Structural and molecular basis for bacterial chromosome organisation, segregation, and maintenance

Adam Suffian Bin Jalal

A thesis submitted to the University of East Anglia for the degree of Doctor of Philosophy

Department of Molecular Microbiology
John Innes Centre
Norwich

March 2021

Abstract

Proper chromosome segregation is essential in all living organisms. In most bacteria, faithful chromosome segregation is mediated by the ParAB*S* system, consisting of the ATPase protein ParA, the CTPase and DNA-binding protein ParB, and a centromere-like *parS* DNA. ParB nucleates on *parS* before binding to adjacent non-specific DNA (spreading) to form a multimeric nucleoprotein complex. ParA in turn powers the movement of the ParB-DNA nucleoprotein complex to each daughter cell. In Firmicutes, another ParB-like protein, Noc, nucleates onto *NBS* sites before spreading to form the membrane-associated nucleoprotein complex that physically occludes the assembly of the divisome. However, the molecular basis of ParB/Noc nucleation and spreading is unclear. Here, I elucidate the molecular basis for the DNA-binding specificity of ParB and Noc. I show that specificity is encoded by four residues at the protein-DNA interface, and a combination of permissive and specificity-switching mutations is required to reprogram their DNA-binding specificity. Next, I demonstrate that cytidine triphosphate (CTP) facilitates ParB escape from the *parS* site, enabling ParB to spread by sliding along the non-specific DNA. Using X-ray crystallography, I elucidate the structural basis for the transition of ParB from the nucleating state to the spreading state. Furthermore, I show that, *C. crescentus* ParB does not condense non-specific DNA *in vitro* in absence of CTP. Engineered *C. crescentus* ParB variants with enhanced DNA condensation activity failed to display any increase in spreading ability *in vivo*. Overall, I propose that ParB functions primarily as a CTP-dependent molecular switch. Finally, I report Noc as the first example of a CTPase enzyme whose membrane-binding activity is directly regulated by CTP. By *in vitro* reconstitution and X-ray crystallography, I show that CTP couples membrane-binding activity of Noc to nucleoprotein complex formation. My findings suggest that CTP switches may be more widespread in biology than previously appreciated.

Abbreviations

Å	Ångström
ASU	asymmetric unit
ATP	adenine triphosphate
BLI	Bio-layer interferometry
bp	base pair
CDP	cytidine diphosphate
COOT	Crystallographic Object-Oriented Toolkit
CTD	C-terminal domain
CTP	cytidine triphosphate
CTPγS	cytosine 5'-(γ-thio)triphosphate
DBD	DNA-binding domain
DMSO	Dimethyl sulphoxide
DNA	deoxyribonucleic acid
dH_20	distilled water
EDTA	ethylenediaminetetraacetic acid
GTP	guanosine triphosphate
h	hour
His	Histidine
IPTG	Isopropyl β-D-thiogalactopyranoside
ITC	Isothermal titration calorimetry
kDa	kilodaltons
kb	kilobase pairs
LB	Lysogeny broth
maoS	MaoP-binding site
matS	MatP-binding site
min	minute
MW	Molecular weight
NBS	Noc-binding site
NTD	N-terminal domain
NTP	nucleoside triphosphate
P	pellet
PAGE	Polyacrylamide gel electrophoresis
parS	ParB-binding site
PCR	Polymerase chain reaction
PDB	Protein Data Bank

PEG	Polyethylene glycol
PLD	ParB-like domain
^{R}	resistance
RMSD	Root mean square deviation
rpm	revolution per minute
S	supernatant
s	seconds
SBS	SlmA-binding site
SDS	Sodium dodecyl sulphate
SPR	Surface plasma resonance
SUV	single unilamellar vesicles
ter	replication terminus
TLS	Translation-Libration-Screw-rotation
OD	optical density
O/N	overnight
ori	origin of replication
UTP	uridine triphosphate
UV	ultraviolet
v/v	volume/volume
w/v	weight/volume
WT	wild type
ΔCTD	C-terminal truncation

Acknowledgements

"It ain't what you got, it's what you do with what you have."
Moodymann.

"We have all the answer to your fears, it's short, it's simple, it's crystal clear"
Nick Cave & The Bad Seeds, O' children

Firstly, I would like to extend my sincerest gratitude to my supervisor, Tung Le, for his guidance and support throughout my PhD. I am very thankful for his feedback on my experiments, presentations, and written reports and manuscripts. Through his guidance, I have truly developed as a much better scientist. I genuinely believe that joining this lab was one of the best decisions I could have made. I would also like to thank my secondary supervisor, Mark Buttner, for his suggestions and encouragement during my project. I am also extremely grateful to my secondary supervisor, Dave Lawson, for introducing me to the world of X-ray crystallography and for his assistance with the crystal structures I report here.

A special thank you goes out to Clare Stevenson for her help and advice with crystallography and biophysical analysis. I also deeply appreciate the wonderful JIC media kitchen staffs for providing such excellent support during my time here. I would also like to thank César López Pastrana and Fernando Moreno-Herrero for conducting the magnetic tweezer experiments presented in this thesis. Additionally, I would like to thank Ling Wu and Jeff Errington for performing the microscopic analysis of *Bacillus subtilis* I present here.

I am grateful to all current and former members of the Le group, especially Ngat Tran, for her valuable technical assistance throughout my PhD, Roan Hulks, a summer student I supervised, and Karunakaran Ramakrishnan for his help. I would also like to thank everyone in the Molecular Microbiology Department at the JIC for creating such a friendly environment to work in. I am very fortunate and proud to have been a part of such a fantastic department. I am also very appreciative for all my friends, both in and outside of Norwich, for their continuous encouragement during the past four years. Additionally, I would like to acknowledge the Royal Society and the John Innes Centre for their part in funding my PhD.

Finally, I am extremely grateful for the unconditional love my family have given me, especially my Mum, Dad, and brothers who have provided me with their unyielding support that has helped me with every step of this journey. My parents used to entertain the idea of me having

my own ‘lab’ in my room when I was much younger, and without that encouragement, I don’t think I could’ve made it this far.

Table of contents

Chapter 1: General Introduction

Parts of this chapter have been published in Open Biology, for which I wrote the first draft of the review:

Jalal, A.S.B., and Le, T.B.K. (2020). Bacterial chromosome segregation by the ParABS system. Open Biol. **10**, 200097.

1.1 Global chromosome organisation

1.2 Bacterial chromosome segregation

1.3 The ParB superfamily: domain organisation and shared features

1.3.1 The ParB superfamily: domain organisation and shared features

1.3.2 The crystal structure of a C-terminal truncated (ΔCTD) *Thermus thermophilus* ParB

1.3.3 The co-crystal structure of *Helicobacter pylori* ParBΔCTD-*parS* complex

1.3.4 The NMR structure of the C-terminal domain (CTD) of *B. subtilis* ParB

1.3.5 The co-crystal structure of *B. subtilis* ParBΔCTD-CDP complex

1.3.6 The structure of the *Myxococcus xanthus* PadC (ParB-like domain)-CTP complex

1.4 Multiple models of ParB-*parS* nucleoprotein complex assembly

1.4.1 Model 1 - One-dimensional filamentation of ParB

1.4.2 Model 2 - Bridging and condensing DNA

1.4.3 Model 3 - Nucleation and caging

1.4.4 Model 4 - Lateral sliding of a ParB-CTP clamp on DNA

1.5 ParB-DNA interaction with ParA and segregation of the origin-proximal chromosomal region

1.6 The ParB-DNA and SMC coordinate chromosome segregation with chromosome organization

1.7 ParB interactions with other protein partners to establish cell polarity

1.8 Bacterial cell division

1.1 Global chromosome organisation

All living organisms require mechanisms for DNA compaction, as DNA length exceeds the size of the cell by several orders of magnitude. In eukaryotes, chromosomal DNA is packaged inside the nucleus into a repeating unit known as the nucleosome, originally described as 'beads on a string' (Olins and Olins, 1972). These structural units are composed of ~147 bp of DNA that wraps around the core histone protein octamer (Luger et al., 1997). Bacteria, however, do not possess such DNA-compacting mechanisms like eukaryotes. Instead, bacterial cells utilise a range of DNA-folding factors, such as nucleoid-associated proteins and DNA supercoiling, to ensure a proper chromosome organisation (Dame et al., 2019). Initially, bacterial chromosomes were thought to encompass unstructured bodies of DNA dispersed randomly within the cell. Since then, a combination of fluorescence microscopic analysis and advances in genome-wide mapping and super-resolution microscopy techniques have shown the bacterial chromosome is much more complex and is assembled into multiple higher order structures that influence a myriad biological processes (Azam et al., 2000; Bakshi et al., 2012; Fisher et al., 2013; Hadizadeh Yazdi et al., 2012; Le et al., 2013; Lewis et al., 2000; Viollier et al., 2004).

Initial fluorescence *in situ* hybridisation studies revealed the *Escherichia coli* nucleoid is organised into higher-ordered structures that are physically separated between one another (macrodomains) (Valens et al., 2004). The *E. coli* chromosome is further divided into four macrodomains, with the origin of replication (*ori*) at one end and the replication terminus (*ter*) at the other (Duigou and Boccard, 2017; Valens et al., 2004, 2016). Two additional domains (Left and Right) flank the Ter macrodomain while two non-structured regions are adjacent to the *ori*. Nucleoid-associated proteins promote the establishment of these boundaries; the Ter domain is the only region that contains *matS* sites that MatP specifically binds (Mercier et al., 2008). Binding of MatP to *matS* results in MatP tetramerization that bridges distal *matS* sites on the chromosome, thus condensing the Ter macrodomain (Dupaigne et al., 2012). Additionally, the *ori* macrodomain is organised by the DNA-binding protein, MaoP, which specifically binds to *maoS* to constrict the mobility of the *ori* macrodomain (Duigou and Boccard, 2017; Valens et al., 2004).

While in *Caulobacter crescentus*, the tracking of fluorescently labelled chromosomal loci and chromosome conformation capture assays in conjunction with deep sequencing (Hi-C, 5C) have recapitulated organization of the chromosome. Whereby, the *ori* localises towards one cell pole while the *ter* accumulates at the opposite cell pole (Figure 1C) (Le et al., 2013; Umbarger et al., 2011; Viollier et al., 2004; Yildirim and Feig, 2018). The left and right chromosomal arms run in parallel down the axis of the cell, generating the *ori-ter* configuration

(Le et al., 2013). Unlike *E.* coli, macrodomains have not been observed in *C. crescentus*, instead Hi-C analysis revealed the *C. crescentus* chromosome is organized into ~23 chromosomal interaction domains, loops of supercoiled genomic DNA that are analogous to topologically associated domains in eukaryotes (Dixon et al., 2012; Eser et al., 2017; Sexton et al., 2012; Sullivan et al., 2009). Curiously, chromosomal interaction domains are not only specific to *C. crescentus* as Hi-C analysis also revealed that the *Bacillus subtilis* chromosome is organized into ~20 chromosomal interaction domains, while the *E. coli* chromosome and *Corynebacterium glutamicum* chromosome is compacted into ~31 chromosomal interaction domains and ~ 11 chromosomal interaction domains respectively (Böhm et al., 2020; Lioy et al., 2018; Marbouty et al., 2015). It is therefore likely that chromosomal interaction domains are a conserved feature in bacterial chromosome organisation. In both chromosomal interaction domains and topologically associated domains, DNA loci displayed preferred interactions with other loci in the same domain (Dixon et al., 2012; Eser et al., 2017; Le and Laub, 2016; Nora et al., 2012; Sexton et al., 2012). The boundaries between such domains are commonly associated with long and highly expressed genes (Le and Laub, 2016), with other systems also promoting formation of chromosomal interaction domains boundaries, contributing towards the formation of higher-order structures in the chromosome respectively (Böhm et al., 2020; Lioy et al., 2018; Marbouty et al., 2015). As global chromosome organisation in bacteria undergo arrangement at different stages of the cell cycle, bacterial cells require a diverse range of regulatory components to ensure chromosomal rearrangement is compatible with a myriad of biological processes.

1.2 Bacterial chromosome segregation

Faithful chromosome segregation is essential to ensure each daughter cell inherits a full copy of the genetic information of the parent. Chromosome segregation is not a trivial process, especially in bacteria, because DNA must be maintained in a compacted state to fit within the limited volume of the cells, and chromosome segregation often occurs concomitantly with DNA replication rather than being separated temporally, as in eukaryotes. Bacterial chromosome segregation can be divided into multiple overlapping steps: (i) segregation of DNA proximal to the origin of replication, (ii) segregation of the bulk of the chromosome, and (iii) segregation of DNA near the terminus of replication. In this chapter, I focus on progress towards understanding the molecular basis for segregating the origin-proximal region, specifically by the tripartite ParA-ParB-*parS* system.

The *par* locus was first discovered in low-copy-number plasmids, and was shown to be essential for their stable inheritance (Abeles et al., 1985; Austin and Abeles, 1983a, 1983b) (Mori et al., 1986). A functionally equivalent *par* locus was later found to be important for

chromosome segregation in *B. subtilis* (Ireton et al., 1994; Lin and Grossman, 1998; Mysliwiec et al., 1991). In *C. crescentus*, *Hyphomonas neptunium* and *Myxococcus xanthus*, genes encoded in the *par* locus (ParABS) were found to be essential for cell viability (Iniesta, 2014; Jung et al., 2019; Mohl et al., 2001), whereas in other bacterial species engineered strains lacking ParABS were viable but had an elevated number of anucleate cells owing to defects in chromosome segregation (Bartosik et al., 2009; Charaka and Misra, 2012; Donczew et al., 2016; Donovan et al., 2010; Du et al., 2016; Jecz et al., 2015; Kadoya et al., 2011; Lagage et al., 2016; Lee and Grossman, 2006; Lewis et al., 2002; Li, 2019; Li et al., 2015; Minnen et al., 2016; Santi and McKinney, 2015; Yamaichi et al., 2007; Yu et al., 2010). A comparative genomic study suggested that the chromosomal ParABS system is conserved in two-thirds of bacterial species (Livny et al., 2007). In most bacteria, one or multiple *parS* sites are commonly found near the origin of replication (Livny et al., 2007). The *parS* site is the first DNA locus to be segregated after chromosome replication (Harms et al., 2013; Lagage et al., 2016; Lin and Grossman, 1998; Toro et al., 2008). ParB is a DNA-binding protein that nucleates on *parS* to recruit additional ParB molecules to adjacent non-specific DNA to form a network of protein-DNA complexes (Funnell, 2016). The ParB-DNA nucleoprotein complex stimulates the ATPase activity of ParA, creating a gradient of ParA-ATP that drives the movement of the origin-proximal region of the chromosome (and subsequently, the whole chromosome) along this gradient to the opposite pole of the cell (Le Gall et al., 2016; Hwang et al., 2013; Leonard et al., 2005; Lim et al., 2014; Mohl et al., 2001; Vecchiarelli et al., 2010, 2013a, 2014). ParB also recruits the Structural Maintenance of Chromosomes (SMC) complex onto the chromosome to reduce DNA entanglement, thereby promoting the individualization of replicated chromosomes (Böhm et al., 2020; Gruber and Errington, 2009; Gruber et al., 2014; Minnen et al., 2016; Sullivan et al., 2009; Tran et al., 2017; Wang et al., 2014, 2015).

Since the discovery of the ParABS system over 35 years ago, tremendous progress has been made towards answering some of the key questions about how this system works:

- What are the structure-function insights into ParB-mediated DNA organisation and segregation? (discussed in chapter 1.3)
- How does ParB recruit tens to hundreds more ParB proteins to assemble a higher-order nucleoprotein complex? (discussed in chapter 1.4)
- What is the molecular mechanism of ParA-mediated DNA segregation? (discussed in section 1.5)
- How does ParB recruits SMC and other protein partners to coordinate chromosome segregation with chromosome organisation? (discussed in chapter 1.5)

In the next subchapters, I summarise recent progress and compare the competing models for addressing these key questions.

1.3 ParB-*parS* interaction and the assembly of a ParB-DNA higher-order nucleoprotein complex

ParB binding to *parS* nucleates the recruitment of additional ParB molecules which associate with neighbouring DNA, a process known as spreading, to form a higher-order ParB-DNA nucleoprotein complex (Funnell, 2016). The purpose of this higher-order complex, whether to strengthen the physical link between DNA and ParA or to provide a specific DNA topology to facilitate DNA segregation, is still under debate. However, since bacterial strains harbouring nucleation-competent but spreading-defective mutants of *parB* are either unviable or have elevated number of anucleate cells, it is clear that a higher-order nucleoprotein complex is a prerequisite for faithful chromosome segregation (Breier and Grossman, 2007; Kusiak et al., 2011; Lin and Grossman, 1998; Song et al., 2017; Tran et al., 2018). In order to deduce the molecular basis underpinning the assembly of the ParB-DNA nucleoprotein complex, a detailed understanding of the domain organisation and structural features shared within the ParB superfamily is required. In the next subchapters, I describe the domain architecture shared by proteins in the ParB superfamily, and discuss the structure-function insights obtained from various crystal structures of chromosomally encoded ParBs.

1.3.1 The ParB superfamily: domain organisation and shared features

Proteins that belong in the ParB superfamily generally display a modest sequence conservation. Nevertheless, chromosomal ParB proteins share a common domain architecture, consisting of an N-terminal domain (NTD), a central DNA-binding domain (DBD), and a C-terminal domain (CTD) (Fig. 1.1A) (Funnell, 2016). A highly conserved arginine-rich motif (GERRxRA) resides in the NTD and mediates protein-protein and protein-ligand interactions (Fig. 1.1A) (Chen et al., 2015; Osorio-Valeriano et al., 2019; Soh et al., 2019). The DBD contains a helix-turn-helix motif that enables ParB to specifically bind to *parS.* The CTD, which is the least conserved domain among ParB homologs, contains a leucine zipper motif that allows ParB to homodimerise (Fig. 1.1A). The CTD of *B. subtilis* ParB also has a lysine-rich amino acid patch that provides additional non-specific DNA-binding and DNA condensation activities (Fisher et al., 2017).

Currently, there exists no full-length structure of a chromosomal ParB. The flexibility of ParB, endowed by amino acid linkers that connect consecutive domains, has hindered the effort to crystallize and solve the structure of a full-length protein. Nevertheless, structure-function insights have been gained from X-ray crystallography/NMR studies using a single domain or

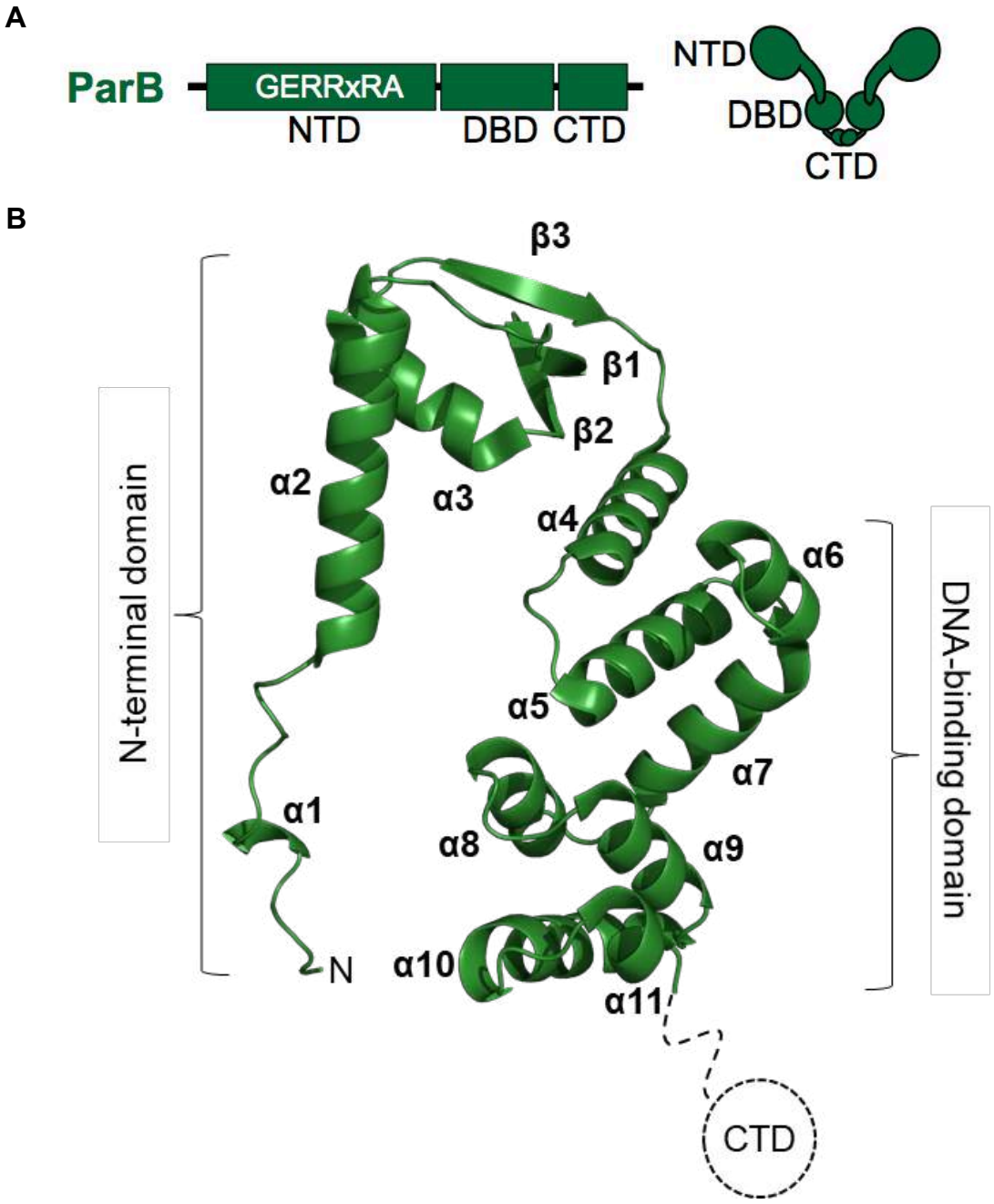

Figure 1.1 The crystal structure of the *T. thermophilus* ParBΔCTD (A) Chromosomal ParB proteins share a common domain architecture, consisting of an N-terminal domain (NTD), a central DNA-binding domain (DBD) and a C-terminal domain (CTD). The NTD harbours a conserved arginine-rich motif (GERRxRA) that mediates ParB–ParB and ParB–cytidine triphosphate (CTP) interactions. **(B)** The crystal structure of a C-terminal truncated (ΔCTD) *T. thermophilus* ParB monomer with key features highlighted.

domain-truncated variants of ParB from various bacterial species (Chen et al., 2015; Fisher et al., 2017; Leonard et al., 2004; Osorio-Valeriano et al., 2019; Soh et al., 2019). Structural comparisons suggested that ParB, especially its NTD, can adopt multiple alternative conformations that might facilitate the assembly of a higher-order nucleoprotein complex that enables faithful chromosome partitioning (Chen et al., 2015; Leonard et al., 2004; Osorio-Valeriano et al., 2019; Soh et al., 2019). In the next subchapters I describe the different structures of chromosomally encoded ParB that are available.

1.3.2 The crystal structure of a C-terminal truncated (ΔCTD) *Thermus thermophilus* ParB

The first structure of a chromosomally encoded ParB was a ΔCTD variant from *T. thermophilus* (Leonard et al., 2004). The crystal structure was solved using selenomethionine SAD phasing to a resolution of 2.3 Å. The construct for the *T. thermophilus* ParBΔCTD variant contained residues 1-222, whereas the full-length *T. thermophilus* ParB contains 269 residues. Although, no electron density was observed for residues 1-22 and 210-222, suggesting these residues were disordered in the crystal.

The asymmetric unit of the crystal contained eight copies of the ParB monomers, which arranged into four dimers in the crystal (Leonard et al., 2004). The overall structure of the *T. thermophilus* ParBΔCTD complex is shown in Figure 1.1B, with the *T. thermophilus* ParBΔCTD variant containing both the NTD and the DBD. The secondary structure of the ParBΔCTD is composed of 3β-pleated sheets and 11 α-helices, with the NTD consisting of three β-pleated-sheets (β1-β3) and three α-helices (α1-α3), while the last eight helices (α4-α11) form the DBD of *T. thermophilus* ParB (Fig. 1.1B). In the N-terminal region of *T. thermophilus* ParBΔCTD, a long linker containing a short α1 and a long α2 connects to β1. The NTD is further composed of β2 and β3 which are separated by α3 (Fig. 1.1B). The DBD is formed of the remaining α-helices observed in the crystal, whereby a long linker containing α4 and α5 connects to the helix-turn-helix forming α6 and α7 that enables DNA binding (Fig. 1.1B). Helices α4-α11 then pack together to form a compact helical bundle, whereby helices α6, α7, α9, α11 are positioned across helices α4, α5, α8 and α10 (Fig. 1.1B). In the *T. thermophilus* ParBΔCTD, the NTD folds into a tight dimer, forming “open” conformation that stabilises the overall structure (Leonard et al., 2004).

As no such obvious protein-protein ParB spreading interactions were observed in the *T. thermophilus* ParBΔCTD crystal structure, Leonard *et. al.,* (2004) proposed that the CTD of ParB (that was absent in the crystal), likely mediated ParB spreading as a one-dimensional

filament on the DNA. Nevertheless, the crystal structure of the *T. thermophilus* ParBΔCTD provided structural evidence that chromosomal ParB contains a helix-turn-helix motif that enables ParB nucleation to *parS*.

1.3.3 The co-crystal structure of *Helicobacter pylori* ParBΔCTD-*parS* complex

More than a decade after the structure of the *T. thermophilus* ParBΔCTD was reported (Leonard et al., 2004), Chen *et. al*. (2015) solved the co-crystal structure of a chromosomal ParB from *H. pylori* in complex with *parS* (Chen et al., 2015). Much like the *T. thermophilus* ParBΔCTD structure, the *H. pylori* ParB variant was also truncated at the CTD, likely to reduce the flexibility of the protein to favour crystallization (Chen et al., 2015; Leonard et al., 2004). The crystal structure was solved using selenomethionine SAD phasing to a resolution of 3.1 Å. The *H. pylori* ParBΔCTD variant contained residues 1-240, while the full-length *H. pylori* ParB contains 290 residues (Chen et al., 2015). Noticeably, certain chains in the crystal structure were more complete than others, with the most complete chain lacking electron density was for residues 1-34 and 228-240, suggesting these residues were disordered in the crystal (Chen et al., 2015). These observations further highlight the flexibility of ParB molecules that enables these proteins to undergo the drastic conformational changes required for their various functions.

The asymmetric unit of the *H. pylori* ParBΔCTD-*parS* complex consisted of four ParBΔCTD monomers and two copies of the *parS* DNA (Chen et al., 2015). In the co-crystal complex, each ParB monomer binds to half a *parS* site and array on the opposite sides of the *parS* site, with the *parS* DNA duplex forms the pseudo-continuous filament that stabilizes the complex (Chen et al., 2015). The overall structure of the *H. pylori* ParBΔCTD-*parS* complex is shown in Figure 1.2A, with the *H. pylori* ParBΔCTD variant containing both the NTD and the DBD. The secondary structure of the ParBΔCTD-*parS* is composed of 10 α helices and 3 β-pleated sheets, with the NTD consisting of three α-helices (α1-α3) and three β-pleated-sheets (β1-β3), while the last seven helices (α4-α10) make up the DBD of the *H. pylori* ParB (Fig 1.2A). In the NTD, a linker region consisting of α1 connects to β1. A short linker then connects β1 to β2, which is then followed by a longer region containing α2 that connects β2 to β3 ParB (Fig 1.2A). The NTD is further composed of α3 which connects to the remaining helices that form the DBD of *H. pylori* ParB (Fig 1.2A). The DBD is then followed by α4 which links to the helix-turn-helix motif forming α5 and α6 that docks into the major groove of the *parS* site (Fig 1.2A). α6 then links the remaining helices which pack to form a compact bundle in the structure, whereby helices α7 and α9 are positioned across helices α8 and α1 (Fig 1.2A).

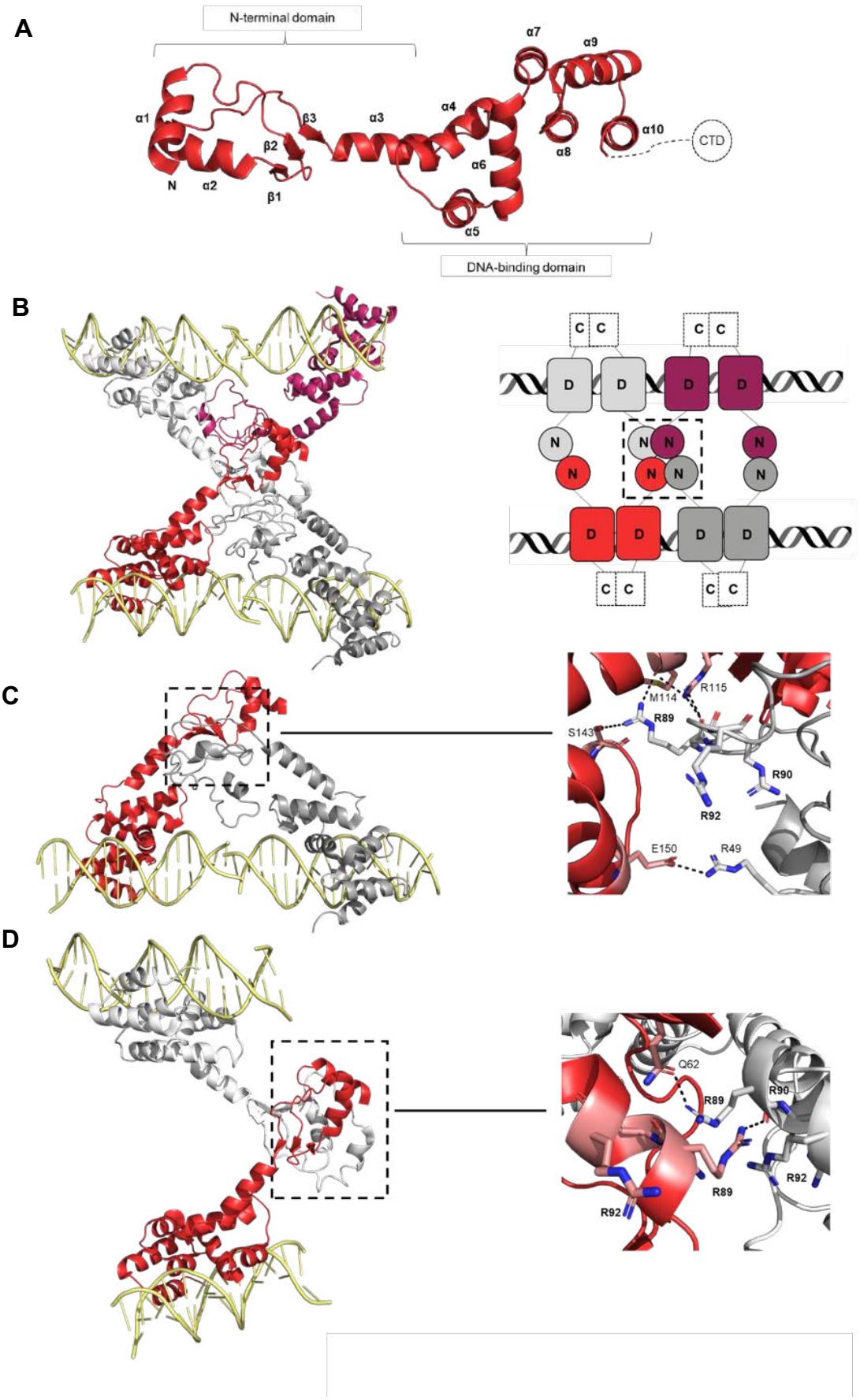
A
N-terminal domain
α1
β3
α3
α4
α7
α9
α10
CTD
β2
α8
α6
N
α2
β1
α5
DNA-binding domain
B
C C
D
N
C
M114
R115
R89
S143
R90
R92
E150
R49
D
Q62
R89
R90
R92

Figure 1.2 The crystal structure of the *H. pylori* ParBΔCTD-*parS* complex (A) The structure of the *H. pylori* ParBΔCTD monomer with key features highlighted. **(B)** The co-crystal structure of *H. pylori* ParB in complex with *parS*, within the crystal, four *H. pylori* ParB molecules form a tetramer, a cartoon representation is shown on the left, where N: N-terminal domain, D: DNA-binding domain and C: C-terminal domain **(C)** ParB-ParB *in cis* (spreading), the arginine patch shown to the right mediates the adjacent interactions **(D)** ParB-ParB *in trans* (bridging) interactions. The arginine patch shown to the right mediates the traverse interactions.

Interestingly, the co-crystal structure of the *H. pylori* ParBΔCTD-*parS* complex demonstrated ParB oligomerisation in the presence of *parS* (Fig. 1.2B-D). Indeed, ParB was shown to interact with an adjacent ParB on a pseudo-continuous DNA in the crystal lattice (*in cis* interactions) (Fig. 1.2C). Additionally, ParB was also shown interact with an adjacent ParB monomer on a disconnected DNA duplex (*in trans* interactions) (Fig. 1.2D). The arginine rich motif (GERRxRA) required for ParB spreading *in vivo* (Breier and Grossman, 2007; Graham et al., 2014; Tran et al., 2018) mediated the NTD-NTD interactions observed in the crystal (Fig. 1.2C-D). From comparing the *H. pylori* ParBΔCTD-*parS* monomer and the *T. thermophilus* apo-ParBΔCTD structure, Chen *et. al.* (2015) proposed that the nucleation of ParB to *parS* induces the conformational change at the NTD that enables the arginine rich motif to participate in these NTD-NTD interactions (Chen et al., 2015; Leonard et al., 2004). While the NTD of *T. thermophilus* apo-ParB adopts an "open" conformation, the NTD *H. pylori* ParBΔCTD-*parS* complex adopts an "extended" conformation that exposes the arginine-rich patch. Furthermore, the DBD of either an apo- or *parS* bound ParB shared a similar subunit arrangement. It is therefore likely that apo-ParB exists in a nucleation-competent conformation that favours *parS* binding.

1.3.4 The NMR structure of the C-terminal domain (CTD) of *B. subtilis* ParB

Although both structures of chromosomally encoded ParB from *T. thermophilus* and *H. pylori* greatly improved our understanding of ParB, both structures were solved in absence of the CTD that mediates ParB dimerisation (Chen et al., 2015; Leonard et al., 2004). Interestingly, in *B. subtilis* the CTD also possess non-specific DNA condensation activity *in vitro* (Fisher et al., 2017; Madariaga-Marcos et al., 2019; Taylor et al., 2015). To better understand the structural determinants of this non-specific DNA condensation activity, Fisher *et. al.,* (2017) solved the structure of the CTD only of *B. subtilis* ParB by solution NMR (Fisher et al., 2017) (Fig. 1.3A). As expected, the reported structure formed a dimer, with each monomer consisting of two α-helices and two β-sheets, and is arranged in an α1-β1-β2-α2 arrangement (Fig. 1.3A). The dimerisation interface is formed by β-sheets and domain swapping between the two α-helices, whereby a leucine rich zipper is formed between α1 and α2 (Fig. 1.3A-B). Interestingly, the NMR structure of the CTD revealed a highly positively charged surface composed of lysine residues that facilitates the non-specific binding/condensation activity of *B. subtilis* ParB (Fig. 1.3C) (Fisher et al., 2017).

1.3.5 The co-crystal structure of *B. subtilis* ParBΔCTD-CDP complex

More recent studies have uncovered a new co-factor of ParB. Various plasmid- and chromosome-encoded ParB and ParB-like proteins have been found to bind and hydrolyse

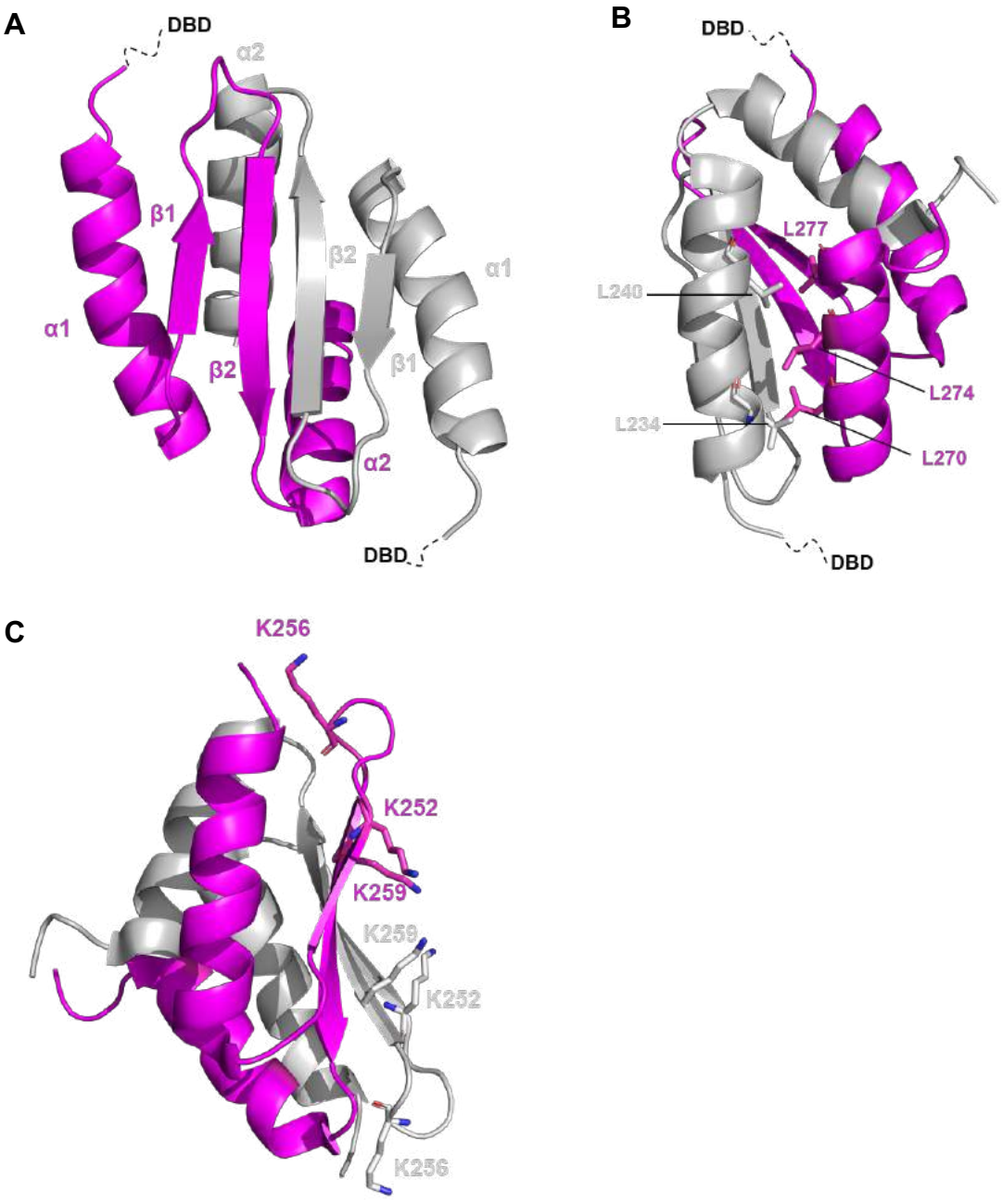

Figure 1.3 The solution NMR structure of the *B. subtilis* ParB C-terminal domain (CTD). **(A)** Two copies of the *B. subtilis* ParB CTD are shown with one copy in purple and the other in grey with key features highlighted. **(B)** The leucine-zipper interaction between the two CTD monomers are shown with the leucine residues being represented as sticks. **(C)** The lysine rich surface that mediates the DNA condensation activity of *B. subtilis* ParB is shown with the lysine residues being represented as sticks.

cytidine triphosphate (CTP) to cytidine diphosphate (CDP) and inorganic phosphate (Osorio-Valeriano et al., 2019; Soh et al., 2019). Indeed, Soh *et. al.,* first reported the co-crystal structure of the *B. subtilis* ParBΔCTD-CDP complex, where a molecule of CDP was observed in the arginine-rich patch at the NTD of a ParB monomer (Soh et al., 2019). As CTP and Ca^{2+} were included in the crystallisation process, it is likely that CTP was hydrolysed to CDP during crystallisation (Soh et al., 2019). The *B. subtilis* ParBΔCTD-CDP co-crystal structure was solved using selenomethionine SAD phasing to a resolution of 1.8 Å (Soh et al., 2019). The *B. subtilis* ParBΔCTD construct contained residues 21-218, while the full-length *B. subtilis* ParB contains 282 residues (Soh et al., 2019).

The asymmetric unit of the crystal contained four copies of the *B. subtilis* ParB monomers (two dimers) and four CDP molecules (Soh et al., 2019), with each ParBΔCTD chain being associated with a CDP molecule and two coordinated Ca^{2+} ions (Soh et al., 2019). The overall structure of the *B. subtilis* ParBΔCTD complex is shown in Figure 1.4A, with the *B. subtilis* ParBΔCTD variant containing both the NTD and the DBD. The secondary structure of the *B. subtilis* ParBΔCTD-CDP is composed of 5 β-pleated sheets and 10 α-helices, with the NTD consisting of five β-pleated-sheets (β1-β5) and two α-helices (α1-α2) while the last eight helices (α3-α10) form the DBD of *B. subtilis* ParB (Soh et al., 2019) (Fig. 1.4A). In the NTD, β1 and β2 are connected by a short linker, which is then followed by a longer α1 containing linker region that connects to β3. Another short linker connects β3 to β4 before a longer linker region containing α2 connects to β5. Both β2 and α2 in the NTD packs into the DBD of *B. subtilis* ParBΔCTD, which is formed of the remaining α-helices observed in the crystal (Fig. 1.4A). The DBD is then followed by a long linker region containing α3 and α4, which then connects to α5 and α6 that forms the classical helix-turn-helix motif that enables DNA binding (Fig. 1.4A). α6 then links the remaining helices which pack to form a compact bundle in the structure, whereby helices α7 and α9 are positioned across helices α8 and α10 (Fig. 1.4A).

Noticeably, two CDP molecules are then sandwiched between the two NTD of the *B. subtilis* ParB, generating a new self-dimerisation interface (Fig. 1.4B) (Soh et al., 2019). Additionally, residues G77 and R80 in the arginine rich motif interacts with the β- phosphate group of CDP (Fig. 1.4B) (Soh et al., 2019). Indeed, previous mutations in this motif prevented ParB spreading *in vivo*, thus implying the loss of ParB spreading is caused by a defective CTP binding/hydrolysis (Breier and Grossman, 2007; Tran et al., 2018). A three way structural comparison between *B. subtilis* ParBΔCTD-CDP complex, the *H. pylori* ParBΔCTD-*parS* and the *T. thermophilus* apo-ParBΔCTD displayed that both the NTD and the DBD of *B. subtilis* ParBΔCTD harboured a different orientation between the NTD and DBD of either the *T.*

thermophilus ParBΔCTD or the *H. pylori* ParBΔCTD-*parS* complex (Chen et al., 2015; Leonard et al., 2004; Soh et al., 2019, Jalal et al., 2019). While the NTD of *T. thermophilus* ParBΔCTD adopts an 'open' conformation and the NTD of *H. pylori* ParBΔCTD-*parS* is in an 'extended' conformation, the NTD of the *B. subtilis* ParBΔCTD-CDP exists in a 'closed' conformation, whereby CDP-interactions results in NTD self-dimerisation (Fig. 1.4B) (Chen et al., 2015; Leonard et al., 2004; Soh et al., 2019). Furthermore, the DBD of the CDP bound *B. subtilis* ParBΔCTD adopts a conformational change at the central DNA-binding domain that is incompatible with *parS* binding (Fig. 1.4A) (Chen et al., 2015; Soh et al., 2019), as it became clear that one DBD from the adjacent *B. subtilis* ParBΔCTD monomer clashes with the *parS* DNA. Thus, from these findings it was proposed that CTP-interactions result in a conformational change that promotes ParB spreading by sliding on the DNA as a lateral clamp (see 1. 4.4 Model 4 - Lateral sliding of a ParB-CTP clamp on DNA).

1.3.6 The structure of the *Myxococcus xanthus* PadC (ParB-like domain)-CTP complex

Almost at the same time as Soh *et. al.* (2019), Osorio-Valeriano (2019) solved the first crystal structure of the ParB-like protein, PadC from *M. xanthus* (Osorio-Valeriano et al., 2019; Soh et al., 2019) The co-crystal complex contained the ParB-like protein PadC in complex with CTP and was solved using selenomethionine SAD phasing to 1.7 Å resolution (Osorio-Valeriano et al., 2019). The ParB-like domain (PLD) of PadC construct lacked the first 281 residues, however no electron density was observed in the first 8 residues at the N-terminus and the remaining 422-489 at the C-terminus, suggesting these region was flexible in the crystal (Osorio-Valeriano et al., 2019).

The asymmetric unit of the crystal contained two copies of the PadC (PLD) monomer and two molecules of CTP. With each PadC (PLD) chain being associated with a CTP molecule and a coordinated Mg^{2+} ion (Osorio-Valeriano et al., 2019). The overall structure of the *M. xanthus* PadC (PLD)-CTP complex is shown in figure 1.4B. The secondary structure of the *M. xanthus* PadC (PLD) consists of four β-sheets (β1-β4) and six α-helices (α1-α6) (Osorio-Valeriano et al., 2019) (Fig. 1.4C). Each chain consists of a globular N-terminal PLD domain contain β-sheets, with β1 and β2 being connected by a long flexible loop containing a short α1 and α2, while β3 and β4 are connected by α3 (Fig 1.4C). The N-terminal PLD is then followed by a linker region which contains α4, followed by a linker region that linkers the remaining two helices α5 and α6 observed in the crystal. Noticeably, the two PadC (PLD) molecules cross over in this linker region causing α5 and α6 to be oriented in a juxtaposed to α4 in the adjacent PadC (PLD) monomer to stabilise the dimer in a closed conformation (Fig 1.4D) (Osorio-

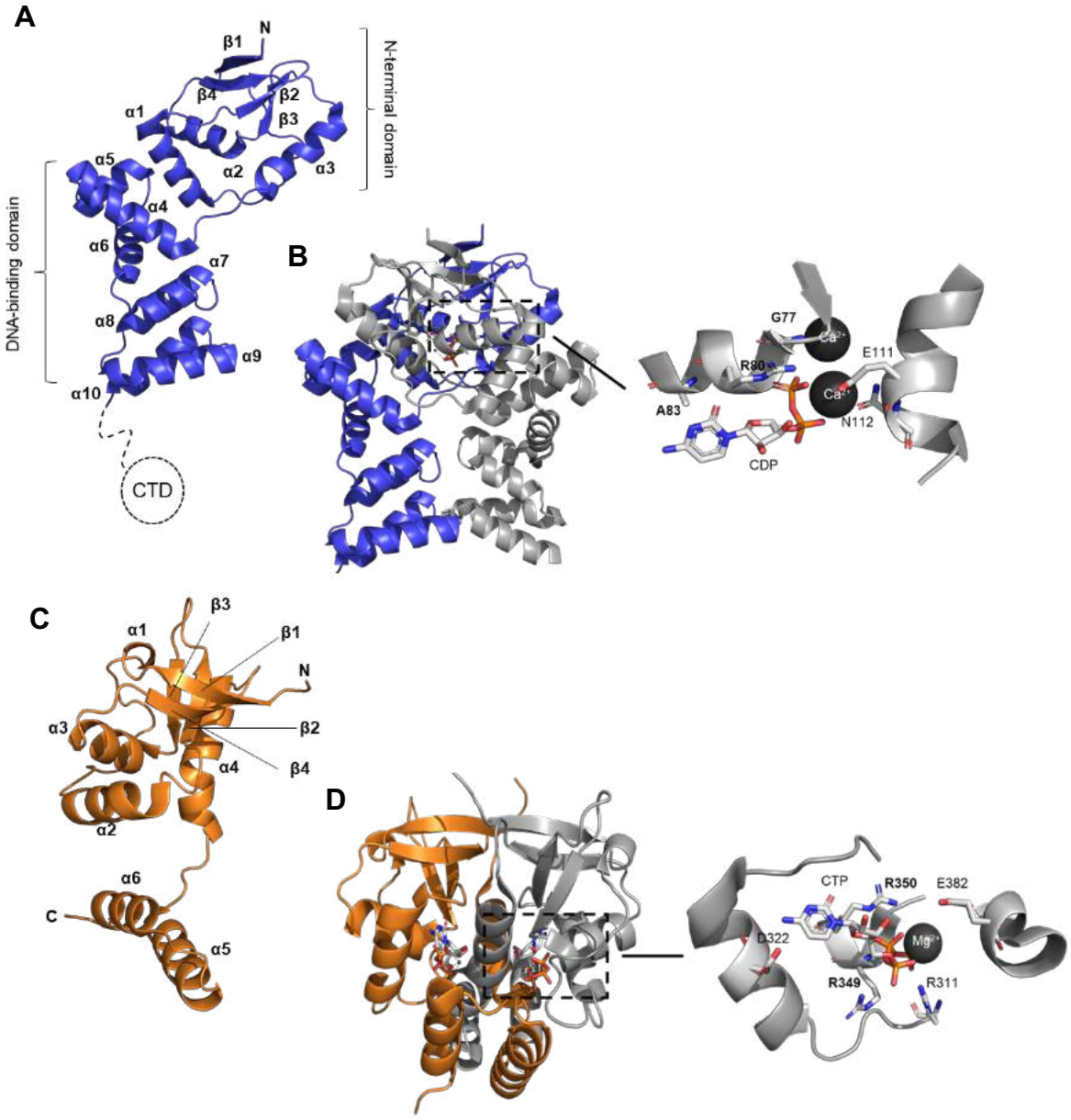

Figure 1.4 The co-crystal structures of the *B. subtilis* ParBΔCTD-CDP and *M. xanthus* PadC (PLD)-CTP complex. **(A)** The structure of the *B. subtilis* ParBΔCTD monomer with key features highlighted. **(B)** The co-crystal structure of *B. subtilis* ParB-CDP complex, the nucleotide binding pocket is shown to the left, GxxRxxA residues are highlighted in bold. One ParB monomer is shown in blue while the other ParB monomer is shown in grey **(C)** The structure of the *M. xanthus* PadC (PLD) monomer with key features highlighted. **(D)** The co-crystal structure of *M. xanthus* PadC-CTP complex, the nucleotide binding pocket is shown to the left. One PadC (PLD) monomer is shown in bronze while the other PadC (PLD) monomer is shown in grey.

Valeriano et al., 2019).

As observed in the *B. subtilis* ParBΔCTD-CDP complex, two CTP molecules are sandwiched between the two PLD of *M. xanthus* PadC, generating a new self-dimerisation interface (Fig. 1.4B, 1.4D) (Osorio-Valeriano et al., 2019; Soh et al., 2019). PadC harbours a similar arginine rich patch (GxxRxxA) motif to ParB, and is shown to form the CTP binding pocket in the *M. xanthus* PadC(PLD)-CTP co-crystal structure (Fig 1.4B). Indeed, a structural comparison between the PadC (PLD) structure with *T. thermophilus* ParBΔCTD and *H. pylori* ParBΔCTD and *B. subtilis* ParBΔCTD structure demonstrated that the NTD of *M. xanthus* PadC shares a high structural similarity with the arginine rich motif containing NTD of the solved ParBΔCTD proteins (Chen et al., 2015; Leonard et al., 2004; Osorio-Valeriano et al., 2019; Soh et al., 2019). Thus, these findings demonstrate that CTP-binding promotes a new protein-protein interface that enables the self-dimerisation of PadC, and that CTP-interactions are likely conserved feature of the ParB-family of proteins.

The existence of these various crystal structures of ParB have shed light into the various models of the higher order ParB-DNA nucleoprotein complex assembly. In the next subchapters, I assess the evidence for and against each model, before highlighting outstanding questions and challenges for fully understanding the ParABS system and chromosome segregation in bacteria.

1.4 Multiple models of ParB-DNA nucleoprotein complex assembly

1.4.1 Model 1 - One-dimensional filamentation of ParB

The earliest evidence of a higher-order ParB-DNA nucleoprotein complex came from studies of a plasmid-borne ParB. Overexpression of an F-plasmid ParB protein ($ParB_F$ or SopB) was observed to repress the expression of antibiotic resistance genes several kilobases away from the *parS* (*sopC*) site on the plasmid (Lynch and Wang, 1995). Moreover, $ParB_F$ overexpression also prevents DNA gyrase and restriction enzyme access to DNA regions neighbouring the *parS* site (Lynch and Wang, 1995). Similarly, a P1-plasmid ParB ($ParB_{P1}$) also silences expression of genes adjacent to *parS* in both directions for several kilobases, with the efficiency of gene silencing decreasing as the genomic distance from *parS* increases. A direct association of $ParB_{P1}$ with the silenced DNA was demonstrated by chromatin immunoprecipitation PCR (ChIP-PCR) assay (Rodionov et al., 1999). Based on these observations, it was proposed the growth of a filament of ParB proteins nucleated at *parS* and then spread outward to neighbouring DNA (Fig. 1.5A) (Rodionov et al., 1999). This model was further supported by the observation that a site-specific DNA-binding protein, RepA, could

attenuate the $ParB_{P1}$-mediated gene silencing effect, presumably by acting as a roadblock to partially stop the filamentation of ParB (Fig. 1.5A) (Rodionov et al., 1999). Multiple chromosomal ParBs have subsequently been observed by ChIP-chip/seq to associate with an extended DNA region beyond *parS* (Böhm et al., 2020; Breier and Grossman, 2007; Donczew et al., 2016; Graham et al., 2014; Lagage et al., 2016; Minnen et al., 2016; Murray et al., 2006; Tran et al., 2018), hence chromosomal ParBs were also thought to oligomerize to form a nucleoprotein filament. The highly conserved arginine-rich patch (GERRxRA) at the NTD has been implicated in mediating ParB filamentation, as mutations in this region impair the ability of ParB to associate extensively with DNA beyond *parS* (Breier and Grossman, 2007; Graham et al., 2014; Kawalek et al., 2018; Tran et al., 2018). This early model of ParB spreading is straightforward and attractive, however later studies have argued that the intracellular concentration of ParB is too low to support such an extensive 1D filamentation *in vivo*. Moreover, at native expression levels, *B. subtilis* ParB (Spo0J) does not silence genes adjacent to *parS*, suggesting that the ParB-DNA nucleoprotein complex might be more dynamic than can be explained by the 1D filamentation model (Breier and Grossman, 2007).

1.4.2 Model 2 - Bridging and condensing DNA

A combination of quantitative immunoblotting and immunofluorescence microscopy approaches led to the estimate that ~20 ParB dimers are associated with each *parS* site in *B. subtilis*, allowing for maximally ~500 bp of DNA to be covered by a continuous filament of ParB (Graham et al., 2014). This is substantially lower than the ~10-20 kb of ParB-bound DNA observed by ChIP-chip, arguing against the 1D filamentation model (Breier and Grossman, 2007; Murray et al., 2006). Instead, a new model was proposed based on the observation that *B. subtilis* ParB can bridge different segments of DNA (Fig. 1.5A). In a single-molecule microscopy-based assay, bacteriophage λ DNA (~50 kb) was tethered at one end to a microscope slide and stretched out by a buffer flow (Graham et al., 2014). The introduction of purified *B. subtilis* ParB compacted the flow-extended DNA, demonstrating that ParB can form bridges and condense bound DNA (Graham et al., 2014). Moreover, mutations in the arginine-rich patch which eliminate the extensive *in vivo* ChIP-seq profile of *B. subtilis* ParB also impair *in vitro* DNA-bridging activity (Graham et al., 2014).

ParB-mediated DNA bridging was also observed using magnetic-tweezers assays (Fisher et al., 2017; Madariaga-Marcos et al., 2019; Taylor et al., 2015). The additional non-specific DNA-binding activity owing to a surface-exposed lysine-rich patch at the CTD of *B. subtilis* ParB was found to be essential for this function (Fisher et al., 2017). Mutations in these lysine residues eliminate DNA bridging and condensation *in vitro* and reduce ParB-DNA nucleoprotein formation *in vivo*, as assessed by the less extensive ChIP-qPCR profile and by

the dimmer and fuzzier appearance of fluorescently labelled ParB foci (Fisher et al., 2017). It is important to emphasize that interactions among NTD of *B. subtilis* ParB are also necessary for bridging DNA (Fig. 1.5B); neither CTD alone nor ParB with mutations at the arginine-rich patch (at the NTD) can condense DNA *in vitro* (Fisher et al., 2017; Madariaga-Marcos et al., 2019). The non-specific DNA-binding activity of the CTD is thought to provide multiple anchors on DNA that can be brought spatially close together by the NTD-NTD interactions (Fig. 1.5B). Insights into the molecular mechanism of NTD-NTD interactions were provided by the co-crystal structure of a CTD-truncated *H. pylori* ParB in complex with a *parS* DNA duplex (Chen et al., 2015). This structure shows *H. pylori* ParB interacting with an adjacent ParB on a pseudo-continuous DNA in the crystal lattice (in *cis* interactions or 1D filamentation) and also with ParB on a disconnected DNA duplex (in *trans* interactions or 3D bridging) (Fig 1.2B-D), with the arginine-rich patch at the core of the NTD-NTD interaction interface (Chen et al., 2015). By comparison with the *T. thermophilus* apo-ParB structure, it was proposed that the nucleation of ParB onto *parS* induces a conformational change at the NTD that exposes the arginine-rich patch for the NTD-NTD interactions (Chen et al., 2015; Leonard et al., 2004).

In sum, it has been proposed that DNA-bridging activity allows a limited number of ParB molecules to bring regions of DNA that are several kilobases apart together in 3D space to form a compacted nucleoprotein complex (Fig. 1.5B). Nevertheless, a computational modelling study has suggested that a combination of both 1D filamentation and 3D bridges are required to recreate the condensed ParB-DNA nucleoprotein complex observed *in vivo* (Broedersz et al., 2014). Thus, while the DNA-bridging model is an important step towards understanding the assembly of the ParB-DNA nucleoprotein complex, it is unlikely to be the final say. The main caveat is that *B. subtilis* ParB can bridge to condense DNA *in vitro* regardless of the presence of *parS* (Fisher et al., 2017; Graham et al., 2014; Taylor et al., 2015). This contradicts *in vivo* data showing *parS* is absolutely required for the clustering of fluorescently labelled ParB molecules into a tight focus (Erdmann et al., 1999; Graham et al., 2014). Moreover, the lysine-rich patch (at the CTD of *B. subtilis* ParB) is not highly conserved; for example, ParB from *C. crescentus* lacks the equivalent lysine residues and does not bridge/condense DNA *in vitro*. As such, it is not yet clear how prevalent DNA-bridging activity is among chromosomal ParB homologues.

1.4.3 Model 3 - Caging ParB and DNA

A model broadly similar to bridging and condensing DNA that aims to better explain the observed *parS*-dependent confinement of ParB *in vivo* has been proposed (Sanchez et al., 2015). In this nucleation and caging model, the *parS* site acts as a ParB nucleation centre, while weak but synergistic protein-protein and protein-DNA interactions cage ParB spatially

into a confined volume inside the cells (Fig. 1.5C) (Sanchez et al., 2015). Supporting this model, single-molecule super resolution microscopy demonstrated that the binding of $ParB_F$ to *parS* results in a very high local concentration of protein *in vivo,* where greater than 90% of $ParB_F$ in the cell are confined in clusters at *parS* (Sanchez et al., 2015). Similarly, the local concentration of *C. crescentus* ParB near *parS* has been estimated to reach ~500 μM (500 times more concentrated than typically used for *in vitro* experiments) (Lim et al., 2014). Despite $ParB_F$ (or *C. crescentus* ParB) having expectedly low-affinity interactions with non-specific DNA, these interactions may occur stochastically at very high frequency, especially at the extreme local concentration of ParB *in vivo*, to create a cage of dynamically exchanged ParB-DNA complexes (Fig. 1.5C). Fluorescence recovery after photo-bleaching (FRAP) experiments have shown that $ParB_F$ molecules rapidly exchange between different clusters, further highlighting the dynamic nature of cages of ParB-DNA *in vivo* (Debaugny et al., 2018). The nucleation and caging model has also been shown applicable to the *Vibrio cholerae* chromosomal ParB-*parS* system, suggesting that this dynamic self-assembly mechanism might be conserved from plasmids to chromosomes (Debaugny et al., 2018).

1.4.4 Model 4 - Lateral sliding of a ParB-CTP clamp on DNA

Recent studies have uncovered a new co-factor of ParB (Jalal et al., 2020; Osorio-Valeriano et al., 2019; Soh et al., 2019). Various plasmid- and chromosome-encoded ParB and ParB-like proteins have been found to bind and hydrolyse cytidine triphosphate (CTP) to cytidine diphosphate (CDP) and inorganic phosphate (Jalal et al., 2020; Osorio-Valeriano et al., 2019; Soh et al., 2019) A co-crystal structure showed CDP binding to the arginine-rich patch at the NTD of *B. subtilis* ParB (CTP was hydrolysed to CDP during crystallization). At the same time, a co-crystal structure showed a *M. xanthus* ParB-like protein (PadC) in complex with CTP. CTP (or CDP) is sandwiched between two NTDs, thus promoting a new NTD self-dimerisation interface that has not been observed previously (Osorio-Valeriano et al., 2019). Employing site-specific cross-linking assays and single-molecule imaging, it was demonstrated that CTP-induced self-dimerisation creates a clamp-like ParB that entraps DNA within its central cavity (Fig. 1.5D). A comparison between the *B. subtilis* ParB-CDP structure and the *H. pylori* ParB-*parS* structure suggested that CTP binding induces a conformational change at the central DNA-binding domain that is incompatible with *parS* binding (Chen et al., 2015; Soh et al., 2019). Studies with *C. crescentus* and *M. xanthus* ParBs further showed that CTP binding reduces ParB nucleation at *parS* and/or liberates pre-bound ParB from *parS*, thereby facilitating the escape of ParB from a high-affinity nucleation site to a low-affinity neighbouring DNA (Jalal et al., 2020; Osorio-Valeriano et al., 2019). Therefore, CTP most likely serves to switch ParB from a nucleating to a sliding mode (Fig. 1.5D). Overall, it was suggested that ParB clamp can self-load at *parS*, without the need of a dedicated loading factor, and spreads

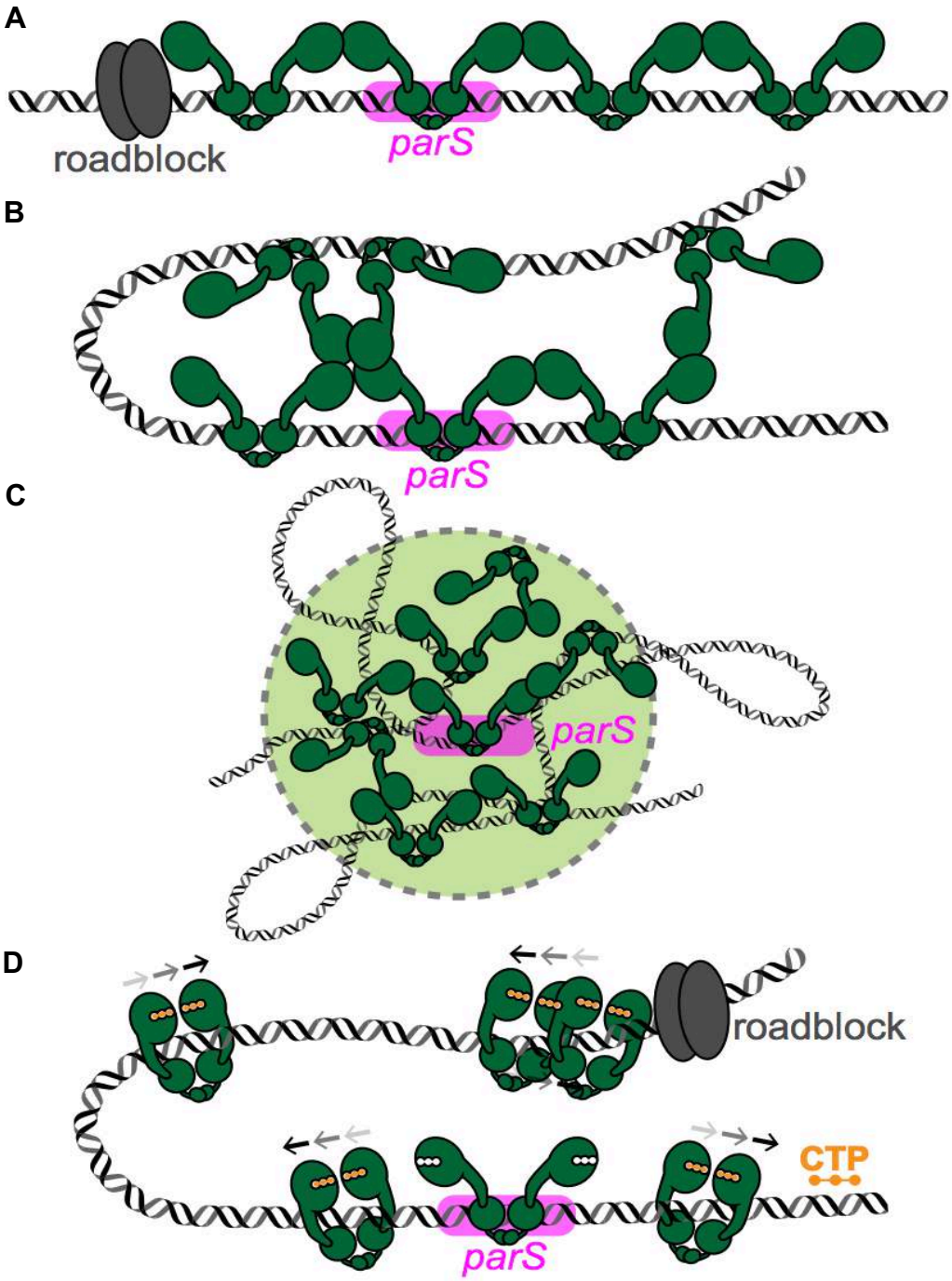

Figure 1.5 The assembly of a higher-order ParB–DNA nucleoprotein complex. **(A)** Model 1: ParB spreading by a one-dimensional filamentation. **(B)** Model 2: ParB spreading by bridging and condensing DNA. **(C)** Model 3: ParB spreading by caging DNA. **(D)** Model 4: ParB spreading by sliding on DNA. ParB switches from an open to a closed clamp upon binding to CTP (orange). ParB and *parS* are coloured green and magenta, respectively. The arrows above the ParB–CTP complexes indicate their progressive sliding on DNA. A tight DNA-binding protein (grey) can unidirectionally block the one-dimensional filamentation or the sliding of ParB on DNA.

by sliding to the neighbouring DNA while still entrapping DNA (Fig. 1.5D) (Jalal et al., 2020). The interpretation of a sliding ParB-CTP clamp on DNA is further backed up by several lines of evidence: (i) tight DNA-binding proteins, such as a catalytic-dead EcoRI (E111Q) variant or TetR, can block the spreading of *B. subtilis* and *C. crescentus* ParB-CTP on DNA *in vitro* (Fig. 1.5D), and (ii) *C. crescentus* ParB only accumulates on DNA that has both ends blocked (by a bulky biotin-streptavidin complex) to prevent a run-off (Jalal et al., 2020). However, it is not yet clear whether the translocation of ParB-CTP on DNA is entirely a passive 1D diffusion process or whether it is facilitated by unknown interactions between the protein and DNA. CTP hydrolysis is unlikely to provide energy for ParB translocation since its hydrolysis rate is extremely low, ranging from ~3 to ~36 CTP molecules per hour. Moreover, ParB in complex with a slow-hydrolyzable CTPγS analogue can still self-load and accumulate on DNA, albeit with a reduced stability. It has been speculated that CTP hydrolysis might contribute to recycling of ParB between the nucleation and translocation modes (Soh et al., 2019). Mutant proteins (N112S and N172A of *B. subtilis* and *M. xanthus* ParB, respectively), which bind CTP but are deficient for hydrolysis, fail to form tight foci inside the cells; however this is weak evidence for the *in vivo* role of CTP hydrolysis since *B. subtilis* ParB (N112S) is already impaired at forming a protein clamp (Osorio-Valeriano et al., 2019; Soh et al., 2019). A better understanding of the CTPase mechanism that enables the design of a mutation at the catalytic site to eliminate CTP hydrolysis while allowing NTD self-dimerisation is likely to provide a key insight into the role of CTP hydrolysis.

Whether CTP plays a regulatory role in chromosome segregation, in addition to being a co-factor of ParB, is also unknown. The concentration of nucleoside triphosphate (NTP) ranges from ~0.3 to ~3 mM inside bacterial cells (Buckstein et al., 2008). Their concentrations can decrease by ~tenfold as cells enter the stationary phase but it is unlikely to impact ParB-CTP binding significantly (Buckstein et al., 2008). Indeed, foci of a fluorescently tagged ParB do not disappear when *C. crescentus* cells enter the stationary phase or during starvation (Britos et al., 2011). For these reasons, I speculate that the assembly of ParB-DNA nucleoprotein complex is not regulated by varying the intracellular concentration of CTP. However, there is a formal possibility that other NTP-related small molecules, whose diversity has only been realized recently, could have a regulatory impact (Whiteley et al., 2019). Future work will undoubtedly continue to provide important new insights into the assembly of the ParB-DNA nucleoprotein complex and its roles in chromosome segregation.

1.5 ParB-DNA interaction with ParA and segregation of the origin-proximal chromosomal region

ParA is a deviant Walker A ATPase protein that enables a directional movement of ParB-bound DNA (Koonin, 1993). Early studies of plasmid and chromosome segregation proposed a mechanism for DNA-pulling by either a linear or a helical ParA filament (Adachi et al., 2006; Ebersbach and Gerdes, 2004; Ebersbach et al., 2006; Fogel and Waldor, 2006; Hatano et al., 2007; Pratto et al., 2008; Ptacin et al., 2010; Ringgaard et al., 2009), akin to the mitotic spindle apparatus in eukaryotes. According to this model, ParA-ATP polymerizes into a filamentous structure along the cell length, with the edge of the filament capturing the ParB-DNA nucleoprotein complex. ParB binds ParA and stimulates its ATPase activity to hydrolyse ATP, thereby depolymerizing the ParA filament and concomitantly pulling the ParB-DNA complex (hence, the plasmid/chromosome) along the retracting filament to the opposite cell pole (Gerdes et al., 2010; Ptacin et al., 2014; Ringgaard et al., 2009). While purified ParA from various bacterial species could self-aggregate into filament-like structures in the presence of ATP/ADP (Barillà et al., 2005; Bouet et al., 2007; Dunham et al., 2009; Ebersbach et al., 2006; Havey et al., 2012; Hui et al., 2010; Leonard et al., 2005; Lim et al., 2014; Machón et al., 2007; Pratto et al., 2008; Ptacin et al., 2010), no such continuous polymer was seen in recent co-crystal structures of ParA with DNA, even at the high concentration of protein and DNA used to generate crystals. Furthermore, the spatial distribution of an F-plasmid ParA and *C. crescentus* ParA *in vivo* is inconsistent with a continuous filamentous structure, instead they form small patches or a cloud-like gradient of sparsely distributed molecules inside the cells, as observed by super-resolution microscopy (Le Gall et al., 2016; Lim et al., 2014). As such, it is uncertain whether a DNA-pulling mechanism by a ParA filament is operating *in vivo*.

It has been proposed that a ParA filament is not necessary for DNA segregation, and that a diffusion-ratchet mechanism can also explain the directional movement of segregating DNA (Hu et al., 2017; Hwang et al., 2013; Vecchiarelli et al., 2010, 2012, 2013a, 2014)(Fig. 1.6A-B). In this model, ParA binds ATP to homodimerize and to associate with non-specific DNA. X-ray crystallographic and hydrogen/deuterium exchange mass spectrometry analysis of ParA with nucleotides and DNA have revealed the dimerisation interface and a multifaced DNA-binding surface (Chu et al., 2019; Corrales-Guerrero et al., 2020; Zhang and Schumacher, 2017). ParB, via its N-terminal peptide, binds ParA directly and stimulates the ATPase activity of ParA, thereby dissociating ParA dimer into individual monomers that no longer bind DNA (Barillà et al., 2007; Leonard et al., 2005; Vecchiarelli et al., 2013b; Volante and Alonso, 2015) (Fig. 1.6A). This stimulation in the ATPase activity creates a local gradient of ParA-ATP with the least DNA-bound ParA-ATP near the ParB-DNA complex (Fig. 1.6A). The ParB-DNA complex then diffuses up the gradient, by Brownian motion, to rebind ParA-ATP, resulting in a net movement of the ParB-anchored DNA (Fig. 1.6A). The initial movement of the ParB-DNA complex in one chosen direction enforces the continued movement in the same direction,

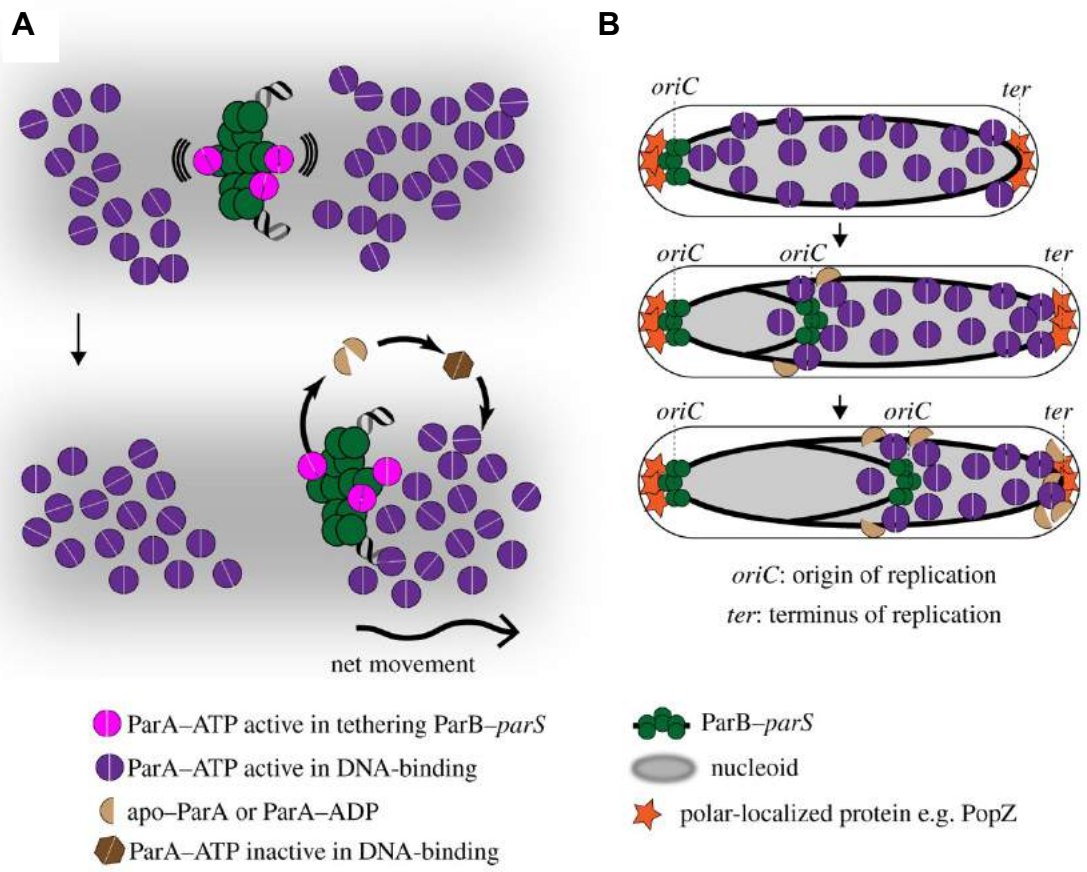
A
net movement
ParA–ATP active in tethering ParB–parS
ParA–ATP active in DNA-binding
apo–ParA or ParA–ADP
ParA–ATP inactive in DNA-binding
B
oriC
ter
oriC
oriC
ter
oriC
oriC
ter
oriC: origin of replication
ter: terminus of replication
ParB–parS
nucleoid
polar-localized protein e.g. PopZ
C
diffusion-binding
DNA-relay
HDR 1
HDR 2
HDR 3
HDR 4
hitch-hiking via high-density
DNA regions (HDR)

Figure 1.6 ParA drives the movement of ParB-bound DNA to segregate plasmids and chromosomes. (A) A diffusion-ratchet model for ParA-mediated transport of ParB-bound DNA. A ParB-DNA complex (green) interacts with ParA-ATP (violet) to tether to the nucleoid (grey), and to stimulate the ATPase activity of ParA. ParA-ATP dimers (violet) bind the nucleoid non-specifically. After ATP hydrolysis, monomers of apo-ParA/ParA-ADP (light brown) no longer bind DNA, thus creating a zone of depletion of ParA-ATP surrounding the ParB-DNA complex. By thermal fluctuation (wavy lines), the ParB–DNA complex moves to the edge of the zone of depletion to rebind ParA-ATP. The initial movement of the ParB-DNA complex in one chosen direction enforces the continued movement in the same direction, resulting in a long-range directional movement of the DNA (see *b*). The released apo-ParA/ParA-ADP (light brown) rebinds ATP but cannot immediately bind DNA (the dark brown hexagon) until a transition occurs in the ParA-ATP structure. **(B)** The segregation of the origin-proximal region of the chromosome by the ParABS system. For example, in *C. crescentus*, one ParB-DNA complex remains at the pole after chromosome replication, while the other moves along the gradient of ParA-ATP, via the diffusion-ratchet mechanism, to the opposite cell pole. The polarly localised proteins (e.g. PopZ, orange) contribute to maintaining the ParA-ATP gradient by sequestering apo-ParA/ParA-ADP away from the nucleoid and to regenerate them at the pole. **(C)** Other variations of the diffusion-ratchet model have been proposed to include an element of DNA elasticity (i.e. the DNA-relay model) or high-density DNA regions (HDR) (i.e. the hitch-hiking model). A wavy arrow indicates the directional movement of the partition complex.

resulting in a long-range directional movement of the DNA (Fig. 1.6A-B). The released monomeric apo-ParA/ParA-ADP can rebind ATP to homodimerise and later regains its non-specific DNA-binding activity (Fig. 1.6A). It is worth noting that the released apo-ParA/ParA-ADP can rebind ATP but cannot immediately bind DNA until a transition occurs in the ParA-ATP structure (Fig. 1.6A); this transitional state presumably introduces a time delay mechanism to ensure the existence of a ParA-ATP gradient surrounding the ParB-DNA complex (Vecchiarelli et al., 2010; Zhang and Schumacher, 2017). Without this delay, regenerated ParA-ATP will instantly rebind DNA in the same location, thus dissipating the gradient. Other organism specific factors, for example, the polarly localised proteins PopZ and TipN in *C. crescentus*, may also contribute to maintain the ParA-ATP gradient by sequestering apo-ParA/ ParA-ADP away from the nucleoid and to regenerate ParA-ATP only at the cell pole (Ptacin et al., 2014; Schofield et al., 2010) (Fig. 1.6B). Based on computational modelling it has been argued that the shortrange diffusion of a ParB-DNA complex up the gradient of ParA-ATP might not be sufficient to explain a robust unidirectional segregation of chromosome towards the new cell pole (Fig. 1.6B) and that the diffusion-ratchet model should be extended to incorporate a component of DNA elasticity. In this model, DNA-bound ParA-ATP complexes can harness the elastic dynamics of the chromosome to relay the partition complex over a long distance from one DNA location to another (Lim et al., 2014) (Fig. 1.6C). Similarly, it has also been proposed that partition complexes can also hitchhike from one high-density DNA region to another on the chromosome to move the ParB-bound DNA progressively (Fig. 1.6C) (Le Gall et al., 2016). High-density DNA regions have been observed in *B. subtilis* and *E. coli* by super-resolution microscopy and may represent highly compacted domains of the chromosomes (Le Gall et al., 2016; Marbouty et al., 2015). The preferred association of ParA-ATP with high-density DNA regions, via its non-specific DNA-binding activity, might create the required directional bias in the movement of the ParABS complex (Fig. 1.6C).

The diffusion-ratchet model emphasizes the crucial role of ParB in stimulating the ATPase activity of ParA to create the ParA–ATP gradient. However, an alternative view on the ATPase-stimulating role of ParB, at least for the F-plasmid ParAB system (SopAB) suggested that the stimulation of ParAF ATPase activity mainly serves to spatially separate F-plasmid clusters following replication and to prevent them from re-forming later (Ah-Seng et al., 2013). The directional movement of replicated F plasmids might depend on a basal ATPase activity of ParAF but does not need further stimulation by ParBF (Ah-Seng et al., 2013).

1.6 The ParB-DNA and SMC coordinate chromosome segregation with chromosome organisation

In addition to its role in DNA segregation, ParB also participates in other biological processes such as chromosome organisation, nucleoid occlusion, regulation of DNA replication initiation and regulation of gene expression (Attaiech et al., 2015; Dubarry et al., 2019; Gruber and Errington, 2009; Kadoya et al., 2011; Maurya et al., 2016; Mercy et al., 2019; Minnen et al., 2011; Murray and Errington, 2008; Nourikyan et al., 2015; Pióro et al., 2019; Schofield et al., 2010; Sullivan et al., 2009; Szafran et al., 2013; Thanbichler and Shapiro, 2006; Toro-Nahuelpan et al., 2019; Yamaichi et al., 2012). The wide range of ParB-interacting partners reflects (i) the central role of the ParB-DNA nucleoprotein as a hub to couple chromosome segregation with other biological processes and (ii) the capacity of ParB to evolve additional functions. For a further discussion, I refer the reader to recent reviews (Kawalek et al., 2020; Pióro and Jakimowicz, 2020). In this section, I instead focus on the interaction between ParB and the SMC complex that is directly relevant to the segregation of the origin-proximal region of the chromosome. A canonical bacterial SMC is composed of an ATPase domain (the head), a dimerisation domain (the hinge) and an extended antiparallel coiled-coil region in the middle (Nolivos and Sherratt, 2014) (Fig. 1.7A). Two SMC monomers homodimerize together with the accessory proteins (ScpA and ScpB) to form a ring like protein complex that can bring distal DNA segments close together spatially to organize the chromosome (Mascarenhas et al., 2002; Nolivos et al., 2016; Soppa et al., 2002) (Fig. 1.7A). This entrapment of DNA has been shown for *B. subtilis* SMC (Wilhelm et al., 2015) and for *eukaryotic* SMC homologues such as cohesin and condensin (Cuylen et al., 2011; Haering et al., 2008; Murayama and Uhlmann, 2014). Application of chromosome conformation capture assays (Hi-C/ 3C-seq) to cells from a range of bacterial species lacking SMC have revealed a reduced interaction between opposite arms of the chromosome, suggesting that SMC entraps and tethers the two chromosome arms together (Böhm et al., 2020; Le et al., 2013; Marbouty et al., 2015; Val et al., 2016; Wang et al., 2017) (Fig. 1.7B). SMC is recruited onto the chromosome by ParB at the origin-proximal parS sites (Minnen et al., 2011)(Böhm et al., 2020; Gruber and Errington, 2009; Sullivan et al., 2009; Tran et al., 2017) (Fig. 1.7C).

After loading, SMC redistributes directionally away from *parS* towards the replication terminus (ter) while maintaining the tethers between the *parS*-proximal regions of the chromosome arms (Tran et al., 2017; Wang et al., 2017) (Fig. 1.7C). Given that *parS* sites are often found near the origin of replication, *parS*-loaded SMCs preferably condense newly replicated DNA to package them into individual entities and away from each other (Fig. 1.7B). This DNA-unlinking activity is independent of topoisomerase IV, at least in *B. subtilis*, and might help to prevent catenation between replicated chromosomes at the replication fork or promote their resolution behind the fork (Gruber et al., 2014; Wang et al., 2014). If replicated chromosomes are not resolved, their entanglement might hinder movement of individual chromosomes to

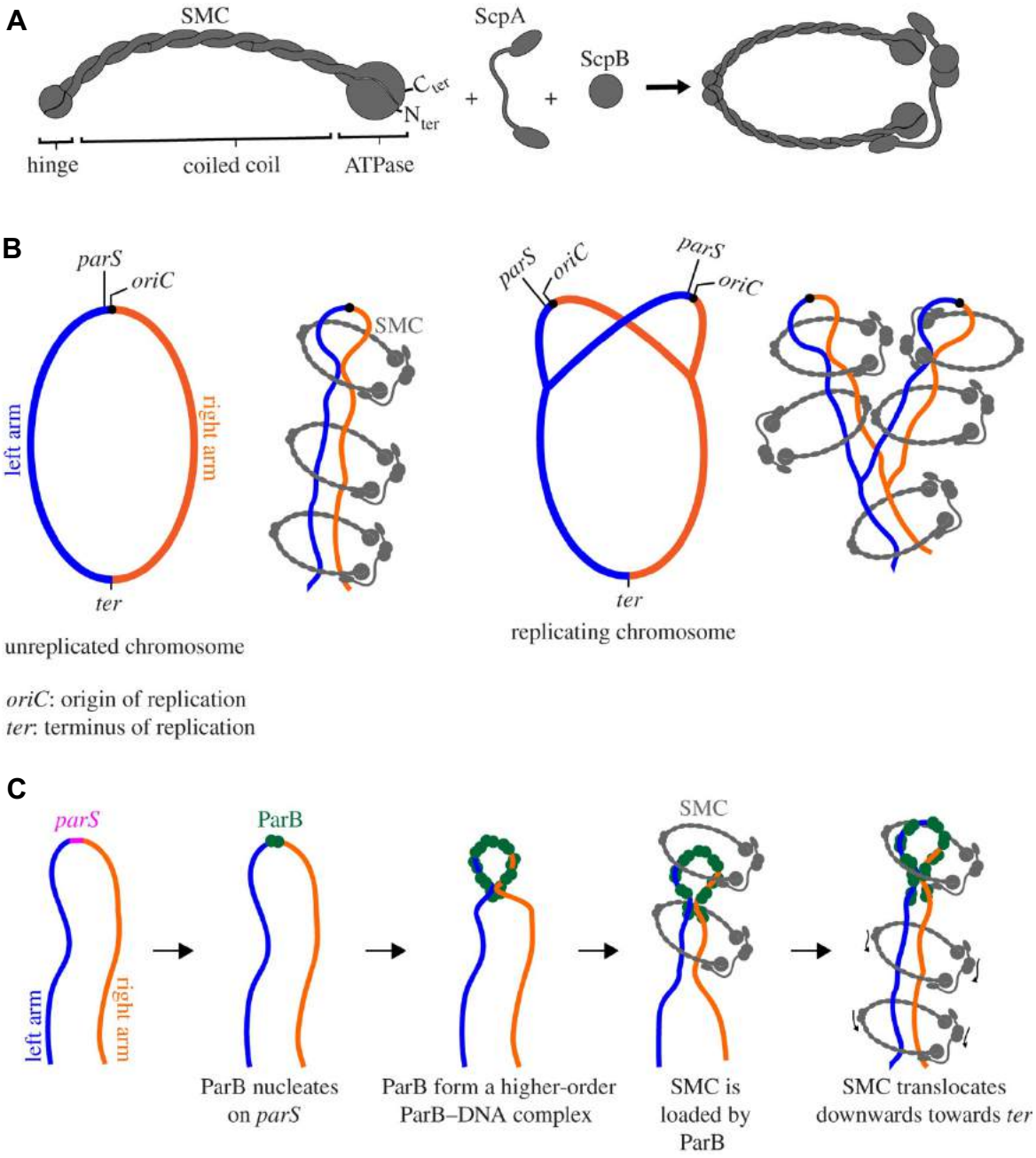

Figure 1.7 The ParB–DNA nucleoprotein complex recruits SMC to coordinate chromosome segregation and chromosome organisation. (A) Components of the bacterial SMC complex. **(B)** SMC (grey) tethers the two arms (blue and orange) of a circular chromosome together. An SMC–ScpA–ScpB complex can either hold both the left and the right arm of the chromosome within its lumen or two SMC complexes, each encircles one chromosome arm, can handcuff to tether both chromosome arms together. For simplicity, only SMCs entrapping both chromosome arms are shown. SMC probably packages sister chromosomes into individual entities and away from each other, thus minimising DNA entanglement between replicating chromosomes. **(C)** A schematic model of how SMC is loaded at *parS* by ParB and translocates on the chromosome towards the replication terminus (*ter*). For simplicity, alternative conformations of SMC (ring or rod) are not illustrated; the SMC complex is shown as a generic ring that entraps DNA. Schematic pictures are not drawn to scale.

opposite cell poles by the ParABS system. In *C. crescentus*, segregation of origin-proximal DNA occurs in two steps; the duplicated origins are released from the pole and separate slightly from one another first before one of the origins is moved unidirectionally by ParABS to the opposite cell pole (Shebelut et al., 2010). While the initial separation does not require ParA, it might be facilitated by the DNA-unlinking activity of SMC (Shebelut et al., 2010; Taylor et al., 2017).

Precisely how SMC translocates on the chromosome is not yet clear; several models have been proposed, and I refer the reader to a recent review for an in-depth discussion (Yatskevich et al., 2019). How ParB loads SMC onto the chromosome is also not fully understood; the weak and transient interaction between ParB and SMC has made efforts to study their interactions by traditional methodologies (such as bacterial two-hybrid or co-immunoprecipitation) difficult (Böhm et al., 2020; Sullivan et al., 2009; Tran et al., 2017). However, it was suggested that DNA-bound ParB probably interacts directly with SMC to recruit it to the DNA (Gruber and Errington, 2009). Indeed, a ParB-interacting area has been identified in the neck region in between the ATPase head domain and the coiled coil of *B. subtilis* SMC (Minnen et al., 2016), while mutations that eliminate SMC recruitment have been mapped onto the N-terminal domain of *B. subtilis* ParB (Gruber and Errington, 2009; Wang et al., 2015). Those same mutations also impair the ability of ParB to assemble into a higher-order nucleoprotein complex, hence it is tempting to speculate that either (i) a high local concentration of DNA-bound ParB is necessary to recruit sufficient SMC molecules or (ii) the DNA-bridging/ clamping activity of ParB ensures SMC entraps DNA correctly at the loading step. Future experiments, particularly a cell-free reconstitution of a ParB-dependent SMC recruitment and translocation, will provide further insights into the mechanism of actions of bacterial SMC and its contribution to chromosome segregation.

1.7 ParB interactions with other protein partners to establish cell polarity

The spatiotemporal organisation of cells are dependent on the accurate and distinct localisation of proteins and protein complexes. As such, the establishment of cell polarity is essential in various processes, including chromosome organisation and segregation. In rod-shaped bacteria, cell poles act as hubs for the intracellular localisation of proteins, nucleic acids and lipids (Surovtsev and Jacobs-Wagner, 2018). When cell division is initiated, a new cell pole forms at the site of the division plane, polar organising proteins play a role in ensuring the newly divided chromosome migrates towards the appropriate cell pole. Polar organisers display variability in primary structure and function across various bacterial lineages (Laloux and Jacobs-Wagner, 2014; Surovtsev and Jacobs-Wagner, 2018). In this section, I focus on

the polar organising proteins that interact directly or indirectly with components of the ParABS system.

During cell division in *C. crescentus,* the polar anchoring protein, PopZ localises towards the new cell pole (Bowman et al., 2008, 2010) (Fig 1.8A). PopZ is inherently disordered and in *C. crescentus*, PopZ also accumulates at the old cell pole, where it self-aggregates into a proteinaceous matrix that interacts with ParB to tether the *ori*-proximal *parS* sequence (and hence the non-replicating chromosome) (Fig 1.8A) (Bowman et al., 2008, 2010; Holmes et al., 2016). Concomitantly, the polar localisation of PopZ towards the new pole captures the new ParB-*parS* complex and tethers the replicated chromosome towards the newly diving cell (Bowman et al., 2008). By doing so, the PopZ-ParB-*parS* complex ensures the directional movement of the replicating chromosome towards the new cell pole in *C. crescentus*. PopZ has also been shown to interact and recruit ParA towards the cell pole via its NTD, hence regulating the dynamics of ParA during chromosome segregation (Ptacin et al., 2014). Ptacin *et. al.* (2014) demonstrated that PopZ binds and sequesters an inactive population of ParA monomers towards the original cell pole and regenerates ATP-bound ParA which can then associate with the nucleoid again to start the next chromosome segregation cycle (Ptacin et al., 2014). Although PopZ is not well conserved between other bacterial species, homologues of PopZ have been reported in *Brucella abortus* and *Agrobacterium tumefaciens* (Deghelt et al., 2014; Ehrle et al., 2017). In *A. tumefaciens*, PopZ also anchors the chromosome centromere towards the cell pole through its interaction with the *A. tumefaciens* ParB homologue, ParBI (Ehrle et al., 2017).

In the Gram-negative γ-proteobacteria *Vibrio cholerae*, a transposon-based screening of mutants impaired in mobility identified the polar landmark protein, HubP (Yamaichi et al., 2012). HubP is a multi-domain protein, that anchors the *V. cholerae* chromosome to the cell pole through its interaction with ParA-like proteins (Fig. 1.8B). HubP contains a LysM domain in the NTD that allows its interaction with peptidoglycan, allowing non-covalent interactions with the bacterial cell wall, whilst its large cytoplasmic domain interacts with three ParA-like ATPase spatial regulators (ParA1, FlhG and ParC) (Mesnage et al., 2014; Yamaichi et al., 2012). It is likely that ParA1 interacts with ParB1, which in turn nucleates onto the *parS* site located towards the *ori* region (Fig. 1.8B). Direct interactions were shown between ParA1 and FlhG, while HubP and ParC interact indirectly (Yamaichi et al., 2012). In *Vibrio alginolyticus*, HubP through its polar anchoring of FlhG regulates the formation of flagellar biogenesis (Takekawa et al., 2016). In the γ-proteobacterium *Sewanella putrefaciens*, HubP also contributes in polar anchoring but in a FlhG- independent manner. Fluorescent microscopic analysis of *S. putrefaciens* cells displayed co-localisation between ParB and HubP, suggesting

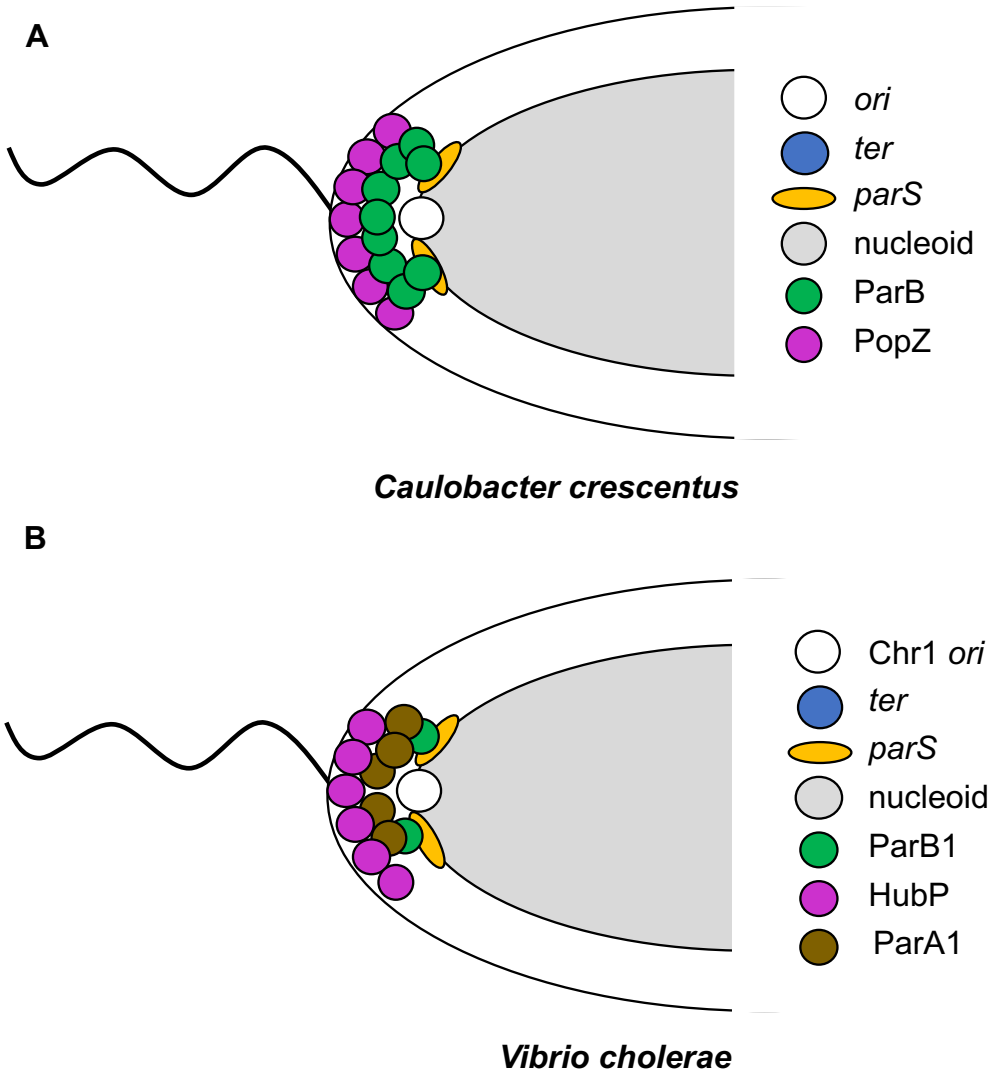

Figure 1.8 The protein-based systems that anchors specific DNA regions in *C. crescentus* and *V. cholerae*. (A) Schematic illustration of the polar anchoring complex in *C. crescentus*. PopZ (purple circle) self-aggregates into a proteinaceous matrix towards the old cell pole and directly interacts with ParB (green circle), which in turn tethers the *ori*-proximal *parS* sequences (white circle and yellow oval respectively). **(B)** Schematic illustration of a polar anchoring complex in *V. cholerae*. HubP (purple circle) anchors the *ori* of the large chromosome Chr1 to the cell pole through directly interacting with ParA1 (brown circle) which likely interacts with the ParB1-*parS* sequences tethered towards the Chr1 *ori*.

that HubP anchoring of the chromosome is dependent on ParB-*parS ori* interactions (Rossmann et al., 2019).In bacteria lacking PopZ, such as those in the actinobacteria and firmicutes clade, the establishment of cell polarity is mediated by the peripheral membrane protein, DivIVA that binds to the concave curvature of the bacterial membrane (reviewed in Hammond et al., 2019). Much like PopZ, DivIVA also anchors at the chromosomal origins located at the cell poles. In *Streptomyces coelicolor,* DivIVA is essential and localises towards the tips of the aerial hyphae to promote the synthesis of peptidoglycan at the cell poles (Flärdh, 2003; Hempel et al., 2008). Fluorescence microscopy experiments in *S. coelicolor* displayed colocalisation between DivIVA, Scy and FilP (Ditkowski et al., 2013; Fuchino et al., 2013; Holmes et al., 2013). Colocalisation of Scy with DivIVA serves as molecular assembly to assemble the polarisome (Holmes et al., 2013). Scy then recruits ParA towards the cell tips of aerial hyphae as sporulation is initiated allowing the chromosome to be equally partitioned into spores. A direct interaction between *S. coelicolor* DivIVA and ParB was seen when heterologous expressed in *E. coli* (Donovan et al., 2012). In the actinomycete *Corynebacterium diphtheria*, DivIVA is also essential and functions by tethering the chromosome towards the cell pole (Hempel et al., 2008; Ramos et al., 2003). A direct interaction between ParB and ParB in complex with *parS* was observed with DivIVA when expressed in *E. coli*, suggesting that DivIVA tethering to the cell pole is also dependent on ParB-*parS*-*ori* interactions (Donovan et al., 2012). In Firmicutes such as *B. subtilis* DivIVA interacts with ParA, ParB and RacA, a protein that binds sites near *ori*. During sporulation, DivIVA accumulates towards the old cell pole where interaction with RacA and ParA/ParB tethers the *ori*-proximal regions of the chromosome to one side of the cell pole (Ben-Yehuda et al., 2003).

Although ParB plays a crucial role in ensuring faithful chromosome segregation, ParB participates in a wide range of biological activities outside chromosome segregation that are beyond the scope of this review, in *B. subtilis* for example, ParB (and ParA) regulate chromosome replication through their interaction with DnaA (reviewed in Kawalek *et. al.,* 2020) (Ireton et al., 1994; Kawalek et al., 2020; Murray and Errington, 2008; Schofield et al., 2010). Remarkably, evolution has repurposed various ParA and ParB proteins with novel functions. In the next sections I discuss the existence of ParA-like and ParB-like proteins that function in protecting the nucleoid during cell division.

1.8 Bacterial cell division

Cell division represents a fundamental biological process that enables the proliferation of both prokaryotic and eukaryotic cells (Adams et al., 2014). Crucial to cell division is the formation

of a complex of proteins that forms the division machinery (divisome). The assembly of the divisome however must be spatially and temporally regulated to ensure that the replicated daughter cells are of equal size and have both inherit an equal amount of genetic information. Most bacteria divide by binary fission which involves the formation of the division septum at the midcell through the polymerisation of FtsZ (Z-ring) (Bi and Lutkenhaus, 1993). FtsZ however is not only found in bacteria, as it is an ancient protein that mediates cell division in multiple archaea, chloroplasts and primitive mitochondria (Adams et al., 2014; Bi and Lutkenhaus, 1991; Margolin, 2005; McQuillen and Xiao, 2020). The assembly of the Z-ring acts as the scaffold that leads to the dynamic recruitment of more than 30 proteins to assemble of the divisome (McQuillen and Xiao, 2020). The fully matured divisome then forms the septal ring complex that interacts with the septal and intermembrane peptidoglycan precursors to facilitate cytokinesis (McQuillen and Xiao, 2020). The core components of the divisome include peptidoglycan remodelling proteins (such as peptidoglycan synthases and peptidoglycan glycosyltransferases), proteins that stabilizes the Z-ring (such as ZapA) (Pichoff and Lutkenhaus, 2002), proteins involved in chromosome segregation (FtsK) (Wang and Lutkenhaus, 1998) and proteins that regulate the activity of septum peptidoglycan enzymes (McQuillen and Xiao, 2020). Indeed, with exception to MapZ in *Streptococcus pneumoniae*, the localisation of all these proteins are dependent on the positioning of the Z-ring at future division sites (Fleurie et al., 2014; Holečková et al., 2014). In rod-shaped bacteria such as *B. subtilis* and *E. coli*, division site selection occurs at the midcell, which lies at the midpoint of the rod, perpendicular to the long axis of the cell (Adams et al., 2014). Nevertheless, to better understand bacterial cell division, further studies using differently shaped non-model organisms that undergo complex lifecycles are required (Eswara and Ramamurthi, 2017).

1.9 FtsZ and Z-ring assembly

Initial insights into the genes that control cell division came from a study probing temperature sensitive cell division *E. coli* mutants (Hirota et al., 1968). One particular mutant retained its ability to replicate and segregate the chromosome, but was impaired in constricting the cell envelope at the division site (Hirota et al., 1968). Later Bi and Lutkenhaus mapped the mutation of this strain to a single gene termed *ftsZ* (filamentous temperature sensitive gene) (Bi and Lutkenhaus, 1990, 1991). Immuno-electron microscopy approaches demonstrated that FtsZ localises towards the midcell and self-assembles into a ring-like structure to initiate cell division (Bi and Lutkenhaus, 1991). A few years later, the first crystal structure of FtsZ from the archaeon *Methanococcus jannaschii* was solved (Löwe and Amos, 1998). Intriguingly, although FtsZ shares very little sequence identity with tubulin, the crystal structure of FtsZ shared a similar secondary and tertiary structure to tubulin and was proposed to the tubulin homologue (Erickson, 1995; Löwe and Amos, 1998; Oliva et al., 2004). Since then,

various studies have demonstrated that FtsZ functions as a GTPase protein and polymerises in a GTP binding-dependent manner (De Boer et al., 1992; Bramhill and Thompson, 1994; Mukherjee et al., 1993; Nogales et al., 1998; RayChaudhuri and Park, 1992).

FtsZ proteins generally share a similar domain architecture where they are composed of a short typically disordered N-terminal region, a globular tubulin-like domain, followed by a flexible linker and the C-terminal tail (Löwe and Amos, 1998; Löwe and Van den Ent, 2001). The globular domain of FtsZ binds to GTP, resulting in the generation of a continuous linear protofilament, hence causing FtsZ to polymerize to form a septal ring-like structure known as the Z-ring (McQuillen and Xiao, 2020). The Z-ring then acts as a scaffold resulting in the dynamic assembly of the divisome that mediates cell division. The initiation of the Z-ring assembly begins by the targeting of FtsZ monomers towards the cell membrane. Depending on the species of bacteria, a variety of proteins can be involved in this process. In model organisms such as *E. coli*, *C. crescentus* and *B. subtilis* FtsA tethers FtsZ to the bacterial membrane through its conserved C-terminal amphipathic helix (Din et al., 1998; Jensen et al., 2005; Pichoff and Lutkenhaus, 2002). Additionally, in both *E. coli* and *C. crescentus* the transmembrane protein ZipA localises FtsZ towards the cell membrane (Mosyak et al., 2000; Osorio et al., 2017; Pichoff and Lutkenhaus, 2002). While no homologue of ZipA exists in *B. subtilis*, instead SepF interacts with the C-terminal tail of FtsZ to direct FtsZ towards the cell membrane (Duman et al., 2013).

Interestingly, across various bacterial species, the intracellular levels of FtsZ remains constant throughout the cell cycle and generally exceeds the concentration required for Z-ring assembly (Erickson et al., 2010; Lutkenhaus et al., 2012; Schumacher, 2017). Other determinants must therefore mediate the correct positioning of the Z-ring to ensure a proper cell division. These proteins can act either directly or indirectly interact with FtsZ to inhibit FtsZ polymerisation, or conversely to promote the assembly and maturation of the Z-ring. Fascinatingly, the existence of such effectors are extremely diverse in bacteria, highlighting the natural variation that exists between bacterial species (Huang et al., 2013; Schumacher, 2017). Additionally, these proteins generally interact with different regions of FtsZ, explaining the prevalence of such effectors in bacteria. Whereas, these proteins are not essential and bacterial strains depleted or lacking such factors only display impaired cell division under certain conditions (such as being DNA replication deficient). The diversity of these effectors therefore suggests that they are only needed in specific conditions that may not be faithfully reconstituted in the laboratory. Moreover, recent evidence have demonstrated that cell metabolism itself regulates the activities of FtsZ, as cell size is dependent on nutrient availability. Such studies have demonstrated that metabolic enzymes can either directly or indirectly inhibit FtsZ activity. In

B. subtilis, UgtP, an enzyme that catalyses the transfer of glucose from UDP-glucose to a diacylglycerol-containing sugar acceptor directly inhibits FtsZ polymerisation in a UDP-glucose dependent manner (Weart et al., 2007). While in *E. coli*, regulation of Z-ring assembly is mediated by another UDP-glucose utilizing enzyme, OpgH (Hill et al., 2013). Furthermore, in *C. crescentus*, under conditions of nitrogen limitation, the NAD-dependent glutamate dehydrogenase GdhZ and the oxidoreductase-like KidO act in conjunction to promote FtsZ disassembly (Beaufay et al., 2015). While such FtsZ regulators function in response to particular cues, other protein-based complexes function to specifically inhibit Z-ring polymerisation at the cell poles and over the replicating nucleoid. Indeed, one of the first and most characterised protein based machinery (Min system) was first identified in *E. coli* (de Boer et al., 1989; De Boer et al., 1990).

1.10 The Min system

Over 50 years ago, Adler *et. al.,* (1967) discovered small, anucleate *E. coli* cells that they termed minicells (Adler et al., 1967). Noticeably, these cells failed to divide and contained much less DNA than the WT *E. coli* cells, yet remarkably these cells remained metabolic active for several hours (Adler et al., 1967). Although minicells could easily be separated from WT cells through the use of a sucrose gradient centrifugation, the factors causing this striking phenotype was not fully understood. Moreover, the formation of these minicells were not specific to *E. coli*, as a few years later minicells were also reported in *B. subtilis* (Reeve et al., 1973). Subsequent studies proposed that minicells are the result of pre-mature cell division, due to mispositioning of the division apparatus (Taheri-Araghi et al., 2015). Bacterial cells must therefore possess regulatory mechanisms that ensures cell division only occurs once the cell is of adequate size and has inherited a proper amount of genetic information. Indeed, initial insights into these mechanisms came from genetic studies in *E. coli*, whereby mutations in the *minB* locus generated *E. coli* minicells (De Boer et al., 1988). Later, de Boer *et. al.,* (1990) proposed that the *minB* operon is composed of three components: MinC (directly inhibits FtsZ polymerisation), MinD (ATPase-localising protein of MinC) and MinE (ATPase-activating protein of MinD) (Fig 1.9A) (De Boer et al., 1990; Hu and Lutkenhaus, 2000; Hu et al., 1999).

MinD belongs to the family of cytoskeletal Walker ATPases and localises towards the cell poles (Fig 1.9A) (Hu et al., 2002). Similar to ParA, ATP-binding results in the dimerisation of MinD which increases its affinity to the membrane; endowed by its amphipathic helix that binds the membrane at a higher valency (Hu et al., 2002; Leonard et al., 2005). MinD directly interacts with MinC to localise MinC towards the cell pole (Fig 1.9A) (Bramkamp et al., 2008; Hu and Lutkenhaus, 2003; Hu et al., 1999). Additionally, MinD interacts with MinE, which in

turn stimulates the ATPase activity of MinD (Hu and Lutkenhaus, 2001; Hu et al., 2002; Suefuji et al., 2002). This promotes MinD monomerisation, resulting in its dissociation from the cell membrane (Hu et al., 2002). Additionally, in dividing cells, MinE assembles into a ring like structure at the midcell and migrates towards the cell pole (Fig 1.9A) (Fu et al., 2001; Raskin and De Boer, 1997). The interactions between the MinE ring and the MinCD complex results in an oscillation between cell poles, thus preventing FtsZ assembly at the polar regions of the cell (Fig 1.9A) (de Boer et al., 1989). Much like MinD, MinE also possess an amphipathic helix that enables MinE to remain localised at the cell membrane following the displacement of MinD from the cell membrane (Fig 1.9A) (Raskin and De Boer, 1997). This is likely to inhibit MinD from rebinding at the same location on the membrane (Huang et al., 2003; Loose et al., 2011; Park et al., 2011). While MinC, rather than participating in MinDE dynamics functions as the effector of the Min system (de Boer et al., 1989). MinC consists of two domains joined together by a linker that confers flexibility towards the NTD (Hu and Lutkenhaus, 2000). While the CTD contains the dimerisation interface that primarily consists of hydrophobic residues. Interestingly, both domains contributes towards inhibiting Z-ring assembly (Hu and Lutkenhaus, 2000). MinC binds to the FtsZ-FtsZ subunit interface through its NTD, preventing the head-to-tail assembly of FtsZ promoters (LaBreck et al., 2019). While the CTD of MinC interacts with the C-terminal tail of FtsZ to prevent the lateral association of FtsZ filaments (LaBreck et al., 2019).

The Min system has been extensively studied in *E. coli* and represents one of the earliest example of the spatiotemporal regulation of cell division. Indeed, *B. subtilis* also possess a Min system, however MinE is not present (Cha and Stewart, 1997; El Karoui and Errington, 2001; Marston et al., 1998). Instead, MinJ/DivIVA fulfils the role of MinE, by recruiting the MinCD complex towards the cell poles (Edwards and Errington, 1997; Patrick and Kearns, 2008). Despite this, the Min system only inhibits Z-ring assembly at the cell poles; other factors must therefore prevent the mispositioning of the Z-ring over the actively replicating nucleoid. The existence of such factors was speculated in the 'nucleoid occlusion' hypothesis, and over the past few decades, various proteins across different bacterial species have been identified to fulfil this role.

1.11 Noc-mediated nucleoid occlusion

1.11.1 The nucleoid occlusion hypothesis

Over three decades ago a direction relationship between the bacterial nucleoid and division site selection was observed (Mulder and Woldringh, 1989; Mulder et al., 1990; Woldringh et al., 1991). By studying temperature sensitive *E. coli* mutants deficient in chromosome

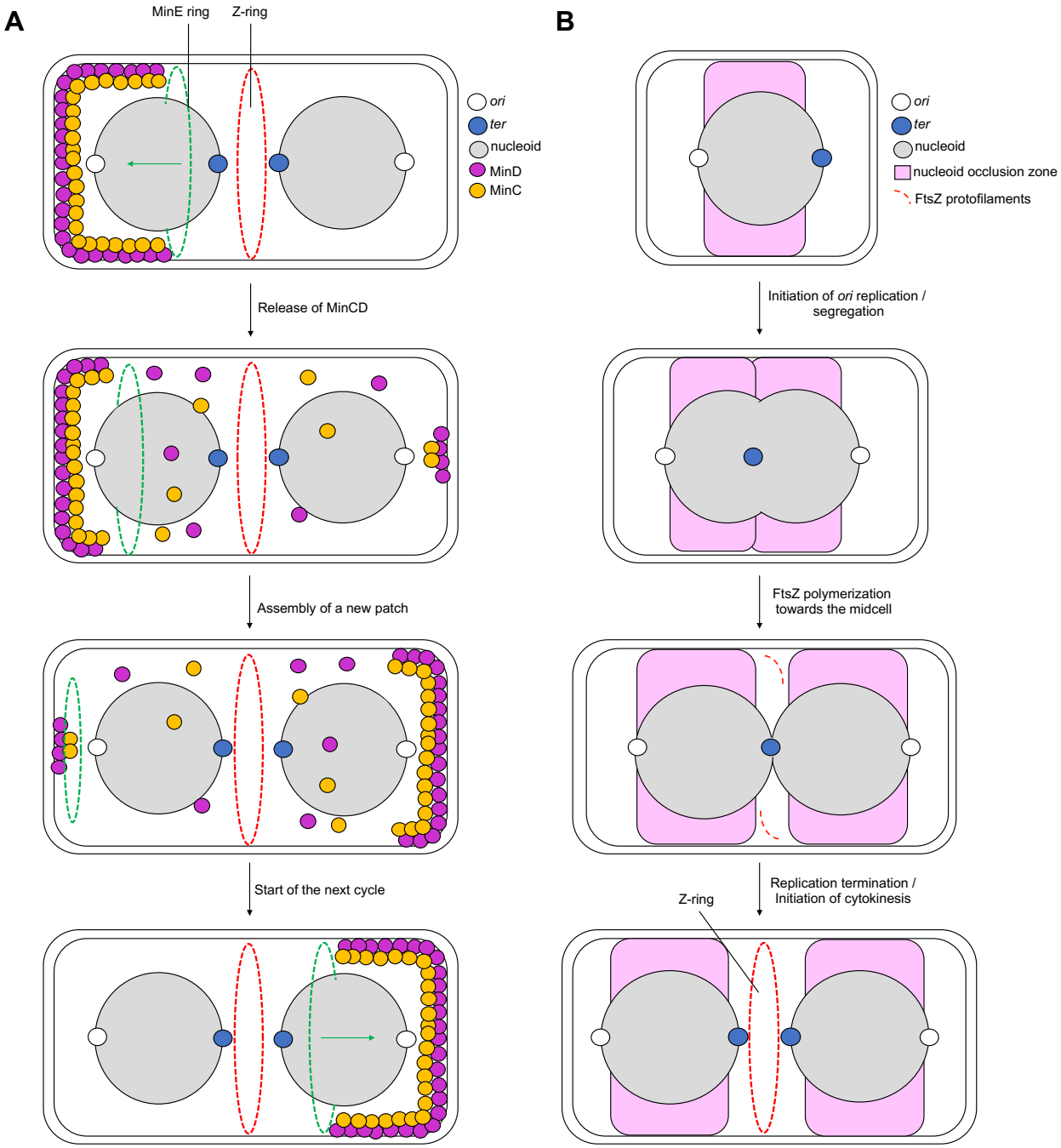
A
MinE ring
Z-ring
ori
ter
nucleoid
MinD
MinC
Release of MinCD
Assembly of a new patch
Start of the next cycle
B
ori
ter
nucleoid
nucleoid occlusion zone
FtsZ protofilaments
Initiation of ori replication / segregation
FtsZ polymerization towards the midcell
Replication termination / Initiation of cytokinesis
Z-ring

Figure 1.9 Model for the positioning of the Z-ring by the Min system and nucleoid occlusion. (A) Inhibition of cell division at the cell poles by the Min system. MinD (purple circle) localises the FtsZ-inhibitor MinC (yellow circle) onto the cytoplasmic membrane. MinC in turn inhibits FtsZ polymerisation at the polar regions of the cell. MinE (green dotted ring) organises into a ring-shaped structure that gradually displaces MinCD from the cell membrane. Free MinC and MinD subunits migrate towards the opposite end of the cell to establish a new polar cap and hence restart the cycle. **(B)** Nucleoid occlusion spatiotemporally regulates cell division in bacteria. Nucleoid occlusion factors such as Noc or SlmA preferentially associates towards the pole-proximal regions of the nucleoid. During the initiation of chromosome replication and segregation, the longitudinal dimensions of the nucleoid is small, placing Noc and SlmA within close proximity to the midcell to restrict Z-ring assembly. As chromosome replication and segregation progresses the two nascent daughter nucleoids start to partition. As a result, the midcell is free of Noc and SlmA enabling FtsZ to polymerize at the midcell. Other nucleoid occlusion factors (not illustrated in the model, discussed below) may localise towards the midcell to promote Z-ring assembly.

replication/segregation, Mulder and Woldrich (1989) observed that division site selection was influenced by DNA replication within the bacterial nucleoid (Mulder and Woldringh, 1989). The initial nucleoid occlusion model proposed that the nucleoid alone inhibits the formation of divisome (Fig 1.9B) (Mulder and Woldringh, 1989). Later, Woldrich and co-workers would refine their nucleoid occlusion hypothesis by proposing that a molecular 'crowding' effect occurs from a process termed 'transertion' (Woldringh, 2002). Whereby the active transcription, translation and insertion of proteins into the cell membrane produces strong but short-range inhibitors that prevent the assembly of the cell division apparatus (Woldringh, 2002). Thus, nucleoid occlusion protects the bacterial nucleoid from pre-mature bisection by ensuring a proper division site selection. Indeed, further studies have uncovered several protein factors from various bacterial species that contributes towards the nucleoid occlusion phenomenon. Nucleoid occlusion factors generally coordinate cell division with chromosome segregation by spatiotemporally regulating the assembly of the divisome. Despite this, these protein are typically non-essential (with exception to MipZ in *C. crescentus*) and only prevents premature cell division when chromosome replication/segregation is perturbed (Bernhardt and De Boer, 2005; Fleurie et al., 2014; Mercy et al., 2019; Thanbichler and Shapiro, 2006; Treuner-Lange et al., 2013; Veiga et al., 2011; Wu and Errington, 2004). Nevertheless, it is likely that the existence of these nucleoid occlusion factors improve the survival of bacterial cells in their respective niches. In the following sub-chapters, I discuss examples of nucleoid occlusion factors across various bacterial species and review their mechanism in ensuring proper division site selection.

1.11.2 The nucleoid occlusion protein, Noc

The first ever nucleoid occlusion factor, Noc (initially termed YyaA) was discovered in *B. subtilis* (Sievers et al., 2002). Due to its high sequence similarity with ParB (43% sequence identity with *B. subtilis* ParB), initial studies attempted to elucidate its role in chromosome segregation. Deletion of *yyaA* however produced no obvious defects in chromosome partitioning and/or organisation (Sievers et al., 2002). Later, a combination of null mutations helped elucidate the function of YyaA. Whereby the deletion of both the Min system as well as *yyaA*, produced *B. subtilis* cells that were not viable (Wu and Errington, 2004). While the depletion of *minD* in a *yyaA* knockout strain of *B. subtilis* introduced cell division defects, evidenced by the growth of long filamentous cells (Wu and Errington, 2004). Noticeably, FtsZ assembly was dispersed along the nucleoid, preventing FtsZ from reaching the concentration required for Z-ring formation (Wu and Errington, 2004). Furthermore, the overexpression of *yyaA* impaired sporulation and partially inhibited cell division in *B. subtilis*. Additionally, the deletion of *yyaA* in a *dnaA* (a key initiator of DNA replication in *B. subtilis*) depleted background resulted in the pre-mature guillotining of the *B. subtilis* nucleoid (Wu and

Errington, 2004). Early microscopic observations suggested that YyaA binds non-specially to the *B. subtilis* nucleoid, and this property was reported to be essential for *yyaA* mediated nucleoid occlusion. Further characterisation revealed YyaA as a nucleoid occlusion factor and was renamed Noc (Nucleoid occlusion protein) (Wu and Errington, 2004).

While initially Noc was proposed to non-specifically bind to the *B. subtilis* nucleoid, an absence of Noc localising towards the replication terminus (*ter*) region was observed (Wu et al., 2009). To investigate further, Wu *et. al.,* (2009) used ChAP-on-Chip approaches to reveal the consensus Noc-binding DNA sequence (termed *NBS*) (Wu et al., 2009). Indeed, ~74 *NBS* sites were found dispersed through the nucleoid but were largely absent at the *ter* (Wu et al., 2009). While the introduction of an *NBS* array at the *ter* recruited Noc towards the midcell, resulting in impaired cell division (Wu et al., 2009). These findings suggest that *NBS* recruits Noc towards the nucleoid, and the positioning of *NBS* on the chromosome mediates the nucleoid occlusion activity of Noc. As the *ter* is the final region that is segregated, the absence of *NBS* bound Noc would direct Z-ring formation towards the midcell. Despite this, the mechanism underpinning the inhibition of Z-ring assembly by Noc is unclear.

1.11.3 A model for Noc mediated nucleoid occlusion

Despite a thorough interrogation, no direct interaction between Noc and FtsZ (and other known cell division proteins) was observed (Adams et al., 2015). This contrasts the mechanism of other nucleoid occlusion proteins (such as SlmA) that directly interacts with FtsZ, complicating our understanding on Noc mediated nucleoid occlusion (Bernhardt and De Boer, 2005). Nevertheless, microscopic analysis of fluorescently labelled Noc revealed the formation of a dynamic foci at the cell periphery (Adams et al., 2015). Treatment with carbonyl cyanide m-chlorophenyl hydrazine (CCCP), a compound that disrupts membrane potential, impaired the localisation of Noc towards the cell membrane (Adams et al., 2015). While subsequent analysis of the Noc sequence predicted that the first 10 amino acid residues of Noc forms an amphipathic helix. Indeed, both the deletion of the entire amphipathic helix and mutations that perturb its amphipathic nature prevented the association of Noc to the cell membrane (Adams et al., 2015). While complementing the native Noc amphipathic helix with one from the hepatitis C virus protein NS4B, restored the membrane binding activity of Noc (Adams et al., 2015).

Nevertheless, Adams *et. al.,* (2015) observed a weak affinity between Noc and the cell membrane (Adams et al., 2015). It was speculated that Noc likely assembles into a higher-nucleoprotein complex to increase its affinity to the cell membrane (Adams et al., 2015; Wu et al., 2009). In support for this, previous ChAP-on-Chip assays demonstrated Noc binding to

the non-specific DNA adjacent to *NBS* (Wu et al., 2009). Moreover, Noc possess the highly conserved arginine rich motif (GxRRxRA) in the NTD (crucial for ParB spreading), and mutations in this motif prevented nucleoprotein complex assembly *in vivo* (Adams et al., 2015; Breier and Grossman, 2007; Tran et al., 2018). From the crystal structures of the Noc homologue ParB, it was speculated that the nucleation of Noc onto *NBS* would induce a conformational change at the NTD, exposing the arginine-rich patch for NTD-NTD oligomeric interactions (Chen et al., 2015; Leonard et al., 2004; Schumacher, 2017). This results in the assembly of the Noc-DNA nucleoprotein complex, increasing the local concentration of Noc at *NBS* and promoting its association to the cell membrane (Fig. 1.10A). Concomitantly, the assembly of a large Noc-DNA-membrane nucleoprotein complex would aggregate and cause a crowding effect in the cell (Fig. 1.10A). Indeed, Woldringh and colleagues previously proposed that the formation of a large complex coupled with the transertion of membrane proteins would physically occlude the assembly of the cell division machinery (Fig. 1.9B, 1.10A) (Woldringh, 2002). It is likely that molecular crowding of Noc-*NBS*-membrane complex would bias the division machinery towards areas that are unoccupied by nucleoid/membrane bound Noc. The lack of *NBS* sites at the *ter* region would hence bias Z-ring assembly towards the midcell (Fig 1.10A) (Adams et al., 2015; Wu et al., 2009). Despite this, whether the arginine rich patch of Noc mediates the oligomeric NTD-NTD interactions as observed in the *H. pylori* ParBΔCTD-*parS* co-crystal complex is uncertain (Chen et al., 2015). The lack of any structural information of Noc (until those presented in this thesis) has hindered our understanding on the assembly of the Noc-*NBS*-membrane complex. Indeed, Adams *et. al.,* (2015) demonstrated that mutations in the arginine patch impaired Noc foci formation at the cell periphery and were lethal in absence of *min* (Adams et al., 2015). Yet, Soh *et. al.,* (2019) recently proposed the arginine-rich patch forms the CTP binding/hydrolysis pocket of ParB (Soh et al., 2019). Indeed, ParB mutants impaired in binding or hydrolysing CTP failed to assemble the ParB-*parS* nucleoprotein complex *in vivo* (Osorio-Valeriano et al., 2019). Furthermore, Noc was reported to bind and hydrolyse CTP, with *NBS* stimulating its CTPase activity (Soh et al., 2019). However, it is unclear whether the arginine-rich patch forms the CTP-binding pocket of Noc or if CTP is required to assemble the Noc-DNA-membrane nucleoprotein complex.

More recently, both Noc and ParB have been shown to coordinate faithful Z-ring positioning in the initial steps of chromosome replication (Hajduk et al., 2019). Microscopic analysis of *B. subtilis* cells lacking both ParB and Noc, revealed a higher amount of Z-ring assembly at the new division sites and more frequent guillotining of the nucleoid (Hajduk et al., 2019). Interestingly, Hadjuk *et. al.,* (2019) proposed that both the formation of the ParB-*parS* complex and recruitment of SMC indirectly prevents Z-ring assembly over the early replicating nucleoid (Hajduk et al., 2019). It is likely that this interplay between ParB and Noc finetunes the

spatiotemporal regulation of division sites in replicating cells (Hajduk et al., 2019). Finally, Yu *et. al.,* (2021) recently demonstrated an alternative view of Noc mediated nucleoid occlusion, whereby Noc was proposed to corral Z-rings undergoing cytokinesis to restrict the migration of protofilaments along the cell, instead of preventing Z-ring assembly over the nucleoid (Yu et al., 2021). Using time-lapse microscopy of *noc* lacking *B. subtilis* cells, Yu *et. al.,* (2021) demonstrated that the decondensed spiral-like FtsZ intermediates were not formed *de novo*, but were split off pre-existing Z-rings (Yu et al., 2021). Additionally, Noc was proposed to function in a manner akin to ZapA (Buss et al., 2013; Caldas et al., 2019) and eukaryotic septin (Caudron and Barral, 2009; Dobbelaere and Barral, 2004). Indeed, the overexpression of ZapA restored the stabilization of the Z-ring in the *noc* lacking *B. subtilis* mutant. Whether Noc functions primarily in Z-ring positioning or by corralling FtsZ is not fully understood (Yu et al., 2021). Nevertheless, it is clear that the formation of the higher-order Noc-*NBS*-membrane complex is essential for the nucleoid occlusion activity of Noc.

1.11.4 Noc mediates DNA replication in *S. aureus*

Noc proteins are found widespread in the Firmicute clade; it is likely that Noc serves a conserved function by ensuring proper Z-ring positioning during cell division. Unlike *B. subtilis*, *S. aureus* lacks the Min system but possess a functional Noc protein (Veiga et al., 2011). Microscopic analysis demonstrated that Noc colocalises with the nucleoid but was largely absent at the midcell (Veiga et al., 2011). Whereas the deletion of *noc* resulted in Z-ring assembly over the nucleoid and caused DNA breaks on the chromosome (Veiga et al., 2011). Thus, in contrast to *B. subtilis*, Noc in *S. aureus* plays an essential nucleoid occlusion role. Despite this, in *S. aureus*, *noc* is not an essential gene as cells lacking *noc* were still viable (Veiga et al., 2011). Further analysis demonstrated that the *noc* lacking *S. aureus* contained a higher DNA content relative to cell volume (Pang et al., 2017). Pang *et. al.,* (2017) proposed that Noc negatively regulates replication initiation by interacting with DnaA in a post-translational manner (Pang et al., 2017). Indeed, *noc* deleted cells harbouring *dnaA* suppressor mutants, prevented the formation of large cells and reduced the number of mis-localised Z-rings (Pang et al., 2017). These findings suggest that cell division phenotype may be caused by the over-initiation of DNA replication in *S. aureus* (Pang et al., 2017).

Intriguingly, *S. aureus* Noc shares 48% sequence identity with *B. subtilis* Noc, with key features such as the amphipathic helix, GERRxR motif and DNA-binding domain being highly conserved (Pang et al., 2017). Additionally the distribution of *NBS* sites towards the *ori* but not at the *ter* is similar in *S. aureus* and *B. subtilis* (Pang et al., 2017). While the ChIP-seq profile of *S. aureus* Noc displayed an enrichment that spanned 8-10 kb from the *NBS* site, suggesting that *S. aureus* Noc also spreads to form the higher-order nucleoprotein complex (Pang et al.,

2017). Thus, it is likely that both *S. aureus* and *B. subtilis* Noc share a similar mechanism to mediate nucleoid occlusion. Despite this, *S. aureus* Noc, was unable to complement the deletion of *noc* in a strain of *B. subtilis* which requires a functional Noc for cell viability (Pang et al., 2017). These observations indicate that Noc may interact with a species-specific component of the divisome, likely to prevent its assembly in the vicinity of the Noc-DNA-membrane complex. The identification of this elusive partner of Noc however remains uncertain.

1.12 SlmA mediates faithful nucleoid occlusion in *E. coli*

To identify a nucleoid occlusion factor in *E.* coli, Bernhardt and De Boer (2005) characterised *E. coli* mutants that were synthetic lethal in a *min* defective background (Bernhardt and De Boer, 2005). Strikingly, the deletion of both the twenty-three-kDa protein (*ttk*) and *min* generated *E. coli* cells that were not viable, hence *ttk* was renamed SlmA (synthetic lethality with a defective Min system) (Bernhardt and De Boer, 2005). Subsequent analysis of *slmA* suggested it encoded a TetR-like DNA-binding protein (Bernhardt and De Boer, 2005). The TetR family of proteins represent one of the largest family of transcriptional regulators in *prokaryotes* (Cuthbertson and Nodwell, 2013). Interestingly, *E. coli* cells harbouring the deletion of both *slmA* and *minD* were impaired in cell division due to improper positioning of the Z-ring (Bernhardt and De Boer, 2005). While microscopic analysis of GFP-labelled SlmA demonstrated that SlmA localises towards the nucleoid. Furthermore, light-scattering assays displayed a direct interaction between SlmA and FtsZ. Thus, in contrast with Noc, the nucleoid occlusion activities of SlmA are mediated by a direct interaction with FtsZ (Bernhardt and De Boer, 2005).

To obtain further insights into the function of SlmA, Tonthat *et. al.* (2011) reported the crystal structure of SlmA from *E. coli* (Tonthat et al., 2011). Noticeably, the crystal structure demonstrated that SlmA possess a canonical helix-turn-helix motif (Tonthat et al., 2011). This, coupled with the nucleoid-binding ability of SlmA suggested that SlmA must have a specific DNA sequence on the chromosome (Bernhardt and De Boer, 2005; Tonthat et al., 2011). Indeed, both ChIP-on-chip and restriction endonuclease protection, selection and amplification assays identified the consensus SlmA DNA binding site (termed *SBS*) on the chromosome (Cho et al., 2011; Tonthat et al., 2011). Furthermore, Cho *et. al.,* (2011) demonstrated that the location of *SBS* regulates the polymerisation of the Z-ring *in vivo*, as the introduction of extra copies of *SBS* on the chromosome impaired cell division in a SlmA-FtsZ manner (Cho et al., 2011). Similar to the distribution of *NBS*, *SBS* were also absent in the *ter* region of the *E. coli* chromosome (Cho et al., 2011; Tonthat et al., 2011). Indeed, the introduction of an *SBS* array at the *ter* region in *E. coli* cells grown under growth inhibiting

conditions, resulted in elongated cells that were impaired in cell division (Cho et al., 2011). The absence of *SBS* sites at the *ter* region likely creates a SlmA-free region that biases Z-ring assembly towards the midcell.

Initial biochemical reconstitutions of SlmA and FtsZ however produced contradictory findings that SlmA promotes FtsZ polymerisation; it was clear that *SBS* was required to promote the activity of SlmA *in vitro* (Bernhardt and De Boer, 2005; Cho et al., 2011). Initially Cho *et. al.,* (2011) demonstrated that the nucleation of SlmA to *SBS* promotes SlmA dimerisation, which inhibits FtsZ polymerisation by enhancing the GTPase activity of FtsZ (Cho et al., 2011). Although, later studies produced contradictory findings as no significant change in the GTPase activity of FtsZ was observed in the presence of SlmA or the SlmA-*SBS* complex (Cabré et al., 2015; Du and Lutkenhaus, 2014; Tonthat et al., 2013). Additionally, these studies also demonstrated that SlmA exists in a dimeric state even in the absence of *SBS* (Cabré et al., 2015; Tonthat et al., 2013). Nevertheless, it was clear that SlmA must be bound to *SBS* to inhibit Z-ring polymerisation. Thus, to obtain the molecular mechanism of nucleoid occlusion mediated by SlmA, Tonthat *et. al.,* (2013) reported the co-crystal structures of SlmA from *E. coli*, *V. cholera* and *Klebsiella pneumonia* in complex with *SBS* (Tonthat et al., 2013). Despite being crystallised in various conditions, the SlmA-*SBS* co-crystal structures all demonstrated that SlmA binds to *SBS* as a dimer-of-dimers (Tonthat et al., 2013). Indeed, ChIP analysis previously demonstrated that SlmA binds to non-specific DNA adjacent to *SBS* (spreading) (Cho et al., 2011). Hence by spreading and occupying the DNA flanking *SBS*, SlmA can directly occlude the formation of FtsZ in the areas occupied by the SlmA-*SBS* complex (Fig. 1.10B). Despite this, the molecular basis underpinning SlmA and FtsZ interactions, crucial for the nucleoid occlusion activity of SlmA was not fully understood.

Initial attempts at determining the SlmA-FtsZ interaction interface through small angle X-ray scattering (SAXS) were unsuccessful largely due to the resolution of the solved complex (Tonthat et al., 2011). Nevertheless, Tonthat *et. al.* proposed that a dimer of SlmA is likely sandwiched between two molecules of FtsZ (Tonthat et al., 2011, Tonthat et al., 2013). Later, using a genetics approach Cho and Bernhardt (2013), identified the residues in SlmA that mediates the interactions with FtsZ (Cho and Bernhardt, 2013). Intriguingly, this FtsZ-interacting interface exists in close proximity to the DNA-binding domain of SlmA. Thus, it was proposed that SlmA likely undergoes a conformational change when bound to *SBS*, increasing its affinity for FtsZ (Cho and Bernhardt, 2013). Subsequently, Du and Lutkenhaus mapped the FtsZ-SlmA interface onto the C-terminal tail of FtsZ, which is essential for SlmA-mediated antagonization of FtsZ polymerisation (Du and Lutkenhaus, 2014) (Du et al., 2015). In order to deduce the molecular basis underpinning SlmA-FtsZ interactions, Schumacher and Zeng

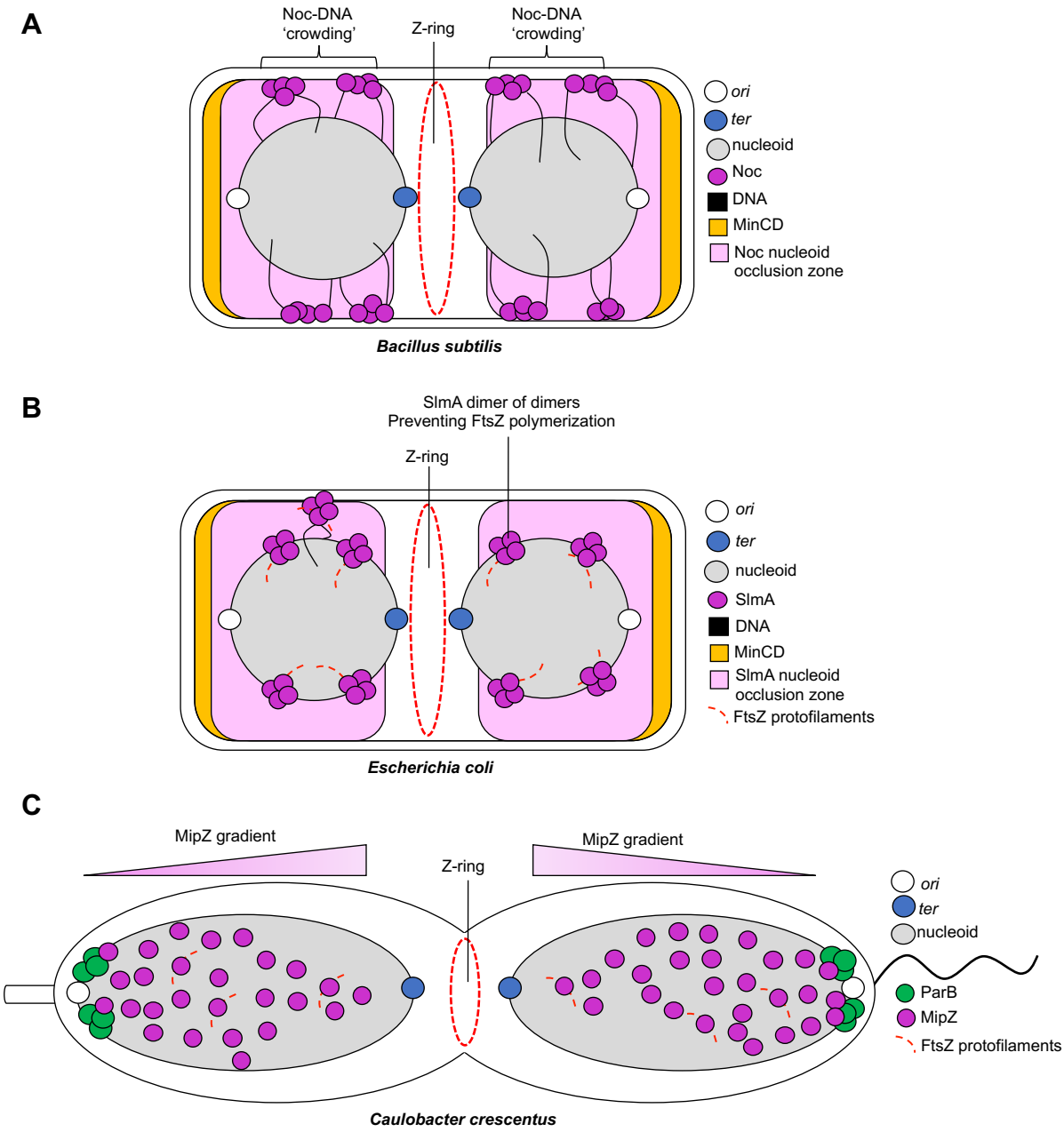
A
Noc-DNA
'crowding'
Z-ring
Noc-DNA
'crowding'
ori
ter
nucleoid
Noc
DNA
MinCD
Noc nucleoid
occlusion zone
Bacillus subtilis
B
SlmA dimer of dimers
Preventing FtsZ polymerization
Z-ring
ori
ter
nucleoid
SlmA
DNA
MinCD
SlmA nucleoid
occlusion zone
FtsZ protofilaments
Escherichia coli
C
MipZ gradient
Z-ring
MipZ gradient
ori
ter
nucleoid
ParB
MipZ
FtsZ protofilaments
Caulobacter crescentus

Figure 1.10 Negative regulators of Z-ring positioning in *B. subtilis*, *E. coli* and *C. crescentus*. (A) A model for Noc-mediated nucleoid occlusion. A schematic illustration of *B. subtilis* undergoing cell division, whereby the Z-ring has polymerized at the midcell (red dotted ring) concomitant with the segregation of the two nucleoids (grey circles). Noc binds to *NBS* sites that are widely distributed on the genome except near the *ter* region. Upon nucleating to *NBS*, Noc binds to the non-specific DNA along *NBS* to form a higher order nucleoprotein complex that associates and recruits DNA towards cell-membrane. The formation of the Noc-*NBS*-membrane complex indirectly inhibits Z-ring polymerisation over the actively replicating and segregating nucleoid. As *NBS* sites are not present in the *ter* region, Z-ring assembly would be biased towards the midcell. **(B)** A model of SlmA-mediated nucleoid occlusion. A schematic illustration of *E. coli* undergoing cell division in which the Z-ring has polymerized at the midcell (red ring) concomitant with segregation of the two nucleoids (grey circles). A dimer-of-dimers of SlmA (purple circles) binds *SBS* that are clustered towards the *ori*, but never found at the *ter* regions. SlmA-DNA complexes bind FtsZ protofilaments preventing their polymerisation. These interactions dissociate FtsZ protofilaments in the vicinity of the DNA. Additionally, SlmA recruits *SBS* sites towards the cell membrane to further sequester FtsZ protofilaments. Thus, SlmA creates a negative zone for Z-ring polymerisation around the nucleoid. As *SBS* sites are not found towards the *ter* region, Z-ring assembly would be biased towards the midcell. **(C)** A model of MipZ-mediated nucleoid occlusion. A schematic illustration of *C. crescentus* undergoing cell division is shown with a stalked cell (left) and swarmer cell (right). The Z-ring has polymerized at the midcell (red ring) concomitant with segregation of the two nucleoids (grey circles). MipZ (purple circle) directly interacts with FtsZ (red dotted lines), inhibiting FtsZ polymerisation. Furthermore, MipZ binds to the nucleoid non-specifically and also interacts with ParB (green circle) to generate a bipolar gradient of MipZ that restricts Z-ring assembly towards the midcell where the concentration of MipZ is the lowest. Additionally, polar-anchored ParB sequesters a population of MipZ for the next cycle of cell division.

(2016) solved the co-crystal structures of the SlmA-*SBS*-FtsZ(CTD) complex from *E. coli*, *Klebsiella pneumonia* and *Vibrio cholera* (Schumacher and Zeng, 2016). Indeed, the co-crystal structure demonstrated that SlmA-*SBS* interactions results in the conformational change that enables the residues previously identified by Cho and Bernhardt (2013) to interact with the C-terminal tail of FtsZ (Cho and Bernhardt, 2013; Schumacher and Zeng, 2016). It is likely that this interaction results in SlmA out-competing other effectors of FtsZ (such as FtsA or ZipA). However, the C-terminal tail is not required for the Z-ring polymerisation, and the SlmA-*SBS* complexes directly inhibits the polymerisation of FtsZ protofilaments. Furthermore, Robles-Ramos *et. al.,* (2020) recently provided *in vitro* evidence that SlmA binds to the lipid membranes, and this membrane binding activity is regulated by both *SBS* and FtsZ (Robles-Ramos et al., 2020). While *SBS* reduced the affinity of SlmA towards the purified lipids, a combination of both FtsZ and *SBS* facilitated the recruitment of the SlmA-*SBS*-FtsZ complex towards the membrane (Fig. 1.10B) (Robles-Ramos et al., 2020). It is possible that the recruitment of FtsZ towards cell membrane by the SlmA-*SBS* complex further prevents other FtsZ effectors from localising FtsZ towards the cell membrane. Despite this, the membrane targeting motif that enables SlmA to interact to the purified phospholipids is uncertain, and how SlmA promotes the disassembly of the Z-ring is not fully understood. Further studies are required to refine our understanding on SlmA-mediated nucleoid occlusion, nevertheless, it is clear that the lack of *SBS* towards *ter* region, biases the formation of the cell division machinery towards the midcell (Fig. 1.10B).

1.13 Noc/SlmA-independent nucleoid occlusion

Although both Noc and SlmA play important roles in protecting the nucleoid from pre-mature bisection, neither proteins are essential in their respective bacterium (Bernhardt and De Boer, 2005; Sievers et al., 2002). Indeed, *B. subtilis* or *E. coli* cells harbouring impaired Min and nucleoid occlusion systems still display a bias of Z-ring formation towards the inter-nucleoid spaces (Bailey et al., 2014; Rodrigues and Harry, 2012). Furthermore division site selection still occurred at the midcell when FtsZ was overexpressed in either a *B. subtilis noc min* double mutant or an *E. coli slmA, min* double mutant (Bernhardt and De Boer, 2005; Rodrigues and Harry, 2012). It is therefore likely that other nucleoid occlusion factors in these bacterial cells play a role in protecting the nucleoid from pre-mature bisection.

Furthermore, protein-based factors that promote the organisation of the bacterial chromosome may also regulate the positioning of the Z-ring. Indeed, in *E. coli*, MatP a DNA-binding protein that condenses the *ter* macrodomain interacts with a component of the divisome, ZapB (Castillo et al., 2016; Espéli et al., 2012). ZapB is a coiled coil protein that interacts with the FtsZ effector ZapA to form the ZapAB complex that promotes Z-ring assembly by anchoring

FtsZ molecules onto the cell membrane (Ebersbach et al., 2008; Gueiros-Filho and Losick, 2002). MatP directly interacts with ZapB upon assembly of the ZapA-ZapB-FtsZ complex, which ultimately promotes the assembly of the Z-ring towards the midcell (Buss et al., 2017; Galli and Gerdes, 2010).

1.14 MipZ ensures faithful Z-ring positioning in *C. crescentus*

Unlike *B. subtilis* and *E. coli*, C*. crescentus* lacks both the Min system and Noc. Nevertheless, *C. crescentus* utilises an alternative mechanism that encompasses the properties of both systems. In *C. crescentus*, ParB has been shown to directly interact with the P-loop ATPase MipZ, a MinD-like protein that promotes the midcell arrangement of FtsZ (Thanbichler and Shapiro, 2006). Initial attempts at deleting *mipZ* were unsuccessful, as a functional MipZ is required for the viability of *C. crescentus* (Thanbichler and Shapiro, 2006). Depletion of *mipZ* resulted in Z-ring assembly occurring at random locations throughout the nucleoid (Thanbichler and Shapiro, 2006). While the overexpression of *mipZ* blocked cell division by preventing FtsZ polymerisation in the cell (Thanbichler and Shapiro, 2006). These findings suggested that MipZ is essential for cell division in *C. crescentus* by ensuring the proper positioning of the Z-ring in the cell.

MipZ mediates its functions by interacting with ParB and the bacterial nucleoid (Kiekebusch et al., 2012). In doing so, MipZ generates a bipolar protein gradient that restricts FtsZ polymerisation towards the midcell, where MipZ concentration is the lowest (Fig. 1.10C) (Corrales-Guerrero et al., 2020; Kiekebusch et al., 2012; Thanbichler and Shapiro, 2006). Furthermore, MipZ was shown to function as an ATP-dependent molecular switch, whereby ATP regulates its interactions with the bacterial nucleoid (Kiekebusch et al., 2012). Mechanistic insights into bipolar gradient formation by MipZ was provided through the crystal structures of an apo-MipZ and MipZ in complex with the slow-hydrolysable ATP analogue, ATPγS (Kiekebusch et al., 2012). Indeed, MipZ was revealed to contain a P-loop Walker-box fold that resembles ParA. While both ParA and MipZ form a bipolar gradient throughout the cell, the generation of either a ParA or MipZ gradient is temporarily separated from one another through their interactions with ParB. Similar to ParA, MipZ dimerizes upon binding to ATP (Kiekebusch et al., 2012; Leonard et al., 2005). However, in contrast to ParA, ParB stimulates the formation of MipZ dimers (rather than promoting ParA monomerisation). Monomers of MipZ are then recaptured by ParB which in turn re-dimerizes MipZ, exposing an array of positively charged residues at the MipZ dimer interface that enables non-specific nucleoid binding (Corrales-Guerrero et al., 2020; Kiekebusch et al., 2012) (Fig. 1.10C). Due to the self-intrinsic ATPase activity of MipZ, MipZ hydrolyses ATP to ADP, promoting MipZ monomerisation. This leads to the disassociation from the chromosome and the re-association

towards the cell pole localised PopZ-ParB, to restart a new localisation cycle (Fig. 1.8A, 1.10C) (Kiekebusch et al., 2012). The recycling of such interactions with the ParB-*pars* complex results in the formation of a subcellular gradient of MipZ, with a higher concentration at the cell poles and a lower concentration at the midcell. MipZ also directly inhibits the polymerisation of FtsZ by promoting its GTPase activity, thus by associating with ParB-*parS*, MipZ is localised towards polar regions, guiding FtsZ polymerisation towards the midcell (Thanbichler and Shapiro, 2006).

Additionally, in *Mycobacterium gryphiswaldense* the MipZ homologue, MipZ1 also localises towards the cell poles through its interaction with polar ParB-*parS* complexes (Toro-Nahuelpan et al., 2019). MipZ1 also inhibits FtsZ polymerisation by stimulating its GTPase activity, thus its placement away from the mid-cell facilitates proper divisome assembly (Toro-Nahuelpan et al., 2019). While in *Rhodobacter sphaeroides*, MipZ monomers also associate with cell pole localised ParB-*parS* complexes, while dimeric forms of MipZ colocalise with FtsZ (Dubarry et al., 2019).

1.15 SsgA and SsgB as positive spatial regulators of Z-ring position in *Streptomyces coelicolor*

Much like *C. crescentus*, *S. coelicolor* lacks both the Min system and Noc. While MinD and DivIV homologs exist in *S. coelicolor,* neither of which contributes towards the localisation of the Z-ring (Flärdh, 2003; Willemse et al., 2011). Instead *S. coelicolor* harbours a positive spatial regulator of Z-ring positioning through the action of SsgA and SsgB (Willemse et al., 2011). To uncover the roles of SsgA and SsgB in *S. coelicolor*, Willemse *et. al.,* (2011) tracked the localisation of SsgA and SsgB with FtsZ (Willemse et al., 2011). Unique to *Streptomyces*, are the formation of long filaments of FtsZ in the areal hyphae during sporulation. This is then followed by the localisation of a focal pattern during the initiation of cell division before the formation of the Z-ring which form 'FtsZ ladders' along the hyphae. Intriguingly, SsgB formed a similar localisation pattern to FtsZ in *S. coelicolor*, suggesting that SsgB and FtsZ interact *in vivo* (Willemse et al., 2011). While Z-ring formation was impaired in *S. coelicolor* strains lacking either SsgA or SsgB, as fluorescence microscopic analysis displayed hampered formation of the FtsZ ladders in the areal hyphae (Willemse et al., 2011).

Interestingly, in absence of FtsZ, both SsgA and SsgB retained their localisation pattern. This indicates that SsgB is able to localise to the midcell independently of FtsZ and before FtsZ in the cell cycle (Willemse et al., 2011). The localisation of SsgB was also shown to be dependent on SsgA, as SsgB was shown to co-localise with SsgA at later stages of the developmental cycle. Thus, the model by Willemse *et. al.,* (2011) proposed that at the onset of sporulation,

FtsZ is recruited towards the future division sites by a direct interaction with SsgB, which in turn interacts SsgA to localise SsgB towards the midcell (Fig. 1.11A) (Willemse et al., 2011). Despite this, the factors that promote the localisation of SsgA or SsgB were uncertain. Later, Schlimpert *et. al.,* (2017) reported two dynamin like proteins, DynA and DynB that form components of the *S. venezuelae* divisome (Schlimpert et al., 2017). Bacterial two hybrid approaches demonstrated that both DynA and DynB directly interacts with SsgB, but not SsgA or FtsZ (Schlimpert et al., 2017). Although microscopy analysis demonstrated that DynA and DynB colocalise with FtsZ, it is likely that DynA and DynB interact indirectly with FtsZ through SsgB (Schlimpert et al., 2017). Thus by forming a network of protein-protein contacts, both DynA and DynB recruit SsgB towards the midcell to promote Z-ring assembly during sporulation-specific cell division (Fig. 1.11A) (Schlimpert et al., 2017).

1.16 The PomXYZ complex regulates division site placement in *Myxococcus xanthus*

Much like *C. crescentus* and *S. coelicolor*, *M. xanthus* lacks both the Min system and Noc. Nevertheless, initial insights into proper Z-ring positioning in *M. xanthus* came from the identification of the ParA-like protein, PomZ (Treuner-Lange et al., 2013). Deletion of *pomZ* resulted in the formation of chromosome lacking-minicell that were impaired in cell division (Treuner-Lange et al., 2013). Further microscopic analysis of *pomZ* lacking cells demonstrated diffusive patterns of FtsZ in the cytoplasm. Thus, PomZ likely functions to ensure faithful division site selection (Treuner-Lange et al., 2013). Similar to its ParA and MipZ counterparts, PomZ also dimerises and non-specifically binds to the nucleoid in the presence of ATP (Fig. 11.B) (Hester and Lutkenhaus, 2007; Kiekebusch et al., 2012; Leonard et al., 2005; Thanbichler and Shapiro, 2006; Treuner-Lange et al., 2013). However, in contrast to MipZ, PomZ was shown to localise towards the midcell where it co-localises and directly interacts with FtsZ. In doing so, PomZ positively regulates division site selection by directly recruiting FtsZ towards the midcell (Fig. 11.B) (Treuner-Lange et al., 2013).

A later study uncovered two additional proteins, PomX and PomY that together with PomZ, ensures proper Z-ring positioning at the midcell in *M. xanthus* (Fig. 11.B) (Schumacher et al., 2017). Deletion of any of these components impaired FtsZ polymerisation as the Z-ring was found dispersed along the nucleoid (Schumacher et al., 2017). Noticeably, both PomX and PomY are rich in protein-protein interacting domains. Indeed, PomX, PomY and PomZ interact directly with one another to form the PomXYZ complex (Schumacher et al., 2017). Microscopic tracking of the PomXYZ complex revealed that PomX and PomY localises towards the midcell in a PomZ dependent manner (Fig. 11.B) (Schumacher et al., 2017). Whereby PomX and PomY interact to form a complex that stimulates the ATPase activity of nucleoid bound PomZ, PomZ in turn recruits PomX and PomY to the nucleoid and translocates the PomXYZ complex

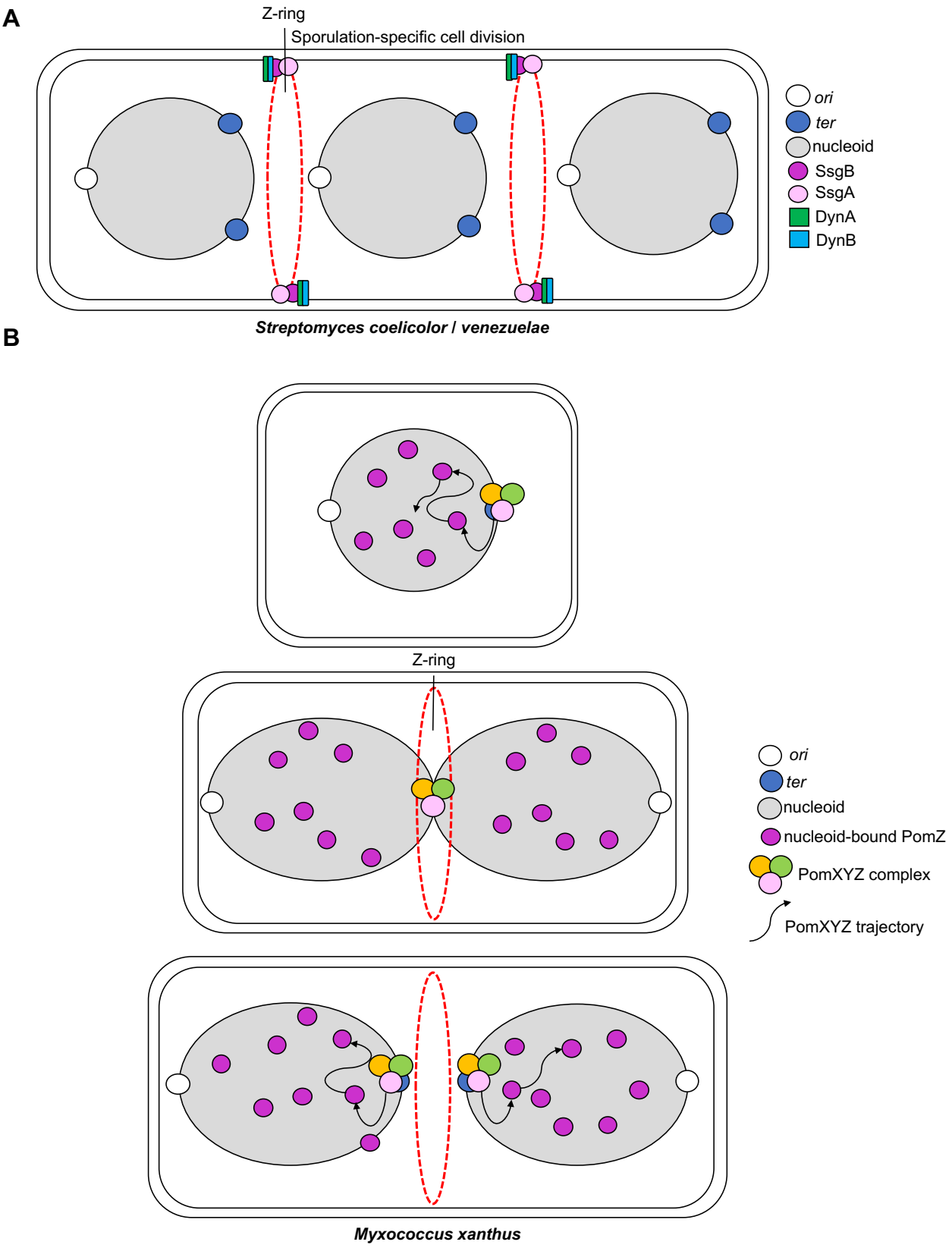
A
Z-ring
Sporulation-specific cell division
ori
ter
nucleoid
SsgB
SsgA
DynA
DynB
Streptomyces coelicolor / venezuelae
B
Z-ring
ori
ter
nucleoid
nucleoid-bound PomZ
PomXYZ complex
PomXYZ trajectory
Myxococcus xanthus

Figure 1.11 Positive regulators of Z-ring positioning in *Streptomyces* and *M. xanthus* **(A)** A model describing SsgB mediated Z-ring positioning in *Streptomyces*. During sporulation-specific cell division DynA (green box) and DynB (blue box) localises towards the midcell and interact with the divisome through interacting with SsgB. Additionally SsgA (pink circle) localises SsgB (purple circle) towards the midcell which in turn recruits FtsZ to form the Z-ring (red dotted ring). **(B)** Schematic illustration of Z-ring positioning by the PomXYZ complex in *M. xanthus*. PomZ (purple circle) binds non-specifically along the nucleoid. Additionally, PomZ interacts with PomY and PomZ to form the PomXYZ complex (yellow, green and pink circles). Prior to chromosome replication and segregation, the PomXYZ complex localises towards the midcell. The initiation of chromosome replication and segregation results in the translocation of the PomXYZ complex towards the midcell to promote Z-ring assembly via the diffusive flux of nucleoid bound PomZ.

towards the midcell both in the absence and presence of FtsZ. The formation of the PomXYZ complex towards the midcell would directly localise FtsZ towards midcell of *M. xanthus.* (Schumacher et al., 2017). Through a combination of mathematical modelling and experimental validation, Schumacher *et. al.,* (2017) proposed that the translocation of the PomXYZ complex is based on an bias/unbias Brownian movement (Schumacher et al., 2017). In which the migration of the PomXYZ complex depends on the diffusive fluxes of PomZ, Additionally, the difference in diffusive PomZ fluxes into the complex acts as a proxy for the asymmetry of the PomXYZ complex on the nucleoid, which converts the global cellular asymmetry of the PomXYZ complex into the local PomZ gradient complex (Fig. 11.B) (Schumacher et al., 2017). Currently however, no structural information for any components of the PomXYZ complex is available, although PomZ is likely to contain a ParA/MipZ like fold. The crystal or cryo-electron microscopy structure of the PomXYZ complex with FtsZ may yet reveal the molecular basis underpinning PomXYZ mediated nucleoid occlusion in *M. xanthus*.

1.17 MapZ and RocS mediate nucleoid occlusion in *Streptococcus pneumoniae*

Much like *C. crescentus*, *S. coelicolor* and *M. xanthus*, the human pathogen *S. pneumoniae* does not possess the Min system or Noc. Unique to *S. pneumoniae*, is the essential role of the StkP kinase for cell division, peptidoglycan synthesis, and the maintenance of cell shape (Beilharz et al., 2012; Fleurie et al., 2012; Jarick et al., 2018; Nováková et al., 2010; Sasková et al., 2007). To gain further insights into StkP function, Fleurie *et. al.,* (2014) characterised an endogenous target of StkP, Spr0334 which encoded a membrane protein of unknown function (Fleurie et al., 2014). Microscopic analysis of *spr0334* deleted *S. pneumoniae* strains displayed *S. pneumoniae* cells that were misshaped due to the improper positioning of the division septa (Fleurie et al., 2014). Subsequent observations led to the renaming of Spr0334 to MapZ (Mid-cell anchored protein Z). While almost at the same time, Holečková *et. al.,* (2014) identified the same protein which they termed LocZ (Localising at the midcell of FtsZ) (Holečková et al., 2014).

MapZ was predicted to contain a single transmembrane segment in between the cytoplasmic NTD and the extracellular CTD (Fleurie et al., 2014). The CTD binds peptidoglycan to position MapZ towards the midcell, while the NTD functions as a pedestal for the CTD (Manuse et al., 2016). Microscopic analysis displayed that MapZ forms a ring that localises towards the midcell and at future division sites (Fleurie et al., 2014; Holečková et al., 2014). In newly replicated daughter cells, GFP-MapZ was observed to colocalise with FtsZ at the midcell. As the *S. pneumoniae* cell elongates, the MapZ ring divides into two separate rings, while the Z-ring remains at the midcell. Co-immunoprecipitation studies confirmed that MapZ interacts with FtsZ, and MapZ-FtsZ interactions were mediated by the NTD cytoplasmic domain of

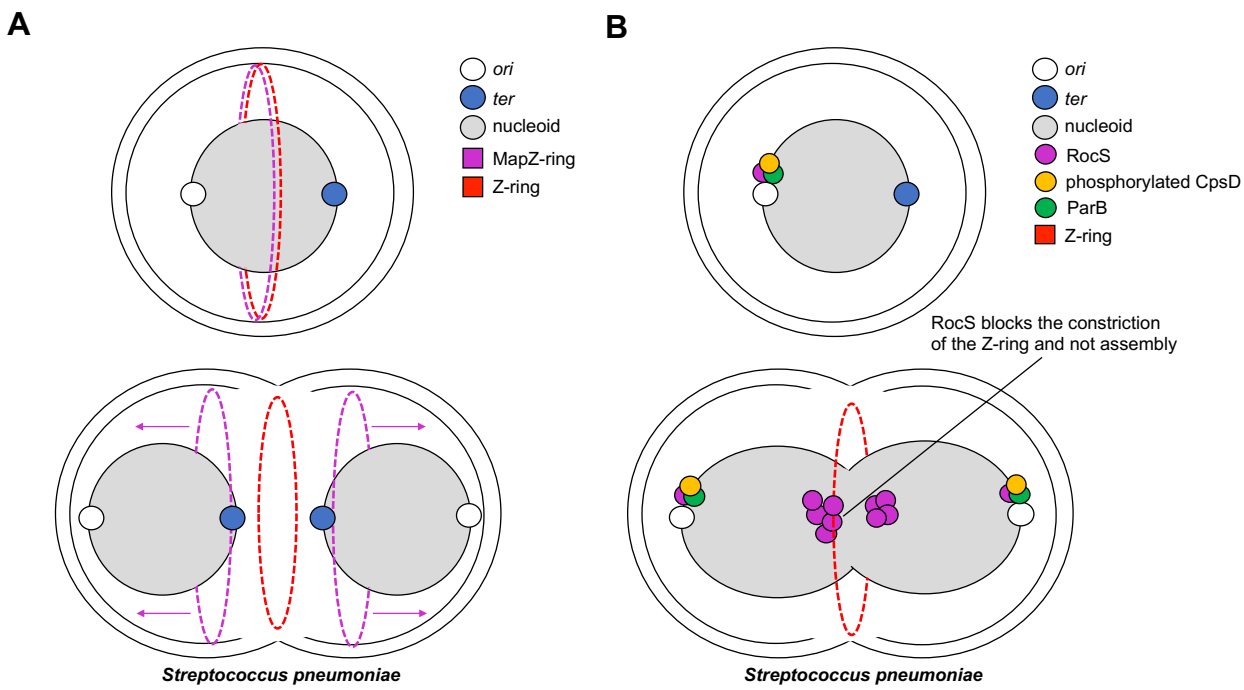

Figure 1.12 *S. pneumoniae* utilises both positive and negative regulators of Z-ring positioning (A) A model for MapZ positively regulating Z-ring positioning in *S. pneumoniae*. Both FtsZ (red dotted ring) and MapZ (purple dotted ring) colocalise at the midcell in newborn cells. MapZ rings then split into two rings that migrates toward the dividing daughter cells to mark future division sites. **(B)** A model for RocS negatively regulating Z-ring positioning in *S. pneumoniae*. During the early stages of the cell cycles RocS (purple circle) localises with ParB (green circle) and CpsD (orange circle) towards the *ori*. RocS binds non-specifically on the nucleoid and interacts directly with FtsZ at the midcell to prevent the contraction of the Z-ring.

MapZ (Fleurie et al., 2014). These findings suggest that MapZ in *S. pneumoniae* acts as a positive regulator of FtsZ polymerisation by promoting the assembly of the Z-ring towards the midcell (Fig. 1.12A). Homologues of MapZ were also found in *streptococci*, *lactococci* and most *enterococci*, suggesting this mechanism of cell division selection is conserved across these various bacteria (Fleurie et al., 2014).

Furthermore, the newly discovered RocS was shown to protect the nucleoid in a CpsD dependent manner (Mercy et al., 2019). *S. pneumoniae* harbours ParB and *parS*, but lacks ParA. Instead ParB interacts with the ParA-like protein CpsD, a key regulator in the assembly of the polysaccharide capsule (Nourikyan et al., 2015). Unique to *S. pneumoniae*, a CpsD-dependent phosphorylation mechanism powers the movement of the ParB-*parS* nucleoprotein complex (Nourikyan et al., 2015). Prior to the discovery of RocS, cell division blockage through phosphorylation dependent CpsD movement of ParB prevented the pre-mature bisection of the nucleoid. Interestingly in *S. pneumoniae* cells lacking *rocS*, newly replicated chromosomes either failed to segregate, or were partly segregated and guillotined by the division machinery (Mercy et al., 2019). Indeed, deletion of *rocS* in strains mimicking defective phosphorylation of CpsD suppressed the elongated phenotype previously observed when CpsD was impaired in phosphorylation (Mercy et al., 2019). These findings suggest that both RocS and CpsD phosphorylation levels, are able to block cell division to protect the nucleoid from pre-mature bisection (Fig. 1.12B) (Mercy et al., 2019). Further microscopy analysis displayed RocS and CpsD colocalise in the early stage of the cell cycle. It is likely that RocS and CpsD only interacts when the chromosome is impaired in segregating. These findings therefore suggest that RocS acts as a nucleoid occlusion factor in *S. pneumoniae* (Mercy et al., 2019). Unlike Noc however, RocS does not influence the localisation of the divisome and instead interacts directly with FtsZ to constrict Z-ring assembly (Fig. 1.12B) (Mercy et al., 2019). The ability of RocS to non-specifically bind to the bacterial nucleoid and the cell membrane likely contributes towards its nucleoid occlusion function. However, in absence of any structural data, the molecular basis of RocS mediated nucleoid occlusion in *S. pneumoniae* remains poorly understood. Nevertheless, by interacting with both ParB and CpsD, RocS acts as the link that combines chromosome segregation with nucleoid occlusion (Mercy et al., 2019; Nourikyan et al., 2015).

1.18 Project aims

Bacteria exhibit great diversity in the Nature and as such have evolved complex mechanisms to ensure both daughter cells inherit a full copy of the chromosome during cell division. Despite decades of research, it is clear that future work is needed to reveal the underlying forces of nucleoid occlusion and how they are intimately linked with the organisation and segregation

of the bacterial chromosome. The central goal of my thesis is to provide additional structural and mechanistic insights into the role ParB and Noc in bacterial chromosome segregation and maintenance. Here in this thesis, I aim:

- To investigate the molecular basis for DNA-binding specificity by ParB and Noc (Chapter 3).

- To determine the structural basis for the translocation/spreading of ParB along the chromosome (Chapter 4).

- To characterise the relationship between *in vitro* DNA condensation and *in vivo* spreading ability of ParB (Chapter 5).

- To characterise the role of CTP in the formation of the tripartite Noc-DNA-membrane complex (Chapter 6).

1.19 References

1. Abeles, A.L., Friedman, S.A., and Austin, S.J. (1985). Partition of unit-copy miniplasmids to daughter cells. III. The DNA sequence and functional organization of the P1 partition region. J. Mol. Biol. **185**, 261–272.
2. Adachi, S., Hori, K., and Hiraga, S. (2006). Subcellular positioning of F plasmid mediated by dynamic localisation of SopA and SopB. J. Mol. Biol. **356**, 850–863.
3. Adams, D.W., Wu, L.J., and Errington, J. (2014). Cell cycle regulation by the bacterial nucleoid. Curr. Opin. Microbiol. **22**, 94–101.
4. Adams, D.W., Wu, L.J., and Errington, J. (2015). Nucleoid occlusion protein N oc recruits DNA to the bacterial cell membrane . EMBO J. **34**, 491–501.
5. Adler, H.I., Fisher, W.D., Cohen, A., and Hardigree, A.A. (1967). MINIATURE escherichia coli CELLS DEFICIENT IN DNA. Proc. Natl. Acad. Sci. **57**, 321–326.
6. Ah-Seng, Y., Rech, J., Lane, D., and Bouet, J.Y. (2013). Defining the Role of ATP Hydrolysis in Mitotic Segregation of Bacterial Plasmids. PLoS Genet. **9**, e1003956.
7. Attaiech, L., Minnen, A., Kjos, M., Gruber, S., and Veening, J.W. (2015). The ParB-parS chromosome segregation system modulates competence development in Streptococcus pneumoniae. MBio. **6**, e00662–15.
8. Austin, S., and Abeles, A. (1983a). Partition of unit-copy miniplasmids to daughter cells. I. P1 and F miniplasmids contain discrete, interchangeable sequences sufficient to promote equipartition. J. Mol. Biol. **169**, 373–387.
9. Austin, S., and Abeles, A. (1983b). Partition of unit-copy miniplasmids to daughter

cells. II. The partition region of miniplasmid P1 encodes an essential protein and a centromere-like site at which it acts. J. Mol. Biol. **169**, 353–372.

10. Azam, T.A., Hiraga, S., and Ishihama, A. (2000). Two types of localisation of the DNA-binding proteins within the Escherichia coli nucleoid. Genes to Cells. **5**, 61–626.
11. Bailey, M.W., Bisicchia, P., Warren, B.T., Sherratt, D.J., and Männik, J. (2014). Evidence for Divisome Localisation Mechanisms Independent of the Min System and SlmA in Escherichia coli. PLoS Genet. **10**, e1004504.
12. Bakshi, S., Siryaporn, A., Goulian, M., and Weisshaar, J.C. (2012). Superresolution imaging of ribosomes and RNA polymerase in live Escherichia coli cells. Mol. Microbiol. **85**, 21–38.
13. Barillà, D., Rosenberg, M.F., Nobbmann, U., and Hayes, F. (2005). Bacterial DNA segregation dynamics mediated by the polymerizing protein ParF. EMBO J. **24**, 1453–1464.
14. Barillà, D., Carmelo, E., and Hayes, F. (2007). The tail of the ParG DNA segregation protein remodels ParF polymers and enhances ATP hydrolysis via an arginine finger-like motif. Proc. Natl. Acad. Sci. U. S. A. **104**, 1811–1816.
15. Bartosik, A.A., Mierzejewska, J., Thomas, C.M., and Jagura-Burdzy, G. (2009). ParB deficiency in Pseudomonas aeruginosa destabilizes the partner protein ParA and affects a variety of physiological parameters. Microbiology. **155**, 1080–1092.
16. Beaufay, F., Coppine, J., Mayard, A., Laloux, G., De Bolle, X., and Hallez, R. (2015). A NAD -dependent glutamate dehydrogenase coordinates metabolism with cell division in Caulobacter crescentus . EMBO J. **34**, 1786–1800.
17. Beilharz, K., Nováková, L., Fadda, D., Branny, P., Massidda, O., and Veening, J.W. (2012). Control of cell division in Streptococcus pneumoniae by the conserved Ser/Thr protein kinase StkP. Proc. Natl. Acad. Sci. U. S. A. **109**, E905–E913.
18. Ben-Yehuda, S., Rudner, D.Z., and Losick, R. (2003). RacA, a bacterial protein that anchors chromosomes to the cell poles. Science. **299**, 532–536.
19. Bernhardt, T.G., and De Boer, P.A.J. (2005). SlmA, a nucleoid-associated, FtsZ binding protein required for blocking septal ring assembly over chromosomes in E. coli. Mol. Cell. **18**, 555–564.
20. Bi, E., and Lutkenhaus, J. (1990). FtsZ regulates frequency of cell division in Escherichia coli. J. Bacteriol. **172**, 2765–2768.
21. Bi, E., and Lutkenhaus, J. (1991). FtsZ ring structure associated with division in Escherichia coli. Nature. **354**, 161–164.
22. Bi, E., and Lutkenhaus, J. (1993). Cell division inhibitors SulA and MinCD prevent formation of the FtsZ ring. J. Bacteriol. **175**, 1118–1125.
23. de Boer, P.A.J., Crossley, R.E., and Rothfield, L.I. (1989). A division inhibitor and a

topological specificity factor coded for by the minicell locus determine proper placement of the division septum in E. coli. Cell. **56**, 641–649.

24. De Boer, P., Crossley, R., and Rothfield, L. (1992). The essential bacterial cell-division protein FtsZ is a GTPase. Nature. **359**, 254–256.
25. De Boer, P.A.J., Crossley, R.E., and Rothfield, L.I. (1988). Isolation and properties of minB, a complex genetic locus involved in correct placement of the division site in Escherichia coli. J. Bacteriol. **170**, 2106–2112.
26. De Boer, P.A.J., Crossley, R.E., and Rothfield, L.I. (1990). Central role for the Escherichia coli minC gene product in two different cell division-inhibition systems. Proc. Natl. Acad. Sci. U. S. A. **87**, 1129–113.
27. Böhm, K., Giacomelli, G., Schmidt, A., Imhof, A., Koszul, R., Marbouty, M., and Bramkamp, M. (2020). Chromosome organization by a conserved condensin-ParB system in the actinobacterium Corynebacterium glutamicum. Nat. Commun. **11**, 1485.
28. Bouet, J.Y., Ah-Seng, Y., Benmeradi, N., and Lane, D. (2007). Polymerisation of SopA partition ATPase: Regulation by DNA binding and SopB. Mol. Microbiol. **63**, 468–481.
29. Bowman, G.R., Comolli, L.R., Zhu, J., Eckart, M., Koenig, M., Downing, K.H., Moerner, W.E., Earnest, T., and Shapiro, L. (2008). A Polymeric Protein Anchors the Chromosomal Origin/ParB Complex at a Bacterial Cell Pole. Cell. **134**, 945–955.
30. Bowman, G.R., Comolli, L.R., Gaietta, G.M., Fero, M., Hong, S.H., Jones, Y., Lee, J.H., Downing, K.H., Ellisman, M.H., McAdams, H.H., et al. (2010). Caulobacter PopZ forms a polar subdomain dictating sequential changes in pole composition and function. Mol. Microbiol. **76**, 173–189.
31. Bramhill, D., and Thompson, C.M. (1994). GTP-dependent polymerisation of Escherichia coli FtsZ protein to form tubules. Proc. Natl. Acad. Sci. U. S. A. **91**, 5813–5817.
32. Bramkamp, M., Emmins, R., Weston, L., Donovan, C., Daniel, R.A., and Errington, J. (2008). A novel component of the division-site selection system of Bacillus subtilis and a new mode of action for the division inhibitor MinCD. Mol. Microbiol. **70**, 1556–1559.
33. Breier, A.M., and Grossman, A.D. (2007). Whole-genome analysis of the chromosome partitioning and sporulation protein Spo0J (ParB) reveals spreading and origin-distal sites on the Bacillus subtilis chromosome. Mol. Microbiol. **64**, 703–718.
34. Britos, L., Abeliuk, E., Taverner, T., Lipton, M., McAdams, H., and Shapiro, L. (2011). Regulatory response to carbon starvation in caulobacter crescentus. PLoS One. **6**, e18179.
35. Broedersz, C.P., Wang, X., Meir, Y., Loparo, J.J., Rudner, D.Z., and Wingreen, N.S. (2014). Condensation and localisation of the partitioning protein ParB on the bacterial chromosome. Proc. Natl. Acad. Sci. U. S. A. **111**, 8809–8814.

36. Buckstein, M.H., He, J., and Rubin, H. (2008). Characterization of nucleotide pools as a function of physiological state in Escherichia coli. J. Bacteriol. **190**, 718–726.
37. Buss, J., Coltharp, C., Huang, T., Pohlmeyer, C., Wang, S.C., Hatem, C., and Xiao, J. (2013). In vivo organization of the FtsZ-ring by ZapA and ZapB revealed by quantitative super-resolution microscopy. Mol. Microbiol. **89**, 1099–1120.
38. Buss, J.A., Peters, N.T., Xiao, J., and Bernhardt, T.G. (2017). ZapA and ZapB form an FtsZ-independent structure at midcell. Mol. Microbiol. **104**, 652–663.
39. Cabré, E.J., Monterroso, B., Alfonso, C., Sánchez-Gorostiaga, A., Reija, B., Jiménez, M., Vicente, M., Zorrilla, S., and Rivas, G. (2015). The nucleoid occlusion SlmA protein accelerates the disassembly of the FtsZ protein polymers without affecting their GTPase activity. PLoS One. **10**, e0126434.
40. Caldas, P., López-Pelegrín, M., Pearce, D.J.G., Budanur, N.B., Brugués, J., and Loose, M. (2019). Cooperative ordering of treadmilling filaments in cytoskeletal networks of FtsZ and its crosslinker ZapA. Nat. Commun. **10**, 5744.
41. Castillo, D.E., Yang, D., Siopsis, G., and Männik, J. (2016). The role of MatP, ZapA and ZapB in chromosomal organization and dynamics in Escherichia coli. Nucleic Acids Res. **44**, 1216–1226.
42. Caudron, F., and Barral, Y. (2009). Septins and the Lateral Compartmentalization of Eukaryotic Membranes. Dev. Cell. **16**, 493–506.
43. Cha, J.H., and Stewart, G.C. (1997). The divIVA minicell locus of Bacillus subtilis. J. Bacteriol. **5**, 1671–1683.
44. Charaka, V.K., and Misra, H.S. (2012). Functional characterization of the role of the chromosome I partitioning system in genome segregation in Deinococcus radiodurans. J. Bacteriol. **194**, 5739–5748.
45. Chen, B.W., Lin, M.H., Chu, C.H., Hsu, C.E., and Sun, Y.J. (2015). Insights into ParB spreading from the complex structure of Spo0J and parS. Proc. Natl. Acad. Sci. U. S. A. **112**, 6613–6618.
46. Cho, H., and Bernhardt, T.G. (2013). Identification of the SlmA Active Site Responsible for Blocking Bacterial Cytokinetic Ring Assembly over the Chromosome. PLoS Genet. **9**, e1003304.
47. Cho, H., McManus, H.R., Dove, S.L., and Bernhardt, T.G. (2011). Nucleoid occlusion factor SlmA is a DNA-activated FtsZ polymerisation antagonist. Proc. Natl. Acad. Sci. U. S. A. **108**, 3773–3778.
48. Chu, C.H., Yen, C.Y., Chen, B.W., Lin, M.G., Wang, L.H., Tang, K.Z., Hsiao, C.D., and Sun, Y.J. (2019). Crystal structures of HpSoj-DNA complexes and the nucleoid-adaptor complex formation in chromosome segregation. Nucleic Acids Res. **47**, 2113–2129.

49. Corrales-Guerrero, L., He, B., Refes, Y., Panis, G., Bange, G., Viollier, P.H., Steinchen, W., and Thanbichler, M. (2020). Molecular architecture of the DNA-binding sites of the P-loop ATPases MipZ and ParA from Caulobacter crescentus. Nucleic Acids Res. **48**, 4769–4779.
50. Cuthbertson, L., and Nodwell, J.R. (2013). The TetR Family of Regulators. Microbiol. Mol. Biol. Rev. **69**, 326–456.
51. Cuylen, S., Metz, J., and Haering, C.H. (2011). Condensin structures chromosomal DNA through topological links. Nat. Struct. Mol. Biol. **18**, 894–901.
52. Dame, R.T., Rashid, F.Z.M., and Grainger, D.C. (2019). Chromosome organization in bacteria: mechanistic insights into genome structure and function. Nat. Rev. Genet. **21**, 227–242.
53. Debaugny, R.E., Sanchez, A., Rech, J., Labourdette, D., Dorignac, J., Geniet, F., Palmeri, J., Parmeggiani, A., Boudsocq, F., Anton Leberre, V., et al. (2018). A conserved mechanism drives partition complex assembly on bacterial chromosomes and plasmids. Mol. Syst. Biol. **14**, e8516.
54. Deghelt, M., Mullier, C., Sternon, J.F., Francis, N., Laloux, G., Dotreppe, D., Van Der Henst, C., Jacobs-Wagner, C., Letesson, J.J., and De Bolle, X. (2014). G1-arrested newborn cells are the predominant infectious form of the pathogen Brucella abortus. Nat. Commun. **9**, 4366.
55. Din, N., Quardokus, E.M., Sackett, M.J., and Brun, Y. V. (1998). Dominant C-terminal deletions of FtsZ that affect its ability to localise in Caulobacter and its interaction with FtsA. Mol. Microbiol. **27**, 1051–1063.
56. Ditkowski, B., Holmes, N., Rydzak, J., Donczew, M., Bezulska, M., Ginda, K., Kędzierski, P., Zakrzewska-Czerwińska, J., Kelemen, G.H., and Jakimowicz, D. (2013). Dynamic interplay of ParA with the polarity protein, Scy, coordinates the growth with chromosome segregation in Streptomyces coelicolor. Open Biol. **3**, 130006.
57. Dixon, J.R., Selvaraj, S., Yue, F., Kim, A., Li, Y., Shen, Y., Hu, M., Liu, J.S., and Ren, B. (2012). Topological domains in mammalian genomes identified by analysis of chromatin interactions. Nature. **485**, 376–380.
58. Dobbelaere, J., and Barral, Y. (2004). Spatial coordination of cytokinetic events by compartmentalization of the cell cortex. Science. **305**, 393–396.
59. Donczew, M., Mackiewicz, P., Wróbel, A., Flärdh, K., Zakrzewska-Czerwińska, J., and Jakimowicz, D. (2016). ParA and ParB coordinate chromosome segregation with cell elongation and division during Streptomyces sporulation. Open Biol. **6**, 150263.
60. Donovan, C., Schwaiger, A., Krämer, R., and Bramkamp, M. (2010). Subcellular localisation and characterization of the ParAB system from Corynebacterium glutamicum. J. Bacteriol. **192**, 3441–3451.

61. Donovan, C., Sieger, B., Krämer, R., and Bramkamp, M. (2012). A synthetic Escherichia coli system identifies a conserved origin tethering factor in Actinobacteria. Mol. Microbiol. **84**, 105–116.
62. Du, S., and Lutkenhaus, J. (2014). SlmA Antagonism of FtsZ Assembly Employs a Two-pronged Mechanism like MinCD. PLoS Genet. **10**, e1004460.
63. Du, S., Park, K.T., and Lutkenhaus, J. (2015). Oligomerization of FtsZ converts the FtsZ tail motif (conserved carboxy-terminal peptide) into a multivalent ligand with high avidity for partners ZipA and SlmA. Mol. Microbiol. **95**, 173–188.
64. Du, W.L., Dubarry, N., Passot, F.M., Kamgoué, A., Murray, H., Lane, D., and Pasta, F. (2016). Orderly Replication and Segregation of the Four Replicons of Burkholderia cenocepacia J2315. PLoS Genet. **12**, e1006172.
65. Dubarry, N., Willis, C.R., Ball, G., Lesterlin, C., and Armitage, J.P. (2019). In vivo imaging of the segregation of the 2 chromosomes and the cell division proteins of rhodobacter sphaeroides reveals an unexpected role for MipZ. MBio. **10**, e02515-18.
66. Duigou, S., and Boccard, F. (2017). Long range chromosome organization in Escherichia coli: The position of the replication origin defines the non-structured regions and the Right and Left macrodomains. PLoS Genet. **13**, e1006758.
67. Duman, R., Ishikawa, S., Celik, I., Strahl, H., Ogasawara, N., Troc, P., Löwe, J., and Hamoen, L.W. (2013). Structural and genetic analyses reveal the protein SepF as a new membrane anchor for the Z ring. Proc. Natl. Acad. Sci. U. S. A. **110**, E4601–E4610.
68. Dunham, T.D., Xu, W., Funnell, B.E., and Schumacher, M.A. (2009). Structural basis for ADP-mediated transcriptional regulation by P1 and P7 ParA. EMBO J. **28**, 1792–1802.
69. Dupaigne, P., Tonthat, N.K., Espéli, O., Whitfill, T., Boccard, F., and Schumacher, M.A. (2012). Molecular Basis for a Protein-Mediated DNA-Bridging Mechanism that Functions in Condensation of the E. coli Chromosome. Mol. Cell. **48**, 560–571.
70. Ebersbach, G., and Gerdes, K. (2004). Bacterial mitosis: Partitioning protein ParA oscillates in spiral-shaped structures and positions plasmids at mid-cell. Mol. Microbiol. **52**, 385–398.
71. Ebersbach, G., Ringgaard, S., Møller-Jensen, J., Wang, Q., Sherratt, D.J., and Gerdes, K. (2006). Regular cellular distribution of plasmids by oscillating and filament-forming para ATPase of plasmid pB171. Mol. Microbiol. **61**, 1428–1442.
72. Ebersbach, G., Galli, E., Møller-Jensen, J., Löwe, J., and Gerdes, K. (2008). Novel coiled-coil cell division factor ZapB stimulates Z ring assembly and cell division. Mol. Microbiol. **68**, 720–735.
73. Edwards, D.H., and Errington, J. (1997). The Bacillus subtilis DivIVA protein targets to

the division septum and controls the site specificity of cell division. Mol. Microbiol. **24**, 905–915.

74. Ehrle, H.M., Guidry, J.T., Iacovetto, R., Salisbury, A.K., Sandidge, D.J., and Bowman, G.R. (2017). Polar organizing protein PopZ is required for chromosome segregation in Agrobacterium tumefaciens. J. Bacteriol. **199**, 111–117.
75. Erdmann, N., Petroff, T., and Funnell, B.E. (1999). Intracellular localisation of P1 ParB protein depends on ParA and parS. Proc. Natl. Acad. Sci. U. S. A. **96**, 14905–14910.
76. Erickson, H.P. (1995). FtsZ, a prokaryotic homolog of tubulin? Cell. **80**, 367–370.
77. Erickson, H.P., Anderson, D.E., and Osawa, M. (2010). FtsZ in Bacterial Cytokinesis: Cytoskeleton and Force Generator All in One. Microbiol. Mol. Biol. Rev. **74**, 504–528.
78. Eser, U., Chandler-Brown, D., Ay, F., Straight, A.F., Duan, Z., Noble, W.S., and Skotheim, J.M. (2017). Form and function of topologically associating genomic domains in budding yeast. Proc. Natl. Acad. Sci. U. S. A. **114**, E3061–E3070.
79. Espéli, O., Borne, R., Dupaigne, P., Thiel, A., Gigant, E., Mercier, R., and Boccard, F. (2012). A MatP-divisome interaction coordinates chromosome segregation with cell division in E. coli. EMBO J. **31**, 3198–3211.
80. Eswara, P.J., and Ramamurthi, K.S. (2017). Bacterial Cell Division: Nonmodels Poised to Take the Spotlight. Annu. Rev. Microbiol. **71**, 393–411.
81. Fisher, G.L.M., Pastrana, C.L., Higman, V.A., Koh, A., Taylor, J.A., Butterer, A., Craggs, T., Sobott, F., Murray, H., Crump, M.P., et al. (2017). The structural basis for dynamic DNA binding and bridging interactions which condense the bacterial centromere. Elife. **6**, e28086.
82. Fisher, J.K., Bourniquel, A., Witz, G., Weiner, B., Prentiss, M., and Kleckner, N. (2013). Four-dimensional imaging of E. coli nucleoid organization and dynamics in living cells. Cell. **153**, 882–895.
83. Flärdh, K. (2003). Essential role of DivIVA in polar growth and morphogenesis in Streptomyces coelicolor A3(2). Mol. Microbiol. **49**, 1523–1536.
84. Fleurie, A., Cluzel, C., Guiral, S., Freton, C., Galisson, F., Zanella-Cleon, I., di Guilmi, A.M., and Grangeasse, C. (2012). Mutational dissection of the S/T-kinase StkP reveals crucial roles in cell division of Streptococcus pneumoniae. Mol. Microbiol. **83**, 746–758.
85. Fleurie, A., Lesterlin, C., Manuse, S., Zhao, C., Cluzel, C., Lavergne, J.P., Franz-Wachtel, M., MacEk, B., Combet, C., Kuru, E., et al. (2014). MapZ marks the division sites and positions FtsZ rings in Streptococcus pneumoniae. Nature. **516**, 259–262.
86. Fogel, M.A., and Waldor, M.K. (2006). A dynamic, mitotic-like mechanism for bacterial chromosome segregation. Genes Dev. **20**, 3269–3282.
87. Fu, X., Shih, Y.L., Zhang, Y., and Rothfield, L.I. (2001). The MinE ring required for

proper placement of the division site is a mobile structure that changes its cellular location during the Escherichia coli division cycle. Proc. Natl. Acad. Sci. U. S. A. **98**, 980–985.

88. Fuchino, K., Bagchi, S., Cantlay, S., Sandblad, L., Wu, D., Bergman, J., Kamali-Moghaddam, M., Flärdh, K., and Ausmees, N. (2013). Dynamic gradients of an intermediate filament-like cytoskeleton are recruited by a polarity landmark during apical growth. Proc. Natl. Acad. Sci. U. S. A. **110**, E1889–E1897.
89. Funnell, B.E. (2016). ParB partition proteins: Complex formation and spreading at bacterial and plasmid centromeres. Front. Mol. Biosci. **3**, 44.
90. Le Gall, A., Cattoni, D.I., Guilhas, B., Mathieu-Demazière, C., Oudjedi, L., Fiche, J.B., Rech, J., Abrahamsson, S., Murray, H., Bouet, J.Y., et al. (2016). Bacterial partition complexes segregate within the volume of the nucleoid. Nat. Commun. **7**, 12107.
91. Galli, E., and Gerdes, K. (2010). Spatial resolution of two bacterial cell division proteins: ZapA recruits ZapB to the inner face of the Z-ring. Mol. Microbiol. **76**, 1514–1526.
92. Gerdes, K., Howard, M., and Szardenings, F. (2010). Pushing and pulling in prokaryotic DNA segregation. Cell. **141**, 927–942.
93. Graham, T.G.W., Wang, X., Song, D., Etson, C.M., van Oijen, A.M., Rudner, D.Z., and Loparo, J.J. (2014). ParB spreading requires DNA bridging. Genes Dev. **28**, 1228–1238.
94. Gruber, S., and Errington, J. (2009). Recruitment of Condensin to Replication Origin Regions by ParB/SpoOJ Promotes Chromosome Segregation in B. subtilis. Cell. **137**, 685–696.
95. Gruber, S., Veening, J.W., Bach, J., Blettinger, M., Bramkamp, M., and Errington, J. (2014). Interlinked sister chromosomes arise in the absence of condensin during fast replication in B. subtilis. Curr. Biol. **24**, 293–298
96. Gueiros-Filho, F.J., and Losick, R. (2002). A widely conserved bacterial cell division protein that promotes assembly of the tubulin-like protein FtsZ. Genes Dev. **16**, 2544–2556
97. Hadizadeh Yazdi, N., Guet, C.C., Johnson, R.C., and Marko, J.F. (2012). Variation of the folding and dynamics of the Escherichia coli chromosome with growth conditions. Mol. Microbiol. **86**, 1318–1333.
98. Haering, C.H., Farcas, A.M., Arumugam, P., Metson, J., and Nasmyth, K. (2008). The cohesin ring concatenates sister DNA molecules. Nature. **454**, 297–301.
99. Hajduk, I. V., Mann, R., Rodrigues, C.D.A., and Harry, E.J. (2019). The ParB homologs, Spo0J and Noc, together prevent premature midcell Z ring assembly when the early stages of replication are blocked in Bacillus subtilis. Mol. Microbiol. **112**, 766–

784.

100. Hammond, L.R., White, M.L., and Eswara, P.J. (2019). ¡vIVA la DivIVA! J. Bacteriol. **201**, e00245-19.

101. Harms, A., Treuner-Lange, A., Schumacher, D., and Søgaard-Andersen, L. (2013). Tracking of Chromosome and Replisome Dynamics in Myxococcus xanthus Reveals a Novel Chromosome Arrangement. PLoS Genet. **9**, e1003802.

102. Hatano, T., Yamaichi, Y., and Niki, H. (2007). Oscillating focus of SopA associated with filamentous structure guides partitioning of F plasmid. Mol. Microbiol. **64**, 1198–1213.

103. Havey, J.C., Vecchiarelli, A.G., and Funnell, B.E. (2012). ATP-regulated interactions between P1 ParA, ParB and non-specific DNA that are stabilized by the plasmid partition site, parS. Nucleic Acids Res. **40**, 801–812.

104. Hempel, A.M., Wang, S.B., Letek, M., Gil, J.A., and Flärdh, K. (2008). Assemblies of DivIVA mark sites for hyphal branching and can establish new zones of cell wall growth in Streptomyces coelicolor. J. Bacteriol. **190**, 7579–7583,

105. Hester, C.M., and Lutkenhaus, J. (2007). Soj (ParA) DNA binding is mediated by conserved arginines and is essential for plasmid segregation. Proc. Natl. Acad. Sci. U. S. A. **104**, 20326–20331.

106. Hill, N.S., Buske, P.J., Shi, Y., and Levin, P.A. (2013). A Moonlighting Enzyme Links Escherichia coli Cell Size with Central Metabolism. PLoS Genet. **9**, e1003663.

107. Hirota, Y., Ryter, A., and Jacob, F. (1968). Thermosensitive mutants of E. coli affected in the processes of DNA synthesis and cellular division. Cold Spring Harb. Symp. Quant. Biol. **33**, 677–693.

108. Holečková, N., Doubravová, L., Massidda, O., Molle, V., Buriánková, K., Benada, O., Kofroňová, O., Ulrych, A., and Branny, P. (2014). LocZ is a new cell division protein involved in proper septum placement in Streptococcus pneumoniae. MBio. **6**, e01700-14.

109. Holmes, J.A., Follett, S.E., Wang, H., Meadows, C.P., Varga, K., and Bowman, G.R. (2016). Caulobacter PopZ forms an intrinsically disordered hub in organizing bacterial cell poles. Proc. Natl. Acad. Sci. U. S. A. **113**, 12490–12495.

110. Holmes, N.A., Walshaw, J., Leggett, R.M., Thibessard, A., Dalton, K.A., Gillespie, M.D., Hemmings, A.M., Gust, B., and Kelemen, G.H. (2013). Coiled-coil protein Scy is a key component of a multiprotein assembly controlling polarized growth in Streptomyces. Proc. Natl. Acad. Sci. U. S. A. **110**, E397–E406.

111. Hu, Z., and Lutkenhaus, J. (2000). Analysis of MinC reveals two independent domains involved in interaction with MinD and FtsZ. J. Bacteriol. **182**, 3965–3971.

112. Hu, Z., and Lutkenhaus, J. (2001). Topological regulation of cell division in E.

coli: Spatiotemporal oscillation of MinD requires stimulation of its ATPase by MinE and phospholipid. Mol. Cell. **7**, 1137–1343.

113. Hu, Z., and Lutkenhaus, J. (2003). A conserved sequence at the C-terminus of MinD is required for binding to the membrane and targeting MinC to the septum. Mol. Microbiol. **47**, 345–355.

114. Hu, L., Vecchiarelli, A.G., Mizuuchi, K., Neuman, K.C., and Liu, J. (2017). Brownian ratchet mechanisms of ParA-mediated partitioning. Plasmid. **92**, 12–16.

115. Hu, Z., Mukherjee, A., Pichoff, S., and Lutkenhaus, J. (1999). The MinC component of the division site selection system in Escherichia coli interacts with FtsZ to prevent polymerisation. Proc. Natl. Acad. Sci. U. S. A. **96**, 14819–14824.

116. Hu, Z., Gogol, E.P., and Lutkenhaus, J. (2002). Dynamic assembly of MinD on phospholipid vesicles regulated by ATP and MinE. Proc. Natl. Acad. Sci. U. S. A. **99**, 6761–6766.

117. Huang, K.C., Meir, Y., and Wingreen, N.S. (2003). Dynamic structures in Escherichia coli: Spontaneous formation of MinE rings and MinD polar zones. Proc. Natl. Acad. Sci. U. S. A. **100**, 12724–12728.

118. Huang, K.H., Durand-Heredia, J., and Janakiraman, A. (2013). FtsZ ring stability: Of bundles, tubules, crosslinks, and curves. J. Bacteriol. **195**, 1859–1868.

119. Hui, M.P., Galkin, V.E., Yu, X., Stasiak, A.Z., Stasiak, A., Waldor, M.K., and Egelman, E.H. (2010). ParA2, a Vibrio cholerae chromosome partitioning protein, forms left-handed helical filaments on DNA. Proc. Natl. Acad. Sci. U. S. A. **107**, 4590–4595.

120. Hwang, L.C., Vecchiarelli, A.G., Han, Y.W., Mizuuchi, M., Harada, Y., Funnell, B.E., and Mizuuchi, K. (2013). ParA-mediated plasmid partition driven by protein pattern self-organization. EMBO J. **32,** 1238–1249.

121. Iniesta, A.A. (2014). ParABS system in chromosome partitioning in the bacterium Myxococcus xanthus. PLoS One. **9**, e86897.

122. Ireton, K., Gunther IV, N.W., and Grossman, A.D. (1994). spo0J is required for normal chromosome segregation as well as the initiation of sporulation in Bacillus subtilis. J. Bacteriol. **176**, 5320–5329.

123. Jalal, A.S.B., and Le, T.B.K. (2020). Bacterial chromosome segregation by the ParABS system. Open Biol. **10**, 200097.

124. Jalal, A.S., Tran, N.T., and Le, T.B. (2020). ParB spreading on DNA requires cytidine triphosphate in vitro. Elife. **9**, e53515.

125. Jarick, M., Bertsche, U., Stahl, M., Schultz, D., Methling, K., Lalk, M., Stigloher, C., Steger, M., Schlosser, A., and Ohlsen, K. (2018). The serine/threonine kinase Stk and the phosphatase Stp regulate cell wall synthesis in Staphylococcus aureus. Sci.

Rep. **8**, 13693.

126. Jecz, P., Bartosik, A.A., Glabski, K., and Jagura-Burdzy, G. (2015). A single parS sequence from the cluster of four sites closest to oriC is necessary and sufficient for proper chromosome segregation in Pseudomonas aeruginosa. PLoS One. **10**, e0120867.

127. Jensen, S.O., Thompson, L.S., and Harry, E.J. (2005). Cell division in Bacillus subtilis: FtsZ and FtsA association is Z-ring independent, and FtsA is required for efficient midcell Z-ring assembly. J. Bacteriol. **187**, 6536–6544.

128. Jung, A., Raßbach, A., Pulpetta, R.L., van Teeseling, M.C.F., Heinrich, K., Sobetzko, P., Serrania, J., Becker, A., and Thanbichler, M. (2019). Two-step chromosome segregation in the stalked budding bacterium Hyphomonas neptunium. Nat. Commun. **10**, 3290.

129. Kadoya, R., Baek, J.H., Sarker, A., and Chattoraj, D.K. (2011). Participation of chromosome segregation protein ParAI of Vibrio cholerae in chromosome replication. J. Bacteriol. **193**, 1504–1514.

130. El Karoui, M., and Errington, J. (2001). Isolation and characterization of topological specificity mutants of minD in Bacillus subtilis. Mol. Microbiol. **42**, 1211–1221.

131. Kawalek, A., Bartosik, A.A., Glabski, K., and Jagura-Burdzy, G. (2018). Pseudomonas aeruginosa partitioning protein ParB acts as a nucleoid-associated protein binding to multiple copies of a parS-related motif. Nucleic Acids Res. **46**, 4592–4606.

132. Kawalek, A., Wawrzyniak, P., Bartosik, A.A., and Jagura-Burdzy, G. (2020). Rules and exceptions: The role of chromosomal ParB in DNA segregation and other cellular processes. Microorganisms. **8**.

133. Kiekebusch, D., Michie, K.A., Essen, L.O., Löwe, J., and Thanbichler, M. (2012). Localised Dimerisation and Nucleoid Binding Drive Gradient Formation by the Bacterial Cell Division Inhibitor MipZ. Mol. Cell. **46**, 245–259.

134. Koonin, E. V. (1993). A superfamily of ATPases with diverse functions containing either classical or deviant ATP-binding motif. J. Mol. Biol. **229**, 1165–1174.

135. Kusiak, M., Gapczyńska, A., Płochocka, D., Thomas, C.M., and Jagura-Burdzy, G. (2011). Binding and spreading of ParB on DNA determine its biological function in Pseudomonas aeruginosa. J. Bacteriol. **193**, 3342–3355.

136. LaBreck, C.J., Conti, J., Viola, M.G., and Camberg, J.L. (2019). MinC N- and C-Domain interactions modulate ftsz assembly, division site selection, and minD-dependent oscillation in Escherichia coli. J. Bacteriol. **201**, e00374–18.

137. Lagage, V., Boccard, F., and Vallet-Gely, I. (2016). Regional Control of

Chromosome Segregation in Pseudomonas aeruginosa. PLoS Genet. **12**, e1006428.

138. Laloux, G., and Jacobs-Wagner, C. (2014). How do bacteria localise proteins to the cell pole? J. Cell Sci. **127**, 11–9.

139. Le, T.B., and Laub, M.T. (2016). Transcription rate and transcript length drive formation of chromosomal interaction domain boundaries. EMBO J. **35**, 1582–1595.

140. Le, T.B.K., Imakaev, M. V., Mirny, L.A., and Laub, M.T. (2013). High-resolution mapping of the spatial organization of a bacterial chromosome. Science. **342**. 731–734.

141. Lee, P.S., and Grossman, A.D. (2006). The chromosome partitioning proteins Soj (ParA) and Spo0J (ParB) contribute to accurate chromosome partitioning, separation of replicated sister origins, and regulation of replication initiation in Bacillus subtilis. Mol. Microbiol. **60**, 853–869.

142. Leonard, T.A., Butler, P.J.G., and Löwe, J. (2004). Structural analysis of the chromosome segragation protein Spo0J from Thermus thermophilus. Mol. Microbiol. **53**, 419–432.

143. Leonard, T.A., Butler, P.J., and Löwe, J. (2005). Bacterial chromosome segregation: Structure and DNA binding of the Soj dimer - A conserved biological switch. EMBO J. **24**, 270–282.

144. Lewis, P.J., Thaker, S.D., and Errington, J. (2000). Compartmentalization of transcription and translation in Bacillus subtilis. EMBO J. **19**, 710–718.

145. Lewis, R.A., Bignell, C.R., Zeng, W., Jones, A.C., and Thomas, C.M. (2002). Chromosome loss from par mutants of Pseudomonas putida depends on growth medium and phase of growth. Microbiology. **148**, 537–548.

146. Li, H. (2019). Random chromosome partitioning in the polyploid bacterium Thermus thermophilus HB27. G3 Genes, Genomes, Genet. **9**, 1249–1261.

147. Li, H., Angelov, A., Pham, V.T.T., Leis, B., and Liebl, W. (2015). Characterization of chromosomal and megaplasmid partitioning loci in Thermus thermophilus HB27. BMC Genomics. **16**, 317.

148. Lim, H.C., Surovtsev, I. V., Beltran, B.G., Huang, F., Bewersdorf, J., and Jacobs-Wagner, C. (2014). Evidence for a DNA-relay mechanism in ParABS-mediated chromosome segregation. Elife. **3**, e02758.

149. Lin, D.C.H., and Grossman, A.D. (1998). Identification and characterization of a bacterial chromosome partitioning site. *Cell* **92**, 675–685.

150. Lioy, V.S., Cournac, A., Marbouty, M., Duigou, S., Mozziconacci, J., Espéli, O., Boccard, F., and Koszul, R. (2018). Multiscale Structuring of the E. coli Chromosome by Nucleoid-Associated and Condensin Proteins. Cell. **172**, 771–783.

151. Livny, J., Yamaichi, Y., and Waldor, M.K. (2007). Distribution of centromere-

like parS sites in bacteria: Insights from comparative genomics. J. Bacteriol. **189**, 8693–8703.

152. Loose, M., Fischer-Friedrich, E., Herold, C., Kruse, K., and Schwille, P. (2011). Min protein patterns emerge from rapid rebinding and membrane interaction of MinE. Nat. Struct. Mol. Biol. **18**, 577–583.

153. Löwe, J., and Amos, L.A. (1998). Crystal structure of the bacterial cell-division protein FtsZ. Nature. **391**, 203–206.

154. Löwe, J., and Van den Ent, F. (2001). Conserved sequence motif at the C-terminus of the bacterial cell-division protein FtsA. Biochimie. **83**, 117–120.

155. Luger, K., Mäder, A.W., Richmond, R.K., Sargent, D.F., and Richmond, T.J. (1997). Crystal structure of the nucleosome core particle at 2.8 Å resolution. Nature. **389**, 251–260.

156. Lutkenhaus, J., Pichoff, S., and Du, S. (2012). Bacterial cytokinesis: From Z ring to divisome. Cytoskeleton. **69**, 778–790.

157. Lynch, A.S., and Wang, J.C. (1995). SopB protein-mediated silencing of genes linked to the sopC locus of Escherichia coli F plasmid. Proc. Natl. Acad. Sci. U. S. A. **92**, 1896–1900.

158. Machón, C., Fothergill, T.J.G., Barillà, D., and Hayes, F. (2007). Promiscuous Stimulation of ParF Protein Polymerisation by Heterogeneous Centromere Binding Factors. J. Mol. Biol. **374**, 1–8.

159. Madariaga-Marcos, J., Pastrana, C.L., Fisher, G.L.M., Dillingham, M.S., and Moreno-Herrero, F. (2019). ParB dynamics and the critical role of the CTD in DNA condensation unveiled by combined force-fluorescence measurements. Elife. **8**, e43812.

160. Manuse, S., Jean, N.L., Guinot, M., Lavergne, J.P., Laguri, C., Bougault, C.M., Vannieuwenhze, M.S., Grangeasse, C., and Simorre, J.P. (2016). Structure-function analysis of the extracellular domain of the pneumococcal cell division site positioning protein MapZ. Nat. Commun. **7**, 12071.

161. Marbouty, M., Le Gall, A., Cattoni, D.I., Cournac, A., Koh, A., Fiche, J.B., Mozziconacci, J., Murray, H., Koszul, R., and Nollmann, M. (2015). Condensin- and Replication-Mediated Bacterial Chromosome Folding and Origin Condensation Revealed by Hi-C and Super-resolution Imaging. Mol. Cell. **59**, 588–602

162. Margolin, W. (2005). FtsZ and the division of prokaryotic cells and organelles. Nat. Rev. Mol. Cell Biol. **6**, 862–871.

163. Marston, A.L., Thomaides, H.B., Edwards, D.H., Sharpe, M.E., and Errington, J. (1998). Polar localisation of the MinD protein of Bacillus subtilis and its role in selection of the mid-cell division site. Genes Dev. **12**, 3419–3430.

164. Mascarenhas, J., Soppa, J., Strunnikov, A. V., and Graumann, P.L. (2002). Cell cycle-dependent localisation of two novel prokaryotic chromosome segregation and condensation proteins in Bacillus subtilis that interact with SMC protein. EMBO J. **12**, 3108–3118.

165. Maurya, G.K., Modi, K., and Misra, H.S. (2016). Divisome and segrosome components of Deinococcus radiodurans interact through cell division regulatory proteins. Microbiol. (United Kingdom). **162**, 1321–2334.

166. McQuillen, R., and Xiao, J. (2020). Insights into the Structure, Function, and Dynamics of the Bacterial Cytokinetic FtsZ-Ring. Annu. Rev. Biophys. **49**, 309–341.

167. Mercier, R., Petit, M.A., Schbath, S., Robin, S., El Karoui, M., Boccard, F., and Espéli, O. (2008). The MatP/matS Site-Specific System Organizes the Terminus Region of the E. coli Chromosome into a Macrodomain. Cell. **135**, 475–485.

168. Mercy, C., Ducret, A., Slager, J., Lavergne, J.P., Freton, C., Nagarajan, S.N., Garcia, P.S., Noirot-Gros, M.F., Dubarry, N., Nourikyan, J., et al. (2019). RocS drives chromosome segregation and nucleoid protection in Streptococcus pneumoniae. Nat. Microbiol. **4**, 1661–1670.

169. Mesnage, S., Dellarole, M., Baxter, N.J., Rouget, J.B., Dimitrov, J.D., Wang, N., Fujimoto, Y., Hounslow, A.M., Lacroix-Desmazes, S., Fukase, K., et al. (2014). Molecular basis for bacterial peptidoglycan recognition by LysM domains. Nat. Commun. **5**, 4269.

170. Minnen, A., Attaiech, L., Thon, M., Gruber, S., and Veening, J.W. (2011). SMC is recruited to oriC by ParB and promotes chromosome segregation in Streptococcus pneumoniae. Mol. Microbiol. **81**, 676–688.

171. Minnen, A., Bürmann, F., Wilhelm, L., Anchimiuk, A., Diebold-Durand, M.L., and Gruber, S. (2016). Control of Smc Coiled Coil Architecture by the ATPase Heads Facilitates Targeting to Chromosomal ParB/parS and Release onto Flanking DNA. Cell Rep. **14**, 2003–2016.

172. Mohl, D.A., Easter, J., and Gober, J.W. (2001). The chromosome partitioning protein, ParB, is required for cytokinesis in Caulobacter crescentus. Mol. Microbiol. **42**, 741–755.

173. Mori, H., Kondo, A., Ohshima, A., Ogura, T., and Hiraga, S. (1986). Structure and function of the F plasmid genes essential for partitioning. J. Mol. Biol. **192**, 1–15.

174. Mosyak, L., Zhang, Y., Glasfeld, E., Haney, S., Stahl, M., Seehra, J., and Somers, W.S. (2000). The bacterial cell-division protein ZipA and its interaction with an FtsZ fragment revealed by X-ray crystallography. EMBO J. **19**, 3179–3191.

175. Mukherjee, A., Dai, K., and Lutkenhaus, J. (1993). Escherichia coli cell division protein FtsZ is a guanine nucleotide binding protein. Proc. Natl. Acad. Sci. U. S. A. **90**,

1053–1057.

176. Mulder, E., and Woldringh, C.L. (1989). Actively replicating nucleoids influence positioning of division sites in Escherichia coli filaments forming cells lacking DNA. J. Bacteriol. **171**, 4303–4314.

177. Mulder, E., El'Bouhali, M., Pas, E., and Woldringh, C.L. (1990). The Escherichia cohi minB mutation resembles gyrB in defective nucleoid segregation and decreased negative supercoiling of plasmids. MGG Mol. Gen. Genet. **221**, 87–93.

178. Murayama, Y., and Uhlmann, F. (2014). Biochemical reconstitution of topological DNA binding by the cohesin ring. Nature. **505**, 367–371.

179. Murray, H., and Errington, J. (2008). Dynamic Control of the DNA Replication Initiation Protein DnaA by Soj/ParA. *Cell* **135**, 74–84.

180. Murray, H., Ferreira, H., and Errington, J. (2006). The bacterial chromosome segregation protein Spo0J spreads along DNA from parS nucleation sites. Mol. Microbiol. **61**, 1352–1361.

181. Mysliwiec, T.H., Errington, J., Vaidya, A.B., and Bramucci, M.G. (1991). The Bacillus subtilis spo0J gene: Evidence for involvement in catabolite repression of sporulation. J. Bacteriol **173**, 1911–1919.

182. Nogales, E., Downing, K.H., Amos, L.A., and Löwe, J. (1998). Tubulin and FtsZ form a distinct family of GTPases. Nat. Struct. Biol. **5**, 451–458.

183. Nolivos, S., and Sherratt, D. (2014). The bacterial chromosome: Architecture and action of bacterial SMC and SMC-like complexes. FEMS Microbiol. Rev. **38**, 380–392.

184. Nolivos, S., Upton, A.L., Badrinarayanan, A., Müller, J., Zawadzka, K., Wiktor, J., Gill, A., Arciszewska, L., Nicolas, E., and Sherratt, D. (2016). MatP regulates the coordinated action of topoisomerase IV and MukBEF in chromosome segregation. Nat. Commun. **7**, 10466.

185. Nora, E.P., Lajoie, B.R., Schulz, E.G., Giorgetti, L., Okamoto, I., Servant, N., Piolot, T., Van Berkum, N.L., Meisig, J., Sedat, J., et al. (2012). Spatial partitioning of the regulatory landscape of the X-inactivation centre. Nature. **485**, 381–385.

186. Nourikyan, J., Kjos, M., Mercy, C., Cluzel, C., Morlot, C., Noirot-Gros, M.F., Guiral, S., Lavergne, J.P., Veening, J.W., and Grangeasse, C. (2015). Autophosphorylation of the Bacterial Tyrosine-Kinase CpsD Connects Capsule Synthesis with the Cell Cycle in Streptococcus pneumoniae. PLoS Genet. **11**, e1005518.

187. Nováková, L., Bezoušková, S., Pompach, P., Špidlová, P., Sasková, L., Weiser, J., and Branny, P. (2010). Identification of multiple substrates of the StkP Ser/Thr protein kinase in Streptococcus pneumoniae. J. Bacteriol. **192**, 3629–3638.

188. Olins, D.E., and Olins, A.L. (1972). Physical studies of isolated eucaryotic nuclei. J. Cell Biol. **53**, 715–736.

189. Oliva, M.A., Cordell, S.C., and Löwe, J. (2004). Structural insights into FtsZ protofilament formation. Nat. Struct. Mol. Biol. **11**, 1243–1250.

190. Osorio-Valeriano, M., Altegoer, F., Steinchen, W., Urban, S., Liu, Y., Bange, G., and Thanbichler, M. (2019). ParB-type DNA Segregation Proteins Are CTP-Dependent Molecular Switches. Cell. **179**, 1512–1524.e15.

191. Osorio, A., Camarena, L., Cevallos, M.A., and Poggio, S. (2017). A new essential cell division protein in Caulobacter crescentus. J. Bacteriol. **199**, e00811–16.

192. Pang, T., Wang, X., Lim, H.C., Bernhardt, T.G., and Rudner, D.Z. (2017). The nucleoid occlusion factor Noc controls DNA replication initiation in Staphylococcus aureus. PLoS Genet. **13**, e1006908.

193. Park, K.T., Wu, W., Battaile, K.P., Lovell, S., Holyoak, T., and Lutkenhaus, J. (2011). The min oscillator uses MinD-dependent conformational changes in MinE to spatially regulate cytokinesis. Cell. **146**, 396–407.

194. Patrick, J.E., and Kearns, D.B. (2008). MinJ (YvjD) is a topological determinant of cell division in Bacillus subtilis. Mol. Microbiol. **70**, 1166–1179.

195. Pichoff, S., and Lutkenhaus, J. (2002). Unique and overlapping roles for ZipA and FtsA in septal ring assembly in Escherichia coli. EMBO J. **21**, 685–693.

196. Pióro, M., and Jakimowicz, D. (2020). Chromosome Segregation Proteins as Coordinators of Cell Cycle in Response to Environmental Conditions. Front. Microbiol. **11**, 588.

197. Pióro, M., Małecki, T., Portas, M., Magierowska, I., Trojanowski, D., Sherratt, D., Zakrzewska-Czerwińska, J., Ginda, K., and Jakimowicz, D. (2019). Competition between DivIVA and the nucleoid for ParA binding promotes segrosome separation and modulates mycobacterial cell elongation. Mol. Microbiol. **111**, 204–220.

198. Pratto, F., Cicek, A., Weihofen, W.A., Lurz, R., Saenger, W., and Alonso, J.C. (2008). Streptococcus pyogenes pSM19035 requires dynamic assembly of ATP-bound ParA and ParB on parS DNA during plasmid segregation. Nucleic Acids Res. **36**, 3676–3689.

199. Ptacin, J.L., Lee, S.F., Garner, E.C., Toro, E., Eckart, M., Comolli, L.R., Moerner, W.E., and Shapiro, L. (2010). A spindle-like apparatus guides bacterial chromosome segregation. Nat. Cell Biol. **12**, 791–798.

200. Ptacin, J.L., Gahlmann, A., Bowman, G.R., Perez, A.M., Von Diezmann, A.R.S., Eckart, M.R., Moerner, W.E., and Shapiro, L. (2014). Bacterial scaffold directs pole-specific centromere segregation. Proc. Natl. Acad. Sci. U. S. A. **111**, E2046–E2055

201. Ramos, A., Honrubia, M.P., Valbuena, N., Vaquera, J., Mateos, L.M., and Gil, J.A. (2003). Involvement of DivIVA in the morphology of the rod-shaped actinomycete Brevibacterium lactofermentum. Microbiology. **149**, 3531–3542.

202. Raskin, D.M., and De Boer, P.A.J. (1997). The MinE ring: An FtsZ-independent cell structure required for selection of the correct division site in E. coli. Cell. **91**, 685–694.

203. RayChaudhuri, D., and Park, J.T. (1992). Escherichia coli cell-division gene ftsZ encodes a novel GTP-binding protein. Nature. **359**, 251–254.

204. Reeve, J.N., Mendelson, N.H., Coyne, S.I., Hallock, L.L., and Cole, R.M. (1973). Minicells of Bacillus subtilis. J. Bacteriol. **114**, 860–873.

205. Ringgaard, S., Van Zon, J., Howard, M., and Gerdes, K. (2009). Movement and equipositioning of plasmids by ParA filament disassembly. Proc. Natl. Acad. Sci. U. S. A. **106**, 19369–19374.

206. Robles-Ramos, M.Á., Margolin, W., Sobrinos-Sanguino, M., Alfonso, C., Rivas, G., Monterroso, B., and Zorrilla, S. (2020). The nucleoid occlusion protein SlmA binds to lipid membranes. MBio. **11**, e02094–20.

207. Rodionov, O., ŁObocka, M., and Yarmolinsky, M. (1999). Silencing of genes flanking the P1 plasmid centromere. Science. **283**, 546–549.

208. Rodrigues, C.D.A., and Harry, E.J. (2012). The min system and nucleoid occlusion are not required for identifying the division site in bacillus subtilis but ensure its efficient utilization. PLoS Genet. **8**, e1002561.

209. Rossmann, F.M., Rick, T., Mrusek, D., Sprankel, L., Dörrich, A.K., Leonhard, T., Bubendorfer, S., Kaever, V., Bange, G., and Thormann, K.M. (2019). The GGDEF domain of the phosphodiesterase PdeB in Shewanella putrefaciens mediates recruitment by the polar landmark protein HubP. J. Bacteriol. **201**, e00534–18

210. Sanchez, A., Cattoni, D.I., Walter, J.C., Rech, J., Parmeggiani, A., Nollmann, M., and Bouet, J.Y. (2015). Stochastic Self-Assembly of ParB Proteins Builds the Bacterial DNA Segregation Apparatus. Cell Syst. **1**, 163–173.

211. Santi, I., and McKinney, J.D. (2015). Chromosome organization and replisome dynamics in Mycobacterium smegmatis. MBio. **6**, e01999-14.

212. Sasková, L., Nováková, L., Basler, M., and Branny, P. (2007). Eukaryotic-type serine/threonine protein kinase StkP is a global regulator of gene expression in Streptococcus pneumoniae. J. Bacteriol. **189**, 4168–4179.

213. Schlimpert, S., Wasserstrom, S., Chandra, G., Bibb, M.J., Findlay, K.C., Flärdh, K., and Buttner, M.J. (2017). Two dynamin-like proteins stabilize FtsZ rings during Streptomyces sporulation. Proc. Natl. Acad. Sci. U. S. A. **114**, E6176–E6183.

214. Schofield, W.B., Lim, H.C., and Jacobs-Wagner, C. (2010). Cell cycle

coordination and regulation of bacterial chromosome segregation dynamics by polarly localised proteins. EMBO J. **29**, 3068–3081.

215. Schumacher, M.A. (2017). Bacterial nucleoid occlusion: Multiple mechanisms for preventing chromosome bisection during cell division. Subcell. Biochem. **84**, 267–298.

216. Schumacher, M.A., and Zeng, W. (2016). Structures of the nucleoid occlusion protein SlmA bound to DNA and the C-terminal domain of the cytoskeletal protein FtsZ. Proc. Natl. Acad. Sci. U. S. A. **113**, 4988–4993.

217. Schumacher, D., Bergeler, S., Harms, A., Vonck, J., Huneke-Vogt, S., Frey, E., and Søgaard-Andersen, L. (2017). The PomXYZ Proteins Self-Organize on the Bacterial Nucleoid to Stimulate Cell Division. Dev. Cell. **41**, 299–314.

218. Sexton, T., Yaffe, E., Kenigsberg, E., Bantignies, F., Leblanc, B., Hoichman, M., Parrinello, H., Tanay, A., and Cavalli, G. (2012). Three-dimensional folding and functional organization principles of the Drosophila genome. Cell. **148**, 458–472.

219. Shebelut, C.W., Guberman, J.M., Van Teeffelen, S., Yakhnina, A.A., and Gitai, Z. (2010). Caulobacter chromosome segregation is an ordered multistep process. Proc. Natl. Acad. Sci. U. S. A. **107**, 14194–14198.

220. Sievers, J., Raether, B., Perego, M., and Errington, J. (2002). Characterization of the parB-like yyaA gene of Bacillus subtilis. J. Bacteriol. **184**, 1102–1111.

221. Soh, Y.-M., Davidson, I.F., Zamuner, S., Basquin, J., Bock, F.P., Taschner, M., Veening, J.-W., De, P., Rios, L., Peters, J.-M., et al. (2019). Self-organization of *parS* centromeres by the ParB CTP hydrolase. Science. **366**, 1129–1133.

222. Song, D., Rodrigues, K., Graham, T.G.W., and Loparo, J.J. (2017). A network of cis and trans interactions is required for ParB spreading. Nucleic Acids Res. **45**, 7106–7117.

223. Soppa, J., Kobayashi, K., Noirot-Gros, M.F., Oesterhelt, D., Ehrlich, S.D., Dervyn, E., Ogasawara, N., and Moriya, S. (2002). Discovery of two novel families of proteins that are proposed to interact with prokaryotic SMC proteins, and characterization of the Bacillus subtilis family members ScpA and ScpB. Mol. Microbiol. **45**, 59–71.

224. Suefuji, K., Valluzzi, R., and RayChaudhuri, D. (2002). Dynamic assembly of MinD into filament bundles modulated by ATP, phospholipids, and MinE. Proc. Natl. Acad. Sci. U. S. A. **99**, 16776–16781.

225. Sullivan, N.L., Marquis, K.A., and Rudner, D.Z. (2009). Recruitment of SMC by ParB-parS Organizes the Origin Region and Promotes Efficient Chromosome Segregation. Cell. **137**, 697–707.

226. Surovtsev, I. V., and Jacobs-Wagner, C. (2018). Subcellular Organization: A

Critical Feature of Bacterial Cell Replication. Cell. **172**, 1271–1293.

227. Szafran, M., Skut, P., Ditkowski, B., Ginda, K., Chandra, G., Zakrzewska-Czerwińska, J., and Jakimowicz, D. (2013). Topoisomerase I (topA) is recruited to ParB complexes and is: Required for proper chromosome organization during streptomyces Coelicolor sporulation. J. Bacteriol. **195**, 4445–4455.

228. Taheri-Araghi, S., Bradde, S., Sauls, J.T., Hill, N.S., Levin, P.A., Paulsson, J., Vergassola, M., and Jun, S. (2015). Cell-size control and homeostasis in bacteria. Curr. Biol. **27**, 1392.

229. Takekawa, N., Kwon, S., Nishioka, N., Kojima, S., and Homma, M. (2016). HubP, a polar landmark protein, regulates flagellar number by assisting in the proper polar localisation of FlhG in Vibrio alginolyticus. J. Bacteriol. **198**, 3091–3098.

230. Taylor, J.A., Pastrana, C.L., Butterer, A., Pernstich, C., Gwynn, E.J., Sobott, F., Moreno-Herrero, F., and Dillingham, M.S. (2015). Specific and non-specific interactions of ParB with DNA: Implications for chromosome segregation. Nucleic Acids Res. **43**, 719–731.

231. Taylor, J.A., Panis, G., Viollier, P.H., and Marczynski, G.T. (2017). A novel nucleoid-associated protein coordinates chromosome replication and chromosome partition. Nucleic Acids Res. **45**, 8916–8929.

232. Thanbichler, M., and Shapiro, L. (2006). MipZ, a Spatial Regulator Coordinating Chromosome Segregation with Cell Division in Caulobacter. Cell. **126**, 147–162.

233. Tonthat, N.K., Arold, S.T., Pickering, B.F., Van Dyke, M.W., Liang, S., Lu, Y., Beuria, T.K., Margolin, W., and Schumacher, M.A. (2011). Molecular mechanism by which the nucleoid occlusion factor, SlmA, keeps cytokinesis in check. EMBO J. **30**, 154–164.

234. Tonthat, N.K., Milam, S.L., Chinnam, N., Whitfill, T., Margolin, W., and Schumacher, M.A. (2013). SlmA forms a higher-order structure on DNA that inhibits cytokinetic Z-ring formation over the nucleoid. Proc. Natl. Acad. Sci. U. S. A. **110**, 10586–10591.

235. Toro-Nahuelpan, M., Corrales-Guerrero, L., Zwiener, T., Osorio-Valeriano, M., Müller, F.D., Plitzko, J.M., Bramkamp, M., Thanbichler, M., and Schüler, D. (2019). A gradient-forming MipZ protein mediating the control of cell division in the magnetotactic bacterium Magnetospirillum gryphiswaldense. Mol. Microbiol. **112**, 1423–1439.

236. Toro, E., Hong, S.H., McAdams, H.H., and Shapiro, L. (2008). Caulobacter requires a dedicated mechanism to initiate chromosome segregation. Proc. Natl. Acad. Sci. U. S. A. **105**, 15435–15440.

237. Tran, N.T., Laub, M.T., and Le, T.B.K. (2017). SMC Progressively Aligns

Chromosomal Arms in Caulobacter crescentus but Is Antagonized by Convergent Transcription. Cell Rep. **20**, 2057–2071.

238. Tran, N.T., Stevenson, C.E., Som, N.F., Thanapipatsiri, A., Jalal, A.S.B., and Le, T.B.K. (2018). Permissive zones for the centromere-binding protein ParB on the Caulobacter crescentuschromosome. Nucleic Acids Res. **46**, 1196–1209.

239. Treuner-Lange, A., Aguiluz, K., van der Does, C., Gómez-Santos, N., Harms, A., Schumacher, D., Lenz, P., Hoppert, M., Kahnt, J., Muñoz-Dorado, J., et al. (2013). PomZ, a ParA-like protein, regulates Z-ring formation and cell division in Myxococcus xanthus. Mol. Microbiol. **87**, 235–253.

240. Umbarger, M.A., Toro, E., Wright, M.A., Porreca, G.J., Baù, D., Hong, S.H., Fero, M.J., Zhu, L.J., Marti-Renom, M.A., McAdams, H.H., et al. (2011). The three-dimensional architecture of a bacterial genome and its alteration by genetic perturbation. Mol. Cell. **44**, 252–264.

241. Val, M.E., Marbouty, M., De Lemos Martins, F., Kennedy, S.P., Kemble, H., Bland, M.J., Possoz, C., Koszul, R., Skovgaard, O., and Mazel, D. (2016). A checkpoint control orchestrates the replication of the two chromosomes of Vibrio cholerae. Sci. Adv. **22**, e1501914.

242. Valens, M., Penaud, S., Rossignol, M., Cornet, F., and Boccard, F. (2004). Macrodomain organization of the Escherichia coli chromosome. EMBO J. **23**, 4330–4341.

243. Valens, M., Thiel, A., and Boccard, F. (2016). The MaoP/maoS Site-Specific System Organizes the Ori Region of the E. coli Chromosome into a Macrodomain. PLoS Genet. **12**, e1006309.

244. Vecchiarelli, A.G., Han, Y.W., Tan, X., Mizuuchi, M., Ghirlando, R., Biertümpfel, C., Funnell, B.E., and Mizuuchi, K. (2010). ATP control of dynamic P1 ParA-DNA interactions: A key role for the nucleoid in plasmid partition. Mol. Microbiol. **78**, 78–91.

245. Vecchiarelli, A.G., Mizuuchi, K., and Funnell, B.E. (2012). Surfing biological surfaces: Exploiting the nucleoid for partition and transport in bacteria. Mol. Microbiol. **86**, 513–523.

246. Vecchiarelli, A.G., Hwang, L.C., and Mizuuchi, K. (2013a). Cell-free study of F plasmid partition provides evidence for cargo transport by a diffusion-ratchet mechanism. Proc. Natl. Acad. Sci. U. S. A. **110**, E1390-1397

247. Vecchiarelli, A.G., Havey, J.C., Ing, L.L., Wong, E.O.Y., Waples, W.G., and Funnell, B.E. (2013b). Dissection of the ATPase active site of P1 ParA reveals multiple active forms essential for plasmid partition. J. Biol. Chem. **288**, 17823–17831.

248. Vecchiarelli, A.G., Neuman, K.C., and Mizuuchi, K. (2014). A propagating ATPase gradient drives transport of surface-confined cellular cargo. Proc. Natl. Acad.

Sci. U. S. A. **111**, 4880–4885.

249. Veiga, H., Jorge, A.M., and Pinho, M.G. (2011). Absence of nucleoid occlusion effector Noc impairs formation of orthogonal FtsZ rings during Staphylococcus aureus cell division. Mol. Microbiol. **80**, 1366–1380.

250. Viollier, P.H., Thanbichler, M., McGrath, P.T., West, L., Meewan, M., McAdams, H.H., and Shapiro, L. (2004). Rapid and sequential movement of individual chromosomal loci to specific subcellular locations during bacterial DNA replication. Proc. Natl. Acad. Sci. U. S. A. **101**, 9257–9262.

251. Volante, A., and Alonso, J.C. (2015). Molecular anatomy of ParA-ParA and ParA-ParB interactions during plasmid partitioning. J. Biol. Chem. **290**, 18782–18795.

252. Wang, L., and Lutkenhaus, J. (1998). FtsK is an essential cell division protein that is localised to the septum and induced as part of the SOS response. Mol. Microbiol. **29**, 731–740.

253. Wang, X., Tang, O.W., Riley, E.P., and Rudner, D.Z. (2014). The SMC condensin complex is required for origin segregation in Bacillus subtilis. Curr. Biol. **24**, 287–292.

254. Wang, X., Le, T.B.K., Lajoie, B.R., Dekker, J., Laub, M.T., and Rudner, D.Z. (2015). Condensin promotes the juxtaposition of dna flanking its loading site in Bacillus subtilis. Genes Dev. **29**, 1661–1675.

255. Wang, X., Brandão, H.B., Le, T.B.K., Laub, M.T., and Rudner, D.Z. (2017). Bacillus subtilis SMC complexes juxtapose chromosome arms as they travel from origin to terminus. Science. **355**, 524–527.

256. Weart, R.B., Lee, A.H., Chien, A.C., Haeusser, D.P., Hill, N.S., and Levin, P.A. (2007). A Metabolic Sensor Governing Cell Size in Bacteria. Cell. **130**, 335–347.

257. Whiteley, A.T., Eaglesham, J.B., de Oliveira Mann, C.C., Morehouse, B.R., Lowey, B., Nieminen, E.A., Danilchanka, O., King, D.S., Lee, A.S.Y., Mekalanos, J.J., et al. (2019). Bacterial cGAS-like enzymes synthesize diverse nucleotide signals. Nature. **567**, 194–199.

258. Wilhelm, L., Bürmann, F., Minnen, A., Shin, H.C., Toseland, C.P., Oh, B.H., and Gruber, S. (2015). SMC condensin entraps chromosomal DNA by an ATP hydrolysis dependent loading mechanism in Bacillus subtilis. Elife. **4**, e06659.

259. Willemse, J., Borst, J.W., De Waal, E., Bisseling, T., and Van Wezel, G.P. (2011). Positive control of cell division: FtsZ is recruited by SsgB during sporulation of Streptomyces. Genes Dev. **25**, 89–99.

260. Woldringh, C.L. (2002). The role of co-transcriptional translation and protein translocation (transertion) in bacterial chromosome segregation. Mol. Microbiol. **45**, 17–29.

261. Woldringh, C.L., Mulder, E., Huls, P.G., and Vischer, N. (1991). Toporegulation of bacterial division according to the nucleoid occlusion model. Res. Microbiol. **142**, 309–320.

262. Wu, L.J., and Errington, J. (2004). Coordination of cell division and chromosome segregation by a nucleoid occlusion protein in Bacillus subtilis. Cell. **117**, 915–925.

263. Wu, L.J., Ishikawa, S., Kawai, Y., Oshima, T., Ogasawara, N., and Errington, J. (2009). Noc protein binds to specific DNA sequences to coordinate cell division with chromosome segregation. EMBO J. **28**, 1940–1952.

264. Yamaichi, Y., Fogel, M.A., McLeod, S.M., Hui, M.P., and Waldor, M.K. (2007). Distinct centromere-like parS sites on the two chromosomes of Vibrio spp. J. Bacteriol. **189**, 5314–5324.

265. Yamaichi, Y., Bruckner, R., Ringgaard, S., Möll, A., Ewen Cameron, D., Briegel, A., Jensen, G.J., Davis, B.M., and Waldor, M.K. (2012). A multidomain hub anchors the chromosome segregation and chemotactic machinery to the bacterial pole. Genes Dev. **26**, 2348–2360.

266. Yatskevich, S., Rhodes, J., and Nasmyth, K. (2019). Organization of Chromosomal DNA by SMC Complexes. Annu. Rev. Genet. **53**, 445–482.

267. Yildirim, A., and Feig, M. (2018). High-resolution 3D models of Caulobacter crescentus chromosome reveal genome structural variability and organization. Nucleic Acids Res. **46**, 3937–3952.

268. Yu, W., Herbert, S., Graumann, P.L., and Götz, F. (2010). Contribution of SMC (Structural Maintenance of Chromosomes) and spoIIIE to chromosome segregation in staphylococci. J. Bacteriol. **192**, 4067–4073.

269. Yu, Y., Zhou, J., Gueiros-Filho, F.J., Kearns, D.B., and Jacobson, S.C. (2021). Noc Corrals Migration of FtsZ Protofilaments during Cytokinesis in Bacillus subtilis . MBio. **12**, e02964–20.

270. Zhang, H., and Schumacher, M.A. (2017). Structures of partition protein para with nonspecific dna and parb effector reveal molecular insights into principles governing walker-box dna segregation. Genes Dev. **31**, 481–492.

Chapter 2: Materials and Methods

2.7 *In vitro* measurement of protein-DNA interactions

2.7.1 Measurement of protein-DNA interactions by Bio-layer interferometry (BLI)

2.7.2 Measurement of protein-DNA interactions by Surface Plasmon Resonance (SPR)

2.8 Measurement of protein-NTP interactions by isothermal titration calorimetry (ITC)

2.9 X-ray crystallisation and cryoprotection of ParB and Noc variants

2.9.1 General X-ray crystallography data collection and reduction

2.9.2 Crystallisation and cryoprotection of the DNA-binding domain (DBD) of *C. crescentus* ParB in complex with *parS*

2.9.3 Crystallisation and cryoprotection of the C-terminally truncated (ΔCTD) ParB (QKKR+K227) in complex with *NBS*

2.9.4 Crystallisation and cryoprotection of the Noc (DBD) in complex with 22-bp *NBS*

2.9.5 Crystallisation and cryoprotection of the *C. crescentus* ParBΔCTD-*parS* complex

2.9.6 Crystallisation and cryoprotection of the *C. crescentus* ParBΔCTD-CTPɣS complex

2.9.7 Crystallisation and cryoprotection of the *C. crescentus* ParBΔ44NΔCTD-CDP complex

2.9.8 Crystallisation and cryoprotection of the *G. thermoleovorans* NocΔCTD

2.9.9 Crystallisation and cryoprotection of the *G. thermoleovorans* NocNΔ26ΔCTD Noc

2.10 Structure determination and refinement of ParB and Noc variant structures

2.10.1 Structure determination and refinement of the *C. crescentus* ParB (DBD)-*parS* complex

2.10.2 Structure determination and refinement of the *C. crescentus* ParBΔCTD (QKKR+K227)-*NBS* complex

2.10.3 Structure determination and refinement of the *B. subtilis* Noc (DBD)-*NBS* structure

2.10.4 Structure determination and refinement of the *C. crescentus* ParBΔCTD-*parS* structure

2.10.5 Structure determination and refinement of the *C. crescentus* ParBΔCTD-CTPɣS co-crystal structure

2.10.6 Structure determination and refinement of the *C. crescentus* ParBΔ44NΔCTD-CDP complex

2.10.7 Structure determination and refinement of the *G. thermoleovorans* NocΔCTD structure

2.10.8 Structure determination and refinement of the *G. thermoleovorans* NocNΔ26ΔCTD structure

2.11 Analysis of crystal structures

2.12 Differential radial capillary action of ligand assay (DRaCALA) or membrane-spotting assay

2.13 Magnetic tweezer assays

2.14 Immunoblot analysis

2.15 Genome-wide techniques

2.16.1 Chromatin immunoprecipitation coupled with deep sequencing (ChIP-seq)

2.16.2 Generation of ChIP-seq profiles

2.16 Measurement of NTPase activity by EnzChek phosphate assay

2.17 *In vitro* crosslinking using a sulfhydryl-to-sulfhydryl crosslinker bismaleimidoethane (BMOE)

2.17.1 General in vitro crosslinking using BMOE

2.17.2 DNA loading assays

2.17.3 Nuclease treatment assays

2.18 Liposomes preparation

2.19 Liposome co-sedimentation assays

2.19.1 General liposome co-sedimentation assays

2.19.2 Nuclease treatment assays

2.19.3 Liposome re-sedimentation experiments

2.20 Liposome flotation assays

2.21 References

2.1 Bacterial strains, plasmids and primers

2.1.1 E. coli strains

Strains	Strains/descriptions	Source
DH5α	*E. coli* host for DNA cloning and propagation of plasmid	Le lab collection
Rosetta (DE3)	*E. coli* host for protein overexpression from an IPTG-inducible T7 promoter	Merck

2.1.2 C. crescentus strains

Strains	Strains/descriptions	Source
CB15N	Wild type synchronizable *C. crescentus*	Le lab collection
MT148	CB15N *parB*::P_{xyl}-*parB mipZ::mipZ-yfp*	Gift from Martin Thanbichler
AJS35	CB15N + pMT158::1xFLAG-*C. crescentus* ParB (D275K), kanamycin^R	This study
AJS44	CB15N + pMT158::1xFLAG-*C. crescentus* ParB (G278K), kanamycin^R	This study
AJS37	CB15N + pMT158::1xFLAG-*C. crescentus* ParB (S279K), kanamycin^R	This study
AJS43	CB15N + pMT158::1xFLAG-*C. crescentus* ParB (T280K), kanamycin^R	This study
AJS36	CB15N + pMT158::1xFLAG-*C. crescentus* ParB (T282K), kanamycin^R	This study
AJS46	CB15N + pMT158::1xFLAG-*C. crescentus* ParB (D275K, G278K), kanamycin^R	This study
AJS45	CB15N + pMT158::1xFLAG-*C. crescentus* ParB (D275K, T282K), kanamycin^R	This study
AJS47	CB15N + pMT158::1xFLAG-*C. crescentus* ParB (D275K, G278K, T282K), kanamycin^R	This study
AJS81	CB15N + pMT158::1xFLAG-*C. crescentus* ParB, (D275K, G278K, T280K, T282K), kanamycin^R	This study
AJS82	CB15N + pMT158::1xFLAG-*C. crescentus* ParB, (D275K, G278K, S279K, T280K, T282K), kanamycin^R	This study
	MT148+ vanA::Pvan 1xFLAG-C. crescentus ParB, kanamycin^R	This study

	MT148+ vanA::Pvan 1xFLAG-yfp	This study
TLS1858	MT148+ vanA::Pvan 1xFLAG-*C. crescentus* ParB (D275K), kanamycin^R	This study
TLS1859	MT148+ vanA::Pvan 1xFLAG-*C. crescentus* ParB (G278K), kanamycin^R	This study
AJS49	MT148+ vanA::Pvan 1xFLAG-*C. crescentus* ParB (S279K), kanamycin^R	This study
AJS48	MT148+ vanA::Pvan 1xFLAG-*C. crescentus* ParB (T280K), kanamycin^R	This study
TLS1860	MT148+ vanA::Pvan 1xFLAG-*C. crescentus* ParB (T282K), kanamycin^R	This study
AJS51	MT148+ vanA::Pvan 1xFLAG-*C. crescentus* ParB (D275K, G278K), kanamycin^R	This study
AJS50	MT148+ vanA::Pvan 1xFLAG-*C. crescentus* ParB (D275K, T282K), kanamycin^R	This study
AJS52	MT148+ vanA::Pvan 1xFLAG-*C. crescentus* ParB (D275K, G278K, T282K), kanamycin^R	This study
AJS82	MT148+ vanA::Pvan 1xFLAG-*C. crescentus* ParB (D275K, G278K, T280K, T282K), kanamycin^R	This study
AJS83	MT148+ vanA::Pvan 1xFLAG-*C. crescentus* ParB, (D275K, G278K, S279K, T280K, T282K), kanamycin^R	This study
DWA117	*B. subtilis* 168CA (*trpC2*) *Δnoc::tet*	(Adams et. al., 2015)
DWA206	*B. subtilis* 168CA (trpC2) *Δnoc::tet ΩamyE::[spc Pxyl-noc (WT)-myfp)*	(Adams et. al., 2015)
DWA382	*B. subtilis* 168CA (trpC2) *Δnoc::tet ΩamyE::[spc Pxyl-nocNΔ10-myfp*)	(Adams et. al., 2015)
DWA546	*B. subtilis* 168CA (trpC2) *Δnoc::tet ΩamyE*::[*spc Pxyl-nco (R89A)-myfp*)	(Adams et. al., 2015)
4746	*B. subtilis* 168CA (trpC2) Δnoc::tet ΩamyE::[*spc Pxyl-nco (N121S)-yfpmut1*)	This study
DWA564	*B. subtilis 168CA* (trpC2) *Δnoc::tet ΔminCD::kan ΩamyE*::[*spc Pxyl-noc (WT)-myfp*)	(Adams et. al., 2015)
DWA566	*B. subtilis 168CA* (trpC2) Δnoc::tet ΔminCD::kan ΩamyE::[spc Pxyl-nocNΔ10-myfp)	(Adams et. al., 2015)

DWA600	*B. subtilis 168CA* (trpC2) *Δnoc::tet ΔminCD::kan ΩamyE*::[*spc Pxyl-nco (R89A)-myfp*)	(Adams et. al., 2015)
4747	*B. subtilis* 168CA (trpC2) *Δnoc::tet ΔminCD::kan ΩamyE::[spc Pxyl-noc (N121S)-yfpmut1*)	This study

2.1.3 Plasmids

Plasmid	**Description**	**Source**
pET21b	ENTRY vector for Gateway cloning, carbenicillin^R	Invitrogen
pET21b::ParB-$(His)_6$	overexpression of ParB-$(His)_6$ from an IPTG-inducible T7 promoter	Gift of Christine Jacob-Wagner
pET21b::ParB (R104A)-$(His)_6$	pET21b::*C. crescentus*-ParB- (R104A) $(His)_6$	Gift of Ngat Tran
pET21b::DBD ParB $(His)_6$	pET21b::*C. crescentus*-ParB-$(His)_6$ (residue 126-243) (DBD only)	This study
pET21b::ParB (Q162A)-$(His)_6$	pET21b::*C. crescentus*-ParB- (Q162A) $(His)_6$	This study
pET21b::ParB (K171A)-$(His)_6$	pET21b::*C. crescentus*-ParB- (K171A) $(His)_6$	This study
pET21b::ParB (S172A)-$(His)_6$	pET21b::*C. crescentus*-ParB- (S172A) $(His)_6$	This study
pET21b::ParB (R173A)-$(His)_6$	pET21b::*C. crescentus*-ParB- (R173A) $(His)_6$	This study
pET21b::ParB (S174A)-$(His)_6$	pET21b::*C. crescentus*-ParB- (S174A) $(His)_6$	This study
pET21b::ParB (N178A)-$(His)_6$	pET21b::*C. crescentus*-ParB- (N178A) $(His)_6$	This study
pET21b::ParB (R181A)-$(His)_6$	pET21b::*C. crescentus*-ParB- (R181A) $(His)_6$	This study
pET21b::ParB (V226A)-$(His)_6$	pET21b::*C. crescentus*-ParB- (V226A) $(His)_6$	This study
pET21b::ParB (R227A)-$(His)_6$	pET21b::*C. crescentus*-ParB- (R227A) $(His)_6$	This study
pET21b::ParB (R234A)-$(His)_6$	pET21b::*C. crescentus*-ParB- (R234A) $(His)_6$	This study
pET21b::ParB (K245A)-$(His)_6$	pET21b::*C. crescentus*-ParB- (K245A) $(His)_6$	This study

pET21b::ParB-$(His)_6$ chimera 1	pET21b::ParB-$(His)_6$ chimera 1, with residue 162-230 from *Bacillus subtilis* Noc	This study
pET21b::ParB-$(His)_6$ chimera 4	pET21b::ParB-$(His)_6$ chimera 4, with residue 162-207 from *Bacillus subtilis* Noc	This study
pET21b::PtoN1	pET21b::PtoN1-$(His)_6$ (Q173T179A184G201)	This study
pET21b::PtoN2	pET21b::PtoN2-$(His)_6$ (R173K179A184G201)	This study
pET21b::PtoN3	pET21b::PtoN3-$(His)_6$ (R173T179K184G201)	This study
pET21b::PtoN4	pET21b::PtoN4-$(His)_6$ (R173T179A184R201)	This study
pET21b::PtoN5	pET21b::PtoN5-$(His)_6$ (Q173K179A184G201)	This study
pET21b::PtoN6	pET21b::PtoN6-$(His)_6$ (Q173T179K184G201)	This study
pET21b::PtoN7	pET21b::PtoN7-$(His)_6$ (Q173T179A184R201)	This study
pET21b::PtoN8	pET21b::PtoN8-$(His)_6$ (R173K179K184G201)	This study
pET21b::PtoN9	pET21b::PtoN9-$(His)_6$ (R173K179A184R201)	This study
pET21b::PtoN10	pET21b::PtoN10-$(His)_6$ (R173T179K184R201)	This study
pET21b::PtoN11	pET21b::PtoN11-$(His)_6$ (Q173K179K184G201)	This study
pET21b::PtoN12	pET21b::PtoN12-$(His)_6$ (Q173K179A184R201)	This study
pET21b::PtoN13	pET21b::PtoN13-$(His)_6$ (Q173T179K184R201)	This study
pET21b::PtoN14	pET21b::PtoN14-$(His)_6$ (R173K179K184R201)	This study
pET21b::PtoN15	pET21b::PtoN15-$(His)_6$ (Q173K179K184R201)	This study
pET21b::PtoN16	pET21b::PtoN16-$(His)_6$ (R173T179A184G201+R227K)	This study
pET21b::Noc-(N163A) $(His)_6$	pET21b::*B. subtilis*-Noc- (N163A) $(His)_6$	This study
pET21b::Noc-K169A) $(His)_6$	pET21b::*B. subtilis*-Noc- (K169A) $(His)_6$	This study
pET21b::Noc-T182A) $(His)_6$	pET21b::*B. subtilis*-Noc- (T182A) $(His)_6$	This study
pET21b::Noc-R186A) $(His)_6$	pET21b::*B. subtilis*-Noc- (R186A) $(His)_6$	This study
pET21b::Noc-R189A) $(His)_6$	pET21b::*B. subtilis*-Noc- (R189A) $(His)_6$	This study
pET21b::Noc-N213A) $(His)_6$	pET21b::*B. subtilis*-Noc- (N213A) $(His)_6$	This study
pET21b::Noc-V214A) $(His)_6$	pET21b::*B. subtilis*-Noc- (V214A) $(His)_6$	This study
pET21b::Noc-R230A) $(His)_6$	pET21b::*B. subtilis*-Noc- (R230A) $(His)_6$	This study

pET21b::Ct ParB	pET21b::*C. crescentus*-ParB-$(His)_6$ (residue 11-154)	This study
pET21b::ParB (D275K)-$(His)_6$	pET21b::*C. crescentus*-ParB- (D275K) $(His)_6$	This study
pET21b::ParB (G282K)-$(His)_6$	pET21b::*C. crescentus*-ParB- (G278K) $(His)_6$	This study
pET21b::ParB (S279K)-$(His)_6$	pET21b::*C. crescentus*-ParB- (S279K) $(His)_6$	This study
pET21b::ParB (T280K)-$(His)_6$	pET21b::*C. crescentus*-ParB- (T280K) $(His)_6$	This study
pET21b::Noc-(T282K)$(His)_6$	pET21b::*C. crescentus*-ParB- (T282K) $(His)_6$	This study
pET21b::ParB-(D275K, G278K)$(His)_6$	pET21b::*C. crescentus*-ParB- (D275K, G278K) $(His)_6$	This study
pET21b::ParB-(D275K, T282K) $(His)_6$	pET21b::*C. crescentus*-ParB- (D275K, T282K) $(His)_6$	This study
pET21b::ParB-(3K) $(His)_6$	pET21b::*C. crescentus*-ParB- (D275K, G278K, T282K) $(His)_6$	This study
pET21b::ParB-(4K) $(His)_6$	pET21b::*C. crescentus*-ParB- (D275K, G278K, T280K, T282K) $(His)_6$	This study
pET21b::ParB-(5K) $(His)_6$	pET21b::*C. crescentus*-ParB- (D275K, G278K, S279K, T280K, T282K) $(His)_6$	This study
pMT571-1xFLAG-DEST	Destination vector for Gateway cloning, 1xFLAG tag fused to the N-terminus of protein of interest, integrative to the van locus, tetracycline^R	This study
pMT571-1xFLAG:: ParB	pMT571-1xFLAG::*C. crescentus* ParB, kanamycin^R	This study
pMT571-1xFLAG::*yfp*	pMT571-1xFLAG::yfp	This study
pMT571-1xFLAG:: ParB (D275K)	pMT571-1xFLAG::C. *crescentus*-ParB (D275K)	This study
pMT571-1xFLAG:: ParB (G278K)	pMT571-1xFLAG::C. *crescentus*-ParB (G278K)	This study

pMT571-1xFLAG:: ParB (S279K)	pMT571-1xFLAG::*C. crescentus*-ParB (S279K)	This study
pMT571-1xFLAG:: ParB (T280K)	pMT571-1xFLAG::*C. crescentus*-ParB (T280K)	This study
pMT571-1xFLAG:: ParB (T282K)	pMT571-1xFLAG::*C. crescentus*-ParB (T282K)	This study
pMT571-1xFLAG:: ParB (D275K, G278K)	pMT571-1xFLAG::*C. crescentus*-ParB (D275K, G278K)	This study
pMT571-1xFLAG:: ParB (D275K, T282K)	pMT571-1xFLAG::*C. crescentus*-ParB (D275K, T282K)	This study
pMT571-1xFLAG:: ParB (D275K, G278K, T282K)	pMT571-1xFLAG::*C. crescentus*-ParB (D275K, G278K, T282K)	This study
pMT571-1xFLAG:: ParB (D275K, G278K, T280K, T282K)	pMT571-1xFLAG::*C. crescentus*-ParB (D275K, G278K, T280K, T282K)	This study
pMT571-1xFLAG:: ParB (D275K, G278K, S279K, T280K, T282K)	pMT571-1xFLAG::*C. crescentus*-ParB (D275K, G278K, S279K, T280K, T282K)	This study
pET21b::Noc(NΔ10) $(His)_6$	pET21b::*B. subtilis*-Noc- (NΔ10) $(His)_6$	This study
pET21b::Noc- (R89A) $(His)_6$	pET21b::*B. subtilis*-Noc- (R89A) $(His)_6$	This study
pET21b::Noc- (N121S) $(His)_6$	pET21b::*B. subtilis*-Noc- (N121S) $(His)_6$	This study
pET21b::Noc- (E29C) $(His)_6$	pET21b::*B. subtilis*-Noc- (E29C) $(His)_6$	This study
pET21b::Noc (S253C) $(His)_6$	pET21b::*B. subtilis*-Noc- (S253C) $(His)_6$	This study
pET21b::Noc- (E29C, R89A) $(His)_6$	pET21b::*B. subtilis*-Noc- (E29C, R89A) $(His)_6$	This study

pET21b::Noc-(E29C, N121S) $(His)_6$	pET21b::*B. subtilis*-Noc- (E29C, N121S) $(His)_6$	This study
pET21b::Noc-(NΔ10, E29C) $(His)_6$	pET21b::B. subtilis subtilis-Noc- (NΔ10, E29C) $(His)_6$	This study
pET21b::Gt NocΔCTD $(His)_6$	pET21b::*G. thermoleovorans* Noc residues (1-239) $(His)_6$	This study
pET21b::Gt NocNΔ26ΔCTD $(His)_6$	pET21b::*G. thermoleovorans* Noc residues (25-239) $(His)_6$	This study
pMCS5-4x*NBS*	pMCS5 plasmid that harbours four NBS sites, tetracycline^R	This study
pMCS5::empty	pMCS5 plasmid with an intact multiple cloning site	This study
pUC19-4x*NBS*	pUC19 plasmid that harbours four *NBS* sites, carbenicillin^R	This study
pUC19-scrambled *NBS*	pUC19 plasmid that harbours four scrambled *NBS* sites	This study

2.1.4 Primers

Primers	**Sequence**
AJ1	TAACTTTAAGAAGGAGATATACATATGTCCGAAGGGCGTCGTGGTCTGGGTC
AJ2	GGTGGTGCTCGAGTGCGGCCGCAAGCTTGTCCTTCACGCGTGGGGGGCGGCC
3286	GTGGTGCTCGAGTGCGGCCGCAAGCTTATCTCTGCTGAATGCTTTGCGTCTC
3287	TAACTTTAAGAAGGAGATATACATATGACGGAAACCGCTTCTGTGGCGTTA
P3296	TTTAACTTTAAGAAGGAGATATACAT
P3297	TGGTGCTCGAGTGCGGCCGCAAGCTT
AJ30	GTTCGCAATCGTCGACGCCCCTTTTCCCAAACG
AJ31	CGTTTGGGAAAAGGGGCGTCGACGATTGCGAAC
AJ32	GACAGGTTGCGGCAACGCCAGTAAGCGCAGTTT
AJ33	AAACTGCGCTTACTGGCGTTGCCGCAACCTGTC
AJ34	CAGGGCACGTGCGTGCGCCTCCGTAATCTTTTT
AJ35	AAAAAGATTACGGAGGCGCACGCACGTGCCCTG
AJ36	TTTGTTCGCAATCGTCGCCTGCCCTTTTCCCAA
AJ37	TTGGGAAAAGGGCAGGCGACGATTGCGAACAAA
AJ40	CGGCAACTTCAGTAACGCCAGTTTGTTCGCAAT
AJ41	ATTGCGAACAAACTGGCGTTACTGAAGTTGCCG

AJ46	GTCTTCTGTCTGTTTCGCGTTTAACGATTTCTC
AJ47	GAGAAATCGTTAAACGCGAAACAGACAGAAGAC
AJ55	CAGTTTGTTCGCAATCGCCGACTGCCCTTTTCC
AJ56	GGAAAAGGGCAGTCGGCGATTGCGAACAAACTG
AJ57	ACGCGGTTTCGGCTTCGCCTGTCCCTGTTCCAA
AJ58	TTGGAACAGGGACAGGCGAAGCCGAAACCGCGT
AJ65	TAACTTTAAGAAGGAGATATACATATGTTGGGTGAAAAGGAGCAAGAACCG
AJ66	TAACTTTAAGAAGGAGATATACATATGTTGGGTGAAAAGGAGCAAGAACCG
AJ73	CTGAACCGCGCGCCACGCGCGTTCTCCCGCAAT
AJ74	ATTGCGGGAGAACGCGCGTGGCGCGCGGTTCAG
AJ84	GATACCAATAAGGAATGCATTTTAGAAATTCCA
AJ85	TGGAATTTCTAAAATGCATTCCTTATTGGTATC
AJ86	GTGGCCTTAATTGAGTCTTTGCAACGCGAGGAG
AJ87	CTCCTCGCGTTGCAAAGACTCAATTAAGGCCAC
AJ88	AATACTATTCGTCAGTGCTTATCAATGGTGGAA
AJ89	TTCCACCATTGATAAGCACTGACGAATAGTATT
M13-F	CGCCAGGGTTTTCCCAGTCACGAC
M 13-R	ATGGTCATAGCTGTTTCCT

2.1.5 Other oligonucleotides and gBlocks DNA fragments

Oligos	**Sequence (5'-3')**
170bp *parS*	CGCCAGGGTTTTCCCAGTCACGACGTTGTAAAACGACGGCCAGAATT CGCAACGTGTGTTTCACGTGAAACAGCCTTGAACTGATAACGACTCT ATCATTGATAGAGTGTTCTCTCCACG**GGATCC**CCAGGCATGCAAGCT TGGCGTAATCATGGTCATAGCTGTTTCCT
170bp *NBS*	CGCCAGGGTTTTCCCAGTCACGACGTTGTAAAACGACGGCCAGAATT CGCAACGTGTATTTCCCGGGAAATAGCCTTGAACTGATAACGACTCT ATCATTGATAGAGTGTTCTCTCCACG**GGATCC**CCAGGCATGCAAGCT TGGCGTAATCATGGTCATAGCTGTTTCCT
20 bp *parS*	GATGTTTCACGTGAAACATC
22 bp *parS*	GGATGTTTCACGTGAAACATCC
22 bp *NBS*	GGATATTTCCCGGGAAATATCC
4x*NBS*-F	GCCCAGGCCCTGGAGCGCATCTC
4x*NBS*-R	CAAGACGCTCGCCTCAATGCGAAC
22 bp *NBS*	GGATATTTCCCGGGAAATATCC

2.2 Growth conditions and storage of bacterial strains

2.2.1 E. coli strains

E. coli was grown on solid or liquid LB media supplemented with the appropriate antibiotics at 37°C. DMSO stocks were made from fresh overnight cultures by adding (10%) (v/v) DMSO to an equal volume of culture and storing at -70°C.

2.2.2 C. crescentus strains

C. crescentus cultures were grown on solid or liquid PYE media supplemented with the appropriate antibiotics and/or sugars at 30°C. DMSO stocks were made from fresh overnight cultures by adding (10%) (v/v) DMSO to an equal volume of culture and storing at -70°C.

2.2.3 Antibiotic concentrations for E. coli and C. crescentus strains

Growth medium were supplemented with the appropriate antibiotics at the following concentrations (liquid/solid media for *E. coli*, liquid/solid media for *C. crescentus* [µg/mL]): carbenicillin (only *E. coli*: 50/100), chloramphenicol (20/30; 1/2), kanamycin (30/50; 5/25) and oxytetracycline (12/12; 1/2).

2.3 General cloning methods

For protein overexpression and purification related experiments, DNA fragments were either amplified by PCR using Phusion® High-fidelity DNA polymerase (NEB) or chemically synthesized (gBlocks dsDNA fragments, IDT). For PCR amplified fragments, the DNA was analysed using agarose gel electrophoresis using either a 1% (w/v) or 2% (w/v) TAE agarose gel with 1 µg/mL ethidium bromide. The PCR amplified and gBlocks DNA fragments contained a 23-bp sequence shared between the *Nde*I-*Hind*III-cut pET21b backbone thus enabling cloning by Gibson assembly. In the PCR amplified fragment, the 23-bp region of homology was incorporated in the primers used to amplify the fragment, whereas for the gBlocks fragments, the 23-bp regions were incorporated during the synthesis of gBlocks fragments. The PCR amplified fragments and gBlocks fragments and a *Nde*I-*Hind*III-digested pET21b backbone were assembled together using a 2x Gibson master mix (NEB). Two and a half µL of each fragment at equimolar concentration was added to 5 µL 2x Gibson master mix (NEB), and the mixture was incubated at 50°C for 60 min. Five µL was used to transform chemically competent *E. coli* DH5α cells. The cloned plasmids was then purified using a miniprep column (Qiagen) and the resulting plasmids were sequence verified by Sanger sequencing by Eurofins or Genewiz.

For site-directed mutagenesis related experiments a Gibson assembly-based method was used to introduce the desired mutation of interest. Briefly 4 primers were generated to incorporate the mutation into the gene. 2 primers (33 nucleotides in length) were designed to flank the left and right regions of the substituted residue, resulting in an amplicon that contained 15 bp overlap and the desired mutation. 2 additional primers 3296 and 3297 were used to generate the 23-bp region of homology to the *Nde*I-*Hind*III digested pET21b backbone. The PCR-amplified fragments were then analysed using agarose gel electrophoresis using a 2% (w/v) TAE agarose gel with 1 µg/mL ethidium bromide. The PCR-amplified fragments were then gel-purified before being mixed with the *Nde*I-*Hind*III-digested pET21b backbone and the 2x Gibson master mix (NEB) and the mixture was incubated at 50°C for 60 min. Five µL was used to transform chemically competent *E. coli* DH5α cells. The cloned plasmids was then purified using a miniprep column (Qiagen) and the resulting plasmids were sequence verified by Sanger sequencing by Eurofins or Genewiz.

For *in vivo* genome-wide approaches related experiments, the vectors used were generated using LR cloning. Briefly, the *parB* (WT) and variant encoding genes were chemically synthesized and cloned into a pUC57 plasmid. LR cloning was then used to shuttle *parB* (WT) and variants into the pMT571-*flag* plasmid. In brief 2 µl of pUC57kan-*parB* (WT) or variants were mixed with 2µl of pMT751-*flag* and 1 µl of LR Clonase (Thermo Fisher). The mixture was left to incubate for 1 hour at room temperature before being used to transform chemically competent *E. coli* DH5α by heat-shock transformation. Cells were then plated on to LB agar plates supplemented with oxytetracycline or kanamycin. Colonies were selected for oxytetracycline resistance and were subsequently patched to obtain oxytetracycline-resistant and kanamycin-sensitive colonies. Individual colonies were then used to inoculate a 10ml of LB with chloramphenicol and was left to grow for ~8 hours at 37˚C. The cloned plasmid was then extracted from the overnight culture using the Qiagen miniprep kit (Qiagen).

2.3.1 Constructions of plasmids

To construct the *pET21b::parBΔCTD-(his)$_6$* plasmid, the coding sequence of a C-terminally truncated *C. crescentus* ParB (ParBΔCTD, lacking the last 50 amino acids) was amplified by PCR using primers AJF1 and AJR2 and pET21b::*parB-(his)$_6$* as template. The pET21b plasmid backbone was generated via a double digestion of pET21b::*parB-(his)$_6$* with NdeI and HindIII. The resulting backbone was subsequently gel-purified and assembled with the PCR-amplified fragment of *parBΔCTD* using a 2x Gibson master mix (NEB). Gibson assembly was possible owing to a 23-bp sequence shared between the NdeI-HindIII-cut pET21b backbone and the PCR fragment. These 23-bp regions were incorporated during the synthesis of primers

NdeI-Ct-ParB-F and HindIII-Ct-ParB-R. The resulting plasmids were sequence verified by Sanger sequencing (Eurofins, Germany).

To construct the *pET21b:: C. crescentus ParB (variants)-His$_6$* plasmids, all sequences of ParB variants were designed in VectorNTI (ThermoFisher) and chemically synthesized as gBlocks dsDNA fragments (IDT). Individual gBlocks fragment and a NdeI-HindIII-digested pET21b backbone were assembled using a 2x Gibson master mix (NEB). Gibson assembly was possible due to a 23-bp sequence shared between the NdeI-HindIII-cut pET21b backbone and the gBlocks fragment. These 23-bp regions were incorporated during the synthesis of gBlocks fragments. The resulting plasmids were sequence verified by Sanger sequencing (Eurofins, Germany).

To construct the *pET21b:: B. subtilis noc-his$_6$* plasmid, a double-stranded DNA (dsDNA) fragment containing a codon-optimized *B. subtilis noc* gene was chemically synthesized (gBlocks, IDT). The pET21b plasmid backbone was generated via a double digestion of pET21b::*Caulobacter crescentus parB-(his)$_6$* with NdeI and HindIII. The resulting backbone was subsequently gel-purified and assembled with the *noc* gBlocks fragment using a 2x Gibson master mix. Briefly, 2.5 µL of the gBlocks fragment and 2.5 µL of NdeI-HindIII-cut pET21b at equimolar concentration were added to 5 µL of a 2x Gibson master mix (NEB). The mixture was incubated at 50°C for 60 min. Subsequently, 5 µL was used to transform chemically competent *E. coli* DH5α cells. Gibson assembly was possible owing to a 23-bp sequence shared between the NdeI-HindIII-cut pET21b backbone and the gBlocks fragment. The resulting plasmid was verified by Sanger sequencing (Eurofins, Germany).

To construct the *pET21b:: B. subtilis noc (DBD)-his$_6$* plasmid, the coding sequence of only the DNA-binding domain (DBD) of Noc was amplified by PCR using primers X and X, and pET21b::*noc-his$_6$* as template. The resulting PCR product was gel-purified and assembled into an NdeI-HindIII-cut pET21b using a 2x Gibson master mix. Gibson assembly was possible owing to a 23-bp sequence shared between the NdeI-and-HindIII cut pET21b backbone and the PCR amplified fragment. The 23-bp homologous region was introduced during the synthesis of primers 3286 and 3287. The resulting plasmid was verified by Sanger sequencing (Eurofins, Germany).

To construct the *pET21b:: B. subtilis nocNΔ10-his$_6$* plasmid, the coding sequence of a 10-amino-acid N-terminally truncated Noc (NocNΔ10) was amplified by PCR using primers AJ65 and AJ66, and pET21b::*noc-his$_6$* as template. The resulting PCR product was gel-purified and assembled into an NdeI-HindIII-cut pET21b using a 2x Gibson master mix. Gibson assembly

was possible owing to a 23-bp sequence shared between the NdeI-and-HindIII cut pET21b backbone and the PCR amplified fragment. The 23-bp homologous region was introduced during the synthesis of primers AJ65 and AJ66. The resulting plasmid was verified by Sanger sequencing (Eurofins, Germany).

To construct the *pET21b::noc (Q158A)-his$_6$* plasmid, the Q158A mutation was introduced into the coding sequence of Noc, primers P3296 and AJ30, and primers P3297 and AJ31 were used in PCR reactions to amplify the left half and the right half of *noc (R89A)*, respectively, from the *pET21b::noc-his$_6$* template. A 15-bp overlapping region between the two PCR fragments contained the point mutation and also enabled their assembly by a Gibson master mix. Briefly, 1.7 µL of each PCR-amplified DNA fragment and 1.6 µL of a gel purified NdeI-HindIII-cut pET21b at equimolar concentration were added to 5 µL of a 2x Gibson master mix. The mixture was incubated at 50°C for 60 min. Subsequently, 5 µL was used to transform chemically competent *E. coli* DH5α cells. The resulting plasmid was verified by Sanger sequencing (Eurofins, Germany).

To construct the *pET21b::noc (K169A)-his$_6$* plasmid, the same procedure as above, except to introduce the K169A mutation in the coding sequence of Noc, primers P3296 and AJ32, and primers P3297 and AJ33 were used in PCR reactions to amplify the left half and the right half of *noc (K169A)*, respectively, from the *pET21b::noc-his$_6$* template.

To construct the *pET21b::noc (R186A)-his$_6$* plasmid, the same procedure as above, except to introduce the R186A mutation in the coding sequence of Noc, primers P3296 and AJ34, and primers P3297 and AJ35 were used in PCR reactions to amplify the left half and the right half of *noc (R186A)*, respectively, from the *pET21b::noc-his$_6$* template.

To construct the *pET21b::noc (S159A)-his$_6$* plasmid, the same procedure as above, except to introduce the R186A mutation in the coding sequence of Noc, primers P3296 and AJ36, and primers P3297 and AJ37 were used in PCR reactions to amplify the left half and the right half of *noc (S159A)*, respectively, from the *pET21b::noc-his$_6$* template.

To construct the *pET21b::noc (R166A)-his$_6$* plasmid, the same procedure as above, except to introduce the R166A mutation in the coding sequence of Noc, primers P3296 and AJ41, and primers P3297 and AJ42 were used in PCR reactions to amplify the left half and the right half of *noc (R166A)*, respectively, from the *pET21b::noc-his$_6$* template.

To construct the *pET21b::noc (V214A)-his$_6$* plasmid, the same procedure as above, except to introduce the V214A mutation in the coding sequence of Noc, primers P3296 and AJ46, and primers P3297 and AJ47 were used in PCR reactions to amplify the left half and the right half of *noc (V214A)*, respectively, from the *pET21b::noc-his$_6$* template.

To construct the *pET21b::noc (T160A)-his$_6$* plasmid, the same procedure as above, except to introduce the T160A mutation in the coding sequence of Noc, primers P3296 and AJ55, and primers P3297 and AJ56 were used in PCR reactions to amplify the left half and the right half of *noc (T160A)*, respectively, from the *pET21b::noc-his$_6$* template.

To construct the *pET21b::noc (R230A)-his$_6$* plasmid, the same procedure as above, except to introduce the R230A mutation in the coding sequence of Noc, primers P3296 and AJ57, and primers P3297 and AJ58 were used in PCR reactions to amplify the left half and the right half of *noc (R230A)*, respectively, from the *pET21b::noc-his$_6$* template.

To construct the *pET21b::noc (R89A)-his$_6$* plasmid, the same procedure as above, except to introduce the R89A mutation in the coding sequence of Noc, primers P3296 and AJ73, and primers P3297 and AJ74 were used in PCR reactions to amplify the left half and the right half of *noc (R89A)*, respectively, from the *pET21b::noc-his$_6$* template.

To construct the *pET21b::noc (N121S)-his$_6$* plasmid, the same procedure as above was used to introduce the N121S mutation into the coding sequence of Noc, except that primers P3296 and AJ87, and primers P3297 and AJ86 were used to amplify the left half and the right half of *noc (N121S)*, respectively, from the *pET21b::noc-his$_6$* template.

To construct the *pET21b::noc (E29C)-his$_6$* plasmid, the same procedure as above was used to introduce the E29C mutation into the coding sequence of Noc, except that primers P3296 and AJ85, and primers P3297 and AJ84 were used to amplify the left half and the right half of *noc (E29C)*, respectively, from the *pET21b::noc-his$_6$* template.

To construct the *pET21b::noc (S253C)-his$_6$* plasmid, the same procedure as above was used to introduce the S253C mutation into the coding sequence of Noc, except that primers P3296 and AJ89, and primers P3297 and AJ88 were used to amplify the left half and the right half of *noc (S253C)*, respectively, from the *pET21b::noc-his$_6$* template.

To construct the *pET21b::noc (E29C R89A)-his$_6$* plasmid, the same procedure as above was used to introduce the R89A mutation into the coding sequence of Noc (E29C), except that

primers P3296 and AJ73, and primers P3297 and AJ74 were used to amplify the left half and the right half of *noc (E29C R89A)*, respectively, from the *pET21b::noc (E29C)-his$_6$* template.

To construct the *pET21b::Noc (E29C N121S)-his$_6$* plasmid, the same procedure as above was used to introduce the N121S mutation into the coding sequence of Noc (E29C), except that primers P3296 and AJ86, and primers P3297 and AJ87 were used to amplify the left half and the right half of *noc (E29C N121S)*, respectively, from the *pET21b::noc (E29C)-his$_6$* template.

To construct the *pET21b::noc (E29C S253C)-his$_6$* plasmid, the same procedure as above was used to introduce the E29C mutation into the coding sequence of Noc (S253C), except that primers P3296 and AJ85, and primers P3297 and AJ84 were used to amplify the left half and the right half of *noc (E29C S253C)*, respectively, from the *pET21b::noc (S253C)-his$_6$* template.

Construction of *pET21b:: Geobacillus thermoleovorans NocΔCTD-his$_6$*

To construct the *pET21b:: Geobacillus thermoleovorans NocΔCTD-his$_6$* plasmid, a dsDNA fragment containing the coding sequence of a 42-amino-acid C-terminally truncated *G. thermoleovorans* Noc was chemically synthesized (gBlocks, IDT). The gBlocks fragment was assembled into an NdeI-HindIII-cut pET21b using a 2x Gibson master mix. Gibson assembly was possible owing to a 23-bp sequence shared between the NdeI-HindIII-cut pET21b backbone and the gBlocks fragment. The resulting plasmid was verified by Sanger sequencing (Eurofins, Germany).

To construct the *pET21b:: Geobacillus thermoleovorans NocNΔ26ΔCTD-his$_6$* plasmid, the coding sequence of a 26-amino-acid N-terminally truncated and 42-amino-acid C-terminally truncated *G. thermoleovorans* Noc was amplified by PCR using primers AJ76 and AJ81, and pET21b:: *Geobacillus thermoleovo*rans NocΔCTD-his$_6$ as template. The resulting PCR product was gel-purified and assembled into an NdeI-HindIII-cut pET21b using a 2x Gibson master mix. Gibson assembly was possible owing to a 23-bp sequence shared between the NdeI-and-HindIII cut pET21b backbone and the PCR amplified fragment. The 23-bp homologous region was introduced during the synthesis of primers AJ76 and AJ81. The resulting plasmid was verified by Sanger sequencing (Eurofins, Germany).

To construct the *pMCS5-4xNBS* plasmid, a dsDNA fragment containing four *NBS* sites were chemically synthesized (gBlocks, IDT). The gBlocks fragment was assembled into an EcoRI-cut pMCS5 using a 2x Gibson master mix. Gibson assembly was possible owing to a 23-bp sequence shared between the EcoRI-cut pMCS5 backbone and the gBlocks fragment. The resulting plasmid was verified by Sanger sequencing (Eurofins, Germany).

To construct the *pUC19-4xNBS* plasmid, a 260-bp DNA region containing four *NBS* sites were amplified by PCR using primers 4xNBS-F and 4xNBS-R, and pMCS5-4x*NBS* as template. The resulting PCR product was gel-purified, 5'-phosphorylated using T4 PNK enzyme (NEB), and subsequently ligated into a SmaI-cut pUC19 backbone. The resulting plasmid was verified by Sanger sequencing (Eurofins, Germany).

2.4 Protein overexpression and purification

2.4.1 Overexpression and purification of ParB and ParB variants

Plasmid pET21b-ParB (Hexa-histidine tag at the C-terminus of ParB, a gift from Christine Jacob-Wagner) was transformed into E. coli BL21/pRARE, and 10 mL overnight culture was used to inoculate 2 L LB medium + carbenicillin + chloramphenicol. Cells were grown at 37° C to OD_{600} of ~0.4. The culture was then cooled to 30° C before isopropyl-β-D-thiogalactopyranoside (IPTG) was added to a final concentration of 0.5 mM. The culture was left shaking for an additional 3 hrs at 30° C before cells were harvested by centrifugation. Pelleted cells were resuspended in a buffer containing 100 mM Tris-HCl pH 8.0, 300 mM NaCl, 5% (v/v) glycerol, EDTA-free protease inhibitor tablet (Roche), and lysed by sonication (three cycles of 20 s with 40 s resting on ice in between each cycle). The cell debris was removed by centrifugation at 84,000 g for 30 min and the supernatant was filtered through a 0.45 µm membrane before being applied to a 1-ml Ni-loaded Hi-Trap Chelating HP column (GE Healthcare) that had been equilibrated with buffer A [100 mM Tris-HCl, pH 8.0, 300 mM NaCl, 10 mM imidazole]. Protein was eluted from the column using an increasing (10 mM to 500 mM) imidazole gradient in the same buffer. ParB-(His)6 fractions were identified using SDS-PAGE, pooled together, and applied to a Heparin HP column (GE Healthcare) that had been equilibrated with buffer A [100mM Tris-HCl pH 8.0, 25mM NaCl, 5% (v/v) glycerol]. Protein was eluted from the column using an increasing (25 mM to 1 M NaCl) salt gradient in the same buffer A. ParB-(His)6 fractions were identified using SDS-PAGE, pooled together, and concentrated to approximately 2 mg/mL using a Vivaspin6 10 kDa cut-off protein concentrator (Vivascience). The concentrated protein was then exchanged into a storage buffer [50mM Tris-HCl, pH 8.0, 250 mM NaCl and 10% glycerol] using a Zeba desalting column (Thermo Scientific) before flash-frozen in liquid nitrogen. The concentration of ParB dimer was measured by Bradford method.

For crystallography experiments ParB was further polished via a gel-filtration column. To do so, purified ParB variants were concentrated by centrifugation in an Amicon Ultra-15 3-kDa cut-off spin filters (Merck) before being loaded into a Superdex 200 gel filtration column (GE

Healthcare). The gel filtration column was pre-equilibrated with 10 mM Tris-HCl pH 8.0, 250 mM NaCl. ParB fractions were then pooled and analysed for purity by SDS-PAGE.

C. crescentus ParB (G101S) was purified using the same procedure as ParB (WT), except pET21b::ParB (G101S)-His_6 was introduced into *E. coli* Rosetta (DE3) competent cells (Merck). The final gel filtration step was omitted, and 8 L of culture was used.

C. crescentus ParB (R104A) was purified using the same procedure as ParB (WT), except pET21b::ParB (R104A)-His_6 was introduced into *E. coli* Rosetta (DE3) competent cells (Merck). The final gel filtration step was omitted, and 6 L of culture was used.

C. crescentus ParB (R173A) was purified using the same procedure as ParB (WT), except pET21b::ParB (R173A)-His_6 was introduced into *E. coli* Rosetta (DE3) competent cells (Merck). The final gel filtration step was omitted, and 2 L of culture was used.

C. crescentus ParB (K171A) was purified using the same procedure as ParB (WT), except pET21b::ParB (K17A)-His_6 was introduced into *E. coli* Rosetta (DE3) competent cells (Merck). The final gel filtration step was omitted, and 2 L of culture was used.

C. crescentus ParB (S172A) was purified using the same procedure as ParB (WT), except pET21b::ParB (S172A)-His_6 was introduced into *E. coli* Rosetta (DE3) competent cells (Merck). The final gel filtration step was omitted, and 2 L of culture was used.

C. crescentus ParB (S174A) was purified using the same procedure as ParB (WT), except pET21b::ParB (S174A)-His_6 was introduced into *E. coli* Rosetta (DE3) competent cells (Merck). The final gel filtration step was omitted, and 2 L of culture was used.

C. crescentus ParB (R181A) was purified using the same procedure as ParB (WT), except pET21b::ParB (R181A)-His_6 was introduced into *E. coli* Rosetta (DE3) competent cells (Merck). The final gel filtration step was omitted, and 2 L of culture was used.

C. crescentus ParB (N178A) was purified using the same procedure as ParB (WT), except pET21b::ParB (N178A)-His_6 was introduced into *E. coli* Rosetta (DE3) competent cells (Merck). The final gel filtration step was omitted, and 2 L of culture was used.

C. crescentus ParB (R204A) was purified using the same procedure as ParB (WT), except pET21b::ParB (R204A)-His_6 was introduced into *E. coli* Rosetta (DE3) competent cells (Merck). The final gel filtration step was omitted, and except 2 L of culture was used.

C. crescentus ParB (D275K) was purified using the HIS-Select® Cobalt gravity flow columns as follows. *C. crescentus* ParB (D275K) was expressed the same way as ParB (WT) except, plasmid pET21b::*parB* (D275K) was introduced into *E. coli* Rosetta (DE3) competent cells (Merck) by heat-shock transformation. For purification, the cell lysate was transferred to a gravity flow column containing 2 mL of HIS-Select® Cobalt Affinity Gel (Sigma Aldrich) that was pre-equilibrated with 40 mL of buffer A [100 mM Tris-HCl pH 8.0, 300 mM NaCl, 10 mM Imidazole, 5% (v/v) glycerol]. The column was rotated at 4˚C for 1 hour to allow for binding to His-tagged proteins to the resin. After the binding step, unbound proteins were washed off using 60 mL of buffer A. Proteins were eluted using 2.7 mL of buffer B [100 mM Tris-HCl pH 8.0, 300 mM NaCl, 500 mM Imidazole, 5% (v/v) glycerol]. The purified protein was desalted using a PD-10 column (GE Healthcare), concentrated using an Amicon Ultra-4 10 kDa cut-off spin column (Merck), and stored at -80˚C in a storage buffer [100 mM Tris-HCl pH 8.0, 300 mM NaCl, and 10% (v/v) glycerol]. The purified protein was desalted using a PD-10 column (GE Healthcare), concentrated using an Amicon Ultra-4 10 kDa cut-off spin column (Merck), and stored at -80˚C in a storage buffer [100 mM Tris-HCl pH 8.0, 300 mM NaCl, and 10% (v/v) glycerol].

C. crescentus ParB (G278K) was purified using the same procedure as ParB (D275K), except pET21b::ParB (G278K)-His_6 was introduced into *E. coli* Rosetta (DE3) competent cells (Merck).

C. crescentus ParB (S279K) was purified using the same procedure as ParB (D275K), except pET21b::ParB (S279K)-His_6 was introduced into *E. coli* Rosetta (DE3) competent cells (Merck).

C. crescentus ParB (T280K) was purified using the same procedure as ParB (D275K), except pET21b::ParB (T280K)-His_6 was introduced into *E. coli* Rosetta (DE3) competent cells (Merck).

C. crescentus ParB (T282K) was purified using the same procedure as ParB (D275K), except pET21b::ParB (T282K)-His_6 was introduced into *E. coli* Rosetta (DE3) competent cells (Merck).

C. crescentus ParB (D275K, G278K) was purified using the same procedure as ParB (D275K), except pET21b::ParB (D275K, G278K)-His_6 was introduced into *E. coli* Rosetta (DE3) competent cells (Merck).

C. crescentus ParB (D275K, T282K) was purified using the same procedure as ParB (D275K), except pET21b::ParB (D275K, T282K)-His_6 was introduced into *E. coli* Rosetta (DE3) competent cells (Merck).

C. crescentus ParB (D275K, G278K, T282K) was purified using the same procedure as ParB (D275K), except pET21b::ParB (D275K, G278K, T282K)-His_6 was introduced into *E. coli* Rosetta (DE3) competent cells (Merck). For magnetic tweezer experiments, the same three-step purification procedure used to purify proteins used in crystallography experiments was used to purify the *C. crescentus* ParB (D275K, G278K, T282K) variant. In which a Ni^{2+}, heparin and a final gel filtration step was used. Except the final gel filtration buffer consists of 100 mM TRIS pH 8.0, 250 mM NaCl and 5% (v/v) glycerol was used. Proteins were then stored in a buffer containing 100 mM TRIS pH 8.0, 250 mM NaCl and 10% (v/v) glycerol.

C. crescentus ParB (D275K, G278K, T280K, T282K) was purified using the same procedure as ParB (D275K), except pET21b::ParB (D275K, G278K, T280K, T282K)-His_6 was introduced into *E. coli* Rosetta (DE3) competent cells (Merck). For magnetic tweezer experiments, the same three-step purification procedure used to purify the *C. crescentus* ParB (D275K, G278K, T282K) variant was used to purify the *C. crescentus* ParB (D275K, G278K, T280K, T282K) variant.

C. crescentus ParB (D275K, G278K, S279K, T280K, T282K) was purified using the same procedure as ParB (D275K), except pET21b::ParB (D275K, G278K, S279K, T280K, T282K)-His_6 was introduced into *E. coli* Rosetta (DE3) competent cells (Merck). For magnetic tweezer experiments, the same three-step purification procedure used to purify the *C. crescentus* ParB (D275K, G278K, T282K) variant was used to purify the *C. crescentus* ParB (D275K, G278K, S279K, T280K, T282K) variant.

2.4.2 Overexpression and purification of Noc and Noc variants

Full-length *B. subtilis* Noc and Noc (R89A) were purified using a similar protocol used to purify *C. crescentus* ParB as described previously. Briefly, pET21b::Noc-His_6 (WT) was introduced into *E. coli* Rosetta (DE3) competent cells (Merck), A 10 mL overnight culture was used to inoculate 1 L of LB medium + carbenicillin + chloramphenicol. Cells were grown at 37°C with shaking at 250 rpm to an OD_{600} of 0.4. The culture was then left to cool to 4°C before isopropyl-

β-D-thiogalactopyranoside (IPTG) was added to a final concentration of 1 mM. The culture was shaken for 3 hr at 28°C before cells were harvested by centrifugation. The protein was then loaded into a 1 mL HisTrap column (GE Healthcare) that had been equilibrated with buffer A [100 mM Tris-HCl pH 8.0, 300 mM NaCl, 10 mM Imidazole, and 5% glycerol]. Protein was eluted from the column using an increasing (10 mM to 500 mM) imidazole gradient in the same buffer. ParB-containing fractions were pooled and diluted to a conductivity of 16 mS/cm before being loaded onto a 1 mL Heparin HP column (GE Healthcare) that had been equilibrated with 100 mM Tris-HCl pH 8.0, 25 mM NaCl, and 5% glycerol. Protein was eluted from the Heparin column using an increasing (25 mM to 1 M NaCl) salt gradient in the same buffer. For Noc (WT) used in cross-linking experiments, the pH for all buffers used was adjusted to 7.4.

For crystallography experiments, proteins were polished via a gel-filtration column. To do so, purified Noc (WT) and variants were concentrated by centrifugation in an Amicon Ultra-15 3-kDa cut-off spin filters (Merck) before being loaded into a Superdex 200 gel filtration column (GE Healthcare). The gel filtration column was pre-equilibrated with 10 mM Tris-HCl pH 8.0, 250 mM NaCl. Noc variant fractions were then pooled and analysed for purity by SDS-PAGE.

For ITC experiments, proteins were polished via a gel-filtration column. To do so, purified Noc (WT) and variants were concentrated by centrifugation in an Amicon Ultra-15 3-kDa cut-off spin filters (Merck) before being loaded into a Superdex 200 gel filtration column (GE Healthcare). The gel filtration column was pre-equilibrated with 100 mM Tris-HCl pH 8.0, 150 mM NaCl and 5 mM $CaCl_2$. Noc variant fractions were then pooled and analysed for purity by SDS-PAGE.

C-terminally truncated *G. thermoleovorans* Noc (Noc∆CTD) was purified using the same procedure as above with a further polishing step using a gel-filtration column. To do so, purified Gt Noc was concentrated using an Amicon Ultra-15 3 kDa cut-off spin filters (Merck) before being loaded onto a Superdex 75 gel filtration column (GE Healthcare). The gel filtration column was pre-equilibrated with 10 mM TRIS-HCl pH 8.0 and 250 mM NaCl.

G. thermoleovorans Noc (Noc∆26N∆CTD) was expressed and purified using the same procedure as above.

B. subtilis Noc (R89A) was and expressed purified using a similar protocol as Noc (WT), with a two-step Ni^{2+} and heparin procedure except pET21b::Noc-His_6 (R89A) was introduced into *E. coli* Rosetta (DE3) competent cells (Merck).

B. subtilis Noc (Q158A) was and expressed purified using a similar protocol as Noc (WT) except pET21b::Noc-His_6 (Q158A) was introduced into *E. coli* Rosetta (DE3) competent cells (Merck). The final gel-filtration step was also omitted.

B. subtilis Noc (R186A) was and expressed purified using a similar protocol as Noc (WT) except pET21b::Noc-His_6 (R186A) was introduced into *E. coli* Rosetta (DE3) competent cells (Merck). The final gel-filtration step was also omitted.

B. subtilis Noc (K169A) was and expressed purified using a similar protocol as Noc (WT) except pET21b::Noc-His_6 (K169A) was introduced into *E. coli* Rosetta (DE3) competent cells (Merck). The final gel-filtration step was also omitted.

B. subtilis Noc (T160A) was expressed using a similar protocol as Noc (WT), except pET21b::Noc (T160A)-His_6 was introduced into *E. coli* Rosetta (DE3) competent cells (Merck). was purified using the HIS-Select® Cobalt gravity flow columns as follows. For purification, the cell lysate was transferred to a gravity flow column containing 2 mL of HIS-Select® Cobalt Affinity Gel (Sigma Aldrich) that was pre-equilibrated with 40 mL of buffer A [100 mM Tris-HCl pH 8.0, 300 mM NaCl, 10 mM Imidazole, 5% (v/v) glycerol] . The column was rotated at 4˚C for 1 hour to allow for binding to His-tagged proteins to the resin. After the binding step, unbound proteins were washed off using 60 mL of buffer A. Proteins were eluted using 2.7 mL of buffer B [100 mM Tris-HCl pH 8.0, 300 mM NaCl, 500 mM Imidazole, 5% (v/v) glycerol]. The purified protein was desalted using a PD-10 column (GE Healthcare), concentrated using an Amicon Ultra-4 10 kDa cut-off spin column (Merck), and stored at -80˚C in a storage buffer [100 mM Tris-HCl pH 8.0, 300 mM NaCl, and 10% (v/v) glycerol]. The purified protein was desalted using a PD-10 column (GE Healthcare), concentrated using an Amicon Ultra-4 10 kDa cut-off spin column (Merck), and stored at -80˚C in a storage buffer [100 mM Tris-HCl pH 8.0, 300 mM NaCl, and 10% (v/v) glycerol].

B. subtilis Noc (S159A) was expressed using a similar protocol as Noc (T160A), except pET21b::Noc (S159A)-His_6 was introduced into *E. coli* Rosetta (DE3) competent cells (Merck). Noc (S159A) subsequently purified using a one-step the HIS-Select® Cobalt gravity flow columns using the same buffer used to purify the *B. subtilis* Noc (T160A)-His_6.

B. subtilis Noc (R166A) was expressed using a similar protocol as Noc (T160A), except pET21b::Noc (R166A)-His_6 was introduced into *E. coli* Rosetta (DE3) competent cells (Merck).

Noc (R166A) subsequently purified using a one-step the HIS-Select® Cobalt gravity flow columns using the same buffer used to purify the *B. subtilis* Noc (T160A)-His_6.

B. subtilis Noc (R186A) was expressed using a similar protocol as Noc (WT), except pET21b::Noc (R186A)-His_6 was introduced into *E. coli* Rosetta (DE3) competent cells (Merck). Noc (R186A) subsequently purified using a one-step the HIS-Select® Cobalt gravity flow columns using the same buffer used to purify the *B. subtilis* Noc (T160A)-His_6.

B. subtilis Noc (R189A) was expressed using a similar protocol as Noc (WT), except pET21b::Noc (R189A)-His_6 was introduced into *E. coli* Rosetta (DE3) competent cells (Merck). Noc (R189A) subsequently purified using a one-step the HIS-Select® Cobalt gravity flow columns using the same buffer used to purify the *B. subtilis* Noc (T160A)-His_6.

B. subtilis Noc (V214A) was expressed using a similar protocol as Noc (WT), except pET21b::Noc (V214A)-His_6 was introduced into *E. coli* Rosetta (DE3) competent cells (Merck). Noc (V214A) subsequently purified using a one-step the HIS-Select® Cobalt gravity flow columns using the same buffer used to purify the *B. subtilis* Noc (T160A)-His_6.

B. subtilis Noc (R230A) was expressed using a similar protocol as Noc (WT), except pET21b::Noc (R230A)-His_6 was introduced into *E. coli* Rosetta (DE3) competent cells (Merck). Noc (R230A) subsequently purified using a one-step the HIS-Select® Cobalt gravity flow columns using the same buffer used to purify the *B. subtilis* Noc (T160A)-His_6.

B. subtilis Noc (Δ10) was expressed using a similar protocol as Noc (WT), except pET21b::Noc (Δ10Noc)-His_6 was introduced into *E. coli* Rosetta (DE3) competent cells (Merck). Noc (Δ10) subsequently purified using a one-step the HIS-Select® Cobalt gravity flow columns using the same buffer used to purify the *B. subtilis* Noc (T160A)-His_6.

B. subtilis Noc (N121S) was expressed using a similar protocol as Noc (WT), except pET21b::Noc (N121S)-His_6 was introduced into *E. coli* Rosetta (DE3) competent cells (Merck). Noc (N121S) subsequently purified using a one-step the HIS-Select® Cobalt gravity flow columns using the same buffer used to purify the *B. subtilis* Noc (T160A)-His_6.

B. subtilis Noc (E29C) was expressed using a similar protocol as Noc (WT), except pET21b::Noc (E29C)-His_6 was introduced into *E. coli* Rosetta (DE3) competent cells (Merck).

Noc (E29C) subsequently purified using a one-step the HIS-Select® Cobalt gravity flow columns using the same buffer used to purify the *B. subtilis* Noc (T160A)-His_6.

B. subtilis Noc (E29C, R89A) was expressed using a similar protocol as Noc (WT), except pET21b::Noc (E29C, R89A)-His_6 was introduced into *E. coli* Rosetta (DE3) competent cells (Merck). Noc (E29C, R89A) subsequently purified using a one-step the HIS-Select® Cobalt gravity flow columns using the same buffer used to purify the *B. subtilis* Noc (T160A)-His_6.

B. subtilis Noc (E29C, N121S) was expressed using a similar protocol as Noc (WT), except pET21b::Noc (E29C, N121S)-His_6 was introduced into *E. coli* Rosetta (DE3) competent cells (Merck). Noc (E29C, N121S) subsequently purified using a one-step the HIS-Select® Cobalt gravity flow columns using the same buffer used to purify the *B. subtilis* Noc (T160A)-His_6.

B. subtilis Noc (NΔ10, E29C) was expressed using a similar protocol as Noc (WT), except pET21b::Noc (NΔ10,E29C)-His_6 was introduced into *E. coli* Rosetta (DE3) competent cells (Merck). Noc (NΔ10, E29C) subsequently purified using a one-step the HIS-Select® Cobalt gravity flow columns using the same buffer used to purify the *B. subtilis* Noc (T160A)-His_6.

B. subtilis Noc (S253C) was expressed using a similar protocol as Noc (WT), except pET21b::Noc (S253C)-His_6 was introduced into *E. coli* Rosetta (DE3) competent cells (Merck). Noc (S253C) subsequently purified using a one-step the HIS-Select® Cobalt gravity flow columns using the same buffer used to purify the *B. subtilis* Noc (T160A)-His_6.

B. subtilis Noc (E29C, S253C) was expressed using a similar protocol as Noc (WT), except pET21b::Noc (E29C, S253C)-His_6 was introduced into *E. coli* Rosetta (DE3) competent cells (Merck). Noc (E29C, S253C) subsequently purified using a one-step the HIS-Select® Cobalt gravity flow columns using the same buffer used to purify the *B. subtilis* Noc (T160A)-His_6.

Noc variants that were used in crosslinking experiments were purified using a one-step Ni-affinity column, and all buffers were adjusted to pH 7.4 which was optimal for crosslinking reactions. Purified proteins were desalted using a PD-10 column (Merck), concentrated using an Amicon Ultra-4 10 kDa cut-off spin column (Merck), and stored at -80˚C in a storage buffer [100 mM Tris-HCl pH 7.4, 250 mM NaCl, 10% (v/v) glycerol, and 1 mM TCEP].

2.5 Strain construction

2.5.1 Transformation of commercial E. coli DH5α cells

For transformation, the frozen commercial competent cells (Invitrogen) were quickly thawed. DNA was added to 50 µl of competent cells, which were incubated on ice for 30 min. The suspension was heat-shocked at 42°C for 25 s, then transferred to ice for 2 min. 0.6 ml of warm LB broth was added to the suspension, which was incubated for 1 h at 37°C. The transformed cells were plated out onto L agar plates containing the appropriate antibiotic and incubated at 37°C

2.5.2 General transformation of C. crescentus cells

2.5.2.1 Electroporation of electro-competent C. crescentus cells

50 µL of electro-competent *C. crescentus* cells was mixed with 5 µL of plasmid on ice. The mixture was then transferred into a 1 mL electroporation cuvette before being electroporated at 1500 V. Ice cold PYE was immediately added before the electroporated cells were left to grow at 28 °C for 3 h. The electroporated cells were then plated onto solid PYE supplemented with the appropriate antibiotics.

2.5.2.2 ΦCr30 transduction of C. crescentus cells

Electroporated CB15N *C. crescentus* cells were streaked for single colonies, and isolated colonies were then used to inoculate 20 mL of PYE and grown overnight (O/N). O/N cultures were then used as a template for PCR using primers 973 and 974 to verify the integration of *parB* into the *van* locus of CB15N. 100 µL of O/N cultures was then incubated with 1 µL of ΦCr30 (10^{10} pfu/mL phage stock) for 15 min at 28 °C. In parallel, molten 0.3% PYE agar [0.3 g of Bacto agar in 100 mL of PYE) was prepared. The ΦCr30 infected *C. crescentus* cells were then mixed with 15 mL of molten 0.3% PYE agar before being plated onto PYE plates and left to incubate O/N at 28 °C. The ΦCr30 infected *C. crescentus* molten PYE agar mixture was then scrapped into a 50 mL falcon tube before 100 µL of 100% chloroform was added and the mixture was subsequently vortexed and stores at 4 °C O/N. The mixture was then vortexed vigorously before being centrifuged at 8500 g for 10 m. The supernatant was then poured on to a clean petri dish and irradiated at 1500 UV, twice to inactivate the ΦCr30 phage. 1 mL of supernatant was aspirated and mixed with 50 µL of 100% chloroform. After vortexing the supernatant-chloroform mixture was spun at 10,000 rpm for 60 s and stored at 4 °C. For transduction of MT148 cells, a mixture consisting of [40 µL phage culture, 460 µL PYE, 10 µL 30% xylose and 500 µL of O/N MT148 culture] was incubated with shaking at 28 °C, before being plated on PYE agar supplemented with xylose and the appropriate antibiotics. Grown colonies were streaked twice on PYE agar supplemented with xylose and the appropriate antibiotics to isolate single colonies. The isolated single colonies were then used to inoculate 20 mL of PYE and grown O/N, before being stored at -70 °C for future use.

2.5.2.3 Generation of C. crescentus strains

To generate strain AJS35, electro-competent *C. crescentus* cells were electroporated with pMT571::*flag-parB* (D275K) plasmid to allow for a single integration at the vanA locus. Correct integration was subsequently verified via PCR using primers 973 and 974.

To generate strain AJS36,the same procedure as shown above was used, except that plasmid pMT571::flag-parB (G278K) was used.

To generate strain AJS37 the same procedure as shown above was used, except that plasmid pMT571::flag-parB (T282K) was used.

To generate strain AJS43, the same procedure as shown above was used, except that plasmid pMT571::flag-parB (T280K) was used.

To generate strain AJS44, the same procedure as shown above was used, except that plasmid pMT571::flag-parB (S279K) was used.

To generate strain AJS45, the same procedure as shown above was used, except that plasmid pMT571::flag-parB (D275K, T282K) was used.

To generate strain AJS46, the same procedure as shown above was used, except that plasmid pMT571::flag-parB (D275K, G278K) was used.

To generate strain AJS47, the same procedure as shown above was used, except that plasmid pMT571::flag-parB (D275K, G278K, T282K) was used.

To generate strain TLS1858, van::Pvan-1xflag-parB (D275K), marked with chloramphenicol^R, was transduced by phage ΦCr30 from AJ35 to MT148 to result in TLS1858.

To generate strain TLS1859, van::Pvan-1xflag-parB (G278K), marked with chloramphenicol^R, was transduced by phage ΦCr30 from AJ36 to MT148 to result in TLS1859.

To generate strain TLS1860, van::Pvan-1xflag-parB (T282K), marked with chloramphenicol^R, was transduced by phage ΦCr30 from AJ37 to MT148 to result in TLS1860.

To generate strain AJS48, van::Pvan-1xflag-parB (T280K), marked with chloramphenicol^R, was transduced by phage ΦCr30 from AJ43 to MT148 to result in AJS48.

To generate strain AJS49, van::Pvan-1xflag-parB (S279K), marked with chloramphenicol^R, was transduced by phage ΦCr30 from AJ44 to MT148 to result in AJS49.

To generate strain AJS50, van::Pvan-1xflag-parB (D275K, T282K), marked with chloramphenicol^R, was transduced by phage ΦCr30 from AJ45 to MT148 to result in AJS50.

To generate strain AJS51, van::Pvan-1xflag-parB (D275K, G278K), marked with chloramphenicol^R, was transduced by phage ΦCr30 from AJ46 to MT148 to result in AJS51.

To generate strain AJS52, van::Pvan-1xflag-parB (D275K, G278K, T282K), marked with chloramphenicol^R, was transduced by phage ΦCr30 from AJ47 to MT148 to result in AJS52.

To generate strain AJS81, electro-competent C. crescentus cells were electroporated with pMT571::*flag-parB* (D275K, G278K, S279K, T282K) plasmid to allow for a single integration at the vanA locus. Correct integration was subsequently verified via PCR using primers 973 and 974.

To generate strain AJS82, the same procedure as shown above was used, except that plasmid pMT571::flag-parB (D275K, G278K, T280K, T282K) was used.

To generate strain AJS83, the same procedure as shown above was used, except that plasmid pMT571::*flag-parB* (D275K, G278K, S279K, T280K, T282K) plasmid was used.

To generate strain AJS100, van::Pvan-1xflag-parB (D275K, G278K, S279K, T282K), marked with chloramphenicol^R, was transduced by phage ΦCr30 from AJS81 to MT148 to result in AJS100.

To generate strain AJS101, van::Pvan-1xflag-parB (D275K, G278K, T280K, T282K), marked with chloramphenicol^R, was transduced by phage ΦCr30 from AJS82 to MT148 to result in AJS101.

To generate strain AJS102 van::Pvan-1xflag-parB (D275K, G278K, S279K, T280K, T282K), marked with chloramphenicol^R, was transduced by phage ΦCr30 from AJS83 to MT148 to result in AJS102.

To generate strain AJS127, electro-competent *C. crescentus* cells were electroporated with pMT571::*flag-parB* (WT) plasmid to allow for a single integration at the vanA locus. Correct integration was subsequently verified via PCR using primers 973 and 974.

To generate strain AJS128, the same procedure as shown above was used, except that plasmid pMT571::flag-*yfp* was used.

To generate strain AJS154, van::Pvan-1xflag-parB (WT) marked with chloramphenicol^R, was transduced by phage ΦCr30 from AJS127 to MT148 to result in AJS154.

To generate strain AJS156, van::Pvan-1xflag-*yfp*, marked with chloramphenicol^R, was transduced by phage ΦCr30 from AJS128 to MT148 to result in AJS156.

2.6 Reconstitution of DNA for *in vitro* experiments

2.6.1 Reconstitution of parS DNA for X-ray crystallography

A 20-bp palindromic DNA fragment (5'-GATGTTTCACGTGAAACATC-3') (3600 μM in buffer that contains 10 mM Tris-HCl pH 8.0 and 250 mM NaCl) was heated to 95°C for 5 min before being left to cool at room temperature overnight to form a double stranded *parS* DNA (final concentration: 1800 μM). The 14-bp *parS* site sequences are underlined.

A 22-bp palindromic single-stranded DNA fragment (5'GGATGTTTCACGTGAAACATCC-3') (3600 μM in 10 mM Tris-HCl pH 8.0, 250 mM NaCl buffer) was heated at 95°C for 5 min before being left to cool down to room temperature (RT) overnight to form a double stranded *parS* DNA (final concentration: 1800 μM). The 14-bp *parS* site sequences are underlined.

2.6.1.2 Reconstitution of NBS DNA for X-ray crystallography

A 22-bp DNA fragment (5'-GGATATTTCCCGGGAAATATCC-3') (3600 μM in buffer that contains 10 mM Tris-HCl pH 8.0 and 250 mM NaCl) was heated to 95°C for 5 min before being left to cool at room temperature overnight to form a double stranded *NBS* DNA (final concentration: 1800 μM). The 14-bp *NBS* site sequences are underlined.

2.6.2 Reconstitution of DNA for Bio-layer Interferometry (BLI)

2.6.2.1 20 bp parS or NBS- containing DNA

A 22-bp palindromic single-stranded DNA (ssDNA) oligomer (*NBS*: GGATATTTCCCGGGAAATATCC or *parS*: GGATGTTTCACGTGAAACATCC) [dissolved to 100 μM in buffer containing 1 mM Tris-HCl pH 8.0 and 5 mM NaCl] was heated at 98°C for 5

min before being left to cool down to room temperature overnight to form 50 µM *parS* or *NBS* DNA duplex. The core sequences of *NBS* and *parS* are underlined.

2.6.2.2 170 bp parS or NBS- containing DNA

All DNA constructs were designed in VectorNTI (Thermo Fisher) and were chemically synthesized (gBlocks dsDNA fragments, IDT). All linear DNA constructs were designed with an M13F and M13R homologous region at each end. To generate a dual biotin-labeled DNA substrate, PCR reactions were performed using a 2x GoTaq PCR master mix (Promega), biotin-labelled M13F and biotin-labelled M13R primers, and gBlocks fragments as template. PCR products were resolved by electrophoresis using a 2% TAE agarose gel and subsequently gel purified.

2.6.3 Reconstitution of DNA for surface plasmon resonance (SPR)

Single-stranded oligomers containing *parS*, scrambled *parS* or *NBS* sequences were purchased from Sigma and reconstituted to 100 µM in water. Complementary oligos were annealed together in an annealing buffer (10 mM Tris–HCl pH 8.0, 50 mM NaCl, and 1 mM EDTA) to form double stranded DNA before being diluted to a working concentration of 1 µM in HPS-EP+ buffer (0.01 M HEPES pH 7.4, 0.15 M NaCl, 3 mM EDTA, 0.005% v/v Surfactant P20) for each SPR experiment.

2.7 *In vitro* measurement of protein-DNA interactions

2.7.1 Measurement of protein-DNA interactions by Bio-layer Interferometry (BLI)

Bio-layer interferometry experiments were conducted using a BLItz system equipped with Dip-and-Read Streptavidin (SA) Biosensors (Molecular Devices). BLItz monitors wavelength shifts (nm) resulting from changes in the optical thickness of the sensor surface during association or dissociation of the analyte. All BLI experiments were performed at 22°C. The streptavidin biosensor was hydrated in a low-salt binding buffer [100 mM Tris-HCl pH 8.0, 150 mM NaCl, 1 mM $MgCl_2$, and 0.005% Tween 20] for at least 10 min before each experiment. Biotinylated double-stranded DNA (dsDNA) was immobilized onto the surface of the SA biosensor through a cycle of Baseline (30 s), Association (120 s), and Dissociation (120 s). For experiments done using *B. subtilis* Noc, an association time of (600s), and Dissociation time of (600s) was used. Briefly, the tip of the biosensor was dipped into a binding buffer for 30 s to establish the baseline, then to 1 µM biotinylated dsDNA for 120 s, and finally to a low salt binding buffer for 120 s to allow for dissociation.

After the immobilization of DNA on the sensor, association reactions were monitored at 1 µM dimer concentration of Noc (with or without 1 µM TetR or NTPs at various concentrations) for

600 s. At the end of each binding step, the sensor was transferred into a protein-free binding buffer to follow the dissociation kinetics for 600 s. The sensor can be recycled by dipping in a high-salt buffer [100 mM Tris-HCl pH 8.0, 2000 mM NaCl, 1mM EDTA, 0.005% Tween 20] for 10 min to remove bound Noc.

For experiments where a closed DNA was cleaved to generate a free DNA end, DNA-coated tips were dipped into 300 µL of cutting solution [266 µL of water, 30 µL of 10x CutSmart buffer (NEB), and 4 µL of *Eco*RI-HF or *Bam*HI-HF restriction enzyme (20,000 units/mL)] for 30 min at 37°C. NTP (stock concentration: 100 mM) used in BLI assays was purchased from ThermoFisher.

2.7.2 Measurement of protein-DNA interactions by Surface Plasmon Resonance (SPR)

The sequences of DNA oligos used in this study are reported in 2.1.5. SPR measurements were recorded at 25°C using a Biacore T200 system (GE Healthcare). All experiments were performed using *R*e-usable *D*NA *Ca*pture *T*echnique (ReDCaT) exactly as described in (Stevenson et al., 2013). Briefly, ReDCaT uses a Sensor Chip SA (GE Healthcare), which has streptavidin pre-immobilized to a carboxymethylated dextran matrix, to which a 20-base biotinylated ReDCaT linker is immobilised. This is then used to immobilize *parS*-containing biotin-labelled double stranded oligos on the chip surface as each contain a single stranded overhand complimentary to the ReDCaT linker on the surface. The DNA to be tested is flowed over one flow cell on the chip at a flow rate of 10 µL/min and it anneals through the complementary DNA to the ReDCaT linker. *C. crescentus* ParB-$(His)_6$ or *B. subtilis* ParB-$(His)_6$, pre-diluted in HBS-EP+ buffer, was then flowed over the chip surface (the blank surface and the one with the DNA immobilised) and then HBS-EP+ buffer was then passed over to allow ParB-$(His)_6$ to dissociate from DNA. A high-salt wash buffer was injected to the chip to wash off any residual ParB-$(His)_6$ protein on the chip's surface. The test DNA could then be removed using a wash with 1M NaCl, 50mM NaOH. The chip could then be used again to load a new piece of test DNA. The SPR signal (Response Units) was monitored continuously throughout the process. Each cycle was repeated for increasing concentrations of ParB-$(His)_6$. For each concentration, the amount of ParB bound was measured and plotted against the concentration to construct a ParB-*parS* binding curve. All sensorgrams recorded during ReDCaT experiments were analysed using Biacore T200 BiaEvaluation software version 1.0 (GE Healthcare). Data were then plotted using Microsoft Excel or R, and K_d was estimated from best-fit curves.

2.8 Measurement of protein-NTP interactions by isothermal titration calorimetry (ITC)

All ITC experiments were recorded using a MicroCal PEAQ ITC instrument (Malvern Panalytical, UK). Experiments were performed at 4°C and both protein and ligand were in the buffer 100 mM Tris-HCl pH 8.0, 100 mM NaCl, and 5 mM $CaCl_2$. The calorimetric cell was filled with 100 µM monomer concentration of either B. subtilis Noc (WT), Noc (R89A), or Noc (N121S), and was titrated with 3 mM CTPɣS. For each ITC run, a single injection of 0.5 µL of 3 mM CTPɣS was performed first, following by 19 injections of 2 µL each. Injections were made at 120 s intervals with a stirring speed of 750 rpm. Each experiment was run in duplicate. The raw titration data were integrated and fitted to a one-site binding model using the built-in software of the MicroCal PEAQ ITC. Controls (CTPɣS into buffer and buffer into protein) were performed and no signal was observed.

2.9 Crystallisation and cryoprotection of ParB and Noc variants

2.9.1 General X-ray crystallography data collection and reduction

Crystallisation screens were set up in sitting-drop vapour diffusion format in MRC2 96-well crystallisation plates with drops comprised of 0.3 µL precipitant solution and 0.3 µL of protein and incubated at 293 K. After optimization of an initial hit, suitable crystals were cryoprotected with 20% (v/v) glycerol and mounted in Litholoops (Molecular Dimensions) before flash-cooling by plunging into liquid nitrogen. X-ray data were recorded on beamline I04-1 at the Diamond Light Source (Oxfordshire, UK) using a Pilatus 6M-F hybrid photon counting detector (Dectris), with crystals maintained at 100 K by a Cryojet cryocooler (Oxford Instruments). Diffraction data were integrated and scaled using DIALS (Winter et al., 2018) via the XIA2 (Winter, 2010) expert system then merged using AIMLESS (Evans and Murshudov, 2013). The majority of the downstream analysis was performed through the CCP4i2 graphical user interface (Potterton et al., 2018).

2.9.2 Crystallisation of the DNA-binding domain (DBD) of C. crescentus ParB in complex with parS

His-tagged (DBD)-ParB (10 mg/mL) was mixed with a 20-bp *parS* site at a molar ratio of 1:1.2 (protein:DNA) in the elution buffer (10 mM Tris-HCl pH8.0, 250 mM NaCl). The DBD ParB-*parS* complex crystals grew in a solution containing 19% (w/v) PEG 3350 and 49 mM lithium citrate. Suitable crystals were then cryoprotected in a solution containing 19% (w/v) PEG3350, 49 mM lithium citrate and 20% glycerol.

2.9.3 Crystallisation and the C-terminally truncated (ΔCTD) ParB (QKKR+K227) in complex with NBS

His-tagged ParBΔCTD (QKKR+K227) (10 mg/mL) was mixed with a 20-bp *NBS* site at a molar ratio of 1:1.2 (protein:DNA) in the elution buffer (10mM Tris-HCl pH8.0, 250 mM NaCl). The ParBΔCTD (QKKR+K227)-*NBS* complex crystals grew in a solution containing 20% (w/v) PEG3350, 263 mM magnesium formate and 10% (v/v) glycerol. Suitable crystals were then cryoprotected in a solution containing 20% (w/v) PEG 3350, 263 mM magnesium formate and 20% glycerol.

2.9.4 Crystallisation and cryoprotection of the DNA-binding domain (DBD) Noc in complex with 22-bp NBS

His-tagged Noc (DBD)-His_6 (10 mg/mL) was mixed with a 22-bp *NBS* duplex at a molar ratio of 1:1.2 protein:DNA in buffer containing 10 mM Tris-HCl pH 8.0 and 250 mM NaCl. The Noc (DBD)-*NBS* crystals grew in a solution containing 20% (w/v) PEG 3350 and 200 mM di-potassium phosphate. Suitable crystals were then cryoprotected in a solution containing 20% (w/v) PEG3350, 200 mM di-potassium phosphate and 20% glycerol.

2.9.5 Crystallisation and cryoprotection of the C-terminal truncated C. crescentus ParBΔCTD-parS complex

His-tagged ParBΔCTD (10 mg/mL) was mixed with a 22-bp *parS* duplex DNA at a molar ratio of 2:1.2 (protein monomer: DNA) in the gel filtration elution buffer (10 mM Tris-HCl pH 8.0, 250 mM NaCl). The ParBΔCTD-*parS* crystals grew in a solution containing 20.5% (w/v) PEG 3350, 263 mM magnesium formate, and 10% (v/v) glycerol. Suitable crystals were then cryoprotected in a solution containing 20% (w/v) PEG3350, 200 mM di-potassium phosphate and 20% glycerol.

2.9.6 Crystallisation and cryoprotection of the C. crescentus ParBΔCTD-CTPɣS complex

His-tagged ParBΔCTD (10 mg/mL) was premixed with 1 mM CTPɣS and 1 mM $MgCl_2$ in buffer [10 mM Tris-HCl pH 8.0 and 250 mM NaCl] before crystallisation. The ParBΔCTD-CTPɣS crystals grew in a solution containing 15% (w/v) PEG 3350, 260 mM calcium acetate, 10% (v/v) glycerol, 1 mM CTPɣS, and 1 mM $MgCl_2$. Suitable crystals were then cryoprotected in a solution containing 15% (w/v) PEG3350, 260 mM calcium acetate and 20% glycerol.

2.9.7 Crystallisation and cryoprotection of the C. crescentus ParBΔ44NΔCTD-CDP complex

His-tagged ParBΔ44NΔCTD (10 mg/mL) was premixed with 1 mM CTP and 1 mM MgCl2 in buffer [10 mM Tris-HCl pH 8.0 and 250 mM NaCl] before crystallisation. The crystals grew in a solution containing X (w/v) PEG 400 and 0.1M MES pH 6.5.

2.9.8 Crystallisation and cryoprotection of the G. thermoleovorans NocΔCTD Noc

His-tagged NocΔCTD Noc (10 mg/mL) was premixed with 1 mM CTP and 1 mM MgCl2 in buffer [10 mM Tris-HCl pH 8.0 and 250 mM NaCl] before crystallisation. Crystals grew in a solution containing 2000 mM ammonium sulphate and 50 mM tri-sodium citrate and were cryoprotected in the crystallisation solution supplemented with 20% (v/v) glycerol, 1 mM CTP and 1 mM $MgCl_2$. For iodide derivatization, the cryoprotectant comprised of the crystallisation solution supplemented with 25% (v/v) ethylene glycol, 1 mM CTP, 1 mM $MgCl_2$, and 500 mM potassium iodide; crystals were soaked in this solution for less than 30 seconds before cryocooling. Despite the presence of CTP in the crystallisation buffer, no density for CTP was found in the NocΔCTD structure, presumably because *NBS* DNA was not included to facilitate CTP binding.

2.9.9 Crystallisation and cryoprotection of the G. thermoleovorans NocNΔ26ΔCTD Noc

His-tagged NocNΔ26ΔCTD Noc (10 mg/mL) was premixed with 1 mM CTPɣS and 1 mM $MgCl_2$ in buffer [10 mM Tris-HCl pH 8.0 and 250 mM NaCl] before crystallisation. NocNΔ26ΔCTD crystals grew in a solution containing 211 mM di-ammonium phosphate and 2293 mM ammonium sulphate.

2.10 Structure determination and refinement of ParB and Noc variant structures

2.10.1 Structure determination and refinement of the C. crescentus DBD-ParB-parS complex

The ParB (DBD)-*parS* complex crystallized in space group *C*2 with approximate cell parameters of *a* = 122.1, *b* = 40.7, *c* = 94.0 Å and β = 121.4° (Table 2.12.1). Analysis of the likely composition of the asymmetric unit (ASU) suggested that it would contain two copies of the ParB (DBD) bound to a single DNA duplex, giving an estimated solvent content of ~49%. A molecular replacement template covering the DBD was generated by manually editing the protein component of the structure of the Spo0J-*parS* complex from *Helicobacter pylori* (PDB accession code 4UMK; 42% identity over 75% of the sequence) (Chen et al., 2015) and truncating all side-chains to Cβ atoms. For the DNA component, an ideal B-form DNA duplex was generated in COOT (Emsley and Cowtan, 2004) from the 20-bp palindromic sequence of *parS*. PHASER (McCoy et al., 2007) was used to place the DNA duplex, followed by two copies of the DBD into the ASU. The placement of the DNA-binding domains with respect to the DNA duplex was analogous to that seen in the *H. pylori* Spo0J-*parS* (Chen et al., 2015), and an analysis of crystal contacts revealed that the DNA formed a pseudo-continuous filament spanning the crystal due to base-pair stacking between adjacent DNA fragments. After restrained refinement in REFMAC5 (Murshudov et al., 1997) at 2.4 Å resolution, the protein component of the model was completely rebuilt using BUCCANEER (Cowtan, 2006).

The model was finalized after several iterations of manual editing in COOT (Emsley and Cowtan, 2004) and further refinement in REFMAC5 (Murshudov et al., 1997). The model statistics are reported in Table 3.1 (Chapter 3).

2.10.2 Structure determination and refinement of the C. crescentus ParBΔCTD (QKKR+K227)-NBS complex

The ParBΔCTD (QKKR+K227)-*NBS* complex crystallized in space group I4122 with approximate cell parameters of a = b = 117.9, c = 249.6 Å (Table 2.12.1). The data were weak and anisotropic and, as a consequence, were truncated to a resolution of 3.6 Å. Despite multiple attempts, we were not able to collect a better dataset. Analysis of the likely composition of the asymmetric unit (ASU) suggested that it would contain two copies of ParBΔCTD (QKKR+K227) bound to a single DNA duplex, giving an estimated solvent content of ~61%. A preliminary model was obtained using PHASER (McCoy et al., 2007), which was able to place the full ParB (DBD)-*parS* complex structure in the ASU. As with the previous structure, crystal contacts gave a pseudo-continuous DNA filament spanning the crystal via base-pair stacking between adjacent DNA fragments. After correcting for sequence changes in both the protein and DNA and applying rigid body adjustments to several α-helices in the electron density, the model was refined in REFMAC5 (Murshudov et al., 1997) to give a slightly improved map (to enhance interpretability, a sharpening factor of 100 Å2 was applied to the map calculations). At this point it was possible to dock one of the missing N-terminal domains into electron density adjacent to the A chain (this was a poly-Ala model derived from the *H. pylori* ParB model; PDB accession code 4UMK) (Chen et al., 2015), whilst the second could not be placed with confidence. The final model was obtained after further iterations of manual editing in COOT and refinement with tight geometrical restraints in REFMAC5 (Murshudov et al., 1997). The model statistics are reported in Table 3.1 (Chapter 3).

2.10.3 Structure determination and refinement of the B. subtilis DBD-Noc-NBS structure

The Noc DBD-*NBS* complex crystallized in space group *C*2 with approximate cell parameters of *a* = 134.1, *b* = 60.6, *c* = 81.0 Å and β = 116.9°. The data were collected in two 360° sweeps separated by a χ offset of 20°. Data reduction in AIMLESS (Evans and Murshudov, 2013) indicated that the diffraction was highly anisotropic, and thus before using the dataset, it was corrected using STARANISO with a local mean *I/σ(I)* threshold of 1.2, giving maximum and minimum anisotropic resolution cut-offs of 2.23 and 4.02 Å, respectively (Table 2.12.1). Analysis of the likely composition of the asymmetric unit (ASU) suggested that it would contain two copies of the Noc DBD bound to a single DNA duplex, giving an estimated solvent content of ~69%. A molecular replacement template covering the DBD was generated from the ParB DBD structure above using SCULPTOR (41% identity overall) (Bunkóczi and Read, 2011).

For the DNA component, an ideal B-form DNA duplex was generated from the 22-bp palindromic sequence of *NBS*. PHASER (McCoy et al., 2007) was used to place the DNA duplex, followed by two copies of the DBD template into the ASU. This generated a complex that was consistent with that of ParB DBD-*parS* determined above, again with the DNA forming a pseudo-continuous filament spanning the crystal due to base-pair stacking between adjacent DNA fragments. After restrained refinement in REFMAC5 (Murshudov et al., 1997) at 2.23 Å resolution, the protein component of the model was completely rebuilt using BUCCANEER (Cowtan, 2006). The model was finalized after several iterations of manual editing in COOT (Emsley and Cowtan, 2004) and further refinement in REFMAC5 (Murshudov et al., 1997) incorporating TLS restraints. To avoid model bias resulting from the feature of REFMAC5 (Murshudov et al., 1997) to approximate missing reflections within the spherical resolution cut-off to their calculated values, these filled-in reflections were removed prior to map inspection. Subsequently, the map connectivity was improved by applying a blurring factor of 60 $Å^2$. The model statistics are reported in Table 3.1 (Chapter 3).

2.10.4 Structure determination and refinement of the C. crescentus ParBΔCTD-parS structure

The ParBΔCTD-*parS* complex crystallized in space group P21 with cell parameters of a = 54.25, b = 172.93, c = 72.85 Å and β = 90.54° (Table 2.12.1). Analysis of the likely composition of the asymmetric unit (ASU) suggested that it would contain four copies of the ParBΔCTD monomers and two copies of the 22-bp parS DNA duplex, giving an estimated solvent content of ~46.6%. Interrogation of the Protein Data Bank with the sequence of the *C. crescentus* ParBΔCTD revealed two suitable template structures for molecular replacement: apo-ParB from *T. thermophilus* (Leonard et al., 2004) (PDB accession code: 1VZ0; 46% identity over 82% of the sequence) and *H. pylori* ParB bound to *parS* DNA (Chen et al., 2015) (PDB accession code: 4UMK; 42% identity over 75% of the sequence).

First, single subunits taken from these two entries were trimmed using SCULPTOR (Bunkóczi and Read, 2011) to retain the parts of the structure that aligned with the *C. crescentus* ParBΔCTD sequence, and then all side chains were truncated to Cβ atoms using CHAINSAW (Stein, 2008). Comparison of these templates revealed a completely different relationship between the N-terminal domain and the DNA-binding domain. Thus, I prepared search templates based on the individual domains rather than the subunits. The pairs of templates for each domain were then aligned and used as ensemble search models in PHASER (McCoy et al., 2007). For the DNA component, an ideal B-form DNA duplex was generated in COOT (Emsley and Cowtan, 2004) from a 22- bp palindromic sequence of *parS*. A variety of protocols were attempted in PHASER (McCoy et al., 2007), the best result was obtained by searching for the two DNA duplexes first, followed by four copies of the DNA-binding domain, giving a

TFZ score of 10.5 at 4.5 Å resolution. We found that the placement of the DNA-binding domains with respect to the DNA duplexes was analogous to that seen in the *H. pylori* ParBΔCTD-*parS* complex. After several iterations of rebuilding in COOT and refining the model in REFMAC5 (Murshudov et al., 1997), it was possible to manually dock one copy of the N-terminal domain template (from 1VZ0) into weak and fragmented electron density such that it could be joined to one of the DNA-binding domains. A superposition of this more complete subunit onto the other three copies revealed that in only one of these did the N-terminal domain agree with the electron density. Inspection of the remaining unfilled electron density showed evidence for the last two missing N-terminal domains, which were also added by manual docking of the domain template (from 1VZ0). For the final stages, TLS refinement was used with a single TLS domain defined for each protein chain and for each DNA strand. The statistics of the final refined model, including validation output from MolProbity (Davis et al., 2007), are summarized in Table 4.1.

2.10.5 Structure determination and refinement of the C. crescentus ParBΔCTD-CTPγS co-crystal structure

The ParBΔCTD-CTPγS complex crystallized in space group $P2_1$ with cell parameters of a = 69.5, b = 56.1, c = 71.4 Å and β = 98.4° (Table 2.12.2). Analysis of the likely composition of the asymmetric unit (ASU) suggested that it contains two copies of the ParBΔCTD monomer giving an estimated solvent content of ~50%. Molecular replacement templates were generated from the ParBΔCTD-*parS* complex solved above. Attempts to solve the structure in PHASER (McCoy et al., 2007) using individual subunits taken from the latter in both conformations did not yield any convincing solutions, suggesting that the subunits had adopted new conformations. Given that the two subunit conformations observed in the previous structure differed largely in the relative dispositions of DBD and NTDs, we reasoned that a better outcome might be achieved by searching for the DNA-binding domains and N-terminal domains separately. This time PHASER (McCoy et al., 2007) successfully placed two copies of each domain in the ASU such that they could be reconnected to give two subunits in a new conformation. The result was subjected to 100 cycles of jelly-body refinement in REFMAC5 (Murshudov et al., 1997) before rebuilding with BUCCANEER (Cowtan, 2006) to give a model in which 77% of the expected residues had been fitted into two chains and sequenced. The model was completed after further iterations of model editing in COOT and refinement with REFMAC5 (Murshudov et al., 1997). In this case, TLS refinement was not used as this gave poorer validation results. The statistics of the final refined model, including validation output from MolProbity (Davis et al., 2007), are summarized in Table 4.1.

2.10.6 Structure determination and refinement of the C. crescentus ParBΔ44NΔCTD-CDP complex

The ParBD44NΔCTD crystallized in space group P21212 with cell parameters of a = 56.130, b = 69.406, c = 55.260 Å and β = 90°. Analysis of the likely composition of the asymmetric unit (ASU) suggested that it would contain a single copy of the ParBΔ44NΔCTD monomer, giving an estimated cell content of ~43%. The structure was solved by molecular replacement with PHASER (McCoy et al., 2007) using Chain A from the *C. crescentus* ParBΔCTD-*parS* structure as a template. The search model was split into two separate ensembles comprising residues 44-120 and 121-230 respectively. PHASER (McCoy et al., 2007) successfully placed all three ensembles, although one of these had to be interchanged with a symmetry mate in order to restore the connectivity of the starting template. Several iterations of model building in COOT (Emsley and Cowtan, 2004) and refinement REFMAC5 (Murshudov et al., 1997) yielded the final model with R_{work} and R_{free} values of 0.185 and 0.205, respectively, to 1.28 Å resolution. The statistics of the final refined model, including validation output from MolProbity (Davis et al., 2007), are summarized in Table 4.1.

2.10.7 Structure determination and refinement of the G. thermoleovorans NocΔCTD structure

Three 360° passes of X-ray data were taken at a wavelength of 1.8 Å from different parts of a single crystal and merged to give a highly redundant dataset to 3.4 Å resolution in space group P213 with cell parameters a = b = c = 136.6 Å. Solvent content estimation gave a value of 66% for two copies of the 29 kDa subunit per asymmetric unit (ASU). The structure was subsequently solved by single-wavelength anomalous dispersion using the CRANK2 pipeline (Skubák and Pannu, 2013), which located 12 iodide sites, and BUCCANEER (Cowtan, 2006) was able to build and sequence 339 residues in two chains corresponding to 67% of those expected for two monomers, giving R_{work} and R_{free} values of 0.318 and 0.362, respectively, to 3.4 Å resolution after refinement with REFMAC5 (Murshudov et al., 1997). At this point, this preliminary model was used as a starting point for refinement against a native data set processed to 2.5 Å resolution in the same space group, but with a significantly longer cell edge of 146.8 Å corresponding to a solvent content of 72.6%. Thus, it was necessary to resolve the structure by molecular replacement using PHASER (McCoy et al., 2007) before further refinement in REFMAC5 (Murshudov et al., 1997). After a complete rebuild in BUCCANEER (Cowtan, 2006), several iterations of model building in COOT (Emsley and Cowtan, 2004) and REFMAC5 (Murshudov et al., 1997) refinement jobs yielded the final model with R_{work} and R_{free} values of 0.210 and 0.240, respectively, to 2.5 Å resolution. The statistics of the final refined model, including validation output from MolProbity (Davis et al., 2007), are summarized in Table 5.1.

2.10.8 Structure determination and refinement of the G. thermoleovorans NocNΔ26ΔCTD structure

NocNΔ26ΔCTD crystallized in the space group C2221 with cell parameters of a = 105.1, b = 106.6, c = 42.2 Å. Analysis of the likely composition of the ASU suggested that it contained a single copy of the 26 kDa NocNΔ26ΔCTD Noc monomer, giving an estimated solvent content of 46%. The structure was solved by molecular replacement with PHASER (McCoy et al., 2007) using chain A from the *G. thermoleovorans* NocΔCTD structure above as the template. The search model was split into three separate ensembles comprising residues 26-100, 101-140, and 141-230, respectively. PHASER (McCoy et al., 2007) successfully placed all three ensembles, although one of these had to be interchanged with a symmetry mate in order to restore the connectivity of the starting template. Several iterations of model building in COOT (Emsley and Cowtan, 2004) and refinement REFMAC5 (Murshudov et al., 1997) yielded the final model with R_{work} and R_{free} values of 0.267 and 0.288, respectively, to 2.95 Å resolution. The statistics of the final refined model, including validation output from MolProbity (Davis et al., 2007), are summarized in Table 5.1.

2.11 Analysis of crystal structures

Superpositions of structures presented in this thesis were performed either by using the *align*/*cealign* function in PyMOL (DeLano, 2002) or by using the superpose function on CCP4 QtMG (Potterton et al., 2018). Protein-DNA, Protein-Protein contacts were determined using the jsPISA webserver (Krissinel, 2015). Curves+ (Blanchet et al., 2011) was used to determine DNA shape parameters reported from the crystal structures, while the shape parameters for unbound DNA was predicted using the DNAshape webserver (Zhou et al., 2013).

2.12 Differential radial capillary action of ligand assay (DRaCALA) or membrane-spotting assay

Purified *C. crescentus* 25 μM ParB-His_6 or 25 μM TetR-His_6 or 40 μM *B. subtilis* Noc were incubated with 3 nM radiolabelled P^{32}-α-CTP (Perkin Elmer), 30 μM of unlabelled cold CTP (Thermo Fisher), 0.5 μM of 22-bp *parS* or *NBS* DNA duplex in the reaction buffer [100 mM Tris pH 8.0, 100 mM NaCl, and 10 mM $MgCl_2$] for 5 minutes at room temperature. For the NTP competition assay, the mixture was further supplemented with 500 μM of either unlabelled cold CTP, ATP, GTP, or UTP. Four μL of samples were spotted slowly onto a dry nitrocellulose membrane and air-dried. The nitrocellulose membrane was wrapped in cling film before being exposed to a phosphor screen (GE Healthcare) for two minutes. Each DRaCALA assay was triplicated and a representative autoradiograph was shown.

2.13 Magnetic tweezer assays

Magnetic tweezer assays Magnetic tweezer experiments were performed using a home-made setup as described previously (Fisher et al., 2017; Taylor et al., 2015). Briefly, images of micrometer-sized superparamagnetic beads tethered to the surface of a glass slide by DNA constructs are acquired with a 100x oil immersion objective and a CCD camera. Real-time image analysis was used to determine the spatial coordinates of beads with nm accuracy in x, y and z. A step-by-step motor located above the sample moves a pair of magnets allowing the application of stretching forces to the bead-DNA system. We used horizontally aligned magnets coupled to an iron holder. Applied forces can be quantified from the Brownian excursions of the bead and the extension of the DNA tether. Data were acquired at 150 Hz to minimize sampling artifacts in force determination. We used horizontally aligned magnets coupled to an iron holder to achieve force up to 15 pN.

Fabrication of DNA substrates for magnetic tweezer experiments containing a single *parS* sequence with biotins and digoxigenins at the tails was described previously (Taylor et al., 2015).The DNA molecules were incubated with 2.8 µm streptavidin-coated beads (MyOne, Invitrogen) for 10 min. Then, the DNA bead complex was injected in a liquid cell functionalized with anti-digoxigenin antibodies (Roche) and incubated for 10 min before applying force. Torsionally constrained molecules and beads with more than a single DNA molecule were identified from its distinct rotation-extension curves and discarded for further analysis. All the experiments were performed in a reaction buffer composed of 10 mM HEPES pH 7.5, 150 mM NaCl, 3 mM EDTA, 0.1% (v/v) Tween-20 and 100 µg/ml BSA.

Force-extension curves were obtained by decreasing the applied force in steps from 15 pN to ~0.02 pN for a total measuring time of 15 min. First, we measured the force-extension response for bare DNA molecules. Then, the force was reset to 15 pN and ParB variants were flown and incubated for 2 min before starting the measurement of a force-extension curve at the same magnet positions in absence of proteins. The force applied to each bead was determined based on the force-extension data of bare DNA molecules. Bare DNA curves were fitted to the worm-like chain model and fitted values of persistence length and contour length were used as a quality control. Molecules with a large discrepancy for contour length or persistence with respect to expected parameters (45 nm persistence length, 2.1 µm contour length) were discarded from the analysis.

2.14 Immunoblot analysis

To confirm the presence of FLAG-tagged ParB variants, O/N cultures of *C. crescentus* harbouring FLAG-tagged ParB variants were used to inoculate 25 mL of PYE supplemented

with the appropriate antibiotics, xylose and vanillate to an OD_{600} of 0.1. Cultures were then left to grow for ~3 h when the OD_{600} of 0.4, before *C. crescentus* cells were pelleted and resuspended directly in 1xSDS buffer. Samples were then heated to 95°C for 5 min before loading. Total protein was run on 10% Tris-HCL gels (Bio-Rad) at 150 V for separation. Resolved proteins were transferred to polyvinylidene fluoride membranes using the Trans-Blot Turbo Transfer System (BioRad) and probed with 1:10,000 dilution of primary α-FLAG antibodies (Sigma Aldrich). Blots were imaged using an Amersham Imager 600 (GE Healthcare).

For protein expression related experiments, isolated single colonies of *C. crescentus* strains were used to inoculate 25 mL of PYE supplemented with xylose or glucose + vanillate with the appropriate antibiotics and left to grow O/N. For proline harbouring ParB variants, the O/N culture was then used to inoculate 25 mL of PYE supplemented with xylose and the appropriate antibiotics to an OD_{600} of 0.1. Cultures were then left to grow for ~3 h when the OD_{600} of 0.4, before cells were pelleted and washed 2x to remove remaining xylose. The pelleted cells were then resuspended in 25 mL of PYE supplemented with glucose and vanillate and left to grow for 2 h before being pelleted and resuspended directly in 1xSDS sample buffer, then heated to 95°C for 5 min before loading. Bradford assay was used to measure the total protein in sample and an equal volume of protein between each sample was run on 10% Tris-HCL gels (Bio-Rad) at 150 V for separation. Resolved proteins were transferred to polyvinylidene fluoride membranes using the Trans-Blot Turbo Transfer System (BioRad) and probed with 1:10,000 dilution of primary α-FLAG antibodies (Sigma Aldrich). Blots were imaged using an Amersham Imager 600 (GE Healthcare).

For the lysine harbouring ParB variants, the O/N cultures were prepared in PYE supplemented with glucose + vanillate with the appropriate antibiotics. The O/N culture was then used to inoculate 25 mL of PYE supplemented with glucose and vanillate and the appropriate antibiotics to an OD_{600} of 0.1. Cultures were then left to grow for ~3 h when the OD_{600} of 0.4 before being *C. crescentus* cells were pelleted and resuspended directly in 1xSDS sample buffer, then heated to 95°C for 5 min before loading. Bradford assay was used to measure the total protein in sample and an equal volume of protein between each sample was run on 10% Tris-HCL gels (Bio-Rad) at 150 V for separation. Resolved proteins were transferred to polyvinylidene fluoride membranes using the Trans-Blot Turbo Transfer System (BioRad) and probed with 1:10,000 dilution of primary α-FLAG antibodies (Sigma Aldrich). Blots were imaged using an Amersham Imager 600 (GE Healthcare).

2.15 Genome-wide techniques

2.15.1 Chromatin immunoprecipitation coupled with deep sequencing (ChIP-seq)

C. crescentus cell cultures (25 mL) were grown in PYE (in the presence of appropriate antibiotics, 0.3% glucose, and 0.5 mM vanillate) before fixation with formaldehyde to a final concentration of 1%. Fixed cells were incubated at RT for 30 minutes, then quenched with 0.125 M glycine for 15 minutes at RT. Cells were washed three times with 1× PBS (pH 7.4) and resuspended in 1 ml of buffer 1 (20 mM K-HEPES pH 7.9, 50 mM KCl, 10% Glycerol and Roche EDTA-free protease inhibitors). Subsequently, the cell suspension was sonicated on ice using a probe-type sonicator (8 cycles, 15 s ON, 15 s OFF, at setting 8) to shear the chromatin to below 1 kb, and the cell debris was cleared by centrifugation (20 min at 13 000 rpm at 4°C).

The supernatant was then transferred to a new 2 ml tube and the buffer conditions were adjusted to 10 mM Tris–HCl pH 8, 150 mM NaCl and 0.1% NP-40. Fifty microliters of the supernatant were transferred to a separate tube for control (the INPUT fraction) and stored at –20°C. In the meantime, antibodies-coupled beads were washed off storage buffers before adding to the above supernatant. I then used α-FLAG antibodies coupled to agarose beads (Sigma, UK) for ChIP-seq of FLAG-ParB (WT) and variants, and FLAG-YFP. Briefly, 25 µl of beads was washed off storage buffer by repeated centrifugation and resuspension in IPP150 buffer (10 mM Tris–HCl pH 8, 150 mM NaCl and 0.1% NP-40). Beads were then introduced to the cleared supernatant and incubated with gentle shaking at 4°C overnight. In the next day, beads were then washed five times at 4°C for 2 min each with 1 ml of IPP150 buffer, then twice at 4°C for 2 min each in 1× TE buffer (10 mM Tris–HCl pH 8 and 1 mM EDTA). Protein–DNA complexes were then eluted twice from the beads by incubating the beads first with 150 µl of the elution buffer (50 mM Tris–HCl pH 8, 10 mM EDTA and 1% SDS) at 65°C for 15 min, then with 100 µl of 1× TE buffer + 1% SDS for another 15 min at 65°C. The supernatant (the ChIP fraction) was then separated from the beads and further incubated at 65°C overnight to completely reverse crosslink. The INPUT fraction was also de-crosslinked by incubation with 200 µl of 1× TE buffer + 1% SDS at 65°C overnight. DNA from the ChIP and INPUT fraction were then purified using the PCR purification kit (Qiagen) according to the manufacturer's instruction, then eluted out in 50 µl of EB buffer (Qiagen). The purified DNA was then used directly for qPCR or being constructed into library suitable for Illumina sequencing using the NEXT Ultra library preparation kit (NEB). ChIP libraries were sequenced on the Illumina Hiseq 2500 at the Tufts University Genomics facility.

2.15.2 Generation of ChIP-seq profiles

For analysis of ChIP-seq data, Hiseq 2500 Illumina short reads (50 bp) were mapped back to the *C. crescentus* NA1000 reference genome (NCBI Reference Sequence: NC-011916.1) using Bowtie 1 and the following command:

bowtie -m 1 -n 1 –best –strata -p 4 –chunkmbs 512 NA1000-bowtie –sam *.fastq > output.sam

Subsequently, the sequencing coverage at each nucleotide position was computed using BEDTools using the following command:

bedtools genomecov -d -ibam output.sorted.bam -g NA1000.fna > coverage_output.txt

2.16 Measurement of NTPase activity by EnzChek phosphate assay

NTP hydrolysis was monitored using an EnzChek Phosphate Assay Kit (Thermo Fisher). Samples (100 µL) containing a reaction buffer ± 0 to 1 mM of CTP ± 1 µM *NBS*/*parS* dsDNA + 1 µM of purified Noc (WT or mutants) were assayed in a Biotek EON plate reader for 15 hrs with readings every minute. The reaction buffer (1 mL) typically contained 640 µL ultrapure water, 100 µL 10x customized reaction buffer [100 mM Tris pH 8.0, 2 M NaCl, and 20 mM $MgCl_2$], 200 µL MESG substrate solution, and 10 µL purine nucleoside phosphorylase (1 unit). Reactions with buffer only, buffer + protein only or buffer + NTP only were also included as controls. The plates were shaken at 280 rpm continuously for 15 hrs at 25°C. The inorganic phosphate standard curve was also constructed according to the manual. Each assay was triplicated. The NTPase rates were calculated using a linear regression fitting in Excel.

2.17 *In vitro* crosslinking using a sulfhydryl-to-sulfhydryl crosslinker bismaleimidoethane (BMOE)

2.17.1 General in vitro crosslinking using BMOE

A 50 µL mixture of 10 µM Noc (WT/mutants) ± 1 mM NTP ± 1 µM 22-bp *NBS*/*parS* dsDNA was assembled in a reaction buffer [10 mM Tris-HCl pH 7.4, 200 mM NaCl, and 1 mM $MgCl_2$] and was incubated for 10 min at 22ºC or for 1, 5, 10, 15, and 30 min at 4°C. Subsequently, BMOE was added to the final concentration of 1 mM, and the reaction was quickly mixed by three pulses of vortexing. SDS-PAGE sample buffer containing 23 mM β-mercaptoethanol was then added immediately to quench the crosslinking reaction. Samples were heated to 50°C for 10 min before being loaded on 12% WedgeWell Tris-Glycine polyacrylamide gels (Thermo Fisher). Each experiment was triplicated. Polyacrylamide gels were stained in an InstantBlue Coomassie solution (Abcam) and band intensity was quantified using Image Studio Lite (LI-COR Biosciences). The crosslinked fractions were averaged, and their standard errors were calculated in Excel.

2.17.2 DNA loading assays

DNA loading assays were performed similarly to the *in vitro* BMOE crosslinking experiments above. A 50 µL mixture of 10 µM Noc (E29C S253C) ± 1 mM CTP ± 100 nM *NBS*-harboring/*NBS*-scrambled plasmid was assembled in a reaction buffer [10 mM Tris-HCl pH 7.4, 200 mM NaCl, and 1 mM $MgCl_2$] and was incubated for 10 min at 22°C. Subsequently, BMOE was added to the final concentration of 1 mM, and the reaction was quickly mixed by three pulses of vortexing. SDS-PAGE sample buffer containing 23 mM β-mercaptoethanol was then added immediately to quench the crosslinking reaction. Samples were heated to 50°C for 10 min before being loaded on 4-12% WedgeWell Tris-Glycine polyacrylamide gels.

2.17.3 Nuclease treatment assays

For nuclease treatment, crosslinking reactions were performed as described above, however the reaction were quenched using a quenching buffer [10 mM Tris-HCl pH 7.4, 200 mM NaCl, 1 mM $MgCl_2$, and 2.3 mM β-mercaptoethanol] instead. Subsequently, 0.5 µL of a non-specific DNA nuclease (Benzonase, 250 units/µL, Merck) was added, the mixture was incubated at 22°C for 10 min before SDS-PAGE sample buffer was added. Samples were heated to 50°C for 10 min before being loaded on 4-12% WedgeWell Tris-Glycine polyacrylamide gels. Gels were either stained in an InstantBlue Coomassie solution (to detect protein bands) or in a Sybr Green solution (to detect DNA bands).

2.18 Liposomes preparation

E. coli total lipid extract (25 mg/mL in chloroform, Avanti) was used to generate liposomes. Briefly, an argon stream was used to evaporate chloroform from the lipids, and the resulting lipid cake was further dried under vacuum for 2 hrs. The lipids were subsequently re-suspended in a buffer containing 100 mM Tris-HCl pH 7.4 and 200 mM NaCl. The mixture was incubated at 30°C for 30 min with vigorous vortexing every 5 min. The final concentration of the resuspended lipids was 50 mg/mL. The resuspended lipids were then extruded to ~100 nm single unilamellar vesicles (SUV) using a mini-extruder (Avanti) equipped with polycarbonate membranes (0.1 µm pore size). The size of the resulting SUVs was confirmed by dynamic light scattering.

2.19 Liposome co-sedimentation assays

2.19.1 General liposome co-sedimentation assays

A 500 µL mixture of 0.75 µM Noc (WT/mutants) ± 1.0 mg/mL liposomes ± 1 mM NTP ± DNA (either 1 µM of 22-bp *NBS*/*parS* dsDNA or 100 nM of *NBS*-harboring/empty plasmid) was assembled in a binding buffer [100 mM Tris-HCl pH 7.4, 200 mM NaCl, and 1 mM $MgCl_2$]. The mixture was incubated at 22°C for 20 min before being centrifuged at 50,000 rpm for 20 min

at 22°C (TLA120.2 rotor, Optima Max-E Benchtop Ultracentrifuge). After centrifugation, the supernatant was transferred to a new 1.5 mL Eppendorf tube. The pellet was resuspended in 500 µL of binding buffer before being transferred to another 1.5 mL Eppendorf tube. SDS-PAGE sample buffer was then added, and the samples were heated at 70ºC for 5 min before being loaded onto either 12% WedgeWell Tris-Glycine polyacrylamide gels, Novex 20% TBE polyacrylamide gels, or 1% agarose gels. Gels were subsequently stained in an InstantBlue Coomassie solution (to detect protein bands) or in a Sybr Green solution (to detect DNA bands). Each assay was triplicated. Protein/DNA band intensity was quantified using Image Studio Lite (LI-COR Biosciences). The protein/DNA fractions were averaged, and their standard errors were calculated in Excel.

2.19.2 Nuclease treatment assays

For nuclease treatment, a 500 µL mixture of 0.75 µM Noc (WT/mutants) ± 1.0 mg/mL liposomes ± 1 mM NTP ± 100 nM of *NBS*-harbouring/empty plasmid was incubated at room temperature for 10 min. Afterwards, 1 µL of Benzonase (250 units/ µL) was added, and the mixture was incubated for another 10 min at 22ºC before ultracentrifugation.

2.19.3 Liposome re-sedimentation experiments

For re-sedimentation experiments, the pellet (from the first round of ultracentrifugation) was resuspended either in 500 µL of binding buffer [100 mM Tris-HCl pH 7.4, 200 mM NaCl, and 1 mM $MgCl_2$] or in a stripping buffer [100 mM Tris-HCl pH 7.4, 200 mM NaCl, and 10 mM EDTA]. The resuspended pellet was centrifuged for the second time at 50,000 rpm for 20 min at 22°C. After the second centrifugation, the supernatant was transferred to a new 1.5 mL Eppendorf tube. The pellet was resuspended in 500 µL of binding buffer before being transferred to another 1.5 mL Eppendorf tube. SDS-PAGE sample buffer was then added to the supernatant and the pellet fractions, and the samples were analysed on denaturing polyacrylamide gels.

2.20 Liposome flotation assays

A 200 µL mixture of 0.75 µM Noc (WT/mutants) ± 1.0 mg/mL liposomes ± 1 mM NTP ± 20 nM *NBS*-harbouring/empty plasmid was assembled in a 30% sucrose buffer [100 mM Tris-HCl pH 7.4, 200 mM NaCl, 1 mM $MgCl_2$, and 30% sucrose]. The mixture was incubated at 22ºC for 5 min before being overlaid with 250 µL of a 25% sucrose buffer [100 mM Tris-HCl pH 7.4, 200 mM NaCl, 1 mM $MgCl_2$, and 25% sucrose]. Finally, 150 µL of a 0% sucrose buffer [100 mM Tris-HCl pH 7.4, 200 mM $NaCl_2$, and 1 mM $MgCl_2$] was added as the top layer. The solution was incubated for 15 min at the 22ºC before being centrifuged at 70,000 rpm at 22°C for 20

min (TLA120.2 rotor, Optima Max-E Benchtop Ultracentrifuge). After centrifugation, three equal fractions (200 µL each) were gently drawn sequentially from bottom of the ultracentrifugation tube using a Hamilton syringe. SDS-PAGE sample buffer was added to each fraction, and samples were heated at 70ºC for 5 min before being loaded onto either 12% WedgeWell Tris-Glycine polyacrylamide gels or 1% agarose gels. Gels were subsequently stained in an InstantBlue Coomassie solution (to detect protein bands) or in a Sybr Green solution (to detect DNA bands). Each assay was triplicated. Protein/DNA band intensity was quantified using Image Studio Lite (LI-COR Biosciences). The protein/DNA fractions were averaged, and their standard errors were calculated in Excel.

2.21 References

1. Adams, D.W., Wu, L.J., and Errington, J. (2015). Nucleoid occlusion protein N oc recruits DNA to the bacterial cell membrane . EMBO J. **34**, 491–501.
2. Blanchet, C., Pasi, M., Zakrzewska, K., and Lavery, R. (2011). CURVES+ web server for analyzing and visualizing the helical, backbone and groove parameters of nucleic acid structures. Nucleic Acids Res. **39**, 68–73.
3. Bunkóczi, G., and Read, R.J. (2011). Improvement of molecular-replacement models with Sculptor. Acta Crystallogr. Sect. D Biol. Crystallogr. **67**, 303–312.
4. Chen, B.W., Lin, M.H., Chu, C.H., Hsu, C.E., and Sun, Y.J. (2015). Insights into ParB spreading from the complex structure of Spo0J and parS. Proc. Natl. Acad. Sci. U. S. A. **112**, 6613–6618.
5. Cowtan, K. (2006). The Buccaneer software for automated model building. 1. Tracing protein chains. Acta Crystallogr. Sect. D Biol. Crystallogr. **62**, 1002–1011.
6. Davis, I.W., Leaver-Fay, A., Chen, V.B., Block, J.N., Kapral, G.J., Wang, X., Murray, L.W., Arendall, W.B., Snoeyink, J., Richardson, J.S., et al. (2007). MolProbity: All-atom contacts and structure validation for proteins and nucleic acids. Nucleic Acids Res. **35**, W375–W83.
7. DeLano, W.L. (2002). Pymol: An open-source molecular graphics tool. {CCP4} Newsl. Protein Crystallogr.PyMOL. http://www.pymol.org.
8. Emsley, P., and Cowtan, K. (2004). Coot: Model-building tools for molecular graphics. Acta Crystallogr. Sect. D Biol. Crystallogr. **60**, 2126–2132.
9. Evans, P.R., and Murshudov, G.N. (2013). How good are my data and what is the resolution? Acta Crystallogr. Sect. D Biol. Crystallogr. **69**, 1204–1214.
10. Fisher, G.L.M., Pastrana, C.L., Higman, V.A., Koh, A., Taylor, J.A., Butterer, A., Craggs, T., Sobott, F., Murray, H., Crump, M.P., et al. (2017). The structural basis for dynamic DNA binding and bridging interactions which condense the bacterial centromere. Elife. **6**, e28086.

11. Krissinel, E. (2015). Stock-based detection of protein oligomeric states in jsPISA. Nucleic Acids Res. **43**, W314–W319.
12. Leonard, T.A., Butler, P.J.G., and Löwe, J. (2004). Structural analysis of the chromosome segragation protein Spo0J from Thermus thermophilus. Mol. Microbiol. **53**, 419–432.
13. McCoy, A.J., Grosse-Kunstleve, R.W., Adams, P.D., Winn, M.D., Storoni, L.C., and Read, R.J. (2007). Phaser crystallographic software. J. Appl. Crystallogr. **40**, 658–674.
14. Murshudov, G.N., Vagin, A.A., and Dodson, E.J. (1997). Refinement of macromolecular structures by the maximum-likelihood method. Acta Crystallogr. Sect. D Biol. Crystallogr. **53**, 240–255.
15. Potterton, L., Agirre, J., Ballard, C., Cowtan, K., Dodson, E., Evans, P.R., Jenkins, H.T., Keegan, R., Krissinel, E., Stevenson, K., et al. (2018). CCP 4 i 2: The new graphical user interface to the CCP 4 program suite. Acta Crystallogr. Sect. D Struct. Biol. **74**, 68–84.
16. Skubák, P., and Pannu, N.S. (2013). Automatic protein structure solution from weak X-ray data. Nat. Commun. **4**, 2777.
17. Stein, N. (2008). CHAINSAW: A program for mutating pdb files used as templates in molecular replacement. J. Appl. Crystallogr. **41**, 641–643.
18. Stevenson, C.E.M., Assaad, A., Chandra, G., Le, T.B.K., Greive, S.J., Bibb, M.J., and Lawson, D.M. (2013). Investigation of DNA sequence recognition by a streptomycete MarR family transcriptional regulator through surface plasmon resonance and X-ray crystallography. Nucleic Acids Res. **41**. 7009–7022.
19. Taylor, J.A., Pastrana, C.L., Butterer, A., Pernstich, C., Gwynn, E.J., Sobott, F., Moreno-Herrero, F., and Dillingham, M.S. (2015). Specific and non-specific interactions of ParB with DNA: Implications for chromosome segregation. Nucleic Acids Res. **43**, 719–731.
20. Winter, G. (2010). Xia2: An expert system for macromolecular crystallography data reduction. J. Appl. Crystallogr. **69**, 1260–1273.
21. Winter, G., Waterman, D.G., Parkhurst, J.M., Brewster, A.S., Gildea, R.J., Gerstel, M., Fuentes-Montero, L., Vollmar, M., Michels-Clark, T., Young, I.D., et al. (2018). DIALS: Implementation and evaluation of a new integration package. Acta Crystallogr. Sect. D Struct. Biol. **74**, 85–97.
22. Zhou, T., Yang, L., Lu, Y., Dror, I., Dantas Machado, A.C., Ghane, T., Di Felice, R., and Rohs, R. (2013). DNAshape: a method for the high-throughput prediction of DNA structural features on a genomic scale. Nucleic Acids Res. **41**, W56–W62.

Chapter 3: Determinants of DNA-binding specificity in the ParB/Noc protein family

Parts of this chapter have been published in Cell Reports, for which I share first authorship with Dr. Ngat Tran:

Jalal, A.S.B., Tran, N.T., Stevenson, C.E., Chan, E.W., Lo, R., Tan, X., Noy, A., Lawson, D.M., and Le, T.B.K. (2020). Diversification of DNA-Binding Specificity by Permissive and Specificity-Switching Mutations in the ParB/Noc Protein Family. Cell Rep. **32**, 107928.

3.1 Introduction

3.2 Crystallisation of the DNA-binding domain (DBD) of *C. crescentus* ParB in complex with *parS*

3.3 The co-crystal structure of *C. crescentus* ParB (DBD) in complex with *parS*

3.4 Residues that mediate the recognition of *C. crescentus* ParB to *parS*

3.5 Validating the observed ParB-*parS* interactions in the *C. crescentus* ParB (DBD)-*parS* co-crystal structure

3.6 Four amino acid residues dictate the DNA-binding specificity between ParB and Noc

3.7 Systematic dissection of ParB-*parS* and Noc-*NBS* interfaces reveals the genetic contribution of each specificity residue to the DNA-binding preference

3.8 Crystallisation of a C-terminal truncated (ΔCTD) *C. crescentus* ParB (QKKR+K227) variant with *NBS*

3.9 The crystal structure of the *C. crescentus* ParBΔCTD (QKKR+K227) variant with *NBS*

3.10 Co-crystal structure of the specificity-altered ParB variant with *NBS* reveals the contribution of each specificity residue to the DNA-binding preference

3.11 Crystallisation of the *B. subtilis* Noc (DBD) variants in complex with *NBS*

3.12 The co-crystal structure of the *B. subtilis* Noc (DBD)-*NBS* complex

3.13 The residues that mediate the recognition of *B. subtilis* Noc to *NBS*

3.14 Validating the observed Noc-*NBS* interactions in the *B. subtilis* Noc (DBD)-*NBS* co-crystal structure

3.15 Superimposing the structure of *C. crescentus* ParB (DBD) and *B. subtilis* Noc (DBD) reveals the mechanistic basis that defines specificity

3.16 Discussion

3.17 References

3.1 Introduction

In all living organisms, DNA-binding proteins play a plethora of roles in homeostasis, transcriptional regulation in response to stress, and in maintenance and transmission of genetic information. Crucial to the function of such proteins are their distinct ability to recognise specific cognate DNA-binding sites found on the genome. Despite this, it remains unclear how related proteins, sometimes with a very similar DNA-recognition motif, are able to recognise entirely different DNA-binding sites. What were the changes at the molecular level that brought about the diversification in DNA-binding specificity? As these proteins evolved, did the intermediates in this process drastically switch DNA-binding specificity or did they transit gradually through promiscuous states that recognised multiple DNA sequences? Among many ways to evolve new biological innovations, gene duplication and neo-functionalization have been widely implicated as a major force in evolution (Conrad and Antonarakis, 2007; Kaessmann, 2010; Lynch and Conery, 2000; Qian and Zhang, 2014; Teichmann and Babu, 2004). In this process, after a gene was duplicated, one copy retained the original function while the other accumulated beneficial and diverging mutations that produced a different protein with a new function. In the case of DNA-binding proteins, a new function could be the recognition of an entirely different DNA site. In this work, I employed a pair of related DNA-binding proteins (ParB and Noc) that are crucial for bacterial chromosome segregation and maintenance to better understand factors that might have influenced the evolution of a new DNA-binding specificity.

ParB ensures faithful chromosome segregation in roughly two-thirds of known bacterial species (Lin and Grossman, 1998; Livny et al., 2007) The centromere-like *parS* DNA is the first loci to be segregated following chromosome replication (Lagage et al., 2016; Lin and Grossman, 1998; Livny et al., 2007; Toro et al., 2008). *parS* is nucleated by ParB to form a ParB-*parS* nucleoprotein complex, which in turn interacts with ParA and SMC proteins to partition the ParB-*parS* nucleoprotein complex, hence the chromosome, into each daughter cell (Fig. 3.1) (Fisher et al., 2017; Fogel and Waldor, 2006; Gruber and Errington, 2009; Ireton et al., 1994; Lin and Grossman, 1998; Mohl and Gober, 1997; Tran et al., 2017, 2018). ParB specifically recognises and binds to *parS*, a palindromic sequence (Fig. 3.1) that can be present as multiple copies on the bacterial chromosome but must almost always be located towards the origin of replication (*ori*) on the chromosome (Fig. 3.1). ParB proteins also appear to be widely distrusted in bacteria and thus must have appeared early in evolution.

Noc (Nucleoid Occlusion Factor), a ParB-related protein, was first discovered in *Bacillus subtilis* (Sievers et al., 2002; Wu and Errington, 2004). Noc has a similar three-domain architecture to ParB, consisting of an N-terminal domain for protein-protein interactions and

for targeting Noc to the cell membrane, a central DNA-binding domain, and a C-terminal dimerization domain (Fig. 3.1) (Wu and Errington, 2004; Wu et al., 2009). Due to its similarity to ParB, initial experiments attempted to elucidate its function in chromosome segregation. In contrast to ParB, Noc recognises a different palindromic DNA-binding site termed *NBS* (Noc Binding Site) (Pang et al., 2017; Wu et al., 2009) (Fig. 3.1). The function of Noc is also divergent from ParB; Noc preserves the integrity of bacterial chromosome by preventing the assembly of the cell division machinery in the vicinity of the nucleoid. In doing so, Noc prevents the premature assembly of the cell division apparatus which may guillotine the nucleoid and damage the DNA (Fig. 3.1) (Wu and Errington, 2004; Wu et al., 2009). In other words, Noc has a role in preserving the integrity of the chromosome. Interestingly, the genome-wide distribution of *NBS* is drastically different from that of *parS*. While *parS* sites are found clustered towards the *ori*, *NBS* are found widely distributed on the genome but never near the replication terminus (*ter*). The absence of *NBS* near *ter* is thought to direct the formation of the FtsZ ring and cell division apparatus towards the mid-cell (Fig. 3.1). Due to their genomic proximity (Fig. 3.2A) and high sequence identity, it is likely that *noc* resulted from a gene duplication and neo-functionalisation event from *parB* (Sievers et al., 2002; Wu and Errington, 2012). A phylogenetic tree displayed that *parB* genes are widely distributed in bacteria but *noc* genes are confined within the Firmicutes clade (Fig. 3.2A). As such, it is probable that appearance of the *parB* gene appeared early in evolution, predating the split between Gram-positive and Gram-negative bacteria, and that the occurrence of *noc* is a later event that happened only in Firmicutes (Fig. 3.2B).

Initial experiments using ChIP-seq/qPCR of 17 different ParB and 4 different Noc from various bacterial species expressed heterologously in *E. coli* harbouring a single *parS* or *NBS* site demonstrated that ParB specifically recognises *parS* over *NBS* and that Noc in turn recognises *NBS* over *parS* (Fig 3.2 C-D) (Jalal et al., 2020). Thus, there must be residues that mediate sequence specificity that enables ParB and Noc to recognise their individual cognate sites. In this chapter, I used X-ray crystallography to identify the specificity defining residues that mediate ParB-*parS* and Noc-*NBS* recognition. I was able to demonstrate that specificity towards each respective DNA-binding site is mediated by a small set of specificity defining residues at the protein-DNA interface. Mutations in these specificity-defining residues are enough to reprogram ParB to interact with a non-cognate *NBS* DNA site. By combining structural data with systematic scanning mutagenesis, I propose a model explaining how DNA-binding specificity was switched during evolution: through the introduction of both negative and positive determinants of specificity, in the presence of permissive substitutions.

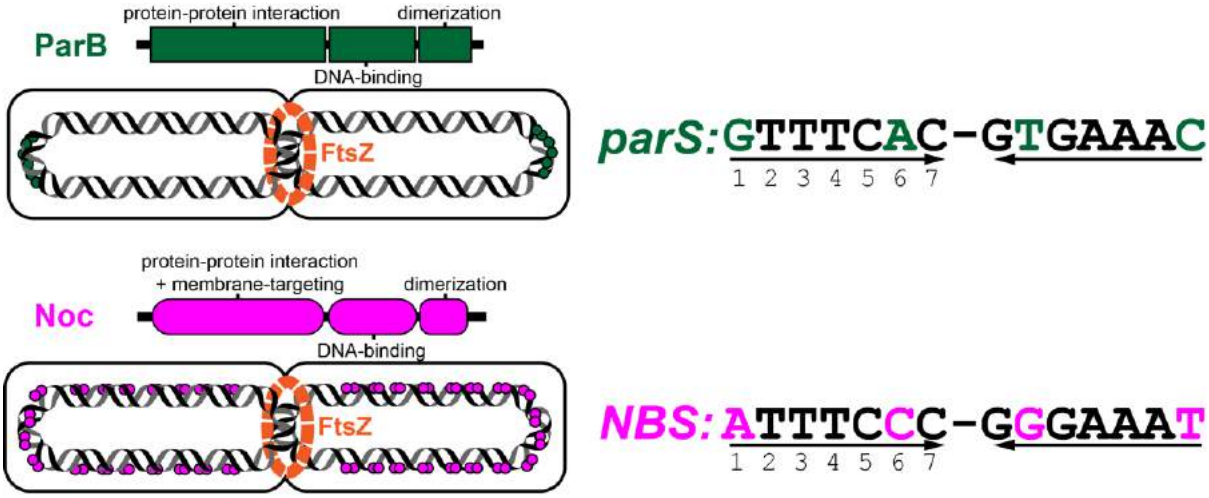

Figure 3.1 Schematic illustration of ParB and Noc and their respective specific DNA-binding site *parS* and *NBS*. The domain architecture of ParB (dark green) and Noc (magenta) together with their respective cognate DNA-binding sites, *parS* and *NBS*. Different bases between *parS* and *NBS* are highlighted in colours (*parS*: dark green, *NBS*: magenta). The genome-wide distributions of *parS* and *NBS* sites (dark green and magenta circles, respectively) are also shown schematically.

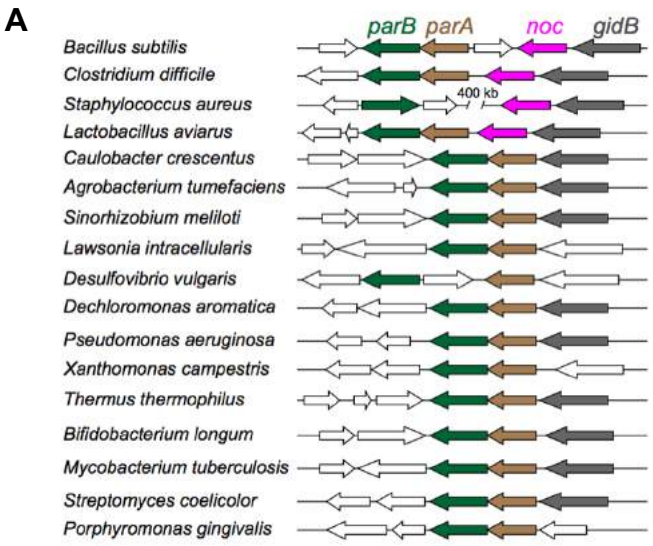
A
parB parA noc gidB
Bacillus subtilis
Clostridium difficile
Staphylococcus aureus
400 kb
Lactobacillus aviarus
Caulobacter crescentus
Agrobacterium tumefaciens
Sinorhizobium meliloti
Lawsonia intracellularis
Desulfovibrio vulgaris
Dechloromonas aromatica
Pseudomonas aeruginosa
Xanthomonas campestris
Thermus thermophilus
Bifidobacterium longum
Mycobacterium tuberculosis
Streptomyces coelicolor
Porphyromonas gingivalis

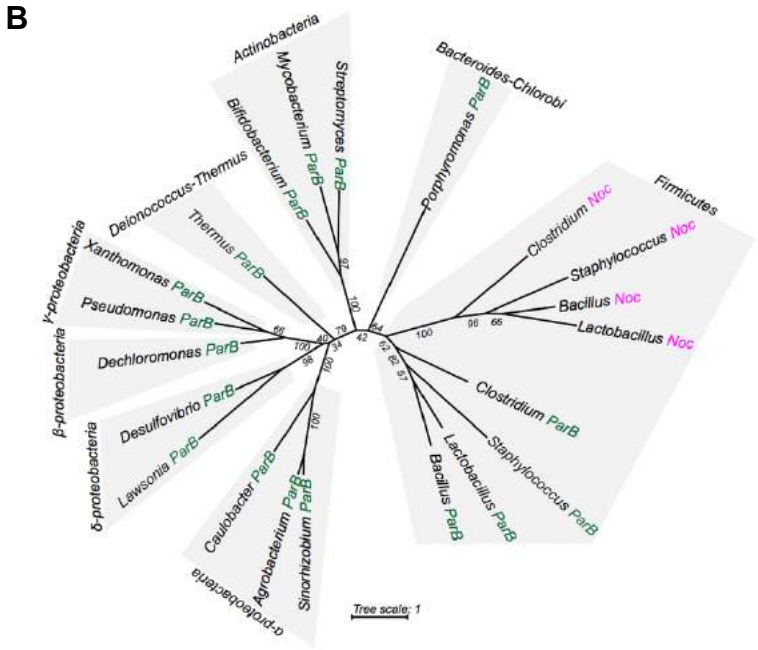
B
Actinobacteria
Mycobacterium ParB
Streptomyces ParB
Bifidobacterium ParB
Bacteroides-Chlorobi
Porphyromonas ParB
Firmicutes
Clostridium Noc
Staphylococcus Noc
Bacillus Noc
Lactobacillus Noc
Deinococcus-Thermus
Thermus ParB
γ-proteobacteria
Xanthomonas ParB
Pseudomonas ParB
β-proteobacteria
Dechloromonas ParB
Desulfovibrio ParB
Lawsonia ParB
δ-proteobacteria
Clostridium ParB
Staphylococcus ParB
Lactobacillus ParB
Bacillus ParB
Caulobacter ParB
Agrobacterium ParB
Sinorhizobium ParB
α-proteobacteria
Tree scale: 1

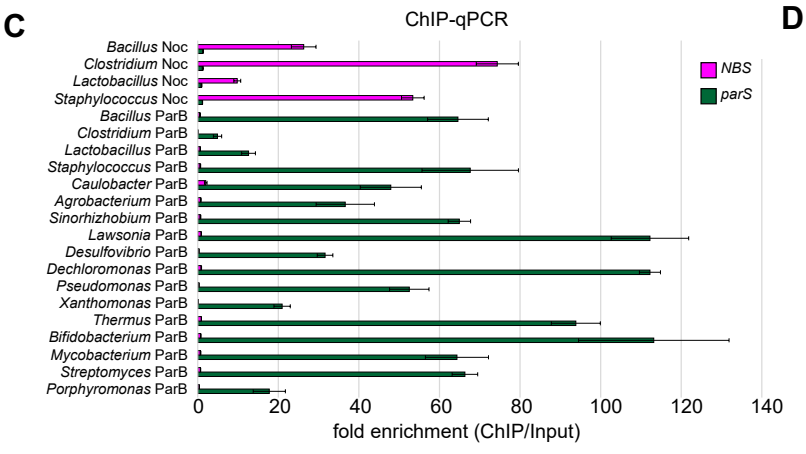
C
ChIP-qPCR
Bacillus Noc
Clostridium Noc
Lactobacillus Noc
Staphylococcus Noc
Bacillus ParB
Clostridium ParB
Lactobacillus ParB
Staphylococcus ParB
Caulobacter ParB
Agrobacterium ParB
Sinorhizobium ParB
Lawsonia ParB
Desulfovibrio ParB
Dechloromonas ParB
Pseudomonas ParB
Xanthomonas ParB
Thermus ParB
Bifidobacterium ParB
Mycobacterium ParB
Streptomyces ParB
Porphyromonas ParB
NBS
parS
0
20
40
60
80
100
120
140
fold enrichment (ChIP/Input)

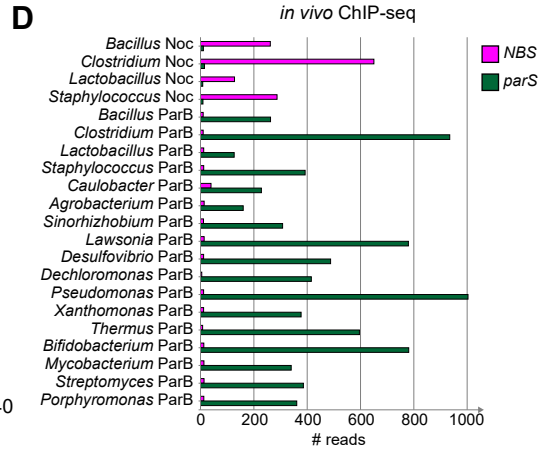
D
in vivo ChIP-seq
Bacillus Noc
Clostridium Noc
Lactobacillus Noc
Staphylococcus Noc
Bacillus ParB
Clostridium ParB
Lactobacillus ParB
Staphylococcus ParB
Caulobacter ParB
Agrobacterium ParB
Sinorhizobium ParB
Lawsonia ParB
Desulfovibrio ParB
Dechloromonas ParB
Pseudomonas ParB
Xanthomonas ParB
Thermus ParB
Bifidobacterium ParB
Mycobacterium ParB
Streptomyces ParB
Porphyromonas ParB
NBS
parS
0
200
400
600
800
1000
reads

Figure 3.2 DNA-binding specificity for *parS* and *NBS* is conserved among ParB and Noc orthologs (A) Genomic context of ParB- and Noc-encoding genes in various bacterial species. *parB*, *parA*, *noc*, and the highly conserved *gidB* gene (which encodes a methyltransferase that confers antibiotic resistance to streptomycin) (Mikeil et. al., 2012), are coloured in dark green, brown, magenta, and grey, respectively. Genes at the border of the *parB-parA-noc* cluster (open arrows) vary between bacterial species. **(B)** An unrooted maximum likelihood tree that shows the restrictive distribution of Noc orthologs (magenta branches) to the Firmicutes clade. Bootstrap support values are shown for branches. **(C)** The *in vivo* binding preferences of ParB/Noc to *parS*/*NBS* as measured by ChIP-qPCR. Error bars represent standard deviation (SD) from three replicates. An *E. coli* strain with a single *parS* and *NBS* site engineered onto the chromosome was used as a heterologous host for expression of FLAG-tagged ParB/Noc. **(D)** The *in vivo* binding preferences of ParB-*parS*/Noc-*NBS* as measured by ChIP-seq. An *E. coli* strain with a single *parS* and *NBS* site engineered onto the chromosome was used as a heterologous host for expression of FLAG-tagged ParB/Noc. For ChIP-seq data, reads in a 100-bp window surrounding the *parS/NBS* site were quantified and used as a proxy for the enrichment of immunoprecipitated *parS* or *NBS* DNA.

3.2 Crystallisation of the DNA-binding domain (DBD) of *C. crescentus* ParB in complex with *parS*

As the first step in identifying the specificity defining residues that enables *C. crescentus* ParB to recognise *parS*, I sought to crystallise the *C. crescentus* ParB-*parS* co-crystal complex. ParB proteins generally compose of three different domains, each of which are connected by flexible linkers (Fig. 3.1). This often results in a flexibility in the organisation of the domain orientation which could impair the protein from forming an orderly-packaged crystal. To date the only crystal structures of chromosomally encoded ParB have been solved have been truncated, principally at the CTD. Previous studies have highlighted the role of the DBD of ParB in facilitating *parS* recognition, although a positive charged lysine surface in the CTD of *B. subtilis* ParB has been shown to bind non-specific DNA (Fisher et al., 2017; Tran et al., 2018). The CTD between ParBs however are highly divergent and this lysine-rich surface is not present in *C. crescentus* ParB. Additionally, *C. crescentus* ParB does not possess any non-specific DNA binding activity *in vitro* (Tran et al., 2018). As I was primarily interested identifying the specificity-defining residues that enables ParB-*parS* recognition, I decided to crystallise only the DBD of *C. crescentus* ParB in complex with *parS*. After screening several conditions and different lengths of *parS* DNA, I was able to obtain crystals of the *C. crescentus* ParB (DBD) in complex with a 20 bp *parS* site. Diffraction data for the *C. crescentus* ParB (DBD)-*parS* co-crystal was collected to a resolution of 2.6 Å, and the phase was solved by molecular replacement using the 3.1 Å structure of the *H. pylori* ParBΔCTD-*parS* complex (Chen et al., 2015). The X-ray crystallographic data are summarized in Table 3.1.

3.3 The co-crystal structure of *C. crescentus* ParB (DBD) in complex with *parS*

The final model contained two copies of the *C. crescentus* ParB (DBD) monomers in the asymmetric unit; each complex consists of two ParB (DBD) molecules and one copy of the half *parS* DNA (Fig 3.3A). Superimposition of both monomers suggest that they are near identical to one another with an RMSD value of 0.1 Å, with chain B being more complete than chain A (Fig 3.3B). The DBD of *C. crescentus* ParB consists of eight α-helices with an additional α-helix representing the His_6-tag used to purify the *C. crescentus* DBD ParB variant (Fig. 3.4B). Residues: A127-V137 (α1), V144-P158 (α2), Q162-I169 (α3), S172-A184 (α4), D187-S195 (α5), A200-I206 (α6), P212-G222 (α7) and V226-K235 (α8). Noticeably, an extended linker between residues 236-254 was observable due to non-specific DNA contacts stabilizing the loop in the crystal (Fig 3.4A, 3.4B). The helix-turn-helix motif is formed by helices α3 and α4 observed in various repressors and DNA-binding proteins (Fig 3.4B). Helix α4 then connects to the remaining three helix that form a compact bundle (Fig 3.4A-B). Furthermore,

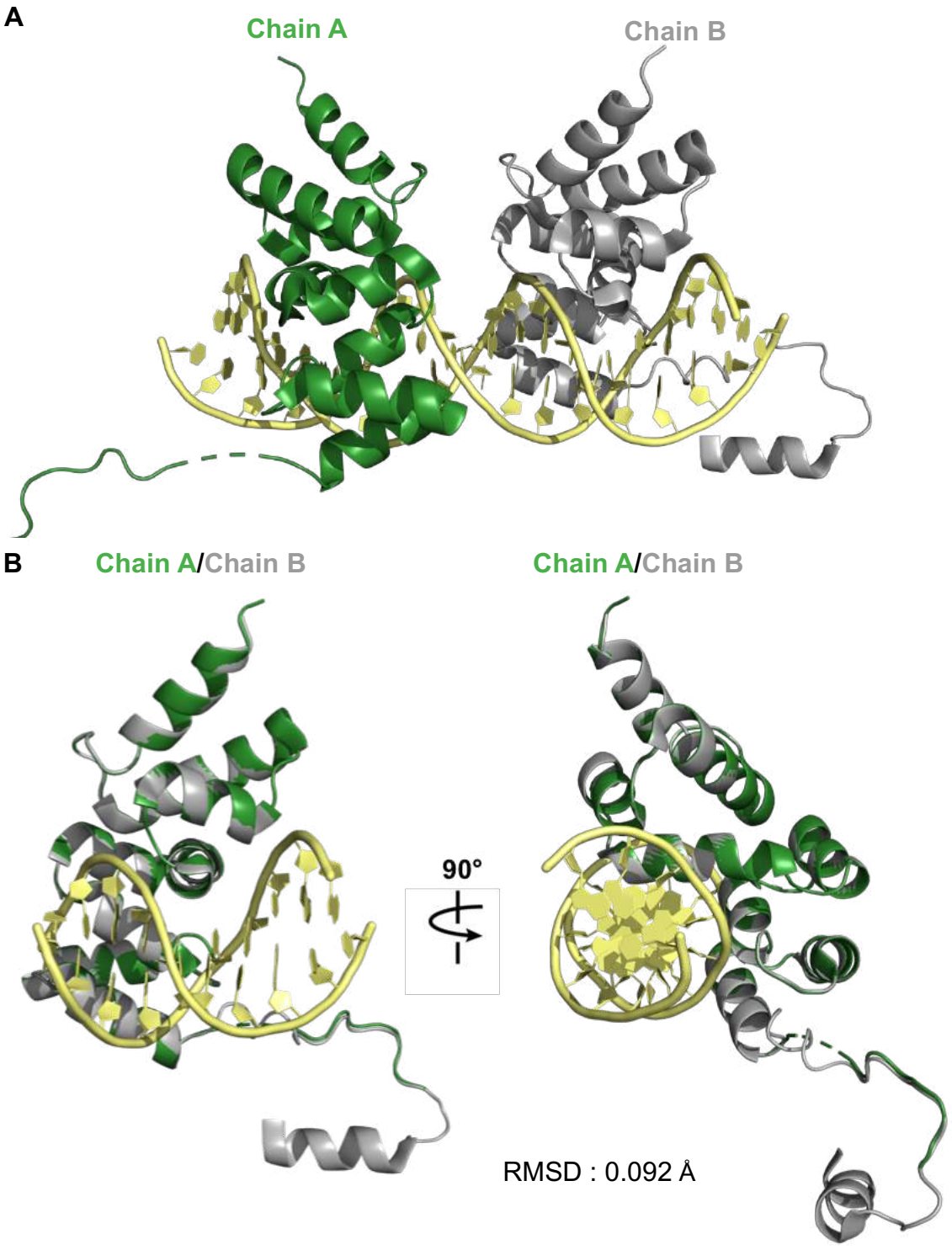

Figure 3.3 Composition of the asymmetric unit (ASU) of the DNA-binding domain (DBD) of *Caulobacter* ParB in complex with *parS*. (A) The ASU of the *C. crescentus* ParB (DBD)-*parS* co-crystal complex. Two ParB (DBD) monomers are shown (Chain A : dark green and Chain B : grey) in complex with a 20-bp *parS* DNA (yellow) **(B)** Superimposition of chain A and chain B of wild-type *Caulobacter* ParB DNA-binding domain (DBD). Root-mean- square deviation (RMSD) value is also shown.

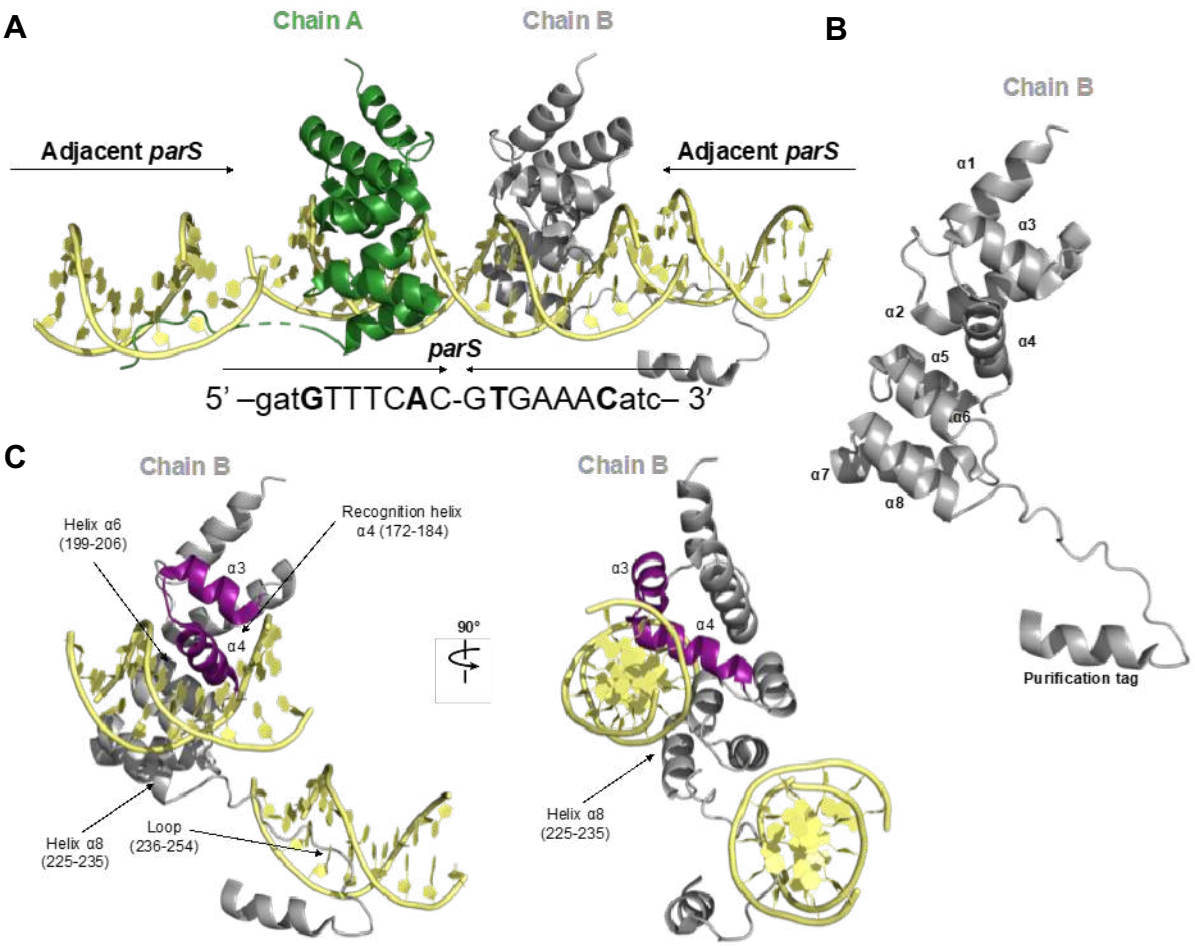

Figure 3.4 ParB-*parS* interactions observed in the *Caulobacter* DBD ParB-*parS* co-crystal structure. (A) The 2.4-Å resolution structure of two ParB (DBD) monomers (chain A: dark green, chain B: grey) in complex with a 20-bp *parS* DNA (yellow). The nucleotide sequence of the 20-bp *parS* is shown; bases (Guanine 1 and Adenine 6) that are different from *NBS* are shown. The purification tag is also visible in one of the DBD monomers. Loop (236–254) contacts the adjacent DNA in the crystal lattice. **(B)** Same as panel A but only chain B and half-*parS* sites are shown. Key features of the ParB-*parS* complex are highlighted. The helix-turn-helix motif (purple) docks into the major groove of the *parS* site.

the 20bp *parS* site also forms a pseudo-continuous filament, by interacting with *parS* sites in the adjacent subunit, thus stabilizing the *C. crescentus* DBD ParB-*parS* crystal complex (Fig 3.4A).

3.4 The residues that mediate the recognition of *C. crescentus* ParB to *parS*

In the co-crystal structure of *C. crescentus* ParB (DBD)-*parS* complex, the two very similar ParB (DBD) monomers (RMSD = 0.1 Å) bind in a two-fold symmetric fashion to a full-size *parS* DNA duplex, with one monomer interacting with half a *parS* site (Fig 3.4A). In the co-crystal complex, ParB binds to *parS* through a classical helix-turn-helix motif (α3 and α4) that inserts into the major grooves of the palindromic *parS* site (Fig 3.4C). However, several other ParB-*parS* contacts outside the helix-turn-helix are also observed in the *C. crescentus* ParB (DBD) ParB-*parS* co-crystal structure. Various residues found in helix α8 (225-235) and a loop (236-254) region interacts with the *parS* site, either by forming hydrogen bonds with specific bases or through interactions with the phosphate backbone (Fig. 3,4C)

First, the recognition helix α4 (res. 172-184) of the helix-turn-helix motif inserts into the major grooves of the palindromic *parS* site (Fig. 3.4C, Fig. 3.5). In the recognition helix α4, residues R173, S174, N178 interact directly to the *parS* site by making specific base contacts via hydrogen bonds, while residues Q162 and R181 interacts with the phosphate backbone (Fig. 3.5). In helix α6, a single arginine residue R204 forms hydrogen bonds with two bases on the *parS* site, while G201 makes a non-specific contact with the phosphate backbone (Fig. 3.5). In addition, in helix α8 (225-235), residues R227 and E230 both make specific contacts by hydrogen bonding to specific bases on the *parS* site, while R234 interacts with the phosphate backbone of the *parS* site (Fig. 3.5). Finally, several lysine and arginine residues in the loop spanning residues 236-254 which interacts with the minor groove in the *parS* site found in the adjacent complex of the crystal (Fig. 3.5). Noticeably, K245, R248, and R251 form a positively charged surface that interacts with the phosphate backbone of *parS* (Fig 3.5). Thus, from solving the *C. crescentus* ParB DBD-*parS* co-crystal structure, I was able to identify residues that make specific and non-specific contacts, either by hydrogen bonding with *parS* bases or by interacting with the phosphate backbone.

3.5 Validating the observed ParB-*parS* interactions in the *C. crescentus* ParB (DBD)-*parS* co-crystal structure

Next, I sought to validate the protein-DNA interactions observed in the *C. crescentus* ParB (DBD)-*parS* crystal structure. To do so, I performed alanine scanning mutagenesis on the ParB-*parS* interface and determined their ability to bind to *parS in vitro*. In brief, the gene encoding the residues observed to mediate *parS* recognition in *C. crescentus* ParB (DBD)-

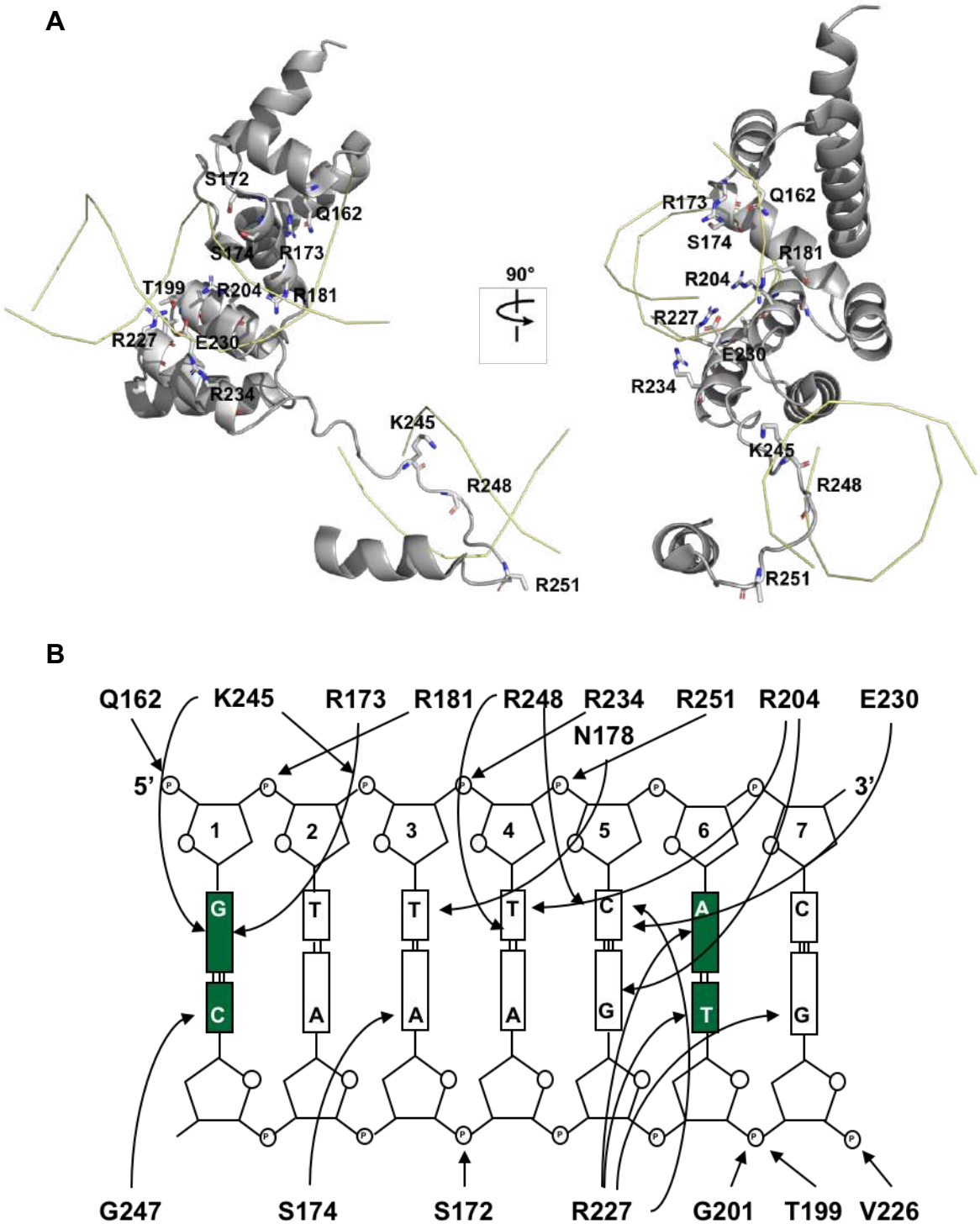

Figure 3.5 ParB-*parS* interactions observed in the *C. crescentus* ParB(DBD)-*parS* co-crystal structure. (A) One monomer of ParB (DBD) is shown in complex with a *parS* half-site; residues that contact the DNA are labelled. For simplicity, the *parS* site is shown as wires. **(B)** Schematic representation of ParB (DBD)-*parS* interactions. For simplicity, only half-site a *parS* site is shown. The two bases at position 1 and 6 that are different between *parS* and *NBS* are highlighted in dark green.

parS co-crystal structure were mutated to alanine and the corresponding variant proteins were subsequently purified. In the recognition helix (α4) residues S172, R173, S174, N178 were mutated to alanine to generate the ParB (S172A), ParB (R173A), ParB (S174A), ParB (N178A) variants. Additionally, in α6 residue R204 was mutated to alanine to generate the ParB (R204A) variant and in α8 residues V226, R227, E230 and R234A was mutated to alanine to generate the ParB (R227A), ParB (E230A), ParB (R234A) mutant proteins. Finally, in the loop spanning residues 236-254 residues K245, R248, R251 were subsequently mutated to alanine to generate the ParB (K245A), ParB (R248A) and ParB (R251A) variants. All variant proteins were purified to homogeneity (Fig 3.6) and analysed by a quantitative bio-layer interferometry (BLI) assay that directly assessed their binding to the *parS* DNA. A linear 20-bp biotinylated *parS* DNA to a streptavidin-coated probe to measure the BLI. BLI assay monitors wavelength shifts (responses) resulting from changes in the optical thickness of the probe surface during association or dissociation of the analyte. The interactions between the immobilized *parS* DNA and the purified *C. crescentus* ParB (WT) and variants were then monitored. In agreement with previous observations, *C. crescentus* ParB (WT) binds to the *parS* DNA with a K_D of 11 $\pm$ 7.0 nM (Tran et al., 2018). In contrast, I was unable to detect any noticeable *parS* binding activity when protein-DNA interacting residues found in the recognition helix (α4), α6 and α8 (except E230 K_D = 47 $\pm$ 17 nM) were substituted for alanine. Moreover, in the loop spanning residues 236-254, both the ParB (K245A) and ParB (R251A) variants retained their *parS* binding ability albeit with a reduced affinity of K_D = 450 $\pm$ 67 nM and 34 $\pm$ 10 respectively, while no *parS* binding was observed with the R248A variant. These findings therefore further support the ParB-*parS* interactions observed in the *C. crescentus* ParB (DBD)-*parS* co-crystal complex. As most of the residues crucial for *parS* binding were found in the helix-turn-helix motif and in α8, I suggest these residues are important in recognizing DNA specifically. Thus, I reasoned that specificity residues for *parS* (and *NBS*) must localize within this amino acid region in ParB (and in an equivalent region in Noc).

3.6 Four amino acid residues dictate the specificity between ParB and Noc

To determine which amino acid region contains the specificity residues for *NBS*, we constructed a series of chimeric proteins in which different regions of *C. crescentus* ParB were replaced with the corresponding regions of *B. subtilis* Noc (Fig. 3.8A). Replacing the entire region (res. 162-230) containing the helix-turn-helix motif, helix (res. 200-207), and helix (res. 226-230) with the corresponding region of *B. subtilis* Noc produced a chimera that binds to both *parS* and *NBS* but with a clear preference for *NBS* (Chimera 1, Fig. 3.8B). Swapping a smaller region containing just the helix-turn-helix motif and an adjacent helix (res. 200-207) created a chimera that has an improved specificity to the *NBS* site (Chimera 4, Fig. 3.8B).

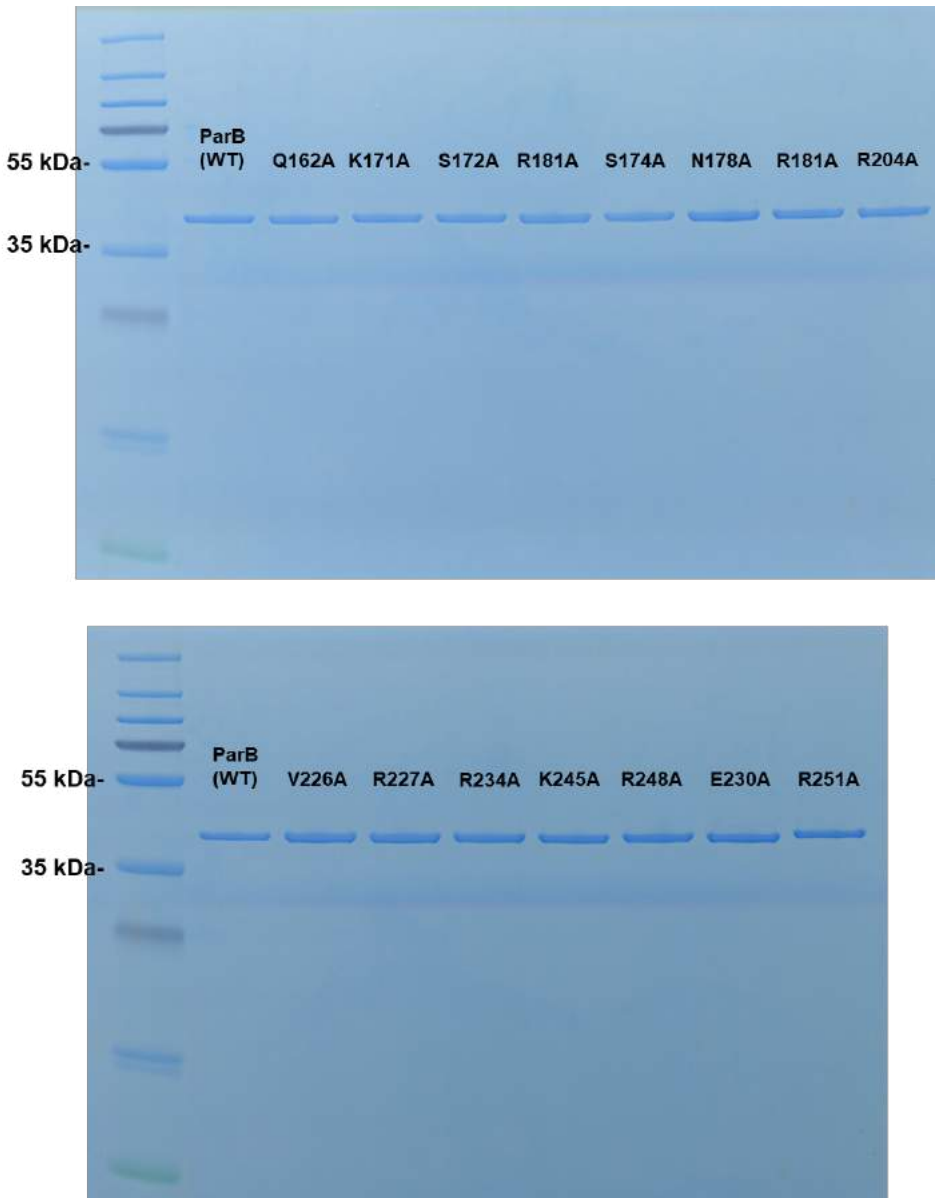

Figure 3.6 SDS-PAGE analysis of purified ParB variants used in this study. Their identities are shown above the corresponding lane.

	variants	K_D (nM)
	WT	11 ± 7.0
	Q162A	no binding
	K171A	no binding
recognition helix α4 (172-184)	S172A	no binding
	R173A	no binding
	S174A	no binding
	N178A	no binding
	R181A	no binding
helix α6 (199-206)	R204A	no binding
helix 8 (225-235)	V226A	no binding
	R227A	no binding
	E230A	47 ± 17
	R234A	no binding
loop (236-254)	K245A	450 ± 67
	R248A	no binding
	R251A	34 ± 10

Figure 3.7 Alanine scanning mutagenesis of the ParB-*parS* interface. Alanine scanning mutagenesis and the *in vitro* dissociation constant (K_D) ± standard deviation (SD) of ParB variants to *parS* DNA.

These results indicate that the region (res. 162-207) contains most of the specificity residues for *NBS*. To better understand the high degree of specificity conserved within the ParB and Noc families, we mapped a sequence alignment of ~1800 ParB and ~400 Noc orthologs onto the ParB DBD-*parS* crystal structure to determine amino acid sequence preferences for those residues required for interaction specificity (Fig. 3.8A). We focused our attention on the region between residues 162 and 207, which was shown above to contain the specificity residues (Fig. 3.8B). Of those amino acids that contact *parS* (Fig. 2B-C), six residues (Q162, G170, K171, S172, N178, and R204) are conserved between ParB and Noc family members (Fig. 3.8B). Two residues (R173 and G201) in ParB contact *parS* but are changed to Q173 and R201, respectively, in Noc homologues (Fig. 3.8B). Other residues at position 179 and 184 vary among ParB homologues but are almost invariably a lysine in Noc family members (Fig. 3.8B). We hypothesized that these amino acids (Q173, K179, K184, and R201) (Fig. 3.8B) are specificity residues that dictate Noc preference for *NBS*. To test this hypothesis, we generated a variant of *Caulobacter* ParB in which these four residues were introduced at the structurally equivalent positions (i.e. R173Q, T179K, A184K and G201R). We purified and tested this variant in a bio-layer interferometry assay with *parS* and *NBS*. As shown in Fig. 3.8, this *C. crescentus* ParB (RTAG→QKKR) variant completely switched its binding preference to a non-cognate *NBS* site. In addition to these four residues, we identified other highly conserved residues, namely E200 and K227 (Fig. 3.8A-C), that also contribute to the *NBS* binding preference. However, just four residues are enough to reprogram the DNA-binding specificity. Our results were strengthened by the fact that *C. crescentus* (a Gram-negative) ParB is far apart from *B. subtilis* (a Gram-positive) ParB in phylogenetic distance (Fig. 3.2B), and that *C. crescentus* does not have a native Noc homologue. Taken together, our data indicate that these four amino acids are the main specificity-determining residues, and that they are likely the key players in the evolutionary switch in binding preference from *parS* to *NBS*.

3.7 Systematic dissection of ParB-*parS* and Noc-*NBS* interfaces reveals the genetic contribution of each specificity residue to the DNA-binding preference

To systematically dissect the role of each specificity residue on DNA-binding preference, Dr. Ngat Tran constructed a complete set of ParB mutants that have either single, double, or triple amino acid changes between the four specificity positions, from a *parS*-preferred wild-type *C. crescentus* ParB ($R^{173}T^{179}A^{184}G^{201}$) to an *NBS*-preferred variant ($Q^{173}K^{179}K^{184}R^{201}$). We named them ParB-to-Noc intermediates (PtoN for short, 15 variants in total). To simplify the nomenclature, we named the mutants based on the specificity residues being considered, for example, an *NBS*-preferred variant ($Q^{173}K^{179}K^{184}R^{201}$) is shortened to PtoN15 (QKKR). PtoN variants were C-terminally $(His)_6$ tagged, expressed in *E. coli*, and purified to homogeneity

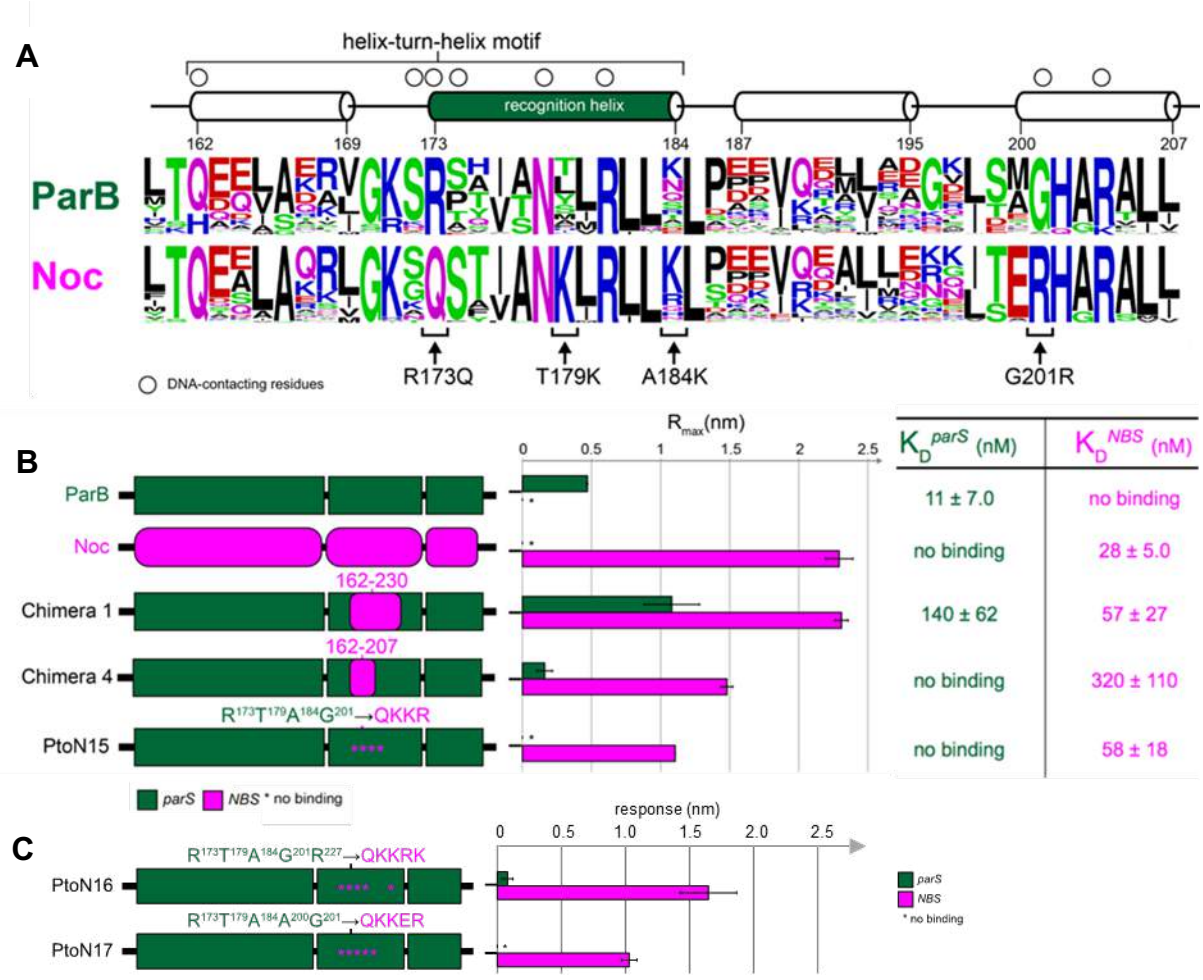

Figure 3.8 Four amino acids dictate amino acid specificity between ParB and Noc. (A) The sequence alignment of ParB (~1800 sequences) and Noc (~400 sequences) orthologs. Amino acids are coloured based on their chemical properties (GSTYC: polar; QN: neutral; KRH: basic; DE: acidic; and AVLIPWFM: hydrophobic). The secondary structure of the amino acid region (res. 162-207) is shown above the sequence alignment, together with residues (open circles) that contact DNA in the ParB (DBD)-*parS* structure. **(B)** Mutations in a subset of residues in the region between res. 162-207 (ParB's numbering) can reprogram interaction specificity. ParB (or segments of amino acids from ParB) and Noc (or equivalent segment in Noc) are shown in dark green and magenta, respectively. The affinity of protein-DNA interaction was expressed as dissociation constant (K_D) ± SD. **(C)** Same as panel except only PtoN16 and PtoN17 variants were used. The level of protein-DNA interaction was expressed as an averaged response value. Error bars represent SD from three replicates.

(Fig. 3.9A). Subsequently, we tested ParB and 15 PtoN variants with a series of 16 different DNA sites, each representing a transitional state from *parS* to *NBS* with each of the two variable positions (1 and 6) changed to any of other four DNA bases (Fig. 3.9A). We visualised 16x16 interactions as a heatmap where each matrix position reflects a dissociation constant (K_D).

This systematic pairwise interaction screen led to several notable observations (Fig. 3.9A). First, there are two non-functional variants (PtoN1: QTAG and PtoN7: QTAR) that were unable to interact with any of the 16 DNA sites (Fig. 3.9A). Second, six variants (PtoN4: RTAR, PtoN5: QKAG, PtoN6: QTKG, PtoN9: RKAR, PtoN10: RTKR, and PtoN11: QKKG) switched their specificity to a DNA site that has features borrowed from both *parS* and *NBS*. Meanwhile, four variants (PtoN2: RKAG, PtoN3: RTKG, PtoN8: RKKG, PtoN14: RKKR) were promiscuous i.e. binding to multiple different DNA sites (Fig. 3.9A). We noted that functional PtoN variants have a lysine at either position 179, or 184, or both. This observation became even clearer after we performed hierarchical clustering of the interaction profile in both the protein and the DNA dimensions (Fig. 3.9B). A single lysine at either position 179 or 184 is enough to license the DNA-binding capability to PtoN variants (nodes a, d, i, and k on the clustering tree, Fig. 3.9B), while PtoN1 (QTAG) and PtoN7 (QTAR) that do not possess any lysine at 179/184 are non-functional (node j, Fig. 3.9B). We suggest that K179/184 has a permissive effect that might permit Q173 and R201 to contact DNA.

Next, we wondered which base of the *NBS* site that Q173 might contact specifically. To find out, we clustered only PtoN variants that share the Q amino acid at position 173 (Fig. 3.9C). We discovered that those variants preferred DNA sites that possess an Adenine at position 1 (Fig. 3.9C). We applied the same approach to find the base that residue R201 might contact (Fig. 3.9D). The emerging trend is that PtoN variants that share an R amino acid at 201 preferred DNA sites with a Cytosine at position 6 (Fig. 3.9D). Taken together, our results suggest a model in which each specificity residue has a distinct role: Q173 recognises Adenine 1, R201 recognises Cytosine 6, but they can only do so in the presence of a permissive K at either position 179 or 184, or both. In the next section, we used X-ray crystallography to provide evidence to support this model.

3.8 Crystallisation of a C-terminally truncated (ΔCTD) *C. crescentus* ParB (QKKR+K227) variant with *NBS*

To determinate the molecular basis that enables the recognition *NBS* over *parS* by the *C. crescentus* ParB (QKKR) variant, I sought to crystallise a co-crystal complex of a specificity-altered ParB variant (QKKR+K227) mutant with a 20-bp *NBS* DNA. K227 was shown to

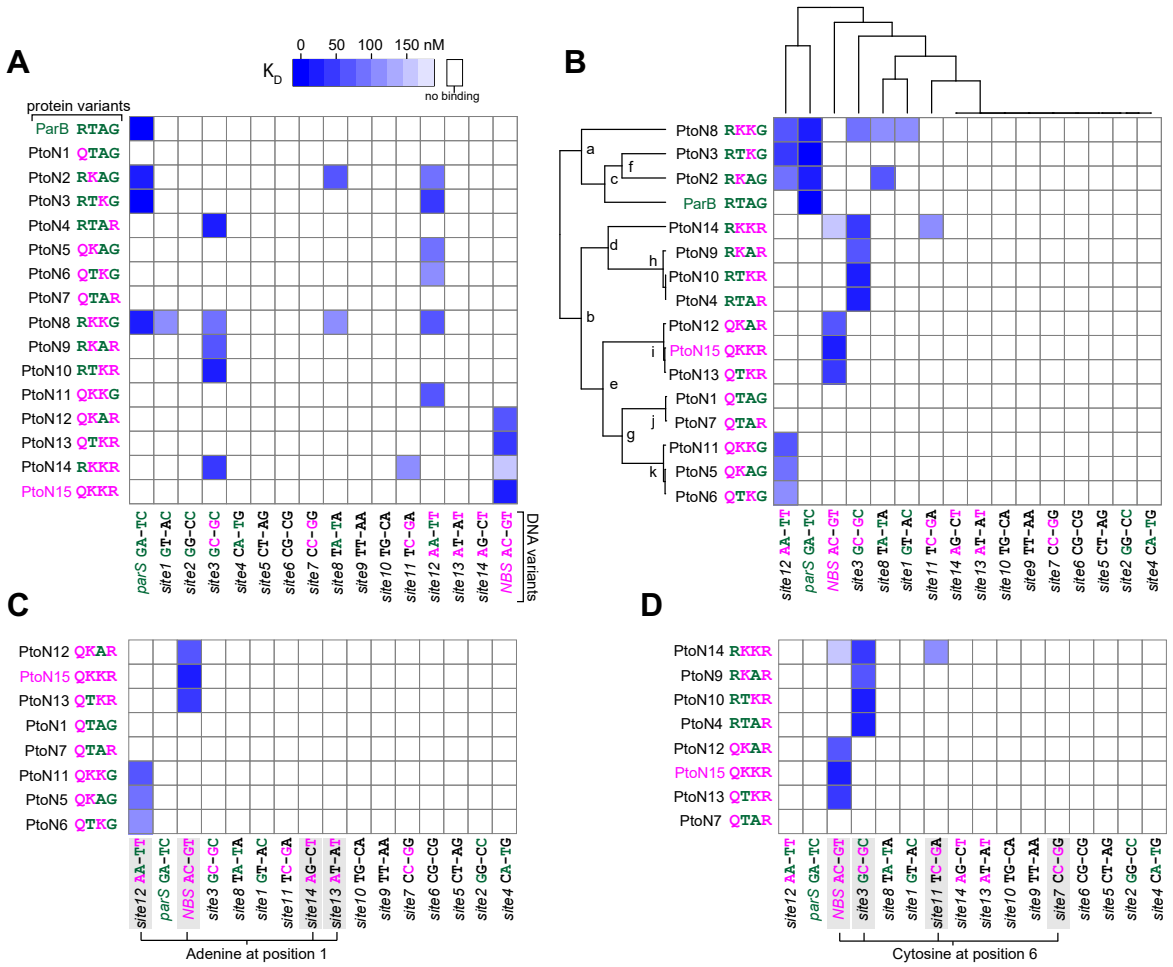

Figure 3.9 Systemic scanning mutagenesis of the protein-DNA interface revealed the contribution of each specificity-defining residue in the protein-DNA interface. (A) Systematic scanning mutagenesis of the protein-DNA interface reveals the contribution of each specificity residue to the DNA-binding preference. Interactions between ParB + 15 PtoN intermediates with 16 DNA sites are represented as a heatmap where each matrix position reflects a K_D value. Amino acid residues/bases from ParB/*parS* are coloured in dark green, and those from Noc/*NBS* in magenta. **(B)** A hierarchical clustering of data in panel A in both protein and DNA dimensions. **(C)** A simplified heatmap where only PtoN intermediates with a glutamine (Q) at position 173 are shown. **(D)** A simplified heatmap where only PtoN intermediates with an arginine (R) at position 201 are shown.

enhance *NBS* binding but is not part of the core specificity residues (Fig. 3.8C). After screening several constructs with different length of the specificity-altered ParB variant and *NBS*, I obtained crystals of a 50 amino acid C-terminally truncated (ΔCTD) ParB (residues 1-243) in complex with a 20-bp *parS* duplex *NBS*. The construct contains the DNA-binding domain and the N-terminal domain of ParB (QKKR+K227) but lacks the CTD. Diffraction data for the *C. crescentus* DBD ParB-*NBS* co-crystal was collected to a resolution of 3.6 Å, a the phase was solved by molecular replacement using the 3.1 Å structure of the *H. pylori* ParBΔCTD-*parS* complex (Chen et al., 2015; Leonard et al., 2004). The X-ray crystallographic data are summarized in Table 3.1.

3.9 The crystal structure of *C. crescentus* ParBΔCTD (QKKR+K227) variant with *NBS*

The final model contained two copies of the *C. crescentus* ParBΔCTD (QKKR+K227) monomers in the asymmetric unit; each complex consists of two ParBΔCTD (QKKR+K227) ParB molecules symmetrically bound to half an *NBS* site (Fig. 3.10). Superimposition of both monomers suggest that they are identical to one another with an RMSD value of 0.137 Å (Fig 3.10B-C). Noticeably, chain A was more complete than chain B. Despite being in the construct, the electron density was not observed in the first 30 aa residues in the structure owing to the flexibility of ParB. The secondary structure of the *C. crescentus* ParBΔCTD (QKKR+K227) complex consists of 4 β-sheets and 10 α-helices, with residues R45-R54 forming β1, L85-P88 (β2), W96-A100 (β3) and T115-I118 (β4). While residues E65-R76 form α1, E102-A111 (α2), D125-R139 (α3), V144-K157 (α4), Q162-I169 (α5), Q173-L182 (α6), D187-S195 (α7), A200-A207 (α8), P212-G222 (α9) and V226-A233 (α10). Noticeably helices α3 and α4 of the NTD are packed against the DBD. The highly conserved arginine-rich motif (GERRxR), crucial for *C. crescentus* ParB spreading and NTP interactions, resides on helix α2. The helix-turn-helix is formed by helices α5 and α6 observed in various repressors and DNA-binding proteins. Helix α6 then connects to the remaining four helices that form a compact bundle. In the crystal, the 20bp *NBS* site also forms a pseudo-continuous filament, by interacting with *NBS* sites in the adjacent subunit, thus stabilizing the *C. crescentus* ParBΔCTD (QKKR+K227) *NBS* crystal complex.

3.10 Co-crystal structure of the specificity-altered ParB variant with *NBS* reveals the contribution of each specificity residue to the DNA-binding preference

While the resolution was modest, the protein-DNA interface was well resolved and strongly supported by the electron density. By superimposing the structures of the WT *C. crescentus* ParB (DBD)-*parS* complex and the ParBΔCTD (QKKR+K227) complex, I observed several

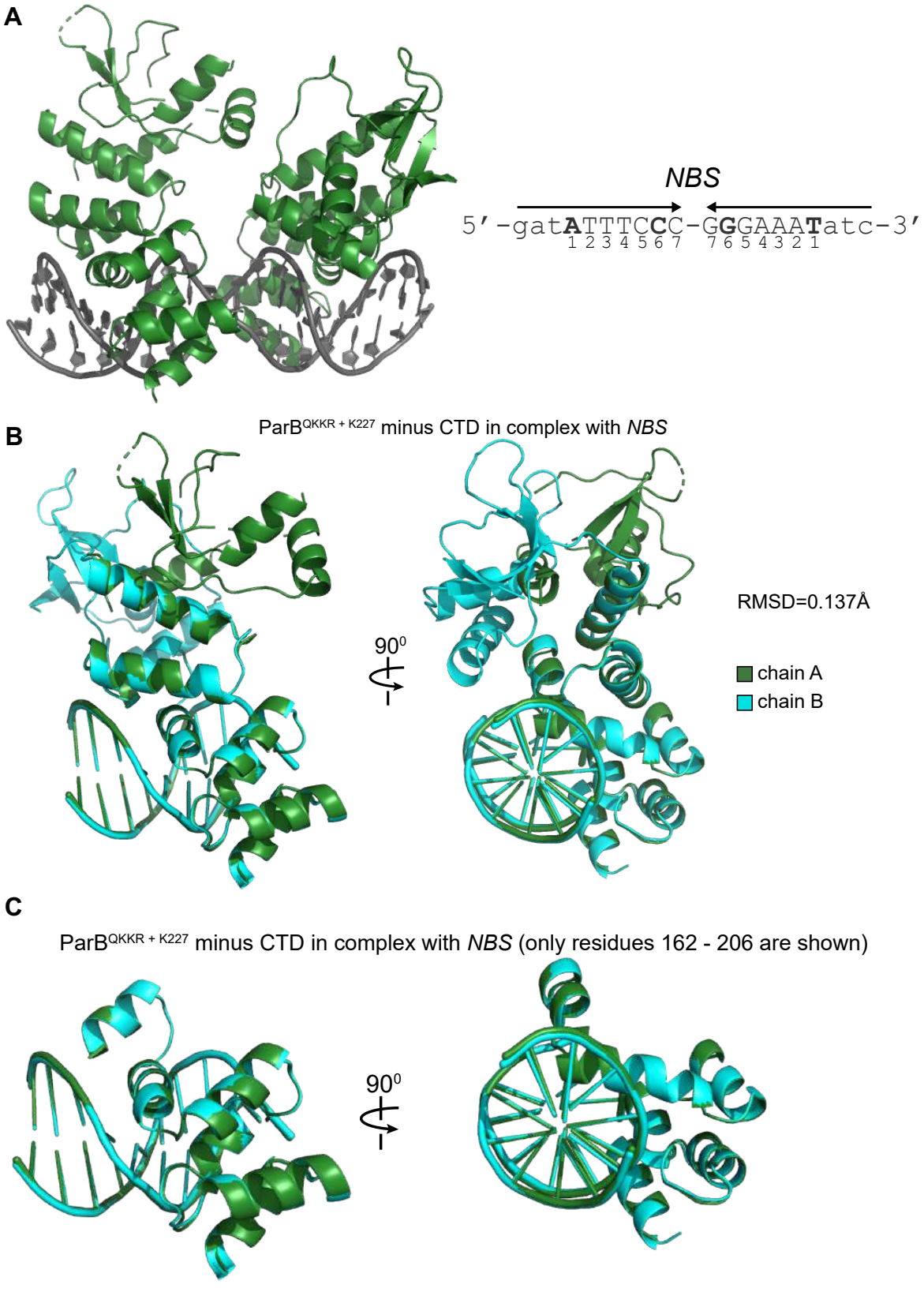
A
NBS
5′-gatATTTCCC-GGGAAATatc-3′
1 2 3 4 5 6 7 7 6 5 4 3 2 1
B
ParBQKKR + K227 minus CTD in complex with NBS
90⁰
RMSD=0.137Å
chain A
chain B
C
ParBQKKR + K227 minus CTD in complex with NBS (only residues 162 - 206 are shown)
90⁰

Figure 3.10 Co-crystal structure of the *NBS*-preferred *Caulobacter* ParB variant with *NBS*. (A) The structure of two ParB (QKKR + K227) monomers (dark green) in complex with a 20-bp *NBS* DNA (grey). Each ParB (QKKR + K227) monomer contains the N-terminal domain and the central DNA-binding domain but lacks the C-terminal dimerization domain. The nucleotide sequence of the 20-bp *NBS* site is shown on the left-hand side; bases (Adenine 1 and Cytosine 6) that are different from *parS* are bolded. **(B)** Superimposition of chain A and chain B of the *NBS*-preferred ParB (QKKR +K227) variant. Chain A/B contains both the N-terminal domain and the central DNA-binding domain but lacks the C-terminal dimerization domain. **(C)** Superimposition of chain A and chain B of the *NBS*-preferred ParB (QKKR +K227) variant, but only the core DBD is shown.

.

changes in both the protein and DNA that enables specific interactions. First, R173 in a wild-type ParB hydrogen bonds with *parS* Guanine 1. A shorter side chain of Q173 (in an *NBS*-preferred ParB mutant) is unable to bind to Guanine 1. However, a corresponding base in *NBS* (Adenine 1) positions itself closer to hydrogen bond with this Q173 residue (Fig. 3.12A); this is possible due to conformational changes in the *NBS* site that narrows the minor groove width at the Adenine 1:Thymine -1 position (from 7.5 to 3.8Å, Fig. 3.12A-B). The switch from R173 to Q173 served to eliminate the ability of ParB to contact *parS* Guanine 1 while simultaneously establishing a new contact with *NBS* Adenine 1. Other notable changes between the two co-crystal structures occur at residues G201 and R201 (Fig. 3.12B). Due to the lack of a side chain for G201 it is unable to contact Thymine -6 (Fig. 3.12B) and only binds to the phosphate backbone. Whereas, the equivalent residue R201 in an *NBS*-preferred ParB variant readily forms hydrogen bonds with Guanine -6 (Fig. 3.12B). Superimposition and analysis of the *parS* and *NBS* site demonstrated that both the minor groove and the major groove widths increase significantly at the Cytosine 6:Guanine -6 position of *NBS* (from 7.0 to 9.0Å, and from 10.2 to 12.5Å, respectively), presumably to move Guanine -6 outwards to be compatible with the longer side chain of R201 (Fig. 3.12). The co-crystal structures are therefore consistent with data from the systematic scanning mutagenesis, and support the model that R201 is a positive determinant of specificity which enables the recognition of Cytosine 6:Guanine -6, and that Q173 is a dual positive and negative determinant which enables the recognition of Adenine 1:Thymine -1 on *NBS*.

The ParBΔCTD (QKKR+K227)-*NBS* complex structure, however, did not yield extra information on the specificity residues K179 and K184 because no clear electron density was seen for the side chains of these residues (Fig. 3.12). It is possible that these residues do not contact specific bases but interact with the phosphate backbone non-specifically at multiple positions, leading to a blurring of the electron-density. Indeed a previous study comparing 129 protein-DNA interactions available on the PDB noted that lysine residues make up most of the interaction with the phosphate backbone (Luscombe et al., 2001). Thus, the most parsimonious explanation for the “enabling” capability of K179 and K184 (data from systematic scanning mutagenesis experiments-Fig.3.9A) is that they increase DNA-binding affinity non-specifically to overcome the initial energy barrier and permit specific base contacts from Q173 and R201, perhaps by interacting with the phosphate backbone non-specifically. Another hypothesis for the “enabling” effect of K179/184 is that they induce conformational changes at the recognition helix and helix (res. 200-207), thereby positioning Q173 and R201 favourably to interact with *NBS* Adenine 1 and Guanine -6. However, the two helices were not seen to change their positions or conformations significantly between the two co-crystal structures,

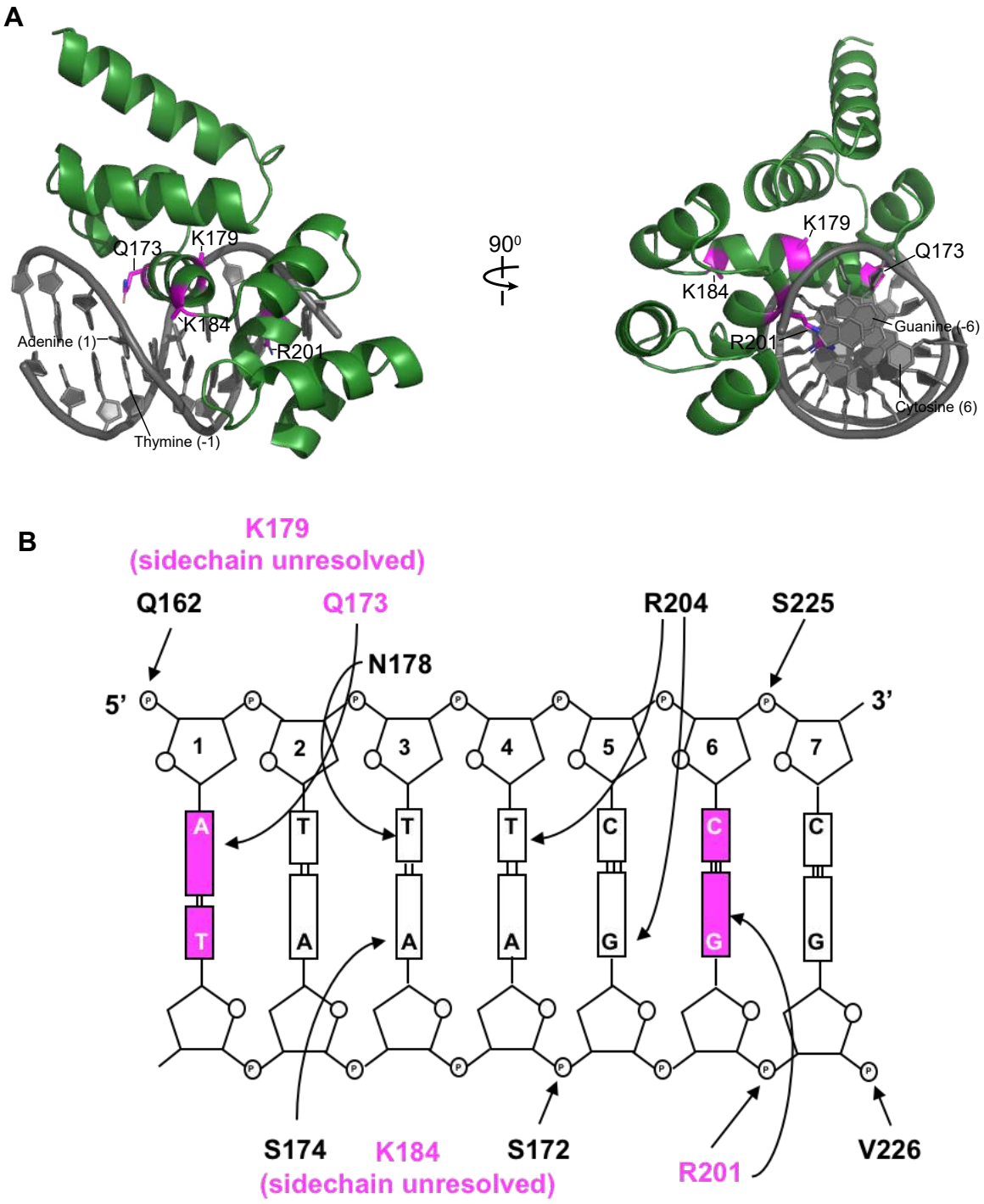

Figure 3.11 Interactions between ParB (QKKR + K227) variant and the *NBS* DNA. One monomer of ParB (DBD) is shown in complex with an *NBS* half-site; only specificity residues are labelled and coloured in magenta. **(C)** Schematic representation of ParB (QKKR + K227)-*NBS* interactions. For simplicity, only half of *NBS* is shown. The two bases at position 1 and 6 that are different between *parS* and *NBS* are highlighted in magenta.

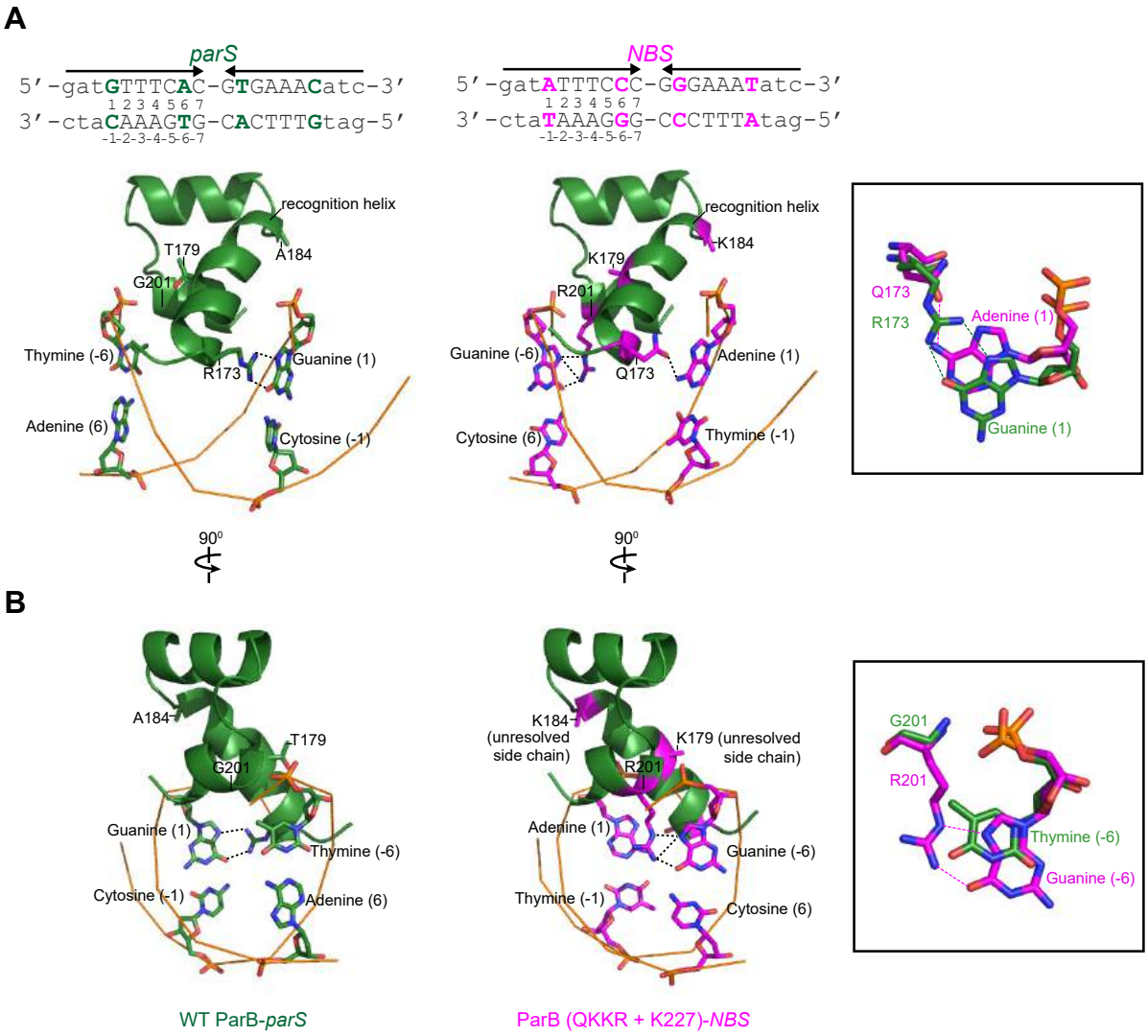

Figure 3.12 Superimposition of the wild-type ParB-*parS* structure on the ParB (QKKR+K227)-*NBS* structure reveals the contribution of specificity residues to *NBS* binding. To simplify and highlight the roles of specificity residues, only the side chains of specificity residues and their contacting bases are shown. The amino acid region (173-207) and the DNA backbones are shown in cartoon representation. DNA bases are numbered according to their respective positions on *parS/NBS* site. The insets show interactions between either Q/R at position 173 **(A)** or G/R201 **(B)** with their corresponding bases on *parS/NBS*.

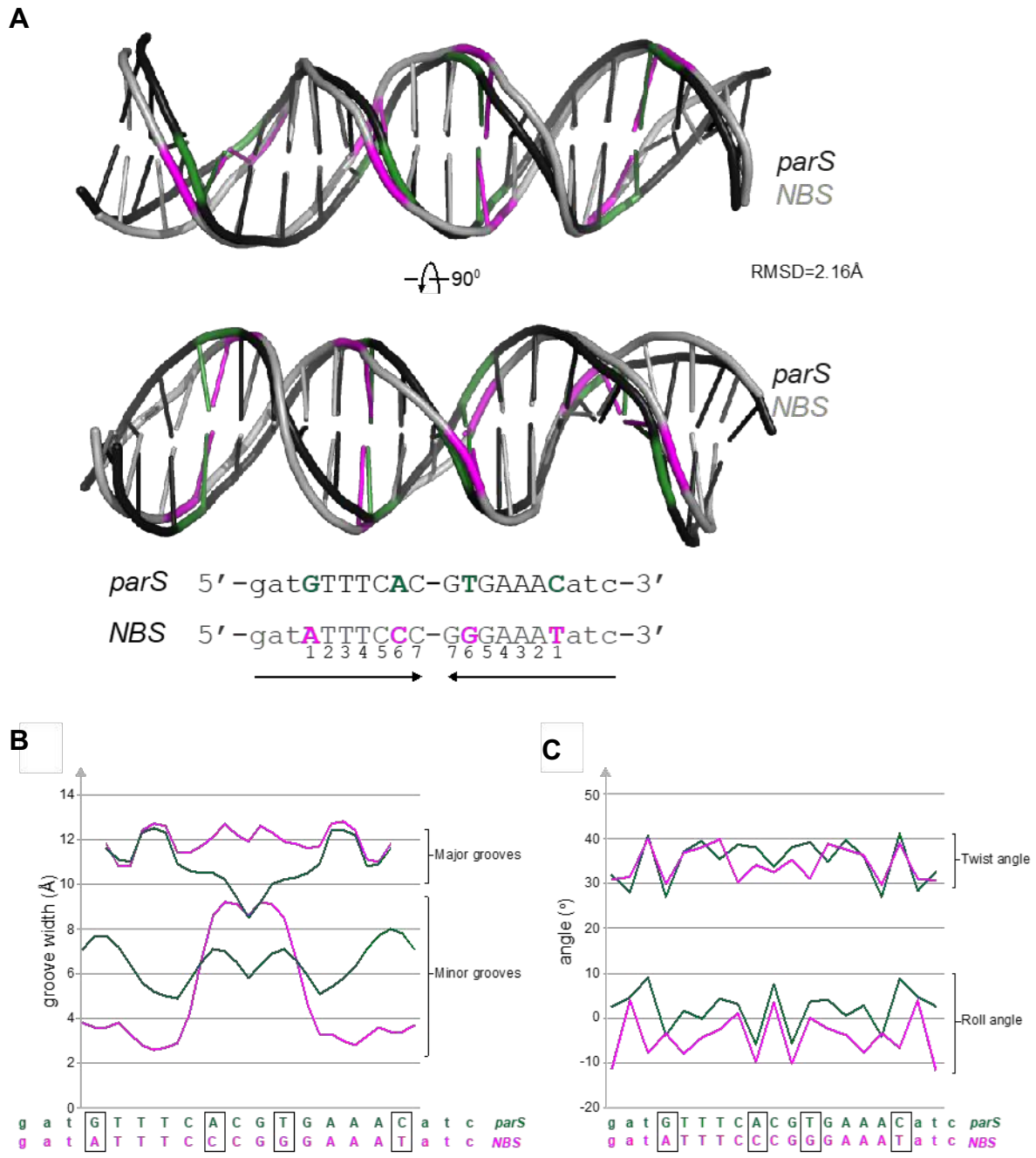

Figure 3.13 Conformational changes at *parS* and *NBS* DNA within the two co-crystal structures. (A) A superimposition of *parS* and *NBS* DNA structures, root-mean-square deviation (RMSD) values are also shown. Bases that are different between *parS* (dark green) and *NBS* (magenta) are highlighted in colours. **(B)** The major and minor groove widths of the bound DNA (*parS*: dark green, *NBS*: magenta). **(B)** The roll and twist angles for each base pair step of the bound DNA (*parS*: dark green, *NBS*: magenta).

arguing against this hypothesis (Fig. 3.12). Thus, to unambiguously determine the contribution of the K179 and K184 residues in mediating the recognition of *NBS* over *parS*. I sought to obtain a higher resolution of data set, which may reveal the electron density for the side chains of these residues. Despite various attempts, I was unable to obtain crystals of the ParBΔCTD (QKKR + K227)-*NBS* variant that diffracted better than 3.6 Å. To overcome this, I decided to solve the crystal structure of *B. subtilis* Noc in complex with *NBS* to obtain a Noc-*NBS* co-crystal that would diffract at a much better resolution.

3.11 Crystallisation of the *B. subtilis* DNA-binding domain (DBD) in complex with *NBS*

To understand the determinants of specificity between *B. subtilis* Noc and its DNA substrate, *NBS*. I sought to crystalise *B. subtilis* Noc in complex with *NBS*. Noc proteins are generally composed of three different domains, each of which are connected by flexible linkers (Fig. 3.1A). This often results in a flexibility in the organisation of the domain orientation which could impair the protein from forming an orderly-packaged crystals. To overcome this flexibility and produce suitable crystals, I decided to crystallise only the DBD of *Bacillus* Noc in complex with *NBS*, After screening several conditions and different lengths of *NBS* DNA, I was able to obtain crystals of the *B. subtilis* Noc (DBD) in complex with a 22 bp *NBS* site. Diffraction data for the *B. subtilis* Noc (DBD)-*NBS* co-crystal was collected to a resolution of 2.6 Å, although the dataset was highly anisotropic. The phase was solved using the *C. crescentus* ParB (DBD)-*parS* complex as a search template. The X-ray crystallographic data are summarized in Table 3.1.

3.12 The co-crystal structure of the *B. subtilis* Noc (DBD)-*NBS* complex

The final model contained two copies of the *B. subtilis* Noc (DBD) monomers in the asymmetric unit; each complex consists of two DBD Noc molecules symmetrically bound to half a *NBS* site (Fig. 3.14A and 3.15A). Noticeably, chain B was more complete than chain A, with the first helix α1 only seen in chain B. Superimposition of both monomers suggest that they are identical to one another with an RMSD value of 0.1 Å (Fig 3.14B). The secondary structure of *B. subtilis* Noc (DBD) consists of eight α-helices, with residues T113-R124 forming α1, S129-H143 (α2), Q147-L154 (α3), Q158-K169 (α4), Q172-E180 (α5), E185-I192 (α6), P197-K210 (α7) and V214-R230 (α8) (Fig. 3.15B). The helix-turn-helix is formed by helices α3 and α4 observed in various repressors and DNA-binding proteins (Fig. 3.15B). Helix α4 then connects to the remaining three helix that form a compact bundle. In the crystal, the 22-bp *NBS* site also forms a pseudo-continuous filament, by interacting with *NBS* sites in the adjacent subunit, thereby stabilizing the *B. subtilis* Noc (DBD)-*NBS* crystal complex (Fig. 3.15B).

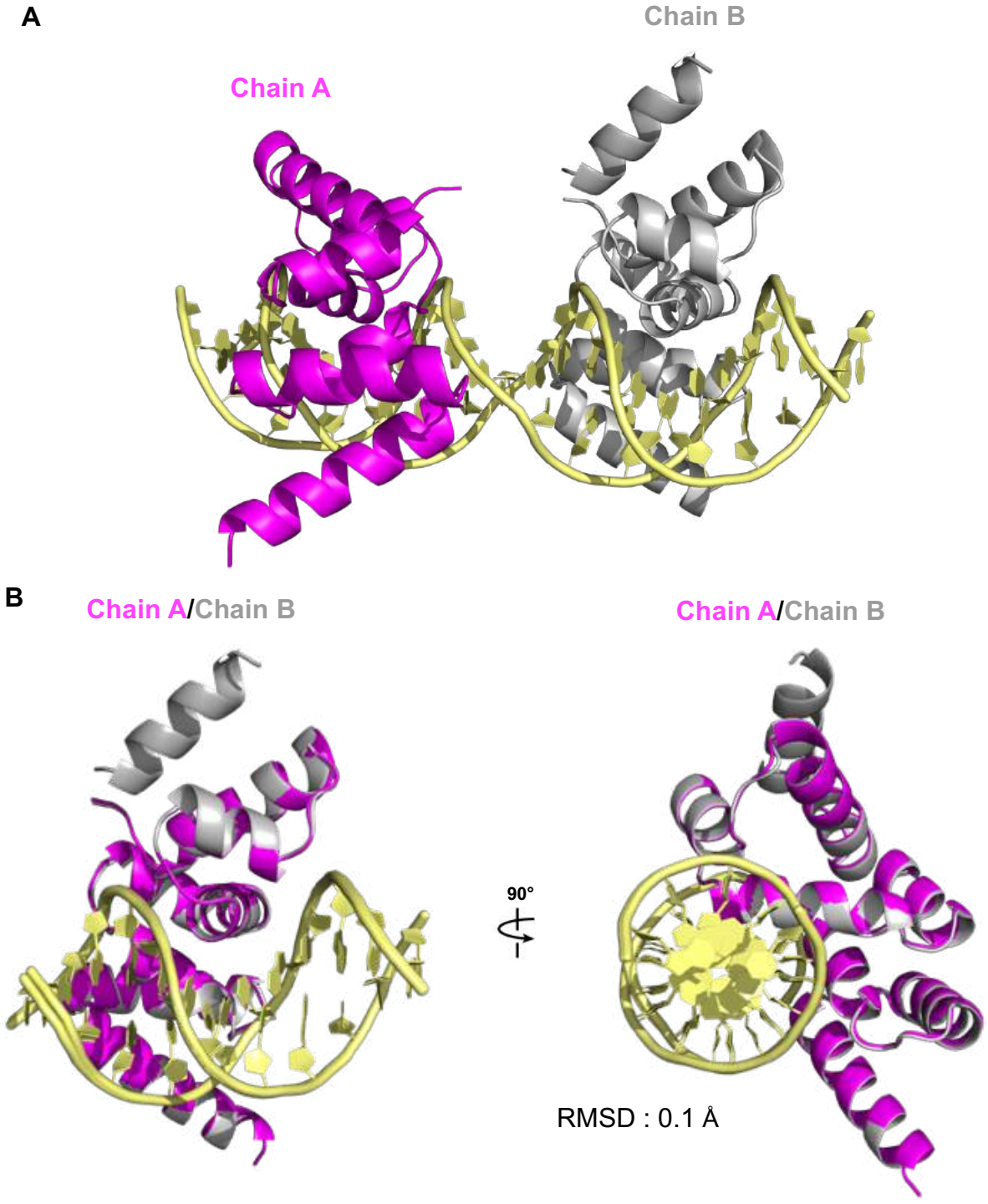

Figure 3.14 Composition of the asymmetric unit (ASU) of the DNA-binding domain (DBD) of *B. subtilis* Noc in complex with *NBS*. (A) The ASU of the *B. subtilis* Noc (DBD)-*NBS* co-crystal complex. Two DBD monomers of Noc are shown (Chain A : magenta and Chain B : grey) in complex with a 22-bp *NBS* DNA (yellow) **(B)** Superimposition of chain A and chain B of *B. subtilis* Noc(DBD). Root-mean- square deviation (RMSD) value is also shown.

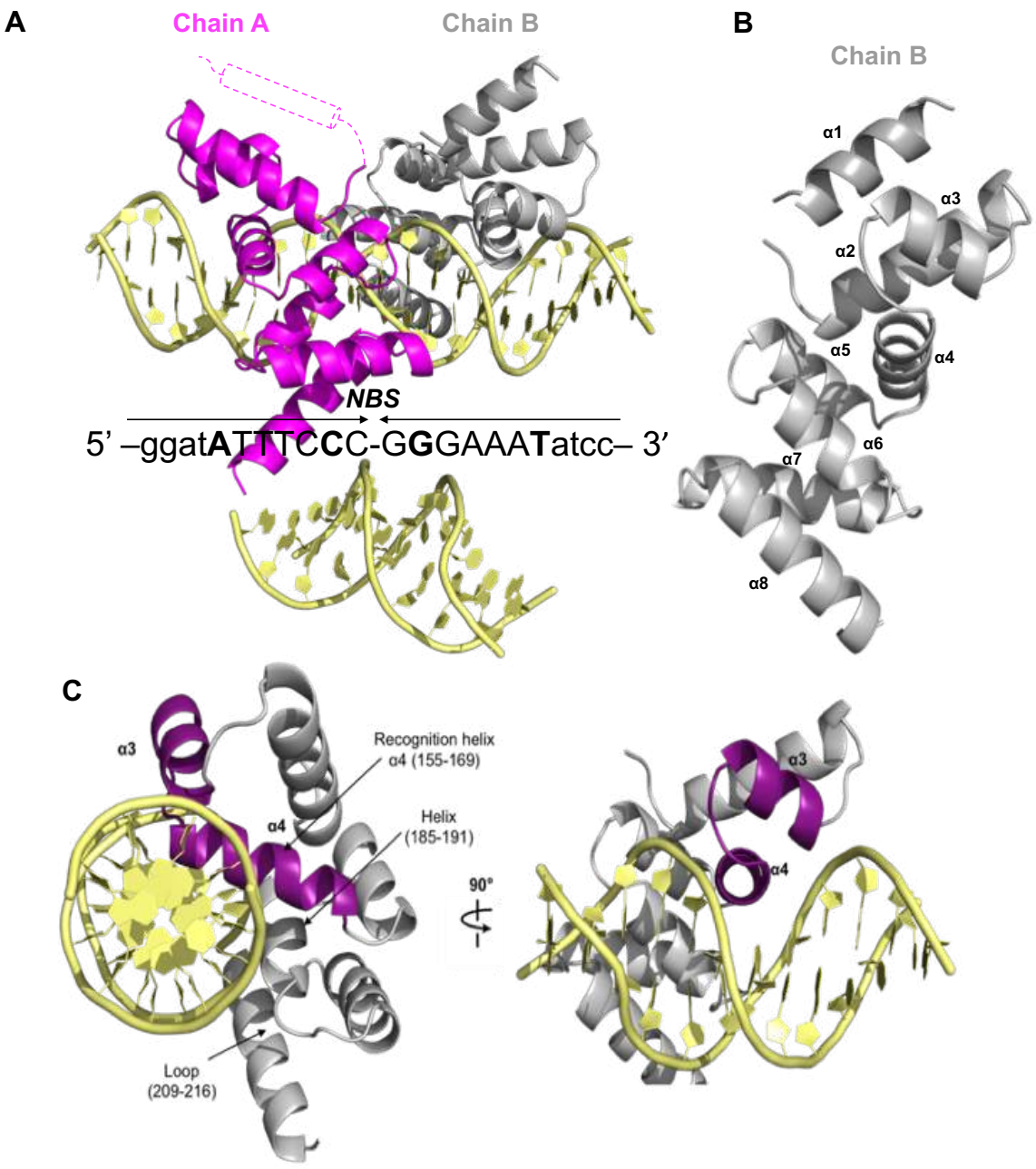

Figure 3.15 The co-crystal structure of the DNA-binding domain of *B. subtilis* ParB in complex with a 22-bp *NBS* DNA. (A) The 2.4-Å resolution structure of two ParB (DBD) monomers (chain A: dark green, chain B: grey) in complex with a 20-bp *parS* DNA (yellow). The nucleotide sequence of the 20-bp *parS* is shown; bases (Guanine 1 and Adenine 6) that are different from *NBS* are shown. The purification tag is also visible in one of the DBD monomers. Loop (236–254) contacts the adjacent DNA in the crystal lattice. One monomer of ParB (DBD) is shown in complex with an *NBS* half-site; only specificity residues are labelled and coloured in magenta.

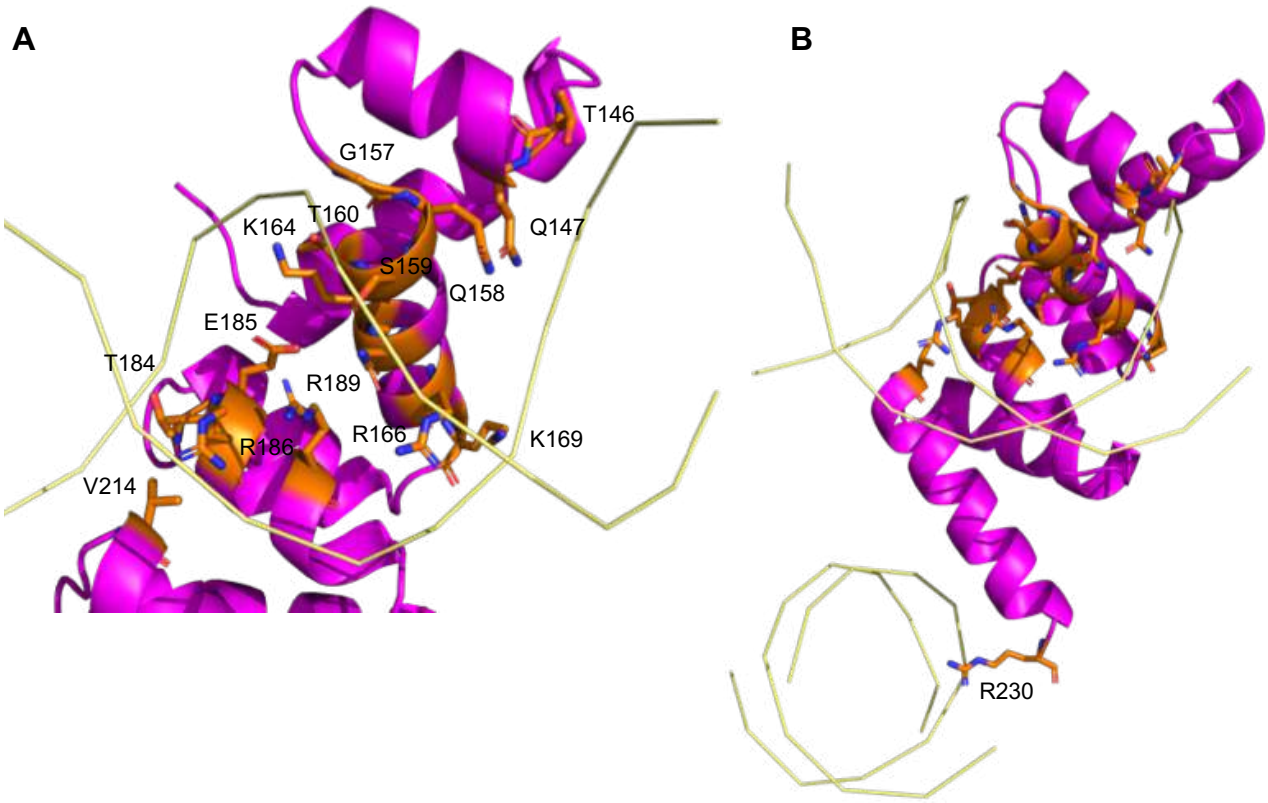
A
T146
G157
K164
T160
Q147
S159
Q158
E185
T184
R189
R186
R166
K169
V214
B
R230

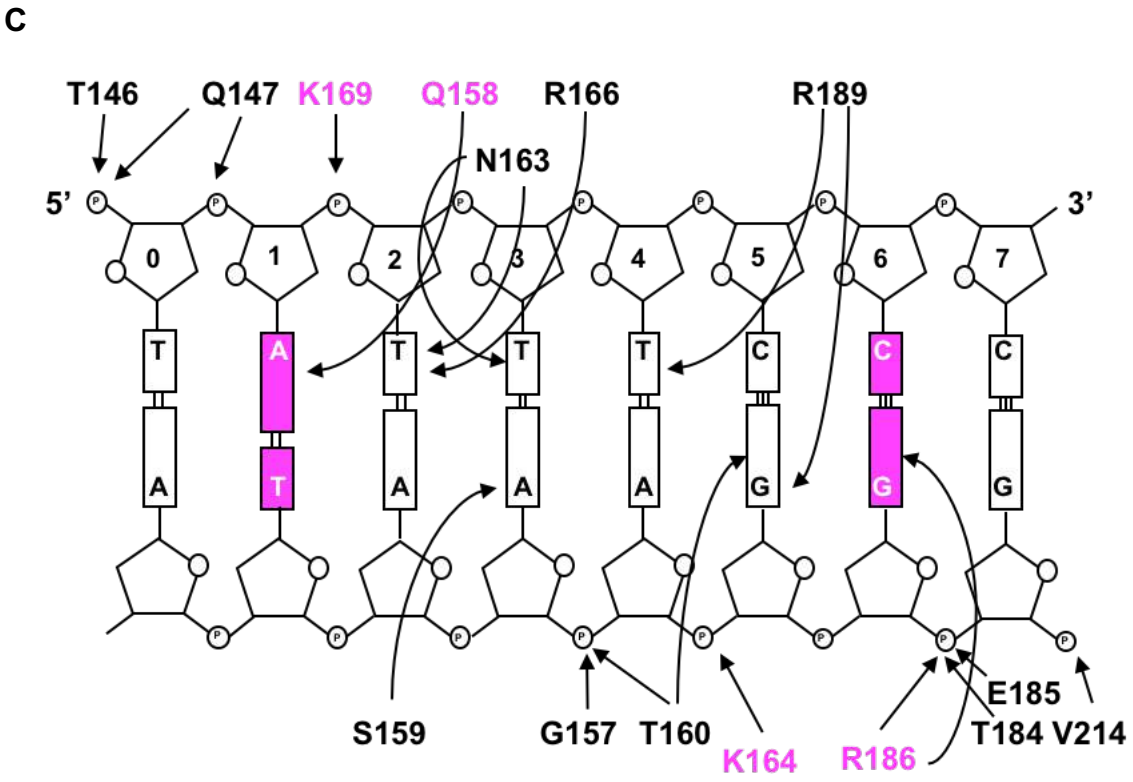
C
T146
Q147
K169
Q158
R166
R189
N163
5'
3'
0
1
2
3
4
5
6
7
T
A
T
A
T
A
T
A
C
G
C
G
C
G
S159
G157
T160
K164
R186
E185
T184
V214

Figure 3.16 Interactions between the DBD of Noc and the *NBS* DNA. **(A)** One monomer of the DBD only of *B. subtilis* Noc is shown in complex with an *NBS* half-site; residues that contact the DNA are labelled. For simplicity, the *parS* site is shown as wires. **(B)** In the Noc (DBD)-*NBS* co-crystal structure, Noc interacts with an *NBS* DNA in the adjacent subunit. Residue R230 hydrogen bonds with Guanine1 and Guanine2 in the adjacent 22 bp *NBS* DNA. These nucleotides however are not present in the cognate *NBS* sequence and this Noc-*NBS* interaction is likely an artefact of crystallization. **(C)** Schematic representation of Noc (DBD)-*NBS* interactions. For simplicity, only half-site a *NBS* site is shown. The two bases at position 1 and 6 that are different between *parS* and *NBS* as well as the specificity defining residues of Noc are highlighted in magenta.

3.13 The residues that mediate the recognition of *B. subtilis* Noc to *NBS*

In the co-crystal structure of *B. subtilis* Noc (DBD)-*NBS*, two very similar Noc (DBD) monomers (RMSD = 0.1 Å) bind in a two-fold symmetric fashion to a full-size *NBS* DNA duplex, with one monomer interacting with half an *NBS* site. The DBD of *B. subtilis* Noc binds to *NBS* through helices α3 and α4, which form the helix-turn-helix motif that inserts into the major grooves of the palindromic *NBS* site (Fig. 3.15C). Furthermore, several other protein-DNA interaction are observed outside of the helix-turn-helix motif. First, in the helix α3 of the helix-turn-helix motif, residue Q147 makes a non-specific contact with the phosphate backbone of the *NBS* site (Fig. 3.16A, 3.16C). Then, the recognition helix (α4) of the helix-turn-helix motif inserts into the major grooves of the palindromic *NBS* site. In α4, residues Q158, S159, T160, N163 and R166 interact directly to the *NBS* site by making specific base contacts via hydrogen bonds, while residues G159, T160, K164 and K169 interacts with the phosphate backbone (Fig. 3.16A, 3.16C). Indeed, the electron density for the side chains of residues K164 and K169 were not resolved in the 3.6 Å *C. crescentus* ParB (QKKR+K227)-*NBS* co-crystal structure (Fig 3.12A-B). Furthermore, in helix α6 a single arginine residue, R189 forms hydrogen bonds with two bases on the *NBS* site, while residues T184, E185 and R186 interacts with the phosphate backbone (Fig. 3.16A, 3.16C). Next, a single valine residue V214 in the loop spanning res. 209-216 makes a non-specific contact with the phosphate backbone of *NBS* (Fig. 3.16A, 3.16C). Finally, a single arginine residue R230 in α8 shown to interact with the *NBS* site in the adjacent asymmetric unit, by hydrogen bonding with Guanine 1 and Guanine 2 in the 22-bp *NBS* site (Fig. 3.16B). Nevertheless, these bases are not part of the cognate *NBS* site, thus these interaction are likely an artefact from crystal packing (discussed below) (Wu et al., 2009). Thus, from solving this co-crystal structure, I was able to identify residues that mediate specific and non-specific contacts between Noc and *NBS,* either through hydrogen bonding with *NBS* bases or by interacting with the phosphate backbone.

3.14 Validating the Noc-*NBS* interactions observed in the *B. subtilis* Noc (DBD)-*NBS* co-crystal structure

Next, I sought to validate the protein-DNA interactions observed in the *B. subtilis* Noc (DBD)-*NBS* crystal structure. To do so, I performed an alanine scanning mutagenesis on the Noc-*NBS* interface and determined their ability to bind to *NBS in vitro*. In brief, the gene encoding the residues observed to mediate *NBS* recognition in *B. subtilis* Noc (DBD)-*NBS* co-crystal structure were mutated to alanine and the corresponding variant proteins were subsequently purified. In the recognition helix (α4) residues Q158, S159, T160, R166, K169 were mutated to alanine to generate the Noc (Q158A), Noc (S159A), Noc (T160A), Noc (R166A) and Noc (K169A) variants. Additionally, in α6 residue R186 was mutated to alanine to generate the Noc (R186A) variant and in the loop spanning residues 236-254, N214 was mutated to alanine to

generate the Noc (N214A) mutant protein. Finally, in α8 a single residue, R230 was mutated to alanine to generate and Noc (R230A) variant. All variant proteins were purified to homogeneity (Fig 3.17A) and analysed by a surface plasmon resonance (SPR) assay that directly assessed their binding to the *NBS* DNA. To measure the percentage of the theoretical maximum response ($\%R_{max}$) of Noc binding to a 24-bp double stranded oligonucleotides containing individual *NBS* sites by SPR, before being tethered onto the chip surface within the SPR flow cell. Purified Noc (WT) and variants were then flowed over the DNA. Interactions between Noc and *NBS* was measured by recording the change in response units during Noc injections. After each injection, the chip was washed in a high salt containing buffer to remove any bound Noc. The cycle was repeated using 3 different concentrations of Noc (WT) and variants, consisting of 1000 nM, 500 nM and 50 nM concentrations. In agreement with previous observations, *B. subtilis* Noc (WT) binds to immobilized *NBS* DNA (Fig. 3.17B) (Wu et al., 2009). While I was unable to detect any noticeable binding when residues Q158, T160 and R166 in the recognition helix (α4) and R166 in (α6) were substituted for alanine, both Noc (S159A) and Noc (K169A) retained their *NBS* binding albeit with ~11 and ~6 fold reduced binding respectively at 1000 nM concentration (Fig. 3.17B). Moreover, in the loop spanning residues 236-254, the Noc (N214A) displayed a ~8 fold reduced binding at 1000 nM concentration to the *NBS* DNA when compared to Noc (WT). Finally while R230 in α8 was shown to interact with the *NBS* DNA in the adjacent ASU of the *B. subtilis* Noc DBD-*NBS*, the Noc (R230A) variant displayed a WT-like binding to the *NBS* site, thus it is likely that this interaction is an artefact of crystal packing (Fig. 3.17B). Taken together, these findings further support the Noc-*NBS* interactions observed in the *B. subtilis* Noc (DBD)-*NBS* co-crystal complex.

3.15 Superimposing the structure of *C. crescentus* ParB (DBD) and *B. subtilis* Noc (DBD) reveals the mechanistic basis that defines specificity

To determine the changes in both protein and the DNA sites that enabled specific interactions, I superimposed the structures of the ParB (DBD)-*parS* and Noc (DBD)-*NBS* complexes (Fig. 3.18A-B). By doing so, I observed several changes in both the protein and the DNA sites that enabled specific interactions (Fig. 3.18B). These findings were similar with the observations made when I compared the ParB (DBD)-*parS* structure with the ParBΔCTD (QKKR+K227)-*NBS* structure. R173 in ParB forms a hydrogen bond with *parS* Guanine1, while the shorter side chain of the corresponding Q158 in Noc is unable to bond with Guanine 1 (Fig. 3.18A). Instead, the corresponding base in *NBS* (Adenine 1) positions itself closer to enable hydrogen bonding with this Q158 residue (Fig. 3.18B). Indeed comparison between *parS* and *NBS* demonstrated conformational changes in the *NBS* site that narrows the minor groove width at the Adenine1:Thymine1 position (from ~7.7 to ~3.7 Å, Fig. 3.19). The switch from arginine to

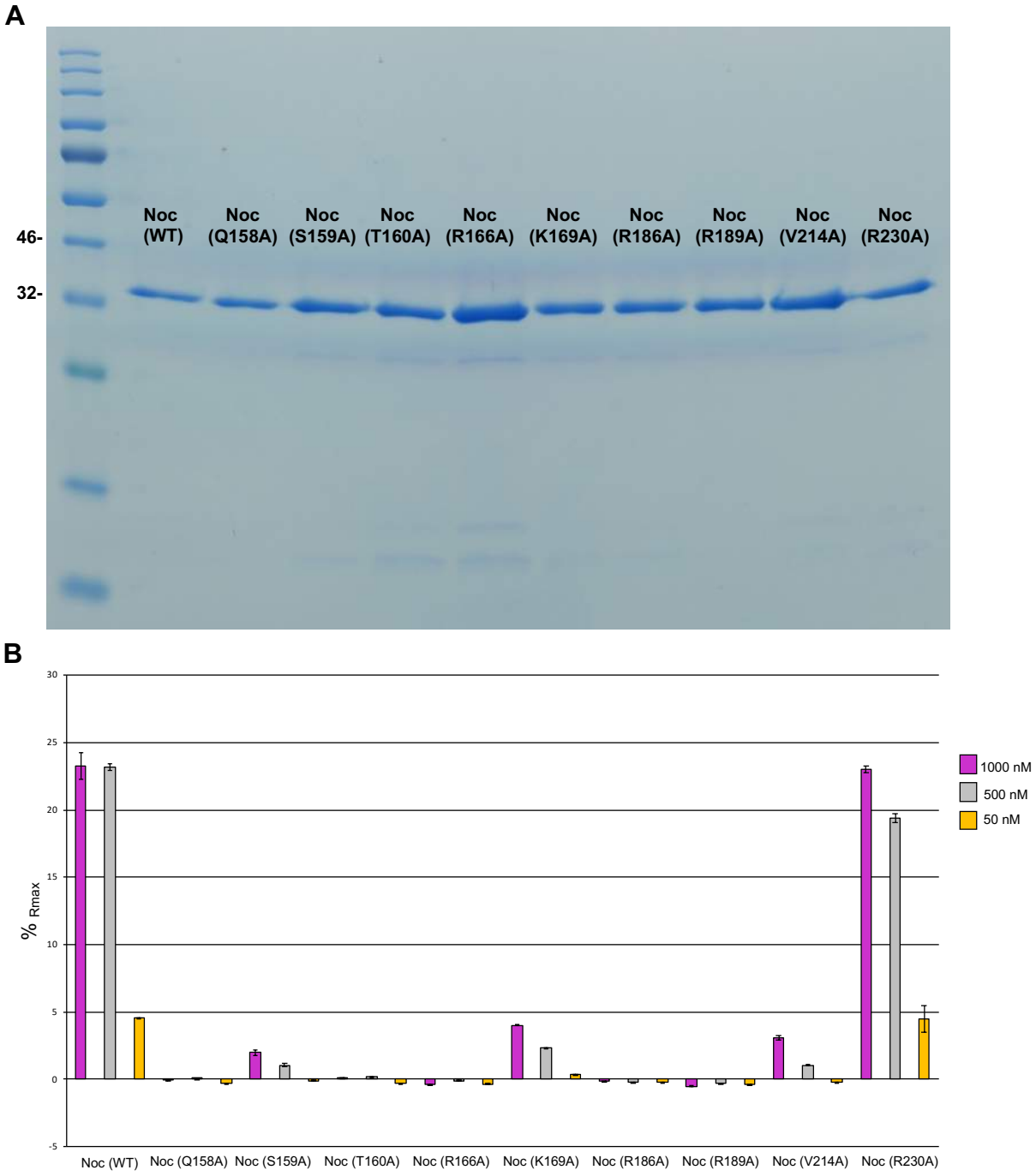

Figure 3.17 Alanine scanning mutagenesis of the Noc-*NBS* interface. (A) SDS-PAGE analysis of purified Noc variants used in this study. Their identities are shown above the corresponding lane. **(B)** Surface Plasmon Resonance (SPR) was used to measure binding affinity of Noc (WT) and Noc variants (50, 500 and 1000 nM) to 24-bp double-stranded DNA that contains the *NBS* site. The level of Noc (WT) and variants binding to DNA was expressed as a percentage of the theoretical maximum response, R_{max}, assuming a single Noc dimer binding to one immobilized double-stranded DNA oligomer. This normalization process enabled the various responses to be readily compared, irrespective of the quantity and length of the DNA tethered on an SPR chip surface.

glutamine serves to eliminate the ability of ParB to contact *parS* at Guanine 1 while simultaneously forming a new hydrogen bond with NBS at Adenine 1. Another notable difference between the two co-crystal structures occurs at position 201 (Fig. 3.18B-C). G201 from ParB has no side chain, hence cannot contact Thymine -6 and only contacts the phosphate backbone non-specifically (Fig. 3.18B-C). However, the equivalent residue R186 in Noc readily forms hydrogen bonds with Guanine -6 (Fig. 3.18B-C). Indeed, comparison of *parS* and *NBS* revealed a DNA unwinding that increased both the minor and the major groove widths at the Cytosine 6:Guanine -6 position of NBS (from ~7.1 to ~8.1 Å, and from ~10.5 to ~11.8 Å, respectively), possibly to position Guanine -6 outwards to accommodate a longer side chain of arginine (Fig. 3.19). Furthermore, the Noc (DBD)-*NBS* structure revealed the side chains of K164 and K169 which makes hydrogen bonds with the phosphate groups of Guanine (-5) and Thymine (2) of *NBS* rather than contacting any bases specifically (Fig. 3.16A-B and 3.18B-C). Interestingly, in absence of K164 and/or K169, prevented the interaction between PtoN variants with *NBS*, even in the presence of the Q173 and R201 substitutions (Fig. 3.9). Thus, the binding of K164 and K169 to the phosphate backbone of *NBS* likely increases the DNA-binding affinity of PtoN/Noc towards the *NBS* site to overcome the initial energy barrier and primes both Q173 and R201 to favourably interact with *NBS* Adenine -1 and Guanine -6 respectively. Thus, through a combination of X-ray crystallography and systemic mutagenesis, I propose that permissive mutations (K164 and K169) and specificity swapping mutations (Q158 and R201) are required for DNA-binding proteins to switch the recognition of their cognate DNA substrate.

3.16 Discussion

Both *parS* and *NBS* differ from each other by only 2 bases (position 1 and 6, Fig. 4.1A), yet both ParB and Noc recognise and binds them with exquisite specificity. By obtaining co-crystal structures of the *C. crescentus* ParB (DBD)-*parS* complex and the *B. subtilis* Noc DBD-*NBS* complex, along with the scanning mutagenesis of the protein-DNA interface, we demonstrated that DNA-binding specificity was switched from *parS* to *NBS* through the combined action of negative and positive determinants of specificity, and permissive mutations. A single R173Q substitution alone removed the *parS*-binding capability (a negative determinant), while at the same time enabled the protein to recognise Adenine 1 of *NBS* (a positive determinant). The specificity for *NBS* was further improved by a G201R substitution that introduced a hydrogen-bonding capability to recognise Cytosine 6 of *NBS* (a positive determinant) (Fig. 3.18B-C). However, as observed by the systemic scanning mutagenesis assays, Q173 and R201 alone/together are not enough; and permissive amino acids (K179 and/or K184) must have been introduced. Without these permissive substitutions, Q173 and R201 were poised to recognise specific bases but could not achieve sufficient affinity to bind *NBS* strongly. Due to

A

```
CcParB      DLNVLEEALSYKVLMEKFERTQENIAQTIGKSRSHVA  177
BsNoc       ELSSIEEAHAYARLLELHDLTQEALAQRLGKGQSTIA  162

CcParB      NTMRLLALPDEVQSYLVSGELTAGHARAIAAAADPV-  213
BsNoc       NKLRLLKLPQPVQEAIMEKKITERHARALIPLKQPEL  199

CcParB      --ALAKQIIEGGLSVRETEALARKAPNLSAG 242
BsNoc       QVTLLTEIIEKSLNVKQTEDRVVKMLEQGQR 230
```

B

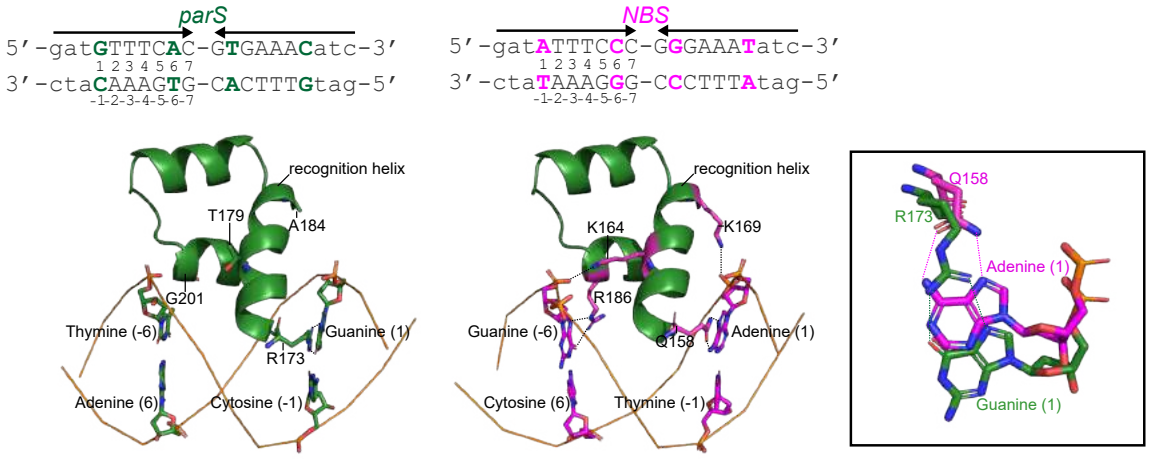

C

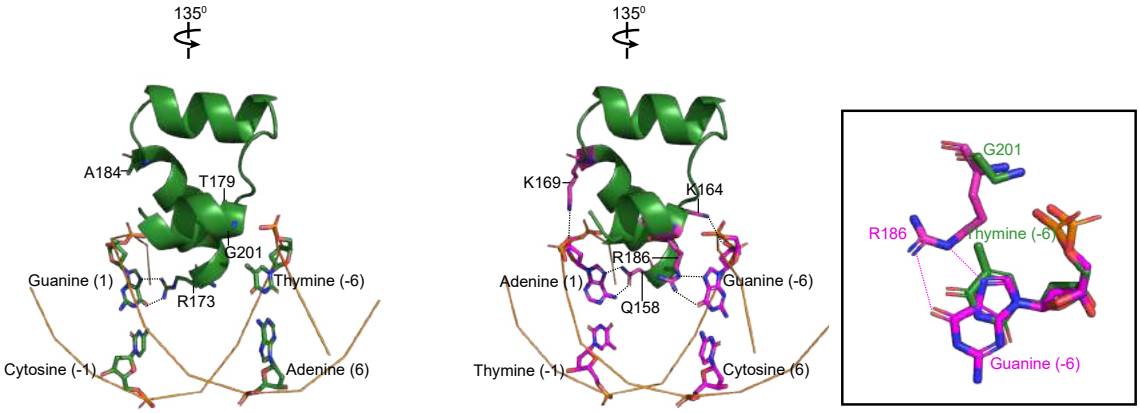

ParB (DBD)-*parS* Noc (DBD)-*NBS*

Figure 3.18 Superimposition of the ParB (DBD)-*parS* structure on the Noc (DBD)-*NBS* structure reveals the contribution of specificity residues to *NBS* binding. (A) Amino acid sequences of *C. crescentus* ParB and *B. subtilis* Noc with the positions of four specificity residues highlighted in dark green and magenta, respectively. Secondary structures are shown above the sequence alignment. To simplify and highlight the roles of specificity residues, only the side chains of specificity residues and their contacting bases are shown. The amino acid regions (173-207 in ParB and the corresponding 158-192 in Noc) and the DNA backbones are shown in cartoon representation. DNA bases are numbered according to their respective positions on *parS/NBS* site. The insets show interactions between either **(B)** R173 (ParB's numbering) and Q158 (Noc's numbering) or **(C)** G201 (ParB's numbering) and R186 (Noc's numbering) and with their corresponding bases on *parS/NBS*. The side chains of K164 and K169 in Noc (DBD)-*NBS* structure contact the phosphate groups of Guanine (-5) and Thymine (2) of *NBS*, respectively (See also Figure S2D). For Guanine (-5) and Thymine (2) in *NBS*, only their phosphate groups are shown.

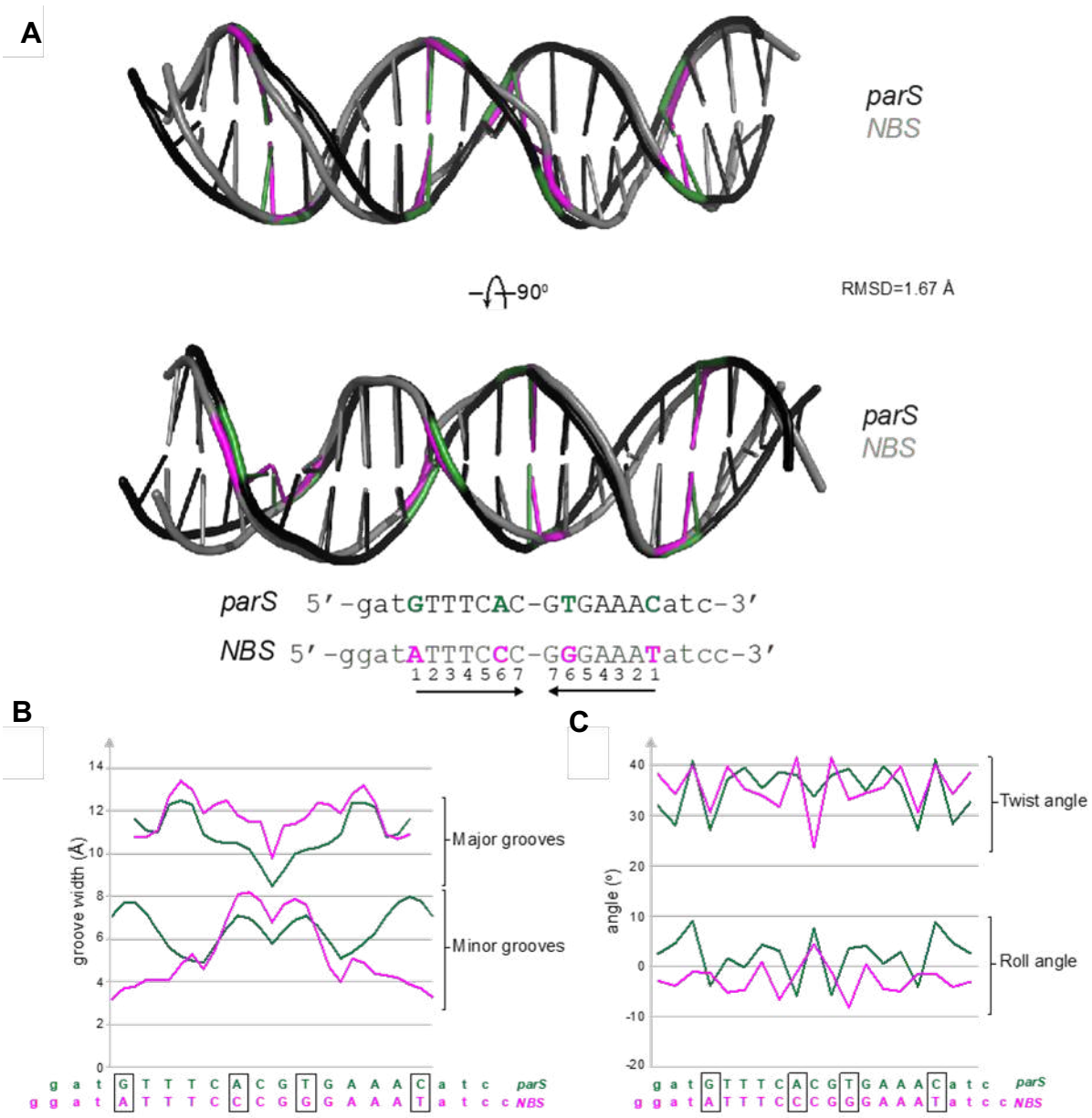

Figure 3.19 Conformational changes at *parS* and *NBS* DNA within the *C. crescentus* ParB (DBD)-*parS* and *B. subtilis* Noc (DBD)-*NBS* co-crystal structures. (A) A superimposition of *parS* and *NBS* DNA structures, root-mean-square deviation (RMSD) values are also shown. Bases that are different between *parS* (dark green) and *NBS* (magenta) are highlighted in colours. **(B)** The major and minor groove widths of the bound DNA (*parS*: dark green, *NBS*: magenta). **(B)** The roll and twist angles for each base pair step of the bound DNA (*parS*: dark green, *NBS*: magenta).

Structure	**ParB (DBD)-*parS* complex**	**ParBΔCTD (QKKR+K227)-*NBS* complex**	**Noc (DBD)-*NBS* complex**
Data collection			
Diamond Light Source beamline	I04	I03	I03
Wavelength (Å)	0.980	0.970	0.970
Detector	Pilatus 6M-F	Pilatus3 6M	Eiger2 XE 16M
Resolution range (Å)	40.12 – 2.40 (2.49 – 2.40)	83.36 – 3.60 (3.94 – 3.60)	72.30 – 2.23 (2.66 – 2.23)
Space Group	*C*2	$I4_122$	*C*2
Cell parameters (Å/°)	*a* = 122.1, *b* = 40.7, *c* = 94.0, β = 121.4	*a* = *b* = 117.9, *c* = 249.6	*a* = 134.1 *b* = 60.6, *c* = 81.1, β = 116.9
Total no. of measured intensities	105021 (10942)	194558 (47223)	142152 (6183)
Unique reflections	16317 (1662)	10637 (2491)	10830 (542)
Multiplicity	6.4 (6.6)	18.3 (19.0)	13.1 (11.4)
Mean $I/\sigma(I)$	7.0 (2.0)	10.5 (2.7)	9.3 (1.5)
Completeness (%)	99.7 (99.2)	100.0 (99.9)	38.1 (4.7)
R_{merge}[a]	0.137 (0.801)	0.148 (0.799)	88.4 (57.2)
R_{meas}[b]	0.150 (0.869)	0.152 (0.821)	0.108 (0.851)
$CC_{½}$[c]	0.992 (0.850)	0.999 (0.994)	1.000 (0.847)
Wilson *B* value (Å^2)	42.1	140.9	115.7
Refinement			
Resolution range (Å)	40.12 – 2.40	83.36 – 3.60	72.30 – 2.23
Reflections: working/free[d]	15480/826	10078/527	10231/599
R_{work}[e]	0.216	0.319	0.231
R_{free}[e]	0.232	0.340	0.279
Ramachandran plot: favoured/allowed/disallowed[f] (%)	96.5/3.5/0.0	95/5.0/0.0	95.4/4.6/0.0
R.m.s. bond distance deviation (Å)	0.003	0.003	0.002
R.m.s. bond angle deviation (°)	1.08	1.09	1.03
No. of protein residues per chain	121/140	194/113	105/116
No. of DNA bases per chain	20/20	20/20	22/22
No. of water/glycerol molecules	82/2	0/0	0/0
Mean *B* factors: protein/DNA/ water/glycerol/overall (Å^2)	51/46/38/60/49	206/226/-/-/212	155/148/0/154
PDB accession code	**6S6H**	**6S6P**	**6Y93**

Table 3.1 X-ray data collection and processing statistics for the crystal structures of the ParB (DBD)-*parS* complex, ParBΔCTD (QKKR+K227)-*NBS* complex and Noc (DBD)-*NBS* complex

Values in parentheses are for the outer resolution shell. [a] Rmerge = $\sum_{hkl} \sum_i |I_i(hkl) - \langle I(hkl) \rangle| / \sum_{hkl} \sum_i I_i(hkl)$.

[b] Rmeas = $\sum_{hkl} [N/(N-1)]^{1/2} \times \sum_i |I_i(hkl) - \langle I(hkl) \rangle| / \sum_{hkl} \sum_i I_i(hkl)$, where $I_i(hkl)$ is the ith observation of reflection hkl, $\langle I(hkl) \rangle$ is the weighted average intensity for all observations i of reflection hkl and N is the number of observations of reflection hkl.

[c] $CC1/2$ is the correlation coefficient between symmetry equivalent intensities from random halves of the dataset.

[d] The dataset was split into "working" and "free" sets consisting of 95 and 5% of the data respectively. The free set was not used for refinement.

[e] The R-factors Rwork and Rfree are calculated as follows: $R = \sum(|F\text{obs} - F\text{calc}|)/\sum|F\text{obs}|$, where Fobs and Fcalc are the observed and calculated structure factor amplitudes, respectively.

[f] As calculated using MolProbity (Davis et al., 2007).

the resolution of the co-crystal structure of the ParB (QKKR+K227) variant in complex with *NBS*, the contribution of K179 and/or K184 to *NBS* binding remained enigmatic, as no electron density was observed for the side chains of either residues. To overcome this, I was able to crystallise and solve a higher resolution structure of DBD only of *B. subtilis* Noc in complex with *NBS*, which revealed that the K179 and/or K184 substitutions binds to phosphate backbone of the *NBS* site, providing evidence of their role as permissive substitutions for *NBS* recognition. Intriguingly, permissive mutations were also observed in the evolution of influenza resistance to the antiviral drug oseltamivir (Bloom et al., 2010). The acquisition of two permissive mutations, enabled the virus to tolerate the subsequent accumulation of a H274Y mutation that impaired oseltamivir binding to the viral neuraminidase enzyme. By acquiring these permissive mutations, the virus managed to improve the stability of neuraminidase before the introduction of the structurally destabilizing H274Y mutation (Bloom et al., 2010). Similarly, a permissive mutation located far away from the active site of an antibiotic-degrading β- lactamase (TEM1) had little effect on its enzymatic activity by itself, but restored stability loss by a subsequent mutation that increased TEM1 activity against cephalosporin antibiotics (Wang et al., 2002). While in another example, 11 permissive mutations were introduced to diversify the DNA-binding specificity of an ancestral steroid receptor to recognise a new cognate DNA site. Indeed, these 11 mutations were found outside of the DNA-recognition helix, but non-specifically increased the affinity for both estrogen response elements and steroid response elements, thereby permitting three additional substitutions in the recognition helix to alter the protein specificity to the new DNA site (McKeown et al., 2014). In the case of ParB/Noc, the introduction of a lysine residues, either at position 179 or 184, was enough to enable Gln173 and Arg201 to bind and recognise *NBS* specifically, by increasing the affinity to both *parS* and *NBS* non-specifically.

In summary, the work I present in this chapter revealed the molecular basis underpinning ParB-*parS* and Noc-*NBS* recognition. In doing so, I was able to provide a model explaining how protein-DNA interaction specificity can change (Fig 3.20). By combining X-ray crystallography and systemic scanning mutagenesis, we identified a small set of four specificity residues at the protein-DNA interface, and dissected at the molecular level the role of individual residues in reprogramming specificity. The work in this chapter may be useful for understanding the diversification of other classes of DNA-binding proteins. Nevertheless, evolution has most likely exploited more mutations and amino acid residues to fine-tune DNA-binding specificity than the core set of four residues in this work. Other compensatory mutations that alter the structural stability of proteins might also contribute and dictate the course of evolution to new biological functions (Ivankov et al., 2014; Sikosek and Chan, 2014; Starr and Thornton, 2016). An important challenge for future work is to study all contributing

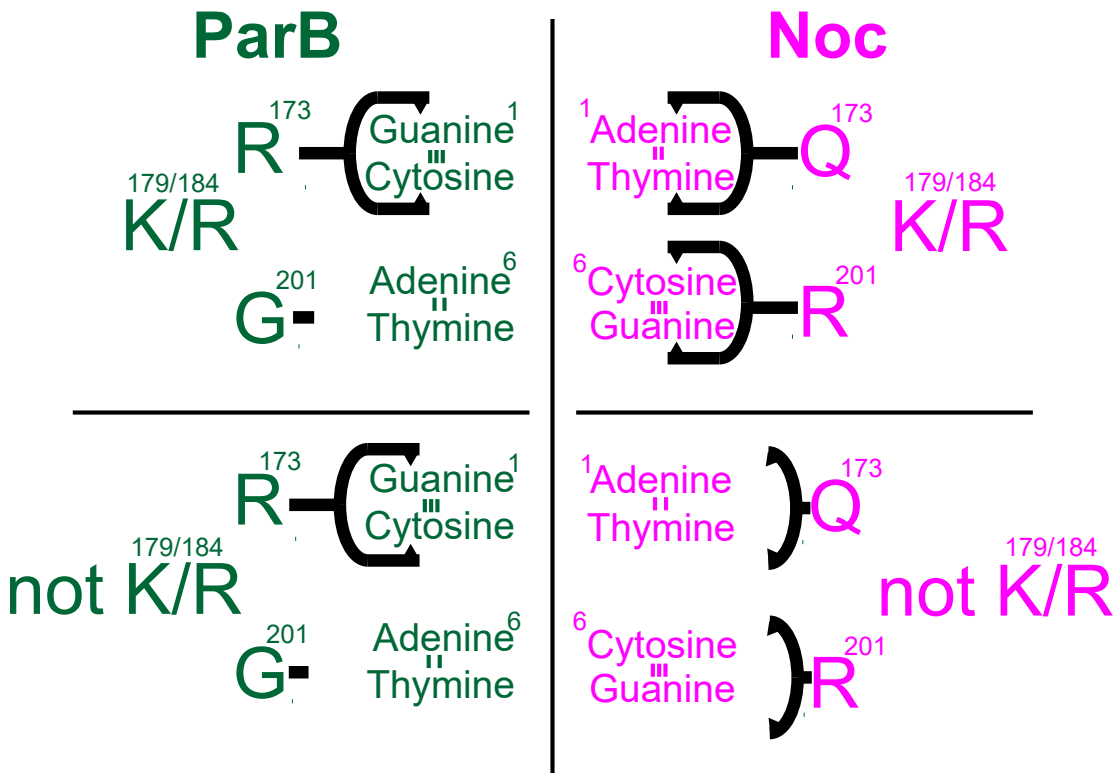

Figure 3.20 A model for the determinants of *NBS*-binding specificity. Contributions of each specificity residue to enable a switch in binding specificity from *parS* to *NBS*. An R173Q substitution enabled interactions with Adenine 1:Thymine -1 (of *NBS*). A G201R substitution enabled interactions with Cytosine 6: Guanine -6 (of *NBS*). Q173 and R201 could only do so in the presence of permissive residues K at either 179, 184, or both. Without K179/184, Q173 and R201 were poised to interact with specific bases but could not, possibly because of insufficient affinity for DNA.

factors (permissive, specificity-switching, and other compensatory substitutions) in a systematic manner to better understand the course of evolution to new biological innovations.

3.17 References

1. Bloom, J.D., Gong, L.I., and Baltimore, D. (2010). Permissive secondary mutations enable the evolution of influenza oseltamivir resistance. Science. **328**, 1272–1275.
2. Chen, B.W., Lin, M.H., Chu, C.H., Hsu, C.E., and Sun, Y.J. (2015). Insights into ParB spreading from the complex structure of Spo0J and parS. Proc. Natl. Acad. Sci. U. S. A. **112**, 6613–6618.
3. Conrad, B., and Antonarakis, S.E. (2007). Gene duplication: A drive for phenotypic diversity and cause of human disease. Annu. Rev. Genomics Hum. Genet. **8**, 17–35.
4. Fisher, G.L.M., Pastrana, C.L., Higman, V.A., Koh, A., Taylor, J.A., Butterer, A., Craggs, T., Sobott, F., Murray, H., Crump, M.P., et al. (2017). The structural basis for dynamic DNA binding and bridging interactions which condense the bacterial centromere. Elife **6**, e28086.
5. Fogel, M.A., and Waldor, M.K. (2006). A dynamic, mitotic-like mechanism for bacterial chromosome segregation. Genes Dev. **20**, 3269–3282.
6. Gruber, S., and Errington, J. (2009). Recruitment of Condensin to Replication Origin Regions by ParB/SpoOJ Promotes Chromosome Segregation in B. subtilis. Cell. **137**, 685–696.
7. Ireton, K., Gunther IV, N.W., and Grossman, A.D. (1994). spo0J is required for normal chromosome segregation as well as the initiation of sporulation in Bacillus subtilis. J. Bacteriol. **176**, 5320–5329.
8. Ivankov, D.N., Finkelstein, A. V., and Kondrashov, F.A. (2014). A structural perspective of compensatory evolution. Curr. Opin. Struct. Biol. **26,** 104–112.
9. Jalal, A.S.B., Tran, N.T., Stevenson, C.E., Chan, E.W., Lo, R., Tan, X., Noy, A., Lawson, D.M., and Le, T.B.K. (2020). Diversification of DNA-Binding Specificity by Permissive and Specificity-Switching Mutations in the ParB/Noc Protein Family. Cell Rep. **32**, 107928.
10. Kaessmann, H. (2010). Origins, evolution, and phenotypic impact of new genes. Genome Res. **20**, 1313–1326.
11. Lagage, V., Boccard, F., and Vallet-Gely, I. (2016). Regional Control of Chromosome Segregation in Pseudomonas aeruginosa. PLoS Genet. **12**, e1006428.
12. Leonard, T.A., Butler, P.J.G., and Löwe, J. (2004). Structural analysis of the chromosome segragation protein Spo0J from Thermus thermophilus. Mol. Microbiol. **53**, 419–432.

13. Lin, D.C.H., and Grossman, A.D. (1998). Identification and characterization of a bacterial chromosome partitioning site. Cell. **92**, 675–685.
14. Livny, J., Yamaichi, Y., and Waldor, M.K. (2007). Distribution of centromere-like parS sites in bacteria: Insights from comparative genomics. J. Bacteriol. **189**, 8693–8703.
15. Luscombe, N.M., Laskowski, R.A., and Thornton, J.M. (2001). Amino acid-base interactions: A three-dimensional analysis of protein-DNA interactions at an atomic level. Nucleic Acids Res. **29**, 2860–2874
16. Lynch, M., and Conery, J.S. (2000). The evolutionary fate and consequences of duplicate genes. Science. **290**, 1151–1155.
17. McKeown, A.N., Bridgham, J.T., Anderson, D.W., Murphy, M.N., Ortlund, E.A., and Thornton, J.W. (2014). Evolution of DNA specificity in a transcription factor family produced a new gene regulatory module. Cell. **159**, 58–68.
18. Mikheil, D.M., Shippy, D.C., Eakley, N.M., Okwumabua, O.E., and Fadl, A.A. (2012). Deletion of gene encoding methyltransferase (gidB) confers high-level antimicrobial resistance in Salmonella. J. Antibiot. **65**, 185–192
19. Mohl, D.A., and Gober, J.W. (1997). Cell cycle-dependent polar localization of chromosome partitioning proteins in Caulobacter crescentus. Cell. **88**, 675–684.
20. Pang, T., Wang, X., Lim, H.C., Bernhardt, T.G., and Rudner, D.Z. (2017). The nucleoid occlusion factor Noc controls DNA replication initiation in Staphylococcus aureus. PLoS Genet. **13**, e1006908.
21. Qian, W., and Zhang, J. (2014). Genomic evidence for adaptation by gene duplication. Genome Res. **24**, 1356–1362.
22. Sievers, J., Raether, B., Perego, M., and Errington, J. (2002). Characterization of the parB-like yyaA gene of Bacillus subtilis. J. Bacteriol. **184**, 1102–1111.
23. Sikosek, T., and Chan, H.S. (2014). Biophysics of protein evolution and evolutionary protein biophysics. J. R. Soc. Interface. **11**, 20140419.
24. Starr, T.N., and Thornton, J.W. (2016). Epistasis in protein evolution. Protein Sci. **25**, 1204–1218.
25. Teichmann, S.A., and Babu, M.M. (2004). Gene regulatory network growth by duplication. Nat. Genet. **36**, 492–496
26. Toro, E., Hong, S.H., McAdams, H.H., and Shapiro, L. (2008). Caulobacter requires a dedicated mechanism to initiate chromosome segregation. Proc. Natl. Acad. Sci. U. S. A. **105**, 15435–15440.
27. Tran, N.T., Laub, M.T., and Le, T.B.K. (2017). SMC Progressively Aligns Chromosomal Arms in Caulobacter crescentus but Is Antagonized by Convergent Transcription. Cell Rep. **20**, 2057–2071.
28. Tran, N.T., Stevenson, C.E., Som, N.F., Thanapipatsiri, A., Jalal, A.S.B., and Le,

T.B.K. (2018). Permissive zones for the centromere-binding protein ParB on the Caulobacter crescentuschromosome. Nucleic Acids Res. **46**, 1196–1209

29. Wang, X., Minasov, G., and Shoichet, B.K. (2002). Evolution of an antibiotic resistance enzyme constrained by stability and activity trade-offs. J. Mol. Biol. **320**, 85–95.
30. Wu, L.J., and Errington, J. (2004). Coordination of cell division and chromosome segregation by a nucleoid occlusion protein in Bacillus subtilis. Cell. **117**, 915–925.
31. Wu, L.J., and Errington, J. (2012). Nucleoid occlusion and bacterial cell division. Nat. Rev. Microbiol. **10**, 8–12.
32. Wu, L.J., Ishikawa, S., Kawai, Y., Oshima, T., Ogasawara, N., and Errington, J. (2009). Noc protein binds to specific DNA sequences to coordinate cell division with chromosome segregation. EMBO J. **28**, 1940–1952.

Chapter 4: A CTP-dependent gating mechanism enables ParB spreading on DNA

Parts of this chapter have been deposited in BioRxiv, for which I performed most of the experiments and wrote the first draft of the manuscript:

Jalal, A.S., Pastrana, C.L., Tran, N.T., Stevenson, C.E., Lawson, D.M., Moreno-Herrero, F., and Le, T.B.. (2019). Structural and biochemical analyses of Caulobacter crescentus ParB reveal the role of its N-terminal domain in chromosome segregation. BioRxiv. 816959.

Additionally, other data I present here have also been published in two papers in eLife:

Jalal, A.S., Tran, N.T., and Le, T.B. (2020a). ParB spreading on DNA requires cytidine triphosphate in vitro. Elife. **9**, e53515.

Jalal, A.S., Tran, N.T., Stevenson, C.E.M., Chimthanawala, A., Badrinarayanan, A., Lawson, D. M., and Le, T.B. (2021). A CTP-dependent gating mechanism enables ParB spreading on DNA in Caulobacter crescentus. Elife. **10**, e69676.

4.1 Introduction

4.2 Crystallisation of the C-terminal truncated (∆CTD) *C. crescentus* ParB-*parS* complex

4.3 The crystal structure of *C. crescentus* ParB∆CTD in complex with *parS*

4.4 Structural comparison reveals the flexibility at the NTD of ParB

4.5 *parS* DNA increases the CTP-binding and hydrolysis rate of *C. crescentus* ParB

4.6 CTP reduces the nucleation of *C. crescentus* ParB on *parS*

4.7 CTP facilitates ParB association with a closed DNA substrate beyond nucleation

4.8 A closed DNA substrate is required for an increased ParB association with DNA

4.9 The crystal structure of *C. crescentus* ParBΔCTD in complex with the slow hydrolysable CTP analogue, CTPɣS

4.10 The CTP-binding pocket (C-pocket) of *C. crescentus* ParB

4.11 Conformational changes between the nucleating and spreading state of *C. crescentus* ParB

4.12 The crystal structure of the *C. crescentus* ParBΔ44NΔCTD in complex with CDP

4.13 Discussion

4.14 References

4.1 Introduction

Proper chromosome segregation is essential in all domains of life. In most bacterial species, faithful chromosome segregation is mediated by the tripartite ParA-ParB-*parS* system (Donczew et al., 2016; Fogel and Waldor, 2006; Harms et al., 2013; Ireton et al., 1994; Jakimowicz et al., 2002; Jalal and Le, 2020; Kawalek et al., 2018; Lin and Grossman, 1998; Mohl et al., 2001; Tran et al., 2018). The centromere *parS* is the first DNA locus to be segregated following chromosome replication (Lagage et al., 2016; Lin and Grossman, 1998; Livny et al., 2007; Toro et al., 2008). ParB nucleates on *parS* before associating with adjacent non-specific DNA, in a process known as spreading, to form a higher-order nucleoprotein complex (Breier and Grossman, 2007; Broedersz et al., 2014; Graham et al., 2014; Jalal and Le, 2020; Murray et al., 2006; Sanchez et al., 2015; Taylor et al., 2015). The ParB-DNA nucleoprotein complex stimulates the ATPase activity of ParA, driving the movement of the *parS* locus (and subsequently, the whole chromosome) to the opposite pole of the cell (Hwang et al., 2013; Leonard et al., 2005; Lim et al., 2014; Vecchiarelli et al., 2012, 2014). This nucleoprotein complex recruits SMC to disentangle and organize replicated DNA (Böhm et al., 2020; Gruber and Errington, 2009; Tran et al., 2017; Wang et al., 2017).

The assembly of the ParB-*parS* nucleoprotein complex is a crucial event; bacterial cells harbouring a nucleation-competent but spreading-defective *parB* allele are impaired in plasmid/chromosome segregation (Breier and Grossman, 2007; Murray et al., 2006; Song et al., 2017). Spreading was first discovered for the P1 plasmid-encoded ParB protein (Rodionov et al., 1999), and was subsequently found to be a general feature of many plasmid and chromosomal ParB proteins in bacteria (Breier and Grossman, 2007; Chen et al., 2015; Kusiak et al., 2011; Murray et al., 2006; Song et al., 2017; Tran et al., 2018) In addition to a linear spreading on DNA, *Bacillus subtilis* ParB can also bridge distal DNA together to coalesce into a large nucleoprotein network in a process known as “spreading and bridging” (Fisher et al., 2017; Graham et al., 2014; Madariaga-Marcos et al., 2019; Song et al., 2017; Taylor et al., 2015). While a broadly similar “nucleation and caging” mechanism was also proposed to explain the ability of an F1-plasmid ParB and *Vibrio cholerae* chromosomal ParB to form a large nucleoprotein network (Debaugny et al., 2018; Sanchez et al., 2015). In this model, the nucleation of ParB on *parS* creates a high local concentration of ParB, thereby caging ParB molecules together with non-specific DNA surrounding *parS* to create a loose but fluid protein-DNA network (Debaugny et al., 2018; Sanchez et al., 2015).

Chromosomal ParB protein consists of an N-terminal domain (NTD), a central *parS*-specific DNA-binding domain (DBD), and a C-terminal domain (CTD) (Fig. 4.1A). Previously the structure of a CTD-truncated (ΔCTD) *Helicobacter pylori* ParB with *parS* provided a possible

structural basis for spreading. In this structure, four *H. pylori* ParBΔCTD monomers bind to four individual half *parS* sites and tetramerize to bring distal DNA closer together (Fig. 1.2, Chapter 1) (Chen et al., 2015). In comparison to the structure of an apo-ParBΔCTD from *Thermus thermophilus*, the NTD of *H. pylori* ParBΔCTD adopts an alternative conformation to position the highly conserved arginine-rich patch (GERRxR, Fig. 4.1) outwards to mediate ParB-ParB oligomerization (Chen et al., 2015; Leonard et al., 2004). Based on this pairwise structural comparison, Chen et al., (2015) proposed that the nucleation on *parS* induces a transition (at the NTD of ParB) from a spreading-incompetent closed conformation to a spreading-competent open conformation (Chen et al., 2015; Leonard et al., 2004). While more recent works by Soh et al., (2019) and Osorio-Valeriano et al., (2019) on *Bacillus subtilis* and *Myxococcus xanthus* ParB, respectively, showed that ParB binds and hydrolyses cytidine triphosphate (CTP) to cytidine diphosphate (CDP), and that CTP modulates the binding affinity of ParB to *parS* (Osorio-Valeriano et al., 2019; Soh et al., 2019). Co-crystal structures of a *B. subtilis* ParB (ParBΔCTD) with CDP and an N-terminal domain truncated (ΔNTD) *Myxococcus xanthus* PadC (PadCΔNTD) with CTP showed nucleotides sandwiching between the two opposite subunits, thus promoting their self-dimerization (Osorio-Valeriano et al., 2019; Soh et al., 2019). The self-dimerization at the N-terminal domain (NTD) of *B. subtilis* ParB creates a clamp-like molecule that enables DNA entrapment (Soh et al., 2019). Additionally, ParB can hydrolyse CTP to CDP and inorganic phosphate, however hydrolysis is not required for spreading since ParB in complex with a slow-hydrolysable CTP analogue (CTPγS) can still self-load on the DNA (Soh et al., 2019). Also, *M. xanthus* PadC, a ParB-like protein, does not possess noticeable CTPase activity (Osorio-Valeriano et al., 2019). Overall, the role of CTP hydrolysis in bacterial chromosome segregation is not yet clear.

Here, we demonstrate that CTP facilitates ParB escape from the *parS* site and promotes the accumulation of ParB on a closed DNA substrate. Furthermore, I report the co-crystal structures of a C-terminal domain truncated *C. crescentus* ParB in complex with either *parS* or CTPγS to better understand the roles of CTP binding and hydrolysis. Consistent with a previous finding (Soh et al., 2019), the NTDs of *C. crescentus* ParB also self-dimerize upon binding to nucleotides, thus closing a molecular gate at this domain (the NTD gate). Furthermore, the two opposite DNA-binding domains (DBD) move closer together to close a second molecular gate (the DNA-gate). Collectively, I suggest a CTP-operated gating mechanism that regulates ParB nucleation and spreading in *C. crescentus*.

4.2 Crystallisation of the *C. crescentus* ParB(ΔCTD)-*parS* complex

Chromatin immunoprecipitation coupled to deep sequencing (ChIP-seq) approaches have demonstrated that *C. crescentus* ParB binds to the non-specific DNA flanking the *parS* sites

to spread on the chromosome (Tran et al., 2018). Thus, to elucidate the structural basis of ParB spreading, I first sought to determine a co-crystal structure of the ParB-*parS* complex from *C. crescentus.* ParB proteins generally compose of three different domains, each of which are connected by flexible linkers (Fig. 4.1A). This often results in a flexibility in the organization of the domain orientation which could impair the protein from forming an orderly-packaged crystals. To reduce the flexibility of the ParB protein, I generated a shorter ParB variant by truncating the CTD (50 amino acids) (Fig. 4.1B). The C-terminal region of ParB has the weakest homology to ParB homologues from different bacterial species (Figure 4.2). Indeed, the crystal structures of apo-ParB from *T. thermophilus* and ParB-*parS* from *H. pylori* were both solved by using the ΔCTD proteins (Chen et al., 2015; Leonard et al., 2004). While the CTD of *B. subtilis* ParB was found to interact with DNA non-specifically due to a series of lysine residues in this domain (Fisher et al., 2017; Madariaga-Marcos et al., 2019), the equivalent residues are not found in *C. crescentus* ParB. Thus, I hypothesised that the *C. crescentus* CTD may not bind DNA and solely function as a dimerization interface (see Chapter 5).

To generate a C-terminal truncated (ΔCTD) variant of ParB, the *parB* gene from *C. crescentus* encoding residues 1–244 of 291 amino acids found in the full-length proteins were cloned, overexpressed, and the protein was purified (see Chapter 2) (Fig 4.1B). To verify whether the ParBΔCTD variant retains *parS* binding ability *in vitro*, I performed a quantitative DNA binding assay using bio-layer interference (BLI). In brief, a linear 20 bp biotinylated *parS* or scrambled-*parS* containing DNA was attached to a streptavidin-coated probe to measure by BLI. BLI assay monitors wavelength shifts (responses) resulting from changes in the optical thickness of the probe surface during association or dissociation of the analyte (see Chapter 2). Observed protein-DNA interactions were recorded as BLI-responses (nm), and three different concentrations of protein (1000 nm, 500nm, 250nm) of ParB (WT) and ParBΔCTD were used. As previously observed in Chapter 3, at 150 mM NaCl, no binding between ParB (WT) and ParBΔCTD was observed with the scrambled- *parS* containing DNA (Fig 4.1C) (Tran et al., 2018). Indeed, BLI-analysis confirmed that ParBΔCTD retains its *parS* binding ability *in vitro*, albeit much weaker than the full-length ParB protein (Fig 4.1D). After conducting crystal trials with either the full-length or ParBΔCTD and several different length of *parS* DNA duplexes, I obtained crystals of a ParBΔCTD in complex with a 22-bp *parS* duplex DNA. Diffraction data for the *C. crescentus* ParBΔCTD-*parS* co-crystal was collected to a resolution of 2.9 Å, and the phase was solved by molecular replacement using the 3.1 Å structure of the *H. pylori* ParBΔCTD-*parS* complex and the 2.3 Å structure of apo-*T. thermophilus* ParBΔCTD as search templates (Chen et al., 2015; Leonard et al., 2004). The X-ray crystallographic data are summarised in Table 4.1.

A

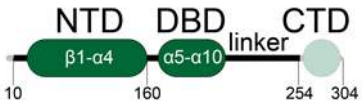
NTD
DBD
CTD
linker
β1-α4
α5-α10
10
160
254
304

B

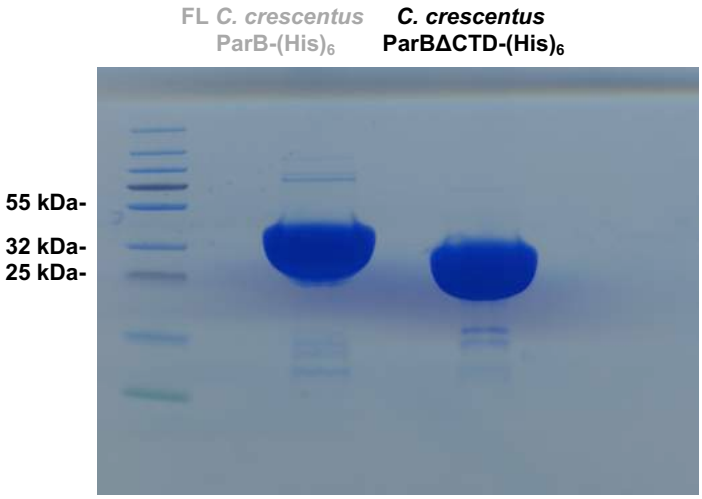
FL C. crescentus ParB-(His)6
C. crescentus ParBΔCTD-(His)6
55 kDa-
32 kDa-
25 kDa-

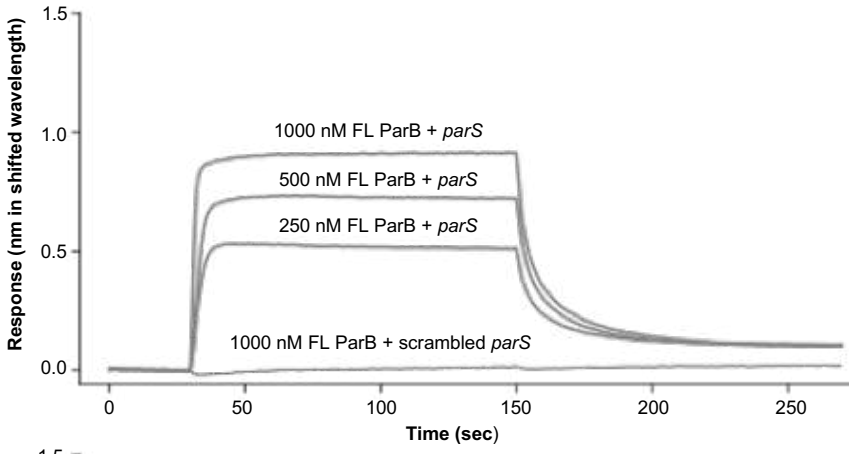
Response (nm in shifted wavelength)
1.5
1.0
0.5
0.0
1000 nM FL ParB + parS
500 nM FL ParB + parS
250 nM FL ParB + parS
1000 nM FL ParB + scrambled parS
0
50
100
150
200
250
Time (sec)

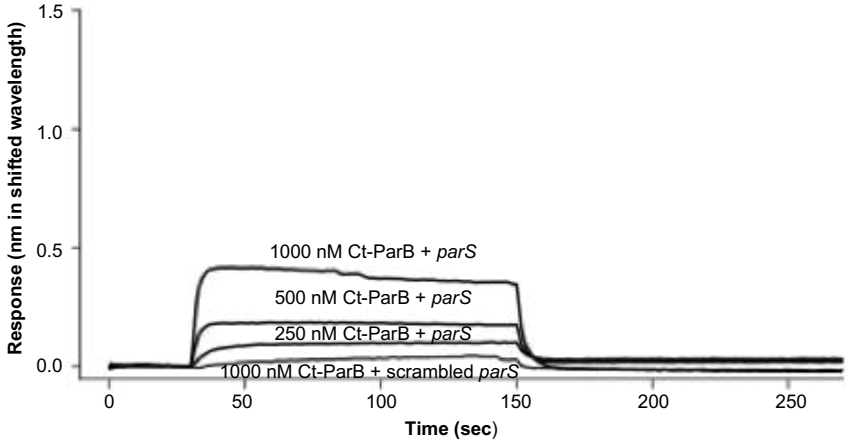
Response (nm in shifted wavelength)
1.5
1.0
0.5
0.0
1000 nM Ct-ParB + parS
500 nM Ct-ParB + parS
250 nM Ct-ParB + parS
1000 nM Ct-ParB + scrambled parS
0
50
100
150
200
250
Time (sec)

Figure 4.1 Purified *C. crescentus* Par B variants and their parS DN A-binding activities. **(A)** The domain architecture of *C. crescentus* ParB: the N-terminal domain (NTD, dark green), the central DNA-binding domain (DBD, dark green), the C-terminal domain (CTD, faded green), and a linker that connects the DBD and the CTD together. The ParBΔCTD variant that was used for Crystallisation lacks the CTD (faded green). **(B)** Full-length *C. crescentus* ParB and the C-terminally truncated variant (ParBΔCTD) were expressed in E. coli and purified to near homogeneity. All variants were C-terminally His-tagged (KLAAALEHHHHHH). **(C)** ParBΔCTD retains its ability to bind parS DNA, albeit weaker than a full-length protein. Bio-layer interferometric analysis of the interaction between a full-length *C. crescentus* ParB (grey) or a C-terminally truncated ParBΔCTD (black) and a 20-bp parS-containing duplex DNA or the scrambled parS DNA. Sensors loaded with biotinylated parS DNA were probed with 5000 nM, 1000 nM, and 500 nM dimer concentrations of proteins. The interaction kinetics were followed by monitoring the wavelength shifts (response unit, nm) resulting from changes in the optical thickness of the sensor surface during association or dissociation of the proteins.

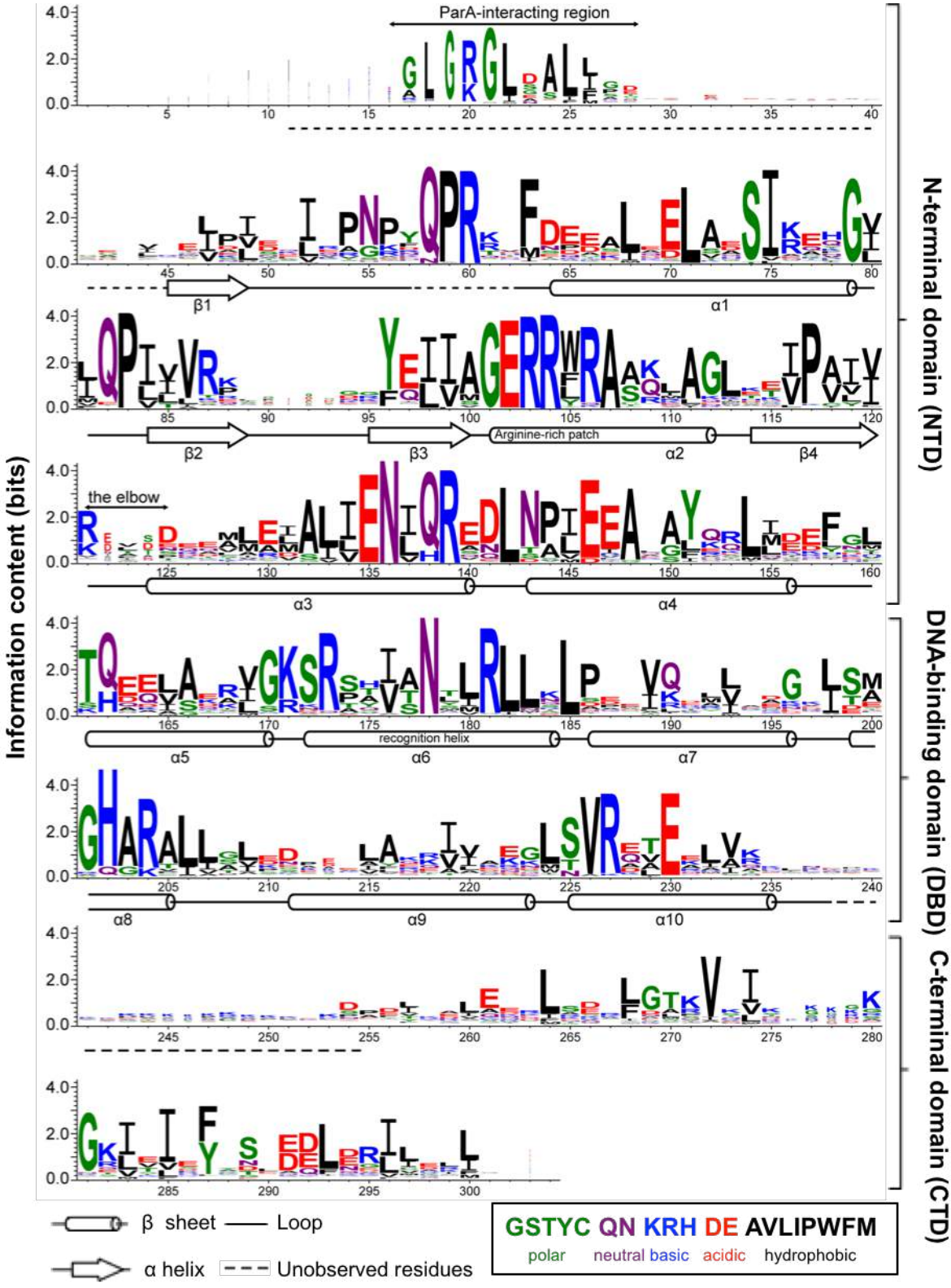
ParA-interacting region
Information content (bits)
N-terminal domain (NTD)
DNA-binding domain (DBD)
C-terminal domain (CTD)
β1
α1
β2
β3
Arginine-rich patch
α2
β4
the elbow
α3
α4
α5
recognition helix
α6
α7
α8
α9
α10
β sheet
Loop
α helix
Unobserved residues
GSTYC QN KRH DE AVLIPWFM
polar
neutral basic
acidic
hydrophobic

Figure 4.2 Sequence alignment of the chromosomal ParB superfamily. An alignment of ~1800 chromosomal ParB proteins was constructed and presented as a sequence logo. The height of the stack indicates the sequence conservation, while the height of symbols within the stack indicates the relative frequency of each amino acid residue at that position. Amino acids are coloured based on their chemical properties. Secondary-structure elements for *C. crescentus* ParBΔCTD are shown below the alignment. Dashed lines indicate unmodeled residues due to poor electron density in the *C. crescentus* ParBΔCTD-*parS* co-crystal structure.

4.3 The crystal structure of *C. crecentus* ParBΔCTD in complex with *parS*

The asymmetric unit of the crystal contained four copies of the ParB monomer (Chain A-D) (two dimers) and two copies of the *parS* DNA (Fig 4.3A-B). Each ParBΔCTD binds to a half *parS* site but there is no protein-protein contact between the two adjacent subunits (Fig 4.4A). The bases at the end of the *parS* site stack and interact to form the pseudo-continuos filament that runs through the crystal. The overall structure of the ParBΔCTD-*parS* complex is shown in Figure 4.4, with the ParBΔCTD variant containing both the NTD and the DBD (Fig 4.4A-B). The secondary structure of the ParBΔCTD-*parS* is composed of 10 α-helix and 4 β-pleated sheets that span residues 45-48 (β1), 65-73 (α1), 84-88 (β2), 96-100 (β3), 102-111 (α2), 114-120 (β4), 125-138 (α3), 144-158 (α4), 162-169 (α5), 173-184 (α6), 187-195 (α7), 200-206 (α8), 212-222 (α9) and 226-235 (α10) (Fig. 4.4B). The NTD contains helixes α1 to α2 and pleated-sheets β1 to β4, while the last eight helices (α3- α10) make up the DBD of ParB (Fig. 4.4B). I noticed similar interactions between ParB and *parS* as previously observed in the *C. crescentus* ParB (DBD)-*parS* co-crystal structure (Chapter 3) (Jalal et al., 2020b). Since both chain A and chain B in the asymmetric unit are almost identical to chain C and chain D, I decided to use chain C-D-*parS* for subsequent structural analysis (Fig. 4.3A).

From the co-crystal structure, I noticed that helices α3 and α4 of the NTD are packed against the DBD. A flexible loop found between α3 and β4 (V120-L123) connects the rest of the NTD to the DBD. The highly conserved arginine-rich motif (GERRxR), crucial for *C. crescentus* ParB spreading, resides on helix α2. By superimposing different chains found in the co-crystal structure, I observe that while the DBD and the NTD α3-α4 are almost identical between chain C and D (RMSD=0.19 Å), the rest of the NTD (α1-β4) adopts completely different arrangement (Fig 4.4C) (Tran et al., 2018). The NTD (α1-β4) of chain C and D are oriented ~80^{o} apart from each other (Fig. 4.4C); this is due to a loop (V120-L123) (flexible elbow) connecting α3 and β4 together (Fig. 4.4C-D). The role of this elbow in orientating the NTD became clearer upon comparing the *C. crescentus* ParBΔCTD-*parS* structure to two other available structures of chromosomal ParBs from *H. pylori* and *T. thermophilus*.

4.4 Structural comparison reveals the flexibility of the NTD of ParB

In the co-crystal structure of the *H. pylori* ParBΔCTD-*parS* complex, ParB adopts a different conformation in which its NTD projects outwards and contacts a nearby ParB monomer in the adjacent asymmetric unit (Chen et al., 2015) (Fig. 4.5A). In contrast, I was unable to observe any such interaction between the NTD of the two adjacent *C. crescentus* ParB monomers (Fig. 4.5A). By superimposing the structure of *H. pylori* ParBΔCTD onto the *C. crescentus*

A

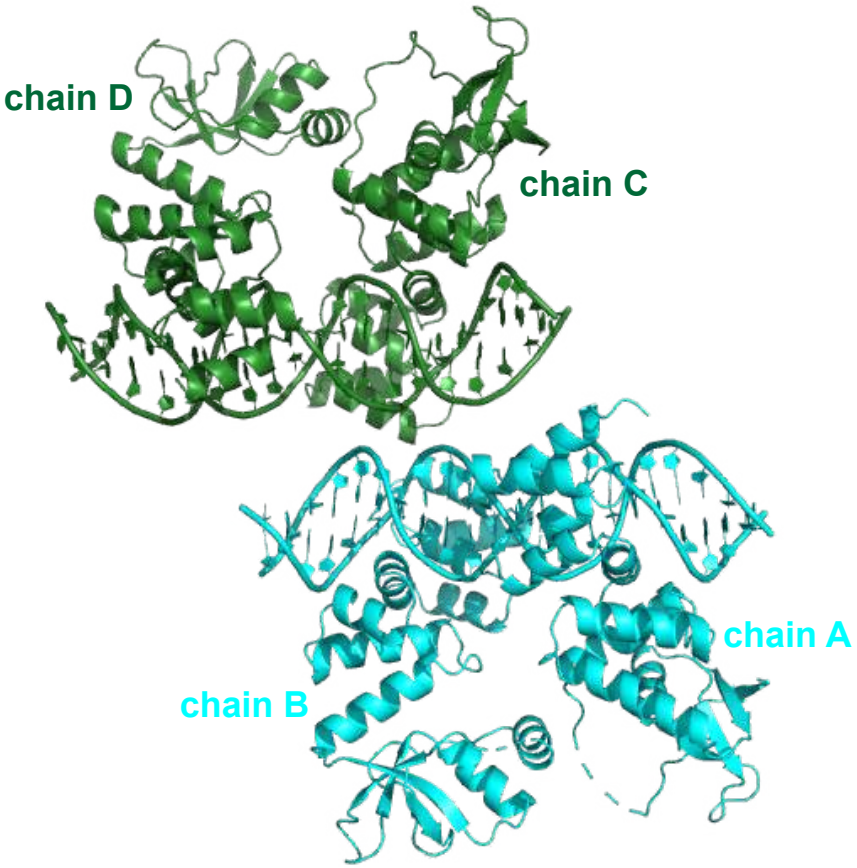

B

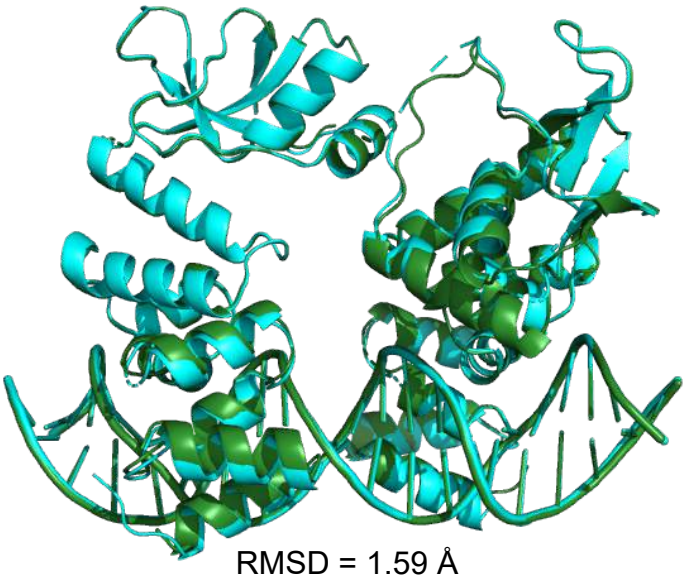

RMSD = 1.59 Å

C. crescentus ParBΔCTD-*parS* chain C/D
C. crescentus ParBΔCTD-*parS* chain A/B

Figure 4.3 Composition of the asymmetric unit of the co-crystal *C. crescentus* Ct-ParB-*parS* structure. (A) The asymmetric unit consists of four copies of the *C. crescentus* ParBΔCTD (chain A, B, C and D) and two copies of the 22 bp full size *parS* DNA. **(B)** Superimposition of chains A (cyan) and B (light grey) onto chains C (green) and D (dark grey) displayed the near identical orientation of the two complexes in the asymmetric unit.

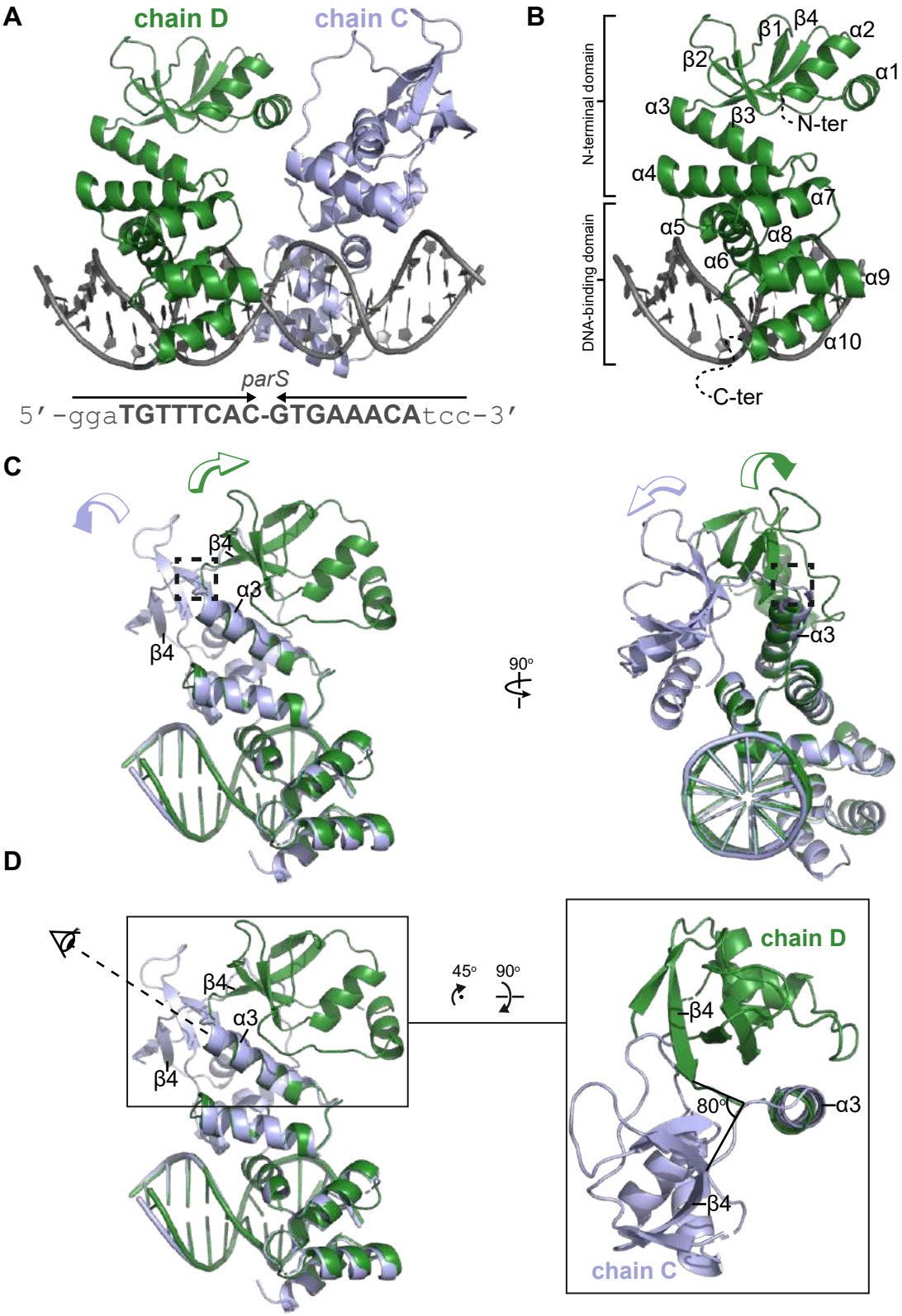
A
chain D
chain C
parS
5′-ggaTGTTTCAC-GTGAAACAtcc-3′
B
N-terminal domain
DNA-binding domain
β1
β4
α2
β2
α1
α3
β3
N-ter
α4
α7
α5
α8
α6
α9
α10
C-ter
C
β4
α3
β4
90°
α3
D
β4
α3
β4
45°
90°
chain D
β4
80°
α3
β4
chain C

Figure 4.4 Co-crystal structure of a C-terminal domain truncated ParBΔCTD-*parS* complex from *Caulobacter crescentus* revealed the multiple conformations of the N-terminal domain. (A) Co-crystal structure of two *C. crescentus* ParBΔCTD monomers (dark green and light blue) bound on a 22-bp *parS* DNA. The nucleotide sequence of the 22-bp *parS* is shown below the co-crystal structure, the core *parS* sequence is highlighted in bold. **(B)** The structure of ParBΔCTD chain D bound to a *parS* half site with key features highlighted. **(C)** Superimposition of *C. crescentus* ParBΔCTD chain C and D (light blue and dark green, respectively) shows two different orientations of the NTD (α1-β4). The arrow above each chain shows the direction each NTD projects towards. The dashed box shows the flexible loop (elbow) that connects helix α3 and sheet β4 together. **(D)** A top-down view of the superimposition of chain C and D shows that the NTD (α1-β4) of chain C and D are oriented ~80^{o} apart from each other.

ParBΔCTD structure, I observed that each NTD is orientated differently (Fig. 4.5B, Fig. 4.6A-B). In the *H. pylori* ParB-*parS* co-crystal structure, the NTD extends outwards (in an extended conformation), while the *C. crescentus* ParB points either inwards (chain D) or side-ways (chain C) (Fig 4.5A-C).

By superimposing all three chains, I noted that the elbow (V120-L123) swivels around the α3 axis, hence permitting the NTD to adopt three distinct conformations (Fig. 4.5B). Sequence alignment of ~1800 ParB orthologs displayed an enrichment for charged and polar uncharged residues in the elbow region (Fig. 4.5B). This amino acid preference is typically found in intrinsically disordered proteins and may confer flexibility to the elbow connecting α3 and β4 together (Romero et al., 2001; Vucetic et al., 2003). A subsequent structure superimposition and showed that the NTD of an apo-*T. thermophilus* ParBΔCTD also adopts a similar open conformation, to chain D in the *C. crescentus* ParBΔCTD-*parS* co-crystal structure (Fig. 4.5C). Next, I observed a second level of flexibility of the N-terminal most peptide (residues 1-64) of ParB. This amino acid region is extended in the *T. thermophilus* ParBΔCTD structure (pink dashed line, Fig 4.5C), however in the *C. crescentus* ParBΔCTD this region folds back to contribute the fourth strand to the core β-sheet at the NTD (green dashed line, Fig. 4.5C). Interestingly, the equivalent region was not observed in the *H. pylori* ParBΔCTD co-crystal structure. Due to the alternate conformations of this N-terminal region and of the NTD as a whole, the ParA-interacting region (residues 1-30, Fig. 1 and Fig. 4.5), it is likely that this region can potentially explore a very large space surrounding ParB.

Altogether, by performing a three-way structural comparison, I suggest that the NTD of ParB can adopt multiple alternate conformations regardless whether ParB is in complex with *parS*. Our finding contrasts previous observations made by Chen et al., (2015), as my *C. crescentus* ParBΔCTD-*parS* co-crystal structure demonstrated that nucleation to *parS* alone is not sufficient enough to induce a transition (at the NTD) from a spreading-incompetent to a spreading-competent state. Indeed while ParB spreading has been observed in various bacterial species *in vivo*, (Breier and Grossman, 2007; Graham et al., 2014; Lagage et al., 2016; Murray et al., 2006; Rodionov et al., 1999; Tran et al., 2018) *parS*-dependent ParB spreading has resisted biochemical reconstitutions (in agreement with my *C. crescentus* ParBΔCTD-*parS* structure) (Fisher et al., 2017; Graham et al., 2014; Madariaga-Marcos et al., 2019; Taylor et al., 2015). These unsuccessful attempts at reconstituting ParB spreading *in vitro* suggests that additional factors may be missing. In the next section, I further expand on the co-factor required for ParB spreading *in vitro*.

4.5 *parS* DNA increases the CTP binding and hydrolysis rate of *C. crescentus* ParB

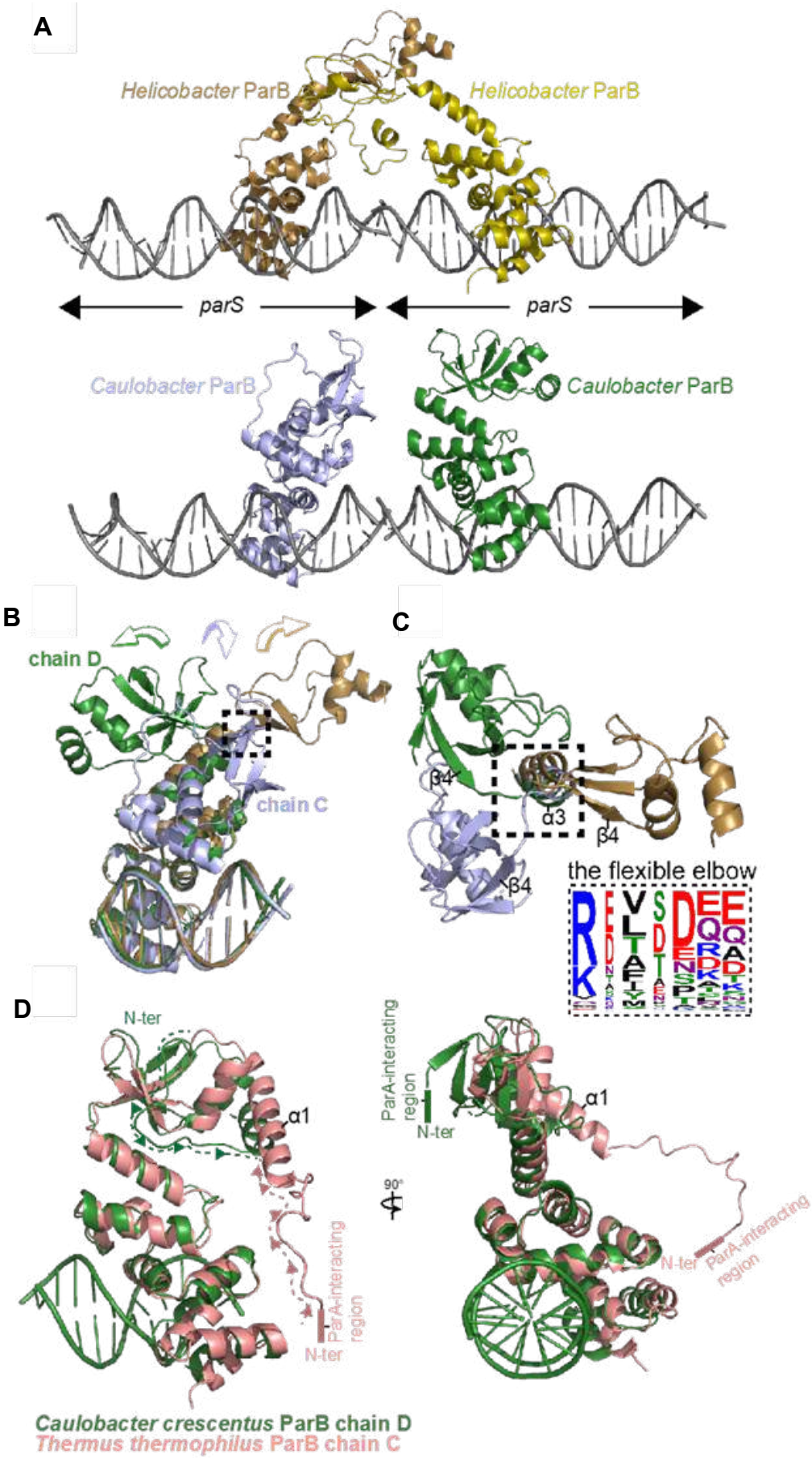
A
Helicobacter ParB
Helicobacter ParB
parS
parS
Caulobacter ParB
Caulobacter ParB
B
chain D
chain C
C
β4
α3
β4
β4
the flexible elbow
D
N-ter
α1
ParA-interacting region
N-ter
ParA-interacting region
α1
N-ter
N-ter
ParA-interacting region
Caulobacter crescentus ParB chain D
Thermus thermophilus ParB chain C

Figure 4.5 Structural comparisons of the *C. crescentus* ParBΔCTD-*parS* complex to other ParB family members. (A) Structures of two adjacent symmetry complexes of *H. pylori* (upper panel) and *C. crescentus* ParBΔCTD -*parS* (lower panel). In the *H. pylori* ParBΔCTD-*parS* complex, ParB adopts an open conformation in which its NTD projects outwards to contact a neighbouring monomer. However, no such interaction was seen between the NTD of the two adjacent *C. crescentus* ParB monomers. **(B)** A side-view of the superimposition between *C. crescentus* ParBΔCTD chain C (light blue), chain D (dark green), and *H. pylori* ParBΔCTD (golden) shows the three distinct orientations of the NTD (see also Fig. 4.6). **(C)** A top view of the superimposition between *C. crescentus* ParBΔCTD chain C, chain D, and *H. pylori* ParBΔCTD. The dashed box shows the flexible loop (elbow) that connects helix α3 and sheet β4 together. The conservation of amino acids at the flexible elbow is presented as sequence logos. Amino acids are coloured based on their chemical properties (GSTYC: polar; QN: neutral; KRH: basic; DE: acidic; and AVLIPWFM: hydrophobic). **(D)** Superimposition of *C. crescentus* ParBΔCTD chain D (dark green) and *T. thermophilus* ParBΔCTD chain C (pink) shows the two different conformations of the N-terminal-most peptide (dashed dark green and pink lines).

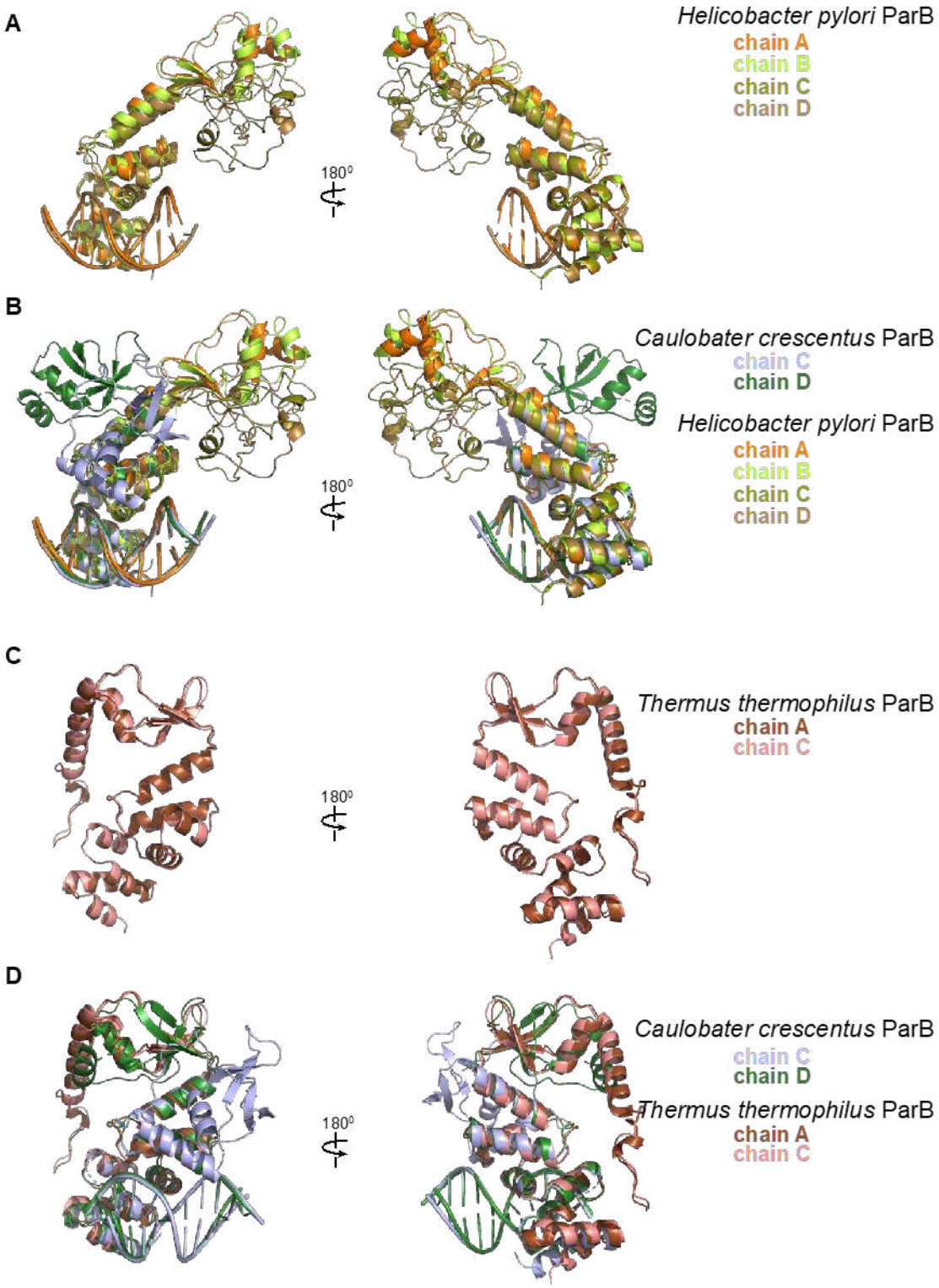

Figure 4.6 Structural comparisons of the *C. crescentus* ParB-*parS* complex to other ParB family members. Superposition of all crystallographic independent subunits from **(A)** *H. pylori* ParB-*parS*; **(B)** *H. pylori* ParB-*parS* and chain C and D of *C. crescentus* Ct-ParB-*parS*; **(C)** *T. thermophilus* apo-ParBΔCTD; **(D)** *T. thermophilus* Ct-ParBΔCTD and chain C and D of *C. crescentus* ParBΔCTD-*parS*. Superimposition was based on the DNA-binding domain and helices α3-α4 of the N-terminal domain.

More recent studies have demonstrated that *B. subtilis* ParB and *M. xanthus* PadC are members of a new CTPase protein family that bind and hydrolyse cytidine triphosphate (CTP) to cytidine diphosphate (CDP) (Osorio-Valeriano et al., 2019; Soh et al., 2019). By employing a membrane-spotting assay (DRaCALA), we showed that *C. crescentus* ParB binds to radiolabelled CTP in the presence of *parS* DNA (Fig. 4.7A). An excess of unlabelled CTP, but no other NTPs, could compete with radioactive CTP for binding to *C. crescentus* ParB, suggesting that *C. crescentus* ParB does not bind other NTPs (Fig. 4.7B). The CTP binding of ParB was reduced when a non-cognate DNA site (*NBS*) (Wu et al., 2009) was used instead of *parS*. We also failed to detect CTP binding in our DRaCALA assay or by isothermal titration calorimetry when DNA was omitted. Nevertheless, we robustly detected CTP hydrolysis to CDP and inorganic phosphate when *C. crescentus* ParB and CTP were included, albeit at a very low rate of ~0.4 CTP molecules per ParB per hour (Fig. 4.7C). A background level of inorganic phosphate was observed when *C. crescentus* ParB was incubated with ATP, GTP, or UTP (Fig. 4.7C). Crucially, the addition of a 22-bp *parS* DNA, but not a non-cognate 22-bp *NBS* DNA, increased CTP turnover rate sevenfold to ~3 CTP molecules per ParB per hour (Fig. 4.7C). Lastly, the CTP hydrolysis was reduced to the background in the nucleation-competent but spreading-defective ParB (R104A) variant (Fig. 4.7C). Altogether, our data suggest that *parS* DNA stimulates *C. crescentus* ParB to bind and hydrolyse CTP. Next we sought to determine whether CTP influence the nucleation of ParB to *parS*.

4.6 CTP reduces the nucleation of *C. crescentus* ParB on *parS*

To determine if CTP or other NTP alone affects ParB-*parS* interaction, we attached a linear 20-bp biotinylated *parS* DNA to a streptavidin-coated probe to measure the bio-layer interference (BLI). We monitored in real-time interactions between immobilized *parS* DNA and purified *C. crescentus* ParB or a premix of ParB + NTP (Fig. 4.8A). Consistent with previous reports (Figge et al., 2003; Tran et al., 2018), *C. crescentus* ParB bound site-specifically to *parS* (Fig. 4.8B). In the presence of ATP, GTP, or UTP, we observed a small reduction in ParB-*parS* binding at steady state regardless of whether Mg^{2+} was included in binding buffer or not (Fig. 4.8B-C), suggesting that *C. crescentus* ParB is slightly sensitive to highly negatively charged compounds or possibly to counter-ions (Na^{+}) in NTP solutions. However, we noted that CTP had a pronounced effect on ParB-*parS* interaction, specifically in the presence of Mg^{2+} (Fig. 4.8B-C). An increasing concentration of CTP (but not CMP or CDP) gradually reduced the binding of ParB to *parS* (Fig 4.8D-E). On closer inspection, we noted that ParB + CTP slowly dissociated from *parS* even before the probe was returned to a protein-free buffer (a gradual downward slope between 30^{th} and 150^{th} sec, Fig. 4.8A), suggesting that CTP facilitated ParB removal from a 20-bp *parS* DNA. To investigate further, we monitored the dissociation rates of pre-bound CTP-free ParB-*parS* complexes after probes were returned

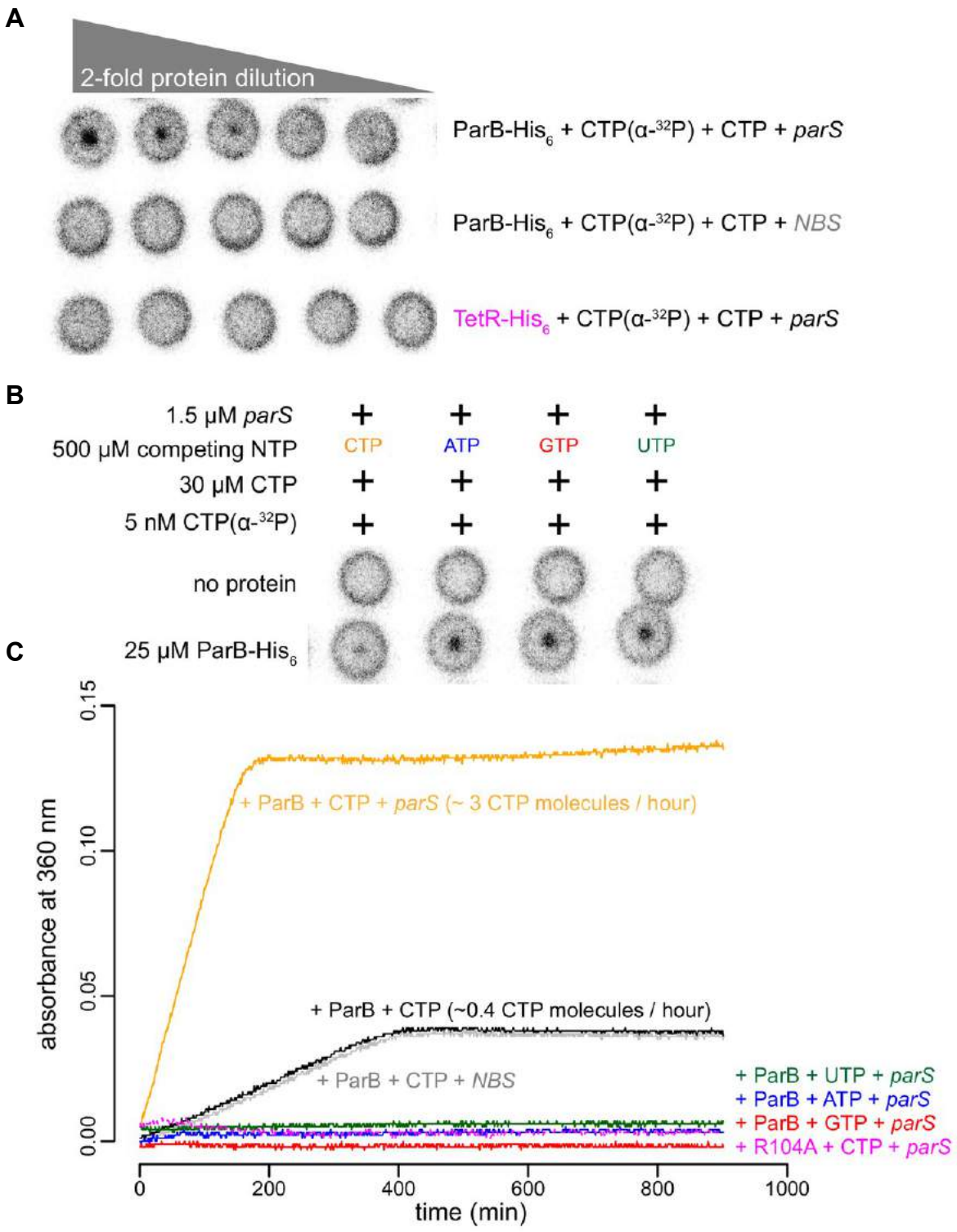
A
2-fold protein dilution
ParB-His6 + CTP(α-32P) + CTP + parS
ParB-His6 + CTP(α-32P) + CTP + NBS
TetR-His6 + CTP(α-32P) + CTP + parS
B
1.5 µM parS
500 µM competing NTP
CTP
ATP
GTP
UTP
30 µM CTP
5 nM CTP(α-32P)
no protein
25 µM ParB-His6
C
absorbance at 360 nm
0.00
0.05
0.10
0.15
+ ParB + CTP + parS (~ 3 CTP molecules / hour)
+ ParB + CTP (~0.4 CTP molecules / hour)
+ ParB + CTP + NBS
+ ParB + UTP + parS
+ ParB + ATP + parS
+ ParB + GTP + parS
+ R104A + CTP + parS
0
200
400
600
800
1000
time (min)

Figure 4.7 *parS* DNA increases the CTP binding and hydrolysis rate by *C. crescentus* ParB. (**A–B**) CTP binding as monitored by DRaCALA assay using radiolabelled CTP α-P^{32}. The bulls-eye staining indicates CTP binding due to a more rapid immobilization of protein-ligand complexes compared to free ligands alone. The starting concentration of proteins used in panel A was 25 μM. The same concentration of radioactive CTP, unlabelled CTP, and DNA was used in experiments shown in panels A and B. (**C**) A continuous monitoring of inorganic phosphate (Pi) released by recording absorbance at 360 nm overtime at 25°C. The rates of CTP hydrolysis were inferred from a Pi standard. The NTP hydrolysis of *C. crescentus* ParB was also monitored in the presence of ATP, GTP, or UTP, with a 22 bp *parS* DNA duplex or a non-cognate 22 bp *NBS* DNA duplex (a DNA-binding site of Noc protein (Wu and Errington, 2004). The nucleation-competent but spreading-defective ParB (R104A) mutant did not hydrolyse CTP in the presence of *parS* DNA. All buffers used for experiments in this figure contained Mg^{2+}.

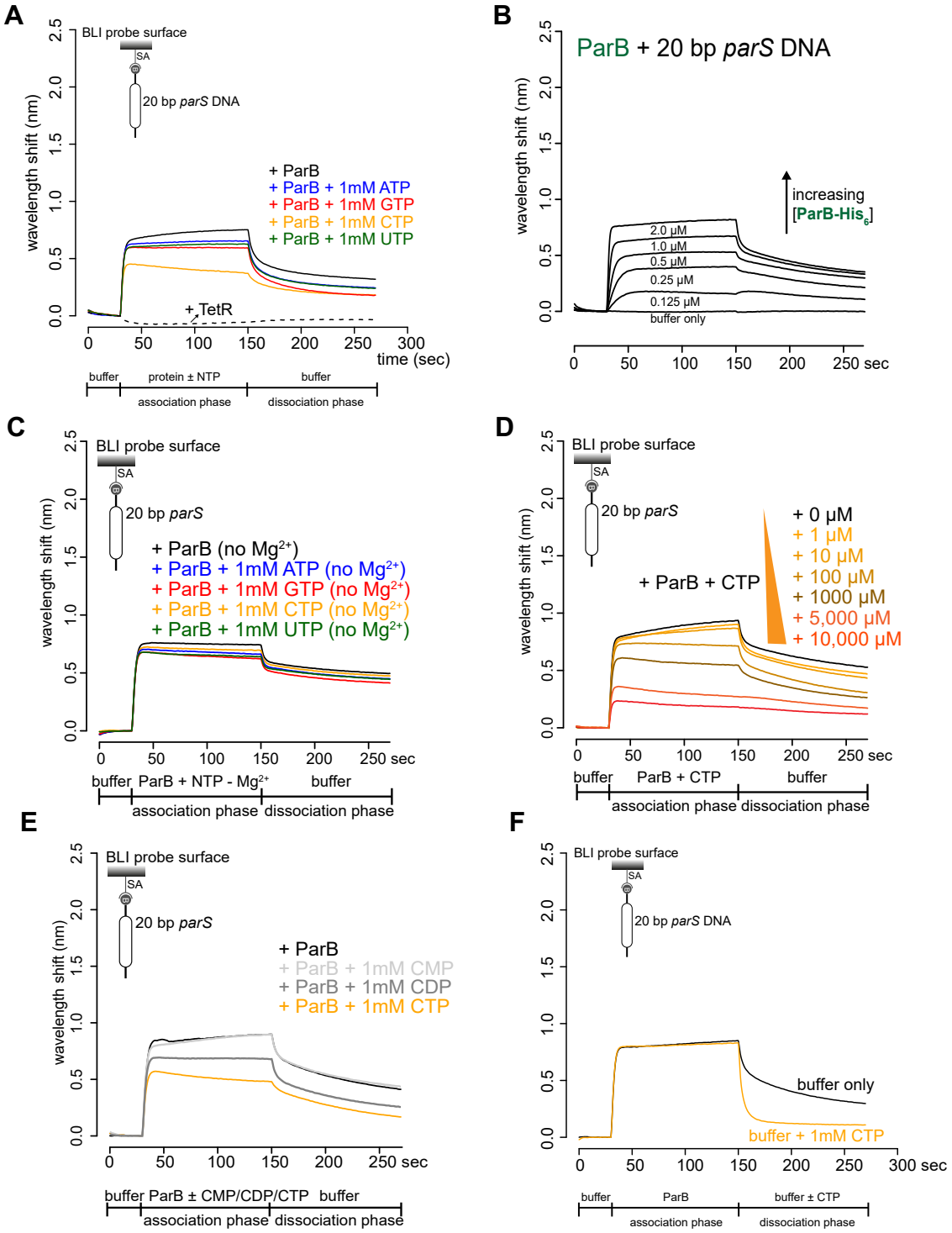
A
BLI probe surface
SA
20 bp parS DNA
wavelength shift (nm)
+ ParB
+ ParB + 1mM ATP
+ ParB + 1mM GTP
+ ParB + 1mM CTP
+ ParB + 1mM UTP
+ TetR
time (sec)
buffer
protein ± NTP
buffer
association phase
dissociation phase
B
ParB + 20 bp parS DNA
wavelength shift (nm)
increasing
[ParB-His6]
2.0 µM
1.0 µM
0.5 µM
0.25 µM
0.125 µM
buffer only
C
BLI probe surface
SA
20 bp parS
wavelength shift (nm)
+ ParB (no Mg2+)
+ ParB + 1mM ATP (no Mg2+)
+ ParB + 1mM GTP (no Mg2+)
+ ParB + 1mM CTP (no Mg2+)
+ ParB + 1mM UTP (no Mg2+)
buffer
ParB + NTP - Mg2+
buffer
association phase
dissociation phase
D
BLI probe surface
SA
20 bp parS
wavelength shift (nm)
+ ParB + CTP
+ 0 µM
+ 1 µM
+ 10 µM
+ 100 µM
+ 1000 µM
+ 5,000 µM
+ 10,000 µM
buffer
ParB + CTP
buffer
association phase
dissociation phase
E
BLI probe surface
SA
20 bp parS
wavelength shift (nm)
+ ParB
+ ParB + 1mM CMP
+ ParB + 1mM CDP
+ ParB + 1mM CTP
buffer
ParB ± CMP/CDP/CTP
buffer
association phase
dissociation phase
F
BLI probe surface
SA
20 bp parS DNA
buffer only
buffer + 1mM CTP
buffer
ParB
buffer ± CTP
association phase
dissociation phase

Figure 4.8 CTP reduces the nucleation of *C. crescentus* ParB at *parS*. (A) Bio-layer interferometric (BLI) analysis of the interaction between a premix of 1 μM ParB-His_6 dimer ± 1 mM NTP and a 20-bp DNA duplex containing *parS*. Biotinylated DNA fragments were immobilized onto the surface of a Streptavidin (SA)-coated probe (See Materials and Methods). The BLI probe was dipped into a buffer only solution (0-30 sec), then to a premix of protein ± NTP (30-150 sec: association phase), and finally returned to a buffer only solution (150-270 sec: dissociation phase). Sensorgrams were recorded over time. **(B)** BLI analysis of the interaction between purified *C. crescentus* ParB-His_6 (0.125 to 2 μM) and a 20-bp *parS* DNA probe **(C)** Same as panel except Mg^{2+} was omitted in the buffer solution **(D)** BLI analysis of the interaction between purified *C. crescentus* ParB and an increasing concentration of CTP-Mg^{2+}. ParB-His_6 (1 μM dimer) + 0-10 mM CTP, and a 20-bp DNA duplex containing *parS* were used for this experiment. **(E)** BLI analysis of the interaction between a premix of 1 μM *C. crescentus* ParB-His_6 ± 1 mM cytidine mono-, di-, or triphosphate, and a 20-bp *parS* DNA. Schematic of the DNA substrate is shown above the sensorgram **(F)** BLI analysis of the interaction between 1 μM *C. crescentus* ParB-His_6 (without CTP) and a 20-bp *parS* DNA. For the dissociation phase, the probe was returned to a buffer only or buffer supplemented with 1 mM CTP. All buffers used for experiments in this figure (with exception of Figure 4.8C) contained Mg^{2+}. Each BLI experiment was triplicated and a representative sensorgram was presented.

to a protein-free buffer with or without CTP, we found ParB dissociating ~seven times faster in buffer with CTP than in buffer only solution (Fig. 4.8F). Given the short length of a 20-bp *parS* DNA duplex that has only sufficient room for nucleation, our results suggest that CTP might decrease ParB nucleation on *parS* or liberates pre-bound ParB from *parS* site.

4.7 CTP facilitates ParB association with a closed DNA substrate beyond nucleation

Next, we investigated the effect of CTP on ParB-DNA interaction by employing a longer 169-bp *parS*-containing DNA fragment that has been labelled at both 5' ends with biotin (Fig. 4.9A). Immobilizing a dual biotin-labelled DNA on a streptavidin-coated BLI probe created a DNA substrate where both ends were blocked (a closed DNA). The interactions between immobilized DNA and purified *C. crescentus* ParB in the presence or absence of NTP was then monitored. In the absence of NTP, we observed the usual nucleation event on *parS* with 1 μM ParB protein (Fig. 4.9A). Premixing ATP, GTP, or UTP with ParB did not change the sensorgrams markedly (Fig. 4.9A). However, the addition of CTP significantly increased the response by ~12 fold (Fig. 4.9A) suggesting that more ParB associated with a 169-bp *parS* probe at steady state than by nucleation at *parS* alone. We observed that DNA-bound ParB was salt sensitive and dissociated easily to the solution when the BLI probe was returned to a low-salt protein-free buffer without CTP (Fig. 4.9A, dissociation phase). Noticeably, no increase in response was observed when a 169-bp dual biotin-labelled DNA containing a scrambled *parS* was employed instead (Fig. 4.9A). Furthermore, we observed that a nucleation-competent but spreading-defective *C. crescentus* ParB (R104A) mutant did not respond to the addition of CTP to the same extent as ParB (WT) (Fig. 4.9B). Our results suggest that CTP is required for the increase in *parS*-dependent ParB accumulation *in vitro*.

To independently verify the BLI data, we performed an *in vitro* pull-down of purified His-tagged *C. crescentus* ParB (Fig. 4.9C). Streptavidin-coated paramagnetic beads were incubated with 2.8-kb dual biotin-labelled DNA fragments containing either *parS* or scrambled *parS* sites. Again, a dual biotin-labelled DNA formed a closed substrate on the surface of the beads. DNA-coated beads were incubated with purified *C. crescentus* ParB either in the presence or absence of NTP before being pulled down magnetically. Pulled-down ParB was released from beads and their protein level was analysed by an α-His_6 immunoblot (Fig. 4.9C). We found~13-15 fold more pulled-down ParB when CTP was included (Fig. 4.9C). No enrichment was observed when scrambled *parS*-coated beads were used, confirming that the extensive *in vitro* association of ParB with DNA is dependent on *parS* (Fig. 4.9C). Also, consistent with the BLI experiments, no further enrichment of ParB was seen when ATP, GTP or UTP was included (Fig. 4.9C). Furthermore, a nucleation-competent but spreading-defective ParB

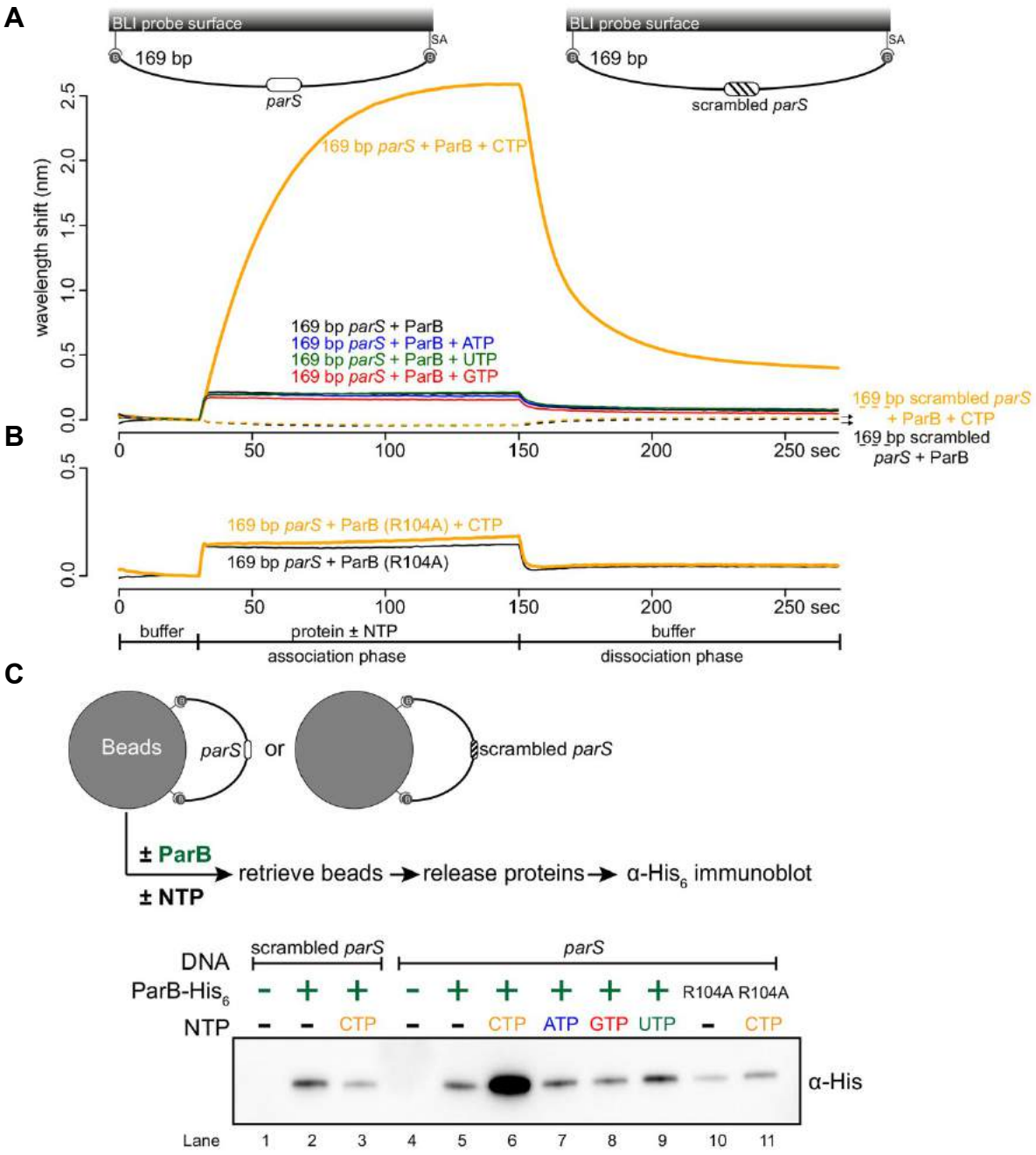

Figure 4.9 Cytidine triphosphate (CTP) enhances ParB association with a *parS* containing DNA beyond by nucleation alone (A) BLI analysis of the interaction between a premixed of 1 µM *C. crescentus* ParB-His6 ± 1mM NTP and a 169-bp dual biotin-labelled DNA containing a parS or a scrambled parS site. Interactions between a dual biotinylated DNA and a streptavidin (SA)-coated probe created a topologically closed DNA substrate (see the schematic cartoon of the BLI probe above the sensorgram). **(B)** Interactions between a nucleation-competent but spreading-defective ParB (R104) variant with a 169 parS DNA fragment in the presence or absence of CTP were also recorded. **(C)** A schematic of the pull-down assay and immunoblot analysis of pulled-down *C. crescentus* ParB-His_6. The length of bound DNA is ~2.8 kb. Beads were incubated with ParB protein for five minutes before being pulled down magnetically. All buffers used for experiments in this figure contained Mg^{2+}.

(R104A) variant was not enriched in our pull-down assay regardless of whether CTP was present or not (Fig. 4.9C). Altogether, our results suggest that the *parS*-dependent spreading ability of ParB on a closed DNA substrate requires CTP.

4.8 A closed DNA substrate is required for an increased ParB association with DNA

Next, we investigated whether a DNA substrate with a free end (an open DNA) can also support ParB accumulation *in vitro*. The 169-bp dual biotin-labelled DNA was designed with unique *Bam*HI and *Eco*RI recognition sites flanking the *parS* site (Fig. 4.10A). To generate an open end on DNA, we immerged the DNA-coated probes in buffers contained either *Bam*HI or *Eco*RI (Fig. 4.10A-C). Subsequently, probes were washed of restriction enzymes and returned to a binding buffer. Before restriction enzyme digestion, we again observed an enhanced ParB association with a closed DNA substrate in the presence of CTP (Fig. 4.10A). After restriction enzyme digestion, the inclusion of CTP had no effect on the BLI response, indicating that ParB did not accumulate on an open DNA substrate *in vitro* (Fig. 4.10A-C). Taken together, these findings suggest that ParB spreads but quickly escapes by sliding off the free DNA end.

4.9 The crystal structure of the C-terminal truncated (ΔCTD) *Caulobacter* ParB in complex with the slow hydrolysable CTP analogue, CTPγS

Next, to gain insights into the spreading state of ParB, I attempted to crystallise *C. crescentus* ParB in complex with the slow hydrolysable analogue of CTP, CTPγS. After screening several constructs, I was able to obtain crystals of the *C. crescentus* ParBΔCTD in complex with CTPγS. Diffraction data was collected to a resolution of 2.7 Å and the structure was solved using molecular replacement with the *C. crescentus* ParBΔCTD as a template (Chapter 2). The X-ray crystallographic data are summarised in Table 4.1. At this resolution, it was not possible to assign the position of the ligand sulphur atom. Indeed, the placement of the sulphur atom may vary from one ligand to the next leading to an averaging of the electron density. Hence, CTP instead of CTPγS was modelled into the electron density (Fig. 4.11A). The asymmetric unit contains two copies of ParBΔCTD, each with a CTPγS molecule and a coordinated Mg^{2+} ion bound at the NTD (Fig. 4.11A). In contrast to the open conformation of the ParBΔCTD-*parS* structure, nucleotide-bound NTDs from opposite subunits self-dimerize (with an interface area of 2111 $Å^2$, as determined by PISA) (Krissinel, 2015) (Fig. 4.11A). Multiple CTPγS-contacting residues also directly contribute to the NTD self-dimerization interface (summarized in Fig. 4.12), indicating a coupling between nucleotide binding and self-dimerization. Furthermore, the *C. crescentus* ParBΔCTD-CTPγS structure is similar to that of the CDP-bound *B. subtilis* ParBΔCTD (RMSD=1.48 Å) (Soh et al., 2019) and the CTP-bound

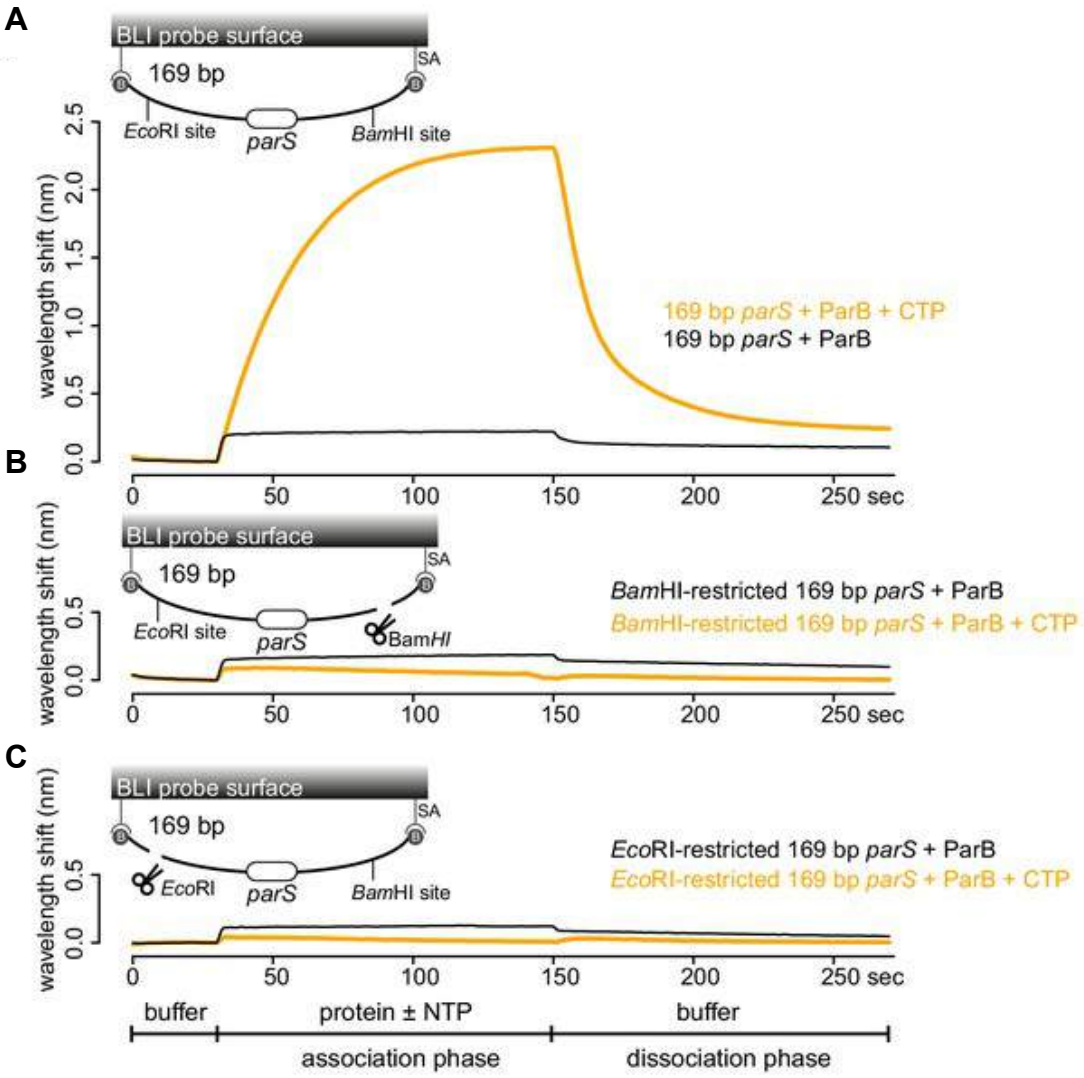

Figure 4.10 A closed DNA substrate is required for an increased association of ParB with DNA. (A) BLI analysis of the interaction between a premix of 1 µM *C. crescentus* ParB-His_6 ± 1mM CTP and a 169-bp dual biotin-labelled *parS* DNA. **(B)** Same as panel A but immobilized DNA fragments have been restricted with *Bam*HI before BLI analysis. **(C)** Same as panel A but immobilized DNA fragments have been restricted with *Eco*RI before BLI analysis. Schematic of DNA fragments with the relative positions of *parS* and restriction enzyme recognition sites are shown above the sensorgram. Each BLI experiment was triplicated and a representative sensorgram was presented. All buffers used for experiments in this figure contained Mg^{2+}.

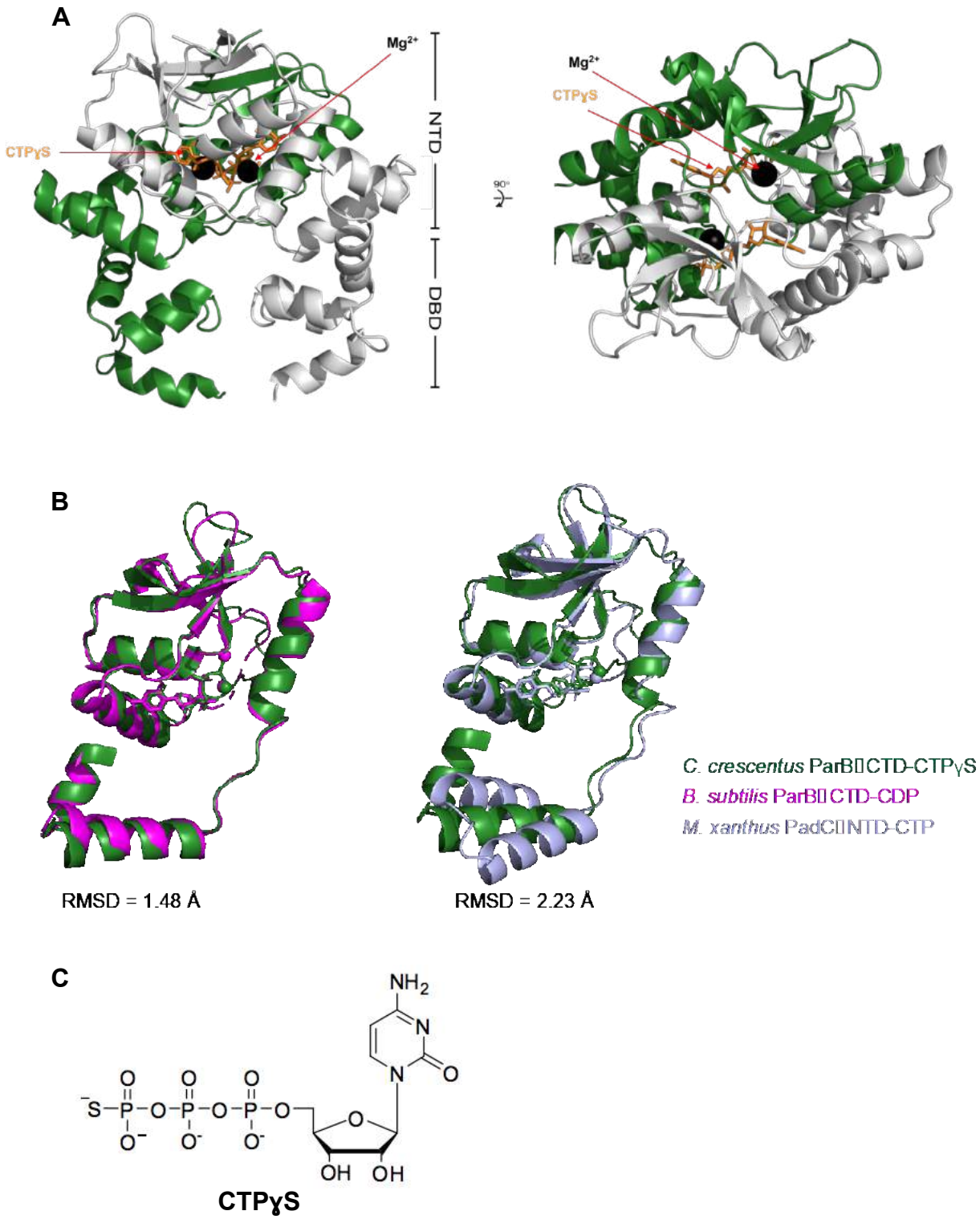
A
Mg2+
CTPγS
NTD
DBD
90°
Mg2+
CTPγS
B
RMSD = 1.48 Å
RMSD = 2.23 Å
C. crescentus ParBCTD-CTPγS
B. subtilis ParBCTD-CDP
M. xanthus PadCNTD-CTP
C
NH2
N
N
O
O
O
O
O
O
O
O
S
P
P
P
O
O
O
OH
OH
CTPγS

Figure 4.11 Co-crystal structure of a *C. crescentus* ParBΔCTD-CTPɣS complex reveals a closed conformation at the NTD. (A) (Left panel) The front view of the co-crystal structure of *C. crescentus* ParBΔCTD (dark green and grey) bound to a non-hydrolysable analogue CTPɣS (orange) and Mg^{2+} ions (dark green and grey spheres). **(Right panel)** The top view of the *C. crescentus* ParBΔCTD-CTPɣS co- crystal structure. **(B)** Structural comparisons of the *C. crescentus* ParBΔCTD-CTPɣS complex to the *B. subtilis* ParBΔCTD-CDP complex and the *M. xanthus* PadCΔNTD-CTP complex. Superimposition of nucleotide-bound structures of *C. crescentus* ParBΔCTD (dark green), *B. subtilis* ParBΔCTD (magenta) PDB: 6SDK, and *M. xanthus* PadCΔNTD PDB: 6RYK (light blue) with their corresponding pairwise root- mean-square deviation values (RMSD). **(C)** The chemical structure of CTPɣS.

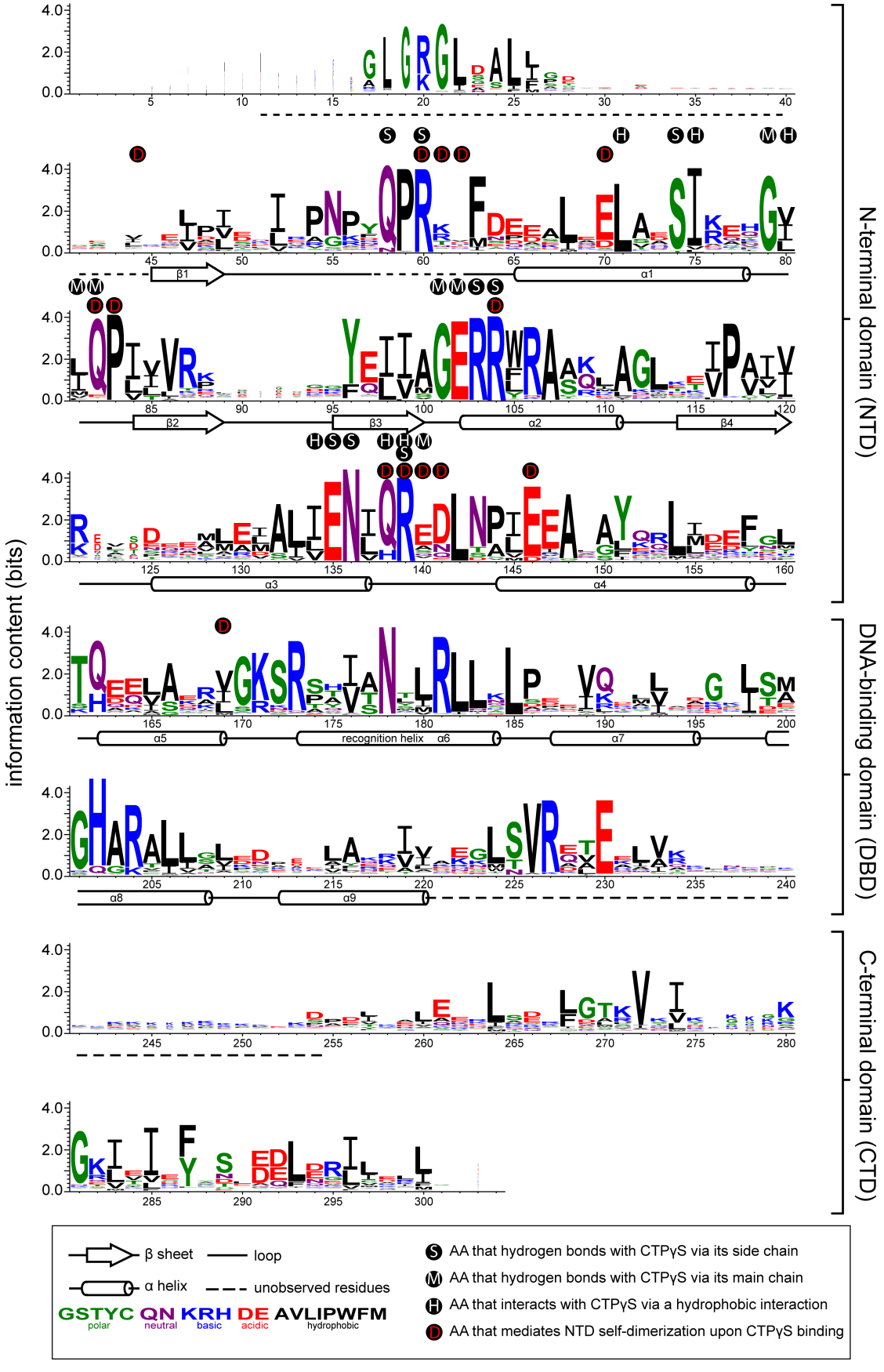
information content (bits)
N-terminal domain (NTD)
DNA-binding domain (DBD)
C-terminal domain (CTD)
β1
α1
β2
β3
α2
β4
α3
α4
α5
recognition helix
α6
α7
α8
α9
β sheet
loop
α helix
unobserved residues
GSTYC polar
QN neutral
KRH basic
DE acidic
AVLIPWFM hydrophobic
AA that hydrogen bonds with CTPγS via its side chain
AA that hydrogen bonds with CTPγS via its main chain
AA that interacts with CTPγS via a hydrophobic interaction
AA that mediates NTD self-dimerization upon CTPγS binding

Figure 4.12 Sequence alignment of the chromosomal ParB protein family. An alignment of ~1800 chromosomal ParB proteins was constructed and presented as a sequence logo. The height of the stack indicates the sequence conservation, while the height of symbols within the stack indicates the relative frequency of each amino acid residue at that position. Amino acids are coloured based on their chemical properties. Secondary-structure elements for *C. crescentus* ParBΔCTD are shown below the alignment. Dashed lines indicate unmodeled residues due to poor electron density in the *C. crescentus* ParBΔCTD-CTPγS co-crystal structure. Residues that contact CTPγS-Mg^{2+} and/or mediate the NTD self-dimerization are also labelled.

M. xanthus PadCΔNTD (RMSD=2.23 Å) (Osorio-Valeriano et al., 2019) (Fig. 4.11B), suggesting that the closed conformation at the NTD is structurally conserved in nucleotide-bound ParB/ParB-like proteins.

4.10 The CTP-binding pocket (C-pocket) of *C. crescentus* ParB

In the co-crystal structure of the *C. crescentus* ParBΔCTD-CTPγS complex, two CTPγS molecules are sandwiched between helices α1, α2, α3 from one subunit and helix α3' from the opposite subunit (Fig. 4.11A, 4.13A-B). Ten amino acids form hydrogen-bonding contacts with three phosphate groups of CTPγS, either directly or via the coordinated Mg^{2+} ion (Fig. 4.13A-B). These phosphate-contacting residues were referred to as P-motifs 1 to 3, respectively (P for phosphate motif, Fig. 4.13A-B). Four amino acids at helix α1 and the α1-β2 intervening loop provide hydrogen-bonding interactions to the cytosine ring, hence were termed the C- motif (C for cytosine motif, Fig. 4.13A-B). Lastly, six additional residues contact the ribose moiety and/or the pyrimidine moiety via hydrophobic interactions (Fig. 4.13A-B). Nucleotide- contacting residues in *C. crescentus* ParB and their corresponding amino acids in ParB/ParB-like homologs were summarized in figure 4.12 and figure 4.20. The C-motif forms a snug fit to the pyrimidine moiety, thus is incompatible with larger purine moieties such as those from ATP or GTP. Hydrogen-bonding contacts from the G79 main chain and the S74 side chain to the amino group at position 4 of the cytosine moiety further distinguish CTP from UTP (Fig. 4.13A-B). Taken all together, my structural data is consistent with the known specificity of *C. crescentus* ParB for CTP (Fig. 4.7A-B).

4.11 Conformational changes between the nucleating and spreading state of *C. crescentus* ParB

A direct comparison of the *C. crescentus* ParBΔCTD-*parS* structure to the ParBΔCTD-CTPγS structure further revealed the conformational changes upon nucleotide binding. In the nucleating state, as represented by the ParBΔCTD-*parS* structure, helices α3 and α4 from each subunit bundle together (32° angle between α3 and α4, Fig. 4.14). However, in the spreading state, as represented by the ParBΔCTD-CTPγS structure, α3 swings outwards by CTP 101° to pack itself with α4' from the opposite subunit (Fig. 4.14). Nucleotide binding most likely facilitates this "swinging-out" conformation since both α3 and the α3-α4 loop i.e. P- motif 3 make numerous contacts with the bound CTPγS and the coordinated Mg^{2+} ion (Fig. 4.15A-B). The reciprocal exchange of helices ensures the packing in the α3-α4 protein core remains intact, while driving the conformational changes for the rest of the NTD as well as the DBD (Fig. 4.15A). Indeed, the residues 44-121 at the NTD wholesale rotates by 94° to dimerize with its counterpart from the opposite subunit (Fig. 4.15A, 4.16A). Also, residues 161-221 at

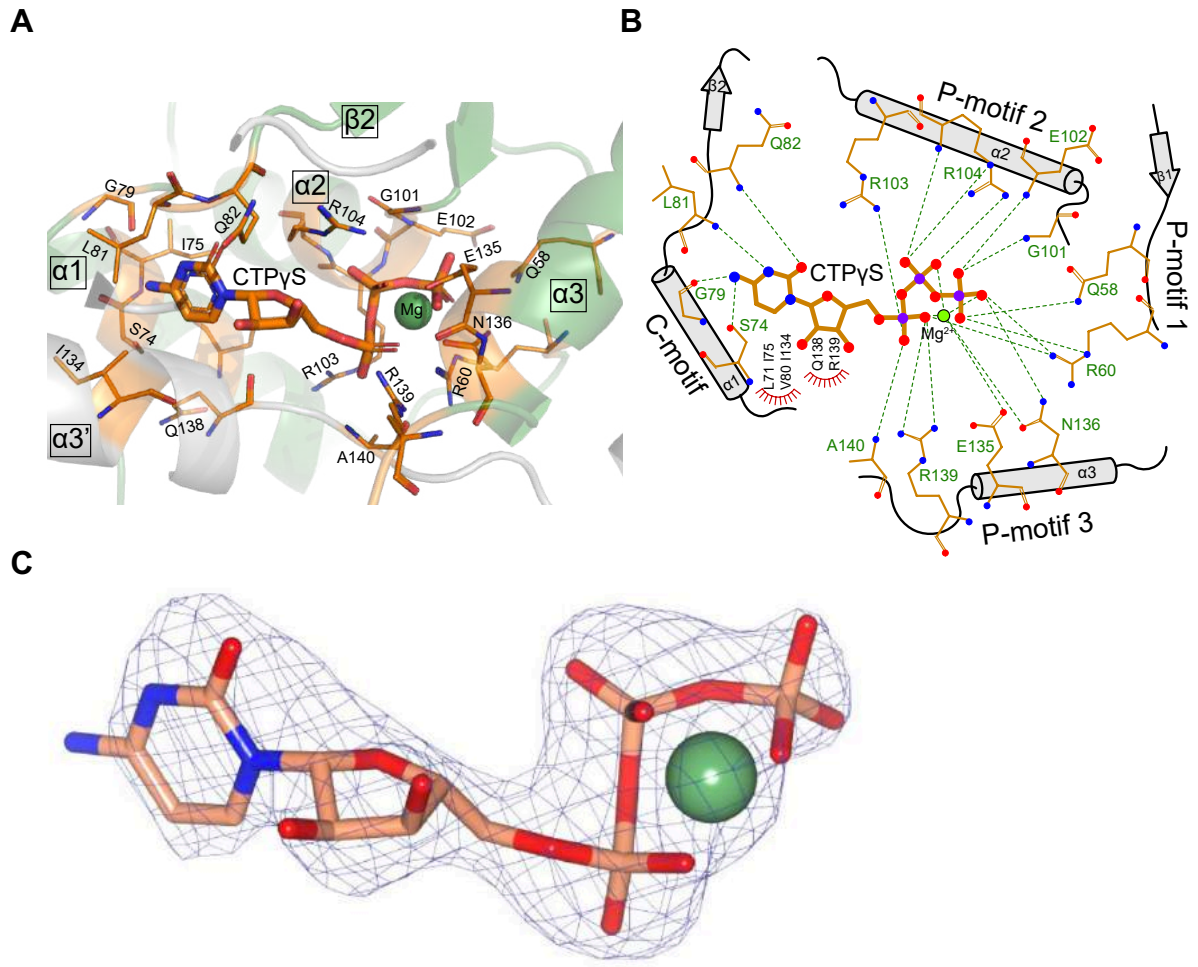

Figure 4.13 The nucleotide-binding pocket of *C. crescentus* ParB. (A) The amino acid residues that contact the CTPɣS molecule and the coordinated Mg^{2+} ion are shown **(B)** Protein-ligand interaction map of CTPɣS bound to *C. crescentus* ParBΔCTD. Hydrogen bonds are shown as dashed green lines and hydrophobic interactions as red semi-circles. Nitrogen, oxygen, phosphate, and magnesium atoms are shown as blue, red, purple, and green filled circles, respectively. **(C)** Omit mFobs-DFcalc difference electron density calculated at 2.73 Å resolution for Mg-CTP. The omit map was calculated using phases from the final model, with the displayed atoms omitted, after the application of small random shifts to the atomic coordinates, re-setting temperature factors, and re-refining to convergence (rendered in blue mesh at a contour level of ~3.5σ).

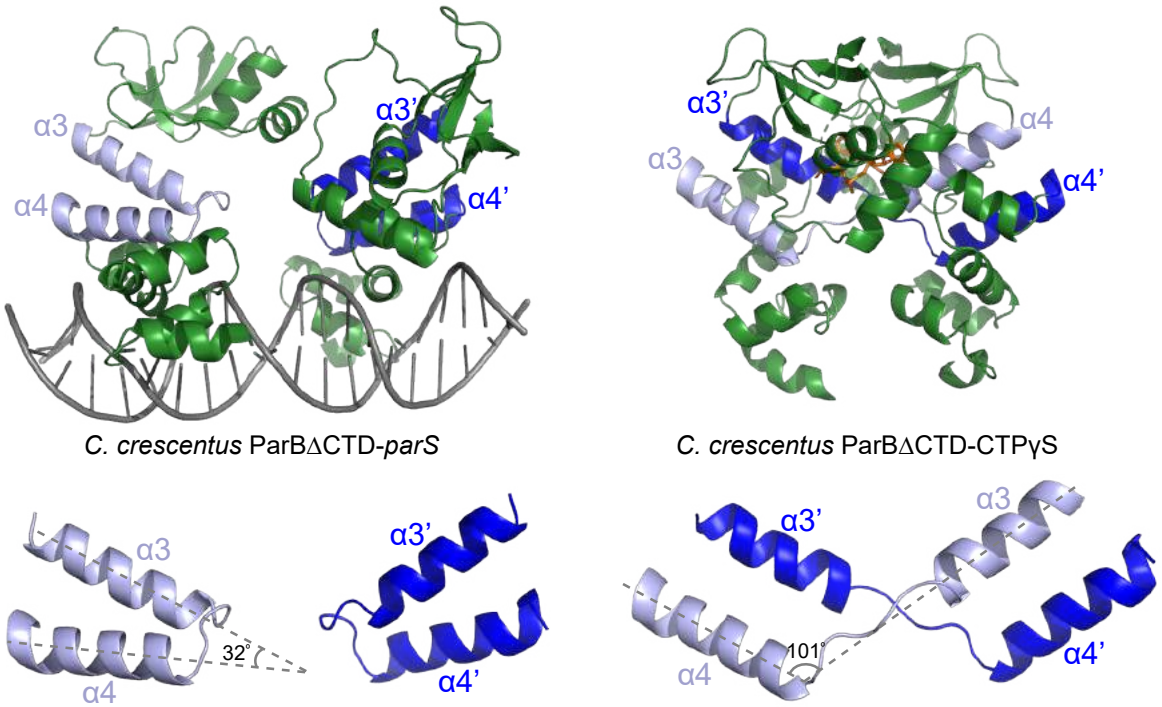

Figure 4.14 Conformational changes between the nucleating and the spreading state of *C. crescentus* ParB. Structures of *C. crescentus* ParBΔCTD in complex with *parS* **(left panel)** and with CTPγS **(right panel)**, with the pairs of helices (α3-α4, and α3'-α4' for the opposite subunit) shown in light blue and dark blue, respectively. Below each structure, only the α3-α4, α3'-α4' pairs, and the angles between these helices are shown.

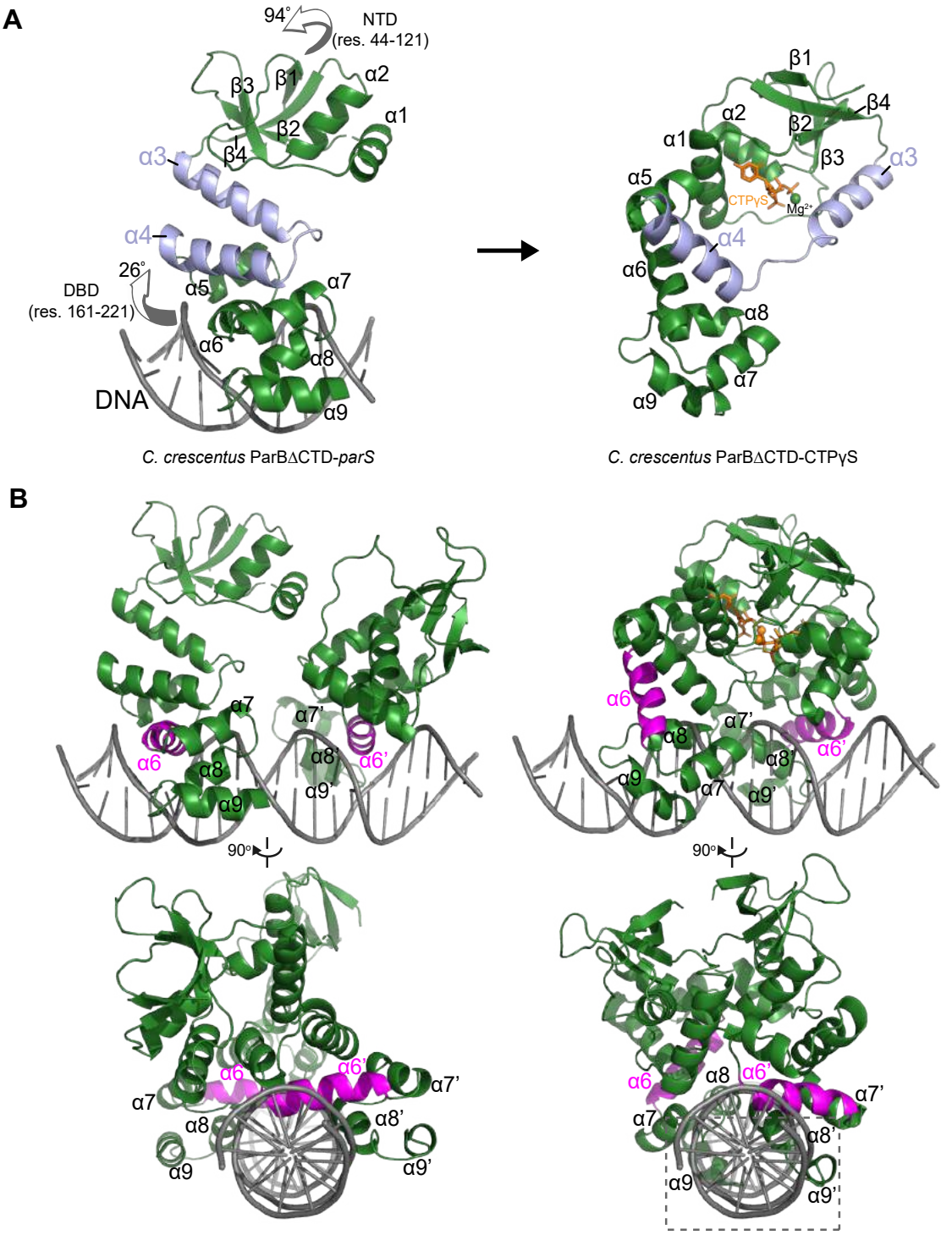
A
94°
NTD
(res. 44-121)
β3
β1
α2
α1
β2
α3
β4
α4
26°
DBD
(res. 161-221)
α5
α7
α6
α8
DNA
α9
β1
α2
β2
β4
α1
β3
α3
α5
CTPγS
Mg2+
α4
α6
α8
α7
α9
C. crescentus ParBΔCTD-parS
C. crescentus ParBΔCTD-CTPγS
B
α7
α7'
α6
α8
α8'
α6'
α9
α9'
90°
α6
α8
α6'
α7'
α7
α8'
α9
α9'
α6
α7'
α8
α8'
α6'
α9
α7
α9'
90°
α6
α8
α6'
α7'
α7
α8'
α9
α9'
C. crescentus ParBΔCTD-parS
C. crescentus ParBΔCTD-CTPγS, superimposed on parS

Figure 4.15 The structure of a nucleotide-bound *C. crescentus* ParBΔCTD is incompatible with specific *parS* binding at the DBD. (A) Structural changes between *C. crescentus* ParBΔCTD-*parS* and ParBΔCTD-CTPɣS structures. Helices α3 and α4 are shown in light blue. The arrows next to the NTD (residues 44 to 1221) and the DBD (residues 161 to 21) show the direction that these domains rotate towards in the nucleotide-bound state. **(B)** Superimposing the *C. crescentus* ParBΔCTD-CTPɣS structure onto *parS* DNA shows DNA-recognition helices (α6 and α6', magenta) positioning away from the two consecutive major grooves of *parS*, and helices α8-α9 and α8'-α9' at the DBD (dashed box) clashing with *parS* DNA.

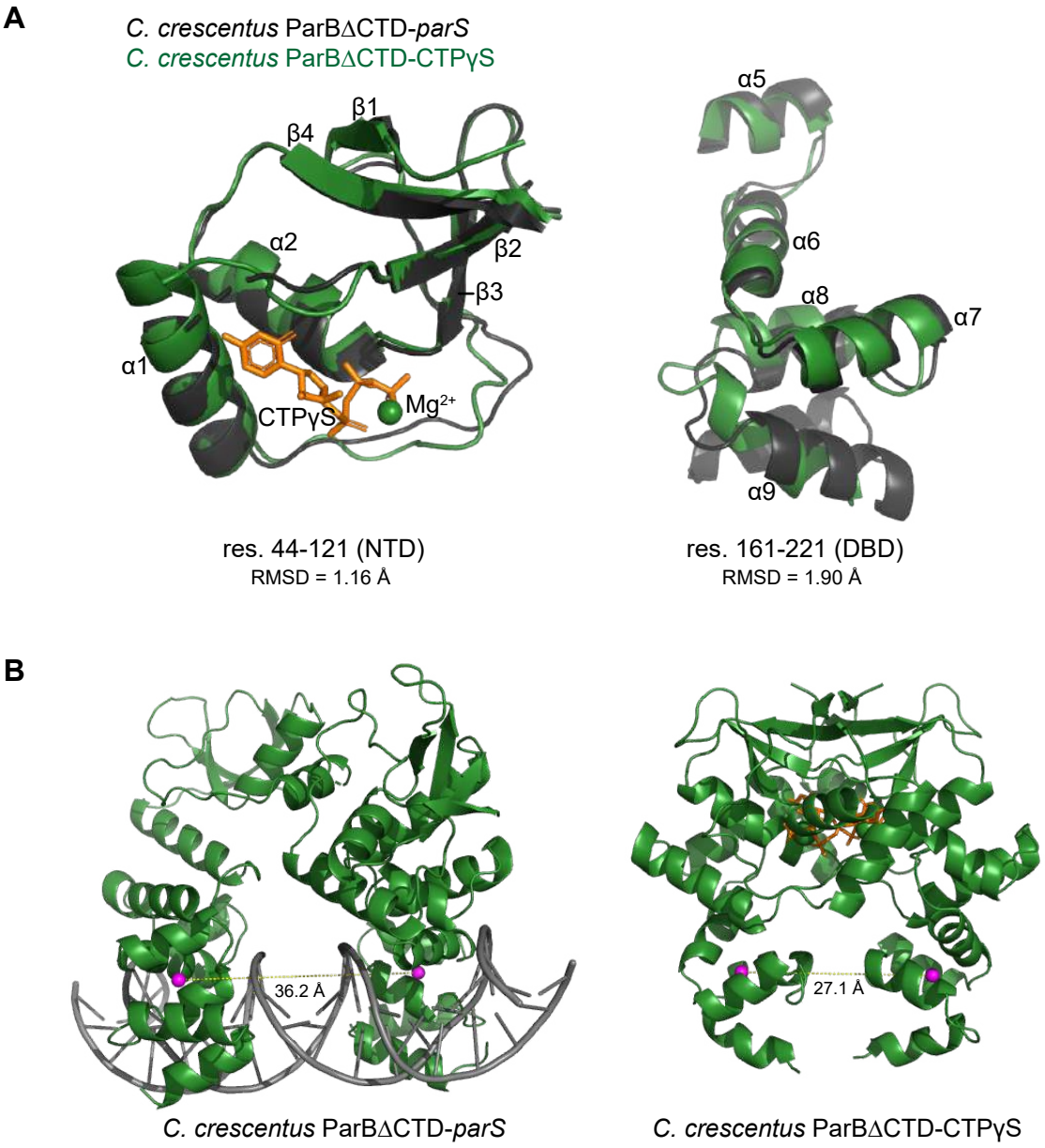

Figure 4.16 The structure of nucleotide-bound *C. crescentus* ParBΔCTD is incompatible with specific *parS* binding at the DBD. (A) Residues 44 to 121 of the NTD and residues 161 to 221 of the DBD move in a near rigid-body motion between the ParBΔCTD-*parS* and the ParBΔCTD-CTPγS structures. **(Left panel)** Structural comparison between the NTDs (residues 44 to 121) from the ParBΔCTD-*parS* structure (black) and the ParBΔCTD-CTPγS structure (dark green). **(Right panel)** Structural comparison between the DBDs (residues 161 to 221) from the ParBΔCTD-*parS* structure (black) and the ParBΔCTD-CTPγS structure (dark green). The corresponding root-mean- square deviation value (RMSD) is shown below each structural alignment. **(B)** The inter-domain distances between opposite DBDs in the ParBΔCTD-*parS* and the ParBΔCTD-CTPγS structures. Distances (yellow dashed lines) were measured between the centroid (magenta sphere) of each DBD.

the DBD rotates upward by 26° in a near rigid- body movement (Fig. 4.15A, 4.16A). As the result, the opposite DBDs of ParB are closer together in the spreading state (inter-domain distance = 27.1 Å) than in the nucleating state (inter-domain distance = 36.2 Å) (Fig. 4.16B). By overlaying the CTPγS-bound structure onto the *parS* DNA, it then became clear that the DBDs in the spreading state clash severely with DNA, hence are no longer compatible with *parS* DNA binding (Fig. 4.15B). My structural data are therefore consistent with our biochemical reconstitutions that CTP decreases *C. crescentus* ParB nucleation on *parS* or liberates pre- bound ParB from *parS* site (Fig. 4.8, 4.9). Overall, I suggest that CTP binding induces a DNA-binding incompatible conformation that facilitates ParB escape from the high-affinity nucleation *parS* site.

4.12 The crystal structure of the *Caulobacter* ParBΔ44N in complex with CDP

As the CTPγS-bound *C. crescentus* ParB crystals diffracted to 2.7 Å, I was unable to confidently model any potential catalytic water molecules, preventing our understanding of the mechanism of CTP hydrolysis by the ParB CTPase. To obtain a structural insight into ParB mediated CTP hydrolysis, I sought to obtain a ParB-CTPγS co-crystal complex that would diffract at a higher resolution. From comparing both ParBΔCTD crystal structures, I observed that the electron density for the first 44 residues of ParBΔCTD were not present in the structure, likely due to a disordered conformation. Indeed, truncating this region generated the *C. crescentus* ParBΔ44NΔCTD variant generated crystals that diffracted to a much higher resolution of 1.28 Å. The phase was then solved by molecular replacement using the 2.9 Å structure of the *C. crescentus* ParBΔCTD ParB-*parS* as a search template. The X-ray crystallographic data are summarised in Table 4.1.

The asymmetric unit of the crystal contained a single molecule of ParBΔ44NΔCTD-CDP monomer which forms a dimer due to the symmetry of crystal packing (Fig 4.17A-B). In the crystal, *C. crescentus* ParBΔ44NΔCTD forms a compact dimer composed of two interlocking polypeptide chains. Despite the ParBΔ44NΔCTD being co-crystallised with CTPγS, I was unable to confidently model the third sulphur containing phosphate group, as such CDP was modelled instead. Thus, despite the higher resolution, I was unable to determine the structural basis of CTP-hydrolysis by the ParB CTPase. Structural comparisons between the *C. crescentus* ParBΔ44NΔCTD-CDP complex and the *C. crescentus* ParBΔCTD-CTPγS revealed that both proteins adopt a similar conformation of the NTD and DBD (RMSD = 0.7. Å) (Fig. 4.18A). Nevertheless, from comparing the C-pocket of the ParBΔCTD-CTPγS I was able to compare the contacts mediated between ParB-CTPγS and CDP (Fig. 4.19). Noticeably both E135 and N136 which form side chain contacts through a coordinated Mg^{2+} ion with P-

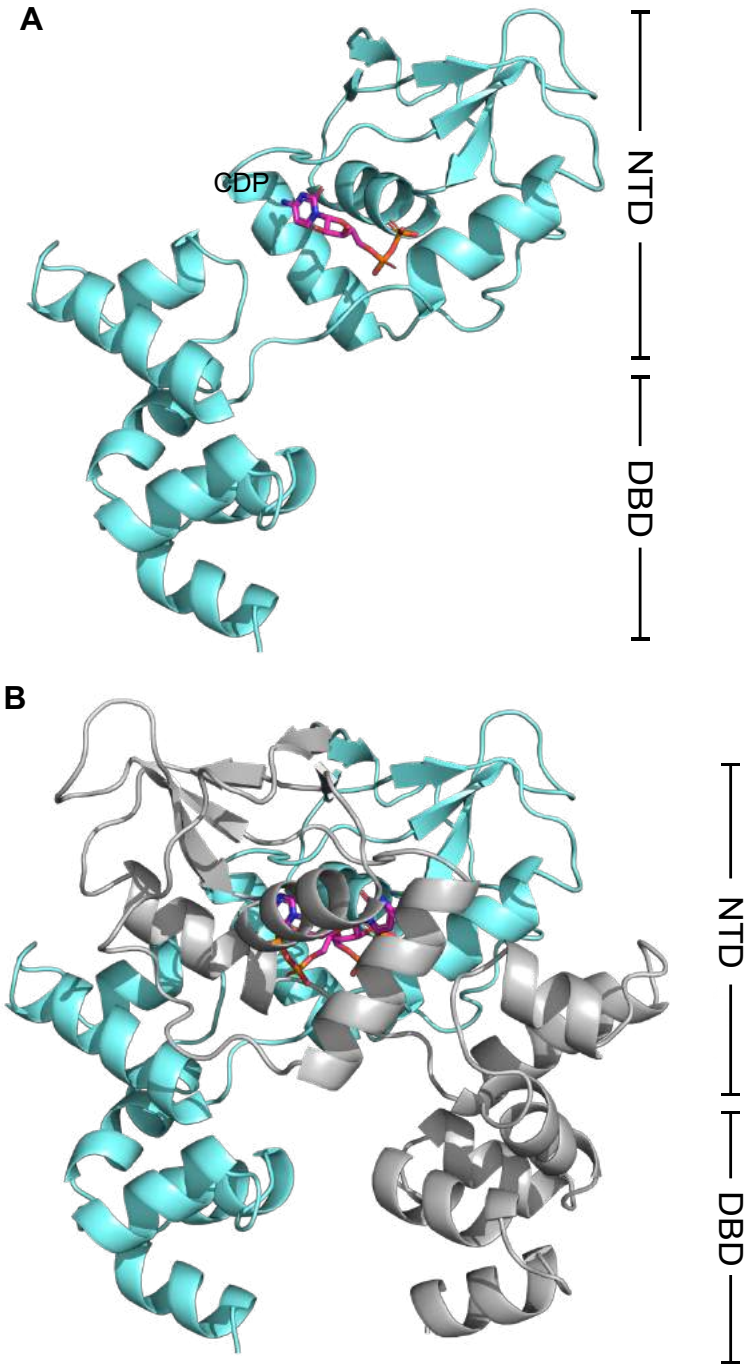

Figure 4.17 The crystal structure of a *C. crescentus* ParBΔ44NΔCTD in complex with cytidine diphosphate (CDP) (A) The asymmetric unit contained one copy of the *C. crescentus* ParBΔ44NΔCTD (aquamarine and grey) bound to CDP (magenta). **(B)** A dimer of the *C. crescentus* ParBΔ44NΔCTD that self-dimerizes at the N-terminal domain (NTD).

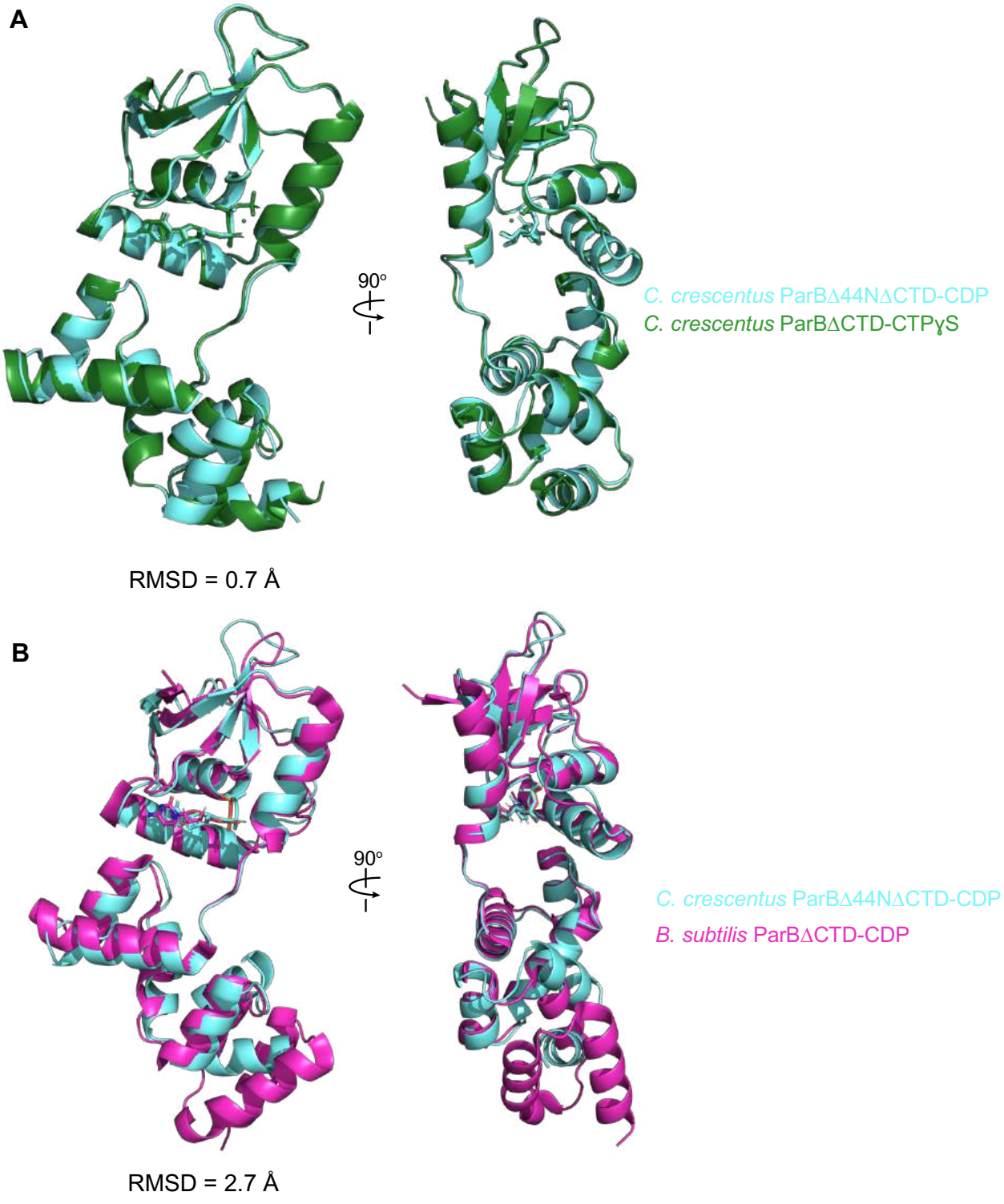

Figure 4.18 Structural superimposition between the *C. crescentus* ParBΔ44NΔCTD-CDP complex, *C. crescentus* ParBΔCTD-CTPγS, and *B. subtilis* ParBΔCTD-CDP complex. (A) Superimposition of nucleotide-bound structures of *C. crescentus* ParBΔ44NΔCTD (aquamarine) *C. crescentus* ParBΔCTD (green) **(B)** Superimposition of nucleotide-bound structures of *C. crescentus* ParBΔ44NΔCTD (aquamarine) and *B. subtilis* ParBΔCTD (magenta) with their corresponding pairwise root- mean-square deviation values (RMSD).

A

C. crescentus ParBΔCTD-CTPγS

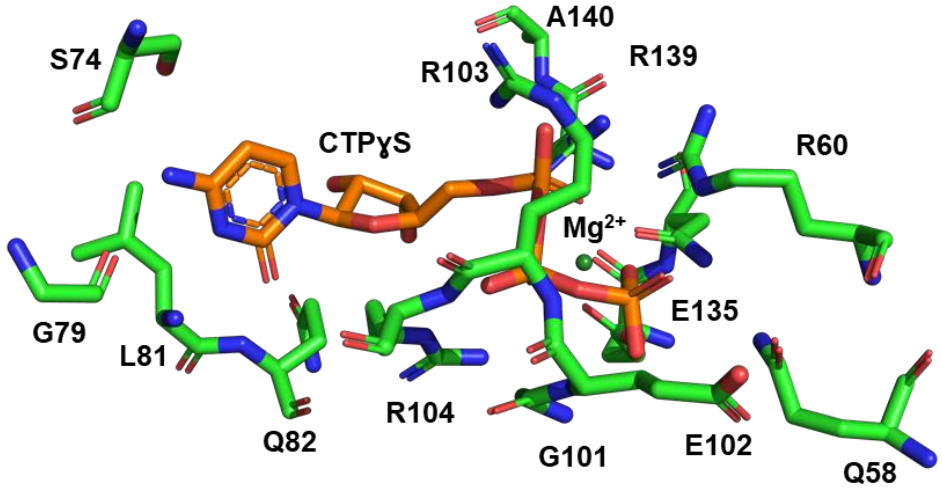

B

C. crescentus ParBΔ44NΔCTD-CDP

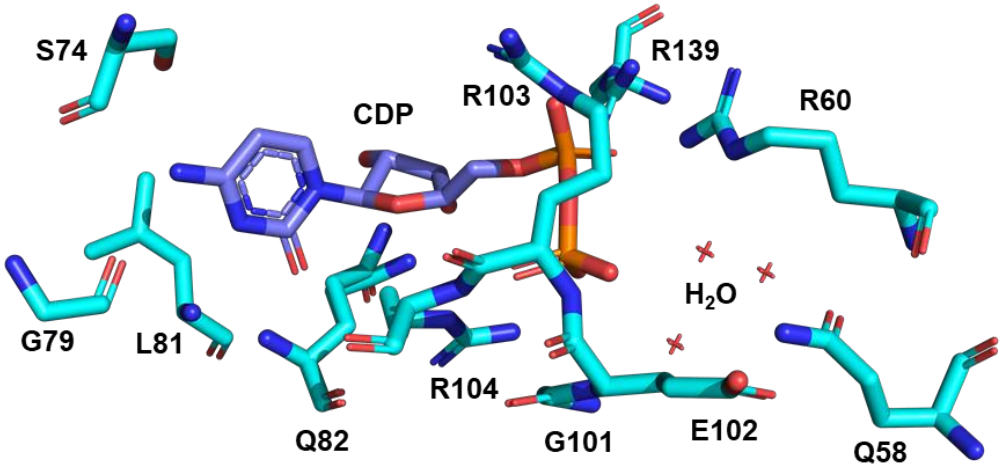

C

C. crescentus ParBΔCTD-CTPγS

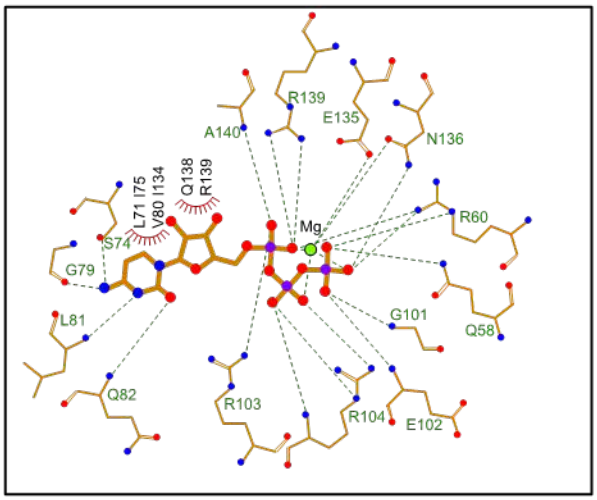

D

C. crescentus ParBΔ44NΔCTD-CDP

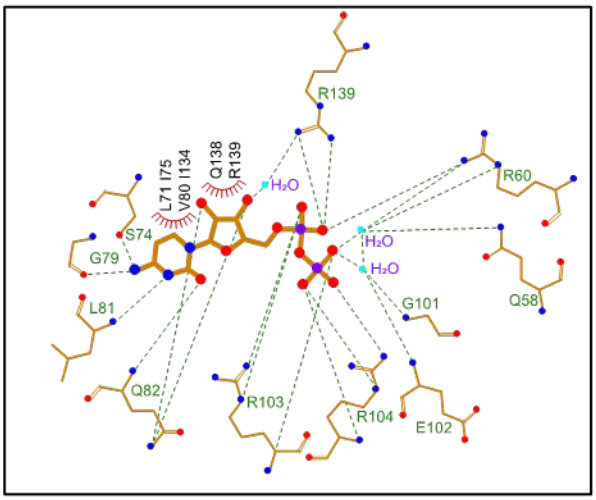

Figure 4.19 Comparison of the nucleotide binding pocket between the CTPγS bound *C. crescentus* ParBΔCTD and the CDP bound *C. crescentus* ParBΔ44NΔCTD (A) The amino acid residues that contact the CTPγS molecule and the coordinated Mg^{2+} ion are shown **(B)** The amino acid residues that contact the CDP molecule and water molecules are shown (**C)** Protein-ligand interaction map of CTPγS bound to *C. crescentus* ParBΔCTD. Hydrogen bonds are shown as dashed green lines and hydrophobic interactions as red semi-circles. Nitrogen, oxygen, phosphate, and magnesium atoms are shown as blue, red, purple, and green filled circles, respectively. (**D)** Protein-ligand interaction map of CDP bound to *C. crescentus* ParBΔ44NΔCTD.

	C. crescentus ParBΔC-CTPγS	*C. crescentus* ParBΔC-CDP	*Bacillus subtilis* ParBΔC-CDP (6SDK, Soh *et al*., 2019)	*Myxococcus xanthus* PadCΔN-CTP (6RYK, Osorio-Valeriano *et al*., 2019)
P-region 1	Q58 (side chain) R60 (side chain)	Q58 (side chain, via H_20) R60 (side chain, via H_20)	Q37 (no contact to CDP) R39 (side chain)	F308 (no contact to CTP) R311 (side chain)
C-pocket	S74 (side chain) G79 (main chain) L81 (main chain) Q82 (main chain)	S74 (side chain) G79 (main chain) L81 (main chain) Q82 (main chain)	S53 (side chain) G58 (main chain) L60 (main chain) Q61 (main chain)	E322 (side chain) G327 (main chain) L329 (main chain) F330 (main chain)
P-region 2	G101 (main chain) E102 (main chain) R103 (side chain) R104 (side chain)	G101 (side chain, via H_20) E102 (side chain, via H_20) R103 (side chain) R104 (side chain)	G77 (main chain, via Ca^{2+}) E78 (main chain, via Ca^{2+}) R79 (side chain) R80 (side chain)	G347 (main chain) F348 (main chain) R349 (side chain) R350 (side chain)
P-region 3	E135 (side chain, via Mg^{2+}) N136 (side chain, via Mg^{2+}) R139 (side chain) A140 (main chain)	E135 (no contact to CDP) N136 (no contact to CDP) R139 (side chain) A140 (no contact to CDP)	E111 (side chain, via H_20 and Ca^{2+}) N112 (side chain, via H_20 and Ca^{2+}) R115 (side chain) E116 (main chain)	E382 (side chain, via H_20 and Mg^{2+}) A383 (no contact to CTP) A386 (no contact to CTP) T387 (main chain)
Hydrophobic interactions to the cytidine moiety	L71 (side chain) I134 (side chain) I75 (side chain) V80 (side chain)	L71 (side chain) I134 (side chain) I75 (side chain) V80 (side chain)	L50 (side chain) I110 (side chain) V54 (side chain) I59 (side chain)	L319 (side chain) A381 (no contact with CTP) I323 (side chain) Q328 (side chain)
to the ribose moiety	R139 (side chain)	R139 (side chain)	R115 (side chain)	A386 (no contact to CTP)
to the cytidine and ribose moiety	Q138 (side chain)	Q138 (side chain)	Q114 (side chain)	H385 (side chain)

Figure 4.20 Summary of nucleotide-contacting residues of ParB. The nucleotide-binding residues from *C. crescentus* ParBΔCTD-CTPγS structure, *C. crescentus* ParBΔ44NΔCTD structure, *B. subtilis* ParBΔCTD-CDP structure (PDB accession code: 6SDK), and *M. xanthus* PadCΔNTD structure (PDB accession code: 6RYK) are shown. Positional equivalent residues that do not contact nucleotides are shown in light grey.

Structure	***C. crescentus* ParBΔCTD-*parS* complex**	***C. crescentus* ParBΔCTD CTPγS complex**	***C. crescentus* ParBΔ44NΔCTD CDP complex**
Data collection			
Diamond Light Source beamline	I04-1	I03	I04
Wavelength (Å)	0.916	0.976	0.980
Detector	Pilatus 6M-F	Eiger2 XE 16M	Eiger2 XE 16M
Resolution range (Å)	72.96 – 2.90 (3.08 – 2.90)	70.59 – 2.73 (2.86 – 2.73)	69.38 – 1.26 (1.28 – 1.26)
Space Group	$P2_1$	$P2_1$	$P2_12_12$
Cell parameters (Å/°)	a = 54.3, b = 172.9, c = 72.9, β = 90.5	a = 69.5, b = 56.1, c = 71.4, β = 98.4	a = 56.1, b = 69.4, c = 55.2
Total no. of measured intensities	198135 (33888)	92266 (8473)	2057626 (2872)
Unique reflections	29654 (4775)	14516 (1756)	58976 (2872)
Multiplicity	6.7 (7.1)	6.4 (4.8)	34.9 (14.5)
Mean $I/\sigma(I)$	8.7 (1.4)	5.4 (1.2)	24.0 (1.0)
Completeness (%)	99.7 (100.0)	98.8 (91.4)	100.0 (99.4)
R_{merge}[a]	0.135 (1.526)	0.195 (1.210)	0.061 (2.100)
R_{meas}[b]	0.146 (1.646)	0.212 (1.357)	0.062 (2.173)
$CC_{½}$[c]	0.997 (0.677)	0.991 (0.825)	0.999 (0.522)
Wilson B value (Å^2)	81.6	57.7	19.1
Refinement			
Resolution range (Å)	72.96 – 2.90 (2.98 – 2.90)	70.59 – 2.73 (2.80 – 2.73)	69.42 – 1.26 (1.29 – 1.26)
Reflections: working/free[d]	28155/1466	13824/678	56152/2763
R_{work}[e]	0.240 (0.366)	0.248 (0.371)	0.176 (0.343)
R_{free}[e]	0.263 (0.369)	0.284 (0.405)	0.200 (0.366)
Ramachandran plot: favoured/allowed/disallowed[f] (%)	95.2/4.8/0	95.5/4.5/0	98.9/1.1/0
R.m.s. bond distance deviation (Å)	0.005	0.002	0.008
R.m.s. bond angle deviation (°)	1.05	1.19	1.482
Mean B factors: protein/DNA/water /other/ overall (Å^2)	98/74/-/-/92	81/-/-/61/77	31/-/39/23/31
PDB accession code	**6T1F**	**7BM8**	

Table 4.1 X-ray data collection and processing statistics for the crystal structures of the *C. crescentus* ParBΔCTD-parS complex, *C. crescentus* ParBΔCTD-CTPγS complex and *C. crescentus* ParBΔ44NΔCTD-CDP complex

Values in parentheses are for the outer resolution shell. [a] Rmerge = $\sum_{hkl} \sum_i |I_i(hkl) - \langle I(hkl) \rangle| / \sum_{hkl} \sum_i I_i(hkl)$.

[b] Rmeas = $\sum_{hkl} [N/(N-1)]^{1/2} \times \sum_i |I_i(hkl) - \langle I(hkl) \rangle| / \sum_{hkl} \sum_i I_i(hkl)$, where $I_i(hkl)$ is the ith observation of reflection hkl, $\langle I(hkl) \rangle$ is the weighted average intensity for all observations i of reflection hkl and N is the number of observations of reflection hkl.

[c] $CC1/2$ is the correlation coefficient between symmetry equivalent intensities from random halves of the dataset.

[d] The dataset was split into "working" and "free" sets consisting of 95 and 5% of the data respectively. The free set was not used for refinement.

[e] The R-factors Rwork and Rfree are calculated as follows: $R = \sum(|F\text{obs} - F\text{calc}|)/\sum|F\text{obs}|$, where Fobs and Fcalc are the observed and calculated structure factor amplitudes, respectively.

[f] As calculated using MolProbity (Davis et al., 2007).

region 3 of CTPγS no longer forms any covalent interaction with CDP (Fig 4.19A-D). Next, A140 which hydrogen bonds through its main chain with CTPγS no longer interacts with CDP in the ParBΔ44NΔCTD-CDP complex (Fig 4.19A-D). Additionally, the sidechains of Q58 and R59 which form a direct interaction with the γ-phosphate of CTPγS now forms water mediated contacts with the 2nd phosphate group in CDP (Fig 4.19A-D). Furthermore, despite being co-crystallised in the presence of $MgCl_2$, I was unable to observe any clear density to model in any Mg^{2+} atoms in the C-pocket of the ParBΔ44NΔCTD-CDP complex (Fig 4.19A-D). It is therefore likely that CTPγS was hydrolysed during the crystallisation of ParBΔ44NΔCTD-CTPγS complex and the ParBΔ44NΔCTD-CDP complex exists in a post-hydrolysis state. Indeed structural comparison between ParBΔ44NΔCTD-CDP complex and the previously solved *B. subtilis* ParBΔCTD-CDP (Soh et al., 2019) demonstrated both proteins adopt a similar conformation of both the NTD and DBD (Fig. 4.18B). While *M. xanthus* ParB displayed a weak affinity to CDP and NTD of *B. subtilis* failed to self-engage in the presence of CDP (Osorio-Valeriano et al., 2019; Soh et al., 2019), it is likely that the ParBΔ44NΔCTD-CDP complex still maintained NTD self-dimerization due to the high concentration of protein in the crystal.

4.13 Discussion

In this chapter, we report that a small molecule (CTP) is required to enable *C. crescentus* ParB proteins to spread *in vitro*. Furthermore, I provide the structural insights into the nucleating and sliding states of *C. crescentus* ParB. Nucleating ParB is an open clamp in which *parS* DNA is held tightly (nM affinity) at the DBD (Tran et al., 2018). The NTDs of nucleating ParB can adopt multiple alternative conformations, and crucially there is no contact between opposite NTDs. We liken this conformation of the NTD to that of an open gate (NTD-gate), through which *parS* DNA might gain access to the DNA-binding domain (Fig. 4.18). In the sliding state, CTP promotes the self-dimerization of the NTDs, thus closing the NTD-gate (Fig. 4.18). Opposite DBDs also move approx. 10 Å closer together, bringing about a DNA incompatible conformation. Again, I liken this conformation of the DBDs to that of a closed gate (DNA-gate) (Fig. 4.18). Overall, the DNA-gate closure explains how CTP binding might switch ParB from a nucleating to a sliding state. These findings support our observations from BLI analysis that CTP facilitates the dissociation of ParB from *parS* (Fig. 4.8). Upon escaping *parS*, CTP-bound ParB is then able to spread or diffuse along the non-specific DNA flanking *parS*. Indeed, we demonstrated CTP-bound *C. crescentus* ParB did not accumulate on an open DNA suggesting that *C. crescentus* ParB diffuses laterally along the DNA (Fig. 4.10). Similarly, cross-linking experiments on *Bacillus* ParB (Soh et al., 2019) proposed that the ParB-CTP complex forms a sliding clamp that moves along the DNA.

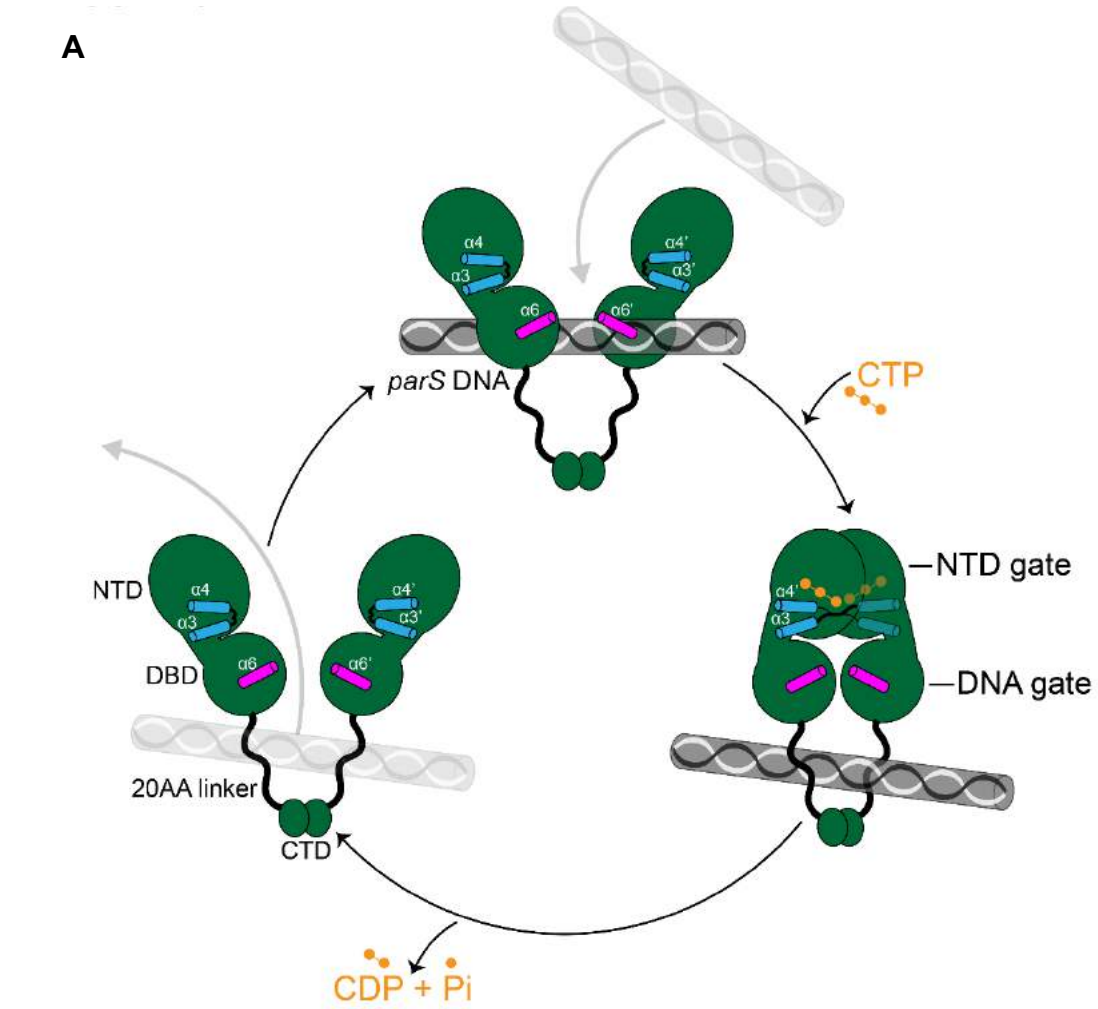
A
α4
α3
α6
α4'
α3'
α6'
parS DNA
CTP
NTD
DBD
20AA linker
CTD
NTD gate
DNA gate
CDP + Pi

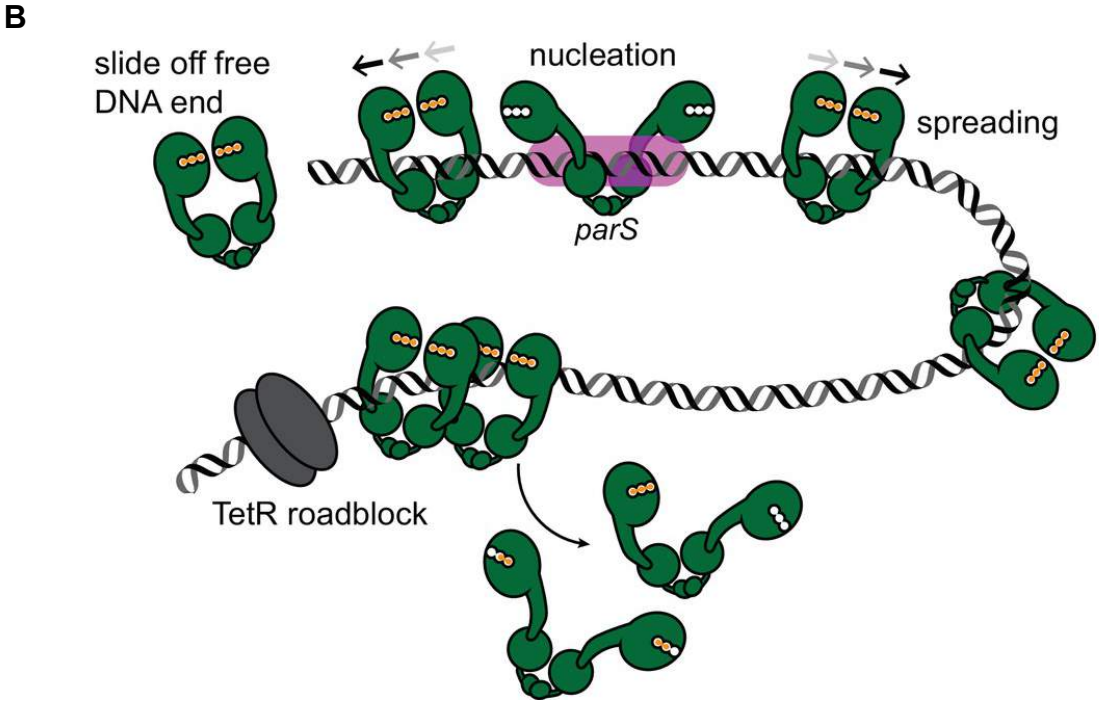
B
slide off free
DNA end
nucleation
spreading
parS
TetR roadblock

Figure 4.21 A model for *C. crescentus* ParB nucleating and sliding cycle. (A) ParB (dark green) consists of three domains: an N-terminal CTP-binding domain (NTD), a central *parS* DNA-binding domain (DBD), a C-terminal dimerization domain (CTD), and a 20 amino acid linker that connects the DBD and the CTD together. Nucleating ParB is an open clamp, in which *parS* DNA is captured at the DNA-binding domain (the DNA-gate). Upon binding CTP (orange), the N-terminal domain (NTD) self-dimerizes to close the NTD-gate of the clamp. CTP-binding and the exchange of helices α4 and α4' (blue) stabilize this closed conformation. The DNA-binding domains also move closer together to close the DNA-gate, potentially driving *parS* DNA into a compartment between the DNA-gate and the CTD. In the nucleotide-bound state, the DBD and the DNA-recognition helices (α6 and α6', magenta) are incompatible with DNA binding. CTP hydrolysis and/or the release of hydrolytic products (CDP and inorganic phosphate Pi) may re-open the gates to discharge DNA. **(B)** *C. crescentus* ParB sliding and spreading on DNA. CTP-bound ParBs diffuse from the nucleation site *parS* and can run off the free DNA end unless they are blocked by DNA-bound roadblocks such as transcriptional regulators e.g. TetR. CTP hydrolysis is not required for ParB to escape from the nucleation *parS* site but might contribute to ParB recycling. It is not yet known whether both CTP molecules on a ParB dimer are concertedly hydrolysed/dissociated for ParB to escape from the chromosome or a heterodimer state of ParB with a single CTP bound also exists *in vivo*.

The closure of the two gates most likely drives *parS* DNA into a compartment in between the DBD and the CTD. Previously, Soh *et. al.,* (2019) compared *B. subtilis* ParBΔCTD-CDP co-crystal structure to that of a *H. pylori* ParBΔCTD-*parS* complex and proposed that DNA must be entrapped in the DBD-CTD compartment (Soh et al., 2019). Here, the available structures of nucleating and sliding ParB from the same bacterial species provides further support that the compartment between the DBD and CTD likely acts as the DNA-entrapping compartment. The linker that connects the DBD and the CTD together is not conserved in amino acid sequence among chromosomal ParB orthologs (Fig. 4.12), however I noted that the linker is invariably ~20 amino acid in length and positively charge lysines are over-represented (Fig. 4.12) The biological significance of the linker length and its lysines, if any, is currently unknown. However, it is worth noting that a human PCNA clamp was proposed to recognize DNA via lysine-rich patches lining the clamp channel, and that these lysine residues help PCNA slides by tracking the DNA backbone (De March et al., 2017). Investigating whether these lysine residues in the DBD-CTD linker of ParB have a similar role is an important subject for the future. If not already bound on DNA, the closed ParB clamp presumably cannot self-load onto *parS* due to its now inaccessible DBD. Indeed, Soh *et. al.,* (2019) *parS* DNA enhances the CTP-dependent NTD-gate closure, thus is likely a built-in mechanism to ensure gate closure results in a productive DNA entrapment (Soh et al., 2019). However, the molecular basis for the parS-enhanced gate closure remains unclear due to the lack of a crystal structure of *C. crescentus* apo-ParB despite my extensive effort.

Herein both the *C. crescentus* ParBΔ44NΔCTD-CDP and the previous structure of a *B. subtilis* ParBΔCTD-CDP complex also have the NTD-gate closed (CTP was hydrolysed to CDP during the crystallisation), hence it is likely that both CTP hydrolysis and the subsequent release of hydrolytic products are necessary to re-open the gates (Soh et al., 2019). However, ParB has a weak to negligible affinity to CDP, hence the CDP-bound ParB species might be short-lived in solution and might not play a significant biological role (Osorio-Valeriano et al., 2019). Once the clamp is re-opened, entrapped DNA might escape via the same route that it first enters. Other well-characterized DNA clamps, for examples, topoisomerases II open their CTD to release trapped DNA. However, the CTDs ParB are stably dimerized independently of *parS* and CTP, hence we speculate that the CTD of ParB is mostly impassable to the entrapped DNA. The released ParB clamp might re-nucleate on *parS* and binds CTP to close the gate, hence restarting the nucleation and sliding cycle. The CTP-bound structure of a *M. xanthus* ParB-like protein, PadC, was solved to a high resolution (1.7 Å), however, PadC does not possess noticeable CTPase activity (Osorio-Valeriano et al., 2019). While the co-crystal of *B. subtilis* and *C. crescentus* ParB with CDP was also solved to a high resolution (1.8 Å and 1.28 Å resolution respectively) but represents a post-hydrolysis state instead. Lastly, our CTPγS-

bound *C. crescentus* ParB crystals diffracted to 2.7 Å, thus preventing water molecules, including a potential catalytic water, from being assigned with confidence. Therefore, the mechanism of CTP hydrolysis by a ParB CTPase remains unresolved. Given that ParB is a founding member of a new CTPase protein family, further studies are needed to fully understand the molecular mechanism of CTP hydrolysis so that the knowledge gained might be generalized to other CTPases.

Taken together I propose the structural basis for a CTP-operated gating mechanism that regulate the opening and closing of a DNA-clamp ParB. CTP functions as a molecular switch that converts ParB from a nucleating to a sliding and DNA-entrapping state. Overall, CTP is crucial for the formation of the higher-order ParB-DNA complex *in vivo*, and ultimately for the faithful chromosome segregation in the majority of bacterial species. Nevertheless, as all the crystal structures I report in this chapter were truncated at the CTD, the role of the CTD in addition to being a dimerization interface is less clear. In the next chapter I investigate the role of the CTD of *C. crescentus* ParB in bacterial chromosome segregation.

4.14 References

1. Böhm, K., Giacomelli, G., Schmidt, A., Imhof, A., Koszul, R., Marbouty, M., and Bramkamp, M. (2020). Chromosome organization by a conserved condensin-ParB system in the actinobacterium Corynebacterium glutamicum. Nat. Commun. **11**, 1485.
2. Breier, A.M., and Grossman, A.D. (2007). Whole-genome analysis of the chromosome partitioning and sporulation protein Spo0J (ParB) reveals spreading and origin-distal sites on the Bacillus subtilis chromosome. Mol. Microbiol. **64**, 703–718
3. Broedersz, C.P., Wang, X., Meir, Y., Loparo, J.J., Rudner, D.Z., and Wingreen, N.S. (2014). Condensation and localization of the partitioning protein ParB on the bacterial chromosome. Proc. Natl. Acad. Sci. U. S. A. **111**, 8809–8814.
4. Chen, B.W., Lin, M.H., Chu, C.H., Hsu, C.E., and Sun, Y.J. (2015). Insights into ParB spreading from the complex structure of Spo0J and parS. Proc. Natl. Acad. Sci. U. S. A. **112**, 6613– 6618.
5. Debaugny, R.E., Sanchez, A., Rech, J., Labourdette, D., Dorignac, J., Geniet, F., Palmeri, J., Parmeggiani, A., Boudsocq, F., Anton Leberre, V., et al. (2018). A conserved mechanism drives partition complex assembly on bacterial chromosomes and plasmids. Mol. Syst. Biol. **14**, e8516.
6. Donczew, M., Mackiewicz, P., Wróbel, A., Flärdh, K., Zakrzewska-Czerwińska, J., and Jakimowicz, D. (2016). ParA and ParB coordinate chromosome segregation with cell elongation and division during Streptomyces sporulation. Open Biol. **6**, 150263.
7. Figge, R.M., Easter, J., and Gober, J.W. (2003). Productive interaction between the

chromosome partitioning proteins, ParA and ParB, is required for the progression of the cell cycle in Caulobacter crescentus. Mol. Microbiol. **47**, 1225–1237.

8. Fisher, G.L.M., Pastrana, C.L., Higman, V.A., Koh, A., Taylor, J.A., Butterer, A., Craggs, T., Sobott, F., Murray, H., Crump, M.P., et al. (2017). The structural basis for dynamic DNA binding and bridging interactions which condense the bacterial centromere. Elife. **6**, e28086.
9. Fogel, M.A., and Waldor, M.K. (2006). A dynamic, mitotic-like mechanism for bacterial chromosome segregation. Genes Dev. **20**, 3269–3282.
10. Graham, T.G.W., Wang, X., Song, D., Etson, C.M., van Oijen, A.M., Rudner, D.Z., and Loparo, J.J. (2014). ParB spreading requires DNA bridging. Genes Dev. **28**, 1228–1238.
11. Gruber, S., and Errington, J. (2009). Recruitment of Condensin to Replication Origin Regions by ParB/SpoOJ Promotes Chromosome Segregation in B. subtilis. Cell. **137**, 685-696
12. Harms, A., Treuner-Lange, A., Schumacher, D., and Søgaard-Andersen, L. (2013). Tracking of Chromosome and Replisome Dynamics in Myxococcus xanthus Reveals a Novel Chromosome Arrangement. PLoS Genet. **9**, e1003802.
13. Hwang, L.C., Vecchiarelli, A.G., Han, Y.W., Mizuuchi, M., Harada, Y., Funnell, B.E., and Mizuuchi, K. (2013). ParA-mediated plasmid partition driven by protein pattern self-organization. EMBO J. **32,** 1238–1249.
14. Ireton, K., Gunther IV, N.W., and Grossman, A.D. (1994). spo0J is required for normal chromosome segregation as well as the initiation of sporulation in Bacillus subtilis. J. Bacteriol. **176**, 5320–5329.
15. Jakimowicz, D., Chater, K., and Zakrzewska-Czerwínska, J. (2002). The ParB protein of Streptomyces coelicolor A3(2) recognizes a cluster of parS sequences within the origin-proximal region of the linear chromosome. Mol. Microbiol. **45**, 1365–1377.
16. Jalal, A.S.B., and Le, T.B.K. (2020). Bacterial chromosome segregation by the ParABS system. Open Biol. **10**, 200097.
17. Jalal, A.S.., Pastrana, C.L., Tran, N.T., Stevenson, C.E., Lawson, D.M., Moreno-Herrero, F., and Le, T.B.. (2019). Structural and biochemical analyses of Caulobacter crescentus ParB reveal the role of its N-terminal domain in chromosome segregation. BioRxiv. 816959.
18. Jalal, A.S., Tran, N.T., and Le, T.B. (2020a). ParB spreading on DNA requires cytidine triphosphate in vitro. Elife. **9**, e53515.
19. Jalal, A.S.B., Tran, N.T., Stevenson, C.E., Chan, E.W., Lo, R., Tan, X., Noy, A., Lawson, D.M., and Le, T.B.K. (2020b). Diversification of DNA-Binding Specificity by Permissive and Specificity-Switching Mutations in the ParB/Noc Protein Family. Cell

Rep. **32**, 107928.

20. Jalal, A.S., Tran, N.T., Stevenson, C.E.M., Chimthanawala, A., Badrinarayanan, A., Lawson, D. M., and Le, T.B. (2021). A CTP-dependent gating mechanism enables ParB spreading on DNA in Caulobacter crescentus. Elife. **10**, e69676.
21. Kawalek, A., Bartosik, A.A., Glabski, K., and Jagura-Burdzy, G. (2018). Pseudomonas aeruginosa partitioning protein ParB acts as a nucleoid-associated protein binding to multiple copies of a parS-related motif. Nucleic Acids Res. **46**, 4592–4606
22. Krissinel, E. (2015). Stock-based detection of protein oligomeric states in jsPISA. Nucleic Acids Res. **43**, W314–W319.
23. Kusiak, M., Gapczyńska, A., Płochocka, D., Thomas, C.M., and Jagura-Burdzy, G. (2011). Binding and spreading of ParB on DNA determine its biological function in Pseudomonas aeruginosa. J. Bacteriol. **193**, 3342–3355.
24. Lagage, V., Boccard, F., and Vallet-Gely, I. (2016). Regional Control of Chromosome Segregation in Pseudomonas aeruginosa. PLoS Genet. **12**, e1006428.
25. Leonard, T.A., Butler, P.J.G., and Löwe, J. (2004). Structural analysis of the chromosome segragation protein Spo0J from Thermus thermophilus. Mol. Microbiol. **53**, 419–432.
26. Leonard, T.A., Butler, P.J., and Löwe, J. (2005). Bacterial chromosome segregation: Structure and DNA binding of the Soj dimer - A conserved biological switch. EMBO J. 24, 270–282.
27. Lim, H.C., Surovtsev, I. V., Beltran, B.G., Huang, F., Bewersdorf, J., and Jacobs-Wagner, C. (2014). Evidence for a DNA-relay mechanism in ParABS-mediated chromosome segregation. Elife. **3**, e02758.
28. Lin, D.C.H., and Grossman, A.D. (1998). Identification and characterization of a bacterial chromosome partitioning site. Cell. **92**, 675–685.
29. Livny, J., Yamaichi, Y., and Waldor, M.K. (2007). Distribution of centromere-like parS sites in bacteria: Insights from comparative genomics. J. Bacteriol. **189**, 8693–8703.
30. Madariaga-Marcos, J., Pastrana, C.L., Fisher, G.L.M., Dillingham, M.S., and Moreno-Herrero, F. (2019). ParB dynamics and the critical role of the CTD in DNA condensation unveiled by combined force-fluorescence measurements. Elife. **9**. e43812.
31. De March, M., Merino, N., Barrera-Vilarmau, S., Crehuet, R., Onesti, S., Blanco, F.J., and De Biasio, A. (2017). Structural basis of human PCNA sliding on DNA. Nat. Commun. **8**, 13935.
32. Mohl, D.A., Easter, J., and Gober, J.W. (2001). The chromosome partitioning protein, ParB, is required for cytokinesis in Caulobacter crescentus. Mol. Microbiol. **42**, 741–755.

33. Murray, H., Ferreira, H., and Errington, J. (2006). The bacterial chromosome segregation protein Spo0J spreads along DNA from parS nucleation sites. Mol. Microbiol. **61**, 1352– 1361.
34. Osorio-Valeriano, M., Altegoer, F., Steinchen, W., Urban, S., Liu, Y., Bange, G., and Thanbichler, M. (2019). ParB-type DNA Segregation Proteins Are CTP-Dependent Molecular Switches. Cell. **179,** 1512–1524.e15.
35. Rodionov, O., ŁObocka, M., and Yarmolinsky, M. (1999). Silencing of genes flanking the P1 plasmid centromere. Science. **283**, 546–549.
36. Romero, P., Obradovic, Z., Li, X., Garner, E.C., Brown, C.J., and Dunker, A.K. (2001). Sequence complexity of disordered protein. Proteins Struct. Funct. Genet. **42**, 38–48.
37. Sanchez, A., Cattoni, D.I., Walter, J.C., Rech, J., Parmeggiani, A., Nollmann, M., and Bouet, J.Y. (2015). Stochastic Self-Assembly of ParB Proteins Builds the Bacterial DNA Segregation Apparatus. Cell Syst. **1**, 163–173.
38. Soh, Y.-M., Davidson, I.F., Zamuner, S., Basquin, J., Bock, F.P., Taschner, M., Veening, J.-W., De, P., Rios, L., Peters, J.-M., et al. (2019). Self-organization of *parS* centromeres by the ParB CTP hydrolase. Science. **366**, 1129–1133.
39. Song, D., Rodrigues, K., Graham, T.G.W., and Loparo, J.J. (2017). A network of cis and trans interactions is required for ParB spreading. Nucleic Acids Res. **45**, 7106–7117.
40. Taylor, J.A., Pastrana, C.L., Butterer, A., Pernstich, C., Gwynn, E.J., Sobott, F., Moreno-Herrero, F., and Dillingham, M.S. (2015). Specific and non-specific interactions of ParB with DNA: Implications for chromosome segregation. Nucleic Acids Res. **43**, 719–731.
41. Toro, E., Hong, S.H., McAdams, H.H., and Shapiro, L. (2008). Caulobacter requires a dedicated mechanism to initiate chromosome segregation. Proc. Natl. Acad. Sci. U. S. A. **2**, a000349.
42. Tran, N.T., Laub, M.T., and Le, T.B.K. (2017). SMC Progressively Aligns Chromosomal Arms in Caulobacter crescentus but Is Antagonized by Convergent Transcription. Cell Rep. **32**, 107928
43. Tran, N.T., Stevenson, C.E., Som, N.F., Thanapipatsiri, A., Jalal, A.S.B., and Le, T.B.K. (2018). Permissive zones for the centromere-binding protein ParB on the Caulobacter crescentuschromosome. Nucleic Acids Res. **46**, 1196–1209.
44. Vecchiarelli, A.G., Mizuuchi, K., and Funnell, B.E. (2012). Surfing biological surfaces: Exploiting the nucleoid for partition and transport in bacteria. Mol. Microbiol. **86**, 513–523.
45. Vecchiarelli, A.G., Neuman, K.C., and Mizuuchi, K. (2014). A propagating ATPase gradient drives transport of surface-confined cellular cargo. Proc. Natl. Acad. Sci. U.

S. A. **111**, 4880–4885.

46. Vucetic, S., Brown, C.J., Dunker, A.K., and Obradovic, Z. (2003). Flavors of protein disorder. Proteins Struct. Funct. Genet. **52**, 573–584.
47. Wang, X., Brandão, H.B., Le, T.B.K., Laub, M.T., and Rudner, D.Z. (2017). Bacillus subtilis SMC complexes juxtapose chromosome arms as they travel from origin to terminus. Science. **355**, 524–527.
48. Wu, L.J., and Errington, J. (2004). Coordination of cell division and chromosome segregation by a nucleoid occlusion protein in Bacillus subtilis. Cell. **117**, 915–925.
49. Wu, L.J., Ishikawa, S., Kawai, Y., Oshima, T., Ogasawara, N., and Errington, J. (2009). Noc protein binds to specific DNA sequences to coordinate cell division with chromosome segregation. EMBO J. **28**, 1940–1952.

Chapter 5: Dissecting the role of the C-terminal domain of *C. crescentus* ParB in chromosome segregation

Parts of this chapter have been deposited in BioRxiv, for which I performed most of the experiments and wrote the first draft of the manuscript:

Jalal, A.S., Pastrana, C.L., Tran, N.T., Stevenson, C.E., Lawson, D.M., Moreno-Herrero, F., and Le, T.B.. (2019). Structural and biochemical analyses of Caulobacter crescentus ParB reveal the role of its N-terminal domain in chromosome segregation. BioRxiv. 816959.

5.1 Introduction

5.2 Engineering a lysine-rich surface into the *C. crescentus* ParB C-terminal domain (CTD) resulted in variants with non-specific DNA-binding *in vitro*

5.3 Engineering a lysine-rich surface into the *C. crescentus* ParB CTD resulted in variants with enhanced non-specific DNA condensation activity *in vitro*

5.4 *C. crescentus* cells harbouring ParB variants with *in vitro* DNA condensation activity are viable *in vivo*

5.5 *C. crescentus* ParB variants with enhanced *in vitro* condensation do not spread out more extensively *in vivo*

5.6 Discussion

5.7 References

5.1 Introduction

In roughly two-thirds of known bacterial species, the conserved ParA-ParB-*parS* complex ensures faithful chromosome segregation (Donczew et al., 2016; Fogel and Waldor, 2006; Harms et al., 2013; Ireton et al., 1994; Jakimowicz et al., 2002; Kawalek et al., 2018; Lin and Grossman, 1998; Livny et al., 2007; Mohl et al., 2001; Tran et al., 2018). The *parS* site is the first DNA locus to be segregated after chromosome replication (Lagage et al., 2016; Lin and Grossman, 1998; Livny et al., 2007; Toro and Shapiro, 2010). ParB, a DNA-binding protein, nucleates on *parS* before binding to cytidine triphosphate (CTP) to slide along the adjacent non-specific DNA (spreading) to form a network of protein-DNA complexes (Jalal et al., 2020; Osorio-Valeriano et al., 2019; Soh et al., 2019). This nucleoprotein network in turn interacts with ParA to partition the *parS* locus, hence the chromosome to each daughter cell. Chromosomally encoded ParBs contains an N-terminal domain (NTD), a central *parS*-specific DNA-binding domain (DBD), and a C-terminal domain (CTD) (Figure 5.1). The NTD and DBD are generally conserved between ParB orthologs, while the CTD exhibits high sequence variability, with exception to a conserved leucine-zipper residues that mediate ParB dimerisation (Fisher et al., 2017). The NTD contains the highly conserved arginine rich patch (GERRXR) that has been shown to be essential for ParB spreading by forming the CTP interacting pocket (Jalal et al., 2020; Osorio-Valeriano et al., 2019; Soh et al., 2019).

In the previous chapter (Chapter 4), I provided the structural basis for the transition between nucleation to spreading by solving co-crystal structures of were truncated at the CTD *C. crescentus* ParB with *parS* and with a CTP analogue. ParB nucleates as an open clamp, whereby *parS* is captured by the DNA-binding domain (DNA-gate). Upon binding CTP, the N-terminal domain (NTD) self-engages to form a patch clamp. The DNA-gate also closes to likely drive *parS* into compartment between the DNA-gate and the C-terminal domain, thus enabling ParB to spread by sliding along the non-specific DNA flanking the *parS* site as patch clamp ring. However, as both co-crystal structures lacked the CTD, the role of the CTD in ParB spreading by *C. crescentus* ParB remains less clear. Interestingly, in *B. subtilis*, in addition to the NTD, the CTD of ParB has been proposed to mediate the formation of the ParB-DNA nucleoprotein complex (Fisher et al., 2017; Madariaga-Marcos et al., 2019; Taylor et al., 2015). *B. subtilis* ParB was shown to bind non-specific DNA to condense both DNA *in vitro*; these activities were attributed to a positively charged lysine rich surface found within the CTD (Fisher et al., 2017; Taylor et al., 2015). Despite this, the sequence of the CTD diverges more rapidly than other domains of ParB, thus it is unclear whether ParBs from other bacterial species also possess a functionally equivalent CTD. Moreover, the relationship between the *in vitro* DNA condensation and the *in vivo* spreading is unclear.

In this chapter we show that the CTD of *C. crescentus* ParB, in contrast to that of *B. subtilis* ParB, does not display non-specific DNA-binding or DNA condensation activities *in vitro* (Fisher et al., 2017; Taylor et al., 2015). Engineered *C. crescentus* ParB variants with an enhanced non-specific DNA-binding activity can condense DNA *in vitro* but do not spread further than wild-type protein *in vivo*. Overall, these results suggest that the CTD in *C. crescentus* ParB most likely functions as a primary dimerisation interface.

5.2 Engineering a lysine-rich surface into the *C. crescentus* ParB CTD resulted in variants with non-specific DNA-binding *in vitro*

Previously, *B. subtilis* ParB was reported to condense DNA *in vitro* independently of *parS* and the DNA condensation activity was mediated by a positively charged lysine rich surface on the CTD (Fisher et al., 2017; Taylor et al., 2015). However, unlike *B. subtilis* ParB, the CTD of *C. crescentus* ParB lacks a lysine-rich patch and the wild-type protein does not bind or displays weak affinity to non-specific DNA *in vitro* (Tran et al., 2018) (Fig 5.2A). Thus, I hypothesised that the introduction of a lysine rich surface into the CTD of *C. crescentus* would generate *C. crescentus* ParB with enhanced non-specific DNA-binding activity *in vitro*. To test this hypothesis, I systematically introduced either single (1K), double (2K), triple (3K), quadruple (4K), or quintuple (5K) lysine substitutions from the *B. subtilis* ParB CTD into equivalent positions on the CTD of *C. crescentus* ParB (Fig. 5.1A-B). Ten variants were purified to homogeneity using a one-step Ni^{2+} affinity column as detailed in Chapter 2 (Material and Methods), and purity of each protein was assessed by SDS-PAGE analysis (Fig. 5.1B). To directly assess their binding to a *parS* or a scrambled *parS* DNA i.e. non-specific DNA, I attached a linear 20 bp biotinylated *parS* or scrambled- *parS* containing DNA to a streptavidin-coated probe to measure by bio-layer interference (BLI). BLI assay monitors wavelength shifts (responses) resulting from changes in the optical thickness of the probe surface during association or dissociation of the analyte (see Chapter 2). Observed protein-DNA interactions were recorded as BLI-responses (nm), and three different concentrations of protein (1000 nm, 500nm, 250nm) were used.

As expected, all ten tested ParB variants retained their binding activities to *parS* (Fig. 5.2). Interestingly, BLI response (nm) of the lysine-bearing ParB variant with the *parS* containing DNA was much higher than that to *C. crescentus* ParB (WT). Hence, it is likely that the presence of these lysine residues increases the overall affinity of ParB towards the *parS* site. I was unable to detect any noticeable non-specific DNA-binding activity for the 1K and 2K variants (Fig. 5.2), suggesting that the introduction of more lysine residues at the CTD is required to generate a *C. crescentus* ParB with enhanced non-specific DNA binding activity *in*

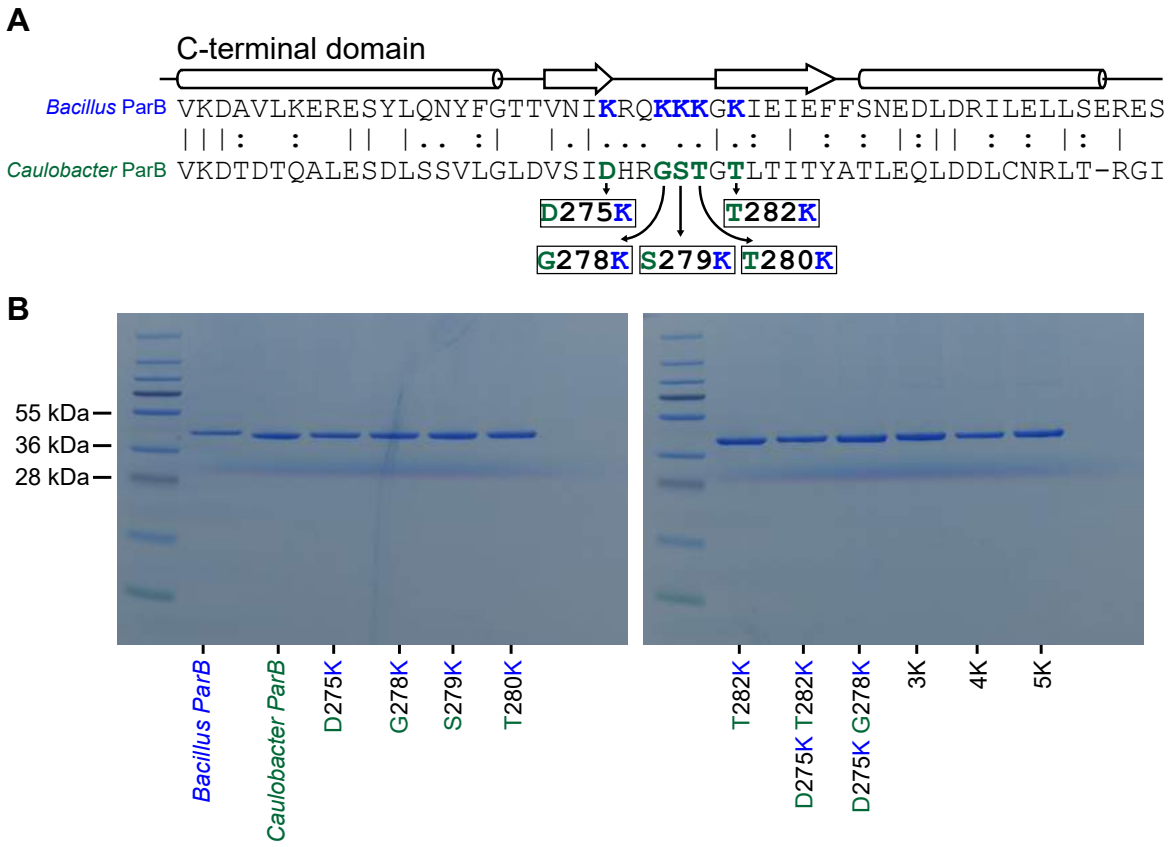

Figure 5.1 Lysine bearing *C. crescentus* ParB variants at the C-terminal domain (CTD) **(A)** Sequence alignment between *C. crescentus* (dark green) and *B. subtilis* ParB (blue) shows that *C. crescentus* ParB lacks the equivalent lysine-rich amino acid patch at its CTD. Lysine residues that are important for the nonspecific DNA-binding and DNA condensation activities in *B. subtilis* ParB, and positional equivalent residues in *C. crescentus* ParB are highlighted in blue and green, respectively. Secondary-structure elements for *B. subtilis* ParB CTD (PDB accession number: 5NOC) are shown above the sequence alignment. **(B)** *C. crescentus* ParB (WY) and lysine bearing variants were expressed in *E. coli* and purified to near homogeneity. All variants were C-terminally His-tagged (KLAAALEHHHHHH).

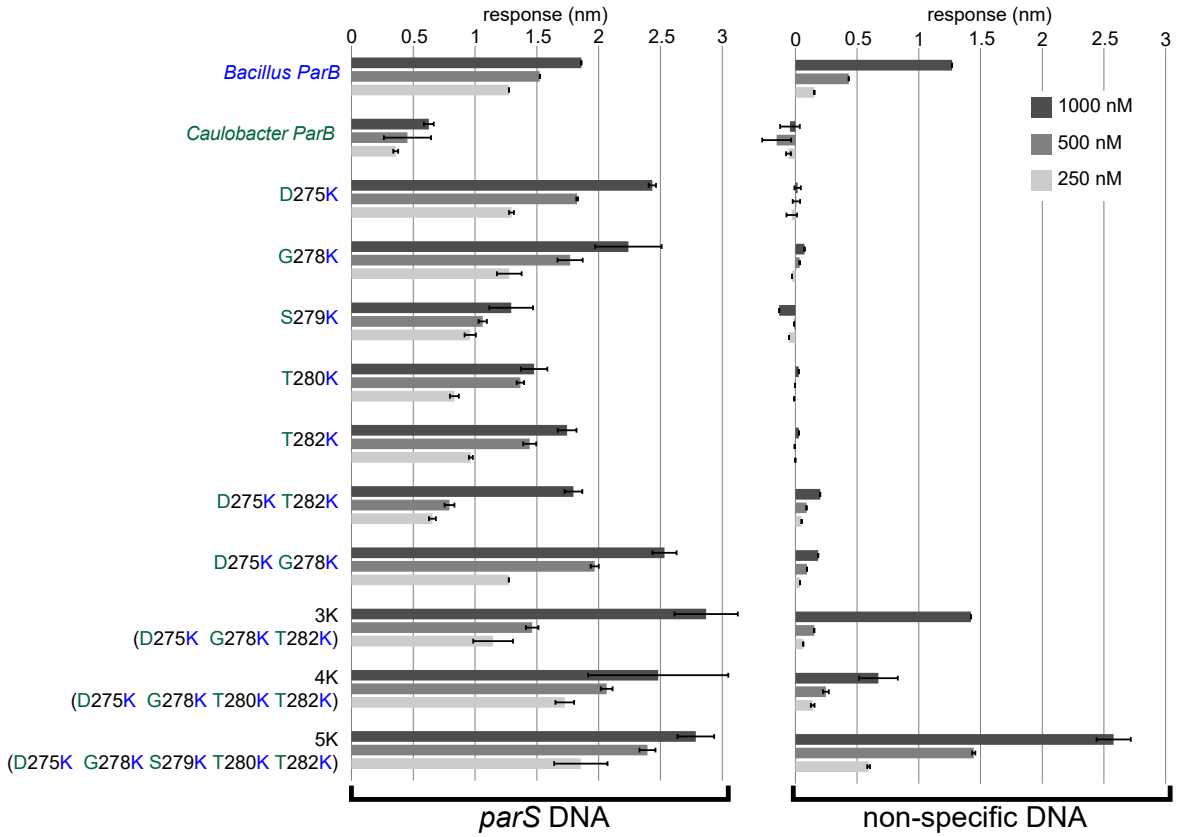

Figure 5.2 Lysine bearing *C. crescentus* ParB variants at the C-terminal domain (CTD) binds non-specific DNA *in vitro*. Introducing three or more lysine residues to the *C. crescentus* CTD resulted in ParB variants with enhanced non-specific DNA-binding activity. In vitro binding affinities between ParB variants and parS DNA (left panel), and non-specific scrambled parS DNA (right panel). Bio-layer interferometry assays were used to measure the binding affinity of ParB (250, 500, and 1000 nM) to 20-bp double-stranded DNA that contains a parS site or a scrambled parS site. The level of ParB binding to DNA was expressed as response units (nm in shifted wavelength). Error bars represent standard deviation (SD) from three replicates.

vitro. Indeed, the further introduction of lysine residues created 3K, 4K, and 5K variants that binds with nonspecific DNA similarly to that of *B. subtilis* ParB (Fig. 5.2). Next, I wondered whether these *C. crescentus* ParB variants with *B. subtilis*-like *in vitro* non-specific DNA binding would also condense DNA *in vitro*.

5.3 Engineering a lysine-rich surface into the *C. crescentus* ParB CTD resulted in variants with enhanced non-specific DNA condensation activity *in vitro*

To determine whether the engineered non-specific DNA-binding activity of *C. crescentus* ParB (3K-5K) variants (Fig. 5.3) would also condense DNA *in vitro*, we performed magnetic tweezer experiments on these variants and compared their ability to condense DNA to that of wild-type *C. crescentus* and *B. subtilis* ParBs (Fig. 5.3A) (A collaboration with Dr. Cesar L. Pastrana and Prof. Fernando Herrero-Moreno, CSIC, Spain). Briefly, in this setup, a DNA containing a single *parS* site is attached onto a glass slide on one end and onto a magnetic bead on the other (Taylor et al., 2015). Above the bead are a pair of magnets which allows the application of force onto the DNA, hence permitting the change in the extension of the DNA. The extension of a tethered DNA is then tracked, and any observation of a decrease in extension that was substantially larger than by the applied force alone is an indication of DNA condensation (Fig. 5.3A).

The *C. crescentus* ParB (WT) and variants (3K-5K) with engineered non-specific DNA-binding activity were purified using a three-step column-procedure (as detailed in Chapter 2). In brief, overproduced His_6-tagged ParB variants (3K-5K) were purified from an *E. coli* cell lysate using a Ni^{2+} affinity column, followed by a Heparin column, and a final gel filtration purification step. The purity of each eluted fraction was assessed by SDS-PAGE. Magnetic tweezer experiments were performed at 1 μM concentration of proteins and at different forces using an identical setup and conditions described in experiments with *B. subtilis* ParB (Fisher et al., 2017; Taylor et al., 2015). Previously, *B. subtilis* ParB was shown to condense both non-*parS* DNA and *parS* containing DNA (Fisher et al., 2017; Taylor et al., 2015). As expected, no noticeable change in extension in relation to applied force was observed when *C. crescentus* ParB (WT) was incubated with either *parS* or the non-*parS* containing DNA 1 μM concentration (Fig.5.3B). Therefore, in contrast to *B. subtilis* ParB, *C. crescentus* ParB does not possess any noticeably DNA condensation activity *in vitro*, likely due to *C. crescentus* ParB (WT) displaying a low binding affinity to non-specific DNA *in vitro*. However, the incubation of the 3K, 4K, or 5K ParB variants with the tethered *parS* or scrambled *parS* containing DNA, resulted in a decrease in the DNA extension that was greater than that attributable to a decrease in applied force alone (Fig. 5.3B). These findings demonstrate that introduction of three to five lysine residues to the *C. crescentus* ParB CTD resulted in the ability to condense

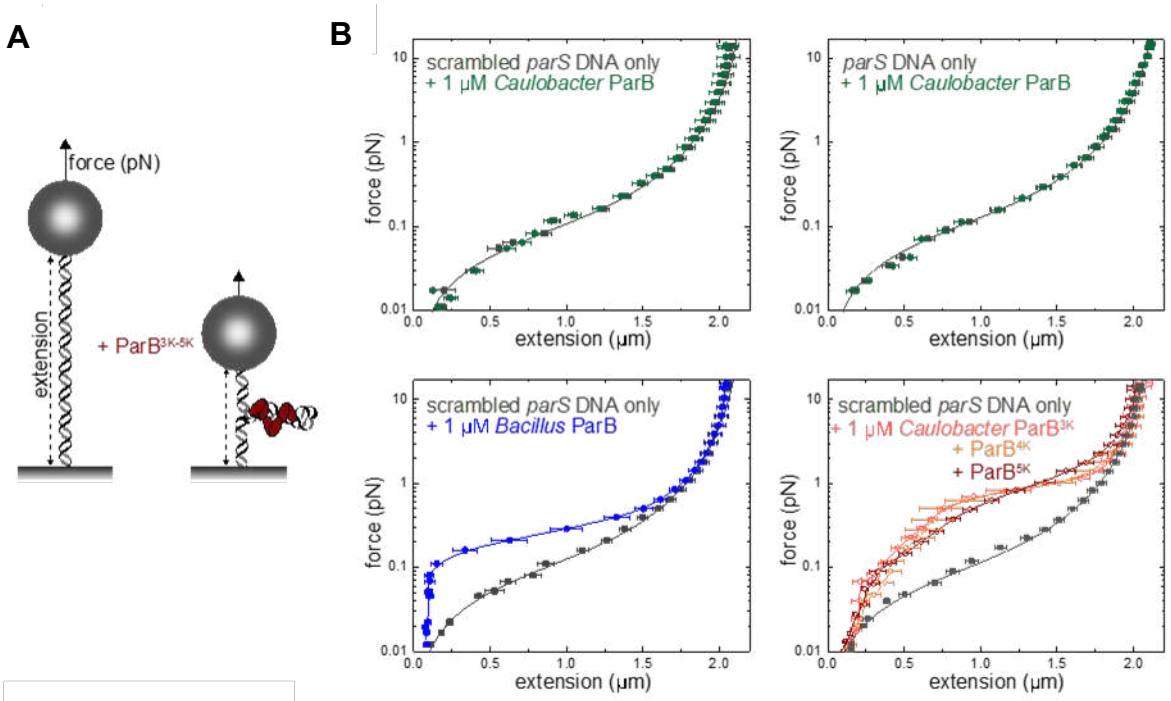

Figure 5.3 Lysine bearing *C. crescentus* ParB variants at the C-terminal domain (CTD) condense non-specific DNA *in vitro*. (A) Schematic of the magnetic tweezer assay that monitored ParB-dependent DNA condensation (see also the Materials and Methods). **(B)** Mean force-extension curves for parS DNA or scrambled parS DNA in the presence of 2 μM *C. crescentus* ParB (WT) (dark green), *B. subtilis* ParB (WT) (blue), and *C. crescentus* ParB (3K-5K) variants (pink, orange, and brown). Data for bare DNA were fitted to the worm-like chain model. Solid lines for data in the presence of ParB variants serve as a guide to the eye. Data for non-condensed DNA were fitted to the worm-like chain model. Errors are the standard error of measurements on different molecules (N ≥ 15 molecules).

DNA non-specifically *in vitro*. In the next section, I sought to determine whether the generated ParB with enhanced *in vitro* DNA condensation activity would affect ParB function *in vivo*.

5.4 *C. crescentus* cells harbouring ParB variants with *in vitro* DNA condensation activity are viable *in vivo*

Next, I wondered whether these *C. crescentus* ParB variants with enhanced *in vitro* DNA condensation activity were functional *in vivo*. In *C. crescentus*, ParB is essential for cell viability, thus mutations that perturb ParB function are lethal. A *flag* tag was fused into the ParB-encoding gene of each lysine-bearing variant (1K-5K) and each allele was cloned downstream of a vanillate-inducible promoter (P_{van}) (Thanbichler et al., 2007). I then used transduction to transform a strain of *C. crescentus* where its native *parB* is under the control of a P_{xyl} and repressed by glucose with the vanillate-inducible FLAG-ParB lysine-bearing variants. Western blotting using anti-FLAG antibodies was then used to confirm the presence of the FLAG-ParB lysine-bearing variants in these *C. crescentus* strains (Fig. 5.4A). When PYE was supplemented with xylose, the P_{xyl} promoter is able to drive the transcription of the native *parB*, thereby allowing chromosome segregation and cell viability. The addition of glucose however inhibits *parB* transcription in this strain of *C. crescentus* and results in ParB depletion, followed by cell death. *C. crescentus* cells were viable when the PYE medium was supplemented with both vanillate and glucose as the P_{van} promoter was able to initiate the transcription of *parB* (1K-5K) variants (Fig 5.4B-C). These findings therefore suggest that the additional lysine residues at the CTD did not impair ParB function in *C. crescentus*.

Western blot analysis using anti-FLAG antibodies was then performed to determine whether these lysine-bearing ParB variants were produced at a stable level *in vivo*. Overnight cultures of *C. crescentus* strains harbouring the ParB lysine-bearing variants were grown in PYE supplemented with vanillate and glucose. Cells were left to grow at an ~OD_{600}, before being pelleted and loaded onto an equal volume of total protein was loaded SDS-PAGE gel. Indeed, western blotting using α-FLAG antibodies confirmed that the ParB variants were produced at a roughly equal level compared to ParB (WT) (Fig 5.4D). I then sought to use chromatin immunoprecipitation coupled to deep sequencing (ChIP-seq) to determine whether these ParB variants would spread further on the *C. crescentus* chromosome.

5.5 *C. crescentus* ParB variants with an in vitro DNA condensation activity did not spread more extensively *in vivo*

Next, I wondered whether these *C. crescentus* ParB with enhanced DNA-condensation activity of the ParB (3K-5K) variants would display an increased spreading ability *in vivo*. To test this,

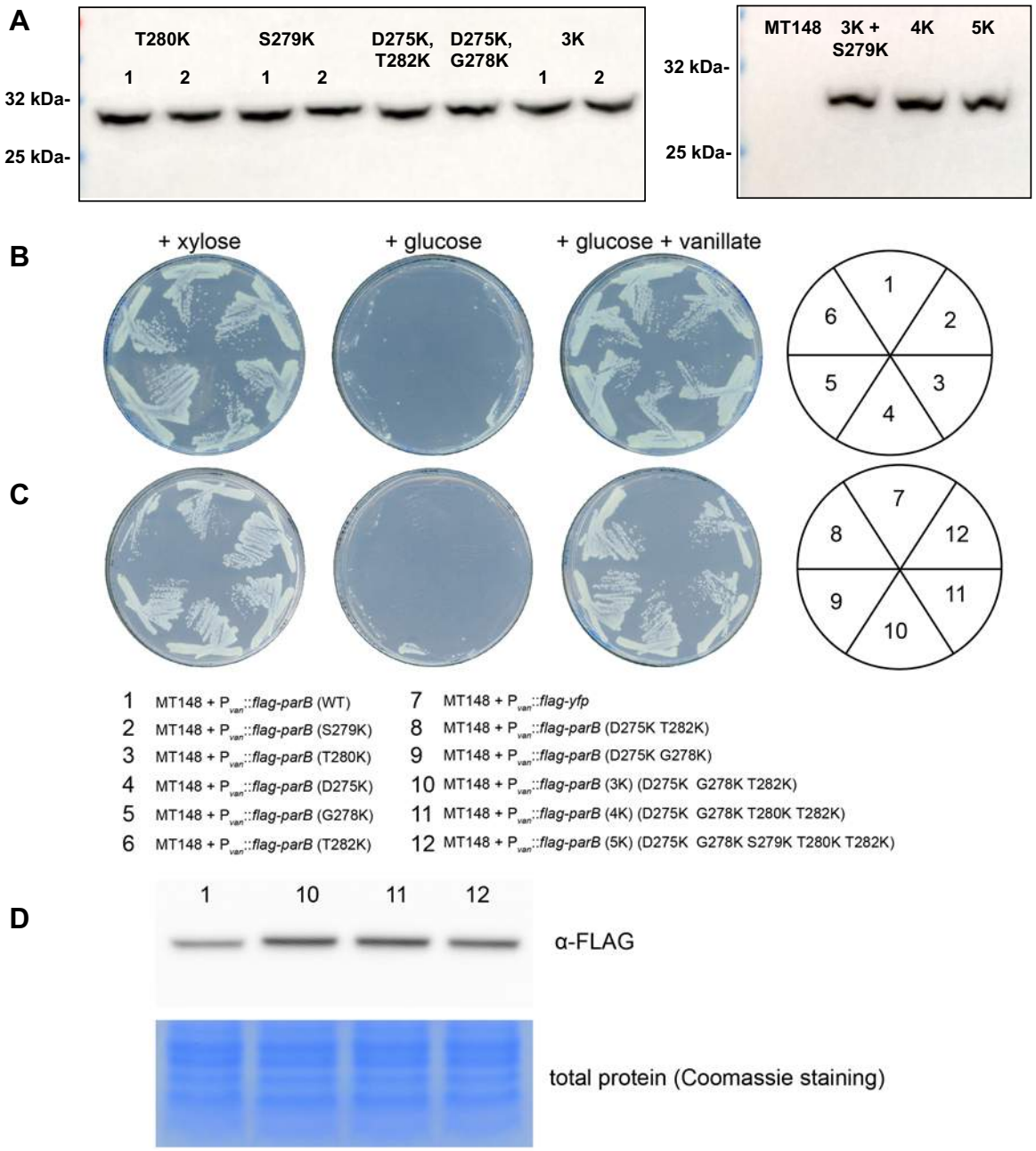

Figure 5.4 Lysine bearing *C. crescentus* ParB variants at the CTD are functional *in vivo*. (**A**) α-FLAG immunoblot analysis of the generated *C. crescentus* strains to confirm the presence *C. crescentus* ParB (1K to 5K) variants. Strains were grown in medium supplemented with xylose and vanillate. (**B-C**) *C. crescentus* ParB (1K to 5K) variants were expressed from the van locus (vanillate inducible) in the ParB (WT)-depletable background (*C. crescentus* MT148: parB::Pxyl-parB). In the presence of xylose, ParB (WT) was produced and all strains were viable, including strain 7 that expressed yfp from the van locus. On the other hand, the addition of glucose repressed the production of ParB (WT) while other ParB variants were not produced, leading to loss of viability. In the presence of both glucose and vanillate, only ParB (1K to 5K) variants were produced. Cell growth for strains (2 to 6, and 8 to 12) indicated that ParB (1K to 5K) variants can complement the lack of ParB (WT) in *C. crescentus*. (**D**) α-FLAG immunoblot analysis of *C. crescentus* strains 1, 10, 11, 12 (see panel B) grown in medium supplemented with glucose and vanillate.

I performed α-FLAG ChIP-seq experiments on *C. crescentus* strains expressing individual FLAG-tagged ParB variant in a ParB (WT)-depletable background (Thanbichler and Shapiro, 2006). As a positive control for these ChIP-seq experiments, I used a strain of *C. crescentus* expressing a FLAG-tagged version of ParB (WT). While as a negative control, a non-spreading FLAG-ParB (R104A) mutant (Tran et al., 2018), and a non-DNA-binding protein FLAG-YFP were included. *C. crescentus* cells were depleted of the native untagged ParB, and the expression of the ParB (WT) and variants were induced by the addition and glucose and vanillate before cells were fixed with 1% formaldehyde for ChIP-seq. DNA-bound to FLAG-ParB (WT), variants and FLAG-YFP was then pulled down through the use of α-FLAG antibody coupled to sepharose beads.

Consistent with the previous findings, the ChIP-seq profile of a FLAG-ParB (WT) showed a clear enrichment above the background in the ~10 kb region from 4030 to 4040 kb on the chromosome (Fig. 5.5) (Tran et al., 2018). This extensive ChIP-seq profile is consistent with ParB (WT) spreading on the chromosome *in vivo* and contrasts the ChIP-seq profile observed in the spreading impaired FLAG-ParB (R104A) in which the enrichment was confined to just ~500 bp immediately surrounding *parS* sites (Tran et al., 2018) (Fig. 5.5). As expected for a negative control, no enrichment was seen in the ChIP-seq profile for the FLAG-YFP. Interestingly, the ChIP-seq profiles of the FLAG-ParB (3K-5K) variants were less extended than the FLAG-ParB (WT), despite these ParB variants displaying enhanced DNA condensation activity *in vitro*. Noticeably, the overall heights of the ChIP-seq profiles of ParB (3K-5K) were lower when compared to the ChIP-seq profile of ParB (WT). It is likely that ParB (3K-5K) might bind DNA non-specifically along the chromosome, thereby titrating ParB molecules away from the *parS* cluster, hence resulting in a lower concentration of DNA-bound ParB near *parS*. Another possibility is ParB (3K-5K) are defective at the *parS* nucleation step, however this is unlikely as ParB (3K-5K) retain their *pars* binding activities *in vitro* (Fig. 5.2) and were expressed to a comparable level to wild-type protein *in vivo* (Fig. 5.4D). Thus, these results demonstrate that the *C. crescentus* ParB variants with an enhanced *in vitro* DNA condensation activity do not display any increase in intrinsic spreading ability *in vivo*.

5.6 Discussion

In this chapter, I characterise the relationship between the CTP-independent *in vitro* DNA condensation and *in vivo* spreading abilities of ParB, by generating *C. crescentus* ParB variants with enhanced *in vitro* DNA condensation activity. Previously (Chapter 4), I demonstrated the structural basis of ParB spreading, whereby CTP-binding promotes NTD-NTD engagement and the DNA-binding domain adopts a conformation that no longer favours

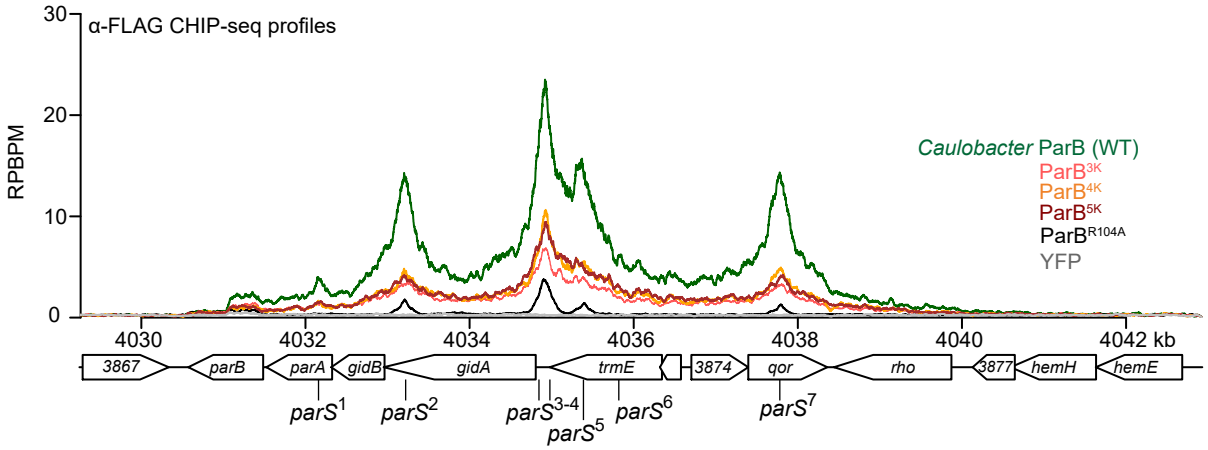

Figure 5.5. Engineered *C. crescentus* ParB variants with an enhanced DNA condensation activity in vitro do not spread further than the wild-type protein in vivo. ChIP-seq profiles of a FLAG-tagged *C. crescentus* ParB (WT) (dark green), a spreading-incompetent FLAG-ParB (R104A), a non-DNA-binding protein FLAG-YFP (grey), and FLAG-ParB (3K-5K) variants (pink, orange, and brown). ChIP-seq signals were reported as the number of reads at every nucleotide along the genome (RPBPM value). The genomic context (4030 kb to 4042 kb) and parS sites are shown below the ChIP-seq profiles.

were truncated at the CTD, thus the role of the CTD (in addition to dimerisation) is less clear. While in *B. subtilis*, the CTD of ParB contributes of towards the formation of the ParB-DNA nucleoprotein complex by acting as both as a dimerisation and DNA-binding and bridging interface via its non-specific DNA binding and condensation activities, the CTD is poorly conserved and *C. crescentus* ParB lacks lysine rich surface and does not condense DNA *in vitro* (Fisher et al., 2017; Graham et al., 2014; Madariaga-Marcos et al., 2019; Taylor et al., 2015). Indeed, *C. crescentus* ParB possessing a *B. subtilis* like DNA condensation activity, displayed no enhancement in ParB spreading. It is therefore likely that CTD of *C. crescentus* ParB may function primarily as a dimerisation interface.

Initially, it was surprising to find that *C. crescentus* ParB displays little affinity to non-specific DNA *in vitro* since both current models for ParB-DNA nucleoprotein complex assembly ("spreading and bridging", "nucleation and caging" and "spread by sliding") require some degree of interaction between ParB and nonspecific DNA (Broedersz et al., 2014; Debaugny et al., 2018; Fisher et al., 2017; Graham et al., 2014; Jalal et al., 2020; Osorio-Valeriano et al., 2019; Sanchez et al., 2015; Soh et al., 2019; Taylor et al., 2015). However, while I did not observe non-specific DNA-binding activity at 1 μM *C. crescentus* ParB in vitro, the local concentration of ParB in close proximity to *parS* has been estimated to reach ~500 μM inside *C. crescentus* cells (Lim et al., 2014). At this high concentration, it can be speculated that the central DBD can bind to DNA non-specifically. Intriguingly, in *C. crescentus* the five *parS* sites that displays the strongest affinity to *C. crescentus* ParB cluster more closely (within a ~5 kb DNA segment (Tran et al., 2018) whereas in *B. subtilis*, the four strongest *parS* sites are dispersed within a ~57 kb region on the chromosome (Lee and Grossman, 2006). Thus, it is likely that a closer clustering *parS* sites, promotes the formation of the *C. crescentus* ParB-*parS* nucleoprotein complex, despite *C. crescentus* ParB displaying a lower affinity for non-specific DNA. Interestingly, in *B. subtilis* cells, the concentration of ParB is much lower than in *C. crescentus* (~140 dimers compared to ~360 dimers per origin of replication (Lim et al., 2014). As the *parS* sites in *B. subtilis* is more dispersed than in *C. crescentus*, it is likely that *B. subtilis* ParB requires the enhanced non-specific DNA binding/condensation activity to promote the formation of the ParB-DNA nucleoprotein complex.

Furthermore, the role of CTP in the DNA bridging and condensation activities of *B. subtilis* ParB is not fully understood. Certainly our single-molecule biophysical approaches have demonstrated that *C. crescentus* ParB is unable to condense DNA, despite being able to form the higher order ParB-*parS* complex *in vivo* (Tran et al., 2018). As CTP was required to reconstitute the spreading ability of ParB *in vitro*, it is not unreasonable to speculate that CTP may promote the DNA bridging and condensation activities of *C. crescentus* ParB (Jalal et al.,

2020). Studies utilizing *B. subtilis* ParB has complicated attempts to distinguish the difference between ParB bridging (NTD-NTD oligomerization) and DNA condensation (Chen et al., 2015; Fisher et al., 2017; Graham et al., 2014; Madariaga-Marcos et al., 2019; Song et al., 2017; Taylor et al., 2015). Although it is clear that NTD-NTD oligomerization of ParB is also necessary for DNA condensation, neither *B. subtilis* CTD alone nor *B. subtilis* ParB with mutations at the arginine-rich patch (at the NTD) can condense DNA *in vitro* (Fisher et al., 2017; Madariaga-Marcos et al., 2019). As *C. crescentus* ParB lacks this CTP-independent DNA condensation activity *in vitro*, perhaps future studies utilizing *C. crescentus* ParB may enable us to further distinguish between the bridging and condensation activities of ParB and clarify the involvement of CTP in these functions.

5.7 References

1. Broedersz, C.P., Wang, X., Meir, Y., Loparo, J.J., Rudner, D.Z., and Wingreen, N.S. (2014). Condensation and localization of the partitioning protein ParB on the bacterial chromosome. Proc. Natl. Acad. Sci. U. S. A. **111**, 8809–8814.
2. Chen, B.W., Lin, M.H., Chu, C.H., Hsu, C.E., and Sun, Y.J. (2015). Insights into ParB spreading from the complex structure of Spo0J and parS. Proc. Natl. Acad. Sci. U. S. A. **112**, 6613– 6618.
3. Debaugny, R.E., Sanchez, A., Rech, J., Labourdette, D., Dorignac, J., Geniet, F., Palmeri, J., Parmeggiani, A., Boudsocq, F., Anton Leberre, V., et al. (2018). A conserved mechanism drives partition complex assembly on bacterial chromosomes and plasmids. Mol. Syst. Biol. **14**, e8516.
4. Donczew, M., Mackiewicz, P., Wróbel, A., Flärdh, K., Zakrzewska-Czerwińska, J., and Jakimowicz, D. (2016). ParA and ParB coordinate chromosome segregation with cell elongation and division during Streptomyces sporulation. Open Biol. **6**, 150263.
5. Fisher, G.L.M., Pastrana, C.L., Higman, V.A., Koh, A., Taylor, J.A., Butterer, A., Craggs, T., Sobott, F., Murray, H., Crump, M.P., et al. (2017). The structural basis for dynamic DNA binding and bridging interactions which condense the bacterial centromere. Elife. **6**. e28086
6. Fogel, M.A., and Waldor, M.K. (2006). A dynamic, mitotic-like mechanism for bacterial chromosome segregation. Genes Dev. **20**, 3269–3282
7. Graham, T.G.W., Wang, X., Song, D., Etson, C.M., van Oijen, A.M., Rudner, D.Z., and Loparo, J.J. (2014). ParB spreading requires DNA bridging. Genes Dev. **28**, 1228–1238.
8. Harms, A., Treuner-Lange, A., Schumacher, D., and Søgaard-Andersen, L. (2013). Tracking of Chromosome and Replisome Dynamics in Myxococcus xanthus Reveals a Novel Chromosome Arrangement. PLoS Genet. **9**, e1003802.

9. Ireton, K., Gunther IV, N.W., and Grossman, A.D. (1994). spo0J is required for normal chromosome segregation as well as the initiation of sporulation in Bacillus subtilis. J. Bacteriol. **176**, 5320–5329.
10. Jakimowicz, D., Chater, K., and Zakrzewska-Czerwínska, J. (2002). The ParB protein of Streptomyces coelicolor A3(2) recognizes a cluster of parS sequences within the origin-proximal region of the linear chromosome. Mol. Microbiol. **45**, 1365–1377.
11. Jalal, A.S.., Pastrana, C.L., Tran, N.T., Stevenson, C.E., Lawson, D.M., Moreno-Herrero, F., and Le, T.B.. (2019). Structural and biochemical analyses of Caulobacter crescentus ParB reveal the role of its N-terminal domain in chromosome segregation. BioRxiv. 816959.
12. Jalal, A.S., Tran, N.T., and Le, T.B. (2020). ParB spreading on DNA requires cytidine triphosphate in vitro. Elife. **9**, e53515.
13. Kawalek, A., Bartosik, A.A., Glabski, K., and Jagura-Burdzy, G. (2018). Pseudomonas aeruginosa partitioning protein ParB acts as a nucleoid-associated protein binding to multiple copies of a parS-related motif. Nucleic Acids Res. **46**, 4592–4606.
14. Lagage, V., Boccard, F., and Vallet-Gely, I. (2016). Regional Control of Chromosome Segregation in Pseudomonas aeruginosa. PLoS Genet. **12**, e1006428.
15. Lee, P.S., and Grossman, A.D. (2006). The chromosome partitioning proteins Soj (ParA) and Spo0J (ParB) contribute to accurate chromosome partitioning, separation of replicated sister origins, and regulation of replication initiation in Bacillus subtilis. Mol. Microbiol. **60**, 853-869.
16. Lim, H.C., Surovtsev, I. V., Beltran, B.G., Huang, F., Bewersdorf, J., and Jacobs-Wagner, C. (2014). Evidence for a DNA-relay mechanism in ParABS-mediated chromosome segregation. Elife. **3**, e02758.
17. Lin, D.C.H., and Grossman, A.D. (1998). Identification and characterization of a bacterial chromosome partitioning site. Cell. **92**, 675–685.
18. Livny, J., Yamaichi, Y., and Waldor, M.K. (2007). Distribution of centromere-like parS sites in bacteria: Insights from comparative genomics. J. Bacteriol. **189**, 8693–8703.
19. Madariaga-Marcos, J., Pastrana, C.L., Fisher, G.L.M., Dillingham, M.S., and Moreno-Herrero, F. (2019). ParB dynamics and the critical role of the CTD in DNA condensation unveiled by combined force-fluorescence measurements. Elife. **9**. e43812.
20. Mohl, D.A., Easter, J., and Gober, J.W. (2001). The chromosome partitioning protein, ParB, is required for cytokinesis in Caulobacter crescentus. Mol. Microbiol. **42**, 741–755.
21. Osorio-Valeriano, M., Altegoer, F., Steinchen, W., Urban, S., Liu, Y., Bange, G., and Thanbichler, M. (2019). ParB-type DNA Segregation Proteins Are CTP-Dependent

Molecular Switches. Cell. **179,** 1512–1524.e15.

22. Sanchez, A., Cattoni, D.I., Walter, J.C., Rech, J., Parmeggiani, A., Nollmann, M., and Bouet, J.Y. (2015). Stochastic Self-Assembly of ParB Proteins Builds the Bacterial DNA Segregation Apparatus. Cell Syst. **1**, 163–173.
23. Soh, Y.-M., Davidson, I.F., Zamuner, S., Basquin, J., Bock, F.P., Taschner, M., Veening, J.-W., De, P., Rios, L., Peters, J.-M., et al. (2019). Self-organization of *parS* centromeres by the ParB CTP hydrolase. Science. **366**, 1129-1133.
24. Song, D., Rodrigues, K., Graham, T.G.W., and Loparo, J.J. (2017). A network of cis and trans interactions is required for ParB spreading. Nucleic Acids Res. **45**, 7106–7117.
25. Taylor, J.A., Pastrana, C.L., Butterer, A., Pernstich, C., Gwynn, E.J., Sobott, F., Moreno-Herrero, F., and Dillingham, M.S. (2015). Specific and non-specific interactions of ParB with DNA: Implications for chromosome segregation. Nucleic Acids Res. **43**, 719–731.
26. Thanbichler, M., and Shapiro, L. (2006). MipZ, a Spatial Regulator Coordinating Chromosome Segregation with Cell Division in Caulobacter. Cell. **126**, 147–162.
27. Thanbichler, M., Iniesta, A.A., and Shapiro, L. (2007). A comprehensive set of plasmids for vanillate - And xylose-inducible gene expression in Caulobacter crescentus. Nucleic Acids Res. **35**, e137.
28. Toro, E., and Shapiro, L. (2010). Bacterial chromosome organization and segregation. Cold Spring Harb. Perspect. Biol. ***2***, a000349.
29. Tran, N.T., Stevenson, C.E., Som, N.F., Thanapipatsiri, A., Jalal, A.S.B., and Le, T.B.K. (2018). Permissive zones for the centromere-binding protein ParB on the Caulobacter crescentuschromosome. Nucleic Acids Res. **46**, 1196–1209.

Chapter 6: CTP regulates the membrane-binding activity of the nucleoid occlusion protein Noc

This chapter has been deposited published in Molecular Cell, for which I performed almost all of the experiments and wrote the first draft of the manuscript:

Jalal ASB, Tran NT, Wu LJ, Ramkrishnan K, Rejzek M, Stevenson CEM, Lawson, DM, Errington, J and Le TBK. 2020. CTP regulates membrane-binding activity of the nucleoid occlusion protein Noc. Molecular Cell, **21**, S1097–2765.

6.1 Introduction

6.2 *NBS* DNA increases the CTP binding and hydrolysis rate of Noc

6.3 CTP and *NBS* DNA stimulate the engagement of the N-terminal domain of Noc *in vitro*

6.4 A clamp-like Noc associates with a closed *NBS* DNA substrate in a CTP-dependent manner

6.5 Noc binds liposomes in the presence of CTP

6.6 Noc recruits *NBS* plasmid to liposomes in the presence of CTP

6.7 The association of Noc-*NBS* DNA with liposomes is reversible

6.8 Crystal structure of *Geobacillus thermoleovorans* NocΔCTD shows the membrane-targeting amphipathic helix in an autoinhibitory conformation

6.9 Crystal structure of the *G. thermoleovorans* NocNΔ26ΔCTD variant is incompatible with an autoinhibitory conformation of the amphipathic helix

6.10 Discussion

6.11 References

6.1 Introduction

While ATP and GTP switches are ubiquitous in biology, CTP switches have rarely been identified but may be more widespread than previously appreciated. A recent discovery showed ParB, a crucial protein for bacterial chromosome segregation, is the founding member of a new class of CTP-dependent molecular switch (Osorio-Valeriano et al., 2019; Soh et al., 2019). ParB nucleates on a *parS* DNA sequence and must associate with neighbouring DNA, a process known as spreading, to enable faithful chromosome segregation (Breier and Grossman, 2007; Funnell, 2016; Graham et al., 2014; Jalal and Le, 2020; Murray et al., 2006; Sanchez et al., 2015). CTP induces ParB self-dimerisation to create a clamp-like molecule. The ParB clamp self-loads at *parS*, then spreads by sliding to neighbouring DNA while still entrapping DNA (Breier and Grossman, 2007; Funnell, 2016; Graham et al., 2014; Jalal and Le, 2020; Jalal et al., 2020a; Murray et al., 2006; Sanchez et al., 2015; Soh et al., 2019) Essentially, CTP serves to switch ParB from a *parS*-nucleating open clamp to a DNA-sliding closed clamp state (Jalal et al., 2020a; Soh et al., 2019). The end result is the formation of a higher-order nucleoprotein complex with multiple ParB-CTP clamps entrapped at the vicinity of the *parS* locus. The higher-order nucleoprotein complex stimulates the ATPase activity of ParA, a partner of ParB, driving the segregation of replicated chromosomes to daughter cells (Hwang et al., 2013; Jalal and Le, 2020; Lim et al., 2014; Vecchiarelli et al., 2013, 2014).

In Firmicutes, the nucleoid occlusion protein Noc is a paralogue of ParB (Jalal et al., 2020b; Sievers et al., 2002; Wu and Errington, 2012), however the role of Noc is different from that of a canonical ParB (Pang et al., 2017; Veiga et al., 2011; Wu et al., 2009). Noc directs the assembly of the cell division machinery towards the middle of a dividing cell where the concentration of chromosomal DNA (the nucleoid) is the least, thus ensuring a binary cell division (Adams et al., 2014; Rodrigues and Harry, 2012; Wu and Errington, 2004). Noc does so by nucleating on 16-bp *NBS* sites scattered around the chromosome before spreading to neighbouring DNA to form large Noc-DNA nucleoprotein complexes (Adams et al., 2015; Wu et al., 2009). Unusually, Noc is also a peripheral membrane protein that directly associates with the cell membrane via an N-terminal amphipathic helix (Fig. 6.1A) (Adams et al., 2015). The recruitment of the chromosomal DNA to the membrane is crucial to prevent the division machinery formation over the chromosome; a Noc variant lacking the amphipathic helix is impaired in nucleoid occlusion activity. In *Bacillus subtilis*, Noc was observed to associate with the cell membrane in a transient manner *in vivo* (Wu et al., 2009). It was thought that a strong membrane-binding activity of Noc might have been selected against since a stable association with the membrane might hamper chromosome replication and segregation, yet it is unclear how the membrane-binding activity of Noc is regulated. Furthermore, Noc must bring the chromosomal DNA to the membrane to physically inhibit the division machinery formation; an

unregulated membrane-binding activity would likely confine apo-Noc permanently to the cell membrane, thus unfavourably limiting the recruitment of DNA to the membrane (Adams et al., 2015). Again, it remains unclear whether the membrane-binding activity of Noc is regulated, and if so how.

To investigate further, I biochemically reconstitute *NBS*-dependent Noc spreading and membrane association events using purified *B. subtilis* Noc protein and phospholipid vesicles (liposomes). I show that, similar to a canonical ParB, Noc is a CTPase enzyme that binds CTP to form a protein clamp that can slide and entrap DNA. Importantly, CTP binding, but not hydrolysis, is required to switch Noc-DNA from a membrane inactive to an active state, thus locking Noc into a pathway in which it has to spread before associating with the cell membrane. I solve an X-ray crystal structure of a C-terminal domain truncated apo-Noc from *Geobacillus thermoleovorans*, in which its membrane-targeting amphipathic helix adopts an autoinhibitory conformation, restricted from interacting with the membrane. I suggest that CTP binding might liberate the amphipathic helix, thereby switching Noc to a membrane-active state. Altogether, I demonstrate that CTP directly regulates the membrane-binding activity of the nucleoid occlusion protein Noc, further expanding the role of CTP switches in biology.

6.2 *NBS* DNA increases the CTP binding and hydrolysis rate of Noc

Given the shared ancestry between ParB and Noc, we wondered if *B. subtilis* Noc also binds and hydrolyses CTP. To investigate, Ngat Tran employed a membrane-spotting assay (DRaCALA) and showed that *B. subtilis* Noc binds radiolabelled CTP but only in the presence of a cognate 22-bp *NBS* DNA (Fig. 6.2A). An excess of unlabelled CTP, but no other NTP, outcompeted radiolabelled CTP for binding to Noc, suggesting that *B. subtilis* Noc binds CTP specifically (Fig. 6.2B). Similarly, an N-terminally truncated Noc variant lacking the 10-AA membrane targeting amphipathic helix (NocNΔ10) also bound radiolabelled CTP in the presence of *NBS* DNA (Fig. 6.2C). However, the Noc (R89A) and Noc (N121S) (with both R89 and N121S being found in the NTD) variants, whose equivalent substitutions in ParB have been shown to impair spreading and CTP binding (Fig. 6.1B), did not bind radiolabelled CTP at the tested concentration (Fig. 6.2C) (Jalal et al., 2020a; Osorio-Valeriano et al., 2019; Soh et al., 2019). Next, I performed a quantitative nucleotide-binding assay using isothermal titration calorimetry (ITC) with a non/slow hydrolysable CTP analogue (CTPɣS) to ensure the heat exchange was solely due to nucleotide-binding but not hydrolysis or DNA binding. I found that *B. subtilis* Noc binds CTPɣS with a moderate affinity (K_d = 67.5 ± 23 μM), while Noc (N121S) bound CTPɣS weaker at K_d = 231.5 ± 66 μM, and Noc (R89A) did not detectably bind nucleotide (Fig. 6.3). Consistent with a previous report, *B. subtilis* Noc also showed CTP hydrolysis activity, albeit at a low rate of ~1 CTP per Noc per hour when only the purified

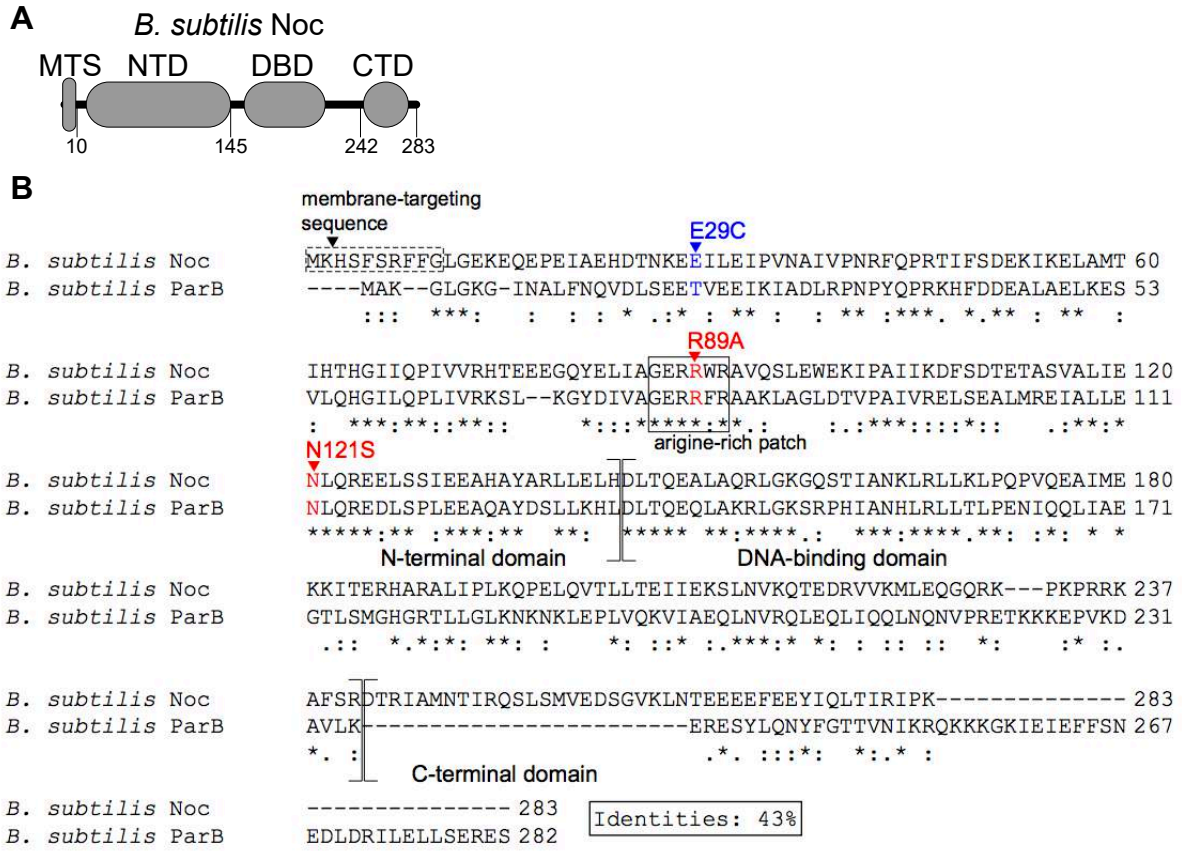

Figure 6.1 Schematic representation of the Noc protein (A) The domain architecture of *B. subtilis* Noc: a membrane-targeting sequence (MTS) that contains an amphipathic helix, an N-terminal domain (NTD), a central DNA-binding domain (DBD), and a C-terminal domain (CTD). **(B)** A sequence alignment between *B. subtilis* Noc and its paralog ParB. The conserved arginine-rich patch that mediates CTP binding in *B. subtilis* ParB is shown in a solid box. Residues E29 (blue), R89 (red) and N121 (red) in *B. subtilis* Noc, whose equivalent substitutions in *B. subtilis* ParB have been showed to impair spreading and CTP binding, were substituted by alanine and serine, respectively.

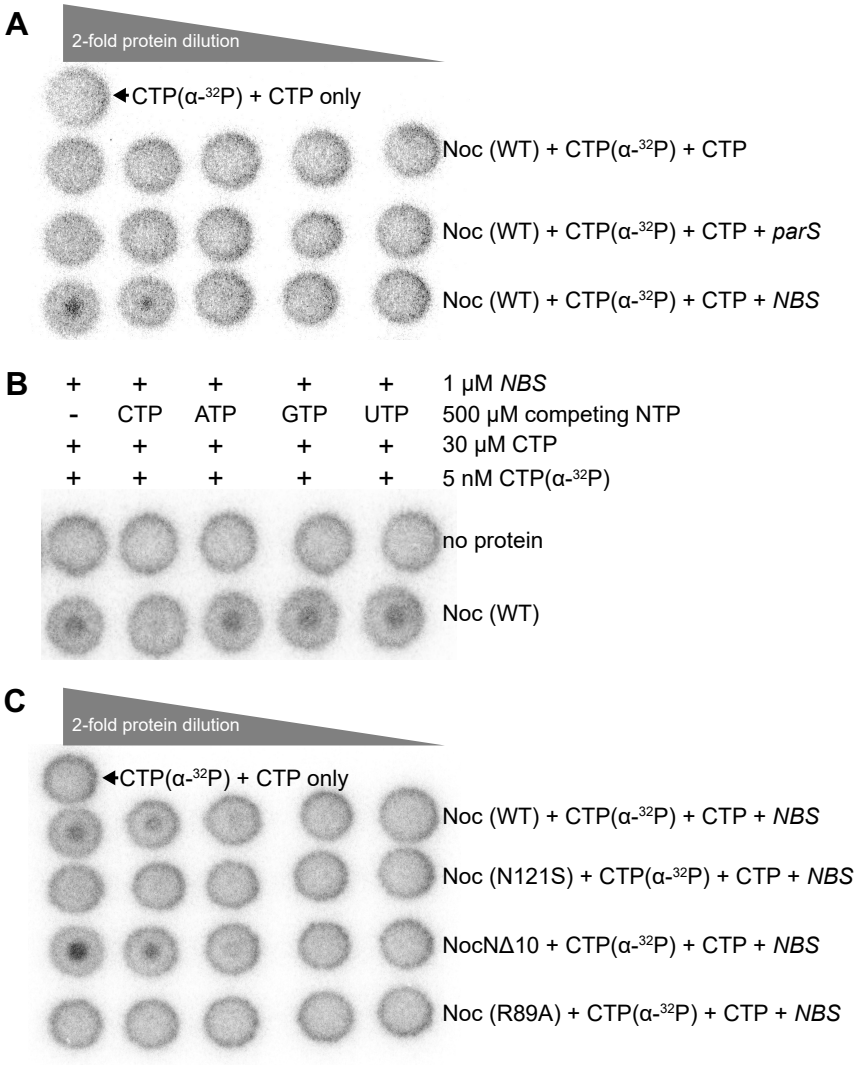

Figure 6.2 Noc binds CTP in the presence of *NBS* DNA. CTP binding as monitored by DRaCALA assay using radiolabelled CTP α-P^{32}. The bulls-eye staining indicates CTP binding due to a more rapid immobilization of protein-ligand complexes compared to free ligands. The starting concentration of Noc used in all panels was 30 μM. The concentrations of CTP α-P^{32}, unlabelled CTP, and a 22-bp *parS*/*NBS* DNA used in all panels were 5 nM, 30 μM, and 1 μM, respectively.

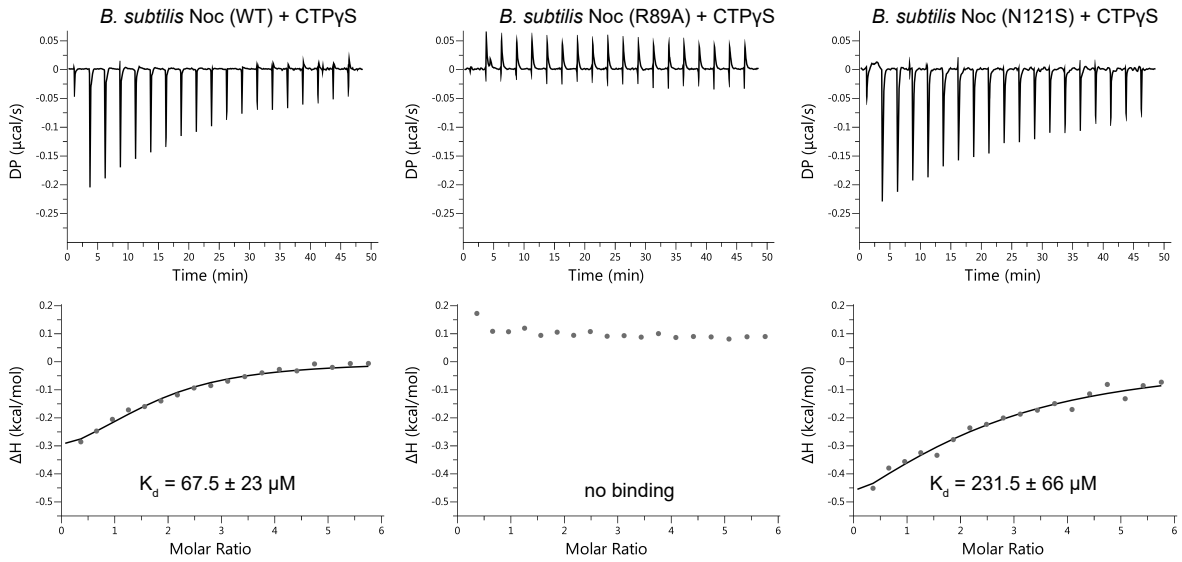

Figure 6.3 Interactions between Noc (WT and mutants) with a slow hydrolysable analogue of CTP, CTPɣS. Analysis of the interaction of *B. subtilis* Noc (WT and mutants) with CTPɣS by isothermal calorimetry (ITC). Each experiment was duplicated. Regression curves were fitted, and binding affinities (K_d) are shown.

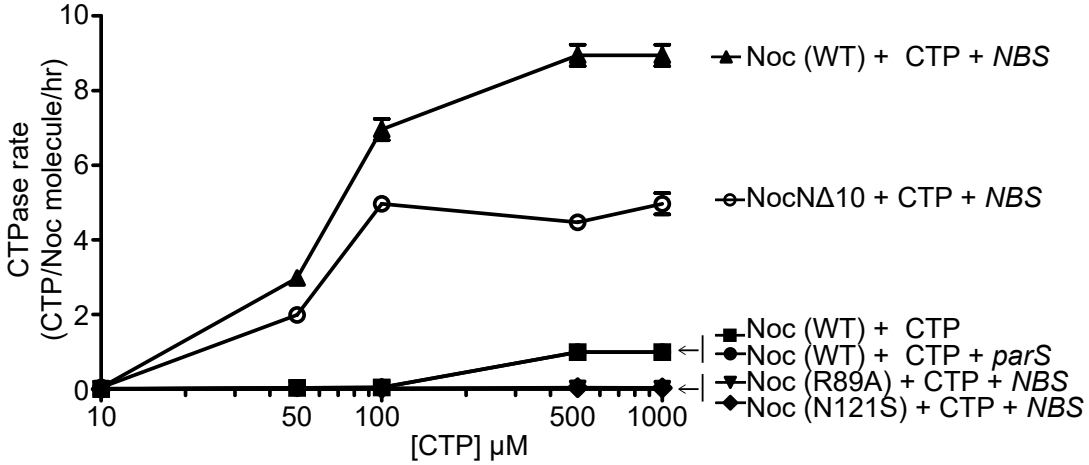

Figure 6.4 Noc hydrolyses CTP in the presence of *NBS* DNA. CTP hydrolysis rate of Noc (WT) and variants, measured by a continuous detection of released inorganic phosphates (see Materials and Methods). CTPase rates were measured at increasing concentration of CTP. All reactions contained 1 µM Noc (WT/variants) ± 1 µM 22-bp *NBS* or *parS* DNA and an increasing concentration of CTP (0, 10, 50, 100, 500, and 1000 µM). Experiments were triplicated and standard deviation of the CTPase rates were presented.

protein and CTP were included (Fig. 6.4) (Soh et al., 2019). The addition of 22-bp *NBS* DNA, but not a non-cognate 22-bp *parS* DNA, increased the CTP hydrolysis rate nine fold to ~9 CTP per Noc per hour (Fig. 6.4) (Soh et al., 2019). The Noc (R89A) and Noc (N121S) variants did not show noticeable CTP-hydrolysing activity (Fig. 6.4). Lastly, despite binding CTP equally or more strongly than the WT (Fig. 6.4), NocNΔ10 hydrolysed CTP at a reduced rate of ~5 CTP per Noc per hour (Fig. 6.4) (see Discussion). Altogether, our data suggest that *B. subtilis* Noc is a CTPase enzyme that binds and hydrolyses CTP in the presence of cognate DNA.

6.3 CTP and *NBS* DNA stimulate the engagement of the N-terminal domain of Noc *in vitro*

In the presence of CTP, ParB self-engages at the N-terminal domain (NTD) to create a clamp-like molecule (Jalal et al., 2020a; Soh et al., 2019). To investigate whether CTP elicits a similar response in Noc, I employed site-specific crosslinking of a purified *B. subtilis* Noc (E29C) variant by a sulfhydryl-to-sulfhydryl crosslinker bismaleimidoethane (BMOE). Residue E29 at the NTD were substituted by cysteine on an otherwise cysteine-less Noc (WT) background (Fig. 6.5A) to create a variant in which symmetry-related cysteines become covalently linked together if they are within 8 Å of each other. The cross-linked form was detectable as a protein form with reduced mobility on SDS-PAGE (labelled X in Figure 6.5B). In the absence of CTP, Noc (E29C) crosslinked minimally (~10% crosslinked fraction, lanes 2-4 of Fig. 6.5B). The crosslinking efficiency increased threefold (~30%) in the presence of CTP (lane 8 of Fig. 6.5B), but not CDP or ATP (Fig. 6.5B and Fig. 6.5C). The crosslinking efficiency further increased fivefold (~55%) when both CTP and a 22-bp *NBS* were included (lane 10 of Fig 6.5B, and Fig. 6.5E). However, the addition of a non-cognate 22-bp *parS* DNA did not result in the same high level of crosslinking even when CTP was present (lane 9 of Fig. 6.5B). Noticeably, a slow-hydrolysable CTP analogue CTPɣS readily promoted crosslinking (~45% crosslinked fraction) regardless of the presence or absence of *NBS* DNA (lanes 8-10 of Fig. 6.5D, and Fig. 6.5F). Therefore, my data suggest that CTP binding, but not hydrolysis, is required for the NTD engagement of *B. subtilis* Noc. Consistent with the requirement of CTP binding for NTD engagement, the Noc (E29C R89A) variant, in which the R89A substitution incapacitated CTP binding, did not crosslink beyond the background level in any tested condition (Fig. 6.6A). The Noc (E29C N121S) variant, which binds CTP (albeit at a reduced affinity) but cannot hydrolyse CTP, crosslinked similarly to Noc (E29C) (~30% crosslinked fraction) at the saturating concentration of 1 mM CTP, though the *NBS*-stimulated crosslinking was abolished (Fig. 6.6B). Lastly, the NocNΔ10 (E29C) variant, which lacks the N-terminal amphipathic helix, crosslinked similarly to Noc (E29C) in the presence of CTP and *NBS* DNA (Fig. 6.6C).

6.4 A Noc clamp associates with a closed *NBS* substrate in a CTP-dependent manner

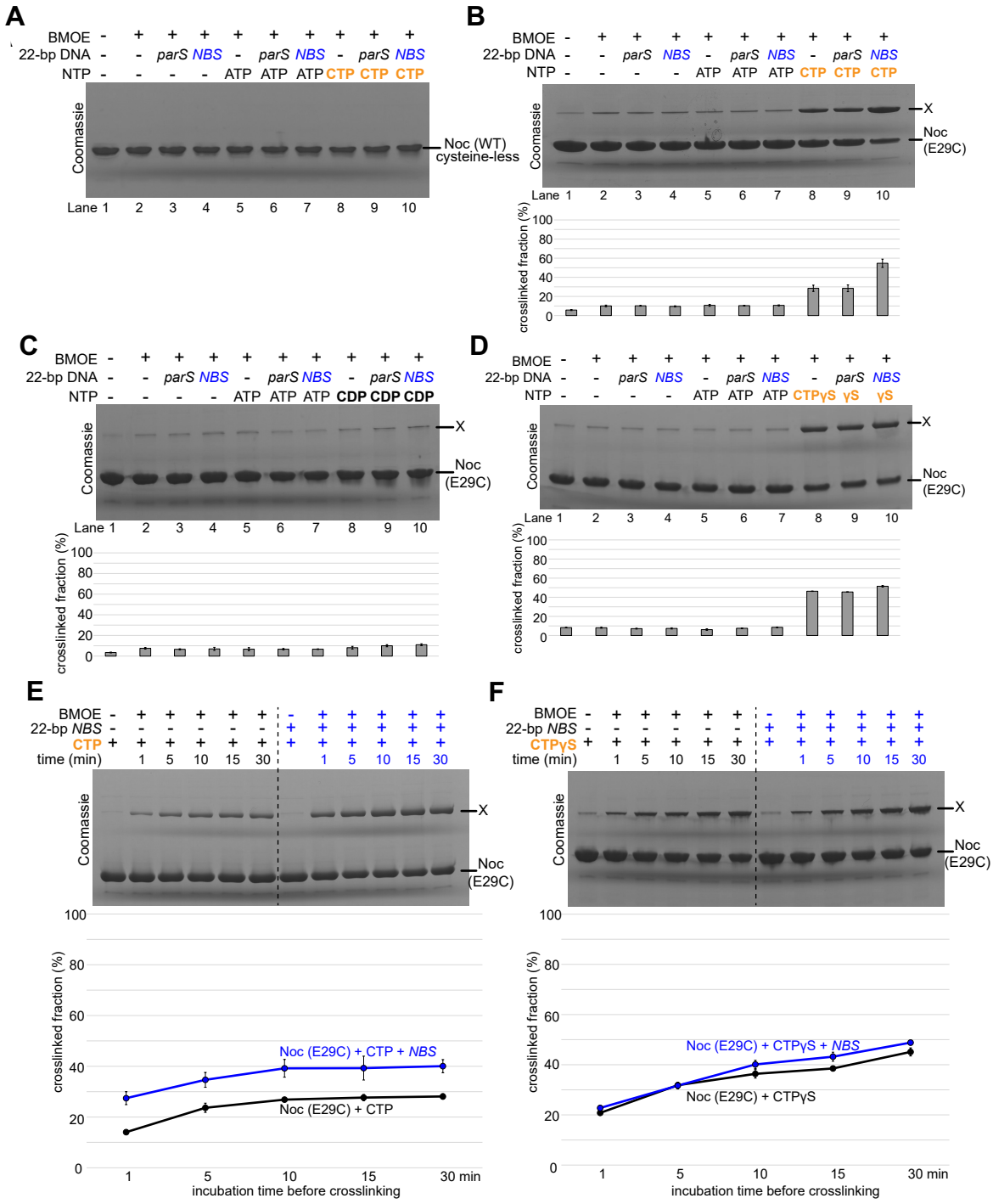
A
BMOE
22-bp DNA
NTP
Coomassie
Noc (WT) cysteine-less
Lane 1 2 3 4 5 6 7 8 9 10
B
X
Noc (E29C)
crosslinked fraction (%)
C
CDP CDP CDP
D
CTPγS γS γS
E
22-bp NBS
CTP
time (min)
Noc (E29C) + CTP + NBS
Noc (E29C) + CTP
incubation time before crosslinking
F
CTPγS
Noc (E29C) + CTPγS + NBS
Noc (E29C) + CTPγS

Figure 6.5 CTP and *NBS* DNA promote the self-engagement of the N-terminal domain of Noc. (A) SDS-PAGE analysis of BMOE crosslinking products of 10 μM *B. subtilis* Noc (WT) protein ± 1.0 μM 22-bp *parS*/*NBS* DNA ± 1.0 mM NTP. Wild-type Noc naturally lacks cysteine, hence does not crosslink in the presence of BMOE. All crosslinking reactions were performed at 22°C unless indicated otherwise. Quantification of the crosslinked fraction is shown below each representative image. Error bars represent SEM from three replicates. **(B)** Same as panel A but Noc (E29C) was used instead. X indicates a crosslinked form of Noc (E29C). **(C)** Same as panel B expect CDP instead of CTP was used. **(D)** Same as panel A but CTPɣS instead of CTP was used. **(E)** Time-course of Noc (E29C) crosslinking with CTP in the presence or absence of 22-bp *NBS* DNA. Purified Noc (E29C) was preincubated with 1.0 mM CTP ± 1 μM 22-bp *NBS* DNA for 1, 5, 10, 15, or 30 min at 4°C (instead of the usual 22°C) before BMOE was added. A lower incubation temperature was needed to slow down the reaction. Quantification of the crosslinked fraction is shown below each representative image. Error bars represent SE from three replicates. **(F)** Same as panel D, but 1.0 mM CTPɣS was used instead.

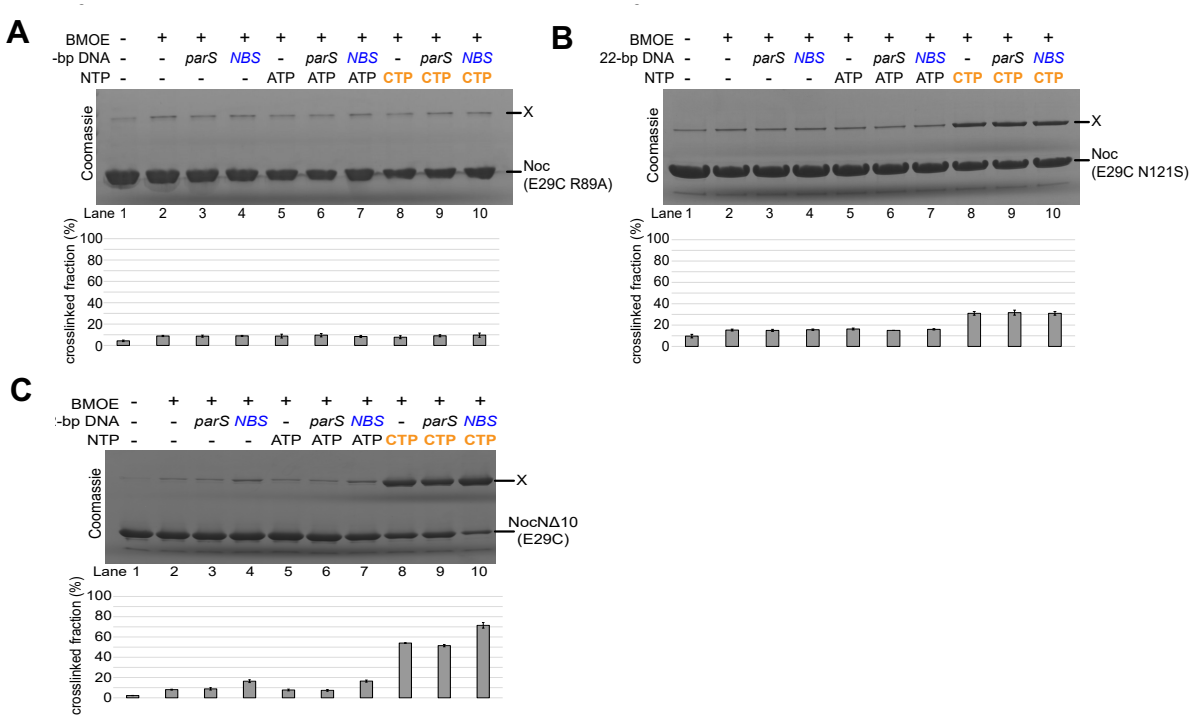

Figure 6.6 CTP and *NBS* DNA promote the self-engagement of the N-terminal domain of Noc. (A) SDS-PAGE analysis of BMOE crosslinking products of 10 μM *B. subtilis* Noc (E29C, R89A) protein ± 1.0 μM 22-bp *parS*/*NBS* DNA ± 1.0 mM NTP. All crosslinking reactions were performed at 22°C unless indicated otherwise. Quantification of the crosslinked fraction is shown below each representative image. Error bars represent SEM from three replicates. **(B)** Same as panel A, but Noc (E29C, N121S) was used instead. **(C)** Same as panel A, but Noc (Δ10, E29C) was used instead.

To further investigate if the NTD engagement produces a clamp-like Noc that can entrap DNA, I performed crosslinking reactions on a dual-cysteine Noc (E29C S253C) variant (Fig. 6.7B). Residues E29 and S253 at the NTD and the C-terminal domain (CTD) of Noc, respectively, were substituted by cysteine (Fig. 6.7B). While Noc (E29C) crosslinked in a CTP and *NBS*-dependent manner (Fig. 6.7B), Noc (S253C) crosslinked efficiently (~80% crosslinked fraction) but independently of CTP and/or *NBS* (Fig. 6.7A), consistent with the known role of the CTD as a primary dimerisation domain (Adams et al., 2015; Leonard et al., 2004). I observed that purified Noc (E29C S253) formed a high molecular weight (HMW) species near the top of the polyacrylamide gel in the presence of CTP, a circular *NBS*-harbouring plasmid, and the crosslinker BMOE (lane 7 of Fig. 6.7B-C and Fig. 6.7D). The HMW smear contained both protein and DNA, as apparent from dual staining with a protein stain (Coomassie) and a DNA stain (Sybr green) (Fig. 6.7C). The slowly migrating DNA-stained bands were also observed when the crosslinking products were resolved on an agarose gel (Fig. 6.7D). Therefore, the HMW smear most likely contained protein-DNA catenates between a circular *NBS* plasmid and a denatured but otherwise circularly crosslinked Noc (E29C S253C) polypeptide. To verify the nature of the catenates, crosslinking products were treated with Benzonase, a non-specific DNase, before SDS-PAGE analysis (lane 8 of Fig. 6.7B-C). Here, the use of Benzonase eliminated the HMW smear, likely by unlinking the protein-DNA catenates. Lastly, the HMW smear was not observed when an empty plasmid was employed or when CTP was omitted from the reaction (lanes 4-5 and 9-10 of Fig. 6.7B-C). Altogether, our results indicate that *B. subtilis* Noc entraps DNA in an *NBS*- and CTP-dependent manner.

To follow the DNA entrapment and spreading of Noc in real-time, I employed a 170-bp dual biotin-labelled *NBS* DNA that had been tethered at both ends onto a streptavidin-coated probe to form a closed DNA and measured bio-layer interferometry (BLI) signal (Fig. 6.8) (Jalal et al., 2020a). BLI monitors wavelength shifts resulting from changes in the optical thickness of the probe during the association/dissociation of Noc from the closed *NBS* DNA substrate. In the absence of CTP, I observed only the nucleation event on *NBS* DNA with 1 µM purified Noc (Fig. 6.8A). Premixing Noc with ATP, GTP, or UTP did not change the sensorgram markedly, however the addition of 1 mM CTP increased the BLI response by ~sixfold (Fig. 6.8A), consistent with Noc-CTP spreading from *NBS* to accumulate more on the 170-bp closed DNA substrate than by nucleation alone. I did not observe a noticeable BLI response when a 170-bp closed *parS* DNA substrate was employed instead (Fig. 6.8A), confirming that nucleation and spreading by *B. subtilis* Noc is strictly dependent on the *NBS*. I further observed by BLI

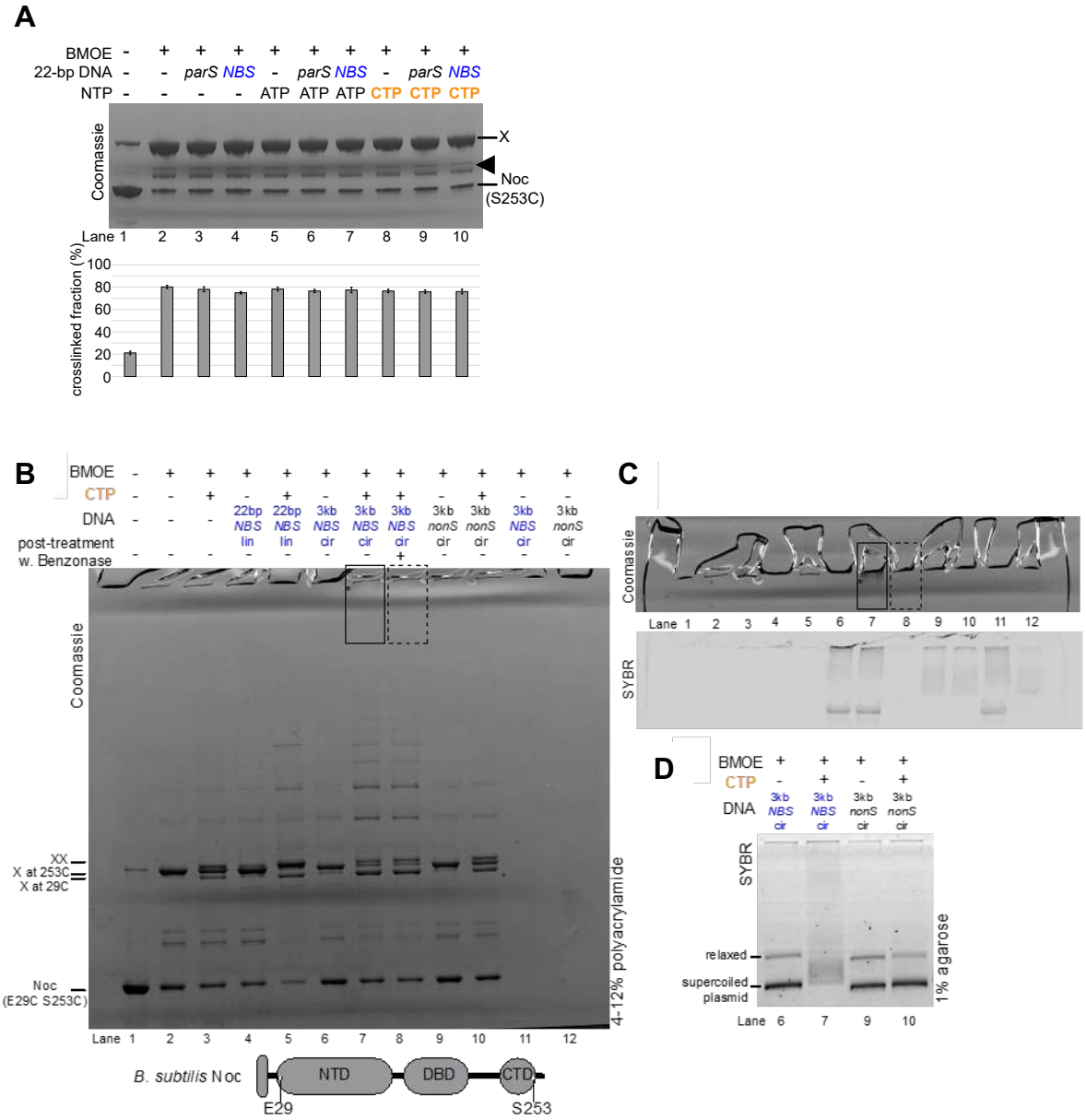
A
BMOE
22-bp DNA
NTP
parS NBS
ATP
CTP
Coomassie
X
Noc
(S253C)
Lane 1 2 3 4 5 6 7 8 9 10
crosslinked fraction (%)
100
80
60
40
20
0
B
BMOE
CTP
DNA
post-treatment w. Benzonase
22bp NBS lin
3kb NBS cir
3kb nonS cir
Coomassie
XX
X at 253C
X at 29C
Noc (E29C S253C)
4-12% polyacrylamide
Lane 1 2 3 4 5 6 7 8 9 10 11 12
B. subtilis Noc
NTD
DBD
CTD
E29
S253
C
Coomassie
SYBR
Lane 1 2 3 4 5 6 7 8 9 10 11 12
D
BMOE
CTP
DNA
3kb NBS cir
3kb nonS cir
SYBR
relaxed
supercoiled plasmid
1% agarose
Lane 6 7 9 10

Figure 6.7 (A) SDS-PAGE analysis of BMOE crosslinking products of 10 μM *B. subtilis* Noc (S253C) protein ± 1.0 μM 22-bp *parS*/*NBS* DNA ± 1.0 mM NTP. All crosslinking reactions were performed at 22^{o}C unless indicated otherwise. The black arrow represents proteolysed cross-linked Noc (S253C). Quantification of the crosslinked fraction is shown below each representative image. Error bars represent SEM from three replicates. **(B**) SDS-PAGE analysis of BMOE crosslinking of 10 μM dual-cysteine Noc (E29C S253C) variant ± DNA ± 1.0 mM NTP. Different DNAs were employed in crosslinking reactions: a linear 22-bp *NBS* DNA (22bp *NBS* lin, 1.0 μM), a circular 3-kb *NBS* plasmid (3kb *NBS* cir, 100 nM), or a circular 3-kb scrambled *NBS* plasmid (3kb *nonS* cir, 100 nM). The high-molecular weight (HMW) smear near the well of the polyacrylamide gel is marked with a solid box and an asterisk (see also panel 6.7C). When the crosslinking reaction was subsequently treated with a non-specific DNA nuclease, Benzonase, the HMW smear was no longer observed (dashed box, lane 8). X indicates a singly crosslinked form of Noc (E29C S253C). XX indicates a doubly crosslinked form of Noc (E29C S253C). **(C)** Same as panel 6.7B but fivefold more volume of each sample was loaded in each well to enhance the visualization of the HMW smear, only the top of the polyacrylamide gel was shown. The gel was also stained with a DNA-dye, Sybr Green (SYBR), and only the top section of the gel was shown. A smaller 22-bp *NBS* DNA migrated out of the gel, thus was not observed. **(D)** Agarose gel analysis of BMOE crosslinking products. A subset of crosslinking reactions (lanes 6,7,9, and 10) were loaded and resolved on a 1% agarose gel. The gel was subsequently stained with Sybr Green for DNA.

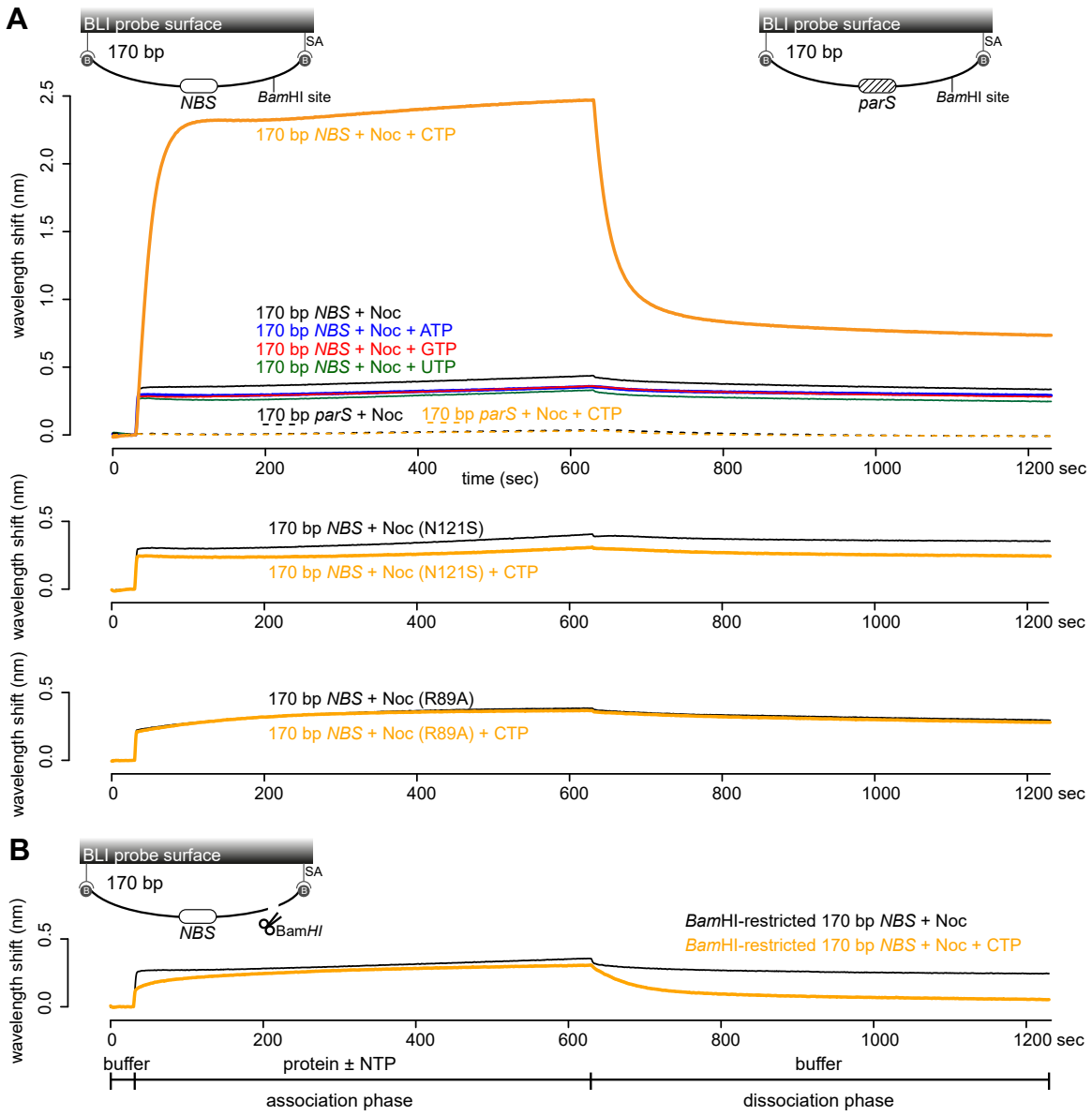

Figure 6.8 CTP facilitates the association of Noc with a closed *NBS* DNA substrate beyond nucleation. (A) Bio-layer interferometry (BLI) analysis of the interaction between a premix of 1.0 μM *B. subtilis* Noc ± 1.0 mM NTP and a 170-bp dual biotin-labelled DNA that contains either an *NBS* or a non-cognate *parS* site. Interactions between a dual biotinylated DNA and a streptavidin (SA)-coated probe created a closed DNA molecule where both ends were blocked (see also the schematic diagram of the BLI probes). Other Noc variants, Noc (R89A) and Noc (N121S), were also analysed in the same assay. **(B)** BLI analysis of the interaction between a premix of 1.0 μM *B. subtilis* Noc ± 1.0 mM CTP and a BamHI-restricted dual biotinylated *NBS* DNA. The 170-bp *NBS* DNA substrate was also designed with a BamHI recognition site (see the schematic diagram of the probes). The intact dual biotinylated DNA was first immobilized onto the probe surface, then an open end was generated by digestion with BamHI (See Materials and Methods). Afterwards, the probe was used in a BLI analysis with a premix of Noc ± CTP. Each experiment was triplicated and a representative sensorgram was shown.

assay that the Noc (R89A) and Noc (N121S) variants could nucleate but could not spread to accumulate on nucleation alone. I did not observe a noticeable BLI response when a 170-bp closed *parS* DNA substrate was employed instead (Fig. 6.8A), confirming that nucleation and spreading by the closed *NBS* substrate even in the presence of 1 mM CTP (Fig. 6.8A), consistent with the requirement of NTD engagement for DNA entrapment (see also Fig. 6.7B-D).

Next, I investigated whether a DNA substrate with a free end (an open DNA) can also support Noc accumulation in our BLI setup. The 170-bp dual biotin-labelled was designed with an unique BamHI recognition site flanking the *NBS* site (Fig. 6.8B). To generate a free end on the DNA, the DNA-coated probe was immersed in a buffer containing *Bam*HI restriction enzyme. Before *Bam*HI digestion, Noc showed an enhanced association on a closed DNA substrate in the presence of CTP (Fig. 6.8A). However, after *Bam*HI digestion, the addition of CTP did not affect the BLI response beyond the nucleation of Noc at the *NBS* (Fig. 6.8B). I reasoned that, similar to the canonical ParB, Noc spreads but quickly escapes by sliding off a free DNA end (Jalal et al., 2020a). Overall, my BLI analysis is consistent with the site-specific crosslinking analysis and suggests a clamp-like Noc-CTP that can spread and accumulate on a closed DNA substrate by entrapping DNA.

6.5 Noc binds liposomes in the presence of CTP

It has been shown previously *in vivo* that Noc possesses membrane-binding activity and it must bring chromosomal DNA to the cell membrane to prevent the formation of cell division machinery (Adams et al., 2015). Puzzlingly, however, I could not observe noticeable association between purified *B. subtilis* Noc and liposomes by a co-sedimentation assay (lanes 1-4 of Fig. 6.9A). I wondered if CTP might be the missing co-factor that activates the membrane-binding activity of Noc. To test this possibility, purified Noc was incubated with liposomes with or without CTP and 22-bp *NBS* DNA, and ultracentrifuged (Fig. 6.9A-B). The pellet contained sedimented liposomes and associating protein while the supernatant contained unbound protein; protein and DNA species from both fractions were analysed by polyacrylamide gel electrophoresis. I did not observe a significant increase in the amount of Noc in the pellet when CTP alone, CTP and a non-cognate 22-bp *parS* DNA (lanes 5-8 of Fig. 6.9A), or other nucleotides were employed (Fig. 6.9C). However, in the presence of both CTP and a 22-bp *NBS* DNA, ~45% of the total amount of Noc was detected robustly in the pellet (lane 9-12 of Fig. 6.9A), suggesting that the *in vitro* membrane-binding activity of Noc is CTP- and *NBS*-dependent. *NBS* DNA is most likely required to stimulate CTP binding, hence the membrane-binding activity of Noc, rather than to concentrate a large amount of weakly

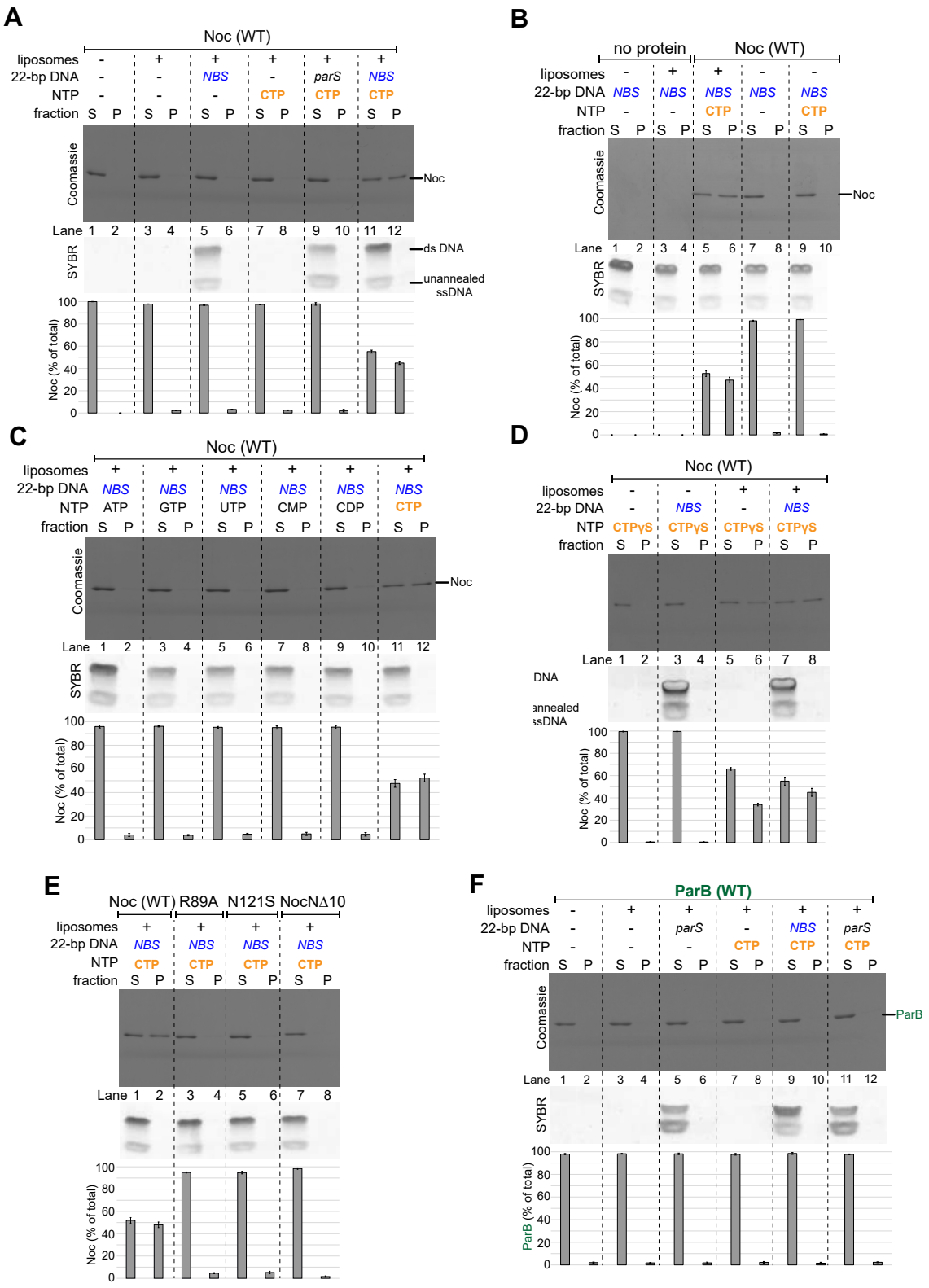
A
Noc (WT)
liposomes
22-bp DNA
NTP
fraction
Coomassie
Noc
Lane
SYBR
ds DNA
unannealed ssDNA
Noc (% of total)
B
no protein
Noc (WT)
C
Noc (WT)
ATP
GTP
UTP
CMP
CDP
CTP
D
Noc (WT)
CTPγS
DNA
annealed ssDNA
E
Noc (WT)
R89A
N121S
NocNΔ10
F
ParB (WT)
ParB
ParB (% of total)

Figure 6.9 Noc binds liposomes in the presence of CTP and *NBS* DNA, and the phenotypic effects of the Noc variants. (A) Analysis of *B. subtilis* Noc binding to membranes by a liposome co-sedimentation assay. A premix of 0.75 µM *B. subtilis* Noc protein ± 1.0 µM 22-bp linear *parS*/*NBS* DNA ± 1.0 mM CTP ± 1.0 mg/mL liposomes was incubated at 22°C for 5 min before ultracentrifugation. The resulting supernatant (S) and pellet (P) fractions were analysed by SDS-PAGE. Samples were also loaded onto a 20% TBE PAGE, and the gel was subsequently stained with Sybr Green for DNA. Quantification of Noc in each fraction is shown below each representative image. Error bars represent SEM from three replicates. **(B)** Analysis of *B. subtilis* Noc binding to membranes by a liposome co-sedimentation assay. A premix of 1.0 µM 22-bp linear *NBS* DNA ± 0.75 µM *B. subtilis* Noc protein ± 1.0 mM CTP ± 1.0 mg/mL liposomes was incubated at 22°C for 5 min before ultracentrifugation. The resulting supernatant (S) and pellet (P) fractions were analysed by SDS-PAGE. Without Noc, 22-bp *NBS* DNA did not co-sediment on its own (lanes 1-2) or with liposomes (lanes 3-4). Samples were also loaded onto a 20% TBE PAGE, and gel was subsequently stained with Sybr Green for DNA. Quantification of Noc in each fraction is shown below each representative image. Error bars represent SEM from three replicates. **(C)** CTP but no other nucleotide enables Noc to co-sediment with liposomes. A premix of 0.75 µM *B. subtilis* Noc protein + 1.0 µM 22-bp *NBS* DNA ± 1.0 mM NTP + 1.0 mg/mL liposomes was incubated at 22°C for 5 min before ultracentrifugation. The resulting supernatant (S) and pellet (P) fractions were analysed by SDS-PAGE. **(D)** Same as panel A but 1.0 mM CTPɣS was used instead. **(E)** Other Noc variants, Noc (R89A), Noc (N121S), and NocNΔ10, were also analysed in a liposome co-sedimentation assay. **(F)** *Caulobacter crescentus* ParB does not co-sediment with liposomes in any tested conditions. A premix of 0.75 µM *C. crescentus* ParB protein ± 1.0 µM 22-bp linear *parS*/*NBS* DNA ± 1.0 mM CTP ± 1.0 mg/mL liposomes was incubated at 22°C for 5 min before ultracentrifugation. The resulting supernatant (S) and pellet (P) fractions were analysed by SDS-PAGE.

binding Noc in the vicinity of *NBS* to collectively enhance its affinity for the cell membrane. Supporting this proposition, the short length of a 22-bp *NBS* DNA duplex means that only a dimer of Noc or Noc-CTP complex can occupy the DNA at a time. Furthermore, nearly all of the 22-bp *NBS* DNA was present in the supernatant (instead of in the pellet) after centrifugation (Fig. 6.9A), most likely because Noc-CTP clamps rapidly escaped the open linear *NBS* DNA, further arguing that individual Noc-CTP possesses a substantial membrane-binding capability.

Next, I observed that the addition of CTPγS alone caused ~35% of Noc to associate with the pelleted vesicles (lanes 5-6, Fig. 6.9D). The vesicle-bound fraction further increased to ~45% when both CTPγS and a 22-bp *NBS* DNA were present (lanes 7-8, Fig. 6.9D). I infer that CTP binding, but not hydrolysis, is required for the *in vitro* Noc-liposomes interaction. Consistent with the requirement of CTP binding for membrane-binding activity, the Noc (R89A) and Noc (N121S) variants which do not bind CTP or bind CTP weakly failed to co-sediment with liposomes even when CTP and *NBS* were included (lanes 3-4 and 5-6, Fig. 6.10E). The N-terminal amphipathic helix was previously shown *in vivo* to be the membrane-targeting determinant of *B. subtilis* Noc. Here, I also confirmed that a purified NocNΔ10 lacking this amphipathic helix was unable to co-sediment with liposomes *in vitro* regardless of the presence or absence of CTP or *NBS* DNA (lanes 7-8, Fig. 6.9E). Lastly, in another control experiment, *C. crescentus* ParB, which binds CTP but not the cell membrane, did not co-sediment with liposomes in the presence of CTP ± *parS* or *NBS* DNA (Fig. 6.9F) (Jalal et al., 2020a; Lim et al., 2014; Toro et al., 2008).

6.6 Noc recruits *NBS* plasmid to liposomes in the presence of CTP

Next I wondered if the Noc-dependent recruitment of DNA to the membrane can be biochemically reconstituted. To this end, I assembled a reaction containing purified Noc, liposomes, CTP, and a ~5-kb circular *NBS*-harbouring plasmid before ultracentrifugation (Fig. 6.10). Unlike the 22-bp *NBS* DNA, the *NBS* plasmid is topologically closed and therefore should not be able to escape entrapment by Noc-CTP clamps. Unfortunately, owing to its high molecular weight, ~45 to 55% of the circular plasmid sedimented independently of the liposomes (lanes 5-6 of Fig. 6.10A, and lanes 1-4 of Fig. 6.10B). Nevertheless, in the presence of liposomes and CTP, the *NBS* plasmid completely co-sedimented with Noc (lanes 11-12 of Fig. 6.10A), demonstrating that Noc can recruit plasmid DNA to liposomes in the presence of CTP. The pellet/supernatant distribution of a control plasmid with no *NBS* (“empty”) was unaffected by the presence of Noc and CTP, and only ~2% of Noc was found in the pellet (lanes 9-10 of Fig. 6.10A). Next, in an attempt to minimize the sedimentation of a plasmid by itself, I performed a vesicle flotation assay in which liposomes and associating protein/DNA

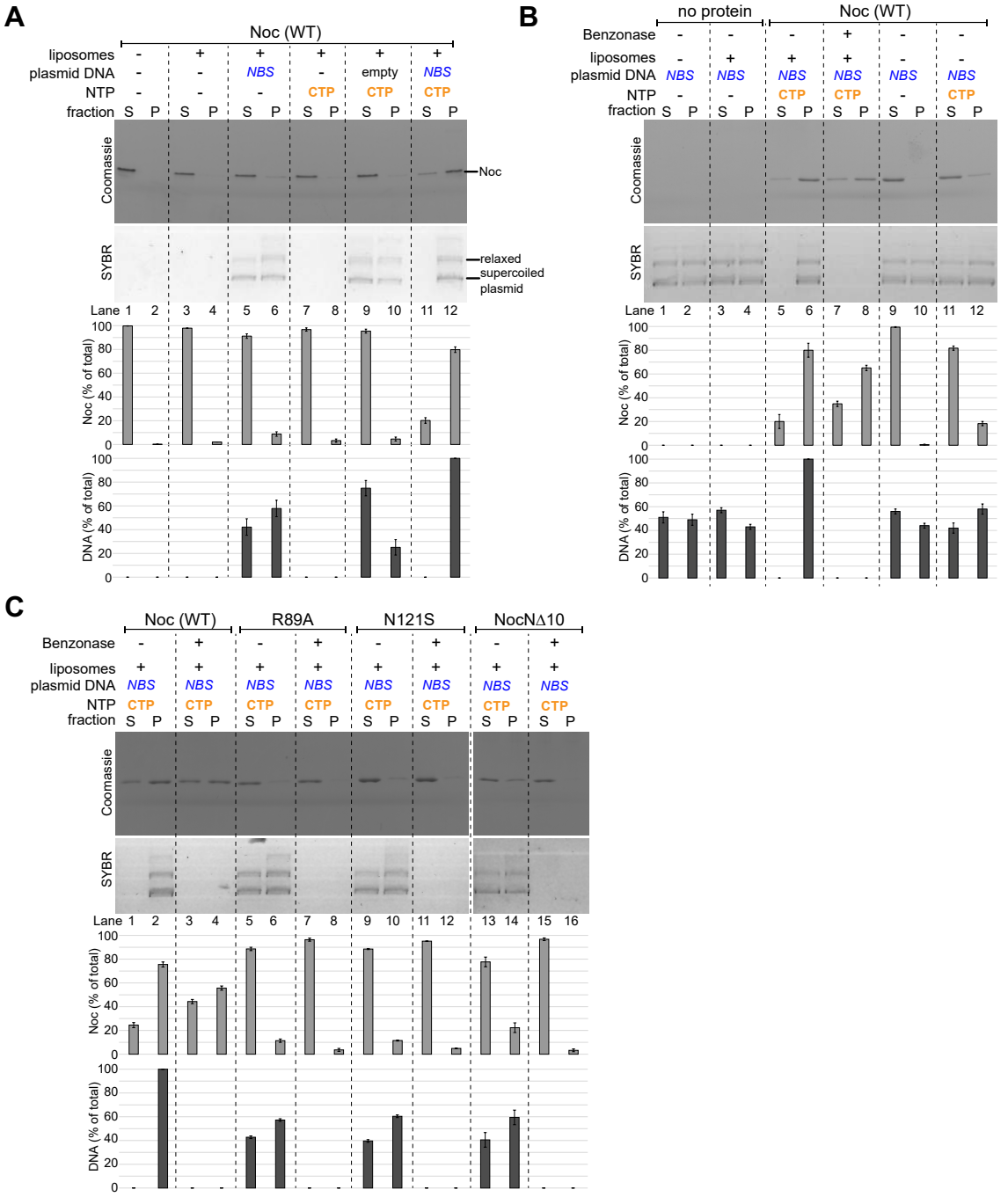
A
Noc (WT)
liposomes
plasmid DNA
NTP
fraction
S P
Coomassie
SYBR
Noc
relaxed
supercoiled
plasmid
Lane
Noc (% of total)
DNA (% of total)
B
no protein
Noc (WT)
Benzonase
C
Noc (WT)
R89A
N121S
NocNΔ10

Figure 6.10 Noc recruits *NBS* plasmid to liposomes in the presence of CTP. (A) Analysis of *B. subtilis* Noc binding to membranes and the recruitment of plasmid DNA to the membranes by a liposome co-sedimentation assay. A premix of 0.75 μM *B. subtilis* Noc protein ± 100 nM 5-kb plasmid DNA ± 1.0 mM CTP ± 1.0 mg/mL liposomes was incubated at 22°C for 5 min before ultracentrifugation. Either an empty plasmid or an *NBS*-harbouring plasmid was employed in this assay. The resulting supernatant (S) and pellet (P) fractions were analysed by SDS-PAGE. Samples were also loaded onto a 1% agarose gel, and was subsequently stained with Sybr Green for DNA. Quantification of Noc or DNA in each fraction is shown below each representative image. Error bars represent SEM from three replicates. **(B)** Similar to panel A, a premix of 100 nM *NBS* plasmid ± 0.75 μM Noc ± 1.0 mM CTP ± 1.0 mg/mL liposomes was first assembled and incubated at 22°C for 5 min. However, before ultracentrifugation, a non-specific DNA nuclease (Benzonase) was either added or omitted from the samples, as indicated. **(C)** Other Noc variants, Noc (R89A), Noc (N121S), and NocNΔ10, were also analysed in a liposome co-sedimentation assay. Benzonase was either added or omitted, as indicated, before ultracentrifugation.

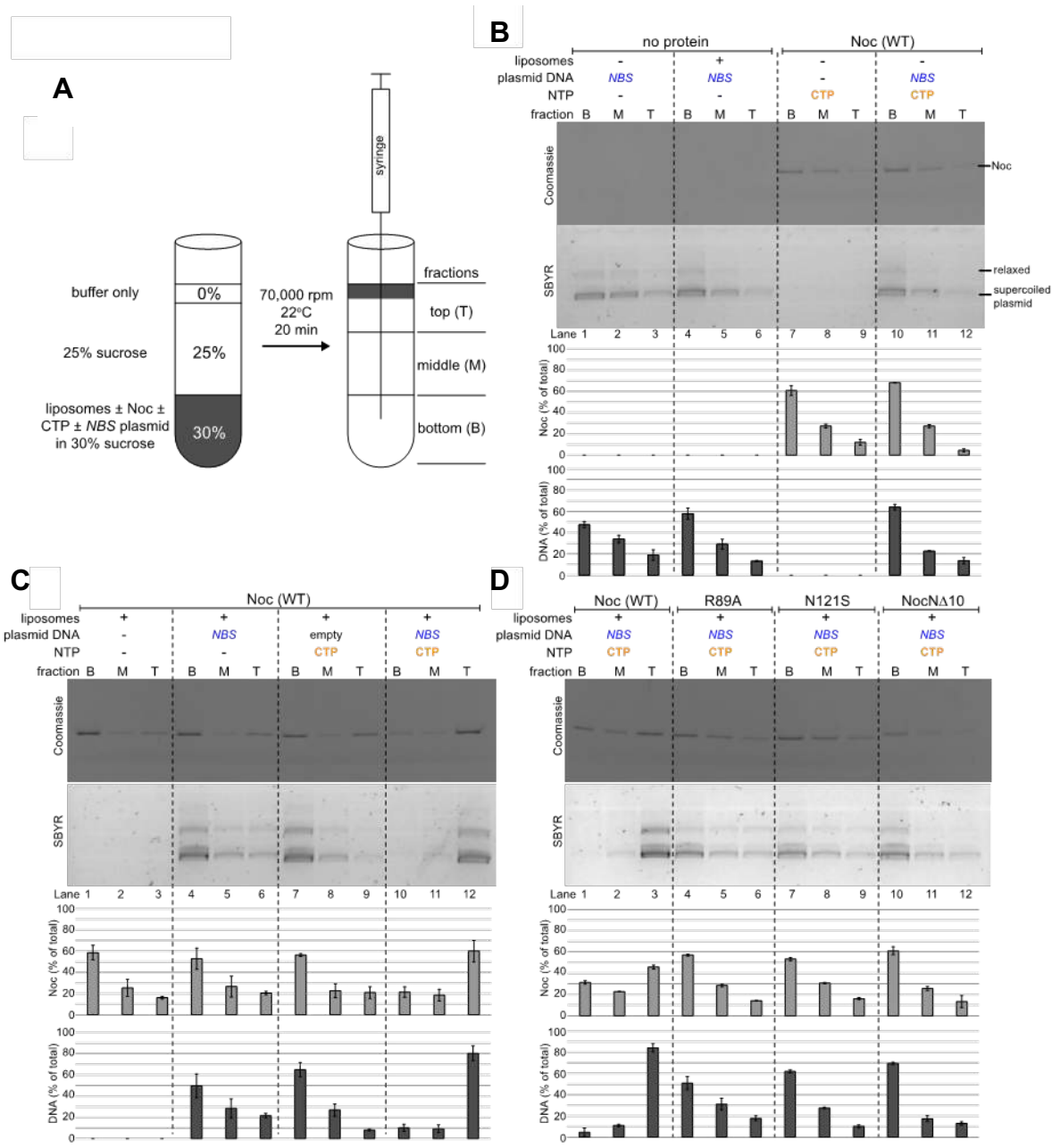
A
buffer only
0%
25% sucrose
25%
liposomes ± Noc ±
CTP ± NBS plasmid
in 30% sucrose
30%
70,000 rpm
22°C
20 min
syringe
fractions
top (T)
middle (M)
bottom (B)
B
no protein
Noc (WT)
liposomes
plasmid DNA
NTP
fraction
Coomassie
SBYR
Noc
relaxed
supercoiled plasmid
Lane
Noc (% of total)
DNA (% of total)
C
Noc (WT)
empty
D
Noc (WT)
R89A
N121S
NocNΔ10

Figure 6.11 Liposome flotation assays shows Noc can recruit *NBS* plasmid to membrane in the presence of CTP. (A) The principle of a liposome flotation assay. Liposomes ± purified Noc ± CTP ± *NBS* plasmid were incubated in a 30% sucrose binding buffer. Buffer only with 25% sucrose and 0% sucrose were subsequently layered on top sequentially. After ultracentrifugation, liposomes and associated protein/DNA migrate along the sucrose gradient i.e. floating to the upper most fractions. Three equal fractions (bottom, middle, and top) were drawn out sequentially using a Hamilton syringe, and their protein and DNA contents were analysed. **(B)** Control experiments: liposome flotation assays in which one component, either Noc protein, a 5-kb plasmid DNA, CTP, or liposomes, was omitted. **(C)** Analysis of *B. subtilis* Noc binding to membranes and the recruitment of plasmid DNA to membranes by a liposome flotation assay. A premix of 0.75 μM *B. subtilis* Noc ± 100 nM 5-kb plasmid DNA ± 1.0 mM CTP ± 1.0 mg/mL liposomes was incubated at 22°C for 5 min before ultracentrifugation. Either an empty plasmid or an *NBS*-harbouring plasmid were employed in this assay. The resulting fractions (Bottom B, Middle M, and Top T) were analysed by SDS-PAGE. Samples were also loaded onto a 1% agarose gel and was subsequently stained with Sybr Green for DNA. Quantification of Noc or DNA in each fraction is shown below each representative image. Error bars represent SEM from three replicates. **(D)** Other Noc variants, Noc (R89A), Noc (N121S), and NocNΔ10, were also analysed in a liposome flotation assay. A premix of 0.75 μM *B. subtilis* Noc protein (WT or mutants) + 100 nM *NBS* plasmid + 1.0 mM CTP + 1.0 mg/mL liposomes was ultracentrifuges, and the resulting fractions were analysed for protein and DNA contents.

migrate up a sucrose gradient to the topmost faction rather than down into the pellet (Fig. 6.11A). Despite the basal level of ~20% total *NBS* plasmid in the top fraction even when liposomes were omitted (lane 3 of Fig. 6.11B), I again observed ~80% of total *NBS* plasmid being recruited to the liposomes when purified Noc and CTP were also present (lane 12 of Fig. 6.11C). In light of the above results, I wondered if the role of *NBS* was to stimulate the membrane-binding activity of Noc-CTP. To test this possibility, I first assembled a co-sedimentation reaction as described above. Subsequently, Benzonase was added to eliminate *NBS* plasmid before ultracentrifugation (lanes 7-8 of Fig. 6.10B). The nuclease treatment eliminated intact *NBS* plasmid from both the supernatant and the pellet fractions, however ~65% of the total amount of Noc still remained co-sedimented to the pellet in comparison to ~80% when nuclease was omitted (lanes 7-8 vs. lanes 5-6 of Fig. 6.10B). In parallel, I tested spreading-defective Noc (R89A) and Noc (N121S), and a membrane-binding-defective NocNΔ10 for their ability to recruit *NBS* plasmid to liposomes in a co-sedimentation assay (Fig. 6.10C) as well as in a flotation assay (Fig. 6.11D). Consistent with previous and the above *in vivo* data, these mutants could not recruit DNA to the pellet fraction beyond the basal level (Fig. 6.10C and Fig. 6.11D) (Adams et al., 2015). Altogether, these results suggest that the *NBS* specifically activates the membrane-binding activity of Noc in the presence of CTP, thereby recruiting Noc-DNA complexes to the membrane.

6.7 The association of Noc-*NBS* DNA with liposomes is reversible

Once the membrane-associated Noc-DNA nucleoprotein complexes form, can this process be reversed? To investigate, I employed a buffer supplemented with EDTA to sequester coordinated Mg^{2+} cation to disrupt CTP binding from the preformed liposome-bound Noc-DNA complexes (Fig. 6.12). In this experiment, the pellet containing preformed liposomes-bound Noc-DNA complexes (lanes 2 or 4 of Fig. 6.12) was either resuspended in EDTA-minus or EDTA-plus buffer before being ultracentrifuged again. After the second round of centrifugation, both the pellet and the supernatant fractions were analysed for the presence of protein and DNA (lanes 5-8 of Fig. 6.12). I observed that while nearly all *NBS* plasmid remained in the pellet when an EDTA-minus buffer was used (lane 6 of Fig. 6.12), ~38% of total plasmid returned to the supernatant in the presence of EDTA (lane 7 of Fig. 6.12). These results demonstrate that the membrane-binding activity of Noc can be reversed and suggest a possible inhibitory mechanism that keeps apo-Noc in the membrane inactive mode in the absence of CTP.

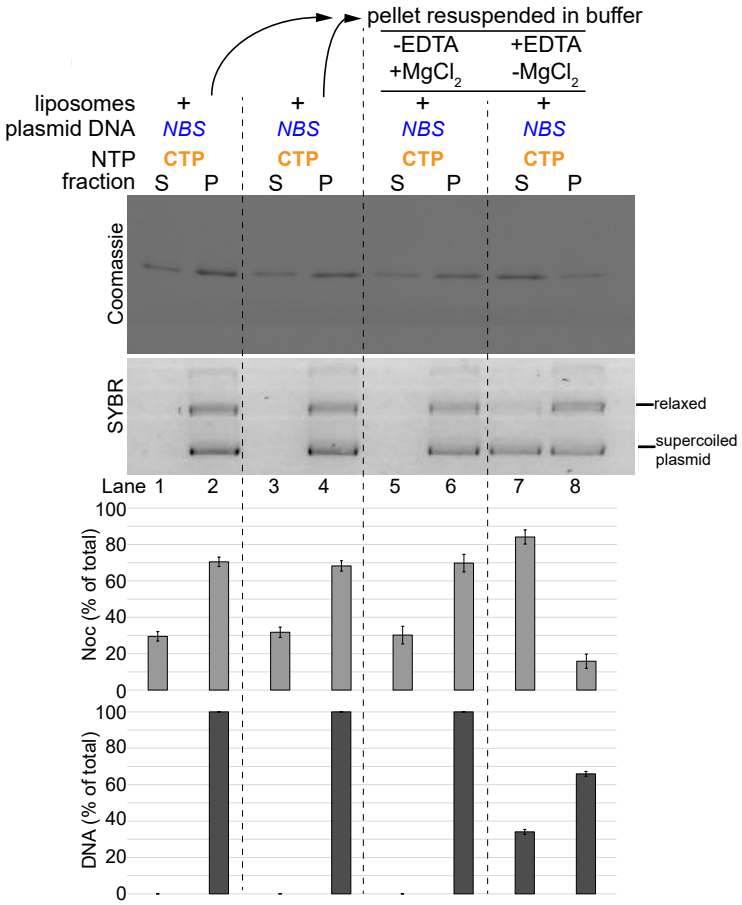

Figure 6.12 The association of Noc-*NBS* DNA with liposomes is reversible. A premix of 0.75 µM *B. subtilis* Noc protein + 100 nM *NBS* plasmid + 1.0 mM CTP + 1.0 mg/mL liposomes was ultracentrifuges, and the resulting fractions were analysed for protein and DNA contents (lanes 1-2 and 3-4). The resulting pellet (lanes 2 and 4) were subsequently resuspended in either a binding buffer (- EDTA + 1 mM $MgCl_2$) or in a stripping buffer (+ 10 mM EDTA - $MgCl_2$). The resuspensions were ultracentrifuged for the second time, and the resulting fractions were analysed for protein and DNA contents (lanes 5-6 and 7-8).

6.8 Crystal structure of *G. thermoleovorans* NocΔCTD shows the membrane-targeting amphipathic helix in an autoinhibitory conformation

To gain further insights into the membrane inactive state, I sought to solve a crystal structure of Noc. I could not obtain high quality crystals of *B. subtilis* Noc either in full-length or truncated forms despite extensive effort. However, I could grow crystals and collect diffraction data for a C-terminal domain truncated apo-Noc (NocΔCTD) from a thermophilic bacterium, *Geobacillus thermoleovorans*, to 2.5 Å resolution. *B. subtilis* Noc and *G. thermoleovorans* Noc share 72% sequence identity (Fig. 6.13). The structure was solved by iodine SAD phasing since no other Noc protein family structure was available as a template for molecular replacement. The X-ray crystallographic data are summarised in Table 6.1. The asymmetric unit contains two similar copies of apo-Noc (RMSD = 0.9 Å) (Fig. 6.14A), hence I used the more complete subunit for all further analysis.

Each NocΔCTD subunit contains an N-terminal domain (NTD) (helices α1-α6) and an *NBS*-specific DNA-binding domain (DBD) (helices α7-α12) (Fig. 6.14B) (Jalal et al., 2020b; Wu et al., 2009). Each *G. thermoleovorans* NocΔCTD subunit is composed of an NTD (helixes and sheets) with the amphipathic helix and the CTP interacting motif being formed by helixes α1 and α4 respectively, and the DBD (helixes), where the helix-turn-helix motif is formed by helixes α7 and α8 (Fig. 6.14B). The secondary structure of the *G. thermoleovorans* NocΔCTD is composed of 12 α-helix and 4 β-pleated sheets, with the NTD consisting of three α-helixes (α1-α5) and four β-pleated-sheets (β1-β4), while the last seven helices (α6-α12) make up the DBD of *G. thermoleovorans* Noc. In the NTD, a short linker connects the amphipathic helix, α1 (5-11) with α2 (13-21), which is then followed by a long flexible loop (flexible arm) that connects to β1(27-31). A long linker then connects β1 to α3 (49-63), which is then followed by region containing β2 (68-73), β3 (77-82), α4 (84-89) and β4 (97-102), with the CTP interacting motif being in α4. The remaining NTD is composed of α5 (107-121) which connects to the remaining helixes that forms the DBD of *G. thermoleovorans* NocΔCTD. The DBD is then followed by α6 (126-140) which links to α7 (144-151) and α8 (155-165) that forms the helix-turn-helix motif. α8 then links to the remaining helixes which pack to form a compact bundle in the structure, whereby helixes α9 (169-177) and α11 (190-207) are positioned across helixes α10 (182-191) and α12 (211-223) (Fig. 6.14B).

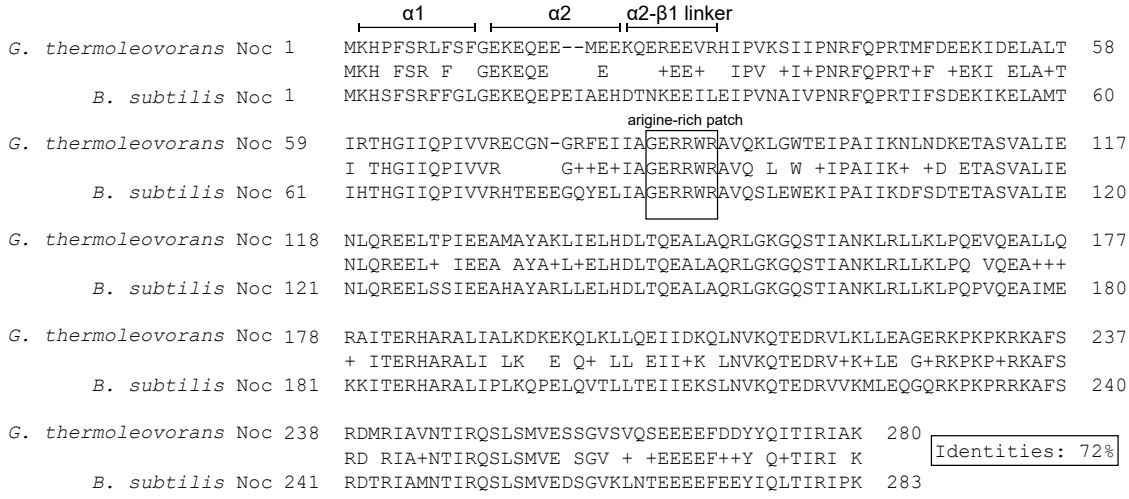

Figure 6.13 A sequence alignment between *B. subtilis* Noc and its homologue *G. thermoleovorans* Noc. The conserved arginine-rich patch that mediates CTP binding in *B. subtilis* ParB is shown in the solid box. The sequences of amphipathic helix α1, helix α2, and the α2-β1 connecting loop are also indicated on the sequence alignment.

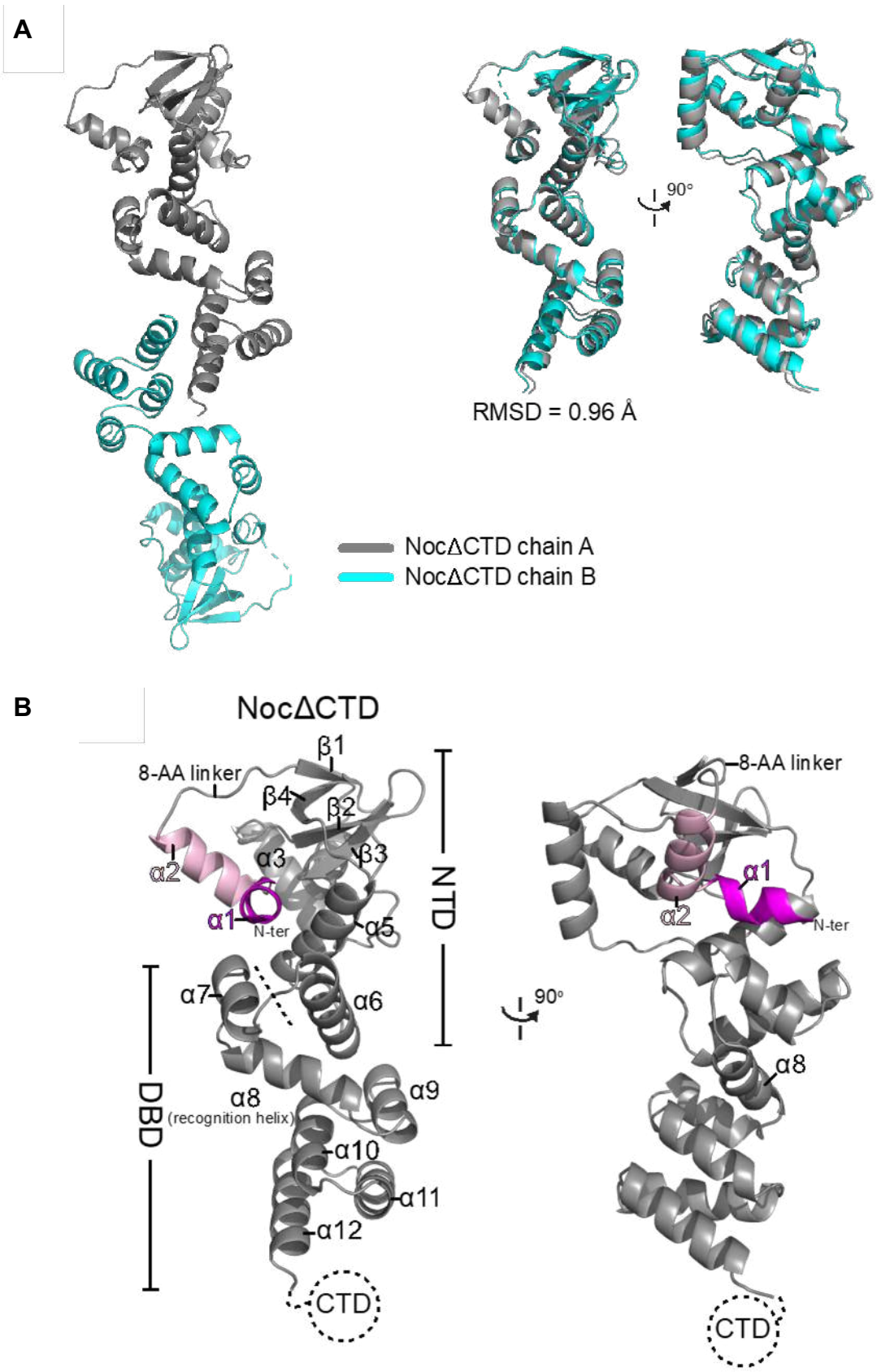
A
90°
RMSD = 0.96 Å
NocΔCTD chain A
NocΔCTD chain B
B
NocΔCTD
β1
8-AA linker
β4
β2
α3
β3
α2
α1
N-ter
α5
NTD
α7
α6
DBD
α8
(recognition helix)
α9
α10
α11
α12
CTD
8-AA linker
α1
α2
N-ter
90°
α8
CTD

Figure 6.14 The crystal structure of *Geobacillus thermoleovorans* NocΔCTD (A) The asymmetric unit of *G. thermoleovorans* NocΔCTD contains two copies of NocΔCTD monomers (left panel). Chains A and B are structurally similar, RMSD = 0.96 Å (right panel) **(B)** Crystal structure of a *G. thermoleovorans* NocΔCTD monomer (grey) with an N-terminal amphipathic helix α1 (magenta) and helix α2 (pink). Helix α2 is connected to the main N-terminal domain (NTD) via an eight amino-acid loop. The dashed line demarcates the NTD from the DNA-binding domain (DBD). Helix α8 at the DBD is the recognition helix that contributes to the specific recognition of the *NBS* site.

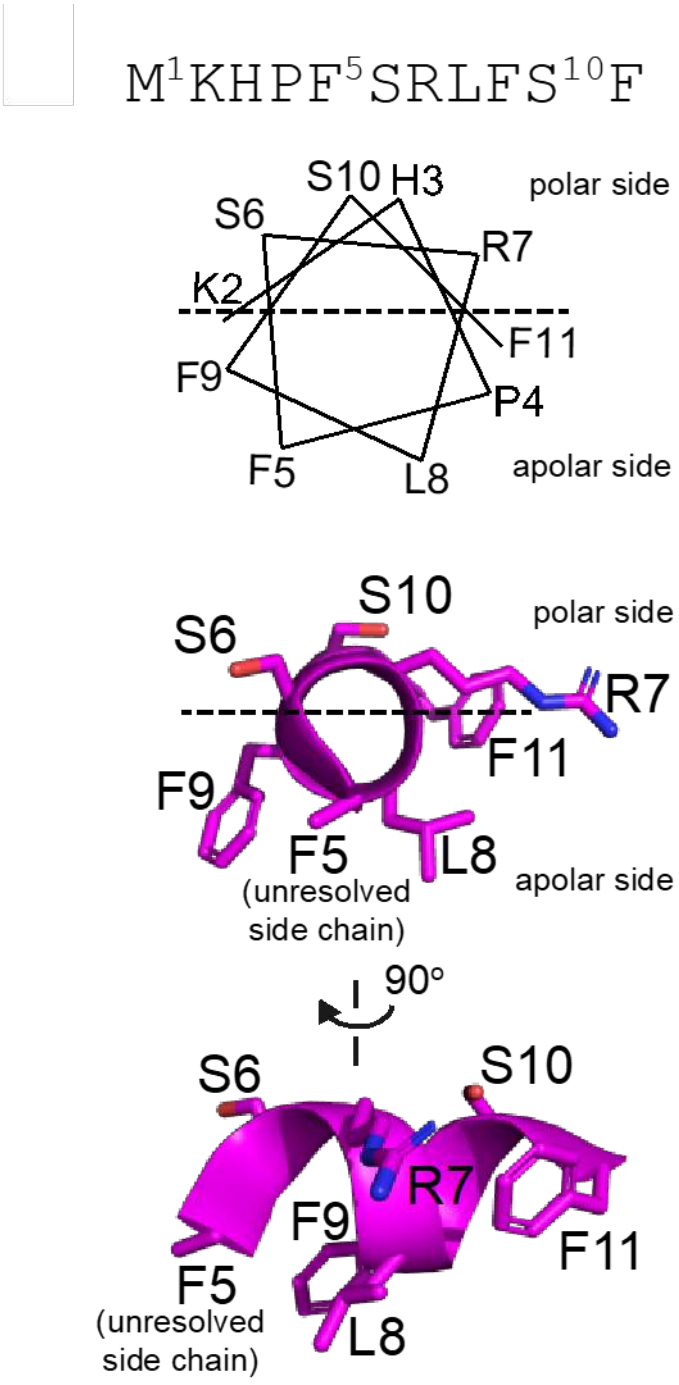

Figure 6.15 The membrane-targeting amphipathic helix α1. A helical wheel representation of the 10-amino acid at the N-terminus of *G. thermoleovorans* Noc. While the first five amino acids were unresolved in the NocΔCTD crystal structure, the next five amino acids adopt a 3_{10} helical conformation with distinct polar and hydrophobic sides.

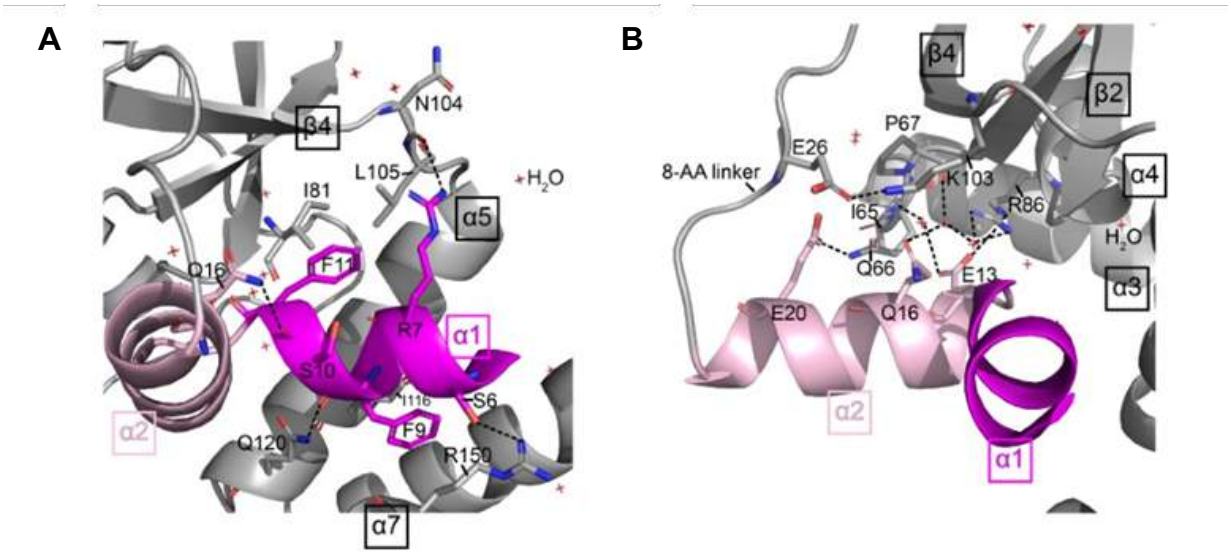

Figure 6.16 Crystal structure of *Geobacillus thermoleovorans* NocΔCTD shows the membrane-targeting amphipathic helix in an autoinhibitory conformation. (A-B) Helices α1 (magenta) and α2 (pink) pack themselves into the core N-terminal domain (grey). Hydrogen bonds are shown as dashed lines, water molecules are also shown.

The primary dimerisation domain at the C-terminal side of Noc was truncated in NocΔCTD, hence is not present in this structure. Most notably, electron density for five out of 10 AA at the membrane-targeting helix α1 are visible and adopt a 3_{10} helical conformation (Fig. 6.15). From the structure, it is apparent that the membrane-targeting sequence of Noc is indeed amphipathic, with distinct polar and hydrophobic faces (Fig. 6.15). The amphipathic helix α1 is immediately followed by helix α2 and subsequently by an 8-AA α2-β1 loop that precedes the main NTD (Fig. 6.15). By sequence comparison with a canonical ParB, the main NTD (β1-α6) of Noc contains the CTP-binding motifs, while the amphipathic α1, α2, and the α2-β1 loop are specific to Noc protein family (Fig. 6.13) (Soh et al., 2019). I noted that the hydrophobic face of the amphipathic α1 helix is buried towards α5 and α7 at the core of Noc (Fig. 6.16A-B), thus is unexposed and unlikely to be available for membrane interaction. Specifically, the side chain of S6 hydrogen bonds with the side chain of R150, and the side chain of R7 hydrogen bonds with the main chain oxygen of N104 (Fig. 6.16A). Additionally, the main chain oxygen of S10 hydrogen bonds with the side chain of Q16, and lastly, the main chain oxygen of F11 hydrogen bonds with the side chain of Q120 (Fig. 6.16A). Sidechains of F9 and F11 also interact hydrophobically with side chains of I116 and I81, respectively (Fig. 6.16A). These interactions thus bury α1 in a potential autoinhibitory conformation. I further noted that α2, which does not target the membrane *per se* but is conserved in Noc homologs (Fig. 6.13), also contributes to holding α1 in the repressed state (Fig. 6.16B) (Adams et al., 2015). Specifically, the side chains of both E13 and Q16 form water-mediated networks with the side chains of I65, R86, and K103, while the side chain of E20 forms a hydrogen bond with Q66 (Fig. 6.16B). Overall, our apo-NocΔCTD structure suggests a repressed state that might keep Noc in the membrane inactive state in the absence of CTP.

6.9 Crystal structure of the *G. thermoleovorans* NocNΔ26ΔCTD variant is incompatible with an autoinhibitory conformation of the amphipathic helix

Next, I attempted to obtain a co-crystal structure of Noc in complex with nucleotides. In the presence of CTPγS, we were able to grow and collect 2.95 Å diffraction data for a crystal of a *G. thermoleovorans* NocNΔ26ΔCTD variant, which lacks both the N-terminal membrane-targeting helix and the C-terminal domain. The X-ray crystallographic data are summarised in Table 6.1. After solving its structure, it is apparent that NocNΔ26ΔCTD has adopted an alternative conformation to that of NocΔCTD (Fig. 6.17A-B, 6.18A-C). This alternative conformation of NocΔN26ΔCTD is compatible with homodimer formation, giving an interfacial area of ~2700 $Å^2$ (as evaluated with jsPISA) (Krissinel, 2015), which resembles that observed for a co-crystal structure of *B. subtilis* ParBΔCTD with bound cytidine diphosphate (CDP) (Fig. 6.19A) and my *C. crescentus* ParBΔCTD- CTPγS co-crystal structure (RMSD = 2.6 Å) (Fig. 6.19B) (Soh et al., 2019). However, there was no clear electron density for a bound nucleotide

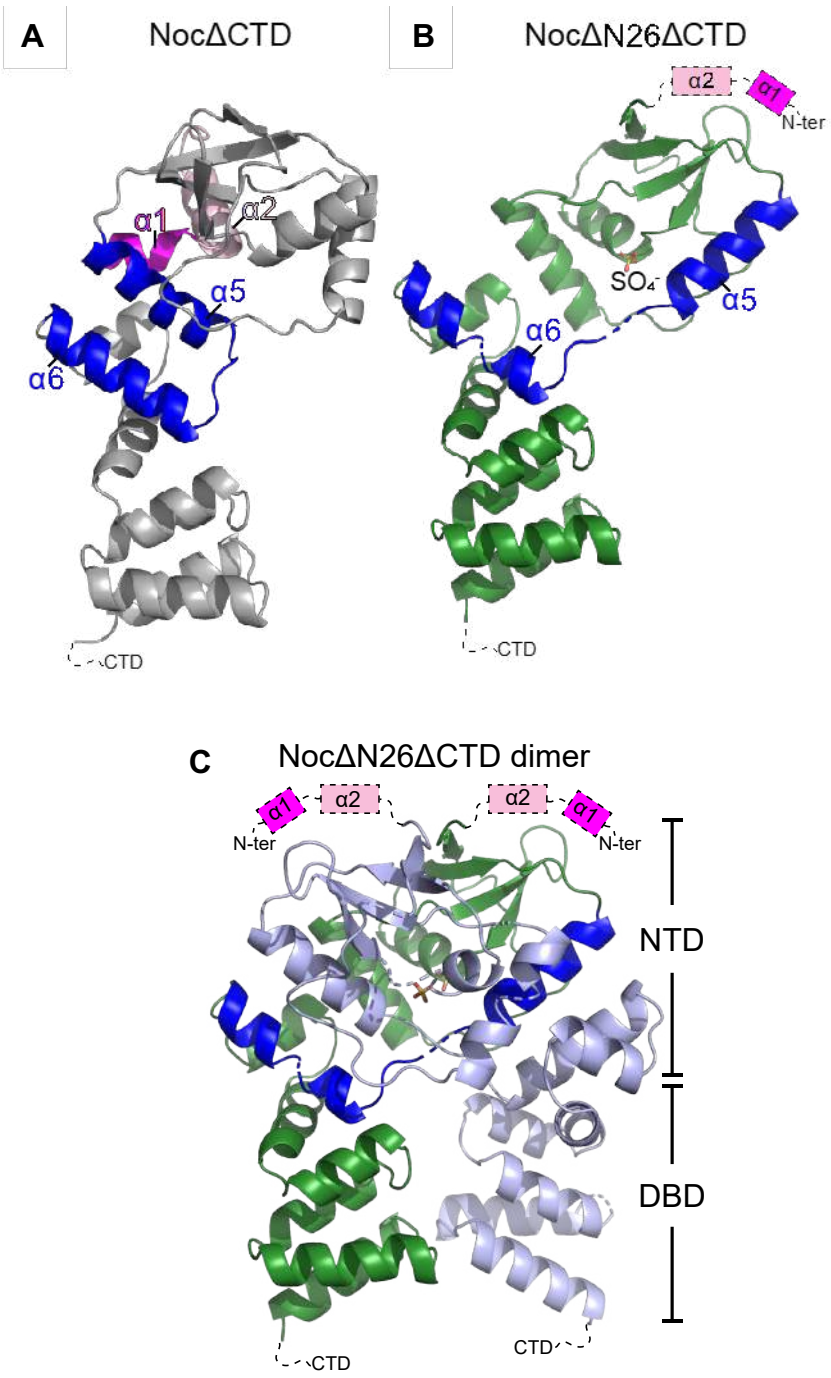

Figure 6.17 The crystal structure of the *G. thermoleovorans* NocNΔ26ΔCTD (A) Crystal structure of *G. thermoleovorans* NocΔCTD (same as Fig. 6A) with helices α5 and α6 highlighted in blue. The amphipathic helix α1 and α2 are shown in magenta and pink, respectively. **(B)** Crystal structure of a *G. thermoleovorans* NocNΔ26ΔCTD variant that lacks both the C-terminal domain (CTD) and helices α1 and α2 (dashed boxes). Helices α5 and α6 are shown in blue. **(C)** A dimer of *G. thermoleovorans* NocNΔ26ΔCTD that self-dimerizes at the N-terminal domain (NTD). Helices α5 and α6 in one of the subunits are shown in blue.

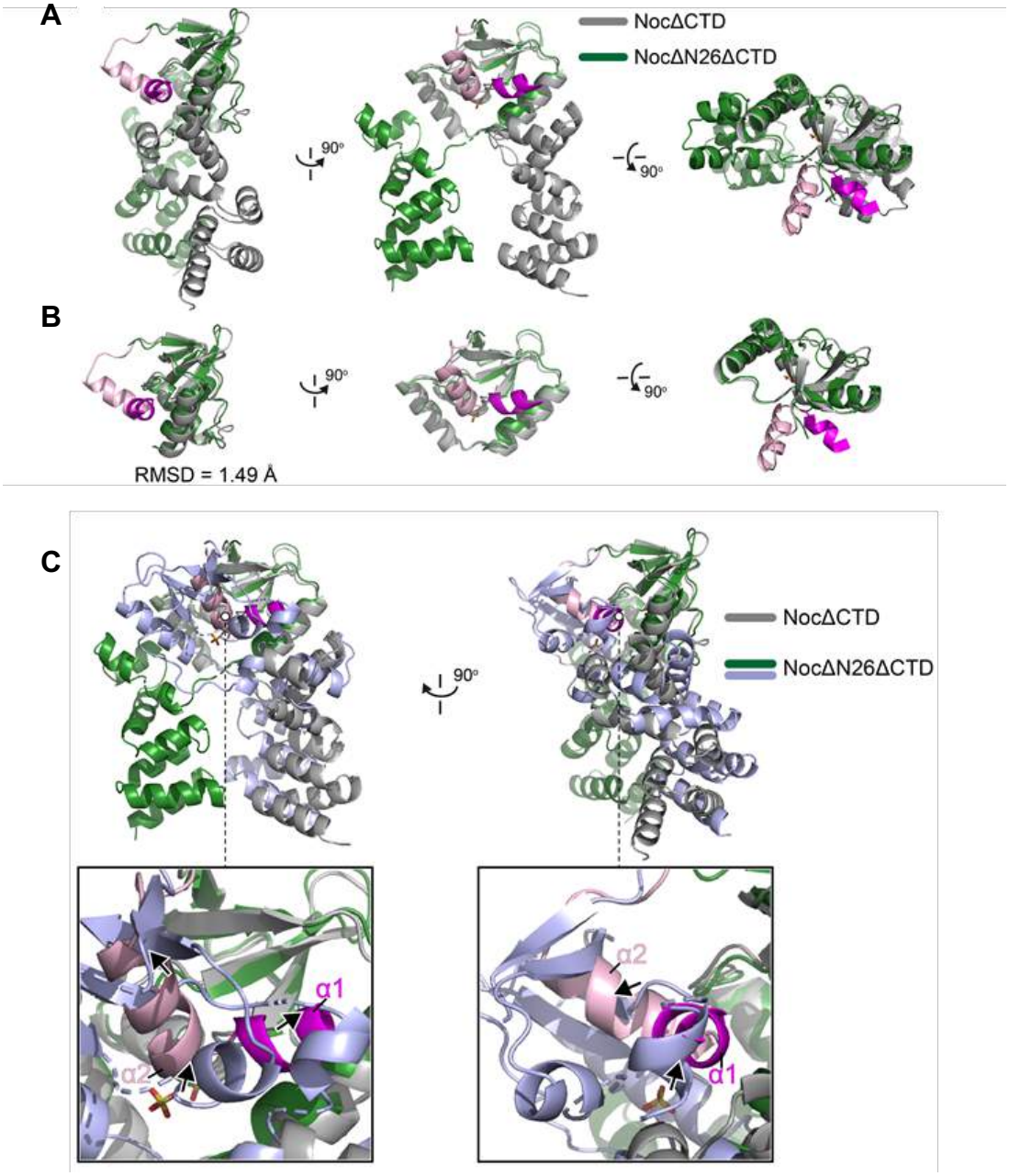

Figure 6.18 The conformation of Noc in the crystal structure of *G. thermoleovorans* NocNΔ26ΔCTD is incompatible with an autoinhibitory state of the amphipathic helix. (A) A superimposition at the N-terminal domains of a NocΔCTD monomer (grey) and a NocNΔ26ΔCTD monomer (green). The amphipathic helix α1 and helix α2 are shown in magenta and pink, respectively. **(B)** Same as panel B, but only the N-terminal domain (NTD) is shown for clarity. **(C)** A superimposition at the NTDs of NocΔCTD monomer (grey) and NocNΔ26ΔCTD dimer (green and light blue) shows a severe clash (arrows) between α1 (magenta), α2 (pink) and the opposite subunit of NocNΔ26ΔCTD (light blue).

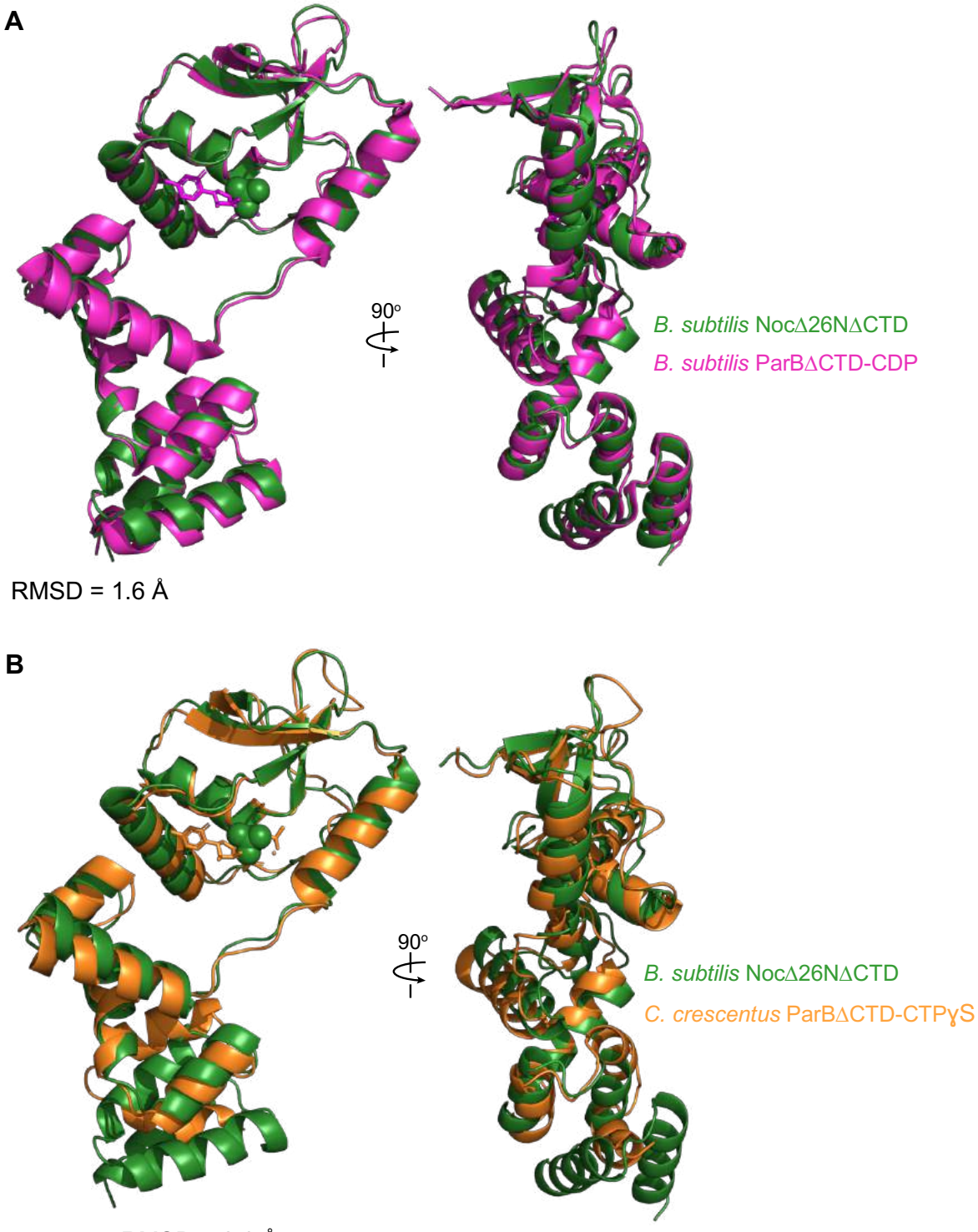
A
90°
B. subtilis NocΔ26NΔCTD
B. subtilis ParBΔCTD-CDP
RMSD = 1.6 Å
B
90°
B. subtilis NocΔ26NΔCTD
C. crescentus ParBΔCTD-CTPγS
RMSD = 2.6 Å

Figure 6.19 The conformation of *G. thermoleovorans* NocNΔ26ΔCTD is similar to that of a nucleotide-bound *B. subtilis* ParBΔCTD and *C. crescentus* ParBΔCTD (A) Superimposition between a *G. thermoleovorans* NocNΔ26ΔCTD dimer (green) and a *B. subtilis* ParBΔCTD-CDP dimer (magenta). CDP molecules are shown in magenta and the sulphate anion is shown in green. **(B)** Superimposition between a *G. thermoleovorans* NocNΔ26ΔCTD dimer (green) and a *C. crescentus* ParBΔCTD-CTPɣS dimer (yellow). CDP molecules are shown in magenta and the sulphate anion is shown in green.

Structure	***G. thermoleovorans* NocΔCTD - iodide**	***G. thermoleovorans* NocΔCTD - native**	***G. thermoleovorans* NocNΔ26ΔCTD**
Data collection			
Diamond Light Source beamline	I04	I04-1	I04
Wavelength (Å)	1.800	0.912	0.980
Detector	Eiger2 XE 16M	Pilatus 6M-F	Eiger2 XE 16M
Resolution range (Å)	96.61 – 3.40 (3.67 – 3.40)	84.89 – 2.50 (2.60 – 2.50)	37.44 – 2.95 (3.13 – 2.95)
Space Group	$P2_13$	$P2_13$	$C222_1$
Cell parameters (Å/°)	$a = b = c = 136.6$	$a = b = c = 146.8$	$a = 105.1$, $b = 106.6$, $c = 42.2$
Total no. of measured intensities	2147484 (426036)	1458851 (163435)	66966 (10641)
Unique reflections	11990 (2445)	36704 (4119)	5285 (835)
Multiplicity	179.1 (174.2)	39.7 (39.7)	12.6 (12.0)
Mean $I/\sigma(I)$	15.9 (3.3)	28.5 (1.8)	5.5 (1.5)
Completeness (%)	100.0 (100.0)	100.0 (100.0)	100.0 (100.0)
R_{merge}[a]	0.500 (3.392)	0.091 (2.654)	0.281 (1.343)
R_{meas}[b]	0.501 (3.402)	0.093 (2.688)	0.293 (1.399)
$CC_{½}$[c]	0.999 (0.894)	1.000 (0.670)	0.997 (0.885)
Wilson B value (Å^2)	88.7	68.0	38.2
Refinement			
Resolution range (Å)	-	84.89 – 2.50 (2.57 – 2.50)	37.44 – 2.95 (3.03 – 2.95)
Reflections: working/free[d]	-	34843/1794	4752/522
R_{work}[e]	-	0.210 (0.328)	0.267 (0.438)
R_{free}[e]	-	0.240 (0.386)	0.288 (0.443)
Ramachandran plot: favoured/allowed/disallowed[f] (%)	-	98.1/1.9/0.0	98.0/2.0/0.0
R.m.s. bond distance deviation (Å)	-	0.010	0.007
R.m.s. bond angle deviation (°)	-	1.55	1.33
Mean B fa protein/sulfate/water/ overall (Å^2)	-	85/118/71/86	74/70/0/74
PDB accession code		**7NFU**	**7NG0**

Values in parentheses are for the outer resolution shell. [a] *R*merge = $\sum hkl \sum i |I_i(hkl) - \langle I(hkl) \rangle| / \sum hkl \sum i I_i(hkl)$.

[b] *R*meas = $\sum hkl [N/(N-1)]^{1/2} \times \sum i |I_i(hkl) - \langle I(hkl) \rangle| / \sum hkl \sum i I_i(hkl)$, where $I_i(hkl)$ is the *i*th observation of reflection *hkl*, $\langle I(hkl) \rangle$ is the weighted average intensity for all observations *i* of reflection *hkl* and *N* is the number of observations of reflection *hkl*.

[c] *CC1/2* is the correlation coefficient between symmetry equivalent intensities from random halves of the dataset.

[d] The dataset was split into "working" and "free" sets consisting of 95 and 5% of the data respectively. The free set was not used for refinement.

[e] The R-factors *R*work and *R*free are calculated as follows: $R = \sum(|F\text{obs} - F\text{calc}|)/\sum|F\text{obs}|$, where *F*obs and *F*calc are the observed and calculated structure factor amplitudes, respectively.

[f] As calculated using MolProbity (Davis et al., 2007).

Table 6.1 X-ray data collection and processing statistics for the crystal structures of the *G. thermoleovorans* NocΔCTD-iodide, *G. thermoleovorans* NocΔCTD-native and *G. thermoleovorans* NocNΔ26ΔCTD.

in our structure, instead a sulphate anion occupies a similar nucleotide-binding pocket to the *B. subtilis* ParB-CDP structure (Fig. 6.19A-B) (Soh et al., 2019). I further observed that helix α5 in the NocΔN26ΔCTD structure swings outwards by 104 degrees and no longer bundles with helix α6 from the same subunit (Fig. 6.18C), and that this movement might drive the self-dimerisation at the N-terminal domain of Noc i.e. the NTD engagement (Fig. 6.18C). By superimposing the NTDs of NocΔCTD and NocNΔ26ΔCTD (RMSD = 1.49 Å), I detected severe clashes between α1, α2, and the opposite subunit of NocNΔ26ΔCTD (Fig. 6.18A-C). Therefore, it is clear that the autoinhibitory state of α1 and α2 (as observed in NocΔCTD) is not compatible with the alternative conformation in the NocNΔ26ΔCTD structure. I speculate that the amphipathic helix α1 and α2 might be liberated from its autoinhibitory conformation to be compatible with the NTD-engagement conformation in the NocNΔ26ΔCTD structure.

6.10 Discussion

The nucleoid occlusion protein Noc increases cell division efficiency by directing the division machinery towards midcell either by inhibiting FtsZ formation over the nucleoid and/or by concentrating FtsZ in the vicinity of a pre-existing mid-cell Z-ring (Pang et al., 2017; Rodrigues and Harry, 2012). The extensive Noc-mediated DNA-membrane interaction is at the heart of both models for nucleoid occlusion (Adams et al., 2015; Wu et al., 2009). In this study, I show that CTP regulates the nucleoid occlusion activity of Noc. I provide evidence that (i) CTP is required for Noc to form the *NBS*-dependent nucleoprotein complex, and (ii) CTP binding switches Noc from a membrane-inactive auto-repressed state to a membrane-active state. I propose that the dual dependency of Noc's membrane-binding activity on *NBS* and CTP might ensure productive recruitment of DNA to the bacterial cell membrane to exert the nucleoid occlusion activity (Fig. 6.20). It has been estimated that the intracellular concentrations of Noc and CTP are ~5 μM and ~1 mM, respectively (Buckstein et al., 2008; Wu et al., 2009). At these concentrations, if the membrane-binding activity of Noc was solely dependent on CTP, most intracellular DNA-unbound Noc would be in the CTP-bound state and confined to the cell membrane, thus potentially limiting the recruitment of chromosomal DNA to the cell membrane. I therefore reason that the *NBS*-stimulated Noc-CTP interaction provides a mechanism to commit Noc into a pathway in which only DNA-entrapped Noc molecules are able to associate with the cell membrane (Fig. 6.20). Another consequence of coupling membrane activity to *NBS* binding is that membrane-associated nucleoprotein complexes are spatially confined near the vicinity of *NBS* sites. This spatial confinement is important for directing division machinery formation towards midcell where the concentration of *NBS* sites, hence the nucleoid occlusion activity, is lowest (Wu et al., 2009).

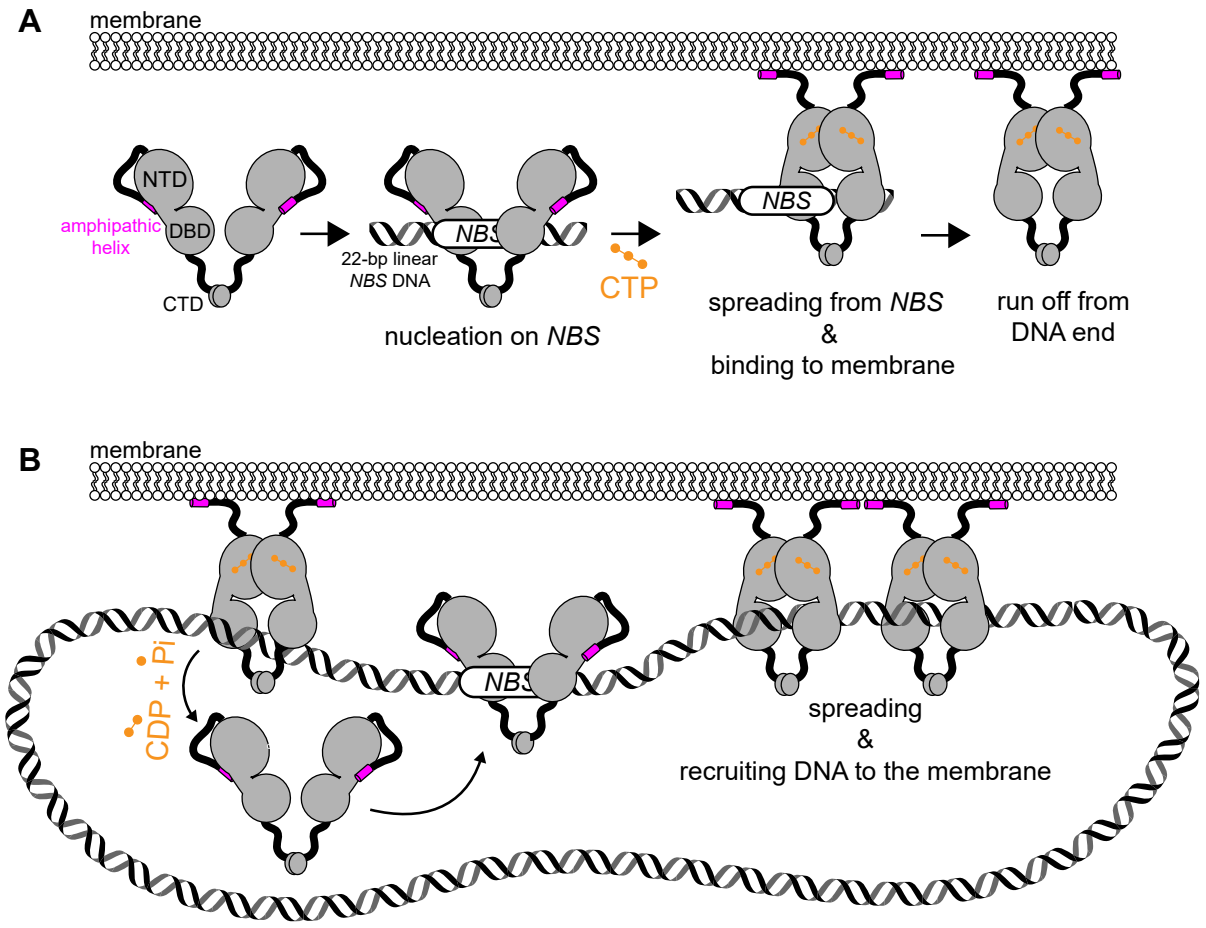

Figure 6.20 A model for a CTP-dependent regulation of membrane-binding activity of Noc. (A) Noc binds specifically to *NBS* site to nucleate on DNA. In the apo- or *NBS*-associated form, the amphipathic helix (magenta) adopts an autoinhibitory conformation, thus cannot bind to the membrane. *NBS*-binding stimulates Noc to bind CTP (orange). Concomitantly, CTP induces a sliding clamp conformation in Noc that can run off open ends of a linear 22-bp *NBS* DNA. In this state, the amphipathic helix is likely liberated from the autoinhibitory conformation, thus enable Noc-CTP to bind to the membrane. **(B)** When a circular *NBS* plasmid with no open end was employed, a sliding clamp of Noc entraps plasmid DNA and recruit DNA to the membrane. In the presence of CTD, a tripartite membrane-protein-DNA linkage is formed. CTP hydrolysis is not required for membrane binding or DNA recruitment but might has a role in releasing Noc from DNA and the membrane.

The lack of a bound nucleotide in the NocNΔ26ΔCTD structure forbids me from drawing a conclusion on the role of CTP and the possible conformational liberation of the amphipathic helix α1. However, several lines of evidence suggest that CTP might favour the NTD-engagement conformation as observed in our NocNΔ26ΔCTD structure: (i) CTP/CTPɣS promoted the crosslinking between symmetrical E29C residues, a readout for NTD-engagement (Fig. 6.5B), (ii) the conformation of NocNΔ26ΔCTD is highly similar to that of a CDP-bound *B. subtilis* ParB and CTPɣS-bound *C. crescentus* ParB (Fig. 6.20A-B), and (iii) CTP/CTPɣS enables Noc (WT) to co-sediment with liposomes (Fig. 6.9) (Chapter 4) (Soh et al., 2019). Altogether, it is not unreasonable to speculate that the CTP-induced NTD engagement might liberate the amphipathic helix from its autoinhibitory state to interact with the cell membrane. The 8-AA loop that connects the amphipathic helix to the rest of Noc might offer the flexibility to orient the amphipathic helix parallel to the membrane plane for binding (Fig. 6.20).

This study also provides evidence that *B. subtilis* Noc possesses CTPase activity, but CTP hydrolysis is neither required for the clamp formation nor membrane association. What might possibly the role of CTP hydrolysis be? Similar to the counterpart ParB, CTP hydrolysis and/or the subsequent release of hydrolytic products might disengage the NTD to open the clamp to release entrapped DNA (Fig. 6.20B) (Jalal et al., 2020a; Osorio-Valeriano et al., 2019; Soh et al., 2019). Concomitantly, Noc might revert to the membrane-inactive state, enabling its extraction from the cell membrane. Our experiment that employed EDTA to sequester coordinated Mg^{2+} to artificially promote the dissociation of CTP from Noc supports the proposal that membrane association can be reversible (Fig. 6.12). Furthermore, *B. subtilis* Noc foci associate with the cell membrane in a transient manner, perhaps suggesting a weak and fast on/off membrane interaction *in vivo* (Adams et al., 2015). The transient association with the membrane, possibly endowed by a CTP hydrolysis event that facilitates the release of Noc, might be advantageous for the cells because a strong and permanent mode of binding might hamper chromosome replication or damage DNA. Supporting this view, fusing NocNΔ10 to a synthetic transmembrane helix led to broken, bisected chromosomes and eventually chromosome segregation defects in many *B. subtilis* cells (Adams et al., 2015; Nyholm et al., 2007). Lastly, we noted that NocNΔ10 binds CTP equally/slightly stronger than Noc (WT) (Fig. 1D) yet its CTPase rate is reduced by a half (Fig. 6.4). It is still unclear why this is the case; however, we speculate that the autoinhibitory conformation of this N-terminal most region might play a role in CTP binding/hydrolysis. Lending support to our speculation, this N-terminal-most region interacts with residues Q66 and R86 (apo-NocΔCTD structure, Fig. 6.16B) whose equivalent residues in *C. crescentus* and *B. subtilis* ParB are known to be critical for CTP binding (Soh et al., 2019).

ATP and GTP switches that control membrane activity are widespread in all domains of life. For example, ATP binding promotes the dimerisation of MinD (role in bacterial cell division site selection) and concomitantly increases its affinity for the cell membrane (Hu and Lutkenhaus, 2003; Hu et al., 2002; Ramm et al., 2019; Wu et al., 2011). MinE, a partner of MinD, stimulates the ATPase activity of MinD, promoting MinD dissociation from the membrane. In eukaryotes, both the Ras-related protein (Sar) and ADP-ribosylation factor (Arf) (role in vesicle trafficking) function as GTP-dependent switches, cycling between the active GTP-bound form and the inactive GDP-bound form (Beck et al., 2008; Bielli et al., 2005; Bos et al., 2007; Dodonova et al., 2017; Hanna et al., 2016; Krauss et al., 2008; Lee et al., 2005; Zhukovsky et al., 2019). In the GDP-bound form, the amphipathic helix of Sar/Arf1 adopts a repressed conformation by burying itself into a hydrophobic pocket (Goldberg, 1998; Zhukovsky et al., 2019). The exchange of GDP for GTP induces conformational changes that push the myristoylated amphipathic helix out of the hydrophobic pocket, enabling membrane association (Goldberg, 1998; Zhukovsky et al., 2019). Our study provides evidence for a first CTP switch that controls membrane activity (Fig. 6.20), suggesting that CTP switches are likely to control more diverse functions in biology than previously appreciated.

Taken together my findings unveils a nucleotide-dependent regulatory layer, in addition to the previously described DNA-dependent regulation, in the nucleoid occlusion protein Noc (Adams et al., 2015). The dual dependency on nucleotide and DNA guarantees a productive formation of the tripartite DNA-protein-membrane super-complex for nucleoid occlusion. In this work, we also provide evidence for a CTP switch that controls membrane-binding activity, adding the control of membrane association in Noc to the role of ParB-CTP in bacterial chromosome segregation. It is likely that CTP switches are pervasive in biology but have so far been underappreciated (Basu and Koonin, 2005; Osorio-Valeriano et al., 2019; Soh et al., 2019). Finally, evolution is replete with examples of functional domains being adapted to diversify functions of proteins. Gene encoding Noc resulted from gene duplication and neo-functionalization from *parB*, our work furthers the understanding of how CTP switch has been adapted to a new function, hence might have implications in understanding biological innovations by evolution (Jalal et al., 2020b; Sievers et al., 2002; Wu and Errington, 2012).

6.11 References

1. Adams, D.W., Wu, L.J., and Errington, J. (2015). Nucleoid occlusion protein Noc recruits DNA to the bacterial cell membrane . EMBO J. **34**, 491–501.
2. Basu, M.K., and Koonin, E. V. (2005). Evolution of eukaryotic cysteine sulfinic acid reductase, sulfiredoxin (Srx), from bacterial chromosome partitioning protein ParB.

Cell Cycle. **4**, 947–952.

3. Beck, R., Sun, Z., Adolf, F., Rutz, C., Bassler, J., Wild, K., Sinning, I., Hurt, E., Brügger, B., Béthune, J., et al. (2008). Membrane curvature induced by Arf1-GTP is essential for vesicle formation. Proc. Natl. Acad. Sci. U. S. A. **105**, 11731–11736.
4. Bielli, A., Haney, C.J., Gabreski, G., Watkins, S.C., Bannykh, S.I., and Aridor, M. (2005). Regulation of Sar1 NH2 terminus by GTP binding and hydrolysis promotes membrane deformation to control COPII vesicle fission. J. Cell Biol. **171**, 919–924 (2005).
5. Bos, J.L., Rehmann, H., and Wittinghofer, A. (2007). GEFs and GAPs: Critical Elements in the Control of Small G Proteins. Cell. **129**, 865–877 (2007).
6. Breier, A.M., and Grossman, A.D. (2007). Whole-genome analysis of the chromosome partitioning and sporulation protein Spo0J (ParB) reveals spreading and origin-distal sites on the Bacillus subtilis chromosome. Mol. Microbiol. **64**, 703–718 (2007).
7. Buckstein, M.H., He, J., and Rubin, H. (2008). Characterization of nucleotide pools as a function of physiological state in Escherichia coli. J. Bacteriol. **190**, 718–726 (2008).
8. Dodonova, S.O., Aderhold, P., Kopp, J., Ganeva, I., Röhling, S., Hagen, W.J.H., Sinning, I., Wieland, F., and Briggs, J.A.G. (2017). 9Å structure of the COPI coat reveals that the Arf1 GTPase occupies two contrasting molecular environments. Elife. **6**, e26691
9. Funnell, B.E. (2016). ParB partition proteins: Complex formation and spreading at bacterial and plasmid centromeres. Front. Mol. Biosci. **3,** 44
10. Goldberg, J. (1998). Structural basis for activation of ARF GTPase: Mechanisms of guanine nucleotide exchange and GTP-myristoyl switching. Cell. **95**, 237–248
11. Graham, T.G.W., Wang, X., Song, D., Etson, C.M., van Oijen, A.M., Rudner, D.Z., and Loparo, J.J. (2014). ParB spreading requires DNA bridging. Genes Dev. **28**, 1228–1238.
12. Hanna, M.G., Mela, I., Wang, L., Henderson, R.M., Chapman, E.R., Edwardson, J.M., and Audhya, A. (2016). Sar1 GTPase activity is regulated by membrane curvature. J. Biol. Chem. **291**, 1014–1027.
13. Hu, Z., and Lutkenhaus, J. (2003). A conserved sequence at the C-terminus of MinD is required for binding to the membrane and targeting MinC to the septum. Mol. Microbiol. **47**, 345–355.
14. Hu, Z., Gogol, E.P., and Lutkenhaus, J. (2002). Dynamic assembly of MinD on phospholipid vesicles regulated by ATP and MinE. Proc. Natl. Acad. Sci. U. S. A. **99**, 6761–6766.
15. Hwang, L.C., Vecchiarelli, A.G., Han, Y.W., Mizuuchi, M., Harada, Y., Funnell, B.E., and Mizuuchi, K. (2013). ParA-mediated plasmid partition driven by protein pattern

self-organization. EMBO J. **32**, 1238– 1249.

16. Jalal, A.S.B., and Le, T.B.K. (2020). Bacterial chromosome segregation by the ParABS system. Open Biol. **10**, 200097.
17. Jalal, A.S., Tran, N.T., and Le, T.B. (2020a). ParB spreading on DNA requires cytidine triphosphate in vitro. Elife. 9, e53515.
18. Jalal, A.S.B., Tran, N.T., Stevenson, C.E., Chan, E.W., Lo, R., Tan, X., Noy, A., Lawson, D.M., and Le, T.B.K. (2020b). Diversification of DNA-Binding Specificity by Permissive and Specificity-Switching Mutations in the ParB/Noc Protein Family. Cell Rep. **32**, 107928.
19. Jalal A.S.B., Tran N.T., Wu L.J., Ramkrishnan K, Rejzek M, Stevenson C.E.M., Lawson, D.M., Errington, J and Le T.B.K. 2020. CTP regulates membrane-binding activity of the nucleoid occlusion protein Noc. Mol. Cell., **21**, S1097–2765.
20. Krauss, M., Jia, J.Y., Roux, A., Beck, R., Wieland, F.T., De Camilli, P., and Haucke, V. (2008). Arf1-GTP-induced tubule formation suggests a function of arf family proteins in curvature acquisition at sites of vesicle budding. J. Biol. Chem. **283**, 27717–27723.
21. Krissinel, E. (2015). Stock-based detection of protein oligomeric states in jsPISA. Nucleic Acids Res. **43**, W314–319.
22. Lee, M.C.S., Orci, L., Hamamoto, S., Futai, E., Ravazzola, M., and Schekman, R. (2005). Sar1p N-terminal helix initiates membrane curvature and completes the fission of a COPII vesicle. Cell. **122**, 605–617.
23. Leonard, T.A., Butler, P.J.G., and Löwe, J. (2004). Structural analysis of the chromosome segragation protein Spo0J from Thermus thermophilus. Mol. Microbiol. **53**, 419–432.
24. Lim, H.C., Surovtsev, I. V., Beltran, B.G., Huang, F., Bewersdorf, J., and Jacobs-Wagner, C. (2014). Evidence for a DNA-relay mechanism in ParABS-mediated chromosome segregation. Elife. **3**, e02758.
25. Murray, H., Ferreira, H., and Errington, J. (2006). The bacterial chromosome segregation protein Spo0J spreads along DNA from parS nucleation sites. Mol. Microbiol. **61**, 1352–1361.
26. Nyholm, T.K.M., Özdirekcan, S., and Antoinette Killian, J. (2007). How protein transmembrane segments sense the lipid environment. Biochemistry. **46**, 1457–1465.
27. Osorio-Valeriano, M., Altegoer, F., Steinchen, W., Urban, S., Liu, Y., Bange, G., and Thanbichler, M. (2019). ParB-type DNA Segregation Proteins Are CTP-Dependent Molecular Switches. Cell. **179**, 1512- 1524.e15.
28. Pang, T., Wang, X., Lim, H.C., Bernhardt, T.G., and Rudner, D.Z. (2017). The nucleoid occlusion factor Noc controls DNA replication initiation in Staphylococcus aureus. PLoS Genet. **13**, e1006908.

29. Ramm, B., Heermann, T., and Schwille, P. (2019). The E. coli MinCDE system in the regulation of protein patterns and gradients. Cell. Mol. Life Sci. **76**, 4245–4273.
30. Rodrigues, C.D.A., and Harry, E.J. (2012). The min system and nucleoid occlusion are not required for identifying the division site in bacillus subtilis but ensure its efficient utilization. PLoS Genet. **8**, e1002561.
31. Sanchez, A., Cattoni, D.I., Walter, J.C., Rech, J., Parmeggiani, A., Nollmann, M., and Bouet, J.Y. (2015). Stochastic Self-Assembly of ParB Proteins Builds the Bacterial DNA Segregation Apparatus. Cell Syst. **1**, 163– 173.
32. Sievers, J., Raether, B., Perego, M., and Errington, J. (2002). Characterization of the parB-like yyaA gene of Bacillus subtilis. J. Bacteriol. **184**, 1102–1111
33. Soh, Y.-M., Davidson, I.F., Zamuner, S., Basquin, J., Bock, F.P., Taschner, M., Veening, J.-W., De, P., Rios, L., Peters, J.-M., et al. (2019). Self-organization of *parS* centromeres by the ParB CTP hydrolase. Science. **366**, 1129–1133
34. Toro, E., Hong, S.H., McAdams, H.H., and Shapiro, L. (2008). Caulobacter requires a dedicated mechanism to initiate chromosome segregation. Proc. Natl. Acad. Sci. U. S. A. **105**, 15435–15440.
35. Vecchiarelli, A.G., Hwang, L.C., and Mizuuchi, K. (2013). Cell-free study of F plasmid partition provides evidence for cargo transport by a diffusion-ratchet mechanism. Proc. Natl. Acad. Sci. U. S. A. **110**, E1390-1397
36. Vecchiarelli, A.G., Neuman, K.C., and Mizuuchi, K. (2014). A propagating ATPase gradient drives transport of surface-confined cellular cargo. Proc. Natl. Acad. Sci. U. S. A. 111, 4880–4885.
37. Veiga, H., Jorge, A.M., and Pinho, M.G. (2011). Absence of nucleoid occlusion effector Noc impairs formation of orthogonal FtsZ rings during Staphylococcus aureus cell division. Mol. Microbiol. **80**, 1366–1380.
38. Wu, L.J., and Errington, J. (2004). Coordination of cell division and chromosome segregation by a nucleoid occlusion protein in Bacillus subtilis. Cell. **117**, 915–925.
39. Wu, L.J., and Errington, J. (2012). Nucleoid occlusion and bacterial cell division. Nat. Rev. Microbiol. **10**, 8–12.
40. Wu, L.J., Ishikawa, S., Kawai, Y., Oshima, T., Ogasawara, N., and Errington, J. (2009). Noc protein binds to specific DNA sequences to coordinate cell division with chromosome segregation. EMBO J. **28**, 1940–1952.
41. Wu, W., Park, K.T., Holyoak, T., and Lutkenhaus, J. (2011). Determination of the structure of the MinD-ATP complex reveals the orientation of MinD on the membrane and the relative location of the binding sites for MinE and MinC. Mol. Microbiol. **79**, 1515–1528.
42. Zhukovsky, M.A., Filograna, A., Luini, A., Corda, D., and Valente, C. (2019). Protein

Amphipathic Helix Insertion: A Mechanism to Induce Membrane Fission. Front. Cell Dev. Biol. **7**, 291.

Chapter 7: General discussion

Parts of this chapter have been published in Open Biology, for which I wrote the first draft of the review:

Jalal, A.S.B., and Le, T.B.K. (2020). Bacterial chromosome segregation by the ParABS system. Open Biol. **10**, 200097.

7.1 Evolution shapes the factors involved in bacterial genomic maintenance

7.2 Multiple models for ParB spreading on the bacterial chromosome

7.3 A stepwise model describing the formation of the Noc-DNA-membrane complex

7.4 Cytidine-triphosphate (CTP) molecular switches: a common theme in biology?

7.5 Final perspectives

7.6 References

7.1 Evolution shapes the factors involved in bacterial genomic maintenance

The maintenance of genomic integrity is a sophisticated process that requires the involvement of multiple biological factors. Remarkably, through gene duplication and neo-functionalisation, Nature has repurposed various proteins with novel functions to promote genomic maintenance (Qian and Zhang, 2014). One such example includes the evolutionarily related proteins, ParB and Noc. The close genomic proximity and high sequence similarity between ParB and Noc suggests that *noc* evolved from *parB* through a gene duplication event (Sievers et al., 2002; Wu and Errington, 2012). Through the loss of a ParA-interacting domain and the acquisition of an amphipathic helix, ParB was reengineered to no longer function in chromosome segregation, but rather in nucleoid occlusion (Adams et al., 2015). The mutational event that resulted in the grafting of an amphipathic helix might have been the evolutionary mechanism that once granted a novel function to Noc. However, the evolutionary trajectory that replaced the ParA-interacting region in favour of an amphipathic helix remains enigmatic. Recently, Knopp *et. al.* (2019) generated a diverse library of randomised DNA sequences encoding short peptides in *E. coli* and demonstrated that the *de novo* emergence of such peptides can confer resistance towards antibiotics (Knopp et al., 2019). Using a similar approach, it may be possible to reconstitute the evolution of the Noc amphipathic helix by replacing the DNA sequence encoding the amphipathic helix with one that would encode library of random encoding peptides. This diverse library could then be expressed into a strain of *B. subtilis* where a functional Noc is required for cell viability (live-or-dead selection). Deep sequencing of the region encoding the amphipathic helix of these *noc* variants, both pre- and post-selection, coupled with network analysis might reconstitute the evolutionary paths that enabled the grafting of the amphipathic helix.

Furthermore, in contrast to ParB, Noc does not bind *parS* but instead recognizes a different DNA substrate, *NBS* (Wu et al., 2009). *NBS* differs from *parS* by only two bases yet Noc and ParB recognise them with exquisite specificity (Chapter 3). The difference in the distribution of *parS* and *NBS* on the chromosome also contributes towards the divergence in the roles of ParB and Noc (Livny et al., 2007; Pang et al., 2017; Wu et al., 2009). The clustering of *parS* towards the *ori*, promotes efficient DNA replication/segregation and ParB-dependent chromosome anchoring. Whereas the distribution of *NBS* sites all over the genome except near the *ter*, directs Z-ring assembly towards the midcell (Wu et al., 2009). By combining X-ray crystallography with systemic mutagenesis approaches, we have identified that the recognition of ParB to *parS* and Noc to *NBS* is encoded by a small set of four specificity defining-residues (Chapter 3) (Jalal et al., 2020b). Indeed, a ParB protein harbouring four of the specificity defining-residues from Noc, no longer recognised *parS*, but prefers *NBS* as its DNA substrate. From comparing the co-crystal structures of the *C. crescentus* ParB (DBD)-

parS complex with the *B. subtilis* Noc (DBD)-*NBS* complex, I demonstrate the molecular basis that enabled the diversification of DNA-binding specificity between ParB and Noc (Chapter 3) (Jalal et al., 2020b). Indeed, a combination of permissive mutations which increased the overall binding affinity of Noc to the *NBS* site and a series of sequence specific mutations generated a ParB variant that specifically binds *NBS* and no longer recognises *parS*. Later, deep mutational scanning of these four residues reconstituted the evolutionary trajectory that reprogramed the DNA-binding specificity of ParB to Noc (Jalal et al., 2020b), demonstrating permissive mutations were first introduced before specificity-switching substitutions to change the DNA-binding specificity of ParB to Noc (Jalal et al., 2020b). Interestingly, from our systemic scanning approach, we demonstrated that various ParB-to-Noc (PtoN) variants displayed promiscuous interactions with their cognate DNA sites. Future approaches to better understand the co-evolution of ParB and Noc with their respective DNA sites may involve the generation of a bacterial one-hybrid library with each PtoN variant that displayed a promiscuous interaction. A combination of biochemical reconstitutions, X-ray crystallography and modelling approaches (molecular dynamic simulations) may yet reveal the molecular basis underpinning the DNA-binding specificity mediated by these PtoN variants. Nevertheless, the small number of required mutations and the large number of mutational paths to reprogram DNA-binding specificity demonstrates how evolvable the ParABS system is. This in combination with the widespread distribution of the ParABS system over various species of bacteria illustrates that evolution likely repurposed various proteins belonging to the ParA/ParB superfamily to function outside of chromosome segregation (Livny et al., 2007).

Outside of the ParB/Noc protein family, other examples include the existence of different ParA homologs across various bacterial species. In *Rhodobacter sphaeroides*, an orphan ParA-like protein (PpfA) uses non-specific nucleoid binding to separate cytoplasmic clusters of chemotaxis proteins (Roberts et al., 2012). Similar to the canonical ParABS system, the ATPase activity of PpfA is modulated by the N terminus of a ParB analogue (TlpT) (Roberts et al., 2012). In *C. crescentus*, another ParA homologue (MipZ) coordinates chromosome segregation with cell division by directly interfering with FtsZ polymerization (Thanbichler and Shapiro, 2006). MipZ binds DNA non-specifically and also interacts with ParB to create a bipolar protein gradient in the cells that restricts FtsZ ring formation to the midcell, where the concentration of MipZ is lowest (Corrales-Guerrero et al., 2020; Kiekebusch et al., 2012; Thanbichler and Shapiro, 2006). In *V. cholerae*, three ParA-like ATPases (ParA1, FlhG, and ParC) interact with a polar transmembrane protein HubP to control polar localization of the chromosome origin, the chemotactic machinery, and the flagellum (Yamaichi et al., 2012). Another such example includes the nucleoid occlusion protein SlmA, found in *E. coli.* Noticeably, the crystal structure of SlmA, revealed a similar fold to the tetracycline repressor

(TetR) superfamily (Cuthbertson and Nodwell, 2013; Schumacher and Zeng, 2016; Tonthat et al., 2013). It is likely that by swapping its sequence specificity for *SBS*, over the TetR operator site (*tetO*) that enables TetR to repress the expression of the TetA efflux pump, SlmA was repurposed to function in nucleoid occlusion (Cho and Bernhardt, 2013; Cuthbertson and Nodwell, 2013). Additionally, the ligand binding domain of TetR was reengineered, allowing SlmA to interact with the CTD of FtsZ to impair FtsZ polymerisation instead of tetracycline. Intriguingly, unlike TetR, where ligand binding results in dissociation from *tetO*, SlmA must be in complex with *SBS* to interact with its ligand, FtsZ (Schumacher and Zeng, 2016; Tonthat et al., 2013). These examples illustrate how diverse functions in biology can evolve from a general mechanism, and are therefore interesting from both evolutionary and mechanistic standpoints.

Moreover, research in various model organisms and an ever-increasing number of sequenced bacterial genomes have highlighted the diversification in the mechanism of bacterial chromosome segregation. Roughly one-third of bacterial species lack ParABS homologs entirely and thus likely utilize other systems to facilitate their chromosome partitioning (Livny et al., 2007). Intriguingly some species, for example *Streptococcus pneumoniae* or *Staphylococcus aureus*, lack ParA but both ParB-*parS* as well as SMC are present. Even in bacterial species that possess the canonical ParABS system, wide variation in the number of *parS* sites exists; examples include, *Xanthomonas campestris* has a single *parS* site while *Streptomyces coelicolor* and *Listeria innocua* accumulated up to 20-23 *parS* sites clustered towards the *ori* (Jakimowicz et al., 2002; Livny et al., 2007). Why does a variation in the number of *parS* sites exists, when a single *parS* site is often sufficient for chromosome segregation (Graham et al., 2014; Jecz et al., 2015; Lagage et al., 2016)? How does this variation in the number of *parS* sites influence chromosome segregation in different bacterial species in their respective niches? Why do *parS* sites position closely on the genome and what drives their clustering over evolutionary time? For the last question, a transposon-based saturated insertion of a *parS* site on the *Pseudomonas aeruginosa* and *C. crescentus* chromosome offered some insights; it was discovered that the insertion of a *de novo* or a second *parS* site is only tolerable in ~600 kb region surrounding the native *parS* locus or the origin of replication without severely affecting cell fitness (Lagage et al., 2016; Tran et al., 2018). These results suggest a self-reinforcing mechanism for the expansion of the bacterial centromere region by restricting the multiplication of *parS* to a narrow region near the original site.

Finally, a DNA segregation system that combines bacterial ParAB-like and eukaryotic histone-like components has been identified in the archaea *Sulfolobus* (Schumacher et al., 2015). This

system consists of an ATPase ParA, an atypical ParB adaptor, and a novel centromere-binding protein AspA. The NTD of the archaeal ParB is similar to the bacterial ParB NTD, however its CTD resembles an eukaryotic histone protein CenpA. A long amino acid linker that connects the two domains of the archaeal ParB interacts with ParA while its N-terminal domain binds AspA (Schumacher et al., 2015). AspA binds the centromere, thereby serves as a physical link between the archaeal ParA-ParB and the segregating DNA. The hybrid nature of the archaeal DNA segregation machinery demonstrates how evolution has diversified DNA segregation systems, possibly to adapt to the specific needs of each organism, while keeping the general mechanism conserved across the three domains of life.

7.2 Multiple models for the formation of the ParB-*parS* nucleoprotein complex

Over 35 years of research into the ParB family of proteins have resulted in the proposal of various models for ParB nucleoprotein complex assembly. With the unexpected finding that ParB belonging to a new family of CTPase proteins challenging our current thinking on the assembly of the ParB-DNA nucleoprotein complex, and in turn bacterial chromosome segregation/maintenance (Osorio-Valeriano et al., 2019; Soh et al., 2019). Despite this, it is too early to suggest that the ParB-CTP "spreading by sliding" model supersede each previously proposed models, as various mechanistic insights are still poorly understood. Indeed, Osorio-Valeriano *et. al.,* (2019) proposed an alternative view on ParB-CTP interactions, whereby *parS* binding enhances the CTPase activity in *M. xanthus* ParB, thus switching *M. xanthus* ParB from a closed CTP-bound conformation to an open CDP-bound conformation (Osorio-Valeriano et al., 2019). The weak affinity of *M. xanthus* ParB to CDP would favour the dissociation of bound CDP, enabling the NTD of *M. xanthus* ParB to participate in DNA-bridging and caging interactions (Osorio-Valeriano et al., 2019). Though, whether *M. xanthus* ParB can also participate in similar protein-protein and protein-DNA interactions to condense distal loci like *B. subtilis* ParB has yet to be confirmed experimentally (Fisher et al., 2017; Graham et al., 2014; Taylor et al., 2015). It is likely that two different models of ParB function inside the cells: one that enables the bridging/caging of DNA together, and another that enables the lateral sliding of ParB as a ring on DNA. Investigating the relative contribution of the two different modes of action to chromosome segregation, especially *in vivo*, represents an important challenge for the future.

The initial model for the assembly of the ParB-*parS* complex came from studies using plasmid borne ParB, whereby ParB was proposed to form a one-dimensional filament that binds the DNA flanking the *parS* site (Rodionov et al., 1999). Later, a combination of quantitative immunoblotting and immunofluorescence microscopy approaches, estimated that the number of ParB molecules in the cell is too low to support ParB spreading as a one-dimensional

filament (Graham et al., 2014). Instead, using single-molecule TIRF microscopy, Graham *et. al.,* (2014) proposed the 'spreading and bridging model' whereby the non-specific binding of *B. subtilis* ParB results in the three-dimensional bridging and looping of DNA (Graham et al., 2014). Indeed, mutations in the arginine-rich patch that have previously been shown to impair ParB spreading *in vivo* also hampered the DNA-bridging activity of *B. subtilis* ParB (Graham et al., 2014). Almost at the same time, Taylor *et. al.,* (2015) using *in vitro* magnetic tweezer approaches demonstrated that the combination of *B. subtilis* ParB-ParB and ParB-non-specific DNA interactions results in the condensation of DNA (Taylor et al., 2015). While the co-crystal structure of *H. pylori* ParBΔCTD-*parS* complex demonstrated that the arginine rich patch mediates ParB spreading, by acting as a protein-protein interface that mediates ParB-ParB oligomerization (Chen et al., 2015). Later, Fisher *et. al.,* (2017) proposed that the CTD of *B. subtilis* ParB, in addition to acting as a dimerization interface, also possess a series of lysine residues that mediates the binding and compaction of non-specific DNA networks *in vitro* (Fisher et al., 2017). In contrast to *B. subtilis* ParB, *C. crescentus* ParB failed to display any non-specific DNA condensation activity *in vitro* (Chapter 5). While, *C. crescentus* ParB could only condense DNA *in vitro* using magnetic tweezer assays when the CTD was engineered to possess a *B. subtilis* like non-specific DNA binding activity. It is important to emphasize that both NTD-NTD interactions of ParB and non-specific DNA binding of the CTD is required for DNA condensation activity *in vitro* (Fisher et al., 2017; Taylor et al., 2015). Thus, these findings suggests that *C. crescentus* ParB can also participate in such ParB-ParB interactions in absence of CTP to condense DNA (when the additional three-five lysine residues are present at the CTD). Despite this, the role of CTP in the bridging and condensation ability of ParB needs to be addressed, as the single-molecule imaging approaches that led to the proposal of the 'bridging and condensation' models were done in the absence of CTP. The modest affinity between ParB and CTP suggests that the purified ParB proteins used in these assays were likely CTP free (Osorio-Valeriano et al., 2019; Soh et al., 2019). Nevertheless, as *C. crescentus* lacks any noticeable non-specific DNA binding/condensation activity *in vitro*, future experiments may seek to use *C. crescentus* ParB as a model protein to better understand the role of CTP in regulating its ability to bridge and condense distal loci.

Initially I was surprised by the lack of NTD mediated ParB-ParB interactions in my *C. crescentus* ParBΔCTD-*parS* co-crystal structure, despite *C. crescentus* ParB being able to spread *in vivo* (Chapter 4) (Tran et al., 2018). Nevertheless, through *in vitro* reconstitution we were able to demonstrate that *parS*-dependent spreading requires CTP as a co-factor (Jalal et al., 2020a). Furthermore, from solving the *C. crescentus* ParBΔCTD-CTPɣS complex I was

able to better understand the role of CTP in ParB spreading. We demonstrate that CTP functions as molecular switch to convert ParB from a nucleating-*parS* bound open clamp, to a CTP-bound closed sliding patch clamp (Chapter 4). Structural comparisons between the *C. crescentus* ParBΔCTD-*parS* and the *C. crescentus* ParBΔCTD-CTPɣS complex demonstrated that the DBDs also move approximately 10 Å closer together, bringing about a conformation that is incompatible with *parS* binding. Overall, the closure of the DNA-gate explains how CTP binding switches ParB from a nucleating to a sliding state. It is likely that the closure of the opposing DNA-gates drives *parS* DNA into a compartment in between the DBD and the CTD. Indeed, Soh *et al*. (2019) previously compared the *B. subtilis* ParBΔCTD-CDP co-crystal structure to that of a *H. pylori* ParBΔCTD-*parS* complex and proposed that the non-specific DNA must be entrapped in the DBD-CTD compartment (Soh et al., 2019). While the DBD-CTD linked displays little amino acid sequence conservation among chromosomal ParB orthologs, this linker region is invariably ~20 amino acid in length and is over-represented with positively charged lysine residues. Indeed, a fraction of the DBD-CTD compartment is observed in our *C. crescentus* ParB DBD-*parS* co-crystal structure, whereby a set of positively charged residues were observed to make non-specific contacts with the *parS* DNA in the adjacent subunit (Chapter 3). While Fisher *et. al.,* (2017) demonstrated that mutations in a series of lysine residues in the CTD of *B. subtilis* ParB impaired ParB-DNA nucleoprotein formation *in vivo* (Fisher et al., 2017). It is tantalizing to speculate that these over-represented positively charged residues found in the linker between the DBD-CTD of ParB forms non-specific contacts with the DNA flanking the *parS* site, promoting ParB spreading along the DNA. Nevertheless, the biological significance of these residues along with the length of linker is unknown. Determining the contribution of these positively charged residues in the DBD-CTD linker in ParB spreading is important study for the future.

Despite the tremendous amount of progress in understanding the mechanistic basis of ParB spreading, several questions still remain. In particular, it is uncertain weather the ParB clamp can entrap two or more DNA segments together. The lack of a full-length chromosomal ParB has hindered our understanding on the linker compartment between the DBD and CTD. A full-length structure of ParB would enable a better identification of the size of the lumen and would refine modelling approaches to determine how many DNA segments can be entrapped by the patch clamp. Additionally, the dynamics of the opening and closing of the camp during *parS* and CTP interactions is not fully understood. Single-molecule FRET approaches may better reveal the conformational changes of the ParB clamp during *parS* and CTP interactions. Furthermore, it is uncertain whether the translocation of ParB along the DNA also induces DNA supercoiling, thereby compacting the *parS* site. Various gel-based DNA assays have been used to study DNA supercoiling induced by DNA gyrase proteins (Nitiss et al., 2012).

Perhaps such approaches may be utilised to further characterise ParB-DNA interactions mediated by CTP?

Finally, the recent discovery of CTP as a cofactor of both plasmid- and chromosome-encoded ParB raises many important questions. Does ParB-CTP further stimulate the ATPase activity of ParA, and conversely, does ParA accelerate the CTP hydrolysis rate of ParB? Early evidence suggested that CTP can modulate ParA-ParB interaction; mutations at the CTP-binding pocket of a ParB-like protein PadC were shown to impair PadC–ParA binding in vitro (i.e. ParA preferentially binds to PadC-CTP, rather than to apo-PadC, and gave rise to aberrant ParA localization patterns in vivo) (Osorio-Valeriano et al., 2019). Future works, especially with the canonical ParABS system, will provide important insights to refine current models for the ParA-directed DNA segregation. Addressing these key questions will undoubtedly reveal new insights into the formation of the ParB-DNA nucleoprotein complex and its roles in bacterial chromosome segregation.

7.3 A stepwise model describing the formation of the Noc-DNA-membrane complex

Noc was discovered over 19 years ago, as such it remains less characterised than its ParB paralogue (Sievers et al., 2002). While several models of ParB-*parS* nucleoprotein complex assembly have been described (albeit several important questions remain), the molecular basis underpinning the assembly of the Noc-*NBS*-membrane complex remains less understood, as no structural information, until those presented here have been reported. A refined understanding in the assembly of the Noc-*NBS*-membrane complex is essential to provide a mechanistic basis for Noc mediated nucleoid occlusion. Previously it was speculated that formation of Noc-*NBS*-membrane complex, utilises a ParB-like ‘spreading and bridging’ mechanism through the oligomerization of the NTD to form the Noc-DNA nucleoprotein complex that associates with the cell membrane (Adams et al., 2015). Such proposals were made due to observations that mutations in the arginine-rich motif (required for ParB spreading), impaired foci formation and membrane localization of Noc *in vivo* (Adams et al., 2015). The formation of the Noc-DNA complex at the cell membrane would cause a considerable crowding effect that would prevent the assembly of the Z-ring in the membrane of their vicinity. In this thesis, I demonstrate that the arginine-rich motif of Noc likely forms the CTP binding pocket of Noc, as a mutation in the arginine rich patch prevented the CTP binding and hydrolysis activities of Noc. It is therefore possible that the striking phenotypes arising from mutations in the arginine-rich patch were due to Noc being unable to participate in CTP interactions.

Taken together I propose a stepwise model describing the CTP mediated formation of the Noc-DNA-membrane complex (Fig. 6.21). **Step1: The amphipathic helix adopts an auto-inhibitory conformation preventing premature Noc-membrane interactions.** The data from X-ray crystallography provided evidence that both the α1 amphipathic helix adopts an auto-inhibitory conformation by forming a network of covalent interactions to prevent premature NTD-NTD self-engagement prior to CTP binding. This auto-inhibitory mechanism likely serves to prevent the amphipathic helix from prematurely binding to the cell membrane before Noc nucleates onto *NBS* which would occlude its DNA recruitment activity. **Step 2: Noc nucleates onto *NBS*, enhancing its interaction with CTP.** The modest affinity of Noc to CTPγS, as shown by my ITC analysis suggests that Noc likely exists in the inactive apo-state prior to nucleating onto *NBS*. While the results from our DRaCALA and cross-linking approaches demonstrated that *NBS* acts as the catalyst that promotes the CTP-binding and enhances NTD self-dimerization. The requirement of *NBS* to stimulate Noc-CTP interactions likely commits Noc into a pathway where only DNA-entrapped Noc molecules are able to associate with the cell membrane. **Step 3: Noc spreads by sliding and entrapping the non-specific DNA flanking the *NBS* site.** Both my cross-linking and BLI experiments provide biochemical evidence that CTP-binding induces NTD self-dimerization, enabling Noc to form a patch clamp ring that slides along and entraps the non-specific DNA. Furthermore, from comparing the co-crystal structures of the *C. crescentus* ParBΔCTD-*parS* and ParBΔCTD-CTPγS, I suggested that the linker region between the DBD-CTD of ParB, is the compartment that entraps non-specific DNA (Chapter 4). Bioinformatic predictions suggests that this linker region is conserved with Noc, thus it likely serves a similar function in Noc. **Step 4: Noc associates and recruits DNA towards the cell membrane.** The lack of a nucleotide bound NocNΔ26ΔCTD structure forbids us from drawing a conclusion on the role of CTP and the possible conformational liberation of the amphipathic helix α1. However, several lines of evidence suggest that CTP might favour the NTD-engagement conformation as observed in our NocNΔ26ΔCTD structure (as discussed in Chapter 6). Thus, I speculate that the CTP-induced NTD engagement would liberate the amphipathic helix from its autoinhibitory state to interact with the cell membrane. While the 8-AA loop that lies in between the amphipathic helix and the rest of Noc might offer the flexibility to orient the amphipathic helix parallel to the membrane plane for binding.

The work I present in this thesis has contributed towards our understanding regarding the assembly of the Noc-DNA-membrane complex, nevertheless several unresolved questions still remain. While I have demonstrated that *B. subtilis* Noc possess CTPase activity, it is clear that CTP hydrolysis is not required for clamp formation nor membrane association. Future

studies to further understand the role of CTP hydrolysis is therefore required. I hypothesise that, similar to ParB, CTP hydrolysis likely promotes the disengagement of the NTD, releasing the entrapped DNA, and reverts Noc back to its membrane-inactive state. In support of this, I demonstrated that the association of Noc to the cell-membrane is reversible when CTP is artificially dissociated from Noc (Fig. 6.13, Chapter 6). Additionally, the low CTPase activity of Noc is also intriguing. Is it likely that Noc, like MinD, require an additional protein partner to stimulate its NTPase activity (Hu et al., 2002). Pang *et. al.* (2017) previously demonstrated that *S. aeurus* Noc, despite functioning in a manner akin to *B. subtilis* Noc, was unable to complement the deletion of Noc in a *B. subtilis* Δ*min* Δ*noc* genetic background (Pang et al., 2017). These observations raise the possibility that Noc may interact with a species-specific component of the divisome, likely to prevent its assembly in the vicinity of the Noc-DNA-membrane complex. If this is indeed the case, it is not unreasonable to speculate that an additional protein factor may stimulate the CTPase activity of Noc, and that CTP may promote such interactions. In support of this, the Noc-like protein, PadC was only able to interact with ParA in the presence of CTP (Osorio-Valeriano et al., 2019).

Furthermore, it is unclear whether the amphipathic helix acts as the sole membrane targeting motif of Noc. From my liposome sedimentation assays, I was unable to demonstrate a direct interaction between a 28-aa peptide containing both the amphipathic helix and adjacent helix of Noc and the purified vesicles (data not shown). Additionally, despite various attempts I was unsuccessful in obtaining a crystal structure of an amphipathic helix containing Noc variant in complex with CTP. This is likely due to the insolubility of the hydrophobic surface of the amphipathic helix preventing the formation of suitable crystals in solution. Future experiments may employ the use of detergents or the inclusion of lipids in crystal screens to promote the solubility of the amphipathic helix (Loll, 2014). Another approach to directly investigate whether the amphipathic helix is indeed more solvent-exposed in the presence of CTP is to employ the use Hydrogen-Deuterium Exchange Mass Spectrometry (HDX-MS). HDX-MS is a powerful biophysical technique that determines the conformational dynamics of proteins by monitoring the accessibility of the amide protein backbone hydrogens to the deuterons in the solvent environment (Masson et al., 2019). Indeed, Osorio-Valeriano et. al., (2019) previously used HDX-MS to demonstrate that CTP-binding stabilised the CTP-binding pocket and the helix-turn-helix motif of *M. xanthus* ParB (Osorio-Valeriano et al., 2019). *In lieu* with our findings, I hypothesise that HDX-MS analysis of Noc-CTP complex would reveal a striking difference in HDX uptake of the Noc amphipathic helix in the presence of CTPɣS. If this indeed the case, these findings would provide a direct evidence that CTP-binding liberates the amphipathic helix, switching Noc from a membrane-inactive to a membrane-active state.

More recent work has proposed that Noc rather than promoting division-site placement, functions to condense FtsZ filaments towards the midcell during cytokinesis (Yu et al., 2021). Whether Noc primarily functions in division site placement or through stabilizing FtsZ assembly at the midcell is uncertain (Wu et al., 2009; Yu et al., 2021), though it is clear that these roles rely on the accumulation of Noc on the DNA and membrane. Certainly, in *E. coli*, SlmA was recently reported to bind and recruit DNA (*SBS*) towards lipid membranes in an FtsZ and *SBS*- mediated manner (Robles-Ramos et al., 2020). These findings suggest that membrane association and DNA recruitment may be a common feature of nucleoid occlusion. Further work is therefore required to further elucidate the mechanism of Noc mediated nucleoid occlusion, nevertheless it is most likely that CTP plays a key role in this poorly understood process. The widespread availability of the CTPase domain in various protein sequences also raises the exciting possibility that other crucial biological processes, perhaps even outside bacterial chromosome biology, may be regulated by CTP (Soh et al., 2019).

7.4 CTP molecular switches: a common theme in biology?

ATP and GTP-dependent molecular switches are widespread in all domains of life, where they are used to regulate the functions of various proteins. For example, in bacteria, an ATP-dependent molecular switch, MinD plays a crucial role in bacterial cell division site selection. ATP binding promotes MinD dimerization, concomitantly increasing its affinity to the cell membrane (Hu and Lutkenhaus, 2003; Hu et al., 2002; Ramm et al., 2019; Wu et al., 2011). While MinE, a protein partner of MinD stimulates the ATPase activity of MinD, thus promoting its monomerization and hence its dissociation from the membrane. While in eukaryotes, both the Ras-related protein (Sar) and ADP-ribosylation factor (Arf), which function in vesicle trafficking act as GTP-dependent molecular switches. In the GDP-bound state, the amphipathic helix of Sar/Arf1 adopts a sequestered conformation by burying itself into a hydrophobic pocket (Beck et al., 2008; Bielli et al., 2005; Bos et al., 2007; Dodonova et al., 2017; Hanna et al., 2016; Krauss et al., 2008; Lee et al., 2005; Zhukovsky et al., 2019). The exchange of GDP for GTP results in a conformational change that releases the myristoylated amphipathic helix out of the hydrophobic pocket, fostering membrane association (Goldberg, 1998; Zhukovsky et al., 2019). In this thesis, I further characterise ParB and Noc as a new class of CTP-dependent molecular switches, raising the possibility that CTP switches are highly diverse and may control various functions in biology than previously appreciated.

While CTP has been demonstrated to participate in nucleotide metabolism, with the discovery of new enzymes such as LarC, which functions in the biosynthesis of nickel-pincer nucleotide (Desguin et al., 2018). My finding that CTP regulates the membrane binding activity of Noc raises the exciting possibility that CTP may play additional regulatory roles that remains

undiscovered. One such example includes KorB, a DNA-binding transcriptional factor involved in the regulation of genes required for the stability and transmission of RK2 plasmids (Thomas and Hussain, 1984). Noticeably, KorB is able to regulate the expression of genes found several kilobases away from its operator site (O_B) (Bingle et al., 2005). In addition to this, KorB also harbours the highly conserved GxRRxR motif. It is therefore tantalizing to speculate that KorB may utilize CTP as a co-factor to spread in a manner akin to ParB and Noc. As plasmids are widely used in Nature to confer resistance to a plethora of antibiotics, the CTP-binding pocket may yet serve as a novel target in the development of new antibiotics (Bennett, 2008).

Last but not least, studies to dissect the mechanism of CTP hydrolysis by the ParB/Noc CTPase are crucial to improve our understanding of CTP-dependent molecular switches. As ParB/Noc are a founding members of a the new CTPase family of proteins, knowledge gained from future work might be generalized to other CTPases. Our work have demonstrated that CTP-binding, but not CTP-hydrolysis is required for spreading ability of ParB and Noc, and the membrane-binding activity of Noc. Despite various attempts, I was unable to obtain a high-resolution structure of either ParB or Noc in complex with CTPγS, thus preventing me from confidently modelling any catalytic water molecules. Therefore, the mechanism of CTP hydrolysis by a ParB CTPase remains unresolved. Indeed proteins (N112S and N172A of *B. subtilis* and *M. xanthus* ParB and N121S of *B. subtilis* Noc respectively) which bind CTP but are deficient for hydrolysis, fail to form tight foci inside the cells (Osorio-Valeriano et al., 2019; Soh et al., 2019) (Chapter 6); however, this is weak evidence for the *in vivo* role of CTP hydrolysis since *B. subtilis* ParB (N112S) and Noc (N121S) is already impaired at forming a protein clamp (Soh et al., 2019). Future studies using alanine scanning experiments with reference to my *C. crescentus* ParBΔCTD-CTPγS complex may provide some catalytic insights into the ParB CTPase. Identifying a mutant ParB/Noc protein that retains both CTP-binding and NTD clamp formation, but is unable to hydrolyse CTP will further reveal the role of CTP hydrolysis in the ParB/Noc family of CTPases.

7.5 Final perspectives

Research with bacterial systems has already benefited tremendously from the recent explosion of interest and technological advances obtained from the eukaryotic chromosome field. It is likely that novel high throughput sequencing-based methodologies, single-molecule imaging, single-molecule biophysics as well as traditional biochemistry and genetics will continue to provide further insights into the mechanisms of chromosome segregation and genomic maintenance in bacteria. Various, orthogonal ParB-*parS* systems have been exploited to label and image DNA loci *in vivo*, in both bacteria and eukaryotes (Germier et al., 2017, 2018; Le and Laub, 2014; Mariamé et al., 2018). Recent studies have also expanded

the utilization of the ParABS system in synthetic biology, for example, as part of a genetic circuit to enable asymmetric cell division in *E. coli* (Molinari et al., 2019; Mushnikov et al., 2019). Such exciting developments will benefit from ongoing research into the mechanistic details of the ParB/Noc protein family and their evolvability to acquire new functions.

7.6 References

1. Adams, D.W., Wu, L.J., and Errington, J. (2015). Nucleoid occlusion protein Noc recruits DNA to the bacterial cell membrane . EMBO J. **34**, 491–501.
2. Beck, R., Sun, Z., Adolf, F., Rutz, C., Bassler, J., Wild, K., Sinning, I., Hurt, E., Brügger, B., Béthune, J., et al. (2008). Membrane curvature induced by Arf1-GTP is essential for vesicle formation. Proc. Natl. Acad. Sci. U. S. A. **10**5, 11731–11736.
3. Bennett, P.M. (2008). Plasmid encoded antibiotic resistance: Acquisition and transfer of antibiotic resistance genes in bacteria. British Journal of Pharmacology. **153**, 347–357.
4. Bielli, A., Haney, C.J., Gabreski, G., Watkins, S.C., Bannykh, S.I., and Aridor, M. (2005). Regulation of Sar1 NH2 terminus by GTP binding and hydrolysis promotes membrane deformation to control COPII vesicle fission. J. Cell Biol. **171**, 919–924.
5. Bingle, L.E.H., Macartney, D.P., Fantozzi, A., Manzoor, S.E., Thomas, C.M., and Karn, J. (2005). Flexibility in repression and cooperativity by KorB of broad host range IncP-1 plasmid RK2. J. Mol. Biol. **349**, 302–316.
6. Bos, J.L., Rehmann, H., and Wittinghofer, A. (2007). GEFs and GAPs: Critical Elements in the Control of Small G Proteins. Cell. **129**, 865–877.
7. Chen, B.W., Lin, M.H., Chu, C.H., Hsu, C.E., and Sun, Y.J. (2015). Insights into ParB spreading from the complex structure of Spo0J and parS. Proc. Natl. Acad. Sci. U. S. A. **112**, 6613–6618.
8. Cho, H., and Bernhardt, T.G. (2013). Identification of the SlmA Active Site Responsible for Blocking Bacterial Cytokinetic Ring Assembly over the Chromosome. PLoS Genet. **9**, e1003304.
9. Corrales-Guerrero, L., He, B., Refes, Y., Panis, G., Bange, G., Viollier, P.H., Steinchen, W., and Thanbichler, M. (2020). Molecular architecture of the DNA-binding sites of the P-loop ATPases MipZ and ParA from Caulobacter crescentus. Nucleic Acids Res. **48**, 4769–4779.
10. Cuthbertson, L., and Nodwell, J.R. (2013). The TetR Family of Regulators. Microbiol. Mol. Biol. Rev. **77**, 440–475.
11. Desguin, B., Fellner, M., Riant, O., Hu, J., Hausinger, R.P., Hols, P., and Soumillion, P. (2018). Biosynthesis of the nickel-pincer nucleotide cofactor of lactate racemase requires a CTP-dependent cyclometallase. J. Biol. Chem. **293**, 12303–12317.

12. Dodonova, S.O., Aderhold, P., Kopp, J., Ganeva, I., Röhling, S., Hagen, W.J.H., Sinning, I., Wieland, F., and Briggs, J.A.G. (2017). 9Å structure of the COPI coat reveals that the Arf1 GTPase occupies two contrasting molecular environments. Elife. **6**. e26691.
13. Fisher, G.L.M., Pastrana, C.L., Higman, V.A., Koh, A., Taylor, J.A., Butterer, A., Craggs, T., Sobott, F., Murray, H., Crump, M.P., et al. (2017). The structural basis for dynamic DNA binding and bridging interactions which condense the bacterial centromere. Elife. **6**. e28086.
14. Germier, T., Kocanova, S., Walther, N., Bancaud, A., Shaban, H.A., Sellou, H., Politi, A.Z., Ellenberg, J., Gallardo, F., and Bystricky, K. (2017). Real-Time Imaging of a Single Gene Reveals Transcription-Initiated Local Confinement. Biophys. J.
15. Germier, T., Sylvain, A., Silvia, K., David, L., and Kerstin, B. (2018). Real-time imaging of specific genomic loci in eukaryotic cells using the ANCHOR DNA labelling system. Methods. **113**, 1383–1394.
16. Goldberg, J. (1998). Structural basis for activation of ARF GTPase: Mechanisms of guanine nucleotide exchange and GTP-myristoyl switching. Cell. **95**, 237–248.
17. Graham, T.G.W., Wang, X., Song, D., Etson, C.M., van Oijen, A.M., Rudner, D.Z., and Loparo, J.J. (2014). ParB spreading requires DNA bridging. Genes Dev. **28**, 1228–1238.
18. Hanna, M.G., Mela, I., Wang, L., Henderson, R.M., Chapman, E.R., Edwardson, J.M., and Audhya, A. (2016). Sar1 GTPase activity is regulated by membrane curvature. J. Biol. Chem. **291**, 1014–1027.
19. Hu, Z., and Lutkenhaus, J. (2003). A conserved sequence at the C-terminus of MinD is required for binding to the membrane and targeting MinC to the septum. Mol. Microbiol. **47**, 345–355.
20. Hu, Z., Gogol, E.P., and Lutkenhaus, J. (2002). Dynamic assembly of MinD on phospholipid vesicles regulated by ATP and MinE. Proc. Natl. Acad. Sci. U. S. A. **99**, 6761–6766.
21. Jakimowicz, D., Chater, K., and Zakrzewska-Czerwínska, J. (2002). The ParB protein of Streptomyces coelicolor A3(2) recognizes a cluster of parS sequences within the origin-proximal region of the linear chromosome. Mol. Microbiol **45**, 1365–1377.
22. Jalal, A.S.B., and Le, T.B.K. (2020). Bacterial chromosome segregation by the ParABS system. Open Biol **10**, 200097.
23. Jalal, A.S., Tran, N.T., and Le, T.B. (2020a). ParB spreading on DNA requires cytidine triphosphate in vitro. Elife. **9**, e53515.
24. Jalal, A.S.B., Tran, N.T., Stevenson, C.E., Chan, E.W., Lo, R., Tan, X., Noy, A., Lawson, D.M., and Le, T.B.K. (2020b). Diversification of DNA-Binding Specificity by

Permissive and Specificity-Switching Mutations in the ParB/Noc Protein Family. Cell Rep. **32**, 107928.

25. Jecz, P., Bartosik, A.A., Glabski, K., and Jagura-Burdzy, G. (2015). A single parS sequence from the cluster of four sites closest to oriC is necessary and sufficient for proper chromosome segregation in Pseudomonas aeruginosa. PLoS One. **11**, e0152541.
26. Kiekebusch, D., Michie, K.A., Essen, L.O., Löwe, J., and Thanbichler, M. (2012). Localized Dimerization and Nucleoid Binding Drive Gradient Formation by the Bacterial Cell Division Inhibitor MipZ. Mol. Cell. **46**, 245–259.
27. Knopp, M., Gudmundsdottir, J.S., Nilsson, T., König, F., Warsi, O., Rajer, F., Ädelroth, P., and Andersson, D.I. (2019). De novo emergence of peptides that confer antibiotic resistance. MBio. **10**, e00837–19
28. Krauss, M., Jia, J.Y., Roux, A., Beck, R., Wieland, F.T., De Camilli, P., and Haucke, V. (2008). Arf1-GTP-induced tubule formation suggests a function of arf family proteins in curvature acquisition at sites of vesicle budding. J. Biol. Chem. **283**, 27717–27723
29. Lagage, V., Boccard, F., and Vallet-Gely, I. (2016). Regional Control of Chromosome Segregation in Pseudomonas aeruginosa. PLoS Genet. **12**, e1006428.
30. Le, T.B.K., and Laub, M.T. (2014). New approaches to understanding the spatial organization of bacterial genomes. Curr. Opin. Microbiol. **22**, 15–21.
31. Lee, M.C.S., Orci, L., Hamamoto, S., Futai, E., Ravazzola, M., and Schekman, R. (2005). Sar1p N-terminal helix initiates membrane curvature and completes the fission of a COPII vesicle. Cell. **122**, 605–617.
32. Livny, J., Yamaichi, Y., and Waldor, M.K. (2007). Distribution of centromere-like parS sites in bacteria: Insights from comparative genomics. J. Bacteriol. **189**, 8693–8703.
33. Loll, P.J. (2014). Membrane proteins, detergents and crystals: What is the state of the art? Acta Crystallogr. Sect. FStructural Biol. Commun. **70**, 1576–1583.
34. Mariamé, B., Kappler-Gratias, S., Kappler, M., Balor, S., Gallardo, F., and Bystricky, K. (2018). Real-Time Visualization and Quantification of Human Cytomegalovirus Replication in Living Cells Using the ANCHOR DNA Labeling Technology. J. Virol. **92**, e00571-18.
35. Masson, G.R., Burke, J.E., Ahn, N.G., Anand, G.S., Borchers, C., Brier, S., Bou-Assaf, G.M., Engen, J.R., Englander, S.W., Faber, J., et al. (2019). Recommendations for performing, interpreting and reporting hydrogen deuterium exchange mass spectrometry (HDX-MS) experiments. Nat. Methods. **16**, 595–602.
36. Molinari, S., Shis, D.L., Bhakta, S.P., Chappell, J., Igoshin, O.A., and Bennett, M.R. (2019). A synthetic system for asymmetric cell division in Escherichia coli. Nat. Chem. Biol. **15**, 917–924.

37. Mushnikov, N. V., Fomicheva, A., Gomelsky, M., and Bowman, G.R. (2019). Inducible asymmetric cell division and cell differentiation in a bacterium. Nat. Chem. Biol. **15**, 925–931.
38. Nitiss, J.L., Soans, E., Rogojina, A., Seth, A., and Mishina, M. (2012). Topoisomerase assays. Curr. Protoc. Pharmacol. **3**, 3.3
39. Osorio-Valeriano, M., Altegoer, F., Steinchen, W., Urban, S., Liu, Y., Bange, G., and Thanbichler, M. (2019). ParB-type DNA Segregation Proteins Are CTP-Dependent Molecular Switches. Cell. **179,** 1512–1524.e15.
40. Pang, T., Wang, X., Lim, H.C., Bernhardt, T.G., and Rudner, D.Z. (2017). The nucleoid occlusion factor Noc controls DNA replication initiation in Staphylococcus aureus. PLoS Genet. **13**, e1006908.
41. Qian, W., and Zhang, J. (2014). Genomic evidence for adaptation by gene duplication. Genome Res. **24**, 1356–1362
42. Ramm, B., Heermann, T., and Schwille, P. (2019). The E. coli MinCDE system in the regulation of protein patterns and gradients. Cell. Mol. Life Sci. **76**, 4245–4273
43. Roberts, M.A.J., Wadhams, G.H., Hadfield, K.A., Tickner, S., and Armitage, J.P. (2012). ParA-like protein uses nonspecific chromosomal DNA binding to partition protein complexes. Proc. Natl. Acad. Sci. U. S. A. **109**, 6698–6703.
44. Robles-Ramos, M.Á., Margolin, W., Sobrinos-Sanguino, M., Alfonso, C., Rivas, G., Monterroso, B., and Zorrilla, S. (2020). The nucleoid occlusion protein SlmA binds to lipid membranes. MBio. **11**, e02094-20.
45. Rodionov, O., ŁObocka, M., and Yarmolinsky, M. (1999). Silencing of genes flanking the P1 plasmid centromere. Science. **283**, 546–549.
46. Schumacher, M.A., and Zeng, W. (2016). Structures of the nucleoid occlusion protein SlmA bound to DNA and the C-terminal domain of the cytoskeletal protein FtsZ. Proc. Natl. Acad. Sci. U. S. A. **113**, 4988–4993.
47. Schumacher, M.A., Tonthat, N.K., Lee, J., Rodriguez-Castañeda, F.A., Chinnam, N.B., Kalliomaa-Sanford, A.K., Ng, I.W., Barge, M.T., Shaw, P.L.R., and Barillà, D. (2015). Structures of archaeal DNA segregation machinery reveal bacterial and eukary otic linkages. Science. **349**, 1120–1124.
48. Sievers, J., Raether, B., Perego, M., and Errington, J. (2002). Characterization of the parB-like yyaA gene of Bacillus subtilis. J. Bacteriol. **184**, 1102–1111
49. Soh, Y.-M., Davidson, I.F., Zamuner, S., Basquin, J., Bock, F.P., Taschner, M., Veening, J.-W., De, P., Rios, L., Peters, J.-M., et al. (2019). Self-organization of *parS* centromeres by the ParB CTP hydrolase. Science. **366**, 1129–1133.
50. Taylor, J.A., Pastrana, C.L., Butterer, A., Pernstich, C., Gwynn, E.J., Sobott, F., Moreno-Herrero, F., and Dillingham, M.S. (2015). Specific and non-specific

interactions of ParB with DNA: Implications for chromosome segregation. Nucleic Acids Res. **43**, 719–731.

51. Thanbichler, M., and Shapiro, L. (2006). MipZ, a Spatial Regulator Coordinating Chromosome Segregation with Cell Division in Caulobacter. Cell. **126**, 147–162.
52. Thomas, C.M., and Hussain, A.A. (1984). The korB gene of broad host range plasmid RK2 is a major copy number control element which may act together with trfB by limiting trfA expression. EMBO J. **3**, 1513–1519.
53. Tonthat, N.K., Milam, S.L., Chinnam, N., Whitfill, T., Margolin, W., and Schumacher, M.A. (2013). SlmA forms a higher-order structure on DNA that inhibits cytokinetic Z-ring formation over the nucleoid. Proc. Natl. Acad. Sci. U. S. A. **110**, 10586–10591.
54. Tran, N.T., Stevenson, C.E., Som, N.F., Thanapipatsiri, A., Jalal, A.S.B., and Le, T.B.K. (2018). Permissive zones for the centromere-binding protein ParB on the Caulobacter crescentuschromosome. Nucleic Acids Res. **46**, 1196–1209.
55. Wu, L.J., and Errington, J. (2012). Nucleoid occlusion and bacterial cell division. Nat. Rev. Microbiol. **10**, 8–12.
56. Wu, L.J., Ishikawa, S., Kawai, Y., Oshima, T., Ogasawara, N., and Errington, J. (2009). Noc protein binds to specific DNA sequences to coordinate cell division with chromosome segregation. EMBO J. **28**, 1940–1952.
57. Wu, W., Park, K.T., Holyoak, T., and Lutkenhaus, J. (2011). Determination of the structure of the MinD-ATP complex reveals the orientation of MinD on the membrane and the relative location of the binding sites for MinE and MinC. Mol. Microbiol. **79**, 1515–1528.
58. Yamaichi, Y., Bruckner, R., Ringgaard, S., Möll, A., Ewen Cameron, D., Briegel, A., Jensen, G.J., Davis, B.M., and Waldor, M.K. (2012). A multidomain hub anchors the chromosome segregation and chemotactic machinery to the bacterial pole. Genes Dev. **26**, 2348–2360.
59. Yu, Y., Zhou, J., Gueiros-Filho, F.J., Kearns, D.B., and Jacobson, S.C. (2021). Noc Corrals Migration of FtsZ Protofilaments during Cytokinesis in Bacillus subtilis. MBio. **12**, e02964–20.
60. Zhukovsky, M.A., Filograna, A., Luini, A., Corda, D., and Valente, C. (2019). Protein Amphipathic Helix Insertion: A Mechanism to Induce Membrane Fission. Front. Cell Dev. Biol. **7**, 291.

Appendix:

1. Appendixes Chapter 1: Introduction to X-ray crystallography

2.Publications and preprints

Appendixes Chapter 1: Introduction to X-ray crystallography

X-ray crystallography is a powerful method used to determine the atomic structure of crystals. The initial finding that the three-dimensional structure of proteins can be determined by X-ray crystallography dates back to 1934, where Bernal and Crowfoot managed to produce a diffraction pattern from crystals of the endopeptidase Pepsin (Bernal and Crowfoot, 1934). Since then, X-ray crystallography has elucidated the three-dimensional structures of various proteins, providing crucial insight into their architecture and mechanism (Shi, 2014). A detailed understanding of the principles underpinning X-ray crystallography is therefore invaluable in obtaining the structures of proteins.

Crucial to the use of X-ray crystallography in solving the three-dimensional structure of a protein, is the generation of X-rays. X-rays were first discovered in 1895, where they were described as a form of electromagnetic wave that vary over time and space (Röntgen, 1896). Additionally, X-rays were observed to diffract and possessed a wave-like nature. X-rays typically possess a wavelength within the range of 0.1 Å to 100 Å, with wavelengths 0.2 Å - 3 Å being highly relevant in X-ray crystallography. In order to generate X-rays, a readily available source of electrons and a means of accelerating electrons at a high enough speed is required. In a typical X-ray crystallography experiment, X-rays are generated through accelerating electrons in a synchrotron, as moving electrons emit energy at X-ray wavelength (Ren, 2012). The synchrotron functions to accelerate electrons at high levels of energy before making these electrons change directions periodically (Ren, 2012). The principal components of a synchrotron consists of the linear particle accelerator that produces the electrons, the booster synchrotron which accelerates the electrons prior to injection into the storage ring where electrons travel close to the speed of light and pass through various types of magnets to generate X-rays where they are then emitted by the beamline (Ren, 2012). Alternatively, X-rays can be generated in house through the use of a rotating anode, whereby a tungsten disc receives an electron beam from a cathode to generate X-rays. In this thesis, however X-rays were typically generated using the synchrotron at the Diamond light Source (Pooley et al., 2001).

In order to determine the three-dimensional structure, we must first obtain diffracting protein crystals which can often be a challenging endeavour. The basis of crystallisation, is to take a solution of the protein and facilitate it to come out of solution; if this happens too quickly

however the protein will precipitate, but under the right conditions, crystals will grow. As such, the protein sample must be very pure (~95% purity) and highly concentrated (~10 mg/mL) (Smyth and Martin, 2000). Crystallisation of proteins is a multi-step process which involves 3 main stages: nucleation, growth and cessation of growth (Smyth and Martin, 2000). The initial nucleation step involves the formation of a few crystal nuclei, the protein must then stay in a metastable zone over a period of time to enable the crystals to grow (Smyth and Martin, 2000). In this thesis, growth of proteins crystals was achieved primarily through the vapour diffusion method, which enables the protein concentration to slowly increase over time as water vapour diffuses from the protein drop with a low precipitant concentration to the reservoir with a higher precipitant concentration until the concentrations equilibrate (Giegé, 2013). Once suitable crystals have been grown, an X-ray diffraction pattern is then generated through the bombardment of crystals by in a beam of X-rays. The regular arrangement of atoms that are present in the crystal would then act as a three-dimensional diffraction grating whereby X-rays interact with the electrons through elastic collisions, hence generating diffraction. The scattering of X-rays are a direct result of their interaction with the electrons (Smyth and Martin, 2000). This diffraction pattern is viewed as spots, and determining the intensity, symmetry and position of spots are the first steps in obtaining the final three-dimensional structure of the protein (Smyth and Martin, 2000). Despite this, one cannot simply collect one image whereby the crystal was shot by X-rays at only one angle, this is because only a minute number of reflections will be excited by X-rays at a particular angle of the stationary crystal. To overcome this, we commonly collect 3600 images of the crystal, with the crystal being slowly rotated through 360° (i.e. 0.1° per image) thereby enabling each image to be collected at a different angle.

As diffraction results from the scattering of waves by the protein crystal, an understanding of the properties of waves is required. Waves are described by both their amplitude and frequency, and can be expressed as a function of time and position in space (McClintock, 2018). When represented as a function of time, waves can be mathematically expressed as $A\cos(2\pi vtr)$ whereby A : amplitude, t : time and v : frequency (McClintock, 2018). While when expressed as a function of a position in space, waves are mathematically expressed by the equation $A\cos[2\pi\ (vt - x\ /\lambda)]$ (McClintock, 2018). As waves are stationary in a typical X-ray crystallography experiment, we are principally concerned with waves as a function of a position in space. Additionally, waves can be represented as the x-component of a rotating vector, where the x-component equals the amplitude of the wave, and the angle between rotating vectors equals the phase of the vector (Fig 1.A). As we are principally interested in the properties of a photon in X-ray crystallography (which has a single wavelength) we can summarize the length of the wave axis as the phase (Smyth and Martin, 2000). Moreover,

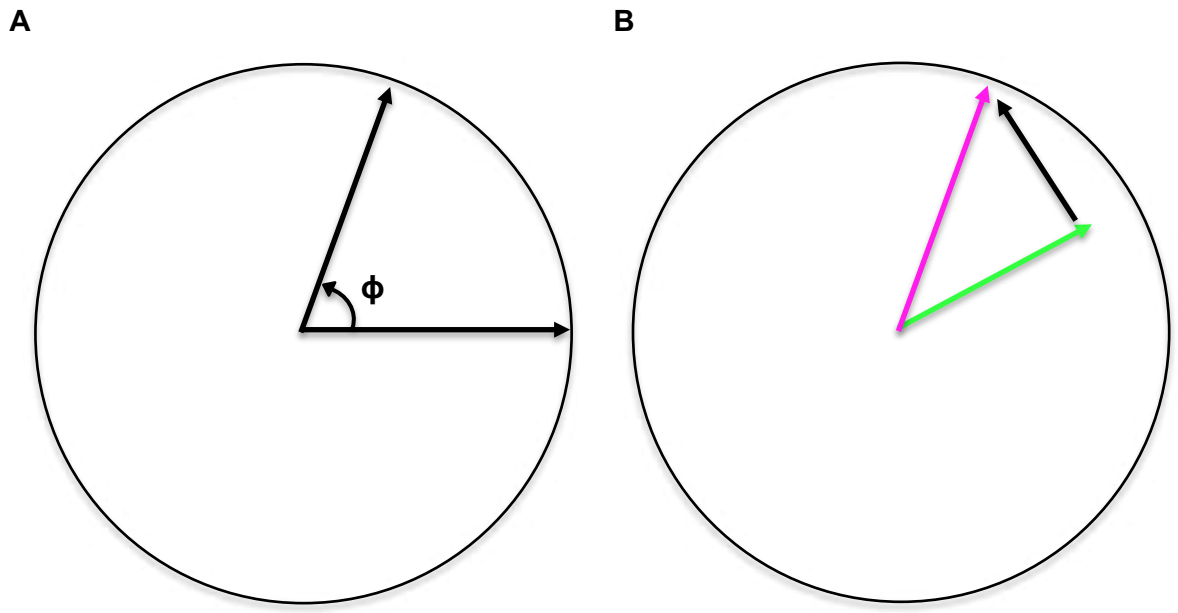

Figure 1. Vector representation of waves. (A) Schematic representation of a wave as a vector. The initial rotation provides the initial phase shift (ϕ). **(B)** The addition of two waves is equivalent to the addition of two vectors. Two different vectors are represented by different coloured arrows (green arrow vs. purple arrow). The addition of two vectors results in a cosine wave with the same wavelength, however the difference between the amplitudes and phases are provided through the sum of two vectors.

when adding the expression of two waves we end up with the equation: A $\cos(\alpha+\varphi_1)$ + B $\cos(\alpha+\varphi_2)$. By utilising the sum of two independent wave vectors, we are able to satisfy this equation which provides us with a cosine wave with the same wavelength but different amplitudes and waves (Fig 1.B). Hence, the representation of waves as vectors enables us to identify both the amplitude and phase.

Diffraction spots can also be described as reflections, due to crystals being able to reflect X-rays. The reflection of these diffracted spots are called Bragg planes (Bragg and Bragg, 1913). Due to the reflective properties of the crystal, Bragg planes and the angle of incidence is equal to the angle of reflection (Bragg and Bragg, 1913). Hence, Bragg's law describes the relationship between scattering angle and the interplanar spacing. This was first proposed in 1913, when W. L. Bragg observed that crystalline solids have remarkably characteristic patterns of reflected X-ray radiation (Bragg and Bragg, 1913). In the crystal, intense peaks of scattered radiation were observed when exposed to certain wavelengths and incident directions (Bragg and Bragg, 1913). To account for this, W. L. Bragg proposed that a crystal consists of a parallel plane of atoms, spaced by distance (*d*) apart (Bragg and Bragg, 1913). As represented in figure 2.A, the X-ray beam shines into the planes and is then reflected by different planes, with the beam that is reflected in the lower plane traveling an extra distance than the reflected X-ray beam in the upper parallel plane, which is $2d\sin\theta$ (Fig 2.A). When the distance equals $n\lambda$ (whereby n is an integer), the condition for constructive interference is obtained, corresponding to the contrast found in the diffraction pattern. Mathematically, Bragg's law can be represented by the equation $n\lambda = 2d\sin\theta$, whereby n: integer value λ (Bragg and Bragg, 1913). Bragg's law therefore states that the X-ray diffraction pattern generated from single crystals can be mathematically treated as a reflection from sets of equivalent parallel planes of the atoms that are found in the crystal. Diffraction of the crystal however can only occur once Bragg's law is satisfied, and to satisfy Bragg's law, the θ must change as the *d* changes.

Later, Ewald proposed a geometrical visualisation of Bragg planes that are in the correct orientation to diffract (Ewald, 1913). As represented by figure 2B, the diffracted X-ray is represented as vectors with a length of $1/\lambda$ (Fig. 2B). Both the incoming X-ray and the diffracted X-ray are at an angle of θ from a set of Bragg planes. The difference between the reflected X-ray and the directed beam passing through the crystal is perpendicular to Bragg planes. From the small internal triangle, it is clear that the sides corresponding to the two halves of the vector shown in red have a length of $\sin\theta/\lambda$, and using Bragg's law we can determine this as $1/2d$ (Fig. 2.A). As such the red vector represents the reciprocal space

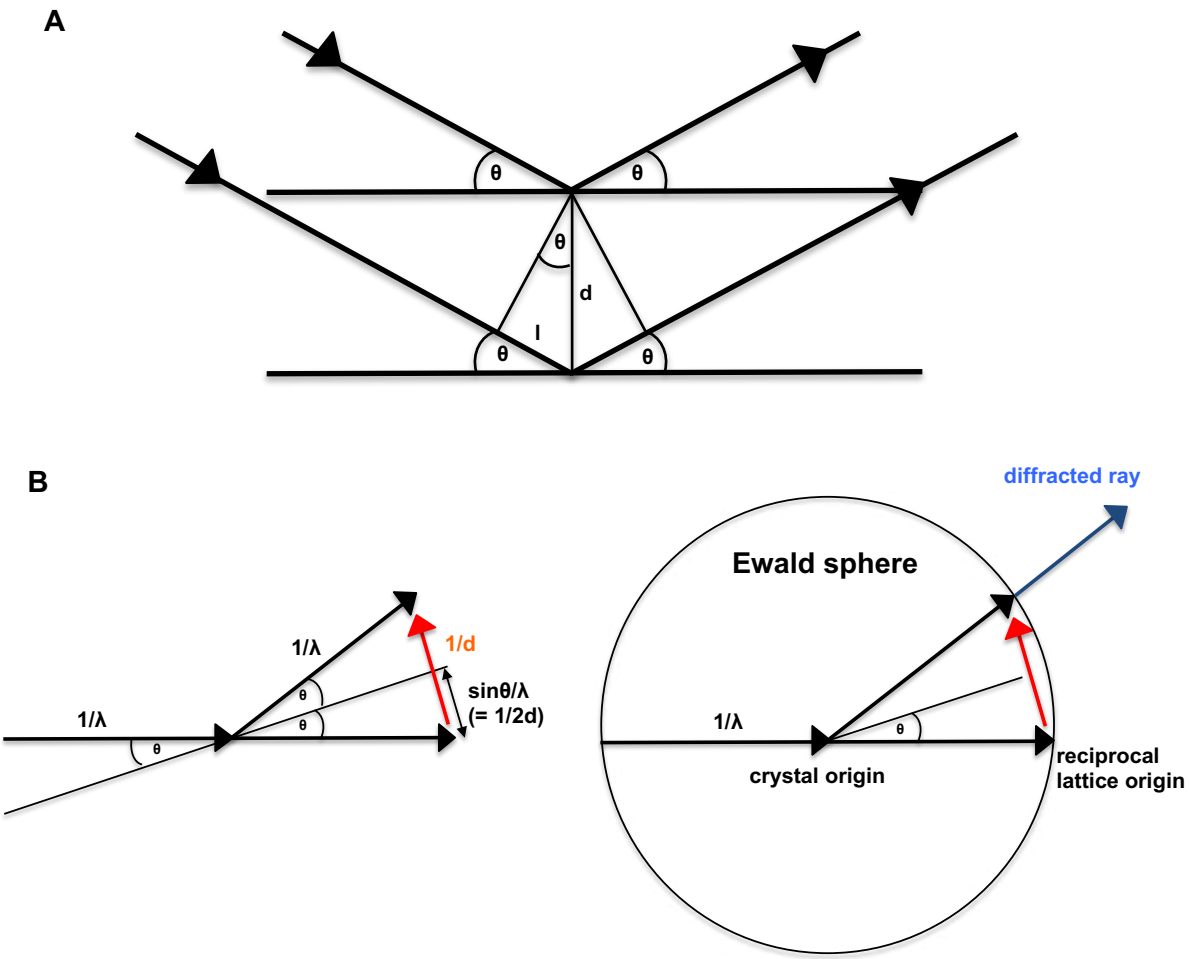

Figure 2. Bragg's planes and Ewald sphere. (A) A schematic representation of Bragg planes from a particular family of lattice planes. The black arrow represents the diffracted X-ray and the black lines represent the planes. The difference between the two reflected X-rays is $2d \sin\theta$. **(B)** A schematic representation of Ewald sphere. The direction of the diffracted ray is indicated by the blue arrow.

vector where Bragg planes can go in any direction (Fig. 2.A). Thus, the representative vector can have its tip at any point of the surface of a sphere (Ewald sphere) whereby the radius is equal to $1/\lambda$. As shown in figure 2B, the diffracted X-ray has a base towards the centre of the circle, which is described as the origin of the crystal, while the origin of the reciprocal space is calculated as the point where the diffracted X-ray exists the Ewald sphere. Thus, rotating the crystal would cause an identical rotation in the reciprocal lattice from its origin. The Ewald sphere therefore demonstrates Bragg's law in the reciprocal space of the crystal, whereby each reciprocal-lattice point must be arranged within respect to the X-ray beam in order to satisfy Bragg's law, thus producing a reflection from the crystal. Thus, utilising the Ewald sphere will allow us to identify which lattice plane in the crystal results in a diffracted signal at a specific wavelength.

The processing of data collected from X-ray diffraction is a mathematically complex and requires well established algorithms and computer based methods available in various software packages, with CCP4i2 being a widely available suite of programs (Potterton et al., 2018). The initial step in data processing is the determination of the crystal system and classification of the unit cell. From this diffraction pattern, the intensity, symmetry and position of each spot is identified. We can schematically describe a crystal as a lattice of points of equal symmetry, and as crystals are composed of the three-dimensional regular arrangement of atoms, the arrangement of which can be represented by a repeat motif known as the unit cell. The unit cell can be classified into 230 different space groups and can be divided into 6 crystal families based on the length of the axes sides and the angles between them (Ladd and Palmer, 2003; Rhodes, 2002). These crystal families are cubic, tetragonal, hexagonal, orthorhombic, monoclinic and triclinic (Ladd and Palmer, 2003; Rhodes, 2002). To describe the atomic planes found within a crystal, Miller indices (*h,k,l*) are used (Ladd and Palmer, 2003; Rhodes, 2002). Miller indices represent the reciprocals of the fractional intercepts that the plane makes with the crystallographic axes. These three indices *hkl* provide a particular set of equivalent, parallel planes (Ladd and Palmer, 2003; Rhodes, 2002). The index *h* provides the overall number of planes in the set per unit cell in direction a. While indices *k* and *l* describes the number of planes in the unit cell in directions b and c, respectively. Once we have identified the cell and orientation of the crystal, indexing can then be performed. In this process, each spot collected from the diffraction experiment is assigned an index: *h*, *k*, and *l*. Autoindexing is then performed through a calculation of the predicted diffraction image based on the cell dimensions and orientation (Evans and Murshudov, 2013). After which, the intensities of each of the diffracted spots are then measured.

During the X-ray diffraction experiment however, different waves of X-rays are superimposed on one another (preventing the identification of the single contribution of each diffraction spot), thus complicating the determination of a crystal's lattice structure. To simplify this, a mathematical tool known as the Fourier transformation can be used (Cochran et al., 1967). If expressed as a mathematical function, the generated diffraction pattern is the Fourier transform of that function. Interestingly, the Fourier transform can be inverted, whereby if you run an inverse of the Fourier transform you would obtain the original function back (Cochran et al., 1967). This is what enables the crystallographer to obtain a snapshot of the electron density. However, this raises another issue known as the Phase problem (discussed below), as both the amplitude and phases of the diffracted waves are required to generate the inverse of the Fourier transform. Nevertheless, the Fourier transform provides the mathematical relationship between the crystal and its X-ray diffraction pattern. This mathematical equation enables us to convert the Fourier-series description of the reflections to a Fourier-series description of the electron density map. Additionally, this mathematical model can also be used to describe the relationship between the electron density and the structure factors (Smyth and Martin, 2000). The structure factor describes a single diffracted X-ray, which produces a single detected reflection (Rhodes, 2002). This is represented by the following equation $F_{hkl} = F_j e^{2\pi(hxj + kyj + lzj)}$ whereby F_{hkl} = the atomic structure factor, F_j = the scattering factor of an atom in the crystal, xj, yj, zj = the coordinates of the atom in the unit cell. Each diffracted spot equates to the sum of diffractive contributions from all the atoms found within the unit cell of the crystal. The structure factor F_{hkl} is a mathematical function used to describe the amplitude and phases generated from the X-ray diffraction experiment. Thus, it can be represented as a complex number and as an equation of the Fourier transform. The inversion of the Fourier transform of the structure factor in reciprocal space can provide the unit cell content in real space. By utilizing an inverse of the Fourier transform, it is therefore possible to convert the structure factors $F(h,k,l)$ to the desired electron density equation $p(x,y,z)$ (Ilari and Savino, 2008; Smyth and Martin, 2000). The electron density of the crystallized protein can be expressed as a wave function as it repeats itself in every unit cell (Ilari and Savino, 2008; Smyth and Martin, 2000). The $F(h,k,l)$ is a wave and therefore have information for the amplitude, frequency and phase. In the X-ray diffraction experiment both the indices of each reflection and its intensity is measured.

Apart from obtaining suitable crystals that can produce a diffraction pattern, the phase problem represents another limiting factor in determining the three-dimensional structure of proteins X-ray crystallography. This is because the structural analysis of proteins requires both the amplitudes from the diffracted X-rays, as well as phases to generate an electron density map. While the amplitude can be calculated by determining the intensity of diffraction

through the use of sensitive X-ray detection methods (such as CCD detectors), all phase information for the waves is lost (Phase Problem) (Gruner et al., 2002). In order to understand the Phase Problem and the various methods crystallographers use to provide a solution to the Phase Problem, a better understanding of Patterson function is required (Patterson, 1935). The Patterson function describes the Fourier transform of the intensities of the diffraction rather than from the structure factor, thus only requiring the measured data (Fultz and Howe, 2008; Patterson, 1935). This results in a map of interatomic vectors in which the weights of the vectors are directly proportional to the atomic numbers of the atoms linked by these vectors. By doing so, we can generate a Patterson map that provides the map of the vectors between the atoms (Fultz and Howe, 2008). Paterson functions are used because they are directly calculated from the observed data without the requirement of any phase information. The Paterson function therefore provides information regarding all the possible inter-atomic vectors that are found within the atomic structure (Fultz and Howe, 2008; Patterson, 1935). From using the Patterson map, it is possible to determine the original position of atoms that gives rise to the Patterson peaks (Rhodes, 2002). However, this method is limited to solving the structures of smaller molecules (Rhodes, 2002). If we assume that crystals consist of similarly-shaped atoms with positive electron density, then we can describe the statistical relationships between the sets of structure factors. We can therefore utilise these statistical relationships to deduce a possible value for the phases. Through the use of direct methods, this relationship is exploited, and hence provides a solution to the Phase problem of small molecules.

Among the various methods crystallographers use to solve the Phase problem includes multiple isomorphous replacement (Taylor, 2010). In this approach, certain changes to the protein crystal are carried out to perturb the structure factor, and through the way they are perturbed, it is possible to deduce the phase values. This is best represented by figure 3A-B, whereby the introduction of a heavy atom causes a significant change in the intensity of scattering (Fig. 3.A-B). From the X-ray diffraction experiment, the scattering of each light atom would essentially cancel each other out, due to these atoms scattering with different phase angles (Taylor, 2010). However, the electrons of heavy atoms will essentially scatter within phase of one another. As a result, the different atoms would contribute to the intensity of scattering within proportion to the number of squared electrons they contain (Fig. 3.A-B). Thus, to utilize this method, the crystallographer would have two separate protein crystals, the native protein crystal which only contains the target protein, and a derivative crystal which contains the protein and an additional heavy atom bound. Due to the small number of heavy atoms present in the derivative crystal, the generated Paterson map will be easy to determine, and once the location of each heavy atom is identified in the crystal, we can then

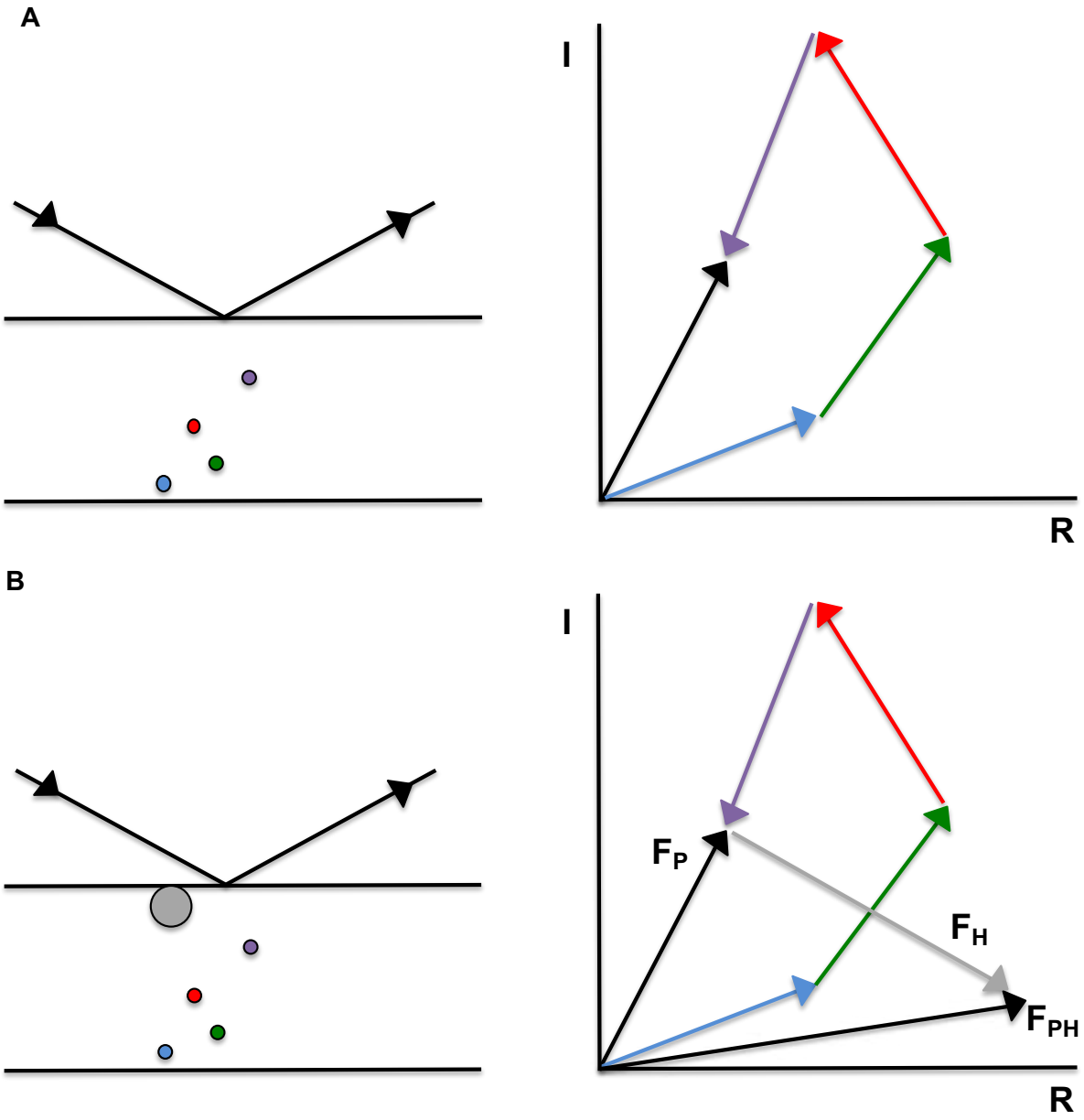

Figure 3. An Argand diagram demonstrating the shift in structure factor caused by the introduction of a heavy atom. (A) The black arrow represents a diffraction event occurring above the planes, while the atoms are represented by different coloured circles. An Argand diagram is shown to the right demonstrating the contribution of the atoms (represented as vectors) to scattering, shown in their respective colours. **(B)** Same as panel A expect a heavy atom, represented by the grey circle is included. An Argand diagram demonstrating the scattering of the electrons by the heavy atom (grey arrow) is shown to the right.

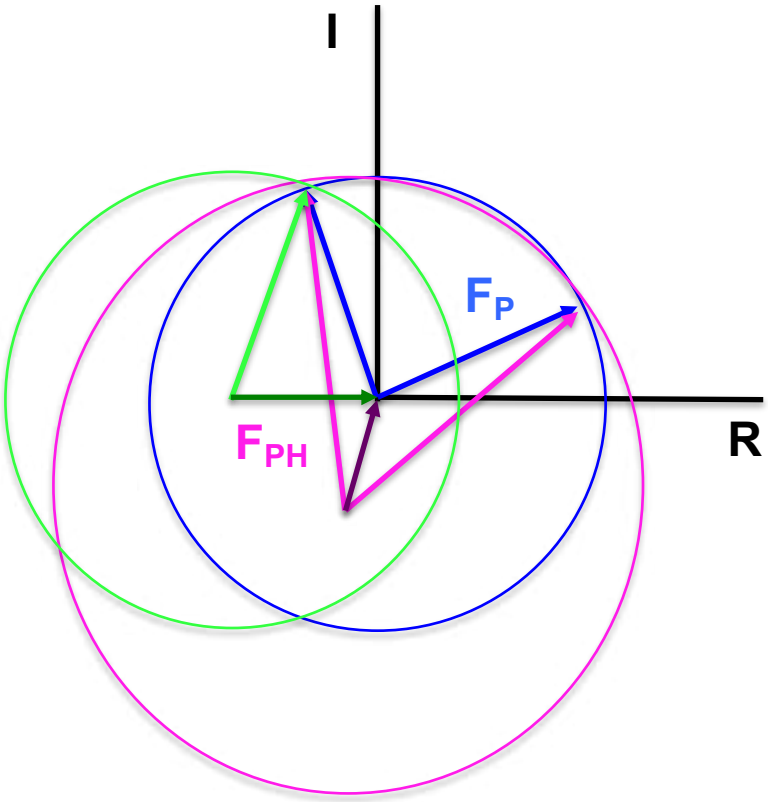

Figure 4. A Harker constitution for a Multiple isomorphous replacement experiment. Multiple isomorphous replacement experiments enable us to solve the phases for the heavy atom containing structure by using the amplitudes from the native and the derivative crystal. By drawing the radius of a circle as the amplitudes of the native crystal (blue circle) around a circle of the amplitudes of heavy atom structure factor (purple circle), we can obtain phases for the native crystal structure (green arrow). More derivative crystals can be used in the experiment to resolve phase ambiguity.

determine their contribution towards the structure factors (Taylor, 2010). This enables the crystallographer to deduce the possible values for each reflection phase angle. If we assume that no change is made to the rest of the structure upon the introduction of the heavy atom, then the structure factor for the derivative crystal (F_{PH}) is equal to the sum of the protein structure factor (F_P) and the heavy atom structure factor (F_H). This can be represented by the equation $F_{PH} = F_P + F_H$. By representing structure factors as vectors, we can then utilize this equation to define a triangle (Fig. 3.A-B). A better representation of the two possible phases is through a Harker construction. This is shown by a circle with a radius equal to the amplitude F_P which is centred towards the origin. This circle represents all possible vectors that can be obtained from every possible phase angles of F_P. In the Harker construction, a second sphere with a radius of F_{PH} with a centre at a point defined by $-|F_H|$ with each point on this second sphere as possible values of F_P to satisfy the $F_{PH} = F_P + F_H$ equation, while still within agreement with the calculated amplitude $|F_{PH}|$ (Fig. 4). Thus, to remove the ambiguity of having two possible phases in the crystal, a derivative heavy atom containing crystal can be used. This is best represented by figure 4, whereby the result from the heavy atom containing crystal is shown in purple (Fig. 4). The calculated information from the derivative crystal would hence only suggest that one phase vector is consistent with other observations. In order to rule out the ambiguous phase information however, multiple derivative crystals are required.

Another method that can be used to solve the phase problem is through anomalous dispersion. Within the protein crystal, most of the electrons will indirectly interact with X-rays (Taylor, 2010). This causes these electrons to diffract with a relative phase of zero, if placed at the origin of the crystal. As such, the diffraction spots generated from the X-ray diffraction experiment would obey Friedel's law (Fig. 5A). This is represented in figure 5.A, whereby a black arrow represents the diffraction event that occurs from above the planes, while an orange arrow represents the diffraction event that occurs at the bottom of the parallel planes. From this figure it is clear that the angles of incidence and reflections are same, thus is the black arrow is defined with Miller indices (h,k,l), while the orange arrow can be defined by Miller indices (-h,-k,-l). The reflection with indices (-h,-k,-l) is referred to as the Friedel mate of (h,k,l). The atoms between Friedel mates would provide the same phase shift, however where the phase shift is positive, they would now be negative, as the orange arrows at the bottom have an opposite phase to the coloured arrows above (Fig 5.A). The use of anomalous scattering can therefore enable us to determine the phase shift of the crystal due to the properties of these anomalous scatterers in breaking Friedel's law. As shown in figure 5.B, the addition of a heavy atom with an anomalous scattering component results in a shift in the amplitudes of Friedel mates (Fig 5.B) (Taylor, 2010). As anomalous scattering is

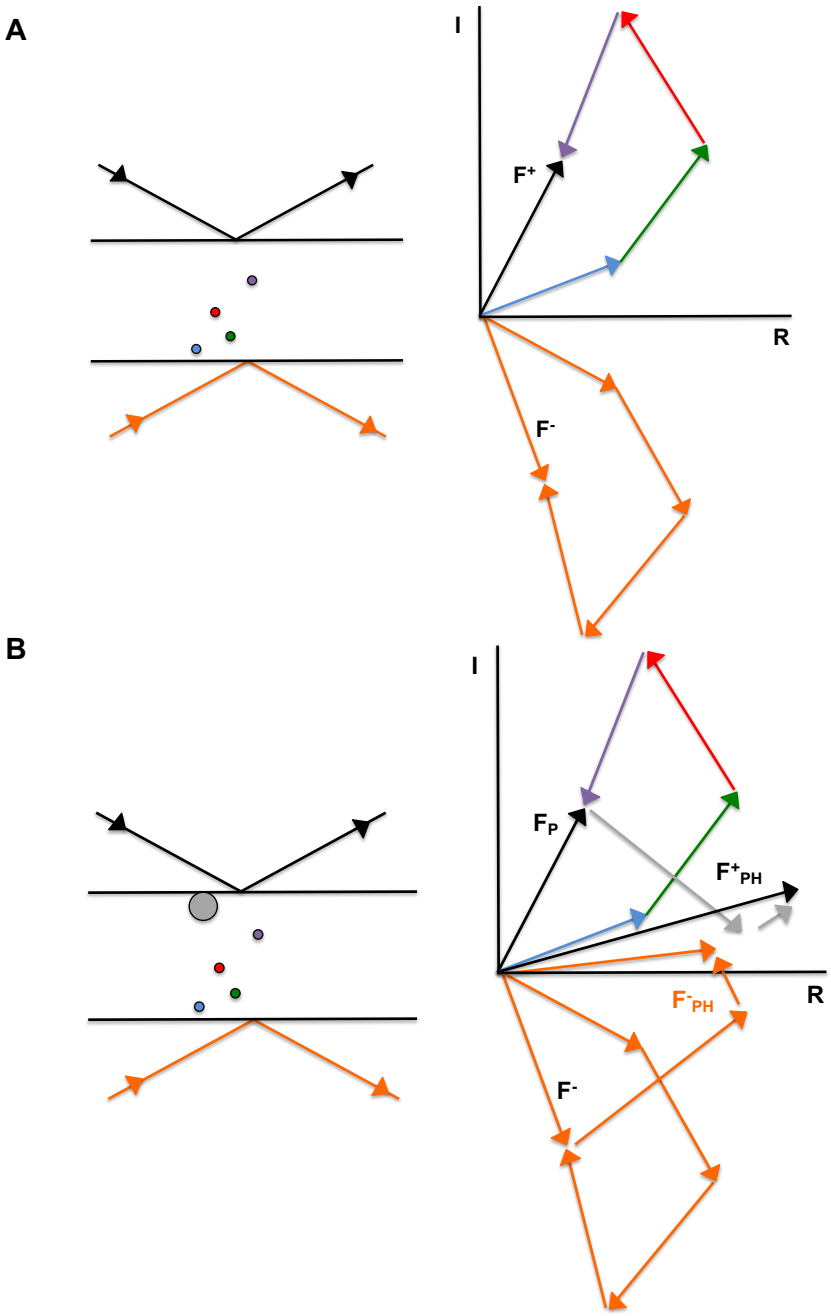

Figure 5. Argand diagram illustrating the breaking of Friedel's law by anomalous scattering. (A) The black arrow represents a diffraction event occurring above the planes, while the orange arrow represents the diffraction event occurring from the bottom of the parallel planes. Atoms are represented by different coloured circles. An argand diagram demonstrating the scattering (represented by vectors) of the diffracted atoms is shown to the right. **(B)** Same as panel A, except an anomalous scatterer represented by a grey circle is included. The changes to the scattering (represented as vectors) is shown to the right by the grey arrow.

dependent on the wavelength of the incident X-rays being close to an atomic absorption edge of the atom, the strength of anomalous scattering is dependent on the wavelength of the X-rays (Taylor, 2010). Thus, to obtain enough phase information, data collected from the crystal must be done at a wavelength close towards the absorption edge of the anomalous scattering element found within the protein crystal (Taylor, 2010).

Since its initial proposal by Rossmann and Blow in 1962, molecular replacement has been the most frequently used method to solve the structure of a protein when a closely related structure of the protein is available (Evans and McCoy, 2007; Rossmann and Blow, 1962; Taylor, 2010). Generally, molecular replacement uses a known molecular model to solve the structure of a closely related molecule. This provides a solution to the phase problem by providing the initial estimates of the phases of the new structure from the previously solved protein structure. For example in this thesis, the *C. crescentus* ParB structures were solved using the previously solved *H. pylori* ParB as a search model (Chen et al., 2015) (Chapter 3 and 4). In this method, the crystallographic calculation occurs in reverse, by which structure factors from a previously known coordinate file is used to calculate the new structure factor (Evans and McCoy, 2007). Thus, one common limitation in this technique is the generation of bias towards the generated model. In this method, we utilise a model which approximates to the unsolved protein structure and a set of measured intensities. Computer based programs such as PHASER utilise every possible orientation and position of the search model in the unsolved protein structure in order to determine the predicted diffraction that best matches the observed diffraction (McCoy et al., 2007). The phases that are calculated from the correctly placed search model are then used to calculate an initial electron density map of the unsolved protein structure. This is used to rebuild the model in order to better resemble the unsolved protein structure.

During molecular replacement, a Patterson function is used to rotate and translate the search model in order to provide a sensible solution for the unsolved target protein (Evans and McCoy, 2007; Patterson, 1935). Initially this is conducted through a rotation function, whereby the search model is rotated until it matches unsolved protein. This is due to the ability of the Patterson function to rotate the search model and the intermolecular vectors by the same angle (Grosse-Kunstleve and Adams, 2001). A second translation function is then carried out to move the reoriented data into the unit cell to fit the position of the new model as accurately as possible (Grosse-Kunstleve and Adams, 2001). Once the model is positioned and orientated as closely as possible, several rounds of refinement are then required to improve the model.

References

1. Bernal, J.D., and Crowfoot, D. (1934). X-ray photographs of crystalline pepsin. Nature. **113**, 794–795.
2. Bragg, W.H. (1913). The Reflection of X-rays by Crystals. Nature. **91**, 477.
3. Chen, B.W., Lin, M.H., Chu, C.H., Hsu, C.E., and Sun, Y.J. (2015). Insights into ParB spreading from the complex structure of Spo0J and parS. Proc. Natl. Acad. Sci. U. S. A. **112**, 6613–6618.
4. Cochran, W.T., Cooley, J.W., Favin, D.L., Helms, H.D., Kaenel, R.A., Lang, W.W., Maling, G.C., Nelson, D.E., Rader, C.M., and Welch, P.D. (1967). What is the Fast Fourier Transform? IEEE Trans. Audio Electroacoust. **15**, 45–55.
5. Evans, P., and McCoy, A. (2007). An introduction to molecular replacement. In Acta Crystallographica Section D: Biological Crystallography. **64**, 1–10.
6. Evans, P.R., and Murshudov, G.N. (2013). How good are my data and what is the resolution? Acta Crystallogr. Sect. D Biol. Crystallogr. **69**, 1204–1214.
7. Ewald, P. P. (1921). Die Berechnung optischer und elektrostatischer Gitterpotentiale. *Annalen der Physik*. **369**, 253–287.
8. Fultz, B., and Howe, J.M. (2008). Transmission electron microscopy and diffractometry of materials. Graduate Texts in Physics.
9. Giegé, R. (2013). A historical perspective on protein crystallization from 1840 to the present day. FEBS J. **280**, 6456–6497.
10. Grosse-Kunstleve, R.W., and Adams, P.D. (2001). Patterson correlation methods: A review of molecular replacement with CNS. Acta Crystallogr. - Sect. D Biol. Crystallogr. **57**, 1390–1396.
11. Gruner, S.M., Tate, M.W., and Eikenberry, E.F. (2002). Charge-coupled device area x-ray detectors. Rev. Sci. Instrum. **73**, 2815.
12. Ilari, A., and Savino, C. (2008). Protein structure determination by X-ray crystallography. Methods Mol. Biol. **452**, 63–87.
13. Ladd, M., and Palmer, R. (2003). Lattices and Space-Group Theory. In Structure Determination by X-Ray Crystallography, p. 51–116.
14. McClintock, P.V.E. (2018). Methods in molecular biophysics: structure, dynamics, function for biology and medicine, 2nd edition. Contemp. Phys.
15. McCoy, A.J., Grosse-Kunstleve, R.W., Adams, P.D., Winn, M.D., Storoni, L.C., and Read, R.J. (2007). Phaser crystallographic software. J. Appl. Crystallogr. **40**, 658–674.
16. Patterson, A.L. (1935). A Direct Method for the Determination of the Components of Interatomic Distances in Crystals. Zeitschrift Für Krist. - Cryst. Mater. **90**, 517–525.
17. Pooley, R.A., McKinney, J.M., and Miller, D.A. (2001). The AAPM/RSNA Physics

Tutorial for Residents. RadioGraphics. **25**, 1087–1099.

18. Potterton, L., Agirre, J., Ballard, C., Cowtan, K., Dodson, E., Evans, P.R., Jenkins, H.T., Keegan, R., Krissinel, E., Stevenson, K., et al. (2018). CCP 4 i 2: The new graphical user interface to the CCP 4 program suite. Acta Crystallogr. Sect. D Struct. Biol. **74**, 84–84.
19. Ren, Y. (2012). High-energy synchrotron x-ray diffraction and its application to in situ structural phase-transition studies in complex sample environments. JOM. **64**, 140–149.
20. Rhodes, G. (2002). Crystallography Made Crystal Clear (Third Edition).
21. Röntgen, W.C. (1896). On a new kind of rays. Science. **3**, 227–231.
22. Rossmann, M.G., and Blow, D.M. (1962). The detection of sub-units within the crystallographic asymmetric unit. Acta Crystallogr. **15**, 24–31.
23. Shi, Y. (2014). A glimpse of structural biology through X-ray crystallography. Cell.
24. Smyth, M.S., and Martin, J.H.J. (2000). x Ray crystallography. J. Clin. Pathol. - Mol. Pathol. **53**, 8–14.
25. Taylor, G.L. (2010). Introduction to phasing. Acta Crystallogr. Sect. D Biol. Crystallogr. **66**, 325–338.

OPEN BIOLOGY

royalsocietypublishing.org/journal/rsob

Review

Cite this article: Jalal ASB, Le TBK. 2020 Bacterial chromosome segregation by the ParABS system. *Open Biol.* **10**: 200097. http://dx.doi.org/10.1098/rsob.200097

Received: 15 April 2020
Accepted: 21 May 2020

Subject Area:
biochemistry/microbiology/molecular biology

Keywords:
chromosome organization, chromosome segregation, chromosome maintenance, ParA–ParB–*parS*, spreading, SMC

Author for correspondence:
Tung B. K. Le
e-mail: tung.le@jic.ac.uk

Bacterial chromosome segregation by the ParABS system

Adam S. B. Jalal and Tung B. K. Le

Department of Molecular Microbiology, John Innes Centre, Norwich NR4 7UH, United Kingdom

ASBJ, 0000-0001-7794-8834; TBKL, 0000-0003-4764-8851

Proper chromosome segregation during cell division is essential in all domains of life. In the majority of bacterial species, faithful chromosome segregation is mediated by the tripartite ParABS system, consisting of an ATPase protein ParA, a CTPase and DNA-binding protein ParB, and a centromere-like *parS* site. The *parS* site is most often located near the origin of replication and is segregated first after chromosome replication. ParB nucleates on *parS* before binding to adjacent non-specific DNA to form a multimeric nucleoprotein complex. ParA interacts with ParB to drive the higher-order ParB–DNA complex, and hence the replicating chromosomes, to each daughter cell. Here, we review the various models for the formation of the ParABS complex and describe its role in segregating the origin-proximal region of the chromosome. Additionally, we discuss outstanding questions and challenges in understanding bacterial chromosome segregation.

1. Introduction

Faithful chromosome segregation is essential to ensure each daughter cell inherits a full copy of the genetic information of the parent. Chromosome segregation is not a trivial process, especially in bacteria, because DNA must be maintained in a compacted state to fit within the limited volume of the cells, and chromosome segregation often occurs concomitantly with DNA replication rather than being separated temporally, as in eukaryotes. Bacterial chromosome segregation can be divided into multiple overlapping steps: (i) segregation of DNA proximal to the origin of replication, (ii) segregation of the bulk of the chromosome, and (iii) segregation of DNA near the terminus of replication. In this review, we focus on progress towards understanding the molecular basis for segregating the origin-proximal region, specifically by the tripartite ParA–ParB–*parS* system.

The *par* locus was first discovered in low-copy-number plasmids, and was shown to be essential for their stable inheritance [1–4]. A functionally equivalent *par* locus was later found to be important for chromosome segregation in *Bacillus subtilis* [5–7]. In *Caulobacter crescentus*, *Hyphomonas neptunium* and *Myxococcus xanthus*, genes encoded in the *par* locus (ParABS) were found to be essential for cell viability [8–11], whereas in other bacterial species engineered strains lacking ParABS were viable but had an elevated number of anucleate cells owing to defects in chromosome segregation [12–27]. A comparative genomic study suggested that the chromosomal ParABS system is conserved in two-thirds of bacterial species [28]. In most bacteria, one or multiple *parS* sites are commonly found near the origin of replication [28]. The *parS* site is the first DNA locus to be segregated after chromosome replication [7,11,13,29]. ParB is a DNA-binding protein that nucleates on *parS* to recruit additional ParB molecules to adjacent non-specific DNA to form a network of protein–DNA complexes [30]. The ParB–DNA nucleoprotein complex stimulates the ATPase activity of ParA, creating a gradient of ParA–ATP that drives the movement of the origin-proximal region of the chromosome (and subsequently, the whole chromosome) along this gradient to the opposite pole of the cell [31–39]. ParB also recruits the structural maintenance of chromosome (SMC) complex onto the chromosome to

THE ROYAL SOCIETY PUBLISHING

reduce DNA entanglement, thereby promoting the individualization of replicated chromosomes [16,40–46].

Since the discovery of the ParABS system over 35 years ago, tremendous progress has been made towards answering some of the key questions about how this system works:

— How does ParB recruit tens to hundreds more ParB proteins to assemble a higher-order nucleoprotein complex? (Discussed in §2.)
— What is the molecular mechanism of ParA-mediated DNA segregation? (Discussed in §3.)
— How does ParB recruits SMC and other protein partners to coordinate chromosome segregation with chromosome organization? (Discussed in §4.)
— How does evolution shape factors that are involved in bacterial chromosome segregation and maintenance? (Discussed in §5.)

In this review, we summarize recent progress and compare the competing models for addressing these key questions, before highlighting outstanding questions and challenges for fully understanding the ParABS system and chromosome segregation in bacteria.

2. ParB–*parS* interaction and the assembly of a higher-order nucleoprotein complex

ParB binding to *parS* nucleates the recruitment of additional ParB molecules which associate with neighbouring DNA, a process known as spreading, to form a higher-order ParB-DNA nucleoprotein complex [30]. The purpose of this higher-order complex, whether to strengthen the physical link between DNA and ParA or to provide a specific DNA topology to facilitate DNA segregation, is still under debate. However, since bacterial strains harbouring nucleation competent but spreading-defective mutants of *parB* are either unviable or have elevated number of anucleate cells, it is clear that a higher-order nucleoprotein complex is a prerequisite for faithful chromosome segregation [7,47–50]. In this section, we describe and discuss the current and emerging models for the assembly of this essential nucleoprotein complex.

2.1. Domain organization and shared features of chromosomal ParB protein family

Chromosomal ParB proteins share a common domain architecture, consisting of an N-terminal domain (NTD), a central DNA-binding domain (DBD) and a C-terminal domain (CTD) (figure 1*a*). A highly conserved arginine-rich motif (GERRxRA) resides in the NTD and mediates protein–protein and protein–ligand interactions [30,51,52] (figure 1*a*). The DBD contains a helix–turn–helix motif that enables ParB to nucleate on *parS* specifically [30]. The CTD, which is the least conserved domain among ParB homologs, contains a leucine zipper motif that allows ParB to homodimerize [30] (figure 1*a*). The CTD of *Bacillus subtilis* ParB also has a lysine-rich amino acid patch that provides additional non-specific DNA-binding and DNA condensation activities [53]. Currently, the structure of a full-length chromosomal ParB is not available. The flexibility of ParB, endowed by amino acid linkers that connect consecutive domains, has hindered the effort to crystallize and solve the structure of a full-length protein. Nevertheless, structure-function insights have been gained from X-ray crystallography/NMR studies using a single-domain or domain-truncated variants of ParB from various bacterial species [52–58]. Structural comparisons suggested that ParB, especially its NTD, can adopt multiple alternative conformations that might facilitate the assembly of a higher-order nucleoprotein complex.

Four models have been proposed relating to the assembly of a higher-order ParB–DNA nucleoprotein complex. Here we assess the evidence for and against each model.

2.2. Model 1—one-dimensional filamentation of ParB

The earliest evidence of a higher-order ParB-DNA nucleoprotein complex came from studies of a plasmid-borne ParB. Overexpression of an F-plasmid ParB protein ($ParB_F$ or SopB) was observed to repress the expression of antibiotic resistance genes several kilobases away from the *parS* (*sopC*) site on the plasmid [59]. Moreover, $ParB_F$ overexpression also prevents DNA gyrase and restriction enzyme access to DNA regions neighbouring the *parS* site [59]. Similarly, a P1-plasmid ParB ($ParB_{P1}$) also silences the expression of genes adjacent to *parS* in both directions for several kilobases, with the efficiency of gene silencing decreasing as the genomic distance from *parS* increases [60]. A direct association of $ParB_{P1}$ with the silenced DNA was demonstrated by chromatin immunoprecipitation PCR (ChIP-PCR) assay [60]. Based on these observations, it was proposed the growth of a filament of ParB proteins nucleated at *parS* and then spread outward to neighbouring DNA (figure 1*b*). This model was further supported by the observation that a site-specific DNA-binding protein, RepA, could attenuate the $ParB_{P1}$-mediated gene silencing effect, presumably by acting as a roadblock to partially stop the filamentation of ParB [60] (figure 1*b*). Multiple chromosomal ParBs have subsequently been observed by ChIP-chip/seq to associate with an extended DNA region beyond *parS* [13,16,19,44,47,48,61,62], hence chromosomal ParBs were also thought to oligomerize to form a nucleoprotein filament. The highly conserved arginine-rich patch (GERRxRA) at the NTD has been implicated in mediating ParB filamentation, as mutations in this region impair the ability of ParB to associate extensively with DNA beyond *parS* [47–49,62,63]. This early model of ParB spreading is straightforward and attractive; however, later studies have argued that the intracellular concentration of ParB is too low to support such an extensive one-dimensional filamentation *in vivo* [62,64]. Moreover, at native expression levels, *B. subtilis* ParB (Spo0 J) does not silence genes adjacent to *parS* [48], suggesting that the ParB-DNA nucleoprotein complex might be more dynamic than can be explained by the one-dimensional filamentation model.

2.3. Model 2—bridging and condensing DNA

A combination of quantitative immunoblotting and immunofluorescence microscopy approaches led to the estimate that approximately 20 ParB dimers are associated with each *parS* site in *B. subtilis*, allowing for maximally approximately 500 bp of DNA to be covered by a continuous filament of ParB [62]. This is substantially lower than the approximately 10–20 kb of ParB-bound DNA observed by ChIP-chip [48,61], arguing against the one-dimensional filamentation model. Instead, a new model was proposed based on the observation that

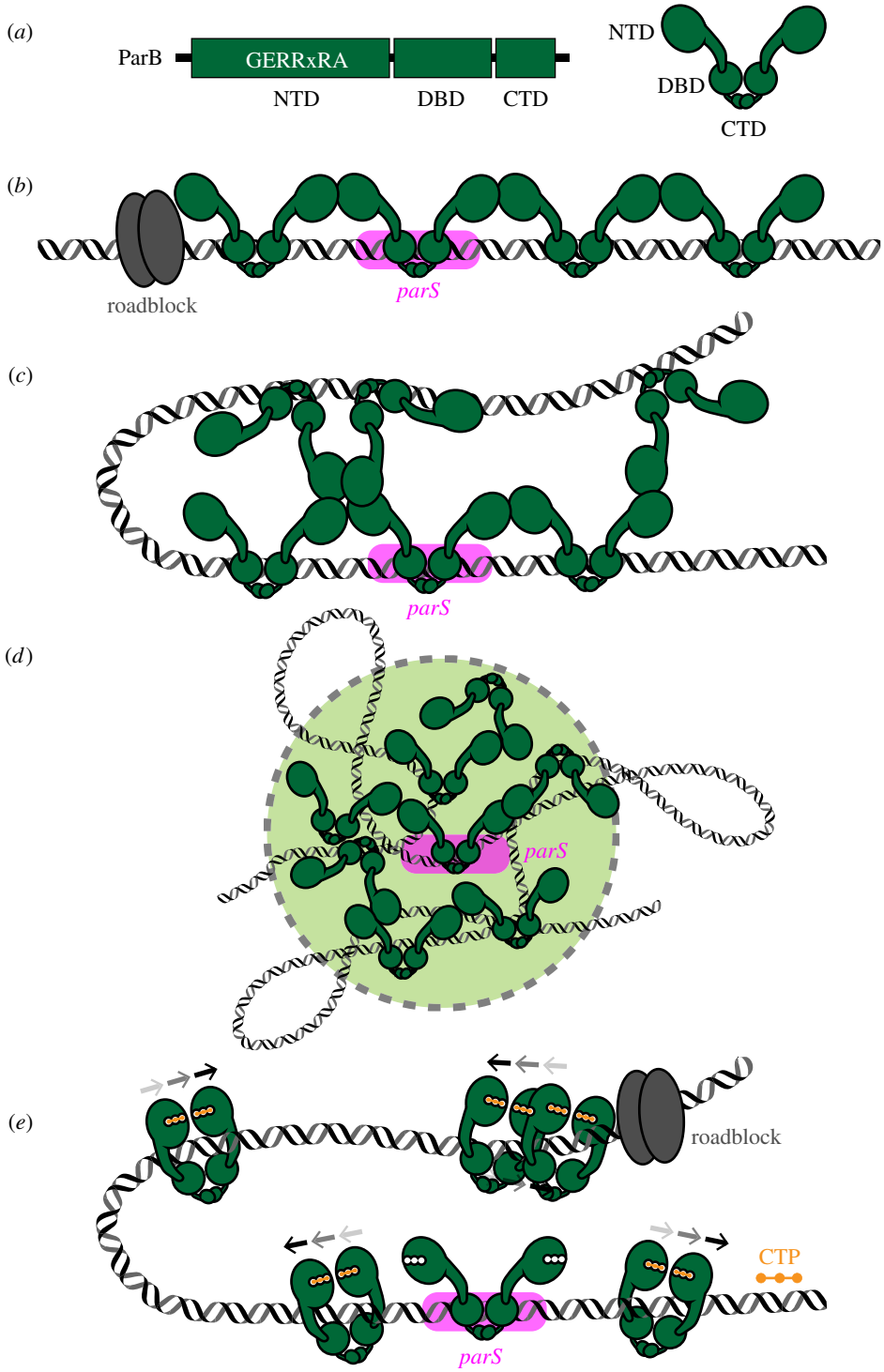

Figure 1. The assembly of a higher-order ParB–DNA nucleoprotein complex. (*a*) Chromosomal ParB proteins share a common domain architecture, consisting of an N-terminal domain (NTD), a central DNA-binding domain (DBD) and a C-terminal domain (CTD). The NTD harbours a conserved arginine-rich motif (GERRxRA) that mediates ParB–ParB and ParB–cytidine triphosphate (CTP) interactions. (*b*) Model 1: ParB spreading by a one-dimensional filamentation. (*c*) Model 2: ParB spreading by bridging and condensing DNA. (*d*) Model 3: ParB spreading by caging DNA. (*e*) Model 4: ParB spreading by sliding on DNA. ParB switches from an open to a closed clamp upon binding to CTP (orange). ParB and *parS* are coloured green and magenta, respectively. The arrows above the ParB–CTP complexes (*e*) indicate their progressive sliding on DNA. A tight DNA-binding protein (grey) can unidirectionally block the one-dimensional filamentation or the sliding of ParB on DNA.

B. subtilis ParB can bridge different segments of DNA (figure 1*c*). In a single-molecule microscopy-based assay, bacteriophage λ DNA (approx. 50 kb) was tethered at one end to a microscope slide and stretched out by a buffer flow. The introduction of purified *B. subtilis* ParB compacted the flow-extended DNA, demonstrating that ParB can form bridges and condense bound DNA [62]. Moreover, mutations in the arginine-rich patch which eliminate the extensive *in vivo* ChIP-seq profile of *B. subtilis* ParB also impair *in vitro* DNA-bridging activity [62].

ParB-mediated DNA bridging was also observed using magnetic-tweezers assays [65]. The additional non-specific DNA-binding activity owing to a surface-exposed lysine-rich patch at the CTD of *B. subtilis* ParB was found to be essential for this function [53,66]. Mutations in these lysine residues eliminate DNA bridging and condensation *in vitro* and reduce ParB-DNA nucleoprotein formation *in vivo*, as assessed by the less extensive ChIP-qPCR profile and by the dimmer and fuzzier appearance of fluorescently labelled ParB foci

[53]. It is important to emphasize that interactions among NTD of *B. subtilis* ParB are also necessary for bridging DNA (figure 1*c*); neither CTD alone nor ParB with mutations at the arginine-rich patch (at the NTD) can condense DNA *in vitro* [53,66]. The non-specific DNA-binding activity of the CTD is thought to provide multiple anchors on DNA that can be brought spatially close together by the NTD–NTD interactions (figure 1*c*). Insights into the molecular mechanism of NTD–NTD interactions were provided by the co-crystal structure of a CTD-truncated *Helicobacter pylori* ParB in complex with a *parS* DNA duplex [54]. This structure shows *H. pylori* ParB interacting with an adjacent ParB on a pseudo-continuous DNA in the crystal lattice (in *cis* interactions or one-dimensional filamentation) and also with ParB on a disconnected DNA duplex (in *trans* interactions or three-dimensional bridging) (figure 1*c*), with the arginine-rich patch at the core of the NTD–NTD interaction interface [54]. By comparison with the *Thermus thermophilus* apo-ParB structure, it was proposed that the nucleation of ParB onto *parS* induces a conformational change at the NTD that exposes the arginine-rich patch for the NTD–NTD interactions [49,54,56].

In sum, it has been proposed that DNA-bridging activity allows a limited number of ParB molecules to bring regions of DNA that are several kilobases apart together in three-dimensional space to form a compacted nucleoprotein complex (figure 1*c*). Nevertheless, a computational modelling study has suggested that a combination of both one-dimensional filamentation and three-dimensional bridges are required to recreate the condensed ParB–DNA nucleoprotein complex observed *in vivo* [67]. Thus, while the DNA-bridging model is an important step towards understanding the assembly of the ParB–DNA nucleoprotein complex, it is unlikely to be the final say. The main caveat is that *B. subtilis* ParB can bridge to condense DNA *in vitro* regardless of the presence of *parS* [53,62,65]. This contradicts *in vivo* data showing *parS* is absolutely required for the clustering of fluorescently labelled ParB molecules into a tight focus [62,68]. Moreover, the lysine-rich patch (at the CTD of *B. subtilis* ParB) is not highly conserved; for example, ParB from *Caulobacter crescentus* lacks the equivalent lysine residues and does not bridge/condense DNA *in vitro* [55]. As such, it is not yet clear how prevalent DNA-bridging activity is among chromosomal ParB homologs.

2.4. Model 3—caging ParB and DNA

A model broadly similar to bridging and condensing DNA that aims to better explain the observed *parS*-dependent confinement of ParB *in vivo* has been proposed [69]. In this nucleation and caging model, the *parS* site acts as a ParB nucleation centre, while weak but synergistic protein–protein and protein–DNA interactions cage ParB spatially into a confined volume inside the cells [69] (figure 1*d*). Supporting this model, single-molecule super-resolution microscopy demonstrated that the binding of $ParB_F$ to *parS* results in a very high local concentration of protein *in vivo*, where greater than 90% of $ParB_F$ in the cell are confined in clusters at *parS* [69]. Similarly, the local concentration of *C. crescentus* ParB near *parS* has been estimated to reach approximately 500 µM (500 times more concentrated than typically used for *in vitro* experiments) [31]. Despite $ParB_F$ (or *C. crescentus* ParB) having expectedly low-affinity interactions with non-specific DNA, these interactions may occur stochastically at very high frequency, especially at the extreme local concentration of ParB *in vivo*, to create a cage of dynamically exchanged ParB–DNA complexes (figure 1*d*). Fluorescence recovery after photo-bleaching (FRAP) experiments have shown that $ParB_F$ molecules rapidly exchange between different clusters, further highlighting the dynamic nature of cages of ParB-DNA *in vivo* [70]. The nucleation and caging model has also been shown applicable to the *Vibrio cholerae* chromosomal ParB–*parS* system, suggesting that this dynamic self-assembly mechanism might be conserved from plasmids to chromosomes [70].

2.5. Model 4—lateral sliding of a ParB–CTP clamp on DNA

Recent studies have uncovered a new cofactor of ParB [51,52]. Various plasmid- and chromosome-encoded ParB and ParB-like proteins have been found to bind and hydrolyse cytidine triphosphate (CTP) to cytidine di-phosphate (CDP) and inorganic phosphate [51,52,71]. A co-crystal structure showed CDP binding to the arginine-rich patch at the NTD of *B. subtilis* ParB (CTP was hydrolysed to CDP during crystallization) [52]. At the same time, another co-crystal structure showed a *M. xanthus* ParB-like protein (PadC) in complex with CTP [51]. CTP (or CDP) is sandwiched between two NTDs, thus promoting a new NTD self-dimerization interface that has not been observed previously [51,52]. Employing site-specific cross-linking assays and single-molecule imaging, it was demonstrated that CTP-induced self-dimerization creates a clamp-like ParB that entraps DNA within its central cavity [52] (figure 1*e*). A comparison between the *B. subtilis* ParB–CDP structure and the *H. pylori* ParB–*parS* structure suggested that CTP binding induces a conformational change at the central DNA-binding domain that is incompatible with *parS* binding [52,54]. Studies with *C. crescentus* and *M. xanthus* ParBs further showed that CTP binding reduces ParB nucleation at *parS* and/or liberates pre-bound ParB from *parS* [51,71], thereby facilitating the escape of ParB from a high-affinity nucleation site to a low-affinity neighbouring DNA. Therefore, CTP probably serves to switch ParB from a nucleating to a sliding mode (figure 1*e*). Overall, it was suggested that ParB clamp can self-load at *parS*, without the need of a dedicated loading factor, and spreads by sliding to the neighbouring DNA while still entrapping DNA [52,71] (figure 1*e*). The interpretation of a sliding ParB–CTP clamp on DNA is further backed up by several lines of evidence: (i) tight DNA-binding proteins, such as a catalytic-dead EcoRI (E111Q) variant or TetR, can block the spreading of *B. subtilis* and *C. crescentus* ParB–CTP on DNA *in vitro* [52,71] (figure 1*e*), and (ii) *C. crescentus* ParB only accumulates on DNA that has both ends blocked (by a bulky biotin-streptavidin complex) to prevent a run-off [71]. However, it is not yet clear whether the translocation of ParB–CTP on DNA is entirely a passive one-dimensional diffusion process or whether it is facilitated by unknown interactions between the protein and DNA. CTP hydrolysis is unlikely to provide energy for ParB translocation since its hydrolysis rate is extremely low, ranging from approximately 3 to approximately 36 CTP molecules per hour [51,52,71]. Moreover, ParB in complex with a non-hydrolysable CTPγS analog can still self-load and accumulate on DNA, albeit with a reduced stability [52,71]. It has been speculated that CTP hydrolysis might contribute to recycling of ParB

between the nucleation and translocation modes [52,71]. Mutant proteins (N112S and N172A of *B. subtilis* and *M. xanthus* ParB, respectively), which bind CTP but are deficient for hydrolysis, fail to form tight foci inside the cells [40,51,52]; however, this is weak evidence for the *in vivo* role of CTP hydrolysis since *B. subtilis* ParB (N112S) is already impaired at forming a protein clamp [52]. A better understanding of the CTPase mechanism that enables the design of a mutation at the catalytic site to eliminate CTP hydrolysis while allowing NTD self-dimerization is likely to provide a key insight into the role of CTP hydrolysis.

2.6. Reconciliation of different models: outstanding questions and challenges

The unexpected finding of the ParB–CTP interaction has fundamentally changed thinking on the assembly of a higher-order nucleoprotein complex and bacterial chromosome segregation by the ParABS system. But does the 'ParB spreading by sliding' model supersede previously proposed models? It is too early to answer this question adequately, given that many mechanistic details are still missing. For example, an alternative view has been proposed wherein *parS* binding stimulates the CTPase activity to switch *M. xanthus* ParB from a CTP-bound closed conformation to an apo/CDP-bound open conformation, liberating the NTD to engage in DNA-bridging/caging interactions [51]. It is possible that there are two different modes of action of ParB inside the cells: one for bridging/caging DNA together, and another for the lateral sliding of ParB on DNA. Investigating the relative contribution of the two different modes of action to chromosome segregation, especially *in vivo*, is an important challenge. Some of other immediate questions to which answers can help refine or reconcile different models include:

— How dynamic is the ParB clamp opening and closing when bound to *parS* and/or to CTP?
— Can the ParB clamp entrap two or more DNA segments together [52], thereby contributing to DNA bridging and condensation?
— What is the mechanism of CTP hydrolysis?
— Does the translocation of ParB supercoil DNA, thereby compacting *parS*-proximal DNA?
— Is there a variation in CTP-binding affinity and CTP hydrolysis rate among ParB orthologs, and how does this natural variation impact chromosome segregation in different bacterial species?

Whether CTP plays a regulatory role in chromosome segregation, in addition to being a co-factor of ParB, is also unknown. The concentration of nucleoside triphosphate (NTP) ranges from approximately 0.3 to approximately 3 mM inside bacterial cells [72]. Their concentrations can decrease by ~tenfold as cells enter the stationary phase [72] but it is unlikely to impact ParB–CTP binding significantly. Indeed, foci of a fluorescently tagged ParB do not disappear when *C. crescentus* cells enter the stationary phase or during starvation [73]. For these reasons, we speculate that the assembly of ParB–DNA nucleoprotein complex is not regulated by varying the intracellular concentration of CTP. However, there is a formal possibility that other NTP-related small molecules, whose diversity has only been realized recently [74], could have a regulatory impact. Future work will undoubtedly continue to provide important new insights into the assembly of the ParB–DNA nucleoprotein complex and its roles in chromosome segregation.

3. ParB–DNA interaction with ParA and segregation of the origin-proximal chromosomal region

ParA is a deviant Walker A ATPase protein [75] that enables a directional movement of ParB-bound DNA. Early studies of plasmid and chromosome segregation proposed a mechanism for DNA-pulling by either a linear or a helical ParA filament [76–83], akin to the mitotic spindle apparatus in eukaryotes. According to this model, ParA–ATP polymerizes into a filamentous structure along the cell length, with the edge of the filament capturing the ParB–DNA nucleoprotein complex. ParB binds ParA and stimulates its ATPase activity to hydrolyse ATP, thereby depolymerizing the ParA filament and concomitantly pulling the ParB–DNA complex (hence, the plasmid/chromosome) along the retracting filament to the opposite cell pole [76,83,84]. While purified ParA from various bacterial species could self-aggregate into filament-like structures in the presence of ATP/ADP [34,76,79,82,85–91], no such continuous polymer was seen in recent co-crystal structures of ParA with DNA, even at the high concentration of protein and DNA used to generate crystals. Furthermore, the spatial distribution of an F-plasmid ParA and *C. crescentus* ParA *in vivo* is inconsistent with a continuous filamentous structure, instead they form small patches or a cloud-like gradient of sparsely distributed molecules inside the cells, as observed by super-resolution microscopy [31,37]. As such, it is uncertain whether a DNA-pulling mechanism by a ParA filament is operating *in vivo*.

It has been proposed that a ParA filament is not necessary for DNA segregation, and that a diffusion-ratchet mechanism can also explain the directional movement of segregating DNA [33,35,36,38,92,93] (figure 2*a*,*b*). In this model, ParA binds ATP to homodimerize and to associate with non-specific DNA. X-ray crystallographic and hydrogen/deuterium exchange mass spectrometry analysis of ParA with nucleotides and DNA have revealed the dimerization interface and a multi-faced DNA-binding surface [94–96]. ParB, via its N-terminal peptide, binds ParA directly and stimulates the ATPase activity of ParA, thereby dissociating ParA dimer into individual monomers that no longer bind DNA [34,36,97,98] (figure 2*a*). This stimulation in the ATPase activity creates a local gradient of ParA–ATP with the least DNA-bound ParA–ATP near the ParB–DNA complex (figure 2*a*). The ParB–DNA complex then diffuses up the gradient, by Brownian motion, to rebind ParA–ATP, resulting in a net movement of the ParB-anchored DNA (figure 2*a*). The initial movement of the ParB–DNA complex in one chosen direction enforces the continued movement in the same direction, resulting in a long-range directional movement of the DNA (figure 2*a*,*b*). The released monomeric apo–ParA/ParA–ADP can rebind ATP to homodimerize and later regains its non-specific DNA-binding activity (figure 2*a*). It is worth noting that the released apo–ParA/ParA–ADP can rebind ATP but cannot immediately bind DNA until a transition occurs in the ParA–ATP structure (figure 2*a*); this transitional state presumably introduces a time delay

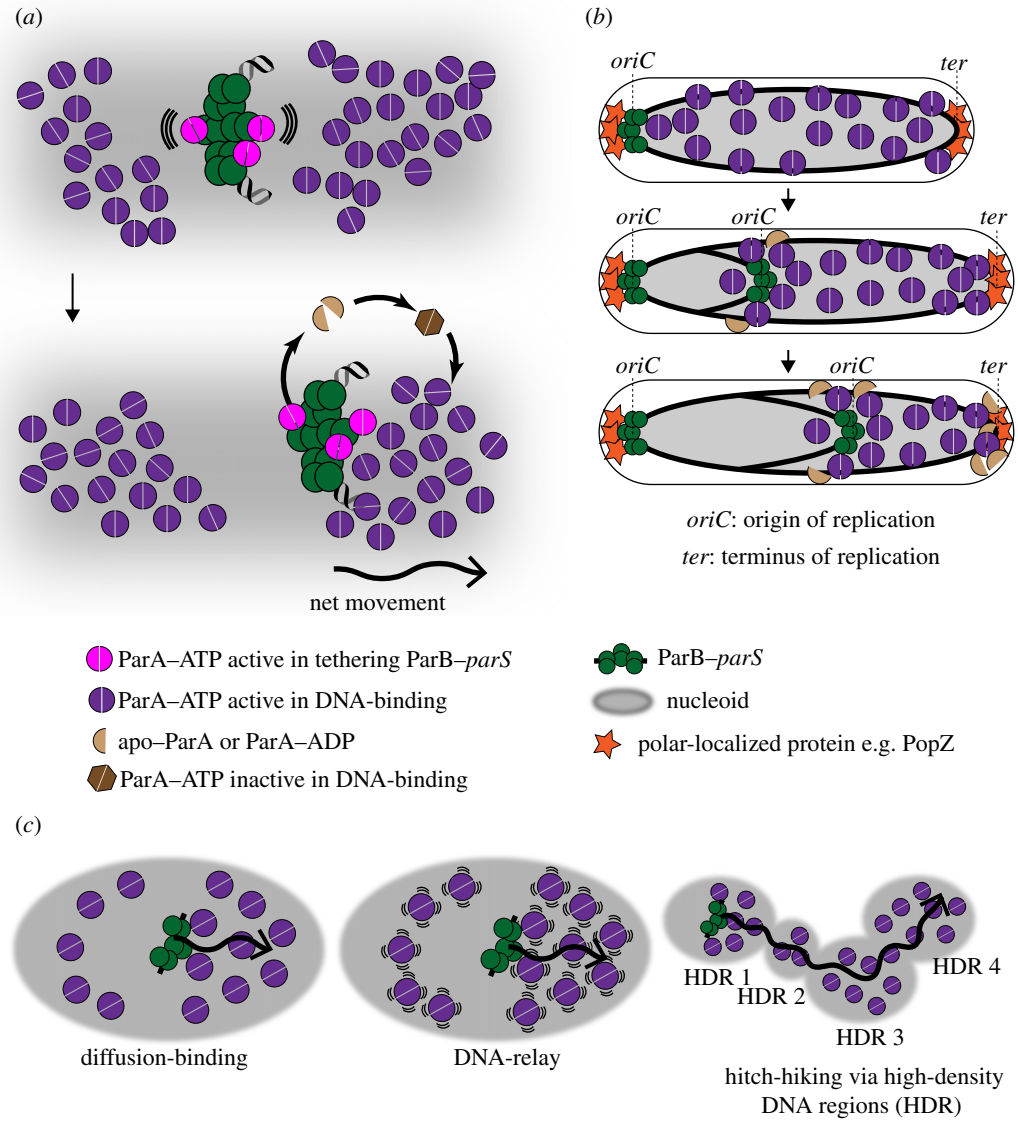

Figure 2. ParA drives the movement of ParB-bound DNA to segregate plasmids and chromosomes. (*a*) A diffusion-ratchet model for ParA-mediated transport of ParB-bound DNA. A ParB–DNA complex (green) interacts with ParA–ATP (violet) to tether to the nucleoid (grey), and to stimulate the ATPase activity of ParA. ParA–ATP dimers (violet) bind the nucleoid non-specifically. After ATP hydrolysis, monomers of apo–ParA/ParA–ADP (light brown) no longer bind DNA, thus creating a zone of depletion of ParA–ATP surrounding the ParB–DNA complex. By thermal fluctuation (wavy lines), the ParB–DNA complex moves to the edge of the zone of depletion to rebind ParA–ATP. The initial movement of the ParB–DNA complex in one chosen direction enforces the continued movement in the same direction, resulting in a long-range directional movement of the DNA (see *b*). The released apo–ParA/ParA–ADP (light brown) rebinds ATP but cannot immediately bind DNA (the dark brown hexagon) until a transition occurs in the ParA–ATP structure. (*b*) The segregation of the origin-proximal region of the chromosome by the ParABS system. For example, in *C. crescentus*, one ParB–DNA complex remains at the pole after chromosome replication, while the other moves along the gradient of ParA–ATP, via the diffusion-ratchet mechanism, to the opposite cell pole. The polarly localized proteins (e.g. PopZ, orange) contribute to maintaining the ParA–ATP gradient by sequestering apo–ParA/ParA–ADP away from the nucleoid and to regenerate them at the pole. (*c*) Other variations of the diffusion-ratchet model have been proposed to include an element of DNA elasticity (i.e. the DNA-relay model) or high-density DNA regions (HDR) (i.e. the hitch-hiking model). A wavy arrow indicates the directional movement of the partition complex.

mechanism to ensure the existence of a ParA–ATP gradient surrounding the ParB–DNA complex [38,94]. Without this delay, regenerated ParA–ATP will instantly rebind DNA in the same location, thus dissipating the gradient. Other organism-specific factors, for example, the polarly localized proteins PopZ and TipN in *C. crescentus*, may also contribute to maintain the ParA–ATP gradient by sequestering apo–ParA/ParA–ADP away from the nucleoid and to regenerate ParA–ATP only at the cell pole [99,100] (figure 2*b*). Based on computational modelling it has been argued that the short-range diffusion of a ParB–DNA complex up the gradient of ParA–ATP might not be sufficient to explain a robust unidirectional segregation of chromosome towards the new cell pole (figure 2*b*) and that the diffusion-ratchet model should be extended to incorporate a component of DNA elasticity. In this model, DNA-bound ParA–ATP complexes can harness the elastic dynamics of the chromosome to relay the partition complex over a long distance from one DNA location to another [31] (figure 2*c*). Similarly, it has also been proposed that partition complexes can also hitchhike from one high-density DNA region to another on the chromosome to move the ParB-bound DNA progressively [37] (figure 2*c*). High-density DNA regions have been observed in *B. subtilis* and *Escherichia coli* by super-resolution microscopy and may represent highly compacted domains of the chromosomes [37,101]. The preferred association of ParA–ATP with high-density DNA

regions, via its non-specific DNA-binding activity, might create the required directional bias in the movement of the ParABS complex (figure 2*c*).

The diffusion-ratchet model emphasizes the crucial role of ParB in stimulating the ATPase activity of ParA to create the ParA–ATP gradient. However, an alternative view on the ATPase-stimulating role of ParB, at least for the F-plasmid ParAB system (SopAB) suggested that the stimulation of $ParA_F$ ATPase activity mainly serves to spatially separate F-plasmid clusters following replication and to prevent them from re-forming later [102]. The directional movement of replicated F plasmids might depend on a basal ATPase activity of $ParA_F$ but does not need further stimulation by $ParB_F$ [102]. Finally, the recent discovery of CTP as a cofactor of both plasmid- and chromosome-encoded ParB raises many important questions. Does ParB–CTP further stimulate the ATPase activity of ParA, and conversely, does ParA accelerate the CTP hydrolysis rate of ParB? Early evidence suggested that CTP can modulate ParA–ParB interaction; mutations at the CTP-binding pocket of a ParB-like protein PadC were shown to impair PadC–ParA binding *in vitro* (i.e. ParA preferentially binds to PadC–CTP, rather than to apo-PadC, and gave rise to aberrant ParA localization patterns *in vivo* [51]). Future works, especially with the canonical ParABS system, will provide important insights to refine current models for the ParA-directed DNA segregation.

4. The ParB-DNA and SMC coordinate chromosome segregation with chromosome organization

In addition to its role in DNA segregation, ParB also participates in other biological processes such as chromosome organization, nucleoid occlusion, regulation of DNA replication initiation and regulation of gene expression [16,24,40,41,100,103–113]. The wide range of ParB-interacting partners reflects (i) the central role of the ParB-DNA nucleoprotein as a hub to couple chromosome segregation with other biological processes and (ii) the capacity of ParB to evolve additional functions. For a further discussion, we refer the reader to recent reviews [114,115]. In this section, we instead focus on the interaction between ParB and the SMC complex that is directly relevant to the segregation of the origin-proximal region of the chromosome.

A canonical bacterial SMC is composed of an ATPase domain (the head), a dimerization domain (the hinge) and an extended antiparallel coiled-coil region in the middle [116] (figure 3*a*). Two SMC monomers homodimerize together with the accessory proteins (ScpA and ScpB) to form a ring-like protein complex that can bring distal DNA segments close together spatially to organize the chromosome [116–118] (figure 3*a*). This entrapment of DNA has been shown for *B. subtilis* SMC [119] and for eukaryotic SMC homologs such as cohesin and condensin [120–123]. Application of chromosome conformation capture assays (Hi-C/3C-seq) to cells from a range of bacterial species lacking SMC have revealed a reduced interaction between opposite arms of the chromosome, suggesting that SMC entraps and tethers the two chromosome arms together [43,44,101,124–126] (figure 3*b*). SMC is recruited onto the chromosome by ParB at the origin-proximal *parS* sites [16,40–42,44] (figure 3*c*). After loading, SMC redistributes directionally away from *parS* towards the replication terminus (*ter*) while maintaining the tethers between the *parS*-proximal regions of the chromosome arms [42,125] (figure 3*c*). Given that *parS* sites are often found near the origin of replication, *parS*-loaded SMCs preferably condense newly replicated DNA to package them into individual entities and away from each other (figure 3*b*). This DNA-unlinking activity is independent of topoisomerase IV, at least in *B. subtilis*, and might help to prevent catenation between replicated chromosomes at the replication fork or promote their resolution behind the fork [45,46]. If replicated chromosomes are not resolved, their entanglement might hinder movement of individual chromosomes to opposite cell poles by the ParABS system. In *C. crescentus*, segregation of origin-proximal DNA occurs in two steps; the duplicated origins are released from the pole and separate slightly from one another first before one of the origins is moved unidirectionally by ParABS to the opposite cell pole [127]. While the initial separation does not require ParA [127,128], it might be facilitated by the DNA-unlinking activity of SMC.

Precisely how SMC translocates on the chromosome is not yet clear; several models have been proposed, and we refer the reader to a recent review [129] for an in-depth discussion. How ParB loads SMC onto the chromosome is also not fully understood; the weak and transient interaction between ParB and SMC has made efforts to study their interactions by traditional methodologies (such as bacterial two-hybrid or co-immunoprecipitation) difficult [41,42,44]. However, it was suggested that DNA-bound ParB probably interacts directly with SMC to recruit it to the DNA [40]. Indeed, a ParB-interacting area has been identified in the neck region in between the ATPase head domain and the coiled coil of *B. subtilis* SMC [130], while mutations that eliminate SMC recruitment have been mapped onto the N-terminal domain of *B. subtilis* ParB [40,43]. Those same mutations also impair the ability of ParB to assemble into a higher-order nucleoprotein complex, hence it is tempting to speculate that either (i) a high local concentration of DNA-bound ParB is necessary to recruit sufficient SMC molecules or (ii) the DNA-bridging/clamping activity of ParB ensures SMC entraps DNA correctly at the loading step. Future experiments, particularly a cell-free reconstitution of a ParB-dependent SMC recruitment and translocation, will provide further insights into the mechanism of actions of bacterial SMC and its contribution to chromosome segregation.

5. The evolution of the ParABS system and bacterial chromosome segregation

Research in multiple model species and an ever-increasing number of sequenced bacterial genomes has highlighted variations in the mechanism for bacterial chromosome segregation. Approximately 25% of bacterial species lack ParABS homologs entirely [28] and thus probably employ other systems to facilitate their chromosome segregation [131–133]. In some species, for example, *Streptococcus pneumoniae* or *Staphylococcus aureus*, only ParB–*parS* and SMC are present while a ParA homolog is missing [28]. Even in species with the canonical ParABS system, there exists a wide variation in the number of *parS* sites; for example, *Xanthomonas campestris* has a single *parS* site while *Streptomyces coelicolor* and *Listeria innocua* accumulated up to 20–23 *parS* sites near the origin of replication

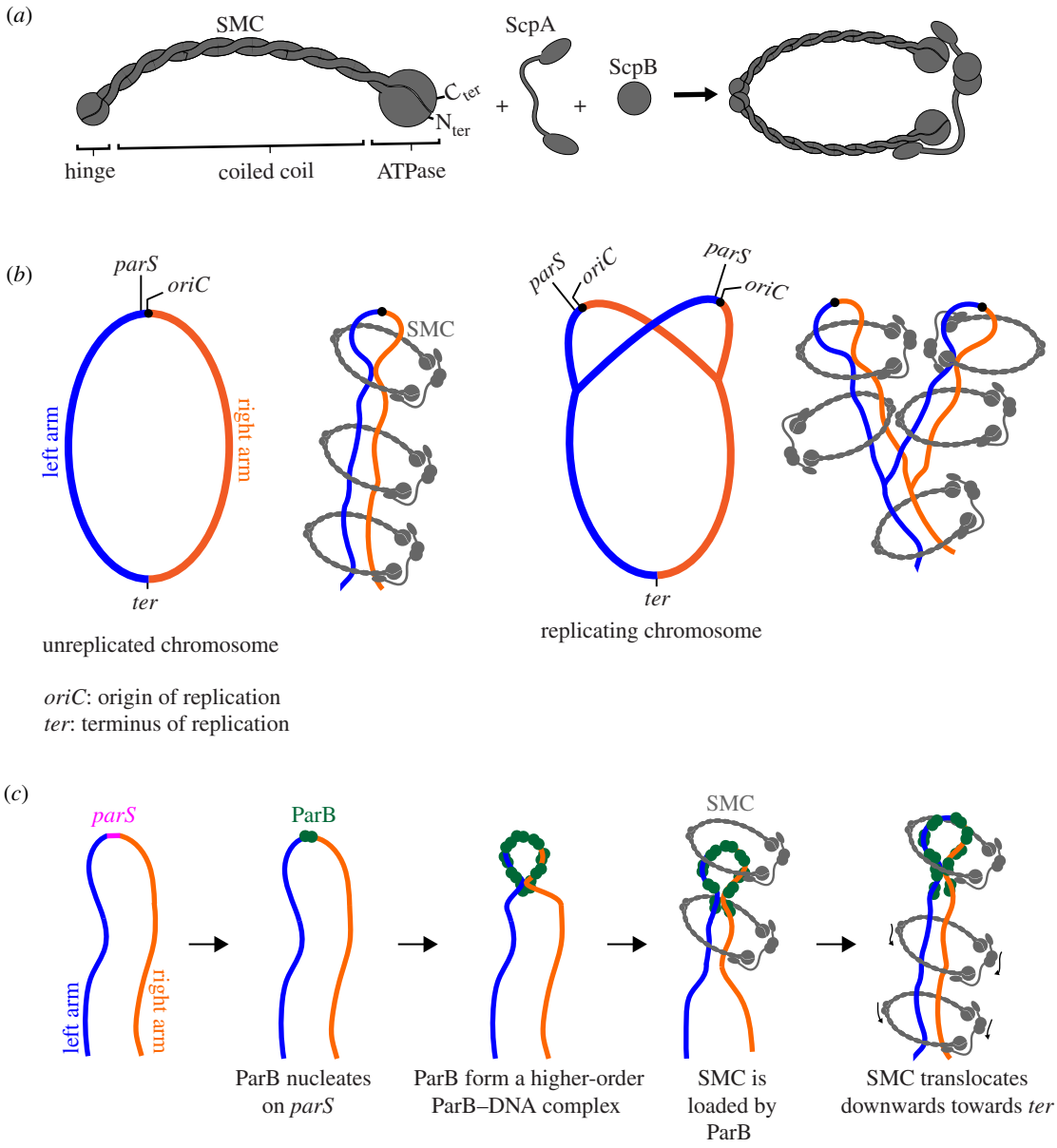

Figure 3. The ParB–DNA nucleoprotein complex recruits SMC to coordinate chromosome segregation and chromosome organization. (*a*) Components of the bacterial SMC complex. (*b*) SMC (grey) tethers the two arms (blue and orange) of a circular chromosome together. An SMC–ScpA–ScpB complex can either hold both the left and the right arm of the chromosome within its lumen or two SMC complexes, each encircles one chromosome arm, can handcuff to tether both chromosome arms together. For simplicity, only SMCs entrapping both chromosome arms are shown. SMC probably packages sister chromosomes into individual entities and away from each other, thus minimizing DNA entanglement between replicating chromosomes. (*c*) A schematic model of how SMC is loaded at *parS* by ParB and translocates on the chromosome towards the replication terminus (*ter*). For simplicity, alternative conformations of SMC (ring or rod) are not illustrated; the SMC complex is shown as a generic ring that entraps DNA. Schematic pictures are not drawn to scale.

[28,134]. Why is the number of *parS* sites variable when a single *parS* site is often sufficient for chromosome segregation [12,13,62]? How does this variation in the number of *parS* sites impact chromosome segregation in different bacterial species in their niches? Why do *parS* sites position closely on the genome and what drives their clustering over evolutionary time? For the last question, a transposon-based saturated insertion of a *parS* site on the *Pseudomonas aeruginosa* and *C. crescentus* chromosome offered some insights; it was discovered that the insertion of a *de novo* or a second *parS* site is only tolerable in approximately 600 kb region surrounding the native *parS* locus or the origin of replication without severely affecting cell fitness [13,47]. These results suggest a self-reinforcing mechanism for the expansion of the bacterial centromere region by restricting the multiplication of *parS* to a narrow region near the original site.

Another noteworthy example of the evolution of the ParABS system is the gene duplication and neo-functionalization event that generated a nucleoid occlusion factor (Noc) in Firmicutes [135–139]. Noc, a ParB-like protein, plays a role in preserving the integrity of the chromosome; it does so by preventing the cell division machinery from assembling in the vicinity of the segregating chromosome, which might be otherwise guillotined, thereby damaging the DNA [136,140,141]. An amphipathic helix is present at the N-terminus of Noc instead of the ParA–ATPase-stimulating peptide commonly found in ParB [141]. Mutations that perturbed the amphipathicity of this helix also eliminated the nucleoid occlusion function, while replacing the native helix with one from the hepatitis C virus protein NS4B restored the nucleoid occlusion activity [141,142]. A mutational event that resulted in the grafting of an amphipathic helix might

have been the evolutionary mechanism that once granted a novel function to a ParB protein [137,141]. Furthermore, in contrast to ParB, Noc does not bind *parS* but recognizes a different DNA-binding sequence called *NBS* (Noc-Binding Site) [140]. *NBS* differs from *parS* by only two bases but Noc and ParB recognize and bind them with exquisite specificity [140,143]. X-ray crystallography and systematic scanning mutagenesis identified a minimal set of just four amino acids that mediate ParB-*parS*/Noc-*NBS* binding specificity [143]. Deep mutational scanning of these four specificity residues enabled an *in silico* reconstitution of possible evolutionary paths that reprogramed DNA-binding specificity from *parS* to *NBS* [143]. A small number of required mutations and the large number of mutational paths to reprogram DNA-binding specificity illustrates the evolvability of the ParABS system.

The existence of various ParA homologs with diverse functions is also intriguing. In *Rhodobacter sphaeroides*, an orphan ParA-like protein (PpfA) uses non-specific nucleoid binding to separate cytoplasmic clusters of chemotaxis proteins [144]. Similar to the canonical ParABS system, the ATPase activity of PpfA is modulated by the N terminus of a ParB analog (TlpT) [144]. In *C. crescentus*, another ParA homolog (MipZ) coordinates chromosome segregation with cell division by directly interfering with FtsZ polymerization [109]. MipZ binds DNA non-specifically and also interacts with ParB to create a bipolar protein gradient in the cells that restricts FtsZ ring formation to the mid cell, where the concentration of MipZ is lowest [95,109,145]. In *V. cholerae*, three ParA-like ATPases (ParA1, FlhG and ParC) interact with a polar transmembrane protein HubP to control polar localization of the chromosome origin, the chemotactic machinery and the flagellum [111]. These examples illustrate how diverse functions in biology can evolve from a general mechanism and are therefore interesting from both evolutionary and mechanistic standpoints.

Last but not least, a DNA segregation system that combines bacterial ParAB-like and eukaryotic histone-like components has been identified in the archaea *Sulfolobus* [146,147]. This system consists of an ATPase ParA, an atypical ParB adaptor and a novel centromere-binding protein AspA. The N-terminal domain of the archaeal ParB is similar to the bacterial ParB NTD; however, its C-terminal domain resembles an eukaryotic histone protein CenpA [146]. A long amino acid linker that connects the two domains of the archaeal ParB interacts with ParA, while its N-terminal domain binds AspA. AspA binds the centromere, thereby serves as a physical link between the archaeal ParA–ParB and the segregating DNA [146]. The hybrid nature of the archaeal DNA segregation machinery demonstrates how evolution has diversified DNA segregation systems, possibly to adapt to the specific needs of each organism, while keeping the general mechanism conserved across the three domains of life.

6. Final perspectives

Over 35 years of research has led to tremendous progress in understanding the molecular mechanism of the ParABS system and its roles in DNA segregation. Nevertheless, many mechanistic details are missing or only now starting to emerge. The recent discovery of cytidine triphosphate as a cofactor of ParB illustrates this point perfectly. Research with bacterial systems has already benefited tremendously from the recent explosion of interest and technological advances from the eukaryotic chromosome field. We predict that novel high–throughput sequencing-based methodologies, single-molecule imaging, single-molecule biophysics, and traditional biochemistry and genetics will continue to provide further insights into the mechanisms of chromosome segregation in bacteria. Finally, various orthogonal ParB–*parS* systems have been exploited to label and image DNA loci *in vivo*, in both bacteria and eukaryotes [148–151]. Recent studies have also expanded the utilization of the ParABS system in synthetic biology, for example, as part of a genetic circuit to enable asymmetric cell division in *E. coli* [152,153]. Such exciting developments will benefit from ongoing research into the mechanistic details of the ParABS system and its evolvability to acquire new functions.

Data accessibility. This article does not contain any additional data.

Authors' contributions. Both authors have contributed to the writing of the manuscript.

Competing interests. We declare we have no competing interests.

Funding. This study was funded by the Royal Society University Research Fellowship no. (UF140053) to T.B.K.L. and the Royal Society Research grant no. (RG150448) to A.S.B.J and T.B.K.L.

References

1. Abeles AL, Friedman SA, Austin SJ. 1985 Partition of unit-copy miniplasmids to daughter cells. III. The DNA sequence and functional organization of the P1 partition region. *J. Mol. Biol.* **185**, 261–272. (doi:10.1016/0022-2836(85)90402-4)
2. Austin S, Abeles A. 1983 Partition of unit-copy miniplasmids to daughter cells. II. The partition region of miniplasmid P1 encodes an essential protein and a centromere-like site at which it acts. *J. Mol. Biol.* **169**, 373–387. (doi:10.1016/s0022-2836(83)80056-4)
3. Austin S, Abeles A. 1983 Partition of unit-copy miniplasmids to daughter cells. I. P1 and F miniplasmids contain discrete, interchangeable sequences sufficient to promote equipartition. *J. Mol. Biol.* **169**, 353–372. (doi:10.1016/s0022-2836(83)80055-2)
4. Mori H, Kondo A, Ohshima A, Ogura T, Hiraga S. 1986 Structure and function of the F plasmid genes essential for partitioning. *J. Mol. Biol.* **192**, 1–15. (doi:10.1016/0022-2836(86)90459-6)
5. Ireton K, Gunther NW, Grossman AD. 1994 spo0 J is required for normal chromosome segregation as well as the initiation of sporulation in *Bacillus subtilis*. *J. Bacteriol.* **176**, 5320–5329. (doi:10.1128/jb.176.17.5320-5329.1994)
6. Mysliwiec TH, Errington J, Vaidya AB, Bramucci MG. 1991 The *Bacillus subtilis* spo0 J gene: evidence for involvement in catabolite repression of sporulation. *J. Bacteriol.* **173**, 1911–1919. (doi:10.1128/jb.173.6.1911-1919.1991)
7. Lin DC, Grossman AD. 1998 Identification and characterization of a bacterial chromosome partitioning site. *Cell* **92**, 675–685. (doi:10.1016/s0092-8674(00)81135-6)
8. Mohl DA, Easter J, Gober JW. 2001 The chromosome partitioning protein, ParB, is required for cytokinesis in *Caulobacter crescentus*. *Mol. Microbiol.* **42**, 741–755. (doi:10.1046/j.1365-2958.2001.02643.x)
9. Jung A, Raßbach A, Pulpetta RL, van Teeseling MCF, Heinrich K, Sobetzko P, Serrania J, Becker A, Thanbichler M. 2019 Two-step chromosome segregation in the stalked budding bacterium

Hyphomonas neptunium. *Nat. Commun.* **10**, 3290. (doi:10.1038/s41467-019-11242-5)

10. Iniesta AA. 2014 ParABS system in chromosome partitioning in the bacterium *Myxococcus xanthus*. *PLoS ONE* **9**, e86897. (doi:10.1371/journal.pone.0086897)
11. Harms A, Treuner-Lange A, Schumacher D, Sogaard-Andersen L. 2013 Tracking of chromosome and replisome dynamics in *Myxococcus xanthus* reveals a novel chromosome arrangement. *PLoS Genet* **9**, e1003802. (doi:10.1371/journal.pgen.1003802)
12. Jecz P, Bartosik AA, Glabski K, Jagura-Burdzy G. 2015 A single parS sequence from the cluster of four sites closest to oriC is necessary and sufficient for proper chromosome segregation in *Pseudomonas aeruginosa*. *PLoS ONE* **10**, e0120867. (doi:10.1371/journal.pone.0120867)
13. Lagage V, Boccard F, Vallet-Gely I. 2016 Regional control of chromosome segregation in *Pseudomonas aeruginosa*. *PLoS Genetics* **12**, e1006428. (doi:10.1371/journal.pgen.1006428)
14. Yu W, Herbert S, Graumann PL, Götz F. 2010 Contribution of SMC (Structural Maintenance of Chromosomes) and SpoIIIE to chromosome segregation in staphylococci. *J. Bacteriol.* **192**, 4067–4073. (doi:10.1128/JB.00010-10)
15. Lee PS, Grossman AD. 2006 The chromosome partitioning proteins Soj (ParA) and Spo0 J (ParB) contribute to accurate chromosome partitioning, separation of replicated sister origins, and regulation of replication initiation in *Bacillus subtilis*. *Mol. Microbiol.* **60**, 853–869. (doi:10.1111/j.1365-2958.2006.05140.x)
16. Minnen A, Attaiech L, Thon M, Gruber S, Veening J-W. 2011 SMC is recruited to oriC by ParB and promotes chromosome segregation in *Streptococcus pneumoniae*. *Mol. Microbiol.* **81**, 676–688. (doi:10.1111/j.1365-2958.2011.07722.x)
17. Donovan C, Schwaiger A, Krämer R, Bramkamp M. 2010 Subcellular localization and characterization of the ParAB system from *Corynebacterium glutamicum*. *J. Bacteriol.* **192**, 3441–3451. (doi:10.1128/JB.00214-10)
18. Santi I, McKinney JD. 2015 Chromosome organization and replisome dynamics in *Mycobacterium smegmatis*. *mBio* **6**, e01999-14. (doi:10.1128/mBio.01999-14)
19. Donczew M, Mackiewicz P, Wróbel A, Flärdh K, Zakrzewska-Czerwińska J, Jakimowicz D. 2016 ParA and ParB coordinate chromosome segregation with cell elongation and division during *Streptomyces sporulation*. *Open Biol.* **6**, 150263. (doi:10.1098/rsob.150263)
20. Du W-L, Dubarry N, Passot FM, Kamgoué A, Murray H, Lane D, Pasta F. 2016 Orderly Replication and Segregation of the Four Replicons of *Burkholderia cenocepacia* J2315. *PLoS Genet.* **12**, e1006172. (doi:10.1371/journal.pgen.1006172)
21. Bartosik AA, Mierzejewska J, Thomas CM, Jagura-Burdzy G. 2009 ParB deficiency in Pseudomonas aeruginosa destabilizes the partner protein ParA and affects a variety of physiological parameters. *Microbiology (Reading, Engl.)* **155**, 1080–1092. (doi:10.1099/mic.0.024661-0)
22. Lewis RA, Bignell CR, Zeng W, Jones AC, Thomas CM. 2002 Chromosome loss from par mutants of *Pseudomonas putida* depends on growth medium and phase of growth. *Microbiology (Reading, Engl.)* **148**, 537–548. (doi:10.1099/00221287-148-2-537)
23. Yamaichi Y, Fogel MA, McLeod SM, Hui MP, Waldor MK. 2007 Distinct centromere-like parS sites on the two chromosomes of *Vibrio* spp. *J. Bacteriol.* **189**, 5314–5324. (doi:10.1128/JB.00416-07)
24. Kadoya R, Baek JH, Sarker A, Chattoraj DK. 2011 Participation of chromosome segregation protein ParAI of *Vibrio cholerae* in chromosome replication. *J. Bacteriol.* **193**, 1504–1514. (doi:10.1128/JB.01067-10)
25. Charaka VK, Misra HS. 2012 Functional characterization of the role of the chromosome I partitioning system in genome segregation in *Deinococcus radiodurans*. *J. Bacteriol.* **194**, 5739–5748. (doi:10.1128/JB.00610-12)
26. Li H, Angelov A, Pham VTT, Leis B, Liebl W. 2015 Characterization of chromosomal and megaplasmid partitioning loci in *Thermus thermophilus* HB27. *BMC Genomics* **16**, 317. (doi:10.1186/s12864-015-1523-3)
27. Li H. 2019 Random chromosome partitioning in the polyploid bacterium *Thermus thermophilus* HB27. *G3 (Bethesda)* **9**, 1249–1261. (doi:10.1534/g3.119.400086)
28. Livny J, Yamaichi Y, Waldor MK. 2007 Distribution of centromere-like parS sites in bacteria: insights from comparative genomics. *J. Bacteriol.* **189**, 8693–8703. (doi:10.1128/JB.01239-07)
29. Toro E, Hong S-H, McAdams HH, Shapiro L. 2008 *Caulobacter* requires a dedicated mechanism to initiate chromosome segregation. *PNAS* **105**, 15 435–15 440. (doi:10.1073/pnas.0807448105)
30. Funnell BE. 2016 ParB partition proteins: complex formation and spreading at bacterial and plasmid centromeres. *Front. Mol. Biosci.* **3**, 44. (doi:10.3389/fmolb.2016.00044)
31. Lim HC, Surovtsev IV, Beltran BG, Huang F, Bewersdorf J, Jacobs-Wagner C. 2014 Evidence for a DNA-relay mechanism in ParABS-mediated chromosome segregation. *Elife* **3**, e02758. (doi:10.7554/eLife.02758)
32. Mohl DA, Gober JW. 1997 Cell cycle-dependent polar localization of chromosome partitioning proteins in *Caulobacter crescentus*. *Cell* **88**, 675–684. (doi:10.1016/s0092-8674(00)81910-8)
33. Hwang LC, Vecchiarelli AG, Han Y-W, Mizuuchi M, Harada Y, Funnell BE, Mizuuchi K. 2013 ParA-mediated plasmid partition driven by protein pattern self-organization. *The EMBO Journal* **32**, 1238–1249. (doi:10.1038/emboj.2013.34)
34. Leonard TA, Butler PJ, Löwe J. 2005 Bacterial chromosome segregation: structure and DNA binding of the Soj dimer—a conserved biological switch. *EMBO J.* **24**, 270–282. (doi:10.1038/sj.emboj.7600530)
35. Vecchiarelli AG, Neuman KC, Mizuuchi K. 2014 A propagating ATPase gradient drives transport of surface-confined cellular cargo. *PNAS* **111**, 4880–4885. (doi:10.1073/pnas.1401025111)
36. Vecchiarelli AG, Hwang LC, Mizuuchi K. 2013 Cell-free study of F plasmid partition provides evidence for cargo transport by a diffusion-ratchet mechanism. *Proc. Natl Acad. Sci. USA* **110**, E1390-E1397. (doi:10.1073/pnas.1302745110)
37. Gall AL *et al.* 2016 Bacterial partition complexes segregate within the volume of the nucleoid. *Nat. Commun.* **7**, 1–10. (doi:10.1038/ncomms12107)
38. Vecchiarelli AG, Han Y-W, Tan X, Mizuuchi M, Ghirlando R, Biertümpfel C, Funnell BE, Mizuuchi K. 2010 ATP control of dynamic P1 ParA–DNA interactions: a key role for the nucleoid in plasmid partition. *Mol. Microbiol.* **78**, 78–91. (doi:10.1111/j.1365-2958.2010.07314.x)
39. Badrinarayanan A, Le TBK, Laub MT. 2015 Bacterial chromosome organization and segregation. *Annu. Rev. Cell Dev. Biol.* **31**, 171–199. (doi:10.1146/annurev-cellbio-100814-125211)
40. Gruber S, Errington J. 2009 Recruitment of condensin to replication origin regions by ParB/SpoOJ promotes chromosome segregation in *B. subtilis*. *Cell* **137**, 685–696. (doi:10.1016/j.cell.2009.02.035)
41. Sullivan NL, Marquis KA, Rudner DZ. 2009 Recruitment of SMC by ParB-parS organizes the origin region and promotes efficient chromosome segregation. *Cell* **137**, 697–707. (doi:10.1016/j.cell.2009.04.044)
42. Tran NT, Laub MT, Le TBK. 2017 SMC progressively aligns chromosomal arms in *Caulobacter crescentus* but is antagonized by convergent transcription. *Cell Rep.* **20**, 2057–2071. (doi:10.1016/j.celrep.2017.08.026)
43. Wang X, Le TBK, Lajoie BR, Dekker J, Laub MT, Rudner DZ. 2015 Condensin promotes the juxtaposition of DNA flanking its loading site in *Bacillus subtilis*. *Genes Dev.* **29**, 1661–1675. (doi:10.1101/gad.265876.115)
44. Böhm K, Giacomelli G, Schmidt A, Imhof A, Koszul R, Marbouty M, Bramkamp M. 2020 Chromosome organization by a conserved condensin-ParB system in the actinobacterium *Corynebacterium glutamicum*. *Nat. Commun.* **11**, 1485. (doi:10.1038/s41467-020-15238-4)
45. Wang X, Tang OW, Riley EP, Rudner DZ. 2014 The SMC condensin complex is required for origin segregation in *Bacillus subtilis*. *Curr. Biol.* **24**, 287–292. (doi:10.1016/j.cub.2013.11.050)
46. Gruber S, Veening J-W, Bach J, Blettinger M, Bramkamp M, Errington J. 2014 Interlinked sister chromosomes arise in the absence of condensin during fast replication in *B. subtilis*. *Curr. Biol.* **24**, 293–298. (doi:10.1016/j.cub.2013.12.049)
47. Tran NT, Stevenson CE, Som NF, Thanapipatsiri A, Jalal ASB, Le TBK. 2018 Permissive zones for the centromere-binding protein ParB on the *Caulobacter crescentus* chromosome. *Nucleic Acids Res.* **46**, 1196–1209. (doi:10.1093/nar/gkx1192)
48. Breier AM, Grossman AD. 2007 Whole-genome analysis of the chromosome partitioning and sporulation protein Spo0 J (ParB) reveals spreading

and origin-distal sites on the *Bacillus subtilis* chromosome. *Mol. Microbiol.* **64**, 703–718. (doi:10.1111/j.1365-2958.2007.05690.x)

49. Song D, Rodrigues K, Graham TGW, Loparo JJ. 2017 A network of cis and trans interactions is required for ParB spreading. *Nucleic Acids Res.* **45**, 7106–7117. (doi:10.1093/nar/gkx271)
50. Kusiak M, Gapczyńska A, Płochocka D, Thomas CM, Jagura-Burdzy G. 2011 Binding and spreading of ParB on DNA determine its biological function in *Pseudomonas aeruginosa*. *J. Bacteriol.* **193**, 3342–3355. (doi:10.1128/JB.00328-11)
51. Osorio-Valeriano M, Altegoer F, Steinchen W, Urban S, Liu Y, Bange G, Thanbichler M. 2019 ParB-type DNA segregation proteins are CTP-dependent molecular switches. *Cell* **179**, 1512–1524. (doi:10.1016/j.cell.2019.11.015)
52. Soh Y-M *et al.* 2019 Self-organization of parS centromeres by the ParB CTP hydrolase. *Science* **366**, 1129–1133. (doi:10.1126/science.aay3965)
53. Fisher GL *et al.* 2017 The structural basis for dynamic DNA binding and bridging interactions which condense the bacterial centromere. *Elife* **6**, e28086. (doi:10.7554/eLife.28086)
54. Chen B-W, Lin M-H, Chu C-H, Hsu C-E, Sun Y-J. 2015 Insights into ParB spreading from the complex structure of Spo0 J and parS. *Proc. Natl. Acad. Sci. USA* **112**, 6613–6618. (doi:10.1073/pnas.1421927112)
55. Jalal ASB, Pastrana CL, Tran NT, Stevenson CE, Lawson DM, Moreno-Herrero F, Le TBK. 2019 Structural and biochemical analyses of *Caulobacter crescentus* ParB reveal the role of its N-terminal domain in chromosome segregation. *bioRxiv*, 816959. (doi:10.1101/816959)
56. Leonard TA, Butler PJG, Löwe J. 2004 Structural analysis of the chromosome segregation protein Spo0 J from *Thermus thermophilus*. *Mol. Microbiol.* **53**, 419–432. (doi:10.1111/j.1365-2958.2004.04133.x)
57. Schumacher MA, Piro KM, Xu W. 2010 Insight into F plasmid DNA segregation revealed by structures of SopB and SopB–DNA complexes. *Nucleic Acids Res* **38**, 4514–4526. (doi:10.1093/nar/gkq161)
58. Schumacher MA, Funnell BE. 2005 Structures of ParB bound to DNA reveal mechanism of partition complex formation. *Nature* **438**, 516–519. (doi:10.1038/nature04149)
59. Lynch AS, Wang JC. 1995 SopB protein-mediated silencing of genes linked to the sopC locus of *Escherichia coli* F plasmid. *PNAS* **92**, 1896–1900. (doi:10.1073/pnas.92.6.1896)
60. Rodionov O, Lobocka M, Yarmolinsky M. 1999 Silencing of genes flanking the P1 plasmid centromere. *Science* **283**, 546–549. (doi:10.1126/science.283.5401.546)
61. Murray H, Ferreira H, Errington J. 2006 The bacterial chromosome segregation protein Spo0 J spreads along DNA from parS nucleation sites. *Mol. Microbiol.* **61**, 1352–1361. (doi:10.1111/j.1365-2958.2006.05316.x)
62. Graham TGW, Wang X, Song D, Etson CM, van Oijen AM, Rudner DZ, Loparo JJ. 2014 ParB spreading requires DNA bridging. *Genes Dev.* **28**, 1228–1238. (doi:10.1101/gad.242206.114)
63. Kawalek A, Bartosik AA, Glabski K, Jagura-Burdzy G. 2018 Pseudomonas aeruginosa partitioning protein ParB acts as a nucleoid-associated protein binding to multiple copies of a parS-related motif. *Nucleic Acids Res.* **46**, 4592–4606. (doi:10.1093/nar/gky257)
64. Bingle LEH, Macartney DP, Fantozzi A, Manzoor SE, Thomas CM. 2005 Flexibility in repression and cooperativity by KorB of broad host range IncP-1 plasmid RK2. *J. Mol. Biol.* **349**, 302–316. (doi:10.1016/j.jmb.2005.03.062)
65. Taylor JA, Pastrana CL, Butterer A, Pernstich C, Gwynn EJ, Sobott F, Moreno-Herrero F, Dillingham MS. 2015 Specific and non-specific interactions of ParB with DNA: implications for chromosome segregation. *Nucleic Acids Res.* **43**, 719–731. (doi:10.1093/nar/gku1295)
66. Madariaga-Marcos J, Pastrana CL, Fisher GL, Dillingham MS, Moreno-Herrero F. 2019 ParB dynamics and the critical role of the CTD in DNA condensation unveiled by combined force-fluorescence measurements. *Elife* **8**, e43812. (doi:10.7554/eLife.43812)
67. Broedersz CP, Wang X, Meir Y, Loparo JJ, Rudner DZ, Wingreen NS. 2014 Condensation and localization of the partitioning protein ParB on the bacterial chromosome. *PNAS* **111**, 8809–8814. (doi:10.1073/pnas.1402529111)
68. Erdmann N, Petroff T, Funnell BE. 1999 Intracellular localization of P1 ParB protein depends on ParA and parS. *Proc. Natl Acad. Sci. USA* **96**, 14 905–14 910. (doi:10.1073/pnas.96.26.14905)
69. Sanchez A, Cattoni DI, Walter J-C, Rech J, Parmeggiani A, Nollmann M, Bouet J-Y. 2015 Stochastic self-assembly of ParB proteins builds the bacterial DNA segregation apparatus. *Cell Syst.* **1**, 163–173. (doi:10.1016/j.cels.2015.07.013)
70. Debaugny RE *et al.* 2018 A conserved mechanism drives partition complex assembly on bacterial chromosomes and plasmids. *Mol. Syst. Biol.* **14**, e8516. (doi:10.15252/msb.20188516)
71. Jalal AS, Tran NT, Le TB. 2020 ParB spreading on DNA requires cytidine triphosphate in vitro. *eLife* **9**, e53515. (doi:10.7554/eLife.53515)
72. Buckstein MH, He J, Rubin H. 2008 Characterization of nucleotide pools as a function of physiological state in *Escherichia coli*. *J. Bacteriol.* **190**, 718–726. (doi:10.1128/JB.01020-07)
73. Britos L, Abeliuk E, Taverner T, Lipton M, McAdams H, Shapiro L. 2011 Regulatory response to carbon starvation in *Caulobacter crescentus*. *PLoS ONE* **6**, e18179. (doi:10.1371/journal.pone.0018179)
74. Whiteley AT *et al.* 2019 Bacterial cGAS-like enzymes synthesize diverse nucleotide signals. *Nature* **567**, 194–199. (doi:10.1038/s41586-019-0953-5)
75. Koonin EV. 1993 A superfamily of ATPases with diverse functions containing either classical or deviant ATP-binding motif. *J. Mol. Biol.* **229**, 1165–1174. (doi:10.1006/jmbi.1993.1115)
76. Ptacin JL, Lee SF, Garner EC, Toro E, Eckart M, Comolli LR, Moerner WE, Shapiro L. 2010 A spindle-like apparatus guides bacterial chromosome segregation. *Nat. Cell Biol.* **12**, 791–798. (doi:10.1038/ncb2083)
77. Ebersbach G, Gerdes K. 2004 Bacterial mitosis: partitioning protein ParA oscillates in spiral-shaped structures and positions plasmids at mid-cell. *Mol. Microbiol.* **52**, 385–398. (doi:10.1111/j.1365-2958.2004.04002.x)
78. Adachi S, Hori K, Hiraga S. 2006 Subcellular positioning of F plasmid mediated by dynamic localization of SopA and SopB. *J. Mol. Biol.* **356**, 850–863. (doi:10.1016/j.jmb.2005.11.088)
79. Ebersbach G, Ringgaard S, Møller-Jensen J, Wang Q, Sherratt DJ, Gerdes K. 2006 Regular cellular distribution of plasmids by oscillating and filament-forming ParA ATPase of plasmid pB171. *Mol. Microbiol.* **61**, 1428–1442. (doi:10.1111/j.1365-2958.2006.05322.x)
80. Fogel MA, Waldor MK. 2006 A dynamic, mitotic-like mechanism for bacterial chromosome segregation. *Genes Dev.* **20**, 3269–3282. (doi:10.1101/gad.1496506)
81. Hatano T, Yamaichi Y, Niki H. 2007 Oscillating focus of SopA associated with filamentous structure guides partitioning of F plasmid. *Mol. Microbiol.* **64**, 1198–1213. (doi:10.1111/j.1365-2958.2007.05728.x)
82. Pratto F, Cicek A, Weihofen WA, Lurz R, Saenger W, Alonso JC. 2008 Streptococcus pyogenes pSM19035 requires dynamic assembly of ATP-bound ParA and ParB on parS DNA during plasmid segregation. *Nucleic Acids Res.* **36**, 3676–3689. (doi:10.1093/nar/gkn170)
83. Ringgaard S, van Zon J, Howard M, Gerdes K. 2009 Movement and equipositioning of plasmids by ParA filament disassembly. *Proc. Natl Acad. Sci. USA* **106**, 19 369–19 374. (doi:10.1073/pnas.0908347106)
84. Gerdes K, Howard M, Szardenings F. 2010 Pushing and pulling in prokaryotic DNA segregation. *Cell* **141**, 927–942. (doi:10.1016/j.cell.2010.05.033)
85. Barillà D, Rosenberg MF, Nobbmann U, Hayes F. 2005 Bacterial DNA segregation dynamics mediated by the polymerizing protein ParF. *EMBO J.* **24**, 1453–1464. (doi:10.1038/sj.emboj.7600619)
86. Bouet J-Y, Ah-Seng Y, Benmeradi N, Lane D. 2007 Polymerization of SopA partition ATPase: regulation by DNA binding and SopB. *Mol. Microbiol.* **63**, 468–481. (doi:10.1111/j.1365-2958.2006.05537.x)
87. Havey JC, Vecchiarelli AG, Funnell BE. 2012 ATP-regulated interactions between P1 ParA, ParB and non-specific DNA that are stabilized by the plasmid partition site, parS. *Nucleic Acids Res.* **40**, 801–812. (doi:10.1093/nar/gkr747)
88. Dunham TD, Xu W, Funnell BE, Schumacher MA. 2009 Structural basis for ADP-mediated transcriptional regulation by P1 and P7 ParA. *EMBO J.* **28**, 1792–1802. (doi:10.1038/emboj.2009.120)
89. Machón C, Fothergill TJG, Barillà D, Hayes F. 2007 Promiscuous stimulation of ParF protein polymerization by heterogeneous centromere binding factors. *J. Mol. Biol.* **374**, 1–8. (doi:10.1016/j.jmb.2007.09.025)

90. Lim GE, Derman AI, Pogliano J. 2005 Bacterial DNA segregation by dynamic SopA polymers. *Proc. Natl Acad. Sci. USA* **102**, 17 658–17 663. (doi:10.1073/pnas.0507222102)
91. Hui MP, Galkin VE, Yu X, Stasiak AZ, Stasiak A, Waldor MK, Egelman EH. 2010 ParA2, a *Vibrio cholerae* chromosome partitioning protein, forms left-handed helical filaments on DNA. *Proc. Nat. Acad. Sci. USA* **107**, 4590–4595. (doi:10.1073/pnas.0913060107)
92. Vecchiarelli AG, Mizuuchi K, Funnell BE. 2012 Surfing biological surfaces: exploiting the nucleoid for partition and transport in bacteria. *Mol. Microbiol.* **86**, 513–523. (doi:10.1111/mmi.12017)
93. Hu L, Vecchiarelli AG, Mizuuchi K, Neuman KC, Liu J. 2017 Brownian ratchet mechanisms of ParA-mediated partitioning. *Plasmid* **92**, 12–16. (doi:10.1016/j.plasmid.2017.05.002)
94. Zhang H, Schumacher MA. 2017 Structures of partition protein ParA with nonspecific DNA and ParB effector reveal molecular insights into principles governing Walker-box DNA segregation. *Genes Dev.* **31**, 481–492. (doi:10.1101/gad.296319.117)
95. Corrales-Guerrero L, He B, Refes Y, Panis G, Bange G, Viollier PH, Steinchen W, Thanbichler M. 2020 Molecular architecture of the DNA-binding sites of the P-loop ATPases MipZ and ParA from *Caulobacter crescentus*. *Nucleic Acids Res.* **48**, 4769–4779. (doi:10.1093/nar/gkaa192)
96. Chu C-H, Yen C-Y, Chen B-W, Lin M-G, Wang L-H, Tang K-Z, Hsiao C-D, Sun Y-J. 2019 Crystal structures of HpSoj–DNA complexes and the nucleoid-adaptor complex formation in chromosome segregation. *Nucleic Acids Res.* **47**, 2113–2129. (doi:10.1093/nar/gky1251)
97. Barillà D, Carmelo E, Hayes F. 2007 The tail of the ParG DNA segregation protein remodels ParF polymers and enhances ATP hydrolysis via an arginine finger-like motif. *Proc. Natl Acad. Sci. USA* **104**, 1811–1816. (doi:10.1073/pnas.0607216104)
98. Volante A, Alonso JC. 2015 Molecular anatomy of ParA-ParA and ParA-ParB interactions during plasmid partitioning. *J. Biol. Chem.* **290**, 18 782–18 795. (doi:10.1074/jbc.M115.649632)
99. Ptacin JL, Gahlmann A, Bowman GR, Perez AM, von Diezmann ARS, Eckart MR, Moerner WE, Shapiro L. 2014 Bacterial scaffold directs pole-specific centromere segregation. *PNAS* **111**, E2046–E2055. (doi:10.1073/pnas.1405188111)
100. Schofield WB, Lim HC, Jacobs-Wagner C. 2010 Cell cycle coordination and regulation of bacterial chromosome segregation dynamics by polarly localized proteins. *EMBO J.* **29**, 3068–3081. (doi:10.1038/emboj.2010.207)
101. Marbouty M *et al.* 2015 Condensin- and replication-mediated bacterial chromosome folding and origin condensation revealed by Hi-C and super-resolution imaging. *Mol. Cell* **59**, 588–602. (doi:10.1016/j.molcel.2015.07.020)
102. Ah-Seng Y, Rech J, Lane D, Bouet J-Y. 2013 Defining the role of ATP hydrolysis in mitotic segregation of bacterial plasmids. *PLoS Genet.* **9**, e1003956. (doi:10.1371/journal.pgen.1003956)
103. Attaiech L, Minnen A, Kjos M, Gruber S, Veening J-W. 2015 The ParB-parS chromosome segregation system modulates competence development in *Streptococcus pneumoniae*. *mBio* **6**, e00662-15. (doi:10.1128/mBio.00662-15)
104. Murray H, Errington J. 2008 Dynamic control of the DNA replication initiation protein DnaA by Soj/ParA. *Cell* **135**, 74–84. (doi:10.1016/j.cell.2008.07.044)
105. Pióro M, Małecki T, Portas M, Magierowska I, Trojanowski D, Sherratt D, Zakrzewska-Czerwińska J, Ginda K, Jakimowicz D. 2019 Competition between DivIVA and the nucleoid for ParA binding promotes segrosome separation and modulates mycobacterial cell elongation. *Mol. Microbiol.* **111**, 204–220. (doi:10.1111/mmi.14149)
106. Nourikyan J *et al.* 2015 Autophosphorylation of the bacterial tyrosine-kinase CpsD connects capsule synthesis with the cell cycle in *Streptococcus pneumoniae*. *PLoS Genet.* **11**, e1005518. (doi:10.1371/journal.pgen.1005518)
107. Mercy C *et al.* 2019 RocS drives chromosome segregation and nucleoid protection in *Streptococcus pneumoniae*. *Nat. Microbiol.* **4**, 1661–1670. (doi:10.1038/s41564-019-0472-z)
108. Szafran M, Skut P, Ditkowski B, Ginda K, Chandra G, Zakrzewska-Czerwińska J, Jakimowicz D. 2013 Topoisomerase I (TopA) is recruited to ParB complexes and is required for proper chromosome organization during *Streptomyces coelicolor* sporulation. *J. Bacteriol.* **195**, 4445–4455. (doi:10.1128/JB.00798-13)
109. Thanbichler M, Shapiro L. 2006 MipZ, a spatial regulator coordinating chromosome segregation with cell division in *Caulobacter*. *Cell* **126**, 147–162. (doi:10.1016/j.cell.2006.05.038)
110. Maurya GK, Modi K, Misra HS. 2016 Divisome and segrosome components of *Deinococcus radiodurans* interact through cell division regulatory proteins. *Microbiology (Reading, Engl.)* **162**, 1321–1334. (doi:10.1099/mic.0.000330)
111. Yamaichi Y, Bruckner R, Ringgaard S, Möll A, Cameron DE, Briegel A, Jensen GJ, Davis BM, Waldor MK. 2012 A multidomain hub anchors the chromosome segregation and chemotactic machinery to the bacterial pole. *Genes Dev.* **26**, 2348–2360. (doi:10.1101/gad.199869.112)
112. Dubarry N, Willis CR, Ball G, Lesterlin C, Armitage JP. 2019 In vivo imaging of the segregation of the 2 chromosomes and the cell division proteins of *Rhodobacter sphaeroides* reveals an unexpected role for MipZ. *mBio* **10**, e02515-18. (doi:10.1128/mBio.02515-18)
113. Toro-Nahuelpan M, Corrales-Guerrero L, Zwiener T, Osorio-Valeriano M, Müller F-D, Plitzko JM, Bramkamp M, Thanbichler M, Schüler D. 2019 A gradient-forming MipZ protein mediating the control of cell division in the magnetotactic bacterium *Magnetospirillum gryphiswaldense*. *Mol. Microbiol.* **112**, 1423–1439. (doi:10.1111/mmi.14369)
114. Kawalek A, Wawrzyniak P, Bartosik AA, Jagura-Burdzy G. 2020 Rules and exceptions: the role of chromosomal ParB in DNA segregation and other cellular processes. *Microorganisms* **8**, 0. (doi:10.3390/microorganisms8010105)
115. Pióro M, Jakimowicz D. 2020 Chromosome segregation proteins as coordinators of cell cycle in response to environmental conditions. *Front. Microbiol.* **11**, 588. (doi:10.3389/fmicb.2020.00588)
116. Nolivos S, Sherratt D. 2014 The bacterial chromosome: architecture and action of bacterial SMC and SMC-like complexes. *FEMS Microbiol. Rev.* **38**, 380–392. (doi:10.1111/1574-6976.12045)
117. Mascarenhas J, Soppa J, Strunnikov AV, Graumann PL. 2002 Cell cycle-dependent localization of two novel prokaryotic chromosome segregation and condensation proteins in *Bacillus subtilis* that interact with SMC protein. *EMBO J.* **21**, 3108–3118. (doi:10.1093/emboj/cdf314)
118. Soppa J, Kobayashi K, Noirot-Gros M-F, Oesterhelt D, Ehrlich SD, Dervyn E, Ogasawara N, Moriya S. 2002 Discovery of two novel families of proteins that are proposed to interact with prokaryotic SMC proteins, and characterization of the *Bacillus subtilis* family members ScpA and ScpB. *Mol. Microbiol.* **45**, 59–71. (doi:10.1046/j.1365-2958.2002.03012.x)
119. Wilhelm L, Bürmann F, Minnen A, Shin H-C, Toseland CP, Oh B-H, Gruber S. 2015 SMC condensin entraps chromosomal DNA by an ATP hydrolysis dependent loading mechanism in *Bacillus subtilis*. *eLife* **4**, e06659. (doi:10.7554/eLife.06659)
120. Cuylen S, Metz J, Haering CH. 2011 Condensin structures chromosomal DNA through topological links. *Nat. Struct. Mol. Biol.* **18**, 894–901. (doi:10.1038/nsmb.2087)
121. Haering CH, Farcas A-M, Arumugam P, Metson J, Nasmyth K. 2008 The cohesin ring concatenates sister DNA molecules. *Nature* **454**, 297–301. (doi:10.1038/nature07098)
122. Murayama Y, Uhlmann F. 2014 Biochemical reconstitution of topological DNA binding by the cohesin ring. *Nature* **505**, 367–371. (doi:10.1038/nature12867)
123. Kanno T, Berta DG, Sjögren C. 2015 The Smc5/6 complex is an ATP-dependent intermolecular DNA linker. *Cell Rep* **12**, 1471–1482. (doi:10.1016/j.celrep.2015.07.048)
124. Le TB, Imakaev MV, Mirny LA, Laub MT. 2013 High-resolution mapping of the spatial organization of a bacterial chromosome. *Science* **342**, 731–734. (doi:10.1126/science.1242059)
125. Wang X, Brandão HB, Le TBK, Laub MT, Rudner DZ. 2017 Bacillus subtilis SMC complexes juxtapose chromosome arms as they travel from origin to terminus. *Science* **355**, 524–527. (doi:10.1126/science.aai8982)
126. Val M-E *et al.* 2016 A checkpoint control orchestrates the replication of the two chromosomes of *Vibrio cholerae*. *Sci. Adv.* **2**, e1501914. (doi:10.1126/sciadv.1501914)
127. Shebelut CW, Guberman JM, van Teeffelen S, Yakhnina AA, Gitai Z. 2010 *Caulobacter* chromosome segregation is an ordered multistep process. *Proc.*

Natl Acad. Sci. USA **107**, 14 194–14 198. (doi:10.1073/pnas.1005274107)

128. Taylor JA, Panis G, Viollier PH, Marczynski GT. 2017 A novel nucleoid-associated protein coordinates chromosome replication and chromosome partition. *Nucleic Acids Res.* **45**, 8916–8929. (doi:10.1093/nar/gkx596)
129. Yatskevich S, Rhodes J, Nasmyth K. 2019 Organization of chromosomal DNA by SMC complexes. *Annu. Rev. Genet.* **53**, 445–482. (doi:10.1146/annurev-genet-112618-043633)
130. Minnen A, Bürmann F, Wilhelm L, Anchimiuk A, Diebold-Durand M-L, Gruber S. 2016 Control of SMC coiled coil architecture by the ATPase heads facilitates targeting to chromosomal ParB/parS and Release onto Flanking DNA. *Cell Reports* **14**, 2003–2016. (doi:10.1016/j.celrep.2016.01.066)
131. Fekete RA, Chattoraj DK. 2005 A cis-acting sequence involved in chromosome segregation in *Escherichia coli*. *Mol. Microbiol.* **55**, 175–183. (doi:10.1111/j.1365-2958.2004.04392.x)
132. Wang X, Sherratt DJ. 2010 Independent segregation of the two arms of the *Escherichia coli* ori region requires neither RNA synthesis nor MreB dynamics. *J. Bacteriol.* **192**, 6143–6153. (doi:10.1128/JB.00861-10)
133. Yamaichi Y, Niki H. 2004 migS, a cis-acting site that affects bipolar positioning of oriC on the *Escherichia coli* chromosome. *EMBO J.* **23**, 221–233. (doi:10.1038/sj.emboj.7600028)
134. Jakimowicz D, Chater K, Zakrzewska-Czerwínska J. 2002 The ParB protein of *Streptomyces coelicolor* A3(2) recognizes a cluster of parS sequences within the origin-proximal region of the linear chromosome. *Mol. Microbiol.* **45**, 1365–1377. (doi:10.1046/j.1365-2958.2002.03102.x)
135. Sievers J, Raether B, Perego M, Errington J. 2002 Characterization of the parB-Like yyaA Gene of *Bacillus subtilis*. *J. Bacteriol.* **184**, 1102–1111. (doi:10.1128/jb.184.4.1102-1111.2002)
136. Wu LJ, Errington J. 2004 Coordination of cell division and chromosome segregation by a nucleoid occlusion protein in *Bacillus subtilis*. *Cell* **117**, 915–925. (doi:10.1016/j.cell.2004.06.002)
137. Wu LJ, Errington J. 2011 Nucleoid occlusion and bacterial cell division. *Nat. Rev. Microbiol.* **10**, 8–12. (doi:10.1038/nrmicro2671)
138. Schumacher MA. 2017 Bacterial nucleoid occlusion: multiple mechanisms for preventing chromosome bisection during cell division. *Subcell. Biochem.* **84**, 267–298. (doi:10.1007/978-3-319-53047-5_9)
139. Pang T, Wang X, Lim HC, Bernhardt TG, Rudner DZ. 2017 The nucleoid occlusion factor Noc controls DNA replication initiation in *Staphylococcus aureus*. *PLoS Genetics* **13**, e1006908. (doi:10.1371/journal.pgen.1006908)
140. Wu LJ, Ishikawa S, Kawai Y, Oshima T, Ogasawara N, Errington J. 2009 Noc protein binds to specific DNA sequences to coordinate cell division with chromosome segregation. *EMBO J.* **28**, 1940–1952. (doi:10.1038/emboj.2009.144)
141. Adams DW, Wu LJ, Errington J. 2015 Nucleoid occlusion protein Noc recruits DNA to the bacterial cell membrane. *EMBO J.* **34**, 491–501. (doi:10.15252/embj.201490177)
142. Lundin M, Monné M, Widell A, von Heijne G, Persson MAA. 2003 Topology of the membrane-associated hepatitis C virus protein NS4B. *J. Virol.* **77**, 5428–5438. (doi:10.1128/JVI.77.9.5428-5438.2003)
143. Jalal ASB, Tran NT, Stevenson CE, Tan X, Lawson DM, Le TBK. 2019 Evolving a new protein-DNA interface via sequential introduction of permissive and specificity-switching mutations. *bioRxiv*, 724823. (doi:10.1101/724823)
144. Roberts MAJ, Wadhams GH, Hadfield KA, Tickner S, Armitage JP. 2012 ParA-like protein uses nonspecific chromosomal DNA binding to partition protein complexes. *Proc. Natl Acad. Sci. USA* **109**, 6698–6703. (doi:10.1073/pnas.1114000109)
145. Kiekebusch D, Michie KA, Essen L-O, Löwe J, Thanbichler M. 2012 Localized dimerization and nucleoid binding drive gradient formation by the bacterial cell division inhibitor MipZ. *Mol. Cell* **46**, 245–259. (doi:10.1016/j.molcel.2012.03.004)
146. Schumacher MA *et al.* 2015 Structures of archaeal DNA segregation machinery reveal bacterial and eukaryotic linkages. *Science* **349**, 1120–1124. (doi:10.1126/science.aaa9046)
147. Barillà D. 2016 Driving apart and segregating genomes in Archaea. *Trends Microbiol.* **24**, 957–967. (doi:10.1016/j.tim.2016.07.001)
148. Le TB, Laub MT. 2014 New approaches to understanding the spatial organization of bacterial genomes. *Current Opin. Microbiol.* **22**, 15–21. (doi:10.1016/j.mib.2014.09.014)
149. Mariamé B, Kappler-Gratias S, Kappler M, Balor S, Gallardo F, Bystricky K. 2018 Real-time visualization and quantification of human cytomegalovirus replication in living cells using the ANCHOR DNA labeling technology. *J. Virol.* **92**, e00571-18. (doi:10.1128/JVI.00571-18)
150. Germier T *et al.* 2017 Real-time imaging of a single gene reveals transcription-initiated local confinement. *Biophys. J.* **113**, 1383–1394. (doi:10.1016/j.bpj.2017.08.014)
151. Germier T, Audibert S, Kocanova S, Lane D, Bystricky K. 2018 Real-time imaging of specific genomic loci in eukaryotic cells using the ANCHOR DNA labelling system. *Methods* **142**, 16–23. (doi:10.1016/j.ymeth.2018.04.008)
152. Molinari S, Shis DL, Bhakta SP, Chappell J, Igoshin OA, Bennett MR. 2019 A synthetic system for asymmetric cell division in *Escherichia coli*. *Nat. Chem. Biol.* **15**, 917–924. (doi:10.1038/s41589-019-0339-x)
153. Mushnikov NV, Fomicheva A, Gomelsky M, Bowman GR. 2019 Inducible asymmetric cell division and cell differentiation in a bacterium. *Nat. Chem. Biol.* **15**, 925–931. (doi:10.1038/s41589-019-0340-4)

1196–1209 *Nucleic Acids Research, 2018, Vol. 46, No. 3* *Published online 23 November 2017*
doi: 10.1093/nar/gkx1192

Permissive zones for the centromere-binding protein ParB on the *Caulobacter crescentus* chromosome

Ngat T. Tran[1,†], Clare E. Stevenson[2,†], Nicolle F. Som[1], Anyarat Thanapipatsiri[1], Adam S. B. Jalal[1] and Tung B. K. Le[1,*]

[1]Department of Molecular Microbiology, John Innes Centre, Norwich NR4 7UH, UK and [2]Department of Biological Chemistry, John Innes Centre, Norwich NR4 7UH, UK

Received August 20, 2017; Revised October 24, 2017; Editorial Decision November 13, 2017; Accepted November 16, 2017

ABSTRACT

Proper chromosome segregation is essential in all living organisms. In *Caulobacter crescentus*, the ParA–ParB–*parS* system is required for proper chromosome segregation and cell viability. The bacterial centromere-like *parS* DNA locus is the first to be segregated following chromosome replication. *parS* is bound by ParB protein, which in turn interacts with ParA to partition the ParB-*parS* nucleoprotein complex to each daughter cell. Here, we investigated the genome-wide distribution of ParB on the *Caulobacter* chromosome using a combination of *in vivo* chromatin immunoprecipitation (ChIP-seq) and *in vitro* DNA affinity purification with deep sequencing (IDAP-seq). We confirmed two previously identified *parS* sites and discovered at least three more sites that cluster ∼8 kb from the origin of replication. We showed that *Caulobacter* ParB nucleates at *parS* sites and associates non-specifically with ∼10 kb flanking DNA to form a high-order nucleoprotein complex on the left chromosomal arm. Lastly, using transposon mutagenesis coupled with deep sequencing (Tn-seq), we identified a ∼500 kb region surrounding the native *parS* cluster that is tolerable to the insertion of a second *parS* cluster without severely affecting cell viability. Our results demonstrate that the genomic distribution of *parS* sites is highly restricted and is crucial for chromosome segregation in *Caulobacter*.

INTRODUCTION

Proper chromosome segregation is essential in all living organisms if daughter cells are each to inherit a full copy of the genome. In eukaryotes, chromosome segregation during mitosis starts with sister chromosome condensation, followed by the formation of spindle fibres that attach to the kinetochore to pull sister chromatids apart. The kinetochore is the protein structure that assembles on the centromere and links each sister chromatid to microtubules polymers from the mitotic spindle. Unlike in eukaryotes, bacterial chromosome segregation happens without a dedicated spindle-like apparatus (1–3). Nevertheless, this process is highly organized and also involves protein-based components (4). The first segregated segment of the chromosome is usually proximal to the origin of replication (*ori*) (5–8). In many bacteria, this region is segregated by the tripartite ParA–ParB–*parS* partitioning system (6,9–11). *parS* is a centromere-like DNA sequence that most often locates near *ori*. ParB is a DNA-binding protein that nucleates on a *parS* sequence. ParB is also capable of binding DNA non-specifically to spread along the chromosome from its cognate *parS* nucleation site (6,12–14). Spreading was first discovered for the P1 plasmid-encoded ParB protein (15), and is subsequently found to be a general feature of many plasmid and chromosomal ParB proteins (13,16–19). Spreading of AspA, a ParB-unrelated DNA segregation protein, has also been described for the archaeal *Sulfolobus* pNOB8 plasmid (20). ParB/Spo0J in a Gram-positive *Bacillus subtilis* might also bridge distal DNA together to coalesce into a large nucleoprotein complex (the 'spreading and bridging' model) (12–14,19). Similarly, the formation of the nucleoprotein complex for the F plasmid ParB–*parS* was proposed to happen via a 'nucleation and caging' mechanism where the nucleation of ParB on *parS* creates a high local concentration of ParB, thereby caging ParB dimer-dimer together with non-specific DNA surrounding *parS* (21). Following ParB binding to *parS*, ParA, a Walker-box ATPase protein, interacts with ParB and powers the segregation of the ParB-DNA nucleoprotein complex to partition replicated chromosomes to each daughter cell (22,23).

In *Caulobacter crescentus*, the ParA–ParB–*parS* system is essential for viability (11,24). In G1-phase *Caulobacter*, *parS*/*ori* reside at one cell pole, the terminus (*ter*) is near the opposite pole, and the two chromosomal arms run orderly in parallel down the long axis of the cell (25,26). After repli-

*To whom correspondence should be addressed. Tel: +44 1603 450776; Fax: +44 1603 450778; Email: tung.le@jic.ac.uk
†These authors contributed equally to this work as first authors.

cation, the duplicated *parS* sites are released from the pole and separated slightly from one another before one *parS* site is translocated unidirectionally to the opposite cell pole. Toro *et al.* identified two *parS* sites located ∼8 kb from the *ori* on the left arm of the *Caulobacter* chromosome (8), while other works predicted six *parS* sites bioinformatically but did not report their sequences nor verify them experimentally (24,27,28). Furthermore, it is not yet known whether *Caulobacter* ParB spreads non-specifically on DNA, and if it does, how far it spreads along the chromosome from the *parS* nucleation site. Regarding the genome-wide distribution of *parS* sites, a comparative genomic study suggested that *parS* sites are not distributed randomly on bacterial chromosomes, rather they are found almost exclusively near the *ori* (7). Notably, in *Pseudomonas aeruginosa*, *parS* sites must be located within a ∼650 kb region surrounding the *ori* for the chromosome segregation to proceed correctly (5).

In this study, we used genome-wide techniques (ChIP-seq and IDAP-seq) together with *in vitro* biochemical characterization to clarify the number and locations of *parS* sites in *Caulobacter*. We show that there are at least five *parS* sites clustered closely near the *ori* of *Caulobacter* chromosome, and that ParB occupies ∼10 kb of DNA on the left arm of the chromosome. We also show that *Caulobacter* ParB nucleates on *parS* and spreads to flanking DNA independent of the location of *parS* on the chromosome. Moreover, using transposon mutagenesis coupled with deep sequencing (Tn-seq), we define a ∼500 kb region surrounding the native *parS* cluster of the *Caulobacter* chromosome that is tolerable to the insertion of a second *parS* cluster without severely affecting cell viability. Our results demonstrate that the genomic location of *parS* is highly biased and crucial for proper chromosome segregation.

MATERIALS AND METHODS

Strains, media and growth conditions

Escherichia coli and *C. crescentus* were grown in LB and PYE, respectively. When appropriate, media were supplemented with antibiotics at the following concentrations (liquid/solid media for *C. crescentus*; liquid/solid media for *Escherichia coli* [μg/ml]): carbenicilin (*E. coli* only: 50/100), chloramphenicol (1/2; 20/30), kanamycin (5/25; 30/50), spectinomycin (25/100; 50/50), oxytetracycline (1/2; 12/12) and apramycin (*E. coli* only: 25/50).

Plasmids and strains construction

All strains used are listed in Supplementary Table S1. All plasmids and primers used in strain and plasmid construction are listed in Supplementary Table S2. For details on plasmids and strains construction, see the Supplementary Materials and Methods.

Chromatin immunoprecipitation with deep sequencing (ChIP-seq)

Caulobacter cell cultures (25 ml) were grown in PYE and fixed with formaldehyde to a final concentration of 1%. Fixed cells were incubated at room temperature for 30 min, then quenched with 0.125 M glycine for 15 min at room temperature. Cells were washed three times with 1× PBS (pH 7.4) and resuspended in 1 ml of buffer 1 (20 mM K-HEPES pH 7.9, 50 mM KCl, 10% Glycerol and Roche EDTA-free protease inhibitors). Subsequently, the cell suspension was sonicated on ice using a probe-type sonicator (8 cycles, 15 s ON, 15 s OFF, at setting 8) to shear the chromatin to below 1 kb, and the cell debris was cleared by centrifugation (20 min at 13 000 rpm at 4°C).

The supernatant was then transferred to a new 2 ml tube and the buffer conditions were adjusted to 10 mM Tris–HCl pH 8, 150 mM NaCl and 0.1% NP-40. Fifty microliters of the supernatant were transferred to a separate tube for control (the INPUT fraction) and stored at –20°C. In the meantime, antibodies-coupled beads were washed off storage buffers before adding to the above supernatant. We employed α-GFP antibodies coupled to sepharose beads (Abcam, UK) for ChIP-seq of CFP-ParB, α-FLAG antibodies coupled to agarose beads (Sigma, UK) for ChIP-seq of FLAG-ParB and FLAG-YFP, and Protein A beads (Sigma, UK) for α-ParB polyclonal antibody ChIP-seq of ParB. Briefly, 25 μl of beads was washed off storage buffer by repeated centrifugation and resuspension in IPP150 buffer (10 mM Tris–HCl pH 8, 150 mM NaCl and 0.1% NP-40). Beads were then introduced to the cleared supernatant and incubated with gentle shaking at 4°C overnight. In the next day, beads were then washed five times at 4°C for 2 min each with 1 ml of IPP150 buffer, then twice at 4°C for 2 min each in 1× TE buffer (10 mM Tris–HCl pH 8 and 1 mM EDTA). Protein–DNA complexes were then eluted twice from the beads by incubating the beads first with 150 μl of the elution buffer (50 mM Tris–HCl pH 8, 10 mM EDTA and 1% SDS) at 65°C for 15 min, then with 100 μl of 1× TE buffer + 1% SDS for another 15 min at 65°C. The supernatant (the ChIP fraction) was then separated from the beads and further incubated at 65°C overnight to completely reverse crosslink. The INPUT fraction was also de-crosslinked by incubation with 200 μl of 1× TE buffer + 1% SDS at 65°C overnight. DNA from the ChIP and INPUT fraction were then purified using the PCR purification kit (Qiagen) according to the manufacturer's instruction, then eluted out in 50 μl of EB buffer (Qiagen). The purified DNA was then used directly for qPCR or being constructed into library suitable for Illumina sequencing using the NEXT Ultra library preparation kit (NEB). ChIP libraries were sequenced on the Illumina Hiseq 2500 at the Tufts University Genomics facility.

For *E. coli* ChIP-seq, cells harboring pUTC18-ParB (WT) or pUTC18-ParB (G101S) were grown in LB (50 ml) at 28°C to mid exponential phase (OD_{600} ∼ 0.4) before 0.5 mM IPTG was added for an hour. Subsequently, formaldehyde is added to a final concentration of 1% to fix the cells. All following steps are identical to ChIP-seq for *Caulobacter*, except that we used α-T18 antibody coupled to sepharose beads (Abcam, UK) to immunoprecipitate ParB–DNA complexes.

For the list of ChIP-seq datasets in this study, see Supplementary Table S3.

Generation and analysis of ChIP-seq profiles

For analysis of ChIP-seq data, Hiseq 2500 Illumina short reads (50 bp) were mapped back to the *Caulobacter* NA1000 reference genome (NCBI Reference Sequence: NC-011916.1) using Bowtie 1 (29) and the following command:

bowtie -m 1 -n 1 –best –strata -p 4 –chunkmbs 512 NA1000-bowtie –sam *.fastq > output.sam

Subsequently, the sequencing coverage at each nucleotide position was computed using BEDTools (30) using the following command:

bedtools genomecov -d -ibam output.sorted.bam -g NA1000.fna > coverage_output.txt

For analysis of *E. coli* ChIP-seq data, reference genomes were first reconstructed *in silico* by inserting the nucleotide sequence of *parS* and apramycin antibiotic resistance cassette to the *ybbD* locus of *E. coli* MG1655 genome. Afterwards, Hiseq 2500 Illumina short reads were mapped back to these reconstructed reference genomes using Bowtie 1. Sequence coverage at each nucleotide position was also computed using BEDTools. Finally, ChIP-seq profiles were plotted with the x-axis representing genomic positions and the y-axis is the number of reads per base pair per million mapped reads (RPBPM) or number of reads per kb per million mapped reads (RPKPM) using custom R scripts.

In vitro DNA affinity purification with deep sequencing (IDAP-seq)

Caulobacter genomic DNA was fragmented using a Diagenode Bioruptor to 200–500 bp in length. Five μg of genomic DNA was incubated with 320 nM of purified ParB-$(His)_6$ in IDAP buffer (20 mM K-HEPES pH7.9, 50 mM KCl, 10% glycerol, 10 mM Tris pH 8, 150 mM NaCl, 0.1% (v/v) Surfactant P20) at room temperature. After 60 min incubation at room temperature, 100 μl of Cu^{2+} Talon Superflow beads (GE Healthcare) were added, and the mixture was left at 4°C with gentle shaking for a further 60 min. Afterward, Talon beads were repeatedly washed in IPP150 buffer (10 mM Tris pH 8, 150 mM NaCl, 0.1% NP40) and 1× TE buffer (10 mM Tris pH 7.4, 1 mM EDTA) to wash off unbound ParB. ParB–DNA complexes were then eluted from the beads by incubating the beads with 150 μl of the elution buffer (50 mM Tris–HCl pH 8, 10 mM EDTA and 1% SDS) at 65°C for 15 min, then with 100 μl of 1× TE buffer + 1% SDS for another 15 min at 65°C. Subsequently, DNA was purified using a Qiaquick PCR clean up kit before being made into a library suitable for Illumina sequencing using the NEXT Ultra library preparation kit (NEB). IDAP-seq libraries were sequenced on the Illumina Hiseq 2500 at the Tufts University Genomics facility. As a control, Talon beads were also incubated with fragmented genomic DNA in the absence of ParB-$(His)_6$. Eluted DNA from the negative control was also made into Illumina sequencing library and sequenced in parallel to control for DNA fragments that bind to the surface of Talon beads non-specifically.

Analysis of IDAP-seq data to pinpoint *parS* sites to a single-nucleotide resolution

For analysis of IDAP-seq data, Hiseq 2500 Illumina short reads (50 bp) were mapped back to the *Caulobacter* NA1000 reference genome (NCBI Reference Sequence: NC-011916.1) using Bowtie 1 (29) and the following command:

bowtie -m 1 -n 1 –best –strata -p 4 –chunkmbs 512 NA1000-bowtie –sam *.fastq > output.sam

Subsequently, sequencing reads were sorted to either being mapped to the upper DNA strand or to the lower strand of the reference genome, as suggested in the original IDAP-seq publication (31). The number of 5′ end of reads that were mapped to the upper strand was counted for each nucleotide position along the *Caulobacter* genome using BEDTools (30) and the following command:

bedtools genomecov -d -5 -strand + -ibam output.sorted.bam -g NA1000.fna > upper_strand_output.txt

To count the number of 5′ end of reads that were mapped to the lower strand, the following command was used instead:

bedtools genomecov -d -5 -strand - -ibam output.sorted.bam -g NA1000.fna > lower_strand_output.txt

The IDAP-seq profile was then plotted using R. The sequence in between the summit of upper strand profile and that of the lower strand profile defines the minimal *parS* sequence required for binding to ParB. See also Supplementary Figure S3 for the principle behind the strand-specific analysis of IDAP-seq data to determine DNA-binding sequence at nucleotide resolution.

Transposon mutagenesis coupled with next-generation sequencing (Tn-seq)

The Tn5 transposon delivery plasmid (pMCS1-Tn5-ME-R6Kγ-kan^R-ME or pMCS1-Tn5-ME-R6Kμ-kan^R-$parS^{345}$-ME) was conjugated from an *E. coli* S17–1 donor into *Caulobacter* cells. Briefly, *E. coli* S17–1 was transformed with the transposon delivery plasmid and plated out on LB + kanamycin. On the next day, colonies forming on LB + kanamycin were scraped off the plates and resuspended in PYE to OD_{600} of 1.0. Cells were pelleted down and resuspended in fresh PYE twice to wash off residual antibiotics. 100 μl of cells were mixed with 1000 μl of exponentially growing *Caulobacter* (either wild-type, *Δsmc*, Flip 1–5, or Flip 2–5 *Caulobacter* cells), then the mixture was centrifuged at 13 000 rpm for 1 minute. The cell pellet was subsequently resuspended in 50 μl of fresh PYE and spotted on a nitrocellulose membrane resting on a fresh PYE plates. Twenty conjugations were performed to generate Tn5 insertion library for each *Caulobacter* strain. PYE plates with nitrocellulose disks were incubated at 30°C for 5 h before being resuspended by vortexing vigorously in fresh PYE liquid to release bacteria. Resuspended cells were plated out on twenty 30 cmx30 cm square Petri disks containing PYE agar supplemented with kanamycin and carbenicilin, and incubated for 3 days at 30°C. After 3-day incubation, cells (∼500 000–1 000 000 single colonies) were scraped off the Petri disk and resuspended in 200 ml of fresh PYE. The culture was pipetted repeatedly using a 10 mL glass pipette to break clumps and homogenize the

culture. Genomic DNA was subsequently extracted from a 2 ml sample using a genomic DNA extraction kit (Qiagen). Genomic DNA (1 μg) was sheared to between 200 and 500 bp using a Diagenode Bioruptor Plus (30 s ON, 30 s OFF, for 20 cycles at low sonication power). The fragmented DNA were resolved on a 2% agarose gel and a band of desired DNA length (200–500 bp) was excised and extracted using a QiaQuick gel extraction kit (Qiagen) before being made into an Illumina deep sequencing libraries.

For the list of Tn-seq libraries in this study, see Supplementary Table S3. For details on the construction of Illumina libraries, see Supplementary Materials and Methods.

Analysis of Tn-seq data

Hiseq 2500 Illumina short reads (50 bp) were mapped back to the *Caulobacter* NA1000 reference genome (NCBI Reference Sequence: NC-011916.1) using Bowtie 1 (29) and the following command:

bowtie -m 1 -n 1 –best –strata -p 4 –chunkmbs 512 NA1000-bowtie –sam *.fastq > output.sam

For *Caulobacter* strains with an inverted DNA segment, a reconstructed fasta file with the correct orientation for the inverted segment was used as reference genome for Bowtie instead. Subsequently, the sequencing coverage for each nucleotide position was computed using BEDTools (30) and the following command:

bedtools genomecov -d -ibam output.sorted.bam -g NA1000.fna > coverage_output.txt

Finally, the ratio between the number of reads of libraries generated from pMCS1-Tn5-ME-R6Kγ-kan^R-ME or pMCS1-Tn5-ME-R6Kγ-kan^R-*parS*$^{4+5+6}$-ME were calculated. Results were binned over 10 kb and represented as a $\log_{10}$ scale.

Measure ParB-*parS* binding affinity by Surface Plasmon Resonance (SPR)

Single-stranded oligomers containing *parS* sequence were purchased from Sigma and reconstituted to 100 μM in water. Complementary oligos were annealed together in an annealing buffer (10 mM Tris–HCl pH 8.0, 50 mM NaCl, and 1 mM EDTA) to form double stranded DNA before being diluted to a working concentration of 1 μM in HPS-EP+ buffer (0.01 M HEPES pH 7.4, 0.15 M NaCl, 3 mM EDTA, 0.005% v/v Surfactant P20) for each SPR experiment. The sequences of DNA oligos used in this study are reported in Supplementary Table S2. SPR measurements were recorded at 25°C using a Biacore T200 system (GE Healthcare). All experiments were performed using *R*e-usable *D*NA *Ca*pture *T*echnique (ReDCaT) exactly as described in (32). Briefly, ReDCAT uses a Sensor Chip SA (GE Healthcare), which has streptavidin pre-immobilized to a carboxymethylated dextran matrix, to which a 20 base biotinylated ReDCaT linker is immobilised. This is then used to immobilize *parS*-containing biotin-labelled double stranded oligos on the chip surface as each contain a single stranded overhand complimentary to the ReDCaT linker on the surface. The DNA to be tested is flowed over one flow cell on the chip at a flow rate of 10 μl/min and it anneals through the complementary DNA to the ReDCaT linker. *C. crescentus* ParB-(His)$_6$ or *B. subtilis* Spo0J-(His)$_6$, pre-diluted in HBS-EP+ buffer, was then flowed over the chip surface (the blank surface and the one with the DNA immobilised) and then HBS-EP+ buffer was then passed over to allow ParB-(His)$_6$ to dissociate from DNA. A high-salt wash buffer was injected to the chip to wash off any residual ParB-(His)$_6$ protein on the chip's surface. The test DNA could then be removed using a wash with 1M NaCl, 50mM NaOH. The chip could then be used again to load a new piece of test DNA. The SPR signal (Response Units) was monitored continuously throughout the process. Each cycle was repeated for increasing concentrations of ParB-(His)$_6$. For each concentration, the amount of ParB bound was measured and plotted against the concentration to construct a ParB-parS binding curve (Supplementary Figure S2). All sensorgrams recorded during ReDCAT experiments were analyzed using Biacore T200 BiaEvaluation software version 1.0 (GE Healthcare). Data were then plotted using Microsoft Excel or R, and K_d was estimated from best-fit curves.

Fluorescence microscopy image analysis

C. crescentus strain MT190 or strains with ectopic *parS*$^{3+4}$ (at +200 kb, +1000 kb or +1800 kb) were grown to OD_{600} = 0.4 in the presence of appropriate antibiotics before being spotted to agarose pad for microscopy observation. Phase contrast (150 ms exposure) and fluorescence images (1000 ms exposure) were collected. MicrobeTracker (http://microtracker.org) was used to detect cell outlines and cell length (33). SpotFinderM was used to manually detect fluorescent foci positions (33). Data (cell length, foci number) were exported to .csv files and subsequently analyzed and plotted in R.

RESULTS AND DISCUSSION

ParB occupies a 10 kb DNA region near the origin of replication

To define the distribution of ParB on the chromosome, we performed chromatin immunoprecipitation with deep sequencing. We fused the *flag* tag to the ParB-encoding gene at its 5′ end and placed this allele downstream of a vanillate-inducible promoter (P_{van}), at the chromosomal *vanA* locus. The vanillate-inducible *flag-parB* was then transduced to a *Caulobacter* strain where the native and untagged *parB* was under the control of a xylose-inducible promoter (P_{xyl}). *Caulobacter* cells were depleted of untagged ParB by addition of glucose for 5 h, then vanillate was added for an additional hour before cells were fixed with 1% formadehyde for ChIP-seq (Figure 1A). *Caulobacter* cells depleted of native ParB while producing the FLAG-tagged ParB version are viable, indicating that the tag does not interfere with ParB function (Supplementary Figure S1A). For ChIP-seq, DNA-bound to FLAG-ParB was pulled down using α-FLAG antibody coupled to sepharose beads. The immunoprecipitated DNA was deep sequenced and mapped back to the *Caulobacter* genome to reveal enriched genomic sites (Figure 1A). As a negative control, we performed α-FLAG ChIP-seq in a *Caulobacter* strain that produces FLAG-tagged YFP, a non-DNA binding protein (Figure 1B). The ChIP-seq profile of FLAG-ParB showed a clear enrichment

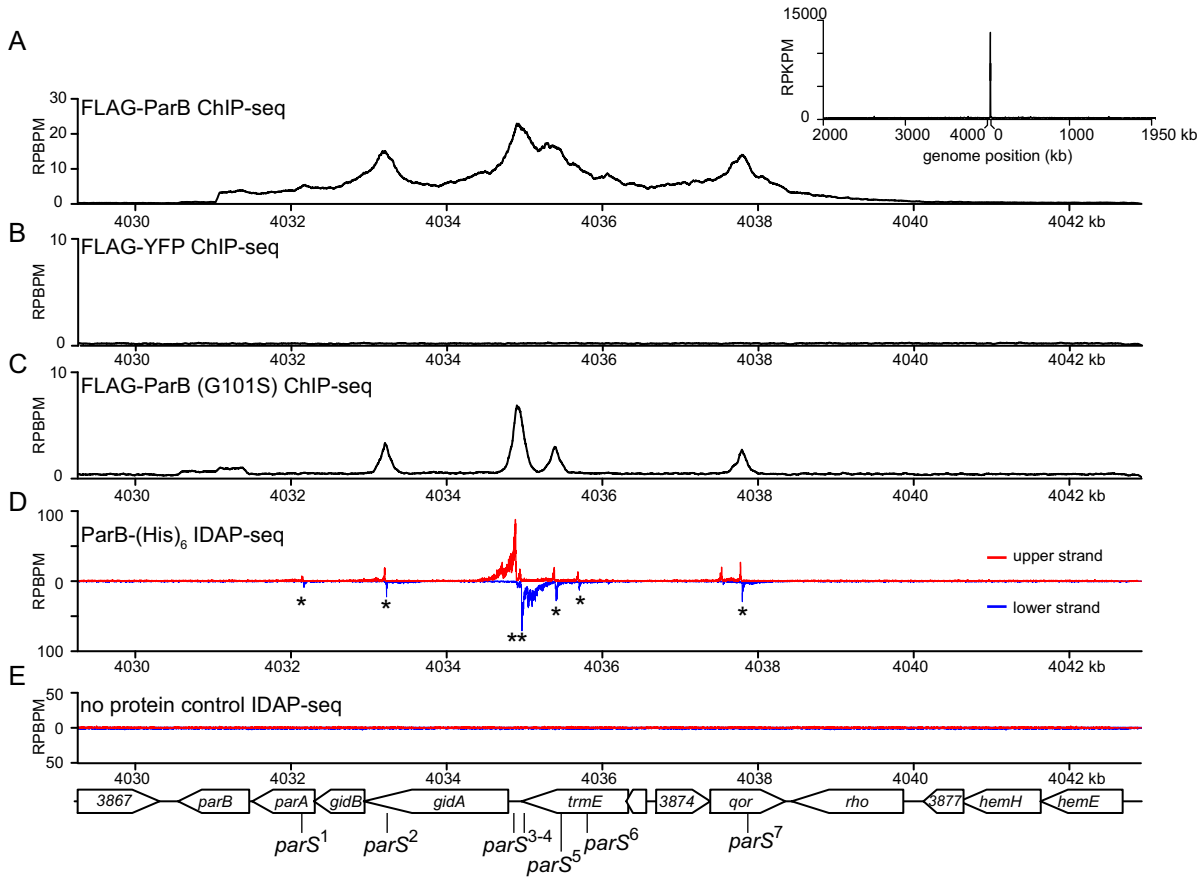

Figure 1. ParB occupies 10 kb DNA region near the origin of replication. (**A**) The distribution of FLAG-tagged ParB on *Caulobacter* chromosome between +4030 kb and +4042 kb. ChIP-seq signals were reported as the number of reads at every nucleotide along the genome (RPBPM value). The whole-genome ChIP-seq profile of ParB is shown in the inset. For the whole genome profile, the ChIP-seq signals were reported as the number of reads at every kb along the genome (RPKPM value). (**B**) ChIP-seq profile of FLAG-tagged YFP. (**C**) ChIP-seq profile of FLAG-tagged ParB (G101S) mutant. (**D**) IDAP-seq profile of ParB-$(His)_6$ with sonication-fragmented genomic DNA from *Caulobacter*. IDAP-seq reads were sorted to either the upper strand (red) or to the lower strand (blue) of the reference genome to enable identification of *parS* sites (see also Figure 2 and Supplementary Figure S3). Putative *parS* sites (1–7) are noted with asterisks (see also Figure 2). (**E**) IDAP-seq profile of a negative control in which ParB-$(His)_6$ was omitted.

in the DNA region on the left chromosomal arm, ∼8 kb away from the origin of replication. No other significant enrichment was observed elsewhere on the chromosome or in the negative control (Figure 1A-B). A closer examination of the *ori*-proximal region revealed an extended ∼10 kb region with significant enrichment above background and four defined peaks (Figure 1A). To independently verify our results, we repeated the ChIP-seq experiment using α-GFP antibody to pull down DNA from a *Caulobacter* strain that produces a CFP-ParB fusion protein from its native location as the only source of ParB in the cell or using a polyclonal α-ParB in a wild-type *Caulobacter* (Supplementary Figure S1B). For all cases, we retrieved very similar ChIP-seq profiles to that of FLAG-ParB, suggesting the extended DNA region associating with ParB is not an artefact of tagging but a property of *Caulobacter* ParB itself.

The extensive 10-kb ParB-binding DNA region cannot be explained by the length of DNA fragments that were sheared as part of a ChIP-seq protocol. We sequenced immunoprecipitated DNA from both ends to determine their exact size distribution (Supplementary Table S3). Pulled-down DNA averages around 150 bp, much smaller than the size of ChIP-seq peaks in our study. However, the extended ParB-binding DNA region can be most easily explained by the non-specific binding of ParB to DNA outside of the *parS* nucleation site, either by a 'spreading and bridging' or 'caging' mechanism. If so, *Caulobacter* ParB mutants that are impaired in binding to non-specific DNA are predicted to spread less. To identify such mutants in *Caulobacter*, we mutated the highly-conserved N-terminal Box II motif which was shown to be important for the non-specific DNA-binding activity of *B. subtilis* ParB (Supplementary Figure S2A) (12,19). Four variants were constructed *parB* (G101S), *parB* (R103A), *parB* (R104A), and *parB* (R106A). We introduced the *flag*-tagged *parB* mutant allele at the *van* locus, in the P_{xyl}-*parB* genetic background, then employed α-FLAG ChIP-seq to assess the distribution of mutated ParB on the chromosome. Two mutants, ParB (G101S) and ParB (R104A), were found to produce well-defined and symmetrical peaks (∼400 bp in width) that are typical of site-specific DNA-binding proteins (Figure 1C and Supplementary Figure S1B). On the contrary, wild-type ParB peaks are much wider and asymmetrical (Figure 1A). These data suggest that *Caulobacter* ParB, similar to *B.*

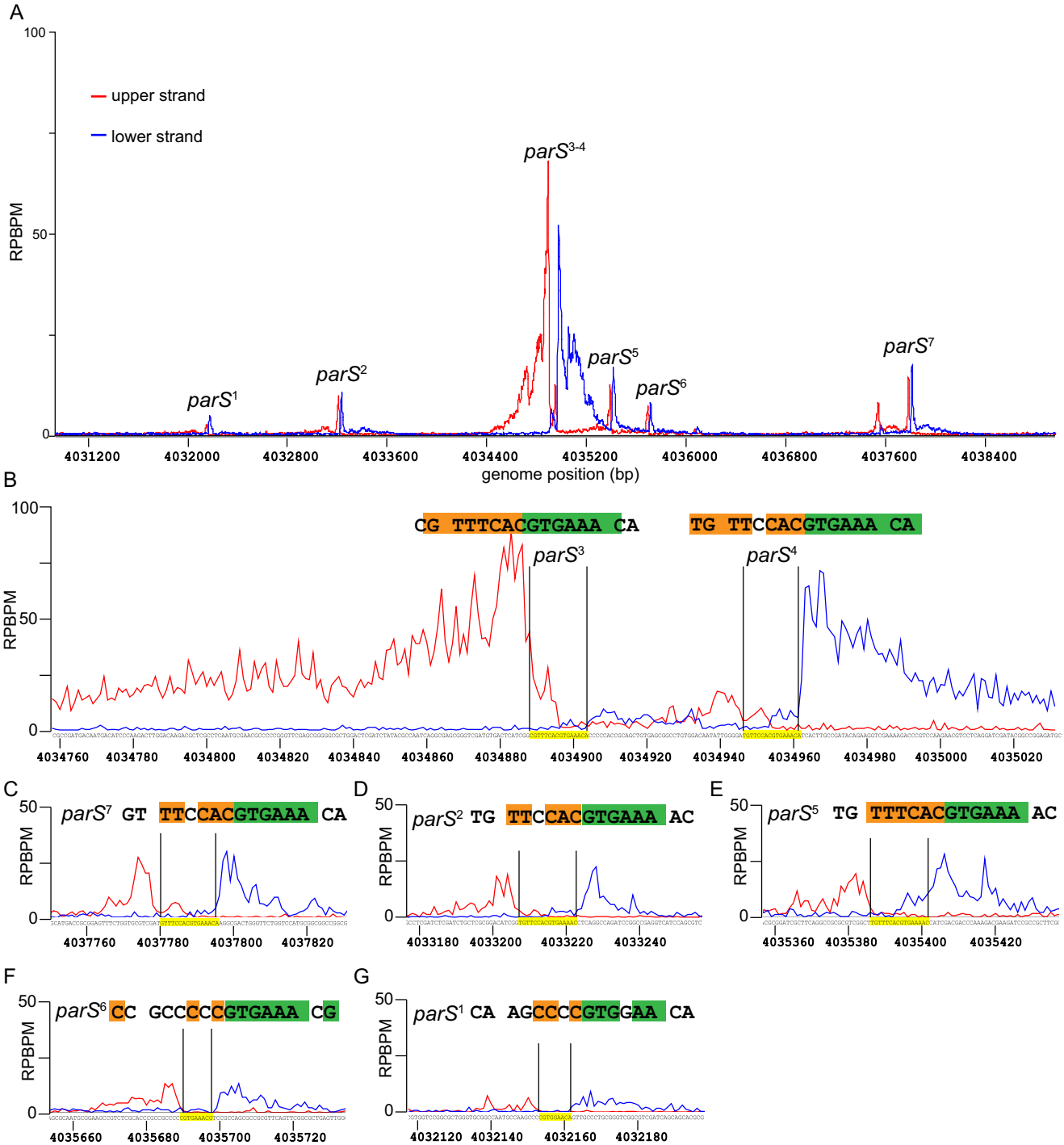

Figure 2. Identification of *parS* sequences by *in vitro* DNA purification with deep sequencing (IDAP-seq). Sequencing reads were sorted to either the upper DNA strand (red) or to the lower strand (blue) of the *Caulobacter* reference gnome, as suggested in the original IDAP-seq publication (31). The sequence in between the summit of the upper strand profile and that of the lower strand profile defines the *parS* sequence required for binding to ParB *in vitro* (see also Supplementary Figure S3). (**A**) IDAP-seq profile of ParB-$(His)_6$ in the genomic region between +4031 kb and +4039 kb. (**B–G**) IDAP-seq profile of ParB-$(His)_6$ surrounding each individual *parS* site. Palindromic nucleotides within the identified *parS* site are shaded in orange and green.

subtilis and *P. aeruginosa* ParB, also spreads along the chromosome. Lastly, we noted that DNA enrichment in ChIP-seq experiments with ParB (G101S) or ParB (R104A) is ∼5 fold less than that of wild-type ParB (Figure 1A–C), despite the fact that ParB variants nucleate equally well on DNA *in vitro* (Supplementary Figure S2B). This is most likely because ParB (G101S) and ParB (R104A) are less stable than wild-type ParB *in vivo* (Supplementary Figure S2C).

Identification of *parS* sites and correlating ParB-*parS in vitro* binding affinities to their *in vivo* ChIP-seq enrichment

Since the large width of ChIP-seq peaks obscures the exact position of *parS*, we employed *in vitro* DNA affinity purification with deep sequencing (IDAP-seq) (31) to pinpoint *parS* sequence to near single-nucleotide resolution. Purified ParB-$(His)_6$ was incubated with randomly-fragmented *Caulobacter* genomic DNA, then ParB-DNA complexes were pulled-down using immobilized Ni^{2+} beads. ParB-bound DNA fragments were eluted out and sequenced *en masse*. The sequencing reads were mapped back to either the upper strand or the lower strand of the *Caulobacter* genome (Figures 1 D and 2). Analysis of the strand-specific coverage map allows identification of seven 16 bp putative *parS* sites (see Figure 1D and Supplementary Figure S3 for the methodology of IDAP-seq data analysis). These included the two *parS* sites (sites 3 and site 4) that were first discovered in Toro *et al* (2008) (8) but revealed five more putative sites (sites 1, 2, 5, 6 and 7).

To correlate the sequence conservation to the binding affinity of ParB, we measured the equilibrium dissociation constant (K_d) of ParB binding to 24-bp double-stranded oligonucleotides containing individual putative *parS* sites by Surface Plasmon Resonance (SPR) (Figure 3 and Supplementary Figure S4). The double-stranded oligonucleotides was tethered to a chip surface within an SPR flow cell. Purified ParB-$(His)_6$ was flowed over the test DNA. ParB binding was recorded by measuring the change in response units during ParB injection. After injection, the chip was washed with buffer and subsequently with high salt buffer to remove any bound ParB. This cycle was repeated for an increasing concentration of ParB dimer to enable the estimation of K_d (Figure 3 and Supplementary Figure S4). Note that the length of the double-stranded oligonucleotides was limited to 24 bp so that only the nucleating event of ParB on *parS* was observed, and not the interaction with DNA flanking *parS*. We observed that sites 2, 3, 4, 5 and 7 have low nM K_d values (Figure 3), consistent with their high ChIP-seq peaks (Figure 1). On the other hand, ParB binds to the putative sites 1 and 6 weakly *in vitro*, albeit more than to a scrambled *parS* control (Figure 3), suggesting that sites 1 and 6 are perhaps unlikely to be significant *in vivo*.

Importantly, the affinity of *Caulobacter* ParB for its *parS* site (30 ± 3 nM) is much stronger than the previously reported K_d for the *B. subtilis* Spo0J-*parS* interaction (230 ± 7 nM) (6,14). To check whether the difference in K_d is due to measurement techniques, we purified *B. subtillis* Spo0J and determined its affinity to a cognate *parS* or to a randomized site by SPR (Supplementary Figure S5). We found that the apparent K_d for *B. subtilis* Spo0J-cognate *parS* is 114 ± 21 nM, and *B. subtilis* Spo0J-randomized *parS* is 183 ± 29 nM (Supplementary Figure S5). These values are in a similar range to those measured previously using a different technique (14). Our experiments also confirmed the previous finding that *B. subtilis* Spo0J does not discriminate well between *parS* and non-*parS* DNA (14). Based on the similar K_d for *parS* and non-*parS* site, it has been suggested that the presence of *parS* site does not promote non-specific DNA binding and/or condensation events by *B. subtilis* Spo0J (14). On the contrary, *Caulobacter* ParB binds *parS* tightly but almost does not bind or binds very weakly to non-*parS* site (Figure 3 and Supplementary Figure S4). Nevertheless, *in vivo* ChIP-seq experiments showed unequivocally that *Caulobacter* ParB spreads to non-specific DNA on both sides of the core *parS* sequence (Figure 1 and Supplementary Figure S1). Our results with *Caulobacter* ParB, therefore, support the idea that the initial ParB–*parS* nucleation event is important for spreading. Why is there a stark contrast between the two ParB proteins of the same class? Recently, it has been showed that the C-terminal domain of *B. subtilis* Spo0J, in addition to the middle helix-turn-helix domain, binds DNA non-specifically and contributes to DNA condensation (14 and M. Dillingham, personal communications). In *Caulobacter*, the C-terminal domain of ParB is not similar to that of the *B. subtilis* Spo0J, hence might not bind non-specific DNA strongly. The DNA-binding property of the Spo0J C-terminal domain might explain why *Bacillus parS* sites do not cluster as closely as in *Caulobacter*. The four strongest *Bacillus parS* sites (*parS* at 354°, *parS* at 355°, *parS* at 356° and *parS* at 359°) are ∼5 kb, 13 kb, and 39 kb apart from each other, respectively. On the contrary, the five strongest *Caulobacter parS* sites are all within a 5-kb DNA segment. The lower capability of *Caulobacter* ParB in binding to non-specific DNA might necessitate a closer clustering of *parS* sites for an efficient 'spreading' in this bacterium. We explore this possibility by investigating the spreading of *Caulobacter* ParB from individual *parS* sites below.

ParB spreads to a maximum of 2 kb around individual *parS* site

Since *parS* sites are located within essential genes or genes that have a high fitness cost, we were not able to ablate individual *parS* sites to investigate the spreading of ParB in *Caulobacter*. Instead, we investigated the spreading of ParB from individual *parS* sites by expressing the *Caulobacter* ParB/*parS* system in *E. coli*. Since *E. coli* does not possess a ParB homolog nor a *Caulobacter parS*-like sequence, it serves as a suitable heterologous host for this experiment. We inserted individual *parS* sites onto the *E. coli* chromosome at the *ybbD* locus (Figure 4). The ParB protein was expressed from an IPTG-inducible promoter as a C-terminal fusion to the T18 fragment of *Bordetella pertussis* adenylate cyclase. The T18-ParB is fully functional in *E. coli* as judged by its interactions with their known partners such as ParB itself, ParA, and MipZ in a bacterial-two hybrid assay (Supplementary Figure S6A). We induced exponentially-growing *E. coli* cells at 28°C with 500 μM IPTG for an hour before fixing with formadehyde for ChIP-seq. DNA bound to T18-ParB was immunoprecipitated using α-T18 conju-

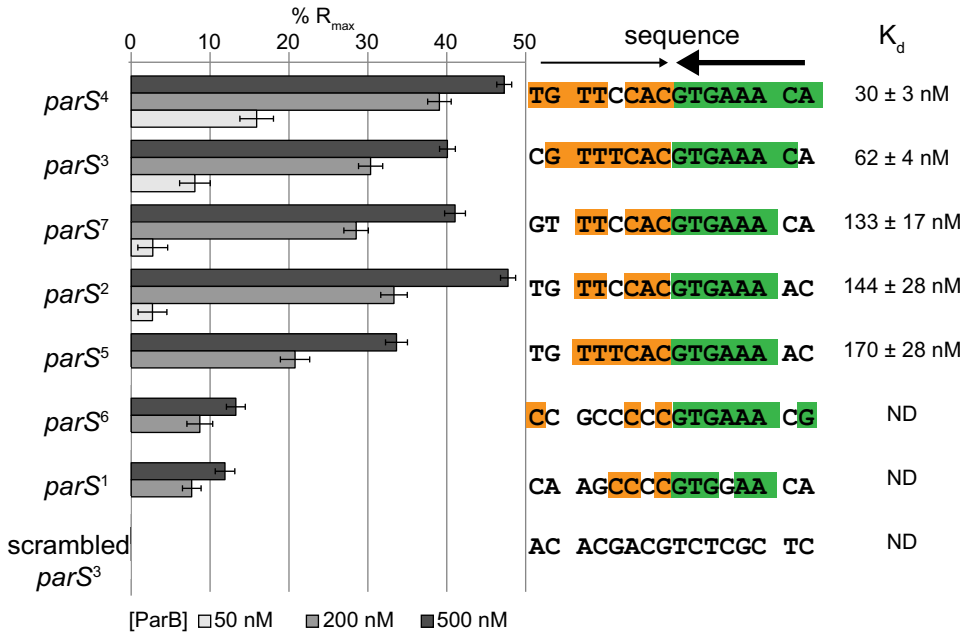

Figure 3. ParB-*parS in vitro* binding affinities correlate to their *in vivo* ChIP-seq enrichment. Surface Plasmon Resonance (SPR) was used to measure binding affinity of ParB (50, 200 and 500 nM) to 24-bp double-stranded DNA that contains individual putative *parS* site. The level of ParB binding to DNA was expressed as a percentage of the theoretical maximum response, R_{max}, assuming a single ParB dimer binding to one immobilized double-stranded DNA oligomer. This normalization process enabled the various responses to be readily compared, irrespective of the quantity and length of the DNA tethered on an SPR chip surface. A wider range of ParB concentration (6.25, 12.5, 25, 50, 100, 200, 400, 600 and 800 nM) was used to estimate the binding constant (K_d) of ParB to individual *parS* site (Supplementary Figure S4). The sequences of *parS* are shown with palindromic nucleotides shaded in orange and green. Convergent arrows on top of *parS* sequence indicate that *parS* sites are palindromic. Thicker arrow signifies that the second half of *parS* sequences (GTGAAA, in green) is conserved among *Caulobacter parS* sites.

gated sepharose beads. A scrambled *parS* site 3 was also inserted at the *ybbD* locus to serve as a negative control. As expected, the strong *parS* sites (sites 2, 3, 4, 5, and 7), on their own showed a high level of DNA enrichment, in agreement with their *in vitro* ParB binding affinity (Figure 4). The weak putative *parS* sites (site 1 and 6) show little to no enrichment above background (Supplementary Figure S6B). Most importantly, we observed that ParB in an *E. coli* host spreads to a maximum of ∼2 kb around each *parS* site (Figure 4), much less than ∼10 kb for *B. subtilis* Spo0J-single *parS* (12). Next, we repeated the ChIP-seq experiment but with a spreading-defective ParB (G101S). This revealed symmetrical peaks with a ∼400-bp width, confirming that *Caulobacter* ParB can spread to any neighbouring DNA and that non-specific interaction with DNA is mainly dependent on an initial ParB-*parS* nucleation event. Lastly, we noted that the spreading of wild-type ParB is not equal on both sides of *parS*. It is likely that the non-specific association of ParB with neighbouring DNA might be influenced by on-going transcription or other nearby DNA-binding proteins. This asymmetrical spreading has been observed previously with ParB homologs from other bacterial species (19,34).

Since *Caulobacter* ParB associates maximally with only ∼2 kb DNA surrounding individual *parS* site, the clustering of *parS* sites might serve to enable a higher concentration of DNA-bound ParB near *ori* than is possible with a single site. A previously study estimated that ∼80% of the total cellular ParB is bound at *parS* sites in *Caulobacter* (1). *Caulobacter* ParA was also found to require a higher concentration of DNA-bound ParB than in *B. subtilis* to activate its ATPase activity, an essential step for chromosome segregation by the ParAB–*parS* system (1). Furthermore, it is known that *Caulobacter* ParB interacts with MipZ, which in turns binds PopZ to anchor the *ori*-proximal DNA to the cell pole (35–37). A high local concentration of DNA-bound ParB would enable a robust anchorage of the *ori* DNA domain to the cell pole. We noted that the nucleation-competent but spreading-defective ParB (G101S) or ParB (R104A) variants are unable to support *Caulobacter* growth, implying that ParB spreading is required for cell viability (Supplementary Figure S1A). In line with our study, *B. subtilis* or *P. aeruginosa* engineered with a single *parS* are defective in chromosome segregation, resulting in elevated numbers of anucleate cells (5,19,38).

Extra copies of *parS* can reduce the fitness of *Caulobacter* depending on their genomic locations

Additional copies of *parS*, for example when is placed on a multi-copy number plasmid, can be lethal for cells because plasmid DNA can be segregated instead of the chromosome, resulting in daughter cells with either zero or two chromosomes (8). Indeed, we found the presence of a *parS*-carrying plasmid caused growth impairment in *Caulobacter*, and the fitness cost correlates well with the ParB–*parS* binding affinity (Figure 5). Plasmid-borne sites 3 and 4, which are the strongest *parS* sites, reduced cell viability by ∼1000-fold compared to a negative control (scrambled site 3). Extra copies of sites 2, 5 and 7 reduced cell viability by

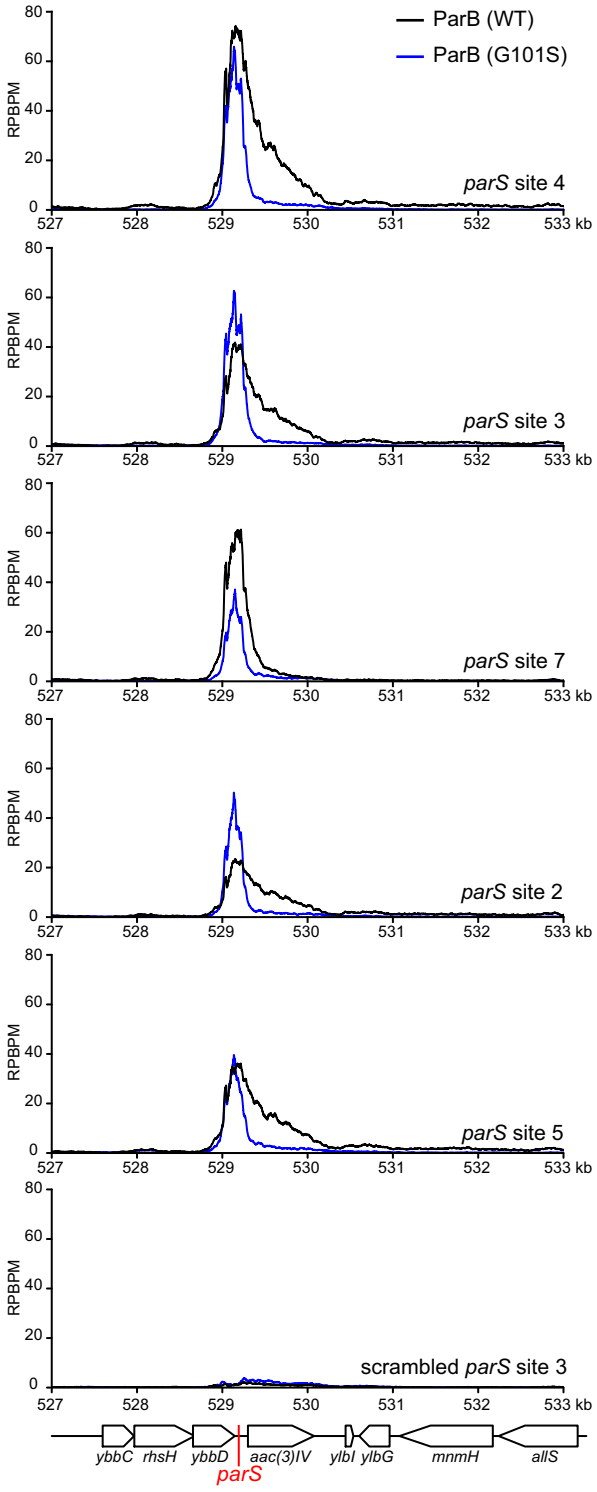

Figure 4. *Caulobacter* ParB binds to *parS* and spreads to flanking DNA in a heterologous *E. coli* host. A cassette composed of individual *parS* (red line) site and an apramycin resistance marker *aac(3)IV* was inserted at the *yybD* locus on an *E. coli* chromosome. T18-ParB (WT) (black) or T18-ParB (G101S) (blue) were expressed from an IPTG-inducible promoter, and their distribution on the *E. coli* chromosome were determined by α-T18 ChIP-seq. ChIP-seq signals were reported as the number of reads at every nucleotide along the genome (RPBPM value). A cassette composed of a scrambled *parS* site 3 and an apramycin resistance marker was also inserted at the *yybD* locus and serves as a negative control.

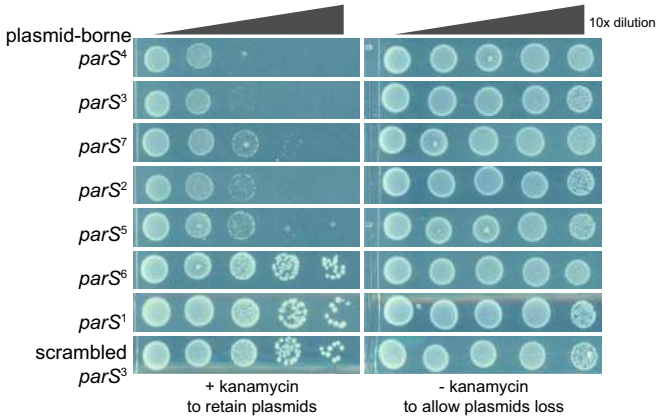

Figure 5. Plasmid-borne *parS* reduces the fitness of *Caulobacter*. Low-copy number plasmid harbouring individual *parS* site was conjugated from *E. coli* S17–1 to wild-type *Caulobacter*. The same number of *E. coli* and *Caulobacter* cells were used for each conjugation. A ten-fold serial dilution was performed and spotted on PYE plates supplemented with both nalidixic acid and kanamycin or just with nalidixic acid. Addition of kanamycin enforces the retention of *parS* plasmid, while omitting kanamycin allows plasmid loss. All cells were spotted on the same +kanamycin or –kanamycin plates, and pictures were taken after 3-day incubation at 30°C.

~100 fold compared to a control, while the weaker *parS* sites 1 and 6 did not impact cell viability when present on a plasmid.

We reasoned that if the toxicity of a plasmid-borne *parS* site was due to the segregation of plasmids instead of the chromosome then having extra *parS* sites on the chromosome should eliminate the toxicity. Indeed, we were able to engineer a 260-bp DNA segment containing both strong *parS* site 3 and site 4 at various positions from *ori* to *ter* on both arms of *Caulobacter* chromosome. On the contrary, a plasmid containing both *parS* sites 3 and 4 is completely lethal to *Caulobacter* cells (8). Nevertheless, we noted a variation in the fitness of *Caulobacter* with extra chromosomal *parS* sites, depending on the location of the ectopic *parS* (Figure 6). An extra $parS^{3+4}$ inserted at +200 kb (near *ori*) or at +1800 kb (near *ter*) did not impact the fitness of the cell dramatically as judged by a normal cell length distribution and a 6-fold increase in the number of anucleate cells (Figure 6B and D). On the contrary, $parS^{3+4}$ inserted at +1000 kb (middle of the right arm of the chromosome) caused a more severe fitness defect. The cells were more elongated (4.74 ± 3.3 μm) compared to WT (2.97 ± 0.77 μm) (Figure 6). Furthermore, the number of cells with no or more than two CFP-ParB foci were elevated ~11-fold in comparison to strains without an ectopic $parS^{3+4}$ (Figure 6C). Lastly, in *Caulobacter*, ParB recruits MipZ, which in turns regulates the positioning of the division plane (37). We found that the number of MipZ-CFP foci are abnormal in strains with an ectopic $parS^{3+4}$ site, suggesting that cell division defects also contribute to a lower cell fitness in those strains (Supplementary Figure S7). Taken all together, our data suggest that the genomic location of an extra chromosomal copy of *parS* is important for the cell fitness in *Caulobacter*.

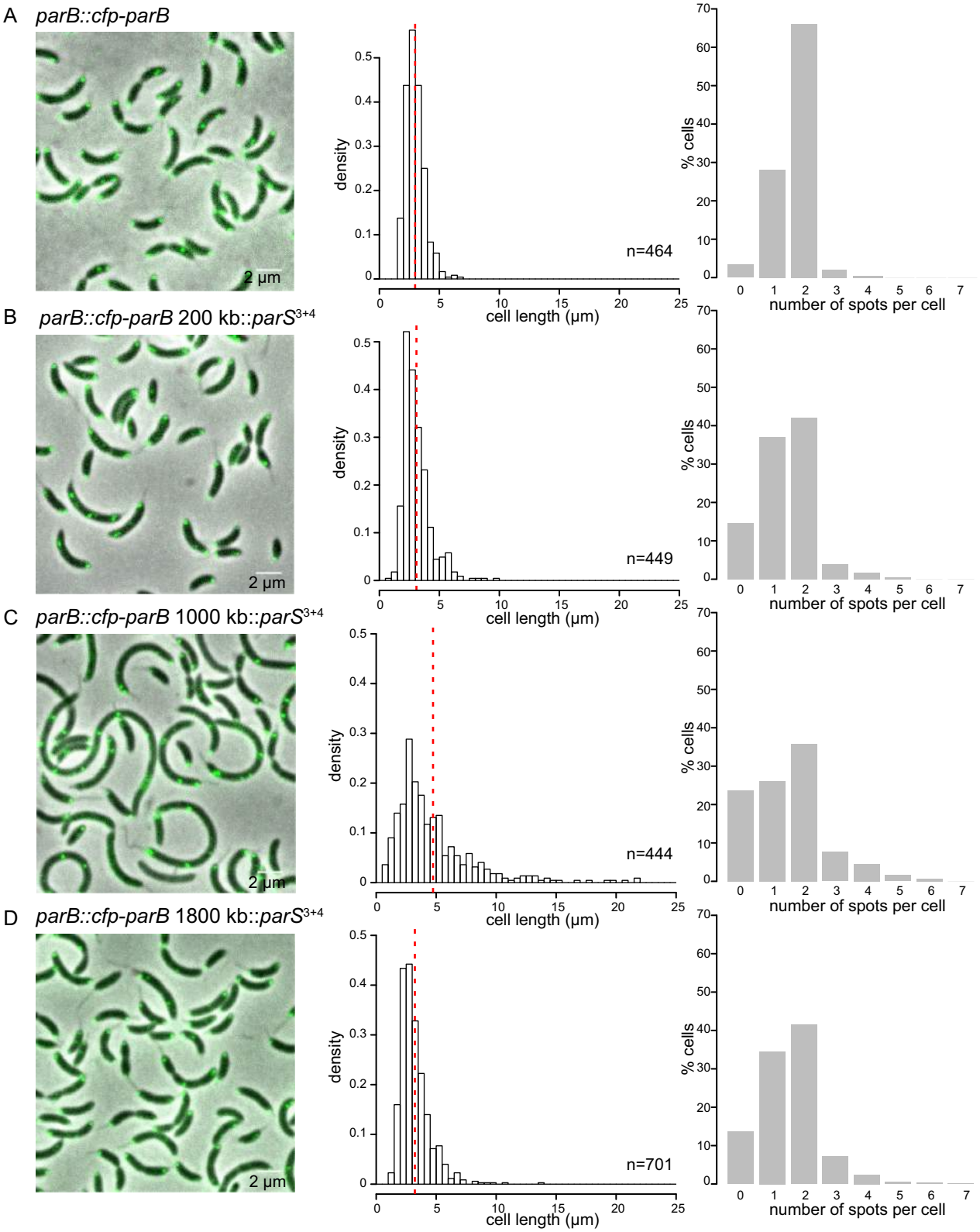

Figure 6. The position of an ectopic *parS* on the chromosome is critical for the fitness of *Caulobacter*. Micrograph of *parB::cfp-parB Caulobacter* cells (**A**) without an extra ectopic $parS^{3+4}$, (**B**) with an extra ectopic $parS^{3+4}$ at +200 kb, (**C**) at +1000 kb or (**D**) at +1800 kb. Cell length of an exponentially-growing cells were quantified and presented as histograms. Vertical dotted red lines indicate the mean cell length. The number of CFP-ParB foci (green) per cell was also quantified and plotted as histograms. Note that we could not observe foci corresponding to an extra ectopic $parS^{3+4}$ perhaps due to the limited numbers of ParB bound to this shorter cluster. Most observable foci are likely due to the original $parS^{1-7}$ cluster that reside ~8 kb near *ori*.

Systematic identification of a permissive zone for *parS* insertion by transposon mutagenesis with deep sequencing (Tn-seq)

Previously, a comparative genomics study surveyed and predicted the positions of *parS* sites over a wide range of bacteria and found that most *parS* sites are located close to the *ori* on the chromosome (7). Here, in *Caulobacter*, we have found that a second *parS* cluster, depending on its location on the chromosome, can affect chromosome segregation and cell fitness. To investigate this positional bias systematically, we employed a genome-wide transposon mutagenesis with deep sequencing (Tn-seq) approach. Briefly, a Tn5 transposon carrying *parS* sites 3, 4 and 5 was used to insert these strong *parS* sites randomly around the chromosome. A library of approximately half a million of single colonies were generated and the genomic locations of the inserted *parS* cluster was then determined *en masse* by deep sequencing. As a control, we generated an insertion library using a transposon that does not carry *parS*. Wild-type *Caulobacter* cells were first mutagenized with $parS^+$ or $parS^-$ transposon, and the number of insertions was binned to 10-kb segments along the *Caulobacter* chromosome. The ratio of the frequency for the $parS^+$ transposon and that of the $parS^-$ transposon was plotted as a $\log_{10}$ scale against genomic position (Figure 7A), and used as a proxy to determine the genomic preference for an extra cluster of *parS*. We observed that a second *parS* cluster is most tolerated within ∼500 kb surrounding *ori* (Figure 7A and Supplementary Figure S8A). In contrast, an ectopic *parS* is strongly disfavoured near the middle of each chromosomal arm (Figure 7A and Supplementary Figure S8B), consistent with our observation that $parS^{3+4}$ at +1000 kb caused cell elongation and chromosome segregation defects. A limited zone of *parS* enrichment was also found within ∼100 kb around the *ter* (Figure 7A and Supplementary Figure S8C). Lastly, we also note the presence of two *parS* insertion 'hot spots'. The first hot spot locates near the native *parS* cluster (Figure 7B), likely strengthening the existing native ParB binding area on the left arm of the chromosome. The second hot spot encompasses the *recF*, *gyrB* and *CCNA0160* genes (Figure 7C). One possibility is that a *parS* insertion in the vicinity of *gyrB* is preferred because it alters the global supercoiling level. However, we found that the *gyrB* transcription was unchanged compared to wild-type cells or cells with an extra *parS* elsewhere on the chromosome. The mechanism responsible for the *gyrB* 'hotspot' therefore remains unknown.

We noted that *parS* insertion frequency decreases gradually from *ori* to the mid-arm without a clear boundary, suggesting that the *parS* permissive zone is perhaps dependent on the genomic distance away either from *ori* or from the native *parS* cluster. To test this hypothesis, we employed a Flip 1–5 strain where the native cluster of *parS* sites were relocated ∼400 kb away from *ori* through an inversion between +3611 and +4038 kb (Figure 7D) (39). The Tn5 transposon with or without the *parS* cluster was again used to randomly mutagenize the Flip 1–5 strain. As a control, we also transposon mutagenized another inversion strain (Flip 2–5) where the native *parS* cluster remains at its original location but a similar chromosome segment (between +3611 and +4030 kb) was inverted (Figure 7D). Results showed that the permissive zone for insertion of an extra *parS* cluster in Flip 1–5 was now centred near the relocated *parS* site at +3611 kb, while the permissive zone remains centred at the native *parS* in the control Flip 2–5 strain (Figure 7D) (39). Altogether, our results suggest that the genomic distance from the original *parS* cluster, not the distance from *ori*, is likely the main determinant of the permissive zone for the insertion of a second *parS* cluster.

Most bacterial species with a ParAB-*parS* system have more than one *parS* site (7), and some species such as *Streptomyces coelicolor* and *Listeria innocua* have accumulated 22 *parS* sites near their origin of replication (7,40). How the bacterial centromere-like region expands and what drives its extension over time are interesting biological questions. Our finding that new *parS* sites can locate near the native *parS* cluster but not elsewhere could potentially explain the clustering of *parS* sites on bacterial chromosomes over time. New *parS* sites preferentially locate near the original *parS* cluster because it is the least disruptive to chromosome segregation, cell division, and cell viability (Figures 6 and 7). In *Caulobacter*, *parS,* not *ori*, is the site at which force is exerted during chromosome segregation (8). ParA forms a gradient emanating from the opposite pole to the ParB–*parS* cluster. A ParA gradient retracts upon contacting ParB-*parS* and this nucleoprotein complex moves in the retreating gradient of ParA to the opposite cell pole. ParA-ParB-*parS* are only required for the segregation of *parS*-proximal DNA, but not of the distal DNA loci (41). Once the *parS*-proximal DNA is properly segregated by ParA–ParB–*parS*, distal DNA regions follow suit, driven by separate molecular machinery, or more likely without the need of a dedicated system (41). It is, therefore, foreseeable that expanding the *parS* region by adding new *parS* sites near the native cluster is least disruptive to chromosome segregation and the subsequent cell division since the *parS*-proximal DNA remains the first locus to be segregated. Similarly, in *P. aeruginosa*, *parS* is also the first segregated locus and it is preferable for cell viability that *parS* segregates soon after DNA replication (5).

In this study, we also discovered that new *parS* sites are also tolerated near the *ter* region, albeit with less preference than near the native *parS* cluster. In *P. aeruginosa* or *B. subtilis*, insertion of *parS* near the *ter* region is strongly discouraged, presumably due to the recruitment of the Structural Maintenance of the Chromosomes (SMC) complex away from *ori* (5,42). SMC is a prominent protein involved in bacterial chromosome organization and segregation (39,42–45). To test if SMC might contribute to shape the distribution of ectopic *parS* sites in *Caulobacter*, we transposon mutagenized the *Δsmc Caulobacter* strain (Supplementary Figure S8D). In *Δsmc* cells, the pattern of *parS* permissive zones does not change dramatically. New *parS* sites remain disfavoured near mid-arms, although they are less favoured near *ter* compared to wild-type cells (Supplementary Figure S8D). Our previous study showed that *Caulobacter* SMC are recruited to the *ter*-located ectopic *parS* and cohese flanking DNA together, nevertheless the global chromosome organization remained largely unchanged with *ori* and *ter* at opposite poles and two chromosomal arms running in parallel down the long axis of the cell (39). All together, we conclude that SMC contributes to the determination of

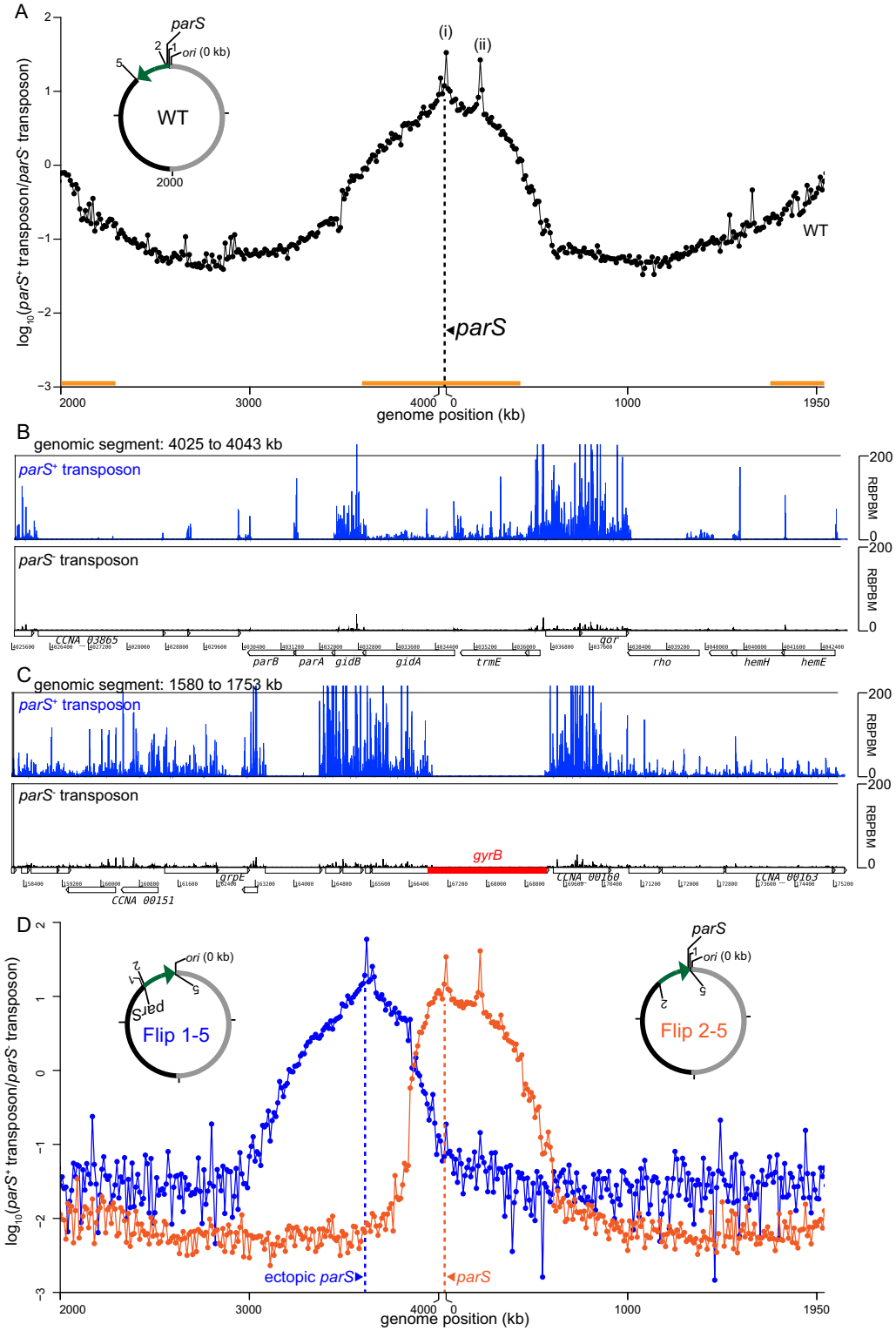

Figure 7. Tn5-seq reveals the positional bias of the centromeric *parS* site on *Caulobacter* chromosome. (**A**) Wild-type *Caulobacter* cells were mutagenized with the $parS^+$ or $parS^-$ transposon, and the number of insertions was binned to 10-kb segments along the *Caulobacter* chromosome. The ratio between insertion frequency for the $parS^+$ transposon and that of the $parS^-$ transposon was calculated and plotted as a $\log_{10}$ scale against genomic position. Two hotspots for insertion of the $parS^+$ transposon are marked with asterisks (*). The vertical dotted line (black) shows the position of the native *parS* cluster. The horizontal bar (orange) indicates the permissive zone for extra *parS* insertions. (**B**) Comparison between $parS^+$ (blue) and $parS^-$ (black) transposon insertions for the genomic segment between +4025 kb and +4043 kb. (**C**) Comparison between $parS^+$ (blue) and $parS^-$ (black) transposon insertions for the genomic segment between +158 kb and +175 kb. (**D**) $parS^+/parS^-$ Tn5-seq profiles for Flip1–5 (blue) and Flip 2–5 (orange) strains. The horizontal axis represents genome position in kilobases for each strain. A schematic genomic map of *Caulobacter* showing the position of *parS* and *ori* are presented in the inset. The inverted DNA segment (green arrow) is indicated together with the end points of the inversion (1, 2 and 5).

parS permissive zones but cannot solely explain some of the preference for the *ter* region and the disfavour for mid-arm regions in *Caulobacter crescentus*. Further investigation into the molecular mechanism that gives raise to the permissive zones of *parS* will undoubtedly improve our understanding of bacterial chromosome segregation and organization.

AVAILABILITY

The accession number for the sequencing data reported in this paper is GEO: **GSE100233**.

SUPPLEMENTARY DATA

Supplementary Data are available at NAR Online.

ACKNOWLEDGEMENTS

We thank Anjana Badrinarayanan, Matthew Bush, Mark Buttner, Michael Laub and Susan Schlimpert for discussion and comments on the manuscript. We thank Christine Jacob-Wagner and Martin Thanbichler for materials.

FUNDING

Royal Society University Research Fellowship [UF140053 to T.B.K.L.]; Royal Society Research Grant [RG150448 to T.B.K.L.]; BBSRC grant-in-add [BBS/E/J/000C0683 to the John Innes Centre); and BBSRC grant [BB/P018165/1 to T.B.K.L.]. Funding for open access charge: Biotechnology and Biological Sciences Research Council (BBSRC).
Conflict of interest statement. None declared.

REFERENCES

1. Lim,H.C., Surovtsev,I.V., Beltran,B.G., Huang,F., Bewersdorf,J. and Jacobs-Wagner,C. (2014) Evidence for a DNA-relay mechanism in ParABS-mediated chromosome segregation. *eLife*, **3**, e02758.
2. Vecchiarelli,A.G., Hwang,L.C. and Mizuuchi,K. (2013) Cell-free study of F plasmid partition provides evidence for cargo transport by a diffusion-ratchet mechanism. *Proc. Natl. Acad. Sci. U.S.A.*, **110**, E1390–E1397.
3. Vecchiarelli,A.G., Neuman,K.C. and Mizuuchi,K. (2014) A propagating ATPase gradient drives transport of surface-confined cellular cargo. *Proc. Natl. Acad. Sci. U.S.A.*, **111**, 4880–4885.
4. Badrinarayanan,A., Le,T.B.K. and Laub,M.T. (2015) Bacterial chromosome organization and segregation. *Annu. Rev. Cell Dev. Biol.*, **31**, 171–199.
5. Lagage,V., Boccard,F. and Vallet-Gely,I. (2016) Regional control of chromosome segregation in *Pseudomonas aeruginosa*. *PLOS Genet.*, **12**, e1006428.
6. Lin,D.C.-H. and Grossman,A.D. (1998) Identification and characterization of a bacterial chromosome partitioning site. *Cell*, **92**, 675–685.
7. Livny,J., Yamaichi,Y. and Waldor,M.K. (2007) Distribution of centromere-like *parS* sites in bacteria: insights from comparative genomics. *J. Bacteriol.*, **189**, 8693–8703.
8. Toro,E., Hong,S.-H., McAdams,H.H. and Shapiro,L. (2008) *Caulobacter* requires a dedicated mechanism to initiate chromosome segregation. *Proc. Natl. Acad. Sci. U.S.A.*, **105**, 15435–15440.
9. Fogel,M.A. and Waldor,M.K. (2006) A dynamic, mitotic-like mechanism for bacterial chromosome segregation. *Genes Dev.*, **20**, 3269–3282.
10. Ireton,K., Gunther,N.W. and Grossman,A.D. (1994) *spo0J* is required for normal chromosome segregation as well as the initiation of sporulation in *Bacillus subtilis*. *J. Bacteriol.*, **176**, 5320–5329.
11. Mohl,D.A., Easter,J. and Gober,J.W. (2001) The chromosome partitioning protein, ParB, is required for cytokinesis in *Caulobacter crescentus*. *Mol. Microbiol.*, **42**, 741–755.
12. Graham,T.G.W., Wang,X., Song,D., Etson,C.M., van Oijen,A.M., Rudner,D.Z. and Loparo,J.J. (2014) ParB spreading requires DNA bridging. *Genes Dev.*, **28**, 1228–1238.
13. Murray,H., Ferreira,H. and Errington,J. (2006) The bacterial chromosome segregation protein Spo0J spreads along DNA from *parS* nucleation sites. *Mol. Microbiol.*, **61**, 1352–1361.
14. Taylor,J.A., Pastrana,C.L., Butterer,A., Pernstich,C., Gwynn,E.J., Sobott,F., Moreno-Herrero,F. and Dillingham,M.S. (2015) Specific and non-specific interactions of ParB with DNA: implications for chromosome segregation. *Nucleic Acids Res.*, **43**, 719–731.
15. Rodionov,O., Lobocka,M. and Yarmolinsky,M. (1999) Silencing of genes flanking the P1 plasmid centromere. *Science*, **283**, 546–549.
16. Kusiak,M., Gapczyńska,A., Płochocka,D., Thomas,C.M. and Jagura-Burdzy,G. (2011) Binding and spreading of ParB on DNA determine its biological function in *Pseudomonas aeruginosa*. *J. Bacteriol.*, **193**, 3342–3355.
17. Chen,B.-W., Lin,M.-H., Chu,C.-H., Hsu,C.-E. and Sun,Y.-J. (2015) Insights into ParB spreading from the complex structure of Spo0J and parS. *Proc. Natl. Acad. Sci. U.S.A.*, **112**, 6613–6618.
18. Song,D., Rodrigues,K., Graham,T.G.W. and Loparo,J.J. (2017) A network of cis and trans interactions is required for ParB spreading. *Nucleic Acids Res.*, **45**, 7106–7117.
19. Breier,A.M. and Grossman,A.D. (2007) Whole-genome analysis of the chromosome partitioning and sporulation protein Spo0J (ParB) reveals spreading and origin-distal sites on the *Bacillus subtilis* chromosome. *Mol. Microbiol.*, **64**, 703–718.
20. Schumacher,M.A., Tonthat,N.K., Lee,J., Rodriguez-Castañeda,F.A., Chinnam,N.B., Kalliomaa-Sanford,A.K., Ng,I.W., Barge,M.T., Shaw,P.L.R. and Barillà,D. (2015) Structures of archaeal DNA segregation machinery reveal bacterial and eukaryotic linkages. *Science*, **349**, 1120–1124.
21. Sanchez,A., Cattoni,D.I., Walter,J.-C., Rech,J., Parmeggiani,A., Nollmann,M. and Bouet,J.-Y. (2015) Stochastic self-assembly of ParB proteins builds the bacterial DNA segregation apparatus. *Cell Syst.*, **1**, 163–173.
22. Easter,J. Jr and Gober,J.W. (2002) ParB-stimulated nucleotide exchange regulates a switch in functionally distinct ParA activities. *Mol. Cell*, **10**, 427–434.
23. Leonard,T.A., Butler,P.J. and Löwe,J. (2005) Bacterial chromosome segregation: structure and DNA binding of the Soj dimer-a conserved biological switch. *EMBO J.*, **24**, 270–282.
24. Mohl,D.A. and Gober,J.W. (1997) Cell cycle-dependent polar localization of chromosome partitioning proteins in *Caulobacter crescentus*. *Cell*, **88**, 675–684.
25. Le,T.B., Imakaev,M.V., Mirny,L.A. and Laub,M.T. (2013) High-resolution mapping of the spatial organization of a bacterial chromosome. *Science*, **342**, 731–734.
26. Viollier,P.H., Thanbichler,M., McGrath,P.T., West,L., Meewan,M., McAdams,H.H. and Shapiro,L. (2004) Rapid and sequential movement of individual chromosomal loci to specific subcellular locations during bacterial DNA replication. *Proc. Natl. Acad. Sci. U.S.A.*, **101**, 9257–9262.
27. Bergé,M., Campagne,S., Mignolet,J., Holden,S., Théraulaz,L., Manley,S., Allain,F.H.-T. and Viollier,P.H. (2016) Modularity and determinants of a (bi-)polarization control system from free-living and obligate intracellular bacteria. *eLife*, **5**, e20640.
28. Figge,R.M., Easter,J. and Gober,J.W. (2003) Productive interaction between the chromosome partitioning proteins, ParA and ParB, is required for the progression of the cell cycle in *Caulobacter crescentus*. *Mol. Microbiol.*, **47**, 1225–1237.
29. Langmead,B., Trapnell,C., Pop,M. and Salzberg,S.L. (2009) Ultrafast and memory-efficient alignment of short DNA sequences to the human genome. *Genome Biol*, **10**, R25.
30. Quinlan,A.R. and Hall,I.M. (2010) BEDTools: a flexible suite of utilities for comparing genomic features. *Bioinformatics*, **26**, 841–842.
31. Belitsky,B.R. and Sonenshein,A.L. (2013) Genome-wide identification of *Bacillus subtilis* CodY-binding sites at single-nucleotide resolution. *Proc. Natl. Acad. Sci. U.S.A.*, **110**, 7026–7031.
32. Stevenson,C.E., Assaad,A., Chandra,G., Le,T.B., Greive,S.J., Bibb,M.J. and Lawson,D.M. (2013) Investigation of DNA sequence

recognition by a streptomycete MarR family transcriptional regulator through surface plasmon resonance and X-ray crystallography. *Nucleic Acids Res*, **41**, 7009–7022.
33. Sliusarenko,O., Heinritz,J., Emonet,T. and Jacobs-Wagner,C. (2011) High-throughput, subpixel precision analysis of bacterial morphogenesis and intracellular spatio-temporal dynamics. *Mol Microbiol*, **80**, 612–627.
34. Attaiech,L., Minnen,A., Kjos,M., Gruber,S. and Veening,J.-W. (2015) The ParB-*parS* chromosome segregation system modulates competence development in *Streptococcus pneumoniae*. *mBio*, **6**, doi:10.1128/mBio.00662-15.
35. Bowman,G.R., Comolli,L.R., Zhu,J., Eckart,M., Koenig,M., Downing,K.H., Moerner,W.E., Earnest,T. and Shapiro,L. (2008) A polymeric protein anchors the chromosomal origin/ParB complex at a bacterial cell pole. *Cell*, **134**, 945–955.
36. Ebersbach,G., Briegel,A., Jensen,G.J. and Jacobs-Wagner,C. (2008) A self-associating protein critical for chromosome attachment, division, and polar organization in *Caulobacter*. *Cell*, **134**, 956–968.
37. Thanbichler,M. and Shapiro,L. (2006) MipZ, a spatial regulator coordinating chromosome segregation with cell division in *Caulobacter*. *Cell*, **126**, 147–162.
38. Jecz,P., Bartosik,A.A., Glabski,K. and Jagura-Burdzy,G. (2015) A single *parS* sequence from the cluster of four sites closest to *oriC* is necessary and sufficient for proper chromosome segregation in *Pseudomonas aeruginosa*. *PLoS One*, **10**, e0120867.
39. Tran,N.T., Laub,M.T. and Le,T.B.K. (2017) SMC progressively aligns chromosomal arms in *Caulobacter crescentus* but is antagonized by convergent transcription. *Cell Rep.*, **20**, 2057–2071.
40. Jakimowicz,D., Chater,K. and Zakrzewska-Czerwi´nska,J. (2002) The ParB protein of *Streptomyces coelicolor* A3(2) recognizes a cluster of *parS* sequences within the origin-proximal region of the linear chromosome. *Mol. Microbiol.*, **45**, 1365–1377.
41. Badrinarayanan,A., Le,T.B.K. and Laub,M.T. (2015) Rapid pairing and resegregation of distant homologous loci enables double-strand break repair in bacteria. *J. Cell Biol.*, **210**, 385–400.
42. Sullivan,N.L., Marquis,K.A. and Rudner,D.Z. (2009) Recruitment of SMC by ParB-*parS* organizes the origin region and promotes efficient chromosome segregation. *Cell*, **137**, 697–707.
43. Gruber,S. and Errington,J. (2009) Recruitment of condensin to replication origin regions by ParB/SpoOJ promotes chromosome segregation in *B. subtilis*. *Cell*, **137**, 685–696.
44. Minnen,A., Attaiech,L., Thon,M., Gruber,S. and Veening,J.-W. (2011) SMC is recruited to oriC by ParB and promotes chromosome segregation in *Streptococcus pneumoniae*. *Mol. Microbiol.*, **81**, 676–688.
45. Schwartz,M.A. and Shapiro,L. (2011) An SMC ATPase mutant disrupts chromosome segregation in *Caulobacter*. *Mol Microbiol*, **82**, 1359–1374.

Cell Reports

Article

Diversification of DNA-Binding Specificity by Permissive and Specificity-Switching Mutations in the ParB/Noc Protein Family

Graphical Abstract

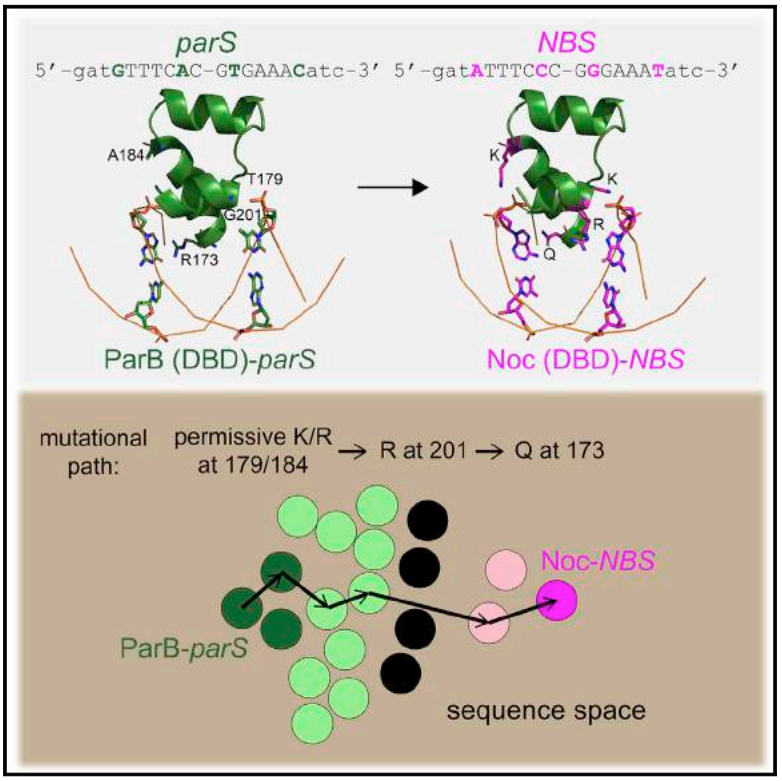

Highlights

- DNA-binding specificity for *parS* and *NBS* is conserved within ParB and Noc family
- Specificity is encoded by a set of four residues at the protein-DNA interface
- Mutations must be introduced in a defined order to reprogram specificity

Authors

Adam S.B. Jalal, Ngat T. Tran, Clare E. Stevenson, ..., Agnes Noy, David M. Lawson, Tung B.K. Le

Correspondence

tung.le@jic.ac.uk

In Brief

Jalal et al. elucidate the molecular basis for how specific protein-DNA interactions can evolve, using ParB and Noc as models. Using X-ray crystallography and deep mutational scanning, they define protein-DNA interfaces and suggest that permissive mutations must be introduced before specificity-switching mutations to reprogram specificity.

Jalal et al., 2020, Cell Reports *32*, 107928
July 21, 2020
https://doi.org/10.1016/j.celrep.2020.107928

CellPress

Cell Reports

CellPress
OPEN ACCESS

Article

Diversification of DNA-Binding Specificity by Permissive and Specificity-Switching Mutations in the ParB/Noc Protein Family

Adam S.B. Jalal,[1,4] Ngat T. Tran,[1,4] Clare E. Stevenson,[2] Elliot W. Chan,[3] Rebecca Lo,[1] Xiao Tan,[1] Agnes Noy,[3] David M. Lawson,[2] and Tung B.K. Le[1,5,*]

[1]Department of Molecular Microbiology, John Innes Centre, Norwich NR4 7UH, UK
[2]Department of Biological Chemistry, John Innes Centre, Norwich NR4 7UH, UK
[3]Department of Physics, Biological Physical Sciences Institute, University of York, York YO10, UK
[4]These authors contributed equally
[5]Lead Contact
*Correspondence: tung.le@jic.ac.uk
https://doi.org/10.1016/j.celrep.2020.107928

SUMMARY

Specific interactions between proteins and DNA are essential to many biological processes. Yet, it remains unclear how the diversification in DNA-binding specificity was brought about, and the mutational paths that led to changes in specificity are unknown. Using a pair of evolutionarily related DNA-binding proteins, each with a different DNA preference (ParB [Partitioning Protein B] and Noc [Nucleoid Occlusion Factor], which both play roles in bacterial chromosome maintenance), we show that specificity is encoded by a set of four residues at the protein-DNA interface. Combining X-ray crystallography and deep mutational scanning of the interface, we suggest that permissive mutations must be introduced before specificity-switching mutations to reprogram specificity and that mutational paths to new specificity do not necessarily involve dual-specificity intermediates. Overall, our results provide insight into the possible evolutionary history of ParB and Noc and, in a broader context, might be useful for understanding the evolution of other classes of DNA-binding proteins.

INTRODUCTION

In living organisms, hundreds of DNA-binding proteins carry out a plethora of roles in homeostasis, in transcriptional regulation in response to stress, and in the maintenance and transmission of genetic information. These DNA-binding proteins do so faithfully due to their distinct DNA-binding specificity toward their cognate DNA sites. Yet, it remains unclear how related proteins, sometimes with a very similar DNA-recognition motif, can recognize entirely different DNA sites. What were the changes at the molecular level that brought about the diversification in DNA-binding specificity? As these proteins evolved, did the intermediates in this process drastically switch DNA-binding specificity, or did they transit gradually through promiscuous states that recognized multiple DNA sequences? Among the many ways to evolve new biological innovations, gene duplication and neo-functionalization have been widely implicated as major forces in evolution (Conrad and Antonarakis, 2007; Kaessmann, 2010; Lynch and Conery, 2000; Qian and Zhang, 2014; Teichmann and Babu, 2004). In this process, after a gene was duplicated, one copy retained the original function, whereas the other accumulated beneficial and diverging mutations that produced a different protein with a new function. In the case of DNA-binding proteins, a new function could be the recognition of an entirely different DNA site. In this work, we used a pair of related DNA-binding proteins (ParB [Partitioning Protein B] and Noc [Nucleoid Occlusion Factor]) that are crucial for bacterial chromosome segregation and maintenance to better understand factors that might have influenced the evolution of a new DNA-binding specificity.

ParB is important for faithful chromosome segregation in two-thirds of bacterial species (Lin and Grossman, 1998; Livny et al., 2007). The centromere-like *parS* DNA locus is the first to be segregated following chromosome replication (Lagage et al., 2016; Lim et al., 2014; Lin and Grossman, 1998; Livny et al., 2007; Toro et al., 2008). *parS* is bound by ParB, which in turn interacts with ParA and SMC proteins to partition the ParB-*parS* nucleoprotein complex and, hence the chromosome, into each daughter cell (Fisher et al., 2017; Fogel and Waldor, 2006; Gruber and Errington, 2009; Ireton et al., 1994; Lin and Grossman, 1998; Mohl and Gober, 1997; Tran et al., 2017, 2018; Wang et al., 2015; Figure 1A). ParB specifically recognizes and binds to *parS*, a palindromic sequence (Figure 1A) that can be present as multiple copies on the bacterial chromosome but is almost always located close to the origin of replication (*oriC*) on each chromosome (Figure 1A; Harms et al., 2013; Jakimowicz et al., 2002; Kawalek et al., 2018; Lagage et al., 2016; Lin and Grossman, 1998; Livny et al., 2007; Murray et al., 2006; Tran et al., 2018). ParB proteins are widely distributed in bacteria and so must have appeared early in evolution (Figure 1B; Livny et al., 2007).

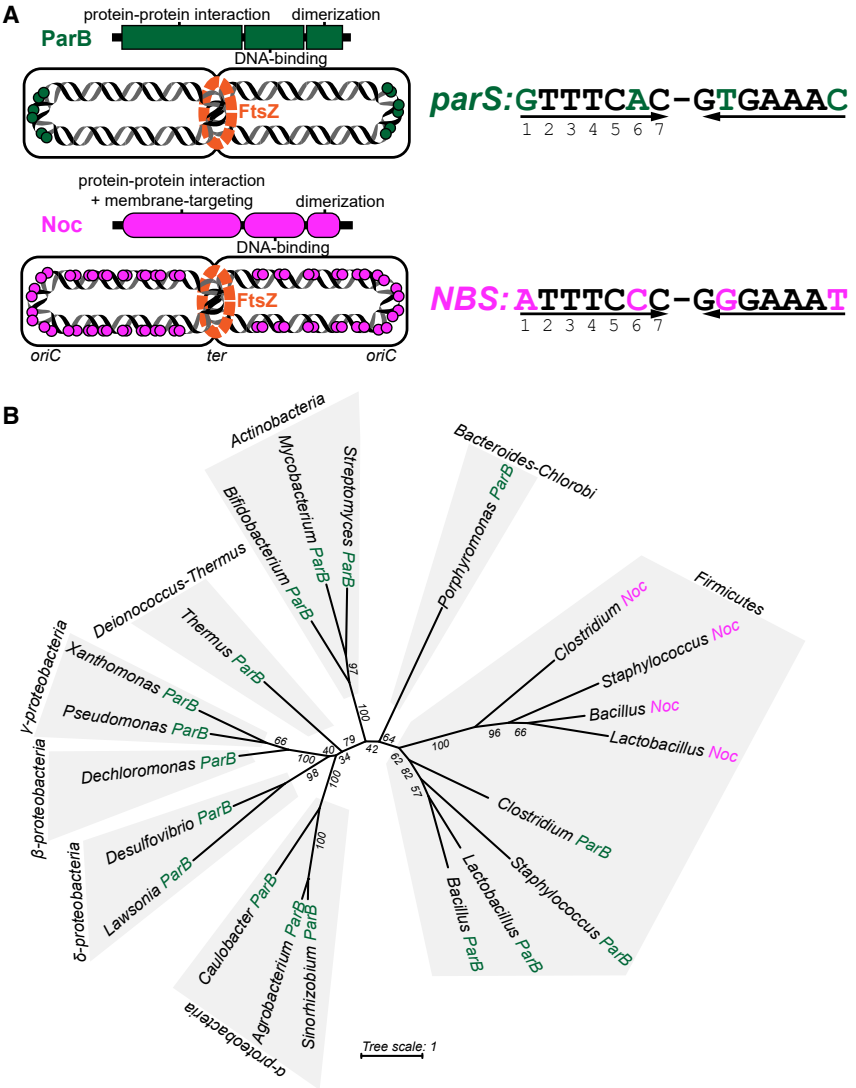

Figure 1. DNA-Binding Specificity for *parS* and *NBS* Is Conserved among ParB and Noc Orthologs

(A) The domain architecture of ParB (dark green) and Noc (magenta) together with their respective cognate DNA-binding sites *parS* and *NBS*. Sequence differences between *parS* and *NBS* are highlighted (*parS*, dark green; *NBS*, magenta). The genome-wide distributions of *parS* and *NBS* sites (dark green and magenta circles, respectively) are also shown schematically.

(B) An unrooted maximum likelihood tree that shows the restrictive distribution of Noc orthologs (magenta branches) to the Firmicutes clade. Bootstrap support values are shown for branches.

(C) The *in vivo* binding preferences of ParB/Noc to *parS*/*NBS*, as measured by ChIP-qPCR. Error bars represent standard deviation (SD) from three replicates. An *E. coli* strain with a single *parS* and *NBS* site engineered onto the chromosome was used as a heterologous host for the expression of FLAG-tagged ParB/Noc.

Noc, a ParB-related protein, was first discovered in *Bacillus subtilis* (Sievers et al., 2002; Wu and Errington, 2004). Like ParB, Noc has a three-domain architecture: an N-terminal domain for protein-protein interactions and for targeting Noc to the cell membrane, a central DNA-binding domain (DBD), and a C-terminal dimerization domain (Wu and Errington, 2004; Wu et al., 2009; Figure 1A). In contrast to ParB, Noc recognizes a DNA-binding sequence called *NBS* (Noc Binding Site) (Pang et al., 2017; Wu et al., 2009; Figure 1A). The role of Noc is also different from ParB; Noc functions to prevent the cell division machinery from assembling in the vicinity of the nucleoid, which might be otherwise guillotined, thereby damaging the DNA (Wu and Errington, 2004; Wu et al., 2009: Figure 1B). In other words, Noc has a role in preserving the integrity of the chromosome. The genome-wide distribution of *NBS* is also drastically different from that of *parS*. Although *parS* sites are restricted in the region around *oriC*, *NBS* distributes widely on the genome, except near the terminus of replication (*ter*) (Pang et al., 2017; Wu et al., 2009). The absence of *NBS* near *ter* is crucial to direct the formation of the FtsZ ring and cell division to mid-cell (Figure 1A). Because of their genomic proximity (Figure S1) and high sequence similarity, it was suggested that *noc* resulted from a gene duplication event from *parB* (Sievers et al., 2002; Wu and Errington, 2011). A phylogenetic tree showed that *parB* genes are widely distributed in bacteria but *noc* genes are confined to the Firmicutes clade (Wu and Errington, 2011; Figure 1B). This phylogenetic distribution is most consistent with *parB* appearing early in evolution, possibly before the split between Gram-positive and Gram-negative bacteria, and that the occurrence of *noc* is a later event that happened only in Firmicutes (Wu and Errington, 2011).

Here, we systematically measure the binding preferences of 17 ParB and 4 Noc family members to *parS* and *NBS* and find that their interactions are specific and conserved among bacterial species. We show that specificity to *parS* or *NBS* is encoded by a small set of four residues at the protein-DNA interface and that mutations in these residues are enough to reprogram DNA-binding specificity. Combining X-ray crystallography and systematic scanning mutagenesis, we show that both permissive and specificity-switching substitutions are required to acquire a new DNA-binding specificity. Guided by these findings, we generate a saturated library with ~10^5 variants of the specificity-defining residues in ParB and select for mutants that bind to *parS* or *NBS* or both. We discover multiple alternative combinations of residues that are capable of binding to *parS* or *NBS*. By analyzing the connectivity of functional variants in the sequence space, we suggest that permissive and specificity-switching mutations, at least when considering the four mutations in this work, must be introduced in an orderly manner to evolve a new protein-DNA interface.

RESULTS

DNA-Binding Specificity for *parS* and *NBS* Is Conserved within ParB and Noc Family

To test whether ParB and Noc family members retained their DNA-binding specificity, we selected a group of 17 ParB and 4 Noc from various bacterial clades for characterization (Figures 1B and S1A). ParB or Noc proteins were expressed individually in *Escherichia coli* and were engineered with an N-terminal FLAG tag for immunoprecipitation. We performed chromatin immunoprecipitation (ChIP)-qPCR and ChIP sequencing (ChIP-seq) experiments to quantify the level of ParB or Noc that are bound at a single *parS* or *NBS* site engineered onto the *E. coli* chromosome (Figures 1C and S1B). *E. coli* is a perfect heterologous host for this experiment, as it does not possess native ParB/Noc homologs and there are no *parS*/*NBS* sites in its genome. As shown in Figure 1C, all tested ParB proteins bind preferentially to *parS* over *NBS*, whereas Noc proteins prefer *NBS* to *parS*. This conservation of DNA preference suggests that there exists a set of conserved residues within each protein family (ParB or Noc) that dictates specificity.

The Co-crystal Structure of the DBD of ParB with *parS* Reveals Residues That Contact DNA

As the first step in identifying specificity residues, we solved a 2.4-Å resolution co-crystal structure of the DBD of *Caulobacter crescentus* ParB bound to a 20-bp *parS* DNA duplex (Figure 2A). In the crystallographic asymmetric unit, two very similar ParB DBD monomers (root-mean-square deviation [RMSD] = 0.1 Å) bind in a 2-fold symmetric fashion to a full-size *parS* DNA duplex (Figure 2A). This structure reveals several regions of each DBD that contact *parS* (Figure 2B). First, the recognition helix α4 of the helix-turn-helix motif inserts into the major grooves of the palindromic *parS* site (Figure 2B). Second, helices α6 and α8 contribute residues to the protein-DNA interface (Figure 2B). Last, several lysine and arginine residues in the loop spanning residues 236–254 contact the minor groove side of *parS* in an adjacent complex in the crystal (Figure 2A). From the structure of the complex, we identified residues that make specific contacts with the DNA bases as well as non-specific contacts with the phosphate backbone (Figure 2C). We verified the protein-DNA contacts by individually mutating each residue to alanine (Figure 2D). We found that most of the crucial residues for binding to *parS* are within the 162–234 region (Figure 2D), suggesting their importance in recognizing DNA specifically. We reasoned that specificity residues for *parS* (and *NBS*) must localize within this amino acid (aa) region in ParB (and in an equivalent region in Noc).

Mutations at Four Residues at the ParB-*parS* Interface Are Sufficient to Reprogram DNA-Binding Specificity toward *NBS*

To discover the region of Noc that determines the specificity for *NBS*, we constructed a series of chimeric proteins in which different regions of *Caulobacter* ParB were replaced with the corresponding regions of *B. subtilis* Noc (Figure 3A). Replacing the entire region (residues 162–230) containing the helix-turn-helix motif, helix α6, and part of helix α8 with the corresponding region of *B. subtilis* Noc produced a chimera that binds to both *parS* and *NBS*, but with a preference for *NBS* (Chimera 1; Figure 3A). Swapping a smaller region (residues 162–207) containing just the helix-turn-helix motif and an adjacent helix α6 created a chimera that has an improved specificity for *NBS*, albeit with a lower binding affinity (Chimera 4; Figure 3A). These results suggest that the region (residues 162–207) might contain the core set of specificity residues for *NBS*.

To better understand the high degree of specificity conserved within the ParB and Noc families, we mapped a sequence alignment of ~1,800 ParB and ~400 Noc orthologs onto the ParB (DBD)-*parS* crystal structure to determine aa sequence preferences for those residues required for interaction specificity

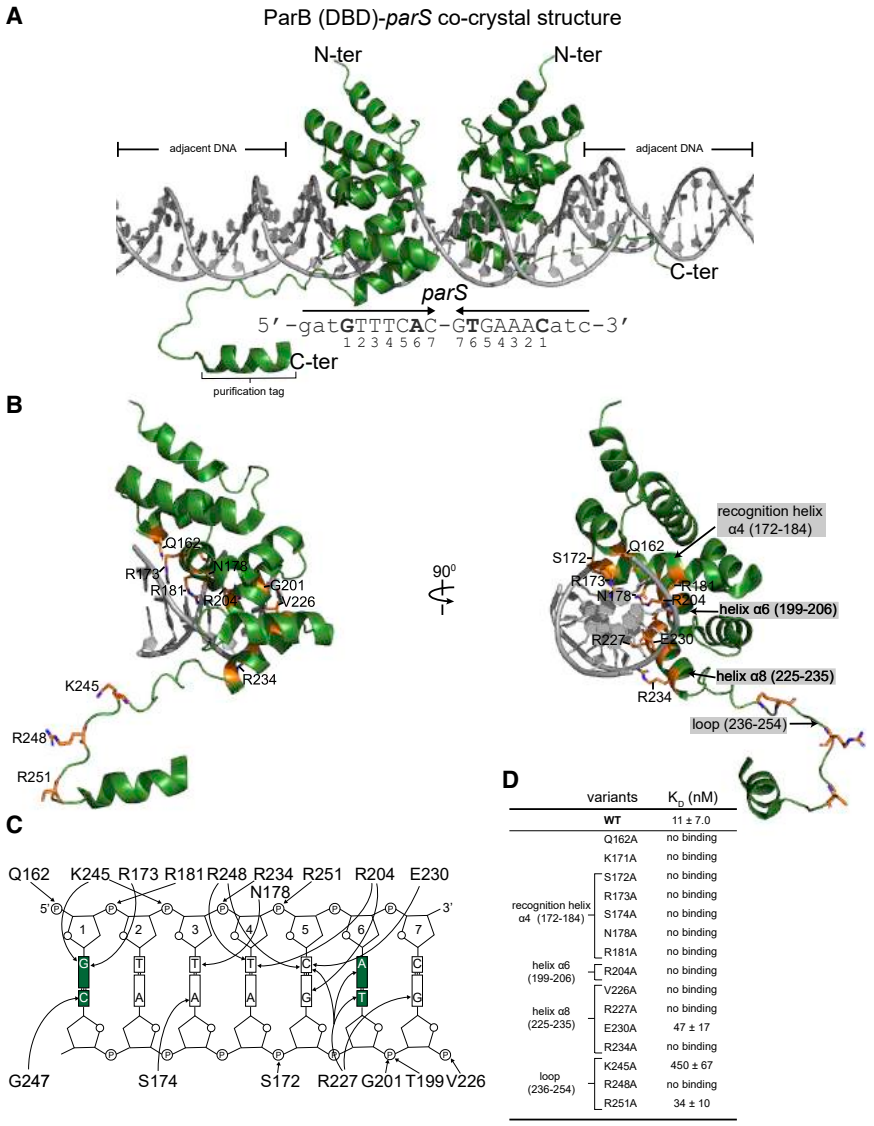

Figure 2. Co-crystal Structure of the DBD of *Caulobacter* ParB with *parS*

(A) The 2.4-Å resolution structure of two ParB (DBD) monomers (dark green) in complex with a 20-bp *parS* DNA (gray). The nucleotide sequence of the 20-bp *parS* is shown below the structure; bases (guanine 1 and adenine 6) that are different from *NBS* are in bold. The purification tag is also visible in one of the DBD monomers. Loop (236–254) contacts the adjacent DNA in the crystal lattice.

(B) One monomer of ParB (DBD) is shown in complex with a *parS* half-site; residues that contact the DNA are labeled and colored in orange.

(C) Schematic representation of ParB (DBD)-*parS* interactions. For simplicity, only a *parS* half-site is shown. The two bases at position 1 and 6 that are different between *parS* and *NBS* are highlighted in dark green.

(D) Alanine scanning mutagenesis and the *in vitro* dissociation constant (K_D) ± standard deviation (SD) of ParB variants to *parS* DNA. See also STAR Methods for details on curve fitting and calculation of SD values.

completely switched its binding preference to a non-cognate *NBS* site. Hence, a core set of four residues are enough to reprogram specificity.

Systematic Dissection of ParB-*parS* and Noc-*NBS* Interfaces Reveals the Contribution of Each Specificity Residue to the DNA-Binding Preference

To systematically dissect the role of each specificity residue, we constructed a complete set of ParB mutants that have either single, double, or triple aa changes between the four specificity positions, from a *parS*-preferred *Caulobacter* ParB ($R^{173}T^{179}A^{184}G^{201}$) to an *NBS*-preferred variant ($Q^{173}K^{179}K^{184}R^{201}$). We named them ParB-to-Noc intermediates (PtoN; 15 variants in total). To simplify the nomenclature, we named the mutants based on the specificity residues being considered, for example, an *NBS*-preferred variant ($Q^{173}K^{179}K^{184}R^{201}$) is shortened to PtoN15 (QKKR). ParB and 15 PtoN variants were purified and tested with a series of 16 different DNA sites, each representing a transitional state from *parS* to *NBS*, with each of the 2 variable positions (1 and 6) changed to any of other 4 DNA bases (Figure 3C). We visualized 16 × 16 interactions as a heatmap where each matrix position reflects a dissociation constant (K_D).

This systematic pairwise interaction screen led to several notable observations (Figure 3C). First, there are 2 non-functional variants (PtoN1: QTAG and PtoN7: QTAR) that were unable to interact with any of the 16 DNA sites (Figure 3C). Second, six variants (PtoN4: RTAR, PtoN5: QKAG, PtoN6: QTKG, PtoN9: RKAR, PtoN10: RTKR, and PtoN11: QKKG) switched their specificity to a DNA site that has features borrowed from both *parS* and *NBS*. Meanwhile, four variants (PtoN2: RKAG, PtoN3: RTKG, PtoN8:

(Figure 3B). We focused our attention on the region between residues 162 and 207, which was shown above to contain the core specificity residues (Figure 3B). Of those residues that contact *parS* (Figures 2B and 2C), six residues (Q162, G170, K171, S172, N178, and R204) are conserved between ParB and Noc family members (Figure 3B). Two residues (R173 and G201) in ParB contact *parS* but are changed to Q173 and R201, respectively, in Noc homologs (Figure 3B). Other residues at positions 179 and 184 vary among ParB homologs but are almost invariably a lysine in Noc family members (Figure 3B). We hypothesized that these residues (Q173, K179, K184, and R201) (Figure 3B) are specificity residues that dictate Noc preference for *NBS*. To test this hypothesis, we generated a variant of *Caulobacter* ParB in which these four residues were introduced at the structurally equivalent positions (R173Q, T179K, A184K, and G201R). We purified and tested this variant in a bio-layer interferometry assay with *parS* and *NBS*. As shown in Figure 3A, a ParB (RTAG→QKKR) (PtoN15) variant

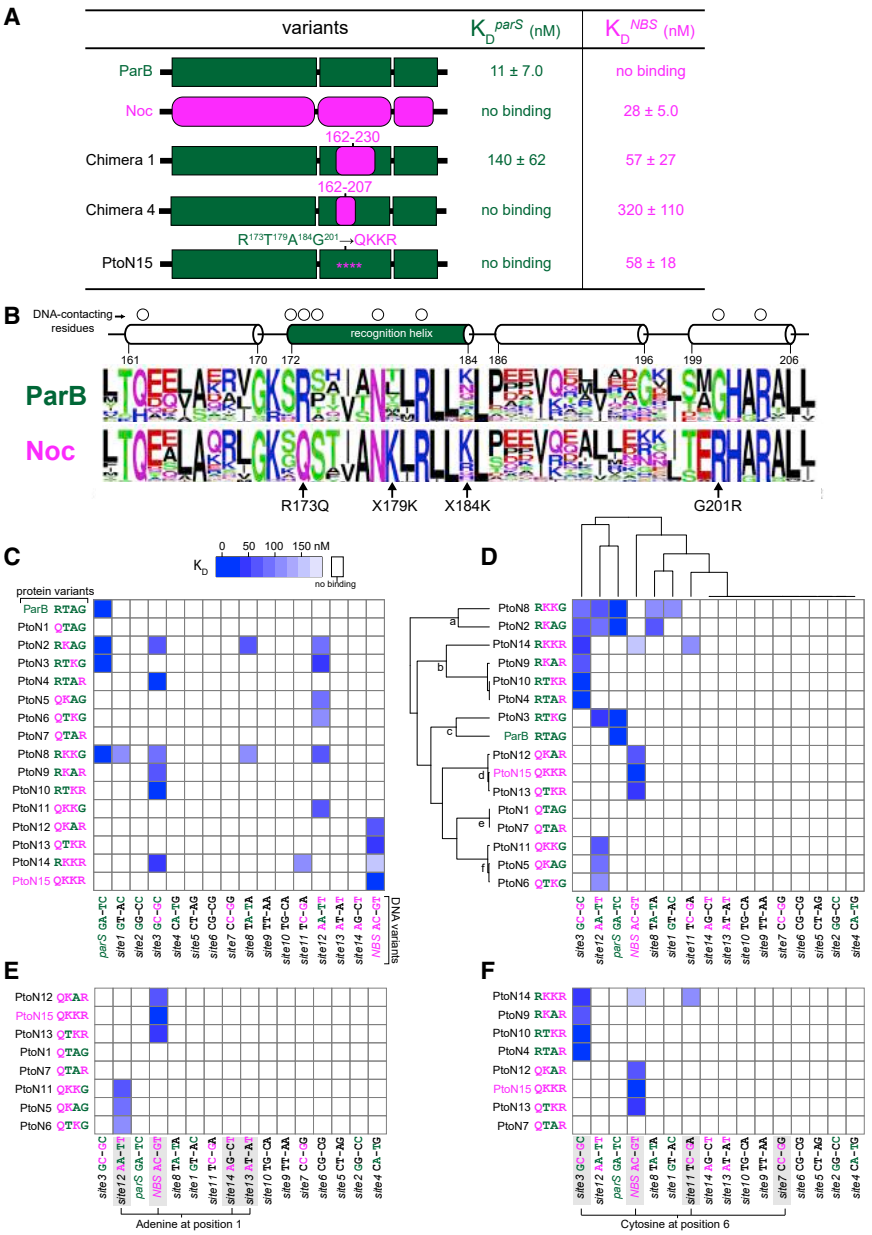

Figure 3. Mutations at Four Residues at the ParB-*parS* Interface Are Sufficient to Reprogram DNA-Binding Specificity Toward *NBS*

(A) Mutations in a subset of residues in the region between residues 162–207 (ParB's numbering) can reprogram interaction specificity. ParB (or segments of amino acids [aas] from ParB) and Noc (or the equivalent segment in Noc) are shown in dark green and magenta, respectively. The affinity of protein-DNA interaction was expressed as dissociation constant (K_D) ± standard deviation (SD). See also STAR Methods for details on curve fitting and calculation of SD values.

(B) The sequence alignment of ParB (~1,800 sequences) and Noc (~400 sequences) orthologs. The aas are colored based on their chemical properties (GSTYC, polar; QN, neutral; KRH, basic; DE, acidic; and AVLIPWFM, hydrophobic). The secondary structure of the aa region (residues 162–207) is shown above the sequence alignment, together with residues (open circles) that contact DNA in the ParB (DBD)-*parS* structure (Figure 2).

(C) Systematic scanning mutagenesis of the protein-DNA interface reveals the contribution of each specificity residue to the DNA-binding preference. Interactions between ParB + 15 PtoN intermediates with 16 DNA sites are represented as a heatmap in which each matrix position reflects a K_D value. The aa residues/bases from ParB/*parS* are colored in dark green, and those from Noc/*NBS* in magenta.

(D) A hierarchical clustering of data in (C) in both protein and DNA dimensions.

(E) A simplified heatmap in which only PtoN intermediates with a glutamine (Q) at position 173 are shown.

(F) A simplified heatmap in which only PtoN intermediates with an arginine (R) at position 201 are shown.

RKKG, and PtoN14: RKKR) were promiscuous, i.e., binding to multiple different DNA sites (Figure 3C). We noted that functional PtoN variants have a lysine at either position 179 or 184 or both. This observation became even clearer after we performed hierarchical clustering of the interaction profile in both the protein and the DNA dimensions (Figure 3D). A single lysine at either position 179 or 184 is enough to license the DNA-binding capability to PtoN variants (nodes a, b, d, and f on the clustering tree; Figure 3D), whereas PtoN1 (QTAG) and PtoN7 (QTAR) that do not possess any lysine at 179/184 are non-functional (node e; Figure 3D). We suggest that K179/184 has a permissive effect that might permit Q173 and R201 to contact DNA.

Next, we wondered which base of the *NBS* site that Q173 might contact specifically. To find out, we clustered only PtoN variants that share the Q aa at position 173 (Figure 3E). We discovered that those variants preferred DNA sites that possess an adenine at position 1 (Figure 3E). We applied the same approach to find the base that residue R201 might contact (Figure 3F). The emerging trend is that PtoN variants that share an R aa at 201 preferred DNA sites with a cytosine at position 6 (Figure 3F). Taken together, our results suggest a model in which each specificity residue has a distinct role, namely, Q173 recognizes adenine 1 and R201 recognizes cytosine 6, but they can only do so in the presence of a permissive K at either position 179 or 184 or both. In the next section, we used X-ray crystallography to provide evidence to support this model.

Co-crystal Structure of the DBD of Noc with *NBS* Reveals the Contribution of Specificity Residues to the DNA-Binding Preference

To understand the biophysical mechanism underlying the specificity to *NBS*, we solved the co-crystal structure of *B. subtilis*

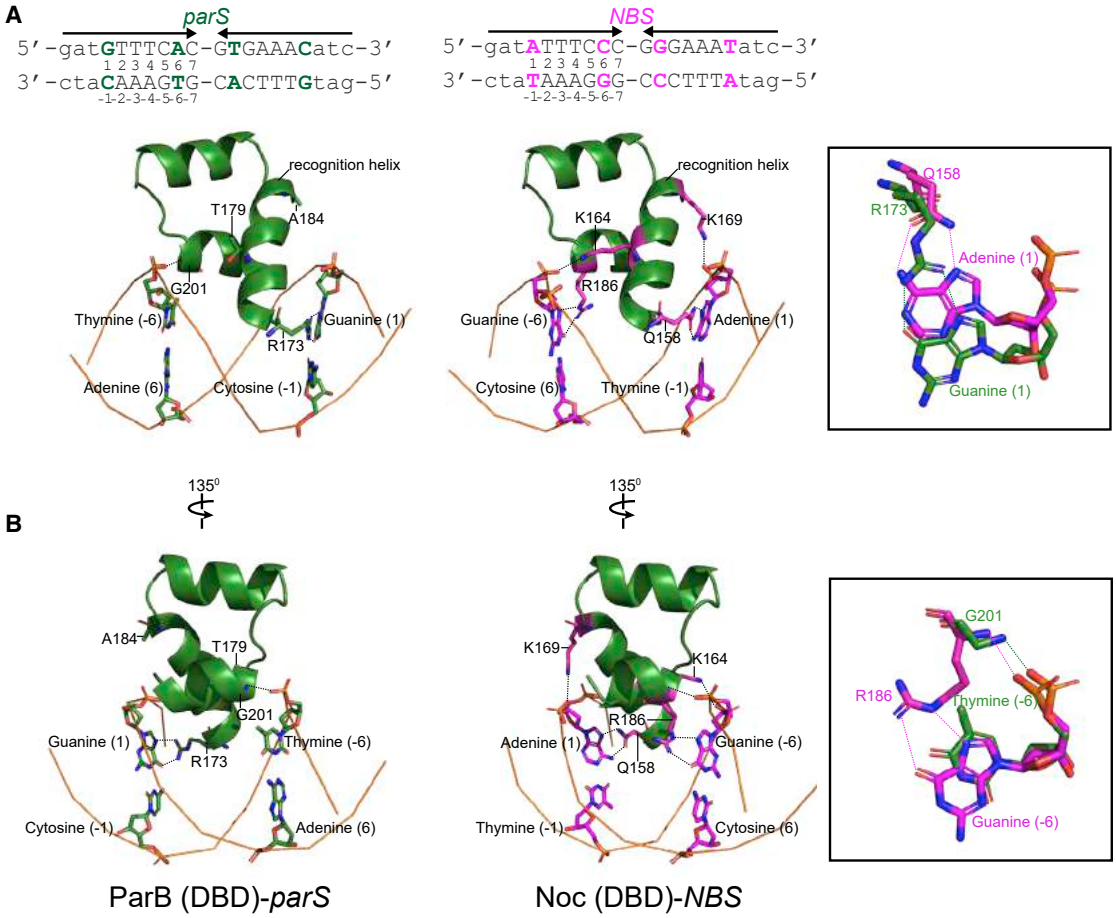

Figure 4. Superimposition of the ParB (DBD)-*parS* Structure on the Noc (DBD)-*NBS* Structure Reveals the Contribution of Specificity Residues to *NBS* Binding

To simplify and highlight the roles of specificity residues, only the side chains of specificity residues and their contacting bases are shown. The aa regions (173–207 in ParB and the corresponding 158–192 in Noc) and the DNA backbones are shown in the cartoon representation. DNA bases are numbered according to their respective positions on the *parS*/*NBS* site. The insets show interactions between either R173 (ParB's numbering) and Q158 (Noc's numbering) (A) or G201 (ParB's numbering) and R186 (Noc's numbering) (B) and with their corresponding bases on *parS*/*NBS*. The side chains of K164 and K169 in the Noc (DBD)-*NBS* structure contact the phosphate groups of guanine (−5) and thymine (2) of *NBS*, respectively (see also Figure S2D). Only the phosphate groups of guanine (−5) and thymine (2) in *NBS* are shown.

Noc (DBD) with a 22-bp *NBS* DNA duplex (Figure S2). The diffraction of the Noc (DBD)-*NBS* crystal was anisotropic. Hence, despite the 2.23-Å resolution limit, because of low completeness in the higher resolution shells resulting from the anisotropic cutoff, the resultant electron density has the appearance of lower resolution maps, approximately a 3-Å resolution (Table S4; STAR Methods). By superimposing the structures of ParB (DBD)-*parS* and Noc (DBD)-*NBS* complexes, we observed several changes in both the protein and the DNA sites that enabled specific interactions (Figure 4). First, R173 in ParB hydrogen bonds with *parS* guanine 1, but the shorter side chain of a corresponding Q158 in Noc is unable to bond with guanine 1 (Figure 4A). However, a corresponding base in *NBS* (adenine 1) positions itself closer to enable hydrogen bonding with this Q173 residue (Figure 4A); this is possibly due to conformational changes in the *NBS* site that narrows the minor groove width at the adenine 1:thymine −1 position (from ~7.7 to ~3.7 Å; Figure S3). The switch from R to Q serves to eliminate the ability of ParB to contact *parS* guanine 1 while simultaneously establishing a new contact with *NBS* adenine 1. The second notable changes between the two co-crystal structures occurs at position 201 (Figure 4B). G201 from ParB has no side chain and hence cannot contact thymine −6 specifically (Figure 4B). However, the equivalent residue R186 in Noc readily forms hydrogen bonds with guanine −6 (Figure 4B). We also observed DNA unwinding that increased both the minor and the major groove widths at the cytosine 6:guanine −6 position of *NBS* (from ~7.1 to ~8.1 Å and from ~10.5 to ~11.8 Å, respectively), possibly to move guanine −6 outward to accommodate a longer side chain of arginine (Figure S3). The NH group in the main chain of both G201 (ParB (DBD)-*parS* structure) and R186 (Noc(DBD)-*NBS* structure) also contact DNA non-specifically by their interaction with the phosphate groups of thymine −6 (*parS*) and guanine −6 (*NBS*), respectively (Figure 4; see also Figures 2C and S2D).

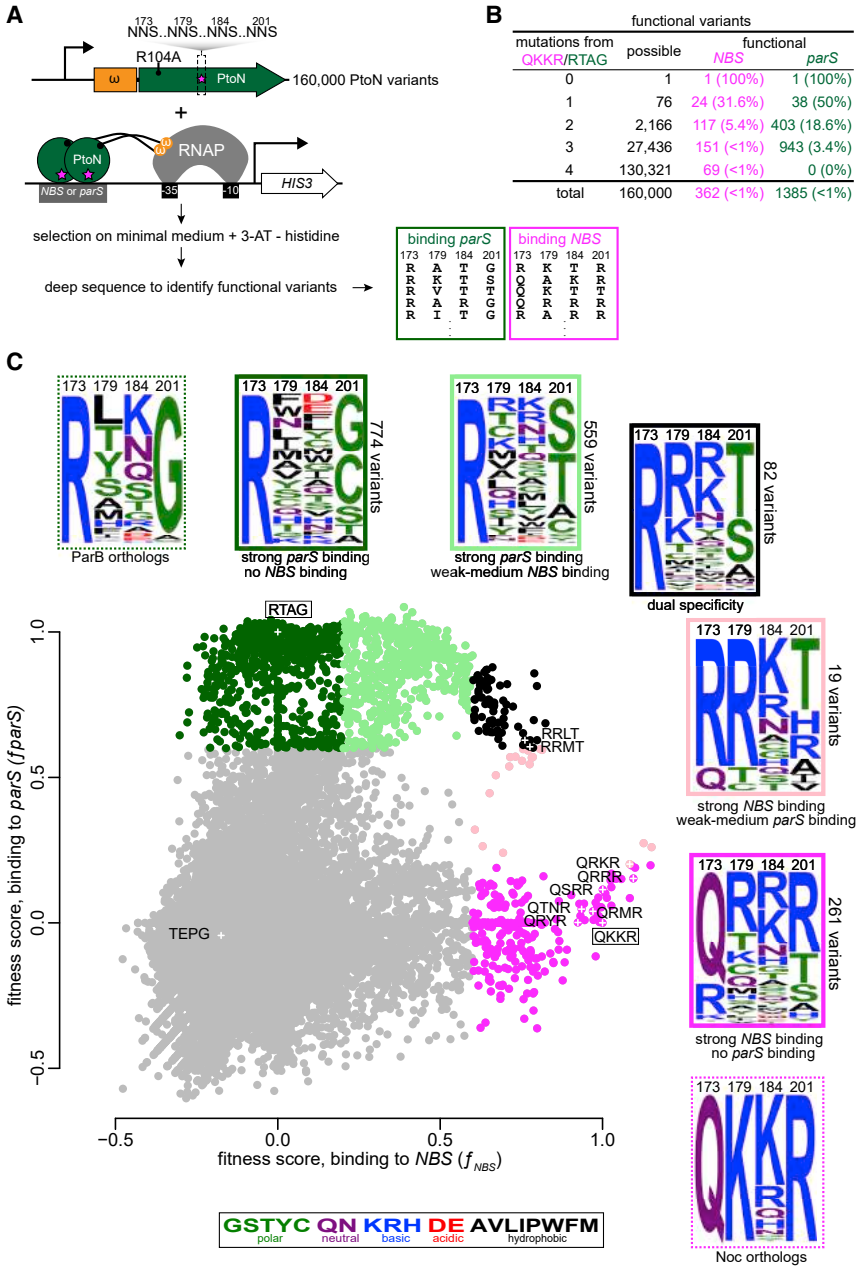

Figure 5. High-Throughput Mapping of the Fitness of Protein-DNA Interface Mutants

(A) The principle and design of the deep mutational scanning experiment that was based on a bacterial one-hybrid assay and high-throughput sequencing.

(B) Summary of functional *NBS*-binding and *parS*-binding variants.

(C) Fitness scores of variants, as assessed by their ability to bind *NBS* (x axis) or *parS* (y axis). Dark green: strong *parS* binding, no *NBS* binding (fitness score: $f_{parS} \geq 0.6$, $f_{NBS} \leq 0.2$); light green: strong *parS* binding, weak-to-medium *NBS* binding ($f_{parS} \geq 0.6$, $0.2 \leq f_{NBS} \leq 0.6$); magenta: strong *NBS* binding, no *parS* binding ($f_{NBS} \geq 0.6$, $f_{parS} \leq 0.2$); pink: strong *NBS* binding, weak-to-medium *parS* binding ($f_{NBS} \geq 0.6$, $0.2 \leq f_{parS} \leq 0.6$); black: dual specificity ($f_{NBS} \geq 0.6$, $f_{parS} \geq 0.6$). Frequency logos of each class of variants are shown together with ones for ParB/Noc orthologs. The amino acids are colored according to their chemical properties. The positions of wild-type (WT) ParB (RTAG), Noc (QKKR), and nine selected variants for an independent validation are also shown and labeled on the scatterplot.

Our Noc (DBD)-*NBS* structure also shows the side chains of K164 and K169 make hydrogen bonds with the phosphate groups of guanine −5 and thymine 2 of *NBS* rather than contacting any bases specifically (Figure S2D). Last, molecular dynamics simulations using the Noc (DBD)-*NBS* structure as initial coordinates also suggested that side chains of K164 and K169 make hydrogen bonds or salt bridges with the DNA backbone, especially when water-mediated contacts were also considered (bonding for >99% of the whole simulation; see also STAR Methods). The most parsimonious explanation for the permissive capability of K164/169 is that they increase DNA-binding affinity non-specifically to overcome the initial energy barrier and permit specific base contacts from Q158 and R186. Overall, our co-crystal structures are consistent with data from the systematic scanning mutagenesis.

A High-Throughput Bacterial One-Hybrid Selection Reveals Multiple Combinations of Specificity Residues That Enable *parS* and *NBS* Recognition

Although the results from our systematic scanning mutagenesis and X-ray crystallography revealed how specificity changed as individual substitutions were introduced, presumably a greater variety of amino acids has been sampled by nature than those presented at the start (RTAG) and endpoint (QKKR). What are the paths, and are there many, to convert a *parS*-binding protein to an *NBS*-preferred one? Does the order of aa substitutions matter? To answer these questions, we explored the entire sequence space at the four specificity residues by generating a combinatorial library of ParB where positions 173, 179, 184, and 201 can be any aa (20^4 or 160,000 variants lacking stop codons). We optimized a bacterial one-hybrid (B1H) assay (Noyes et al., 2008) that is based on transcriptional activation of an imidazoleglycerol-phosphate dehydratase encoding gene HIS3 to enable a selection for *parS* or *NBS*-binding variants (Figure 5A; Figure S4). ParB variants were fused at their N termini to the omega subunit of bacterial RNA polymerase. NNS codons (where N = any nucleotide [nt] and S = cytosine or guanine) were used to randomize the four specificity residues. All ParB

variants were also engineered to contain an additional invariable mutation in the N-terminal domain (R104A) that makes ParB unable to spread (Lee and Grossman, 2006; Tran et al., 2018; Figure 5A). The R104A mutation does not affect the site-specific binding but enables a simpler design of the selection system by converting ParB to a conventional site-specific transcriptional activator (Figure 5A). If a ParB variant binds to a *parS* or *NBS* site engineered upstream of HIS3, it will recruit RNA polymerase to activate HIS3 expression, thereby enabling a histidine-auxotrophic *E. coli* host to survive on a minimal medium lacking histidine (Figure 5A; Figure S4). Deep sequencing of starting libraries revealed that >94% of the predicted variants were represented by at least 10 reads (Figures S5A and S5B) and that libraries prepared on different days were reproducible (R^2 > 0.90; Figure S5C).

To assess the ability of each ParB variant to bind to *parS* or *NBS*, we deep sequenced the relevant region on *parB* variants pre- and post-selection to reveal the underlying sequences and their abundance (Figure 5A; Figure S5C). As the strength of protein-DNA interaction is directly related to the amount of histidine being produced and ultimately to the cell fitness (Noyes et al., 2008), we quantified the fitness of each variant to rank them (Figure 5C). We found 1,385 and 362 variants that show strong binding to *parS* and *NBS*, respectively (Figure 5B). We then selected and verified nine variants that bind either *NBS* or *parS* or both (Figure 5C) by a pairwise B1H assay and by a bio-layer interferometry assay with purified proteins (Figure S6). To systematically probe the sequence space, we generated a scatterplot of ParB variant fitness when screened for binding to *parS* or *NBS* (Figure 5C). Of 362 variants that bind *NBS* strongly, 261 are *NBS* specific (i.e., no *parS* binding, magenta box), 19 show strong *NBS* binding but weak-to-medium *parS* binding (pink box), and 82 dual-specificity variants that bind both *parS* and *NBS* (black box) (Figure 5C). By comparing sequence logos, we observed that *NBS*-specific variants (magenta box) have a high proportion of the Q residue at position 173 but R is allowed, position 201 is dominantly R but polar residues (T and S) are allowed, and positively charged R and K prevail at positions 179 and 184 (Figure 5C). This sequence logo shares some features with Noc orthologs (dashed magenta box, Figure 5C). On the other hand, *parS*-specific variants (dark green box) have an invariable R at position 173, which is the same as ParB orthologs (dashed dark green box) (Figure 5C), but position 201 can be small polar amino acids (C, S, or T, but G is most preferred). Notably, 17 amino acids (except the helix-breaking P or the negatively charged D and E) can occupy position 179, and any of the 20 amino acids is tolerable at position 184 (Figure 5C). Finally, dual-specificity variants (black box) tend to harbor sequence elements from both *parS*- and *NBS*-specific variants (Figure 5C).

NBS-Specific Variants Predominantly Have Lysine or Arginine at Positions 179 and 184

The proportion of *NBS*-specific variants with a K or R aa at position 179 is ~58%, higher than a theoretical 10% value if K/R was chosen randomly (Figure 6A). The same proportion was seen for a K or R at position 184 (Figure 6A). This proportion increased to ~91% for *NBS*-specific variants with either K or R at either position 179 or 184 and ~19% for those with a K or R at both 179 and 184 (Figure 6A). The prevalence of positively charged residues, together with the structure of Noc (DBD)-*NBS*, supports our model that permissive mutations act by increasing protein-DNA binding affinity non-specifically by their interactions with a negatively charged phosphate backbone. We noted that K and R are not preferred more than expected from a random chance in *parS*-specific variants (Figure 6A). Our results suggest that the introduction of permissive substitutions is important to acquire a new specificity.

Mutations Were Introduced in a Defined Order to Reprogram Specificity

We asked if there is an order of substitutions at positions 173, 179, 184, and 201 to create an *NBS*-specific variant. To answer this question, we first reconstructed all possible mutational paths to an *NBS* specificity. We created a force-directed graph that connects functional variants (nodes) together by lines (edges) if they are different by a single aa to visualize the connectivity of functional variants in sequence space (Figure 6B; Podgornaia and Laub, 2015). The node size is proportional to its connectivity (number of edges), and node colors represent different classes of functional variants (Figure 6B). Similarly, we also generated a network graph in which edges represent variants that differ by a single nt substitution (Figures S7A and S7B). Because not all amino acids can be converted to others by a mutation at a single base, a by-nt-substitution network might depict better how long (hard) or short (easy) the mutational paths that *parS*-specific variants might have taken to reprogram their specificity to *NBS*. At first glance, the network is composed of multiple clusters of densely interconnected nodes that share common features in the aa sequence (Figure 6B). Furthermore, there are multiple edges connecting *parS*-preferred variants (dark and light green nodes) to *NBS*-preferred variants (magenta and pink nodes) (Figure 6B). Supporting this observation, we found that it takes at most four aa (or seven nt) substitutions to convert any *parS*-specific variant to an *NBS*-specific QKKR (Figures 6C and S7C). A small number of steps suggested that *NBS*-specific variants can be reached relatively easily from *parS*-specific variants. We focused on *parS*-specific start point RXXG for all analyses below because R173 and G201 are absolutely conserved in all extant ParB orthologs (Figure 5C). We found all the shortest paths (1,232 in total) that connect *parS*-specific RXXG variants (298 dark green nodes) to an *NBS*-specific QKKR and quantified the fractions of intermediates in such paths that contain permissive or specificity-switching residues (Figure 6D). We discovered that permissive substitutions (K or R) at position 179 or 184 happened very early on along the mutational paths (~95% after the first step; Figure 6D). The fraction of R201 increased more gradually after the introduction of permissive substitutions, and Q173 was introduced last (Figure 6D). The same order of substitutions was seen when we analyzed a by-nt-substitution network graph (Figure S7D). In summary, we conclude that the order of aa substitutions matters and suggest that permissive mutations tend to happen before specificity-switching substitutions.

Mutational Paths That Reprogram Specificity Did Not Travel across Dual-Specificity Intermediates

We observed that the fraction of variants with C/T/S residues at position 201 did not increase beyond 0% in any step from RXXG

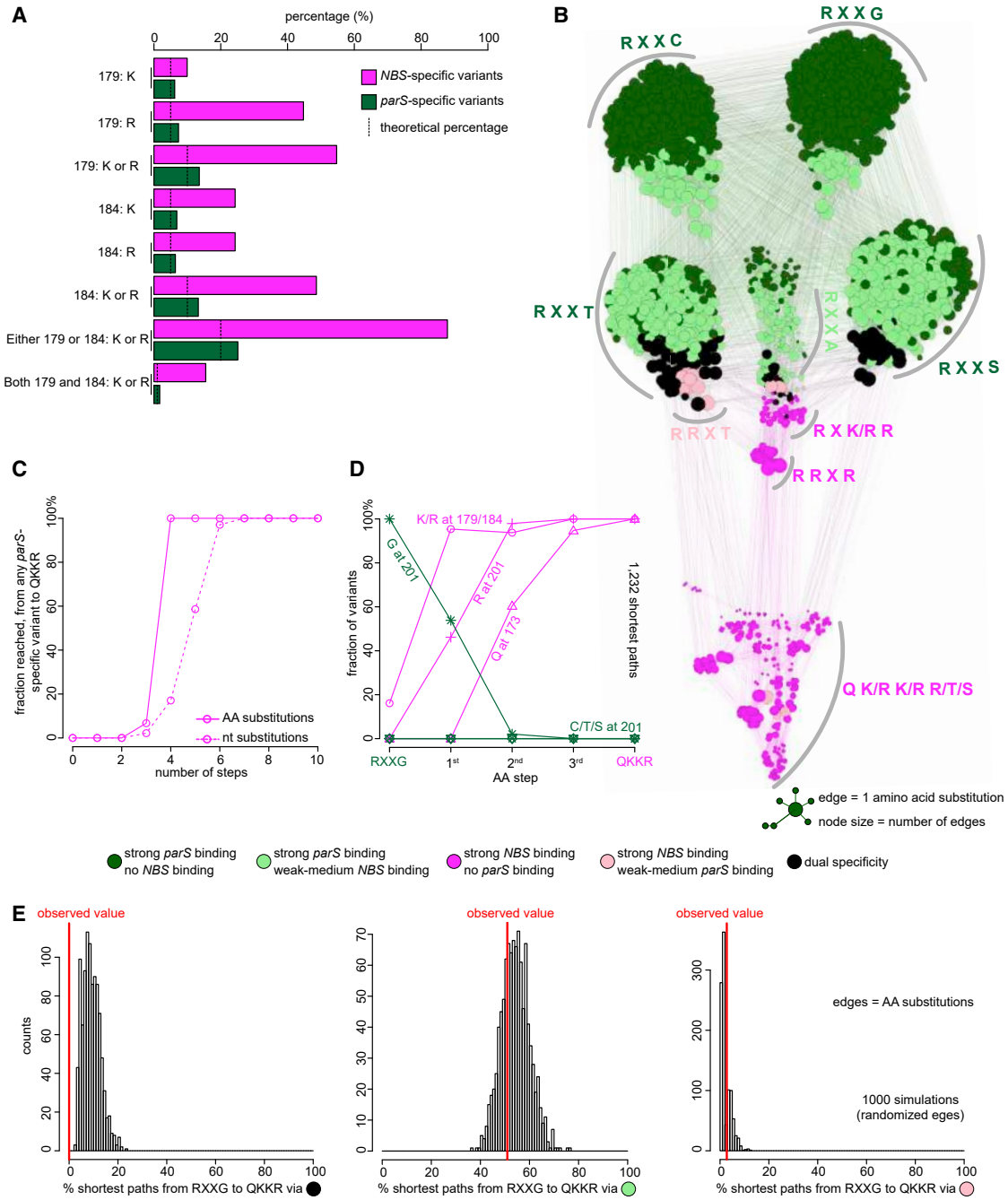

Figure 6. Deep Mutational Scanning Experiments Reveal the Common Properties of the Mutational Paths to a New DNA-Binding Specificity

(A) Fractions of arginine or lysine residues at position 179 or 184 or both, in *parS*-specific (dark green) and *NBS*-specific (magenta) variants. The dotted lines indicate the expected percentage if arginine/lysine was chosen randomly from 20 amino acids.

(B) A force-directed network graph connecting strong *parS*-binding variants to strong *NBS*-binding variants. Nodes represent individual variants, and edges represent single aa substitutions. Node sizes are proportional to their corresponding numbers of edges. Node colors correspond to different classes of variants.

(C) Cumulative fraction of highly *parS*-specific variants that reached an *NBS*-specific QKKR variant in a given number of aa (solid line) or nt (dotted line) substitutions (see also Figure S7A).

(D) Fraction of intermediates on all shortest paths from highly *parS*-specific RXXG variants to the *NBS*-preferred QKKR that have permissive amino acids (K/R) at either position 179 or 184 or both or have R at position 201, or Q at position 173, or C/T/S at position 201 after a given number of aa steps (see also Figure S7D).

(E) Percentage of shortest paths that traversed black, light green, or pink variants to reach QKKR from any of the highly *parS*-specific RXXG variants (red lines). The result was compared to ones from 1,000 simulations where the edges were shuffled randomly while keeping the total number of nodes, edges, and graph density constant.

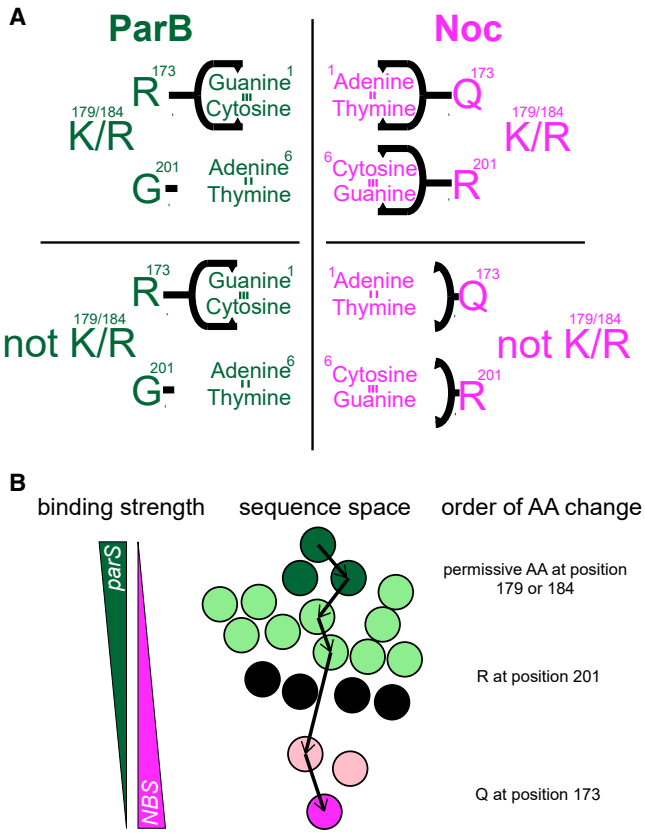

Figure 7. A Model for the Evolution of *NBS*-Binding Specificity

(A) Contributions of each specificity residue to enable a switch in binding specificity from *parS* to *NBS*. An R173Q substitution enabled interactions with adenine 1:thymine −1 (of *NBS*). A G201R substitution enabled interactions with cytosine 6: guanine −6 (of *NBS*). Q173 and R201 could only do so in the presence of permissive residues K at either 179 or 184 or both. Without K179/184, Q173 and R201 were poised to interact with specific bases but could not, possibly because of insufficient affinity for DNA.

(B) Analysis of mutational paths that traversed the network of functional variants showed that the order of introducing specificity-switching substitutions matters and that the shortest paths to *NBS*-specific variants do not necessarily involve dual-specificity nodes to evolve a new DNA-binding preference.

variants to QKKR (Figures 6D and S7D). Given that dual-specificity variants (black box, Figure 5C) mostly have T or S aa at position 201, it suggests that dual-specificity intermediates might have not been exploited to change specificity. Indeed, no shortest path connecting RXXG and QKKR traversed any dual-specificity variant (black nodes) (Figures 6E and S7E). This proportion is significantly smaller than would be expected by chance (estimated from 1,000 random networks where edges were shuffled randomly; Figures 6E and S7E). In contrast, ~51% and ~3% of shortest paths from RXXG variants to QKKR contain light green and pink intermediates, respectively. The proportions of paths with light green or pink intermediates are similar to expected values from random chance (Figure 6E). The preference for traversing light green nodes, therefore, can be explained by the abundance of such variants in the observed graph (Figure 6B). Overall, our network analysis predicted that the *parS*-to-*NBS* reprogram did not exploit truly dual-specificity intermediates and that those with a stricter specificity (light green or pink) were more commonly used.

DISCUSSION

Determinants of Specificity and Implications for Understanding the Evolution of Protein-DNA Interfaces

The *NBS* site differs from the *parS* site by only 2 bases (positions 1 and 6; Figure 1A), but Noc and ParB recognize and bind them with exquisite specificity. We provided evidence that mutations must have been introduced in a defined order to reprogram specificity. Permissive substitutions (K/R at positions 179/184) tend to appear first, presumably to prime *parS*-specific variants for a subsequent introduction of specificity-switching residues (R201 and Q173) which would have otherwise rendered proteins non-functional (Figure 7). Supporting the priming role of permissive amino acids, we noted that ~28% of extant ParB already possess a lysine/arginine residue at position 184 (Figure 5C, a sequence logo in a dashed green box). An early introduction of permissive substitutions is likely to be a recurring principle of evolution. For example, a similar prerequisite for permissive mutations was observed in the evolution of influenza resistance to the antiviral drug oseltamivir (Bloom et al., 2010). Two permissive mutations were first acquired, allowing the virus to tolerate a subsequent occurrence of a H274Y mutation that weakened the binding of oseltamivir to the viral neuraminidase enzyme (Bloom et al., 2010). These permissive mutations improved the stability of neuraminidase before a structurally destabilizing H274Y substitution was introduced (Bloom et al., 2010; Gong et al., 2013). Similarly, a permissive mutation that is far away from the active site of an antibiotic-degrading β-lactamase (TEM1) has little effect on its enzymatic activity by itself but restored stability loss by a subsequent mutation that increased TEM1 activity against cephalosporin antibiotics (Wang et al., 2002). In another case, 11 permissive mutations were required to evolve an ancestral steroid hormone receptor from preferring an estrogen response element (ERE) to a new DNA sequence (steroid response element [SRE]) (McKeown et al., 2014). These 11 mutations were located outside the DNA-recognition motif but non-specifically increased the affinity for both ERE and SRE, thereby licensing three additional substitutions to alter the specificity to SRE (McKeown et al., 2014). Additionally, it has been shown that an early introduction of 11 permissive substitutions dramatically increased the number of SRE-binding variants well beyond the historically observed variants (Starr et al., 2017). In our work, at least when considering just four aa residues, a single introduction of a lysine, either at position 179 or 184, was sufficient to permit Q173 and R201 to recognize *NBS* specifically.

Deep mutational scanning in conjunction with network analysis is a powerful approach to reconstruct possible mutational paths that might have been taken to acquire a new function (Aakre et al., 2015; Podgornaia and Laub, 2015; Starr et al., 2017). Network graph theory was applied to understand the constraints on the evolution of protein-protein interfaces between a histidine kinase and its response regulator partner, between toxin and antitoxin pairs of proteins, and most recently to reveal the alternative evolutionary histories of a steroid hormone

receptor (Aakre et al., 2015; Podgornaia and Laub, 2015; Starr et al., 2017). In our case study, network analysis suggested that mutational paths to a new specificity did not necessarily have to visit dual-specificity intermediates, i.e., those that bind *parS* and *NBS* equally strongly (Figure 6E). Instead, mutational paths to an *NBS*-specific variant tend to be more switch-like, frequently visited dark green nodes (strong *parS* binding, no *NBS* binding) and light green nodes (strong *parS* binding, weak-to-medium *NBS* binding) (Figures 5C and 6E). We reason that most black variants, albeit being dual specific, bind both *parS* and *NBS* at a slightly reduced affinity (compared to the wild-type *parS*-specific RTAG or *NBS*-specific QKKR variants; see the scatterplot on Figure 5C). This might have created an undesirable situation in which dual-specificity intermediates neither could compete with the original copy of ParB to bind *parS* nor had high enough affinity themselves to bind *NBS* sites, i.e., artificially made non-functional due to competition. A similar principle might also apply to other protein-DNA interactions throughout biology. For example, a reconstructed evolutionary history of a steroid hormone receptor indicated that an ancestral receptor (AncSR1) without permissive mutations must always pass through dual-specificity intermediates to acquire the present-day specificity. On the other hand, the presence of 11 permissive mutations (AncSR1+11P) eliminated the absolute requirement for these dual-specificity intermediates. More dramatically, it has been shown that a single substitution (i.e., a truly switch-like mechanism) was enough to reprogram the specificity of homologous repressor proteins (Arc and Mnt) in bacteriophage P22 (Raumann et al., 1995). Nevertheless, we noted that protein-protein interfaces, particularly in the case of paralogous toxin-antitoxin protein pairs, exploited extensively promiscuous intermediates to diversify and evolve instead. In the case of toxin-antitoxin systems, truly promiscuous intermediates might have been favored because many of them bound to and antagonized cognate and non-cognate toxins equally or even better than the wild type (Aakre et al., 2015). It is likely that the topology of the available sequence space and the biology of each system collectively influence the paths to evolve a new biological innovation.

In summary, our work provides a molecular basis for how protein-DNA interaction specificity can change, with a focus on chromosome maintenance proteins ParB/Noc and the minimal set of four specificity residues at their protein-DNA interfaces. A small number of specificity residues enabled a systematic analysis of the protein-DNA interface and possible mutational paths that could have changed specificity. In this regard, our work might be useful for understanding the evolution of other classes of DNA-binding proteins. Nevertheless, evolution has most likely exploited more mutations and aa residues to fine-tune DNA-binding specificity than the core set of four residues in this work. Other compensatory mutations that alter the structural stability of proteins might also contribute and dictate the course of evolution to new biological functions (Ivankov et al., 2014; Sikosek and Chan, 2014; Starr and Thornton, 2016). An important challenge for future work is to study all contributing factors (permissive, specificity-switching, and other compensatory substitutions) in a systematic manner to better understand the course of evolution to new biological innovations.

STAR★METHODS

Detailed methods are provided in the online version of this paper and include the following:

- KEY RESOURCES TABLE
- RESOURCES AVAILABILITY
  - Lead Contact
  - Materials Availability
  - Data and Code Availability
- EXPERIMENTAL MODEL AND SUBJECT DETAILS
  - Bacterial models
  - Growth conditions
  - Plasmids and strains construction
- METHOD DETAILS
  - Identification and alignment of ParB and Noc sequences
  - Phylogenetic analysis of ParB and Noc protein sequences
  - Protein overexpression and purification
  - Selection of *parS* and *NBS* site
  - Reconstitution of *parS* DNA for X-ray crystallography
  - Reconstitution of *NBS* DNA for X-ray crystallography
  - Protein crystallization, structure determination, and refinement
  - DNA-binding domain (DBD) ParB in complex with 20-bp *parS*
  - DNA-binding domain (DBD) Noc in complex with 22-bp *NBS*
  - Identification of protein-DNA contacts and analysis of DNA shapes
  - Molecular dynamics simulations
  - Measure protein-DNA binding affinity by bio-layer interferometry (BLI)
  - Clustering of trajectory-scanning mutagenesis data
  - Chromatin immunoprecipitation with qPCR or deep sequencing
  - Generation and analysis of ChIP-seq profiles
  - Bacterial one-hybrid assay coupled with deep sequencing (B1H-seq)
  - Analysis of data from deep mutational scanning experiments
- QUANTIFICATION AND STATISTICAL ANALYSIS

SUPPLEMENTAL INFORMATION

Supplemental Information can be found online at https://doi.org/10.1016/j.celrep.2020.107928.

ACKNOWLEDGMENTS

This study was supported by the Royal Society University Research Fellowship (UF140053) and a BBSRC grant (BB/P018165/1) to T.B.K.L. A.S.B.J.'s PhD studentship was funded by the Royal Society (RG150448), and N.T.T. was funded by the BBSRC grant-in-aid (BBS/E/J/000PR9791 to the John Innes Centre). Work in the Noy lab was supported by a EPSRC grant (EP/N027639/1). Computational time was secured by HECBioSim, supported by a EPSRC grant (EP/R029407/1) and by the Cambridge Tier-2 system (EPSRC Tier-2 capital grant EP/P020259/1). We acknowledge Tier 3 High Performance Computing facilities at York (Viking and YARCC clusters) for additional

computational resources. We acknowledge Diamond Light Source for access to beamlines I03 and I04 under proposal MX18565 with support from the European Community's Seventh Framework Program (FP7/2007–2013) under Grant Agreement 283570 (BioStruct-X). We also thank Rory Williams and Roan Hulks for help with early experiments.

AUTHOR CONTRIBUTIONS

Conceptualization, A.S.B.J., N.T.T., and T.B.K.L.; Data acquisition, A.S.B.J., N.T.T., C.E.S., E.W.C., R.L., X.T., and T.B.K.L.; Data analysis, A.S.B.J., N.T.T., C.E.S., E.W.C., R.L., A.N., D.M.L., and T.B.K.L. Writing, A.S.B.J., N.T.T., D.M.L., and T.B.K.L. Funding acquisition, A.N., D.M.L., and T.B.K.L.

DECLARATION OF INTERESTS

The authors declare no competing interests.

Received: August 12, 2019
Revised: March 25, 2020
Accepted: June 26, 2020
Published: July 21, 2020

REFERENCES

Aakre, C.D., Herrou, J., Phung, T.N., Perchuk, B.S., Crosson, S., and Laub, M.T. (2015). Evolving new protein-protein interaction specificity through promiscuous intermediates. Cell *163*, 594–606.

Anandakrishnan, R., Aguilar, B., and Onufriev, A.V. (2012). H++ 3.0: automating pK prediction and the preparation of biomolecular structures for atomistic molecular modeling and simulations. Nucleic Acids Res. *40*, W537–W541.

Bloom, J.D., Gong, L.I., and Baltimore, D. (2010). Permissive secondary mutations enable the evolution of influenza oseltamivir resistance. Science *328*, 1272–1275.

Bosley, A.D., and Ostermeier, M. (2005). Mathematical expressions useful in the construction, description and evaluation of protein libraries. Biomol. Eng. *22*, 57–61.

Bunkóczi, G., and Read, R.J. (2011). Improvement of molecular-replacement models with Sculptor. Acta Crystallogr. D Biol. Crystallogr. *67*, 303–312.

Chen, V.B., Arendall, W.B., 3rd, Headd, J.J., Keedy, D.A., Immormino, R.M., Kapral, G.J., Murray, L.W., Richardson, J.S., and Richardson, D.C. (2010). MolProbity: all-atom structure validation for macromolecular crystallography. Acta Crystallogr. D Biol. Crystallogr. *66*, 12–21.

Chen, B.-W., Lin, M.-H., Chu, C.-H., Hsu, C.-E., and Sun, Y.-J. (2015a). Insights into ParB spreading from the complex structure of Spo0J and parS. Proc. Natl. Acad. Sci. USA *112*, 6613–6618.

Chen, C., Esadze, A., Zandarashvili, L., Nguyen, D., Montgomery Pettitt, B., and Iwahara, J. (2015b). Dynamic Equilibria of Short-Range Electrostatic Interactions at Molecular Interfaces of Protein-DNA Complexes. J. Phys. Chem. Lett. *6*, 2733–2737.

Conrad, B., and Antonarakis, S.E. (2007). Gene duplication: a drive for phenotypic diversity and cause of human disease. Annu. Rev. Genomics Hum. Genet. *8*, 17–35.

Cowtan, K. (2006). The Buccaneer software for automated model building. 1. Tracing protein chains. Acta Crystallogr. D Biol. Crystallogr. *62*, 1002–1011.

Crooks, G.E., Hon, G., Chandonia, J.-M., and Brenner, S.E. (2004). WebLogo: a sequence logo generator. Genome Res. *14*, 1188–1190.

Darden, T., York, D., and Pedersen, L. (1993). Particle mesh Ewald: An N·log(N) method for Ewald sums in large systems. J. Chem. Phys. *98*, 10089–10092.

Edgar, R.C. (2004). MUSCLE: multiple sequence alignment with high accuracy and high throughput. Nucleic Acids Res. *32*, 1792–1797.

Emsley, P., and Cowtan, K. (2004). Coot: model-building tools for molecular graphics. Acta Crystallogr. D Biol. Crystallogr. *60*, 2126–2132.

Evans, P.R., and Murshudov, G.N. (2013). How good are my data and what is the resolution? Acta Crystallogr. D Biol. Crystallogr. *69*, 1204–1214.

Fisher, G.L., Pastrana, C.L., Higman, V.A., Koh, A., Taylor, J.A., Butterer, A., Craggs, T., Sobott, F., Murray, H., Crump, M.P., et al. (2017). The structural basis for dynamic DNA binding and bridging interactions which condense the bacterial centromere. eLife *6*, e28086.

Fogel, M.A., and Waldor, M.K. (2006). A dynamic, mitotic-like mechanism for bacterial chromosome segregation. Genes Dev. *20*, 3269–3282.

Gong, L.I., Suchard, M.A., and Bloom, J.D. (2013). Stability-mediated epistasis constrains the evolution of an influenza protein. eLife *2*, e00631.

Gruber, S., and Errington, J. (2009). Recruitment of condensin to replication origin regions by ParB/SpoOJ promotes chromosome segregation in B. subtilis. Cell *137*, 685–696.

Harms, A., Treuner-Lange, A., Schumacher, D., and Søgaard-Andersen, L. (2013). Tracking of chromosome and replisome dynamics in Myxococcus xanthus reveals a novel chromosome arrangement. PLoS Genet. *9*, e1003802.

Ireton, K., Gunther, N.W., 4th, and Grossman, A.D. (1994). spo0J is required for normal chromosome segregation as well as the initiation of sporulation in Bacillus subtilis. J. Bacteriol. *176*, 5320–5329.

Ivani, I., Dans, P.D., Noy, A., Pérez, A., Faustino, I., Hospital, A., Walther, J., Andrio, P., Goñi, R., Balaceanu, A., et al. (2016). Parmbsc1: a refined force field for DNA simulations. Nat. Methods *13*, 55–58.

Ivankov, D.N., Finkelstein, A.V., and Kondrashov, F.A. (2014). A structural perspective of compensatory evolution. Curr. Opin. Struct. Biol. *26*, 104–112.

Jakimowicz, D., Chater, K., and Zakrzewska-Czerwińska, J. (2002). The ParB protein of Streptomyces coelicolor A3(2) recognizes a cluster of parS sequences within the origin-proximal region of the linear chromosome. Mol. Microbiol. *45*, 1365–1377.

Kaessmann, H. (2010). Origins, evolution, and phenotypic impact of new genes. Genome Res. *20*, 1313–1326.

Karimova, G., Pidoux, J., Ullmann, A., and Ladant, D. (1998). A bacterial two-hybrid system based on a reconstituted signal transduction pathway. Proc. Natl. Acad. Sci. USA *95*, 5752–5756.

Kawalek, A., Bartosik, A.A., Glabski, K., and Jagura-Burdzy, G. (2018). Pseudomonas aeruginosa partitioning protein ParB acts as a nucleoid-associated protein binding to multiple copies of a parS-related motif. Nucleic Acids Res. *46*, 4592–4606.

Krissinel, E. (2015). Stock-based detection of protein oligomeric states in jsPISA. Nucleic Acids Res. *43*, W314–W319.

Lagage, V., Boccard, F., and Vallet-Gely, I. (2016). Regional Control of Chromosome Segregation in Pseudomonas aeruginosa. PLoS Genet. *12*, e1006428.

Langmead, B., Trapnell, C., Pop, M., and Salzberg, S.L. (2009). Ultrafast and memory-efficient alignment of short DNA sequences to the human genome. Genome Biol. *10*, R25.

Lavery, R., Moakher, M., Maddocks, J.H., Petkeviciute, D., and Zakrzewska, K. (2009). Conformational analysis of nucleic acids revisited: Curves+. Nucleic Acids Res. *37*, 5917–5929.

Lee, P.S., and Grossman, A.D. (2006). The chromosome partitioning proteins Soj (ParA) and Spo0J (ParB) contribute to accurate chromosome partitioning, separation of replicated sister origins, and regulation of replication initiation in Bacillus subtilis. Mol. Microbiol. *60*, 853–869.

Letunic, I., and Bork, P. (2016). Interactive tree of life (iTOL) v3: an online tool for the display and annotation of phylogenetic and other trees. Nucleic Acids Res. *44*, W242–W245.

Lim, H.C., Surovtsev, I.V., Beltran, B.G., Huang, F., Bewersdorf, J., and Jacobs-Wagner, C. (2014). Evidence for a DNA-relay mechanism in ParABS-mediated chromosome segregation. eLife *3*, e02758.

Lin, D.C.-H., and Grossman, A.D. (1998). Identification and characterization of a bacterial chromosome partitioning site. Cell *92*, 675–685.

Livny, J., Yamaichi, Y., and Waldor, M.K. (2007). Distribution of centromere-like parS sites in bacteria: insights from comparative genomics. J. Bacteriol. *189*, 8693–8703.

Lynch, M., and Conery, J.S. (2000). The evolutionary fate and consequences of duplicate genes. Science *290*, 1151–1155.

Maier, J.A., Martinez, C., Kasavajhala, K., Wickstrom, L., Hauser, K.E., and Simmerling, C. (2015). ff14SB: Improving the Accuracy of Protein Side Chain and Backbone Parameters from ff99SB. J. Chem. Theory Comput. *11*, 3696–3713.

McCoy, A.J., Grosse-Kunstleve, R.W., Adams, P.D., Winn, M.D., Storoni, L.C., and Read, R.J. (2007). Phaser crystallographic software. J. Appl. Cryst. *40*, 658–674.

McKeown, A.N., Bridgham, J.T., Anderson, D.W., Murphy, M.N., Ortlund, E.A., and Thornton, J.W. (2014). Evolution of DNA specificity in a transcription factor family produced a new gene regulatory module. Cell *159*, 58–68.

Miller, M.A., Pfeiffer, W., and Schwartz, T. (2011). The CIPRES Science Gateway: A Community Resource for Phylogenetic Analyses. In Proceedings of the 2011 TeraGrid Conference: Extreme Digital Discovery (ACM), pp. 41:1–41:8.

Mohl, D.A., and Gober, J.W. (1997). Cell cycle-dependent polar localization of chromosome partitioning proteins in Caulobacter crescentus. Cell *88*, 675–684.

Murray, H., Ferreira, H., and Errington, J. (2006). The bacterial chromosome segregation protein Spo0J spreads along DNA from parS nucleation sites. Mol. Microbiol. *61*, 1352–1361.

Murshudov, G.N., Vagin, A.A., and Dodson, E.J. (1997). Refinement of macromolecular structures by the maximum-likelihood method. Acta Crystallogr. D Biol. Crystallogr. *53*, 240–255.

Noy, A., and Golestanian, R. (2010). The chirality of DNA: elasticity cross-terms at base-pair level including A-tracts and the influence of ionic strength. J. Phys. Chem. B *114*, 8022–8031.

Noyes, M.B., Meng, X., Wakabayashi, A., Sinha, S., Brodsky, M.H., and Wolfe, S.A. (2008). A systematic characterization of factors that regulate Drosophila segmentation via a bacterial one-hybrid system. Nucleic Acids Res. *36*, 2547–2560.

Pang, T., Wang, X., Lim, H.C., Bernhardt, T.G., and Rudner, D.Z. (2017). The nucleoid occlusion factor Noc controls DNA replication initiation in Staphylococcus aureus. PLoS Genet. *13*, e1006908.

Podgornaia, A.I., and Laub, M.T. (2015). Protein evolution. Pervasive degeneracy and epistasis in a protein-protein interface. Science *347*, 673–677.

Potterton, L., Agirre, J., Ballard, C., Cowtan, K., Dodson, E., Evans, P.R., Jenkins, H.T., Keegan, R., Krissinel, E., Stevenson, K., et al. (2018). CCP4i2: the new graphical user interface to the CCP4 program suite. Acta Crystallogr. D Struct. Biol. *74*, 68–84.

Price, D.J., and Brooks, C.L., 3rd. (2004). A modified TIP3P water potential for simulation with Ewald summation. J. Chem. Phys. *121*, 10096–10103.

Qian, W., and Zhang, J. (2014). Genomic evidence for adaptation by gene duplication. Genome Res. *24*, 1356–1362.

Quinlan, A.R., and Hall, I.M. (2010). BEDTools: a flexible suite of utilities for comparing genomic features. Bioinformatics *26*, 841–842.

Raumann, B.E., Knight, K.L., and Sauer, R.T. (1995). Dramatic changes in DNA-binding specificity caused by single residue substitutions in an Arc/Mnt hybrid repressor. Nat. Struct. Biol. *2*, 1115–1122.

Roe, D.R., and Cheatham, T.E., 3rd. (2013). PTRAJ and CPPTRAJ: Software for Processing and Analysis of Molecular Dynamics Trajectory Data. J. Chem. Theory Comput. *9*, 3084–3095.

Ryckaert, J.-P., Ciccotti, G., and Berendsen, H.J.C. (1977). Numerical integration of the cartesian equations of motion of a system with constraints: molecular dynamics of n-alkanes. J. Comput. Phys. *23*, 327–341.

Sievers, J., Raether, B., Perego, M., and Errington, J. (2002). Characterization of the parB-like yyaA gene of Bacillus subtilis. J. Bacteriol. *184*, 1102–1111.

Sikosek, T., and Chan, H.S. (2014). Biophysics of protein evolution and evolutionary protein biophysics. J. R. Soc. Interface *11*, 20140419.

Smith, D.E., and Dang, L.X. (1994). Computer simulations of NaCl association in polarizable water. J. Chem. Phys. *100*, 3757–3766.

Stamatakis, A. (2014). RAxML version 8: a tool for phylogenetic analysis and post-analysis of large phylogenies. Bioinformatics *30*, 1312–1313.

Starr, T.N., and Thornton, J.W. (2016). Epistasis in protein evolution. Protein Sci. *25*, 1204–1218.

Starr, T.N., Picton, L.K., and Thornton, J.W. (2017). Alternative evolutionary histories in the sequence space of an ancient protein. Nature *549*, 409–413.

Steinegger, M., Meier, M., Mirdita, M., Vöhringer, H., Haunsberger, S.J., and Söding, J. (2019). HH-suite3 for fast remote homology detection and deep protein annotation. bioRxiv. https://doi.org/10.1101/560029.

Teichmann, S.A., and Babu, M.M. (2004). Gene regulatory network growth by duplication. Nat. Genet. *36*, 492–496.

Toro, E., Hong, S.-H., McAdams, H.H., and Shapiro, L. (2008). Caulobacter requires a dedicated mechanism to initiate chromosome segregation. Proc. Natl. Acad. Sci. USA *105*, 15435–15440.

Tran, N.T., Laub, M.T., and Le, T.B.K. (2017). SMC Progressively Aligns Chromosomal Arms in Caulobacter crescentus but Is Antagonized by Convergent Transcription. Cell Rep. *20*, 2057–2071.

Tran, N.T., Stevenson, C.E., Som, N.F., Thanapipatsiri, A., Jalal, A.S.B., and Le, T.B.K. (2018). Permissive zones for the centromere-binding protein ParB on the Caulobacter crescentus chromosome. Nucleic Acids Res. *46*, 1196–1209.

van Opijnen, T., Bodi, K.L., and Camilli, A. (2009). Tn-seq: high-throughput parallel sequencing for fitness and genetic interaction studies in microorganisms. Nat. Methods *6*, 767–772.

Wang, X., Minasov, G., and Shoichet, B.K. (2002). Evolution of an antibiotic resistance enzyme constrained by stability and activity trade-offs. J. Mol. Biol. *320*, 85–95.

Wang, X., Le, T.B.K., Lajoie, B.R., Dekker, J., Laub, M.T., and Rudner, D.Z. (2015). Condensin promotes the juxtaposition of DNA flanking its loading site in Bacillus subtilis. Genes Dev. *29*, 1661–1675.

Winter, G. (2010). xia2: an expert system for macromolecular crystallography data reduction. J. Appl. Cryst. *43*, 186–190.

Winter, G., Waterman, D.G., Parkhurst, J.M., Brewster, A.S., Gildea, R.J., Gerstel, M., Fuentes-Montero, L., Vollmar, M., Michels-Clark, T., Young, I.D., et al. (2018). DIALS: implementation and evaluation of a new integration package. Acta Crystallogr. D Struct. Biol. *74*, 85–97.

Wu, L.J., and Errington, J. (2004). Coordination of cell division and chromosome segregation by a nucleoid occlusion protein in Bacillus subtilis. Cell *117*, 915–925.

Wu, L.J., and Errington, J. (2011). Nucleoid occlusion and bacterial cell division. Nat. Rev. Microbiol. *10*, 8–12.

Wu, L.J., Ishikawa, S., Kawai, Y., Oshima, T., Ogasawara, N., and Errington, J. (2009). Noc protein binds to specific DNA sequences to coordinate cell division with chromosome segregation. EMBO J. *28*, 1940–1952.

STAR★METHODS

KEY RESOURCES TABLE

REAGENT or RESOURCE	SOURCE	IDENTIFIER
Bacterial and Virus Strains		
Please refer to Table S1		N/A
Chemicals, Peptides, and Recombinant Proteins		
3-AT	Abcam	Cat# ab146281
Benzonase nuclease	Sigma-Aldrich	Cat# E1014
cOmplete, Mini, EDTA-free Protease Inhibitor Cocktail	Roche Applied Science	Cat# 11836170001
Critical Commercial Assays		
Gibson Assembly Master Mix	NEB	Cat# E2611S
Gateway BP Clonase II enzyme mix	ThermoFisher	Cat# 11789020
SYBR® Green JumpStart Taq ReadyMix	Sigma-Aldrich	Cat# S4438
Dip-and-Read Streptavidin (SA) biosensors	Molecular Devices	Cat# 18-5019
HisTrap High Performance column	GE Healthcare	Cat# GE17524801
HiTrap Heparin High Performance column	GE Healthcare	Cat# GE17040601
HiLoad 16/600 Superdex 75pg column	GE Healthcare	Cat# GE28989333
HIS-Select Cobalt Affinity Gel	Sigma-Aldrich	Cat# H8162
PD 10 Desalting Columns	Sigma-Aldrich	Cat# GE17085101
EZview Red ANTI-FLAG® M2 Affinity Gel	Sigma-Aldrich	Cat# F2426; RRID: AB_2616449
QIAquick PCR Purification Kit	QIAGEN	Cat# 28104
NEBNext Ultra DNA Library Prep Kit for Illumina	NEB	Cat# E7370S
Qubit dsDNA HS Assay Kit	ThermoFisher	Cat# Q32851
Deposited Data		
Crystal structures	This paper	PDB: 6S6H, 6Y93
ChIP-seq data	This paper	Gene Expression Omnibus: GSE129285
B1H-seq data	This paper	Gene Expression Omnibus: GSE129285
Other data	This paper	Mendeley Data: https://doi.org/10.17632/8v45kvdtw5.1
Recombinant DNA		
Please refer to Table S2		N/A
Oligonucleotides		
Please refer to Table S3		N/A
Software and Algorithms		
BLItz Pro	Molecular Devices	Cat# 50-0156
Gephi	The Open Graph Viz Platform	https://gephi.org/
R	R Foundation for Statistical Computing	https://www.r-project.org/
igraph	Igraph-The network analysis package	https://igraph.org/
HHsuite	Steinegger et al., 2019	https://github.com/soedinglab/hh-suite
WebLogo 3.0	Crooks et al., 2004	http://weblogo.threeplusone.com/
iTOL	Letunic and Bork, 2016	https://itol.embl.de/
CIPRES	Miller et al., 2011	http://www.phylo.org/
Curves+	Lavery et al., 2009	http://curvesplus.bsc.es/analyse
Bowtie 1	Langmead et al., 2009	http://bowtie-bio.sourceforge.net/index.shtml
BEDTools	Quinlan and Hall, 2010	https://bedtools.readthedocs.io/en/latest/

(*Continued on next page*)

Continued

REAGENT or RESOURCE	SOURCE	IDENTIFIER
FASTX-Toolkit	Hannon Lab	http://hannonlab.cshl.edu/fastx_toolkit/
DIALS	Winter et al., 2018	https://dials.github.io/
AIMLESS	Evans and Murshudov, 2013	http://www.ccp4.ac.uk/html/aimless.html
CCP4i2	Potterton et al., 2018	http://www.ccp4.ac.uk/
COOT	Emsley and Cowtan, 2004	https://www2.mrc-lmb.cam.ac.uk/personal/pemsley/coot/
PHASER	McCoy et al., 2007	https://www.phenix-online.org/
REFMAC5	Murshudov et al., 1997	http://www.ccp4.ac.uk/html/refmac5/description.html
BUCCANEER	Cowtan, 2006	http://www.ccp4.ac.uk/html/cbuccaneer.html
MolProbity	Chen et al., 2010	http://molprobity.biochem.duke.edu/
STARANISO	Global Phasing Limited	http://staraniso.globalphasing.org/cgi-bin/staraniso.cgi
jsPISA	Krissinel, 2015	http://www.ccp4.ac.uk/pisa/
PyMOL	The PyMOL Molecular Graphics System	https://pymol.org/2/
AMBER	AMBER Software, University of California, San Francisco	https://ambermd.org/

RESOURCES AVAILABILITY

Lead Contact

Further information and requests for resources and reagents should be directed to and will be fulfilled by the Lead Contact, Tung Le (tung.le@jic.ac.uk).

Materials Availability

Plasmids and strains used in this study are available from the Lead Contact with a completed Materials Transfer Agreement.

Data and Code Availability

The accession number for the sequencing data reported in this paper is GSE129285. Atomic coordinates for protein crystal structures reported in this paper were deposited in the RCSB Protein Data Bank with the following accession numbers: 6S6H and 6Y93. Original data have been deposited to Mendeley Data (https://doi.org/10.17632/8v45kvdtw5.1).

EXPERIMENTAL MODEL AND SUBJECT DETAILS

Bacterial models

Escherichia coli strains DH5α and Rosetta (DE3) were used as hosts for constructing plasmids, and overexpression of proteins, respectively (Table S1). *E. coli* USO *rpoZ*$^{-}$ *hisB*$^{-}$ *pyrF*$^{-}$ was used as a host for B1H assay (Table S1).

Growth conditions

E. coli was grown in LB. When appropriate, media were supplemented with antibiotics at the following concentrations (liquid/solid media for *E. coli* (μg/mL): carbenicillin (50/100), chloramphenicol (20/30), kanamycin (30/50), and apramycin (25/50).

Plasmids and strains construction

All strains used are listed in Table S1. All plasmids and primers used in strain and plasmid construction are listed in Tables S2 and S3.

pENTR::Noc/ParB. The coding sequences of ParB and Noc from various bacterial species (Figures 1B and S1A) were chemically synthesized (gBlocks dsDNA fragments, IDT). The backbone of pENTR plasmid was amplified by PCR using primers pENTR_gibson_backbone_F and pENTR_gibson_backbone_R from the pENTR-D-TOPO cloning kit (Invitrogen). The resulting PCR product was subsequently treated with DpnI to remove methylated template DNA. The resulting PCR fragment was gel-purified and assembled with the gBlocks fragment using a 2x Gibson master mix (NEB). Gibson assembly was possible due to a 23 bp sequence shared between the PCR fragment and the gBlocks fragment. These 23 bp regions were incorporated during the synthesis of gBlocks fragments. The resulting plasmids were sequence verified by Sanger sequencing (Eurofins, Germany).

pUT18C-1xFLAG-DEST. The backbone of pUT18C was amplified using primers P1936 and P1937, and pUT18C (Karimova et al., 1998) as template. The resulting PCR product was subsequently treated with DpnI to remove the methylated template DNA. The FLAG-*attR1-ccdB*-chloramphenicol^{R}-*attR2* cassette was amplified using primers P1934 and P1935, and pML477 as template. The two PCR fragments were each gel-purified and assembled together using a 2x Gibson master mix (NEB). Gibson assembly was possible due to a 23 bp sequence shared between the two PCR fragments. These 23 bp regions were incorporated during the primer design to amplify the FLAG-*attR1-ccdB*-chloramphenicol^{R}-*attR2* cassette. The resulting plasmid was sequence verified by Sanger sequencing (Eurofins, Germany).

pUT18C::1xFLAG-Noc/ParB. The *parB/noc* genes were recombined into a Gateway-compatible destination vector pUT18C-1xFLAG-DEST via a LR recombination reaction (Invitrogen). For LR recombination reactions: 1 μL of purified pENTR::*parB/noc* was incubated with 1 μL of the destination vector pUT18-1xFLAG-DEST, 1 μL of LR Clonase II master mix, and 2 μL of water in a total volume of 5 μL. The reaction was incubated for an hour at room temperature before being introduced to DH5α *E. coli* cells by heat-shock transformation. Cells were then plated out on LB agar + carbenicillin. Resulting colonies were restruck onto LB agar + carbenicillin and LB agar + kanamycin. Only colonies that survived on LB + carbenicillin plates were subsequently used for culturing and plasmid extraction.

*pB1H2-w2::*Caulobacter *ParB (R104A + Q173K179K184R201) and pB1H2-w2::*Caulobacter *ParB (R104A + R173A179T184G201)*. The coding sequence of *Caulobacter* ParB with the desired mutations was chemically synthesized (gBlocks dsDNA fragments, IDT). The pB1H2-w2 plasmid backbone was generated via a double digestion of pB1H2-w2::Prd plasmid (Noyes et al., 2008) with KpnI and XbaI. The resulting backbone was subsequently gel-purified and assembled with the gBlocks fragments using a 2x Gibson master-mix (NEB). Gibson assembly was possible due to a 23 bp sequence shared between the KpnI-XbaI-cut pB1H2-w2 backbone and the gBlocks fragment. These 23 bp regions were incorporated during the synthesis of gBlocks fragments. The resulting plasmids were sequence verified by Sanger sequencing (Eurofins, Germany).

*pB1H2-w5::*Caulobacter *ParB (R104A + Q173K179K184R201)*. The same procedure as above was used to generate this plasmid, except that pB1H2-w5::Prd plasmid (Noyes et al., 2008) was used.

*pB1H2-w5L::*Caulobacter *ParB (R104A + Q173K179K184R201)*. The same procedure as above was used to generate this plasmid, except that pB1H2-w5L::Prd plasmid (Noyes et al., 2008) was used.

pU3H3::7/14/19/24bp-NBS. The pU3H3 backbone was generated via a double digestion of pU3H3::MCS plasmid (Noyes et al., 2008) with XmaI and EcoRI. The backbone was subsequently gel-purified before being ligated with the DNA insert in the next step. The DNA insert containing *NBS* site with an appropriate spacer (7, 14, 19, or 24 bp) were generated by annealing complementary oligos together (Table S3). The DNA inserts were subsequently 5′ phosphorylated using T4 PNK (NEB), and ligated to the XmaI-EcoRI-cut pU3H3 backbone using T4 DNA ligase (NEB). The resulting plasmids were sequence verified by Sanger sequencing (Eurofins, Germany).

pU3H3::19bp-parS. The same procedure as above was used to generate the plasmid, except that primers *parS*_anneal_19bp_-spacer_F and *parS*_anneal_19bp_spacer_R were used.

pET21b::ParB (variants)-His$_6$. All sequences of ParB variants were designed in VectorNTI (ThermoFisher) and chemically synthesized as gBlocks dsDNA fragments (IDT). Individual gBlocks fragment and a NdeI-HindIII-digested pET21b backbone were assembled using a 2x Gibson master mix (NEB). Gibson assembly was possible due to a 23-bp sequence shared between the NdeI-HindIII-cut pET21b backbone and the gBlocks fragment. These 23-bp regions were incorporated during the synthesis of gBlocks fragments. The resulting plasmids were sequence verified by Sanger sequencing (Eurofins, Germany).

Strains AB1157 ybbD*::*parS*::markerless* ygcE*::*NBS*::markerless*. We use Lambda Red to insert a cassette consisting of a *parS* site and an apramycin antibiotic resistance gene *aac(3)IV* at the *ybbD* locus on the *E. coli* AB1157 chromosome. The *parS*-FRT-apramycin^{R}-FRT cassette was amplified by PCR using primers 1940 and 1941, and pIJ773 (a gift from Keith Chater) as template. These forward and reverse primers also carry a 39 bp homology to the left or the right of the insertion point at the *ybbD* locus. The resulting PCR products were gel-extracted and electroporated into an arabinose-induced *E. coli* AB1157/pKD46 cells. Colonies that formed on LB + apramycin was restruck on LB + apramycin and incubated at 42°C to cure the cells of pKD46 plasmid. Finally, the correct insertion of the *parS*-apramycin^{R} cassette was verified by PCR and Sanger sequencing. To remove the FRT- apramycin^{R}-FRT region while leaving the *parS* site intact, a temperature sensitive FLP recombination plasmid pBT340 (a gift from Keith Chater) was subsequently introduced. To introduce the *NBS* site at the *ygcE* locus on the chromosome of *E. coli* AB1157 *ybbD*::*parS*::markerless, we employed the same procedure, except that the *NBS*-FRT-Apramycin^{R}-FRT cassette was amplified by PCR using primer 3139 and 3140 instead.

METHOD DETAILS

Identification and alignment of ParB and Noc sequences

The sequences used for generating sequence conservation logos were retrieved and aligned using HHblits (-n 4 -e 1E-10 -maxfilt inf -neffmax 20 -nodiff -realign_max inf) and HHfilter (-id 100 -cov 75) in the HHsuite (Steinegger et al., 2019), using *Caulobacter crescentus* ParB protein and *Bacillus subtilis* Noc protein sequences as queries. This procedure resulted in 1800 homologous ParB sequences and 361 homologous Noc sequences. The sequence conservation logos were generated by WebLogo 3.0 (Crooks et al., 2004), using ParB/Noc sequence alignments as input.

Phylogenetic analysis of ParB and Noc protein sequences

Amino acid sequences of ParB and Noc from 21 selected bacterial species were retrieved by BLASTP and used to generate a phylogenetic tree (Figure 1B). Phylogenetic analyses were carried out using MUSCLE (Edgar, 2004) and RAxML (Stamatakis, 2014), which were used through the CIPRES science gateway (Miller et al., 2011), and the trees were visualized using iTOL (Letunic and Bork, 2016). Amino acid sequences were aligned using MUSCLE with the following parameters: muscle -in infile.fasta -seqtype auto -maxiters 16 -maxmb 30000000 -log logfile.txt -weight1 clustalw -cluster1 upgmb -sueff 0.1 -root1 pseudo -maxtrees 1 -weight2 clustalw -cluster2 upgmb -sueff 0.1 -root2 pseudo -objscore sp -noanchors -phyiout outputi.phy

The resulting PHYLIP interleaved output file was then used to generate a maximum likelihood phylogenetic tree using RAxML-HPC BlackBox. The program was configured to perform rapid bootstrapping, followed by a maximum likelihood search to identify the best tree, with the following input parameters: raxmlHPC-HYBRID_8.2.10_comet -s infile.phy -N autoMRE -n result -f a -p 12345 -x 12345 -m PROTCATJTT

Protein overexpression and purification

The DNA-binding domain (DBD) of *Caulobacter* ParB (residues 126-243) was expressed and purified as follows. Plasmid pET21b::*Caulobacter crescentus*-ParB-$(His)_6$ (residue 126-243) was introduced into *E. coli* Rosetta (DE3) competent cells (Merck) by heat-shock transformation. 10 mL overnight culture was used to inoculate 4 L LB medium + carbenicillin + chloramphenicol. Cells were grown at 37°C with shaking at 210 rpm to an OD_{600} of ~0.4. The culture was then left to cool to 28°C before isopropyl-β-D-thiogalactopyranoside (IPTG) was added at a final concentration of 1.0 mM. The culture was left shaking for an additional 3 hours at 28°C before cells were harvested by centrifugation.

Pelleted cells were resuspended in a buffer containing 100 mM Tris-HCl pH 8.0, 300 mM NaCl, 10 mM Imidazole, 5% (v/v) glycerol, 1 μL of Benzonase nuclease (Sigma Aldrich), 1 mg of lysozyme (Sigma Aldrich), and an EDTA-free protease inhibitor tablet (Roche). The pelleted cells were then lyzed by sonification (10 cycles of 15 s with 10 s resting on ice in between each cycle). The cell debris was removed though centrifugation at 28,000 g for 30 min and the supernatant was filtered through a 0.45 μm sterile filter. The protein was then loaded into a 1-mL HiTrap column (GE Healthcare) that had been equilibrated with buffer A [100 mM Tris-HCl pH 8.0, 300 mM NaCl, 10 mM Imidazole, and 5% glycerol]. Protein was eluted from the column using an increasing (10 mM to 500 mM) imidazole gradient in the same buffer. ParB (DBD)-containing fractions were pooled and diluted to a conductivity of 16 mS/cm before being loaded onto a Heparin HP column (GE Healthcare) that had been equilibrated with 100 mM Tris-HCl pH 8.0, 25 mM NaCl, and 5% glycerol. Protein was eluted from the Heparin column using an increasing (25 mM to 1 M NaCl) salt gradient in the same buffer. ParB (DBD) fractions were pooled and analyzed for purity by SDS-PAGE. Glycerol was then added to ParB fractions to a final volume of 10%, followed by 10 mM EDTA and 1 mM DDT. The purified ParB (DBD) was subsequently aliquoted, snap frozen in liquid nitrogen, and stored at −80°C. ParB (DBD) that was used for X-ray crystallography was further polished via a gel-filtration column. To do so, purified ParB (DBD) was concentrated by centrifugation in an Amicon Ultra-15 3-kDa cut-off spin filters (Merck) before being loaded into a Superdex 75 gel filtration column (GE Healthcare). The gel filtration column was pre-equilibrated with 10 mM Tris-HCl pH 8.0 and 250 mM NaCl. ParB (DBD) fractions was then pooled and analyzed for purity by SDS-PAGE.

The DNA-binding domain (DBD) of *Bacillus subtillis* Noc-$(His)_6$ (residue 111-242) was purified using the same 3-column procedure as above. All other ParB/Noc variants were purified using HIS-Select® Cobalt gravity flow columns as follows. Plasmid pET21b::-*parB*/*noc* variants were introduced individually into *E. coli* Rosetta (DE3) competent cells (Merck) by heat-shock transformation. 10 mL overnight culture was used to inoculate 1 L LB medium + carbenicillin + chloramphenicol. Cells were grown at 37°C with shaking at 210 rpm to an OD_{600} of ~0.4. The culture was then left to cool to 28°C before IPTG was added to a final concentration of 0.5 mM. The culture was left shaking for an additional 3 hours at 30°C before cells were harvested by centrifugation. Pelleted cells were resuspended in 25 mL of buffer A [100 mM Tris-HCl pH 8.0, 300 mM NaCl, 10 mM Imidazole, 5% (v/v) glycerol] containing 1 mg lysozyme (Sigma Aldrich), and an EDTA-free protease inhibitor tablet (Roche). The pelleted cells were then lyzed by sonification. The cell debris was removed though centrifugation at 28,000 g for 30 min and the supernatant was transferred to a gravity flow column containing 2 mL of HIS-Select® Cobalt Affinity Gel (Sigma Aldrich) that was pre-equilibrated with 40 mL of buffer A. The column was rotated at 4°C for 1 hour to allow for binding to His-tagged proteins to the resin. After the binding step, unbound proteins were washed off using 60 mL of buffer A. Proteins were eluted using 2.7 mL of buffer B [100 mM Tris-HCl pH 8.0, 300 mM NaCl, 500 mM Imidazole, 5% (v/v) glycerol]. The purified protein was desalted using a PD-10 column (GE Healthcare), concentrated using an Amicon Ultra-4 10 kDa cut-off spin column (Merck), and stored at −80°C in a storage buffer [100 mM Tris-HCl pH 8.0, 300 mM NaCl, and 10% (v/v) glycerol].

Selection of *parS* and *NBS* site

For all experiments described in this work, we employed a consensus *parS* site (TGTTTCAC-GTGAAACA) and consensus *NBS* site (TATTTCCC-GGGAAATA) i.e., the idealized sequence that represents the predominant base at each position. The full position weight matrix (PWM) logos for *parS* and *NBS* sites have been described previously (Livny et al., 2007; Wu et al., 2009).

Reconstitution of *parS* DNA for X-ray crystallography

A 20-bp palindromic DNA fragment (5′-GATGTTTCACGTGAAACATC-3′) (3.6 mM in buffer that contains 10 mM Tris-HCl pH 8.0 and 250 mM NaCl) was heated to 95°C for 5 min before being left to cool at room temperature overnight to form a double stranded *parS* DNA (final concentration: 1.8 mM). The 14-bp *parS* site sequences are underlined.

Reconstitution of *NBS* DNA for X-ray crystallography

A 22-bp DNA fragment (5′-GGATATTTCCCGGGAAATATCC-3′) (3.6 mM in buffer that contains 10 mM Tris-HCl pH 8.0 and 250 mM NaCl) was heated to 95°C for 5 min before being left to cool at room temperature overnight to form a double stranded *NBS* DNA (final concentration: 1.8 mM). The 14-bp *NBS* site sequences are underlined.

Protein crystallization, structure determination, and refinement

Crystallization screens were set up in sitting-drop vapor diffusion format in MRC2 96-well crystallization plates (Swissci) using either an OryxNano or an Oryx8 robot (Douglas Instruments) with drops comprised of 0.3 μL precipitant solution and 0.3 μL of protein-DNA complex, and incubated at 293 K. After optimization of initial hits, suitable crystals were cryoprotected with 20% (v/v) glycerol and mounted in Litholoops (Molecular Dimensions) before flash-cooling by plunging into liquid nitrogen. X-ray data were recorded on either beamline I04 or I03 at the Diamond Light Source (Oxfordshire, UK) using either a Pilatus 6M-F or an Eiger2 XE 16M hybrid photon counting detector (Dectris), respectively, with crystals maintained at 100 K by a Cryojet cryocooler (Oxford Instruments). Diffraction data were integrated and scaled using DIALS (Winter et al., 2018) via the XIA2 expert system (Winter, 2010) then merged using AIMLESS (Evans and Murshudov, 2013). The Noc (DBD)-*NBS* dataset was further subjected to anisotropic correction using the STARANISO server as detailed below. Data collection statistics are summarized in Table S4. The majority of the downstream analysis was performed through the CCP4i2 graphical user interface (Potterton et al., 2018).

DNA-binding domain (DBD) ParB in complex with 20-bp *parS*

For crystallization, His-tagged DBD ParB (10 mg/mL) was mixed with a 20-bp *parS* site at a molar ratio of 1:1.2 (protein:DNA) in the elution buffer [10 mM Tris-HCl pH 8.0, 250 mM NaCl]. The DBD ParB-*parS* complex crystals grew in a solution containing 19% (w/v) PEG3350 and 49 mM lithium citrate.

The ParB (DBD)-*parS* complex crystallized in space group *C*2 with approximate cell parameters of $a = 122.1$, $b = 40.7$, $c = 94.0$ Å and $\beta = 121.4°$ (Table S4). Analysis of the likely composition of the asymmetric unit (ASU) suggested that it would contain two copies of the ParB (DBD) bound to a single DNA duplex, giving an estimated solvent content of ~49%. A molecular replacement template covering the DBD was generated by manually editing the protein component of the structure of the Spo0J-*parS* complex from *Helicobacter pylori* (Chen et al., 2015a) (PDB accession code 4UMK; 42% identity over 75% of the sequence) and truncating all side-chains to Cβ atoms. For the DNA component, an ideal B-form DNA duplex was generated in COOT (Emsley and Cowtan, 2004) from the 20-bp palindromic sequence of *parS*. PHASER (McCoy et al., 2007) was used to place the DNA duplex, followed by two copies of the DBD template into the ASU. The placement of the DNA-binding domains with respect to the DNA duplex was analogous to that seen in the *Helicobacter* Spo0J-*parS* (Chen et al., 2015a), and an analysis of crystal contacts revealed that the DNA formed a pseudo-continuous filament spanning the crystal due to base-pair stacking between adjacent DNA fragments. After restrained refinement in REFMAC5 (Murshudov et al., 1997) at 2.4 Å resolution, the protein component of the model was completely rebuilt using BUCCANEER (Cowtan, 2006). The model was finalized after several iterations of manual editing in COOT and further refinement in REFMAC5 incorporating TLS restraints. The model statistics are reported in Table S4.

DNA-binding domain (DBD) Noc in complex with 22-bp *NBS*

Crystallization screens were set up in sitting-drop vapor diffusion format in MRC2 96-well crystallization plates with drops comprised of 0.3 μL precipitant solution and 0.3 μL of protein-DNA complex, and incubated at 293 K. Noc (DBD)-His_6 (10 mg/mL) was mixed with a 22-bp *NBS* duplex at a molar ratio of 1:1.2 protein:DNA in buffer containing 10 mM Tris-HCl pH 8.0 and 250 mM NaCl. The Noc (DBD)-*NBS* crystals grew in a solution containing 20% (w/v) PEG 3350 and 200 mM di-potassium phosphate.

The Noc (DBD)-*NBS* complex crystallized in space group *C*2 with approximate cell parameters of $a = 134.1$, $b = 60.6$, $c = 81.0$ Å and $\beta = 116.9°$. The data were collected in two 360° sweeps separated by a χ offset of 20°. Data reduction in AIMLESS indicated that the diffraction was highly anisotropic, and thus before using the dataset, it was corrected using STARANISO with a local mean $I/\sigma(I)$ threshold of 1.2, giving maximum and minimum anisotropic resolution cut-offs of 2.23 and 4.02 Å, respectively (Table S4). Analysis of the likely composition of the asymmetric unit (ASU) suggested that it would contain two copies of the Noc (DBD) bound to a single DNA duplex, giving an estimated solvent content of ~69%. A molecular replacement template covering the DBD was generated from the ParB DBD structure above using SCULPTOR (41% identity overall) (Bunkóczi and Read, 2011). For the DNA component, an ideal B-form DNA duplex was generated from the 22-bp palindromic sequence of *NBS*. PHASER was used to place the DNA duplex, followed by two copies of the DBD template into the ASU. This generated a complex that was consistent with that of ParB (DBD)-*parS* determined above, again with the DNA forming a pseudo-continuous filament spanning the crystal due to base-pair stacking between adjacent DNA fragments. After restrained refinement in REFMAC5 at 2.23 Å resolution, the protein component of the model was completely rebuilt using BUCCANEER (Cowtan, 2006). The model was finalized after several iterations of manual editing in COOT and further refinement in REFMAC5 incorporating TLS restraints. To avoid model bias resulting from the feature of REFMAC5

to approximate missing reflections within the spherical resolution cut-off to their calculated values, these filled-in reflections were removed prior to map inspection. Subsequently, the map connectivity was improved by applying a blurring factor of 60 $Å^2$. The model statistics are reported in Table S4.

Identification of protein-DNA contacts and analysis of DNA shapes

Protein-DNA contacts were identified using the jsPISA webserver (Krissinel, 2015). Superpositions of structures were performed using the *align/cealign* function in PyMOL. DNA shape parameters were determined from the structures using Curves+ (Lavery et al., 2009).

Molecular dynamics simulations

We performed simulations of Noc (DBD)-*NBS* complex using its crystallographic structure as initial coordinates. Virginia Tech H++ web server (Anandakrishnan et al., 2012) was used for ensuring the correct protonated state of proteins at pH 7.0. Forcefields ff14SB (Maier et al., 2015) and parmbsc1 (Ivani et al., 2016) were employed for describing protein and DNA, respectively. The system was solvated in a TIP3P octahedral periodic box (Price and Brooks, 2004) with a 12 Å buffer and 100 mM of NaCl ions (Smith and Dang, 1994). Minimization and equilibration were performed following a standard protocol (Noy and Golestanian, 2010) at constant temperature (300 K) and pressure (1 atm). The structures were simulated for 200 ns with an integration time step of 2 fs. SHAKE method (Ryckaert et al., 1977) was used to constrain hydrogen bonds, alongside periodic boundary conditions and Particle-Mesh-Ewald algorithm (Darden et al., 1993). These simulations were performed with CUDA implementation of AMBER 18's PMEMD module. After discarding the first 10 ns, trajectory was analyzed using cpptraj (Roe and Cheatham, 2013) for describing the nature of protein:DNA interactions. Hydrogen bonds were determined using a distance cutoff of 3.5 Å between donor and acceptor atoms and an angle cutoff of 120°. Salt bridges were also established with a distance cutoff of 3.5 Å for a direct ion-pair contact between heavy atoms of charged groups and an increased cutoff of 6.0 Å for a solvent-separated ion-pair (Chen et al., 2015b).

Measure protein-DNA binding affinity by bio-layer interferometry (BLI)

Bio-layer interferometry experiments were conducted using a BLItz system equipped with Dip-and-Read Streptavidin (SA) Biosensors (ForteBio). BLItz monitors wavelength shifts (response, unit: nm) resulting from changes in the optical thickness of the sensor surface during association or dissociation of the analyte over time to obtain kinetics data i.e., k_{off} and k_{on} of interactions. The streptavidin biosensor (ForteBio) was hydrated in a binding buffer [100 mM Tris-HCl pH 7.4, 150 mM NaCl, 1 mM EDTA, and 0.005% Tween 20] for at least 10 min before each experiment. Biotinylated dsDNA was immobilized onto the surface of the SA biosensor through a cycle of Baseline (30 s), Association (120 s), and Dissociation (120 s). Briefly, the tip of the biosensor was dipped into a low salt buffer for 30 s to establish the baseline, then to 1 μM biotinylated dsDNA for 120 s, and finally to a low salt binding buffer for 120 s to allow for dissociation. Biotinylated dsDNA harboring *parS*, *NBS*, or variant of such sites were prepared by annealing a 24-bp biotinylated oligo with its unmodified complementary strand in an annealing buffer [1 mM Tris-HCl pH 8.0 and 5 mM NaCl]. The oligos mixture was heated to 98°C for 2 min and allowed to cool down to room temperature overnight.

After immobilizing DNA on the sensor, we first screened for protein-DNA interactions using a high protein concentration (1000 nM dimer concentration) (282 unique protein-DNA pairs in total, triplicated screens). A protein-DNA pair was regarded as not interacting if no/very weak BLI response above background was observed at this concentration, hence K_D was not determined. For other protein-DNA pairs where we observed BLI responses at 1000 nM, experiments were extended to include a range of protein concentrations. The concentration used were typically 0, 31, 62, 125, 250, 500, and 1000 nM. For weaker protein-DNA pairs, higher concentrations such as 2000 and 4000 nM were also employed. At the end of each protein binding step, the sensor was transferred into a protein-free binding buffer to follow the dissociation kinetics for 120 s. The sensor could be recycled by dipping in a high-salt buffer [100 mM Tris-HCl pH 7.4, 1000 mM NaCl, 1 mM EDTA, and 0.005% Tween 20] for at least 1 min to remove bound proteins.

For every protein-DNA pair, we first measured the kinetics (i.e., response versus time) at 1000 nM in triplicate, using three independent protein aliquots. The kinetic profiles were deemed reproducible, with deviations less than 10%. Then, for Figures 2D and 3C, we measured the kinetics once for each concentration (0, 31, 62, 125, 250, and 500 nM). Kinetics data were fitted locally, using an 1:1 binding model, for each protein concentration using BLItz Pro software (ForteBio) to determine k_{off}, k_{on}, and K_D (a ratio of k_{off}/k_{on}). The χ^2 and R^2 values were calculated, a local fitting was judged to be good if $\chi^2 < 3$ and $R^2 > 0.9$. For a poor local fitting (i.e., $\chi^2 > 3$ and $R^2 < 0.9$), typically because of a low BLI response at a low protein concentration, this datapoint was omitted from K_D calculation (BLI data analysis manual-ForteBio). Each calculated K_D at each concentration is considered as an independent determination of such value, hence we averaged to obtain mean K_D and standard deviation (SD) for each protein-DNA pair. For Figure 3A, we measured the kinetics in triplicate for every concentration in the range.

Clustering of trajectory-scanning mutagenesis data

K_D of interactions between ParB (WT)/PtoN variants and each of the 16 DNA-binding sites were presented as a two-dimensional heatmap using the *heatmap* function in R. Euclidean distances were measured to obtain a distance matrix, and a complete agglomeration method, implemented within the *heatmap* function, was used for clustering.

Chromatin immunoprecipitation with qPCR or deep sequencing

For *E. coli* ChIP-seq, cells harboring pUT18C-1xFLAG-ParB/Noc were grown in LB (25 mL) at 28°C to mid exponential phase (OD_{600} ~0.4) before 1 mM IPTG was added for 1-3 hours. The induction time (either 1, 2 or 3 hours) was chosen so that all ParB/Noc variants were produced to a similar level as judged by an α-FLAG western blot. Subsequently, formaldehyde is added to a final concentration of 1% to fix the cells.

Fixed cells were incubated at room temperature for 30 min, then quenched with 0.125 M glycine for 15 min at room temperature. Cells were washed three times with 1x PBS pH 7.4 and resuspended in 1 mL of buffer 1 [20 mM K-HEPES pH 7.9, 50 mM KCl, 10% Glycerol, and Roche EDTA-free protease inhibitors]. Subsequently, the cell suspension was sonicated on ice using a probe-type sonicator (8 cycles, 15 s on 15 s off, at setting 8) to shear the chromatin to below 1 kb, and the cell debris was cleared by centrifugation (20 min at 13,000 rpm at 4°C).

The supernatant was then transferred to a new 1.5 mL tube and the buffer conditions were adjusted to 10 mM Tris-HCl pH 8, 150 mM NaCl and 0.1% NP-40. Fifty microliters of the supernatant were transferred to a separate tube for control (the INPUT fraction) and stored at −20°C. In parallel, antibodies-coupled beads were washed off storage buffers before adding to the above supernatant. We employed α-FLAG antibodies coupled to agarose beads (Sigma Aldrich) for ChIP-seq of FLAG-ParB/Noc. Briefly, 100 μL of beads was washed off storage buffer by repeated centrifugation and resuspension in IPP150 buffer [10 mM Tris-HCl pH 8, 150 mM NaCl and 0.1% NP-40]. Beads were then introduced to the cleared supernatant and incubated with gentle shaking at 4°C overnight. In the next day, beads were then washed five times at 4°C for 2 min each with 1 mL of IPP150 buffer, then twice at 4°C for 2 min each in 1x TE buffer [10 mM Tris-HCl pH 8 and 1 mM EDTA]. Protein-DNA complexes were then eluted twice from the beads by incubating the beads first with 150 μL of the elution buffer [50 mM Tris-HCl pH 8.0, 10 mM EDTA, and 1% SDS] at 65°C for 15 min, then with 100 μL of 1x TE buffer + 1% SDS for another 15 min at 65°C. The supernatant (the ChIP fraction) was then separated from the beads and further incubated at 65°C overnight to completely reverse crosslink. The INPUT fraction was also de-crosslinked by incubation with 200 μL of 1x TE buffer + 1% SDS at 65°C overnight. DNA from the ChIP and INPUT fraction were then purified using the PCR purification kit (QIAGEN) according to the manufacturer's instruction, then eluted out in 50 μL of EB buffer (QIAGEN). The purified DNA was then used directly for qPCR or being constructed into library suitable for Illumina sequencing using the NEXT Ultra library preparation kit (NEB). ChIP libraries were sequenced on the Illumina HiSeq 2500 at the Tufts University Genomics facility. For the list of ChIP-seq datasets in this study, see Table S5.

Generation and analysis of ChIP-seq profiles

For analysis of ChIP-seq data, Hiseq 2500 Illumina short reads (50 bp) were mapped back to the *Escherichia coli* MG1655 reference genome using Bowtie1 (Langmead et al., 2009) and the following command: bowtie -m 1 -n 1–best–strata -p 4–chunkmbs 512 MG1655-bowtie–sam *.fastq > output.sam

Subsequently, the sequencing coverage at each nucleotide position was computed using BEDTools (Quinlan and Hall, 2010) using the following command: bedtools genomecov -d -ibam output.sorted.bam -g Ecoli_MG1655.fna > coverage_output.txt

ChIP-seq profiles were plotted with the x axis representing genomic positions and the y axis is the number of reads per base pair per million mapped reads (RPBPM) using custom R scripts. To calculate the enrichment of reads at the *parS* or *NBS* site (Figure S1B), we summed the RPBPM values for a 100-bp window surrounding the *parS* or *NBS* site.

Bacterial one-hybrid assay coupled with deep sequencing (B1H-seq)

Optimization of bacterial one-hybrid assays. Bacterial one-hybrid (B1H) assays were performed as described previously (Noyes et al., 2008). Recipes for the minimal medium for B1H selection were described in detail previously (Noyes et al., 2008). Several parameters (promoter strength, spacers between the core −10 −35 promoter and the *NBS*/*parS* site, and IPTG concentration) were empirically optimized for experiments described in this work (Figure S4). We found that induction of ω-*parB** from a weak *lacUV5mut* promoter, using 0.1 mM IPTG, minimizes toxicity to the cells. Also, a 19-bp spacer between the core −10 −35 promoter and the *parS*/*NBS* site is optimal for the induction of HIS3 URA3 but does not auto-induce these genes (Figure S4). Therefore, we employed *pU3H3::19bp-parS* and *pU3H3::19bp-NBS* plasmids for all subsequent B1H selection.

Construction of combinatorial plasmid libraries. To construct combinatorial mutagenesis libraries where codons for Q173, K179, K184, and R201 were replaced with NNS (N = A/T/G/C, S = G/C), we employed round-the-horn PCR using oligos For_B_NNS_HTH, Rev_B_NNS_HTH, and pB1H2-$P_{lacUV5mut}$-*Caulobacter* ParB (R104A + Q173K179K184R201) plasmid as template. Briefly, desalted oligos were reconstituted in 1x T4 ligase buffer, and 5′ phosphorylated using T4 PNK enzyme (NEB). Thirty 50μL PCR reactions were performed before DpnI was added and incubated overnight at 37°C to remove the methylated template. Next, PCR product (~4.5 kb) was gel-purified and re-circularized overnight using T4 DNA ligase (NEB). The product was then ethanol precipitated to remove salts, and the DNA pellet was resuspended in 50 μL of water before being introduced into electrocompetent *E. coli* DH5α cells. Around 15 million carbenicillin-resistant *E. coli* colonies were collected, pooled together, and have their plasmid extracted (QIAGEN MiniPrep kit). The whole procedure was repeated two more times, and on different days, to obtain three independent combinatorial libraries. Libraries from ~15 million individual colonies ensure that at least 99% completeness is achieved (Bosley and Ostermeier, 2005).

Selection of ParB variants that bind to NBS *or* parS. The selection strain TLE3001 (USO *rpoZ- hisB- pyrF-*) harboring either *pU3H3::19bp-NBS* or *pU3H3::19bp-parS* plasmid was made electrocompetent. Next, approximately 2 μg of the combinatorial plasmid library were electroporated into 100 μL of the selection strain. The procedure was repeated for four more times, and electroporated cells were recovered in 10 mL of LB for an hour at 37°C. Subsequently, cells were washed off rich LB medium and resuspended in 5ml of 1x M9 liquid. Cells were then plated out on ten 150 mm Petri plates containing M9-minus-histidine medium

supplemented with 0.1 mM IPTG, 5 mM 3-AT (a competitive inhibitor of HIS3, to increase the stringency of the selection), and appropriate antibiotics. Plates were incubated at 37°C for 48 hours before cells were scrapped off the agar surface, pooled together, and had their plasmids extracted (QIAGEN Miniprep kit).

Construction of deep sequencing libraries. Illumina Truseq-compatible libraries were constructed from pre- and post-selection plasmid libraries via two rounds of PCR.

PCR round 1. Primer 4nns_R (10 μM): 2.5 μL

Mixture in equimolar amount of primers 4nns_offset_0_F; 4nns_offset_1_F; 4nns_offset_2_F; 4nns_offset_3_F; 4nns_offset_4_F (10 μM): 2.5 μL. A mixture of forward primers were used to stagger reads across the amplicon to improve the distribution of base calls at each position during the initial rounds of Illumina sequencing.

dNTP (10mM): 1 μL

DMSO: 1.5 μL

Plasmid template (pre- or post-selection): 1 μL of 500 ng/μL

Phusion polymerase: 0.5 μL

5x HF buffer: 10 μL

Water: 31 μL

PCR program: 98°C for 30 s, (98°C for 10 s, 56°C for 20 s, 72°C for 10 s) x 20 cycles, 72°C for 5 min.

PCR products were gel-purified, quantified by Qubit hsDNA quantification kit (ThermoFisher), and used as template in the second PCR.

PCR round 2. NEBNext Index primer (NEB): 2.5 μL

NEBNext universal primer (NEB): 2.5 μL

dNTP (10mM): 1 μL

DMSO: 1.5 μL

Template: 5 μL of gel-purified DNA from PCR round 1

5x HF buffer: 10 μL

Phusion polymerase: 0.5 μL

Water: 27 μL

PCR program: 98°C for 30 s, (98°C for 10 s, 54°C for 20 s, 72°C for 10 s) x 12 cycles, 72°C for 5 min.

PCR products were gel-purified, quantified by Qubit hsDNA quantification kit (ThermoFisher), and were sequenced on the Illumina HiSeq 2500 (single-end, 150-bp read length, 15% spike-in phiX DNA) at the Tufts University Genomics facility. For the list of B1H-seq datasets in this study, see Table S5.

Analysis of data from deep mutational scanning experiments

Processing deep sequencing reads. We used fastx_trimmer script from the FASTX-Toolkit to remove nucleotides 0 to 20 and 114 to 150 from our reads using the following command: fastx_trimmer -f 20 -l 114 -Q33 -i TLE4_S4_R1_001.fastq -o TLE4_trimmed.fastq. Subsequently, we discarded sequence reads with an average Phred score < 28, using the fastq_quality_filter script in the FASTX-Toolkit: fastq_quality_filter -v -Q33 -q 28 -p 100 -i TLE4_trimmed -o TLE4_trimmed_filtered.fastq. Reads were further filtered for the exact match to the following sequence:[ATGC][ATGC][GC]tctcacgtagcgaat[ATGC][ATGC][GC]atgcgtcttctt[ATGC][ATGC][GC]ttgccggacgaggtacagtcctatcttgtgagtggagagctgacagcg[ATGC][ATGC][GC]. Corresponding codons (bases 1-3, 19-21, 34-36, 85-87) for the four specificity residues were extracted from the above 87-bp nucleotide sequence, and subsequently translated to amino acid sequence, following the standard genetic code. Variants with stop codon (TAG) were removed and were not considered in subsequent steps. Because of a high reproducibility among replicates (Figure S5C), we pooled reads from three replicates together (Figure S5A). We counted the number of occurrences (counts) for each unique variant, and removed variants with less than 10 reads (Figure S5B). Greater than 94% of all 160,000 predicted variants were represented by at least 10 reads. The variant counts for pre-selection and post-selection (for *parS*- or *NBS*-binding) libraries were used in the following steps to estimate the fitness score of each variant.

Calculation of fitness scores. We calculated the fitness of each variant (f_{parS} *and* f_{NBS}), in comparison to WT variants (RTAG or QKKR), as described previously (Aakre et al., 2015; van Opijnen et al., 2009).

$f_{parS,\ raw}$ = $\log_{10}$(N variant, *parS* post-selection library / N wt, *parS* post-selection library) - $\log_{10}$(N variant, pre-selection library / N wt, pre-selection library)

N variant, *parS* post-selection library = counts of each variant in the post-selection library for binding to *parS*.

N wt, *parS* post-selection library = counts of the WT (RTAG) in the post selection library for binding to *parS*.

N variant, pre-selection library = counts of each variant in the pre-selection (starting) library.

N wt, pre-selection library = counts of the WT (RTAG) in the pre-selection (starting) library.

$f_{NBS,\ raw}$ = $\log_{10}$(N variant, *NBS* post-selection library / N wt, *NBS* post-selection library) - $\log_{10}$(N variant, pre-selection library / N wt, pre-selection library)

N variant, *NBS* post-selection library = counts of each variant in the post-selection library for binding to *NBS*.

N wt, *NBS* post-selection library = counts of the WT (QKKR) in the post selection library for binding to *NBS*.

N variant, pre-selection library = counts of each variant in the pre-selection (starting) library.

N wt, pre-selection library = counts of the WT (QKKR) in the pre-selection (starting) library.

These raw fitness scores were further transformed so that f_{parS} of the RTAG variant was 1 and that of QKKR variant was 0, and f_{NBS} of the RTAG variant was 0 and that of QKKR variant was 1. The fitness scores for every variant were presented in the fitness scatterplot (Figure 5C). Dark green: strong *parS* binding, no *NBS* binding (fitness score: $f_{parS} \geq 0.6$, $f_{NBS} \leq 0.2$); light green: strong *parS* binding, weak-to-medium *NBS* binding ($f_{parS} \geq 0.6$, $0.2 \leq f_{NBS} \leq 0.6$); magenta: strong *NBS* binding, no *parS* binding ($f_{NBS} \geq 0.6$, $f_{parS} \leq 0.2$); pink: strong *NBS* binding, weak-to-medium *parS* binding ($f_{NBS} \geq 0.6$, $0.2 \leq f_{parS} \leq 0.6$); black: dual specificity i.e., bind strongly to both *parS* and *NBS* ($f_{NBS} \geq 0.6\, f_{parS} \geq 0.6$). Frequency logos of each class of variants were constructed using WebLogo 3.0 (Crooks et al., 2004)

Reproducibility among replicates. To check the reproducibility among replicates, we plotted $\log_{10}$(counts) of each variant in replicate 1 versus replicate 2 (and versus replicate 3). Only variants with more than four reads were included in such plot. We used R to calculate Pearson's correlation coefficients (R^2) and to plot the linear best fit (Figure S5C). We found that independent experiments were reproducible (R^2 = 0.86-0.98) (Figure S5C). Reads from three independent replicates were subsequently pooled together for the pre-selection, *parS* post-selection, and *NBS* post-selection experiments. Pooled reads were used to construct the scatterplot and frequency sequence logos (Figure 5C), and for the construction of the network graph (Figure 6B).

Generation of force-directed networks graphs and analysis of shortest paths. We constructed a force-directed graph that connects functional variants (nodes) together by lines (edges) if they are different by a single aa (Figure 6B). The node size is proportional to its connectivity (number of edges), and node colors represent different classes of functional variants (Figure 6B). Similarly, we also created a network graph in which edges represent variants that differ by a nt substitution, following a standard codon table (Figure S7A). Force-directed graphs were generated using Gephi network visualization software. Node and edge files were prepared in R. The network layout was generated by running the ForceAtlas algorithm that was implemented in Gephi. Default parameters were used for the ForceAtlas algorithm, except that the repulsion and attraction strength were set to 200 and 10, respectively. The ForceAtlas algorithm arranged nodes in the two-dimensional space based on connectivity: nodes tend to repel each other but they are attracted to each other if these exists a connectivity (an edge). As the result of running the Force Atlas to completion, densely interconnected nodes are clustered together while less well-connected nodes are forced to different spatial locations. To analyze the properties of the network and the mutational paths that traverse the network, we employed the *igraph* package implemented in R. Our network did not include non-functional (gray) variants/nodes.

QUANTIFICATION AND STATISTICAL ANALYSIS

Information about statistical analysis and sample size for each experiment are detailed in the relevant STAR Methods sections.

Cell Reports, Volume *32*

Supplemental Information

Diversification of DNA-Binding Specificity by Permissive and Specificity-Switching Mutations in the ParB/Noc Protein Family

Adam S.B. Jalal, Ngat T. Tran, Clare E. Stevenson, Elliot W. Chan, Rebecca Lo, Xiao Tan, Agnes Noy, David M. Lawson, and Tung B.K. Le

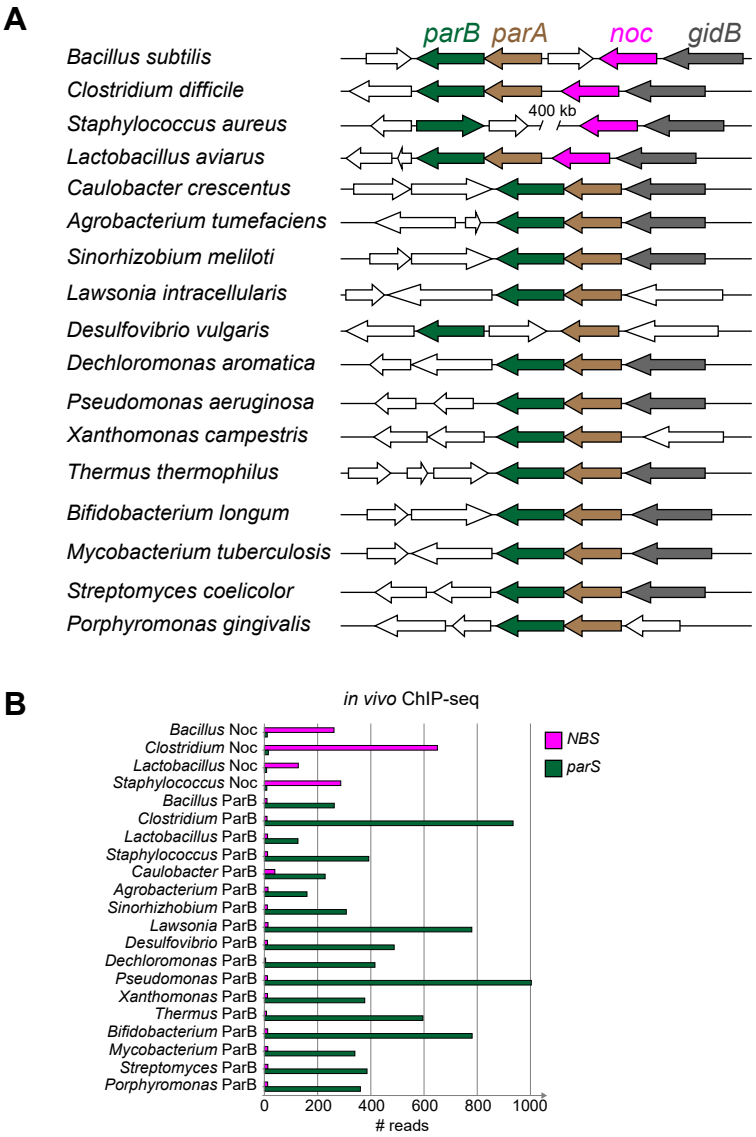

Figure S1. DNA-binding specificity for *parS* and *NBS* is conserved among ParB and Noc orthologs. Related to Figure 1. (A) Genomic context of ParB- and Noc-encoding genes in various bacterial species. *parB*, *parA*, *noc*, and the highly conserved *gidB* gene, are colored in dark green, brown, magenta, and grey, respectively. Genes at the border of the *parB-parA-noc* cluster (open arrows) vary between bacterial species. **(B)** The *in vivo* binding preferences of ParB/Noc to *parS/NBS* as measured by ChIP-seq. An *E. coli* strain with a single *parS* and *NBS* site engineered onto the chromosome was used as a heterologous host for expression of FLAG-tagged ParB/Noc. For ChIP-seq data, reads in a 100-bp window surrounding the *parS/NBS* site were quantified and used as a proxy for the enrichment of immunoprecipitated *parS* or *NBS* DNA.

A Noc (DBD)-*NBS* co-crystal structure

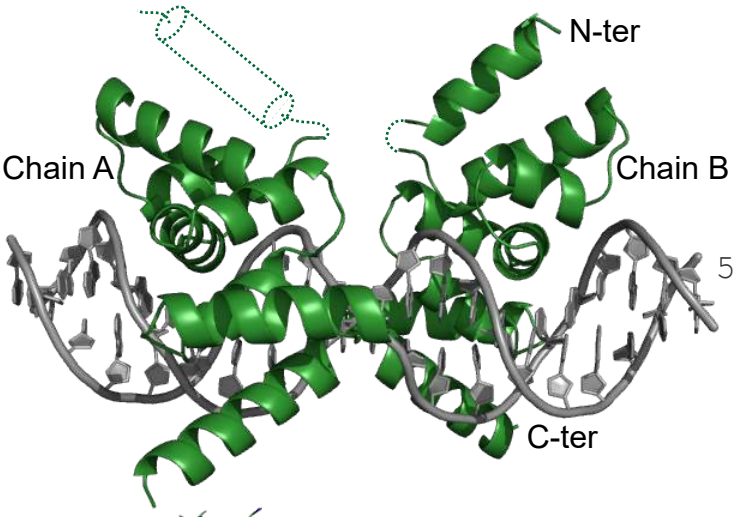

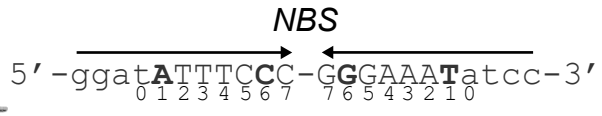

B

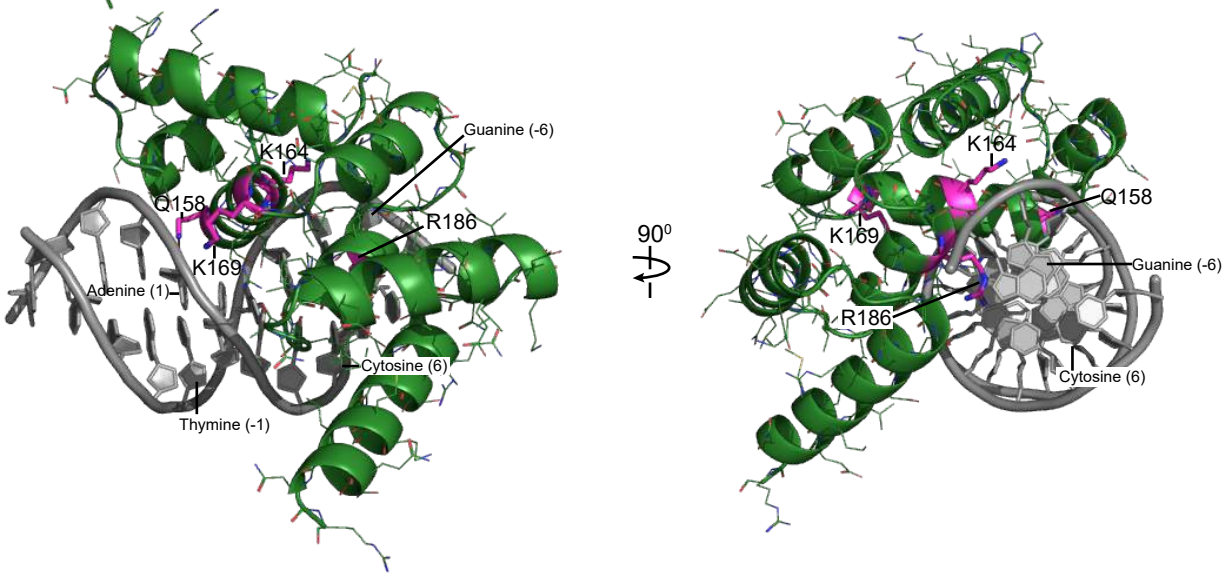

C

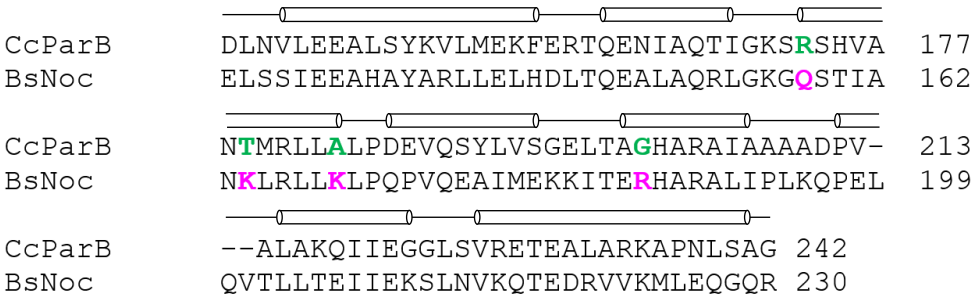

D

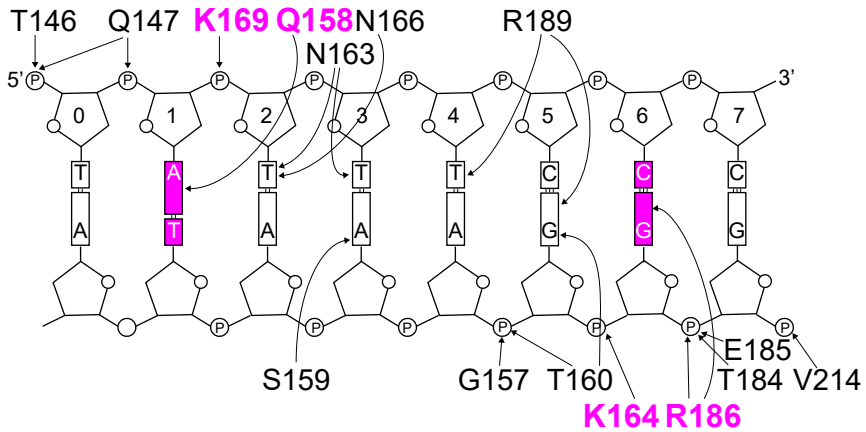

figure legend on the next page

Figure S2. Co-crystal structures of the Noc (DBD)-*NBS* complex. Related to Figure 4. **(A)** The structure of two Noc (DNA-binding domain) monomers (dark green) in complex with a 22-bp *NBS* DNA (grey). A helix (residues 113-125, dotted dark green cylinder) in chain A is not resolved. The nucleotide sequence of the 22-bp *NBS* site is shown on the left-hand side; bases (Adenine 1 and Cytosine 6) that are different from *parS* are in bold. **(B)** One monomer of Noc (DBD) is shown in complex with an *NBS* half-site; four core specificity residues are shown in stick presentation, labeled, and colored in magenta. Other residues surrounding specificity residues are showed as lines and colored in dark green. **(C)** Amino acid sequences of *C. crescentus* ParB and *B. subtilis* Noc with the positions of four specificity residues highlighted in dark green and magenta, respectively. Secondary structures are shown above the sequence alignment. **(D)** Schematic representation of Noc (DBD)-*NBS* interactions. For simplicity, only half of *NBS* is shown. The two bases at position 1 and 6 that are different between *parS* and *NBS* are highlighted in magenta. The four core specificity residues are also colored in magenta.

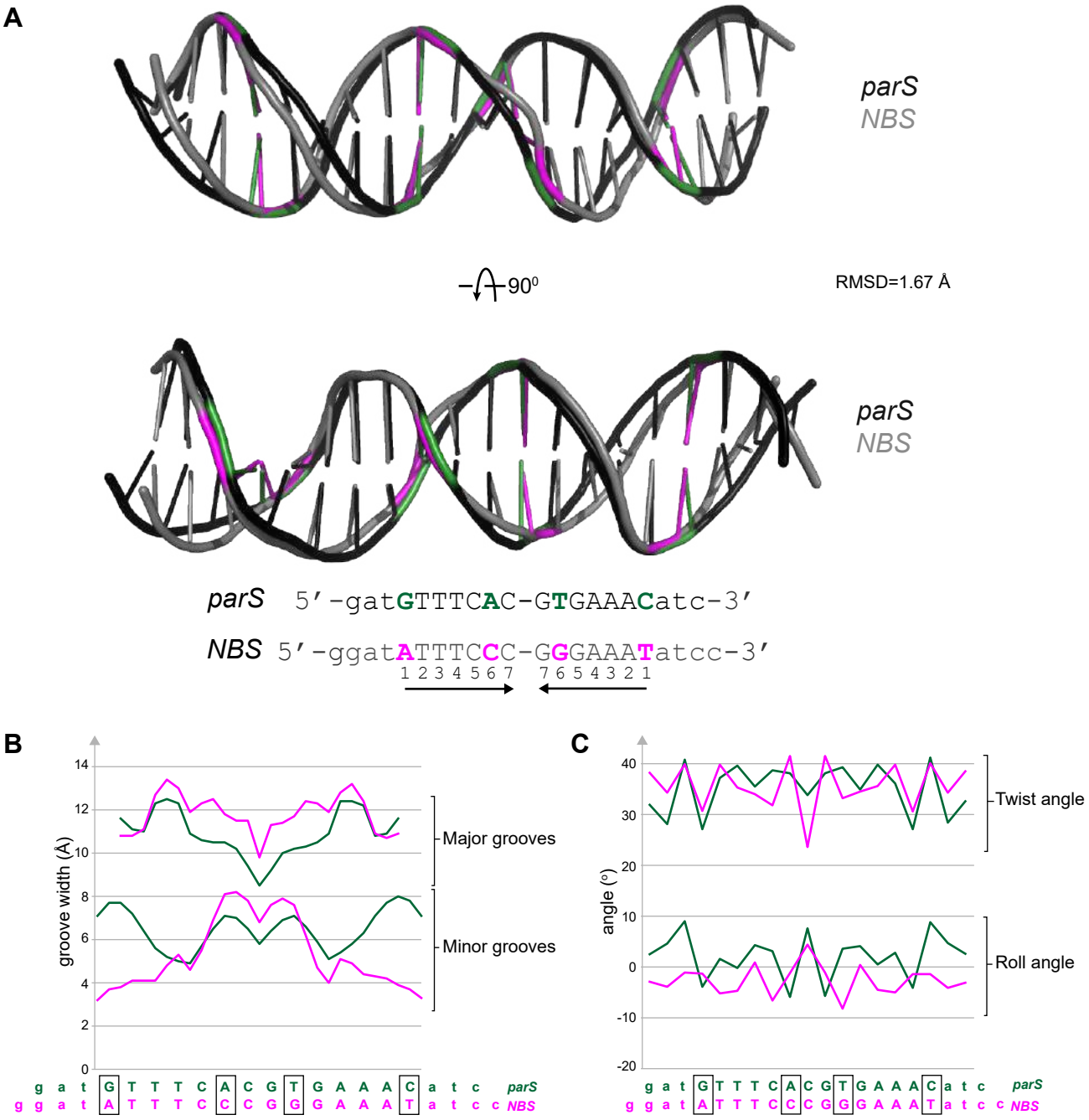

Figure S3. Conformational changes at *parS* and *NBS* DNA within the two co-crystal structures. Related to Figure 4. (A) Superimposition of *parS* and *NBS* DNA structures, root-mean-square deviation (RMSD) value is also shown. Bases that differ between *parS* (dark green) and *NBS* (magenta) are highlighted. **(B)** The major and minor groove widths of the bound DNA (*parS*: dark green, *NBS*: magenta). **(C)** The roll and twist angles for each base pair step of the bound DNA (*parS*: dark green, *NBS*: magenta).

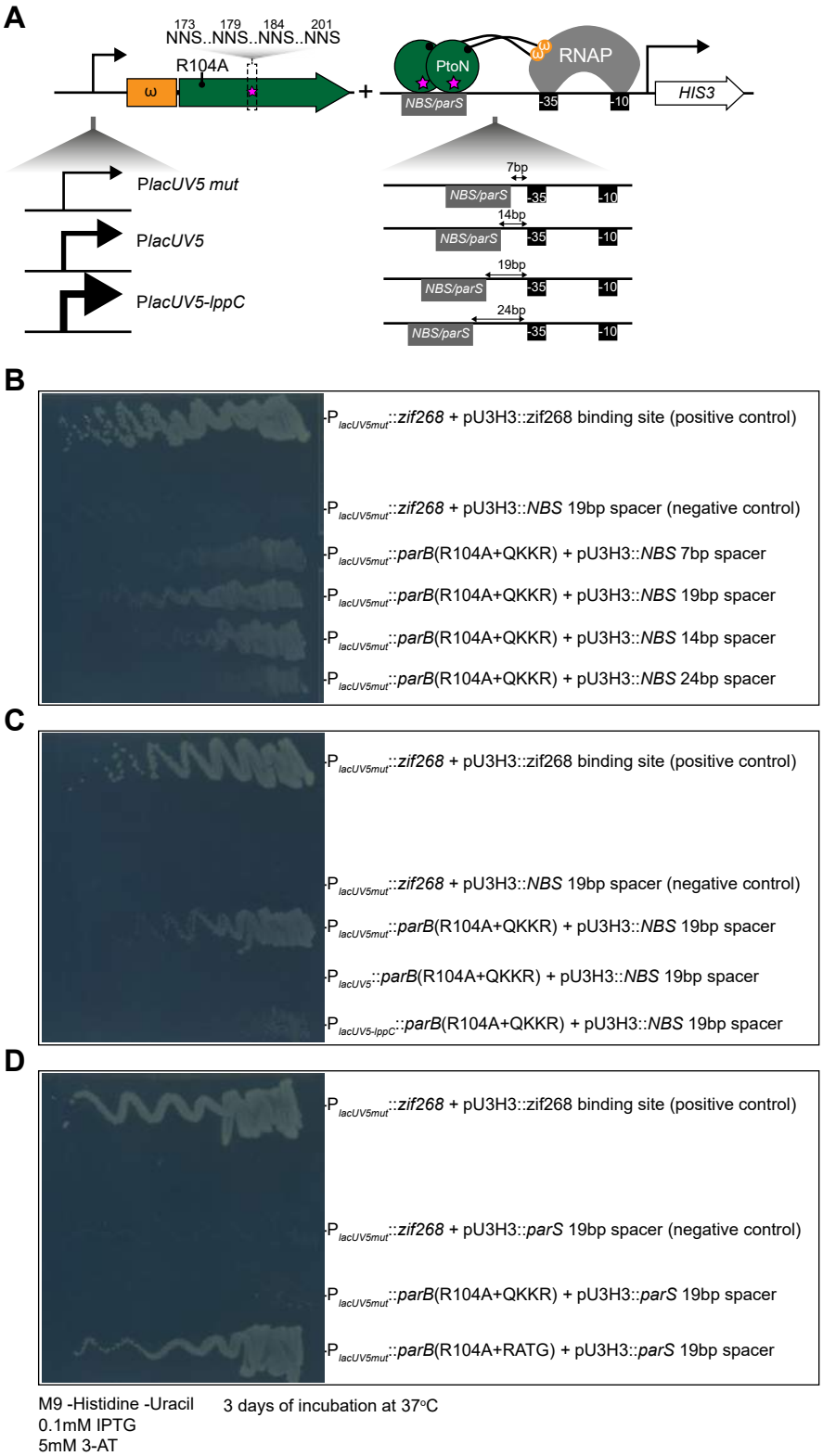

Figure S4. Optimization of bacterial one-hybrid (B1H) assay to select for variants that bind *parS* or *NBS*. Related to Figure 5. (A) The strength of the promoter that drives the expression of *parB* variants and the distances between the *parS* or *NBS* binding site to the core -10 -35 promoter were optimized. **(B)** A 19-bp gap between *NBS/parS* and the core promoter is optimal, based on the streak test for cell growth in a minimal medium lacking histidine. **(C)** A weak promoter ($P_{lacUV5mut}$) is optimal, based on the streak test for cell growth in a minimal medium lacking histidine. **(B and D)** The presence of *parS* or *NBS* upstream of HIS3, in the absence of ParB variants, did not auto-activate its expression.

A

	number of quality-filter reads
Pre-selection, replicate 1	6,954,115
Pre-selection, replicate 2	8,623,273
Pre-selection, replicate 3	7,201,395
Total	22,778,783
Post-selection NBS, replicate 1	6,294,658
Post-selection NBS, replicate 2	7,487,037
Post-selection NBS, replicate 3	6,689,637
Total	20,471,332
Post-selection parS, replicate 1	5,380,569
Post-selection parS, replicate 2	8,572,521
Post-selection parS, replicate 3	7,269,057
Total	21,222,147

B

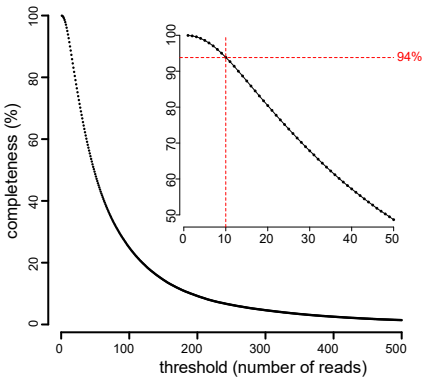

C

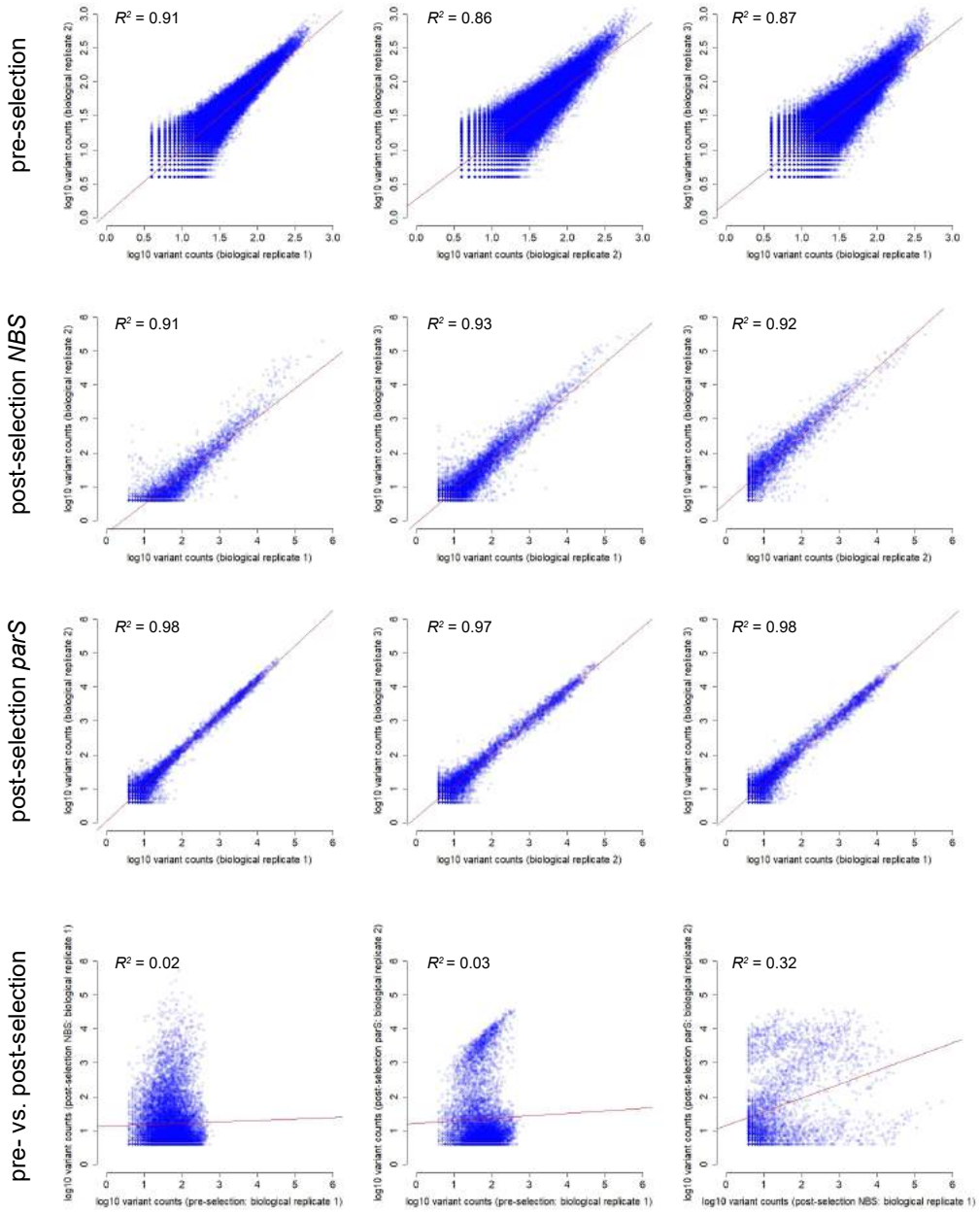

Figure S5. Statistics of deep sequencing reads and completeness of starting libraries. Related to Figure 5. (A) Number of quality-filtered reads for each biological replicate, for pre- and post-selection libraries. **(B)** The completeness of pre-selection libraries at different thresholds. A completeness of 100% means that all 160,000 variants lacking stop codons were present in the pre-selection library. In the starting library, greater than 94% of the predicted variants were represented by at least 10 reads. **(C)** Reproducibility of biological replicates: pre- vs. pre-selection replicates and pre- vs. post-selection replicates. Pearson's correlation coefficients (R^2) are also shown. Red lines show least squares best fits.

A

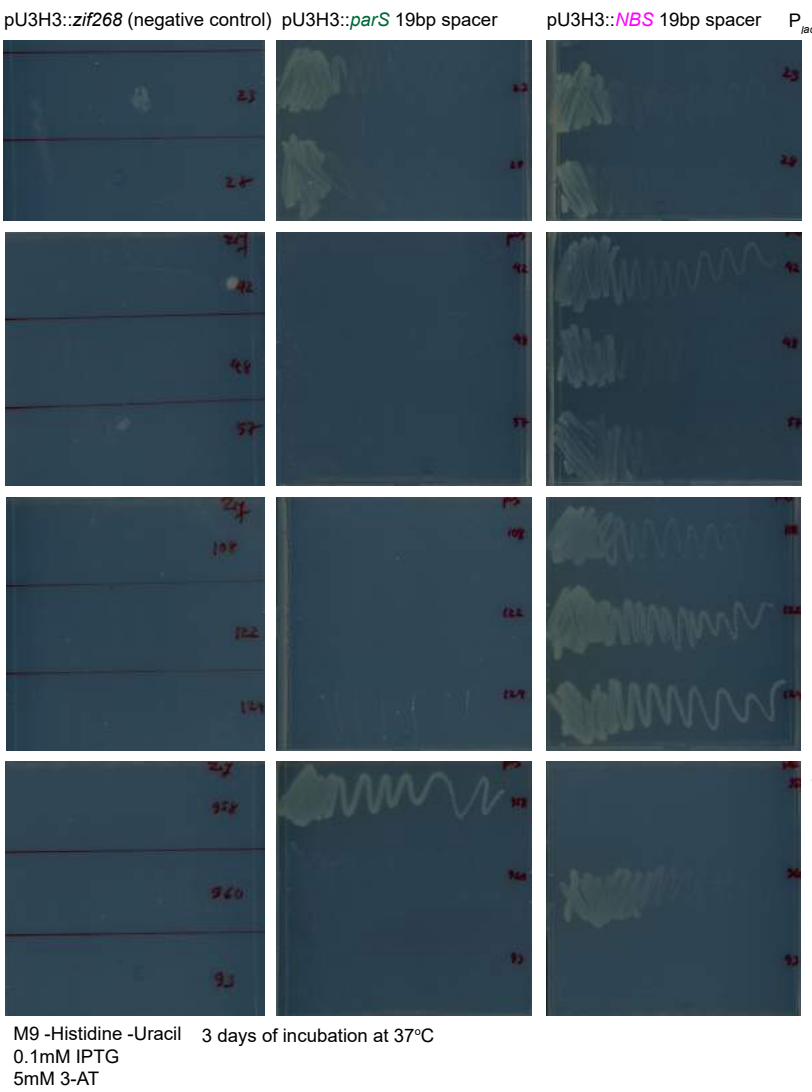

B

	K_D^{parS} (nM)	K_D^{NBS} (nM)
RRMT	12 ± 2.4	45 ± 11
RRLT	7.0 ± 3.0	26 ± 9.0
QRMR	no binding	60 ± 26
QSRR	no binding	30 ± 16
QTNR	no binding	800 ± 92
QRYR	no binding	65 ± 12
QRRR	no binding	4.0 ± 1.2
QRKR	no binding	4.0 ± 3.0
WT (RTAG)	11 ± 7.0	no binding
QKKR	no binding	28 ± 5.0
TEPG	no binding	no binding

Figure S6. Validation of selected variants from the deep mutational scanning experiments. Related to Figure 5. (A) Validation by pairwise bacterial one-hybrid assays. The ability of nine selected variants to grow on a minimal medium lacking histidine (but supplemented with 5mM 3-AT to increase the stringency) was assessed by a streak test. Plasmid harboring a binding site of an eukaryotic transcription factor (*zif268*) served as a negative control. **(B)** Validation by bio-layer interferometry assays. Selected variants were expressed, purified, and K_D ± SD were measured by bio-layer interferometry assay.

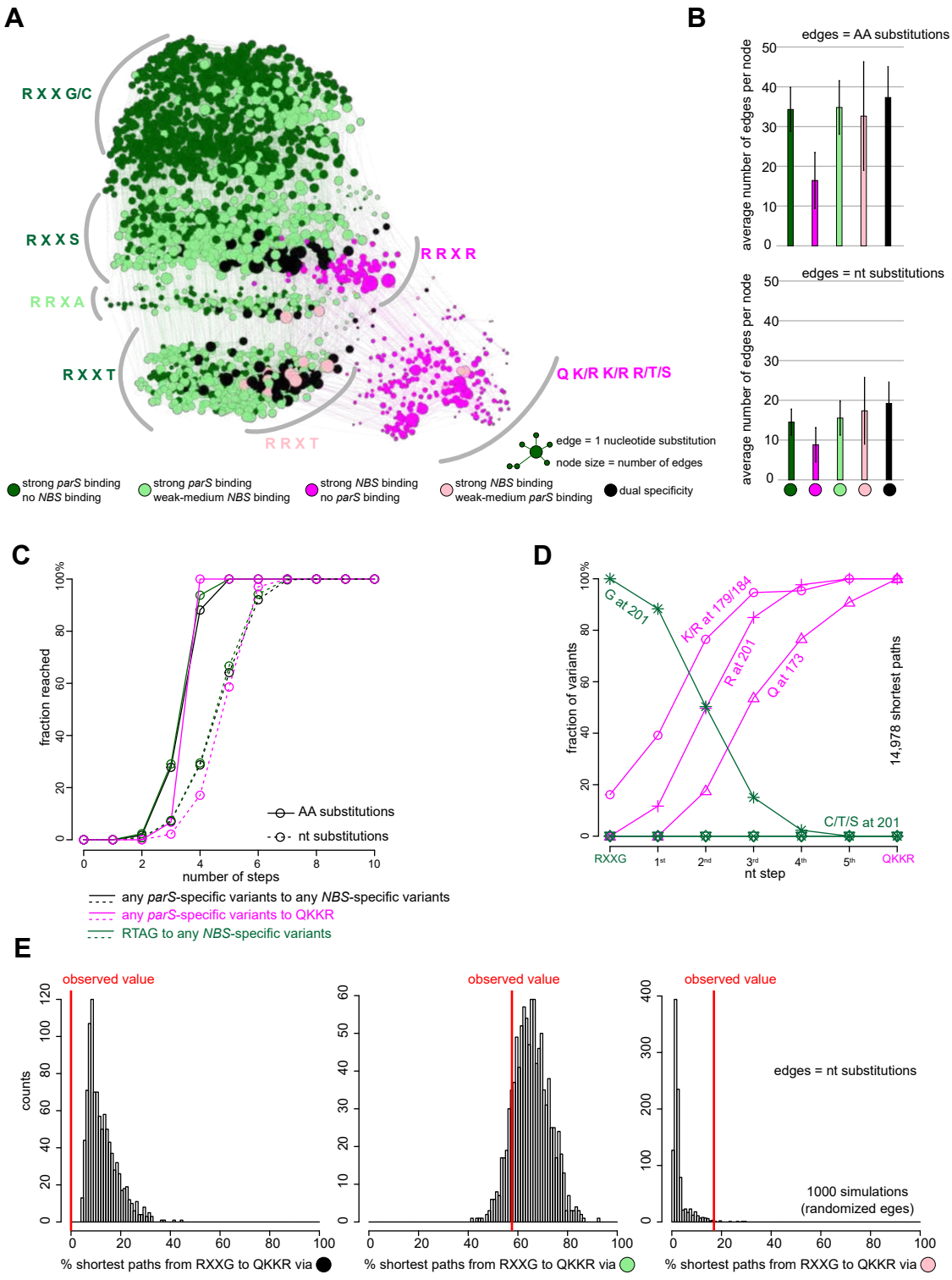

Figure S7. Deep mutational scanning experiments reveal the common properties of mutational paths. Related to Figure 6. (A) A force-directed network graph connecting strong *parS*-binding variants to strong *NBS*-binding variants. Nodes represent individual variants, and edges represent single nucleotide (nt) substitutions. Node sizes are proportional to their corresponding numbers of edges. Node colors correspond to different classes of variants. **(B)** Average number of edges per node. **(C)** Cumulative fraction of variants that reached their destinations in a given number of amino acid (solid line) or nucleotide (dotted line) substitutions. Black lines: from any *parS*-specific variants to any *NBS*-specific variants. Magenta lines: from any *parS*-specific variants to QKKR. Dark green lines: from RTAG to any *NBS*-specific variants. **(D)** Fraction of intermediates on all shortest paths from highly *parS*-specific RXXG variants to the *NBS*-preferred QKKR that have permissive amino acids (K/R) at either position 179/184 or both, or have R at position 201, or Q at position 173, or C/T/S at position 201 after a given number of nt steps. **(E)** Percentage of shortest paths that traversed black, light green, or pink variants to reach QKKR from any of the highly *parS*-specific RXXG variants (red lines). The result was compared to ones from 1,000 simulations where the by-nt-substitution edges were shuffled randomly while keeping the total number of nodes, edges, and graph density constant.

TABLE S1. STRAINS. Related to STAR Methods.

Strains	Strains/descriptions	Source
AB1157	*thr-1, ara-14, leuB6, Δ(gpt-proA)62, lacY1, tsx-33, supE44, galK2, rac-, hisG4(Oc), rfbD1, mgl-51, rpsL31, kdgK51, xyl-5, mtl-1, argE3 (Oc), thi-1, qsr-*	Yale *E. coli* Genetic Stock Center
DH5α	*E. coli* host for DNA cloning and propagation of plasmid	Le lab collection
Rosetta (DE3)	*E. coli* host for protein overexpression from an IPTG-inducible T7 promoter	Merck
CJW4025	BL21 pET21b::*parB-(his)6*	Gift from Christine Jacob-Wagner (Lim et al., 2014)
TLE3000	*AB1157 ybbD::parS::markerless ygcE::NBS::markerless*	This study
TLE3001	*USO rpoZ- hisB- pyrF-*	Scott Wolfe (Noyes et al., 2008) via Addgene
	TLE3000+pUT18C::1xFLAG-*Bacillus subtilis* Noc	This study
	TLE3000+pUT18C::1xFLAG-*Clostridium difficile* Noc	This study
	TLE3000+pUT18C::1xFLAG-*Lactobacillus aviarius* Noc	This study
	TLE3000+pUT18C::1xFLAG-*Staphylococcus aureus* Noc	This study
	TLE3000+pUT18C::1xFLAG-*Bacillus subtilis* ParB	This study
	TLE3000+pUT18C::1xFLAG-*Clostridium difficile* ParB	This study
	TLE3000+pUT18C::1xFLAG-*Lactobacillus aviarius* ParB	This study
	TLE3000+pUT18C::1xFLAG-*Staphylococcus aureus* ParB	This study
	TLE3000+pUT18C::1xFLAG-*Caulobacter crescentus* ParB	This study
	TLE3000+pUT18C::1xFLAG-*Agrobacterium tumefaciens* ParB	This study
	TLE3000+pUT18C::1xFLAG-*Sinorhizobium meliloti* ParB	This study
	TLE3000+pUT18C::1xFLAG-*Lawsonia intracellularis* ParB	This study
	TLE3000+pUT18C::1xFLAG-*Desulfovibrio vulgaris* ParB	This study
	TLE3000+pUT18C::1xFLAG-*Dechloromonas aromatica* ParB	This study
	TLE3000+pUT18C::1xFLAG-*Pseudomonas aeruginosa* ParB	This study
	TLE3000+pUT18C::1xFLAG-*Xanthomonas campestris* ParB	This study
	TLE3000+pUT18C::1xFLAG-*Thermus thermophilus* ParB	This study
	TLE3000+pUT18C::1xFLAG-*Bifidobacterium longum* ParB	This study
	TLE3000+pUT18C::1xFLAG-*Mycobacterium tuberculosis* ParB	This study
	TLE3000+pUT18C::1xFLAG-*Streptomyces coelicolor* ParB	This study
	TLE3000+pUT18C::1xFLAG-*Porphyromonas gingivalis* ParB	This study
	TLE3001 + pB1H2-w2::*zif268* + pU3H3::*zif268* binding site	This study
	TLE3001 + pB1H2-w2::*zif268* + pU3H3::19bp-*NBS*	This study
	TLE3001 + pB1H2-w2::*Caulobacter* ParB (R104A + Q173K179K184R201) + pU3H3::7bp-*NBS*	This study
	TLE3001 + pB1H2-w2::*Caulobacter* ParB (R104A + Q173K179K184R201) + pU3H3::14bp-*NBS*	This study
	TLE3001 + pB1H2-w2::*Caulobacter* ParB (R104A + Q173K179K184R201) + pU3H3::19bp-*NBS*	This study
	TLE3001 + pB1H2-w2::*Caulobacter* ParB (R104A + Q173K179K184R201) + pU3H3::24bp-*NBS*	This study
	TLE3001 + pB1H2-w5::*Caulobacter* ParB (R104A +	This study

	Q173K179K184R201) + pU3H3::19bp-*NBS*	
	TLE3001 + pB1H2-w5L::*Caulobacter* ParB (R104A + Q173K179K184R201) + pU3H3::19bp-*NBS*	This study
	TLE3001 + pB1H2-w2::*zif268* + pU3H3::19bp-*parS*	This study
	TLE3001 + pB1H2-w2::*Caulobacter* ParB (R104A + Q173K179K184R201) + pU3H3::19bp-*parS*	This study
	TLE3001 + pB1H2-w2::*Caulobacter* ParB (R104A + R173A179T184G201) + pU3H3::19bp-*parS*	This study
	BL21 Rosetta pRARE + various pET21b-based protein overexpression vectors (see the plasmid list for the complete collection of protein overexpression plasmids)	This study

TABLE S2. PLASMIDS. Related to STAR Methods.

Plasmids	Description	Source
pENTR::D-TOPO	ENTRY vector for Gateway cloning, kanamycin^R	Invitrogen
	pENTR::*Bacillus subtilis* Noc	This study
	pENTR::*Clostridium difficile* Noc	This study
	pENTR::*Lactobacillus aviarius* Noc	This study
	pENTR::*Staphylococcus aureus* Noc	This study
	pENTR::*Bacillus subtilis* ParB	This study
	pENTR::*Clostridium difficile* ParB	This study
	pENTR::*Lactobacillus aviarius* ParB	This study
	pENTR::*Staphylococcus aureus* ParB	This study
	pENTR::*Caulobacter crescentus* ParB	This study
	pENTR::*Agrobacterium tumefaciens* ParB	This study
	pENTR::*Sinorhizobium meliloti* ParB	This study
	pENTR::*Lawsonia intracellularis* ParB	This study
	pENTR::*Desulfovibrio vulgaris* ParB	This study
	pENTR::*Dechloromonas aromatica* ParB	This study
	pENTR::*Pseudomonas aeruginosa* ParB	This study
	pENTR::*Xanthomonas campestris* ParB	This study
	pENTR::*Thermus thermophilus* ParB	This study
	pENTR::*Bifidobacterium longum* ParB	This study
	pENTR::*Mycobacterium tuberculosis* ParB	This study
	pENTR::*Streptomyces coelicolor* ParB	This study
	pENTR::*Porphyromonas gingivalis* ParB	This study
pML477	Gateway-cloning destination vector for fusion of protein interest to an N-terminally FLAG tag, xylose-inducible promoter, high-copy number plasmid, spectinomycin^R	Gift from Michael Laub
pET21b::ParB-(His)6	overexpression of ParB-$(His)_6$ from an IPTG-inducible T7 promoter	Promega
	pET21b::*Caulobacter crescentus*-ParB-$(His)_6$ (WT)	Gift of Christine Jacob Wagner (Lim et al., 2014)
	pET21b::*Caulobacter crescentus*-ParB-$(His)_6$ (DBD)	This study
	pET21b::*Bacillus subtilis*-Noc-$(His)_6$	This study
	pET21b::*Bacillus subtilis*-Noc-$(His)_6$ (DBD)	This study
	pET21b::PtoN1-$(His)_6$ (Q173T179A184G201)	This study
	pET21b::PtoN2-$(His)_6$ (R173K179A184G201)	This study
	pET21b::PtoN3-$(His)_6$ (R173T179K184G201)	This study
	pET21b::PtoN4-$(His)_6$ (R173T179A184R201)	This study
	pET21b::PtoN5-$(His)_6$ (Q173K179A184G201)	This study
	pET21b::PtoN6-$(His)_6$ (Q173T179K184G201)	This study
	pET21b::PtoN7-$(His)_6$ (Q173T179A184R201)	This study
	pET21b::PtoN8-$(His)_6$ (R173K179K184G201)	This study
	pET21b::PtoN9-$(His)_6$ (R173K179A184R201)	This study
	pET21b::PtoN10-$(His)_6$ (R173T179K184R201)	This study

	pET21b::PtoN11-(His)$_6$ (Q173K179K184G201)	This study
	pET21b::PtoN12-(His)$_6$ (Q173K179A184R201)	This study
	pET21b::PtoN13-(His)$_6$ (Q173T179K184R201)	This study
	pET21b::PtoN14-(His)$_6$ (R173K179K184R201)	This study
	pET21b::PtoN15-(His)$_6$ (Q173K179K184R201)	This study
	pET21b::*Caulobacter crescentus*-ParB-(His)$_6$ (Q162A)	This study
	pET21b::*Caulobacter crescentus*-ParB-(His)$_6$ (K171A)	This study
	pET21b::*Caulobacter crescentus*-ParB-(His)$_6$ (S172A)	This study
	pET21b::*Caulobacter crescentus*-ParB-(His)$_6$ (R173A)	This study
	pET21b::*Caulobacter crescentus*-ParB-(His)$_6$ (S174A)	This study
	pET21b::*Caulobacter crescentus*-ParB-(His)$_6$ (N178A)	This study
	pET21b::*Caulobacter crescentus*-ParB-(His)$_6$ (R181A)	This study
	pET21b::*Caulobacter crescentus*-ParB-(His)$_6$ (V226A)	This study
	pET21b::*Caulobacter crescentus*-ParB-(His)$_6$ (R227A)	This study
	pET21b::*Caulobacter crescentus*-ParB-(His)$_6$ (R234A)	This study
	pET21b::*Caulobacter crescentus*-ParB-(His)$_6$ (K245A)	This study
	pET21b::*Caulobacter crescentus*-ParB-(His)$_6$ (R248A)	This study
	pET21b::*Caulobacter crescentus*-ParB-(His)$_6$ (R204A)	This study
	pET21b::*Caulobacter crescentus*-ParB-(His)$_6$ (E230A)	This study
	pET21b::*Caulobacter crescentus*-ParB-(His)$_6$ (R251A)	This study
	pET21b::ParB-(His)$_6$ chimera 1	This study
	pET21b::ParB-(His)$_6$ chimera 4	This study
	pET21b::*Caulobacter crescentus*-ParB-(His)$_6$ (RRMT)	This study
	pET21b::*Caulobacter crescentus*-ParB-(His)$_6$ (RRLT)	This study
	pET21b::*Caulobacter crescentus*-ParB-(His)$_6$ (QRMR)	This study
	pET21b::*Caulobacter crescentus*-ParB-(His)$_6$ (QSRR)	This study
	pET21b::*Caulobacter crescentus*-ParB-(His)$_6$ (QTNR)	This study
	pET21b::*Caulobacter crescentus*-ParB-(His)$_6$ (QRYR)	This study
	pET21b::*Caulobacter crescentus*-ParB-(His)$_6$ (QRRR)	This study
	pET21b::*Caulobacter crescentus*-ParB-(His)$_6$ (QRKR)	This study
	pET21b::*Caulobacter crescentus*-ParB-(His)$_6$ (TEPG)	This study
pUT18C::1xFLAG-DEST	Destination vector for Gateway cloning, 1xFLAG tag fused to the N-terminus of protein of interest, carbenicillin^R	This study
	pUT18C::1xFLAG-*Bacillus subtilis* Noc	This study
	pUT18C::1xFLAG-*Clostridium difficile* Noc	This study
	pUT18C::1xFLAG-*Lactobacillus aviarius* Noc	This study
	pUT18C::1xFLAG-*Staphylococcus aureus* Noc	This study
	pUT18C::1xFLAG-*Bacillus subtilis* ParB	This study
	pUT18C::1xFLAG-*Clostridium difficile* ParB	This study
	pUT18C::1xFLAG-*Lactobacillus aviarius* ParB	This study
	pUT18C::1xFLAG-*Staphylococcus aureus* ParB	This study
	pUT18C::1xFLAG-*Caulobacter crescentus* ParB	This study
	pUT18C::1xFLAG-*Agrobacterium tumefaciens* ParB	This study
	pUT18C::1xFLAG-*Sinorhizobium meliloti* ParB	This study
	pUT18C::1xFLAG-*Lawsonia intracellularis* ParB	This study

	pUT18C::1xFLAG-*Desulfovibrio vulgaris* ParB	This study
	pUT18C::1xFLAG-*Dechloromonas aromatica* ParB	This study
	pUT18C::1xFLAG-*Pseudomonas aeruginosa* ParB	This study
	pUT18C::1xFLAG-*Xanthomonas campestris* ParB	This study
	pUT18C::1xFLAG-*Thermus thermophilus* ParB	This study
	pUT18C::1xFLAG-*Bifidobacterium longum* ParB	This study
	pUT18C::1xFLAG-*Mycobacterium tuberculosis* ParB	This study
	pUT18C::1xFLAG-*Streptomyces coelicolor* ParB	This study
	pUT18C::1xFLAG-*Porphyromonas gingivalis* ParB	This study
	pB1H2-w2::*zif268*	(Noyes et al., 2008) via Addgene
	pB1H2-w5::*zif268*	(Noyes et al., 2008) via Addgene
	pB1H2-w5L::*zif268*	(Noyes et al., 2008) via Addgene
	pU3H3::MCS	(Noyes et al., 2008) via Addgene
	pU3H3::*zif268* binding site	(Noyes et al., 2008) via Addgene
	pB1H2-w2::*Caulobacter* ParB (R104A + Q173K179K184R201)	This study
	pB1H2-w5::*Caulobacter* ParB (R104A + Q173K179K184R201)	This study
	pB1H2-w5L::*Caulobacter* ParB (R104A + Q173K179K184R201)	This study
	pB1H2-w2::*Caulobacter* ParB (R104A + R173A179T184G201)	This study
	pU3H3::7bp-*NBS*	This study
	pU3H3::14bp-*NBS*	This study
	pU3H3::19bp-*NBS*	This study
	pU3H3::24bp-*NBS*	This study
	pU3H3::19bp-*parS*	This study

TABLE S3. PRIMERS. Related to STAR Methods.

Primers	Sequences
	For construction of pUT18C-1xFLAG-DEST
1934	acaatttcacacaggaaacagctatggactacaaggacgacgacgacaagggctcg
1935	acttagttatatcgatgcatcgaaccactttgtacaagaaagctgaacgagaaac
1936	agctgtttcctgtgtgaaattgttatccgctcacaattc
1937	tcgatgcatcgatataactaagtaatatggtgcac
	For ChIP-qPCR
ybbD_parSF2	GTAAGATACCAGGGCAAGG
ybbD_parSR2	TTACTCTGCACAAGCATCA
ygcE_NBSF2	CGCTACGACGCGATGAATAA
ygcE_NBSR2	CTCTGGATCGAATCCACATTCC
ompG_F1	GCGGAGCCTTCAGTCTATTT
ompG_R1	CAAACCACGTTCCACGTTTAC
	For bio-layer interferometry assays
*NBS*_FOR	[Biotin]GGGAtaTTTCCCGGGAAAta
*NBS*_REV	taTTTCCCGGGAAAtaTCCC
*parS*_FOR	[Biotin]GGGAtgTTTCACGTGAAAca
*parS*_REV	tgTTTCACGTGAAAcaTCCC
site1_FOR	[Biotin]GGGAtgTTTCTCGAGAAAca
site1_REV	tgTTTCTCGAGAAAcaTCCC
site10_FOR	[Biotin]GGGAttTTTCgCGcGAAAaa
site10_REV	ttTTTCgCGcGAAAaaTCCC
site11_FOR	[Biotin]GGGAttTTTCcCGgGAAAaa
site11_REV	ttTTTCcCGgGAAAaaTCCC
site12_FOR	[Biotin]GGGAtaTTTCACGTGAAAta
site12_REV	taTTTCACGTGAAAtaTCCC
site13_FOR	[Biotin]GGGAtaTTTCtCGaGAAAta
site13_REV	taTTTCtCGaGAAAtaTCCC
site14_FOR	[Biotin]GGGAtaTTTCgCGcGAAAta
site14_REV	taTTTCgCGcGAAAtaTCCC
site2_FOR	[Biotin]GGGAtgTTTCGCGCGAAAca
site2_REV	tgTTTCGCGCGAAAcaTCCC
site3_FOR	[Biotin]GGGAtgTTTCCCGGGAAAca
site3_REV	tgTTTCCCGGGAAAcaTCCC
site4_FOR	[Biotin]GGGAtcTTTCACGTGAAAga
site4_REV	tcTTTCACGTGAAAgaTCCC
site5_FOR	[Biotin]GGGAtcTTTCtCGaGAAAga
site5_REV	tcTTTCtCGaGAAAgaTCCC
site6_FOR	[Biotin]GGGAtcTTTCgCGcGAAAga
site6_REV	tcTTTCgCGcGAAAgaTCCC
site7_FOR	[Biotin]GGGAtcTTTCcCGgGAAAga
site7_REV	tcTTTCcCGgGAAAgaTCCC
site8_FOR	[Biotin]GGGAttTTTCACGTGAAAaa
site8_REV	ttTTTCACGTGAAAaaTCCC
site9_FOR	[Biotin]GGGAttTTTCtCGaGAAAaa
site9_REV	ttTTTCtCGaGAAAaaTCCC
	For the construction of pU3H3-*NBS* and pU3H3-*parS*
*NBS*_anneal_7bp_spacer_F	Ccgggtatttcccgggaaataggg

*NBS*_anneal_7bp_spacer_R	aattccctatttcccgggaaatac
*NBS*_anneal_14bp_spacer_F	ccgggtatttcccgggaaataggcgcgccg
*NBS*_anneal_14bp_spacer_R	aattcggcgcgcctatttcccgggaaatac
*NBS*_anneal_19bp_spacer_F	ccgggtatttcccgggaaataggtttcgcgcgccg
*NBS*_anneal_19bp_spacer_R	Aattcggcgcgcgaaacctatttcccgggaaatac
*NBS*_anneal_24bp_spacer_F	ccgggtatttcccgggaaataggtttcttggcgcgcgccg
*NBS*_anneal_24bp_spacer_R	aattcggcgcgcgccaagaa acctatttcccgggaaatac
*parS*_anneal_19bp_spacer_F	ccgggtgtttcacgtgaaacaggtttcgcgcgccg
*parS*_anneal_19bp_spacer_R	ttaagccgcgcgctttggacaaagtgcactttgtg
	For the construction of AB1157 *ybbD*::*parS ygcE*::*NBS* strain
1940	aaatattggagctggattgcctgatgcttgtgcagagtaatgttccacgtggaacaattccggggatccgtcgacctg
1941	ttgacgacttcgatatgggatagactcttaattcaagcaatgtaggctggagctgcttcg
3139	ggggaatgtggattcgatccagagctggtcgaatgcgtaatatttcccgggaaataattccggggatccgtcgacctg
3140	tatgttcaggccgggcagtttcccgcccggccttcctcactgtaggctggagctgcttcgaag
	For generation of Illumina libraries for deep mutational scanning experiments
4nns_offset_0_F	ACACTCTTTCCCTACACGACGCTCTTCCGATCTgctcaaactattggcaagag
4nns_offset_1_F	ACACTCTTTCCCTACACGACGCTCTTCCGATCTtgctcaaactattggcaagag
4nns_offset_2_F	ACACTCTTTCCCTACACGACGCTCTTCCGATCTttgctcaaactattggcaagag
4nns_offset_3_F	ACACTCTTTCCCTACACGACGCTCTTCCGATCTattgctcaaactattggcaagag
4nns_offset_4_F	ACACTCTTTCCCTACACGACGCTCTTCCGATCTcattgctcaaactattggcaagag
4nns_R	GTGACTGGAGTTCAGACGTGTGCTCTTCCGATCTTTTTGCTAACGCTACGGGATC
NEBNext universal primer	AAT GAT ACG GCG ACC ACC GAG ATC TAC ACT CTT TCC CTA CAC GAC GCT CTT CCG ATC-s-T
NEBNext Index primer	CAAGCAGAAGACGGCATACGAGATNNNNNNGTGACTGGAGTTCAGACGTGTGCTCTTCCGATC-s-T
	For generation of the deep mutational scanning library
For_B_NNS_HTH	GAGGTACAGTCCTATCTTGTGAGTGGAGAGCTGACAGCGNNSCATGCGCGTGCGATTGCCGCTGC
Rev_B_NNS_HTH	GTCCGGCAASNNAAGAAGACGCATSNNATTCGCTACGTGAGASNNACTCTTGCCAATAGTTTGAGC
	For the amplification of the pENTR backbone
pENTR_gibson_backbone_R	ggtgaaggggcggccgcggagcctgc
pENTR_gibson_backbone_F	aagggtgggcgcgccgacccagctttcttg

Nucleotides in red font are spacer bases used to increase the diversity of the Illumina library. Underlined nucleotides are either Illumina library barcodes or NNS bases.

TABLE S4. X-RAY DATA COLLECTION AND PROCESSING STATISTICS. Related to Figures 2 and 4.

Structure	**ParB (DBD)-*parS* complex**	**Noc (DBD)-*NBS* complex**
Data collection		
Diamond Light Source beamline	I04	I03
Wavelength (Å)	0.980	0.976
Detector	Pilatus 6M-F	Eiger2 XE 16M
Resolution range (Å)	40.12 – 2.40 (2.49 – 2.40)	72.30 – 2.23 (2.66 – 2.23)[a]
Space Group	*C*2	*C2*
Cell parameters (Å/°)	*a* = 122.1, *b* = 40.7, *c* = 94.0, β = 121.4	*a* = 134.1 *b* = 60.6, *c* = 81.1, β = 116.9
Total no. of measured intensities	105021 (10942)	142152 (6183)
Unique reflections	16317 (1662)	10830 (542)
Multiplicity	6.4 (6.6)	13.1 (11.4)
Mean $I/\sigma(I)$	7.0 (2.0)	9.3 (1.5)
Completeness (spherical; %)	99.7 (99.2)	38.1 (4.7)
Completeness (ellipsoidal; %)	-	88.4 (57.2)
R_{merge}[b]	0.137 (0.801)	0.108 (0.851)
R_{meas}[c]	0.150 (0.869)	0.112 (0.891)
$CC_{½}$[d]	0.992 (0.850)	1.000 (0.847)
Wilson *B* value (Å^2)	42.1	115.7
Refinement		
Resolution range (Å)	40.12 – 2.40	72.30 – 2.23
Reflections: working/free[e]	15480/826	10231/599
R_{work}[f]	0.216	0.231
R_{free}[f]	0.232	0.279
Ramachandran plot: favoured/allowed/disallowed[g] (%)	96.5/3.5/0.0	95.4/4.6/0.0
R.m.s. bond distance deviation (Å)	0.003	0.002
R.m.s. bond angle deviation (°)	1.08	1.03

No. of protein residues per chain	121/140	105/116
No. of DNA bases per chain	20/20	22/22
No. of water/glycerol molecules	82/2	0/0
Mean *B* factors: protein/DNA/ water/overall (Å^2)	51/46/38/49	155/148/0/154
PDB accession code	**6S6H**	**6Y93**

Values in parentheses are for the outer resolution shell.

[a] After correction by STARANISO to remove poorly measured reflections affected by anisotropy, the ellipsoidal resolutions were:

2.23 Å in direction 0.854 a^* + 0.017 b^* - 0.519 c^*

3.83 Å in direction 0.302 a^* + 0.784 b^* + 0.543 c^*

4.02 Å in direction 0.130 a^* + 0.911 b^* + 0.391 c^*

[b] $R_{merge} = \sum_{hkl} \sum_i |I_i(hkl) - \langle I(hkl)\rangle| / \sum_{hkl} \sum_i I_i(hkl)$.

[c] $R_{meas} = \sum_{hkl} [N/(N-1)]^{1/2} \times \sum_i |I_i(hkl) - \langle I(hkl)\rangle| / \sum_{hkl} \sum_i I_i(hkl)$, where $I_i(hkl)$ is the ith observation of reflection hkl, $\langle I(hkl)\rangle$ is the weighted average intensity for all observations i of reflection hkl and N is the number of observations of reflection hkl.

[d] $CC_{½}$ is the correlation coefficient between symmetry equivalent intensities from random halves of the dataset.

[e] The dataset was split into "working" and "free" sets consisting of 95 and 5% of the data respectively. The free set was not used for refinement.

[f] The R-factors R_{work} and R_{free} are calculated as follows: $R = \sum(|F_{obs} - F_{calc}|)/\sum|F_{obs}|$, where F_{obs} and F_{calc} are the observed and calculated structure factor amplitudes, respectively.

[g] As calculated using MolProbity (Chen et al., 2010).

TABLE S5. DEEP MUTATIONAL SCAN AND ChIP-Seq. Related to STAR Methods.

Deep mutational scanning libraries	**GEO**
Pre-selection library, replicate 1	This study (GSE129285)
Pre-selection library, replicate 2	This study (GSE129285)
Pre-selection library, replicate 3	This study (GSE129285)
Post-selection library, selection for *parS*-binding capability, replicate 1	This study (GSE129285)
Post-selection library, selection for *parS* -binding capability, replicate 2	This study (GSE129285)
Post-selection library, selection for *parS* -binding capability, replicate 3	This study (GSE129285)
Post-selection library, selection for *NBS*-binding capability, replicate 1	This study (GSE129285)
Post-selection library, selection for *NBS* -binding capability, replicate 2	This study (GSE129285)
Post-selection library, selection for *NBS* -binding capability, replicate 3	This study (GSE129285)
ChIP-seq datasets	
TLE3000+pUT18C::1xFLAG-Bacillus subtilis Noc, fixation with 1% formaldehyde, α-FLAG antibody (Sigma), ChIP fraction	This study (GSE129285)
TLE3000+pUT18C::1xFLAG-Clostridium difficile Noc, fixation with 1% formaldehyde, α-FLAG antibody (Sigma), ChIP fraction	This study (GSE129285)
TLE3000+pUT18C::1xFLAG-Lactobacillus aviarius Noc, fixation with 1% formaldehyde, α-FLAG antibody (Sigma), ChIP fraction	This study (GSE129285)
TLE3000+pUT18C::1xFLAG-Staphylococcus aureus Noc, fixation with 1% formaldehyde, α-FLAG antibody (Sigma), ChIP fraction	This study (GSE129285)
TLE3000+pUT18C::1xFLAG-Bacillus subtilis ParB, fixation with 1% formaldehyde, α-FLAG antibody (Sigma), ChIP fraction	This study (GSE129285)
TLE3000+pUT18C::1xFLAG-Clostridium difficile ParB, fixation with 1% formaldehyde, α-FLAG antibody (Sigma), ChIP fraction	This study (GSE129285)
TLE3000+pUT18C::1xFLAG-Lactobacillus aviarius ParB, fixation with 1% formaldehyde, α-FLAG antibody (Sigma), ChIP fraction	This study (GSE129285)
TLE3000+pUT18C::1xFLAG-Staphylococcus aureus ParB, fixation with 1% formaldehyde, α-FLAG antibody (Sigma), ChIP fraction	This study (GSE129285)
TLE3000+pUT18C::1xFLAG-Caulobacter crescentus ParB, fixation with 1% formaldehyde, α-FLAG antibody (Sigma), ChIP fraction	This study (GSE129285)
TLE3000+pUT18C::1xFLAG-Agrobacterium tumefaciens ParB, fixation with 1% formaldehyde, α-FLAG antibody (Sigma), ChIP fraction	This study (GSE129285)
TLE3000+pUT18C::1xFLAG-Sinorhizobium meliloti ParB, fixation with 1% formaldehyde, α-FLAG antibody (Sigma), ChIP fraction	This study (GSE129285)
TLE3000+pUT18C::1xFLAG-Lawsonia intracellularis ParB, fixation with 1% formaldehyde, α-FLAG antibody (Sigma), ChIP fraction	This study (GSE129285)
TLE3000+pUT18C::1xFLAG-Desulfovibrio vulgaris ParB, fixation with 1% formaldehyde, α-FLAG antibody (Sigma), ChIP fraction	This study (GSE129285)
TLE3000+pUT18C::1xFLAG-Dechloromonas aromatica ParB, fixation with 1% formaldehyde, α-FLAG antibody (Sigma), ChIP fraction	This study (GSE129285)
TLE3000+pUT18C::1xFLAG-Pseudomonas aeruginosa ParB, fixation with 1% formaldehyde, α-FLAG antibody (Sigma), ChIP fraction	This study (GSE129285)
TLE3000+pUT18C::1xFLAG-Xanthomonas campestris ParB, fixation with 1% formaldehyde, α-FLAG antibody (Sigma), ChIP fraction	This study (GSE129285)
TLE3000+pUT18C::1xFLAG-Thermus thermophilus ParB, fixation with 1% formaldehyde, α-FLAG antibody (Sigma), ChIP fraction	This study (GSE129285)
TLE3000+pUT18C::1xFLAG-Bifidobacterium longum ParB, fixation with 1% formaldehyde, α-FLAG antibody (Sigma), ChIP fraction	This study (GSE129285)

TLE3000+pUT18C::1xFLAG-Mycobacterium tuberculosis ParB, fixation with 1% formaldehyde, α-FLAG antibody (Sigma), ChIP fraction	This study (GSE129285)
TLE3000+pUT18C::1xFLAG-Streptomyces coelicolor ParB, fixation with 1% formaldehyde, α-FLAG antibody (Sigma), ChIP fraction	This study (GSE129285)
TLE3000+pUT18C::1xFLAG-Porphyromonas gingivalis ParB, fixation with 1% formaldehyde, α-FLAG antibody (Sigma), ChIP fraction	This study (GSE129285)

Structural and biochemical analyses of *Caulobacter crescentus* ParB reveal the role of its N-terminal domain in chromosome segregation

Adam S. B. Jalal[1], César L. Pastrana[2], Ngat T. Tran[1], Clare. E. Stevenson[3], David M. Lawson[3], Fernando Moreno-Herrero[2], and Tung B. K. Le[1*]

[1]Department of Molecular Microbiology
John Innes Centre, Norwich, NR4 7UH, United Kingdom
[2]Department of Macromolecular Structures
CSIC-Centro Nacional de Biotechnologia, Madrid, 28049, Spain
[3]Department of Biological Chemistry
John Innes Centre, Norwich, NR4 7UH, United Kingdom

[*]Correspondence: tung.le@jic.ac.uk

ABSTRACT

The tripartite ParA-ParB-*parS* complex ensures faithful chromosome segregation in the majority of bacterial species. ParB nucleates on a centromere-like *parS* site and spreads to neighboring DNA to form a network of protein-DNA complexes. This nucleoprotein network interacts with ParA to partition the *parS* locus, hence the chromosome to each daughter cell. Here, we determine the co-crystal structure of a C-terminal domain truncated ParB-*parS* complex from *Caulobacter crescentus*, and show that its N-terminal domain adopts alternate conformations. The multiple conformations of the N-terminal domain might facilitate the spreading of ParB on the chromosome. Next, using ChIP-seq we show that ParBs from different bacterial species exhibit variation in their intrinsic capability for spreading, and that the N-terminal domain is a determinant of this variability. Finally, we show that the C-terminal domain of *Caulobacter* ParB possesses no or weak non-specific DNA-binding activity. Engineered ParB variants with enhanced non-specific DNA-binding activity condense DNA *in vitro* but do not spread further than wild-type *in vivo*. Taken all together, our results emphasize the role of the N-terminal domain in ParB spreading and faithful chromosome segregation in *Caulobacter crescentus*.

INTRODUCTION

Proper chromosome segregation is essential in all domains of life. In two-thirds of known bacterial species, faithful chromosome segregation is mediated by the conserved ParA-ParB-*parS* system (1–10). This tripartite complex consists of a Walker-box ATPase ParA, a centromere-binding protein ParB, and a centromere-like DNA sequence *parS*. The *parS* site is the first DNA locus to be segregated after chromosome replication (2, 5, 11, 12). ParB, a DNA-binding protein, nucleates on *parS* before binding to adjacent non-specific DNA to form a network of protein-DNA complexes. This nucleoprotein network interacts with ParA to partition the chromosome to each daughter cell. In *Caulobacter crescentus*, ParA forms a protein gradient emanating from the opposite pole of the cell to the ParB-*parS* complex (13–15). The DNA-bound ParB complexes stimulate the ATPase activity of ParA, causing the ParA gradient to retract, bringing the ParB-DNA complex to the opposite pole of the cell in a retreating gradient of ParA (15–19). In *Caulobacter crescentus*, ParA and ParB are essential for chromosome segregation and cell viability (3, 13). In other bacterial species, engineered strains lacking ParB are still viable but have elevated numbers of anucleate cells due to defects in chromosome segregation (2, 7, 9, 12, 16, 20–22).

The binding of multiple ParB molecules onto non-specific DNA after nucleation at *parS* (i.e. spreading) is a crucial event; bacterial cells harboring a nucleation-competent but spreading-defective *parB* allele are impaired in plasmid/chromosome segregation (23–25). Spreading was first discovered for the F-plasmid-encoded SopB protein and the P1 plasmid-encoded ParB protein (26, 27), and was subsequently found to be a general feature of many plasmid and chromosomal ParB proteins in bacteria (10, 23–25, 28, 29). Recently, spreading was also reported for a ParB-unrelated AspA protein that is responsible for plasmid segregation in an archaea *Sulfolobus* (30). In addition to a linear spreading on DNA, *Bacillus subtillis* ParB can also bridge distal DNA together to coalesce into a large nucleoprotein network in a process known as “spreading and bridging” (24, 31–33). Recently, a broadly similar “nucleation and caging” mechanism was also proposed to explain the ability of F1-plasmid and *Vibrio cholerae* chromosomal ParB to form a large ParB-DNA network (34, 35). In this model, the nucleation of ParB on *parS* creates a high local concentration of ParB, thereby caging ParB molecules together with non-specific DNA surrounding *parS* to create a loose but dynamic nucleoprotein network (34, 35).

Chromosomal ParB protein consists of an N-terminal domain (NTD), a middle *parS*-specific DNA-binding domain (DBD), and a C-terminal domain (CTD) (Fig. 1). The NTD and DBD are generally conserved among ParB orthologs, while the CTD exhibits high sequence variability, except for conserved leucine-zipper residues that are crucial for dimerization of ParB monomers (36, 37) (Fig. 1). A recent co-crystal structure of a CTD-truncated *Helicobacter pylori* ParB (Ct-ParB) with *parS* provided a possible structural basis for spreading (29). In this structure, four *Helicobacter* Ct-ParB monomers bind to four individual half *parS* sites and tetramerize to bring distal DNA closer together (29). In comparison to the structure of an apo- Ct-ParB from *Thermus thermophilus*, the NTD of *Helicobacter* Ct-ParB adopts a more open conformation to position the highly conserved arginine-rich patch (GERRxR, Fig. 1) outwards to mediate ParB-ParB oligomerization (29, 38). Based on this pairwise structural comparison, Chen *et al* (2015) proposed that the nucleation on *parS* induces a transition (at the NTD of ParB) from a spreading-incompetent closed conformation to a spreading-competent open conformation (29). In addition to the NTD, the CTD of *Bacillus* ParB was also shown to contribute to the formation of the nucleoprotein network via a positively charged lysine-rich surface that binds and condenses DNA non-specifically (36, 39). However, the sequence of the CTD diverges more rapidly than other domains of ParB so it is not yet clear whether ParBs from other bacterial species also possess a functionally equivalent CTD with non-specific DNA-binding and condensation activities.

Here, we determine the co-crystal structure of a Ct-ParB-*parS* complex from *Caulobacter crescentus* to better understand the function of this protein family. By comparing our co-crystal structure to that of apo- *Thermus* Ct-ParB and *Helicobacter* Ct-ParB-*parS* complex, we show that the NTD can adopt alternate conformations. Using ChIP-seq, we then show that ParBs from different bacterial species

exhibit variation in their intrinsic capability for spreading. We discover “maxi-spreaders” (e.g. ParB from *Moorella thermoacetica*) that spread over ~50 kb, while “mini-spreaders” (e.g. ParB from *Caulobacter crescentus*) spread only ~5 kb from a single *parS* site. We construct a series of chimeric proteins and find that the NTD is a determinant for the inter-species variation in spreading, at least in the case of *Caulobacter* and *Moorella* ParBs. In addition, we show that the CTD of *Caulobacter* ParB does not display non-specific DNA-binding and DNA condensation activities *in vitro*. Engineered *Caulobacter* ParB variants with an enhanced non-specific DNA-binding activity can condense DNA *in vitro* but do not spread further than wild-type protein *in vivo*. Overall, our results emphasize the key role of the NTD in ParB spreading in *Caulobacter* and highlights the inter-species variation that exists within the chromosomal ParB family.

RESULTS AND DISCUSSION

Co-crystal structure of the C-terminal domain truncated ParB-*parS* complex from *Caulobacter crescentus* revealed the multiple conformations of the NTD

We sought to determine a co-crystal structure of a ParB-*parS* complex from *Caulobacter crescentus*. After screening several constructs with different length of ParB and *parS*, we obtained crystals of a 50 amino acid C-terminally truncated ParB (Ct-ParB) in complex with a 22-bp *parS* duplex DNA (Fig. 1 and Fig. 2A). In solution, *Caulobacter* Ct-ParB also binds to *parS*, albeit weaker than a full-length protein (Fig. S1). Diffraction data for the *Caulobacter* Ct-ParB-*parS* complex were collected to a resolution of 2.9 Å, and the structure was solved by molecular replacement using the 3.1 Å structure of the *Helicobacter* Ct-ParB-*parS* complex and the 2.3 Å structure of apo- *Thermus* Ct-ParB as search templates. X-ray crystallographic data are summarized in Table 1.

The asymmetric unit of our co-crystal contains four copies of the Ct-ParB monomer and two copies of the full-size *parS* DNA (Fig. S2A). Each Ct-ParB monomer binds to a half *parS* site via the DNA-binding domain (Fig. 2A-B). Since chain A and B are very similar to chain C and D, respectively (RMSD= 1.59 Å, Fig. S2B), we used chain C-D-*parS* complex for subsequent analysis (Fig. 2A). Each Ct-ParB monomer consists of two domains: an N-terminal domain (NTD) (helices α1-α4 and sheets β1- β3) and a *parS* DNA-binding domain (DBD) (helices α5-α10) (Fig. 1 and Fig. 2B). We previously reported a 2.4 Å co-crystal structure of a *Caulobacter* ParB (DBD only) in complex with *parS* (40), here we discuss the structure of the NTD in depth. We observed that helices α3 and α4 of the NTD are packed against the DBD and are connected to the rest of the NTD via a loop in between α3 and β4 (Fig.1 and Fig. 2B). The rest of the NTD is comprised of a four-stranded β-sheet (β1-β4) and two surrounding helices (α1-α2) (Fig. 2B). The highly conserved arginine-rich patch (G^{101}ERRWR), crucial for *Caulobacter* ParB spreading (10), resides on helix α2 (Fig. 1). We observed that while the DBD and the NTD α3-α4 are near identical between chain C and D (RMSD=0.19 Å, Fig. 2C) the rest of the NTD (α1-β4) adopts completely different arrangement (Fig. 2C-D). The NTD (α1-β4) of chain C and D are oriented ~80^{o} apart from each other (Fig. 2D); this is due to a loop (hereafter, called the elbow) that connects α3 and β4 together (Fig. 2C-D). The role of this elbow in orientating the NTD became clearer upon comparing the *Caulobacter* Ct-ParB-*parS* structure to two other available structures of chromosomal ParBs from *Helicobacter pylori* and *Thermus thermophilus*.

Structural comparisons of the *Caulobacter* Ct-ParB-*parS* complex to other ParB family members

In the co-crystal structure of the *Helicobacter* Ct-ParB-*parS* complex, ParB adopts an open conformation in which its NTD projects outwards to contact a nearby ParB monomer (Fig. 3A, Fig. S3A) (29). In contrast, no such interaction was seen between the NTD of the two adjacent *Caulobacter* ParB monomers (Fig. 3A). By superimposing the structure of *Helicobacter* Ct-ParB onto the *Caulobacter* one, we observed that each NTD has a different orientation (Fig. 3B-C). The *Helicobacter* ParB NTD extends outwards (an open conformation), while the *Caulobacter* ParB NTD points either inwards (chain D) or side-way (chain C) (a closed conformation) (Fig. 3B-C). Superimposition of three chains showed that the elbow (residues 121-125) swivels around the α3 axis, allowing the NTD to adopt three distinct conformations (Fig. 3C). Sequence alignment of ~1800

ParB orthologs showed an enrichment for charged and polar uncharged residues in the elbow region (Fig. 3C). This amino acid preference is typically found in intrinsically disordered proteins (41, 42) and might confer flexibility to the elbow region of ParB. A further structure superimposition showed that the NTD of an apo- *Thermus* Ct-ParB also adopts a closed conformation, most similar to chain D in the *Caulobacter* Ct-ParB-*parS* structure (Fig. S3C-D). Altogether, our three-way structural comparison suggests that the NTD can adopt multiple open or closed conformations regardless of whether ParB is on or off DNA. Our finding contrasts with Chen *et al* (2015) study which proposed that a *parS*-binding event induces a transition (at the NTD) from a spreading-incompetent closed conformation to a spreading-competent open conformation (29). While all currently available structures of chromosomal ParB lack the CTD, it is reasonable to assume that the NTD is also flexible in a full-length protein on/off DNA. Indeed, a co-crystal structure of a full-length SopB (a Type-I ParB protein for F-plasmid segregation) with DNA was previously solved, but only the density for the central DBD was observed (43). Schumacher *et al* (2010) showed that the absence of density for the NTD and CTD of SopB was due to their extreme flexibility rather than proteolysis during crystallization (43). The multiple orientations of the NTD of ParB (on/off DNA) might allow a dynamic ParB-DNA network to form inside cells.

We observed the second level of flexibility at the N-terminal-most peptide (residues 1-64) of ParB. This amino acid region is extended in the *Thermus* Ct-ParB structure (pink dashed line, Fig. 3D) but folds back in the *Caulobacter* Ct-ParB to contribute the fourth strand to the core β-sheet at the NTD (green dashed line, Fig. 3D). The equivalent region was not observed in the *Helicobacter* Ct-ParB structure. Due to the alternate conformations of this N-terminal-most peptide and of the NTD as a whole, the ParA-interacting region (residues 1-30, Fig. 1 and Fig. 3D) can potentially explore a very large space surrounding ParB. This flexibility might be beneficial for the network of ParB-DNA complexes to “fly-fishing” for ParA molecules *in vivo* (15–18).

The inter-species variation in spreading among ParB orthologs is dependent on the NTD

ParB orthologs are divergent in sequence, especially at their C-terminal domain (CTD) (Fig. 1). Therefore, we wondered whether ParBs from different bacterial species have distinct capacities for spreading and if it is dependent on the variable CTD. Exploiting the conservation of the *parS* sequence in bacteria (5), we constructed an *E. coli* heterologous system that allowed us to compare the spreading ability of ten chromosomal ParBs by ChIP-seq (Fig. 4A). *E. coli* does not possess a native ParA-ParB-*parS* system. We inserted a single *parS* site at the *ygcE* locus on the *E. coli* chromosome (Fig. 4A). Genes encoding N-terminally FLAG-tagged ParBs were codon optimized and expressed individually in *E. coli* (Fig. 4B). FLAG-ParBs were produced to a similar level (Fig. S4) before bound DNA was immunoprecipitated using an α-FLAG antibody and deep sequenced to reveal the extent of spreading from a single *parS* to the flanking DNA. From the ten ChIP-seq profiles, we observed that the majority of ParB (seven out of ten, including *Caulobacter* ParB) spread ~5 kb surrounding a single *parS* (Fig. 4B). On the other hand, three ParBs are “maxi-spreaders” that spread between ~20 kb to ~50 kb (Fig. 4B). In particular, *Moorella thermoacetica* ParB, despite its lower expression in *E. coli* (Fig. S4), spread ten times more extensively on DNA than *Caulobacter* ParB (Fig. 4B). Also, by considering only the shape of ChIP-seq profiles, we noted that ChIP signals reduced to the background more gradually for *Moorella* ParB than *Caulobacter* one. We also noted that *Bacillus* ParB spread only ~5 kb surrounding a single *parS;* this is more restrictive than a previous reported ~10 kb spreading distance when ChIP-chip of *Bacillus* ParB was performed in the native bacterium (25). The reason behind this discrepancy is unknown. Due to the caveat that ParB spreading has been taken out of the context of the native organism, the biological significance of the inter-species variation in ParB spreading is unclear. Nevertheless, we utilized this inter-species variation to determine the domain responsible for spreading. To do so, we constructed a series of chimeric proteins in which different regions of a “mini-spreader” *Caulobacter* ParB were replaced with the corresponding regions of a “maxi-spreader” *Moorella* ParB (Fig. 5). These chimeric proteins were produced to the same level in the *E. coli ygcE::parS* host (Fig. S4), and α-FLAG ChIP-seq experiments were performed to determine the extent of spreading (Fig. 5). Replacing a ParA-interacting region of *Caulobacter* ParB with the corresponding region from *Moorella* ParB produced

Chimera A that spread to the same extent as a wild-type *Caulobacter* ParB (Fig. 5). Similarly, Chimera B that had the CTD of *Caulobacter* ParB replaced by an equivalent region from *Moorella* ParB spread to the same extent as a wild-type *Caulobacter* ParB (Fig. 5). However, swapping the NTD (Chimera C) or both the NTD and the DBD (Chimera D) between *Caulobacter* ParB and *Moorella* ParB produced variants that are "maxi-spreaders" i.e. having a similar extensive spreading to the wild-type *Moorella* ParB (Fig. 5). Taken together, our ChIP-seq profiles suggested that the NTD, at least in the case of *Caulobacter* and *Moorella* ParBs, dictates their variation in spreading.

Engineering a lysine-rich surface into the *Caulobacter* ParB CTD resulted in variants with non-specific DNA-binding and condensation activities *in vitro*

In addition to the NTD, the CTD of ParB from *Bacillus subtilis* also contributes to the formation of the ParB-DNA network (32, 36, 39). *Bacillus* ParB was reported to bind non-specific DNA to condense both *parS* and non-*parS* DNA *in vitro*; these activities were mediated by a positively charged lysine-rich surface on the CTD (36, 39). Whether the non-specific DNA-binding activity of the *Bacillus* ParB CTD is a shared feature among ParB orthologs is currently unknown, furthermore, the relationship between the *in vitro* DNA condensation and the *in vivo* spreading is not fully understood. To better understand this relationship, we sought to generate variants of *Caulobacter* ParB with an enhanced non-specific DNA-binding activity. Unlike *Bacillus* ParB, the CTD of *Caulobacter* ParB lacks a lysine-rich patch (Fig. 6A), and the wild-type protein does not bind or binds very weakly to non-specific DNA *in vitro* (10) (Fig. 6B). To engineer a non-specific DNA-binding activity into *Caulobacter* ParB, we introduced additional lysine residues into its CTD. We systematically introduced a single (1K), double (2K), triple (3K), quadruple (4K), and quintuple (5K) lysine substitutions from the *Bacillus* ParB CTD into equivalent positions on the CTD of *Caulobacter* ParB (Fig. 6A). Ten variants were purified to homogeneity (Fig. S5A) and analyzed by a quantitative bio-layer interferometry assay that directly assessed their binding to a *parS* and a scrambled *parS* DNA (i.e. non-specific DNA) (Fig. 6B). All ten tested ParB variants retained their binding activities to *parS* (Fig 6B). We were unable to detect any noticeable non-specific DNA-binding activity for the 1K and 2K variants (Fig. 6B). However, a further introduction of lysine residues created 3K, 4K, and 5K variants that interacted with non-specific DNA similarly to that of *Bacillus* ParB (Fig. 6B).

The non-specific DNA-binding property of *Bacillus* ParB CTD was previously shown to condense DNA *in vitro* by magnetic tweezer assay (32, 36, 39) (Fig. 7A). To test if the engineered non-specific DNA-binding activity of *Caulobacter* ParB (3K-5K) variants (Fig. 6B) also leads to DNA condensation *in vitro*, we performed magnetic tweezer experiments on these variants and compared their activities to that of wild-type *Caulobacter* and *Bacillus* ParBs (Fig. 7B). We performed experiments at 1 μM concentration of proteins and different forces using an identical setup and conditions described in experiments with *Bacillus* ParB (32, 36). The extension of a tethered DNA was tracked, and any observation of a decrease in extension that was substantially larger than by the applied force alone is an indication of DNA condensation (Fig. 7A). *Bacillus* ParB condensed both non-*parS* DNA (Fig. 7B) and *parS* DNA (32, 36). On the contrary, *Caulobacter* ParB (WT) did not display any noticeable *in vitro* DNA condensation activity with either *parS* or non-*parS* DNA substrate at the tested concentration (Fig. 7B). However, upon incubating the 3K, 4K, or 5K ParB variants with tethered DNA resulted in a decrease in the DNA extension that was much greater than that attributable to the decrease in force alone (Fig. 7B). These results indicated that introduction of three to five lysine residues to the *Caulobacter* ParB CTD resulted in DNA condensation *in vitro*.

Caulobacter* ParB variants with an *in vitro* DNA condensation activity did not spread more extensively *in vivo

We then wondered whether the enhanced DNA-condensation activity of the ParB (3K-5K) variants leads to an increase in spreading *in vivo*. To test this, we performed α-FLAG ChIP-seq experiments on *Caulobacter* strains expressing individual FLAG-tagged ParB variant in a ParB (WT)-depletable background (44). *Caulobacter* cells that were completely depleted of a native ParB (WT) while producing the FLAG-tagged ParB (3K-5K) variants were viable (Fig. S5B), suggesting that the additional lysine residues at the CTD did not impair chromosome segregation in *Caulobacter*. As

controls for ChIP-seq experiments, strains expressing FLAG-tagged versions of ParB (WT), a non-spreading FLAG-ParB (R104A) mutant (10), and a non-DNA-binding protein FLAG-YFP were included (Fig. 7C). Consistent with the previous report (10), the ChIP-seq profile of a FLAG-ParB (WT) showed a clear enrichment above the background in the ~10 kb region from 4030 to 4040 kb on the chromosome (Fig. 7C). The extensive ChIP-seq profile is consistent with ParB (WT) spreading on the chromosome *in vivo*. This contrasts with the ChIP-seq profile of a non-spreader FLAG-ParB (R104A) in which the enrichment was confined to just ~500 bp immediately surrounding *parS* sites (10) (Fig. 7C). The profiles of the FLAG-ParB (3K-5K) variants were less extended than the FLAG-ParB (WT). We also noted that the overall heights of the ChIP-seq profiles of ParB (3K-5K) are lower than that of ParB (WT). It is possible that ParB (3K-5K) might bind DNA non-specifically along the chromosome, thereby titrating ParB molecules away from the *parS* cluster, resulting in a lower concentration of DNA-bound ParB near *parS*. Another possibility is ParB (3K-5K) are defective at the *parS* nucleation step, however this scenario is less likely since ParB (3K-5K) retained their *parS*-binding activities *in vitro* (Fig. 6B) and expressed to a comparable level to wild-type protein *in vivo* (Fig. S5).

At first, we were surprised to find that *Caulobacter* ParB has no or a very weak non-specific DNA-binding activity *in vitro* since both current models for ParB-DNA network formation ("spreading and bridging" and "nucleation and caging") require some degree of interaction between ParB and non-specific DNA (31–34, 36). However, while we did not observe non-specific DNA-binding activity at 1 μM *Caulobacter* ParB *in vitro*, the local concentration of ParB near *parS* has been estimated to reach ~500 μM (five times higher than in a crystallization drop) inside *Caulobacter* cells (15). At this extreme concentration, it is entirely possible that the central DNA-binding domain can provide some non-specific DNA-binding activity (Fig 8). We also noted that the five strongest *Caulobacter parS* sites cluster more closely (within a ~5 kb DNA segment (10)), while the four strongest *Bacillus parS* sites are dispersed within a ~57 kb region on the chromosome (30). A closer clustering of tightly bound ParB-*parS* complexes might be more effective in increasing the local concentration of *Caulobacter* ParB, despite its much weaker non-specific DNA-binding activity. On the contrary, the concentration of ParB in *Bacillus* cells is lower than in *Caulobacter* (~140 dimers compared to ~360 dimers per origin of replication (15)) and *parS* sites are more dispersed in this bacterium, in this case an added non-specific DNA-binding activity might enhance the formation of a ParB-DNA network in *Bacillus*.

Final perspectives

In this study, we characterize *Caulobacter* ParB biochemically and structurally to compare to orthologous proteins from different bacterial species. The availability of the *Caulobacter* Ct-ParB-*parS* structure, together with the structures of apo- *Thermus* Ct-ParB and *Helicobacter* Ct-ParB-*parS*, allows us to propose that the NTD can adopt multiple alternate conformations with respect to the DBD regardless of whether ParB is on/off DNA. The multiple conformations of the NTD might be beneficial in promoting the formation of a loose but dynamic ParB-DNA network. This is consistent with both "spreading and bridging" and "nucleation and caging" models. We further show that the NTD, at least in *Caulobacter* and *Moorella* ParB, determines how far the protein spreads on the chromosome from a single *parS* site. Our results emphasize the key role of the NTD in the formation of the ParB-DNA network in *Caulobacter* cells (Fig. 8). Our co-crystal structure lacks the CTD, hence the role of this domain is less clear in *Caulobacter*. In *Bacillus* ParB, the CTD acts both as a dimerization and DNA-binding and bridging interface via its non-specific DNA binding and condensation activities, thereby contributing to the formation of the nucleoprotein network. Here, we discover that the *Caulobacter* ParB CTD lacks these activities, *Caulobacter* CTD might mainly function as a monomer-monomer dimerization interface (37) (Fig. 8B). Taken all together, we suggest that different bacteria might fine-tune the properties of their chromosomal ParBs and there is a noticeable inter-species variation in how each domain contributes to the optimal function of ParB inside cells.

ACCESSION NUMBER

The accession number for the sequencing data reported in this paper is GSE134665. Atomic coordinates for a protein crystal structure reported in this paper were deposited in the RCSB Protein Data Bank with the accession number 6T1F.

ACKNOWLEDGMENTS

This study was supported by a Royal Society University Research Fellowship (UF140053) and a BBSRC grant (BB/P018165/1) to T.B.K.L. A.S.B.J's PhD studentship was funded by the Royal Society (RG150448), and N.T.T was funded by the BBSRC grant-in-add (BBS/E/J/000C0683 to the John Innes Centre). We thank Diamond Light Source for access to beamline I04-1 under proposal MX13467 with support from the European Community's Seventh Framework Program (FP7/2007–2013) under Grant Agreement 283570 (BioStruct-X). F.M.H. thanks the financial support from the Spanish MINECO (project BFU2017-83794-P (AEI/FEDER, UE)) and from European Research Council (ERC) under the European Union Horizon 2020 research and innovation (grant agreement No 681299).

Conflict of interest statement. None declared.

TABLE 1. X-RAY DATA COLLECTION AND PROCESSING STATISTICS

Structure	***Caulobacter* Ct-ParB-*parS* complex**
Data collection	
Diamond Light Source beamline	I04-1
Wavelength (Å)	0.916
Detector	Pilatus 6M-F
Resolution range (Å)	72.96 – 2.90 (3.08 – 2.90)
Space Group	$P2_1$
Cell parameters (Å/°)	a = 54.25, b = 172.93, c = 72.85 Å, β = 90.54°
Total no. of measured intensities	198135 (33888)
Unique reflections	29654 (4775)
Multiplicity	6.7 (7.1)
Mean $I/\sigma(I)$	8.7 (1.4)
Completeness (%)	99.7 (100.0)
R_{merge}[a]	0.135 (1.526)
R_{meas}[b]	0.146 (1.646)
$CC_{½}$[c]	0.997 (0.677)
Wilson B value (Å^2)	81.6
Refinement	
Resolution range (Å)	72.96 – 2.90 (2.98 – 2.90)
Reflections: working/free[d]	28155/1466
R_{work}[e]	0.240 (0.366)

R_{free}[e]	0.263 (0.369)
Ramachandran plot: favored/allowed/disallowed[f] (%)	95.2/4.8/0
R.m.s. bond distance deviation (Å)	0.005
R.m.s. bond angle deviation (°)	1.045
No. of protein residues per chain	191/190/195/187
No. of DNA bases per chain	22/22/22/22
Mean *B* factors: protein/DNA/ overall (Å^2)	98/74/92
PDB accession code	**6T1F**

Values in parentheses are for the outer resolution shell.

[a] $R_{merge} = \sum_{hkl} \sum_i |I_i(hkl) - \langle I(hkl)\rangle| / \sum_{hkl} \sum_i I_i(hkl)$.

[b] $R_{meas} = \sum_{hkl} [N/(N-1)]^{1/2} \times \sum_i |I_i(hkl) - \langle I(hkl)\rangle| / \sum_{hkl} \sum_i I_i(hkl)$, where $I_i(hkl)$ is the *i*th observation of reflection *hkl*, $\langle I(hkl)\rangle$ is the weighted average intensity for all observations *i* of reflection *hkl* and *N* is the number of observations of reflection *hkl*.

[c] $CC_{½}$ is the correlation coefficient between symmetry equivalent intensities from random halves of the dataset.

[d] The dataset was split into "working" and "free" sets consisting of 95 and 5% of the data respectively. The free set was not used for refinement.

[e] The R-factors R_{work} and R_{free} are calculated as follows: $R = \sum(|F_{obs} - F_{calc}|)/\sum|F_{obs}|$, where F_{obs} and F_{calc} are the observed and calculated structure factor amplitudes, respectively.

[f] As calculated using MolProbity (45).

MATERIALS AND METHODS

Strains, media and growth conditions

Escherichia coli and *Caulobacter crescentus* were grown in LB and PYE, respectively. When appropriate, media were supplemented with antibiotics at the following concentrations (liquid/solid media for *Caulobacter*; liquid/solid media for *E. coli* (µg/mL)): carbenicillin (*E. coli* only: 50/100), chloramphenicol (1/2; 20/30), kanamycin (5/25; 30/50), oxytetracycline (1/2; 12/12), and apramycin (*E. coli* only: 25/50).

Plasmids and strains construction

All strains used are listed in Supplementary Table S1. All plasmids and primers used in strain and plasmid construction are listed in Supplementary Table S2. For details on plasmids and strain constructions, see the Supplementary Materials and Methods.

Protein overexpression and purification

Plasmid pET21b::*Caulobacter crescentus* Ct-ParB-$(His)_6$ (Table S1) was introduced into *E. coli* Rosetta pRARE competent cells (Novagen) by heat-shock transformation. 10 mL overnight culture was used to inoculate 4 L of LB medium + carbenicillin + chloramphenicol. Cells were grown at 37˚C with shaking at 210 rpm to an OD_{600} of ~0.4. The culture was then left to cool to 28˚C before isopropyl-β-D-thiogalactopyranoside (IPTG) was added at a final concentration of 1 mM. The culture was left shaking for an additional 3 hours at 30ºC before cells were harvested by centrifugation. Pelleted cells

were resuspended in a buffer containing 100 mM Tris-HCl pH 8.0, 300 mM NaCl, 10 mM Imidazole, 5% (v/v) glycerol, 1 µL of Benzonase nuclease (Sigma Aldrich), 0.1 g of lysozyme (Sigma Aldrich), and an EDTA-free protease inhibitor tablet (Roche). The pelleted cells were then lyzed by sonification (10 cycles of 15 s with 10 s resting on ice in between each cycle). The cell debris was removed through centrifugation at 28,000 g for 30 min and the supernatant was filtered through a 0.45 µm sterile filter (Sartorius Stedim). The protein was then loaded into a 1-mL HiTrap column (GE Healthcare) that had been equilibrated with buffer A (100 mM Tris-HCl pH 8.0, 300 mM NaCl, 10 mM Imidazole, and 5% glycerol). Protein was eluted from the column using an increasing (10 mM to 500 mM) Imidazole gradient in the same buffer. Ct-ParB-containing fractions were pooled and diluted to a conductivity of 16 mS/cm before being loaded onto a Heparin HP column (GE Healthcare) that had been equilibrated with 100 mM Tris-HCl pH 8.0, 25 mM NaCl, and 5% glycerol. Protein was eluted from the Heparin column using an increasing (25 mM to 1 M NaCl) salt gradient in the same buffer. Ct-ParB fractions were pooled and analyzed for purity by SDS-PAGE. Glycerol was then added to ParB fractions to a final volume of 10%, followed by 10 mM EDTA and 1 mM DDT. The purified Ct-ParB was subsequently aliquoted, snap frozen in liquid nitrogen, and stored at -80˚C. Ct-ParB that was used for X-ray crystallography was further polished via a gel-filtration column. To do so, purified Ct-ParB was concentrated by centrifugation in an Amicon Ultra-15 3-kDa cut-off spin filters (Merck) before being loaded into a Superdex 200 gel filtration column (GE Healthcare). The gel filtration column was pre-equilibrated with 10 mM Tris-HCl pH 8.0, 250 mM NaCl. Ct-ParB fractions were then pooled and analyzed for purity by SDS-PAGE (Fig. S1A). Full-length *Caulobacter* ParB-$(His)_6$ and other ParB variants were also purified using the same procedure (Fig. S1A and Fig. S5A).

Reconstitution of *parS* DNA

A 22-bp palindromic single-stranded DNA fragment (5'-GGATGTTTCACGTGAAACATCC-3') (360 µM in 10 mM Tris-HCl pH 8.0, 250 mM NaCl buffer) was heated at 95°C for 5 min before being left to cool down to room temperature (RT) overnight to form a double stranded *parS* DNA (final concentration: 180 µM). The core *parS* site sequence is underlined.

Protein crystallization, structure determination, and refinement

Crystallization screens for the *Caulobacter* Ct-ParB-*parS* complex crystal were set up in sitting-drop vapour diffusion format in MRC2 96-well crystallization plates with drops comprised of 0.3 µL precipitant solution and 0.3 µL of protein-DNA complex, and incubated at 293 K. His-tagged Ct-ParB (10 mg/mL) was mixed with a 22-bp *parS* duplex DNA at a molar ratio of 2:1.2 (protein monomer:DNA) in the gel filtration elution buffer (10 mM Tris-HCl pH 8.0, 250 mM NaCl). The Ct-ParB-*parS* crystals grew in a solution containing 20.5% (w/v) PEG 3350, 263 mM magnesium formate, and 10% (v/v) glycerol. After optimization of an initial hit, suitable crystals were cryoprotected with 20% (v/v) glycerol and mounted in Litholoops (Molecular Dimensions) before flash-cooling by plunging into liquid nitrogen. X-ray data were recorded on beamline I04-1 at the Diamond Light Source (Oxfordshire, UK) using a Pilatus 6M-F hybrid photon counting detector (Dectris), with crystals maintained at 100 K by a Cryojet cryocooler (Oxford Instruments). Diffraction data were integrated and scaled using XDS (46) via the XIA2 expert system (47) then merged using AIMLESS (48). Data collection statistics are summarized in Table 1. The majority of the downstream analysis was performed through the CCP4i2 graphical user interface (49).

The Ct-ParB-*parS* complex crystallized in space group $P2_1$ with cell parameters of a = 54.25, b = 172.93, c = 72.85 Å and β = 90.54° (Table 1). Analysis of the likely composition of the asymmetric unit (ASU) suggested that it would contain four copies of the Ct-ParB monomers and two copies of the 22-bp *parS* DNA duplex (Fig. S2B), giving an estimated solvent content of ~46.6%.

Interrogation of the Protein Data Bank with the sequence of the *Caulobacter* Ct-ParB revealed two suitable template structures for molecular replacement: apo-ParB from *Thermus thermophilus* (38) (PDB accession code: 1VZ0; 46% identity over 82% of the sequence) and *Helicobacter pylori* ParB bound to *parS* DNA (29) (PDB accession code: 4UMK; 42% identity over 75% of the sequence).

First, single subunits taken from these two entries were trimmed using SCULPTOR (50) to retain the parts of the structure that aligned with the *Caulobacter* Ct-ParB sequence, and then all side chains were truncated to Cβ atoms using CHAINSAW (51). Comparison of these templates revealed a completely different relationship between the N-terminal domain and the DNA-binding domain. Thus, we prepared search templates based on the individual domains rather than the subunits. The pairs of templates for each domain were then aligned and used as ensemble search models in PHASER (52). For the DNA component, an ideal B-form DNA duplex was generated in COOT (53) from a 22-bp palindromic sequence of *parS*. A variety of protocols were attempted in PHASER (52), the best result was obtained by searching for the two DNA duplexes first, followed by four copies of the DNA-binding domain, giving a TFZ score of 10.5 at 4.5 Å resolution. We found that the placement of the DNA-binding domains with respect to the DNA duplexes was analogous to that seen in the *Helicobacter* Ct-ParB-*parS* complex. After several iterations of rebuilding in COOT and refining the model in REFMAC5 (54), it was possible to manually dock one copy of the N-terminal domain template (from 1VZ0) into weak and fragmented electron density such that it could be joined to one of the DNA-binding domains. A superposition of this more complete subunit onto the other three copies revealed that in only one of these did the N-terminal domain agree with the electron density. Inspection of the remaining unfilled electron density showed evidence for the last two missing N-terminal domains, which were also added by manual docking of the domain template (from 1VZ0). For the final stages, TLS refinement was used with a single TLS domain defined for each protein chain and for each DNA strand. The statistics of the final refined model, including validation output from MolProbity (45), are summarized in Table 1.

Chromatin immunoprecipitation with deep sequencing (ChIP-seq)

Caulobacter cell cultures (25 mL) were grown in PYE (in the presence of appropriate antibiotics, 0.3% glucose, and 0.5 mM vanillate) before fixation with formaldehyde to a final concentration of 1%. Fixed cells were incubated at RT for 30 minutes, then quenched with 0.125 M glycine for 15 minutes at RT. All subsequent steps were performed exactly as described in Tran *et al* (2018) (10). A detailed protocol was described in the Supplementary Materials and Methods. For the list of ChIP-seq experiments and their replicates in this study, see Supplementary Table S3.

Generation and analysis of ChIP-seq profiles

For analysis of ChIP-seq data, Hiseq 2500 Illumina short reads (50 bp) were mapped back to the *Caulobacter* NA1000 reference genome (NCBI Reference Sequence: NC_011916.1) using Bowtie 1 (29) and the following command: bowtie -m 1 -n 1 --best --strata -p 4 --chunkmbs 512 NA1000-bowtie --sam *.fastq > output.sam. Subsequently, the sequencing coverage at each nucleotide position was computed using BEDTools (30) using the following command: bedtools genomecov -d -ibam output.sorted.bam -g NA1000.fna > coverage_output.txt. For analysis of *E. coli* ChIP-seq data, the same procedure as above was applied, except that short reads were map to the reference genome of the *E. coli* MG1655 (NCBI Reference Sequence: NC_000913.3). Finally, ChIP-seq profiles were plotted with the x-axis representing genomic positions and the y-axis is the number of reads per base pair per million mapped reads (RPBPM) using custom R scripts.

Measurement of protein-DNA binding affinity by bio-layer interferometry (BLI)

Bio-layer interferometry experiments were conducted using a BLItz system equipped with Dip-and-Read© Streptavidin (SA) Biosensors (ForteBio). BLItz measures the wavelength shifts (binding signal or response (R), unit: nm) resulting from changes in the optical thickness of the sensor surface during association or dissociation of the analyte. The streptavidin biosensor (ForteBio) was hydrated in a low salt binding buffer (100 mM Tris-HCl pH 7.4, 100 mM NaCl, 1 mM EDTA, and 0.005% Tween 20) for 10 min. Biotinylated double-stranded DNA was immobilized onto the surface of the SA biosensor through a cycle of baseline (30 s), association (120 s), and dissociation (120 s). Briefly, the tip of the biosensor was dipped into a low salt buffer for 30 s to establish the baseline, then to 1 µM biotinylated double-stranded DNA for 120 s, and finally to a low salt binding buffer for 120 s to allow for dissociation. Biotinylated double-stranded DNA harboring *parS* or a scrambled *parS* site (i.e. non-specific DNA) were prepared by annealing a 20-bp biotinylated oligo with its unmodified

complementary strand in an annealing buffer (1 mM Tris-HCl pH 8.0, 5 mM NaCl). The sequences of oligos are listed in Supplementary Table S2. The oligos mixture was heated to 98°C for 2 min and allowed to cool down to RT overnight. After the immobilization of DNA on the sensor, association reactions were monitored at 250 nM, 500 nM, and 1 µM dimer concentration of ParB (WT) or ParB variants for 120 s. At the end of each binding step, the sensor was transferred into a protein-free low salt buffer to follow the dissociation kinetics for 120 s. The sensor was recycled by dipping in a high-salt buffer (100 mM Tris-HCl pH 7.4, 1000 mM NaCl, 1 mM EDTA, and 0.005% Tween 20) for at least 1 min to remove bound proteins. All interaction kinetics profiles (sensorgrams) recorded during BLItz experiments were analyzed using the BLItz analysis software (ForteBio). Reactions were run in triplicate for each concentration of ParB used, and the equilibrium responses were recorded and averaged. The extent of non-specific binding was assessed by monitoring the interaction of proteins with unmodified sensors and was deemed to be negligible.

Magnetic tweezer assays

Magnetic tweezer experiments were performed using a home-made setup as described previously (32, 36). Briefly, images of micro meter-sized superparamagnetic beads tethered to the surface of a glass slide by DNA constructs are acquired with a 100x oil immersion objective and a CCD camera. Real-time image analysis was used to determine the spatial coordinates of beads with nm accuracy in x, y and z. A step-by-step motor located above the sample moves a pair of magnets allowing the application of stretching forces to the bead-DNA system. We used horizontally-aligned magnets coupled to an iron holder. Applied forces can be quantified from the Brownian excursions of the bead and the extension of the DNA tether. Data were acquired at 150 Hz to minimize sampling artifacts in force determination. We used horizontally-aligned magnets coupled to an iron holder to achieve force up to 15 pN.

Fabrication of DNA substrates for magnetic tweezer experiments containing a single *parS* sequence with biotins and digoxigenins at the tails was described previously (32).The DNA molecules were incubated with 2.8 µm streptavidin-coated beads (MyOne, Invitrogen) for 10 min. Then, the DNA-bead complex was injected in a liquid cell functionalized with anti-digoxigenin antibodies (Roche) and incubated for 10 min before applying force. Torsionally constrained molecules and beads with more than a single DNA molecule were identified from its distinct rotation-extension curves and discarded for further analysis. All the experiments were performed in a reaction buffer composed of 10 mM HEPES pH 7.5, 150 mM NaCl, 3 mM EDTA, 0.1% (v/v) Tween-20 and 100 µg/ml BSA.

Force-extension curves were obtained by decreasing the applied force in steps from 15 pN to ~0.02 pN for a total measuring time of 15 min. First, we measured the force-extension response for bare DNA molecules. Then, the force was reset to 15 pN and ParB variants were flown and incubated for 2 min before starting the measurement of a force-extension curve at the same magnet positions in absence of proteins. The force applied to each bead was determined based on the force-extension data of bare DNA molecules. Bare DNA curves were fitted to the worm-like chain model and fitted values of persistence length and contour length were used as a quality control. Molecules with a large discrepancy for contour length or persistence with respect to expected parameters (45 nm persistence length, 2.1 µm contour length) were discarded from the analysis.

REFERENCES

1. Ireton,K., Gunther,N.W. and Grossman,A.D. (1994) spo0J is required for normal chromosome segregation as well as the initiation of sporulation in Bacillus subtilis. *J. Bacteriol.*, **176**, 5320–5329.
2. Lin,D.C. and Grossman,A.D. (1998) Identification and characterization of a bacterial chromosome partitioning site. *Cell*, **92**, 675–685.
3. Mohl,D.A., Easter,J. and Gober,J.W. (2001) The chromosome partitioning protein, ParB, is required for cytokinesis in Caulobacter crescentus. *Mol. Microbiol.*, **42**, 741–755.
4. Fogel,M.A. and Waldor,M.K. (2006) A dynamic, mitotic-like mechanism for bacterial chromosome segregation. *Genes Dev.*, **20**, 3269–3282.
5. Livny,J., Yamaichi,Y. and Waldor,M.K. (2007) Distribution of Centromere-Like parS Sites in Bacteria: Insights from Comparative Genomics. *J. Bacteriol.*, **189**, 8693–8703.
6. Donczew,M., Mackiewicz,P., Wróbel,A., Flärdh,K., Zakrzewska-Czerwińska,J. and Jakimowicz,D. (2016) ParA and ParB coordinate chromosome segregation with cell elongation and division during Streptomyces sporulation. *Open Biology*, **6**, 150263.
7. Kawalek,A., Bartosik,A.A., Glabski,K. and Jagura-Burdzy,G. (2018) Pseudomonas aeruginosa partitioning protein ParB acts as a nucleoid-associated protein binding to multiple copies of a parS-related motif. *Nucleic Acids Res.*, **46**, 4592–4606.
8. Jakimowicz,D., Chater,K. and Zakrzewska-Czerwi´nska,J. (2002) The ParB protein of Streptomyces coelicolor A3(2) recognizes a cluster of parS sequences within the origin-proximal region of the linear chromosome. *Molecular Microbiology*, **45**, 1365–1377.
9. Harms,A., Treuner-Lange,A., Schumacher,D. and Sogaard-Andersen,L. (2013) Tracking of chromosome and replisome dynamics in Myxococcus xanthus reveals a novel chromosome arrangement. *PLoS Genet*, **9**, e1003802.
10. Tran,N.T., Stevenson,C.E., Som,N.F., Thanapipatsiri,A., Jalal,A.S.B. and Le,T.B.K. (2018) Permissive zones for the centromere-binding protein ParB on the Caulobacter crescentus chromosome. *Nucleic Acids Res*, **46**, 1196–1209.
11. Toro,E., Hong,S.-H., McAdams,H.H. and Shapiro,L. (2008) Caulobacter requires a dedicated mechanism to initiate chromosome segregation. *PNAS*, **105**, 15435–15440.
12. Lagage,V., Boccard,F. and Vallet-Gely,I. (2016) Regional Control of Chromosome Segregation in Pseudomonas aeruginosa. *PLOS Genetics*, **12**, e1006428.
13. Mohl,D.A. and Gober,J.W. (1997) Cell cycle-dependent polar localization of chromosome partitioning proteins in Caulobacter crescentus. *Cell*, **88**, 675–684.
14. Ptacin,J.L., Lee,S.F., Garner,E.C., Toro,E., Eckart,M., Comolli,L.R., Moerner,W.E. and Shapiro,L. (2010) A spindle-like apparatus guides bacterial chromosome segregation. *Nat Cell Biol*, **12**, 791–798.
15. Lim,H.C., Surovtsev,I.V., Beltran,B.G., Huang,F., Bewersdorf,J. and Jacobs-Wagner,C. (2014) Evidence for a DNA-relay mechanism in ParABS-mediated chromosome segregation. *Elife*, **3**, e02758.
16. Vecchiarelli,A.G., Mizuuchi,K. and Funnell,B.E. (2012) Surfing biological surfaces: exploiting the nucleoid for partition and transport in bacteria. *Molecular Microbiology*, **86**, 513–523.
17. Vecchiarelli,A.G., Neuman,K.C. and Mizuuchi,K. (2014) A propagating ATPase gradient drives transport of surface-confined cellular cargo. *PNAS*, **111**, 4880–4885.
18. Hwang,L.C., Vecchiarelli,A.G., Han,Y.-W., Mizuuchi,M., Harada,Y., Funnell,B.E. and Mizuuchi,K. (2013) ParA-mediated plasmid partition driven by protein pattern self-organization. *The EMBO Journal*, **32**, 1238–1249.
19. Leonard,T.A., Butler,P.J. and Löwe,J. (2005) Bacterial chromosome segregation: structure and DNA binding of the Soj dimer--a conserved biological switch. *EMBO J.*, **24**, 270–282.
20. Jecz,P., Bartosik,A.A., Glabski,K. and Jagura-Burdzy,G. (2015) A single parS sequence from the cluster of four sites closest to oriC is necessary and sufficient for proper chromosome segregation in Pseudomonas aeruginosa. *PLoS ONE*, **10**, e0120867.

21. Attaiech,L., Minnen,A., Kjos,M., Gruber,S. and Veening,J.-W. (2015) The ParB-parS Chromosome Segregation System Modulates Competence Development in Streptococcus pneumoniae. *mBio*, **6**, e00662-15.
22. Yu,W., Herbert,S., Graumann,P.L. and Götz,F. (2010) Contribution of SMC (Structural Maintenance of Chromosomes) and SpoIIIE to Chromosome Segregation in Staphylococci. *J Bacteriol*, **192**, 4067–4073.
23. Murray,H., Ferreira,H. and Errington,J. (2006) The bacterial chromosome segregation protein Spo0J spreads along DNA from parS nucleation sites. *Molecular Microbiology*, **61**, 1352–1361.
24. Song,D., Rodrigues,K., Graham,T.G.W. and Loparo,J.J. (2017) A network of cis and trans interactions is required for ParB spreading. *Nucleic Acids Res.*, **45**, 7106–7117.
25. Breier,A.M. and Grossman,A.D. (2007) Whole-genome analysis of the chromosome partitioning and sporulation protein Spo0J (ParB) reveals spreading and origin-distal sites on the Bacillus subtilis chromosome. *Molecular Microbiology*, **64**, 703–718.
26. Rodionov,O., Lobocka,M. and Yarmolinsky,M. (1999) Silencing of genes flanking the P1 plasmid centromere. *Science*, **283**, 546–549.
27. Lynch,A.S. and Wang,J.C. (1995) SopB protein-mediated silencing of genes linked to the sopC locus of Escherichia coli F plasmid. *PNAS*, **92**, 1896–1900.
28. Kusiak,M., Gapczyńska,A., Płochocka,D., Thomas,C.M. and Jagura-Burdzy,G. (2011) Binding and Spreading of ParB on DNA Determine Its Biological Function in Pseudomonas aeruginosa. *J. Bacteriol.*, **193**, 3342–3355.
29. Chen,B.-W., Lin,M.-H., Chu,C.-H., Hsu,C.-E. and Sun,Y.-J. (2015) Insights into ParB spreading from the complex structure of Spo0J and parS. *Proc. Natl. Acad. Sci. U.S.A.*, **112**, 6613–6618.
30. Schumacher,M.A., Tonthat,N.K., Lee,J., Rodriguez-Castañeda,F.A., Chinnam,N.B., Kalliomaa-Sanford,A.K., Ng,I.W., Barge,M.T., Shaw,P.L.R. and Barillà,D. (2015) Structures of archaeal DNA segregation machinery reveal bacterial and eukaryotic linkages. *Science*, **349**, 1120–1124.
31. Graham,T.G.W., Wang,X., Song,D., Etson,C.M., Oijen,A.M. van, Rudner,D.Z. and Loparo,J.J. (2014) ParB spreading requires DNA bridging. *Genes Dev.*, **28**, 1228–1238.
32. Taylor,J.A., Pastrana,C.L., Butterer,A., Pernstich,C., Gwynn,E.J., Sobott,F., Moreno-Herrero,F. and Dillingham,M.S. (2015) Specific and non-specific interactions of ParB with DNA: implications for chromosome segregation. *Nucleic Acids Res*, **43**, 719–731.
33. Broedersz,C.P., Wang,X., Meir,Y., Loparo,J.J., Rudner,D.Z. and Wingreen,N.S. (2014) Condensation and localization of the partitioning protein ParB on the bacterial chromosome. *PNAS*, **111**, 8809–8814.
34. Sanchez,A., Cattoni,D.I., Walter,J.-C., Rech,J., Parmeggiani,A., Nollmann,M. and Bouet,J.-Y. (2015) Stochastic Self-Assembly of ParB Proteins Builds the Bacterial DNA Segregation Apparatus. *Cell Syst.*, **1**, 163–173.
35. Debaugny,R.E., Sanchez,A., Rech,J., Labourdette,D., Dorignac,J., Geniet,F., Palmeri,J., Parmeggiani,A., Boudsocq,F., Anton Leberre,V., *et al.* (2018) A conserved mechanism drives partition complex assembly on bacterial chromosomes and plasmids. *Mol. Syst. Biol.*, **14**, e8516.
36. Fisher,G.L., Pastrana,C.L., Higman,V.A., Koh,A., Taylor,J.A., Butterer,A., Craggs,T., Sobott,F., Murray,H., Crump,M.P., *et al.* (2017) The structural basis for dynamic DNA binding and bridging interactions which condense the bacterial centromere. *Elife*, **6**.
37. Figge,R.M., Easter,J. and Gober,J.W. (2003) Productive interaction between the chromosome partitioning proteins, ParA and ParB, is required for the progression of the cell cycle in Caulobacter crescentus. *Mol. Microbiol.*, **47**, 1225–1237.
38. Leonard,T.A., Butler,P.J.G. and Löwe,J. (2004) Structural analysis of the chromosome segregation protein Spo0J from Thermus thermophilus. *Mol. Microbiol.*, **53**, 419–432.
39. Madariaga-Marcos,J., Pastrana,C.L., Fisher,G.L., Dillingham,M.S. and Moreno-Herrero,F. (2019) ParB dynamics and the critical role of the CTD in DNA condensation unveiled by combined force-fluorescence measurements. *Elife*, **8**.

40. Jalal,A.S.B., Tran,N.T., Stevenson,C.E., Tan,X., Lawson,D.M. and Le,T.B.K. (2019) Evolving a new protein-DNA interface via sequential introduction of permissive and specificity-switching mutations. *bioRxiv*, 10.1101/724823.
41. Romero,P., Obradovic,Z., Li,X., Garner,E.C., Brown,C.J. and Dunker,A.K. (2001) Sequence complexity of disordered protein. *Proteins*, **42**, 38–48.
42. Vucetic,S., Brown,C.J., Dunker,A.K. and Obradovic,Z. (2003) Flavors of protein disorder. *Proteins*, **52**, 573–584.
43. Schumacher,M.A., Piro,K.M. and Xu,W. (2010) Insight into F plasmid DNA segregation revealed by structures of SopB and SopB–DNA complexes. *Nucleic Acids Res*, **38**, 4514–4526.
44. Thanbichler,M. and Shapiro,L. (2006) MipZ, a Spatial Regulator Coordinating Chromosome Segregation with Cell Division in Caulobacter. *Cell*, **126**, 147–162.
45. Chen,V.B., Arendall,W.B., Headd,J.J., Keedy,D.A., Immormino,R.M., Kapral,G.J., Murray,L.W., Richardson,J.S. and Richardson,D.C. (2010) MolProbity: all-atom structure validation for macromolecular crystallography. *Acta Crystallogr. D Biol. Crystallogr.*, **66**, 12–21.
46. Kabsch,W. (2010) XDS. *Acta Crystallogr D Biol Crystallogr*, **66**, 125–132.
47. Winter,G. (2010) xia2: an expert system for macromolecular crystallography data reduction. *J Appl Cryst*, **43**, 186–190.
48. Evans,P.R. and Murshudov,G.N. (2013) How good are my data and what is the resolution? *Acta Cryst D*, **69**, 1204–1214.
49. Potterton,L., Agirre,J., Ballard,C., Cowtan,K., Dodson,E., Evans,P.R., Jenkins,H.T., Keegan,R., Krissinel,E., Stevenson,K., *et al.* (2018) CCP4i2: the new graphical user interface to the CCP4 program suite. *Acta Crystallogr D Struct Biol*, **74**, 68–84.
50. Bunkóczi,G. and Read,R.J. (2011) Improvement of molecular-replacement models with Sculptor. *Acta Crystallogr D Biol Crystallogr*, **67**, 303–312.
51. Stein,N. (2008) CHAINSAW: a program for mutating pdb files used as templates in molecular replacement. *J Appl Cryst*, **41**, 641–643.
52. McCoy,A.J., Grosse-Kunstleve,R.W., Adams,P.D., Winn,M.D., Storoni,L.C. and Read,R.J. (2007) Phaser crystallographic software. *J Appl Crystallogr*, **40**, 658–674.
53. Emsley,P. and Cowtan,K. (2004) Coot: model-building tools for molecular graphics. *Acta Crystallogr. D Biol. Crystallogr.*, **60**, 2126–2132.
54. Murshudov,G.N., Vagin,A.A. and Dodson,E.J. (1997) Refinement of Macromolecular Structures by the Maximum-Likelihood Method. *Acta Cryst D*, **53**, 240–255.

FIG. 1

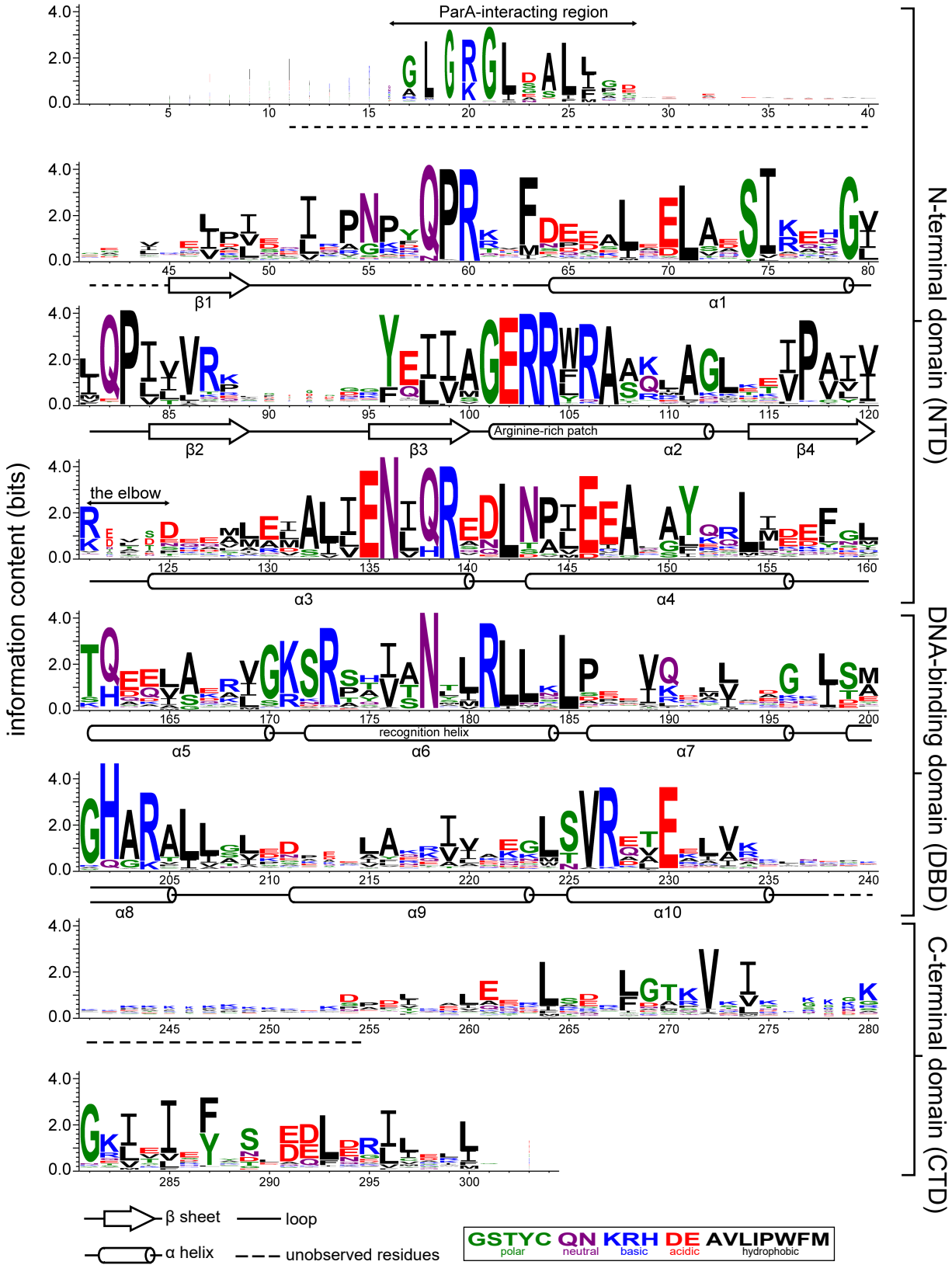

Figure 1. Sequence alignment of the chromosomal ParB protein family. An alignment of ~1800 chromosomal ParB proteins was constructed and presented as a sequence logo. The height of the stack indicates the sequence conservation, while the height of symbols within the stack indicates the relative frequency of each amino acid residue at that position. Amino acids are colored based on their chemical properties. Secondary-structure elements for *Caulobacter* Ct-ParB are shown below the alignment. Dashed lines indicate unmodelled residues due to poor electron density in the *Caulobacter* Ct-ParB-*parS* co-crystal structure.

FIG. 2

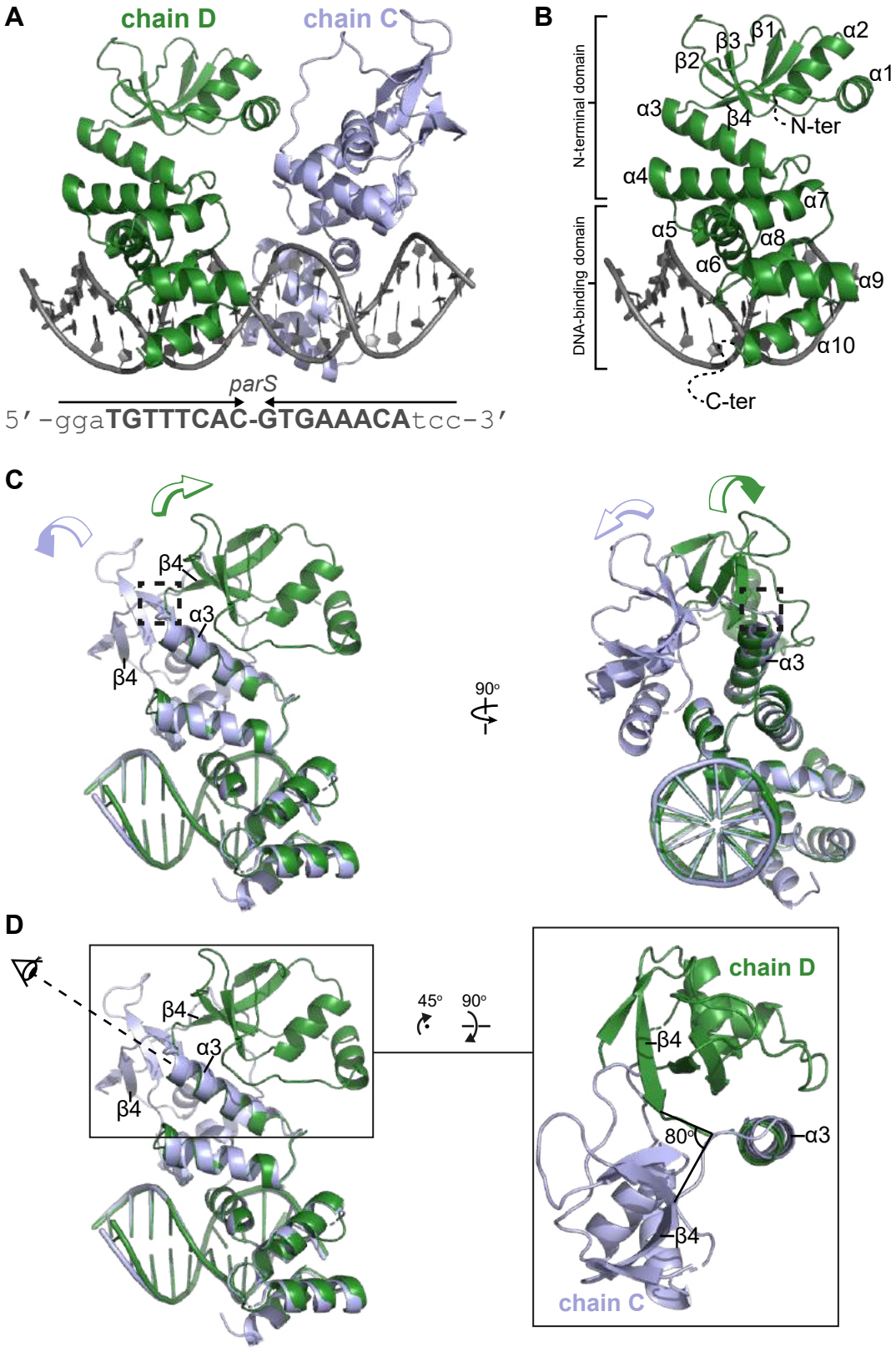

Figure 2. Co-crystal structure of a C-terminal domain truncated Ct-ParB-*parS* complex from *Caulobacter crescentus* reveals alternate conformations of the N-terminal domain. (A) Co-crystal structure of two *Caulobacter* Ct-ParB monomers (dark green and light blue) bound on a 22-bp *parS* DNA. The nucleotide sequence of the 22-bp *parS* is shown below the co-crystal structure, the core *parS* sequence is highlighted in bold. **(B)** The structure of Ct-ParB chain D bound to a *parS* half site with key features highlighted. **(C)** Superimposition of *Caulobacter* Ct-ParB chain C and D (light blue and dark green, respectively) shows two different orientations of the NTD (α1-β4). The arrow above each chain shows the direction each NTD projects towards. The dashed box shows the loop (the elbow) that connects helix α3 and sheet β4 together. **(D)** A top-down view of the superimposition of chain C and D shows that the NTDs (α1-β4) of chain C and D are oriented ~80° apart from each other.

FIG. 3

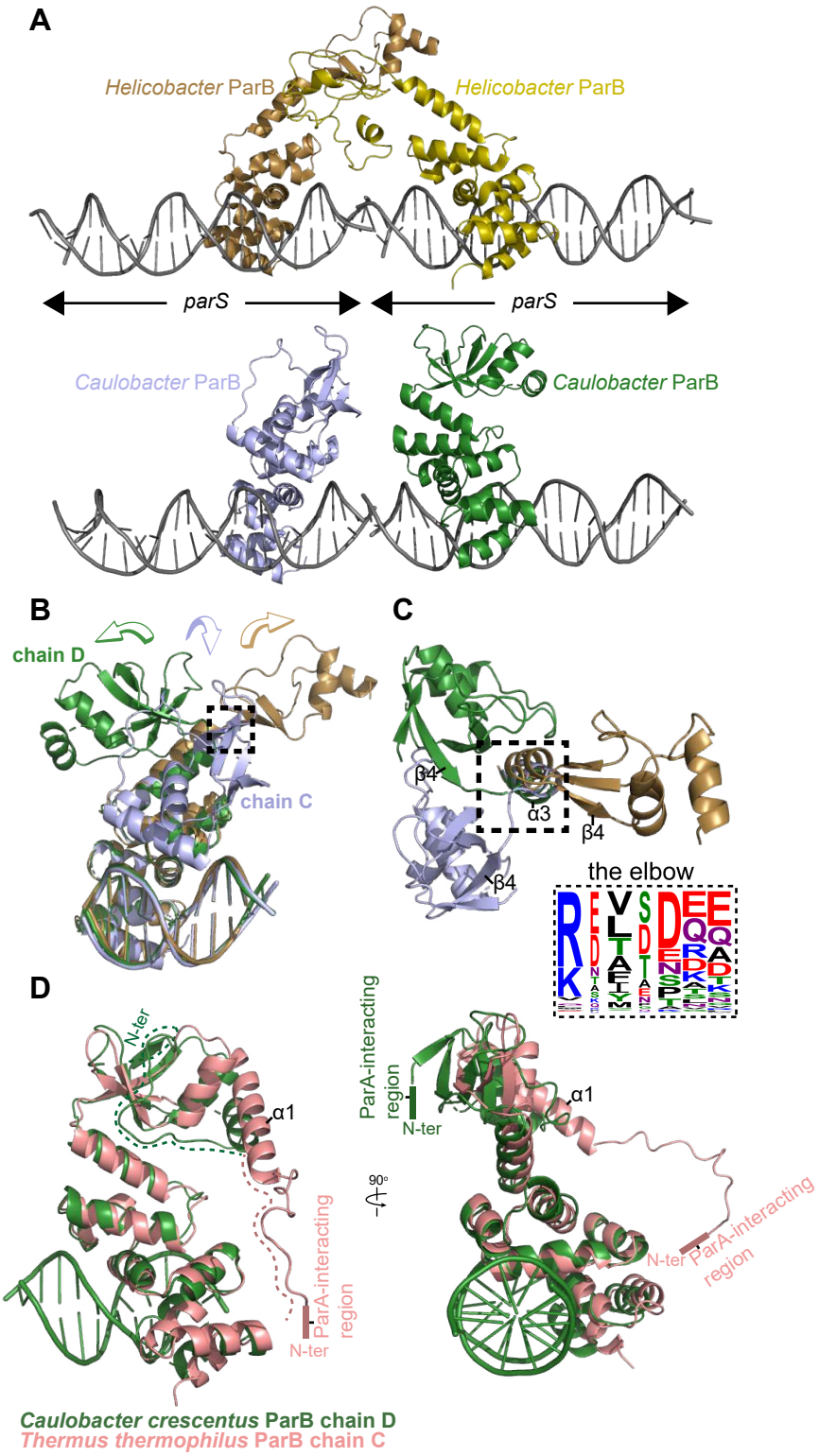

Figure 3. Structural comparisons of the *Caulobacter* Ct-ParB-*parS* complex to other ParB family members. (A) Structures of two adjacent symmetry complexes of *Helicobacter pylori* (upper panel) and *Caulobacter crescentus* Ct-ParB-*parS* (lower panel). In the *Helicobacter* Ct-ParB-*parS* complex, ParB adopts an open conformation in which its NTD projects outwards to contact a neighboring monomer. However, no such interaction was seen between the NTD of the two adjacent *Caulobacter* ParB monomers. **(B)** A side-view of the superimposition between *Caulobacter* Ct-ParB chain C (light blue), chain D (dark green), and *Helicobacter* Ct-ParB (golden) shows the three distinct orientations of the NTD (see also Fig. S3). **(C)** A top-view of the superimposition between *Caulobacter* Ct-ParB chain C, chain D, and *Helicobacter* Ct-ParB. The dashed box shows the loop (the elbow) that connects helix α3 and sheet β4 together. The conservation of amino acids at the flexible elbow is presented as sequence logos. Amino acids are colored based on their chemical properties (GSTYC: polar; QN: neutral; KRH: basic; DE: acidic; and AVLIPWFM: hydrophobic). **(D)** Superimposition of *Caulobacter* Ct-ParB chain D (dark green) and *Thermus* Ct-ParB chain C (pink) shows the two different conformations of the N-terminal-most peptide (dashed dark green and pink lines).

FIG. 4

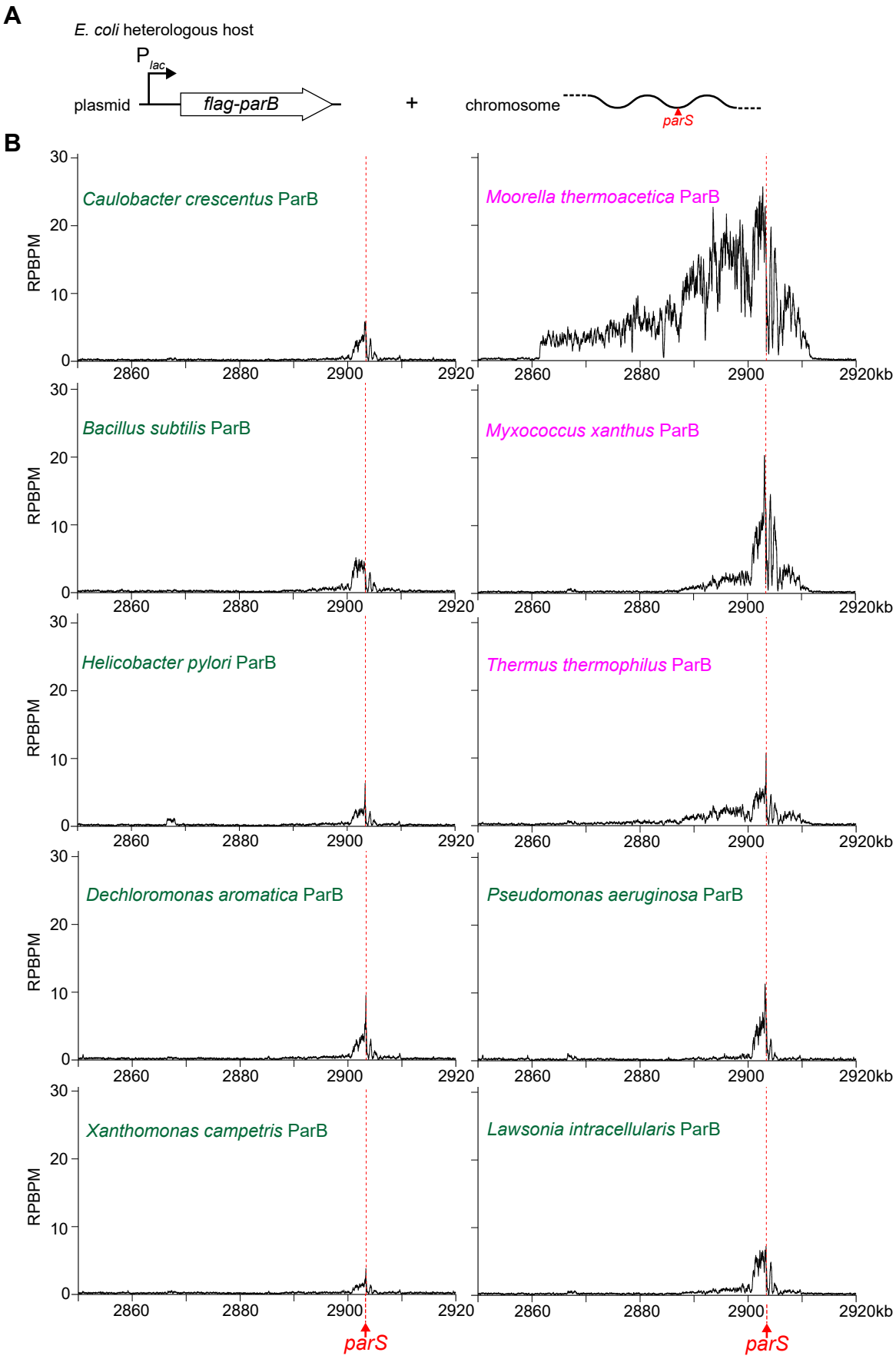

Figure 4. ChIP-seq revealed an inter-species variation in spreading among ParB orthologs. (A) The design of an *E. coli* heterologous host that allowed quantification of ParB spreading by ChIP-seq. A single *parS* site was inserted at the *ygcE* locus on the *E. coli* chromosome. Individual N-terminally FLAG-tagged ParB was produced from an IPTG-inducible P_{lac} promoter on a plasmid. **(B)** ChIP-seq profiles of FLAG-tagged ParBs from a collection of ten bacterial species (mini-spreader ParB: dark green; maxi-spreader ParB: magenta). ChIP-seq signals were reported as the number of reads at every nucleotide along the genome (RPBPM value).

FIG. 5

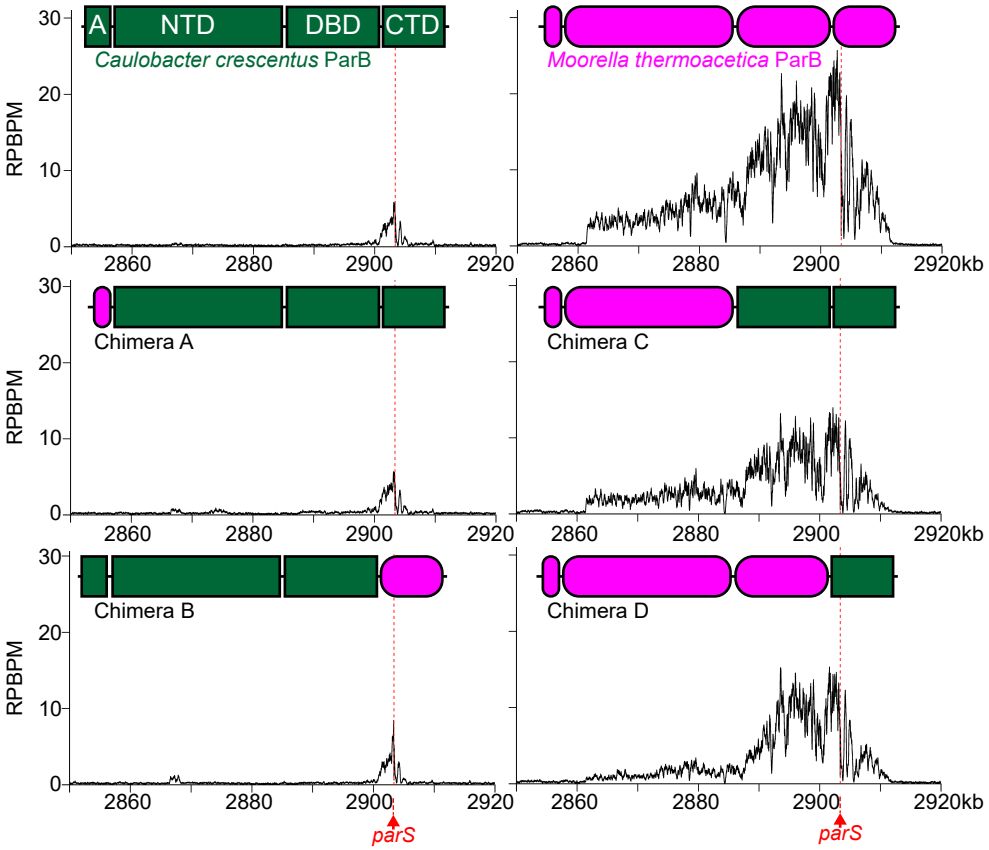

Figure 5. The N-terminal domain determines the inter-species variation in spreading among ParB orthologs. ChIP-seq profiles of a series of chimeric proteins in which different regions of a mini-spreader *Caulobacter* ParB (dark green) were replaced with the corresponding regions of a super-spreader *Moorella* ParB (magenta). N-terminally FLAG-tagged chimeras were expressed in an *E. coli ygcE*::*parS* heterologous host (See Fig. 4A). A: ParA-interacting region (res.1-32, *Caulobacter* ParB numbering); NTD: N-terminal domain (res.33-158); DBD: the *parS* DNA-binding domain (res.159-251); CTD: C-terminal domain (res. 252-end). ChIP-seq signals were reported as the number of reads at every nucleotide along the genome (RPBPM value).

FIG. 6

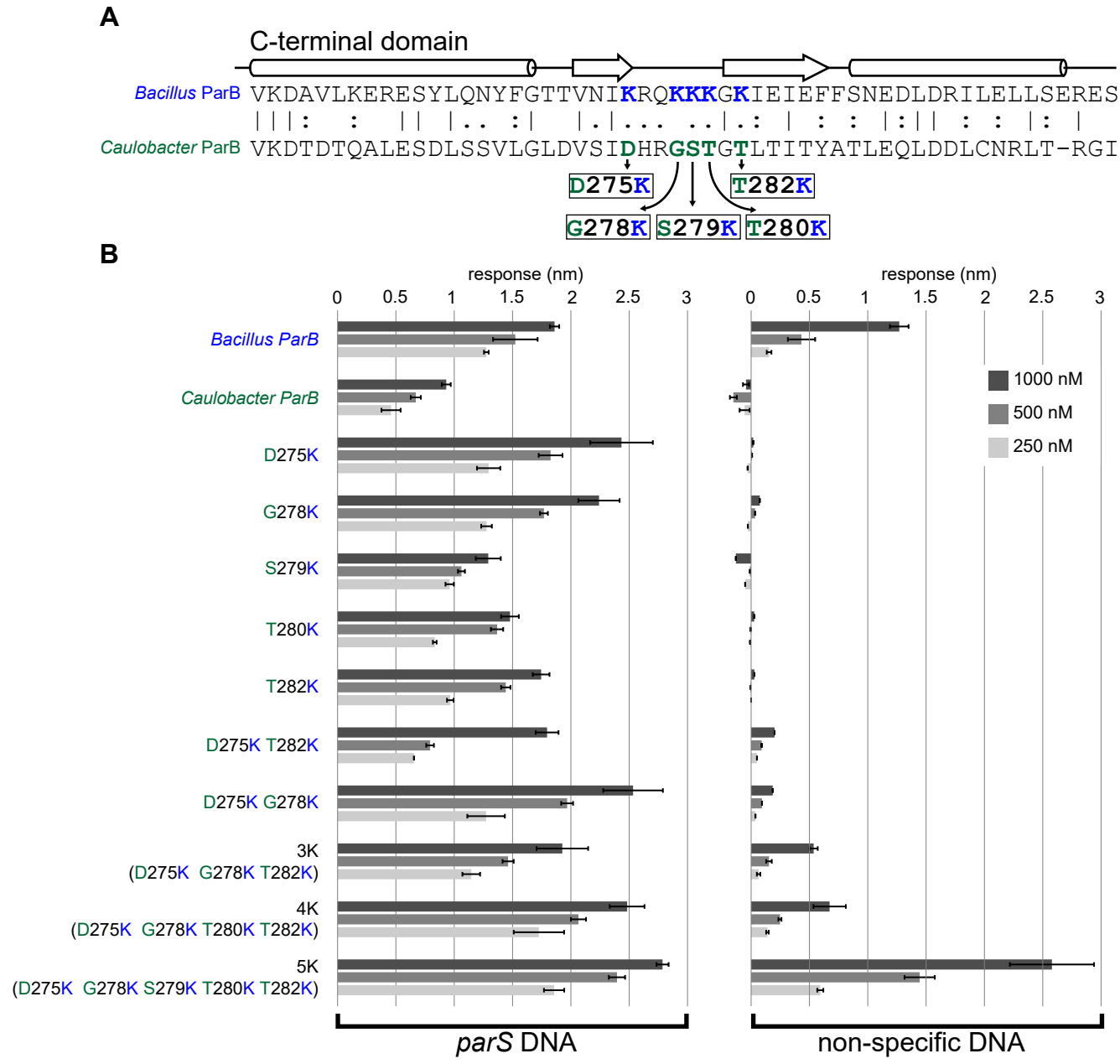

Figure 6. Engineering a lysine-rich surface into the *Caulobacter* ParB C-terminal domain resulted in variants with enhanced non-specific DNA-binding activity. (A) Sequence alignment between *Caulobacter* (dark green) and *Bacillus* ParB (blue) shows that *Caulobacter* ParB lacks the equivalent lysine-rich amino acid patch at its CTD. Lysine residues that are important for the non-specific DNA-binding and DNA condensation activities in *Bacillus* ParB (36), and positional equivalent residues in *Caulobacter* ParB are highlighted in blue and green, respectively. Secondary-structure elements for *Bacillus* ParB CTD (PDB accession number: 5NOC) are shown above the sequence alignment. **(B)** Introducing three or more lysine residues to the *Caulobacter* CTD resulted in ParB variants with enhanced non-specific DNA-binding activity. *In vitro* binding affinities between ParB variants and *parS* DNA (left panel), and non-specific scrambled *parS* DNA (right panel). Bio-layer interferometry assays were used to measure the binding affinity of ParB (250, 500, and 1000 nM) to 20-bp double-stranded DNA that contains a *parS* site or a scrambled *parS* site. The level of ParB binding to DNA was expressed as response units (nm in shifted wavelength). Error bars represent standard deviation (SD) from three replicates.

FIG. 7

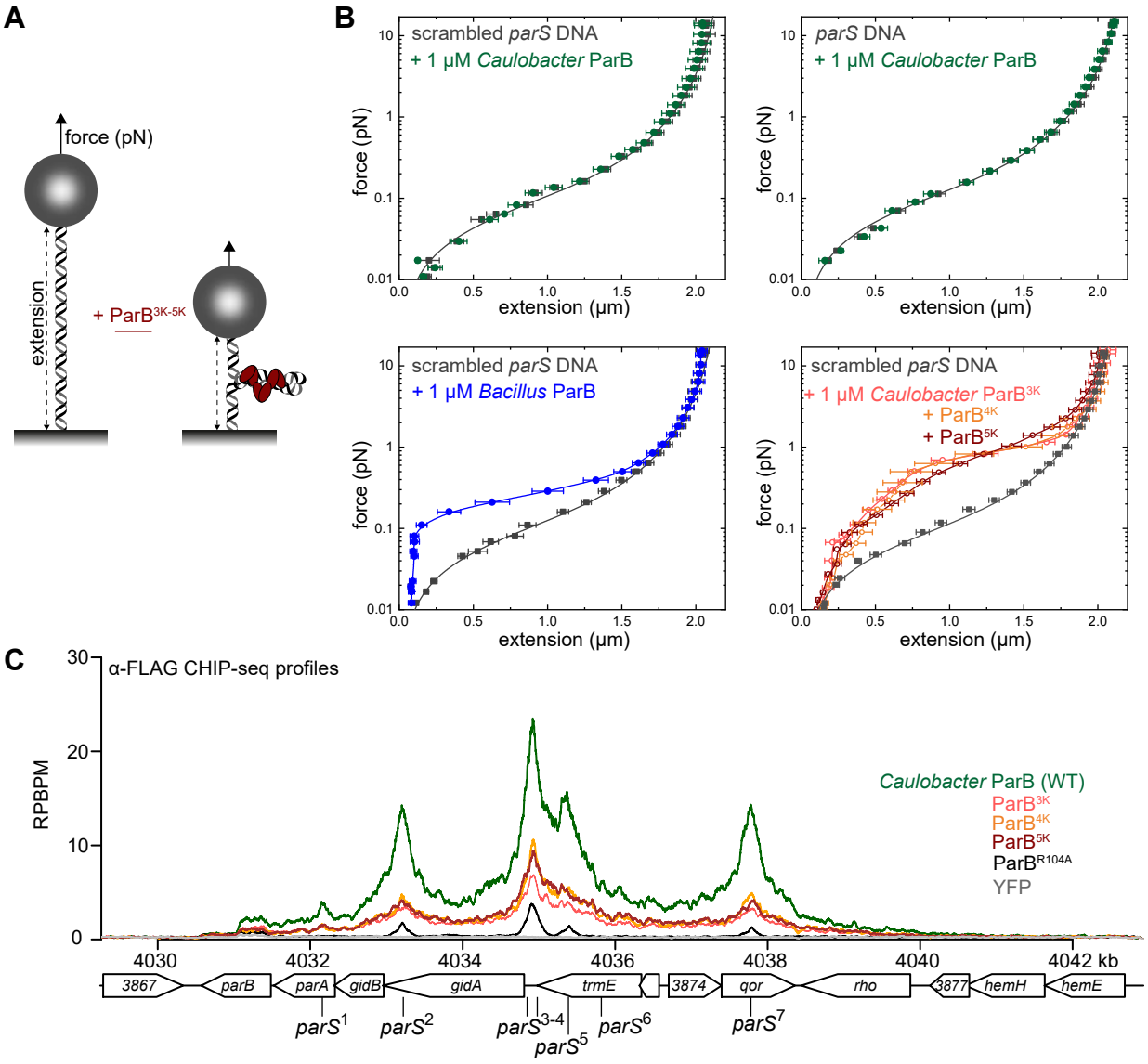

Figure 7. Engineered *Caulobacter* ParB variants with an enhanced non-specific DNA-binding activity condensed DNA *in vitro* but did not spread further than the wild-type protein *in vivo*. **(A)** Schematic of the magnetic tweezer assay that monitored ParB-dependent DNA condensation (see also the Materials and Methods). **(B)** Mean force-extension curves for *parS* DNA or scrambled *parS* DNA in the presence of 2 μM *Caulobacter* ParB (WT) (dark green), *Bacillus* ParB (WT) (blue), and *Caulobacter* ParB (3K-5K) variants (pink, orange, and brown). Data for bare DNA were fitted to the worm-like chain model. Solid lines for data in the presence of ParB variants serve as a guide to the eye. Data for non-condensed DNA were fitted to the worm-like chain model. Errors are the standard error of measurements on different molecules (N ≥ 15 molecules). **(C)** ChIP-seq profiles of a FLAG-tagged *Caulobacter* ParB (WT) (dark green), a spreading-incompetent FLAG-ParB (R104A), a non-DNA-binding protein FLAG-YFP (grey), and FLAG-ParB (3K-5K) variants (pink, orange, and brown). ChIP-seq signals were reported as the number of reads at every nucleotide along the genome (RPBPM value). The genomic context (4030 kb to 4042 kb) and *parS* sites are shown below the ChIP-seq profiles.

FIG. 8

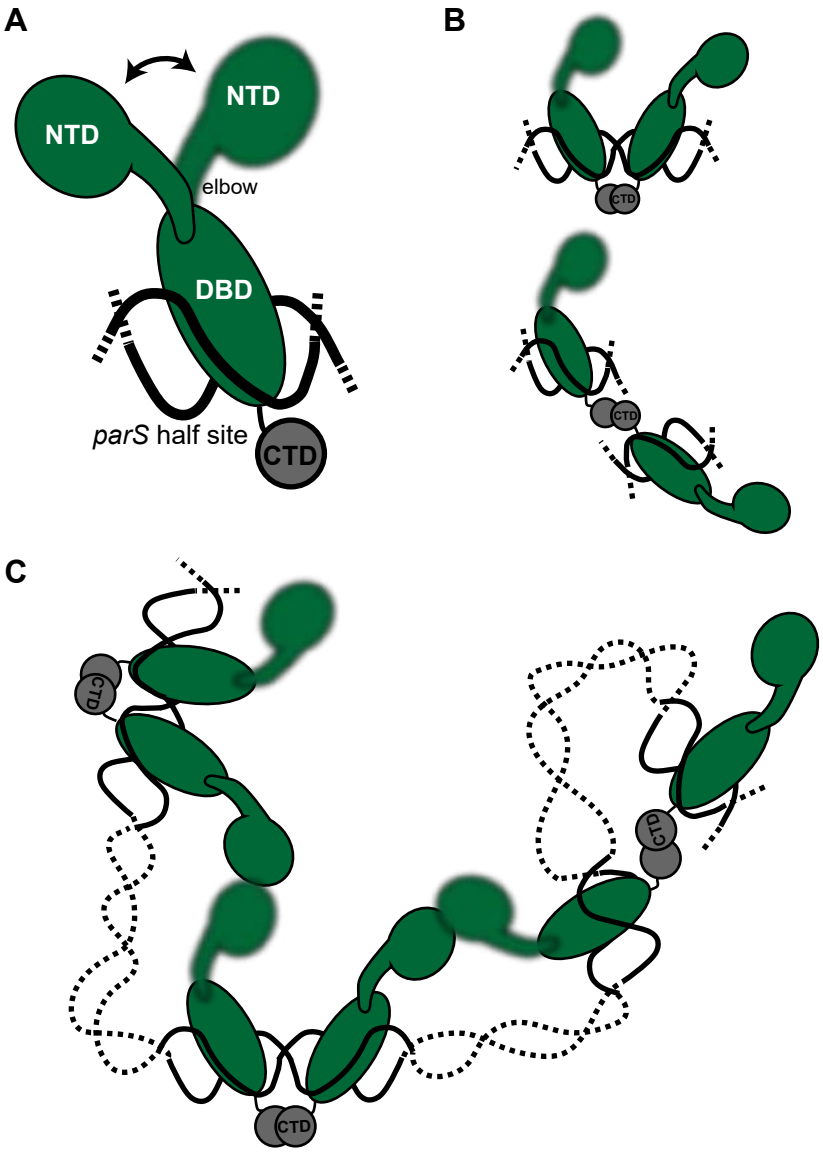

Figure 8. A model for *Caulobacter* ParB-ParB interactions via the N-terminal (NTD) and C-terminal domain (CTD). (A) The flexible elbow that connects α3 and β4 together enables the NTD of ParB to adopt multiple conformations. **(B)** The CTD might mediate the interactions between two ParB monomers bound on two adjacent half-*parS* sites (upper panel) or between two ParB monomers bound on two spatially separated half-*parS* sites (lower panel). **(C)** The coordinated actions of the CTD and the flexible NTD allows a loose but fluid network of ParB-DNA interactions to form inside the cell.

FIG. S1

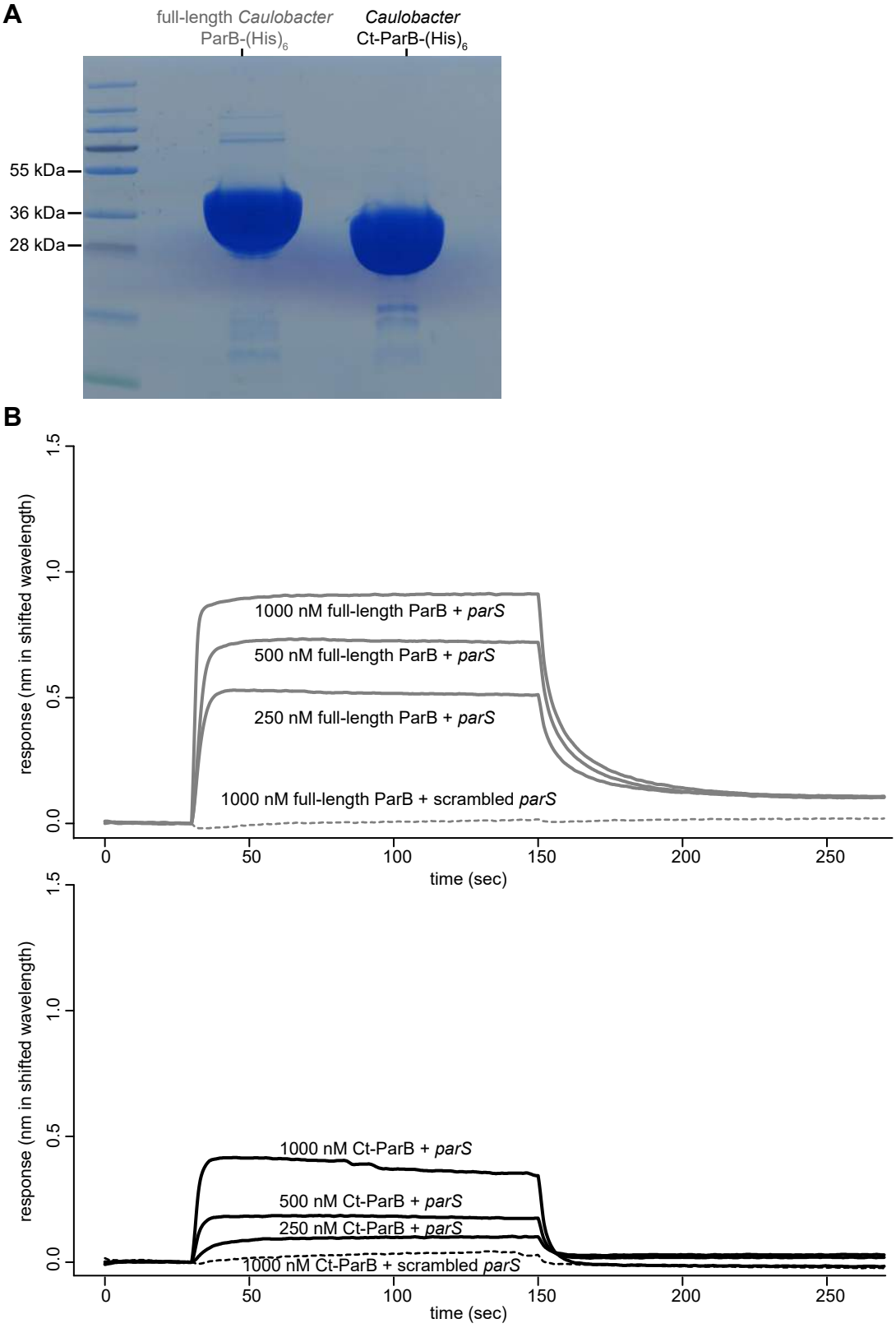

Figure S1. Purified *Caulobacter* ParB variants and their *parS* DNA-binding activities. (A) Full-length *Caulobacter* ParB and the C-terminally truncated variant (Ct-ParB) were expressed in *E. coli* and purified to near homogeneity. All variants were C-terminally His-tagged (KLAAALEHHHHHH). **(B)** Ct-ParB retains its ability to bind *parS* DNA, albeit weaker than a full-length protein. Bio-layer interferometric analysis of the interaction between a full-length *Caulobacter* ParB (grey) or a C-terminally truncated Ct-ParB (black) and a 20-bp *parS*-containing duplex DNA or the scrambled *parS* DNA. Sensors loaded with biotinylated *parS* DNA were probed with 5000 nM, 1000 nM, and 500 nM dimer concentrations of proteins. The interaction kinetics were followed by monitoring the wavelength shifts (response unit, nm) resulting from changes in the optical thickness of the sensor surface during association or dissociation of the proteins.

FIG. S2

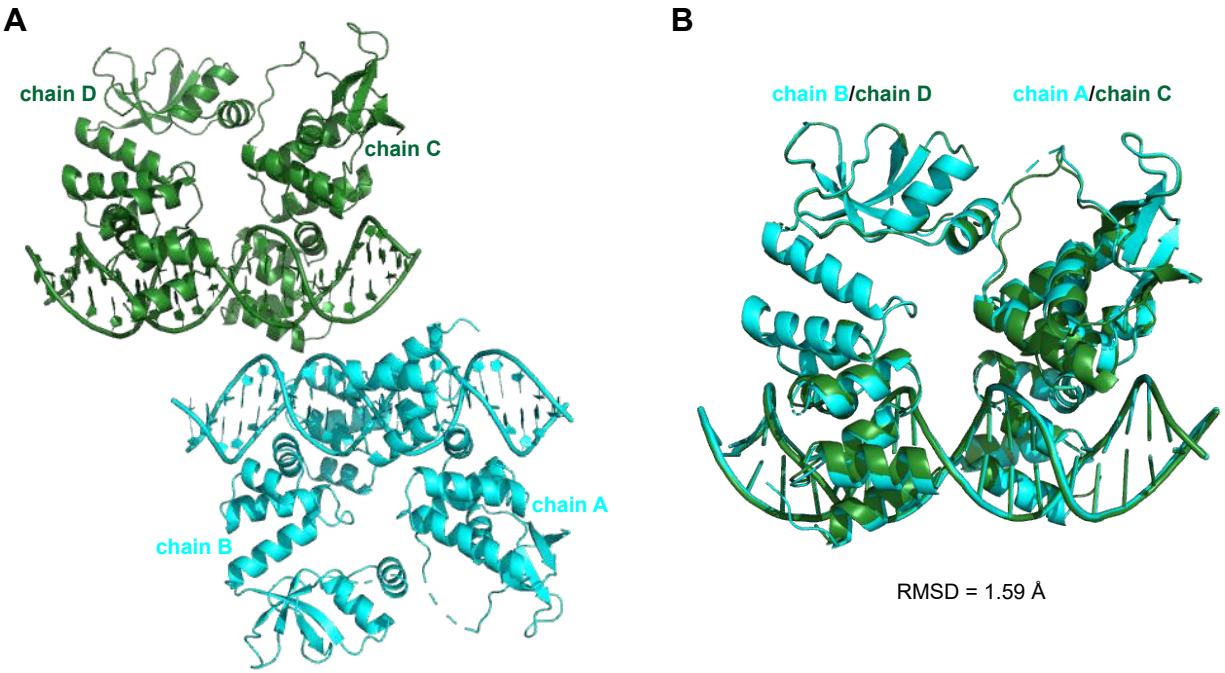

Figure S2. Composition of the asymmetric unit (ASU) of the *Caulobacter* Ct-ParB-*parS* co-crystal. (A) The ASU contains four copies of the *Caulobacter* Ct-ParB monomers (chain A, B, C, and D) and two copies of the full-size *parS* DNA. **(B)** Superimposition of the chain C-D-*parS* complex (dark green) to the chain A-B-*parS* complex (cyan) showed that the two complexes in the ASU are near identical (RMSD = 1.59 Å).

FIG. S3

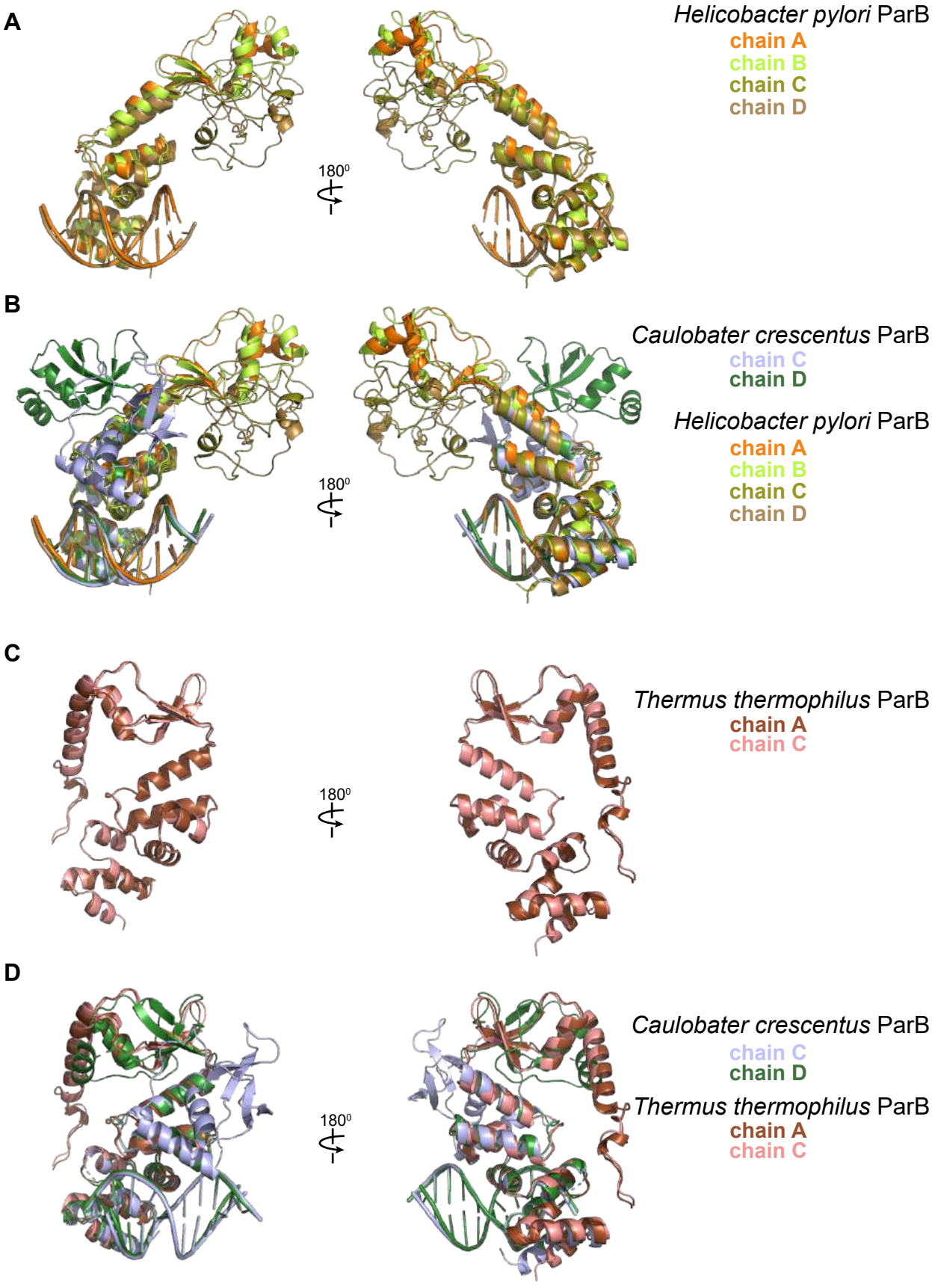

Figure S3. Structural comparisons of the *Caulobacter* Ct-ParB-*parS* complex to other ParB family members. Superposition of all crystallographically independent subunits from **(A)** *Helicobacter* Ct-ParB-*parS*; **(B)** *Helicobacter* Ct-ParB-*parS* and chain C and D of *Caulobacter* Ct-ParB-*parS*; **(C)** *Thermus* apo-Ct-ParB; **(D)** *Thermus* apo-Ct-ParB and chain C and D of *Caulobacter* Ct-ParB-*parS*. Superimposition was based on the DNA-binding domain and helices α3-α4 of the N-terminal domain.

FIG. S4

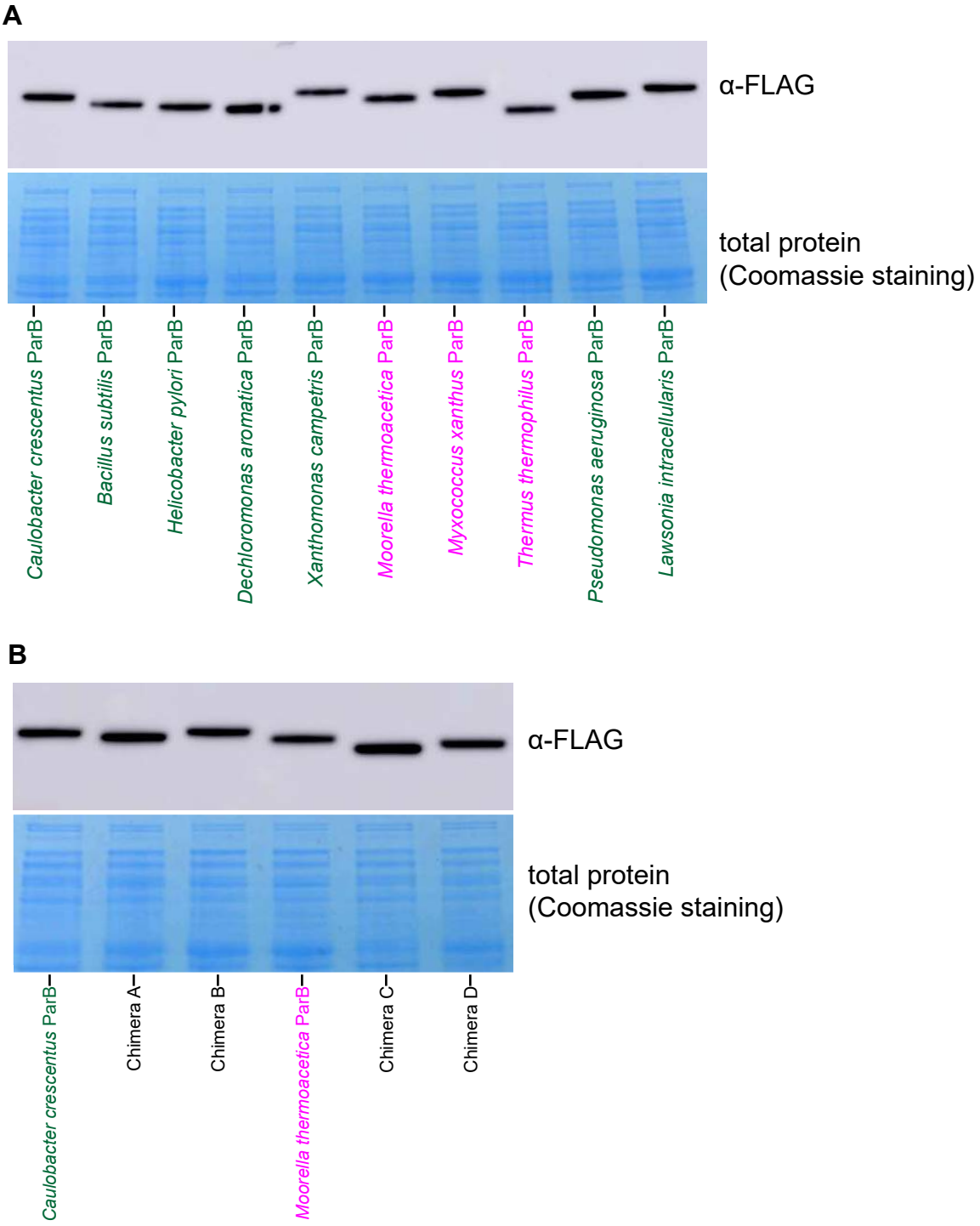

Figure S4. Production of FLAG-tagged ParB proteins from the *E. coli* heterologous host. **(A)** α-FLAG immunoblot analysis of ten FLAG-tagged ParB proteins individually expressed in the *E. coli ygcE::parS* heterologous host. **(B)** α-FLAG immunoblot analysis of FLAG-tagged chimeric ParB proteins individually expressed in the *E. coli ygcE::parS* heterologous host.

FIG. S5

A

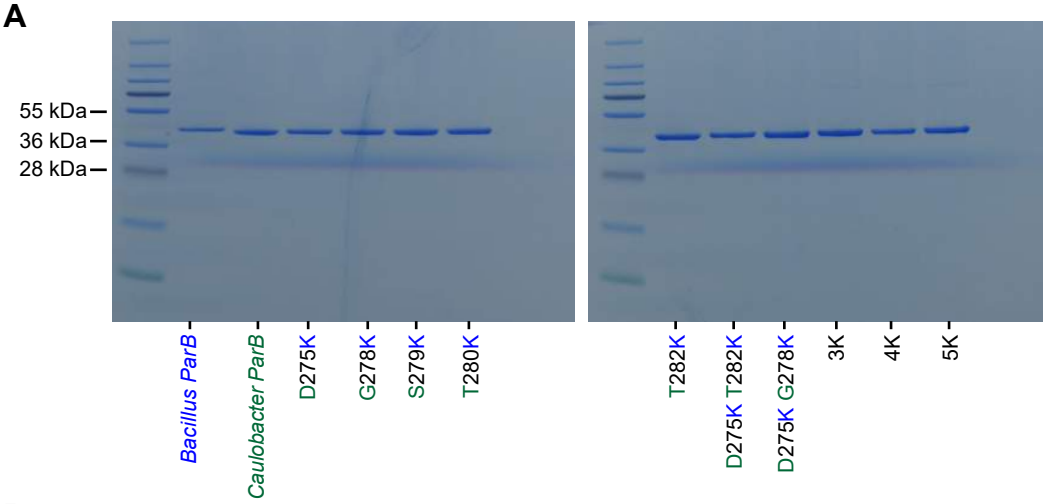

B

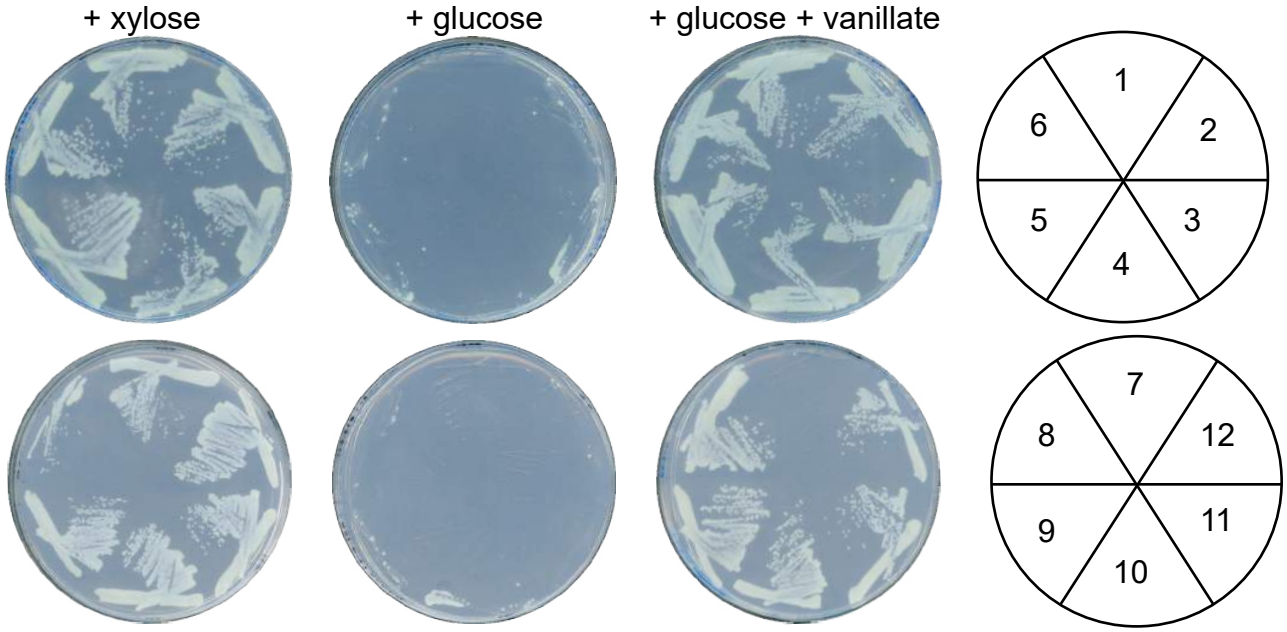

1 MT148 + P_{van}::*flag-parB* (WT)
2 MT148 + P_{van}::*flag-parB* (S279K)
3 MT148 + P_{van}::*flag-parB* (T280K)
4 MT148 + P_{van}::*flag-parB* (D275K)
5 MT148 + P_{van}::*flag-parB* (G278K)
6 MT148 + P_{van}::*flag-parB* (T282K)
7 MT148 + P_{van}::*flag-yfp*
8 MT148 + P_{van}::*flag-parB* (D275K T282K)
9 MT148 + P_{van}::*flag-parB* (D275K G278K)
10 MT148 + P_{van}::*flag-parB* (3K) (D275K G278K T282K)
11 MT148 + P_{van}::*flag-parB* (4K) (D275K G278K T280K T282K)
12 MT148 + P_{van}::*flag-parB* (5K) (D275K G278K S279K T280K T282K)

C

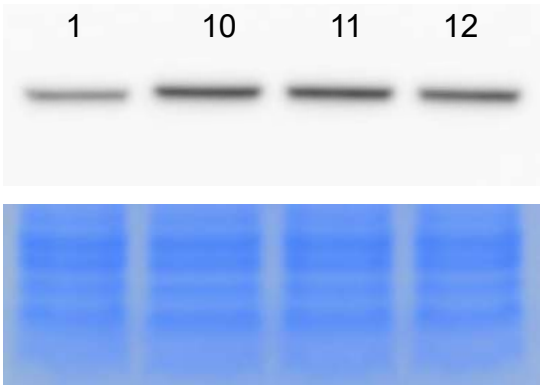

α-FLAG

total protein (Coomassie staining)

figure legend on the next page

FIG. S5

Figure S5. Expression and purification of *Caulobacter* ParB variants with additional lysine residues at their C-terminal domains. (A) *Bacillus* ParB (WT), *Caulobacter* ParB (WT) and its variants were expressed in *E. coli* and purified to near homogeneity. All variants were C-terminally His-tagged (KLAAALEHHHHHH). The identity of each protein variant (i.e. the engineered substitutions at the C-terminal domain) is shown below each lane. **(B)** *Caulobacter* ParB (1K to 5K) variants were expressed from the *van* locus (vanillate inducible) in the ParB (WT)-depletable background (*Caulobacter* MT148: *parB::*P_{xyl}*-parB*). In the presence of xylose, ParB (WT) was produced and all strains were viable, including strain 7 that expressed *yfp* from the *van* locus. On the other hand, the addition of glucose repressed the production of ParB (WT) while other ParB variants were not produced, leading to loss of viability. In the presence of both glucose and vanillate, only ParB (1K to 5K) variants were produced. Cell growth for strains (2 to 6, and 8 to 12) indicated that ParB (1K to 5K) variants can complement the lack of ParB (WT) in *Caulobacter*. **(C)** α-FLAG immunoblot analysis of *Caulobacter* strains 1, 10, 11, 12 (see panel **B**) grown in medium supplemented with glucose and vanillate.

eLIFE elifesciences.org

RESEARCH ARTICLE

ParB spreading on DNA requires cytidine triphosphate in vitro

Adam SB Jalal, Ngat T Tran, Tung BK Le*

Department of Molecular Microbiology, John Innes Centre, Norwich, United Kingdom

Abstract In all living organisms, it is essential to transmit genetic information faithfully to the next generation. The SMC-ParAB-*parS* system is widely employed for chromosome segregation in bacteria. A DNA-binding protein ParB nucleates on *parS* sites and must associate with neighboring DNA, a process known as spreading, to enable efficient chromosome segregation. Despite its importance, how the initial few ParB molecules nucleating at *parS* sites recruit hundreds of further ParB to spread is not fully understood. Here, we reconstitute a *parS*-dependent ParB spreading event using purified proteins from *Caulobacter crescentus* and show that CTP is required for spreading. We further show that ParB spreading requires a closed DNA substrate, and a DNA-binding transcriptional regulator can act as a roadblock to attenuate spreading unidirectionally in vitro. Our biochemical reconstitutions recapitulate many observed in vivo properties of ParB and opens up avenues to investigate the interactions between ParB-*parS* with ParA and SMC.

***For correspondence:** tung.le@jic.ac.uk

Competing interests: The authors declare that no competing interests exist.

Funding: See page 21

Received: 11 November 2019
Accepted: 19 February 2020
Published: 20 February 2020

Reviewing editor: Anthony G Vecchiarelli, University of Michigan, United States

Introduction

Faithful chromosome segregation is essential in all domains of life if daughter cells are each to inherit the full set of genetic information. The SMC-ParAB-*parS* complex is widely employed for chromosome segregation in bacteria (**Donczew et al., 2016**; **Fogel and Waldor, 2006**; **Gruber and Errington, 2009**; **Harms et al., 2013**; **Ireton et al., 1994**; **Jakimowicz et al., 2002**; **Kawalek et al., 2018**; **Lin and Grossman, 1998**; **Livny et al., 2007**; **Mohl et al., 2001**; **Sullivan et al., 2009**; **Tran et al., 2018**; **Wang et al., 2017**). The centromere *parS* is the first DNA locus to be segregated following chromosome replication (**Lin and Grossman, 1998**; **Livny et al., 2007**; **Toro et al., 2008**; **Lagage et al., 2016**). ParB specifically nucleates on *parS* before spreading outwards to the flanking DNA and bridges/cages DNA together to form a nucleoprotein network in vivo (**Breier and Grossman, 2007**; **Murray et al., 2006**; **Taylor et al., 2015**; **Graham et al., 2014**; **Sanchez et al., 2015**; **Debaugny et al., 2018**; **Broedersz et al., 2014**; **Funnell, 2016**). This nucleoprotein complex recruits SMC to disentangle and organize replicated DNA (**Gruber and Errington, 2009**; **Sullivan et al., 2009**; **Wang et al., 2017**; **Tran et al., 2017**; **Minnen et al., 2011**). ParB-*parS* also interacts with an ATPase ParA to power the segregation of replicated chromosomes (**Lim et al., 2014**; **Vecchiarelli et al., 2014**; **Vecchiarelli et al., 2012**; **Hwang et al., 2013**; **Leonard et al., 2005**). Engineered strains harboring a nucleation-competent but spreading-defective mutant of *parB* are either unviable (**Mohl et al., 2001**) or have elevated number of anucleate cells (**Harms et al., 2013**; **Kawalek et al., 2018**; **Lin and Grossman, 1998**; **Lagage et al., 2016**; **Jecz et al., 2015**; **Attaiech et al., 2015**; **Yu et al., 2010**; **Lee and Grossman, 2006**). Despite the importance of spreading for proper chromosome segregation, the mechanism by which a few *parS*-bound ParB can recruit hundreds more ParB molecules to the vicinity of *parS* to assemble a high-molecular-weight nucleoprotein complex is not fully understood.

Since the first report in 1995 (**Lynch and Wang, 1995**), ParB spreading has been observed in vivo by chromatin immunoprecipitation in multiple bacterial species (**Tran et al., 2018**; **Lagage et al., 2016**; **Breier and Grossman, 2007**; **Murray et al., 2006**; **Graham et al., 2014**; **Rodionov et al.,**

1999). The nucleation of ParB on *parS* has also been demonstrated in vitro (**Harms et al., 2013**; **Mohl et al., 2001**; **Breier and Grossman, 2007**; **Murray et al., 2006**; **Sanchez et al., 2015**; **Chen et al., 2015**; **Surtees and Funnell, 2001**; **Ah-Seng et al., 2013**); however, *parS*-dependent ParB spreading has resisted biochemical reconstitution (**Taylor et al., 2015**; **Graham et al., 2014**; **Fisher et al., 2017**; **Madariaga-Marcos et al., 2019**). Unsuccessful attempts to reconstitute spreading in vitro suggests that additional factors might be missing. Recently, works by **Soh et al. (2019)** and **Osorio-Valeriano et al. (2019)** on *Bacillus subtilis* and *Myxococcus xanthus* ParB, respectively, showed that ParB binds and hydrolyzes cytidine triphosphate (CTP) to cytidine diphosphate (CDP), and that CTP modulates the binding affinity of ParB to *parS* (**Osorio-Valeriano et al., 2019**; **Soh et al., 2019**). A co-crystal structure of *Bacillus* ParB with CDP and that of a *Myxococcus* ParB-like protein (PadC) with CTP showed CTP binding promotes a new dimerization interface between N-terminal domains of ParB subunits (**Osorio-Valeriano et al., 2019**; **Soh et al., 2019**). Crucially, **Soh et al. (2019)** showed by single-molecule imaging and cross-linking assays that *Bacillus* ParB, in the presence of CTP, forms a self-loading protein clamp at *parS* and slides away to spread to neighboring DNA (**Soh et al., 2019**). While reproducing a key result from **Easter and Gober (2002)** that showed *Caulobacter crescentus* ParA-ATP dissociated pre-bound ParB from *parS* (**Easter and Gober, 2002**), we found that CTP could also modulate the nucleation of *Caulobacter* ParB on *parS*. Personal communication with Stephan Gruber and the recent work by **Osorio-Valeriano et al. (2019)** and **Soh et al. (2019)** encouraged us to take steps further to investigate the role of CTP for ParB spreading in *Caulobacter crescentus*.

Here, we reconstitute a *parS*-dependent ParB spreading on DNA in real-time, using a label-free purified protein from *Caulobacter crescentus*. Consistent with pioneering works by **Soh et al. (2019)** and **Osorio-Valeriano et al. (2019)**, we confirm that CTP regulates ParB-DNA interaction. We further provide evidence that the accumulation of *Caulobacter* ParB requires a closed DNA substrate, and that a DNA-binding transcription factor, TetR, can act as a roadblock to attenuate ParB accumulation unidirectionally in vitro. Our real-time and label-free reconstitution has successfully recapitulated many well-known aspects of ParB behaviors in vivo and might open up avenues to investigate further the roles of the ParB-*parS* nucleoprotein complex in ensuring faithful chromosome segregation.

Results

CTP reduces the nucleation of *Caulobacter* ParB on *parS*

Easter and Gober (2002) reported that ATP-bound *Caulobacter* ParA dissociated ParB from *parS* (**Easter and Gober, 2002**); however, the authors did not control for the effect of ATP alone on ParB-*parS* binding. NTPs are highly negatively charged and could have affected protein-DNA interactions by binding non-specifically to the often positively charged DNA-binding domain. To determine if ATP or other NTP alone affects ParB-*parS* interaction, we attached a linear 20 bp biotinylated *parS* DNA to a streptavidin-coated probe to measure the bio-layer interference (BLI) (**Figure 1A**). BLI assay monitors wavelength shifts (responses) resulting from changes in the optical thickness of the probe surface during association or dissociation of the analyte (see Materials and Methods). We monitored in real-time interactions between immobilized *parS* DNA and purified *Caulobacter* ParB or a premix of ParB + NTP (**Figure 1B**). Consistent with previous reports (**Tran et al., 2018**; **Figge et al., 2003**), *Caulobacter* ParB bound site-specifically to *parS* but not to non-cognate DNA (**Figure 1—figure supplement 1**). In the presence of ATP, GTP, or UTP, we observed a small reduction in ParB-*parS* binding at steady state regardless of whether Mg^{2+} was included in binding buffer or not (**Figure 1B** and **Figure 1—figure supplement 2**), suggesting that *Caulobacter* ParB is slightly sensitive to highly negatively charged compounds or to counter-ions (Na^{+}) in NTP solutions. However, we noted that CTP had a pronounced effect on ParB-*parS* interaction, specifically in the presence of Mg^{2+} (**Figure 1B** and **Figure 1—figure supplement 2**). An increasing concentration of CTP (but not CMP or CDP) gradually reduced the binding of ParB to *parS* (**Figure 1—figure supplement 3**). In contrast, neither CTP nor other NTPs affected the binding of another protein-DNA pair, for example, the well-characterized TetR-*tetO* interaction (**Saenger et al., 2000**; **Figure 1C**). On closer inspection, we noted that ParB + CTP slowly dissociated from *parS* even before the probe was returned to a protein-free buffer (a gradual downward slope between 30^{th} and 150^{th} sec,

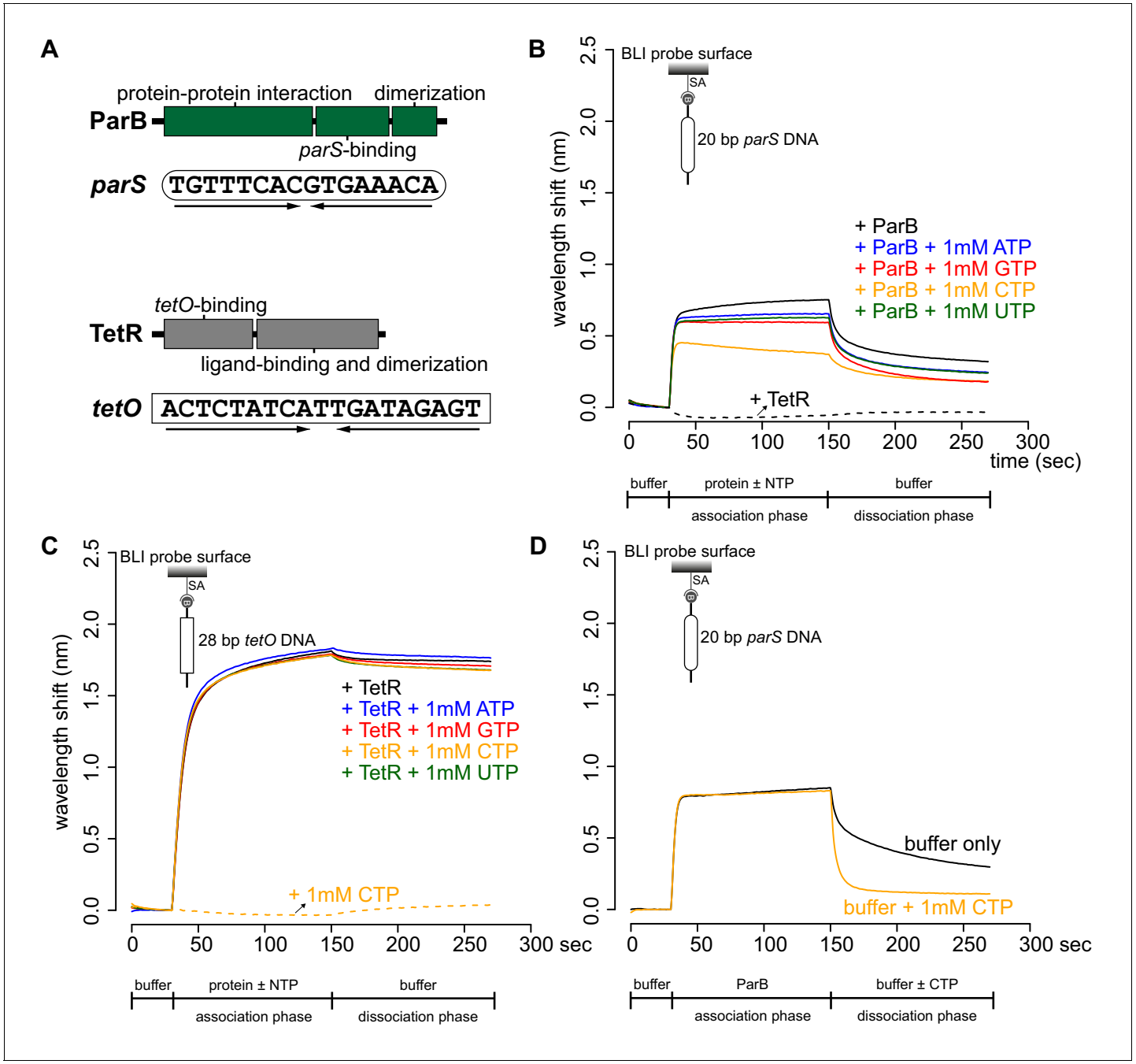

Figure 1. CTP reduces the nucleation of *Caulobacter* ParB at *parS*. (**A**) The domain architecture of ParB (dark green) and TetR (grey), and their respective DNA-binding sites *parS* and *tetO*. Convergent arrows below DNA-binding sites indicate that *parS* and *tetO* are palindromic. (**B**) Bio-layer interferometric (BLI) analysis of the interaction between a premix of 1 µM ParB-His_6 dimer ± 1 mM NTP and a 20 bp DNA duplex containing *parS*. Biotinylated DNA fragments were immobilized onto the surface of a Streptavidin (SA)-coated probe (See Materials and methods). The BLI probe was dipped into a buffer only solution (0–30 s), then to a premix of protein ± NTP (30–150 s: association phase), and finally returned to a buffer only solution (150–270 s: dissociation phase). Sensorgrams were recorded over time. BLI analysis of the interaction between 1 µM TetR-His_6 and a 20 bp *parS* probe was also recorded (a negative control). (**C**) BLI analysis of the interaction between a premix of 1 µM TetR-His_6 ± 1 mM NTP and a 28 bp DNA duplex containing *tetO*. BLI analysis of the interaction between 1 mM CTP and a 28 bp *tetO* probe was also recorded (a negative control). (**D**) BLI analysis of the interaction between 1 µM *Caulobacter* ParB-His_6 (without CTP) and a 20 bp *parS* DNA. For the dissociation phase, the probe was returned to a buffer only or buffer supplemented with 1 mM CTP. All buffers used for experiments in this figure contained Mg^{2+}. Each BLI experiment was triplicated and a representative sensorgram was presented.

The online version of this article includes the following source data and figure supplement(s) for figure 1:

Source data 1. Data used to generate ***Figure 1***.

Figure 1 continued on next page

Figure 1 continued

Figure supplement 1. ParB and TetR bind specifically to their cognate-binding sites *parS* and *tetO*, respectively.
Figure supplement 1—source data 1. Data used to generate ***Figure 1—figure supplement 1***.
Figure supplement 2. BLI analysis of the interaction between purified *Caulobacter* ParB and NTP in buffers lacking Mg^{2+}.
Figure supplement 2—source data 1. Data used to generate ***Figure 1—figure supplement 2***.
Figure supplement 3. BLI analysis of the interaction between purified *Caulobacter* ParB and cytidine mono-, di-, or triphosphate.
Figure supplement 3—source data 1. Data used to generate ***Figure 1—figure supplement 3***.

Figure 1B), suggesting that CTP facilitated ParB removal from a 20 bp *parS* DNA. To investigate further, we monitored the dissociation rates of pre-bound CTP-free ParB-*parS* complexes after probes were returned to a protein-free buffer with or without CTP, we found ParB dissociating ~seven times faster in buffer with CTP than in buffer only solution (***Figure 1D***). Given the short length of a 20 bp *parS* DNA duplex that has only sufficient room for nucleation, our results suggest that CTP might decrease ParB nucleation on *parS* or liberates pre-bound ParB from *parS* site.

CTP facilitates ParB accumulation on a closed DNA substrate

Next, we investigated the effect of CTP on ParB-DNA interaction by employing a longer 169 bp *parS*-containing DNA fragment that has been labeled at both 5' ends with biotin (***Figure 2A***). Immobilizing a dual biotin-labeled DNA on a streptavidin-coated BLI probe created a DNA substrate where both ends were blocked (a closed DNA) (***Onn and Koshland, 2011***; ***Figure 2—figure supplement 1***). We monitored the interactions between immobilized DNA and purified *Caulobacter* ParB in the presence or absence of NTP. In the absence of NTP, we observed the usual nucleation event on *parS* with 1 µM ParB protein (***Figure 2A***). We noted that the BLI signal was not as high as with a 20 bp *parS* probe (***Figure 2A***) due to a less efficient immobilization of a longer DNA fragment on the BLI probe. Premixing ATP, GTP, or UTP with ParB did not change the sensorgrams markedly (***Figure 2A***). However, the addition of CTP significantly increased the response by ~12 fold (***Figure 2A*** and ***Figure 2—figure supplement 2A***), suggesting that more ParB associated with a 169 bp *parS* probe at steady state than by nucleation at *parS* alone. We observed that DNA-bound ParB was salt sensitive and dissociated readily to the solution when the BLI probe was returned to a low-salt protein-free buffer without CTP (***Figure 2A***, dissociation phase). However, the dissociation of pre-bound ParB-CTP from DNA was slowed down by ~fivefold if the probe was returned to a buffer supplemented with CTP (***Figure 2—figure supplement 2B***). The effect on the BLI response was not seen if Mg^{2+} was omitted (***Figure 2—figure supplement 2C***), neither did we observe an equivalent increase in response when a 169 bp dual biotin-labeled DNA containing a scrambled *parS* was employed instead (***Figure 2A***). Furthermore, we observed that a nucleation-competent but spreading-defective *Caulobacter* ParB (R104A) (***Tran et al., 2018***) mutant did not respond to the addition of CTP to the same extent as ParB (WT) (***Figure 2B***). Our results suggest that CTP is required for the increase in *parS*-dependent ParB accumulation in vitro. Lastly, we performed BLI experiments for eight additional chromosomal ParB proteins from a diverse set of bacterial species and consistently observed the specific effect of CTP on enhancing ParB association with a closed DNA in vitro (***Figure 2—figure supplement 3***). It is most likely that ParB-CTP interaction with DNA is conserved among ParB orthologs.

To independently verify the BLI data, we performed an in vitro pull-down of purified His-tagged *Caulobacter* ParB (***Figure 2C***). Streptavidin-coated paramagnetic beads were incubated with 2.8 kb dual biotin-labeled DNA fragments containing either *parS* or scrambled *parS* sites. Again, a dual biotin-labeled DNA formed a closed substrate on the surface of the beads. DNA-coated beads were incubated with purified *Caulobacter* ParB either in the presence or absence of NTP before being pulled down magnetically. Pulled-down ParB was released from beads and their protein level was analyzed by an α-His_6 immunoblot (***Figure 2C***). We found ~13–15 fold more pulled-down ParB when CTP was included (***Figure 2C***). No enrichment was observed when scrambled *parS*-coated beads were used, confirming that the extensive in vitro association of ParB with DNA is dependent on *parS* (***Figure 2C***). Also, consistent with the BLI experiments, no further enrichment of ParB was seen when ATP, GTP or UTP was included (***Figure 2C***). Furthermore, a ParB (R104A) variant was not enriched in our pull-down assay regardless of whether CTP was present or not (***Figure 2C***). Altogether, our

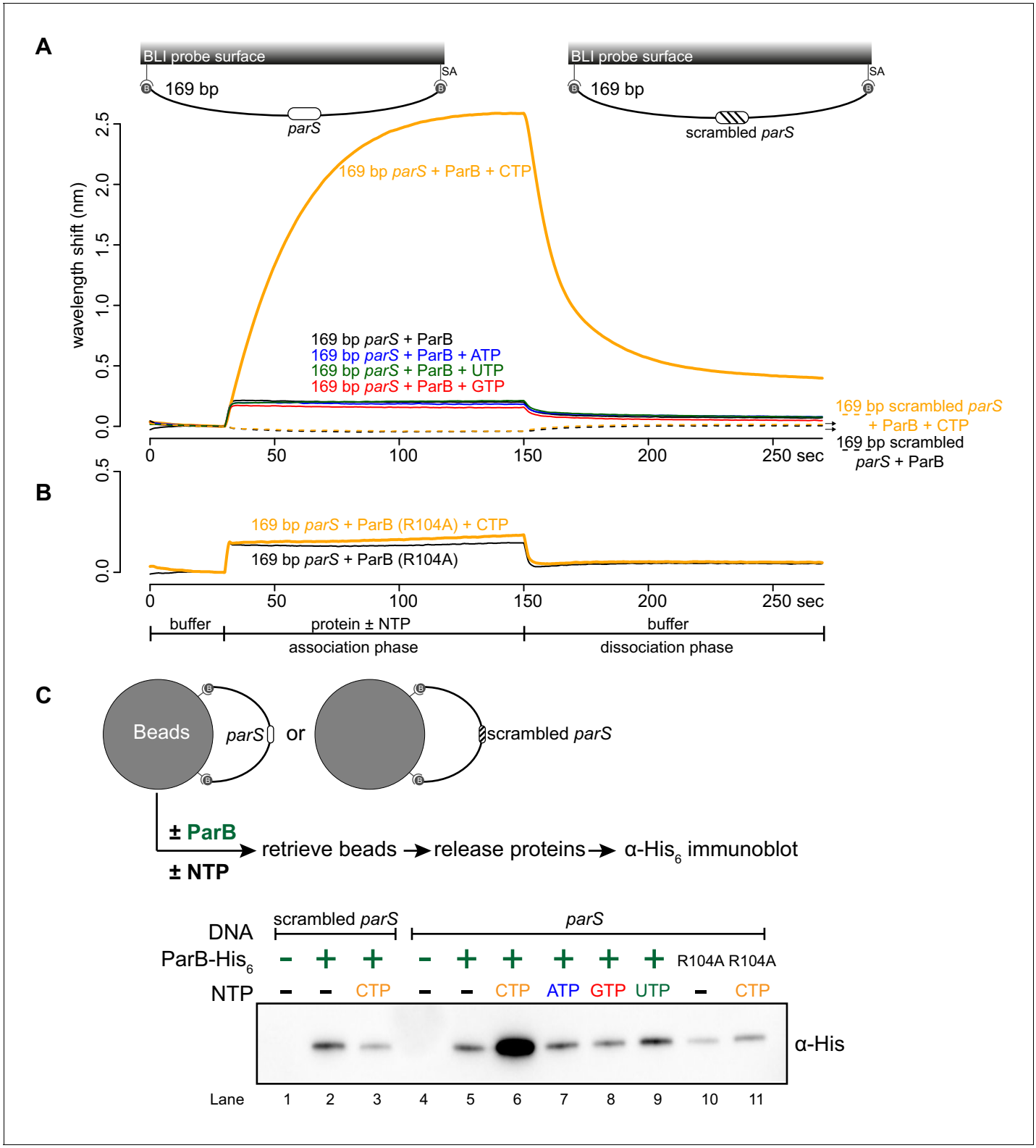

Figure 2. CTP facilitates ParB association with a closed DNA substrate beyond nucleation. (**A**) BLI analysis of the interaction between a premix of 1 µM *Caulobacter* ParB-His_6 ± 1 mM NTP and a 169 bp dual biotin-labeled DNA containing a *parS* or a scrambled *parS* site. Interactions between a dual biotinylated DNA and streptavidin (SA)-coated probe created a DNA substrate where both ends were blocked (a closed DNA substrate) (see the schematic of the BLI probes above the sensorgram). (**B**) Interactions between a nucleation-competent but spreading-defective ParB (R104) variant with a 169 bp *parS* DNA fragment in the presence or absence of CTP were also recorded. Each BLI experiment was triplicated and a representative

Figure 2 continued on next page

Figure 2 continued

sensorgram was presented. (**C**) A schematic of the pull-down assay and immunoblot analysis of pulled-down *Caulobacter* ParB-His_6. The length of bound DNA is ~2.8 kb. Beads were incubated with ParB protein for five minutes before being pulled down magnetically. All buffers used for experiments in this figure contained Mg^{2+}.

The online version of this article includes the following source data and figure supplement(s) for figure 2:

Source data 1. Data used to generate ***Figure 2***.
Figure supplement 1. Dual biotin-labeled DNA fragments form a closed substrate on the surface of the BLI probe.
Figure supplement 1—source data 1. Data used to generate ***Figure 2—figure supplement 1***.
Figure supplement 2. CTP-Mg^{2+} enhances ParB accumulation on a closed DNA substrate.
Figure supplement 2—source data 1. Data used to generate ***Figure 2—figure supplement 2***.
Figure supplement 3. CTP facilitates the association of eight ParB orthologs with DNA.
Figure supplement 3—source data 1. Data used to generate ***Figure 2—figure supplement 3***.

results suggest that a *parS*-dependent accumulation of ParB on a closed DNA substrate requires CTP.

A closed DNA substrate is required for an increased ParB association with DNA

Next, we investigated whether a DNA substrate with a free end (an open DNA) can also support ParB accumulation in vitro. The 169 bp dual biotin-labeled DNA was designed with unique *Bam*HI and *Eco*RI recognition sites flanking the *parS* site (***Figure 3A***). To generate an open end on DNA, we immerged the DNA-coated probes in buffers contained either *Bam*HI or *Eco*RI (***Figure 3A–C*** and ***Figure 3—figure supplement 1***). Before restriction enzyme digestion, we again observed an enhanced ParB association with a closed DNA substrate in the presence of CTP (***Figure 3A***). After digestion by either *Bam*HI or *Eco*RI, the inclusion of CTP had no effect on the BLI response, indicating that ParB did not accumulate on an open DNA substrate in vitro (***Figure 3B–C***). Our conclusion was further supported by results from an experiment in which we added *Bam*HI after ParB + CTP and a closed DNA substrate were preincubated together for 120 s (***Figure 3—figure supplement 2***). Here, in the presence of *Bam*HI, ParB binding to DNA reduced gradually over 30 min, while it was unaffected if heat-inactivated *Bam*HI was employed instead (***Figure 3—figure supplement 2***). Lastly, consistent with BLI experiments, our pull-down assay also showed that ParB-CTP failed to accumulate when a 2.8 kb dual biotin-labeled DNA was linearized by *Hind*III digestion (***Figure 3D***).

Next, we wondered if a tight protein-DNA binding could cap the open end of DNA, thereby mimicking a closed DNA substrate and restoring ParB accumulation. To investigate this possibility, we constructed a 170 bp dual biotin-labeled DNA fragment that contains a single *parS* site, a *tetO* operator, and flanking restriction enzyme recognition sites for *Eco*RI and *Bam*HI (***Figure 4A***). With this closed DNA substrate, we observed an enhanced ParB association with DNA in the presence of CTP (***Figure 4A***). Again, we generated a free DNA end via restriction enzyme digestion. Consistent with previous experiments with a restricted 169 bp DNA probe, the addition of ParB + CTP had no effect on the BLI response (***Figure 4B***). However, it can be partially rescued by incubating a *Bam*HI-restricted DNA probe with a premix of ParB + CTP + TetR (***Figure 4B***). We reason that TetR binding at *tetO* capped the open DNA end, essentially generated a closed DNA substrate. Our conclusion was further supported by results from an experiment in which a premix of ParB + CTP + TetR was tested against an *Eco*RI-restricted DNA instead (***Figure 4C***). Here, we did not observe an enhanced association of ParB with DNA even when TetR was included, most likely because of a persistent open DNA end that could not be blocked by TetR-*tetO* binding (***Figure 4C***). Finally, we observed that the TetR could attenuate ParB-CTP accumulation on a closed DNA substrate (magenta line vs. orange line, ***Figure 4A***). This blocking effect is specific to TetR-*tetO* binding since the addition of anhydrotetracycline (ahTc), a negative effector of TetR (***Saenger et al., 2000***), allowed ParB-CTP to regain its accumulation on DNA (***Figure 4—figure supplement 1***). Overall, the ability of a DNA-bound TetR to act as a roadblock in vitro is consistent with previous ChIP-seq data that showed DNA-binding proteins or RNA polymerases could block or attenuate ParB spreading unidirectionally in vivo (***Breier and Grossman, 2007***; ***Murray et al., 2006***; ***Sanchez et al., 2015***; ***Rodionov et al., 1999***).

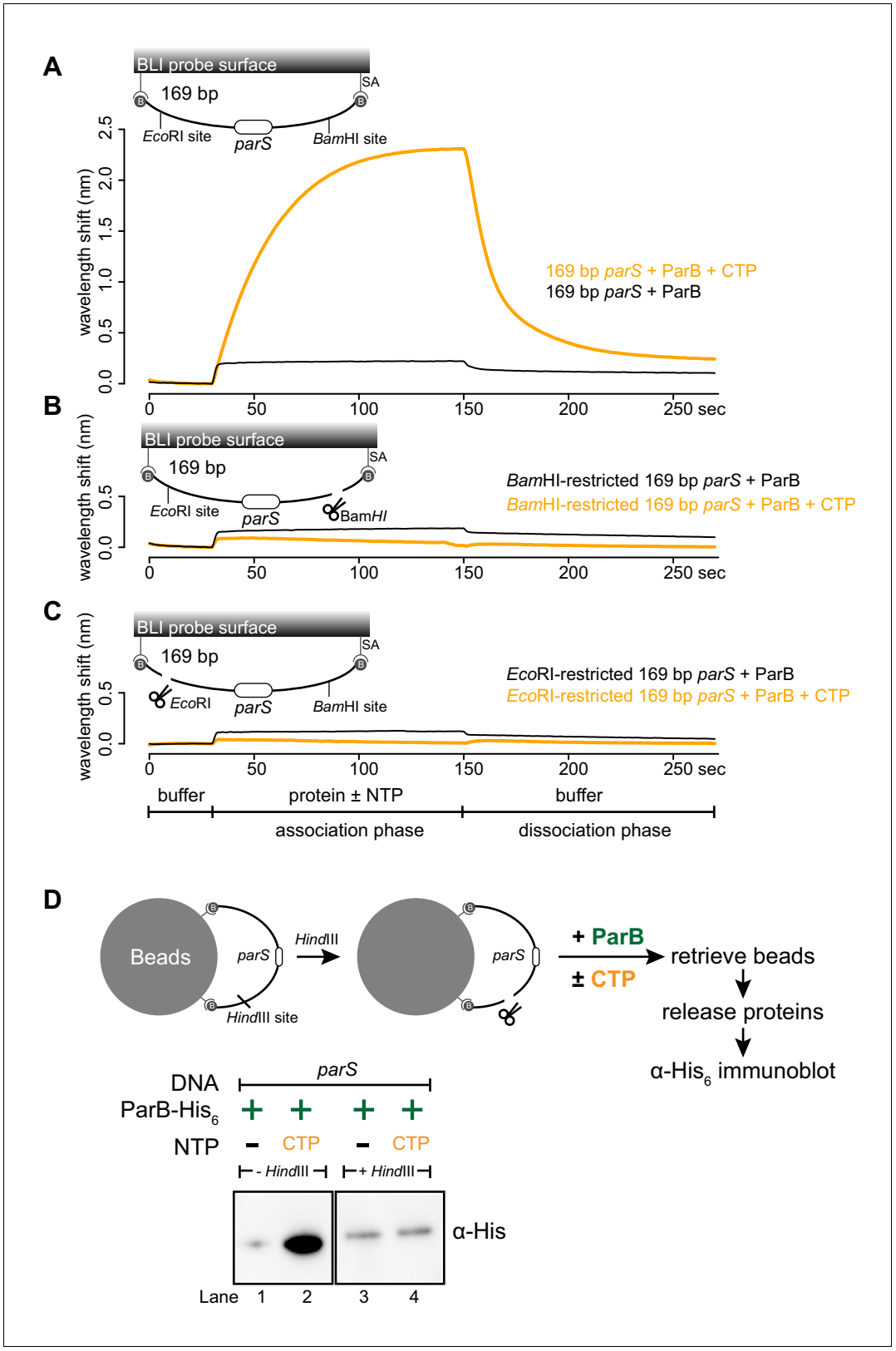

Figure 3. A closed DNA substrate is required for an increased association of ParB with DNA. (**A**) BLI analysis of the interaction between a premix of 1 µM *Caulobacter* ParB-His$_6$ ± 1 mM CTP and a 169 bp dual biotin-labeled *parS* DNA. (**B**) Same as panel A but immobilized DNA fragments have been restricted with *Bam*HI before BLI analysis. (**C**) Same as panel A but immobilized DNA fragments have been restricted with *Eco*RI before BLI analysis.

Figure 3 continued on next page

Figure 3 continued

Schematic of DNA fragments with the relative positions of *parS* and restriction enzyme recognition sites are shown above the sensorgram. Each BLI experiment was triplicated and a representative sensorgram was presented. (**D**) A schematic of the pull-down assay and immunoblot analysis of pulled-down *Caulobacter* ParB-His_6. For lanes 3 and 4, DNA-bound beads were incubated with *Hind*III to linearize bound DNA. Samples in lanes 1–4 were loaded on the same gel, the immunoblot was spliced together for presentation purposes. All buffers used for experiments in this figure contained Mg^{2+}.

The online version of this article includes the following source data and figure supplement(s) for figure 3:

Source data 1. Data used to generate ***Figure 3***.
Figure supplement 1. Restriction enzymes linearize dual biotin-labeled DNA fragments on the surface of the BLI probe.
Figure supplement 1—source data 1. Data used to generate ***Figure 3—figure supplement 1***.
Figure supplement 2. Linearization of a closed DNA substrate by *Bam*HI liberates pre-bound ParB from DNA.
Figure supplement 2—source data 1. Data used to generate ***Figure 3—figure supplement 2***.

parS DNA increases the CTP binding and hydrolysis rate of *Caulobacter* ParB

Recently, *Myxococcus* and *Bacillus* ParB were shown to bind and hydrolyze CTP (***Osorio-Valeriano et al., 2019***; ***Soh et al., 2019***). Our in vitro results so far also hint at CTP binding directly to *Caulobacter* ParB. By employing a membrane-spotting assay (DRaCALA), we showed that *Caulobacter* ParB binds to radiolabeled CTP in the presence of *parS* DNA (***Figure 5A***). An excess of unlabeled CTP, but no other NTPs, could compete with radioactive CTP for binding to *Caulobacter* ParB (***Figure 5B***), suggesting that *Caulobacter* ParB does not bind other NTPs. The CTP binding of ParB was reduced when a non-cognate DNA site (*NBS*) (***Wu and Errington, 2004***) was used instead of *parS* (***Figure 5A***). We also failed to detect CTP binding in our DRaCALA assay or by isothermal titration calorimetry when DNA was omitted. Nevertheless, we robustly detected CTP hydrolysis to CDP and inorganic phosphate when *Caulobacter* ParB and CTP were included, albeit at a very low rate of ~0.4 CTP molecules per ParB per hour (***Figure 5C***). A background level of inorganic phosphate was observed when *Caulobacter* ParB was incubated with ATP, GTP, or UTP (***Figure 5C***). Crucially, the addition of a 22 bp *parS* DNA, but not a non-cognate 22 bp *NBS* DNA, increased CTP turnover rate sevenfold to ~3 CTP molecules per ParB per hour (***Figure 5C***). Lastly, the CTP hydrolysis was reduced to the background in the nucleation-competent but spreading-defective ParB (R104A) variant (***Figure 5C***). Altogether, our data suggest that *parS* DNA stimulates *Caulobacter* ParB to bind and hydrolyze CTP.

ParB accumulation on DNA is unstable in the presence of a non-hydrolyzable analog CTPγS

Next, we investigated the role of CTP hydrolysis by following ParB-*parS* interaction in the presence of a non-hydrolyzable analog CTPγS (***Figure 6A*** and ***Figure 6—figure supplement 1***). ParB was pre-incubated with CTP or CTPγS for 1 to 60 min before binding to a 169 bp closed *parS* DNA substrate (***Figure 6A***). We observed that *Caulobacter* ParB could accumulate on DNA in the presence of CTPγS, but in contrast to when CTP was employed, a longer preincubation time between ParB and CTPγS gradually reduced ParB accumulation on DNA (***Figure 6A***). Our results suggest the possibility that CTPγS, in the absence of *parS* DNA, converts apo-ParB in solution to a nucleation-incompetent form over time. Our observation is reminiscent of a time-course experiment in which CTPγS efficiently promoted the engagement between N-terminal domains of *Bacillus* ParB in the absence of *parS* DNA (***Soh et al., 2019***). The engagement of N-terminal domains was shown to convert *Bacillus* ParB from an open to a closed protein clamp (***Soh et al., 2019***). If not already bound on DNA, the closed form of ParB presumably cannot nucleate/load onto *parS* due to its now inaccessible DNA-binding domain (***Soh et al., 2019***). We wondered if CTPγS also catalyzed the N-domain engagement in *Caulobacter* ParB in the absence of *parS* DNA. To investigate this possibility, we employed site-specific cross-linking of a purified *Caulobacter* ParB (Q35C C297S) variant by a sulfhydryl-to-sulfhydryl crosslinker bismaleimidoethane (BMOE) (***Figure 6B***). A lone cysteine residue on the native ParB was first mutated to serine to create a cysteine-less ParB (C297S) variant, then a glutamine to

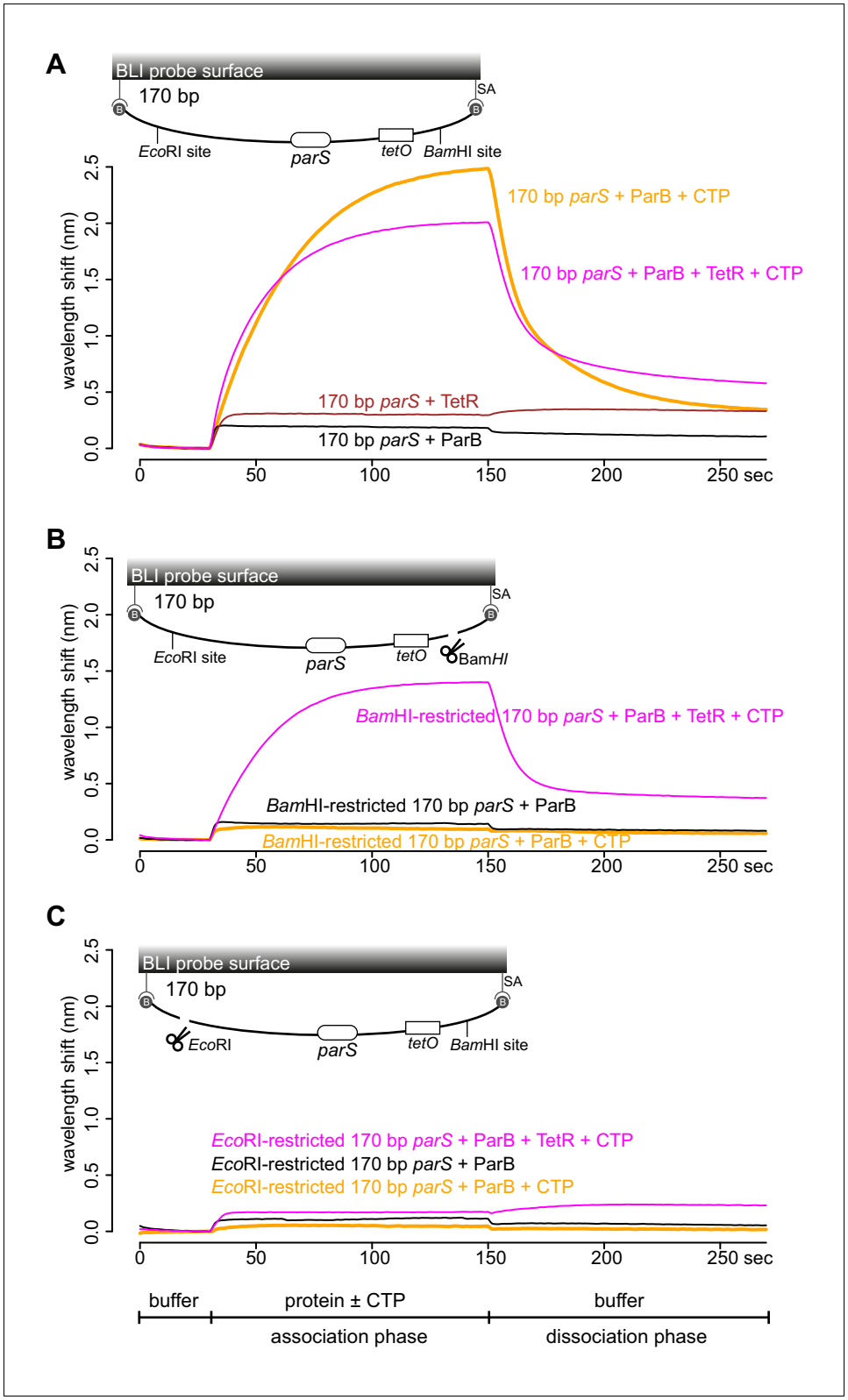

Figure 4. TetR-*tetO* binding restores ParB association with an open DNA substrate. (**A**) BLI analysis of the interaction between a premix of 1 µM *Caulobacter* ParB-His$_6$ ± 1 mM CTP ± 1 µM TetR-His$_6$ and a 170 bp dual biotin-labeled DNA containing a *parS* site. (**B**) Same as panel A but immobilized DNA fragments have been restricted with *Bam*HI before BLI analysis. (**C**) Same as panel A but immobilized DNA fragments have been restricted with *Eco*RI before BLI analysis. Schematic of DNA fragments together with the relative positions of *parS*,

Figure 4 continued on next page

Figure 4 continued

tetO, and restriction enzyme recognition sites are shown above the sensorgram. Each BLI experiment was triplicated and a representative sensorgram was presented. All buffers used for experiments in this figure contained Mg^{2+}.

The online version of this article includes the following source data and figure supplement(s) for figure 4:

Source data 1. Data used to generate ***Figure 4***.

Figure supplement 1. Anhydrotetracycline removes DNA-bound TetR roadblock and allows ParB to accumulate further on DNA.

Figure supplement 1—source data 1. Data used to generate ***Figure 4—figure supplement 1***.

cysteine mutation was engineered at position 35 at the N-terminal domain to create ParB (Q35C C297S). Both ParB (C297S) and ParB (Q35C C297S) were competent at spreading in the presence of CTP (***Figure 6—figure supplement 2A***). The cross-linking of ParB (Q35C C297S) was also enhanced by CTP and CTPγS but not by other NTPs, consistent with the specific role of CTP in ParB spreading (***Figure 6—figure supplement 2B***). We performed a time-course cross-linking of ParB (Q35C C297S) + CTP or CTPγS in the absence of *parS* DNA (***Figure 6B***). As shown in ***Figure 6B***, CTPγS was twice as efficient as CTP in promoting the cross-linked form between N-terminal domains of *Caulobacter* ParB. The rapid increase in the nucleation-incompetent closed form of *Caulobacter* ParB might explain the overall reduction in accumulation overtime when ParB was preincubated with CTPγS (***Figure 6A***).

To further investigate the effect of CTPγS on ParB spreading on a longer time scale, we extended the association phase between 169 bp *parS* DNA and a freshly prepared premix of ParB + CTP or CTPγS from 120 s to 60 min (***Figure 6C***). In the presence of CTP, the reaction reached steady state after 120 s and remained stable for the duration of the association phase (***Figure 6C***). However, in the presence of CTPγS, ParB accumulation rapidly reached the maximal level after 200 s, then declined slowly over 60 min. We suggest that DNA-bound ParB-CTPγS complexes gradually dissociated from DNA into solution (possibly via a transient clamp opening or CTPγS leaving its weak binding pocket rather than by hydrolysis) but were not replenished by a new cycle of nucleation-spreading-dissociation because over time most ParB-CTPγS in solution was in a nucleation-incompetent closed form. Taken together, we suggest that CTP hydrolysis is not required for *parS*-bound ParB to escape the nucleation site to spread, but possibly contributes to maintaining the stability of spreading by recycling ParB.

Discussion

In this work, we report that a small molecule (CTP) is required to enable *Caulobacter* ParB proteins (as well as eight other chromosomal ParB proteins, ***Figure 2—figure supplement 3***) to spread in vitro. Recently, ***Soh et al. (2019)*** observed that F-plasmid and P1-plasmid ParB proteins also bind and hydrolyze CTP (***Soh et al., 2019***). Hence, it is most likely that the effect of CTP on ParB spreading is universal among plasmid and chromosomal ParB orthologs. A classical mutant whose arginine-rich patch (G^{101}ERRxR) has been mutated to alanine for example ParB (R104A) (***Lin and Grossman, 1998***) was not responsive to CTP, suggesting that CTP is bound to the N-terminal domain of *Caulobacter* ParB. Indeed, ***Soh et al. (2019)*** reported a co-crystal structure that showed CDP binding to the arginine-rich patch at the N-terminal domain of *Bacillus* ParB (CTP was hydrolyzed to CDP during crystallization) (***Soh et al., 2019***). ***Osorio-Valeriano et al. (2019)*** also showed a similar binding pocket of CTP at the N-terminal domain of *Myxococcus* ParB by hydrogen-deuterium exchange mass spectrometry (***Osorio-Valeriano et al., 2019***). Intriguingly, a co-crystal structure of a *Helicobacter pylori* ParB-*parS* complex, together with the in vitro magnetic-tweezer and single-molecule TIRF microscopy-based experiments with *Bacillus* ParB showed that the N-terminal domain can oligomerize to bridge DNA together without the need of an additional ligand (***Taylor et al., 2015***; ***Graham et al., 2014***; ***Chen et al., 2015***; ***Fisher et al., 2017***). There might be two different modes of action of ParB on DNA: one for bridging DNA together (that does not require CTP) and another for the lateral spreading of ParB on DNA (that requires CTP). Investigating the relative contribution of these two different modes of action to chromosome segregation in vivo is an important challenge for the future.

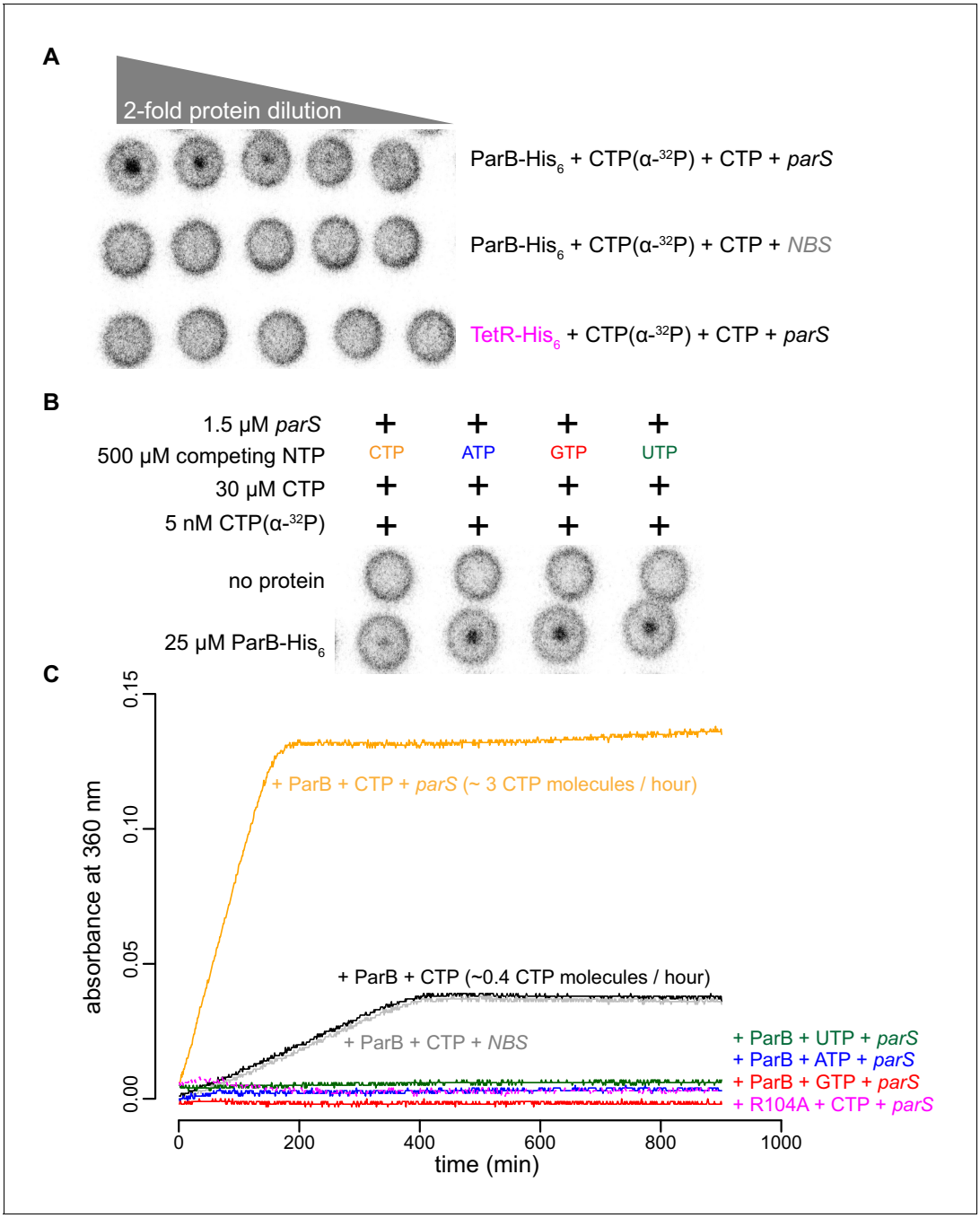

Figure 5. *parS* DNA increases the CTP binding and hydrolysis rate by *Caulobacter* ParB. (**A–B**) CTP binding as monitored by DRaCALA assay using radiolabeled CTP α-P^{32}. The bulls-eye staining indicates CTP binding due to a more rapid immobilization of protein-ligand complexes compared to free ligands alone. The starting concentration of proteins used in panel A was 25 μM. The same concentration of radioactive CTP, unlabeled CTP, and DNA was used in experiments shown in panels A and B. (**C**) A continuous monitoring of inorganic phosphate (Pi) released by recording absorbance at 360 nm overtime at 25˚C. The rates of CTP hydrolysis were inferred from a Pi standard. The NTP hydrolysis of *Caulobacter* ParB was also monitored in the presence of ATP, GTP, or UTP, with a 22 bp *parS* DNA duplex or a non-cognate 22 bp *NBS* DNA duplex (a DNA-binding site of Noc protein ***Wu and Errington, 2004***). The nucleation-competent but spreading-defective ParB (R104A) mutant did not hydrolyze CTP in the presence of *parS* DNA. All buffers used for experiments in this figure contained Mg^{2+}.

The online version of this article includes the following source data for figure 5:

Source data 1. Data used to generate ***Figure 5***.

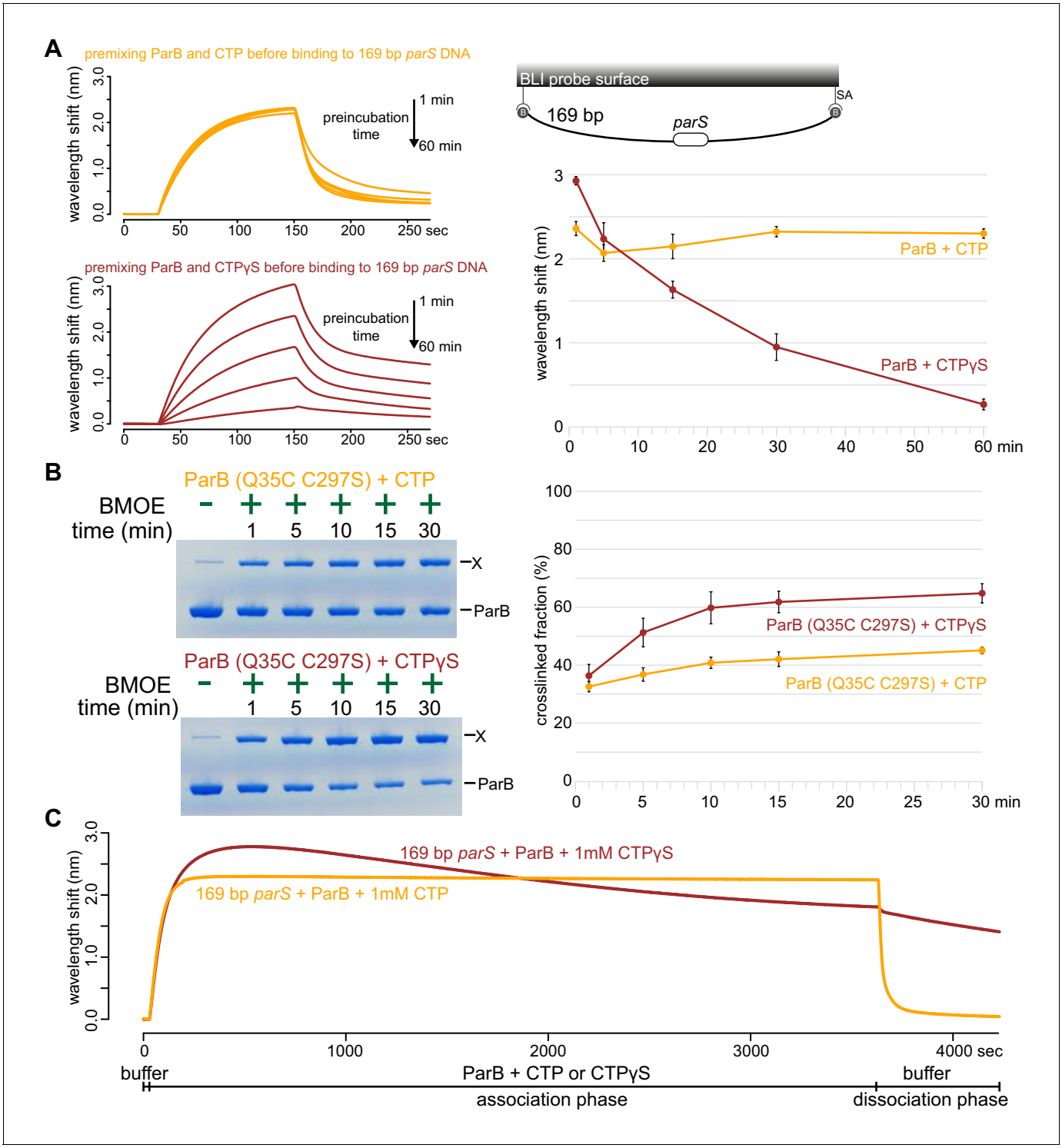

Figure 6. ParB accumulation on DNA is unstable in the presence of a non-hydrolyzable analog CTPγS. (**A**) (Left panel) BLI analysis of the interaction between a premix of 1 µM *Caulobacter* ParB-His_6 ± 1 mM CTP or CTPγS and a 169 bp dual biotin-labeled *parS* DNA. Purified ParB was preincubated with CTP or CTPγS for 1, 5, 15, 30, or 60 min before BLI analysis. (Right panel) Quantification of ParB-DNA interaction at the end of each association phase (150th sec). Error bars represent SD from three replicates. (**B**) (Left panel) Time course of *Caulobacter* ParB (Q35C C297S) cross-linking with CTP or CTPγS in the absence of *parS* DNA. Purified ParB-His_6 (Q35C C297S) (10 µM) were preincubated with 1 mM CTP or CTPγS for 1, 5, 10, 15, or 30 min before BMOE was added. X indicates a cross-linked form of ParB. (Right panel) Quantification of the cross-linked (X) fractions. Error bars represent SD from three replicates. (**C**) BLI analysis of the interaction between a premix of 1 µM *Caulobacter* ParB-His_6 ± 1 mM CTP or CTPγS and a 169 bp dual

Figure 6 continued on next page

Figure 6 continued

biotin-labeled *parS* DNA. CTP or CTPγS was added to purified ParB, and the mixture was immediately used for BLI experiments. All buffers used for experiments in this figure contained Mg^{2+}.

The online version of this article includes the following source data and figure supplement(s) for figure 6:

Source data 1. Data used to generate ***Figure 6***.
Figure supplement 1. *Caulobacter* ParB binds CTP and a non-hydrolyzable analog CTPγS but not CMP-PCP.
Figure supplement 1—source data 1. Data used to generate ***Figure 6—figure supplement 1***.
Figure supplement 2. BLI analysis and gel analysis of cross-linking products of purified *Caulobacter* ParB (Q35C C297S).
Figure supplement 2—source data 1. Data used to generate ***Figure 1—figure supplement 2***.

The requirement of a DNA substrate with blocked ends for ParB accumulation in vitro is suggestive of a lateral ParB diffusion along the DNA that is ParB can escape by running off a free DNA end (***Figure 7***). Inside cells, the spreading and bridging/caging of ParB have been inferred from the compact foci of fluorescently labeled ParB (***Harms et al., 2013***; ***Lagage et al., 2016***; ***Sanchez et al., 2015***; ***Thanbichler and Shapiro, 2006***; ***Kusiak et al., 2011***; ***Lin et al., 1997***; ***Glaser et al., 1997***; ***Erdmann et al., 1999***), presumably resulting from the concentration of fluorescent signal to a defined location in the cytoplasm. Nucleation-competent but spreading-defective ParB mutants formed no or very diffusive foci in vivo (***Graham et al., 2014***; ***Song et al., 2017***). Recently, it has been observed that an artificially engineered double-strand break ~8 kb away from *parS* did not cause a dissolution of ParB foci in *Caulobacter* cells (***Badrinarayanan et al., 2015***). This result seemingly contradicted our findings that *Caulobacter* ParB spreading in vitro requires a closed DNA. However, we reason that the abundant DNA-bound transcription factors and RNA polymerases in vivo act as roadblocks to minimize ParB runoff. This barricading effect has been recapitulated in our experiments with TetR, a tight DNA-binding transcriptional regulator (***Figure 4***).

Our results so far suggest three distinct stages of *Caulobacter* ParB-DNA interactions in vitro:

Stage 1: ParB nucleates on *parS* (***Figure 7A***). Results from experiments in ***Figure 1*** indicate that CTP modulates ParB nucleation on a *parS* site. ***Soh et al. (2019)*** reported that CTP-bound ParB could form a closed protein clamp even in the absence of *parS* DNA, albeit not energetically favorable (***Soh et al., 2019***). The DNA-binding domain of a closed ParB clamp would be inaccessible to DNA, especially to a closed DNA substrate. It might be that only apo-ParB or a transiently formed CDP-bound ParB (from CTP hydrolysis) are able to nucleate on *parS* (***Figure 7A***). Supporting this interpretation, preincubation of *Caulobacter* ParB with a non-hydrolyzable analog CTPγS promoted efficiently the cross-linked form of ParB and subsequently reduced ParB nucleation and spreading on DNA (***Figure 6***). Initially, we were surprised by a weak CTP binding of *Bacillus*, *Caulobacter*, and *Myxococcus* ParBs (***Osorio-Valeriano et al., 2019***; ***Soh et al., 2019***), however, this might be advantageous for the cells as a fraction of intracellular apo-ParB will remain to nucleate on *parS*.

Stage 2: Nucleated ParB escapes from *parS* (***Figure 7B–C***). We showed that *Caulobacter* ParB-*parS* complex binds CTP, and this facilitates ParB dissociation from *parS* (***Figure 1D***). It was reported that the DNA-binding domain in *Bacillus* ParB-CDP co-crystal structure is incompatible with *parS* binding (***Soh et al., 2019***) and this might enable ParB to escape from a high-affinity nucleation site to non-specific flanking DNA. Our observation of a low BLI response with an open DNA (***Figure 3*** and ***Figure 4***) implies that ParB proteins dissociate off the free end well before the next ParB escapes from the *parS* nucleation site. We suggest that the transition from a *parS*-bound ParB to a spreading ParB might be the rate-limiting step.

Stage 3: ParB spreads or diffuses to non-specific DNA flanking *parS*. Our observation that *Caulobacter* ParB did not accumulate on an open DNA suggests that *Caulobacter* ParB diffuses laterally along the DNA. Similarly, cross-linking experiments on *Bacillus* ParB (***Soh et al., 2019***) proposed that the ParB-CTP complex forms a sliding clamp that moves along the DNA (***Soh et al., 2019***). From our experiments with CTPγS (***Figure 6***) and consistent with ***Soh et al. (2019)***, we suggest that the diffusive *Caulobacter* ParB along the DNA is CTP bound. The low CTP hydrolysis rate of *Caulobacter* ParB (~3 CTP molecules per ParB per hour) while ParB spreading could be observed by BLI within minutes also lends support to the interpretation that the diffusive spreading form of *Caulobacter* ParB is most likely CTP-bound (***Figure 7B–C***). For *Bacillus* and *Caulobacter* ParB, CTP hydrolysis is not required for ParB to escape from the nucleation site (***Soh et al., 2019***). *Caulobacter* ParB

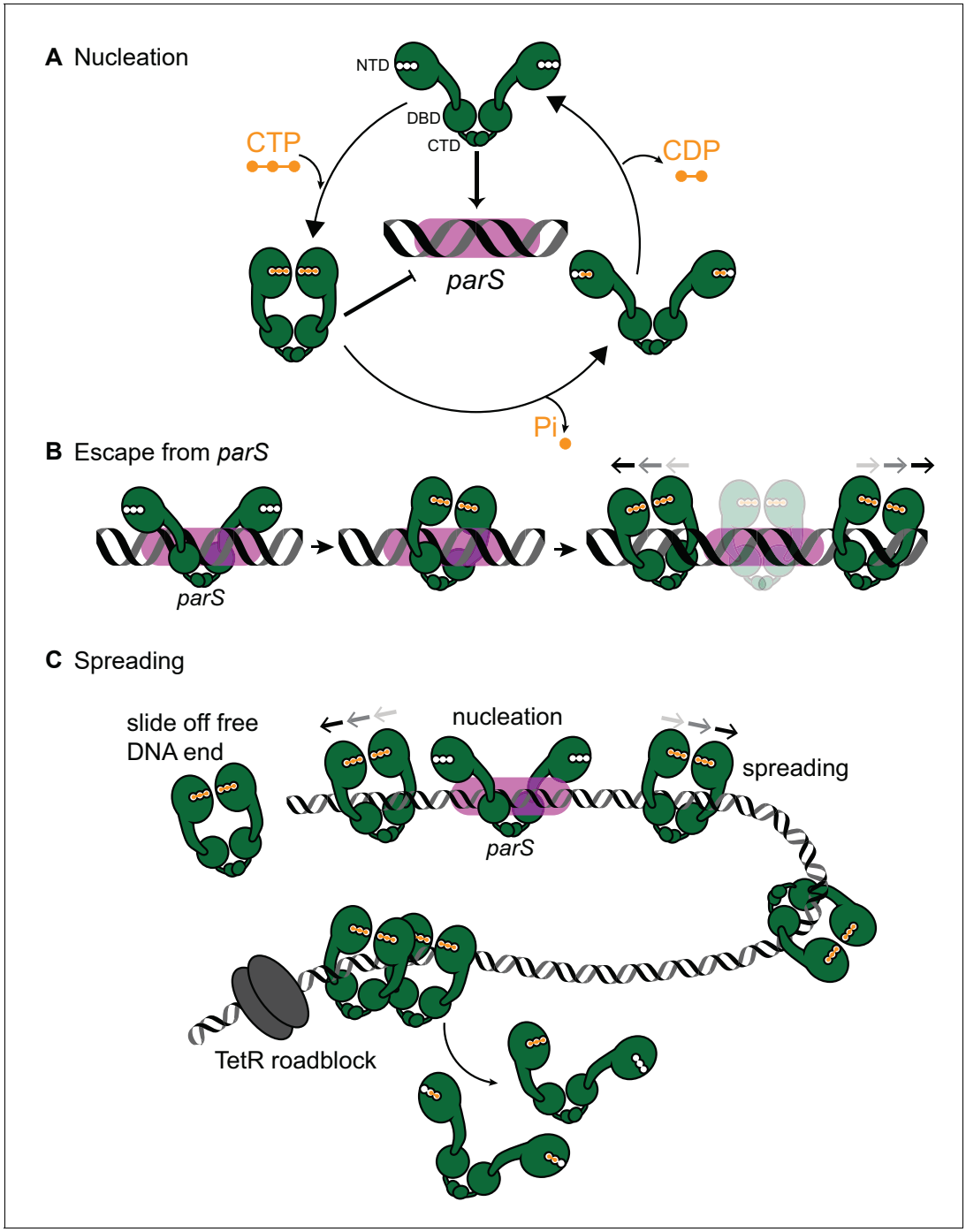

Figure 7. A model for *Caulobacter* ParB nucleation and spreading. (**A**) *Caulobacter* ParB nucleation at *parS*. CTP (orange) reduces *Caulobacter* ParB (dark green) nucleation at *parS* (magenta box), presumably by inducing conformational changes that are incompatible with a site-specific *parS* binding (***Soh et al., 2019***). Only apo- or CDP-bound ParB can nucleate on *parS*. ParB hydrolyzes CTP at a faster rate in the presence of *parS*. The domain architecture of ParB is also shown: NTD: N-terminal domain, DBD: DNA-binding domain, and CTD: C-terminal domain. (**B**) *Caulobacter* ParB escapes from the nucleation site *parS*. Apo-ParB at *parS* binds CTP and slides laterally away from the nucleation site *parS* while still associating with DNA. (**C**) *Caulobacter* ParB sliding and spreading on DNA. CTP-bound ParBs diffuse from the nucleation site *parS* and can run off the free DNA end unless they are blocked by DNA-bound roadblocks such as transcriptional regulators for example TetR. CTP hydrolysis is not required for ParB to escape from the nucleation *parS* site but might contribute to ParB recycling. It is not yet known whether both CTP molecules on a ParB dimer are concertedly hydrolyzed/dissociated for ParB to escape from the chromosome or a heterodimer state of ParB with a single CTP bound also exists in vivo.

could still spread on a DNA when incubated with a non-hydrolyzable CTPγS (***Figure 6***), even though spreading, at least in vitro, was less stable over time in comparison to when CTP was employed (***Figure 6C***). As suggested for *Bacillus* ParB (***Soh et al., 2019***) and supported by our results with *Caulobacter* ParB, CTP hydrolysis might contribute to ParB recycling instead. It is possible that ParB recycling in vivo is achieved via several routes: (i) CTP dissociation from its weak binding pocket, (ii) CTP hydrolysis, (iii) a possible enhanced CTP dissociation/hydrolysis via collisions with DNA-bound roadblocks, or (iv) a transient clamp opening even when ParB is CTP bound. Additional work is required to investigate the dynamics of ParB clamp opening/closing, and whether both CTP molecules on opposite subunits of a ParB dimer are concertedly hydrolyzed/dissociated for ParB to escape from the chromosome or a heterodimer state of ParB with a single CTP bound exists in vivo.

Final perspectives

In this work, we showed the enhancing effect of CTP on *Caulobacter* ParB accumulation on DNA and further demonstrated that ParB spreading requires a closed DNA substrate and that a DNA-binding transcriptional regulator can act as a roadblock to attenuate spreading unidirectionally in vitro. Our real-time and label-free reconstitution of ParB spreading has successfully recapitulated many well-known aspects of ParB behaviors and is consistent with pioneering works by ***Soh et al. (2019)*** and ***Osorio-Valeriano et al. (2019)***. Beyond the biological significance of the findings, our label-free approaches to biochemical reconstitution obviate the often time-consuming and challenging task of site-specifically labeling proteins with fluorophores/chemical crosslinkers without affecting the function of proteins. Here, we have demonstrated the medium-throughput capability of our methodology by investigating the effect of CTP on the spreading of eight additional chromosomal ParB proteins. The ease and medium-throughput manner of our methodology is likely to facilitate future works by the community. Important areas of research in the future are to investigate (i) the effect of ParB-CTP spreading on the supercoiling state of the DNA and vice versa, and (ii) how ParA and SMC interact with ParB-CTP in vivo to organize and faithfully segregate replicated chromosomes to each daughter cell.

Materials and methods

Key resources table

Reagent type (species) or resource	Designation	Source or reference	Identifiers	Additional information
Strain, strain background (*Escherichia coli*)	Rosetta (DE3)	Merck	Cat# 70954	Electro-competent cells
Recombinant DNA reagent	See ***Supplementary file 1***	This paper		See ***Supplementary file 1***
Sequence-based reagent	See ***Supplementary file 1***	This paper		See ***Supplementary file 1***
Antibody	Anti-6xHis tag antibody (HRP) (Rabbit polyclonal)	Abcam	Cat# ab1187	Western blot (1:5,000)
Commercial assay or kit	EnzChek Phosphate Assay Kit	ThermoFisher	Cat# E6646	
Commercial assay or kit	Gibson Assembly Master Mix	NEB	Cat# E2611S	
Commercial assay or kit	Gateway BP Clonase II enzyme mix	ThermoFisher	Cat# 11789020	
Commercial assay or kit	Dip-and-Read Streptavidin (SA) biosensors	Molecular Devices	Cat# 18–5019	
Commercial assay or kit	HisTrap High Performance column	GE Healthcare	Cat# GE17524801	

Continued on next page

Continued

Reagent type (species) or resource	Designation	Source or reference	Identifiers	Additional information
Commercial assay or kit	HiTrap Heparin High Performance column	GE Healthcare	Cat# GE17040601	
Commercial assay or kit	HiLoad 16/600 Superdex 75 pg column	GE Healthcare	Cat# GE28989333	
Commercial assay or kit	Dynabeads MyOne Streptavidin C1	ThermoFisher	Cat# 65001	
Commercial assay or kit	Amersham Protran supported Western blotting membranes, nitrocellulose	GE Healthcare	Cat# GE10600016	pore size 0.45 µm, for DRaCALA assay
Peptide, recombinant protein	*Bam*HI-HF	NEB	Cat# R3136S	20,000 units/mL
Peptide, recombinant protein	*Bam*HI	NEB	Cat# R0136S	20,000 units/mL
Peptide, recombinant protein	*Eco*RI-HF	NEB	Cat# R3101S	20,000 units/mL
peptide, recombinant protein	*Hind*III-HF	NEB	Cat# R3104S	20,000 units/mL
Peptide, recombinant protein	Exonuclease VII	NEB	Cat# M0379S	10,000 units/mL
Peptide, recombinant protein	Exonuclease T7	NEB	Cat# M0263S	10,000 units/mL
Chemical compound, drug	Benzonase nuclease	Sigma-Aldrich	Cat# E1014	
Chemical compound, drug	NTP	ThermoFisher	Cat# R0481	100 mM solution
Chemical compound, drug	CTPγS	Jena Bioscience		A gift from S. Gruber and custom synthesis (purity ≥ 96%)
Chemical compound, drug	CMP-PCP	Jena Bioscience	Cat# NU-254	
Chemical compound, drug	P^{32} -α-CTP	Perkin Elmer	Cat# BLU008H250UC	3000 Ci/mmol, 10 mCi/ml, 250 µCi
Chemical compound, drug	Anhydrotetracycline hydrochloride (ahTc)	Abcam	Cat# ab145350	Dissolved in ethanol
Chemical compound, drug	Bismaleimidoethane (BMOE)	ThermoFisher	Cat# 22323	Dissolved in DMSO
Software, algorithm	BLItz Pro	Molecular Devices	Cat# 50–0156	Version 1.2 https://www.moleculardevices.com/
Software, algorithm	R	R Foundation for Statistical Computing	RRID: SCR_001905	Version 3.2.4
Software, algorithm	Image Studio Lite	LI-COR Biosciences	RRID: SCR_013715	Version 5.2
Software, algorithm	Excel 2016	Microsoft	RRID: SCR_016137	

Protein overexpression and purification

Full-length *Caulobacter* ParB (WT) and ParB (R104A) were purified as described previously (***Tran et al., 2018***). Briefly, pET21b::ParB-His_6 (WT or R104A) was introduced into *E. coli* Rosetta (DE3) competent cells (Merck). A 10 mL overnight culture was used to inoculate 4 L of LB medium + carbenicillin + chloramphenicol. Cells were grown at 37˚C with shaking at 250 rpm to an OD_{600} of 0.4. The culture was then left to cool to 4˚C before isopropyl-β-D-thiogalactopyranoside (IPTG) was

added to a final concentration of 1 mM. The culture was shaken for 3 hr at 30˚C before cells were harvested by centrifugation.

Pelleted cells were resuspended in a buffer containing 100 mM Tris-HCl pH 8.0, 300 mM NaCl, 10 mM Imidazole, 5% (v/v) glycerol, 1 µL of Benzonase nuclease (Sigma Aldrich), 1 mg of lysozyme (Sigma Aldrich), and an EDTA-free protease inhibitor tablet (Roche). The pelleted cells were then lyzed by sonication. The cell debris was removed via centrifugation at 28,000 g for 30 min, and the supernatant was filtered through a 0.45 µm sterile filter (Sartorius Stedim). The protein was then loaded into a 1 mL HisTrap column (GE Healthcare) that had been equilibrated with buffer A [100 mM Tris-HCl pH 8.0, 300 mM NaCl, 10 mM Imidazole, and 5% glycerol]. Protein was eluted from the column using an increasing (10 mM to 500 mM) imidazole gradient in the same buffer. ParB-containing fractions were pooled and diluted to a conductivity of 16 mS/cm before being loaded onto a 1 mL Heparin HP column (GE Healthcare) that had been equilibrated with 100 mM Tris-HCl pH 8.0, 25 mM NaCl, and 5% glycerol. Protein was eluted from the Heparin column using an increasing (25 mM to 1 M NaCl) salt gradient in the same buffer. ParB that was used for EnzChek Phosphate assay and DRaCALA was further polished via a gel-filtration column. To do so, purified ParB was concentrated by centrifugation in an Amicon Ultra-15 3 kDa cut-off spin filters (Merck) before being loaded into a Superdex 75 gel filtration column (GE Healthcare). The gel filtration column was pre-equilibrated with 100 mM Tris-HCl pH 8.0, 250 mM NaCl, and 1 mM $MgCl_2$.

C-terminally His-tagged TetR (class B, from Tn10) were expressed from *E. coli* Rosetta (DE3) harboring a pET21b::TetR-His_6 plasmid (***Supplementary file 1***). TetR-His_6 were purified via a one-step Ni-affinity column using the exact buffers as employed for the purification of *Caulobacter* ParB-His_6.

C-terminally His-tagged ParB (C297S) and ParB (Q35C C297S) were expressed from *E. coli* Rosetta (DE3) harboring a pET21b::ParB-His_6 (C297S) or (Q35C C297S) plasmid (***Supplementary file 1***). ParB-His_6 (C297S) and (Q35C C297S) were purified via a one-step Ni-affinity column using the exact buffers as employed for the purification of *Caulobacter* ParB-His_6. ParB (Q35C C297S) stock solution was supplemented with TCEP (1 mM final concentration) before being flash-frozen in liquid nitrogen.

N-terminally His-tagged MBP-tagged ParB (orthologous proteins from various bacterial species) were expressed from *E. coli* Rosetta (DE3) harboring pET-His-MBP-TEV-DEST::ParB plasmids. His_6-MBP-ParB proteins were purified via a one-step Ni-affinity column as described previously (***Jalal et al., 2019***).

Different batches of proteins were purified by A.S.B.J and N.T.T, and are consistent in all assays used in this work. Both biological (new sample preparations from a fresh stock aliquot) and technical (same sample preparation) replicates were performed for assays described in this study.

Construction of pET21b::ParB-His_6 (C297S and Q35C C297S)

DNA containing the codon-optimized coding sequence of ParB (C297S or Q35C C297S) was chemically synthesized (gBlocks dsDNA fragments, IDT). These gBlocks fragments and a *Nde*I-*Hind*III-digested pET21b backbone were assembled using a 2x Gibson master mix (NEB). Two and a half µL of each fragment at equimolar concentration was added to 5 µL 2x Gibson master mix (NEB), and the mixture was incubated at 50˚C for 60 min. Five µL was used to transform chemically competent *E. coli* DH5α cells. Gibson assembly was possible due to a 23 bp sequence shared between the *Nde*I-*Hind*III-cut pET21b backbone and the gBlocks fragments. These 23 bp regions were incorporated during the synthesis of gBlocks fragments. The resulting plasmids were sequence verified by Sanger sequencing (Eurofins, Germany).

Construction of pET21b::TetR-His_6

DNA containing the coding sequence of TetR (class B, from Tn10) was chemically synthesized (gBlocks dsDNA fragments, IDT). This gBlocks fragment and a *Nde*I-*Hind*III-digested pET21b backbone were assembled together using a 2x Gibson master mix (NEB). Gibson assembly was possible due to a 23 bp sequence shared between the *Nde*I-*Hind*III-cut pET21b backbone and the gBlocks fragment. These 23 bp regions were incorporated during the synthesis of gBlocks fragments. The resulting plasmids were sequence verified by Sanger sequencing (Eurofins, Germany).

Construction of pENTR::ParB orthologs

The coding sequences of ParB orthologs were chemically synthesized (gBlocks dsDNA fragments, IDT) and cloned into pENTR-D-TOPO backbone (Invitrogen) by Gibson assembly (NEB). The resulting plasmids were sequence verified by Sanger sequencing (Eurofins, Germany).

Construction of pET-His-MBP-TEV-DEST::ParB orthologs

The *parB* genes were recombined into a Gateway-compatible destination vector pET-His-MBP-TEV-DEST (***Jalal et al., 2019***) via an LR recombination reaction (ThermoFisher). For LR recombination reactions: 1 µL of purified pENTR::*parB* (~100 ng/µL) was incubated with 1 µL of the destination vector pET-His-MBP-TEV-DEST (~100 ng/µL), 1 µL of LR Clonase II enzyme mix, and 2 µL of water in a total volume of 5 µL.

Construction of DNA substrates for BLI assays

All DNA constructs (***Supplementary file 1***) were designed in VectorNTI (ThermoFisher) and were chemically synthesized (gBlocks dsDNA fragments, IDT). All linear DNA constructs were designed with M13F and M13R homologous regions at each end. To generate a dual biotin-labeled DNA substrate, PCR reactions were performed using a 2x GoTaq PCR master mix (Promega), biotin-labeled M13F and biotin-labeled M13R primers, and gBlocks fragments as template. PCR products were resolved by electrophoresis and gel purified.

Measurement of protein-DNA interaction by bio-layer interferometry (BLI)

Bio-layer interferometry experiments were conducted using a BLItz system equipped with Dip-and-Read Streptavidin (SA) Biosensors (Molecular Devices). BLItz monitors wavelength shifts (nm) resulting from changes in the optical thickness of the sensor surface during association or dissociation of the analyte. All BLI experiments were performed at 22˚C. The streptavidin biosensor was hydrated in a low-salt binding buffer [100 mM Tris-HCl pH 8.0, 100 mM NaCl, 1 mM $MgCl_2$, and 0.005% Tween 20] for at least 10 min before each experiment. Biotinylated double-stranded DNA (dsDNA) was immobilized onto the surface of the SA biosensor through a cycle of Baseline (30 s), Association (120 s), and Dissociation (120 s). Briefly, the tip of the biosensor was dipped into a binding buffer for 30 s to establish the baseline, then to 1 µM biotinylated dsDNA for 120 s, and finally to a low salt binding buffer for 120 s to allow for dissociation.

After the immobilization of DNA on the sensor, association reactions were monitored at 1 µM dimer concentration of ParB (with or without 1 µM TetR or NTPs at various concentrations) for 120 s or 60 min (***Figure 6A***). At the end of each binding step, the sensor was transferred into a protein-free binding buffer to follow the dissociation kinetics for 120 s. The sensor can be recycled by dipping in a high-salt buffer [100 mM Tris-HCl pH 8.0, 1000 mM NaCl, 1 mM $MgCl_2$, and 0.005% Tween 20] for 5 min to remove bound ParB.

For experiments where a closed DNA was cleaved to generate a free DNA end, DNA-coated tips were dipped into 300 µL of cutting solution [266 µL of water, 30 µL of 10x CutSmart buffer (NEB), and 4 µL of *Eco*RI-HF or *Bam*HI-HF restriction enzyme (20,000 units/mL)] for 30 min at 37˚C.

For experiments described in ***Figure 1—figure supplement 2***, $MgCl_2$ was omitted from all binding and protein storage buffers.

For experiments described in ***Figure 3—figure supplement 2***, bio-layer interferometry assays were performed using 1x NEB 3.1 buffer [100 mM NaCl, 50 mM Tris-HCl pH 7.9, 10 mM $MgCl_2$, 100 µg/ml BSA] instead of the low-salt binding buffer [100 mM NaCl, 10 mM Tris-HCl pH 8.0, 1 mM $MgCl_2$, 0.005% Tween20]. After incubating 1 µM ParB and 1 mM CTP with a 169 bp *parS*-coated probe for 120 s, 4 µL of *Bam*HI (20,000 units/mL) or heat-inactivated *Bam*HI was added to a 300 µL reaction to start digesting bound DNA. The reaction was monitored for an additional 30 min. *Bam*HI was inactivated by heat at 65˚C for 30 min.

For experiments described in ***Figure 4—figure supplements 1***, 3 µM of anhydrotetracycline (ahTc) was used to remove bound TetR from DNA. After incubating 1 µM ParB and 1 mM CTP ±1 µM TetR with a 170 bp *parS*-coated probe for 120 s, ahTc (dissolved in ethanol) or ethanol alone was added to a 300 µL reaction to the final concentration of 3 µM or 0.01%, respectively. The reaction was monitored for an additional 120 s.

All sensorgrams recorded during BLI experiments were analyzed using the BLItz analysis software (BLItz Pro version 1.2, Molecular Devices) and replotted in R for presentation. Each experiment was triplicated, the standard deviation of triplicated sensorgrams is less than ten percent, and a representative sensorgram was presented in each figure.

To verify that dual biotin-labeled DNA fragments formed a closed substrate on the surface of the BLI probe, we performed a double digestion with Exonuclease T7 and Exonuclease VII (NEB) (***Figure 2—figure supplement 1***). DNA-coated tips were dipped into 300 µL of cutting solution [266 µL of water, 30 µL of 10x RE buffer 4 (NEB), 2 µL of exonuclease T7 (10,000 units/mL) and 2 µL of exonuclease VII (10,000 units/mL)] for 30 min at 25˚C. Tips were then cut off from the plastic adaptor (***Figure 2—figure supplement 1***) and immerged into a 1x GoTaq PCR master mix [25 µL water, 25 µL 2x GoTaq master mix, 0.5 µL of 100 µM M13F oligo, and 0.5 µL of 100 µM M13R oligo]. Ten cycles of PCR were performed, and the PCR products were resolved on 2% agarose gels (***Figure 2—figure supplement 1***).

NTP (stock concentration: 100 mM) used in BLI assays was purchased from ThermoFisher. CTPγS (stock concentration: 90 mM) was a generous gift from Stephan Gruber and Young-Min Soh. CTPγS was also custom-synthesized and re-purified to 96% purity (Jena Bioscience). Another non-hydrolyzable analog CMP-PCP (Jena Bioscience) was unsuitable for our assays as *Caulobacter* ParB does not bind CMP-PCP (***Figure 6—figure supplement 1***).

Construction of DNA substrates for pull-down assays

A 260 bp DNA fragment containing *Caulobacter parS* sites (genomic position: 4034789–4035048) (***Tran et al., 2018***) or scrambled *parS* sites were chemically synthesized (gBlocks fragments, IDT). These DNA fragments were subsequently 5' phosphorylated using T4 PNK enzyme (NEB), then cloned into a *Sma*I-cut pUC19 using T4 DNA ligase (NEB). The two resulting plasmids are pUC19::260bp-*parS* and pUC19::260bp-scrambled *parS* (***Supplementary file 1***). These plasmids were sequence verified by Sanger sequencing (Eurofins, Germany). To generate dual biotin-labeled DNA substrates, we performed PCR using a pair of biotinylated primers: around_pUC19_F and around_pUC19_R, and either pUC19::260bp-*parS* or pUC19::260bp-scrambled *parS* as a template. Phusion DNA polymerase (NEB) was employed for this round-the-horn PCR reaction. The resulting ~2.8 kb linear DNA fragments were gel-purified and eluted in 50 µL of autoclaved distilled water.

Pull-down assays

Paramagnetic MyOne Streptavidin C1 Dyna beads (ThermoFisher) were used for pull-down assays. Thirty µL of beads were washed twice in 500 µL of high-salt wash buffer [100 mM Tris-HCl pH 8.0, 1 M NaCl, 1 mM $MgCl_2$, and 0.005% Tween 20] and once in 100 µL binding buffer [100 mM Tris-HCl pH 8.0, 100 mM NaCl, 1 mM $MgCl_2$, and 0.005% Tween 20] by repeating a cycle of resuspension and pull-down by magnetic attraction. Five µL of ~50 nM dual biotin-labeled DNA substrate was incubated with 30 µL of beads in 100 µL binding buffer for 30 min at room temperature. The reaction was occasionally mixed by pipetting up and down several times. Afterward, DNA-coated beads were washed once in 500 µL high-salt buffer [100 mM Tris-HCl pH 8.0, 1000 mM NaCl, 1 mM $MgCl_2$, and 0.005% Tween 20] and once in 500 µL of binding buffer. Finally, DNA-coated beads were resuspended in 300 µL of binding buffer. Ninety-six µL of the resuspended beads were used for each pull-down assay. Four µL of *Caulobacter* ParB-His_6 (WT) or (R104A) (stock concentration: 25 µM) were added to 96 µL of suspended beads. NTPs were either omitted or added to the suspended beads to the final concentration of 1 mM. The mixture was pipetted up and down several times and was left to incubate at room temperature for 5 min. Beads were then pulled down magnetically and unwanted supernatant discarded. DNA-coated beads (now with bound protein) were then washed once with 500 µL of binding buffer and once with 100 µL of the same buffer. The unwanted supernatant was discarded, and the left-over beads were resuspended in 30 µL of 1x SDS-PAGE sample buffer. Each experiment was triplicated, and a representative immunoblot was presented.

Immunoblot analysis

For immunoblot analysis, magnetic beads were resuspended directly in 1x SDS sample buffer, then heated to 42˚C for 15 min before loading to 12% Novex Tris-Glycine SDS-PAGE gels (ThermoFisher).

The eluted protein was resolved by electrophoresis at 150 V for 60 min. Resolved proteins were transferred to polyvinylidene fluoride membranes using the Trans-Blot Turbo Transfer System (Bio-Rad) and probed with 1:5000 dilution of α-His_6 HRP-conjugated antibody (Abcam). Blots were imaged and analyzed using an Amersham Imager 600 (GE Healthcare) and Image Studio Lite version 5.2 (LI-COR Biosciences). The band intensities were quantified for lanes 5 and 6 (***Figure 2C***), and the range of fold difference between replicates was reported.

Differential radial capillary action of ligand assay (DRaCALA) or membrane-spotting assay

Purified *Caulobacter* ParB-His_6 or TetR-His_6 (final concentration: 25 µM) were incubated with 5 nM radiolabeled P^{32}-α-CTP (Perkin Elmer), 30 µM of unlabeled cold CTP (Thermo Fisher), 1.5 µM of 22 bp *parS* or *NBS* DNA duplex in the reaction buffer [100 mM Tris pH 8.0, 100 mM NaCl, and 10 mM $MgCl_2$] for 5 min at room temperature. For the NTP competition assay, the mixture was further supplemented with 500 µM of either unlabeled cold CTP, ATP, GTP, or UTP. Four µL of samples were spotted slowly onto a dry nitrocellulose membrane and air-dried. The nitrocellulose membrane was wrapped in cling film before being exposed to a phosphor screen (GE Healthcare) for two minutes. Each DRaCALA assay was triplicated, and a representative autoradiograph was shown.

DNA preparation for EnzCheck phosphate assay and DRaCALA

A 22 bp palindromic single-stranded DNA fragment (*parS*: GGATGTTTCACGTGAAACATCC or *NBS*: GGATATTTCCCGGGAAATATCC) [100 µM in 1 mM Tris-HCl pH 8.0, 5 mM NaCl buffer] was heated at 98˚C for 5 min before being left to cool down to room temperature overnight to form 50 µM double-stranded *parS* or *NBS* DNA. The sequences of *parS* and *NBS* are underlined.

Measurement of NTPase activity by EnzCheck phosphate assay

NTP hydrolysis was monitored using an EnzCheck Phosphate Assay Kit (Thermo Fisher). Samples (100 µL) containing a reaction buffer supplemented with 1 mM of NTP and 1 µM ParB (WT or R104A) were assayed in a Biotek EON plate reader at 25˚C for 15 hr with readings every minute. The reaction buffer (1 mL) typically contained: 740 µL Ultrapure water, 50 µL 20x customized reaction buffer [100 mM Tris pH 8.0, 2 M NaCl, and 20 mM $MgCl_2$], 200 µL MESG substrate solution, and 10 µL purine nucleoside phosphorylase (1 unit). Reactions with buffer only, buffer + protein only or buffer + NTP only were also included as controls. The plates were shaken at 280 rpm continuously for 15 hr at 25˚C. The inorganic phosphate standard curve was also constructed according to the manual. Each assay was triplicated. The results were analyzed using R and the NTPase rates were calculated using a linear regression fitting in R.

In vitro crosslinking using a sulfhydryl-to-sulfhydryl crosslinker bismaleimidoethane (BMOE)

A 50 µL mixture of 10 µM ParB (C297S) or (C297S Q35C) ± 1 mM NTP ± 0.5 µM *parS* dsDNA (22 bp) was assembled in a reaction buffer [10 mM Tris-HCl pH 7.4, 100 mM NaCl, and 1 mM $MgCl_2$] and incubated for 15 min (***Figure 6—figure supplement 2B***) or for 1, 5, 10, 15, and 30 min (***Figure 6B***) at room temperature. BMOE (1 mM final concentration from a 20 mM stock solution) was then added, and the reaction was quickly mixed by three pulses of vortexing. SDS-PAGE sample buffer containing 23 mM β-mercaptoethanol was then added immediately to quench the crosslinking reaction. Samples were heated to 50˚C for 15 min before being loaded on 12% TruPAGE Tris-Glycine Precast gels (Sigma Aldrich). Each assay was triplicated. Gels were stained with InstantBlue solution (Expedeon) and band intensity was quantified using Image Studio Lite version 5.2 (LI-COR Biosciences). The crosslinked fractions were averaged, and their standard deviations calculated in Excel.

Additional information

Funding

Funder	Grant reference number	Author
Biotechnology and Biological Sciences Research Council	BB/P018165/1	Tung BK Le
Royal Society	UF140053	Tung BK Le
Biotechnology and Biological Sciences Research Council	BBS/E/J/000PR9791	Ngat T Tran Tung BK Le
Royal Society	RG150448	Adam SB Jalal Tung BK Le
Biotechnology and Biological Sciences Research Council	BBS/E/J/000PR9778	Tung BK Le

The funders had no role in study design, data collection and interpretation, or the decision to submit the work for publication.

Author contributions

Adam SB Jalal, Ngat T Tran, Formal analysis, Investigation, Methodology; Tung BK Le, Conceptualization, Formal analysis, Supervision, Funding acquisition, Investigation, Visualization, Methodology, Writing - original draft, Writing - review and editing

Author ORCIDs

Adam SB Jalal https://orcid.org/0000-0001-7794-8834
Ngat T Tran https://orcid.org/0000-0002-7186-3976
Tung BK Le https://orcid.org/0000-0003-4764-8851

Decision letter and Author response

Decision letter https://doi.org/10.7554/eLife.53515.sa1
Author response https://doi.org/10.7554/eLife.53515.sa2

Additional files

Supplementary files

- Supplementary file 1. Plasmids, DNA, and protein sequences used in this study.
- Transparent reporting form

Data availability

No deep sequencing data or X-ray crystallography data were generated during this study. All other data (BLI, uncropped gel images etc.) are included in the manuscript, figures, and source data files.

References

Ah-Seng Y, Rech J, Lane D, Bouet JY. 2013. Defining the role of ATP hydrolysis in mitotic segregation of bacterial plasmids. *PLOS Genetics* **9**:e1003956. DOI: https://doi.org/10.1371/journal.pgen.1003956, PMID: 24367270

Attaiech L, Minnen A, Kjos M, Gruber S, Veening JW. 2015. The ParB-parS chromosome segregation system modulates competence development in Streptococcus pneumoniae. *mBio* **6**:e00662. DOI: https://doi.org/10.1128/mBio.00662-15, PMID: 26126852

Badrinarayanan A, Le TB, Laub MT. 2015. Rapid pairing and resegregation of distant homologous loci enables double-strand break repair in Bacteria. *The Journal of Cell Biology* **210**:385–400. DOI: https://doi.org/10.1083/jcb.201505019, PMID: 26240183

Breier AM, Grossman AD. 2007. Whole-genome analysis of the chromosome partitioning and sporulation protein Spo0J (ParB) reveals spreading and origin-distal sites on the *Bacillus subtilis* chromosome. *Molecular Microbiology* **64**:703–718. DOI: https://doi.org/10.1111/j.1365-2958.2007.05690.x, PMID: 17462018

Broedersz CP, Wang X, Meir Y, Loparo JJ, Rudner DZ, Wingreen NS. 2014. Condensation and localization of the partitioning protein ParB on the bacterial chromosome. *PNAS* **111**:8809–8814. DOI: https://doi.org/10.1073/pnas.1402529111, PMID: 24927534

Chen BW, Lin MH, Chu CH, Hsu CE, Sun YJ. 2015. Insights into ParB spreading from the complex structure of Spo0J and parS. *PNAS* **112**:6613–6618. DOI: https://doi.org/10.1073/pnas.1421927112, PMID: 25964325

Debaugny RE, Sanchez A, Rech J, Labourdette D, Dorignac J, Geniet F, Palmeri J, Parmeggiani A, Boudsocq F, Anton Leberre V, Walter JC, Bouet JY. 2018. A conserved mechanism drives partition complex assembly on bacterial chromosomes and plasmids. *Molecular Systems Biology* **14**:e8516. DOI: https://doi.org/10.15252/msb.20188516, PMID: 30446599

Donczew M, Mackiewicz P, Wróbel A, Flärdh K, Zakrzewska-Czerwińska J, Jakimowicz D. 2016. ParA and ParB coordinate chromosome segregation with cell elongation and division during Streptomyces sporulation. *Open Biology* **6**:150263. DOI: https://doi.org/10.1098/rsob.150263, PMID: 27248800

Easter J, Gober JW. 2002. ParB-stimulated nucleotide exchange regulates a switch in functionally distinct ParA activities. *Molecular Cell* **10**:427–434. DOI: https://doi.org/10.1016/S1097-2765(02)00594-4, PMID: 12191487

Erdmann N, Petroff T, Funnell BE. 1999. Intracellular localization of P1 ParB protein depends on ParA and parS. *PNAS* **96**:14905–14910. DOI: https://doi.org/10.1073/pnas.96.26.14905, PMID: 10611311

Figge RM, Easter J, Gober JW. 2003. Productive interaction between the chromosome partitioning proteins, ParA and ParB, is required for the progression of the cell cycle in Caulobacter crescentus. *Molecular Microbiology* **47**:1225–1237. DOI: https://doi.org/10.1046/j.1365-2958.2003.03367.x, PMID: 12603730

Fisher GL, Pastrana CL, Higman VA, Koh A, Taylor JA, Butterer A, Craggs T, Sobott F, Murray H, Crump MP, Moreno-Herrero F, Dillingham MS. 2017. The structural basis for dynamic DNA binding and bridging interactions which condense the bacterial centromere. *eLife* **6**:e28086. DOI: https://doi.org/10.7554/eLife.28086, PMID: 29244022

Fogel MA, Waldor MK. 2006. A dynamic, mitotic-like mechanism for bacterial chromosome segregation. *Genes & Development* **20**:3269–3282. DOI: https://doi.org/10.1101/gad.1496506, PMID: 17158745

Funnell BE. 2016. ParB partition proteins: complex formation and spreading at bacterial and plasmid centromeres. *Frontiers in Molecular Biosciences* **3**:44. DOI: https://doi.org/10.3389/fmolb.2016.00044, PMID: 27622187

Glaser P, Sharpe ME, Raether B, Perego M, Ohlsen K, Errington J. 1997. Dynamic, mitotic-like behavior of a bacterial protein required for accurate chromosome partitioning. *Genes & Development* **11**:1160–1168. DOI: https://doi.org/10.1101/gad.11.9.1160, PMID: 9159397

Graham TGW, Wang X, Song D, Etson CM, van Oijen AM, Rudner DZ, Loparo JJ. 2014. ParB spreading requires DNA bridging. *Genes & Development* **28**:1228–1238. DOI: https://doi.org/10.1101/gad.242206.114

Gruber S, Errington J. 2009. Recruitment of condensin to replication origin regions by ParB/Spo0J promotes chromosome segregation in *B. subtilis*. *Cell* **137**:685–696. DOI: https://doi.org/10.1016/j.cell.2009.02.035, PMID: 19450516

Harms A, Treuner-Lange A, Schumacher D, Søgaard-Andersen L. 2013. Tracking of chromosome and replisome dynamics in Myxococcus xanthus reveals a novel chromosome arrangement. *PLOS Genetics* **9**:e1003802. DOI: https://doi.org/10.1371/journal.pgen.1003802, PMID: 24068967

Hwang LC, Vecchiarelli AG, Han Y-W, Mizuuchi M, Harada Y, Funnell BE, Mizuuchi K. 2013. ParA-mediated plasmid partition driven by protein pattern self-organization. *The EMBO Journal* **32**:1238–1249. DOI: https://doi.org/10.1038/emboj.2013.34

Ireton K, Gunther NW, Grossman AD. 1994. Spo0J is required for normal chromosome segregation as well as the initiation of sporulation in *Bacillus subtilis*. *Journal of Bacteriology* **176**:5320–5329. DOI: https://doi.org/10.1128/JB.176.17.5320-5329.1994, PMID: 8071208

Jakimowicz D, Chater K, Zakrzewska-Czerwínska J. 2002. The ParB protein of Streptomyces coelicolor A3(2) recognizes a cluster of parS sequences within the origin-proximal region of the linear chromosome. *Molecular Microbiology* **45**:1365–1377. DOI: https://doi.org/10.1046/j.1365-2958.2002.03102.x, PMID: 12207703

Jalal ASB, Tran NT, Stevenson CE, Tan X, Lawson DM, Le TBK. 2019. Evolving a new protein-DNA interface via sequential introduction of permissive and specificity-switching mutations. *bioRxiv*. DOI: https://doi.org/10.1101/724823

Jecz P, Bartosik AA, Glabski K, Jagura-Burdzy G. 2015. A single parS sequence from the cluster of four sites closest to oriC is necessary and sufficient for proper chromosome segregation in *Pseudomonas aeruginosa*. *PLOS ONE* **10**:e0120867. DOI: https://doi.org/10.1371/journal.pone.0120867, PMID: 25794281

Kawalek A, Bartosik AA, Glabski K, Jagura-Burdzy G. 2018. *Pseudomonas aeruginosa* partitioning protein ParB acts as a nucleoid-associated protein binding to multiple copies of a parS-related motif. *Nucleic Acids Research* **46**:4592–4606. DOI: https://doi.org/10.1093/nar/gky257, PMID: 29648658

Kusiak M, Gapczynska A, Plochocka D, Thomas CM, Jagura-Burdzy G. 2011. Binding and spreading of ParB on DNA determine its biological function in *Pseudomonas aeruginosa*. *Journal of Bacteriology* **193**:3342–3355. DOI: https://doi.org/10.1128/JB.00328-11, PMID: 21531806

Lagage V, Boccard F, Vallet-Gely I. 2016. Regional control of chromosome segregation in *Pseudomonas aeruginosa*. *PLOS Genetics* **12**:e1006428. DOI: https://doi.org/10.1371/journal.pgen.1006428

Lee PS, Grossman AD. 2006. The chromosome partitioning proteins soj (ParA) and Spo0J (ParB) contribute to accurate chromosome partitioning, separation of replicated sister origins, and regulation of replication initiation in *Bacillus subtilis*. *Molecular Microbiology* **60**:853–869. DOI: https://doi.org/10.1111/j.1365-2958.2006.05140.x, PMID: 16677298

Leonard TA, Butler PJ, Löwe J. 2005. Bacterial chromosome segregation: structure and DNA binding of the Soj dimer–a conserved biological switch. *The EMBO Journal* **24**:270–282. DOI: https://doi.org/10.1038/sj.emboj.7600530, PMID: 15635448

Lim HC, Surovtsev IV, Beltran BG, Huang F, Bewersdorf J, Jacobs-Wagner C. 2014. Evidence for a DNA-relay mechanism in ParABS-mediated chromosome segregation. *eLife* **3**:e02758. DOI: https://doi.org/10.7554/eLife.02758, PMID: 24859756

Lin DC-H, Levin PA, Grossman AD. 1997. Bipolar localization of a chromosome partition protein in *Bacillus subtilis*. *PNAS* **94**:4721–4726. DOI: https://doi.org/10.1073/pnas.94.9.4721

Lin DC, Grossman AD. 1998. Identification and characterization of a bacterial chromosome partitioning site. *Cell* **92**:675–685. DOI: https://doi.org/10.1016/S0092-8674(00)81135-6, PMID: 9506522

Livny J, Yamaichi Y, Waldor MK. 2007. Distribution of centromere-like parS sites in bacteria: insights from comparative genomics. *Journal of Bacteriology* **189**:8693–8703. DOI: https://doi.org/10.1128/JB.01239-07, PMID: 17905987

Lynch AS, Wang JC. 1995. SopB protein-mediated silencing of genes linked to the sopC locus of *Escherichia coli* F plasmid. *PNAS* **92**:1896–1900. DOI: https://doi.org/10.1073/pnas.92.6.1896, PMID: 7534407

Madariaga-Marcos J, Pastrana CL, Fisher GL, Dillingham MS, Moreno-Herrero F. 2019. ParB dynamics and the critical role of the CTD in DNA condensation unveiled by combined force-fluorescence measurements. *eLife* **8**:e43812. DOI: https://doi.org/10.7554/eLife.43812, PMID: 30907359

Minnen A, Attaiech L, Thon M, Gruber S, Veening JW. 2011. SMC is recruited to oriC by ParB and promotes chromosome segregation in Streptococcus pneumoniae. *Molecular Microbiology* **81**:676–688. DOI: https://doi.org/10.1111/j.1365-2958.2011.07722.x, PMID: 21651626

Mohl DA, Easter J, Gober JW. 2001. The chromosome partitioning protein, ParB, is required for cytokinesis in Caulobacter crescentus. *Molecular Microbiology* **42**:741–755. DOI: https://doi.org/10.1046/j.1365-2958.2001.02643.x, PMID: 11722739

Murray H, Ferreira H, Errington J. 2006. The bacterial chromosome segregation protein Spo0J spreads along DNA from parS nucleation sites. *Molecular Microbiology* **61**:1352–1361. DOI: https://doi.org/10.1111/j.1365-2958.2006.05316.x, PMID: 16925562

Onn I, Koshland D. 2011. In vitro assembly of physiological cohesin/DNA complexes. *PNAS* **108**:12198–12205. DOI: https://doi.org/10.1073/pnas.1107504108, PMID: 21670264

Osorio-Valeriano M, Altegoer F, Steinchen W, Urban S, Liu Y, Bange G, Thanbichler M. 2019. ParB-type DNA segregation proteins are CTP-Dependent molecular switches. *Cell* **179**:1512–1524. DOI: https://doi.org/10.1016/j.cell.2019.11.015, PMID: 31835030

Rodionov O, Lobocka M, Yarmolinsky M. 1999. Silencing of genes flanking the P1 plasmid centromere. *Science* **283**:546–549. DOI: https://doi.org/10.1126/science.283.5401.546, PMID: 9915704

Saenger W, Orth P, Kisker C, Hillen W, Hinrichs W. 2000. The tetracycline repressor-A paradigm for a biological switch. *Angewandte Chemie International Edition* **39**:2042–2052. DOI: https://doi.org/10.1002/1521-3773(20000616)39:12<2042::AID-ANIE2042>3.0.CO;2-C, PMID: 10941016

Sanchez A, Cattoni DI, Walter JC, Rech J, Parmeggiani A, Nollmann M, Bouet JY. 2015. Stochastic self-assembly of ParB proteins builds the bacterial DNA segregation apparatus. *Cell Systems* **1**:163–173. DOI: https://doi.org/10.1016/j.cels.2015.07.013, PMID: 27135801

Soh YM, Davidson IF, Zamuner S, Basquin J, Bock FP, Taschner M, Veening JW, De Los Rios P, Peters JM, Gruber S. 2019. Self-organization of *parS* centromeres by the ParB CTP hydrolase. *Science* **366**:1129–1133. DOI: https://doi.org/10.1126/science.aay3965, PMID: 31649139

Song D, Rodrigues K, Graham TGW, Loparo JJ. 2017. A network of cis and trans interactions is required for ParB spreading. *Nucleic Acids Research* **45**:7106–7117. DOI: https://doi.org/10.1093/nar/gkx271

Sullivan NL, Marquis KA, Rudner DZ. 2009. Recruitment of SMC by ParB-parS organizes the origin region and promotes efficient chromosome segregation. *Cell* **137**:697–707. DOI: https://doi.org/10.1016/j.cell.2009.04.044, PMID: 19450517

Surtees JA, Funnell BE. 2001. The DNA binding domains of P1 ParB and the architecture of the P1 plasmid partition complex. *Journal of Biological Chemistry* **276**:12385–12394. DOI: https://doi.org/10.1074/jbc.M009370200, PMID: 11150297

Taylor JA, Pastrana CL, Butterer A, Pernstich C, Gwynn EJ, Sobott F, Moreno-Herrero F, Dillingham MS. 2015. Specific and non-specific interactions of ParB with DNA: implications for chromosome segregation. *Nucleic Acids Research* **43**:719–731. DOI: https://doi.org/10.1093/nar/gku1295, PMID: 25572315

Thanbichler M, Shapiro L. 2006. MipZ, a spatial regulator coordinating chromosome segregation with cell division in Caulobacter. *Cell* **126**:147–162. DOI: https://doi.org/10.1016/j.cell.2006.05.038, PMID: 16839883

Toro E, Hong SH, McAdams HH, Shapiro L. 2008. Caulobacter requires a dedicated mechanism to initiate chromosome segregation. *PNAS* **105**:15435–15440. DOI: https://doi.org/10.1073/pnas.0807448105, PMID: 18824683

Tran NT, Laub MT, Le TBK. 2017. SMC progressively aligns chromosomal arms in Caulobacter crescentus but is antagonized by convergent transcription. *Cell Reports* **20**:2057–2071. DOI: https://doi.org/10.1016/j.celrep.2017.08.026, PMID: 28854358

Tran NT, Stevenson CE, Som NF, Thanapipatsiri A, Jalal ASB, Le TBK. 2018. Permissive zones for the centromere-binding protein ParB on the Caulobacter crescentus chromosome. *Nucleic Acids Research* **46**:1196–1209. DOI: https://doi.org/10.1093/nar/gkx1192, PMID: 29186514

Vecchiarelli AG, Mizuuchi K, Funnell BE. 2012. Surfing biological surfaces: exploiting the nucleoid for partition and transport in Bacteria. *Molecular Microbiology* **86**:513–523. DOI: https://doi.org/10.1111/mmi.12017, PMID: 22934804

Vecchiarelli AG, Neuman KC, Mizuuchi K. 2014. A propagating ATPase gradient drives transport of surface-confined cellular cargo. *PNAS* **111**:4880–4885. DOI: https://doi.org/10.1073/pnas.1401025111, PMID: 24567408

Wang X, Brandão HB, Le TB, Laub MT, Rudner DZ. 2017. *Bacillus subtilis* SMC complexes juxtapose chromosome arms as they travel from origin to terminus. *Science* **355**:524–527. DOI: https://doi.org/10.1126/science.aai8982, PMID: 28154080

Wu LJ, Errington J. 2004. Coordination of cell division and chromosome segregation by a nucleoid occlusion protein in *Bacillus subtilis*. *Cell* **117**:915–925. DOI: https://doi.org/10.1016/j.cell.2004.06.002, PMID: 15210112

Yu W, Herbert S, Graumann PL, Götz F. 2010. Contribution of SMC (Structural Maintenance of Chromosomes) and SpoIIIE to chromosome segregation in staphylococci. *Journal of Bacteriology* **192**:4067–4073. DOI: https://doi.org/10.1128/JB.00010-10, PMID: 20525833

RESEARCH ADVANCE

A CTP-dependent gating mechanism enables ParB spreading on DNA

Adam SB Jalal[1], Ngat T Tran[1], Clare EM Stevenson[2], Afroze Chimthanawala[3,4], Anjana Badrinarayanan[3], David M Lawson[2], Tung BK Le[1]*

[1]Department of Molecular Microbiology, John Innes Centre, Norwich, United Kingdom; [2]Department of Biochemistry and Metabolism, John Innes Centre, Norwich, United Kingdom; [3]National Centre for Biological Sciences, Tata Institute of Fundamental Research, Bangalore, India; [4]SASTRA University, Thanjavur, Tamil Nadu, India

ABSTRACT Proper chromosome segregation is essential in all living organisms. The ParA-ParB-*parS* system is widely employed for chromosome segregation in bacteria. Previously, we showed that *Caulobacter crescentus* ParB requires cytidine triphosphate to escape the nucleation site *parS* and spread by sliding to the neighboring DNA (Jalal et al., 2020). Here, we provide the structural basis for this transition from nucleation to spreading by solving co-crystal structures of a C-terminal domain truncated *C. crescentus* ParB with *parS* and with a CTP analog. Nucleating ParB is an open clamp, in which *parS* is captured at the DNA-binding domain (the DNA-gate). Upon binding CTP, the N-terminal domain (NTD) self-dimerizes to close the NTD-gate of the clamp. The DNA-gate also closes, thus driving *parS* into a compartment between the DNA-gate and the C-terminal domain. CTP hydrolysis and/or the release of hydrolytic products are likely associated with reopening of the gates to release DNA and recycle ParB. Overall, we suggest a CTP-operated gating mechanism that regulates ParB nucleation, spreading, and recycling.

***For correspondence:** tung.le@jic.ac.uk

Competing interest: The authors declare that no competing interests exist.

Funding: See page 25

Preprinted: 05 May 2021
Received: 11 May 2021
Accepted: 03 August 2021
Published: 16 August 2021

Reviewing Editor: Anthony G Vecchiarelli, University of Michigan, United States

Introduction

Proper chromosome segregation is essential in all domains of life. In most bacterial species, faithful chromosome segregation is mediated by the tripartite ParA-ParB-*parS* system (***Donczew et al., 2016***; ***Fogel and Waldor, 2006***; ***Harms et al., 2013***; ***Ireton et al., 1994***; ***Jakimowicz et al., 2002***; ***Jalal and Le, 2020a***; ***Kawalek et al., 2018***; ***Lin and Grossman, 1998***; ***Livny et al., 2007***; ***Mohl et al., 2001***; ***Tran et al., 2018***). ParB, a CTPase and DNA-binding protein, nucleates on *parS* before spreading to adjacent non-specific DNA to form a higher-order nucleoprotein complex (***Breier and Grossman, 2007***; ***Broedersz et al., 2014***; ***Graham et al., 2014***; ***Jalal and Le, 2020a***; ***Murray et al., 2006***; ***Rodionov et al., 1999***; ***Sanchez et al., 2015***; ***Taylor et al., 2015***). The ParB-DNA nucleoprotein complex stimulates the ATPase activity of ParA, driving the movement of the *parS* locus (and subsequently, the whole chromosome) to the opposite pole of the cell (***Hwang et al., 2013***; ***Leonard et al., 2005***; ***Lim et al., 2014***; ***Taylor et al., 2021***; ***Vecchiarelli et al., 2014***; ***Vecchiarelli et al., 2012***). ParB spreads by sliding along the DNA, in a manner that depends on the binding of a co-factor, cytidine triphosphate (CTP) (***Balaguer F de et al., 2021***; ***Jalal et al., 2020c***; ***Osorio-Valeriano et al., 2019***; ***Soh et al., 2019***). A co-crystal structure of a C-terminal domain truncated *Bacillus subtilis* ParB (ParBΔCTD) together with CDP showed the nucleotide to be sandwiched between adjacent subunits, thus promoting their dimerization (***Soh et al., 2019***). A similar arrangement was seen in the co-crystal structure of an N-terminal domain (NTD) truncated version of the *Myxococcus xanthus* ParB homolog, PadC, bound to CTP (***Osorio-Valeriano et al., 2019***). Self-dimerization at the NTD of *B. subtilis* ParB creates a clamp-like molecule that enables DNA entrapment (***Soh et al., 2019***). Biochemical studies

with *M. xanthus* and *C. crescentus* ParBs showed that CTP facilitates the dissociation of ParB from *parS*, thereby switching ParB from a nucleating mode to a sliding mode (**Jalal et al., 2020c**; **Osorio-Valeriano et al., 2019**). ParB can hydrolyze CTP to CDP and inorganic phosphate (**Jalal et al., 2020c**; **Osorio-Valeriano et al., 2019**; **Soh et al., 2019**); however, hydrolysis is not required for spreading since ParB in complex with a non-hydrolyzable CTP analog (CTPγS) can still self-load and slide on DNA (**Jalal et al., 2020c**; **Soh et al., 2019**). Furthermore, *M. xanthus* PadC does not possess noticeable CTPase activity (**Osorio-Valeriano et al., 2019**). As such, the role of CTP hydrolysis in bacterial chromosome segregation is not yet clear.

Here, we solve co-crystal structures of a C-terminal domain truncated *C. crescentus* ParB in complex with either *parS* or CTPγS to better understand the roles of CTP binding and hydrolysis. Consistent with the previous report (**Soh et al., 2019**), the NTDs of *C. crescentus* ParB also self-dimerize upon binding to nucleotides, thus closing a molecular gate at this domain (the NTD-gate). Furthermore, the two opposite DNA-binding domains (DBD) move closer together to close a second molecular gate (the DNA-gate). We provide evidence that the CTP-induced closure of the DNA-gate drives *parS* DNA from the DBD into a 20-amino-acid long compartment between the DNA-gate and the C-terminal domain, thus explaining how CTP binding enables ParB to escape the high-affinity *parS* site to spread while still entrapping DNA. Lastly, we identify and characterize a ParB 'clamp-locked' mutant that is defective in CTP hydrolysis but otherwise competent in gate closing, suggesting a possible role for CTP hydrolysis/release of hydrolytic products in the reopening ParB gates and in recycling ParB. Collectively, we suggest a CTP-operated gating mechanism that might regulate ParB nucleation, spreading, and recycling.

Results

Co-crystal structure of a *C. crescentus* ParBΔCTD-*parS* complex reveals an open conformation at the NTD

We sought to solve a co-crystal structure of *C. crescentus* ParB nucleating at *parS*. After screening several constructs with different lengths of ParB and *parS*, we obtained crystals of a 50 amino acid C-terminally truncated ParB in complex with a 22 bp *parS* DNA (**Figure 1**). This protein variant lacks the C-terminal domain (CTD) responsible for ParB dimerization (**Figure 1A**; **Figge et al., 2003**). Diffraction data for the ParBΔCTD-*parS* co-crystal were collected to 2.9 Å resolution, and the structure was solved by molecular replacement (see Materials and methods). The asymmetric unit contains four copies of ParBΔCTD and two copies of the *parS* DNA (**Figure 1—figure supplement 1A,B**).

Each ParBΔCTD subunit consists of an NTD (helices α1–α4 and sheets β1–β4) and a DBD (helices α5–α10) (**Figure 1B**). Each ParBΔCTD binds to a half *parS* site, but there is no protein-protein contact between the two adjacent subunits (**Figure 1B**). We previously reported a 2.4 Å co-crystal structure of the DBD of *C. crescentus* ParB bound to *parS* (**Jalal et al., 2020b**) and elucidated the molecular basis for specific *parS* recognition, hence we focus on the conformation of the NTD here instead. We observed that helices α3 and α4 are packed towards the DBD and are connected to the rest of the NTD via an α3–β4 loop (**Figure 1B,C**). While the DBD and helices α3–α4 are near identical between the two ParBΔCTD subunits (root-mean-square deviation [RMSD] = 0.19 Å, **Figure 1C**), the rest of the NTD, from α1 to β4, adopts notably different conformations in the two subunits (**Figure 1C,D**). Specifically, NTDs (α1–β4) from the two ParBΔCTD subunits are related by a rotation of approximately 80° due to changes in a flexible loop in between α3 and β4 (**Figure 1D**). Furthermore, by superimposing the *C. crescentus* ParBΔCTD-*parS* structure onto that of *Helicobacter pylori* (**Chen et al., 2015**), we observed that the NTDs of ParB from both species can adopt multiple alternative orientations (**Figure 1—figure supplement 2**). Taken together, these observations suggest that the ability of the NTD to adopt multiple open conformations is likely a general feature of nucleating ParB.

Co-crystal structure of a *C. crescentus* ParBΔCTD-CTPγS complex reveals a closed conformation at the NTD

Next, to gain insight into the spreading state of ParB, we solved a 2.7 Å resolution structure of *C. crescentus* ParBΔCTD in complex with CTPγS (see Materials and methods). At this resolution, it was not possible to assign the position of the ligand's sulfur atom. Indeed, the placement of the sulfur atom relative to the terminal phosphorus atom may vary from one ligand to the next in the crystal,

leading to an averaging of the electron density. Hence, we modeled CTP, instead of CTPγS, into the electron density (***Figure 2*** and ***Figure 2—figure supplement 1***). The asymmetric unit contains two copies of ParBΔCTD, each with a CTPγS molecule and a coordinated Mg^{2+} ion bound at the NTD (***Figure 2A***). In contrast to the open conformation of the ParBΔCTD-*parS* structure, nucleotide-bound NTDs from opposite subunits self-dimerize (with an interface area of 2111 Å^2, as determined by PISA; ***Krissinel, 2015***), thus adopting a closed conformation (***Figure 2A***). Multiple CTPγS-contacting residues also directly contribute to the NTD self-dimerization interface (summarized in ***Figure 2—figure***

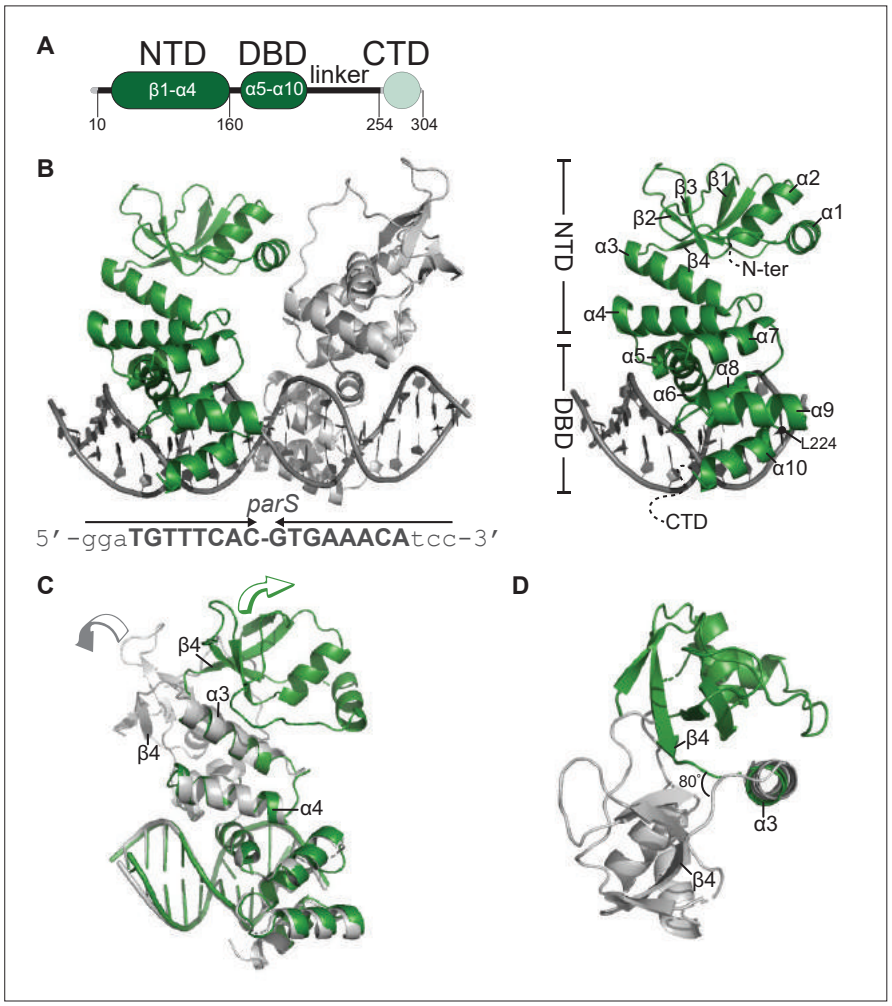

Figure 1. Co-crystal structure of a *C. crescentus* ParBΔCTD-*parS* complex reveals an open conformation at the N-terminal domain (NTD). (**A**) The domain architecture of *C. crescentus* ParB: the NTD (dark green), the central DNA-binding domain (DBD, dark green), the C-terminal domain (CTD, faded green), and a linker that connects the DBD and the CTD together. The ParBΔCTD variant that was used for crystallization lacks the CTD (faded green). (**B**, left panel) Co-crystal structure of two *C. crescentus* ParBΔCTD monomers (dark green and gray) bound to a 22 bp *parS* DNA. The nucleotide sequence of the 22 bp *parS* is shown below the co-crystal structure, the core *parS* sequence is highlighted in bold, and each *parS* half-site is denoted by an arrow. The position of residue L224 is also indicated. (Right panel) The structure of a ParBΔCTD subunit bound to a *parS* half site with key features highlighted. (**C**) Superimposition of *C. crescentus* ParBΔCTD subunits shows two different orientations of the NTD. The arrow above each subunit shows the direction each NTD is projecting towards. (**D**) A top-down view of the superimposition of ParBΔCTD subunits shows their NTDs orienting ~80° apart from each other.

The online version of this article includes the following figure supplement(s) for figure 1:

Figure supplement 1. The composition of the asymmetric unit (ASU) of the *C. crescentus* ParBΔCTD-*parS* co-crystal.

Figure supplement 2. Structural comparisons of the *C. crescentus* ParBΔCTD-*parS* complex to the *H. pylori* ParBΔCTD-*parS* complex.

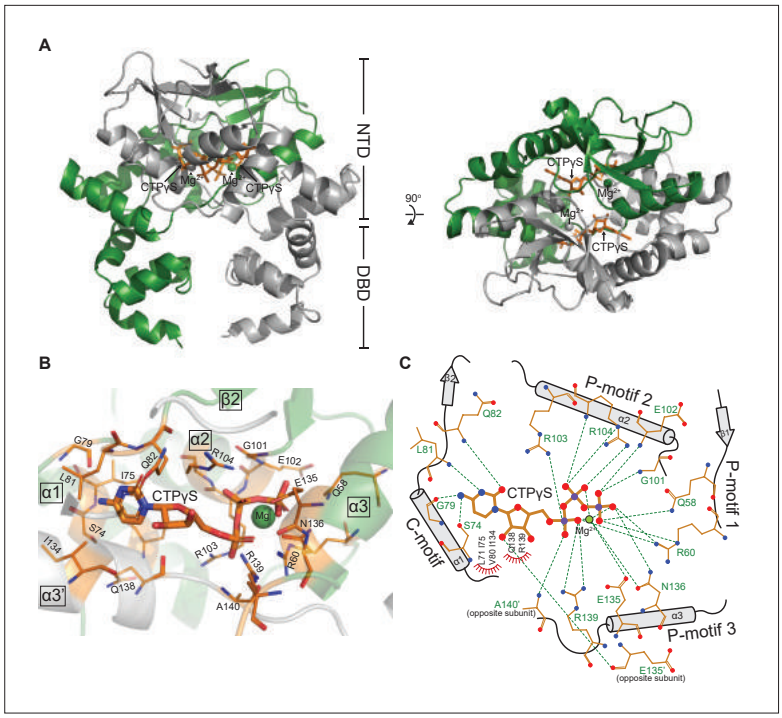

Figure 2. Co-crystal structure of a *C. crescentus* ParBΔCTD-CTPγS complex reveals a closed conformation at the N-terminal domain (NTD). (**A**, left panel) The front view of the co-crystal structure of *C. crescentus* ParBΔCTD (dark green and gray) bound to a non-hydrolyzable analog CTPγS (orange) and Mg^{2+} ions (dark green and gray spheres). (Right panel) The top view of the *C. crescentus* ParBΔCTD-CTPγS co-crystal structure. Note that helix α10 is not resolved in this structure due to a poor electron density in this region. (**B**) The nucleotide-binding pocket of *C. crescentus* ParB showing amino acid residues that contact the CTPγS molecule and the coordinated Mg^{2+} ion. (**C**) Protein-ligand interaction map of CTPγS bound to *C. crescentus* ParBΔCTD. Hydrogen bonds are shown as dashed green lines and hydrophobic interactions as red semi-circles. Nitrogen, oxygen, phosphate, and magnesium atoms are shown as blue, red, purple, and green filled circles, respectively.

The online version of this article includes the following figure supplement(s) for figure 2:

Figure supplement 1. Omit mF_{obs}-DF_{calc} difference electron density calculated at 2.73 Å resolution for Mg-CTP.

Figure supplement 2. Sequence alignment of the chromosomal ParB protein family.

Figure supplement 3. Structural comparisons of the *C. crescentus* ParBΔCTD-CTPγS complex to the *B. subtilis* ParBΔCTD-CDP complex and the *M. xanthus* PadCΔNTD-CTP complex.

supplement 2), indicating a coupling between nucleotide binding and self-dimerization. Furthermore, the *C. crescentus* ParBΔCTD-CTPγS structure is similar to that of the CDP-bound *B. subtilis* ParBΔCTD (RMSD = 1.48 Å) and the CTP-bound *M. xanthus* PadCΔNTD (RMSD = 2.23 Å) (***Figure 2—figure supplement 3A***), suggesting that the closed conformation at the NTD is structurally conserved in nucleotide-bound ParB/ParB-like proteins.

Each CTPγS molecule is sandwiched between helices α1, α2, α3 from one subunit and helix α3′ from the opposite subunit (***Figure 2B***). Ten amino acids form hydrogen-bonding contacts with three phosphate groups of CTPγS, either directly or via the coordinated Mg^{2+} ion (***Figure 2C***). These phosphate-contacting residues are referred to as P-motifs 1–3, respectively (P for phosphate motif, ***Figure 2C***). Four amino acids at helix α1 and the α1–β2 intervening loop provide hydrogen-bonding interactions to the cytosine ring, hence are termed the C-motif (C for cytosine motif, ***Figure 2C***). Lastly, six additional residues contact the ribose moiety and/or the pyrimidine moiety via hydrophobic interactions (***Figure 2C***). Nucleotide-contacting residues in *C. crescentus* ParB and their corresponding amino acids in ParB/ParB-like homologs are summarized in ***Figure 2—figure supplement 2*** and ***Figure 2—figure supplement 3B***. The C-motif forms a snug fit to the pyrimidine moiety, thus is incompatible with larger purine moieties such as those from ATP or GTP. Hydrogen-bonding contacts from the G79 main chain and the S74 side chain to the amino group at position 4 of the cytosine moiety further

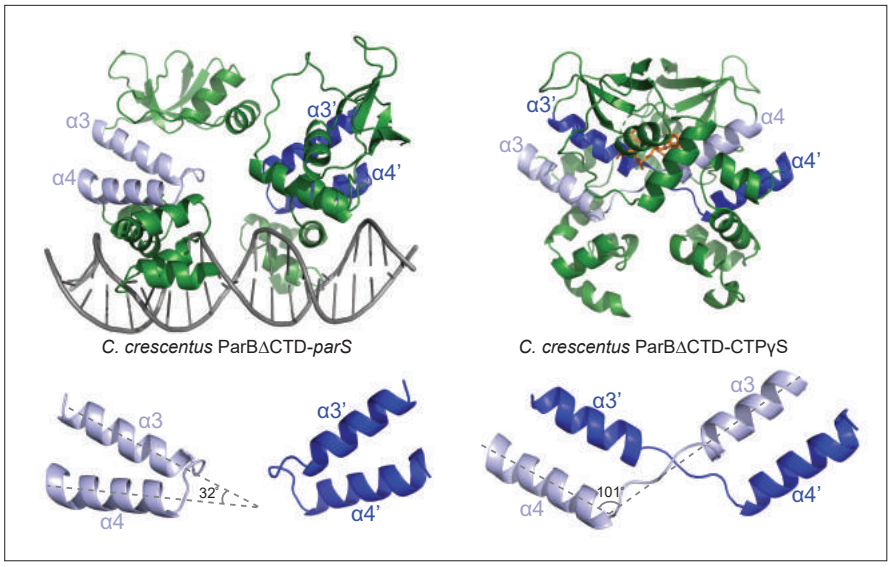

Figure 3. Conformational changes between the nucleating and the spreading states of *C. crescentus* ParB. Structures of *C. crescentus* ParBΔCTD in complex with *parS* (left panel) and with CTPγS (right panel), with the pairs of helices (α3–α4, and α3′–α4′ for the opposite subunit) shown in light blue and dark blue, respectively. Below each structure, only the α3–α4, α3′–α4′ pairs, and the angles between these helices are shown.

distinguish CTP from UTP (***Figure 2C***). Taken all together, our structural data are consistent with the known specificity of *C. crescentus* ParB for CTP (***Jalal et al., 2020c***).

Conformational changes between the nucleating and the spreading state of *C. crescentus* ParB

A direct comparison of the *C. crescentus* ParBΔCTD-*parS* structure to the ParBΔCTD-CTPγS structure further revealed the conformational changes upon nucleotide binding. In the nucleating state, as represented by the ParBΔCTD-*parS* structure, helices α3 and α4 from each subunit bundle together (32° angle between α3 and α4, ***Figure 3***). However, in the spreading state, as represented by the ParBΔCTD-CTPγS structure, α3 swings outwards by 101° to pack itself with α4′ from the opposing subunit (***Figure 3***). Nucleotide binding most likely facilitates this 'swinging-out' conformation since both α3 and the α3–α4 loop, that is, P-motif 3 make numerous contacts with the bound CTPγS and the coordinated Mg^{2+} ion (***Figure 2C***). The reciprocal exchange of helices ensures that the packing in the α3–α4 protein core remains intact, while likely driving the conformational changes for the rest of the NTD as well as the DBD (***Figure 4A***). Indeed, residues 44–121 at the NTD rotate wholesale by 94° to dimerize with their counterpart from the opposing subunit (***Figure 4A*** and ***Figure 4—figure supplement 1A***). Also, residues 161–221 at the DBD rotate upward by 26° in a near rigid-body movement (***Figure 4A*** and ***Figure 4—figure supplement 1A***). As a result, the opposite DBDs are closer together in the spreading state (inter-domain distance = ~ 27 Å) than in the nucleating state (inter-domain distance = ~ 36 Å) (***Figure 4—figure supplement 1B***). By overlaying the CTPγS-bound structure onto the *parS* DNA complex, it is clear that the DBDs in the spreading state clash severely with DNA, hence are no longer compatible with *parS* DNA binding (***Figure 4B***). Our structural data are therefore consistent with the previous finding that CTP decreases *C. crescentus* ParB nucleation on *parS* or liberates pre-bound ParB from *parS* site (***Jalal et al., 2020c***). Overall, we suggest that CTP binding stabilizes a conformation that is incompatible with DNA-binding and that this change might facilitate ParB escape from the high-affinity nucleation *parS* site.

C. crescentus ParB entraps *parS* DNA in a compartment between the DBD and the CTD in a CTP-dependent manner

To verify the CTP-dependent closed conformation of ParB, we performed site-specific crosslinking of purified proteins using a sulfhydryl-to-sulfhydryl crosslinker bismaleimidoethane (BMOE) (***Soh et al., 2019***). Residues Q35, L224, and I304 at the NTD, DBD, and CTD, respectively (***Figure 5A***), were

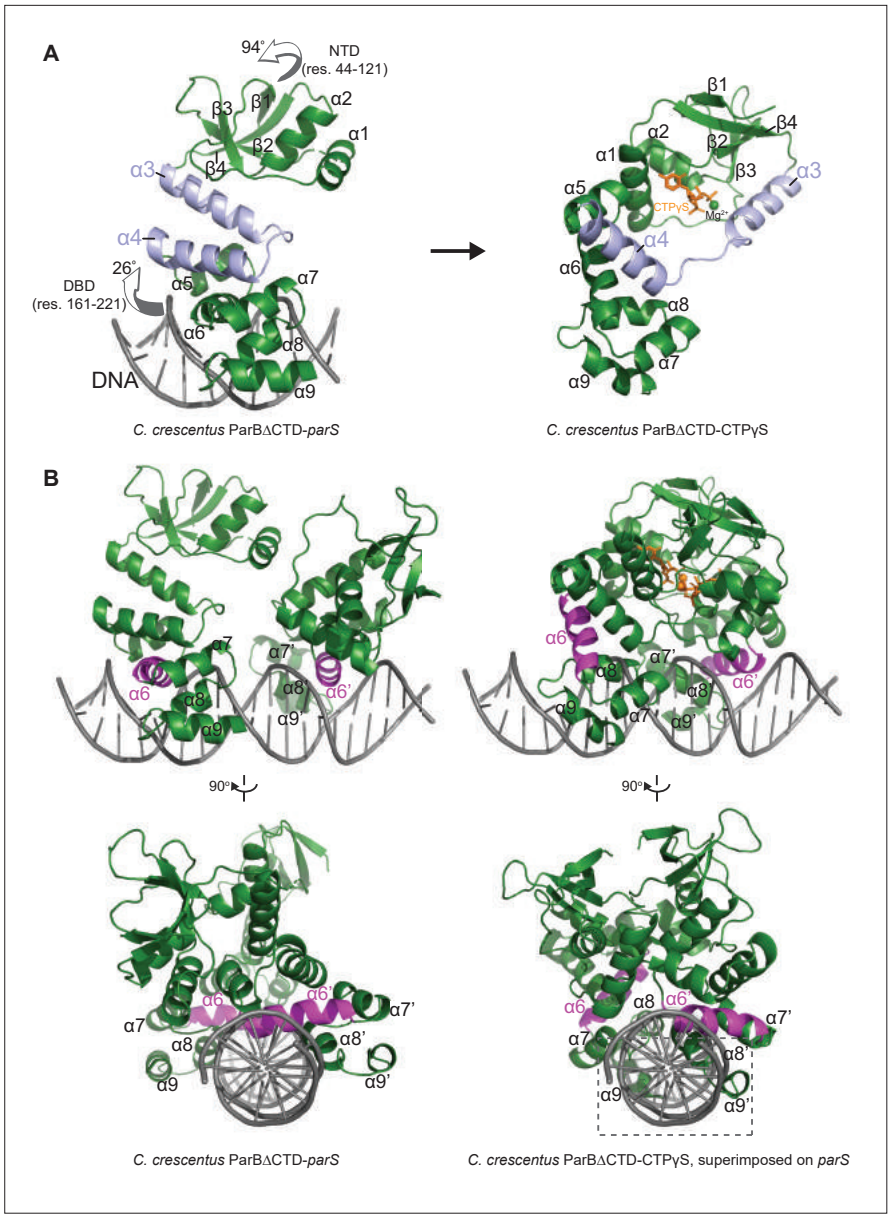

Figure 4. The structure of a nucleotide-bound *C. crescentus* ParBΔCTD is incompatible with specific *parS* binding at the DNA-binding domain (DBD). (**A**) Structural changes between *C. crescentus* ParBΔCTD-*parS* and ParBΔCTD-CTPγS structures. Helices α3 and α4 are shown in light blue. The arrows next to the N-terminal domain (NTD) (residues 44–121) and the DBD (residues 161–221) show the direction that these domains rotate towards in the nucleotide-bound state. (**B**) Superimposing the *C. crescentus* ParBΔCTD-CTPγS structure onto *parS* DNA shows DNA-recognition helices (α6 and α6′, magenta) positioning away from the two consecutive major grooves of *parS*, and helices α8–α9 and α8′–α9′ at the DBD (dashed box) clashing with *parS* DNA.

The online version of this article includes the following figure supplement(s) for figure 4:

Figure supplement 1. The structure of nucleotide-bound *C. crescentus* ParBΔCTD is incompatible with specific *parS* binding at the DNA-binding domain (DBD).

substituted individually to cysteine on an otherwise cysteine-less ParB (C297S) background (***Jalal et al., 2020c***), to create ParB variants where symmetry-related cysteines become covalently linked if they are within 8 Å of each other (***Figure 5B***). We observed that the crosslinking of both ParB (Q35C) and ParB (L224C) was enhanced ~2.5–3-fold in the presence of *parS* DNA and CTP (***Figure 5B***), consistent with CTP favoring a conformation when the NTD and the DBD are close together. In contrast,

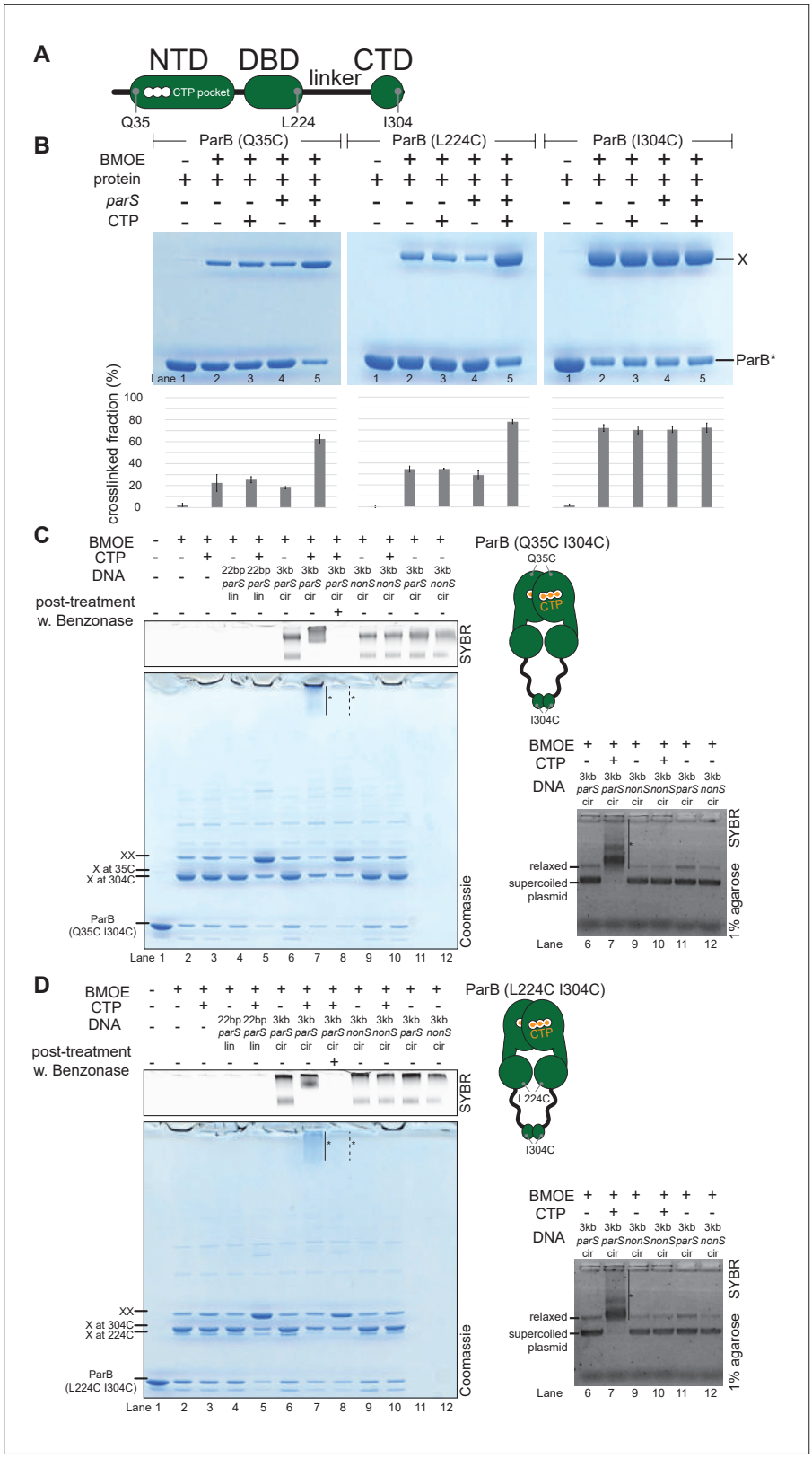

Figure 5. *C. crescentus* ParB entraps *parS* DNA in a compartment between the DNA-binding domain (DBD) and the C-terminal domain (CTD) in a cytidine triphosphate (CTP)-dependent manner. (**A**) A schematic diagram of *C. crescentus* ParB showing the position of Q35 (at the N-terminal domain [NTD]), L224 (at the DBD), and I304 (at the CTD) that were substituted either individually or in combinations for cysteine. (**B**) Denaturing polyacrylamide

Figure 5 continued on next page

Figure 5 continued

gel analysis of bismaleimidoethane (BMOE) crosslinking products of 8 μM single-cysteine ParB (Q35C/L224C/I304C) variant ±0.5 μM 22 bp *parS* DNA ±1 mM CTP. X indicates a crosslinked form of ParB. Quantification of the crosslinked (X) fraction is shown below each representative gel image. Error bars represent SD from three replicates. (**C**, left panel) Denaturing polyacrylamide gel analysis of BMOE crosslinking products of 8 μM dual-cysteine ParB (Q35C I304C) variant ±0.5 μM DNA ±1 mM CTP. Different DNA were employed in crosslinking reactions: a linear 22 bp *parS* DNA (22 bp *parS* lin), a circular 3 kb *parS* plasmid (3 kb *parS* cir), and a circular 3 kb scrambled *parS* plasmid (3 kb *nonS* cir). The high molecular weight (HMW) smear near the top of the polyacrylamide gel is marked with a solid line and an asterisk (lane 7). When the crosslinking reaction was post-treated with a non-specific DNA nuclease, Benzonase, the HMW smear was no longer observed (dashed line and asterisk, lane 8). The polyacrylamide gel was also stained with a DNA dye, Sybr Green (SYBR), and only the top section of the gel is shown. Small 22 bp *parS* DNA duplex migrated out of the gel, thus was not observed near the top of the Sybr-stained gel. A schematic diagram of a dual-cysteine *C. crescentus* ParB dimer is also shown. (Right panel) Agarose gel analysis of BMOE crosslinking products. A subset of crosslinking reactions (lanes 6, 7, and 9–12) were loaded and resolved on 1 % agarose gel. The gel was subsequently stained with Sybr Green for DNA. Shifted gel bands are marked with a solid line and an asterisk. (**D**) Same as panel (**C**) but another dual-cysteine variant, ParB (L224C I304C) was employed instead.

The online version of this article includes the following figure supplement(s) for figure 5:

Source data 1. Original files, annotation of the full raw gels, and data used to generate ***Figure 5***.

Figure supplement 1. Crosslinking ParB (Q35C I304C) and ParB (L224C I304C) did not produce a high molecular weight (HMW) smear in the presence of cytidine triphosphate (CTP) and a linearized *parS* plasmid.

Figure supplement 1—source data 1. Original files, annotation of the full raw gels, and data used to generate ***Figure 5—figure supplement 1***.

Figure supplement 2. Crosslinking ParB (Q35C L224C) did not produce a high molecular weight (HMW) smear despite the presence of cytidine triphosphate (CTP) and a circular *parS* plasmid.

Figure supplement 2—source data 1. Original files, annotation of the full raw gels, and data used to generate ***Figure 5—figure supplement 2***.

Figure supplement 3. The high molecular weight (HMW) smear likely contains catenates between crosslinked ParB dimers and circular *parS* plasmids.

Figure supplement 3—source data 1. Original files, annotation of the full raw gels, and data used to generate ***Figure 5—figure supplement 3***.

Figure supplement 4. A premature closing of ParB clamps prevents their interactions with a 170 bp closed *parS* DNA substrate.

Figure supplement 4—source data 1. Data used to generate ***Figure 5—figure supplement 4***.

ParB (I304C) crosslinked independently of CTP or *parS* (***Figure 5B***), supporting the known role of the CTD as a primary dimerization domain (***Figge et al., 2003***; ***Fisher et al., 2017***).

Previously, it was shown that *B. subtilis* ParB-CTP forms a protein clamp that entraps DNA (***Soh et al., 2019***); however, the location of DNA within the clamp is not yet clear. To locate such DNA-entrapping compartment, we employed a double crosslinking assay while taking advantage of the availability of crosslinkable cysteine residues in all three domains of *C. crescentus* ParB (***Figure 5A***). A *C. crescentus* ParB variant with crosslinkable NTD and CTD interfaces (Q35C I304C) was first constructed and purified (***Figure 5C***). ParB (Q35C I304C) could form high molecular weight (HMW) species near the top of the polyacrylamide gel in the presence of CTP, a 3 kb *parS* plasmid, and the crosslinker BMOE (lane 7, ***Figure 5C***, left panel). The HMW smear on the polyacrylamide gel contained both protein and DNA as apparent from a dual staining with Coomassie and Sybr Green (***Figure 5C***, left panel). Slowly migrating DNA-stained bands were also observed when resolved on an agarose gel (***Figure 5C***, right panel). The HMW smear most likely contained DNA-protein catenates between a circular *parS* plasmid and a denatured but otherwise circularly crosslinked ParB (Q35C I304C) polypeptide. Indeed, a post-crosslinking treatment with Benzonase, a non-specific DNA nuclease (lane 8, ***Figure 5C***, left panel) or the use of a linearized *parS* plasmid (lane 2 vs. lane 4, ***Figure 5—figure supplement 1***) eliminated the HMW smear, presumably by unlinking the DNA-protein catenates. Lastly, the HMW smear was not observed when a plasmid containing a scrambled *parS* site was used (lane 10, ***Figure 5C***, left panel) or when CTP was omitted from the crosslinking reaction (lane 6, ***Figure 5C***, left panel), indicating that the DNA entrapment is dependent on *parS* and CTP. Collectively, these experiments demonstrate

that as with the *B. subtilis* ParB homolog, *C. crescentus* ParB is also a CTP-dependent molecular clamp that can entrap *parS* DNA in between the NTD and the CTD.

Employing the same strategy, we further narrowed down the DNA-entrapping compartment by constructing a ParB (L224C I304C) variant in which both the DBD and the CTD are crosslinkable (***Figure 5D***). We found that crosslinked ParB (L224C I304C) also entrapped circular plasmid efficiently in a *parS*- and CTP-dependent manner, as judged by the appearance of the HMW smear near the top of the gel (lane 7, ***Figure 5D***, left panel). By contrast, ParB (Q35C L224C) that has both the NTD and the DBD crosslinkable was unable to entrap DNA in any tested condition (***Figure 5—figure supplement 2***). We therefore hypothesized that ParB clamps entrap DNA within a compartment created by a 20-amino-acid linker in between the DBD and the CTD. To investigate further, we constructed a ParB (L224C I304C)-TEV variant, in which a TEV protease cleavage site was inserted within the DBD-CTD linker (***Figure 5—figure supplement 3A***). Again, ParB (L224C I304C)-TEV entrapped a circular *parS* plasmid efficiently in the presence of CTP (the HMW smear on lane 7, ***Figure 5—figure supplement 3A***). However, a post-crosslinking treatment with TEV protease eliminated such HMW smear, presumably by creating a break in the polypeptide through which a circular plasmid could escape (lane 8, ***Figure 5—figure supplement 3A***). We also extracted crosslinked ParB (L224C I304C) from gel slices that encompassed the HMW smear and electrophoresed the eluted proteins again on a denaturing gel to find a single band that migrated similarly to a double-crosslinked protein (lane 9, ***Figure 5—figure supplement 2B***). Therefore, our results suggest that a ParB dimer, rather than ParB oligomers, is the major species that entraps DNA. Taken together, we suggest that *C. crescentus* ParB dimer functions as a molecular clamp that entraps *parS*-containing DNA within a DBD-CTD compartment upon CTP binding. This is also consistent with experiments that showed a premature and irreversible closing of ParB clamps, achieved either by an extended preincubation with CTPγS (***Jalal et al., 2020c*** and ***Figure 5—figure supplement 4B***) or by pre-crosslinking a closed clamp form of ParB (***Figure 5—figure supplement 4C***), prevented nucleation at *parS* and DNA entrapment.

C. crescentus ParB (E102A) is a clamp-locked mutant that is defective in clamp reopening

Next, we investigated the potential role(s) of CTP hydrolysis. Hydrolysis is unlikely to be required for DNA entrapment and translocation since ParB in complex with CTPγS can still self-load and slide on DNA (***Jalal et al., 2020c***; ***Soh et al., 2019***). *M. xanthus* ParB (N172A) and *B. subtilis* ParB (N112S) mutants, which bind but cannot hydrolyze CTP, failed to form higher-order protein-DNA complexes inside the cells (***Osorio-Valeriano et al., 2019***; ***Soh et al., 2019***). However, these ParB variants are already impaired in NTD self-dimerization (***Soh et al., 2019***), hence the mechanistic role of CTP hydrolysis is still unclear. We postulated that creation of a ParB variant defective in CTP hydrolysis but otherwise competent in NTD self-dimerization would enable us to investigate the possible role of CTP hydrolysis. To this end, we performed alanine scanning mutagenesis on the CTP-binding pocket of *C. crescentus* ParB (***Figure 2C***). Eleven purified ParB variants were assayed for CTP binding by a membrane-spotting assay (DRaCALA) (***Figure 6A***), and for CTP hydrolysis by measuring the release rate of inorganic phosphate (***Figure 6B***). Moreover, their propensity for NTD self-dimerization was also analyzed by crosslinking with BMOE (***Figure 6C*** and ***Figure 6—figure supplement 1***). Lastly, their ability to nucleate, slide, and entrap a closed *parS* DNA substrate was investigated by a biolayer interferometry (BLI) assay (***Figure 6D*** and ***Figure 6—figure supplement 2A***). Immobilizing a dual biotin-labeled DNA on a streptavidin-coated BLI surface created a closed DNA substrate that can be entrapped by ParB-CTP clamps (***Figure 5—figure supplement 4A***; ***Jalal et al., 2020c***). The BLI assay monitors wavelength shifts resulting from changes in the optical thickness of the probe surface during the association/dissociation of ParB with a closed DNA substrate in real time (***Figure 6—figure supplement 2***).

Overall, we identified several distinct classes of ParB mutants:

1. Class I: ParB (R60A), (R103A), (R104A), (R139A), (N136A), (G79S), and (S74A) did not bind or bound radiolabeled CTP only weakly (***Figure 6A***), thus also showed weak to no CTP hydrolysis (***Figure 6B***) or clamp-closing activity (***Figure 6C,D***).
2. Class II: ParB (Q58A) and (E135A) that are competent in CTP-binding (***Figure 6A***), but defective in CTP hydrolysis (***Figure 6B***) and in entrapping a closed *parS* DNA substrate (***Figure 6D***). We noted that ParB (Q58A) and ParB (E135A) already had an elevated crosslinking efficiency even

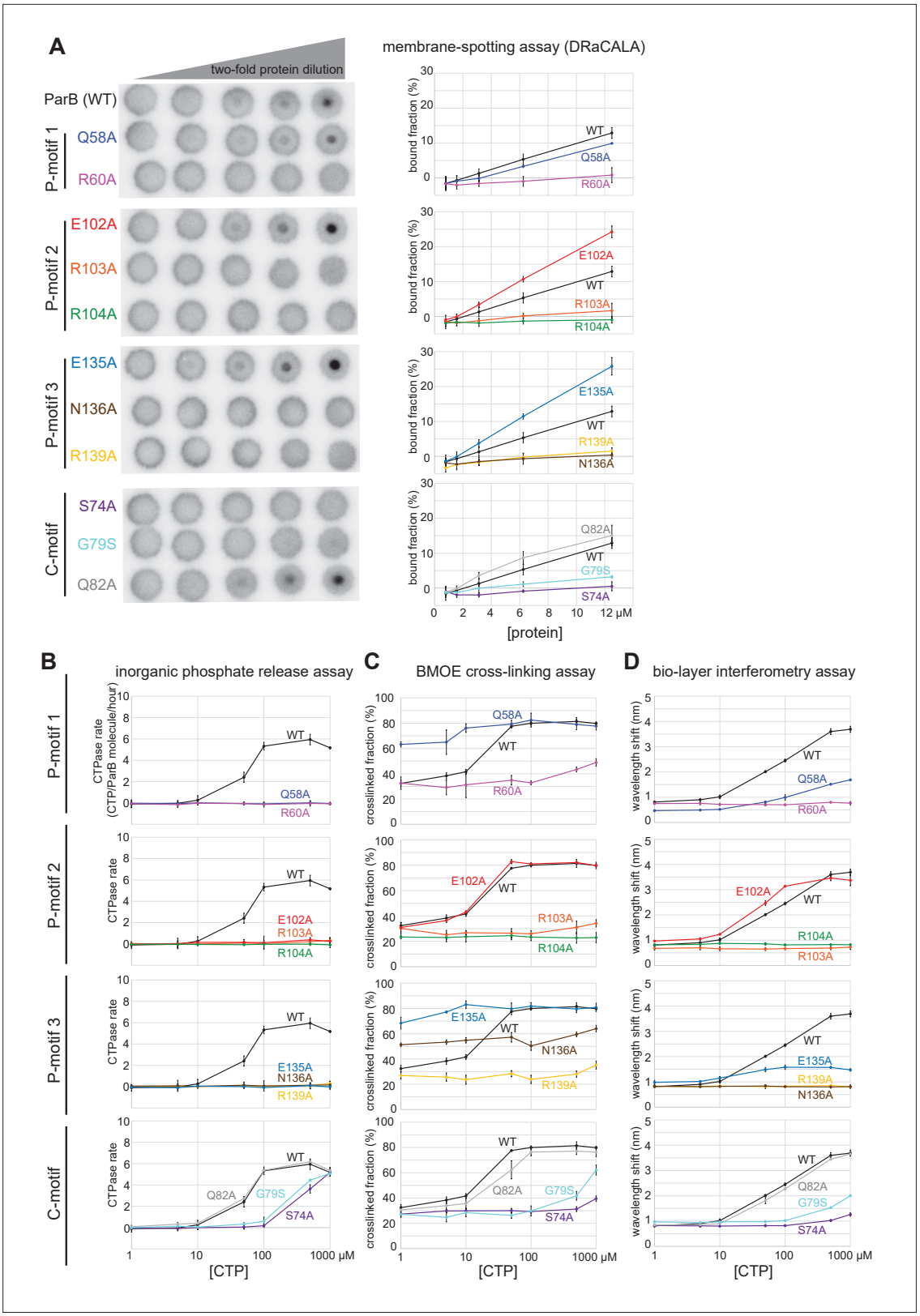

Figure 6. Alanine scanning mutagenesis of the *C. crescentus* ParB cytidine triphosphate (CTP)-binding pocket reveals several classes of clamp mutants. Eleven residues at C-motif and P-motifs 1–3 were individually substituted for alanine or glycine. (**A**) Membrane-spotting assay of ParB variants. CTP binding was monitored by membrane-spotting assay using radiolabeled CTP α-P^{32}. The bulls-eye staining indicates CTP binding due to a more rapid immobilization of protein-ligand complexes compared to free ligands. All reactions contained various concentration of purified ParB, 5 nM radiolabeled

Figure 6 continued on next page

Figure 6 continued

CTP α-P^{32}, 30 μM unlabeled CTP, and 1.5 μM 22 bp *parS* DNA. The bound fractions were quantified, and error bars represent SD from three replicates. All the reactions were spotted on the same membrane, the radiograph was rearranged solely for presentation purposes. (**B**) Inorganic phosphate release assay of ParB variants. The CTPase rates were measured at increasing concentration of CTP. All reactions contained 1 μM purified ParB variant, 0.5 μM 22 bp *parS* DNA, and an increasing concentration of CTP. (**C**) Bismaleimidoethane (BMOE) crosslinking assay of ParB variants. A second set of alanine scanning ParB variants, which harbor an additional Q35C substitution at the N-terminal domain (NTD), were also constructed and subsequently used in BMOE crosslinking experiments. Purified ParB variants (8 μM) were preincubated with 0.5 μM 22 bp *parS* DNA and an increasing concentration of CTP for 5 min before BMOE was added. Crosslinking products were resolved on a 12 % denaturing polyacrylamide gel and the crosslinked fractions were quantified (see also ***Figure 6—figure supplement 1*** for representation images). Error bars represent SD from three replicates. (**D**) Biolayer interferometry (BLI) assay of ParB variants. BLI analysis of the interaction between a premix of 1 μM ParB variant ± an increasing concentration of CTP and a 170 bp closed *parS* DNA substrate. See also ***Figure 5—figure supplement 4A*** for a schematic diagram of the BLI setup and ***Figure 6—figure supplement 2*** for representative BLI sensorgrams. BLI signal at the end of the association phase (± SD from three replicates) was plotted against CTP concentrations.

The online version of this article includes the following figure supplement(s) for figure 6:

Source data 1. Original files, annotation of the full raw gels, and data used to generate ***Figure 6***.

Figure supplement 1. Denaturing polyacrylamide gel analysis of crosslinking products of alanine scanning ParB variants.

Figure supplement 1—source data 1. Original files, annotation of the full raw gels, and data used to generate ***Figure 6—figure supplement 1***.

Figure supplement 2. Biolayer interferometry (BLI) analysis of the interaction between ParB variants and a 170 bp closed *parS* DNA substrate.

Figure supplement 2—source data 1. Data used to generate ***Figure 6—figure supplement 2***.

in the absence of CTP (***Figure 6C***). This premature clamp closing might have resulted in a less than wild-type level of DNA entrapment (***Figure 6D***).

3. Class III: ParB (E102A) did not hydrolyze CTP (***Figure 6B***) but nevertheless bound CTP efficiently (***Figure 6A***) to self-dimerize at the NTD and to entrap DNA to the same level as ParB (WT) at all CTP concentrations (***Figure 6C,D***).

Upon a closer inspection of the BLI sensorgrams (***Figure 6—figure supplement 2B*** and ***Figure 7***), we noted that the entrapped ParB (E102A) did not noticeably dissociate from a closed DNA substrate when the probe was returned to a buffer-only solution (dissociation phase, k_{off} = 8.0 10^{-4} ± 1.9 × 10^{-4} s^{-1}, ***Figure 6—figure supplement 2B*** and ***Figure 7***). By contrast, entrapped ParB (WT) dissociated approximately 15-fold faster into buffer (k_{off} = 1.2 10^{-2} ± 3.7 × 10^{-4} s^{-1}). Further experiments showed that DNA entrapment by ParB (E102A), unlike ParB (WT), is more tolerant to high-salt solution (up to 1 M NaCl, ***Figure 7A***). Nevertheless, ParB (E102A)-CTP could not accumulate on a BamHI-restricted open DNA substrate (***Figure 7B,C***; ***Jalal et al., 2020c***), suggesting that ParB (E102A)-CTP, similar to ParB (WT), also form a closed clamp that runs off an open DNA end. Collectively, our results suggest that *parS* DNA and CTP induced a stably closed clamp conformation of ParB (E102A) in vitro.

To investigate the function of ParB (E102A) in vivo, we expressed a FLAG-tagged version of *parB* (E102A) from a vanillate-inducible promoter (P_{van}) in a *C. crescentus* strain where the native *parB* was under the control of a xylose-inducible promoter (P_{xyl}) (***Figure 8A***). Cells were depleted of the native ParB by adding glucose for 4 hr, subsequently vanillate was added for another hour before cells were fixed with formaldehyde for ChIP-seq. Consistent with the previous report (***Tran et al., 2018***), the ChIP-seq profile of FLAG-ParB (WT) showed an ~10 kb region of enrichment above background with clearly defined peaks that correspond to the positions of *parS* sites (***Figure 8A***). By contrast, the ChIP-seq profile of FLAG-ParB (E102A) is significantly reduced in height but has an extra peak over the *parB* coding sequence (***Figure 8A***, asterisk). The instability of FLAG-ParB (E102A) in its native *C. crescentus* host, and hence the reduced protein level (***Figure 8—figure supplement 1A***), might explain the overall lower height of its ChIP-seq profile (***Figure 8***). The reason for an extra peak over *parB* in the ChIP-seq profile of ParB (E102A) is still, however, unknown. We also noted that expressing ParB (E102A) could not rescue cells with depleted ParB (WT) (***Figure 8—figure supplement 2***). Again, due to the caveat of a lower ParB (E102A) protein level in *C. crescentus* (***Figure 8—figure supplement 1A***), we could not reliably link the in vitro properties of ParB (E102A) to its behaviors in the native host.

To overcome the caveat of protein instability, we instead investigated the spreading of ParB (WT) vs. ParB (E102A) from *parS* by analyzing the *C. crescentus* ParB/*parS* system in *Escherichia coli*. *E. coli* does not possess a ParA/ParB homolog nor a *parS*-like sequence, thus it serves as a suitable heterologous host. *C. crescentus parS* sites 3 and 4 were engineered onto the *E. coli* chromosome at the *ygcE* locus (***Figure 8B***). CFP-tagged ParB (WT/E102A) was expressed from a leaky lactose

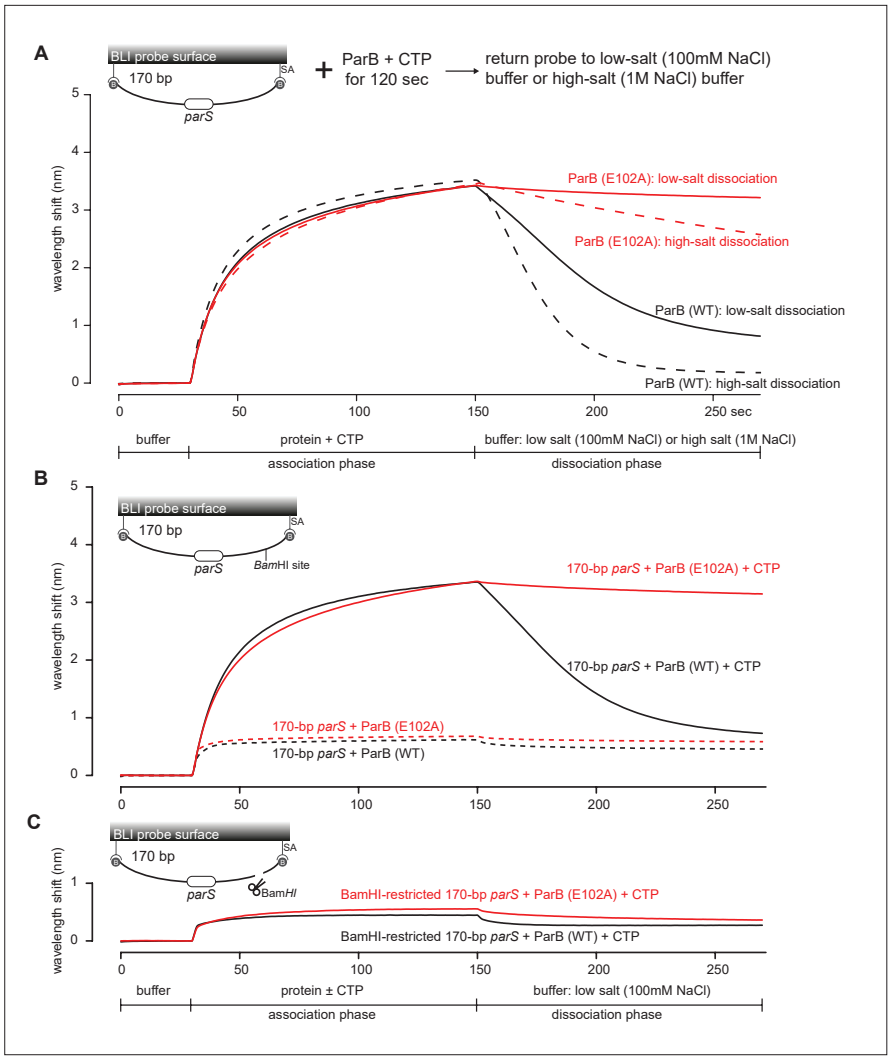

Figure 7. The DNA-entrapped ParB (E102A)-CTP clamp is resistant to high-salt conditions. (**A**) Biolayer interferometry (BLI) analysis of the interaction between a premix of 1 μM *C. crescentus* ParB (WT) or ParB (E102A) + 1 mM cytidine triphosphate (CTP) and 170 bp dual biotin-labeled *parS* DNA. For the dissociation phase, the probe was returned to a low-salt buffer that contains 100 mM NaCl (solid black or red lines) or to a high-salt buffer that contains 1 M NaCl (dashed black or red lines). The schematic diagram of the BLI probe shows a closed *parS* DNA substrate due to the interactions between a dual biotin-labeled DNA and the streptavidin (SA)-coated probe surface. (**B**) BLI analysis of the interaction between a premix of 1 μM *C. crescentus* ParB (WT) or ParB (E102A) + 1 mM CTP (solid lines) or –1 mM CTP (dashed lines) and 170 bp dual biotin-labeled *parS* DNA. (**C**) Same as panel (**B**) but immobilized DNA fragments have been restricted with BamHI before BLI analysis.

The online version of this article includes the following figure supplement(s) for figure 7:

Source data 1. Data used to generate ***Figure 7***.

promoter (P_{lac}, no IPTG was added) on a medium-copy-number plasmid. CFP-ParB (WT/E102A) was produced at the same level, as judged by an immunoblot (***Figure 8—figure supplement 1B***). We observed by ChIP-seq that CFP-ParB (WT) in an *E. coli* host spreads asymmetrically ~5 kb around *parS* sites. By contrast, the shape of the ParB (E102A) distribution was clearly different from that of ParB (WT); the profile was further expanded to both neighboring sides of *parS* (covering in total ~26 kb) at the expense of the enrichment at *parS* itself (***Figure 8B***). The more excessive spreading of ParB (E102A) might suggest that this variant, in the absence of CTP hydrolysis, persisted and perhaps slid further away from the loading site *parS* in *E. coli*. The reduced enrichment of ParB (E102A) at *parS* itself (***Figure 8B***) might be due to reduced cytoplasmic ParB (E102A) available to re-nucleate at *parS* and/or due to stably entrapped ParB (E102A) sterically hindering further nucleation events. We

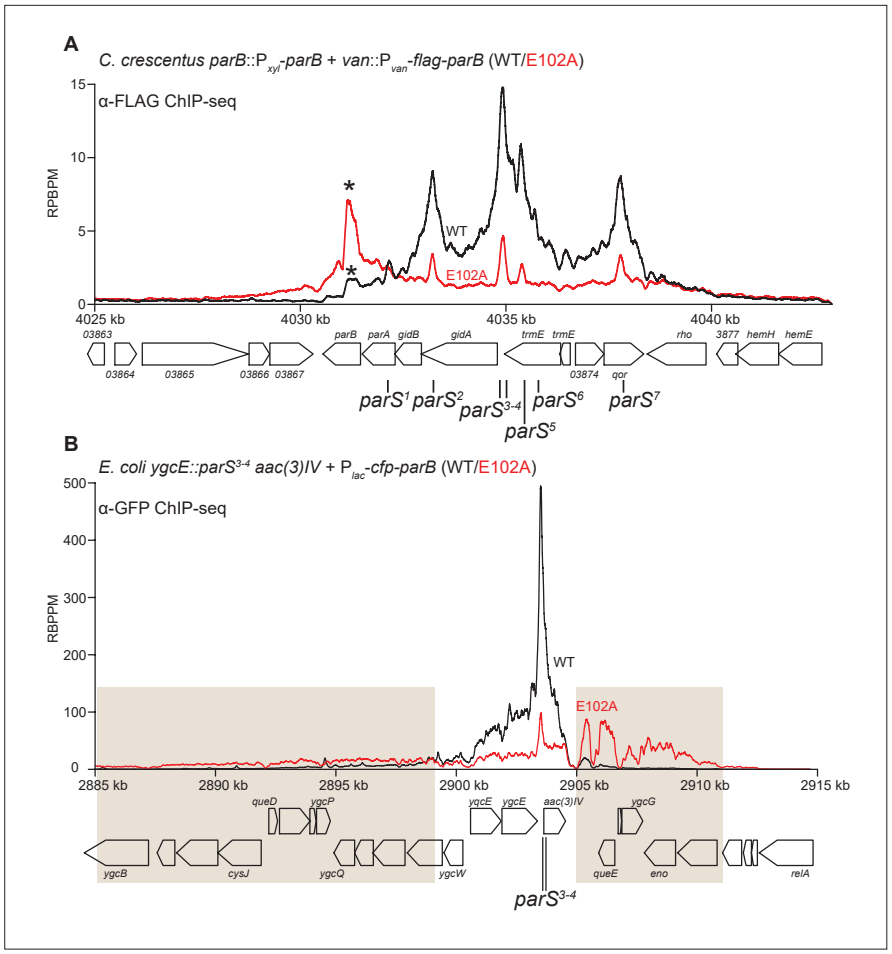

Figure 8. ParB (E102A) occupies a more extended DNA region surrounding *parS* sites than ParB (WT) in a heterologous host (*E. coli*) but not in the native host (*C. crescentus*). (**A**) ChIP-seq showed the distribution of FLAG-tagged ParB (WT) (black) and FLAG-ParB (E102A) (red) on *C. crescentus* chromosome between +4025 kb and +4042 kb. Underlying genes and *parS* sites are also shown below ChIP-seq profiles. An asterisk (*) indicates an extra peak over the *parB* coding sequence in the profile of FLAG-ParB (E102A). ChIP-seq signals were reported as the number of reads per base pair per million mapped reads (RPBPM). (**B**) ChIP-seq showed the distribution of CFP-tagged ParB (WT) (black) and CFP-ParB (E102A) (red) on an *E. coli* chromosome between +2885 kb and +2915 kb. *C. crescentus parS* sites 3 and 4 were engineered onto the *E. coli* chromosome at the *ygcE* locus. CFP-tagged ParB (WT/E102A) was expressed from a leaky lactose promoter (P_{lacI}, no IPTG was added) on a medium-copy-number plasmid. Shaded boxes show areas with more enrichment in the ChIP-seq profile of CFP-ParB (E102A) compared to that of CFP-ParB (WT).

The online version of this article includes the following figure supplement(s) for figure 8:

Figure supplement 1. Immunoblot analysis of ParB (WT) vs. E102A.

Figure supplement 1—source data 1. Original files and annotation of the uncropped blots used to generate ***Figure 8—figure supplement 1***.

Figure supplement 2. Expressing a FLAG-tagged version of ParB (E102A) could not complement the depletion of wild-type untagged ParB.

Figure supplement 2—source data 1. Original files, annotation of the full raw images, and data used to generate ***Figure 8—figure supplement 2***.

Figure supplement 3. The fluorescence intensity of CFP-ParB (E102A) foci in an *E. coli* heterologous host is higher than that of CFP-ParB (WT).

Figure supplement 3—source data 1. Data used to generate ***Figure 8—figure supplement 3***.

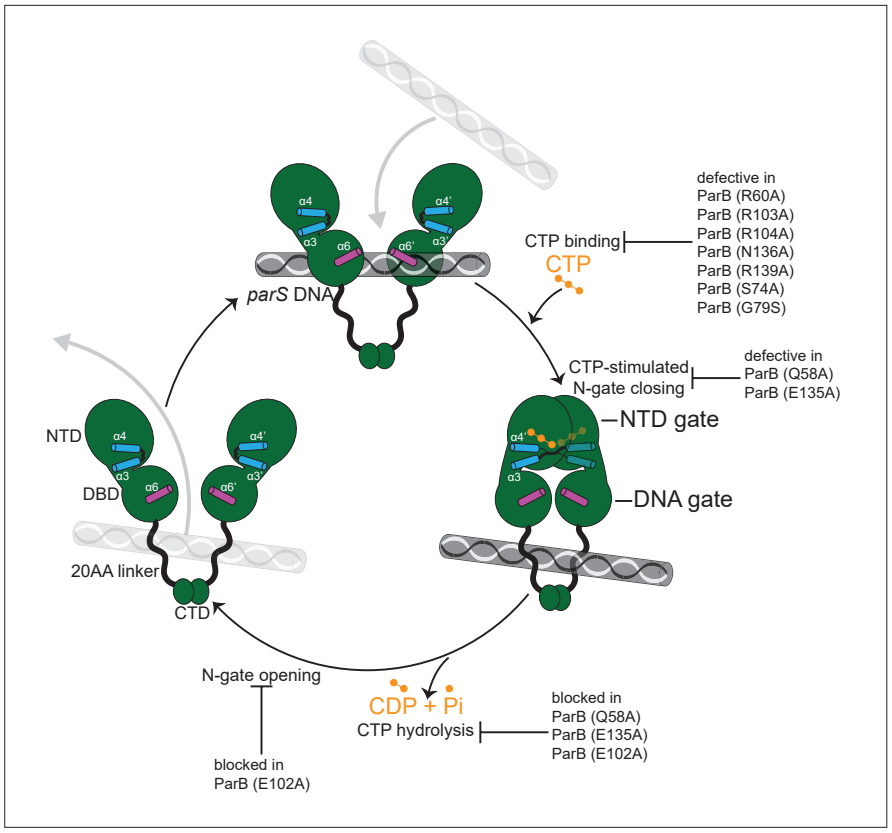

Figure 9. A model for *C. crescentus* ParB nucleating, sliding, and recycling cycle. ParB (dark green) consists of three domains: an N-terminal CTP-binding domain (NTD), a central *parS* DNA-binding domain (DBD), a C-terminal dimerization domain (CTD), and a 20 amino acid linker that connects the DBD and the CTD together. Nucleating ParB is an open clamp, in which *parS* DNA is captured at the DBD (the DNA-gate). Upon binding CTP (orange), the NTD self-dimerizes to close the NTD-gate of the clamp. CTP-binding and the exchange of helices α4 and α4′ (blue) stabilize this closed conformation. The DBD also move closer together to close the DNA-gate, potentially driving *parS* DNA into a compartment between the DNA-gate and the C-terminal domain. In the nucleotide-bound state, the DBD and the DNA-recognition helices (α6 and α6′, magenta) are incompatible with DNA binding. CTP hydrolysis and/or the release of hydrolytic products (CDP and inorganic phosphate Pi) may reopen the gates to release DNA. Substitutions that affect key steps in the CTP biding/hydrolysis cycle are also indicated on the schematic diagram.

also noted that the ChIP-seq profile of CFP-ParB (E102A) in *E. coli* is highly asymmetrical, with more enrichment in the 2905–2911 kb region than the 2885–2899 kb region (shaded areas, ***Figure 8B***). The asymmetrical spreading is possibly due to an impediment in one direction by roadblocks such as RNA polymerases or DNA-bound proteins, which have been shown previously to be able to interfere with ParB spreading (***Balaguer F de et al., 2021***; ***Breier and Grossman, 2007***; ***Jalal et al., 2020c***; ***Murray et al., 2006***; ***Rodionov et al., 1999***; ***Soh et al., 2019***).

Lastly, we quantified the fluorescence intensity of CFP-ParB (WT/E102A) foci inside cells and found a higher CFP signal for CFP-ParB (E102A) when compared with CFP-ParB (WT) (***Figure 8—figure supplement 3***). The higher intensity of the localizations could be due to more DNA-bound ParB (E102A) molecules surrounding the *parS* locus, which is consistent with the ChIP-seq observation showing CFP-ParB (E102A) occupying a more extended genomic area in *E. coli*. Altogether, at least in the heterologous *E. coli* host, the 'clamp-locked' phenotype of ParB (E102A) implies a possible role of CTP hydrolysis and/or the release of hydrolytic products in reopening wild-type ParB clamp to release DNA and to recycle ParB.

Discussion

In this study, we provide structural insights into the nucleating and sliding states of *C. crescentus* ParB. Nucleating ParB is an open clamp in which *parS* DNA is held tightly (nM affinity) at the DBD (***Tran et al., 2018***). The NTDs of nucleating ParB can adopt multiple alternative conformations, and crucially there is no contact between opposing NTDs. We liken this conformation of the NTD to that of an open gate (NTD-gate), through which *parS* DNA might gain access to the DBD (***Figure 9***). In the sliding state, CTP promotes the self-dimerization of the NTDs, thus closing the NTD-gate (***Figure 9***). Opposing DBDs also move approximately 10 Å closer together, bringing about a conformation that is DNA incompatible. Again, we liken this conformation of the DBDs to that of a closed gate (DNA-gate) (***Figure 9***). Overall, the DNA-gate closure explains how CTP binding might switch ParB from a nucleating to a sliding state.

Our data suggest that the closure of the two gates drives *parS* DNA into a compartment in between the DBD and the CTD. Previously, (***Soh et al., 2019***) compared the *B. subtilis* ParBΔCTD-CDP co-crystal structure to that of a *H. pylori* ParBΔCTD-*parS* complex and proposed that DNA must be entrapped in the DBD-CTD compartment (***Soh et al., 2019***). Here, the available structures of nucleating and sliding ParB from the same bacterial species enabled us to introduce a crosslinkable cysteine (L224C) at the DBD, and subsequently provided a direct evidence that the DBD-CTD compartment is the DNA-entrapping compartment. The linker that connects the DBD and the CTD together is not conserved in amino acid sequence among chromosomal ParB orthologs (***Figure 2—figure supplement 2***); however, we noted that the linker is invariably ~20 amino acid in length and positively charged lysines are over-represented (***Figure 2—figure supplement 2***). The biological significance of the linker length and its lysines, if any, is currently unknown. However, it is worth noting that a human PCNA clamp was proposed to recognize DNA via lysine-rich patches lining the clamp channel, and that these lysine residues help PCNA to slide by tracking the DNA backbone (***De March et al., 2017***). Investigating whether lysine residues in the DBD-CTD linker of ParB have a similar role is an important subject for the future.

If not already bound on DNA, the closed ParB clamp presumably cannot self-load onto *parS* owing to its inaccessible DBD. In this study, we showed that *parS* DNA promotes the CTP-dependent NTD-gate closure (***Figure 5B***), thus is likely a built-in mechanism to ensure gate closure results in a productive DNA entrapment. However, the molecular basis for the *parS*-enhanced gate closure remains unclear due to the lack of a crystal structure of *C. crescentus* apo-ParB, despite our extensive efforts.

CTP functions as a molecular latch that stabilizes the closure of the NTD-gate of ParB. Here, we provide evidence that CTP hydrolysis might contribute to reopening the closed NTD-gate. A previous structure of a *B. subtilis* ParBΔCTD-CDP complex also has its NTD-gate closed (CTP was hydrolyzed to CDP during the crystallization) (***Soh et al., 2019***), hence it is likely that both CTP hydrolysis and the subsequent release of hydrolytic products are necessary to reopen the gates. However, ParB has a weak to negligible affinity for CDP, hence the CDP-bound ParB species might be short-lived in solution and might not play a significant biological role. Once the clamp is reopened, entrapped DNA might escape via the same route that it first enters. Other well-characterized DNA clamps, for example, type II topoisomerases open their CTD to release trapped DNA. However, the CTDs of ParB are stably dimerized independently of *parS* and CTP (***Figure 5B***), hence we speculate that the CTD of ParB is likely to be impassable to the entrapped DNA. The released ParB clamp might re-nucleate on *parS* and bind CTP to close the gate, hence restarting the nucleation and sliding cycle. Such a recycling mechanism might provide a biological advantage since a ParB clamp once closed could otherwise become stably trapped on DNA and thus eventually diffuse too far from the *parS* locus, as evidenced by the ChIP-seq profile of the E102A variant (expressed in *E. coli*) that is defective in CTP hydrolysis (***Figure 8B***). However, how CTP hydrolysis contributes to the assembly of the centromere in *C. crescentus* is still unclear due to the caveat that ParB (E102A) is unstable in the native host.

The CTP-bound structure of a *M. xanthus* ParB-like protein, PadC, was solved to a high resolution (1.7 Å); however, PadC does not possess noticeable CTPase activity (***Osorio-Valeriano et al., 2019***). A co-crystal structure of *B. subtilis* ParB with CDP was also solved to a high resolution (1.8 Å) but represents a post-hydrolysis state instead. Lastly, our CTPγS-bound *C. crescentus* ParB crystals diffracted to 2.7 Å, thus preventing water molecules, including a potential catalytic water, from being assigned with confidence. Therefore, the mechanism of CTP hydrolysis by a ParB CTPase remains unresolved. Nevertheless, based on our alanine scanning experiment (***Figure 8***), we speculate that

Q58 (P-motif 1) and E102 (P-motif 2) might be involved in the catalytic mechanism of *C. crescentus* ParB. Supporting this view, we noted that an equivalent Q37 in *B. subtilis* ParB does not contact the hydrolytic product CDP, and this residue is not conserved in the catalytic-dead *M. xanthus* PadC (F308, which does not contact CTP, occupies this position in PadC instead) (***Figure 2—figure supplement 3***). E102 is also not conserved in M. *xanthus* PadC (F348 occupies this equivalent position) (***Figure 2—figure supplement 3***). Given that ParB is the founding member of a new CTPase protein family (***Jalal et al., 2020c***; ***Osorio-Valeriano et al., 2019***; ***Soh et al., 2019***), further studies are needed to fully understand the molecular mechanism of CTP hydrolysis so that the knowledge gained might be generalized to other CTPases.

Recently, an F-plasmid ParB was shown to form biomolecular condensates in vivo that might bridge distal $ParB_F$ dimers together (***Guilhas et al., 2020***; ***Walter et al., 2020***). If and how CTP binding/hydrolysis and the flexibility of the NTD contribute to this process is unclear and will be an important challenge for future studies. It is equally important to better understand the in vivo interaction between ParB and ParA now that CTP is in the picture. Recent in vitro work with $ParAB_F$ showed that two protomers of a single $ParB_F$ dimer interact with a $ParA_F$ dimer in the absence of CTP (***Taylor et al., 2021***). However, two ParBF protomers from two distinct dimers interact with a ParAF dimer in the presence of CTP and *parS* (***Taylor et al., 2021***). Which mode of action is dominant in vivo for a chromosomal ParAB*S* systems and whether interacting with ParA further facilitates CTP hydrolysis by ParB are still unknown. Future works will provide important insights to better understand the mechanism of ParA-directed DNA segregation.

Materials and methods

Key resources table

Reagent type (species) or resource	Designation	Source or reference	Identifiers	Additional information
Strain, strain background (*Escherichia coli*)	See ***Supplementary file 1A***	This paper		See ***Supplementary file 1A***
Strain, strain background (*Caulobacter crescentus*)	See ***Supplementary file 1A***	This paper		See ***Supplementary file 1A***
Recombinant DNA reagent	See ***Supplementary file 1B***	This paper		See ***Supplementary file 1B***
Sequence-based reagent	See ***Supplementary file 1B***	This paper		See ***Supplementary file 1B***
Antibody	Anti-GFP antibody (HRP) (Rabbit polyclonal)	Abcam	Cat# ab190584	Western blot (1:5000)
Antibody	Anti-GFP Sepharose beads	Abcam	Cat# ab69314	For ChIP-seq experiments
Antibody	Anti-FLAG antibody (HRP) (Mouse monoclonal)	Merck	Cat# A8592	Western blot (1:5000)
Antibody	Anti-FLAG M2 affinity agarose beads	Merck	Cat# A2220	For ChIP-seq experiments
Commercial assay or kit	Amersham Protran supported western blotting membranes, nitrocellulose	GE Healthcare	Cat# GE10600016	Pore size 0.45 µm, for DRaCALA assay
Commercial assay or kit	EnzChek Phosphate Assay Kit	ThermoFisher	Cat# E6646	
Commercial assay or kit	Gibson Assembly Master Mix	NEB	Cat# E2611S	
Commercial assay or kit	Gateway BP Clonase II enzyme mix	ThermoFisher	Cat# 11789020	
Commercial assay or kit	Dip-and-Read Streptavidin biosensors SAX2	Sartorius UK	Cat# 18-5019	
Commercial assay or kit	HisTrap High Performance column	GE Healthcare	Cat# GE17524801	
Commercial assay or kit	HisTrap Heparin High Performance column	GE Healthcare	Cat# GE17040601	
Commercial assay or kit	HiLoad 16/600 Superdex 200 pg column	GE Healthcare	Cat# GE28989335	

Continued on next page

Continued

Reagent type (species) or resource	Designation	Source or reference	Identifiers	Additional information
Commercial assay or kit	0.5 mL Zeba spin desalting columns	ThermoFisher	Cat# 89,882	7 K Da molecular weight cutoff
Peptide, recombinant protein	*Bam*HI-HF	NEB	Cat# R3136S	20,000 units/mL
Peptide, recombinant protein	*Hind*III-HF	NEB	Cat# R3104S	20,000 units/mL
Chemical compound, drug	Benzonase nuclease	Merck	Cat# E1014	250 units/µL
Chemical compound, drug	CTP	ThermoFisher	Cat# R0451	100 mM solution
Chemical compound, drug	CTP γ S	Jena Bioscience		Custom synthesis (purity ≥96%)
Chemical compound, drug	P^{32}- α -CTP	Perkin Elmer	Cat# BLU008H250UC	3,000 Ci/mmol, 10 mCi/mL, 250 µCi
Chemical compound, drug	Bismaleimidoethane (BMOE)	ThermoFisher	Cat# 22323	Dissolved in DMSO
Chemical compound, drug	AcTEV protease	ThermoFisher	Cat# 12575015	10 units/µL
Software, algorithm	BLItz Pro	Molecular Devices	Cat# 50-0156	Version 1.2
Software, algorithm	AIMLESS	***Evans and Murshudov, 2013***	http://www.ccp4.ac.uk/	Version 0.7.4
Software, algorithm	BUCCANEER	***Cowtan, 2006***	http://www.ccp4.ac.uk/	Version 1.6.10
Software, algorithm	Coot	***Emsley and Cowtan, 2004***	http://www.ccp4.ac.uk/	Version 0.9.5
Software, algorithm	CHAINSAW	***Stein, 2008***	http://www.ccp4.ac.uk/	Version 7.0.077
Software, algorithm	DIALS	***Winter et al., 2018***	https://dials.github.io	Version 3.1.0
Software, algorithm	Excel 2016	Microsoft	RRID:SCR_016137	Version 16.0
Software, algorithm	GraphPad Prism 8	GraphPad Software	RRID:SCR_002798	Version 8
Software, algorithm	ImageJ	NIH	https://imagej.net/ RRID:SCR_003070	Version 1.50
Software, algorithm	Image Studio Lite	LI-COR Biosciences	RRID:SCR_013715	Version 5.2
Software, algorithm	PISA	***Krissinel, 2015***	http://www.ccp4.ac.uk/pisa/	Version 2.1.1
Software, algorithm	MolProbity	***Williams et al., 2018***	http://molprobity.biochem.duke.edu/	Version 4.5
Software, algorithm	PHASER	***McCoy et al., 2007***	https://www.phenix-online.org/	Version 2.8.2
Software, algorithm	PyMOL	The PyMOL Molecular Graphics System	https://pymol.org/2/	Version 2.4.0
Software, algorithm	R	R Foundation for Statistical Computing	https://www.r-project.org/	Version 3.2.4
Software, algorithm	REFMAC5	***Murshudov et al., 1997***	http://www.ccp4.ac.uk/	Version 5.8.0258
Software, algorithm	SCULPTOR	***Bunkóczi and Read, 2011***	http://www.ccp4.ac.uk/	Version 0.0.3
Software, algorithm	XDS	***Kabsch, 2010***	https://xds.mr.mpg.de/	Version Nov11-2017
Software, algorithm	XIA2	***Winter, 2009***	https://xia2.github.io/index.html	Version 0.3.7.0

Strains, media, and growth conditions

E. coli and *C. crescentus* were grown in LB and PYE, respectively. When appropriate, media were supplemented with antibiotics at the following concentrations (liquid/solid media for *C. crescentus*; liquid/solid media for *E. coli* [μg/mL]): carbenicillin (*E. coli* only: 50/100), chloramphenicol (1/2; 20/30), kanamycin (5/25; 30/50), and oxytetracycline (1/2; 12/12).

Plasmids and strains construction

Construction of pET21b::*parBΔCTD-(his)6*

The coding sequence of a C-terminally truncated *C. crescentus* ParB (ParBΔCTD, lacking the last 50 amino acids) was amplified by PCR using primers NdeI-Ct-ParB-F and HindIII-Ct-ParB-R, and pET21b::*parB-(his)*$_6$ (**Lim et al., 2014**) as template. The pET21b plasmid backbone was generated via a double digestion of pET21b::*parB-(his)*$_6$ with NdeI and HindIII. The resulting backbone was subsequently gel-purified and assembled with the PCR-amplified fragment of *parBΔCTD* using a 2 X Gibson master mix (NEB). Gibson assembly was possible owing to a 23 bp sequence shared between the NdeI-HindIII-cut pET21b backbone and the PCR fragment. These 23 bp regions were incorporated during the synthesis of primers NdeI-Ct-ParB-F and HindIII-Ct-ParB-R. The resulting plasmids were sequence verified by Sanger sequencing (Eurofins, Germany).

Construction of pET21b::*parB-(his)6* (WT and mutants)

DNA fragments containing mutated *parB* genes (*parB**) were chemically synthesized (gBlocks, IDT). The NdeI-HindIII-cut pET21b plasmid backbone and *parB** gBlocks fragments were assembled together using a 2 X Gibson master mix (NEB). Gibson assembly was possible owing to a 23 bp sequence shared between the NdeI-HindIII-cut pET21b backbone and the gBlocks fragment. The resulting plasmids were sequenced verified by Sanger sequencing (Genewiz, UK).

pENTR::*attL1-parB* (WT/mutant)-*attL2*

The coding sequences of *C. crescentus* ParB (WT/mutants) were amplified by PCR and Gibson assembled into plasmid pENTR (Invitrogen) so that *parB* is flanked by phage attachment sites *attL1* and *attL2,* that is, Gateway cloning compatible. Correct mutations were verified by Sanger sequencing (Genewiz, UK).

pMT571-1xFLAG-DEST

Plasmid pMT571 (**Thanbichler et al., 2007**) was first digested with NdeI and NheI. The plasmid backbone was gel-purified and eluted in 50 μL of water. The FLAG-*attR1-ccdB*-chloramphenicol^R-*attR2* cassette was amplified by PCR using primers P1952 and P1953, and pML477 as template. The resulting PCR fragment and the NdeI-NheI-cut pMT571 were assembled together using a 2 X Gibson master mix (NEB). Gibson assembly was possible owing to a 23 bp sequence shared between the two DNA fragments. These 23 bp regions were incorporated during the primer design to amplify the FLAG-*attR1-ccdB*-chloramphenicol^R-*attR2* cassette. The resulting plasmid was sequence verified by Sanger sequencing (Eurofins, Germany).

pMT571-1xFLAG::*parB* (WT/mutants)

The *parB* (WT/mutant) genes were recombined into a Gateway-compatible destination vector pMT571-1xFLAG-DEST via LR recombination reaction (Invitrogen). For LR recombination reactions: 1 μL of purified pENTR::*attL1-parB* (WT/mutant)-*attL2* was incubated with 1 μL of the destination vector pMT571-1xFLAG-DEST, 1 μL of LR Clonase II master mix, and 2 μL of water in a total volume of 5 μL. The reaction was incubated for an hour at room temperature before being introduced into *E. coli* DH5α cells by heat-shock transformation. Cells were then plated out on LB agar+ tetracycline. Resulting colonies were restruck onto LB agar+ kanamycin and LB agar+ tetracycline. Only colonies that survived on LB+ tetracycline plates were subsequently used for culturing and plasmid extraction.

pKTN25::*cfp-parB* (WT/E102A)

The coding sequence of ParB (WT/E102A) was amplified by PCR using primers P3392 and P3393, and pET21b::*C. crescentus* ParB (WT/E102A)-His$_6$ as template. The resulting DNA was gel-purified

and assembled with a BglII-EcoRI-cut pVCFPN-5 (**Thanbichler et al., 2007**) using a 2 X Gibson master mix, to result in vectors where the *cfp* is fused to the 5′-end of *parB* (WT/E102A). Gibson assembly was possible owing to a 23 bp sequence shared between the BglII-EcoRI-cut pVCFPN-5 backbone and the PCR fragment. To create vectors for expressing ParB (WT/E102A) in *E. coli*, the *cfp-parB* (WT/E102A) segment was amplified by PCR using primers P3396 and P3397, and pVCFPN-5::*parB* (WT/E102A) as template. The resulting DNA was then assembled with a HindIII-ClaI-cut pKTN25 (**Karimova et al., 1998**) using a 2 X Gibson master mix. Gibson assembly was possible owing to a 23 bp sequence shared between the HindIII-ClaI-cut pKTN25 backbone and the PCR fragment. Note that the double digestion with HindIII and ClaI removed the T25-encoding gene from the pKTN25 plasmid. The resulting vectors pKTN25::*cfp-parB* (WT/E102A) allow for the expression of CFP-tagged ParB (WT/E102A) from an IPTG-inducible lactose promoter (P_{lac}).

Strains TLE1146 (AB1157 *ygcE*::260 bp *parS*::apramycin^R)

Lambda Red recombineering (**Datsenko and Wanner, 2000**) was used to insert a cassette consisting of 260 bp *C. crescentus parS*$^{3-4}$ sites and an apramycin antibiotic resistance gene *aac(3)IV* at the *ygcE* locus on the *E. coli* chromosome. To generate the first half of the cassette, DNA containing *parS*$^{3-4}$ sites was amplified by PCR using P1304 and P1305, and *C. crescentus* genomic DNA as template. To generate the second half of the cassette, DNA containing *aac(3)IV* was amplified by PCR using P1306 and P1307, and pIJ773 as template (**Gust et al., 2003**). The two resulting PCR products were gel-purified and joined together using a 2X Gibson master mix. The full-length 260 bp *parS*::apramycin^R cassette was further amplified by PCR using P1304 and P1307. P1304 and P1307 also carry 49 bp homology to the left or the right of the insertion point at the *ygcE* locus. The resulting PCR product was gel-extracted and electroporated into an arabinose-induced *E. coli* AB1157/pKD46 cells. Colonies that formed on LB+ apramycin were restruck on LB+ apramycin and incubated at 42 °C to cure of pKD46 plasmid. Finally, the correct insertion of the *parS*-apramycin^R cassette was verified by PCR and Sanger sequencing.

Strains AB1157 + pKTN25::*cfp-parB* (WT/E102A)

E. coli AB1157 cells were made competent chemically and were transformed with pKTN25-*cfp-parB* (WT/E102A) to result in strains TLE3077 and TLE3078, respectively.

Strains TLE1146 + pKTN25::*cfp-parB* (WT/E102A)

E. coli TLE1146 cells were made competent chemically and were transformed with pKTN25-*cfp-parB* (WT/E102A) to result in strains TLE3079 and TLE3080, respectively.

Strains MT148 + pMT571-1xFLAG::*parB* (WT/mutants)

Electro-competent *C. crescentus* CN15N cells were electroporated with pMT571-1xFLAG::ParB (WT/mutants) plasmid to allow for a single integration at the *vanA* locus. The correct integration was verified by PCR, and ΦCr30 phage lysate was prepared from this strain. Subsequently, *van*::P_{van}-*1xflag-parB* (WT/mutant), marked by a tetracycline^R cassette, was transduced by phage ΦCr30 into MT148 (**Thanbichler and Shapiro, 2006**) to result in strains TLS3050-TLS3060.

Protein overexpression and purification

Plasmid pET21b::*parBΔCTD-(his)*$_6$ was introduced into *E. coli* Rosetta (DE3)-competent cells (Merck) by heat-shock transformation. 40 mL overnight culture was used to inoculate 4 L of LB medium + carbenicillin + chloramphenicol. Cells were grown at 37 °C with shaking at 250 rpm to an OD_{600} of ~0.4. The culture was then left in the cold room to cool to 28 °C before isopropyl-β-D-thiogalactopyranoside (IPTG) was added at a final concentration of 0.5 mM. The culture was shaken for an additional 3 hr at 30 °C before cells were pelleted by centrifugation. Pelleted cells were resuspended in a buffer containing 100 mM Tris-HCl pH 8.0, 300 mM NaCl, 10 mM imidazole, 5 % (v/v) glycerol, 1 µL of Benzonase nuclease (Merck), 5 mg of lysozyme (Merck), and an EDTA-free protease inhibitor tablet (Merck). Cells were further lyzed by sonification (10 cycles of 15 s with 10 s resting on ice in between each cycle). The cell debris was removed through centrifugation at 28,000 g for 30 min and the supernatant was filtered through a 0.45 µm sterile filter (Sartorius). The protein was then loaded into a 1 mL HisTrap column (GE Healthcare) that had been pre-equilibrated with buffer A (100 mM Tris-HCl pH

8.0, 300 mM NaCl, 10 mM imidazole, and 5% [v/v] glycerol). Protein was eluted from the column using an increasing (10–500 mM) imidazole gradient in the same buffer. ParBΔCTD-containing fractions were pooled and diluted to a conductivity of 16 mS/cm before being loaded onto a 1 mL Heparin HP column (GE Healthcare) that had been pre-equilibrated with 100 mM Tris-HCl pH 8.0, 25 mM NaCl, and 5 % (v/v) glycerol. Protein was eluted from the Heparin column using an increasing (25 mM to 1 M NaCl) salt gradient in the same buffer. ParBΔCTD fractions were pooled and analyzed for purity by SDS-PAGE. Glycerol was then added to ParBΔCTD fractions to a final volume of 10 % (v/v), followed by 10 mM EDTA and 1 mM DTT. The purified ParBΔCTD was subsequently aliquoted, snap frozen in liquid nitrogen, and stored at –80 °C. ParBΔCTD that was used for X-ray crystallography was further polished via a gel-filtration column. To do so, purified ParBΔCTD was concentrated by centrifugation in an Amicon Ultra-15 3 kDa cutoff spin filters (Merck) before being loaded into a Superdex-200 gel filtration column (GE Healthcare). The gel filtration column was pre-equilibrated with buffer containing 10 mM Tris-HCl pH 8.0 and 250 mM NaCl. ParBΔCTD fractions were then pooled and analyzed for purity by SDS-PAGE.

Other C-terminally His-tagged ParB mutants were purified using HIS-Select Cobalt gravity flow columns as described previously (***Jalal et al., 2020b***). Purified proteins were desalted using a PD-10 column (Merck), concentrated using an Amicon Ultra-4 10 kDa cutoff spin column (Merck), and stored at –80 °C in a storage buffer (100 mM Tris-HCl pH 8.0, 300 mM NaCl, and 10 % [v/v] glycerol). Purified ParB mutants that were used in BMOE crosslinking experiments were buffer-exchanged and stored in a storage buffer supplemented with TCEP instead (100 mM Tris-HCl pH 7.4, 300 mM NaCl, 10 % [v/v] glycerol, and 1 mM TCEP).

Different batches of proteins were purified by ASBJ and NTT. Both biological (new sample preparations from a stock aliquot) and technical (same sample preparation) replicates were performed for assays in this study.

DNA preparation for crystallization, EnzChek phosphate release assay, and differential radical capillary action of ligand assay (DRaCALA)

A 22 bp palindromic single-stranded DNA fragment (*parS*: GGATGTTTCACGTGAAACA TCC) (100 µM in 1 mM Tris-HCl pH 8.0, 5 mM NaCl buffer) was heated at 98 °C for 5 min before being left to cool down to room temperature overnight to form 50 µM double-stranded *parS* DNA. The core sequence of *parS* is underlined.

Protein crystallization, structure determination, and refinement

Crystallization screens for the *C. crescentus* ParBΔCTD-*parS* complex were set up in sitting-drop vapor diffusion format in MRC2 96-well crystallization plates with drops comprising 0.3 µL precipitant solution and 0.3 µL of protein-DNA complex, and incubated at 293 K. His-tagged ParBΔCTD (~10 mg/mL) was mixed with a 22 bp *parS* duplex DNA at a molar ratio of 2:1.2 (protein monomer:DNA) in buffer containing 10 mM Tris-HCl pH 8.0 and 250 mM NaCl. The ParBΔCTD-*parS* crystals grew in a solution containing 20.5 % (w/v) PEG 3350, 260 mM magnesium formate, and 10 % (v/v) glycerol. After optimization of an initial hit, suitable crystals were cryoprotected with 20 % (v/v) glycerol and mounted in Litholoops (Molecular Dimensions) before flash-cooling by plunging into liquid nitrogen. X-ray data were recorded on beamline I04-1 at the Diamond Light Source (Oxfordshire, UK) using a Pilatus 6 M-F hybrid photon counting detector (Dectris), with crystals maintained at 100 K by a Cryojet cryocooler (Oxford Instruments). Diffraction data were integrated and scaled using XDS (***Kabsch, 2010***) via the XIA2 expert system (***Winter, 2009***) then merged using AIMLESS (***Evans and Murshudov, 2013***). Data collection statistics are summarized in ***Table 1***. The majority of the downstream analysis was performed through the CCP4i2 graphical user interface (***Potterton et al., 2018***).

The ParBΔCTD-*parS* complex crystallized in space group $P2_1$ with cell parameters of a = 54.3, b = 172.9, c = 72.9 Å, and β = 90.5° (***Table 1***). Analysis of the likely composition of the asymmetric unit (ASU) suggested that it contains four copies of the ParBΔCTD monomer and two copies of the 22 bp *parS* DNA duplex, giving an estimated solvent content of ~47 %.

Interrogation of the Protein Data Bank with the sequence of the *C. crescentus* ParBΔCTD revealed two suitable template structures for molecular replacement: apo-ParBΔCTD from *Thermus thermophilus* (***Leonard et al., 2004***) (PDB accession code: 1VZ0; 46 % identity over 82 % of the sequence) and *Helicobacter pylori* ParBΔCTD bound to *parS* DNA (***Chen et al., 2015***) (PDB accession code: 4UMK;

Table 1. X-ray data collection and processing statistics.

Structure	*C. crescentus* ParBΔCTD-*parS* complex	*C. crescentus* ParBΔCTD CTPγS complex
Data collection		
Diamond Light Source beamline	I04-1	I03
Wavelength (Å)	0.916	0.976
Detector	Pilatus 6 M-F	Eiger2 XE 16 M
Resolution range (Å)	72.96–2.90 (3.08–2.90)	70.59–2.73 (2.86–2.73)
Space group	$P2_1$	$P2_1$
Cell parameters (Å/°)	a = 54.3, b = 172.9, c = 72.9, β = 90.5	a = 69.5, b = 56.1, c = 71.4, β = 98.4
Total no. of measured intensities	198,135 (33888)	92,266 (8473)
Unique reflections	29,654 (4775)	14,516 (1756)
Multiplicity	6.7 (7.1)	6.4 (4.8)
Mean $I/\sigma(I)$	8.7 (1.4)	5.4 (1.2)
Completeness (%)	99.7 (100.0)	98.8 (91.4)
R_{merge}*	0.135 (1.526)	0.195 (1.210)
R_{meas}†	0.146 (1.646)	0.212 (1.357)
$CC_{½}$‡	0.997 (0.677)	0.991 (0.825)
Wilson B value (Å^2)	81.6	57.7
Refinement		
Resolution range (Å)	72.96–2.90 (2.98–2.90)	70.59–2.73 (2.80–2.73)
Reflections: working/free§	28155/1466	13824/678
R_{work}¶	0.240 (0.366)	0.248 (0.371)
R_{free}¶	0.263 (0.369)	0.284 (0.405)
Ramachandran plot: favored/allowed/disallowed** (%)	95.2/4.8/0	95.5/4.5/0
R.m.s. bond distance deviation (Å)	0.005	0.002
R.m.s. bond angle deviation (°)	1.05	1.19
Mean B factors: protein/DNA/other/ overall (Å^2)	98/74/-/92	81/-/61/77
PDB accession code	6 T1F	7BM8

Values in parentheses are for the outer resolution shell.

*$R_{merge} = \sum_{hkl} \sum_i |I_i(hkl) - \langle I(hkl)\rangle| / \sum_{hkl} \sum_i I_i(hkl)$.

† $R_{meas} = \sum_{hkl} [N/(N-1)]^{1/2} \times \sum_i |I_i(hkl) - \langle I(hkl)\rangle| / \sum_{hkl} \sum_i I_i(hkl)$, where $I_i(hkl)$ is the ith observation of reflection hkl, $\langle I(hkl)\rangle$ is the weighted average intensity for all observations i of reflection hkl, and N is the number of observations of reflection hkl.

‡$CC_{½}$ is the correlation coefficient between symmetry equivalent intensities from random halves of the dataset.

§The dataset was split into 'working' and 'free' sets consisting of 95% and 5% of the data, respectively. The free set was not used for refinement.

¶The R-factors R_{work} and R_{free} are calculated as follows: $R = \Sigma(|F_{obs} - F_{calc}|)/\Sigma|F_{obs}|$, where F_{obs} and F_{calc} are the observed and calculated structure factor amplitudes, respectively.

As calculated using MolProbity (*Chen et al., 2010***).

42 % identity over 75 % of the sequence). First, single subunits taken from these two entries were trimmed using SCULPTOR (***Bunkóczi and Read, 2011***) to retain the parts of the structure that aligned with the *C. crescentus* ParBΔCTD sequence, and then all side chains were truncated to Cβ atoms using CHAINSAW (***Stein, 2008***). Comparison of these templates revealed a completely different relationship between the NTD and the DBD. Thus, we prepared search templates based on the individual domains rather than the subunits. The pairs of templates for each domain were then aligned and used as ensemble search models in PHASER (***McCoy et al., 2007***). For the DNA component, an ideal B-form DNA duplex was generated in COOT (***Emsley and Cowtan, 2004***) from a 22 bp palindromic

sequence of *parS*. A variety of protocols were attempted in PHASER (**McCoy et al., 2007**), the best result was obtained by searching for the two DNA duplexes first, followed by four copies of the DBD, giving a TFZ score of 10.5 at 4.5 Å resolution. We found that the placement of the DBDs with respect to the DNA duplexes was analogous to that seen in the *H. pylori* ParBΔCTD-*parS* complex. After several iterations of rebuilding in COOT and refining the model in REFMAC5 (**Murshudov et al., 1997**), it was possible to manually dock one copy of the NTD template (from 1VZ0) into weak and fragmented electron density such that it could be joined to one of the DBDs. A superposition of this more complete subunit onto the other three copies revealed that in only one of these did the NTD agree with the electron density. Inspection of the remaining unfilled electron density showed evidence for the last two missing NTDs, which were also added by manual docking of the domain template (from 1VZ0). For the final stages, TLS refinement was used with a single TLS domain defined for each protein chain and for each DNA strand. The statistics of the final refined model, including validation output from MolProbity (**Chen et al., 2010**), are summarized in **Table 1**.

Crystallization screens for the *C. crescentus* ParBΔCTD-CTPγS complex crystal were also set up in sitting-drop vapor diffusion format in MRC2 96-well crystallization plates with drops comprising 0.3 µL precipitant solution and 0.3 µL of protein solution (~10 mg/mL) supplemented with 1 mM CTPγS (Jena Biosciences) and 1 mM $MgCl_2$, and incubated at 293 K. The ParBΔCTD-CTPγS crystals grew in a solution containing 15 % (w/v) PEG 3350, 0.26 M calcium acetate, 10 % (v/v) glycerol, 1 mM CTPγS, and 1 mM $MgCl_2$. Suitable crystals were cryoprotected with 20 % (v/v) glycerol and mounted in Litholoops (Molecular Dimensions) before flash-cooling by plunging into liquid nitrogen. X-ray data were recorded on beamline I03 at the Diamond Light Source (Oxfordshire, UK) using an Eiger2 XE 16 M hybrid photon counting detector (Dectris), with crystals maintained at 100 K by a Cryojet cryocooler (Oxford Instruments). Diffraction data were integrated and scaled using DIALS (**Winter et al., 2018**) via the XIA2 expert system (**Winter, 2009**), then merged using AIMLESS (**Evans and Murshudov, 2013**). Data collection statistics are summarized in **Table 1**. The majority of the downstream analysis was performed through the CCP4i2 graphical user interface (**Potterton et al., 2018**).

The ParBΔCTD-CTPγS complex crystallized in space group $P2_1$ with cell parameters of a = 69.5, b = 56.1, c = 71.4 Å, and β = 98.4° (**Table 1**). Analysis of the likely composition of the ASU suggested that it contains two copies of the ParBΔCTD monomer giving an estimated solvent content of ~50 %. Molecular replacement templates were generated from the ParBΔCTD-*parS* complex solved above. Attempts to solve the structure in PHASER using individual subunits taken from the latter in both conformations did not yield any convincing solutions, suggesting that the subunits had adopted new conformations. Given that the two subunit conformations observed in the previous structure differed largely in the relative dispositions of DBD and NTDs, we reasoned that a better outcome might be achieved by searching for the DBD and NTD separately. This time PHASER successfully placed two copies of each domain in the ASU such that they could be reconnected to give two subunits in a new conformation. The result was subjected to 100 cycles of jelly-body refinement in REFMAC5 before rebuilding with BUCCANEER (**Cowtan, 2006**) to give a model in which 77 % of the expected residues had been fitted into two chains and sequenced. The model was completed after further iterations of model editing in COOT and refinement with REFMAC5. In this case, TLS refinement was not used as this gave poorer validation results. The statistics of the final refined model, including validation output from MolProbity (**Chen et al., 2010**), are summarized in **Table 1**.

Measurement of protein-DNA interaction by BLI assay

BLI experiments were conducted using a BLItz system equipped with High Precision Streptavidin 2.0 (SAX2) Biosensors (Molecular Devices). BLItz monitors wavelength shifts (nm) resulting from changes in the optical thickness of the sensor surface during association or dissociation of the analyte. All BLI experiments were performed at 22 °C. The streptavidin biosensor was hydrated in a low-salt-binding buffer (100 mM Tris-HCl pH 8.0, 100 mM NaCl, 1 mM $MgCl_2$, and 0.005 % [v/v] Tween 20) for at least 10 min before each experiment. Biotinylated double-stranded DNA (dsDNA) was immobilized onto the surface of the SA biosensor through a cycle of baseline (30 s), association (120 s), and dissociation (120 s). Briefly, the tip of the biosensor was dipped into a binding buffer for 30 s to establish the baseline, then to 1 µM biotinylated dsDNA for 120 s, and finally to a low-salt-binding buffer for 120 s to allow for dissociation.

After the immobilization of DNA on the sensor, association reactions were monitored at 1 μM dimer concentration of ParB with an increasing concentration of CTP (0, 1, 5, 10, 50, 100, 500, 1000 μM) for 120 s. At the end of each binding step, the sensor was transferred into a protein-free binding buffer to follow the dissociation kinetics for 120 s. The sensor can be recycled by dipping in a high-salt buffer (100 mM Tris-HCl pH 8.0, 1000 mM NaCl, 10 mM EDTA, and 0.005 % [v/v] Tween 20) for 5 min to remove bound ParB.

For the dissociation step in the BLI experiments in ***Figure 7A***, the probe was returned to either a low-salt-binding buffer (100 mM Tris-HCl pH 8.0, 100 mM NaCl, 1 mM $MgCl_2$, and 0.005 % [v/v] Tween 20) for 30 s or a high-salt buffer (100 mM Tris-HCl pH 8.0, 1 M NaCl, 1 mM $MgCl_2$, and 0.005 % [v/v] Tween 20) for 30 s.

For experiments in ***Figure 7C***, DNA-coated tips were dipped into 300 μL of restriction solution (266 μL of water, 30 μL of 10× buffer CutSmart [NEB], and 3 μL of BamHI-HF restriction enzyme [20,000 units/mL]) for 2 hr at 37 °C. As a result, closed DNA on the BLI surface was cleaved to generate a free DNA end.

For experiments in ***Figure 5—figure supplement 4C***, purified ParB (Q35C) was incubated with 1 mM $CTP\gamma S$ in a binding buffer (100 mM Tris-HCl pH 7.4, 100 mM NaCl, 1 mM $MgCl_2$) for 30 min before BMOE was added to 1 mM. DTT was then added to the final concentration of 1 mM to quench the reaction. Subsequently, crosslinked ParB (Q35C) was buffer-exchanged into a storage buffer (100 mM Tris-HCl pH 8.0, 300 mM NaCl, and 10 % glycerol) using 0.5 mL Zeba desalting columns (ThermoFisher). BLITZ assays were performed using 5 μM dimer concentration of crosslinked ParB (Q35C) ± 1 mM CTP.

All sensorgrams recorded during BLI experiments were analyzed using the BLItz analysis software (BLItz Pro version 1.2, Molecular Devices) and replotted in R for presentation. Each experiment was triplicated, standard deviations were calculated in Excel, and a representative sensorgram is presented in ***Figure 5—figure supplement 4***, ***Figure 6—figure supplement 2***, and ***Figure 7***.

Differential radical capillary action of ligand assay (DRaCALA) or membrane-spotting assay

Purified *C. crescentus* ParB-His_6 (WT and mutants, at final concentrations of 0.7, 1.5, 3.1, 6.2, and 12.5 μM) were incubated with 5 nM radiolabeled P^{32}-α-CTP (Perkin Elmer), 30 μM of unlabeled CTP (ThermoFisher), and 1.5 μM of 22 bp *parS* DNA duplex in the binding buffer (100 mM Tris pH 8.0, 100 mM NaCl, and 10 mM $CaCl_2$) for 10 min at room temperature. 4 μL of samples were spotted slowly onto a nitrocellulose membrane and air-dried. The nitrocellulose membrane was wrapped in cling film before being exposed to a phosphor screen (GE Healthcare) for 2 min. Each DRaCALA assay was triplicated, and a representative autoradiograph was shown. Data were quantified using Multi-Gauge software 3.0 (Fujifilm), the bound fraction were quantified as described previously (***Roelofs et al., 2011***). Error bars represent standard deviations from triplicated experiments.

Measurement of CTPase activity by EnzChek phosphate release assay

CTP hydrolysis was monitored using an EnzCheck Phosphate Assay Kit (ThermoFisher). Samples (100 μL) containing a reaction buffer supplemented with an increasing concentration of CTP (0, 1, 5, 10, 50, 100, 500, and 1000 μM), 0.5 μM of 22 bp *parS* DNA, and 1 μM ParB (WT or mutants) were assayed in a Biotek EON plate reader at 25 °C for 8 hr with readings every minute. The reaction buffer (1 mL) typically contained 740 μL Ultrapure water, 50 μL 20× reaction buffer (100 mM Tris pH 8.0, 2 M NaCl, and 20 mM $MgCl_2$), 200 μL MESG substrate solution, and 10 μL purine nucleoside phosphorylase enzyme (one unit). Reactions with buffer only or buffer + CTP + 22 bp *parS* DNA only were also included as controls. The plates were shaken at 280 rpm continuously for 8 hr at 25 °C. The inorganic phosphate standard curve was also constructed according to the manual. The results were analyzed using Excel and the CTPase rates were calculated using a linear regression fitting in Excel. Error bars represent standard deviations from triplicated experiments.

In vitro crosslinking assay using a sulfhydryl-to-sulfhydryl crosslinker BMOE

A 50 μL mixture of 8 μM ParB mutants (with residues at specific positions in the NTD, DBD, or CTD substituted to cysteine) ± CTP (0–1000 μM) ± 0.5 μM DNA (a 22 bp linear DNA or a 3 kb circular *parS*/

scrambled *parS* plasmid) was assembled in a reaction buffer (10 mM Tris-HCl pH 7.4, 100 mM NaCl, and 1 mM $MgCl_2$) and incubated for 5 min at room temperature. BMOE (1 mM final concentration from a 20 mM stock solution) was then added, and the reaction was quickly mixed by three pulses of vortexing. SDS-PAGE sample buffer containing 23 mM β-mercaptoethanol was then added immediately to quench the crosslinking reaction. Samples were heated to 50 °C for 5 min before being loaded on 12 % Novex WedgeWell Tris-Glycine gels (ThermoFisher). Protein bands were stained with an InstantBlue Coomassie solution (Abcam) and band intensity was quantified using Image Studio Lite version 5.2 (LI-COR Biosciences). The crosslinked fractions were averaged, and their standard deviations from triplicated experiments were calculated in Excel.

For the experiment described in lane 8 of ***Figure 5C,D*** and ***Figure 5—figure supplement 2***, crosslinking reactions were performed as described above; however, the reaction was quenched using a quenching buffer (10 mM Tris-HCl pH 7.4, 100 mM NaCl, 1 mM $MgCl_2$, and 2.3 mM β-mercaptoethanol) instead. Subsequently, 1 µL of a non-specific DNA nuclease (Benzonase, 250 units/µL, Merck) was added, and the mixture was incubated at room temperature for a further 10 min before SDS-PAGE sample buffer was added. Samples were heated to 50 °C for 5 min before being loaded on 4–12% Novex WedgeWell Tris-Glycine gels (ThermoFisher).

For the experiments described in lane 8 of ***Figure 5—figure supplement 3A***, crosslinking and quenching reactions were performed as described above before 1 µL of TEV protease (10 units/µL, ThermoFisher) was added. The mixture was incubated at room temperature for a further 30 min before SDS-PAGE sample buffer was added. Samples were heated to 50 °C for 5 min before being loaded on 4–12% Novex WedgeWell Tris-Glycine gels.

For experiments described in lane 9 of ***Figure 5—figure supplement 3B***, proteins were released from gel slices by a 'crush & soak' method. Briefly, 10 gel slices were cut out from unstained SDS-PAGE gels and transferred to a 2 mL Eppendorf tube. Gel slices were frozen in liquid nitrogen and were crushed using a plastic pestle. The resulting paste was soaked in 500 µL of soaking buffer (10 mM Tris-HCl pH 8, 100 mM NaCl, 1 mM $MgCl_2$, and 1 µL of Benzonase [250 units/µL]), and the tube was incubated with rotation in a rotating wheel overnight. On the next day, the tube was centrifuged at 13,000 rpm for 5 min and the supernatant was transferred to a new 1.5 mL Eppendorf tube. The sample volume was reduced to ~50 µL using a SpeedVac vacuum concentrator before SDS-PAGE sample buffer was added in. The entire sample was loaded onto a single well of a 4–12% WedgeWell Tris-Glycine gel.

For experiments described in ***Figure 5—figure supplement 1***, a circular *parS*-harboring plasmid was linearized at an unique HindIII site by HindIII-HF restriction enzyme. After restriction, the linearized DNA was extracted with phenol-chloroform and ethanol precipitated before being used in double-crosslinking experiments.

Polyacrylamide gels were submerged in an InstantBlue Coomassie solution (Abcam) to stain for protein or in a SYBR Green solution (ThermoFisher) to stain for DNA. Denatured samples were also loaded on 1 % TAE agarose gels and electrophoresed at 120 V for 40 min at room temperature. Afterwards, agarose gels were submerged in a SYBR green solution to stain for DNA.

Chromatin immunoprecipitation with deep sequencing (ChIP-Seq)

α-FLAG ChIP-seq experiments on formaldehyde-fixed *C. crescentus* cells, and the subsequent data analysis was performed exactly as reported previously (***Tran et al., 2018***).

For ChIP-seq experiments on fixed *E. coli* cells, cells harboring pKTN25-*cfp-parB* (WT) or pKTN25-*cfp-parB* (E102A) were grown in 50 mL LB at 30 °C to mid exponential phase (OD_{600} ~ 0.4, no IPTG was added). Subsequently, formaldehyde is added to a final concentration of 1 % to fix the cells. All following steps are identical to ChIP-seq for *C. crescentus*, except that α-GFP antibody coupled to sepharose beads (Abcam) was used to immunoprecipitate CFP-tagged ParB–DNA complexes.

Each ChIP-seq experiment was duplicated using biological replicates. For a list of ChIP-seq experiments and their replicates in this study, see ***Supplementary file 1C***.

Immunoblot analysis

For western blot analysis, *C. crescentus* or *E. coli* cells were pelleted and resuspended directly in 1× SDS sample buffer, then heated to 95 °C for 5 min before loading. Total protein was run on 12 % Novex WedgeWell gels (ThermoFisher) at 150 V for separation. The same amount of total protein was

loaded on each lane. Resolved proteins were transferred to PVDF membranes using the Trans-Blot Turbo Transfer System (BioRad) and probed with either a 1:5000 dilution of α-FLAG HRP-conjugated antibody (Merck) antibody or a 1:5000 dilution of α-GFP HRP-conjugated antibody (Abcam). Blots were imaged after incubation with SuperSignal West PICO PLUS Chemiluminescent Substrate (ThermoFisher) using an Amersham Imager 600 (GE Healthcare). Western blot experiments were duplicated using biological replicates.

Fluorescence microscopy and image analysis

TLS3079 and TLS3080 were grown in M9 media supplemented with kanamycin (30 µg/mL) until OD_{600} ~ 0.1 prior to imaging. The expression of *cfp-parB (WT/E102A)* was induced with 0.25 mM IPTG in culture for 60 min before imaging. Imaging was performed using a wide-field epifluorescence microscope (Eclipse Ti-2E, Nikon) with a 63× oil immersion objective (NA 1.41), illumination from pE4000 light source, Hamamatsu Orca Flash 4.0 camera, and a motorized XY stage. Images were acquired using NIS-elements software (version 5.1). For imaging in the CFP channel, 435 nm excitation wavelength was used with 1 s exposure.

Images were analyzed using ImageJ, and plots were generated in GraphPad Prism 8.0. For extracting information on number of ParB foci per cell as well as intensity of ParB in foci, the following analysis pipeline was implemented: cell masks were generated in ImageJ using analyze particle function on thresholds applied to phase profiles. Separately, even background subtraction function was applied to fluorescence profiles, images were convolved (using 'subtract background' and 'convolve' functions in ImageJ), and regions of interest (ROIs) for foci were detected via an application of appropriate thresholds. The cell masks and ROIs thus detected were applied to the raw data (after background correction) to extract intensity information for each ROI as well as total cell fluorescence. ROI intensity was plotted as a ratio of intensity within a focus ($intensity_{loc}$) normalized to total cell intensity ($intensity_{total}$). Along with intensity measurement, number of foci per cell was also recorded. The pipeline was implemented in ImageJ using the following command:

```
n = roiManager("count");for (j = 0; j < n; j++){roiManager("Select", j);run("Analyze Particles...", "size = 3–10 circularity = 0.40–1.00 display summarize add");}
```

Acknowledgements

This study was funded by the Royal Society University Research Fellowship (URF\R\201020), BBSRC grant (BB/P018165/1), and a Wellcome Trust grant (221776/Z/20/Z, to TBKL), and a DST-SERB CRG grant 2019/003321 (to AB). ASBJ's PhD studentship was funded by the Royal Society (RG150448), and NTT was funded by the BBSRC grant-in-add (BBS/E/J/000PR9791 to the John Innes Centre). We thank Diamond Light Source for access to beamlines I04-1 and I03 under proposals MX13467 and MX18565 with support from the European Community's Seventh Framework Program (FP7/2007-2013) under Grant Agreement 283570 (BioStruct-X). We thank Stephan Gruber, Martin Thanbichler, and Manuel Osorio-Valeriano for sharing unpublished results.

Additional information

Funding

Funder	Grant reference number	Author
Royal Society	URF\R\201020	Tung B K Le
Royal Society	RG150448	Adam S B Jalal
Biotechnology and Biological Sciences Research Council	BB/P018165/1	Tung B K Le
Biotechnology and Biological Sciences Research Council	BBS/E/J/000PR9791	Ngat T Tran
Wellcome Trust	221776/Z/20/Z	Tung B K Le

Funder	Grant reference number	Author
Science and Engineering Research Board	2019/003321	Anjana Badrinarayanan

The funders had no role in study design, data collection and interpretation, or the decision to submit the work for publication.

Author contributions

Adam SB Jalal, Formal analysis, Investigation, Methodology, Writing – original draft; Ngat T Tran, Formal analysis, Investigation; Clare EM Stevenson, Investigation; Afroze Chimthanawala, Formal analysis, Investigation, Writing – review and editing; Anjana Badrinarayanan, Formal analysis, Investigation, Supervision, Writing – review and editing; David M Lawson, Formal analysis, Investigation, Methodology, Supervision, Writing – original draft; Tung BK Le, Conceptualization, Formal analysis, Funding acquisition, Investigation, Methodology, Supervision, Visualization, Writing – original draft, Writing – review and editing

Author ORCIDs

Adam SB Jalal http://orcid.org/0000-0001-7794-8834
Ngat T Tran http://orcid.org/0000-0002-7186-3976
Anjana Badrinarayanan http://orcid.org/0000-0001-5520-2134
David M Lawson http://orcid.org/0000-0002-7637-4303
Tung BK Le http://orcid.org/0000-0003-4764-8851

Decision letter and Author response

Decision letter https://doi.org/10.7554/69676.sa1
Author response https://doi.org/10.7554/69676.sa2

Additional files

Supplementary files

- Supplementary file 1. (A) Bacterial strains used in this study. (B) Plasmids, DNA, and protein sequences used in this study. (C) ChIP-seq datasets generated in this study.
- Transparent reporting form

Data availability

The accession number for the sequencing data reported in this paper is GSE168968. Atomic coordinates for protein crystal structures reported in this paper were deposited in the RCSB Protein Data Bank with the accession number 6T1F and 7BM8. All of these sequencing and X-ray crystallography data are already open to the public. All other data generated or analyzed during this study are included in the manuscript.

The following dataset was generated:

Author(s)	Year	Dataset title	Dataset URL	Database and Identifier
Le TBK	2021	A CTP-dependent gating mechanism enables ParB spreading on DNA in Caulobacter crescentus	https://www.ncbi.nlm.nih.gov/geo/query/acc.cgi?acc=GSE168968	NCBI Gene Expression Omnibus, GSE168968
Jalal ASB, Pastrana CL, Tran NT, Stevenson CEM, Lawson DM, Moreno-Herrero F, Le TBK	2020	Crystal structure of the C-terminally truncated chromosome-partitioning protein ParB from Caulobacter crescentus complexed to the centromeric parS site	https://www.rcsb.org/structure/6T1F	RCSB Protein Data Bank, 6T1F

Continued on next page

Continued

Author(s)	Year	Dataset title	Dataset URL	Database and Identifier
Jalal ASB, Pastrana CL, Tran NT, Stevenson CEM, Lawson DM, Moreno-Herrero F, Le TBK	2021	Crystal structure of the C-terminally truncated chromosome-partitioning protein ParB from Caulobacter crescentus complexed with CTP-gamma-S	https://www.rcsb.org/structure/7BM8	RCSB Protein Data Bank, 7BM8

References

Balaguer F de A, Aicart-Ramos C, Fisher GL, de Bragança S, Martin-Cuevas EM, Pastrana CL, Dillingham MS, Moreno-Herrero F. 2021. CTP promotes efficient ParB-dependent DNA condensation by facilitating one-dimensional diffusion from parS. *eLife* **10**: e67554. DOI: https://doi.org/10.7554/eLife.67554, PMID: 34250901

Breier AM, Grossman AD. 2007. Whole-genome analysis of the chromosome partitioning and sporulation protein Spo0J (ParB) reveals spreading and origin-distal sites on the *Bacillus subtilis* chromosome. *Molecular Microbiology* **64**: 703–718. DOI: https://doi.org/10.1111/j.1365-2958.2007.05690.x, PMID: 17462018

Broedersz CP, Wang X, Meir Y, Loparo JJ, Rudner DZ, Wingreen NS. 2014. Condensation and localization of the partitioning protein ParB on the bacterial chromosome. *PNAS* **111**: 8809–8814. DOI: https://doi.org/10.1073/pnas.1402529111, PMID: 24927534

Bunkóczi G, Read RJ. 2011. Improvement of molecular-replacement models with Sculptor. *Acta Crystallogr D Biol Crystallogr* **67**: 303–312. DOI: https://doi.org/10.1107/S0907444910051218, PMID: 21460448

Chen VB, Arendall WB, Headd JJ, Keedy DA, Immormino RM, Kapral GJ, Murray LW, Richardson JS, Richardson DC. 2010. MolProbity: all-atom structure validation for macromolecular crystallography. *Acta Crystallogr D Biol Crystallogr* **66**: 12–21. DOI: https://doi.org/10.1107/S0907444909042073, PMID: 20057044

Chen BW, Lin MH, Chu CH, Hsu CE, Sun YJ. 2015. Insights into ParB spreading from the complex structure of Spo0J and parS. PNAS **112**: 6613–6618. DOI: https://doi.org/10.1073/pnas.1421927112, PMID: 25964325

Cowtan K. 2006. The Buccaneer software for automated model building. 1. Tracing protein chains. *Acta Crystallogr D Biol Crystallogr* **62**: 1002–1011. DOI: https://doi.org/10.1107/S0907444906022116, PMID: 16929101

Datsenko KA, Wanner BL. 2000. One-step inactivation of chromosomal genes in *Escherichia coli* K-12 using PCR products. PNAS **97**: 6640–6645. DOI: https://doi.org/10.1073/pnas.120163297, PMID: 10829079

De March M, Merino N, Barrera-Vilarmau S, Crehuet R, Onesti S, Blanco FJ, De Biasio A. 2017. Structural basis of human PCNA sliding on DNA. *Nature Communications* **8**: 13935. DOI: https://doi.org/10.1038/ncomms13935, PMID: 28071730

Donczew M, Mackiewicz P, Wróbel A, Flärdh K, Zakrzewska-Czerwińska J, Jakimowicz D. 2016. ParA and ParB coordinate chromosome segregation with cell elongation and division during Streptomyces sporulation. *Open Biology* **6**: 150263. DOI: https://doi.org/10.1098/rsob.150263, PMID: 27248800

Emsley P, Cowtan K. 2004. Coot: model-building tools for molecular graphics. *Acta Crystallogr D Biol Crystallogr* **60**: 2126–2132. DOI: https://doi.org/10.1107/S0907444904019158, PMID: 15572765

Evans PR, Murshudov GN. 2013. How good are my data and what is the resolution. *Acta Cryst D* **69**: 1204–1214. DOI: https://doi.org/10.1107/S0907444913000061, PMID: 23793146

Figge RM, Easter J, Gober JW. 2003. Productive interaction between the chromosome partitioning proteins, ParA and ParB, is required for the progression of the cell cycle in Caulobacter crescentus. *Mol Microbiol* **47**: 1225–1237. DOI: https://doi.org/10.1046/j.1365-2958.2003.03367.x, PMID: 12603730

Fisher GL, Pastrana CL, Higman VA, Koh A, Taylor JA, Butterer A, Craggs T, Sobott F, Murray H, Crump MP, Moreno-Herrero F, Dillingham MS. 2017. The structural basis for dynamic DNA binding and bridging interactions which condense the bacterial centromere. *eLife* **6**: 28086. DOI: https://doi.org/10.7554/eLife.28086, PMID: 29244022

Fogel MA, Waldor MK. 2006. A dynamic, mitotic-like mechanism for bacterial chromosome segregation. *Genes Dev* **20**: 3269–3282. DOI: https://doi.org/10.1101/gad.1496506, PMID: 17158745

Graham TGW, Wang X, Song D, Etson CM, van OA, Rudner DZ, Loparo JJ. 2014. ParB spreading requires DNA bridging. *Genes Dev* **28**: 1228–1238. DOI: https://doi.org/10.1101/gad.242206.114, PMID: 24829297

Guilhas B, Walter JC, Rech J, David G, Walliser NO, Palmeri J, Mathieu-Demaziere C, Parmeggiani A, Bouet JY, Le Gall A, Nollmann M. 2020. ATP-driven separation of liquid phase condensates in bacteria. *Mol Cell* **79**: 293–303. DOI: https://doi.org/10.1016/j.molcel.2020.06.034, PMID: 32679076

Gust B, Challis GL, Fowler K, Kieser T, Chater KF. 2003. PCR-targeted Streptomyces gene replacement identifies a protein domain needed for biosynthesis of the sesquiterpene soil odor geosmin. PNAS **100**: 1541–1546. DOI: https://doi.org/10.1073/pnas.0337542100, PMID: 12563033

Harms A, Treuner-Lange A, Schumacher D, Søgaard-Andersen L. 2013. Tracking of chromosome and replisome dynamics in Myxococcus xanthus reveals a novel chromosome arrangement. *PLOS Genetics* **9**: e1003802. DOI: https://doi.org/10.1371/journal.pgen.1003802, PMID: 24068967

Hwang LC, Vecchiarelli AG, Han YW, Mizuuchi M, Harada Y, Funnell BE, Mizuuchi K. 2013. ParA-mediated plasmid partition driven by protein pattern self-organization. *The EMBO Journal* **32**: 1238–1249. DOI: https://doi.org/10.1038/emboj.2013.34, PMID: 23443047

Ireton K, Gunther NW, Grossman AD. 1994. spo0J is required for normal chromosome segregation as well as the initiation of sporulation in *Bacillus subtilis*. *Journal of Bacteriology* **176**: 5320–5329. DOI: https://doi.org/10.1128/jb.176.17.5320-5329.1994, PMID: 8071208

Jakimowicz D, Chater K, Zakrzewska-Czerwi´nska J. 2002. The ParB protein of Streptomyces coelicolor A3(2) recognizes a cluster of parS sequences within the origin-proximal region of the linear chromosome. *Molecular Microbiology* **45**: 1365–1377. DOI: https://doi.org/10.1046/j.1365-2958.2002.03102.x, PMID: 12207703

Jalal ASB, Le TBK. 2020a. Bacterial chromosome segregation by the ParABS system. *Open Biology* **10**: 200097. DOI: https://doi.org/10.1098/rsob.200097, PMID: 32543349

Jalal ASB, Tran NT, Stevenson CE, Chan EW, Lo R, Tan X, Noy A, Lawson DM, Le TBK. 2020b. Diversification of DNA-binding specificity by permissive and specificity-switching mutations in the ParB/Noc protein family. *Cell Reports* **32**: 107928. DOI: https://doi.org/10.1016/j.celrep.2020.107928, PMID: 32698006

Jalal ASB, Tran NT, Le TBK. 2020c. ParB spreading on DNA requires cytidine triphosphate in vitro. *eLife* **9**: e53515. DOI: https://doi.org/10.7554/eLife.53515, PMID: 32077854

Kabsch W. 2010. Xds. *Acta Crystallographica Section D Biological Crystallography* **66**: 125–132. DOI: https://doi.org/10.1107/S0907444909047337

Karimova G, Pidoux J, Ullmann A, Ladant D. 1998. A bacterial two-hybrid system based on a reconstituted signal transduction pathway. *PNAS* **95**: 5752–5756. DOI: https://doi.org/10.1073/pnas.95.10.5752, PMID: 9576956

Kawalek A, Bartosik AA, Glabski K, Jagura-Burdzy G. 2018. *Pseudomonas aeruginosa* partitioning protein ParB acts as a nucleoid-associated protein binding to multiple copies of a parS-related motif. *Nucleic Acids Res* **46**: 4592–4606. DOI: https://doi.org/10.1093/nar/gky257, PMID: 29648658

Krissinel E. 2015. Stock-based detection of protein oligomeric states in jSPISA. *Nucleic Acids Research* **43**: 314-319. DOI: https://doi.org/10.1093/nar/gkv314, PMID: 25908787

Leonard TA, Butler PJG, Löwe J. 2004. Structural analysis of the chromosome segregation protein Spo0J from Thermus thermophilus. *Mol Microbiol* **53**: 419–432. DOI: https://doi.org/10.1111/j.1365-2958.2004.04133.x, PMID: 15228524

Leonard TA, Butler PJ, Löwe J. 2005. Bacterial chromosome segregation: structure and DNA binding of the Soj dimer-a conserved biological switch. *EMBO J* **24**: 270–282. DOI: https://doi.org/10.1038/sj.emboj.7600530, PMID: 15635448

Lim HC, Surovtsev IV, Beltran BG, Huang F, Bewersdorf J, Jacobs-Wagner C. 2014. Evidence for a DNA-relay mechanism in ParABS-mediated chromosome segregation. *eLife* **3**: e02758. DOI: https://doi.org/10.7554/eLife.02758, PMID: 24859756

Lin DC, Grossman AD. 1998. Identification and characterization of a bacterial chromosome partitioning site. *Cell* **92**: 675–685. DOI: https://doi.org/10.1016/S0092-8674(00)81135-6, PMID: 9506522

Livny J, Yamaichi Y, Waldor MK. 2007. Distribution of centromere-like parS sites in bacteria: insights from comparative genomics. *J Bacteriol* **189**: 8693–8703. DOI: https://doi.org/10.1128/JB.01239-07, PMID: 17905987

McCoy AJ, Grosse-Kunstleve RW, Adams PD, Winn MD, Storoni LC, Read RJ. 2007. Phaser crystallographic software. *Journal of Applied Crystallography* **40**: 658–674. DOI: https://doi.org/10.1107/S0021889807021206, PMID: 19461840

Mohl DA, Easter J, Gober JW. 2001. The chromosome partitioning protein, ParB, is required for cytokinesis in Caulobacter crescentus. *Molecular Microbiology* **42**: 741–755. DOI: https://doi.org/10.1046/j.1365-2958.2001.02643.x, PMID: 11722739

Murray H, Ferreira H, Errington J. 2006. The bacterial chromosome segregation protein Spo0J spreads along DNA from parS nucleation sites. *Molecular Microbiology* **61**: 1352–1361. DOI: https://doi.org/10.1111/j.1365-2958.2006.05316.x, PMID: 16925562

Murshudov GN, Vagin AA, Dodson EJ. 1997. Refinement of macromolecular structures by the maximum-likelihood method. *Acta Crystallographica Section D Biological Crystallography* **53**: 240–255. DOI: https://doi.org/10.1107/S0907444996012255

Osorio-Valeriano M, Altegoer F, Steinchen W, Urban S, Liu Y, Bange G, Thanbichler M. 2019. ParB-type DNA segregation proteins are CTP-dependent molecular switches. *Cell* **179**: 1512–1524. DOI: https://doi.org/10.1016/j.cell.2019.11.015, PMID: 31835030

Potterton L, Agirre J, Ballard C, Cowtan K, Dodson E, Evans PR, Jenkins HT, Keegan R, Krissinel E, Stevenson K, Lebedev A, McNicholas SJ, Nicholls RA, Noble M, Pannu NS, Roth C, Sheldrick G, Skubak P, Turkenburg J, Uski V, et al. 2018. Ccp4i2: The new graphical user interface to the CCP4 program suite. *Acta Crystallographica. Section D, Structural Biology* **74**: 68–84. DOI: https://doi.org/10.1107/S2059798317016035, PMID: 29533233

Rodionov O, Lobocka M, Yarmolinsky M. 1999. Silencing of genes flanking the P1 plasmid centromere. *Science* **283**: 546–549. DOI: https://doi.org/10.1126/science.283.5401.546, PMID: 9915704

Roelofs KG, Wang J, Sintim HO, Lee VT. 2011. Differential radial capillary action of ligand assay for high-throughput detection of protein-metabolite interactions. PNAS **108**: 15528–15533. DOI: https://doi.org/10.1073/pnas.1018949108, PMID: 21876132

Sanchez A, Cattoni DI, Walter JC, Rech J, Parmeggiani A, Nollmann M, Bouet JY. 2015. Stochastic self-assembly of ParB proteins builds the bacterial DNA segregation apparatus. *Cell Systems* **1**: 163–173. DOI: https://doi.org/10.1016/j.cels.2015.07.013, PMID: 27135801

Soh YM, Davidson IF, Zamuner S, Basquin J, Bock FP, Taschner M, Veening JW, De Los Rios P, Peters JM, Gruber S. 2019. Self-organization of parS centromeres by the ParB CTP hydrolase. *Science* **366**: 1129–1133. DOI: https://doi.org/10.1126/science.aay3965, PMID: 31649139

Stein N. 2008. CHAINSAW : a program for mutating pdb files used as templates in molecular replacement. *Journal of Applied Crystallography* **41**: 641–643. DOI: https://doi.org/10.1107/S0021889808006985

Taylor JA, Pastrana CL, Butterer A, Pernstich C, Gwynn EJ, Sobott F, Moreno-Herrero F, Dillingham MS. 2015. Specific and non-specific interactions of ParB with DNA: implications for chromosome segregation. *Nucleic Acids Res* **43**: 719–731. DOI: https://doi.org/10.1093/nar/gku1295, PMID: 25572315

Taylor JA, Seol Y, Budhathoki J, Neuman KC, Mizuuchi K. 2021. CTP and parS coordinate ParB partition complex dynamics and ParA-ATPase activation for ParABS-mediated DNA partitioning. *eLife* **10**: e65651. DOI: https://doi.org/10.7554/eLife.65651

Thanbichler M, Shapiro L. 2006. MipZ, a spatial regulator coordinating chromosome segregation with cell division in Caulobacter. *Cell* **126**: 147–162. DOI: https://doi.org/10.1016/j.cell.2006.05.038, PMID: 16839883

Thanbichler M, Iniesta AA, Shapiro L. 2007. A comprehensive set of plasmids for vanillate- and xylose-inducible gene expression in Caulobacter crescentus. *Nucleic Acids Research* **35**: e137. DOI: https://doi.org/10.1093/nar/gkm818, PMID: 17959646

Tran NT, Stevenson CE, Som NF, Thanapipatsiri A, Jalal ASB, Le TBK. 2018. Permissive zones for the centromere-binding protein ParB on the Caulobacter crescentus chromosome. *Nucleic Acids Research* **46**: 1196–1209. DOI: https://doi.org/10.1093/nar/gkx1192, PMID: 29186514

Vecchiarelli AG, Mizuuchi K, Funnell BE. 2012. Surfing biological surfaces: Exploiting the nucleoid for partition and transport in bacteria. *Molecular Microbiology* **86**: 513–523. DOI: https://doi.org/10.1111/mmi.12017, PMID: 22934804

Vecchiarelli AG, Neuman KC, Mizuuchi K. 2014. A propagating atpase gradient drives transport of surface-confined cellular cargo. PNAS **111**: 4880–4885. DOI: https://doi.org/10.1073/pnas.1401025111, PMID: 24567408

Walter JC, Rech J, Walliser NO, Dorignac J, Geniet F, Palmeri J, Parmeggiani A, Bouet JY. 2020. Physical modeling of a sliding clamp mechanism for the spreading of ParB at short genomic distance from bacterial centromere sites. *IScience* **23**: 101861. DOI: https://doi.org/10.1016/j.isci.2020.101861, PMID: 33319179

Williams CJ, Headd JJ, Moriarty NW, Prisant MG, Videau LL, Deis LN, Verma V, Keedy DA, Hintze BJ, Chen VB, Jain S, Lewis SM, Arendall WB, Snoeyink J, Adams PD, Lovell SC, Richardson JS, Richardson DC. 2018. Molprobity: More and better reference data for improved all-atom structure validation. *Protein Science* **27**: 293–315. DOI: https://doi.org/10.1002/pro.3330, PMID: 29067766

Winter G. 2009. xia2 : an expert system for macromolecular crystallography data reduction. *Journal of Applied Crystallography* **43**: 186–190. DOI: https://doi.org/10.1107/S0021889809045701

Winter G, Waterman DG, Parkhurst JM, Brewster AS, Gildea RJ, Gerstel M, Fuentes-Montero L, Vollmar M, Michels-Clark T, Young ID, Sauter NK, Evans G. 2018. Dials: Implementation and evaluation of a new integration package. *Acta Crystallographica Section D, Structural Biology* **74**: 85–97. DOI: https://doi.org/10.1107/S2059798317017235, PMID: 29533234

Molecular Cell

Article

CTP regulates membrane-binding activity of the nucleoid occlusion protein Noc

Graphical abstract

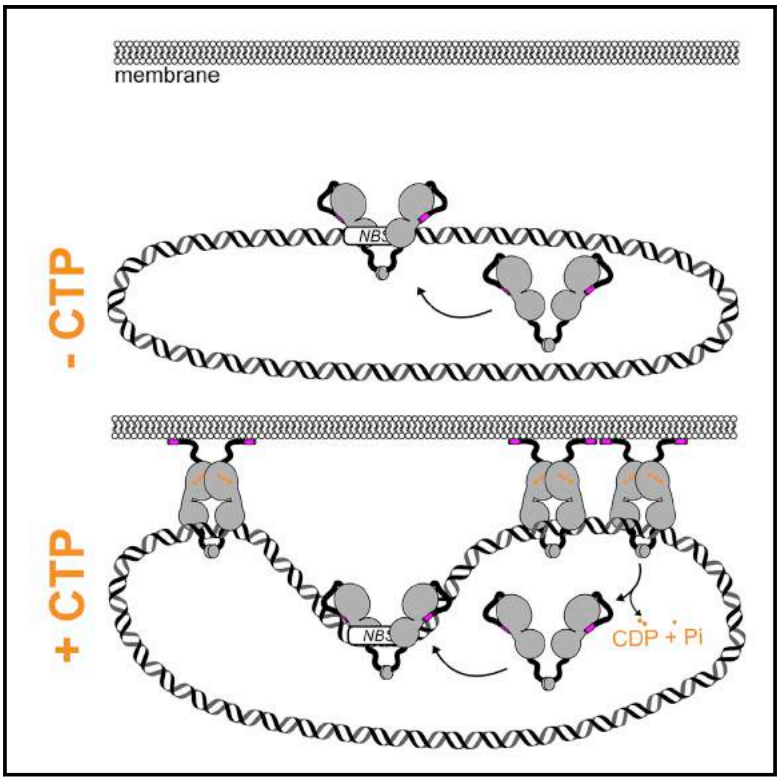

Highlights

- CTP is required for Noc to form a higher-order nucleoprotein complex on DNA
- CTP binding switches DNA-entrapped Noc to a membrane-active state
- CTP hydrolysis likely reverses the association between Noc-DNA and the membrane
- The membrane-targeting helix adopts an autoinhibitory conformation in apo-Noc

Authors

Adam S.B. Jalal, Ngat T. Tran, Ling J. Wu, ..., David M. Lawson, Jeff Errington, Tung B.K. Le

Correspondence

tung.le@jic.ac.uk

In brief

Jalal et al. report that the nucleoid occlusion protein Noc is a CTPase enzyme whose membrane-binding activity is directly regulated by CTP. CTP binding switches the Noc-DNA complex from a membrane-inactive state to an active state, thus ensuring productive recruitment of DNA to the bacterial cell membrane.

Jalal et al., 2021, Molecular Cell *81*, 1–14
September 2, 2021
https://doi.org/10.1016/j.molcel.2021.06.025

CellPress

Please cite this article in press as: Jalal et al., CTP regulates membrane-binding activity of the nucleoid occlusion protein Noc, Molecular Cell (2021), https://doi.org/10.1016/j.molcel.2021.06.025

Molecular Cell

CellPress
OPEN ACCESS

Article

CTP regulates membrane-binding activity of the nucleoid occlusion protein Noc

Adam S.B. Jalal,[1] Ngat T. Tran,[1] Ling J. Wu,[2] Karunakaran Ramakrishnan,[1] Martin Rejzek,[3] Giulia Gobbato,[1] Clare E.M. Stevenson,[4] David M. Lawson,[4] Jeff Errington,[2] and Tung B.K. Le[1,5,*]

[1]Department of Molecular Microbiology, John Innes Centre, Norwich, NR4 7UH, UK
[2]Centre for Bacterial Cell Biology, Biosciences Institute, Medical School, Newcastle University, Newcastle upon Tyne, NE2 4AX, UK
[3]Chemistry Platform, John Innes Centre, Norwich, NR4 7UH, UK
[4]Department of Biological Chemistry, John Innes Centre, Norwich, NR4 7UH, UK
[5]Lead contact
*Correspondence: tung.le@jic.ac.uk
https://doi.org/10.1016/j.molcel.2021.06.025

SUMMARY

ATP- and GTP-dependent molecular switches are extensively used to control functions of proteins in a wide range of biological processes. However, CTP switches are rarely reported. Here, we report that a nucleoid occlusion protein Noc is a CTPase enzyme whose membrane-binding activity is directly regulated by a CTP switch. In *Bacillus subtilis*, Noc nucleates on 16 bp *NBS* sites before associating with neighboring non-specific DNA to form large membrane-associated nucleoprotein complexes to physically occlude assembly of the cell division machinery. By *in vitro* reconstitution, we show that (1) CTP is required for Noc to form the *NBS*-dependent nucleoprotein complex, and (2) CTP binding, but not hydrolysis, switches Noc to a membrane-active state. Overall, we suggest that CTP couples membrane-binding activity of Noc to nucleoprotein complex formation to ensure productive recruitment of DNA to the bacterial cell membrane for nucleoid occlusion activity.

INTRODUCTION

While ATP and GTP switches are ubiquitous in biology, CTP switches have rarely been identified but may be more widespread than previously appreciated. A recent discovery showed that ParB, a crucial protein for bacterial chromosome segregation, is the founding member of a new class of CTP-dependent molecular switches (Osorio-Valeriano et al., 2019; Soh et al., 2019). ParB nucleates on a *parS* DNA sequence and associates with neighboring DNA, a process known as spreading, to enable faithful chromosome segregation (Breier and Grossman, 2007; Funnell, 2016; Graham et al., 2014; Jalal and Le, 2020; Murray et al., 2006; Sanchez et al., 2015). CTP induces ParB self-dimerization to create a clamp-like molecule (Soh et al., 2019). The ParB clamp self-loads at *parS*, then spreads by sliding to neighboring DNA while still entrapping DNA (Jalal et al., 2020a; Soh et al., 2019). Essentially, CTP serves to switch ParB from a *parS*-nucleating open clamp to a DNA-sliding closed-clamp state (Jalal et al., 2020a; Soh et al., 2019). The result is the formation of a higher-order nucleoprotein complex with multiple ParB-CTP clamps entrapped in the vicinity of the *parS* locus. The higher-order nucleoprotein complex stimulates the ATPase activity of ParA, a partner of ParB, driving the segregation of replicated chromosomes to daughter cells (Hwang et al., 2013; Jalal and Le, 2020; Lim et al., 2014; Vecchiarelli et al., 2012, 2013, 2014).

In Firmicutes, the nucleoid occlusion protein Noc is a paralog of ParB (Jalal et al., 2020b; Sievers et al., 2002; Wu and Errington, 2011); however, the role of Noc is different from that of a canonical ParB (Pang et al., 2017; Veiga et al., 2011; Wu and Errington, 2004). Noc helps direct the assembly of the cell division machinery toward the middle of a dividing cell where the concentration of chromosomal DNA (the nucleoid) is the least, thus ensuring a binary cell division (Adams et al., 2015; Rodrigues and Harry, 2012; Wu and Errington, 2004; Yu et al., 2021). Noc does so by nucleating on 16 bp *NBS* (Noc-binding site) sites scattered around the chromosome before spreading to neighboring DNA to form large Noc-DNA nucleoprotein complexes (Wu et al., 2009). Unusually, Noc is also a peripheral membrane protein that directly associates with the cell membrane via a predicted N-terminal amphipathic helix (Adams et al., 2015; Figure 1A). The recruitment of the chromosomal DNA to the membrane is crucial for preventing the assembly of the division machinery over the chromosome; indeed, a Noc variant lacking the amphipathic helix is impaired in nucleoid occlusion activity (Adams et al., 2015). In *Bacillus subtilis*, Noc was observed to associate with the cell membrane in a transient manner *in vivo* (Wu et al., 2009). It was thought that a strong membrane-binding activity of Noc might have been selected against, as a stable association with the membrane might hamper chromosome replication and segregation (Adams et al., 2015), yet it is unclear how the membrane-binding activity of Noc is modulated. Furthermore, Noc must bring the chromosomal DNA to the membrane to physically inhibit the assembly of the division machinery (Adams et al., 2015); an unregulated membrane-binding

Please cite this article in press as: Jalal et al., CTP regulates membrane-binding activity of the nucleoid occlusion protein Noc, Molecular Cell (2021), https://doi.org/10.1016/j.molcel.2021.06.025

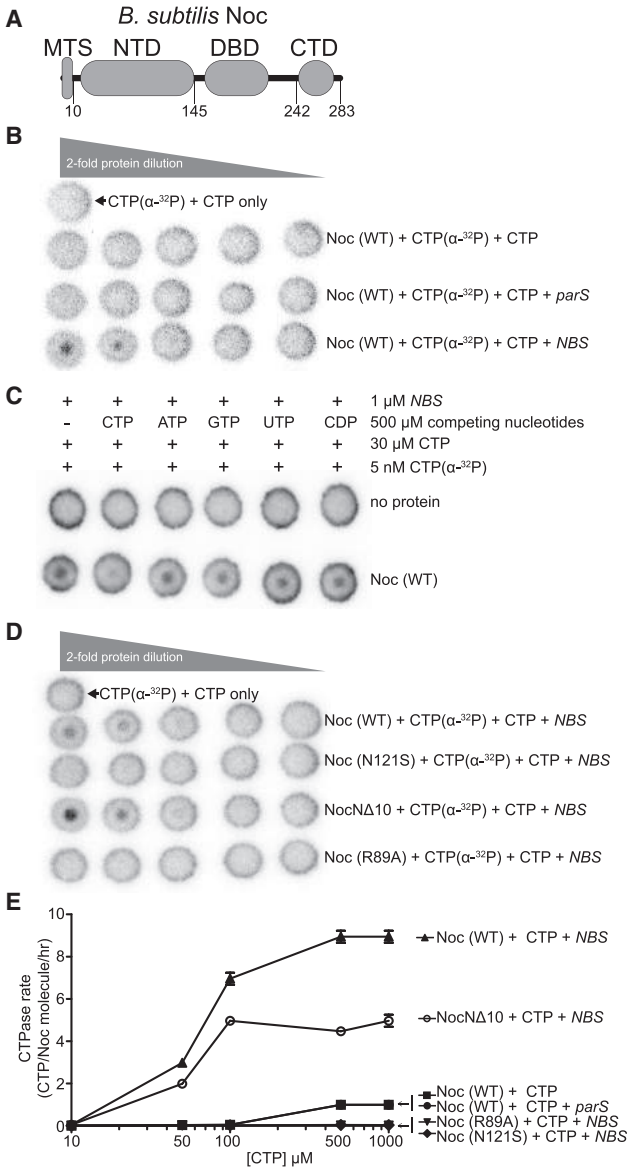

Figure 1. Noc binds and hydrolyzes CTP in the presence of *NBS* DNA

(A) The domain architecture of *B. subtilis* Noc: a membrane-targeting sequence (MTS), an N-terminal domain (NTD), a central DNA-binding domain (DBD), and a C-terminal domain (CTD).

(B–D) CTP binding as monitored by DRaCALA assay using radiolabeled CTP α-P^{32}. The bull's-eye staining indicates CTP binding due to a more rapid immobilization of protein-ligand complexes compared with free ligands. The starting concentration of Noc used in all panels was 30 μM. The concentrations of CTP α-P^{32}, unlabeled CTP, and a 22 bp *parS*/*NBS* DNA used in all panels were 5 nM, 30 μM, and 1 μM, respectively.

(E) CTP hydrolysis rates of Noc (WT) and variants were measured by continuous detection of released inorganic phosphates (see STAR Methods). CTPase rates were measured at increasing concentrations of CTP. All reactions contained 1 μM Noc (WT/variants) ± 1 μM 22 bp *NBS* or *parS* DNA and an increasing concentration of CTP (0, 10, 50, 100, 500, and 1,000 μM). Experiments were triplicated, and the SDs of the CTPase rates were presented.

activity would likely confine apo-Noc permanently to the cell membrane, thus unfavorably limiting the recruitment of DNA to the membrane (Adams et al., 2015). Again, it remains unclear whether the membrane-binding activity of Noc is regulated and, if so, how.

To investigate further, we have biochemically reconstituted *NBS*-dependent Noc spreading and membrane association events using purified *B. subtilis* Noc protein and phospholipid vesicles. We show that, similar to a canonical ParB, Noc is a CTPase enzyme that binds CTP to form a protein clamp that can slide and entrap DNA. Importantly, CTP binding, but not hydrolysis, is required to switch Noc-DNA from a membrane-inactive to an active state, thus locking Noc into a pathway in which it must spread before associating with the cell membrane. We solve an X-ray crystal structure of a C-terminal domain truncated apo-Noc from *Geobacillus thermoleovorans*, in which its membrane-targeting amphipathic helix adopts an autoinhibitory conformation, restricted from interacting with the membrane. We suggest that CTP binding might liberate the amphipathic helix, thereby switching Noc to a membrane-active state. Altogether, we demonstrate that CTP directly regulates the membrane-binding activity of the nucleoid occlusion protein Noc, further expanding the role of CTP switches in biology.

RESULTS

NBS DNA increases the CTP binding and hydrolysis rate of Noc

Given the shared ancestry between ParB and Noc, we wondered if *B. subtilis* Noc also binds and hydrolyses CTP. To investigate, we used a membrane-spotting assay (DRaCALA), and the result showed that *B. subtilis* Noc binds radiolabeled CTP, but only in the presence of a cognate 22 bp *NBS* DNA (Figure 1B). An excess of unlabeled CTP, but no other NTP or CDP, outcompeted radiolabeled CTP for binding to Noc, suggesting that *B. subtilis* Noc binds CTP specifically (Figure 1C). Similarly, an N-terminally truncated Noc variant lacking the 10 amino acid (AA) membrane-targeting sequence (NocNΔ10) also bound radiolabeled CTP in the presence of *NBS* DNA (Figure 1D). However, the Noc (R89A) and Noc (N121S) variants, whose equivalent substitutions in ParB have been shown to impair spreading and CTP binding (Jalal et al., 2020a; Osorio-Valeriano et al., 2019; Soh et al., 2019; Figure S1A), did not bind radiolabeled CTP at the tested concentration (Figure 1D). Next, we performed a quantitative nucleotide-binding assay using isothermal titration calorimetry (ITC) with a non-hydrolyzable CTP analog (CTPγS) to ensure the heat exchange was due solely to nucleotide binding but not hydrolysis or *NBS* DNA binding. We found that *B. subtilis* Noc binds CTPγS with a moderate affinity (K_d = 68 ± 23 μM), while Noc (N121S) bound CTPγS more weakly at K_d = 232 ± 66 μM, and Noc (R89A) did not detectably bind nucleotide (Figure S1B). Consistent with a previous report (Soh et al., 2019), *B. subtilis* Noc also showed CTP hydrolysis activity, albeit at a low rate of about one CTP per Noc per hour when only the purified protein and CTP were included (Figure 1E; Soh et al., 2019). The addition of a 22 bp *NBS* DNA, but not a non-cognate 22 bp *parS* DNA, increased the CTP hydrolysis rate 9-fold to about nine CTP per Noc per hour (Figure 1E; Soh et al., 2019). The Noc

Please cite this article in press as: Jalal et al., CTP regulates membrane-binding activity of the nucleoid occlusion protein Noc, Molecular Cell (2021), https://doi.org/10.1016/j.molcel.2021.06.025

CellPress
OPEN ACCESS

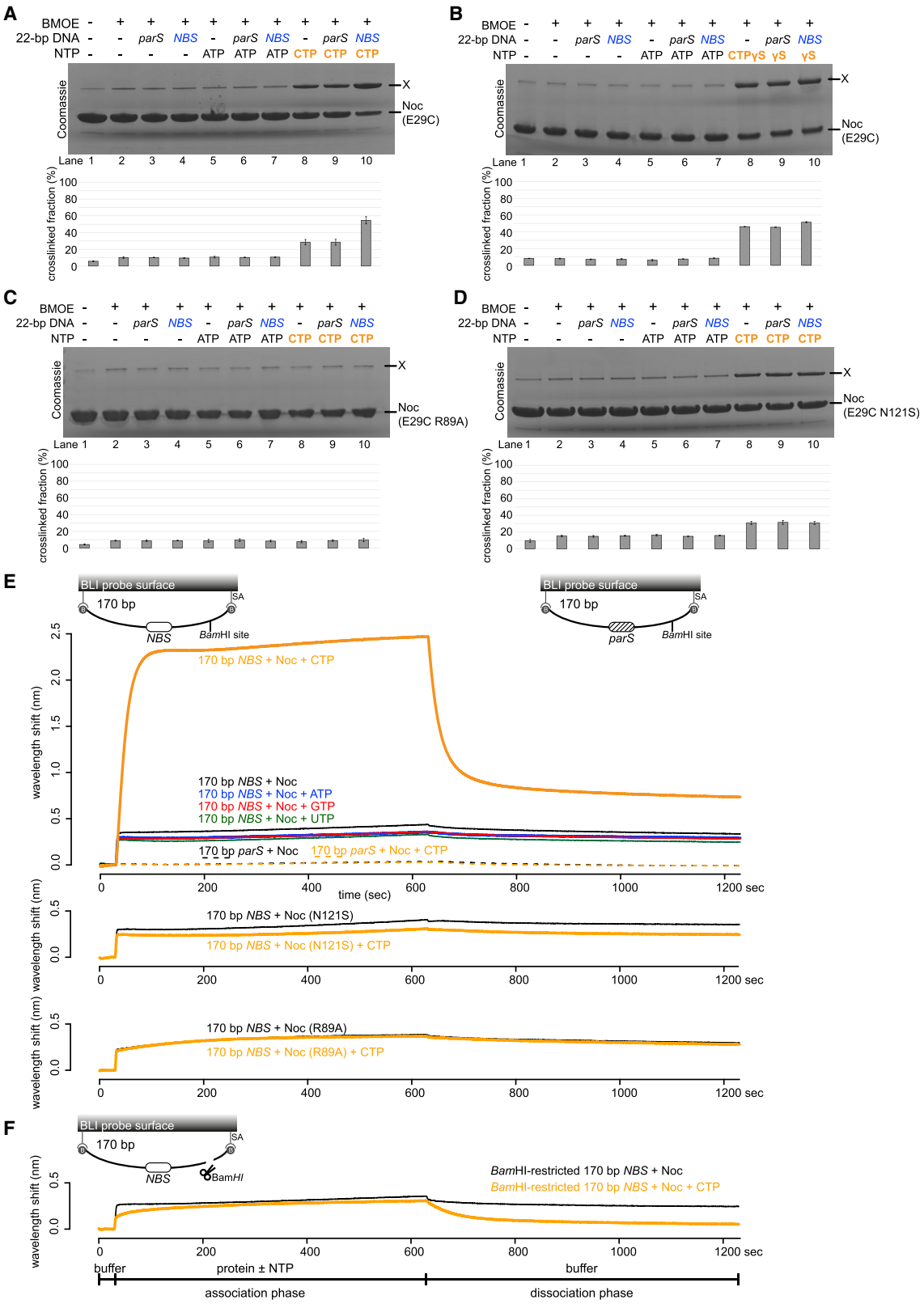

(legend on next page)

Please cite this article in press as: Jalal et al., CTP regulates membrane-binding activity of the nucleoid occlusion protein Noc, Molecular Cell (2021), https://doi.org/10.1016/j.molcel.2021.06.025

(R89A) and Noc (N121S) variants did not show noticeable CTP-hydrolyzing activity (Figure 1E). Last, despite binding CTP equally or more strongly than the wild-type (WT) (Figure 1D), NocNΔ10 hydrolyzed CTP at a reduced rate of about five CTP per Noc per hour (Figure 1E; see Discussion). Altogether, our data suggest that *B. subtilis* Noc is a CTPase enzyme that binds and hydrolyses CTP in the presence of cognate DNA.

CTP and *NBS* DNA stimulate the engagement of the N-terminal domain of Noc *in vitro*

In the presence of CTP, ParB self-engages at the N-terminal domain (NTD) to create a clamp-like molecule (Jalal et al., 2020a; Soh et al., 2019). To investigate whether CTP elicits a similar response in Noc, we used site-specific crosslinking of a purified *B. subtilis* Noc (E29C) variant by a sulfhydryl-to-sulfhydryl crosslinker bismaleimidoethane (BMOE). On the basis of a sequence alignment between *B. subtilis* ParB and Noc (Figure S1A), residue E29 at the NTD was selected and substituted by cysteine on an otherwise cysteine-less Noc (WT) background (Figure S2A) to create a variant in which symmetry-related cysteines become covalently linked together if they are within 8 Å of each other. The crosslinked form was detectable as a protein form with reduced mobility on SDS-PAGE (labeled X in Figure 2). In the absence of CTP, Noc (E29C) crosslinked minimally (~10% crosslinked fraction; Figure 2A, lanes 2–4). The crosslinking efficiency increased threefold (~30%) in the presence of CTP (Figure 2A, lane 8), but not CDP or ATP (Figure 2A; Figure S2B). The crosslinking efficiency further increased fivefold (~55%) when both CTP and a 22 bp *NBS* were included (Figure 2A, lane 10; Figure S2D). However, the addition of a non-cognate 22 bp *parS* DNA did not result in the same high level of crosslinking, even when CTP was present (Figure 2A, lane 9). Noticeably, non-hydrolyzable CTPγS readily promoted crosslinking (~45% crosslinked fraction) regardless of the presence or absence of *NBS* DNA (Figure 2B, lanes 8–10; Figure S2E). Therefore, our data suggest that CTP binding, but not hydrolysis, is required for the NTD engagement of *B. subtilis* Noc. Consistent with the requirement of CTP binding for NTD engagement, the Noc (E29C R89A) variant, in which the R89A substitution incapacitates CTP binding, did not crosslink beyond the background level in any tested condition (Figure 2C). The Noc (E29C N121S) variant, which binds CTP (albeit at a reduced affinity) but cannot hydrolyze CTP, crosslinked similarly to Noc (E29C) (~30% crosslinked fraction) at the saturating concentration of 1 mM CTP, although the *NBS*-stimulated crosslinking was abolished (Figure 2D). Last, the NocNΔ10 (E29C) variant, which lacks the N-terminal membrane-targeting sequence, crosslinked similarly to Noc (E29C) in the presence of CTP and *NBS* DNA (Figure S2C).

Noc associates with a closed *NBS* DNA substrate in a CTP-dependent manner

To further investigate the roles of the NTD engagement, we followed the spreading of Noc in real time. We used a 170 bp dual biotin-labeled *NBS* DNA that had been tethered at both ends onto a streptavidin-coated probe to form a closed DNA and measured the bio-layer interferometry (BLI) signal (Figures 2E and 2F; Jalal et al., 2020a). BLI monitors wavelength shifts resulting from changes in the optical thickness of the probe during the association and dissociation of Noc from the closed *NBS* DNA substrate. In the absence of CTP, we observed only the nucleation event on *NBS* DNA with 1 μM purified Noc (Figure 2E). Premixing Noc with ATP, GTP, or UTP did not change the sensorgram markedly; however, the addition of 1 mM CTP increased the BLI response by ~6-fold (Figure 2E), consistent with Noc-CTP spreading from the *NBS* to accumulate more on the 170 bp closed DNA substrate than by nucleation alone. We did not observe a noticeable BLI response when a 170 bp closed *parS* DNA substrate was used instead (Figure 2E), confirming that nucleation and spreading by *B. subtilis* Noc is strictly dependent on the *NBS*. We also observed that DNA-bound Noc-CTP dissociated readily into the solution when the BLI probe was returned to a protein-free buffer without CTP (Figure 2E; Figure S2F, dissociation phase). However, the dissociation of pre-bound Noc-CTP from DNA was slowed by ~5-fold if the probe was returned to a buffer supplemented with CTP (Figure S2F). Furthermore, we observed that pre-bound Noc-CTPγS was more stable and dissociated slowly into a buffer only solution (Figure S2G).

We then tested the mutant proteins by BLI assay and observed that both the Noc (R89A) and Noc (N121S) variants could nucleate but could not spread to accumulate on the closed *NBS* substrate even in the presence of 1 mM CTP (Figure 2E), suggesting that NTD engagement is required for spreading (see also Figures 2C and 2D).

Next, we investigated whether a DNA substrate with a free end (an open DNA) could also support Noc accumulation in our BLI setup. The 170 bp dual biotin-labeled DNA was designed with

Figure 2. CTP and *NBS* DNA promote the self-engagement of the N-terminal domain of Noc

(A and B) SDS-PAGE analysis of BMOE crosslinking products of 10 μM *B. subtilis* Noc (E29C) ± 1 μM 22 bp *parS*/*NBS* DNA ± 1.0 mM NTP. All crosslinking reactions were performed at 22°C unless indicated otherwise. X indicates a crosslinked form of Noc (E29C). Quantification of the crosslinked fraction is shown below each representative image. Error bars represent SEM from three replicates.

(C) Same as (A), but Noc (E29C R89A) was used instead.

(D) Same as (A), but Noc (E29C N121S) was used instead.

(E) CTP facilitates the association of Noc with a closed *NBS* DNA substrate beyond nucleation. Bio-layer interferometry (BLI) analysis of the interaction between a premix of 1.0 μM *B. subtilis* Noc ± 1.0 mM NTP and a 170 bp dual biotin-labeled DNA that contains either an *NBS* or a non-cognate *parS* site. Interactions between a dual biotinylated DNA and a streptavidin (SA)-coated probe created a closed DNA molecule where both ends were blocked (Jalal et al., 2020a) (see also the schematic diagram of the BLI probes). Other Noc variants, Noc (R89A) and Noc (N121S), were also analyzed in the same assay.

(F) BLI analysis of the interaction between a premix of 1.0 μM *B. subtilis* Noc ± 1.0 mM CTP and a BamHI-restricted dual biotinylated *NBS* DNA. The 170 bp *NBS* DNA substrate was also designed with a BamHI recognition site (see the schematic diagram of the probes). The intact dual biotinylated DNA was first immobilized onto the probe surface, then an open end was generated by digestion with BamHI (see STAR Methods). Afterward, the probe was used in a BLI analysis with a premix of Noc ± CTP. Each experiment was triplicated, and a representative sensorgram was shown.

Please cite this article in press as: Jalal et al., CTP regulates membrane-binding activity of the nucleoid occlusion protein Noc, Molecular Cell (2021), https://doi.org/10.1016/j.molcel.2021.06.025

a unique BamHI recognition site flanking the *NBS* site (Figure 2F). To generate a free end on the DNA, the DNA-coated probe was immersed in buffer containing BamHI restriction enzyme. Before BamHI digestion, Noc showed an enhanced association on a closed DNA substrate in the presence of CTP (Figure 2E). However, after BamHI digestion, the addition of CTP did not affect the BLI response beyond the nucleation of Noc at the *NBS* (Figure 2F). We reasoned that, similar to the canonical ParB clamp (Jalal et al., 2020a), Noc spreads but quickly escapes by sliding off a free DNA end. Overall, our BLI analyses support the idea of a clamp-like Noc-CTP that can spread and accumulate on a closed DNA substrate, most likely by entrapping DNA.

Noc binds liposomes in the presence of CTP

It has been shown previously *in vivo* that Noc possesses membrane-binding activity and that it brings chromosomal DNA to the cell membrane to prevent cell division (Adams et al., 2015). Puzzlingly, however, we could not observe any noticeable association between purified *B. subtilis* Noc and liposomes by a co-sedimentation assay (Figure 3A, lanes 1–4). We wondered if CTP might be the missing co-factor that activates the membrane-binding activity of Noc. To test this possibility, purified Noc was incubated with liposomes with or without CTP and 22 bp *NBS* DNA and ultracentrifuged (Figure 3A; Figure S3A). The pellet contained sedimented liposomes and associating protein, while the supernatant contained unbound protein; protein and DNA species from both fractions were analyzed by polyacrylamide gel electrophoresis. We did not observe a significant increase in the amount of Noc in the pellet when CTP alone, CTP and a non-cognate 22 bp *parS* DNA (Figure 3A, lanes 5–10), or other nucleotides were used (Figure S3B). However, in the presence of both CTP and a 22 bp *NBS* DNA, ~45% of the Noc protein was detected robustly in the pellet (Figure 3A, lane 11 and 12), suggesting that the *in vitro* membrane-binding activity of Noc is CTP and *NBS* dependent. *NBS* DNA is most likely required to promote CTP binding and the membrane-binding activity of Noc, rather than to concentrate a large amount of Noc molecules in the vicinity of *NBS*. Supporting this proposition, the short length of a 22 bp *NBS* DNA duplex should allow only a dimer of Noc or Noc-CTP complex to occupy the DNA at a time. Furthermore, nearly all of the 22 bp *NBS* DNA was present in the supernatant (instead of in the pellet) after centrifugation (Figure 3A), most likely because Noc-CTP clamps rapidly escaped the open linear *NBS* DNA (see also Figure 2F). This result suggests that individual Noc-CTP possesses a substantial membrane-binding capability.

Next, we observed that the addition of CTPγS alone caused ~35% of Noc to associate with the pelleted vesicles (Figure 3B, lanes 5 and 6). The vesicle-bound fraction further increased to ~45% when both CTPγS and a 22 bp *NBS* DNA were present (Figure 3B, lanes 7 and 8). We infer that CTP binding, but not hydrolysis, is required for the *in vitro* Noc-liposome interaction. Consistent with the requirement of CTP binding for membrane-binding activity, the Noc (R89A) and Noc (N121S) variants that do not bind CTP or bind CTP weakly failed to co-sediment with liposomes even when CTP and *NBS* were included (Figure 3C, lanes 3 and 4 and lanes 5 and 6). The 10 AA N-terminal peptide was previously shown *in vivo* to be the membrane-targeting determinant of *B. subtilis* Noc (Adams et al., 2015). Here, we also confirmed that a purified NocNΔ10 lacking this segment was unable to co-sediment with liposomes *in vitro* regardless of the presence or absence of CTP or *NBS* DNA (Figure 3C, lanes 7 and 8). Last, in another control experiment, *C. crescentus* ParB, which binds CTP but not the cell membrane (Jalal et al., 2020a; Lim et al., 2014; Toro et al., 2008), did not co-sediment with liposomes in the presence of CTP ± *parS* or *NBS* DNA (Figure S3C).

Noc recruits *NBS* plasmid to liposomes in the presence of CTP

The recruitment of chromosomal DNA to the membrane is essential for Noc to exert nucleoid occlusion activity *in vivo* (Adams et al., 2015). Indeed, ectopic expression of *noc (R89A)*, *noc (N121S)*, or *nocNΔ10* could not rescue the synthetic cell division defect of a *B. subtilis* Δ*noc*Δ*minCD* double mutant at elevated temperature (Figure 3D; Adams et al., 2015). Epi-fluorescence microscopy of *B. subtilis* cells harboring *yfp*-tagged *noc* mutant alleles also confirmed that Noc (R89A), Noc (N121S), and NocNΔ10 failed to form punctate foci near the cell periphery (i.e., were defective in the formation of large membrane-associated nucleoprotein complexes) (Figure 3E; Adams et al., 2015). We wondered if the Noc-dependent recruitment of DNA to the membrane could be biochemically reconstituted. To this end, we assembled a reaction containing purified Noc, liposomes, CTP, and a ~5 kb circular *NBS*-harboring plasmid before ultracentrifugation (Figure 4). Unlike the 22 bp *NBS* DNA, the *NBS* plasmid is topologically closed and therefore should robustly retain closed Noc-CTP clamps. Unfortunately, because of its high molecular weight, ~45%–55% of the circular plasmid sedimented independently of the liposomes (Figure 4A, lanes 5 and 6; Figure 4B, lanes 1–4). Nevertheless, in the presence of liposomes and CTP, the *NBS* plasmid completely co-sedimented with Noc (Figure 4A, lanes 11 and 12), demonstrating that Noc can recruit plasmid DNA to liposomes in the presence of CTP. The pellet/supernatant distribution of a control plasmid with no *NBS* ("empty") was unaffected by the presence of Noc and CTP, and only ~2% of Noc was found in the pellet (Figure 4A, lanes 9 and 10). Next, in an attempt to minimize the sedimentation of a plasmid by itself, we performed a vesicle flotation assay in which liposomes and associating protein/DNA migrate up a sucrose gradient to the topmost faction rather than down into the pellet (Figure S4A). Despite the basal level of ~20% total *NBS* plasmid in the top fraction even when liposomes were omitted (Figure S4B, lane 3), we again observed ~80% of total *NBS* plasmid being recruited to the liposomes when purified Noc and CTP were also present (Figure S4C, lane 12).

In light of the above results, we wondered if the role of *NBS* was to stimulate the membrane-binding activity of Noc-CTP. To test this possibility, we first assembled a co-sedimentation reaction as described above. Subsequently, a non-specific DNase (Benzonase) was added to eliminate the *NBS* plasmid before ultracentrifugation (Figure 4B, lanes 7 and 8). The nuclease treatment eliminated intact *NBS* plasmid from both the supernatant and the pellet fractions; however, ~65% of the total amount of Noc still co-sedimented to the pellet in comparison with ~80% when nuclease was omitted (Figure 4A, lanes 7 and 8 versus

Please cite this article in press as: Jalal et al., CTP regulates membrane-binding activity of the nucleoid occlusion protein Noc, Molecular Cell (2021), https://doi.org/10.1016/j.molcel.2021.06.025

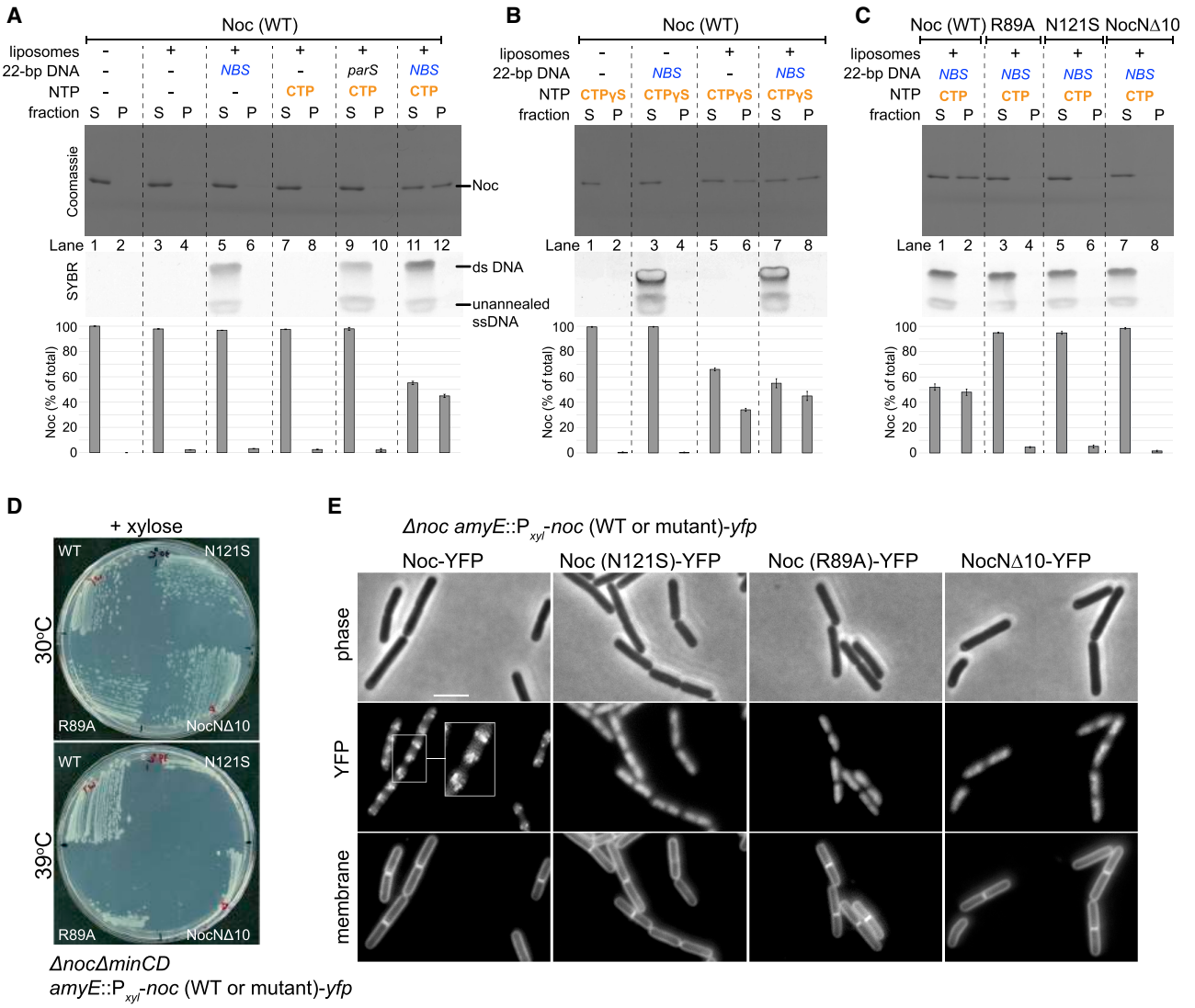

Figure 3. Noc binds liposomes in the presence of CTP and *NBS* DNA, and the phenotypic effects of the Noc variants

(A) Analysis of *B. subtilis* Noc binding to membranes by a liposome co-sedimentation assay. A premix of 0.75 μM *B. subtilis* Noc protein ± 1.0 μM 22 bp linear *parS*/*NBS* DNA ± 1.0 mM CTP ± 1.0 mg/mL liposomes was incubated at 22°C for 5 min before ultracentrifugation. The resulting supernatant (S) and pellet (P) fractions were analyzed using SDS-PAGE. Samples were also loaded onto a 20% TBE PAGE, and the gel was subsequently stained with Sybr Green for DNA. Quantification of Noc in each fraction is shown below each representative image. Error bars represent SEM from three replicates.

(B) Same as (A), but 1.0 mM CTPγS was used instead.

(C) Other Noc variants, Noc (R89A), Noc (N121S), and NocNΔ10, were also analyzed in a liposome co-sedimentation assay.

(D) Complementation of *noc* in a Δ*noc*Δ*minCD* background. Strains Δ*noc*Δ*minCD amyE*::P_{xyl}-*noc* (WT or mutant)-*yfp* were streaked on nutrient agar plates supplemented with 0.5% xylose and incubated at 30°C or 39°C.

(E) Cellular localization of YFP-labeled Noc (WT or mutants). Representative images of Δ*noc amyE*::P_{xyl}-*noc* (WT or mutant)-*yfp* cells grown in the presence of 0.5% xylose. Cell membranes were stained with FM5-95. Scale bar, 3 μm. Inset shows a magnification of a section of cells.

lanes 5 and 6). In parallel, we tested spreading-defective Noc (R89A) and Noc (N121S), and a membrane-binding-defective NocNΔ10 for their ability to recruit the *NBS* plasmid to liposomes in a co-sedimentation assay (Figure 4C) as well as in a flotation assay (Figure S4D). Consistent with previous and the above *in vivo* data (Adams et al., 2015; Figure 3E), these mutants could not recruit DNA to the pellet fraction beyond the basal level (Figure 4C; Figure S4D). Altogether, these results suggest that the *NBS* specifically activates the membrane-binding activity of Noc in the presence of CTP, thereby recruiting Noc-DNA complexes to the membrane.

The association of Noc-*NBS* DNA with liposomes is reversible

Once the membrane-associated Noc-DNA nucleoprotein complexes form, can this process be reversed? To investigate, we

Please cite this article in press as: Jalal et al., CTP regulates membrane-binding activity of the nucleoid occlusion protein Noc, Molecular Cell (2021), https://doi.org/10.1016/j.molcel.2021.06.025

CellPress
OPEN ACCESS

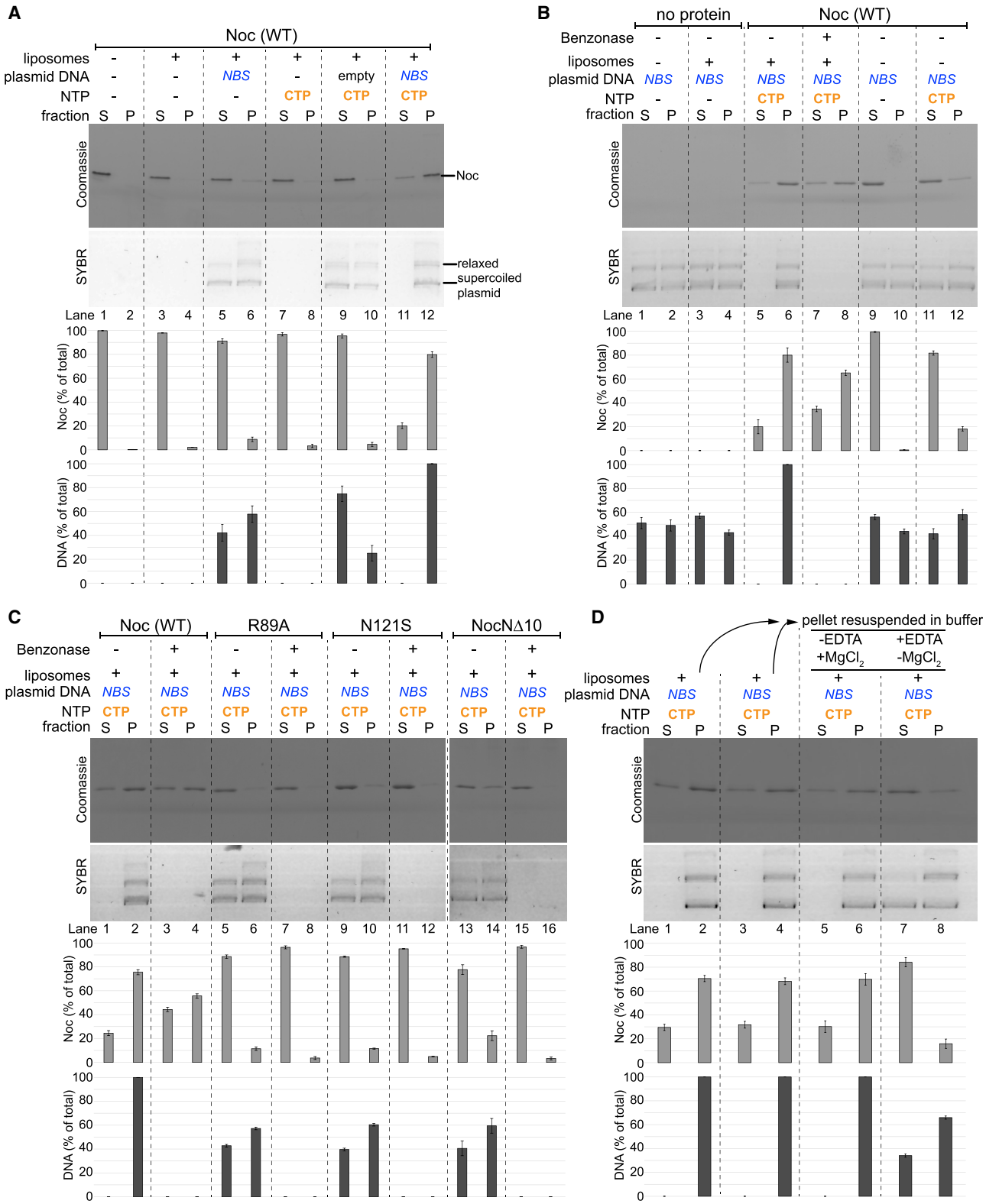

Figure 4. Noc recruits *NBS* plasmid to liposomes in the presence of CTP

(A) Analysis of *B. subtilis* Noc binding to membranes and the recruitment of plasmid DNA to the membranes by a liposome co-sedimentation assay. A premix of 0.75 μM *B. subtilis* Noc protein ± 100 nM 5-kb plasmid DNA ± 1.0 mM CTP ± 1.0 mg/mL liposomes was incubated at 22°C for 5 min before ultracentrifugation.

(legend continued on next page)

Please cite this article in press as: Jalal et al., CTP regulates membrane-binding activity of the nucleoid occlusion protein Noc, Molecular Cell (2021), https://doi.org/10.1016/j.molcel.2021.06.025

used a buffer supplemented with EDTA to sequester Mg^{2+}, thereby disrupting CTP binding in preformed liposome-bound Noc-DNA complexes (Figure 4D). In this experiment, the pellet containing preformed liposome-bound Noc-DNA complexes (Figure 4D, lane 2 or 4) was either resuspended in EDTA-minus or EDTA-plus buffer before being ultracentrifuged again. After the second round of centrifugation, both the pellet and the supernatant fractions were analyzed for the presence of protein and DNA (Figure 4D, lanes 5–8). We observed that although nearly all *NBS* plasmid remained in the pellet when an EDTA-minus buffer was used (Figure 4D, lane 6), ~38% of the total plasmid returned to the supernatant in the presence of EDTA (Figure 4D, lane 7). These results demonstrate that the membrane-binding activity of Noc can be reversed and suggest a possible inhibitory mechanism that keeps apo-Noc in the membrane-inactive mode in the absence of CTP.

Crystal structure of *Geobacillus thermoleovorans* NocΔCTD shows the membrane-targeting amphipathic helix in an autoinhibitory conformation

To gain further insights into the membrane-inactive state, we sought to solve a crystal structure of Noc. We could not obtain high-quality crystals of *B. subtilis* Noc either in full-length or truncated forms despite extensive efforts. However, we could grow and collect diffraction data for a C-terminal domain truncated apo-Noc (NocΔCTD) from a thermophilic bacterium, *Geobacillus thermoleovorans*, to 2.5 Å resolution. *B. subtilis* Noc and *G. thermoleovorans* Noc share 72% sequence identity (see the sequence alignment in Figure S5A). The structure was solved by iodide SAD phasing, as no other Noc protein family structure was available as a template for molecular replacement. The asymmetric unit contains two similar copies of monomeric apo-Noc (root-mean-square deviation [RMSD] = 0.9 Å) (Figure S5B), hence we used the more complete subunit for all further analysis.

Each NocΔCTD subunit contains an NTD (helices α1–α6) and an *NBS*-specific DNA-binding domain (DBD) (helices α7–α12) (Figure 5A; Jalal et al., 2020b; Wu et al., 2009). The primary dimerization domain at the C-terminal side of Noc was truncated in the NocΔCTD and hence was not present in this structure. Most notably, electron density for five of the 10 AA comprising the membrane-targeting helix α1 were visible in a 3_{10} helical conformation (Figures 5A and 5B). From the structure, it is apparent that the visible membrane-targeting sequence (AA 5–10) of Noc is indeed amphipathic, with distinct polar and hydrophobic faces (Figure 5B). The amphipathic helix α1 is immediately followed by helix α2 and subsequently by an 8 AA α2-β1 loop that precedes the main NTD (Figure 5A). By sequence comparison with a canonical ParB (Soh et al., 2019), the main NTD (β1-α6) of Noc contains the CTP-binding motifs, while the amphipathic α1, α2, and the α2-β1 loop are specific to the Noc protein family (Figure S5A). We noted that the hydrophobic face of the amphipathic α1 helix is buried toward α5 and α7 at the core of Noc (Figures 5A and 5C) and thus is unexposed and unlikely to be available for membrane interaction. Specifically, the side chain of S6 hydrogen bonds with the side chain of R150, and the side chain of R7 hydrogen bonds with the main chain oxygen of N104 (Figure 5C). Additionally, the main chain oxygen of S10 hydrogen bonds with the side chain of Q16, and last, the main chain oxygen of F11 hydrogen bonds with the side chain of Q120 (Figure 5C). Sidechains of F9 and F11 also interact hydrophobically with the side chains of I116 and I81, respectively (Figure 5C). These interactions thus bury α1 in a potential autoinhibitory conformation. We further noted that α2, which does not target the membrane per se but is conserved among Noc homologs (Figure S5A; Adams et al., 2015), also contributes to holding α1 in the repressed state (Figure 5D). Specifically, the side chains of both E13 and Q16 form water-mediated contacts with the side chains of I65, R86, and K103, while the side chain of E20 forms a hydrogen bond with Q66 (Figure 5D). Overall, our apo-NocΔCTD structure suggests a repressed state that might keep Noc in the membrane-inactive state in the absence of CTP.

Crystal structure of the *G. thermoleovorans* NocNΔ26ΔCTD variant is incompatible with an autoinhibitory conformation of the amphipathic helix

Next, we attempted to obtain a co-crystal structure of Noc in complex with nucleotides but were not successful when NocΔCTD or NocNΔ10ΔCTD protein variants were used. However, in the presence of CTPγS, we were able to grow and collect 2.95 Å diffraction data for a crystal of a further truncated *G. thermoleovorans* NocNΔ26ΔCTD variant, which lacks both the N-terminal membrane-targeting helix and the C-terminal domain. After solving its structure, it was apparent that NocNΔ26ΔCTD had adopted an alternative conformation to that of NocΔCTD (Figure 6A versus Figures 6B and 6C). This alternative conformation of NocΔN26ΔCTD is compatible with homodimer formation, giving an interfacial area of ~2,700 $Å^2$ (as evaluated with jsPISA), which resembles that observed for a co-crystal structure of *B. subtilis* ParBΔCTD with bound cytidine diphosphate (CDP) (RMSD = 2.17 Å) (Figure S6A; Soh et al., 2019). However, there was no clear electron density for a bound nucleotide in our structure; instead a sulfate anion from the crystallization solution occupies a position equivalent to

Either an empty plasmid or an *NBS*-harboring plasmid was used in this assay. The resulting supernatant (S) and pellet (P) fractions were analyzed using SDS-PAGE. Samples were also loaded onto a 1% agarose gel and were subsequently stained with Sybr Green for DNA. Quantification of Noc or DNA in each fraction is shown below each representative image. Error bars represent SEM from three replicates.

(B) Similar to (A), a premix of 100 nM *NBS* plasmid ± 0.75 μM Noc ± 1.0 mM CTP ± 1.0 mg/mL liposomes was first assembled and incubated at 22°C for 5 min. However, before ultracentrifugation, a non-specific DNA nuclease (Benzonase) was either added or omitted from the samples, as indicated.

(C) Other Noc variants, Noc (R89A), Noc (N121S), and NocNΔ10, were also analyzed in a liposome co-sedimentation assay. Benzonase was either added or omitted, as indicated, before ultracentrifugation.

(D) The association of Noc-*NBS* DNA with liposomes is reversible. A premix of 0.75 μM *B. subtilis* Noc protein + 100 nM *NBS* plasmid + 1.0 mM CTP + 1.0 mg/mL liposomes was ultracentrifuged, and the resulting fractions were analyzed for protein and DNA contents (lanes 1 and 2 and lanes 3 and 4). The resulting pellets (lanes 2 and 4) were subsequently resuspended in either a binding buffer (− EDTA + 1 mM $MgCl_2$) or a stripping buffer (+ 10 mM EDTA − $MgCl_2$). The resuspensions were ultracentrifuged for the second time, and the resulting fractions were analyzed for protein and DNA contents (lanes 5 and 6 and lanes 7 and 8).

Please cite this article in press as: Jalal et al., CTP regulates membrane-binding activity of the nucleoid occlusion protein Noc, Molecular Cell (2021), https://doi.org/10.1016/j.molcel.2021.06.025

CellPress
OPEN ACCESS

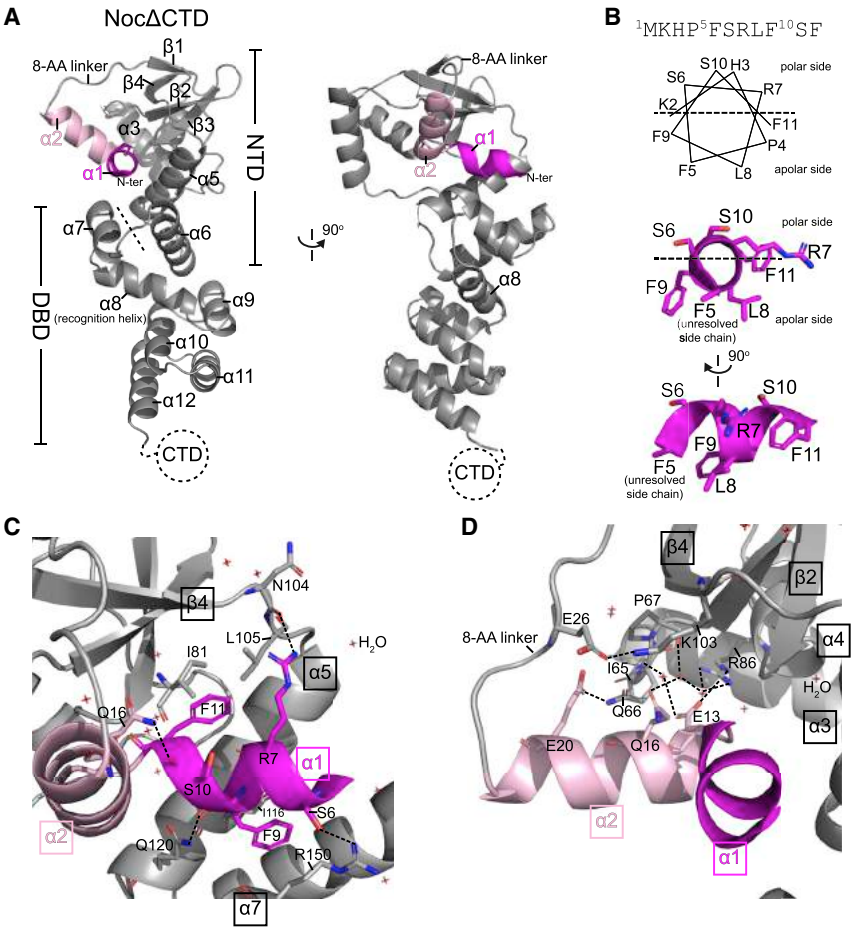

Figure 5. Crystal structure of *Geobacillus thermoleovorans* NocΔCTD shows the membrane-targeting amphipathic helix in an auto-inhibitory conformation

(A) Crystal structure of a *G. thermoleovorans* NocΔCTD monomer (gray) with an N-terminal amphipathic helix α1 (magenta) and helix α2 (pink). Helix α2 is connected to the main N-terminal domain (NTD) via an 8 amino acid loop. The dashed line demarcates the NTD from the DNA-binding domain (DBD). Helix α8 at the DBD is the recognition helix that contributes to the specific recognition of the *NBS* site (Jalal et al., 2020b; Wu et al., 2009).

(B) The membrane-targeting amphipathic helix α1. A helical wheel representation of the 10 amino acid at the N terminus of *G. thermoleovorans* Noc. Although the first 5 amino acids were unresolved in the NocΔCTD crystal structure, the next 5 amino acids adopt a 3_{10} helical conformation with distinct polar and hydrophobic sides.

(C and D) Helices α1 (magenta) and α2 (pink) pack themselves into the core N-terminal domain (gray). Hydrogen bonds are shown as dashed lines, water molecules are also shown.

that of the β-phosphate of the nucleotide in the *B. subtilis* ParBΔCTD-CDP structure (Figure S6B; Soh et al., 2019). We further observed that helix α5 in the NocΔN26ΔCTD structure swings outward by 104° and no longer forms a bundle with helix α6 from the same subunit (Figure 6A versus Figure 6B) and that this movement might drive the self-dimerization at the NTD of Noc (i.e., the NTD engagement) (Figure 6C). By superimposing the NTDs of NocΔCTD and NocNΔ26ΔCTD (RMSD = 1.49 Å), we detected severe clashes between α1, α2, and the opposite subunit of NocNΔ26ΔCTD (Figure 6D; Figures S6C and S6D). Therefore, it is clear that the autoinhibitory state of α1 and α2 (as observed in NocΔCTD) is not compatible with the alternative conformation in the NocNΔ26ΔCTD structure. We speculate that the amphipathic helix α1 and helix α2 might be liberated from the autoinhibitory conformation to be compatible with the NTD-engagement conformation in the NocNΔ26ΔCTD structure.

Last, we overexpressed and purified six *B. subtilis* Noc variants to investigate the effects of N-terminal deletions and substitutions on the membrane-binding ability (Figure S7). Removing a lysine residue at position 2 (NocΔK2) or the first 4 AA (NocΔ4) had a mild effect on the membrane-binding activity of Noc, as judged by liposome co-sedimentation assays (Figure S7, lanes 3 and 4 and lanes 7 and 8). However, hydrophobicity-reducing substitutions such as K2E, F5A, and F5E had a negative effect on Noc-liposome binding (Figure S7, lanes 5 and 6, lanes 9 and 10, and lanes 11 and 12). In contrast, when the hydrophobicity of the first 4 AA segment was increased, as in the S4L variant, Noc (S4L) binding to the liposomes increased compared with Noc (WT) (Figure S7, lanes 13 and 14). Overall, although the conformation of the N-terminal 10 AA sequence of Noc in a membrane-bound state is not yet known, our results suggest that the properties of these amino acids are fine-tuned for membrane-binding activity.

DISCUSSION

Assembly of the membrane-associated Noc-DNA nucleoprotein complex: Roles of CTP

The nucleoid occlusion protein Noc increases cell division efficiency (Rodrigues and Harry, 2012) by directing the division machinery toward mid-cell either by inhibiting FtsZ formation over the nucleoid (Adams et al., 2015; Wu and Errington, 2004) and/or by concentrating FtsZ in the vicinity of a pre-existing mid-cell Z-ring (Yu et al., 2021). The extensive Noc-mediated DNA-membrane interaction is at the heart of both models for nucleoid occlusion (Adams et al., 2015; Yu et al., 2021). In this study, we show that CTP regulates the nucleoid occlusion activity of Noc. We provide evidence that (1) CTP is required for Noc to form the *NBS*-dependent nucleoprotein complex, and (2) CTP binding switches Noc from a membrane-inactive auto-repressed state to a membrane-active state. We propose that the dual dependency of Noc's membrane-binding activity on *NBS* and CTP might ensure productive recruitment of DNA to the bacterial cell membrane to exert the nucleoid occlusion activity (Figure 7). It has been estimated that the intracellular concentrations of Noc

Please cite this article in press as: Jalal et al., CTP regulates membrane-binding activity of the nucleoid occlusion protein Noc, Molecular Cell (2021), https://doi.org/10.1016/j.molcel.2021.06.025

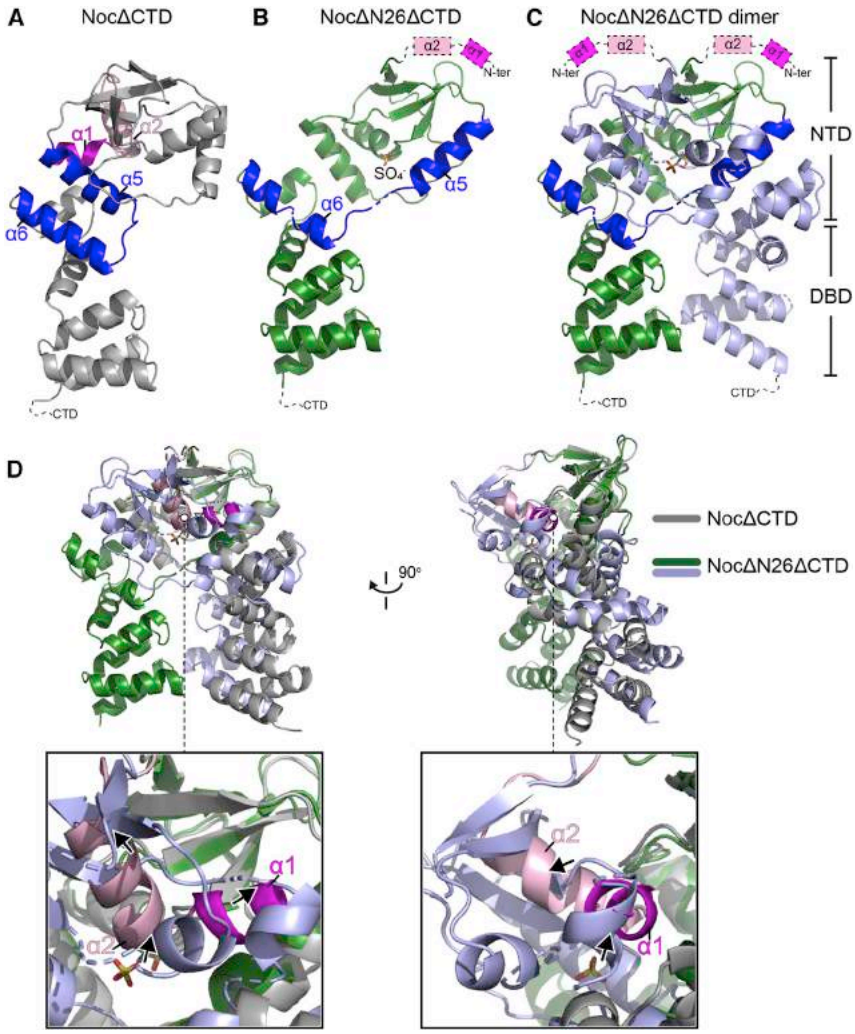

Figure 6. The conformation of Noc in the crystal structure of *G. thermoleovorans* NocNΔ26ΔCTD is incompatible with an autoinhibitory state of the amphipathic helix

(A) Crystal structure of *G. thermoleovorans* NocΔCTD (same as Figure 5A), with helices α5 and α6 highlighted in blue. The amphipathic helix α1 and α2 are shown in magenta and pink, respectively.

(B) Crystal structure of a *G. thermoleovorans* NocNΔ26ΔCTD variant that lacks both the C-terminal domain (CTD) and helices α1 and α2 (dashed boxes). Helices α5 and α6 are shown in blue.

(C) A dimer of *G. thermoleovorans* NocNΔ26ΔCTD that self-dimerizes at the N-terminal domain (NTD). Helices α5 and α6 in one of the subunits are shown in blue.

(D) A superimposition at the NTDs of NocΔCTD monomer (gray) and NocNΔ26ΔCTD dimer (green and light blue) shows a severe clash (arrows) between α1 (magenta), α2 (pink), and the opposite subunit of NocNΔ26ΔCTD (light blue).

and CTP are ~5 μM and ~1 mM, respectively (Buckstein et al., 2008; Wu et al., 2009). At these concentrations, if the membrane-binding activity of Noc were solely dependent on CTP, most intracellular DNA-unbound Noc would be in the CTP-bound state and confined to the cell membrane, thus potentially limiting the recruitment of chromosomal DNA to the cell membrane. We therefore reason that the *NBS*-stimulated Noc-CTP interaction provides a mechanism to commit Noc into a pathway in which only DNA-entrapped Noc molecules are able to associate with the cell membrane (Figure 7B). Another consequence of coupling membrane activity to *NBS* binding is that membrane-associated nucleoprotein complexes are spatially confined near the vicinity of *NBS* sites. This spatial confinement is important for directing division machinery formation toward mid-cell, where the concentration of *NBS* sites, hence the nucleoid occlusion activity, is lowest (Wu et al., 2009).

The lack of a bound nucleotide in the NocNΔ26ΔCTD structure prevents us from drawing a conclusion on the role of CTP and the possible conformational liberation of the amphipathic helix α1. However, several lines of evidence suggest that CTP might favor the NTD-engagement conformation as observed in our NocNΔ26ΔCTD structure: (1) CTP/CTPγS promoted the crosslinking between symmetrical E29C residues, a readout for NTD engagement (Figure 2A); (2) the conformation of NocNΔ26ΔCTD is highly similar to that of a nucleotide-bound *B. subtilis* ParB (Figure S6A; Soh et al., 2019); and (3) CTP/CTPγS enables Noc (WT) to co-sediment with liposomes (Figure 3). Altogether, it is not unreasonable to speculate that the CTP-induced NTD engagement might liberate the amphipathic helix from its autoinhibitory state to interact with the cell membrane. The 8 AA loop that connects the amphipathic helix to the rest of Noc might offer the flexibility to orient the amphipathic helix parallel to the membrane plane for binding (Figure 7).

This study also provides evidence that *B. subtilis* Noc possesses CTPase activity, but CTP hydrolysis is required for neither clamp formation nor membrane association. What might the role of CTP hydrolysis be? Similar to the counterpart ParB (Jalal et al., 2020a; Osorio-Valeriano et al., 2019; Soh et al., 2019), CTP hydrolysis and/or the subsequent release of hydrolytic products might disengage the NTD to open the clamp to release entrapped DNA (Figure 7B). Concomitantly, Noc might revert to the membrane-inactive state, enabling its extraction from the cell membrane. Our experiment that used EDTA to sequester coordinated Mg^{2+} to artificially promote the dissociation of CTP from Noc supports the proposal that membrane association can be reversible (Figure 4D). Furthermore, *B. subtilis* Noc foci associate with the cell membrane in a transient manner, perhaps suggesting a weak and fast on/off membrane interaction *in vivo* (Adams et al., 2015). The transient association with the membrane, possibly endowed by a CTP hydrolysis event that facilitates the release of Noc, might be advantageous for the cells because

Please cite this article in press as: Jalal et al., CTP regulates membrane-binding activity of the nucleoid occlusion protein Noc, Molecular Cell (2021), https://doi.org/10.1016/j.molcel.2021.06.025

CellPress
OPEN ACCESS

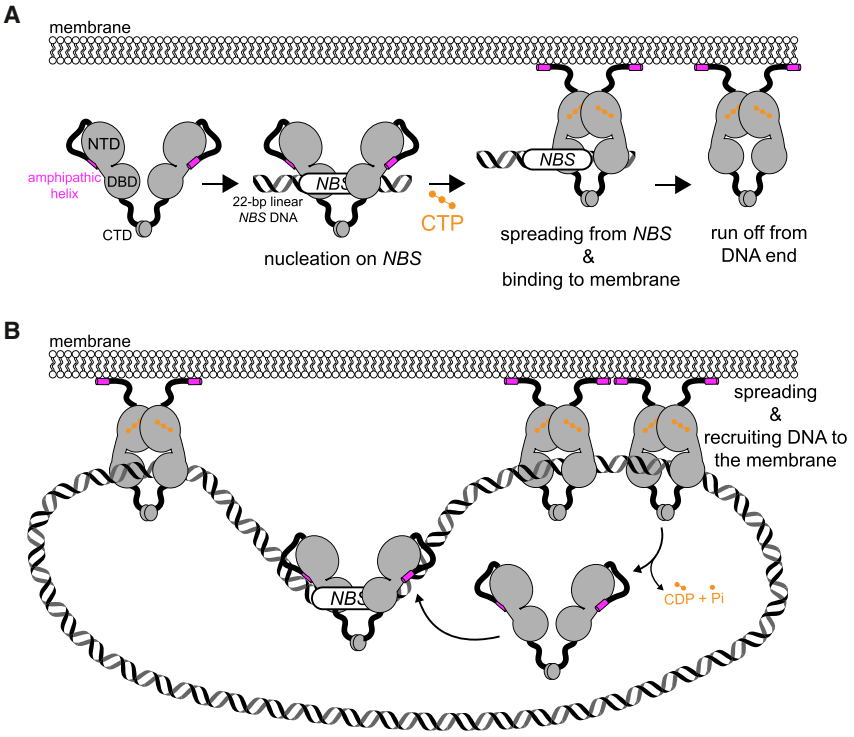

Figure 7. A model for a CTP-dependent regulation of membrane-binding activity of Noc

(A) Noc binds specifically to *NBS* site to nucleate on DNA. In the apo- or *NBS*-associated form, the amphipathic helix (magenta) adopts an auto-inhibitory conformation and thus cannot bind to the membrane. *NBS*-binding stimulates Noc to bind CTP (orange). Concomitantly, CTP induces a sliding clamp conformation in Noc that can run off open ends of a linear 22 bp *NBS* DNA. In this state, the amphipathic helix is likely liberated from the auto-inhibitory conformation, thus enables Noc-CTP to bind to the membrane.

(B) When a circular *NBS* plasmid with no open end was used, a sliding clamp of Noc entraps plasmid DNA and recruit DNA to the membrane. In the presence of CTP, a tripartite membrane-protein-DNA linkage is formed. CTP hydrolysis is not required for membrane binding or DNA recruitment but might have a role in releasing Noc from DNA and the membrane.

a strong and permanent mode of binding might hamper chromosome replication or damage DNA. Supporting this view, fusing NocNΔ10 to a synthetic transmembrane helix led to broken, bisected chromosomes and eventually chromosome segregation defects in many *B. subtilis* cells (Adams et al., 2015; Nyholm et al., 2007). Last, we noted that NocNΔ10 binds CTP equally well as, or slightly stronger than Noc (WT) (Figure 1D), yet its CTPase rate is reduced by half (Figure 1E). It is still unclear why this is the case; however, we speculate that the autoinhibitory conformation of this N-terminal-most region might play a role in CTP binding/hydrolysis. Lending support to our speculation, this N-terminal-most region interacts with residues Q66 and R86 (apo-NocΔCTD structure; Figure 5D) whose equivalent residues in *B. subtilis* ParB are known to be critical for CTP binding (Soh et al., 2019).

Overall, we envision a dynamic cycle inside the cells in which CTP hydrolysis converts a closed clamp Noc-CTP to Noc-CDP. The CDP-bound Noc might exist very briefly, as CDP likely dissociates rapidly from Noc (because of its low affinity to Noc; Figure S1B), thus opening the clamp to release entrapped Noc from the chromosome and the membrane (Figure 7B). The resulting apo-Noc might also be short-lived because it quickly re-nucleates at *NBS* sites (because of its nanomolar binding affinity to *NBS*; Jalal et al., 2020b); nucleating Noc at *NBS* then rebinds CTP to close the clamp to spread and to rebind to the cell membrane, thus essentially restarting the cycle.

The expanding roles of CTP switches in biology

ATP and GTP switches that control membrane activity are widespread in all domains of life. For example, ATP binding promotes the dimerization of MinD (role in bacterial cell division site selection) and concomitantly increases its affinity for the cell membrane (Hu and Lutkenhaus, 2003; Hu et al., 2002; Ramm et al., 2019; Wu et al., 2011). MinE, a partner of MinD, stimulates the ATPase activity of MinD, promoting MinD dissociation from the membrane (Hu et al., 2002; Lutkenhaus, 2012; Park et al., 2012; Ramm et al., 2019). In eukaryotes, both the Ras-related protein (Sar) and ADP-ribosylation factor (Arf) (role in vesicle trafficking) function as GTP-dependent switches, cycling between the active GTP-bound form and the inactive GDP-bound form (Beck et al., 2008; Bielli et al., 2005; Bos et al., 2007; Dodonova et al., 2017; Hanna et al., 2016; Krauss et al., 2008; Lee et al., 2005; Zhukovsky et al., 2019). In the GDP-bound form, the amphipathic helix of Sar/Arf1 adopts a repressed conformation by burying itself into a hydrophobic pocket (Goldberg, 1998; Zhukovsky et al., 2019). The exchange of GDP for GTP induces conformational changes that push the myristoylated amphipathic helix out of the hydrophobic pocket, enabling membrane association (Goldberg, 1998; Zhukovsky et al., 2019). Our study provides the first evidence for a CTP switch that controls membrane-binding activity (Figure 7), suggesting that CTP switches are likely to control more diverse functions in biology than previously appreciated.

Limitations of the study

Several unanswered questions warrant future investigations. First, the conformation (or conformations) of the 10 AA membrane-targeting sequence in a membrane-bound state of Noc-CTP has not been resolved. Second, it is unknown how the Noc-*NBS* DNA binding event mechanistically promotes CTP binding and the subsequent NTD engagement. Relatedly, how a non-hydrolyzable CTP analog (CTPγS) can bypass the requirement for *NBS* DNA to bind to Noc is also not yet clear. Solving a co-crystal structure of a Noc-*NBS* DNA complex; studying the in-solution dynamics of clamp opening and closing in the

presence or absence of *NBS*, CTP, or CTPγS; and the availability of new types of non-hydrolyzable CTP analogs will be required to answer these questions.

Final perspectives

Our work unveils a nucleotide-dependent regulatory layer, in addition to the previously described DNA-dependent regulation (Adams et al., 2015), in the activity of the nucleoid occlusion protein Noc. The dual dependency on nucleotide and DNA guarantees a productive formation of the tripartite DNA-protein-membrane super-complex for nucleoid occlusion while allowing efficient cycling of Noc between the membrane-bound and unbound states. In this work, we also provide evidence for a CTP switch that controls membrane-binding activity, adding the control of membrane association in Noc to the role of ParB-CTP in bacterial chromosome segregation. It is likely that CTP switches are pervasive in biology but have so far been underappreciated (Basu and Koonin, 2005; Osorio-Valeriano et al., 2019; Soh et al., 2019). Finally, evolution is replete with examples of functional domains being adapted to diversify the functions of proteins. The gene encoding Noc apparently resulted from duplication and neo-functionalization of *parB* (Jalal et al., 2020b; Sievers et al., 2002; Wu and Errington, 2011), our work furthers the understanding of how a CTP switch has been adapted to a new function, and hence might have important implications in understanding biological innovations by evolution.

STAR★METHODS

Detailed methods are provided in the online version of this paper and include the following:

- KEY RESOURCES TABLE
- RESOURCE AVAILABILITY
  - Lead contact
  - Materials availability
  - Data and code availability
- EXPERIMENTAL MODEL AND SUBJECT DETAILS
- METHOD DETAILS
  - Plasmid and strain construction
  - DNA preparation for *in vitro* assays
  - Construction of biotinylated DNA substrates for bio-layer interferometry (BLI) analysis
  - Protein overexpression and purification
  - Measurement of NTPase activity by EnzChek phosphate assay
  - *In vitro* crosslinking using a sulfhydryl-to-sulfhydryl crosslinker bismaleimidoethane (BMOE)
  - Measurement of protein-DNA interactions by bio-layer interferometry (BLI)
  - Differential radial capillary action of ligand assay (DRaCALA)
  - Measurement of Noc-CTPγS/CDP interaction by isothermal titration calorimetry (ITC)
  - Liposomes preparation
  - Liposome sedimentation assays
  - Liposome flotation assays
  - Protein crystallization, structure determination, and refinement
  - Fluorescence microscopy
- QUANTIFICATION AND STATISTICAL ANALYSIS

SUPPLEMENTAL INFORMATION

Supplemental information can be found online at https://doi.org/10.1016/j.molcel.2021.06.025.

ACKNOWLEDGMENTS

This study was funded by the Royal Society University Research Fellowship Renewal (URF\R\201020 to T.B.K.L.), and a Wellcome Trust Investigator grant (209500) to J.E. that supported L.J.W. A.S.B.J.'s PhD studentship was funded by the Royal Society (RG150448), and N.T.T. was funded by the Biotechnology and Biological Sciences Research Council (BBSRC) grant-in-add (BBS/E/J/000C0683 to the John Innes Centre). We thank Diamond Light Source for access to beamlines I04 and I04-1 under proposals MX18565 and MX25108 with support from the European Community's Seventh Framework Program (FP7/2007–2013) under grant agreement 283570 (BioStruct-X).

AUTHOR CONTRIBUTIONS

Conceptualization, A.S.B.J. and T.B.K.L.; formal analysis, A.S.B.J., N.T.T., L.J.W., C.E.M.S., and D.M.L.; investigation, A.S.B.J., N.T.T., L.J.W., K.R., G.B., C.E.M.S., D.M.L., J.E., and T.B.K.L.; resources, M.R.; writing, A.S.B.J., L.J.W., D.M.L., J.E., and T.B.K.L.; supervision, T.B.K.L.

DECLARATION OF INTERESTS

The authors declare no competing interests.

Received: February 24, 2021
Revised: May 25, 2021
Accepted: June 18, 2021
Published: July 15, 2021

REFERENCES

Adams, D.W., Wu, L.J., and Errington, J. (2015). Nucleoid occlusion protein Noc recruits DNA to the bacterial cell membrane. EMBO J. *34*, 491–501.

Basu, M.K., and Koonin, E.V. (2005). Evolution of eukaryotic cysteine sulfinic acid reductase, sulfiredoxin (Srx), from bacterial chromosome partitioning protein ParB. Cell Cycle *4*, 947–952.

Beck, R., Sun, Z., Adolf, F., Rutz, C., Bassler, J., Wild, K., Sinning, I., Hurt, E., Brügger, B., Béthune, J., and Wieland, F. (2008). Membrane curvature induced by Arf1-GTP is essential for vesicle formation. Proc. Natl. Acad. Sci. U S A *105*, 11731–11736.

Bielli, A., Haney, C.J., Gabreski, G., Watkins, S.C., Bannykh, S.I., and Aridor, M. (2005). Regulation of Sar1 NH2 terminus by GTP binding and hydrolysis promotes membrane deformation to control COPII vesicle fission. J. Cell Biol. *171*, 919–924.

Bos, J.L., Rehmann, H., and Wittinghofer, A. (2007). GEFs and GAPs: critical elements in the control of small G proteins. Cell *129*, 865–877.

Breier, A.M., and Grossman, A.D. (2007). Whole-genome analysis of the chromosome partitioning and sporulation protein Spo0J (ParB) reveals spreading and origin-distal sites on the Bacillus subtilis chromosome. Mol. Microbiol. *64*, 703–718.

Buckstein, M.H., He, J., and Rubin, H. (2008). Characterization of nucleotide pools as a function of physiological state in Escherichia coli. J. Bacteriol. *190*, 718–726.

Cowtan, K. (2006). The Buccaneer software for automated model building. 1. Tracing protein chains. Acta Crystallogr. D Biol. Crystallogr. *62*, 1002–1011.

Dodonova, S.O., Aderhold, P., Kopp, J., Ganeva, I., Röhling, S., Hagen, W.J.H., Sinning, I., Wieland, F., and Briggs, J.A.G. (2017). 9Å structure of the COPI coat reveals that the Arf1 GTPase occupies two contrasting molecular environments. eLife *6*, e26691.

Emsley, P., and Cowtan, K. (2004). Coot: model-building tools for molecular graphics. Acta Crystallogr. D Biol. Crystallogr. *60*, 2126–2132.

Evans, P.R., and Murshudov, G.N. (2013). How good are my data and what is the resolution? Acta Crystallogr. D Biol. Crystallogr. *69*, 1204–1214.

Funnell, B.E. (2016). ParB partition proteins: complex formation and spreading at bacterial and plasmid centromeres. Front. Mol. Biosci. *3*, 44.

Goldberg, J. (1998). Structural basis for activation of ARF GTPase: mechanisms of guanine nucleotide exchange and GTP-myristoyl switching. Cell *95*, 237–248.

Graham, T.G.W., Wang, X., Song, D., Etson, C.M., van Oijen, A.M., Rudner, D.Z., and Loparo, J.J. (2014). ParB spreading requires DNA bridging. Genes Dev. *28*, 1228–1238.

Hanna, M.G., 4th, Mela, I., Wang, L., Henderson, R.M., Chapman, E.R., Edwardson, J.M., and Audhya, A. (2016). Sar1 GTPase activity is regulated by membrane curvature. J. Biol. Chem. *291*, 1014–1027.

Hu, Z., and Lutkenhaus, J. (2003). A conserved sequence at the C-terminus of MinD is required for binding to the membrane and targeting MinC to the septum. Mol. Microbiol. *47*, 345–355.

Hu, Z., Gogol, E.P., and Lutkenhaus, J. (2002). Dynamic assembly of MinD on phospholipid vesicles regulated by ATP and MinE. Proc. Natl. Acad. Sci. U S A *99*, 6761–6766.

Hwang, L.C., Vecchiarelli, A.G., Han, Y.-W., Mizuuchi, M., Harada, Y., Funnell, B.E., and Mizuuchi, K. (2013). ParA-mediated plasmid partition driven by protein pattern self-organization. EMBO J. *32*, 1238–1249.

Jalal, A.S.B., and Le, T.B.K. (2020). Bacterial chromosome segregation by the ParABS system. Open Biol. *10*, 200097.

Jalal, A.S., Tran, N.T., and Le, T.B. (2020a). ParB spreading on DNA requires cytidine triphosphate in vitro. eLife *9*, e53515.

Jalal, A.S.B., Tran, N.T., Stevenson, C.E., Chan, E.W., Lo, R., Tan, X., Noy, A., Lawson, D.M., and Le, T.B.K. (2020b). Diversification of DNA-Binding specificity by permissive and specificity-switching mutations in the ParB/Noc protein family. Cell Rep. *32*, 107928.

Jenkinson, H.F. (1983). Altered arrangement of proteins in the spore coat of a germination mutant of Bacillus subtilis. J. Gen. Microbiol. *129*, 1945–1958.

Krauss, M., Jia, J.-Y., Roux, A., Beck, R., Wieland, F.T., De Camilli, P., and Haucke, V. (2008). Arf1-GTP-induced tubule formation suggests a function of Arf family proteins in curvature acquisition at sites of vesicle budding. J. Biol. Chem. *283*, 27717–27723.

Krissinel, E. (2015). Stock-based detection of protein oligomeric states in jsPISA. Nucleic Acids Res. *43* (W1), W314–W319.

Lee, M.C.S., Orci, L., Hamamoto, S., Futai, E., Ravazzola, M., and Schekman, R. (2005). Sar1p N-terminal helix initiates membrane curvature and completes the fission of a COPII vesicle. Cell *122*, 605–617.

Lim, H.C., Surovtsev, I.V., Beltran, B.G., Huang, F., Bewersdorf, J., and Jacobs-Wagner, C. (2014). Evidence for a DNA-relay mechanism in ParABS-mediated chromosome segregation. eLife *3*, e02758.

Lutkenhaus, J. (2012). The ParA/MinD family puts things in their place. Trends Microbiol. *20*, 411–418.

McCoy, A.J., Grosse-Kunstleve, R.W., Adams, P.D., Winn, M.D., Storoni, L.C., and Read, R.J. (2007). Phaser crystallographic software. J. Appl. Cryst. *40*, 658–674.

Murray, H., Ferreira, H., and Errington, J. (2006). The bacterial chromosome segregation protein Spo0J spreads along DNA from parS nucleation sites. Mol. Microbiol. *61*, 1352–1361.

Murshudov, G.N., Vagin, A.A., and Dodson, E.J. (1997). Refinement of macromolecular structures by the maximum-likelihood method. Acta Crystallogr. D Biol. Crystallogr. *53*, 240–255.

Nyholm, T.K.M., Özdirekcan, S., and Killian, J.A. (2007). How protein transmembrane segments sense the lipid environment. Biochemistry *46*, 1457–1465.

Osorio-Valeriano, M., Altegoer, F., Steinchen, W., Urban, S., Liu, Y., Bange, G., and Thanbichler, M. (2019). ParB-type DNA segregation proteins are CTP-dependent molecular switches. Cell *179*, 1512–1524.e15.

Pang, T., Wang, X., Lim, H.C., Bernhardt, T.G., and Rudner, D.Z. (2017). The nucleoid occlusion factor Noc controls DNA replication initiation in Staphylococcus aureus. PLoS Genet. *13*, e1006908.

Park, K.-T., Wu, W., Lovell, S., and Lutkenhaus, J. (2012). Mechanism of the asymmetric activation of the MinD ATPase by MinE. Mol. Microbiol. *85*, 271–281.

Partridge, S.R., and Errington, J. (1993). The importance of morphological events and intercellular interactions in the regulation of prespore-specific gene expression during sporulation in Bacillus subtilis. Mol. Microbiol. *8*, 945–955.

Potterton, L., Agirre, J., Ballard, C., Cowtan, K., Dodson, E., Evans, P.R., Jenkins, H.T., Keegan, R., Krissinel, E., Stevenson, K., et al. (2018). CCP4i2: the new graphical user interface to the CCP4 program suite. Acta Crystallogr. D Struct. Biol. *74*, 68–84.

Ramm, B., Heermann, T., and Schwille, P. (2019). The E. coli MinCDE system in the regulation of protein patterns and gradients. Cell. Mol. Life Sci. *76*, 4245–4273.

Rejzek, M., and Le, T.B.K. (2021). Chemical synthesis and purification of a non-hydrolyzable CTP analog CTPγS. BioRxiv. https://doi.org/10.1101/2021.01.13.426546.

Rodrigues, C.D.A., and Harry, E.J. (2012). The Min system and nucleoid occlusion are not required for identifying the division site in Bacillus subtilis but ensure its efficient utilization. PLoS Genet. *8*, e1002561.

Sanchez, A., Cattoni, D.I., Walter, J.-C., Rech, J., Parmeggiani, A., Nollmann, M., and Bouet, J.-Y. (2015). Stochastic self-assembly of ParB proteins builds the bacterial DNA segregation apparatus. Cell Syst. *1*, 163–173.

Sievers, J., Raether, B., Perego, M., and Errington, J. (2002). Characterization of the parB-like yyaA gene of Bacillus subtilis. J. Bacteriol. *184*, 1102–1111.

Skubák, P., and Pannu, N.S. (2013). Automatic protein structure solution from weak X-ray data. Nat. Commun. *4*, 2777.

Soh, Y.-M., Davidson, I.F., Zamuner, S., Basquin, J., Bock, F.P., Taschner, M., Veening, J.-W., De Los Rios, P., Peters, J.-M., and Gruber, S. (2019). Self-organization of *parS* centromeres by the ParB CTP hydrolase. Science *366*, 1129–1133.

Thanbichler, M., Iniesta, A.A., and Shapiro, L. (2007). A comprehensive set of plasmids for vanillate- and xylose-inducible gene expression in Caulobacter crescentus. Nucleic Acids Res. *35*, e137.

Toro, E., Hong, S.-H., McAdams, H.H., and Shapiro, L. (2008). Caulobacter requires a dedicated mechanism to initiate chromosome segregation. Proc. Natl. Acad. Sci. U S A *105*, 15435–15440.

Vecchiarelli, A.G., Mizuuchi, K., and Funnell, B.E. (2012). Surfing biological surfaces: exploiting the nucleoid for partition and transport in bacteria. Mol. Microbiol. *86*, 513–523.

Vecchiarelli, A.G., Hwang, L.C., and Mizuuchi, K. (2013). Cell-free study of F plasmid partition provides evidence for cargo transport by a diffusion-ratchet mechanism. Proc. Natl. Acad. Sci. U S A *110*, E1390–E1397.

Vecchiarelli, A.G., Neuman, K.C., and Mizuuchi, K. (2014). A propagating ATPase gradient drives transport of surface-confined cellular cargo. Proc. Natl. Acad. Sci. U S A *111*, 4880–4885.

Veiga, H., Jorge, A.M., and Pinho, M.G. (2011). Absence of nucleoid occlusion effector Noc impairs formation of orthogonal FtsZ rings during Staphylococcus aureus cell division. Mol. Microbiol. *80*, 1366–1380.

Williams, C.J., Headd, J.J., Moriarty, N.W., Prisant, M.G., Videau, L.L., Deis, L.N., Verma, V., Keedy, D.A., Hintze, B.J., Chen, V.B., et al. (2018). MolProbity: More and better reference data for improved all-atom structure validation. Protein Sci. *27*, 293–315.

Winter, G. (2010). xia2: an expert system for macromolecular crystallography data reduction. J. Appl. Cryst. *43*, 186–190.

Winter, G., Waterman, D.G., Parkhurst, J.M., Brewster, A.S., Gildea, R.J., Gerstel, M., Fuentes-Montero, L., Vollmar, M., Michels-Clark, T., Young, I.D., et al. (2018). DIALS: implementation and evaluation of a new integration package. Acta Crystallogr. D Struct. Biol. *74*, 85–97.

Wu, L.J., and Errington, J. (2004). Coordination of cell division and chromosome segregation by a nucleoid occlusion protein in Bacillus subtilis. Cell *117*, 915–925.

Wu, L.J., and Errington, J. (2011). Nucleoid occlusion and bacterial cell division. Nat. Rev. Microbiol. *10*, 8–12.

Wu, L.J., Ishikawa, S., Kawai, Y., Oshima, T., Ogasawara, N., and Errington, J. (2009). Noc protein binds to specific DNA sequences to coordinate cell division with chromosome segregation. EMBO J. *28*, 1940–1952.

Wu, W., Park, K.-T., Holyoak, T., and Lutkenhaus, J. (2011). Determination of the structure of the MinD-ATP complex reveals the orientation of MinD on the membrane and the relative location of the binding sites for MinE and MinC. Mol. Microbiol. *79*, 1515–1528.

Yu, Y., Zhou, J., Gueiros-Filho, F.J., Kearns, D.B., and Jacobson, S.C. (2021). Noc corrals migration of FtsZ protofilaments during cytokinesis in Bacillus subtilis. MBio *12*, e02964-20.

Zhukovsky, M.A., Filograna, A., Luini, A., Corda, D., and Valente, C. (2019). Protein amphipathic helix insertion: a mechanism to induce membrane fission. Front. Cell Dev. Biol. *7*, 291.

Please cite this article in press as: Jalal et al., CTP regulates membrane-binding activity of the nucleoid occlusion protein Noc, Molecular Cell (2021), https://doi.org/10.1016/j.molcel.2021.06.025

CellPress
OPEN ACCESS

STAR★METHODS

KEY RESOURCES TABLE

REAGENT or RESOURCE	SOURCE	IDENTIFIER
Bacterial and virus strains		
Please refer to Table S1		N/A
Chemicals, peptides, and recombinant proteins		
cOmplete Mini EDTA-free Protease Inhibitor Cocktail	Roche Applied Science	Cat# 11836170001
BamHI	NEB	Cat# R0136S
Bismaleimidoethane (BMOE)	ThermoFisher	Cat# 22323
CTPγS	Jena Bioscience and in-house synthesis (Rejzek and Le, 2021)	N/A
E. coli total lipid extract	Avanti/Merck	Cat# 100500C-100MG
FM 5-95	ThermoFisher	Cat# T23360
NTP	ThermoFisher	Cat# R0481
P^{32}-α-CTP	Perkin Elmer	Cat# BLU008H250UC
Critical commercial assays		
Amersham Protran supported Western blotting membranes, nitrocellulose	GE Healthcare	Cat# GE10600016
Dip-and-Read Streptavidin (SA) biosensors	Molecular Devices	Cat# 18-5019
EnzChek Phosphate Assay Kit	ThermoFisher	Cat# E6646
Gateway BP Clonase II enzyme mix	ThermoFisher	Cat# 11789020
Gibson Assembly Master Mix	NEB	Cat# E2611S
HiLoad 16/600 Superdex 75pg column	GE Healthcare	Cat# GE28989333
HIS-Select Cobalt Affinity Gel	Sigma-Aldrich	Cat# H8162
HisTrap High Performance column	GE Healthcare	Cat# GE17524801
HiTrap Heparin High Performance column	GE Healthcare	Cat# GE17040601
PD 10 Desalting Columns	Sigma-Aldrich	Cat# GE17085101
Deposited data		
Crystal structures	This study	PDB: 7NFU and PDB: 7NG0
Mendeley data	This study	https://doi.org/10.17632/px2k9hr94c.1
Oligonucleotides		
Please refer to Table S2		N/A
Recombinant DNA		
Please refer to Table S2		N/A
Software and algorithms		
AIMLESS	(Evans and Murshudov, 2013)	https://www.ccp4.ac.uk/
BLItz Pro	Molecular Devices	Cat# 50-0156
BUCCANEER	(Cowtan, 2006)	https://www.ccp4.ac.uk/
CCP4i2	(Potterton et al., 2018)	https://www.ccp4.ac.uk/
COOT	(Emsley and Cowtan, 2004)	https://www2.mrc-lmb.cam.ac.uk/personal/pemsley/coot/
CRANK2	(Skubák and Pannu, 2013)	https://www.ccp4.ac.uk/
DIALS	(Winter et al., 2018)	https://dials.github.io/
Excel 2016	Microsoft	RRID: SCR_016137
ImageJ	NIH	https://imagej.net/RRID:SCR_003070
Image Studio Lite	LI-COR Biosciences	RRID: SCR_013715

(*Continued on next page*)

Please cite this article in press as: Jalal et al., CTP regulates membrane-binding activity of the nucleoid occlusion protein Noc, Molecular Cell (2021), https://doi.org/10.1016/j.molcel.2021.06.025

Continued

REAGENT or RESOURCE	SOURCE	IDENTIFIER
jsPISA	(Krissinel, 2015)	http://www.ccp4.ac.uk/pisa/
MetaMorph	Molecular Devices	RRID:SCR_002368
MolProbity	(Williams et al., 2018)	http://molprobity.biochem.duke.edu/
PHASER	(McCoy et al., 2007)	https://phenix-online.org/
PyMOL	The PyMOL Molecular Graphics System	https://pymol.org/2/
R	R Foundation for Statistical Computing	https://www.r-project.org/
REFMAC5	(Murshudov et al., 1997)	https://www.ccp4.ac.uk/
XIA2	(Winter, 2010)	https://xia2.github.io/index.html

RESOURCE AVAILABILITY

Lead contact

Questions about or requests for methods, strains, and resources generated in this study can be directed to the Lead Contact, Tung Le (tung.le@jic.ac.uk).

Materials availability

Plasmids and strains generated in this study are available upon request to the Lead Contact.

Data and code availability

- The crystallographic structure of *G. thermoleovorans* NocΔCTD and *G. thermoleovorans* NocNΔ26ΔCTD have been deposited in the PDB with accession codes PDB: 7NFU and PDB: 7NG0, respectively. All images and source data presented in figures are available in Mendeley Data at https://data.mendeley.com/datasets/px2k9hr94c/1.
- This paper does not report original code.
- Any additional information required to reanalyze the data reported in this paper is available from the Lead Contact upon request.

EXPERIMENTAL MODEL AND SUBJECT DETAILS

Escherichia coli and *B. subtilis* were grown in LB and CH medium (Partridge and Errington, 1993), respectively. Carbenicillin (100 μg/mL), chloramphenicol (50 μg/mL), and tetracycline (12 μg/mL) were used for selection in *E. coli*, as required. Kanamycin (5 μg/mL), spectinomycin (50 μg/mL), and tetracycline (10 μg/mL) were used for selection in *B. subtilis*, as required. Xylose was added as needed at the concentration indicated.

METHOD DETAILS

Plasmid and strain construction

Construction of pET21b::noc (WT)-his$_6$

A double-stranded DNA (dsDNA) fragment containing a codon-optimized *B. subtilis noc* gene was chemically synthesized (gBlocks, IDT). The pET21b plasmid backbone was generated via a double digestion of pET21b::*Caulobacter crescentus parB-his$_6$* with NdeI and HindIII (Lim et al., 2014). The resulting backbone was subsequently gel-purified and assembled with the *noc* gBlocks fragment using a 2x Gibson master mix. Briefly, 2.5 μL of the gBlocks fragment and 2.5 μL of NdeI-HindIII-cut pET21b at equimolar concentration were added to 5 μL of a 2x Gibson master mix (NEB). The mixture was incubated at 50°C for 60 min. Subsequently, 5 μL was used to transform chemically competent *E. coli* DH5α cells. Gibson assembly was possible owing to a 23-bp sequence shared between the NdeI-HindIII-cut pET21b backbone and the gBlocks fragment. The resulting plasmid was verified by Sanger sequencing (Eurofins, Germany).

Construction of pET21b::noc (Δ2K, Δ4, K2E, S4L, F5A, or F5E)-his$_6$

Same procedure as above, except that dsDNA fragments containing codon-optimized *B. subtilis noc* (Δ2K, Δ4, K2E, S4L, F5A, or F5E) variants were chemically synthesized instead (gBlocks, IDT).

Construction of pET21b::nocNΔ10-his$_6$

The coding sequence of a 10-amino-acid N-terminally truncated Noc (NocNΔ10) was amplified by PCR using primers AJ65 and AJ66, and pET21b::*noc-his$_6$* as a template. The resulting PCR product was gel-purified and assembled into an NdeI-HindIII-cut pET21b using a 2x Gibson master mix. Gibson assembly was possible owing to a 23-bp sequence shared between the NdeI- and-HindIII cut pET21b backbone and the PCR amplified fragment. The 23-bp homologous region was introduced during the synthesis of primers AJ65 and AJ66. The resulting plasmid was verified by Sanger sequencing (Eurofins, Germany).

Please cite this article in press as: Jalal et al., CTP regulates membrane-binding activity of the nucleoid occlusion protein Noc, Molecular Cell (2021), https://doi.org/10.1016/j.molcel.2021.06.025

Construction of pET21b::noc (R89A)-his$_6$

To introduce the R89A mutation into the coding sequence of Noc, primers P3296 and AJ73, and primers P3297 and AJ74 were used in PCR reactions to amplify the left half and the right half of *noc (R89A)*, respectively, from the *pET21b::noc-his$_6$* template. A 15-bp overlapping region between the two PCR fragments contained the point mutation and also enabled their assembly by a Gibson master mix. Briefly, 1.7 μL of each PCR-amplified DNA fragment and 1.6 μL of a gel-purified NdeI-HindIII-cut pET21b at equimolar concentration were added to 5 μL of a 2x Gibson master mix. The mixture was incubated at 50°C for 60 min. Subsequently, 5 μL was used to transform chemically competent *E. coli* DH5α cells. The resulting plasmid was verified by Sanger sequencing (Eurofins, Germany).

Construction of pET21b::noc (N121S)-his$_6$

The same procedure as above was used to introduce the N121S mutation into the coding sequence of Noc, except that primers P3296 and AJ87, and primers P3297 and AJ86 were used to amplify the left half and the right half of *noc (N121S)*, respectively, from the *pET21b::noc-his$_6$* template.

Construction of pET21b::noc (E29C)-his$_6$

The same procedure as above was used to introduce the E29C mutation into the coding sequence of Noc, except that primers P3296 and AJ85, and primers P3297 and AJ84 were used to amplify the left half and the right half of *noc (E29C)*, respectively, from the *pET21b::noc-his$_6$* template.

Construction of pET21b::noc (E29C R89A)-his$_6$

The same procedure as above was used to introduce the R89A mutation into the coding sequence of Noc (E29C), except that primers P3296 and AJ73, and primers P3297 and AJ74 were used to amplify the left half and the right half of *noc (E29C R89A)*, respectively, from the *pET21b::noc (E29C)-his$_6$* template.

Construction of pET21b::noc (E29C N121S)-his$_6$

The same procedure as above was used to introduce the N121S mutation into the coding sequence of Noc (E29C), except that primers P3296 and AJ86, and primers P3297 and AJ87 were used to amplify the left half and the right half of *noc (E29C N121S)*, respectively, from the *pET21b::noc (E29C)-his$_6$* template.

Construction of pET21b::Geobacillus thermoleovorans nocΔCTD-his$_6$

A dsDNA fragment containing the coding sequence of a 42-amino-acid C-terminally truncated *G. thermoleovorans* Noc was chemically synthesized (gBlocks, IDT). The gBlocks fragment was assembled into an *Nde*I-HindIII-cut pET21b using a 2x Gibson master mix. Gibson assembly was possible owing to a 23-bp sequence shared between the NdeI-HindIII-cut pET21b backbone and the gBlocks fragment. The resulting plasmid was verified by Sanger sequencing (Eurofins, Germany).

Construction of pET21b::Geobacillus thermoleovorans nocNΔ26ΔCTD-his$_6$

The coding sequence of a 26-amino-acid N-terminally truncated and 42-amino-acid C-terminally truncated *G. thermoleovorans* Noc was amplified by PCR using primers AJ76 and AJ81, and pET21b::*Geobacillus thermoleovo*rans NocΔCTD-his$_6$ as a template. The resulting PCR product was gel-purified and assembled into an NdeI-HindIII-cut pET21b using a 2x Gibson master mix. Gibson assembly was possible owing to a 23-bp sequence shared between the NdeI-and-HindIII cut pET21b backbone and the PCR amplified fragment. The 23-bp homologous region was introduced during the synthesis of primers AJ76 and AJ81. The resulting plasmid was verified by Sanger sequencing (Eurofins, Germany).

Construction of pMCS5-4xNBS

A dsDNA fragment containing four *NBS* sites were chemically synthesized (gBlocks, IDT). The gBlocks fragment was assembled into an EcoRI-cut pMCS5 (Thanbichler et al., 2007) using a 2x Gibson master mix. Gibson assembly was possible owing to a 23-bp sequence shared between the EcoRI-cut pMCS5 backbone and the gBlocks fragment. The resulting plasmid was verified by Sanger sequencing (Eurofins, Germany).

Construction of pSG4926N121S and B. subtilis strains harboring the noc (N121S)-yfp fusion

The N121S substitution was introduced into the *noc(WT)-yfp(mut1)* plasmid pSG4926 by site-directed mutagenesis using PFU Turbo DNA polymerase (Agilent Technologies), and primers Noc(N121S)-F and Noc(N121S)-R. After verification of the mutation by DNA sequencing, the mutagenized plasmid (pSG4926N121S) was introduced into the *B. subtilis* Δ*noc* mutant (DWA117) by transformation (Jenkinson, 1983) to generate strain 4746. To construct strain 4747, the Δ*minCminD* deletion was introduced into strain 4746 by transforming strain 4746 with the chromosomal DNA of strain DWA564, with selection for kanamycin resistance. The transformation plates were incubated at 30°C. Note that fusions to YFP(mut1) or mYFP gave a similar localization pattern and were both functional for the wild-type Noc.

DNA preparation for *in vitro* assays

A 22-bp palindromic single-stranded DNA (ssDNA) oligomer (*NBS*: GGATATTTCCCGGGAAATATCC or *parS*: GGATGTTTCACGTGAAACATCC) [dissolved to 100 μM in buffer containing 1 mM Tris-HCl pH 8.0 and 5 mM NaCl] was heated at 98°C for 5 min before being left to cool down to room temperature overnight to form 50 μM *parS* or *NBS* DNA duplex. The core sequences of *NBS* and *parS* are underlined.

Construction of biotinylated DNA substrates for bio-layer interferometry (BLI) analysis

DNA constructs were chemically synthesized (gBlocks dsDNA fragments, IDT) with M13F and M13R homologous regions at each end. To generate a dual biotin-labeled DNA substrate, PCR reactions were performed using a 2x GoTaq PCR master mix (Promega),

Please cite this article in press as: Jalal et al., CTP regulates membrane-binding activity of the nucleoid occlusion protein Noc, Molecular Cell (2021), https://doi.org/10.1016/j.molcel.2021.06.025

biotin-labeled M13F and biotin-labeled M13R primers, and gBlocks fragments as templates. PCR products were gel purified, and subsequently used in BLI assays.

Protein overexpression and purification

Plasmids pET21b::*noc-his*$_6$ (WT or mutants) were introduced into *E. coli* Rosetta (DE3) competent cells by heat-shock transformation. A 10-mL overnight culture was used to inoculate 1 L of LB medium + carbenicillin + chloramphenicol. Cells were grown at 37°C with shaking at 250 rpm to an OD_{600} of ~0.4. The culture was then left to cool down to 4°C before isopropyl-β-D-thiogalactopyranoside (IPTG) was added to a final concentration of 1 mM. The culture was shaken for an additional 3 hr at 28°C before the cells were pelleted by centrifugation. Pelleted cells were resuspended in a buffer containing 100 mM Tris-HCl pH 8.0, 250 mM NaCl, 10 mM imidazole, 5% (v/v) glycerol, 10 mg of lysozyme, and an EDTA-free protease inhibitor tablet (Merck). Cells were lysed by sonication (10 cycles of 15 s with 10 s resting on ice in between each cycle). The cell debris was removed through centrifugation at 28,000 g for 30 min and the supernatant was filtered through a 0.45 μm filter (Sartorius). The lysate was then loaded into a 1-mL HisTrap column (GE Healthcare) that had been equilibrated with buffer A [100 mM Tris-HCl pH 8.0, 250 mM NaCl, 10 mM imidazole, and 5% (v/v) glycerol]. Protein was eluted from the column using an increasing gradient of imidazole (10 mM to 500 mM) in the same buffer. Noc-containing fractions were pooled together and diluted to a conductivity of 16 mS/cm before being loaded onto a 1-mL Heparin HP column (GE Healthcare) that had been equilibrated with 100 mM Tris-HCl pH 8.0, 25 mM NaCl, and 5% (v/v) glycerol. Protein was eluted from the Heparin column using an increasing gradient of NaCl (25 mM to 1 M) in the same buffer. Lastly, proteins were polished using a gel filtration column. To do so, Noc-containing fractions were concentrated using an Amicon Ultra-15 10 kDa cut-off spin filter (Merck) before being loaded onto a Superdex-75 gel filtration column (GE Healthcare). The gel filtration column was pre-equilibrated with buffer containing 10 mM Tris-HCl pH 8.0 and 250 mM NaCl. Eluted protein fractions were analyzed for purity by SDS-PAGE.

Noc variants that were used in crosslinking experiments were purified using a one-step Ni-affinity column, and all buffers were adjusted to pH 7.4 which was optimal for crosslinking reactions. Purified proteins were desalted using a PD-10 column (Merck), concentrated using an Amicon Ultra-4 10 kDa cut-off spin column (Merck), and stored at −80°C in a storage buffer [100 mM Tris-HCl pH 7.4, 250 mM NaCl, 10% (v/v) glycerol, and 1 mM TCEP].

Measurement of NTPase activity by EnzChek phosphate assay

NTP hydrolysis was monitored using an EnzChek Phosphate Assay Kit (Thermo Fisher). Samples (100 μL) containing a reaction buffer ± 0 to 1 mM of CTP ± 1 μM *NBS*/*parS* dsDNA + 1 μM of purified Noc (WT or mutants) were assayed in a Biotek EON plate reader for 15 hr with readings every minute. The reaction buffer (1 mL) typically contained 640 μL ultrapure water, 100 μL 10x customized reaction buffer [100 mM Tris pH 8.0, 2 M NaCl, and 20 mM $MgCl_2$], 200 μL MESG substrate solution, and 10 μL purine nucleoside phosphorylase (1 unit). Reactions with buffer only, buffer + protein only or buffer + NTP only were also included as controls. The plates were shaken at 280 rpm continuously for 15 hr at 25°C. The inorganic phosphate standard curve was also constructed according to the manual. Each assay was triplicated. The NTPase rates were calculated using a linear regression fitting in Excel.

In vitro crosslinking using a sulfhydryl-to-sulfhydryl crosslinker bismaleimidoethane (BMOE)

A 50 μL mixture of 10 μM Noc (WT/mutants) ± 1 mM NTP ± 1 μM 22-bp *NBS*/*parS* dsDNA was assembled in a reaction buffer [10 mM Tris-HCl pH 7.4, 200 mM NaCl, and 1 mM $MgCl_2$] and was incubated for 10 min at 22°C or for 1, 5, 10, 15, and 30 min at 4°C. Subsequently, BMOE was added to the final concentration of 1 mM, and the reaction was quickly mixed by three pulses of vortexing. SDS-PAGE sample buffer containing 23 mM β-mercaptoethanol was then added immediately to quench the crosslinking reaction. Samples were heated to 50°C for 10 min before being loaded on 12% WedgeWell Tris-Glycine polyacrylamide gels (Thermo Fisher). Each experiment was triplicated. Polyacrylamide gels were stained in an InstantBlue Coomassie solution (Abcam) and band intensity was quantified using Image Studio Lite (LI-COR Biosciences). The crosslinked fractions were averaged, and their standard errors were calculated in Excel.

CTPγS was custom synthesized either in-house (Rejzek and Le, 2021) or by Jena Biosciences.

Measurement of protein-DNA interactions by bio-layer interferometry (BLI)

Bio-layer interferometry (BLI) experiments were conducted using a BLItz system equipped with Dip-and-Read Streptavidin (SA) Biosensors (Molecular Devices). BLItz monitors wavelength shifts (nm) resulting from changes in the optical thickness of the sensor surface during association or dissociation of the analyte. All BLI experiments were performed at 22°C. Briefly, the streptavidin biosensor was hydrated in a low-salt binding buffer [100 mM Tris-HCl pH 8.0, 150 mM NaCl, 1 mM $MgCl_2$, and 0.005% Tween 20] for at least 10 min before each experiment. Biotinylated double-stranded DNA (dsDNA) was immobilized onto the surface of the SA sensor through a cycle of Baseline (30 s), Association (120 s), and Dissociation (120 s). Briefly, the tip of the biosensor was dipped into a binding buffer for 30 s to establish the baseline, then to 1 μM biotinylated dsDNA for 120 s, and finally to a low salt binding buffer for 120 s to allow for dissociation. After the immobilization of DNA on the sensor, association reactions were monitored at 1 μM dimer concentration of Noc (WT/mutants) (with or without 1mM NTP) for 600 s. At the end of each binding step, the sensor was transferred into a protein-free binding buffer to follow the dissociation kinetics for 600 s. The sensor can be recycled by dipping in a high-salt buffer [100 mM Tris-HCl pH 8.0, 2 M NaCl, 1mM EDTA, and 0.005% Tween 20] for 20 min to remove bound Noc.

Please cite this article in press as: Jalal et al., CTP regulates membrane-binding activity of the nucleoid occlusion protein Noc, Molecular Cell (2021), https://doi.org/10.1016/j.molcel.2021.06.025

For experiments where a closed DNA substrate was cleaved to generate a free DNA end, DNA-coated sensors were dipped into 300 μL of restriction solution [266 μL of water, 30 μL of 10x CutSmart buffer (NEB), and 4 μL of BamHI-HF restriction enzyme (20,000 units/mL)] for 30 min at 37°C.

Differential radial capillary action of ligand assay (DRaCALA)

Purified Noc (WT and variants) (final concentration: 30 μM) were incubated with 5 nM radiolabeled P^{32}-α-CTP (Perkin Elmer), 30 μM of unlabeled CTP (Thermo Fisher), 1 μM of 22 bp *NBS* or *parS* DNA in the reaction buffer [100 mM Tris pH 8.0, 100 mM NaCl, and 5 mM $CaCl_2$] for 5 min at room temperature. For the NTP competition assay, the mixture was further supplemented with 500 μM of either unlabeled CTP, CDP, ATP, GTP, or UTP. Four μL of samples were spotted slowly onto a dry nitrocellulose membrane (Amersham Protran 0.45 μm) and air-dried. Subsequently, membranes were exposed to a phosphor screen (GE Healthcare) for two minutes. Each DRaCALA assay was triplicated, and a representative autoradiograph was shown.

Measurement of Noc-CTPγS/CDP interaction by isothermal titration calorimetry (ITC)

All ITC experiments were recorded using a MicroCal PEAQ ITC instrument (Malvern Panalytical, UK). Experiments were performed at 4°C and both protein and ligand were in the buffer 100 mM Tris-HCl pH 8.0, 100 mM NaCl, and 5 mM $CaCl_2$. The calorimetric cell was filled with 100 μM monomer concentration of either *B. subtilis* Noc (WT), Noc (R89A), or Noc (N121S), and was titrated with 3 mM CTPγS. For each ITC run, a single injection of 0.5 μL of 3 mM CTPγS or CDP was performed first, followed by 19 injections of 2 μL each. Injections were carried out at 120 s intervals with a stirring speed of 750 rpm. Each experiment was run in duplicate. The raw titration data were integrated and fitted to a one-site binding model using the built-in software of the MicroCal PEAQ ITC. Controls (CTPγS/CDP into buffer and buffer into protein) were performed and no signal was observed.

Liposomes preparation

E. coli total lipid extract (25 mg/mL in chloroform, Avanti) was used to generate model liposomes. Briefly, an argon stream was used to evaporate chloroform from the lipids, and the resulting lipid cake was further dried under vacuum for 2 hr. The lipids were subsequently re-suspended in a buffer containing 100 mM Tris-HCl pH 7.4 and 200 mM NaCl. The mixture was incubated at 30°C for 30 min with vigorous vortexing every 5 min. The final concentration of the resuspended lipids was 50 mg/mL. The resuspended lipids were then extruded to ~100 nm single unilamellar vesicles (SUV) using a mini-extruder (Avanti) equipped with polycarbonate membranes (0.1 μm pore size). The size of the resulting SUVs was confirmed by dynamic light scattering.

Liposome sedimentation assays

A 500 μL mixture of 0.75 μM Noc (WT/mutants) ± 1.0 mg/mL liposomes ± 1 mM NTP ± DNA (either 1 μM of 22-bp *NBS*/*parS* dsDNA or 100 nM of *NBS*-harboring/empty plasmid) was assembled in a binding buffer [100 mM Tris-HCl pH 7.4, 200 mM NaCl, and 1 mM $MgCl_2$]. The mixture was incubated at 22°C for 20 min before being centrifuged at 50,000 rpm for 20 min at 22°C (TLA120.2 rotor, Optima Max-E Benchtop Ultracentrifuge). After centrifugation, the supernatant was transferred to a new 1.5-mL Eppendorf tube. The pellet was resuspended in 500 μL of binding buffer before being transferred to another 1.5-mL Eppendorf tube. SDS-PAGE sample buffer was then added, and the samples were heated at 70°C for 5 min before being loaded onto either 12% WedgeWell Tris-Glycine polyacrylamide gels, Novex 20% TBE polyacrylamide gels, or 1% agarose gels. Gels were subsequently stained in an InstantBlue Coomassie solution (to detect protein bands) or in a Sybr Green solution (to detect DNA bands). Each assay was triplicated. Protein/DNA band intensity was quantified using Image Studio Lite (LI-COR Biosciences). The protein/DNA fractions were averaged, and their standard errors were calculated in Excel.

For nuclease treatment, a 500 μL mixture of 0.75 μM Noc (WT/mutants) ± 1.0 mg/mL liposomes ± 1 mM NTP ± 100 nM of *NBS*-harboring/empty plasmid was incubated at room temperature for 10 min. Afterward, 1 μL of Benzonase (250 units/ μL) was added, and the mixture was incubated for a further 10 min at 22°C before ultracentrifugation.

For re-sedimentation experiments (Figure 4D), the pellet (from the first round of ultracentrifugation) was resuspended either in 500 μL of binding buffer [100 mM Tris-HCl pH 7.4, 200 mM NaCl, and 1 mM $MgCl_2$] or in a stripping buffer [100 mM Tris-HCl pH 7.4, 200 mM NaCl, and 10 mM EDTA]. The resuspended pellet was centrifuged for the second time at 50,000 rpm for 20 min at 22°C. After the second centrifugation, the supernatant was transferred to a new 1.5-mL Eppendorf tube. The pellet was resuspended in 500 μL of binding buffer before being transferred to another 1.5-mL Eppendorf tube. SDS-PAGE sample buffer was then added to the supernatant and the pellet fractions, and the samples were analyzed on denaturing polyacrylamide gels.

Liposome flotation assays

A 200 μL mixture of 0.75 μM Noc (WT/mutants) ± 1.0 mg/mL liposomes ± 1 mM NTP ± 20 nM *NBS*-harboring/empty plasmid was assembled in a 30% sucrose buffer [100 mM Tris-HCl pH 7.4, 200 mM NaCl, 1 mM $MgCl_2$, and 30% sucrose]. The mixture was incubated at 22°C for 5 min before being overlaid with 250 μL of a 25% sucrose buffer [100 mM Tris-HCl pH 7.4, 200 mM NaCl, 1 mM $MgCl_2$, and 25% sucrose]. Finally, 150 μL of a 0% sucrose buffer [100 mM Tris-HCl pH 7.4, 200 mM NaCl, and 1 mM $MgCl_2$] was added as the top layer. The solution was incubated for 15 min at 22°C before being centrifuged at 70,000 rpm at 22°C for 20 min (TLA120.2 rotor, Optima Max-E Benchtop Ultracentrifuge). After centrifugation, three equal fractions (200 μL each) were gently drawn sequentially from the bottom of the ultracentrifugation tube using a Hamilton syringe. SDS-PAGE sample buffer was added to each

Please cite this article in press as: Jalal et al., CTP regulates membrane-binding activity of the nucleoid occlusion protein Noc, Molecular Cell (2021), https://doi.org/10.1016/j.molcel.2021.06.025

fraction, and samples were heated at 70°C for 5 min before being loaded onto either 12% WedgeWell Tris-Glycine polyacrylamide gels or 1% agarose gels. Gels were subsequently stained in an InstantBlue Coomassie solution (to detect protein bands) or in a Sybr Green solution (to detect DNA bands). Each assay was triplicated. Protein/DNA band intensity was quantified using Image Studio Lite (LI-COR Biosciences). The protein/DNA fractions were averaged, and their standard errors were calculated in Excel.

Protein crystallization, structure determination, and refinement

Crystallization screens were set up in sitting-drop vapor diffusion format in MRC2 96-well crystallization plates with drops comprised of 0.3 μL precipitant solution and 0.3 μL of protein and incubated at 293 K. After optimization of initial hits, suitable crystals were cryoprotected and mounted in Litholoops (Molecular Dimensions) before flash-cooling by plunging into liquid nitrogen. X-ray data were recorded either on beamline I04 or I04-1 at the Diamond Light Source (Oxfordshire, UK) using either an Eiger2 XE 16M or a Pilatus 6M-F hybrid photon counting detector (Dectris), with crystals maintained at 100 K by a Cryojet cryocooler (Oxford Instruments). Diffraction data were integrated and scaled using DIALS (Winter et al., 2018) via the XIA2 expert system (Winter, 2010) then merged using AIMLESS (Evans and Murshudov, 2013). Data collection statistics are summarized in Table S3. The majority of the downstream analysis was performed through the CCP4i2 graphical user interface (Potterton et al., 2018).

Geobacillus thermoleovorans NocΔCTD

His-tagged NocΔCTD Noc (~10 mg/mL) was premixed with 1 mM CTP and 1 mM $MgCl_2$ in buffer [10 mM Tris-HCl pH 8.0 and 250 mM NaCl] before crystallization. Crystals grew in a solution containing 2.0 M ammonium sulfate and 50 mM tri-sodium citrate, and were cryoprotected in the crystallization solution supplemented with 20% (v/v) glycerol, 1 mM CTP and 1 mM $MgCl_2$. For iodide derivatization, the cryoprotectant comprised the crystallization solution supplemented with 25% (v/v) ethylene glycol, 1 mM CTP, 1 mM $MgCl_2$, and 500 mM potassium iodide; crystals were soaked in this solution for less than 30 s before cryo-cooling. Three 360° passes of X-ray data were taken at a wavelength of 1.8 Å from different parts of a single crystal and merged to give a highly redundant dataset to 3.4 Å resolution in space group $P2_13$ with cell parameters $a = b = c = 136.6$ Å. Solvent content estimation gave a value of 66% for two copies of the 29 kDa subunit per asymmetric unit (ASU). The structure was subsequently solved by single-wavelength anomalous dispersion using the CRANK2 pipeline (Skubák and Pannu, 2013), which located 12 iodide sites, and BUCCANEER (Cowtan, 2006) was able to build and sequence 339 residues in two chains corresponding to 67% of those expected for two monomers, giving R_{work} and R_{free} values of 0.318 and 0.362, respectively, to 3.4 Å resolution after refinement with REFMAC5 (Murshudov et al., 1997). At this point, this preliminary model was used as a starting point for refinement against a native dataset processed to 2.5 Å resolution in the same space group, but with a significantly longer cell edge of 146.8 Å corresponding to a solvent content of 72.6%. Thus, it was necessary to resolve the structure by molecular replacement using PHASER (McCoy et al., 2007) before further refinement in REFMAC5. After a complete rebuild in BUCCANEER, several iterations of model building in COOT (Emsley and Cowtan, 2004) and REFMAC5 refinement jobs yielded the final model with R_{work} and R_{free} values of 0.210 and 0.240, respectively, to 2.5 Å resolution.

Despite the presence of CTP in the crystallization buffer, no density for CTP was found in the NocΔCTD structure, presumably because *NBS* DNA was not included to facilitate CTP-binding, or the high concentrations of sulfate (2M) from the precipitant excluded the ligand.

Geobacillus thermoleovorans NocNΔ26ΔCTD

His-tagged NocNΔ26ΔCTD Noc (~10 mg/mL) was premixed with 1 mM CTPγS and 1 mM $MgCl_2$ in buffer [10 mM Tris-HCl pH 8.0 and 250 mM NaCl] before crystallization. Crystals grew in a solution containing 0.2 M di-ammonium phosphate and 2.3 M ammonium sulfate and were cryoprotected in this solution supplemented with 20% (v/v) glycerol. X-ray data were processed to a resolution of 2.95 Å in space group $C222_1$ with cell parameters of $a = 105.1$, $b = 106.6$, $c = 42.2$ Å. Analysis of the likely composition of the ASU suggested that it contained a single copy of the 26 kDa NocNΔ26ΔCTD Noc monomer, giving an estimated solvent content of 46%. The structure was solved by molecular replacement with PHASER (McCoy et al., 2007) using chain A from the *G. thermoleovorans* NocΔCTD structure above as the template. The search model was split into three separate ensembles comprising residues 26-100, 101-140, and 141-230, respectively. PHASER successfully placed all three ensembles, although one of these had to be interchanged with a symmetry mate to restore the connectivity of the starting template. Several iterations of model building in COOT and refinement REFMAC5 yielded the final model with R_{work} and R_{free} values of 0.267 and 0.288, respectively, to 2.95 Å resolution.

Fluorescence microscopy

Cells containing fluorescent protein fusions were grown at 30°C. Xylose (0.5% w/v) was included in the media to induce the expression of YFP fusions in *B. subtilis*. Cell membranes were stained by mixing 15 μL of culture with 0.5 μL of membrane dye FM5-95 (200 μg/ml, Invitrogen). Cells were mounted on microscope slides covered with a thin agarose pad (1.2% w/v in dH_2O) and images were acquired with a Rolera EM-C2 (Q-imaging) camera attached to a Nikon Ti microscope using METAMORPH version 6 (Molecular Devices), with an exposure time of 400 ms for YFP and 1000 ms for membranes. Images were prepared for publication using ImageJ.

QUANTIFICATION AND STATISTICAL ANALYSIS

Information about statistical analysis and sample size for each experiment are detailed in the relevant STAR Methods sections.

Molecular Cell, Volume *81*

Supplemental information

CTP regulates membrane-binding activity of the nucleoid occlusion protein Noc

Adam S.B. Jalal, Ngat T. Tran, Ling J. Wu, Karunakaran Ramakrishnan, Martin Rejzek, Giulia Gobbato, Clare E.M. Stevenson, David M. Lawson, Jeff Errington, and Tung B.K. Le

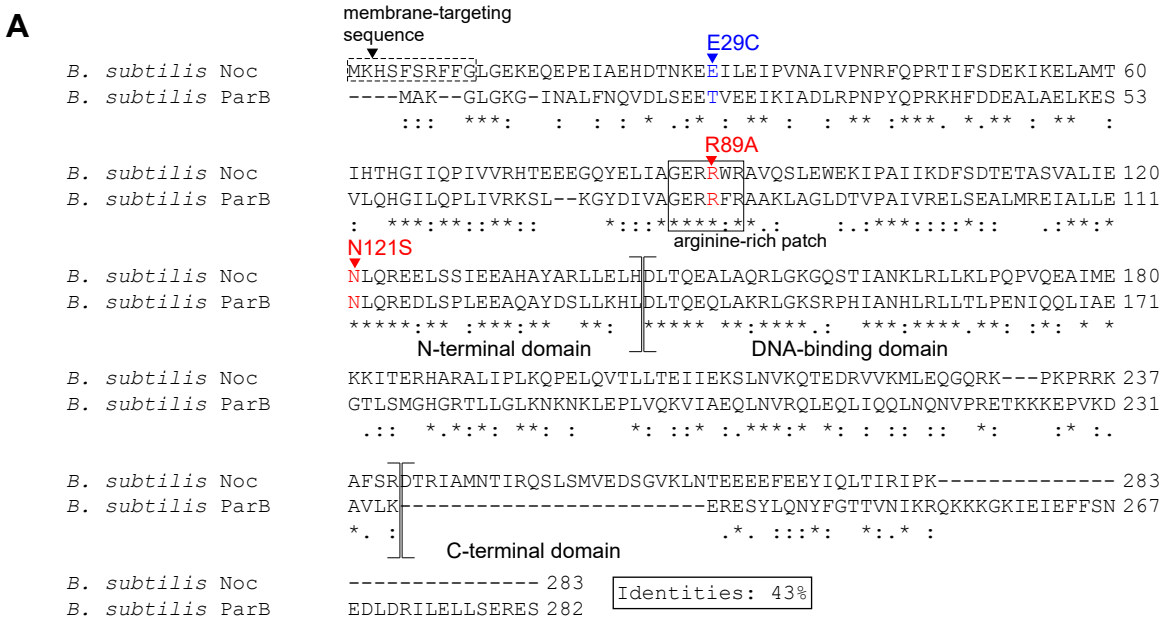

Figure S1. Interactions between Noc (WT and variants) and CTPγS or CDP, related to Figure 1. **(A)** A sequence alignment between *B. subtilis* Noc and its paralog ParB. Residues R89 (red) and N121 (red) in *B. subtilis* Noc, whose equivalent substitutions in *B. subtilis* ParB have been shown to impair spreading and CTP binding (Soh et al., 2019), were substituted by alanine and serine, respectively. Residue E29 (blue) was substituted by cysteine to generate a Noc (E29C) variant which was subsequently used in BMOE crosslinking assays (Figure 2A-D). An equivalent substitution T22C was previously used in BMOE crosslinking assays for in *B. subtilis* ParB (Soh et al., 2019). The conserved arginine-rich patch that mediates CTP binding in *B. subtilis* ParB is shown in a solid box. The 10-amino-acid membrane-targeting sequence of Noc is shown in a dashed box. *B. subtilis* ParB does not possess an equivalent membrane-targeting sequence. The positions of the N-terminal domain, the DNA-binding domain, and the C-terminal domain of Noc and ParB are also indicated on the sequence alignment. **(B)** Analysis of the interaction of *B. subtilis* Noc (WT and mutants) with CTPγS or CDP by isothermal calorimetry (ITC). ITC directly measures the heat released or absorbed during a biomolecular binding event. The large heat exchange from Noc-*NBS* DNA binding (nM binding affinity (Jalal et al., 2020b)) might mask the weaker heat signal from Noc-CTPγS/CDP binding, therefore *NBS* DNA was not included in these ITC experiments. Each experiment was duplicated. Regression curves were fitted, and binding affinities (K_d) are shown.

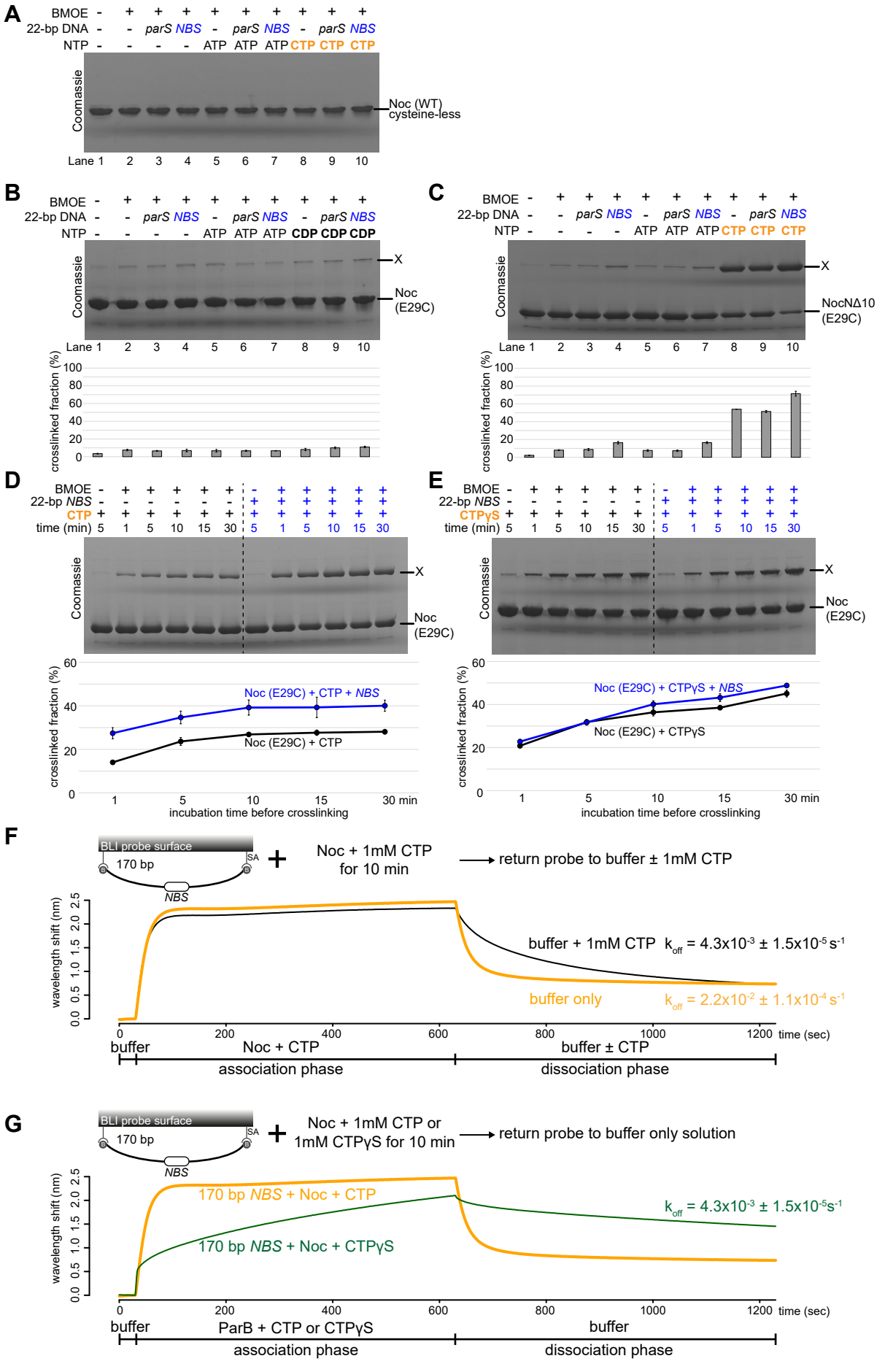

Figure legend (next page)

Figure S2. CTP and CTPγS, but not other nucleotides, promote the engagement of the N-terminal domain of Noc, related to Figure 2. (A) SDS-PAGE analysis of BMOE crosslinking products of 10 μM *B. subtilis* Noc (WT) protein ± 1.0 μM 22-bp *parS*/*NBS* DNA ± 1.0 mM NTP. Wild-type Noc naturally lacks cysteine, hence does not crosslink in the presence of BMOE. All crosslinking reactions were performed at 22°C unless indicated otherwise. **(B)** Same as panel A but Noc (E29C) was used instead. X indicates a crosslinked form of Noc (E29C). Quantification of the crosslinked fraction is shown below each representative image. Error bars represent SEM from three replicates. **(C)** Same as panel A, but NocNΔ10 (E29C) was used instead. **(D)** Time-course of Noc (E29C) crosslinking with CTP in the presence or absence of 22-bp *NBS* DNA. Purified Noc (E29C) was preincubated with 1.0 mM CTP ± 1 μM 22-bp *NBS* DNA for 1, 5, 10, 15, or 30 min at 4°C (instead of the usual 22°C) before BMOE was added. A lower incubation temperature was needed to slow down the reaction. Quantification of the crosslinked fraction is shown below each representative image. Error bars represent SE from three replicates. **(E)** Same as panel D, but 1.0 mM CTPγS was used instead. **(F)** BLI analysis of the interaction between *B. subtilis* Noc-CTP and a 170-bp dual biotin-labeled *NBS* DNA. For the association phase, the interaction between a premix of 1.0 μM *B. subtilis* Noc ± 1.0 mM CTP and a 170-bp dual biotin-labeled *NBS* probe was monitored in real-time for 10 min. For the dissociation phase, the probe was returned to either a buffer-only solution or a buffer supplemented with 1mM CTP. The dissociation rate (k_{off}) of bound Noc into buffer is shown for each reaction. **(G)** BLI analysis of the interaction between *B. subtilis* Noc-CTP or Noc-CTPγS and a 170-bp dual biotin-labeled *NBS* DNA. For the association phase, the interaction between a premix of 1.0 μM *B. subtilis* Noc + 1.0 mM CTP or CTPγS and a 170-bp dual biotin-labeled *NBS* probe was monitored in real-time for 10 min. For the dissociation phase, the probe was returned to a buffer-only solution. The dissociation rate (k_{off}) of bound Noc into buffer is shown for each reaction. Each experiment was triplicated and a representative sensorgram was shown.

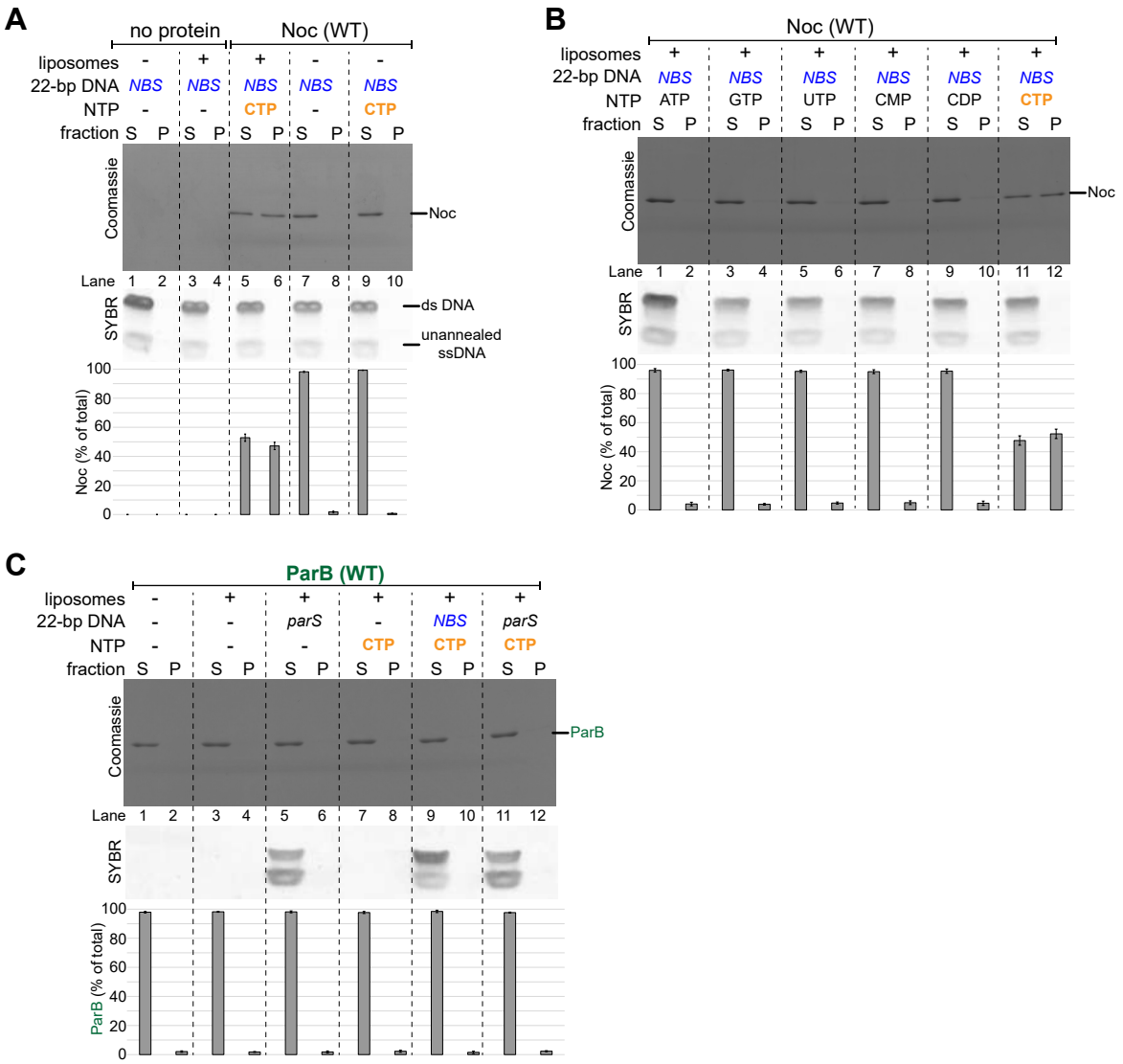

Figure S3. CTP and *NBS* DNA enable Noc binding to liposomes, related to Figure 3. (A) Analysis of *B. subtilis* Noc binding to membranes by a liposome co-sedimentation assay. A premix of 1.0 μM 22-bp linear *NBS* DNA ± 0.75 μM *B. subtilis* Noc protein ± 1.0 mM CTP ± 1.0 mg/mL liposomes was incubated at 22ºC before ultracentrifugation. The resulting supernatant (S) and pellet (P) fractions were analyzed by SDS-PAGE. Without Noc, 22-bp *NBS* DNA did not co-sediment on its own (lanes 1-2) or with liposomes (lanes 3-4). Samples were also loaded onto a 20% TBE PAGE, and the gel was subsequently stained with Sybr Green for DNA. Quantification of Noc in each fraction is shown below each representative image. Error bars represent SEM from three replicates. **(B)** CTP but no other nucleotide enables Noc to co-sediment with liposomes. A premix of 0.75 μM *B. subtilis* Noc protein + 1.0 μM 22-bp *NBS* DNA ± 1.0 mM NTP + 1.0 mg/mL liposomes was incubated at 22ºC for 5 min before ultracentrifugation. The resulting supernatant (S) and pellet (P) fractions were analyzed by SDS-PAGE. **(C)** *Caulobacter crescentus* ParB does not co-sediment with liposomes in any tested conditions. A premix of 0.75 μM *C. crescentus* ParB protein ± 1.0 μM 22-bp linear *parS*/*NBS* DNA ± 1.0 mM CTP ± 1.0 mg/mL liposomes was incubated at 22ºC for 5 min before ultracentrifugation. The resulting supernatant (S) and pellet (P) fractions were analyzed by SDS-PAGE.

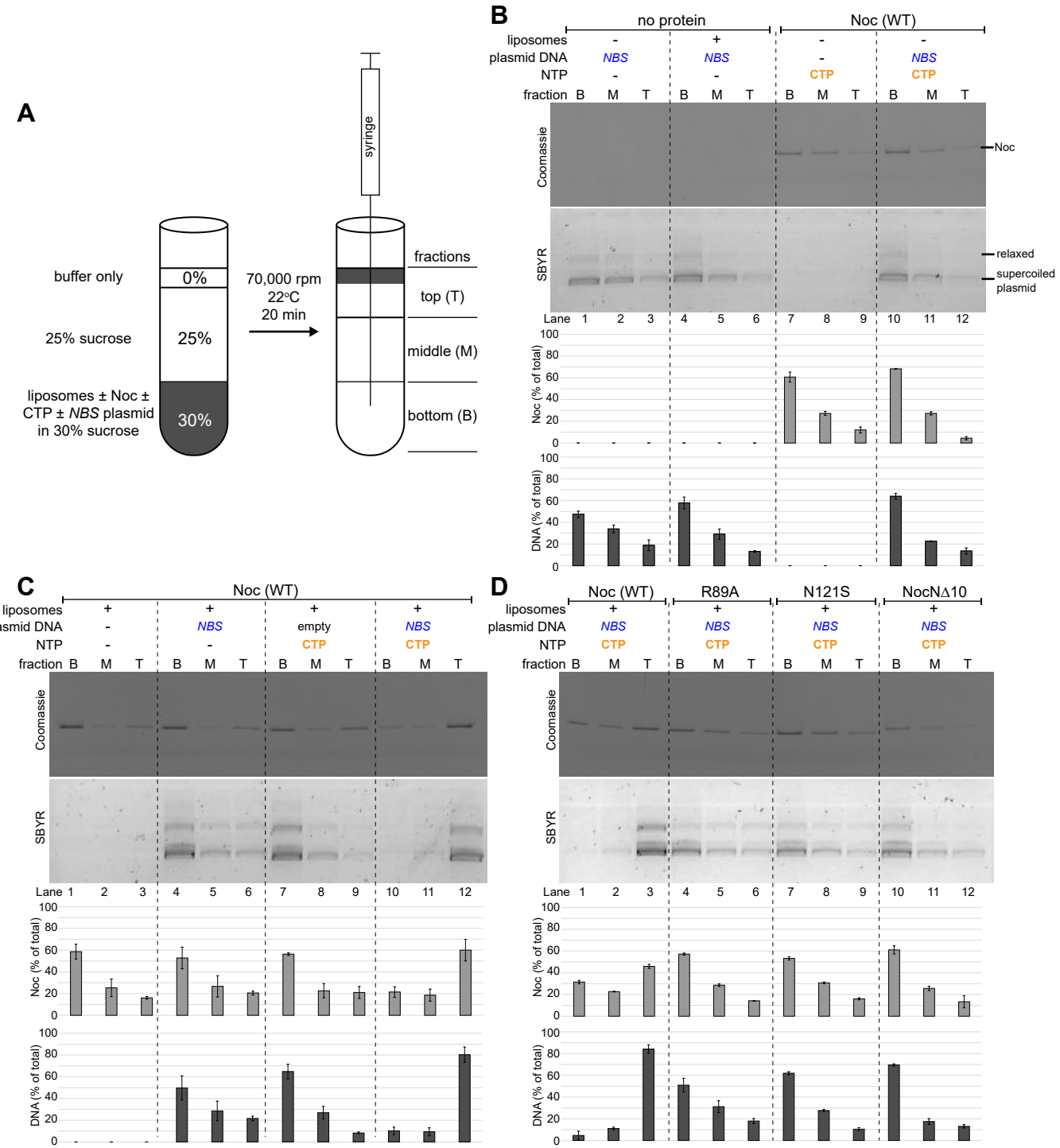

Figure legend (next page)

Figure S4. Liposome flotation assays show Noc can recruit *NBS* plasmid to the membrane in the presence of CTP, related to Figure 4. (A) The principle of a liposome flotation assay. Liposomes ± purified Noc ± CTP ± *NBS* plasmid were incubated in a 30% sucrose binding buffer. Buffer with 25% sucrose and 0% sucrose were subsequently layered on top sequentially. After ultracentrifugation, liposomes and associated protein/DNA migrate along the sucrose gradient i.e. floating to the uppermost fractions. Three equal fractions (bottom, middle, and top) were drawn out sequentially using a Hamilton syringe, and their protein and DNA contents were analyzed. **(B)** Control experiments: liposome flotation assays in which one component, either Noc protein, a 5-kb plasmid DNA, CTP, or liposomes, was omitted. **(C)** Analysis of *B. subtilis* Noc binding to membranes and the recruitment of plasmid DNA to membranes by a liposome flotation assay. A premix of 0.75 μM *B. subtilis* Noc ± 100 nM 5-kb plasmid DNA ± 1.0 mM CTP ± 1.0 mg/mL liposomes was incubated at 22^{o}C for 5 min before ultracentrifugation. Either an empty plasmid or an *NBS*-harboring plasmid was employed in this assay. The resulting fractions (Bottom B, Middle M, and Top T) were analyzed by SDS-PAGE. Samples were also loaded onto a 1% agarose gel and was subsequently stained with Sybr Green for DNA. Quantification of Noc or DNA in each fraction is shown below each representative image. Error bars represent SEM from three replicates. **(D)** Other Noc variants, Noc (R89A), Noc (N121S), and NocNΔ10, were also analyzed in a liposome flotation assay. A premix of 0.75 μM *B. subtilis* Noc protein (WT or mutants) + 100 nM *NBS* plasmid + 1.0 mM CTP + 1.0 mg/mL liposomes was ultracentrifuged, and the resulting fractions were analyzed for protein and DNA contents.

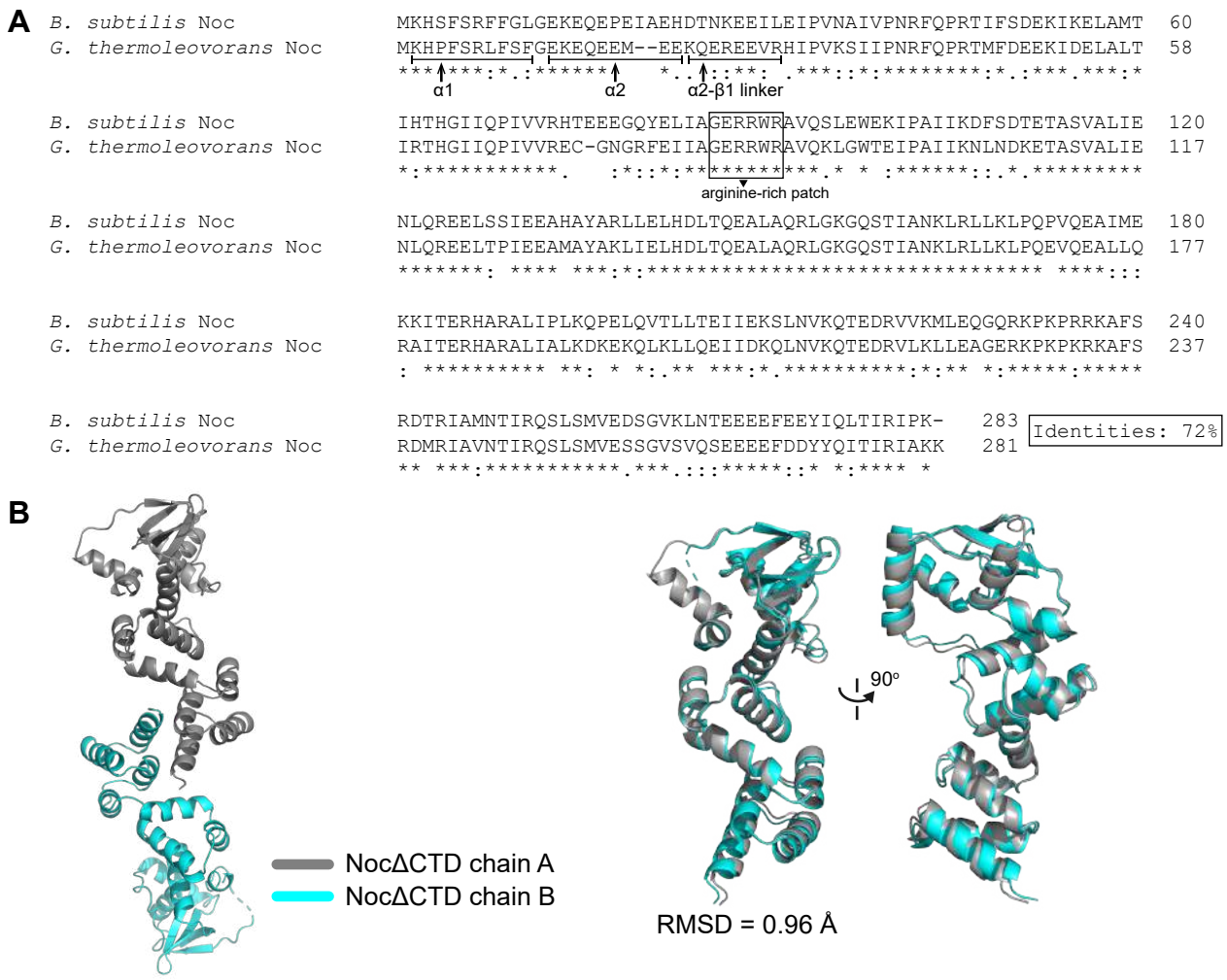

Figure S5. The composition of the asymmetric unit of *G. thermoleovorans* NocΔCTD crystal structure, related to Figure 5. (A) A sequence alignment between *B. subtilis* Noc and its homolog *G. thermoleovorans* Noc. The conserved arginine-rich patch that mediates CTP binding in *B. subtilis* ParB (Soh et al., 2019) is shown in the solid box. The sequences of helix α1, helix α2, and the α2-β1 connecting loop are also indicated on the sequence alignment. **(B)** The asymmetric unit of *G. thermoleovorans* NocΔCTD contains two copies of NocΔCTD monomers (left panel). Chains A and B are structurally similar, RMSD = 0.96 Å (right panel).

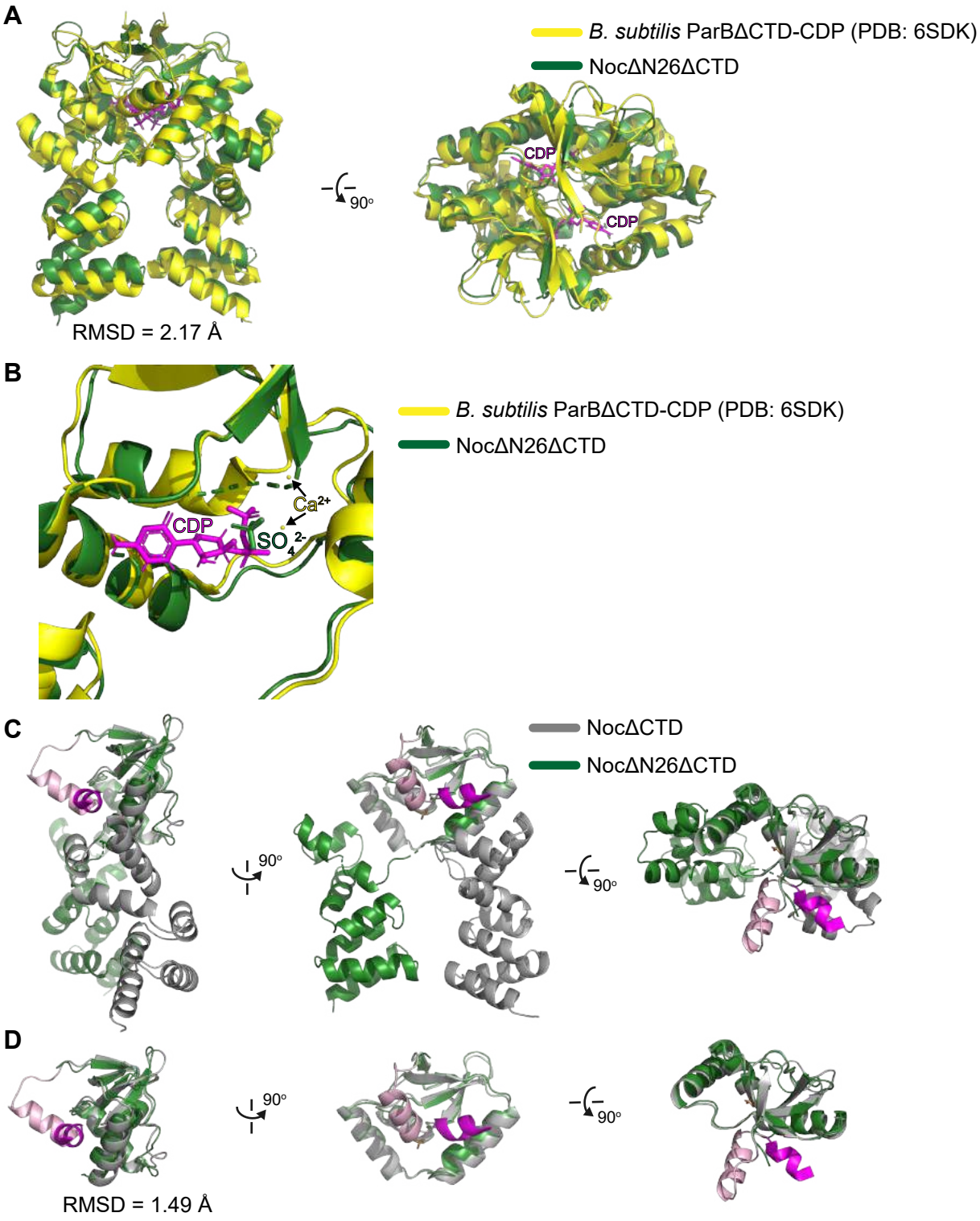

Figure S6. The conformation of *G. thermoleovorans* NocNΔ26ΔCTD is similar to that of a nucleotide-bound *B. subtilis* ParBΔCTD, related to Figure 6. (A) Superimposition between a *G. thermoleovorans* NocNΔ26ΔCTD dimer (green) and a *B. subtilis* ParBΔCTD-CDP dimer (yellow, PDB: 6SDK). CDP molecules are shown in magenta. **(B)** Magnification of the nucleotide-binding pocket of *B. subtilis* ParBΔCTD and *G. thermoleovorans* NocNΔ26ΔCTD. CDP and Ca^{2+} cations that belong to *B. subtilis* ParBΔCTD-CDP co-crystal structure are highlighted in magenta and yellow, respectively. In the *G. thermoleovorans* NocNΔ26ΔCTD structure, a sulfate ion (dark green) occupies a similar position to the β-phosphate group of CDP. **(C)** A superimposition at the N-terminal domains of a NocΔCTD monomer (grey) and a NocNΔ26ΔCTD monomer (green). The amphipathic helix α1 and helix α2 are shown in magenta and pink, respectively. **(D)** Same as panel B, but only the N-terminal domain (NTD) is shown for clarity.

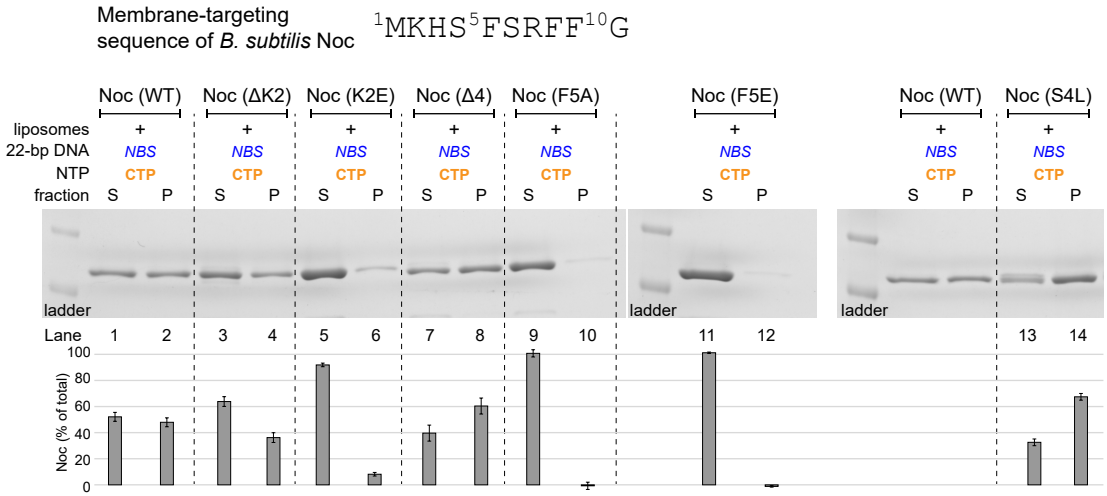

Figure S7. Effects of N-terminal substitutions and deletions on *B. subtilis* Noc-liposomes interaction, related to Figure 6. A premix of 1.0 μM 22-bp linear *NBS* DNA + 1.0 μM *B. subtilis* Noc protein (WT/mutants) + 1.0 mM CTP + 1.0 mg/mL liposomes was incubated at 22°C before ultracentrifugation. The resulting supernatant (S) and pellet (P) fractions were analyzed by SDS-PAGE. Quantification of Noc in each fraction is shown below each representative image. Error bars represent SEM from three replicates.

TABLE S1. Bacterial strains. Related to STAR Methods.

Strains	Description	Source
E. coli Rosetta (DE3)	F^- *ompT hsdS*$_B$(r_B^- m_B^-) *gal dcm* (DE3) pRARE (chloramphenicol^R)	Merck
DWA117	*B. subtilis* 168CA (*trpC2*) *Δnoc::tet*	(Adams et al., 2015)
DWA206	*B. subtilis* 168CA (*trpC2*) *Δnoc::tet ΩamyE::[spc Pxyl-noc (WT)-myfp]*	(Adams et al., 2015)
DWA382	*B. subtilis* 168CA (*trpC2*) *Δnoc::tet ΩamyE::[spc Pxyl-nocNΔ10-myfp]*	(Adams et al., 2015)
DWA546	*B. subtilis* 168CA (*trpC2*) *Δnoc::tet ΩamyE::[spc Pxyl-noc (R89A)-myfp]*	(Adams et al., 2015)
4746	*B. subtilis* 168CA (*trpC2*) *Δnoc::tet ΩamyE::[spc Pxyl-noc (N121S)-yfpmut1]*	This study
DWA564	*B. subtilis* 168CA (*trpC2*) *Δnoc::tet ΔminCD::kan ΩamyE::[spc Pxyl-noc (WT)-myfp]*	(Adams et al., 2015)
DWA566	*B. subtilis* 168CA (*trpC2*) *Δnoc::tet ΔminCD::kan ΩamyE::[spc Pxyl-nocNΔ10-myfp]*	(Adams et al., 2015)
DWA600	*B. subtilis* 168CA (*trpC2*) *Δnoc::tet ΔminCD::kan ΩamyE::[spc Pxyl-noc (R89A)-myfp]*	(Adams et al., 2015)
4747	*B. subtilis* 168CA (*trpC2*) *Δnoc::tet ΔminCD::kan ΩamyE::[spc Pxyl-noc (N121S)-yfpmut1]*	This study

TABLE S2. DNA, plasmids, and oligos. Related to STAR Methods.

Plasmids	Description	Source
pET21b::*Bacillus subtilis noc-his$_6$*	Overexpression of a C-terminally His$_6$-tagged *B. subtilis* Noc, carbenicillin^R	This study
pET21b::*Bacillus subtilis nocNΔ10-his$_6$*	Overexpression of a C-terminally His$_6$-tagged *B. subtilis* Noc that lacks the first 10 amino acids, carbenicillin^R	This study
pET21b::*Bacillus subtilis noc (R89A)-his$_6$*	Overexpression of a C-terminally His$_6$-tagged *B. subtilis* Noc (R89A), carbenicillin^R	This study
pET21b::*Bacillus subtilis noc (N121S)-his$_6$*	Overexpression of a C-terminally His$_6$-tagged *B. subtilis* Noc (N121S), carbenicillin^R	This study
pET21b::*Bacillus subtilis noc (E29C)-his$_6$*	Overexpression of a C-terminally His$_6$-tagged *B. subtilis* Noc (E29C), carbenicillin^R	This study
pET21b::*Bacillus subtilis noc (E29C R89A)-his$_6$*	Overexpression of a C-terminally His$_6$-tagged *B. subtilis* Noc (E29C R89A), carbenicillin^R	This study
pET21b::*Bacillus subtilis noc (E29C N121S)-his$_6$*	Overexpression of a C-terminally His$_6$-tagged *B. subtilis* Noc (E29C N121S), carbenicillin^R	This study
pET21b::*Bacillus subtilis noc ΔK2-his$_6$*	Overexpression of a C-terminally His$_6$-tagged *B. subtilis* Noc that lacks the lysine at position 2, carbenicillin^R	This study
pET21b::*Bacillus subtilis noc Δ4-his$_6$*	Overexpression of a C-terminally His$_6$-tagged *B. subtilis* Noc that lacks the first 4 amino acids, carbenicillin^R	This study
pET21b::*Bacillus subtilis noc (K2E)-his$_6$*	Overexpression of a C-terminally His$_6$-tagged *B. subtilis* Noc (K2E), carbenicillin^R	This study
pET21b::*Bacillus subtilis noc (S4L)-his$_6$*	Overexpression of a C-terminally His$_6$-tagged *B. subtilis* Noc (S4L), carbenicillin^R	This study
pET21b::*Bacillus subtilis noc (F5A)-his$_6$*	Overexpression of a C-terminally His$_6$-tagged *B. subtilis* Noc (F5A), carbenicillin^R	This study
pET21b::*Bacillus subtilis noc (F5E)-his$_6$*	Overexpression of a C-terminally His$_6$-tagged *B. subtilis* Noc (F5E), carbenicillin^R	This study
pET21b::*Bacillus subtilis nocNΔ10 (E29C)-his$_6$*	Overexpression of a C-terminally His$_6$-tagged *B. subtilis* Noc (E29C) variant that also lacks the first 10 amino acids, carbenicillin^R	This study
pET21b::*Geobacillus thermoleovorans NocΔCTD*	Overexpression of a C-terminally His$_6$-tagged *G. thermoleovorans* Noc that lacks the last 42 amino acids, carbenicillin^R	This study
pET21b::*Geobacillus thermoleovorans NocNΔ26ΔCTD*	Overexpression of a C-terminally His$_6$-tagged *G. thermoleovorans* Noc that lacks the first 26 amino acids and the last 42 amino acids, carbenicillin^R	This study
pMCS5-4x*NBS*	pMCS5 plasmid that harbors four *NBS* sites, tetracycline^R	This study

pMCS5::empty	pMCS5 plasmid with an intact multiple cloning site, tetracycline^R	(Thanbichler et al., 2007)
pET21b::*Caulobacter crescentus parB-his$_6$*	Overexpression of a C-terminally His$_6$-tagged *C. crescentus* ParB, carbenicillin^R	Gift from Christine Jacobs-Wagner (Lim et al., 2014)
pSG4926	*bla amyE' spc Pxyl-noc-yfpmut1 'amyE*; shuttle plasmid harboring a xylose-inducible *noc-yfp* fusion for integration at the *B. subtilis amyE* locus	(Wu et al., 2009)
pSG4926 N121S	*bla amyE' spc Pxyl-noc (N121S)-yfpmut1 'amyE*; *B. subtilis* plasmid harboring a xylose-inducible *noc (N121S)-yfp* fusion for integration at the *B. subtilis amyE* locus	This study
Oligos/gBlocks		
170bp-*parS*	CGCCAGGGTTTTCCCAGTCACGACGTTGTAAAACGAC GGCCAGAATTCGCAACGTGTGTTTCACGTGAAACAGC CTTGAACTGATAACGACTCTATCATTGATAGAGTGTTC TCTCCACG**GGATCC**CCAGGCATGCAAGCTTGGCGTAA TCATGGTCATAGCTGTTTCCT	(Jalal et al., 2020a)
170bp-*NBS*	CGCCAGGGTTTTCCCAGTCACGACGTTGTAAAACGAC GGCCAGAATTCGCAACGTGTATTTCCCGGGAAATAGC CTTGAACTGATAACGACTCTATCATTGATAGAGTGTTC TCTCCACG**GGATCC**CCAGGCATGCAAGCTTGGCGTAA TCATGGTCATAGCTGTTTCCT	This study
22bp-*parS*	GGATGTTTCACGTGAAACATCC	(Jalal et al., 2020b)
22bp-*NBS*	GGATATTTCCCGGGAAATATCC	This study
260bp-4x*NBS* gBlocks	GCCCAGGCCCTGGAGCGCATCTCCGGCTATTTCCCGG GAAATAACGTTCTTGGACGGGTCTTTTCGACCTTCTGT ATCGGCAAGTGATATTTCCCGGGAAATATCCCCAATAT TGTCCACAGGCCGCTCACAGCTGCGGTGGGGGTATTT CCCGGGAAATACCGATGAGTCACATCGACCCGCTCGC CTGATTGGCGTATAGATCTATTTCCCGGGAAATACTCG AACCCAGGGGCGTTCGCATTGAGGCGAGCGTCTTG	This study
AJ65	TAACTTTAAGAAGGAGATATACATATGTTGGGTGAAAA GGAGCAAGAACCG	This study
AJ66	GGTGGTGCTCGAGTGCGGCCGCAAGCTTTTTTGGAAT ACGGATTGTAAGCTG	This study
AJ73	CTGAACCGCGCGCCACGCGCGTTCTCCCGCAAT	This study
AJ74	ATTGCGGGAGAACGCGCGTGGCGCGCGGTTCAG	This study
AJ76	GGTGGTGCTCGAGTGCGGCCGCAAGCTTGTCGCGGG AAAAGGCTTTACGTTTAGG	This study
AJ81	TAACTTTAAGAAGGAGATATACATATGGAAGAGGTCCG TCACATCCCCGTCAAA	This study
AJ84	GATACCAATAAGGAATGCATTTTAGAAATTCCA	This study
AJ85	TGGAATTTCTAAAATGCATTCCTTATTGGTATC	This study
AJ86	GTGGCCTTAATTGAGTCTTTGCAACGCGAGGAG	This study
AJ87	CTCCTCGCGTTGCAAAGACTCAATTAAGGCCAC	This study
M13-F	CGCCAGGGTTTTCCCAGTCACGAC	Lab stock
M13-R	ATGGTCATAGCTGTTTCCT	Lab stock
Noc(N121S)-F	GTGGCGTTAATCGAAAGCTTGCAGCGGGAAGAA	This study
Noc(N121S)-R	TTCTTCCCGCTGCAAGCTTTCGATTAACGCCAC	This study

The sequences of *parS/NBS* are underlined. The sequence of BamHI recognition site is bold.

TABLE S3. X-ray data collection and processing statistics. Related to Figures 5 and 6.

Structure	***G. thermoleovorans* NocΔCTD - iodide**	***G. thermoleovorans* NocΔCTD - native**	***G. thermoleovorans* NocNΔ26ΔCTD**
Data collection			
Diamond Light Source beamline	I04	I04-1	I04
Wavelength (Å)	1.800	0.912	0.980
Detector	Eiger2 XE 16M	Pilatus 6M-F	Eiger2 XE 16M
Resolution range (Å)	96.61 – 3.40 (3.67 – 3.40)	84.89 – 2.50 (2.60 – 2.50)	37.44 – 2.95 (3.13 – 2.95)
Space Group	$P2_13$	$P2_13$	$C222_1$
Cell parameters (Å/°)	$a = b = c = 136.6$	$a = b = c = 146.8$	$a = 105.1$, $b = 106.6$, $c = 42.2$
Total no. of measured intensities	2147484 (426036)	1458851 (163435)	66966 (10641)
Unique reflections	11990 (2445)	36704 (4119)	5285 (835)
Multiplicity	179.1 (174.2)	39.7 (39.7)	12.6 (12.0)
Mean $I/\sigma(I)$	15.9 (3.3)	28.5 (1.8)	5.5 (1.5)
Completeness (%)	100.0 (100.0)	100.0 (100.0)	100.0 (100.0)
R_{merge}[a]	0.500 (3.392)	0.091 (2.654)	0.281 (1.343)
R_{meas}[b]	0.501 (3.402)	0.093 (2.688)	0.293 (1.399)
$CC_{½}$[c]	0.999 (0.894)	1.000 (0.670)	0.997 (0.885)
Wilson B value (Å^2)	88.7	68.0	38.2
Refinement			
Resolution range (Å)	-	84.89 – 2.50 (2.57 – 2.50)	37.44 – 2.95 (3.03 – 2.95)
Reflections: working/free[d]	-	34843/1794	4752/522
R_{work}[e]	-	0.210 (0.328)	0.267 (0.438)
R_{free}[e]	-	0.240 (0.386)	0.288 (0.443)
Ramachandran plot: favored/allowed/disallowed[f] (%)	-	98.1/1.9/0.0	98.0/2.0/0.0
R.m.s. bond distance deviation (Å)	-	0.010	0.007
R.m.s. bond angle deviation (°)	-	1.55	1.33
Mean B factors: protein/sulfate/water/ overall (Å^2)	-	85/118/71/86	74/70/0/74
PDB accession code		**7NFU**	**7NG0**

Values in parentheses are for the outer resolution shell.
[a] $R_{merge} = \sum_{hkl} \sum_i |I_i(hkl) - \langle I(hkl)\rangle| / \sum_{hkl} \sum_i I_i(hkl)$.
[b] $R_{meas} = \sum_{hkl} [N/(N-1)]^{1/2} \times \sum_i |I_i(hkl) - \langle I(hkl)\rangle| / \sum_{hkl} \sum_i I_i(hkl)$, where $I_i(hkl)$ is the ith observation of reflection hkl, $\langle I(hkl)\rangle$ is the weighted average intensity for all observations i of reflection hkl and N is the number of observations of reflection hkl.
[c] $CC_{½}$ is the correlation coefficient between symmetry equivalent intensities from random halves of the dataset.
[d] The dataset was split into "working" and "free" sets consisting of 95 and 5% of the data respectively. The free set was not used for refinement.
[e] The R-factors R_{work} and R_{free} are calculated as follows: $R = \sum(|F_{obs} - F_{calc}|)/\sum|F_{obs}|$, where F_{obs} and F_{calc} are the observed and calculated structure factor amplitudes, respectively.
[f] As calculated using MolProbity (Williams et al., 2018)